Published in Journals: Geosciences, Hydrology, IJERPH,
Remote Sensing and Water

Topic Reprint

Groundwater Pollution Control and Groundwater Management

Edited by
Yunhui Zhang, Qili Hu and Liting Hao

mdpi.com/topics

MDPI

Groundwater Pollution Control and Groundwater Management

Groundwater Pollution Control and Groundwater Management

Topic Editors

Yunhui Zhang
Qili Hu
Liting Hao

MDPI

Basel • Beijing • Wuhan • Barcelona • Belgrade • Novi Sad • Cluj • Manchester

Topic Editors

Yunhui Zhang
Faculty of Geosciences and Engineering
Southwest Jiaotong University
Chengdu
China

Qili Hu
School of Chemical and Environmental Engineering
Sichuan University of Science and Engineering
Zigong
China

Liting Hao
School of Environment and Energy Engineering
Beijing University of Civil Engineering and Architecture
Beijing
China

Editorial Office
MDPI AG
Grosspeteranlage 5
4052 Basel, Switzerland

This is a reprint of the Topic, published open access by the journals *Geosciences* (ISSN 2076-3263), *Hydrology* (ISSN 2306-5338), *International Journal of Environmental Research and Public Health* (ISSN 1660-4601), *Remote Sensing* (ISSN 2072-4292) and *Water* (ISSN 2073-4441), freely accessible at: https://www.mdpi.com/topics/groundwater_pollution_management.

For citation purposes, cite each article independently as indicated on the article page online and as indicated below:

Lastname, A.A.; Lastname, B.B. Article Title. *Journal Name* **Year**, *Volume Number*, Page Range.

ISBN 978-3-7258-4635-1 (Hbk)
ISBN 978-3-7258-4636-8 (PDF)
https://doi.org/10.3390/books978-3-7258-4636-8

© 2025 by the authors. Articles in this book are Open Access and distributed under the Creative Commons Attribution (CC BY) license. The book as a whole is distributed by MDPI under the terms and conditions of the Creative Commons Attribution-NonCommercial-NoDerivs (CC BY-NC-ND) license (https://creativecommons.org/licenses/by-nc-nd/4.0/).

Contents

About the Editors . . . . . **ix**

Yunhui Zhang, Zhan Xie, Qili Hu and Liting Hao
Groundwater Pollution Control and Groundwater Management
Reprinted from: *Water* **2024**, *16*, 3542, https://doi.org/10.3390/w16233542 . . . . . **1**

Chaiyathat Imsamranrat and Adisorn Leelasantitham
Assessing Groundwater Resources Vulnerability with the New DRASTIC-LP: A Case Study in Chiang Mai Province, Thailand
Reprinted from: *Water* **2024**, *16*, 547, https://doi.org/10.3390/w16040547 . . . . . **9**

Livinia Saputra, Sang Hyun Kim, Kyung-Jin Lee, Seo Jin Ki, Ho Young Jo, Seunghak Lee and Jaeshik Chung
A Conceptual Framework for Modeling Spatiotemporal Dynamics of Diesel Attenuation Capacity: A Case Study across Namyangju, South Korea
Reprinted from: *Hydrology* **2024**, *11*, 19, https://doi.org/10.3390/hydrology11020019 . . . . . **48**

Julianna Martin and Jeff B. Langman
Leachate Experiments to Evaluate Weathering of Waste Rock for Backfill Aquifers in Restored Coal Mine Pits, Powder River Basin, USA
Reprinted from: *Geosciences* **2024**, *14*, 4, https://doi.org/10.3390/geosciences14010004 . . . . . **60**

Hu Yang, Xingcheng Yuan, Yongling Chen, Jiawei Liu, Chun Zhan, Guosen Lv, et al.
Geochemical Evidence Constraining Genesis and Mineral Scaling of the Yangbajing Geothermal Field, Southwestern China
Reprinted from: *Water* **2024**, *16*, 24, https://doi.org/10.3390/w16010024 . . . . . **77**

Thanh-Tuan Nguyen, Do-Gun Kim and Seok-Oh Ko
Transport of Oxygen-Doped Graphitic Carbon Nitride in Saturated Sand: Effects of Concentration, Grain Size, and Ionic Strength
Reprinted from: *Water* **2024**, *16*, 6, https://doi.org/10.3390/w16010006 . . . . . **97**

Zhongyou Yu, Rongwen Yao, Xun Huang and Yuting Yan
Health Risk Appraisal of Trace Elements in Groundwater in an Urban Area: A Case Study of Sichuan Basin, Southwest China
Reprinted from: *Water* **2023**, *15*, 4286, https://doi.org/10.3390/w15244286 . . . . . **108**

Geumhee Yun, Sunhwa Park, Young Kim and Kyungjin Han
Development of Slow-Releasing Tablets Combined with Persulfate and Ferrous Iron for In Situ Chemical Oxidation in Trichloroethylene-Contaminated Aquifers
Reprinted from: *Water* **2023**, *15*, 4103, https://doi.org/10.3390/w15234103 . . . . . **124**

Jiawei Liu, Chang Yang, Si Chen, Yangshuang Wang, Xingjun Zhang, Wulue Kang, et al.
Hydrochemical Appraisal and Driving Forces of Groundwater Quality and Potential Health Risks of Nitrate in Typical Agricultural Area of Southwestern China
Reprinted from: *Water* **2023**, *15*, 4095, https://doi.org/10.3390/w15234095 . . . . . **137**

Oumar Traoré, Dissinviel Stéphane Kpoda, René Dembélé, Courage Kosi Setsoafia Saba, Johannes Cairns, Nicolas Barro and Kaisa Haukka
Microbiological and Physicochemical Quality of Groundwater and Risk Factors for Its Pollution in Ouagadougou, Burkina Faso
Reprinted from: *Water* **2023**, *15*, 3734, https://doi.org/10.3390/w15213734 . . . . . **158**

Guosen Lv, Xu Zhang, Denghui Wei, Zhongyou Yu, Xingcheng Yuan, Minglu Sun, et al.
Water–Rock Interactions, Genesis Mechanism, and Mineral Scaling of Geothermal Waters in Northwestern Sichuan, SW China
Reprinted from: *Water* **2023**, *15*, 3730, https://doi.org/10.3390/w15213730 . . . . . **172**

Romeo Eftimi, Kastriot Shehu and Franko Sara
Hydrogeological Aspects of the Municipal Water Supply of Albania: Situation and Problems
Reprinted from: *Hydrology* **2023**, *10*, 193, https://doi.org/10.3390/hydrology10100193 . . . . . **195**

Xialin Zhang, Chengdong Deng, Tao Feng and Yunhui Zhang
Geochemical Investigations of the Geothermal Waters in the Kangding Area, SW China: Constraints from Hydrochemistry and D-O-T Isotopy
Reprinted from: *Water* **2023**, *15*, 2761, https://doi.org/10.3390/w15152761 . . . . . **215**

Yi Xiao, Jiahui Zhang, Aihua Long, Shiguang Xu, Tingting Guo, Xinchen Gu, et al.
Hydrochemical Characteristics and Formation Mechanism of Quaternary Groundwater in Baoshan Basin, Western Yunnan, China
Reprinted from: *Water* **2023**, *15*, 2736, https://doi.org/10.3390/w15152736 . . . . . **233**

Alessandra Feo, Federica Lo Medico, Pietro Rizzo, Maurizio Gasparo Morticelli, Riccardo Pinardi, Edoardo Rotigliano and Fulvio Celico
How to Predict the Efficacy of Free-Product DNAPL Pool Extraction Using 3D High-Precision Numerical Simulations: An Interdisciplinary Test Study in South-Western Sicily (Italy)
Reprinted from: *Hydrology* **2023**, *10*, 143, https://doi.org/10.3390/hydrology10070143 . . . . . **251**

Jeerapong Laonamsai, Veeraphat Pawana, Phupha Chipthamlong, Phornsuda Chomcheawchan, Kiattipong Kamdee, Bounhome Kimmany and Phongthorn Julphunthong
Groundwater Quality Variations in Multiple Aquifers: A Comprehensive Evaluation for Public Health and Agricultural Use
Reprinted from: *Geosciences* **2023**, *13*, 195, https://doi.org/10.3390/geosciences13070195 . . . . **271**

Mehaysen Al-Mahasneh, Abeer Al Bsoul, Nada Al-Ananzeh, Hussam Elddin Al-Khasawane, Marwan Al-Mahasneh and Raeda Tashtoush
The Characterization of Groundwater Quality for Safe Drinking Water Wells via Disinfection and Sterilization in Jordan: A Case Study
Reprinted from: *Hydrology* **2023**, *10*, 135, https://doi.org/10.3390/hydrology10060135 . . . . . **293**

Sonia Torres-Rivera, José Ramón Torres-Hernández, Simón Eduardo Carranco-Lozada, María Elena García-Arreola, Rubén Alfonso López-Doncel and Jesús Anibal Montenegro-Ríos
Anthropogenic Contamination in the Free Aquifer of the San Luis Potosí Valley
Reprinted from: *Int. J. Environ. Res. Public Health* **2023**, *20*, 6152,
https://doi.org/10.3390/ijerph20126152 . . . . . **313**

Ying Wang, Rui Li, Xiangchuan Wu, Yuting Yan, Changli Wei, Ming Luo, et al.
Evaluation of Groundwater Quality for Drinking and Irrigation Purposes Using GIS-Based IWQI, EWQI and HHR Model
Reprinted from: *Water* **2023**, *15*, 2233, https://doi.org/10.3390/w15122233 . . . . . **336**

Waleed Al-Zubari, Ali Al-Shaabani and Nadir Abdulhameid
Spatial Optimization of the Groundwater Quality Monitoring Network in the Kingdom of Bahrain
Reprinted from: *Water* **2023**, *15*, 2169, https://doi.org/10.3390/w15122169 . . . . . **365**

Riccardo Pinardi, Alessandra Feo, Andrea Ruffini and Fulvio Celico
Purpose-Designed Hydrogeological Maps for Wide Interconnected Surface–Groundwater Systems: The Test Example of Parma Alluvial Aquifer and Taro River Basin (Northern Italy)
Reprinted from: *Hydrology* **2023**, *10*, 127, https://doi.org/10.3390/hydrology10060127 . . . . . **379**

Hongwei Liu, Lin Gao, Chuanming Ma and Yi Yuan
Analysis of the Seawater Intrusion Process Based on Multiple Monitoring Methods: Study in the Southern Coastal Plain of Laizhou Bay, China
Reprinted from: *Water* **2023**, *15*, 2013, https://doi.org/10.3390/w15112013 . . . . . **392**

Christos Tzimopoulos, Nikiforos Samarinas, Basil Papadopoulos and Christos Evangelides
Fuzzy Analytical Solution of Horizontal Diffusion Equation into the Vadose Zone
Reprinted from: *Hydrology* **2023**, *10*, 107, https://doi.org/10.3390/hydrology10050107 . . . . . **411**

Ismail Mohsine, Ilias Kacimi, Shiny Abraham, Vincent Valles, Laurent Barbiero, Fabrice Dassonville, et al.
Exploring Multiscale Variability in Groundwater Quality: A Comparative Analysis of Spatial and Temporal Patterns via Clustering
Reprinted from: *Water* **2023**, *15*, 1603, https://doi.org/10.3390/w15081603 . . . . . **428**

Runchi Tang, Shuning Dong, Mengfei Zhang, Zhenfang Zhou, Chenghang Zhang, Pei Li and Mengtong Bai
Hydrochemical Characteristics and Water Quality of Shallow Groundwater in Desert Area of Kunyu City, Southern Margin of Tarim Basin, China
Reprinted from: *Water* **2023**, *15*, 1563, https://doi.org/10.3390/w15081563 . . . . . **444**

Ahmed Mohamed, Ahmed Asmoay, Saad S. Alarifi and Musaab A. A. Mohammed
Simulation of Surface and Subsurface Water Quality in Hyper-Arid Environments
Reprinted from: *Hydrology* **2023**, *10*, 86, https://doi.org/10.3390/hydrology10040086 . . . . . **461**

Francesco Chidichimo, Michele De Biase, Francesco Muto and Salvatore Straface
Modeling a Metamorphic Aquifer through a Hydro-Geophysical Approach: The Gap between Field Data and System Complexity
Reprinted from: *Hydrology* **2023**, *10*, 80, https://doi.org/10.3390/hydrology10040080 . . . . . **476**

Ada Vengust, Anja Koroša, Janko Urbanc and Nina Mali
Development of Groundwater Flow Models for the Integrated Management of the Alluvial Aquifer Systems of *Dravsko polje* and *Ptujsko polje*, Slovenia
Reprinted from: *Hydrology* **2023**, *10*, 68, https://doi.org/10.3390/hydrology10030068 . . . . . **492**

Xufeng Zhang, Liyu Du and Wenjuan Jin
Screening and Optimization of Conditions for the Adsorption of Cd^{2+} in Serpentine by Using Response Surface Methodology
Reprinted from: *Int. J. Environ. Res. Public Health* **2022**, *19*, 16848, https://doi.org/10.3390/ijerph192416848 . . . . . **512**

Xiao Yu, Xingcheng Yuan, Hongyang Guo, Yunhui Zhang, Huawen Cao, Tongming Luo, et al.
Coupling Hydrochemistry and Stable Isotopes (δ^2H, $\delta^{18}O$ and $^{87}Sr/^{86}Sr$) to Identify the Major Factors Affecting the Hydrochemical Process of Groundwater and Surface Water in the Lower Reaches of the Yarlung-Zangbo River, Southern Tibet, Southwestern China
Reprinted from: *Water* **2022**, *14*, 3906, https://doi.org/10.3390/w14233906 . . . . . **528**

Liting Hao, Lin Li, Bangyan Wang, Xinli Wang, Jinkai Shi, Chen Shi and Xiaodi Hao
Performance and Enhancement of Various Fillers Guiding Vanadium (V) Bioremediation
Reprinted from: *Int. J. Environ. Res. Public Health* **2022**, *19*, 14926, https://doi.org/10.3390/ijerph192214926 . . . . . **551**

Shuhui Yin, Yuan Tian, Linsheng Yang, Qiqian Wen and Binggan Wei
Dynamics of Spatiotemporal Variation of Groundwater Arsenic Due to Salt-Leaching Irrigation and Saline-Alkali Land
Reprinted from: *Remote Sens.* **2022**, *14*, 5586, https://doi.org/10.3390/rs14215586 . . . . . **562**

Fang Yuan, Jia Zhang, Jian Chen, Honghan Chen and Samuel Barnie
In Situ Pumping–Injection Remediation of Strong Acid–High Salt Groundwater: Displacement–Neutralization Mechanism and Influence of Pore Blocking
Reprinted from: *Water* **2022**, *14*, 2720, https://doi.org/10.3390/w14172720 . . . . . **580**

About the Editors

Yunhui Zhang

Yunhui Zhang , Ph.D., is an Associate Professor at Faculty of Geosciences and Engineering of Southwest Jaiotong University. He is a recipient of the National Natural Science Foundation of China and Scientific Key R&D project of Sichuan Province. Yunhui Zhang has participated in more than 10 scientific projects and has co-authored more than 100 papers. His current research interests include machine learning (AI) and numerical simulation assistance in the management of groundwater resources and the environment.

Qili Hu

Qili Hu graduated as a Doctor of Philosophy in Sustainable Environmental Studies from University of Tsukuba in 2019. He is currently a Lecturer and Master's Supervisor at School of Chemical and Environmental Engineering, Sichuan University of Science and Engineering, a member of Chinese Society for Environmental Sciences and Sichuan Western Returned Scholars Association, and a Youth Editorial Board Member of Chinese Chemical Letters. He was selected for the "High-Level Overseas Talent of Sichuan Province" in 2019 and recognized as one of the "World's Top 2% Scientists" in 2024. His research fields primarily focus on the development of environmental functional materials, industrial wastewater treatment, resource recovery and utilization, and adsorption technologies. He has led two provincial-/ministerial-level research projects, published over 50 academic papers, and held three authorized patents.

Liting Hao

Liting Hao, Ph.D., is an Associate Professor at School of Environment and Energy Engineering of Beijing University of Civil Engineering and Architecture. She is a recipient of the National Natural Science Foundation of China and Young Elite Scientists Sponsorship Program by BAST. Liting Hao has participated in more than 10 scientific projects and has co-authored more than 30 papers. Her current research interests include machine learning (AI)-assisted soil and groundwater pollution remediation, heavy metal biogeochemical processes, environmental remediation materials, risk assessment of emerging pollutants, biological wastewater treatment, and resource utilization.

water

MDPI

Editorial

Groundwater Pollution Control and Groundwater Management

Yunhui Zhang [1,2,3,4,*], Zhan Xie [1,2,3], Qili Hu [5] and Liting Hao [6]

[1] Faculty of Geosciences and Engineering, Southwest Jiaotong University, Chengdu 611756, China; xiez1001@163.com
[2] Sichuan Province Engineering Technology Research Center of Ecological Mitigation of Geohazards in Tibet Plateau Transportation Corridors, Chengdu 611756, China
[3] Yibin Research Institute, Southwest Jiaotong University, Yibin 644000, China
[4] State Key Laboratory of Nuclear Resources and Environment, East China University of Technology, Nanchang 330013, China
[5] School of Chemical and Environmental Engineering, Sichuan University of Science & Engineering, Zigong 643000, China; huqili@suse.edu.cn
[6] School of Environment and Energy Engineering, Beijing University of Civil Engineering and Architecture, Beijing 100044, China; haoliting@bucea.edu.cn
* Correspondence: zhangyunhui@swjtu.edu.cn

1. Introduction

Groundwater, the water that resides beneath the Earth's surface, serves as a crucial resource for human consumption, agriculture, and industrial activities [1–3]. It is estimated that over two billion people globally rely on groundwater as their primary source of drinking water. This vital resource is significant for sustaining life and plays an integral role in the Earth's hydrological cycle [4–6]. Groundwater systems are inherently complex and dynamic, interacting with various environmental components, including soil, surface water, and ecosystems. Given the increasing demand for freshwater due to population growth and climate change, understanding the groundwater environment and its vulnerability to pollution has never been more critical [7–9]. This topic aims to delve into the intricacies of groundwater systems, the factors leading to their contamination, and the implications of pollution on health and the environment.

The contamination of groundwater has emerged as a pressing global concern, with numerous studies highlighting its diverse sources and the complex interactions contributing to its degradation [10–12]. Pollutants such as agricultural runoff, industrial discharges, untreated wastewater, and chemical products infiltrate the groundwater through various pathways [13–15]. These contaminants can significantly alter groundwater quality, posing threats to human health and the ecosystems that depend on this resource. For instance, the presence of heavy metals, nitrates, and pathogens in groundwater has been linked to severe health conditions that primarily affect vulnerable populations, further exacerbating social and economic inequalities [16]. Moreover, the infiltration of pollutants can lead to long-term environmental challenges, compromising the sustainability of freshwater resources and ecosystems.

In addition to understanding the sources and pathways of groundwater pollution, the impacts of anthropogenic activities on this vital resource must also be examined [17–19]. Urbanization and industrialization have increased the pressures on groundwater resources, often leading to overextraction and contamination [20–22]. The correlation between land use changes and groundwater quality illustrates the need for integrated water resource management practices that account for human activities. Effective groundwater management is essential to mitigate pollution and safeguard this invaluable resource. Furthermore, the adoption of best practices in agriculture and industry can significantly reduce the input of contaminants into groundwater systems [23–25]. Public awareness campaigns and community engagement are equally important in promoting the stewardship of groundwater resources and encouraging sustainable practices among users.

To effectively address groundwater pollution, interdisciplinary research and collaboration among scientists, policymakers, and local communities are crucial. This research paper will explore various case studies and scientific findings that elucidate the state of groundwater pollution and the efficacy of different management strategies [26–28]. By synthesizing the existing literature, analyzing field data, and highlighting successful remediation efforts, this study aims to contribute to the ongoing dialog surrounding groundwater sustainability. Ultimately, the goal is to provide a comprehensive understanding of the complexities of groundwater systems, the multifaceted nature of contamination, and the paths toward effective management and conservation efforts. As we navigate the challenges posed by climate change and increasing water demand, safeguarding our groundwater resources is imperative for ensuring a sustainable future for global populations. The topic "Groundwater Pollution Control and Groundwater Management", published in multiple MDPI journals (*Geosciences*, *Hydrology*, *International Journal of Environmental Research and Public Health*, *Remote Sensing*, and *Water*), aims to address these critical areas. With the publication of this Topic, we strive to explore the new knowledge of groundwater pollution control and groundwater management.

2. Findings Reported in the Topic

This Special Issue includes 32 research articles. These 32 papers can be clustered into three main topical groups: hydrochemical characteristics and water quality, groundwater resource management, and groundwater pollution remediation.

The topic of hydrochemical characteristics and water quality is discussed in the following articles: Yin et al. (2022) explored the spatiotemporal correlation of saline–alkali land and salt-leaching irrigation with groundwater in the Hetao Plain [contribution 1]. Yu et al. (2022) investigated the major factors affecting the hydrochemical process of groundwater and surface water in the lower reaches of the Yarlung-Zangbo River, southern Tibet [contribution 2]. Tang et al. (2023) analyzed the hydrochemical characteristics and water quality of shallow groundwater in the desert area of the southern margin of the Tarim Basin [contribution 3]. Mohamed et al. (2023) evaluated the drinking and irrigation qualities of groundwater and surface water in hyper-arid environments of Egypt [contribution 4]. Mohsine et al. (2023) explored multiscale variability in groundwater quality [contribution 5]. Wang et al. (2023) evaluated the suitability of groundwater quality for drinking and irrigation purposes in Suining city of southwestern China [contribution 6]. Al-Mahasneh et al. (2023) assessed the characterization of the quality and safety of groundwater in water wells in Jordan [contribution 7]. Torres-Rivera et al. (2023) investigated anthropogenic contamination by fecal coliform bacteria, total coliform, nitrate, and potentially toxic elements in the free aquifer of the San Luis Potosí Valley [contribution 8]. Laonamsai et al. (2023) analyzed groundwater quality variations in multiple aquifers [contribution 9]. Xiao et al. (2023) analyzed hydrochemical characteristics and the formation mechanism of Quaternary Groundwater in Baoshan Basin, Western Yunnan, China [contribution 10]. Traoré et al. (2023) assessed the quality of urban groundwater in Ouagadougou for the first time [contribution 11]. Liu et al. (2023) explored the hydrochemical processes and conducted a quality assessment of groundwater [contribution 12]. Yu et al. (2023) analyzed trace element pollution levels and the non-carcinogenic and carcinogenic risks posed by groundwater resources in Sichuan Basin, SW China [contribution 13].

The contributions focusing on water resource management are as follows: Zhang et al. (2023) clarified the genetic mechanism of geothermal waters in Kangding area, SW China [contribution 14]. Lv et al. (2023) analyzed the water–rock interactions, genesis mechanism, and mineral scaling of geothermal waters in Northwestern Sichuan, SW China [contribution 15]. Vengust et al. (2023) used a comprehensive approach to conceptualize and identify the functioning of two connected aquifer systems in northeastern Slovenia [contribution 16]. Chidichimo et al. (2023) provided a geological–structural and hydrogeological numerical modeling of a metamorphic aquifer in a large area of the Sila Piccola in Calabria [contribution 17]. Tzimopoulos et al. (2023) used a fuzzy analytical solution of

the horizontal diffusion equation to analyze the vadose zone [contribution 18]. Liu et al. (2023) analyzed the seawater intrusion process in coastal areas [contribution 19]. Pinardi et al. (2023) investigated the hydraulic interconnections and built a hydrogeological map for the Parma Alluvial Aquifer and Taro River Basin (Northern Italy) [contribution 20]. Al-Zubari et al. (2023) evaluated the existing monitoring network of groundwater quality using the geostatistical method of kriging [contribution 21]. Eftimi et al. (2023) analyzed and classified the hydrogeological aspects of the sources of the water supply for the settlements of Albania [contribution 22]. Martin and Langman (2023) evaluated the weathering of waste rock for backfill aquifers in Restored Coal Mine Pits, Powder River Basin, USA [contribution 23]. Saputra et al. (2024) constructed a conceptual framework for modeling the spatiotemporal dynamics of diesel attenuation capacity [contribution 24]. Imsamranrat and Leelasantitham (2024) assessed the vulnerability of groundwater resources using the new DRASTIC-LP in Chiang Mai Province, Thailand [contribution 25]. Yang et al. (2024) analyzed the genesis and mineral scaling of the Yangbajing Geothermal Field, Southwestern China [contribution 26].

Studies focusing on the remediation of groundwater pollution are presented as follows: Hao et al. (2022) conducted V(V) remediation processes using various kinds of auxiliary fillers' agricultural biomass and microbial enhancements [contribution 27]. Yuan et al. (2022) used in situ pumping–injection to remediate strong-acid–high-salt groundwater and achieved optimization [contribution 28]. Zhang et al. (2022) explored the optimal conditions for the adsorption of Cd^{2+} in serpentine by using response surface methodology [contribution 29]. Feo et al. (2023) conducted a series of simulations of free-product DNAPL extraction [contribution 30]. Yun et al. (2023) conducted an in situ groundwater remediation process using a tablet-based, slow-release oxidizer to manage hazardous contaminants in urban areas [contribution 31]. Nguyen et al. (2023) investigated the characteristics and transport of oxygen-doped graphitic carbon nitride (OgCN) and evaluated the transport of OgCN under various conditions [contribution 32].

3. Future Directions

As we look to the future of groundwater management and pollution mitigation, it is imperative to adopt a multifaceted approach that encompasses technological innovation, policy reform, and community engagement [29–31]. Groundwater resources are under increasing pressure from population growth, industrial activities, and climate change, necessitating the development of advanced strategies for monitoring and protection. One promising direction is the integration of cutting-edge technologies such as remote sensing, machine learning, and Internet of Things sensors [32–34]. These tools can enhance our ability to track groundwater levels and quality in real-time, providing invaluable data for decision-makers. By leveraging big data analytics, researchers can identify patterns in groundwater depletion and contamination, allowing for more proactive management strategies. Future studies should focus on refining these technologies, making them more accessible and cost-effective to allow for their widespread application in both urban and rural settings.

Another critical area for future research is the intersection of groundwater management and climate change [35–37]. The impacts of climate variability on hydrological cycles are profound, influencing groundwater recharge rates and pollution dynamics. As extreme weather events become more frequent, understanding these interactions will be vital for developing resilient groundwater systems. Future studies should emphasize the need for adaptive management frameworks that incorporate climate projections into groundwater resource planning. This could involve creating hydrological models that simulate various climate scenarios, enabling stakeholders to anticipate changes and implement mitigation strategies effectively. Furthermore, interdisciplinary research that combines hydrology, ecology, and social science will be essential to address the complex challenges posed by climate change regarding groundwater systems.

In addition to technological and climate-related advancements, the governance of groundwater resources requires urgent attention [38–40]. Effective governance frameworks are essential for ensuring equitable access to groundwater and the sustainable use of groundwater, as well as to protect against pollution. Future research directions should explore collaborative governance models that involve multiple stakeholders, including government agencies, local communities, and private sector entities. Engaging these groups in decision-making processes can lead to more inclusive policies that reflect the diverse needs and values of different user groups. Research should also assess existing legal frameworks governing groundwater use and pollution, identifying gaps and proposing reforms that could enhance accountability and enforcement. By fostering a sense of shared responsibility among stakeholders, we can create more resilient and sustainable groundwater management systems.

Lastly, public awareness and education are crucial for the long-term success of groundwater management initiatives [41–43]. Many communities remain unaware of the critical role groundwater plays in their daily lives and the potential threats it faces from pollution and overextraction. Future efforts should prioritize educational programs that inform the public about groundwater issues, promoting stewardship and responsible usage practices. These could include community workshops, school programs, and outreach campaigns that highlight the importance of groundwater conservation. Additionally, involving local communities in monitoring and management efforts can empower individuals to take action in protecting their water resources. By fostering a culture of awareness and engagement, we can build a stronger collective commitment to safeguarding groundwater for future generations.

In conclusion, the future of groundwater management and pollution mitigation hinges on our ability to innovate, collaborate, and educate. By harnessing advanced technologies, addressing the impacts of climate change, reforming governance structures, and enhancing public awareness, we can develop a comprehensive framework that ensures the sustainable use of groundwater resources. As we move forward, it is essential to remain adaptable and responsive to emerging challenges, prioritizing holistic approaches that integrate scientific research, community involvement, and effective policymaking. Through these concerted efforts, we can secure the health and longevity of our vital groundwater systems.

Author Contributions: Conceptualization, Y.Z., L.H. and Q.H.; investigation, Y.Z., L.H. and Q.H.; writing—original draft preparation, Y.Z.; writing—review and editing, Q.H.; project administration, Y.Z., L.H. and Q.H.; data curation, Z.X.; funding acquisition, Y.Z., L.H. and Q.H. All authors have read and agreed to the published version of the manuscript.

Funding: Financial support has been received from the National Natural Science Foundation of China (42102334, 42072313, and 51908021), Sichuan Science and Technology Program (No. 2023YFS0356, 2024NSFSC0888), Open funding of State Key Laboratory of Nuclear Resources and Environment (East China University of Technology) (No. 2022NRE06) and Young Elite Scientists Sponsorship Program by BAST (No. BYESS2023129).

Data Availability Statement: Not applicable.

Conflicts of Interest: The authors declare no conflicts of interest.

List of Contributions:

1. Yin, S.; Tian, Y.; Yang, L.; Wen, Q.; Wei, B. Dynamics of Spatiotemporal Variation of Groundwater Arsenic Due to Salt-Leaching Irrigation and Saline-Alkali Land. *Remote Sens.* **2022**, *14*, 5586.
2. Yu, X.; Yuan, X.; Guo, H.; Zhang, Y.; Cao, H.; Luo, T.; Gong, Z.; Huang, H. Coupling Hydrochemistry and Stable Isotopes (δ^2H, δ^{18}O and ^{87}Sr/^{86}Sr) to Identify the Major Factors Affecting the Hydrochemical Process of Groundwater and Surface Water in the Lower Reaches of the Yarlung-Zangbo River, Southern Tibet, Southwestern China. *Water* **2022**, *14*, 3906.
3. Tang, R.; Dong, S.; Zhang, M.; Zhou, Z.; Zhang, C.; Li, P.; Bai, M. Hydrochemical Characteristics and Water Quality of Shallow Groundwater in Desert Area of Kunyu City, Southern Margin of Tarim Basin, China. *Water* **2023**, *15*, 1563.

4. Mohamed, A.; Asmoay, A.; Alarifi, S.S.; Mohammed, M.A.A. Simulation of Surface and Subsurface Water Quality in Hyper-Arid Environments. *Hydrology* **2023**, *10*, 86.
5. Mohsine, I.; Kacimi, I.; Abraham, S.; Valles, V.; Barbiero, L.; Dassonville, F.; Bahaj, T.; Kassou, N.; Touiouine, A.; Jabrane, M.; et al. Exploring Multiscale Variability in Groundwater Quality: A Comparative Analysis of Spatial and Temporal Patterns via Clustering. *Water* **2023**, *15*, 1603.
6. Wang, Y.; Li, R.; Wu, X.; Yan, Y.; Wei, C.; Luo, M.; Xiao, Y.; Zhang, Y. Evaluation of Groundwater Quality for Drinking and Irrigation Purposes Using GIS-Based IWQI, EWQI and HHR Model. *Water* **2023**, *15*, 2233.
7. Al-Mahasneh, M.; Al Bsoul, A.; Al-Ananzeh, N.; Al-Khasawane, H.E.; Al-Mahasneh, M.; Tashtoush, R. The Characterization of Groundwater Quality for Safe Drinking Water Wells via Disinfection and Sterilization in Jordan: A Case Study. *Hydrology* **2023**, *10*, 135.
8. Torres-Rivera, S.; Torres-Hernández, J.R.; Carranco-Lozada, S.E.; García-Arreola, M.E.; López-Doncel, R.A.; Montenegro-Ríos, J.A. Anthropogenic Contamination in the Free Aquifer of the San Luis Potosí Valley. *Int. J. Environ. Res. Public Health* **2023**, *20*, 6152.
9. Laonamsai, J.; Pawana, V.; Chipthamlong, P.; Chomcheawchan, P.; Kamdee, K.; Kimmany, B.; Julphunthong, P. Groundwater Quality Variations in Multiple Aquifers: A Comprehensive Evaluation for Public Health and Agricultural Use. *Geosciences* **2023**, *13*, 195.
10. Xiao, Y.; Zhang, J.; Long, A.; Xu, S.; Guo, T.; Gu, X.; Deng, X.; Zhang, P. Hydrochemical Characteristics and Formation Mechanism of Quaternary Groundwater in Baoshan Basin, Western Yunnan, China. *Water* **2023**, *15*, 2736.
11. Traoré, O.; Kpoda, D.S.; Dembélé, R.; Saba, C.K.S.; Cairns, J.; Barro, N.; Haukka, K. Microbiological and Physicochemical Quality of Groundwater and Risk Factors for Its Pollution in Ouagadougou, Burkina Faso. *Water* **2023**, *15*, 3734.
12. Liu, J.; Yang, C.; Chen, S.; Wang, Y.; Zhang, X.; Kang, W.; Li, J.; Wang, Y.; Hu, Q.; Yuan, X. Hydrochemical Appraisal and Driving Forces of Groundwater Quality and Potential Health Risks of Nitrate in Typical Agricultural Area of Southwestern China. *Water* **2023**, *15*, 4095.
13. Yu, Z.; Yao, R.; Huang, X.; Yan, Y. Health Risk Appraisal of Trace Elements in Groundwater in an Urban Area: A Case Study of Sichuan Basin, Southwest China. *Water* **2023**, *15*, 4286.
14. Zhang, X.; Deng, C.; Feng, T.; Zhang, Y. Geochemical Investigations of the Geothermal Waters in the Kangding Area, SW China: Constraints from Hydrochemistry and D-O-T Isotopy. *Water* **2023**, *15*, 2761.
15. Lv, G.; Zhang, X.; Wei, D.; Yu, Z.; Yuan, X.; Sun, M.; Kong, X.; Zhang, Y. Water–Rock Interactions, Genesis Mechanism, and Mineral Scaling of Geothermal Waters in Northwestern Sichuan, SW China. *Water* **2023**, *15*, 3730.
16. Vengust, A.; Koroša, A.; Urbanc, J.; Mali, N. Development of Groundwater Flow Models for the Integrated Management of the Alluvial Aquifer Systems of Dravsko polje and Ptujsko polje, Slovenia. *Hydrology* **2023**, *10*, 68.
17. Chidichimo, F.; De Biase, M.; Muto, F.; Straface, S. Modeling a Metamorphic Aquifer through a Hydro-Geophysical Approach: The Gap between Field Data and System Complexity. *Hydrology* **2023**, *10*, 80.
18. Tzimopoulos, C.; Samarinas, N.; Papadopoulos, B.; Evangelides, C. Fuzzy Analytical Solution of Horizontal Diffusion Equation into the Vadose Zone. *Hydrology* **2023**, *10*, 107.
19. Liu, H.; Gao, L.; Ma, C.; Yuan, Y. Analysis of the Seawater Intrusion Process Based on Multiple Monitoring Methods: Study in the Southern Coastal Plain of Laizhou Bay, China. *Water* **2023**, *15*, 2013.
20. Pinardi, R.; Feo, A.; Ruffini, A.; Celico, F. Purpose-Designed Hydrogeological Maps for Wide Interconnected Surface–Groundwater Systems: The Test Example of Parma Alluvial Aquifer and Taro River Basin (Northern Italy). *Hydrology* **2023**, *10*, 127.
21. Al-Zubari, W.; Al-Shaabani, A.; Abdulhameid, N. Spatial Optimization of the Groundwater Quality Monitoring Network in the Kingdom of Bahrain. *Water* **2023**, *15*, 2169.
22. Eftimi, R.; Shehu, K.; Sara, F. Hydrogeological Aspects of the Municipal Water Supply of Albania: Situation and Problems. *Hydrology* **2023**, *10*, 193.
23. Martin, J.; Langman, J.B. Leachate Experiments to Evaluate Weathering of Waste Rock for Backfill Aquifers in Restored Coal Mine Pits, Powder River Basin, USA. *Geosciences* **2024**, *14*, 4.
24. Saputra, L.; Kim, S.H.; Lee, K.-J.; Ki, S.J.; Jo, H.Y.; Lee, S.; Chung, J. A Conceptual Framework for Modeling Spatiotemporal Dynamics of Diesel Attenuation Capacity: A Case Study across Namyangju, South Korea. *Hydrology* **2024**, *11*, 19.

25. Imsamranrat, C.; Leelasantitham, A. Assessing Groundwater Resources Vulnerability with the New DRASTIC-LP: A Case Study in Chiang Mai Province, Thailand. *Water* **2024**, *16*, 547.
26. Yang, H.; Yuan, X.; Chen, Y.; Liu, J.; Zhan, C.; Lv, G.; Hu, J.; Sun, M.; Zhang, Y. Geochemical Evidence Constraining Genesis and Mineral Scaling of the Yangbajing Geothermal Field, Southwestern China. *Water* **2024**, *16*, 24.
27. Hao, L.; Li, L.; Wang, B.; Wang, X.; Shi, J.; Shi, C.; Hao, X. Performance and Enhancement of Various Fillers Guiding Vanadium (V) Bioremediation. *Int. J. Environ. Res. Public Health* **2022**, *19*, 14926.
28. Yuan, F.; Zhang, J.; Chen, J.; Chen, H.; Barnie, S. In Situ Pumping–Injection Remediation of Strong Acid–High Salt Groundwater: Displacement–Neutralization Mechanism and Influence of Pore Blocking. *Water* **2022**, *14*, 2720.
29. Zhang, X.; Du, L.; Jin, W. Screening and Optimization of Conditions for the Adsorption of Cd^{2+} in Serpentine by Using Response Surface Methodology. *Int. J. Environ. Res. Public Health* **2022**, *19*, 16848.
30. Feo, A.; Lo Medico, F.; Rizzo, P.; Morticelli, M.G.; Pinardi, R.; Rotigliano, E.; Celico, F. How to Predict the Efficacy of Free-Product DNAPL Pool Extraction Using 3D High-Precision Numerical Simulations: An Interdisciplinary Test Study in South-Western Sicily (Italy). *Hydrology* **2023**, *10*, 143.
31. Yun, G.; Park, S.; Kim, Y.; Han, K. Development of Slow-Releasing Tablets Combined with Persulfate and Ferrous Iron for In Situ Chemical Oxidation in Trichloroethylene-Contaminated Aquifers. *Water* **2023**, *15*, 4103.
32. Nguyen, T.-T.; Kim, D.-G.; Ko, S.-O. Transport of Oxygen-Doped Graphitic Carbon Nitride in Saturated Sand: Effects of Concentration, Grain Size, and Ionic Strength. *Water* **2024**, *16*, 6.

References

1. Zhan, Y.; Guo, Z.; Ruzzante, S.; Gleeson, T.; Andrews, C.B.; Babovic, V.; Zheng, C. Assessment of spatiotemporal risks for nationwide groundwater nitrate contamination. *Sci. Total Environ.* **2024**, *947*, 174508. [CrossRef]
2. Akurugu, B.A.; Obuobie, E.; Yidana, S.M.; Stisen, S.; Seidenfaden, I.K.; Chegbeleh, L.P. Groundwater resources assessment in the Densu Basin: A review. *J. Hydrol. Reg. Stud.* **2022**, *40*, 101017. [CrossRef]
3. Marin, M.; Clinciu, I.; Tudose, N.C.; Ungurean, C.; Adorjani, A.; Mihalache, A.L.; Davidescu, A.A.; Davidescu, S.O.; Dinca, L.; Cacovean, H. Assessing the vulnerability of water resources in the context of climate changes in a small forested watershed using SWAT: A review. *Environ. Res.* **2020**, *184*, 109330. [CrossRef]
4. Yu, X.; Zhang, Y.; Liu, P.; Huang, H.; Huang, X. Hydrochemical characteristics and D–O–Sr isotopes of groundwater and surface water in the northern Longzi county of southern Tibet (southwestern China). *Open Geosci.* **2022**, *14*, 111–119. [CrossRef]
5. Wang, Y.; Yuan, X.; Zhang, Y.; Zhang, X.; Xiao, Y.; Duo, J.; Huang, X.; Sun, M.; Lv, G. Hydrochemical, D–O–Sr isotopic and electromagnetic characteristics of geothermal waters from the Erdaoqiao area, SW China: Insights into genetic mechanism and scaling potential. *Ore Geol. Rev.* **2023**, *158*, 105486. [CrossRef]
6. Picetti, R.; Deeney, M.; Pastorino, S.; Miller, M.R.; Shah, A.; Leon, D.A.; Dangour, A.D.; Green, R. Nitrate and nitrite contamination in drinking water and cancer risk: A systematic review with meta-analysis. *Environ. Res.* **2022**, *210*, 112988. [CrossRef]
7. Luo, H.; Zhang, Y.; Liu, J.; Yang, S.; Wu, X.; Wang, Y. Hydrochemical appraisal and suitability for irrigation and portable purposes in eastern Himalayan syntaxis of Tibet Plateau. *Phys. Chem. Earth Parts A/B/C* **2024**, *136*, 103713. [CrossRef]
8. Zhang, Y.; Li, X.; Luo, M.; Wei, C.; Huang, X.; Xiao, Y.; Qin, L.; Pei, Q. Hydrochemistry and Entropy-Based Groundwater Quality Assessment in the Suining Area, Southwestern China. *J. Chem.* **2021**, *2021*, 5591892. [CrossRef]
9. Uddin, M.G.; Nash, S.; Olbert, A.I. A review of water quality index models and their use for assessing surface water quality. *Ecol. Indic.* **2021**, *122*, 107218. [CrossRef]
10. Zhang, Y.; Yan, Y.; Yao, R.; Wei, D.; Huang, X.; Luo, M.; Wei, C.; Chen, S.; Yang, C. Natural background levels, source apportionment and health risks of potentially toxic elements in groundwater of highly urbanized area. *Sci. Total Environ.* **2024**, *935*, 173276. [CrossRef]
11. Li, X.; Huang, X.; Zhang, Y. Spatio-temporal analysis of groundwater chemistry, quality and potential human health risks in the Pinggu basin of North China Plain: Evidence from high-resolution monitoring dataset of 2015–2017. *Sci. Total Environ.* **2021**, *800*, 149568. [CrossRef]
12. Han, J.; Destouni, G.; Jarsjö, J.; Zhang, Q.; Cantoni, J.; Zhang, C. Legacy sources determine current water quality: Nitrogen and phosphorus in streams of Australia, China, Sweden and USA. *Sci. Total Environ.* **2024**, *954*, 176407. [CrossRef]
13. Li, R.; Yan, Y.; Xu, J.; Yang, C.; Chen, S.; Wang, Y.; Zhang, Y. Evaluate the groundwater quality and human health risks for sustainable drinking and irrigation purposes in mountainous region of Chongqing, Southwest China. *J. Contam. Hydrol.* **2024**, *264*, 104344. [CrossRef]
14. Fida, M.; Li, P.; Wang, Y.; Alam, S.M.K.; Nsabimana, A. Water Contamination and Human Health Risks in Pakistan: A Review. *Expo. Health* **2022**, *15*, 619–639. [CrossRef]

15. Lancia, M.; Yao, Y.; Andrews, C.; Wang, X.; Kuang, X.; Ni, J.; Gorelick, S.; Scanlon, B.; Wang, Y.; Zheng, C. The China groundwater crisis: A mechanistic analysis with implications for global sustainability. *Sustain. Horiz.* **2022**, *4*, 100042. [CrossRef]
16. Ruan, D.; Bian, J.; Wang, Y.; Wu, J.; Gu, Z. Identification of groundwater pollution sources and health risk assessment in the Songnen Plain based on PCA-APCS-MLR and trapezoidal fuzzy number-Monte Carlo stochastic simulation model. *J. Hydrol.* **2024**, *632*, 130897. [CrossRef]
17. Yao, R.; Zhang, Y.; Yan, Y.; Wu, X.; Uddin, M.G.; Wei, D.; Huang, X.; Tang, L. Natural Background Level, Source Apportionment and Health Risk Assessment of Potentially Toxic Elements in Multi-layer Aquifers of Arid Area in Northwest China. *J. Hazard. Mater.* **2024**, *479*, 135663. [CrossRef]
18. Tang, L.; Yao, R.; Zhang, Y.; Ding, W.; Wang, J.; Kang, J.; Liu, G.; Zhang, W.; Li, X. Hydrochemical analysis and groundwater suitability for drinking and irrigation in an arid agricultural area of the Northwest China. *J. Contam. Hydrol.* **2023**, *259*, 104256. [CrossRef]
19. Mohammed, S.; Arshad, S.; Bashir, B.; Vad, A.; Alsalman, A.; Harsányi, E. Machine learning driven forecasts of agricultural water quality from rainfall ionic characteristics in Central Europe. *Agric. Water Manag.* **2024**, *293*, 108690. [CrossRef]
20. Yan, Y.; Zhang, Y.; Yao, R.; Wei, C.; Luo, M.; Yang, C.; Chen, S.; Huang, X. Groundwater suitability assessment for irrigation and drinking purposes by integrating spatial analysis, machine learning, water quality index, and health risk model. *Environ. Sci. Pollut. Res.* **2024**, *31*, 39155–39176. [CrossRef]
21. Tao, L.; Zhang, Y.; Yuan, X.; Chen, Q.; Yu, J.; Ma, Y.; Liu, H.; Tu, C. Hydrological processes in multi-layered aquifers of a karst watershed with coal mining activity: Insights from hydrochemistry and isotopes. *J. Hydrol. Reg. Stud.* **2024**, *56*, 102016. [CrossRef]
22. Liu, J.; Lou, K.; Gao, Z.; Wang, Y.; Li, Q.; Tan, M. Comprehending hydrochemical fingerprint, spatial patterns, and driving forces of groundwater in a topical coastal plain of Northern China based on hydrochemical and isotopic evaluations. *J. Clean. Prod.* **2024**, *461*, 142640. [CrossRef]
23. Yan, Y.; Zhang, Y.; Yang, S.; Wei, D.; Zhang, J.; Li, Q.; Yao, R.; Wu, X.; Wang, Y. Optimized groundwater quality evaluation using unsupervised machine learning, game theory and Monte-Carlo simulation. *J. Environ. Manag.* **2024**, *371*, 122902. [CrossRef] [PubMed]
24. Chaudhari, M.P.; George, A.; Sanyal, M.; Shrivastav, P.S. Hydrochemistry and groundwater quality assessment of Gujarat, India: A compendious review. *Phys. Chem. Earth Parts A/B/C* **2024**, *135*, 103635. [CrossRef]
25. Ambade, B.; Sethi, S.S.; Patidar, K.; Gautam, S.; Alshehri, M. Assessing variability and hydrochemical characteristics of groundwater fluoride contamination and its associated health risks in East Singhbhum district of Jharkhand, India. *J. Hazard. Mater.* **2024**, *478*, 135498. [CrossRef] [PubMed]
26. Yan, Y.; Zhang, Y.; Xie, Z.; Wu, X.; Tu, C.; Chen, Q.; Tao, L. Source Apportionment and Human Health Risks of Potentially Toxic Elements in the Surface Water of Coal Mining Areas. *Toxics* **2024**, *12*, 673. [CrossRef]
27. Yao, R.; Yan, Y.; Wei, C.; Luo, M.; Xiao, Y.; Zhang, Y. Hydrochemical Characteristics and Groundwater Quality Assessment Using an Integrated Approach of the PCA, SOM, and Fuzzy c-Means Clustering: A Case Study in the Northern Sichuan Basin. *Front. Environ. Sci.* **2022**, *10*, 907872. [CrossRef]
28. Panagiotou, C.F.; Kyriakidis, P.; Tziritis, E. Application of geostatistical methods to groundwater salinization problems: A review. *J. Hydrol.* **2022**, *615*, 128566. [CrossRef]
29. Abba, S.I.; Yassin, M.A.; Jibril, M.M.; Tawabini, B.; Soupios, P.; Khogali, A.; Shah, S.M.H.; Usman, J.; Aljundi, I.H. Nitrate concentrations tracking from multi-aquifer groundwater vulnerability zones: Insight from machine learning and spatial mapping. *Process Saf. Environ. Prot.* **2024**, *184*, 1143–1157. [CrossRef]
30. Yang, S.; Lian, H.; Xu, B.; Thanh, H.V.; Chen, W.; Yin, H.; Dai, Z. Application of robust deep learning models to predict mine water inflow: Implication for groundwater environment management. *Sci. Total Environ.* **2023**, *871*, 162056. [CrossRef]
31. Yan, J.; Chen, J.; Zhang, W. A new probabilistic assessment process for human health risk (HHR) in groundwater with extensive fluoride and nitrate optimized by non parametric estimation method. *Water Res.* **2023**, *243*, 120379. [CrossRef] [PubMed]
32. Yang, X.; Du, J.; Jia, C.; Yang, T.; Shao, S. Unravelling integrated groundwater management in pollution-prone agricultural cities: A synergistic approach combining probabilistic risk, source apportionment and artificial intelligence. *J. Hazard. Mater.* **2025**, *481*, 136514. [CrossRef] [PubMed]
33. Xue, J.; Yuan, C.; Ji, X.; Zhang, M. Predictive modeling of nitrogen and phosphorus concentrations in rivers using a machine learning framework: A case study in an urban-rural transitional area in Wenzhou China. *Sci. Total Environ.* **2024**, *910*, 168521. [CrossRef] [PubMed]
34. Tian, Y.; Liu, Q.; Ji, Y.; Dang, Q.; Sun, Y.; He, X.; Liu, Y.; Su, J. Prediction of sulfate concentrations in groundwater in areas with complex hydrogeological conditions based on machine learning. *Sci. Total Environ.* **2024**, *923*, 171312. [CrossRef]
35. Huang, Y.; Cai, Y.; He, Y.; Dai, C.; Wan, H.; Guo, H. A water quality prediction approach for the Downstream and Delta of Dongjiang River Basin under the joint effects of water intakes, pollution sources, and climate change. *J. Hydrol.* **2024**, *640*, 131686. [CrossRef]
36. Rotiroti, M.; Sacchi, E.; Caschetto, M.; Zanotti, C.; Fumagalli, L.; Biasibetti, M.; Bonomi, T.; Leoni, B. Groundwater and surface water nitrate pollution in an intensively irrigated system: Sources, dynamics and adaptation to climate change. *J. Hydrol.* **2023**, *623*, 129868. [CrossRef]
37. Xie, C.; Zhao, L.; Eastoe, C.J.; Wang, N.; Dong, X. An isotope study of the Shule River Basin, Northwest China: Sources and groundwater residence time, sulfate sources and climate change. *J. Hydrol.* **2022**, *612*, 128043. [CrossRef]

38. Zheng, P.; Wang, H.; Wei, D.; Pu, C.; He, Z. Environmental governance capability and water quality: A quasi-natural experiment based on the Ten-point Water Plan. *Urban. Clim.* **2022**, *41*, 101050. [CrossRef]
39. Zhong, C.; Yang, Q.; Liang, J.; Ma, H. Fuzzy comprehensive evaluation with AHP and entropy methods and health risk assessment of groundwater in Yinchuan Basin, northwest China. *Environ. Res.* **2022**, *204*, 111956. [CrossRef]
40. Aein, R.; Alizadeh, H. Integrated hydro-economic modeling for optimal design of development scheme of salinity affected irrigated agriculture in Helleh River Basin. *Agric. Water Manag.* **2021**, *243*, 106505. [CrossRef]
41. Pérez-Blanco, C.D.; Essenfelder, A.H.; Gutiérrez-Martín, C. A tale of two rivers: Integrated hydro-economic modeling for the evaluation of trading opportunities and return flow externalities in inter-basin agricultural water markets. *J. Hydrol.* **2020**, *584*, 124676. [CrossRef]
42. Li, H.; Mahmud, M.A.; Arzaghi, E.; Abbassi, R.; Chen, D.; Xu, B. Assessments of economic benefits for hydro-wind power systems: Development of advanced model and quantitative method for reducing the power wastage. *J. Clean. Prod.* **2020**, *277*, 123823. [CrossRef]
43. Knowling, M.J.; White, J.T.; McDonald, G.W.; Kim, J.-H.; Moore, C.R.; Hemmings, B. Disentangling environmental and economic contributions to hydro-economic model output uncertainty: An example in the context of land-use change impact assessment. *Environ. Model. Softw.* **2020**, *127*, 104653. [CrossRef]

Disclaimer/Publisher's Note: The statements, opinions and data contained in all publications are solely those of the individual author(s) and contributor(s) and not of MDPI and/or the editor(s). MDPI and/or the editor(s) disclaim responsibility for any injury to people or property resulting from any ideas, methods, instructions or products referred to in the content.

water

MDPI

Article

Assessing Groundwater Resources Vulnerability with the New DRASTIC-LP: A Case Study in Chiang Mai Province, Thailand

Chaiyathat Imsamranrat and Adisorn Leelasantitham *

Technology of Information System Management Division, Faculty of Engineering, Mahidol University, 25/25 Phutthamonthon Sai 4 Road, Salaya, Phutthamonthon, Nakhon Pathom 73170, Thailand; chaiyathat@hotmail.com
* Correspondence: adisorn.lee@mahidol.ac.th

Abstract: Groundwater vulnerability has gained widespread attention, particularly in Chiang Mai Province, one of Thailand's fastest-growing cities, which is experiencing rapid development in both economic and social sectors. The expansion of urban communities and the industrial, tourism, and agriculture sectors has resulted in the overutilization of available resources, notably water resources. This overuse, coupled with the adoption of modern technology to boost productivity and meet market demands, has led to an increased reliance on groundwater to supplement surface water sources, providing benefits across all sectors. However, the economic and social growth plays a pivotal role in shaping the diversity of land use, encompassing residential, commercial, industrial, and agricultural activities. These activities, in turn, directly contribute to environmental pollution, particularly in terms of the risk of groundwater contamination in Chiang Mai Province. This study aims to predict the future vulnerabilities of groundwater resources under an ensemble of climate change scenarios and changes in land-use patterns. Chiang Mai Province in northern Thailand is one of the fastest-growing cities and therefore is experiencing rapid urbanization, as well as land-use pattern changes, which was important for the case study. The new DRASTIC model, namely the DRASTIC-LP model, combined with GIS-based techniques and overlay techniques, was used to generate the map of groundwater resource vulnerabilities. A point pollution source (P)-related land-use pattern (L) that represents contamination impacts was considered an additional new DRASTIC parameter. The study's findings reveal the high reliability and maximum effectiveness of the new DRASTIC-LP model in assessing groundwater vulnerability and contamination-risk areas under a climate change scenario (by MIROC-ESM-CHEM model under RCP.8.5 scenario) and land-use pattern changes (by CA_Markov Chian Model) for both the current year (2020) and the next 50-year period (2021–2070). Furthermore, the new DRASTIC-LP model is employed to trace the movement of pollutants from high- to very high-risk areas based on the groundwater vulnerability and contamination-risk maps. The results highlight that waste disposal dumping sites pose a more critical distribution and movement of pollutants when compared to industrial sites. Additionally, unconsolidated aquifers and cracked consolidated rock aquifers show a potentially higher occurrence of pollutant distribution and movement when compared to consolidated aquifers. Consequently, the study's outcomes are applied to formulate guidelines for the management and control of groundwater resource contamination. These guidelines serve as valuable tools for decision makers, aiding in pollution prevention and the effective management of contamination risks in groundwater resources.

Keywords: climate change; land-use patterns change; GIS-based techniques; high-risk pollutant; contamination-risk map

1. Introduction

The issue of groundwater pollution has garnered significant attention in Thailand, particularly in the northern region, which holds an estimated 166,860 million cubic meters of groundwater resources, constituting 14.67% of the nation's total groundwater volume [1].

However, due to rapid population growth and extensive development in the tourist, industrial, and agricultural sectors of northern Thailand, the groundwater situation has suffered varying degrees of damage [2,3]. Aligning with prior studies, it has been reported that 80% of shallow groundwater and 30% of deep groundwater in the People's Republic of China exhibit varying levels of pollution [4].

The review of past research indicates that assessing the vulnerability of groundwater resources is crucial for effective planning, policymaking, and decision making, as well as for the sustainable management of these resources. Such assessments not only aid decision makers in adopting effective management strategies to mitigate groundwater pollution, but also contribute to developing a conceptual framework for the allocation of groundwater resources. This framework helps determine appropriate land-use patterns and practices, fostering awareness among the population regarding the risks associated with groundwater contamination [5]. The concept of groundwater resource vulnerability aims to identify and prioritize the most vulnerable areas or regions within a river basin that could lead to groundwater contamination. Additionally, it furnishes essential scientific information for the protection and preservation of groundwater resources [6]. Consequently, a comprehensive review encompassing all methods and approaches used to assess groundwater resources vulnerability from the past to the present is necessary. For instance, Ducci [7] discovered that regional groundwater pollution vulnerability patterns vary between drought, average, and wet climatic conditions. Butscher and Huggenberger [8] conducted an analysis of a karst aquifer system in north-west Switzerland and found that groundwater vulnerability is influenced by climate-affected recharge conditions. Keilholz et al. [9] highlighted the effects of land use and climate change on groundwater and ecosystems at the middle reaches of the Tarim River, using the MIKE SHE-integrated hydrological model. Nistor [10] confirmed the impact of climate change on groundwater vulnerability in the Pannonian basin through a calculation of spatial analysis for groundwater vulnerability, using GIS-based techniques. The groundwater vulnerability maps indicated that the Pannonian basin appears highly vulnerable to climate change in both the present (2020s) and future (2050s) scenarios.

The vulnerability of groundwater resources can undergo changes overtime due to climate fluctuations, alterations in land use, and land cover (LULC). Various methods have been proposed for assessing groundwater resource vulnerability, including the original DRASTIC model [11] and the modified DRASTIC model, as evidenced by studies over the past ten-year period [12–17]. A comprehensive literature review, as presented in Table 1, reveals that there is a gap in past reviews, particularly the lack of studies dealing with groundwater resource vulnerability under the influence of climate change and changes in land-use patterns using modern models. In summarizing the research related to assessing groundwater resource vulnerability, two main groups emerge:

1. Approaches undertaken globally by the original DRASTIC Model [11], combined with the overlay technique and/or the GIS-based technique. This group, totaling 12 research papers, includes studies by Aller et al. [11], Rahman [18], Shirazi et al. [19], Zghibi et al. [20], Abdeslama et al. [21], Rajput et al. [22], Mohammed et al. [23], Nurroh et al. [24], Bera et al. [25], Chilaule et al. [26], Zhang et al. [27], and Wei and Chi [28]. The limitation of these assessments lies in their focus on simulating the susceptibility of groundwater aquifers to contamination from both natural conditions and anthropogenic activities. Notably, these studies primarily concentrate on current scenarios, neglecting any consideration of future scenarios.

2. Applied approaches from the original DRASTIC model to the Modified DRASTIC model. This group, totaling six research papers, encompasses various methodologies, including the overlay technique, the GIS-based technique, and/or remote sensing (RS).

Table 1. Comparisons of the methodology of assessing the groundwater resources vulnerability of this research with the literature reviews.

Literature Review (References)	Methodology of Assessing the Groundwater Resources Vulnerability		Tools	Study Area	Limitation
	Original DRASTIC	Modified DRASTIC			
Aller et al. (1987) [11]	7 indexes		Overlay technique	USA.	These assessments focus on simulating the susceptibility of groundwater aquifers to contamination from both natural conditions and anthropogenic activities. Notably, these studies primarily concentrate on current scenarios, neglecting any consideration of future scenarios.
Rahman (2008) [18]	7 indexes		ILWIS 3.0 model and GIS-based techniques using ArcView 3.2a GIS software	Aligarh, India	
Shirazi et al. (2013) [19]	7 indexes		GIS-based techniques and remote sensing	Melaka State, Malaysia	
Zghibi et al. (2016) [20]	7 indexes		GIS-based techniques	Tunisian Coastal Aquifer	
Abdeslama et al. (2017) [21]	7 indexes		GIS-based techniques using ArcGIS	Northeast of Algeria	
Rajput et al. (2020) [22]	7 indexes		GIS-based techniques	Rajasthan, India	
Mohammed et al. (2020) [23]	7 indexes		GIS-based techniques	Basara Basin, the Iraqi Kurdistan Region	
Nurroh et al. (2020) [24]	7 indexes		GIS-based techniques	Yogyakarta, Indonesia	
Bera et al. (2022) [25]	7 indexes		AHP techniques and GIS-based techniques	Semi-arid Totko River Basin, India	
Chilaule et al. (2023) [26]	7 indexes		GIS-based techniques	Comarca de la Janda, Province of Cádiz, Spain	These assessments focus on simulating the susceptibility of groundwater aquifers to contamination from both natural conditions and anthropogenic activities. Notably, these studies primarily concentrate on current scenarios, neglecting any consideration of future scenarios.
Zhang et al. (2023) [27]	7 indexes		GIS-based techniques	Tangshan City, a Coastal Area in China	
Wei and Chi (2023) [28]	7 indexes		AHP techniques and GIS-based techniques	Remediation of Contaminated Sites in China (PRC)	
Sadat-Noori and Ebrahimi (2016) [14]	7 indexes	7 indexes; using to calibrate and modify the original algorithm	GIS-based techniques and simple statistical techniques	Saveh-Nobaran Plain, the Central Iran	These assessments of the vulnerability of groundwater resources focus mainly on land-use pattern and/or anthropogenic activities (population density, etc.) indices, without considering future scenarios.
Jenifer and Jha (2018) [16]	7 indexes	9 indexes; adding two exogenous factors, namely: lineament density (LD), land-use and land cover (LU)	GIS-based techniques	Tiruchirappalli District, Tamil Nadu, India	
Maqsoom et al. (2020) [17]	7 indexes	8 indexes; adding anthropogenic activity index (A)	GIS-based techniques using ArcGIS 10.3 software	Karakoram Highway (a Part of the CPEC Route (China-Pakistan Economic Corridor)	

Table 1. *Cont.*

Literature Review (References)	Methodology of Assessing the Groundwater Resources Vulnerability		Tools	Study Area	Limitation
	Original DRASTIC	Modified DRASTIC			
Zhang et al. (2022) [29]	7 indexes	11 indexes; adding four exogenous factors, namely: land-use type (L), aquifer thickness (T'), aquifer water potential (P'), and pollution source distance (D')	AHP techniques and GIS-based techniques using ArcGIS environment	Northern part of Shifang City, Sichuan Province, China (PRC)	The traditional DRASTIC model considers the influence of anthropogenic activities based to the current situation. In addition to the seven commonly used factors reflecting natural conditions, four additional evaluation factors—land-use type, aquifer thickness, aquifer water potential, pollution source distance—were considered. A new model, including the DRASTIC-LTPD and AHP-DRASTIC-LTPD models, was proposed, without considering future scenarios.
Lima et al. (2011) [12]		8 indexes (DRASTIC-P); adding land-use index (P) and/or the future agricultural expansion scenarios by Dyna-CLUE model	GIS-based techniques	Dulce Creek Basin, the Southeast of the Bunos Aires City, Argentina	This assessment's primary focus on land-use pattern indices under the current and future scenarios, without considering future climate changes.
Li and Merchant (2013) [13]		7 indexes (DRASTIL) except C; adding land-use index (L)	LTM Model (Land Transformation Model), environmental conditions and GIS-based techniques	Great Plains State, North Dakota, USA.	The assessment of the vulnerability of groundwater resources noted that the groundwater vulnerability maps developed for this research indicate only the "risk" of groundwater pollution on a regional scale, but may not be used to interpret actual local groundwater contamination incidences, due to the site-specific factors, such as hydraulic fracturing for shale oil, which may cause drinking water contamination, not being considered.
Huang et al. (2017) [15]		8 indexes; adding land-use pattern index (L)	LTM Model (Land Transformation Model) and GIS-based techniques	Hunan, China (PRC)	The assessment of groundwater vulnerability confirmed the depth-to-water table (DTW), and that the land-use patterns contribute differently to variations in groundwater vulnerability. Additionally, this study emphasizes the importance of generating an impact model of climate changes and anthropogenic activities on future ground-water resource vulnerability; this would directly link future DTW variations to climate change and associate land-use patterns with anthropogenic activities.

Table 1. *Cont.*

Literature Review (References)	Methodology of Assessing the Groundwater Resources Vulnerability		Tools	Study Area	Limitation
	Original DRASTIC	Modified DRASTIC			
Mkumbo et al. (2022) [30]		8 indexes; adding land-use and land cover (LU/LC)	AHP techniques and GIS-based techniques using ArcGIS environment	Morogoro Municipality, Tanzania	This assessment of groundwater resource vulnera-bility focuses mainly on land use and landcover indexes, without considering future scenarios.
This Paper		9 indexes; adding 2 anthropogenic activities, namely: land-use pattern (L) and point source pollution (P)	CA_Markov Chain Model (Cellular Automata and Markov Chain Model); and MIROC-ESM-CHEM Model under RCP8.5 Scenario; and GIS-based techniques using ArcGIS 10.5 software	Chiang Mai Province, Thailand	A comprehensive review of the literature reveals that past reviews had a narrow focus, and lacked a real coverage of studies, as well as not utilizing state-of-the-art methods to deal with groundwater resource vulnerability. Consequently, this paper focuses on in-depth reviews, considering the best methods and approaches under climate change and land-use pattern changes, while using modern models for analyzing current (2020) scenarios and forecasting future (2070) scenarios.

(a) Approaches without consideration of land-use pattern changes and/or climate change without considering future scenarios: This subgroup consists of three research papers, including Sadat-Noori and Ebrahimi [14], Jenifer and Jha [16], and Maqsoom et al. [17]. The limitation of these assessments of groundwater resource vulnerability is that they mainly focus on land-use pattern and/or anthropogenic activity (population density) indices.

(b) Approaches without consideration of land-use pattern changes and/or climate change without considering future scenarios: This subgroup consists of one research paper: Zhang et al. [29]. This assessment of groundwater resource vulnerability focuses mainly on four additional evaluation factors: land-use type (L), aquifer thickness (T′), aquifer water potential (P′), pollution source distance (D′). These are considered with the new proposed model that includes DRASTIC-LTPD and AHP-DRASTIC-LTPD.

(c) Approaches considering land-use changes and land cover without considering future scenarios: one research paper, Kmumbo et al. [30], is included in this subgroup. The limitation of this assessment is its primary focus on land use and land cover (LU/LC) indexes.

(d) Approaches considering changing land-use patterns under future scenarios, using the Dyna-CLUE model: a study by Lima et al. [12] is included in this subgroup. The limitation of this assessment is its primary focus on land-use pattern indices under both current and future scenarios, without considering future climate changes.

(e) Approaches considering changing land-use patterns using the LTM model (Land Transformation model), and climate changes using the GCMs model for future scenarios: this subgroup consists of two research papers, including Li and Merchant [13] and Huang et al. [15]. The limitations of this assessment of groundwater resource vulnerability were as follows:

    i Li and Merchant [13] found that the groundwater vulnerability maps developed for this research indicate only the risk of groundwater pollution on a regional scale but may not be used to interpret actual local groundwater contamination incidents, due to the site-specific factors, such as hydraulic fracturing for shale oil, which may cause drinking water contamination, not being considered.

    ii Huang et al. [15] confirmed the depth-to-water table (DTW), and also confirmed that the land-use patterns contribute differently to variations in groundwater resource vulnerability. Additionally, this study emphasizes generating an impact model of climate changes and anthropogenic activities on future groundwater resource vulnerability, directly linking future DTW variations to climate change and associating land-use patterns with anthropogenic activities.

Despite the various methodologies applied, addressing future groundwater vulnerability, based on the potential land-use changes and climate change scenarios, is essential for formulating effective policies that ensure sustainable groundwater resource development. This proactive approach aids decision makers in identifying potential future vulnerabilities and taking early steps to protect critical groundwater resources. In the specific context of Chiang Mai Province, Thailand, the assessment of groundwater resource vulnerability utilized the original DRASTIC model [11] and the modified DRASTIC model, incorporating a land-use pattern index (L). Notably, point source pollutions have emerged as critical contributors to groundwater contamination. As mentioned earlier, although many researchers have assessed groundwater vulnerability using the original DRASTIC model and the modified DRASTIC model, these numerous researchers were mainly focused on only current scenarios or land-use patterns change and/or the expansion of anthropogenic activities, without any consideration of climate change scenarios. Little is known, however, about future groundwater resource vulnerability, or the impact of the combination of climate changes and land-use pattern changes under an ensemble of climate change scenarios. The response of groundwater vulnerability to the projected changes in climate change and land-use pattern changes is expected to be profound. Climate change and

land-use pattern changes cannot be neglected during the process of the assessment of groundwater vulnerability.

In Chiang Mai Province in the northern region of Thailand, land-use patterns and point source pollution stand out as primary contributors, directly impacting groundwater resources. Consequently, the vulnerability assessment of groundwater resources, utilizing the new DRASTIC-LP model (modified from Aller et al. [11]), aims to simulate both the current situation and future scenarios, considering climate change under high emission scenarios (or RCP8.5 scenario) and land-use pattern changes. Additionally, the identification of contamination-risk areas is an integral part of this assessment. To identify the impacts of the mentioned factors on groundwater vulnerability, the study proposes an integrated approach, as follows:

1. Assessment of climate change situations: Three models suitable for Thailand are selected, specifically three global climate models (GCMs). The data from the three GCMs AR5 [31] models are modified to incorporate spatial data, aligning with inspection data measures from the past. This modification aims to predict the appearance and behavior of temperature and rainfall conditions.
2. Assessment of land-use change situations: Utilizing the CA_Markov Chain Model, the study analyzes the changes in various types of land-use patterns [32].
3. Assessment of groundwater resource vulnerability: The original DRASTIC model [11] is employed to assess the vulnerability of groundwater resources, both in the current and future scenarios.
4. New approach for risk assessment and management: The research introduces a novel approach for the risk assessment and management of groundwater vulnerability. This approach integrates the aforementioned assessments while incorporating the land-use patterns index, denoted as L, and point source pollutions, marked as P, using Geographic Information System (GIS) techniques. The goal is to produce a comprehensive map depicting the vulnerability of groundwater resources.

2. Site Description and Hydrogeology Condition

2.1. Site Condition

Chiang Mai Province covers a total area of 20,107.06 sq.km. or 12,566,912.50 rais, as shown in Figure 1 [33]. Situated in the upper northern part of Thailand, it stands out as one of the fastest-growing cities, experiencing rapid development in both economic and social sectors. This growth has resulted in the expansion of urban communities, industrial sectors, and the tourism industry. The escalating economic prosperity, coupled with the infusion of modern technology to enhance productivity and meet public sector demands, has led to the overuse of available resources, particularly water. Consequently, a surge in water demand has emerged as a significant challenge. Despite comprising predominantly reserved and conserved areas, covering 15,403.77 sq.km. or 9.627 million rais, constituting 76.61 percent of Chiang Mai's total area [34], legal restrictions prevent the development of medium-to-large surface water reservoirs. The province is situated within the Chiang Mai-Lamphun and Fang groundwater basins [35], with a potential groundwater source. capable of supplying water ranging from less than 2 cubic meters/hour to more than 20 cubic meters/hour [36]. Utilizing groundwater in both basins to replace or supplement surface water sources stands as a beneficial solution across all sectors. The expansive growth in economic and social systems within Chiang Mai Province has significantly influenced the diversity of land-use patterns and the expansion of residential, commercial, industrial, and agricultural sectors. It is evident that activities in these sectors contribute to environmental pollution, posing a threat to groundwater contamination in the Chiang Mai-Lamphun and Fang groundwater basins [2,3].

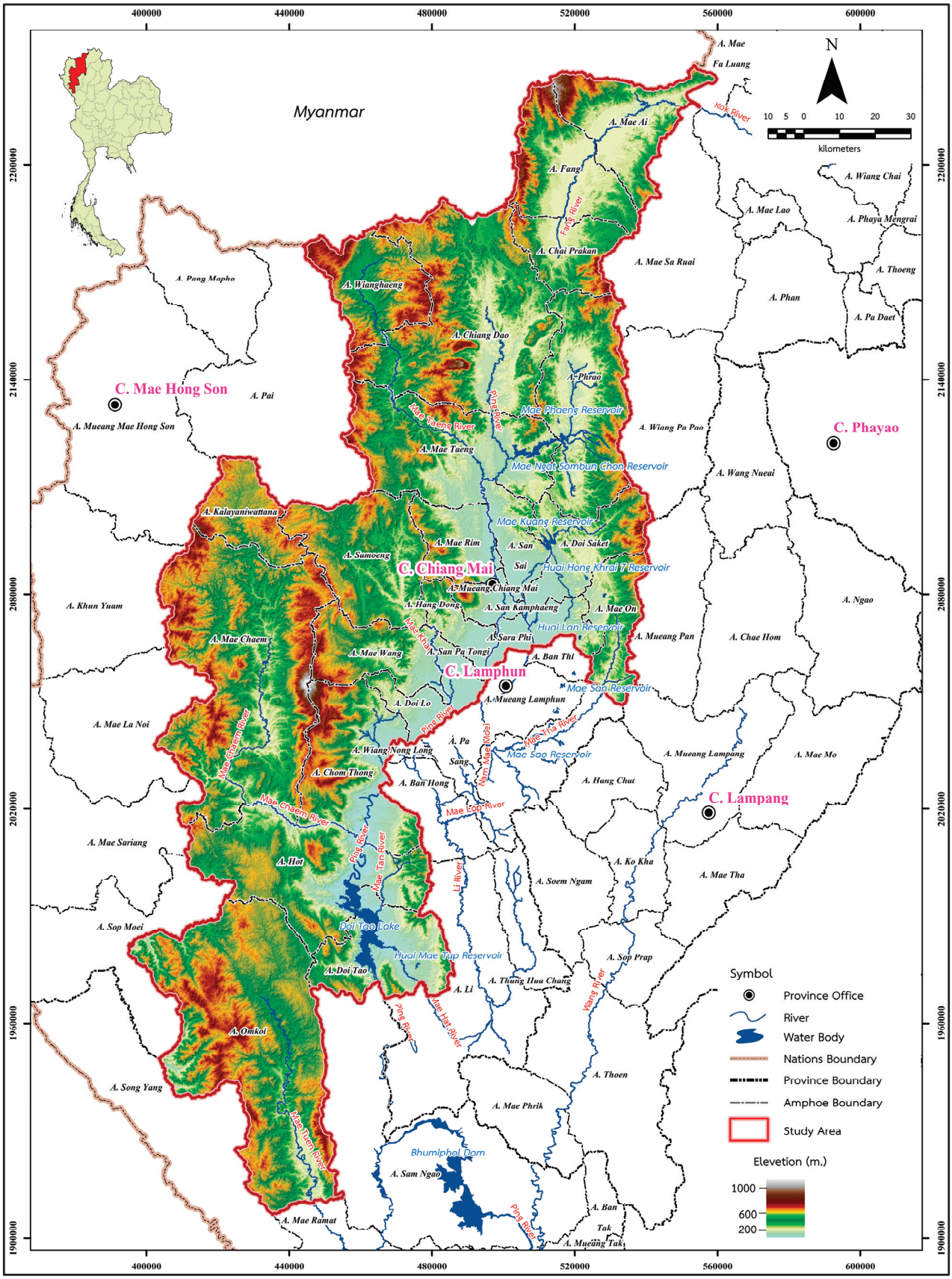

Figure 1. Location of research area, Chiang Mai Province, with a total area of 20,107.06 sq.km. or 12,566,912.50 rais.

2.2. Hydrogeologic Setting of Chiang Mai Province

The hydrogeological characteristics and the geological map of Chiang Mai Province are shown in Figure 2. The province exhibits both unconsolidated and consolidated aquifers. The unconsolidated aquifers in Chiang Mai Province cover an area of approximately 2800 sq.km. or 1,750,000 rais, ranging from 18°30′ to 19° N and from 98°45′ to 99°15′ E. These areas are flanked by mountain ranges on both the east and west sides, with the Ping River being the main river, generally flowing from north to south. The narrowest width of Chiang Mai Province is approximately 20 km. [37]. Various geologic units, spanning from Precambrian to recent ages, are exposed in the area. Unconsolidated Quaternary alluvium deposits overlay older rock formations, dominating most of Chiang Mai Province [38–40]. These aquifers comprise Quaternary sediments, including gravel, sand, silt, and clay, categorized as fluvial deposits aquifers (Qfd), younger terrace aquifers (Qyt), consisting of low terrace aquifers (Qtl) and middle terrace aquifers (Qtm); and the old terrace aquifer (Qot), comparable to high terrace aquifers (Qth) and colluvial aquifers (Qcl). The fluvial deposits aquifer is widespread in the lowlands of the Chiang Mai-Lamphun basin.

On the other hand, consolidated aquifers encompass semi-consolidated aquifers (Tsc), middle Korat aquifers (Jmk), lower Korat aquifers (TRJlk), Lampang aquifers (TRlp), Permian carbonate rocks aquifers (Pc), Permian-Carboniferous metasediments aquifers (PCms), Carboniferous metasediments aquifers (Cms), Ordovician limestone aquifers (Ols), Silurian-Devonian metamorphic aquifers (SDmm), Cambrian metamorphic aquifers (Emm), Precambrian metamorphic aquifers (PEmm), Volcanic aquifers (Vc), and Granitic aquifers (Gr). All these aquifers may undergo fracturing during tectonic events, transforming into cracked consolidated rock aquifers. Groundwater wells in Chiang Mai Province are typically shallow, with a general depth ranging from approximately 20 to 70 m below the ground surface. Figure 3 shows that hydrogeologic cross-sections in lines A0–A1, B0–B1, C0–C1, and D0–D1 (refer to Figure 2) are derived from various lithologic logs, illustrating that semi-consolidated-to-consolidated aquifers are amalgamated into a single, heterogeneous unit, denoted by a dark red color.

The groundwater yield varies across the region, typically falling within the range of 2–10 cubic meters per hour. Notably, the fluvial deposit aquifer (Qfd) exhibits higher groundwater quantities, reaching up to 20 cubic meters per hour, as depicted in Figure 4, modified from the Groundwater Potential Map of Chiang Mai Province (scale 1:100,000, [41]). The flow direction of groundwater resources in the unconsolidated aquifer primarily moves from the edge of the basin towards the center, and ultimately drains into the Ping River. The central alluvial channel of Chiang Mai Province experiences the highest groundwater exploitation. Hydraulic conductivities of these aquifers, as evaluated from pumping tests, range from 0.01 to approximately 20 m per day [42]. Groundwater quality in the region is generally favorable, with the total dissolved solids (TDS) measuring less than 250 mg/L. Fluoride and iron concentrations are consistently low, particularly in the upper part of the aquifer; this can be attributed to the high oxygen levels and flow velocities [2,3].

The research found that it was extremely difficult to delineate the sedimentary units in the Chiang Mai Province, because any correlation was almost impossible due to high heterogeneity [37,43,44]. The hydrostratigraphic model revealed sedimentary facies are associated with varying depths and are intercalated. The correlation between adjacent wells was extremely difficult, due to the lack of key beds or recognizable sequences [44].

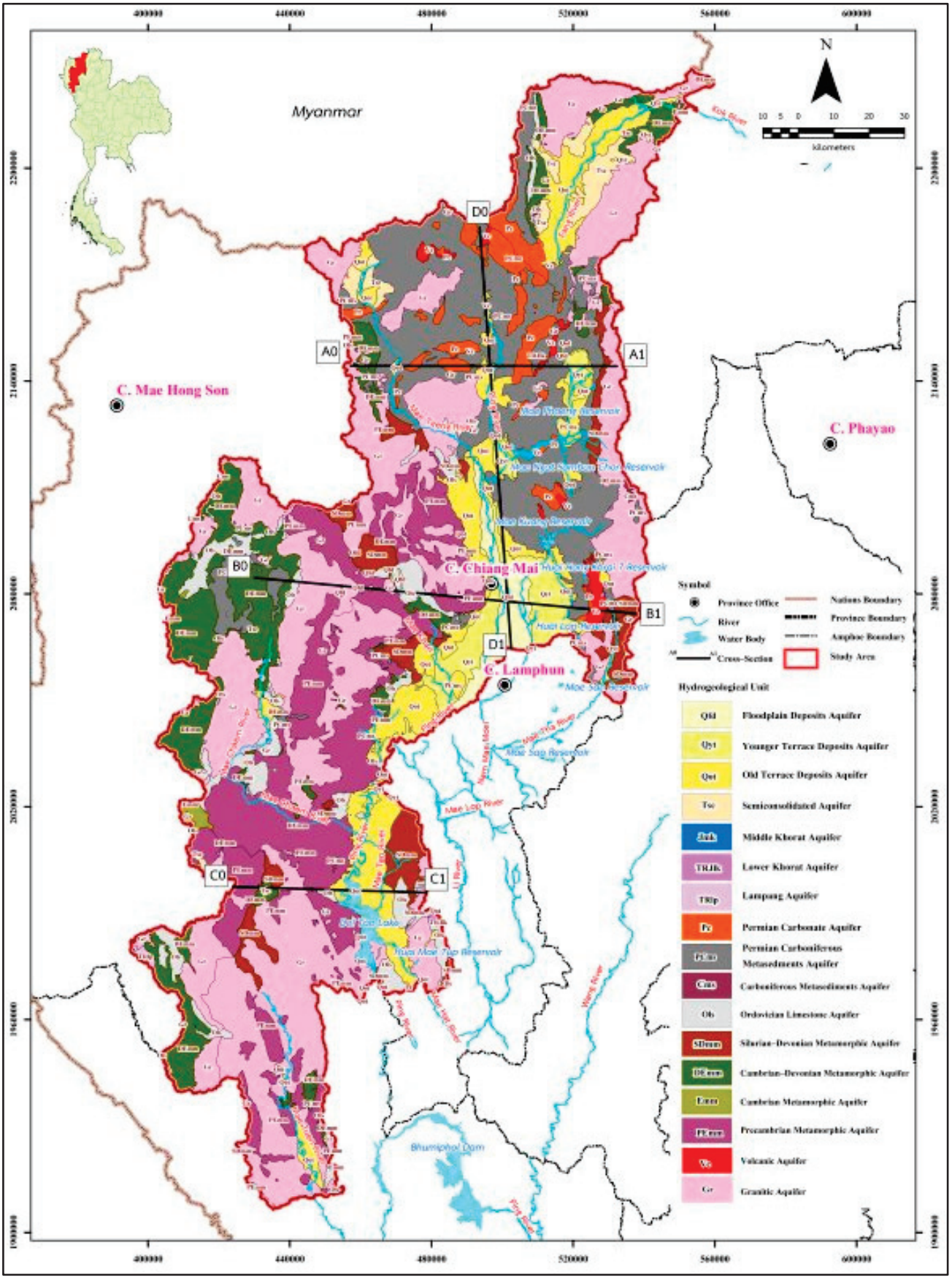

Figure 2. Hydrogeological characteristics of Chiang Mai Province.

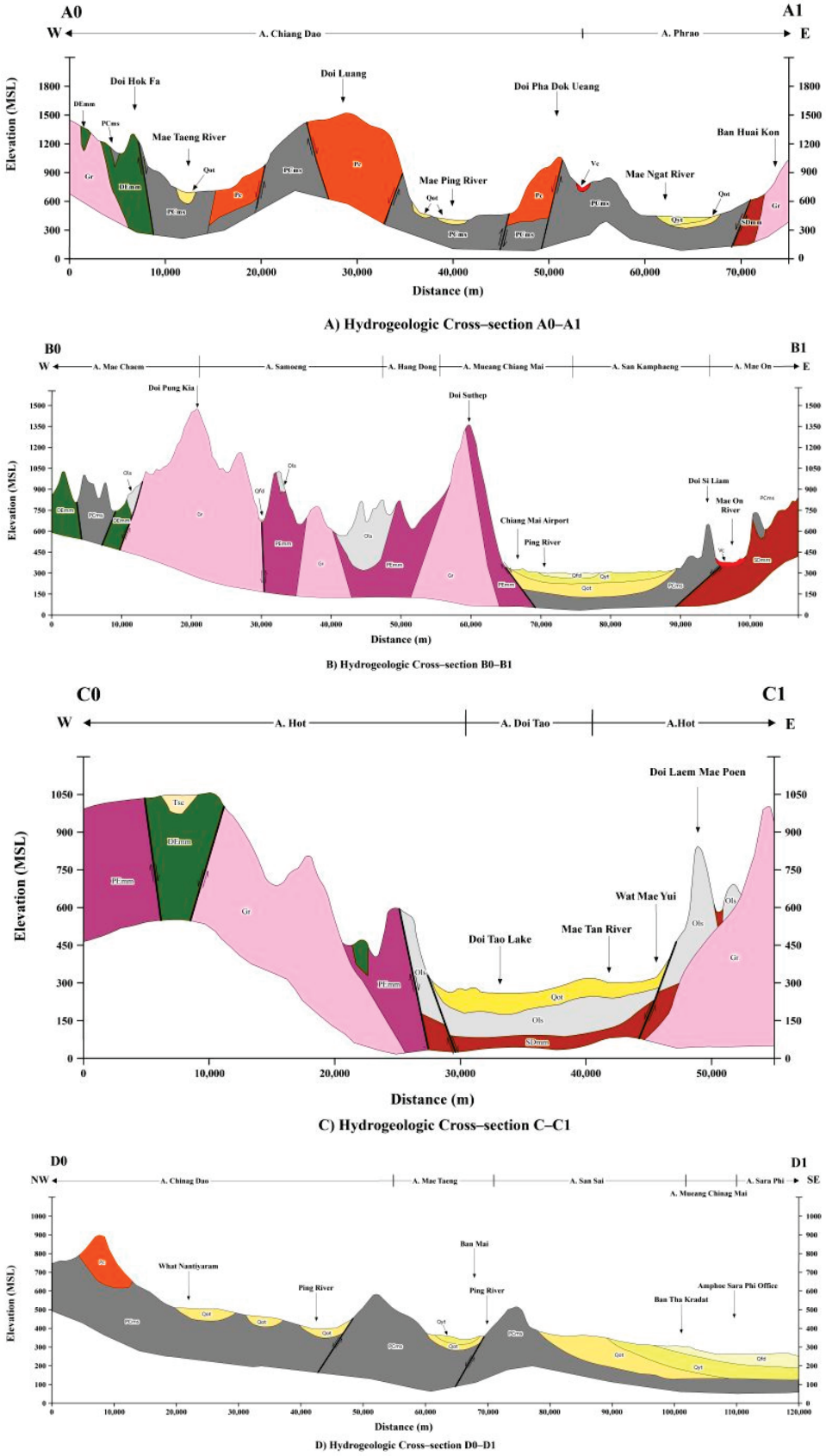

Figure 3. Hydrogeologic cross-sections in lines A0–A1, B0–B1, C0–C1, and D0–D1 (see detail of Hydrogeologic Unit in Figure 2). (**A**) Hydrogeologic cross-sections in lines A0–A1; (**B**) Hydrogeologic cross-sections in lines B0–B1; (**C**) Hydrogeologic cross-sections in lines C0–C1; (**D**) Hydrogeologic cross-sections in lines D0–D1.

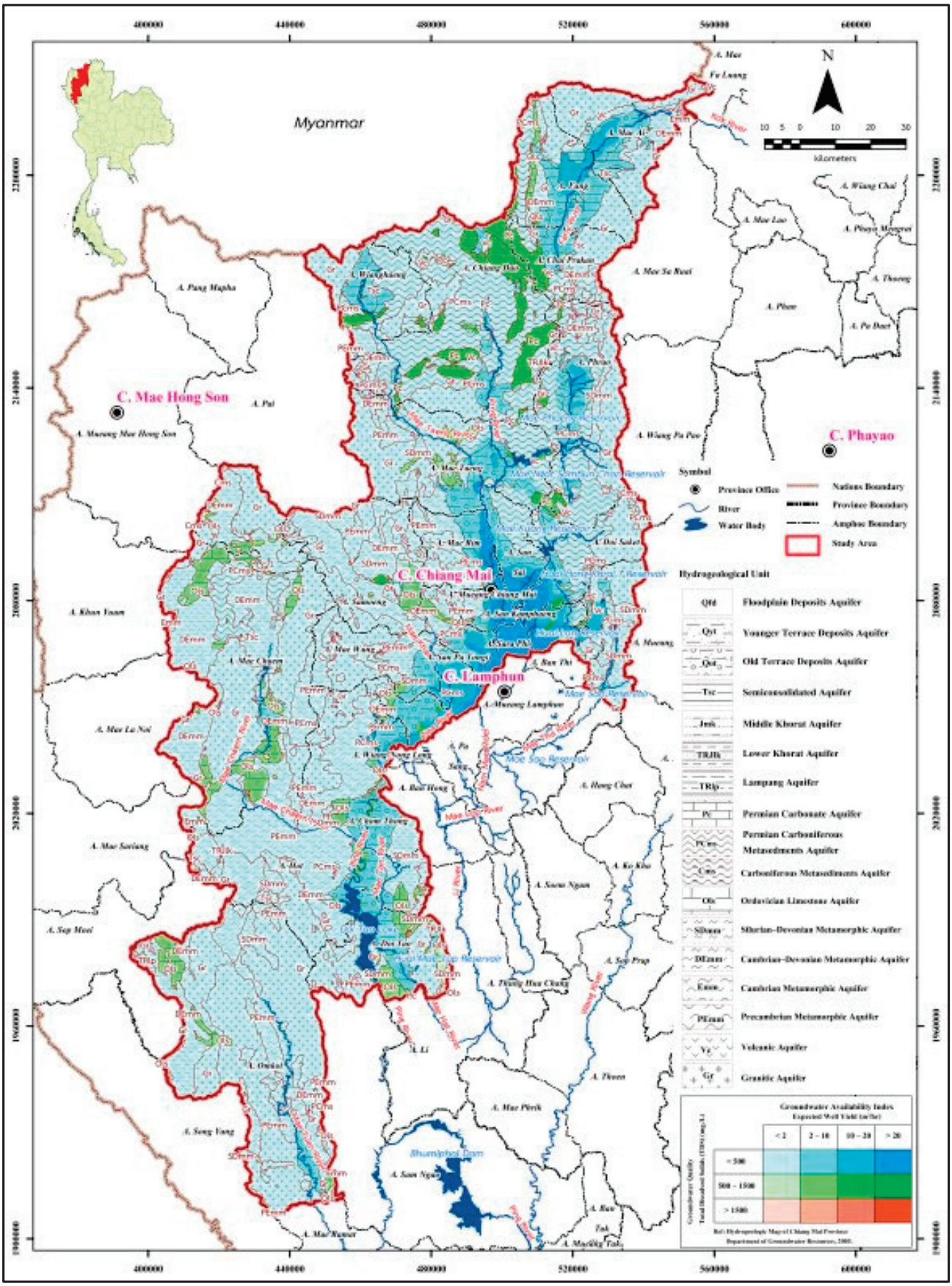

Figure 4. Groundwater potential map of Chiang Mai Province, Thailand.

3. Materials and Methods

3.1. Research Methodology

This study focuses on evaluating the vulnerability of groundwater resources to pollution loads, stemming from both natural and anthropogenic sources. The assessment aims to gauge the risk of groundwater resource vulnerability in Chiang Mai Province, utilizing a new DRASTIC-LP model. This model integrates groundwater resource vulnerability, climate change scenarios featuring very high greenhouse gas emissions (RCP8.5 scenario), land-use change scenarios, and anthropogenic source points, as identified through the CA_Markov Chain model [45].

The overarching goal is to provide insights into future groundwater resource vulnerability management. Identifying areas that are more susceptible to contamination from both natural and anthropogenic sources has become a pivotal aspect for land-use planning and comprehensive resource management in the northern region of Thailand. This study adheres to the established criteria and employs conventional research methodology, ensuring the reliability and efficient management of operating times. The conceptual framework of all the details of the research methodology is shown in Figure 5, and this also clarifies all aspects of the research methodology, tools, and equipment employed. This comprehensive approach not only strengthens the credibility of the study. but also contributes valuable information for informed decision making in groundwater resource management in Chiang Mai Province.

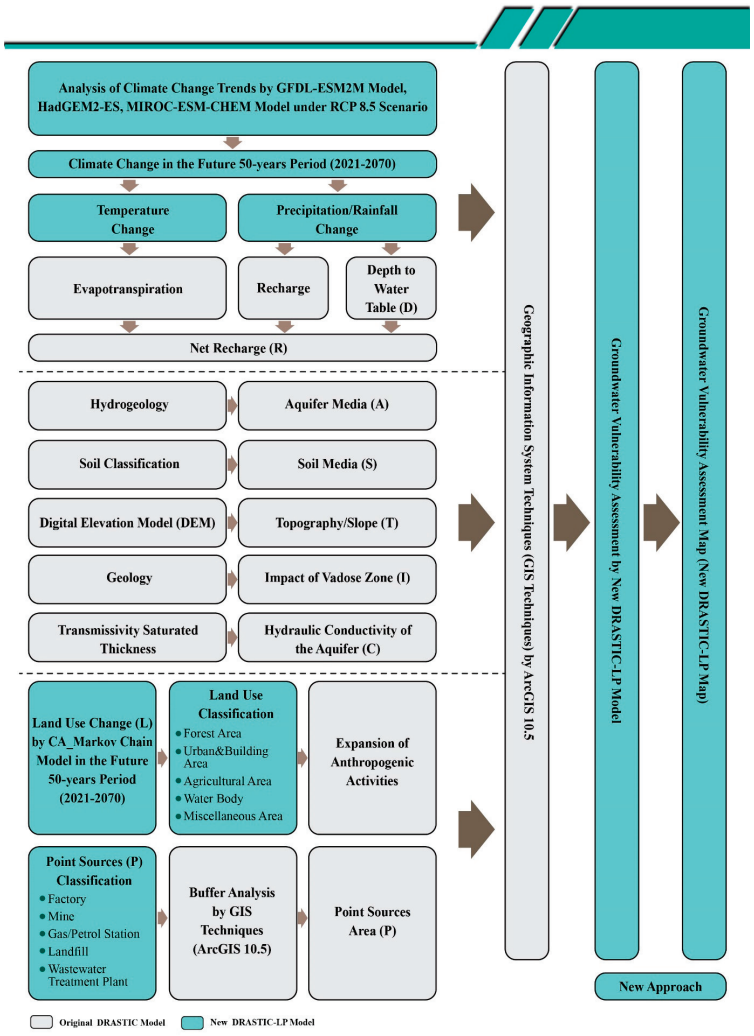

Figure 5. Conceptual framework of risk assessment of groundwater resource vulnerability in Chiang Mai Province, Thailand.

3.2. Data Analysis and Results of the Study

3.2.1. Climate Change Analysis

A performance analysis of the three general climate models (3GCMs), namely the GFDLSM2M model, the HadGEM2-ES model, and the MIROC-ESM-CHEM model, were compared to determine which model was most suitable for predicting both temperature and rainfall, according to the coefficient of determination (R^2 or R-square). From the study, it was revealed that the MIROC-ESM-CHEM model can simulate rainfall behavior in the 30-year period (1991–2020), corresponding to past rainfall behaviors, according to the coefficient of determination (max R^2 = 0.5991); this does so in a much more effective way than the HadGEM2-ES model (max R^2 = 0.5613), and GFDLSM2M model (max R^2 = 0.4503).

1. Monthly temperature data from the 30-year period (1991–2020), provided by the Thai Meteorological Department (TMD) [46] in Chiang Mai Province and its surrounding areas, were collected from eight meteorological stations. These stations were included the Mae Sariang Weather Station (300202), the Mae Hong Son Meteorological Station (300201), the Chiang Mai Meteorological Station (Northern Meteorological Center) (327501), the Lampang Agricultural Weather Station (328301), the Lampang Meteorological Station (328201), the Lamphun Meteorological Station (329201), and the Chiang Rai Meteorological Station (303201). Changes in monthly temperatures over the specified period are depicted in Figure 6.

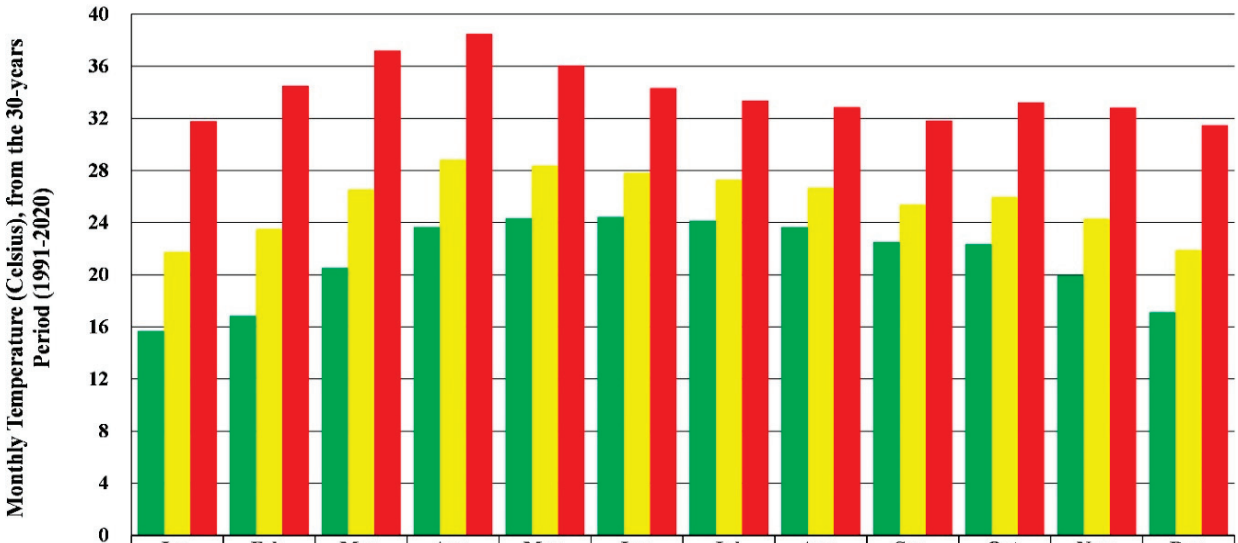

	Jan.	Feb.	Mar.	Apr.	May.	Jun.	Jul.	Aug.	Sep.	Oct.	Nov.	Dec.
Minimum	15.67	16.86	20.52	23.66	24.33	24.43	24.15	23.65	22.52	22.34	19.95	17.13
Average	21.76	23.51	26.55	28.83	28.37	27.82	27.29	26.68	25.39	25.97	24.30	21.90
Maximum	31.78	34.49	37.19	38.48	36.05	34.33	33.38	32.87	31.83	33.22	32.83	31.48

Figure 6. Monthly temperature data from the 30-year period (1991–2020) in Chiang Mai Province.

An analysis of future temperature situations by the MIROC-ESM-CHEM model under the RCP8.5 scenario (very high greenhouse gas (GHG) emissions) is shown in Table 2 and Figure 7. The minimum temperature during the 30-year period (1991–2020) is 20.07 °C for the months of December to February. During the decade of 2021–2030, the minimum temperature is predicted to drop to 18.68 °C, a decrease of −1.38 °C from the 30-year period (1991–2020). Additionally, during the 30-year period (1991–2020), the maximum temperature is 32.08 °C. In the future, specifically across five periods, 2021–2030, 2031–2040, 2041–2050, 2051–2060, and 2061–2070, the maximum temperature is predicted to be 33.44 °C, 33.09 °C, 33.88 °C, 35.43 °C, and 35.48 °C, respectively, with an increase over the 30 years (1991–2020) between +1.02 °C to +3.40 °C. The overall average temperature for the 30 years (1991–2020) is 25.62 °C, while this is predicted to increase from +0.17 °C to +2.55 °C over the 30-year period (1991–2020).

Table 2. Analysis of future temperature situations with the MIROC-ESM-CHEM model under the RCP8.5 scenario.

Month	Average Monthly Temperature (Celsius)					
	Obs.	MIROC-ESM-CHEM under RCP8.5 Scenario; Year				
	1991–2020	2021–2030	2031–2040	2041–2050	2051–2060	2061–2070
January	21.62	21.80	22.62	17.55	24.09	21.37
February	22.86	22.77	24.15	21.84	25.87	24.87
March	26.38	26.54	24.35	27.85	27.48	29.48
April	28.69	29.16	29.38	29.29	31.44	32.53
May	28.38	31.26	28.61	33.03	32.20	29.84
June	27.85	31.68	26.14	29.84	32.16	29.70
July	27.33	28.54	27.02	27.81	28.86	29.16
August	26.83	27.02	27.03	28.73	28.42	29.94
September	25.63	26.57	27.91	28.95	28.55	29.82
October	25.97	25.34	26.54	27.45	28.50	29.15
November	24.23	22.50	25.04	24.97	26.63	27.20
December	21.71	19.55	20.75	22.66	22.39	25.05
Average	25.62	26.06	25.80	26.66	28.05	28.18
Diff. (Obs.-Model), °C		0.44	0.17	1.04	2.43	2.55
Percentage, %		1.71	0.67	4.06	9.47	9.96

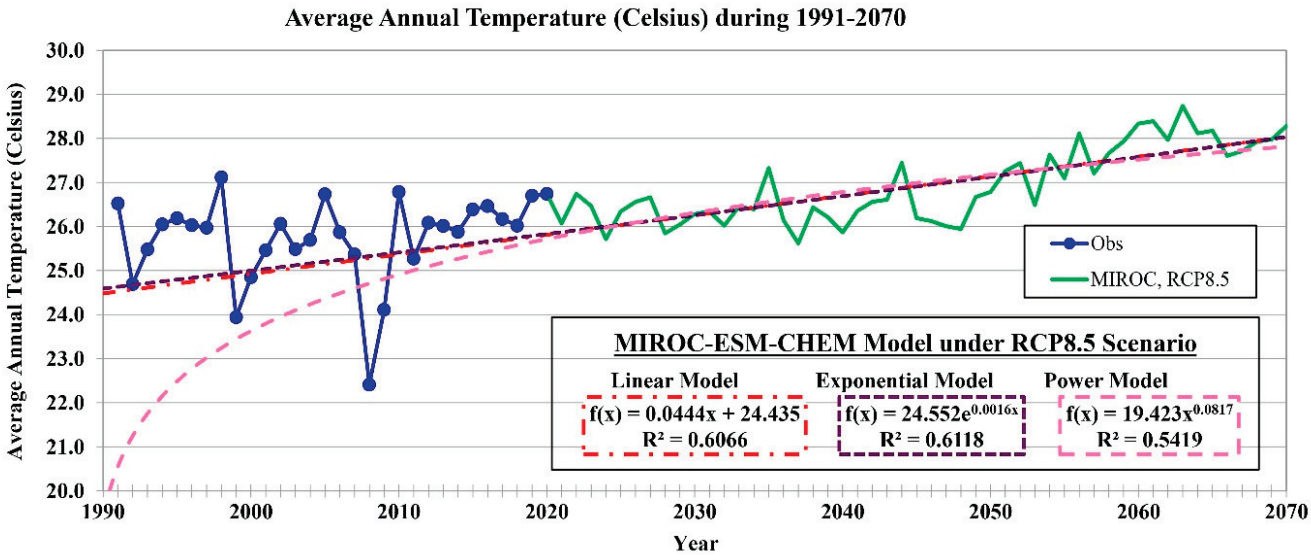

Figure 7. Future temperature situations by the MIROC-ESM-CHEM model under the RCP8.5 scenario.

2. Monthly rainfall data from the same period from the Thai Meteorological Department (TMD) [47], which included 39 stations, and the Royal Irrigation Department (RID) [48], which included 10 stations, but here, the extreme rainfall values were gathered. The continuous monthly rainfall data over a five-year period were used to analyze an average, minimum, and maximum monthly rainfall, as shown in Figure 8.

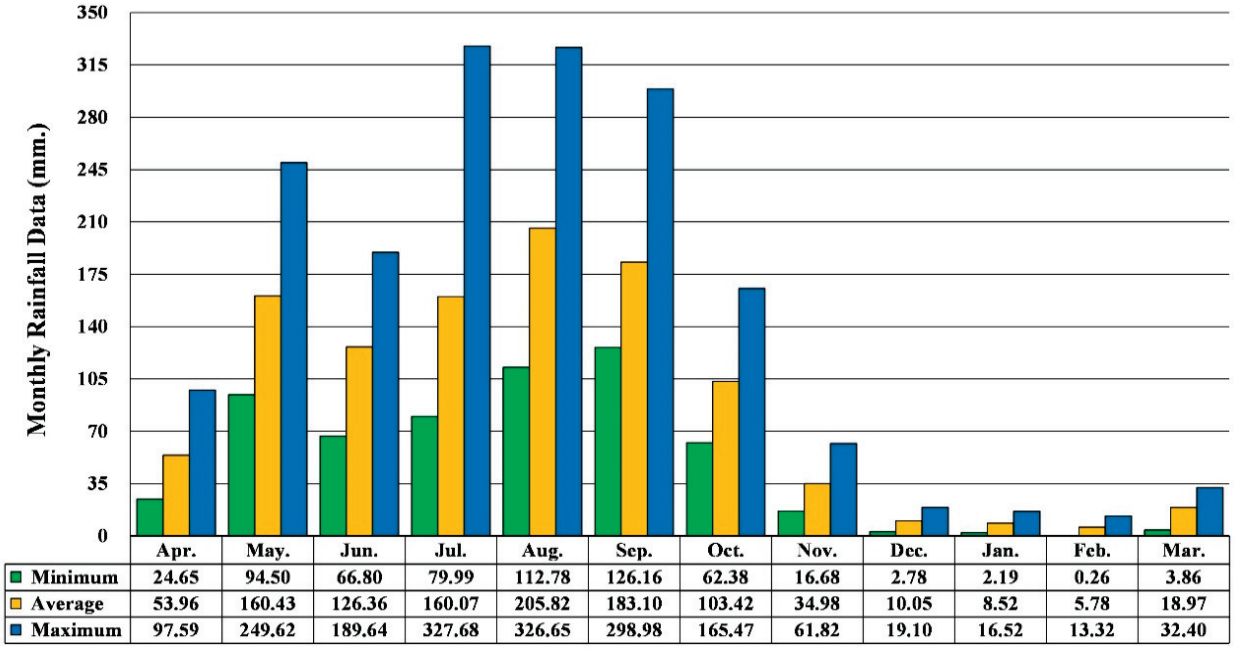

	Apr.	May.	Jun.	Jul.	Aug.	Sep.	Oct.	Nov.	Dec.	Jan.	Feb.	Mar.
Minimum	24.65	94.50	66.80	79.99	112.78	126.16	62.38	16.68	2.78	2.19	0.26	3.86
Average	53.96	160.43	126.36	160.07	205.82	183.10	103.42	34.98	10.05	8.52	5.78	18.97
Maximum	97.59	249.62	189.64	327.68	326.65	298.98	165.47	61.82	19.10	16.52	13.32	32.40

Figure 8. Average, minimum, and maximum monthly rainfall data (mm.), from the 30-year period (1991–2020) in Chiang Mai Province.

Analysis of future rainfall situations by MIROC-ESM-CHEM model under RCP8.5 scenario (very high greenhouse gas (GHG) emissions) as shown in Table 3 and Figure 9. During the 30–year period (1991–2020), the average annual rainfall is 1071.43 mm/year. From the prediction of the model, in the decade of 2021–2030, the average annual rainfall is predicted to be 1241.36 mm/year, with a trend increasing of +15.86% over the 30–year period (1991–2020). During the rainy season (July to October) in this decade (2021–2030), the model predicts to be 209.13–290.25 mm., and the highest monthly rainfall in September is 290.25 mm/year. Moreover, in the decade of 2031–2040, the average annual rainfall is predicted to 1241.36 mm/year, with an increasing trend of +15.86% over than the 30–year period (1991–2020). The overall average annual rainfall for three periods: 2041–2050, 2051–2060, and 2061–2070, the model predicts to be 1377.25, 1250.12, and 1339.16 mm/year, respectively. Their average annual rainfall of them, predicted to increase of +16.68% to +28.54%, over the 30–year period (1991–2020).

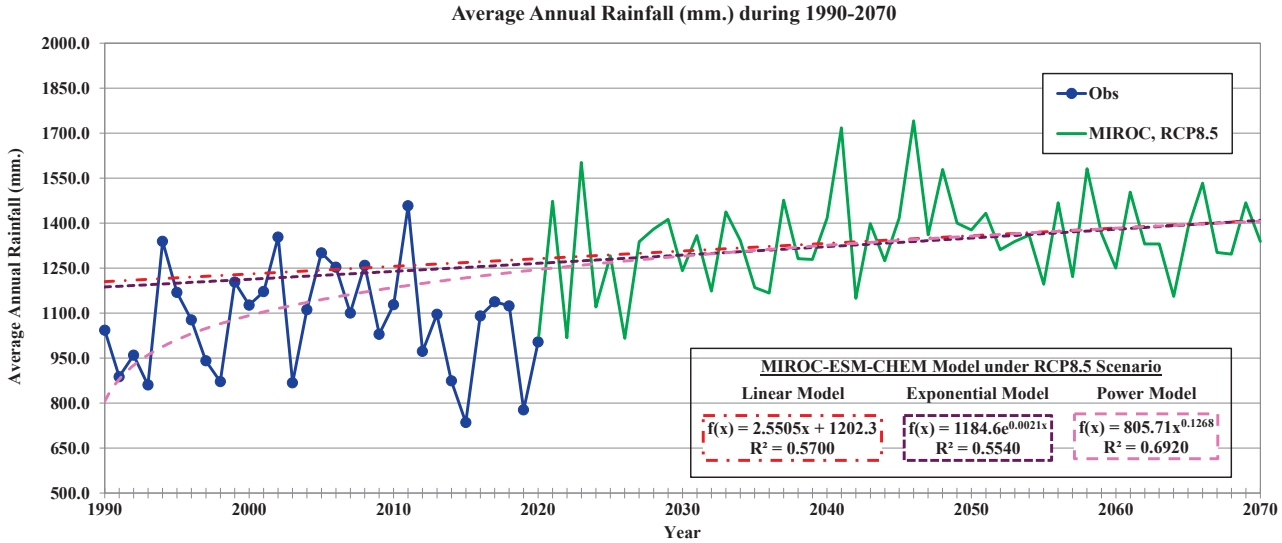

Figure 9. Future rainfall situations using the MIROC-ESM-CHEM model under the RCP8.5 scenario.

Table 3. Analysis of future rainfall situations using the MIROC-ESM-CHEM model under the RCP8.5 Scenario.

Month	Average Monthly Rainfall (mm.)					
	Obs.	MIROC-ESM-CHEM under RCP8.5 Scenario; Year				
	1991–2020	2021–2030	2031–2040	2041–2050	2051–2060	2061–2070
January	8.52	0.51	0.74	11.11	0.97	0.28
February	5.78	1.45	1.21	0.63	1.99	0.39
March	18.97	5.88	80.62	0.85	9.69	6.60
April	53.96	56.84	37.64	93.13	114.97	56.28
May	160.43	87.46	202.90	54.80	82.21	153.49
June	126.36	63.21	209.01	149.00	66.25	163.25
July	160.07	233.26	162.12	204.95	274.34	205.42
August	205.82	290.25	321.52	241.88	280.01	275.15
September	183.10	270.59	225.09	257.89	161.14	306.66
October	103.42	209.13	135.72	320.45	238.75	133.45
November	34.98	18.32	35.37	32.95	3.85	34.92
December	10.05	4.45	4.64	9.61	15.98	3.27
Average Annual Rainfall	1071.43	1241.36	1416.58	1377.25	1250.12	1339.16
Diff. (Model-Obs.), mm.		169.93	345.15	305.82	178.69	267.73
Percentage, %		15.86	32.21	28.54	16.68	24.99

3.2.2. Land-Use Pattern Change Analysis

Satellite data from Landsat-5 and Landsat-8 covering 2001, 2011, and 2020, with a resolution of 30 × 30 m per pixel, has been imported and examined. The existing land-use patterns are applied by a level one land-use map in Chiang Mai Province (GIS), with a scale of 1:25,000 of the Land Development Department (LDD) [49]. These land-use patterns are divided into six categories, namely (i) agricultural areas, (ii) community and buildings areas, (iii) industrial areas, (iv) forest areas, (v) water body, and (vi) miscellaneous areas. A total of twelve scenes of satellite data (Landsat-5/Landsat-8) covering 2001, 2011, and 2020, amounting to four scenes/year, were utilized.

An analysis of trends in land-use pattern changes, as well as community and urban expansion, is undertaken by comparing the changes in land-use patterns over the past 20-year period (2001–2020) using Landsat-8 satellite imagery from 2001, 2011, and 2020. The land-use patterns map for Chiang Mai Province (GIS), 2001, 2011, and 2020, with a scale of 1:25,000 of the Land Development Department (LDD), is shown in Figure 10. Additionally, a topographic map with a scale of 1:4000 (DEM: Digital Elevation Model) is used to verify the accuracy of land-use patterns. Field investigations were conducted in the following time periods: February to March 2020, May to June 2020, and November to December 2020.

An analysis of trends in future land-use patterns changes is conducted for every ten-year period (2030, 2040, 2050, 2060, and 2070) using land-use pattern databases from 2020, in conjunction with Chiang Mai Province Comprehensive Plan. This analysis employs the CA_Markov Chain Model (Cellular Automata and Markov Chain Model) [33], verified at least 5 times to ensure validity and reliability. The analysis of trends in each future land-use pattern changes over a 50-year period (2021–2070) in Chiang Mai Province is represented in Geographic Information System (GIS) maps, as shown in Figure 11 and Table 4.

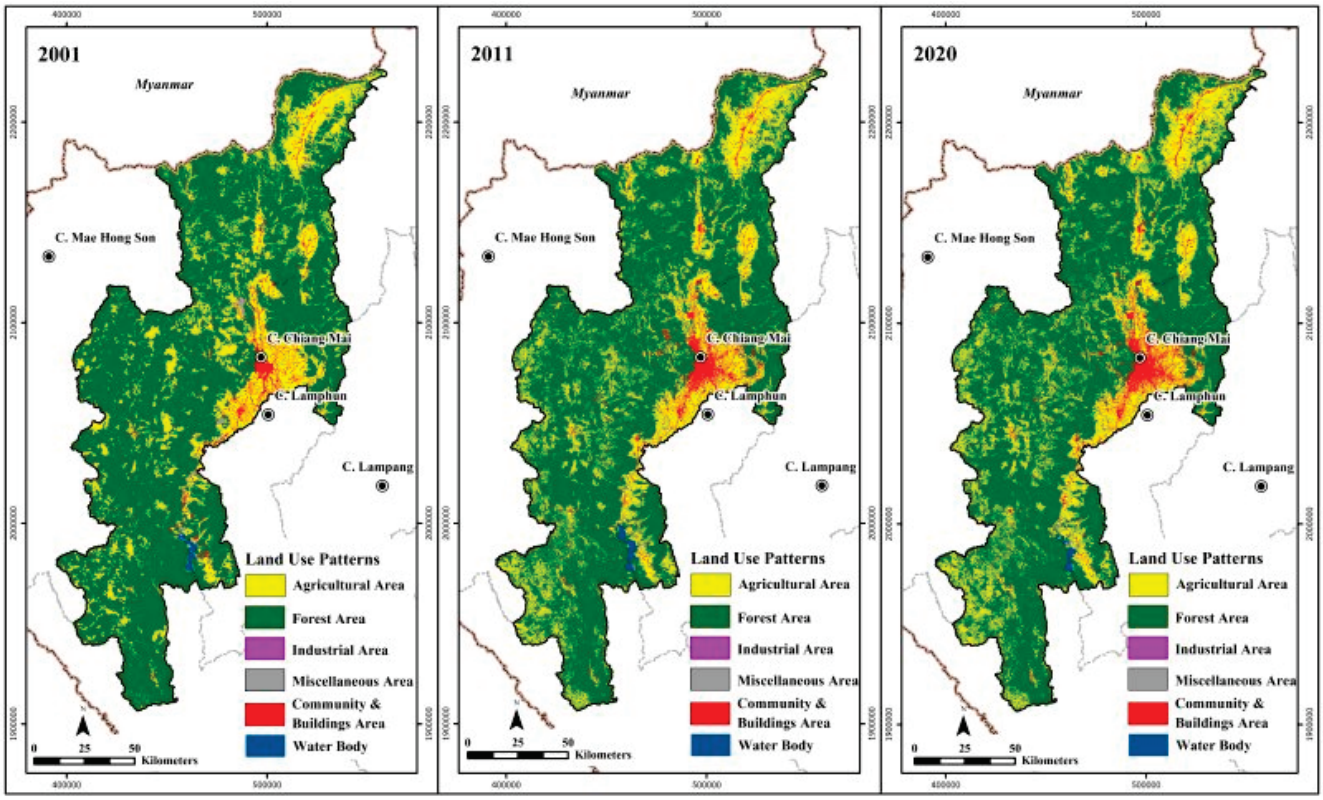

Figure 10. Land-use patterns of Chiang Mai Province level 1 (2001, 2011, and 2020).

Table 4. An analysis of the land-use patterns over a future 50-year period (2021–2070) using the CA_Markov Chain model and GIS-based techniques, covering the area of Chiang Mai Province, totaling 20,107.06 sq.km. or 12,566,912.50 rais.

	Land-Use Pattern Categories	Land-Use Pattern [1,2]					
		2020		2030		2040	
		(sq.km.)	%	(sq.km.)	%	(sq.km.)	%
1.	Agricultural Areas	4718.06	23.46	4906.61	24.40	5066.68	25.20
2.	Community and Building Areas	792.20	3.94	854.06	4.25	901.16	4.48
3.	Industrial Areas	25.05	0.12	25.76	0.13	29.87	0.15
4.	Forest Areas	14,059.72	69.92	13,847.78	68.87	13,641.06	67.84
5.	Water Body	193.68	0.96	170.45	0.85	158.48	0.79
6.	Miscellaneous Areas	318.35	1.58	302.39	1.50	309.81	1.54
	Total Areas	20,107.06	100.00	20,107.06	100.00	20,107.06	100.00
	Land-Use Pattern Categories	**Land-Use Pattern [1,2]**					
		2050		**2060**		**2070**	
		(sq.km.)	**%**	**(sq.km.)**	**%**	**(sq.km.)**	**%**
1.	Agricultural Areas	5190.33	25.81	5304.45	26.38	5401.77	26.87
2.	Community and Building Areas	984.16	4.89	1047.04	5.21	1104.86	5.49
3.	Industrial Areas	41.24	0.21	44.56	0.22	46.61	0.23
4.	Forest Areas	13,430.25	66.79	13,239.69	65.85	13,080.07	65.05
5.	Water Body	148.27	0.74	155.91	0.78	152.66	0.76
6.	Miscellaneous Areas	312.81	1.56	315.42	1.57	321.09	1.60
	Total Areas	20,107.06	100.00	20,107.06	100.00	20,107.06	100.00

Table 4. *Cont.*

	Land-Use Pattern Categories	Land-Use Pattern Change [1/,2/]				Ratio of Annual Change	
		2020–2030		2020–2070		2020–2070	
		(sq.km.)	%	(sq.km.)	%	(sq.km.)	%
1.	Agricultural Areas	61.86	0.21	683.71	3.40	13.67	0.29
2.	Community and Building Areas	0.72	0.03	312.65	1.55	6.25	0.79
3.	Industrial Areas	188.55	0.25	21.57	0.11	0.43	1.72
4.	Forest Areas	−211.94	0.17	−979.65	−4.87	−19.59	−0.14
5.	Water Body	−23.23	−0.37	−41.02	−0.20	−0.82	−0.42
6.	Miscellaneous Areas	−5.96	−0.13	2.74	0.01	0.05	0.02

Notes: [1/] An analysis of the land-use patterns in a future 50-year period (2021–2070), using the CA_Markov Chain Model and a GIS-based technique; [2/] Area size is calculated by ArcGIS 10.5.

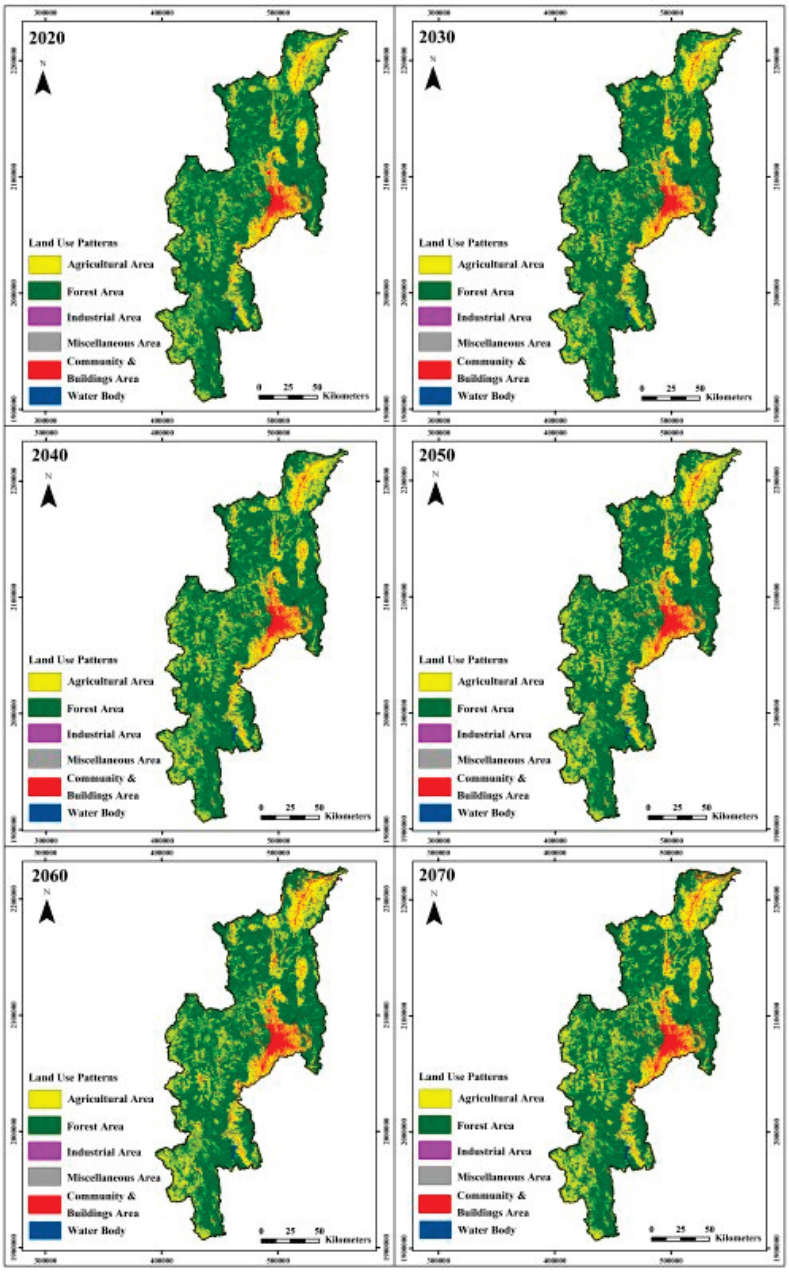

Figure 11. Land-use patterns of baseline (2020) and future 50-year periods (2021–2070), using the CA_Markov Chain model and GIS-based techniques.

3.2.3. An Assessment of the Vulnerability of Groundwater Resources

A process for analyzing the groundwater vulnerability in Chiang Mai Province, using the new DRASTIC-LP model, are shown in Figure 5. It can be explained as follows:

1. Normally, either the traditional method or the original DRASTIC model [11] are used for groundwater vulnerability analysis. This research proposed a new approach to groundwater vulnerability assessments by adding two essential extra indexes, which are land-use pattern (L) and point source pollutions (P), into the conventional DRASTIC Equation (1), as follows:

$$\text{DRASTIC Index } (D_i) = D_r D_w + R_r R_w + A_r A_w + S_r S_w + T_r T_w + I_r I_w + C_r C_w + L_r L_w + P_r P_w \quad (1)$$

D = Depth-to-water table

R = Net recharge has been considered from the amount of rainfall in the area and the rate of rainwater infiltration by the soil-type classification of the Land Development Department (LDD) [50], as shown in Equation (2):

$$r = 0.24(i) + 3.20 \quad (2)$$

The permeability rate was assessed using the percentage of rainfall (r) and the soil permeability coefficient (i), measured using centimeters per hour (cm/hr).

R = Rainfall × Percentage of the permeability rate of water

A = Aquifer media

S = Soil media

T = Topography

I = Impact of vadose zone

C = Hydraulic conductivity of the aquifer

L = Land-use patterns

P = Point sources

r = Weighting values of hydrogeological factors by new DRASTIC-LP model

w = The weights of each determining factor for new DRASTIC-LP model as detailed in Table 5 [11,51].

2. The analysis of vulnerability of the overall groundwater aquifers to pollution is calculated from both secondary data and primary data, obtained from the field investigations.

(a) Depth-to-water table (D): The groundwater development is mainly drilled wells, which are less than 150 m deep. To simulate future net recharge (R) on a large scale, assumptions are proposed based on the very high greenhouse gas (GHG) emissions, using the RCP8.5 scenario provided by the MIROC-ESM-CHEM model. Equation (3), which was used to calculate the depth-to-water table (D), is based on Huang et al. [15]:

$$D = \Delta R(t_i) + H(t_i) \quad (3)$$

$\Delta R(t_i)$ = net recharge occurring between initial time t_0 and ending time t_i; and $H(t_i)$ = baseline depth-to-water table (D), attributed to the recharge period. The predicted scores of the depth-to-water table (D) for the baseline (2020) and the future 50-year periods (2021–2070) are shown in Figure 12.

(b) Net Recharge (R): Considering annual rainfall statistical data from the 30-year period (1991–2020), the rate of rainwater infiltration by the soil-type classification of the Land Development Department (LDD) [50] can be obtained from Equation (2): r = 0.24(i) + 3.20. The permeability rate is assessed as the percentage of rainfall (r) and the soil permeability coefficient (i) in centimeters per hour (cm/h) from the following equation: R = Rainfall × Percentage of the permeability coefficient. The predicted scores of net recharges (R) for the baseline (2020) and the future 50-year period (2021–2070) are shown in Figure 13.

(c) Aquifer Media (A): Considering the aquifer according to the hydrogeological rock unit, there are a total of 17 rock units. Unconsolidated sediment has permeability rates, depending on the properties of the sediment, such as grain size, sorting, and sediment binding, etc. Types of aquifers include fluvial deposit aquifers (Qfd), young terrace deposit

aquifers (Qyt), and old terrace deposit aquifers (Qot), while consolidated rocks are highly fractured with high groundwater permeability.

(d) Soil Media (S): This depends on soil texture and soil depth (less than 1.80 m from the soil surface [50]). Soil characteristics are divided into two types, namely clay varieties (low-lying plain with clay, clay mixed with sandstone fragments, laterite, sandy clay, etc.), as well as terraces (slop complex).

(e) Topography or Slope (T): The plain basin on the east side, surrounded by high mountains, causes most areas to have a slope of >18%, accounting for 70% of the total area. Some areas have a slope of <2% (relatively flat), accounting for 9% of the total area.

(f) Impact of Vadose Zone (I): This is classified according to the characteristics of the soil and bedrock above the groundwater layer.

(g) Hydraulic Conductivity of the Aquifer (C): Data obtained from the pumping tests of the main groundwater resources [51] reveal permeability coefficients between 1.0–10.0 m/day.

(h) Land-use patterns (L): These are divided into six types, namely (i) agricultural areas, (ii) forest areas, (iii) water body, (iv) community and building areas, (v) industrial areas, and (vi) miscellaneous. The scores of land-use patterns (L) are shown in Figure 11.

(i) Point Source Pollutions (P): Various anthropogenic activities consist of eight types of point source pollutions, including 233 landfills, 19 sanitary landfills, 457 factories at risk of contamination, 4 active mining sites related to heavy metal elements, 30 active mining sites (industrial quarry), 7 non-active mining sites (old mine), 216 Gas/Petrol Stations, and 1 wastewater treatment plant. A risk assessment for contamination toxics in groundwater resources is conducted using a buffer distance of 200 m from industrial point sources, as shown in Figure 14.

3. Data preparation for groundwater resource vulnerability assessments involves assessing the vulnerability of groundwater resources using a criteria-based vulnerability index with five levels, namely level 1 (very low), level 2 (low), level 3 (moderate), level 4 (high), and level 5 (very high).

4. The tools for analyzing groundwater vulnerability to pollution are as follows:

(a) ArcGIS Ver. 10.5, comprising a set of tools and commands, is utilized for spatial analysis in a raster-based analysis.

(b) The Model Builder is employed as a process for analyzing the new DRASTIC-LP model to obtain groundwater vulnerability index results (DRASTIC-LP Index Value) regarding pollution.

5. Geo-informatics technology (GIS-based techniques) is selected to create a new groundwater resource vulnerability map (DRASTIC-LP Map). This map is compared with the nitrate (NO_3^-) concentration in groundwater resources from various sources, including the Department of Groundwater Resources (DGR) [51], the Pollution Control Department (PCD, 2020), the Royal Irrigation Department (RID, 2020), and the Environment and Pollution Control Office 1 (Chiang Mai, 2020), etc. These groundwater samples indicate contamination from anthropogenic activities or natural conditions.

6. Calibration of groundwater resource vulnerability using nitrate (NO_3^-) concentration data from field sampling during the rainy (298 samples) and the winter (299 samples) seasons [51]. As nitrate is one of the most important pollutants in the environment, it causes environmental pollution by converting to nitrite (NO_2^-) compounds [52]. It is also found at sites of high levels from anthropogenic activity, such as sewage, septic tank leakages, community, and municipal solid waste. Nitrogen substances are used to make chemical fertilizers, livestock, or non-point pollutions source that runoff from agricultural areas [53]. Moreover, the nitrogen compounds produced by the decomposition of plants and animals accumulated in the soil are converted to nitrate (NO_3^-) compounds by bacteria. Plants absorb nitrogen compounds from the soil in the form of nitrate (NO_3^-) compounds. It can infiltrate into the ground and reach plant roots and, therefore, groundwater resources very easily by rainfall or runoff. Infants below six months old consuming water with high nitrate (NO_3^-) concentrations may experience serious health issues, become seriously

ill, and, if untreated, may die, not to mention conditions such as shortness of breath or blue-baby syndrome. The US EPA reported that when nitrate (NO_3^-) concentrations in groundwater resources exceed 1 mg/L, this indicates contamination from anthropogenic activities [54]. Additionally, concentrations exceeding 3 mg/L suggest contamination affecting domestic consumption [55]. The EPA's maximum contaminant level (MCL) for nitrate (NO_3^-) concentrations to protect against blue-baby syndrome must be over 10 mg/L. The groundwater threshold for monitoring should begin at 5.0 mg/L (Estimated Use of Water in the United States: USGS, 2005) [56], while the groundwater quality standard for drinking purposes, according to the notification of the Ministry of Natural Resources and Environment (2008) [55], is 45.0 mg/L for the maximum allowable concentration of nitrate (NO_3^-). The groundwater resource vulnerability is assessed by with groundwater nitrate (NO_3^-) concentrations from groundwater samples collected during the rainy season (September 2018 to November 2018), comprising 299 samples, and during the winter season (December 2018 to February 2019), consisting of 298 samples [51]. These findings are shown in Figure 15. The results showed concentrations exceeding 3 mg/L in 34 samples of the rainy season, or 11.37% of a total sample, and 4 samples of the winter season, or 8.30% of a total sample. The groundwater nitrate (NO_3^-) concentrations exhibit high vulnerability class in both the young terrace deposits aquifer (Qyt) and the old terrace deposits aquifer (Qot) (Figure 16). These groundwater resources, in both types of aquifers, are used in most intensive agricultural areas along the river bank and tributaries. These results are consistent with the existing literature and regulatory standards. Dubrovsky et al. [57] and Madison and Brunett [58] both indicate the EPA's maximum contaminant level (MCL), as well as the estimated use of water in the United States in 2005 [56], suggesting that groundwater resource vulnerability ranges from moderate to very high classes due to anthropogenic activities in these areas. Although the concentration values in some areas do not exceed the groundwater standard according to the EPA's maximum contaminant level (MCL) and estimated use of water in the United States in 2005 [56], the likelihood of contamination remains significant in areas with high anthropogenic activity.

7. Conventionally, groundwater resource vulnerability is analyzed with the original DRASTIC model (seven indexes) [11]. This research proposes a new approach for groundwater vulnerability analysis (the new DRASTIC-LP model) by adding two essential extra-indexes, which are two risk factors caused by anthropogenic activities: land-use patterns (L) and point source pollutions (P). Thus, groundwater vulnerability can be obtained from the following Equation (4):

$$\text{DRASTIC Index } (D_i) = D_r D_w + R_r R_w + A_r A_w + S_r S_w + T_r T_w + I_r I_w + C_r C_w + L_r L_w + P_r P_w \quad (4)$$

Additionally, groundwater resource vulnerability, as determined by the criteria for assessing the vulnerability index, is divided into 5 levels: <120.00 scores (level 1: very low), 120.00–140.00 scores (level 2: low), 140.01–160.00 scores (level 3: moderate), 160.01–180.00 scores (level 4: high), and >180.00 scores (level 5: very high). The distribution of groundwater vulnerability in Chiang Mai Province, considering the increasing risk factors from anthropogenic activities, land-use patterns (L), and point source pollutions or point sources (P), using the new DRASTIC-LP, is shown in Table 6 and Figure 17. These results reveal that the anthropogenic activities (L, P), and the depth-to-water table (D) directly influence vulnerability and the risk of pollution contaminant in groundwater resources. Moreover, the results of the analysis are more reliable than the conventional analysis as they are simulated in current conditions and situations. The analysis of the groundwater vulnerability using the new DRASTIC-LP model can be a better and more comprehensive analysis than the original DRASTIC model [11] and can also contribute to long-term resource management. Pollution levels are rapidly increasing due to the expansion of urban communities, intensive agricultural areas, and industries/factories/manufactures, etc., highlighting the importance of these results. National resources are heavily used with very few appropriate controls. The variety of pollution depends on the various land-use patterns, as well as point source pollutions. Moreover, the pollutants are directly correlated to the quality of

groundwater resources. Thus, the contamination of pollution to groundwater resources has to be seriously protected, in order to sustain these resources.

Table 5. Weights of each determining factor or weighting values for the new DRASTIC-LP model.

	Main Factor	Weighting Values	Index Score Interval	Score
1.	Depth-to-water table (D) [1/]	5 [1/]	<1.50 m.	10
			1.50–4.50 m.	9
			4.51–9.00 m.	7
			9.01–15.00 m.	5
			15.01–22.50 m.	4
			22.51–30.00 m.	3
			30.01–50.00 m	2
			>50.00 m.	1
2.	Net Recharge (R) [1/]	4 [1/]	<30.00 mm/year	1
			30.01–50.00 mm/year	2
			50.01–70.00 mm/year	4
			70.01–90.00 mm/year	5
			>90.00 mm/year	6
3.	Aquifer Media (A) [1/]	3 [1/]	Fluvial Deposits Aquifer, Qfd	9
			Young Terrace Deposits Aquifer, Qyt	9
			Old Terrace Deposits Aquifer, Qot	9
			Semi-consolidated aquifer, Tsc	6
			Middle Korat Aquifers, Jmk	6
			Lower Korat Aquifer, TRJlk	6
			Lampang Aquifer, TRlp	6
			Permian Carbonate Rocks Aquifer, Pc	7
			Permian-Carboniferous Metasediments Aquifers, PCms	6
			Carboniferous Metasediments Aquifer, Cms	6
			Silurian-Devonian Metamorphic, SDmm	3
			Ordovician Limestone Aquifer, Ols	8
			Cambrian-Devonian Metamorphic Aquifer, DEmm	3
			Cambrian Metamorphic Aquifer, Emm	3
			Precambrian Metamorphic Aquifer, PEmm	2
			Granitic Aquifer, Gr	4
			Volcanic Aquifer, Vc	3
4.	Soil Media (S) [1/]	2 [1/]	Clay consists of 40% or more of clay size particles, 45% or less of sand size particles, and less than 40% of silt size particles.	3
			Silt or silt loam	4
			Loam consists of 7–27% clay size particles, 28–50% silt size particles and less than 52% sand size particles	5
			Sand consists of 85% or more of sand size particles	6
			Terrace (slope complex)	6

Table 5. *Cont.*

	Main Factor	Weighting Values	Index Score Interval	Score
5.	Topography (Slope) (T) [1/]	1 [1/]	<2.00%	10
			2.01–6.00%	9
			6.01–12.00%	5
			12.01–18.00%	3
			>18.00%	1
6.	Impact of Vadose Zone (I) [1/]	5 [1/]	Alluvial deposits unit consists of sand, gravel, silt, clay, laterite. They are fluvial deposits (Qfd); young terrace deposits (Qyt); old terrace deposits (Qot)	9
			Limestone unit consists of limestone and dolomitic limestone. They are Ordovician limestone (Ols) and Permian limestone (Pc)	8
			Sedimentary rock and metasediment units consist of sandstone, shale, conglomerate, mudstone, etc. They are semi-consolidated rock (Tsc), Korat rock (Jmk/TRJlk), Lampang rock (TRlp), Permian Carbonate rocks, Carboniferous metasediments rock (Cms)	6
			Metamorphic and igneous units are Silurian-Devonian rock (SDmm), Cambrian-Devonian rock (DEmm), Metamorphic rock (Emm), Precambrian metamorphic rock (PEmm), Granitic rock (Gr), Volcanic rock (Vc)	4
7.	Hydraulic Conductivity of the Aquifer (C) [1/]	3 [1/]	<0.050 m/day	1
			0.051–0.100 m/day	2
			0.101–0.500 m/day	3
			0.501–1.000 m/day	4
			1.001–10.000 m/day	7
			>10.000 m/day	8
8.	Land-use Pattern (L)	5	Agricultural area	8
			Industrial area	8
			Water body	8
			Community and buildings area	5
			Miscellaneous area	3
			Forest area	1
9.	Point Source (P)	5	Landfill	10
			Sanitary landfill	8
			Factory	8
			Active mining related to heavy metal elements	9
			Active mining (industrial quarry)	7
			Non-active mining (old mine)	6
			Petrol/Gas station	8
			Wastewater treatment plant	5

Notes: Ref: [1/] Aller et al. [11]

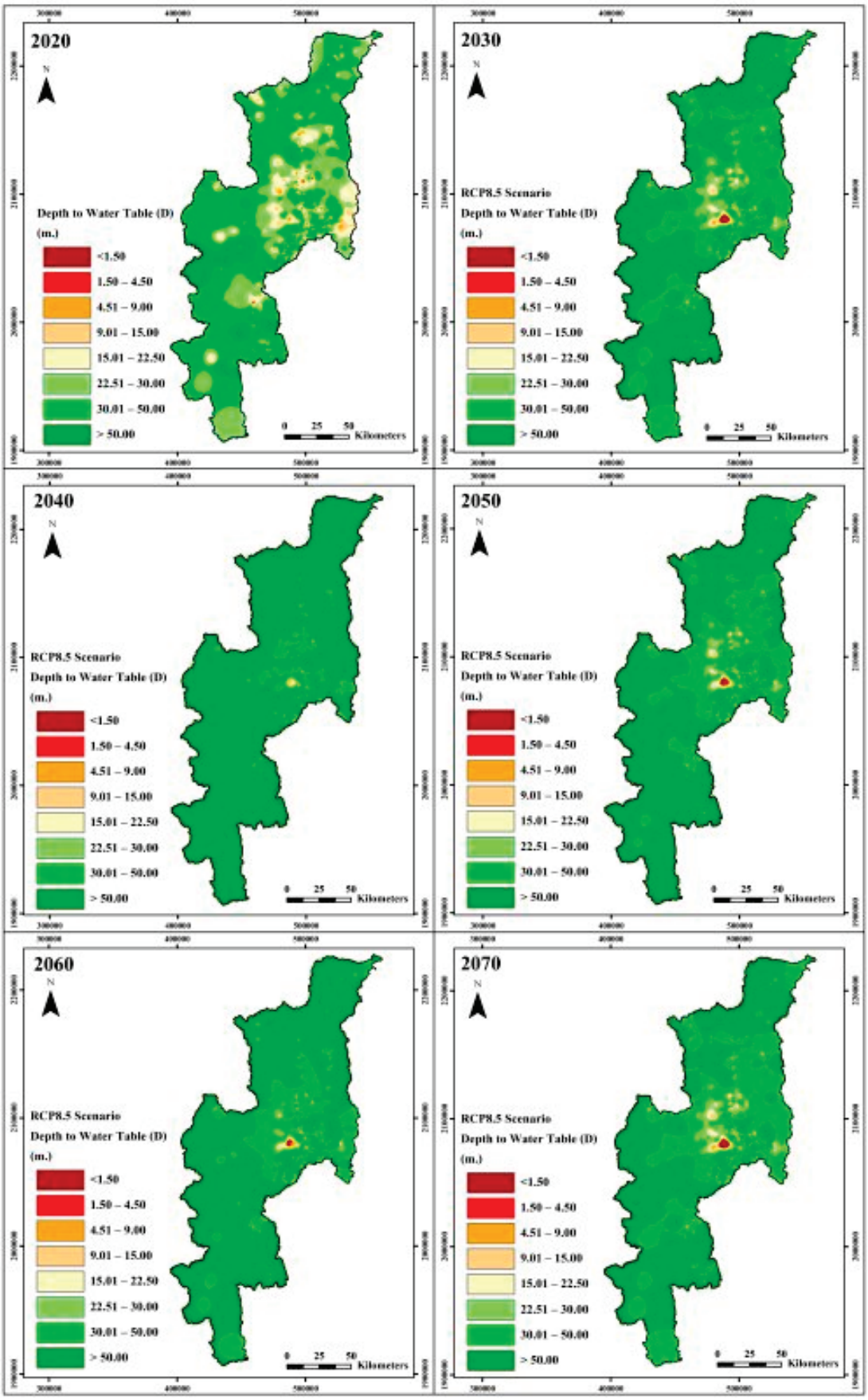

Figure 12. Depth-to-water table (D) of baseline (2020) and future (2030–2070) periods, using the MIROC-ESM-CHEM model with the RCP8.5 scenario.

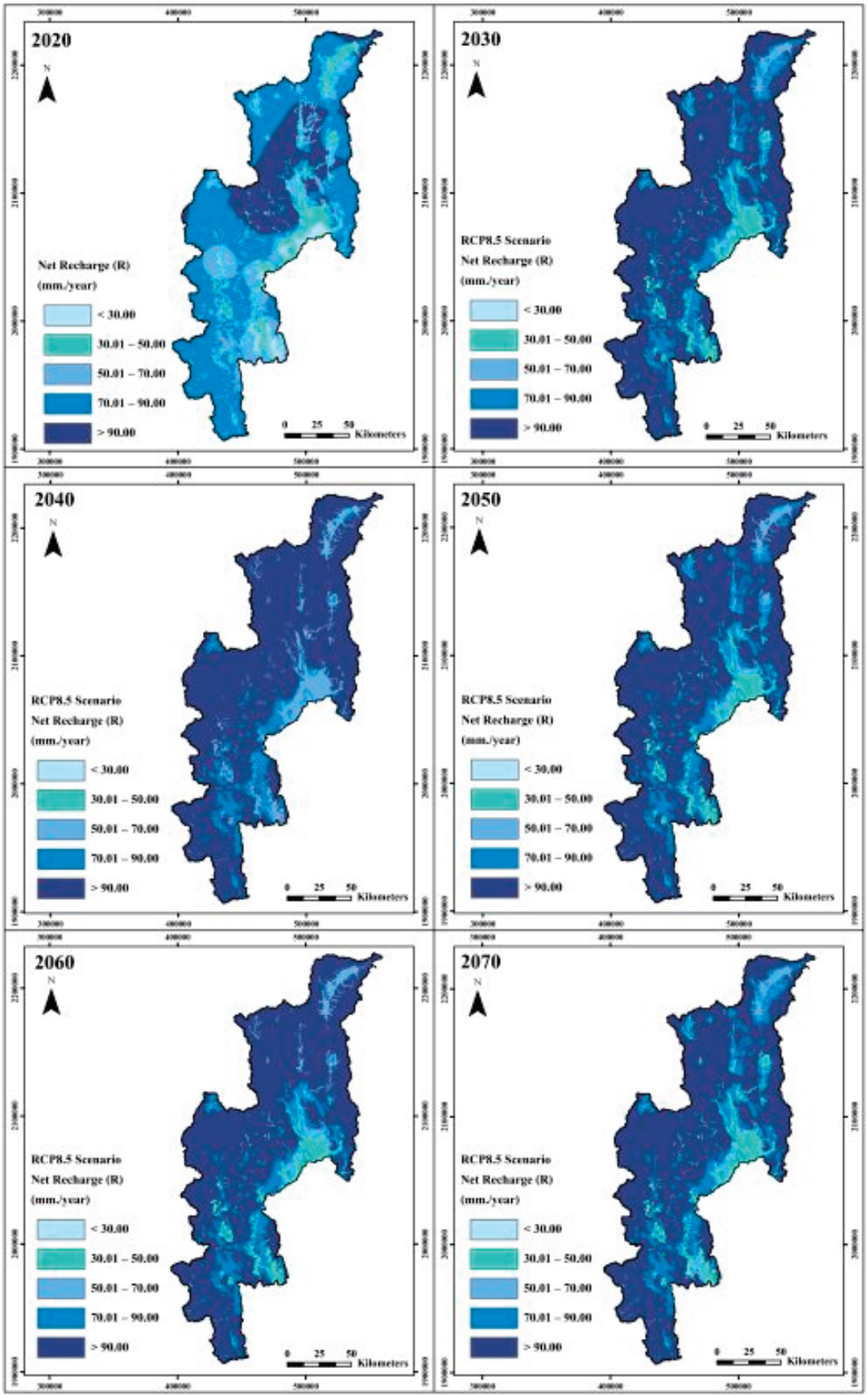

Figure 13. Net recharge (R) of baseline (2020) and future (2030–2070) periods, using the MIROC-ESM-CHEM model with the RCP8.5 scenario.

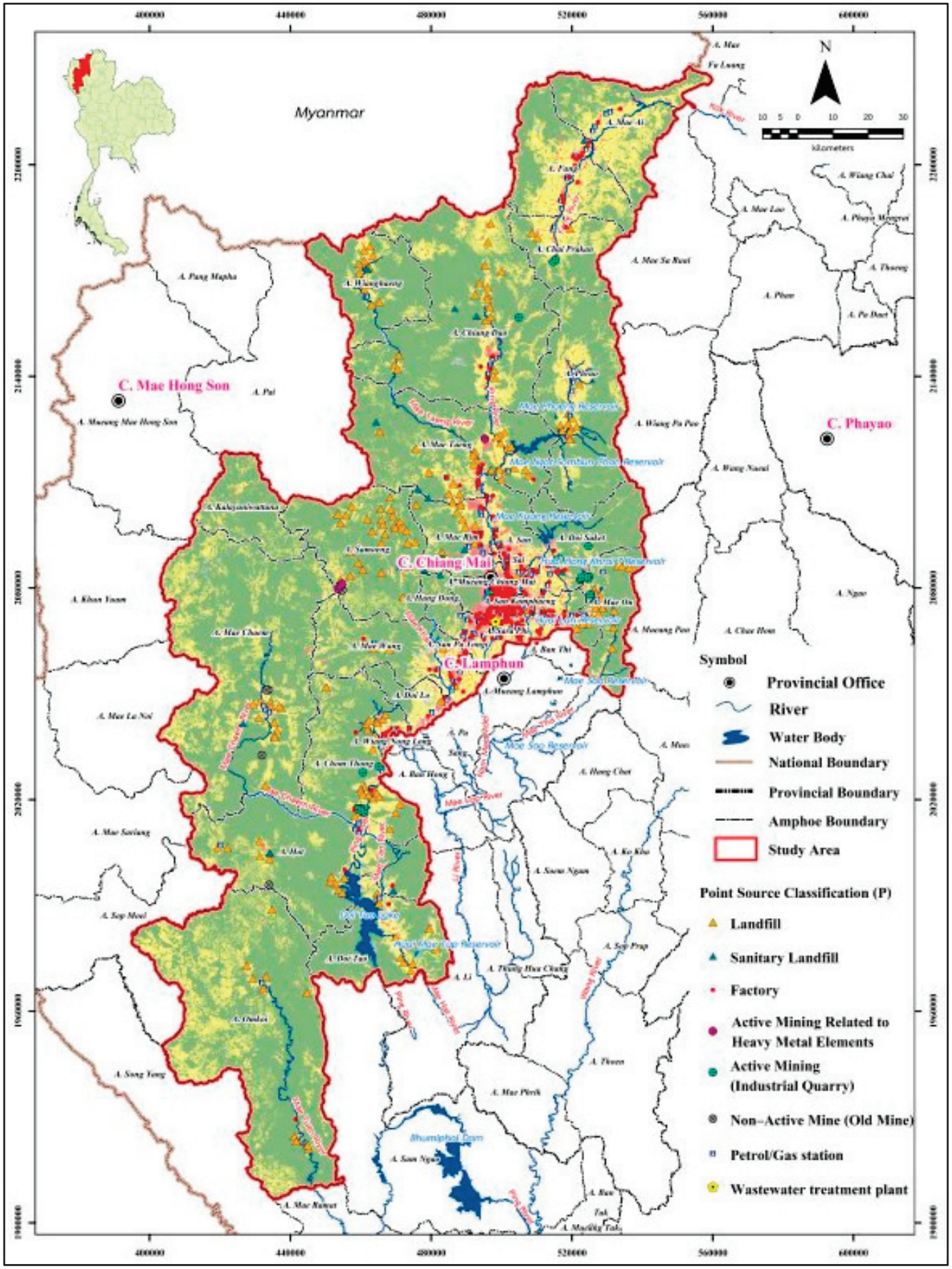

Figure 14. Point pollutions source (P) of baseline (2020) and future (2030–2070) periods.

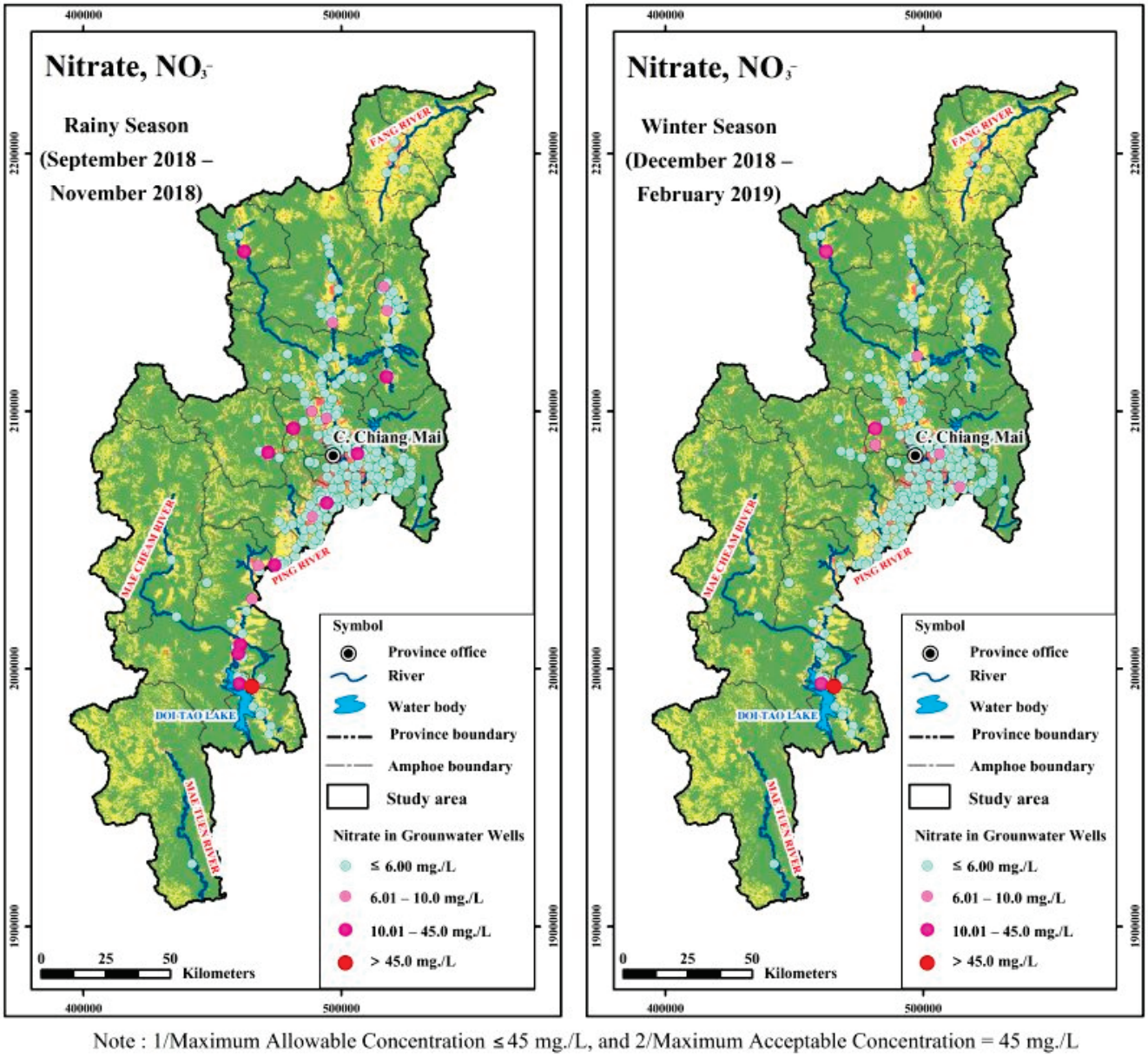

Figure 15. Distribution of groundwater nitrate (NO_3^-) concentrations in the rainy season (September 2018 to November 2018) and the winter season (December 2018 to February 2019).

8. An analysis of groundwater resource vulnerability using the new DRASTIC-LP model was conducted, comparing the present (2020) with the future situations over the 50-year period (2021–2070). Key factors considered include predictions of rainfall behavior under the RCP8.5 scenario [(very high greenhouse gas (GHG) emissions)] and the land-use patterns, as modeled by the CA_Markov Chain Model, which is one of the risk factors that influenced the change of the vulnerability of groundwater resources. These results highlight the trends of decreasing or increasing groundwater vulnerability projected by the MIROC-ESM-CHEM model for future periods of every 10 years (2021–2030, 2031–2040, 2041–2050, 2051–2060, and 2061–2070), as shown in Table 6 and Figure 17. The overall vulnerability changes in groundwater resources in Chiang Mai Province, Thailand during the period ranging 2000–2070 covers 20,107.06 sq.km., with percentages in vulnerability classes for very low (−5.10%), low (+3.44%), moderate (+0.48%), high (−0.24%), and very high (+1.41%). The anticipated groundwater vulnerability changes in the next 50 years (2021–2070) suggest significant shifts in groundwater vulnerability patterns under the

combined influence of climate change and land-use patterns, particularly under the RCP8.5 scenario. Some areas of Chiang Mai Province may face a high risk of groundwater pollution in this period (2021–2070), with vulnerability classes expanding from urban centers, the central business district (CBD), the medium-large industrial areas, and the intensive agricultural areas, etc., to surrounding areas, especially recharge areas and lowland areas along the main rivers, namely Nam Mae Ping, Nam Mae Kok, Nam Mae Khan, and Nam Mae Taeng, etc. These overall areas of vulnerability classes of moderate to very high will directly affect and increase the areas of expansion, corresponding to the risk of increasing groundwater pollution in the future. Furthermore, the areas of vulnerability classes of low to very low will also substantially decrease. Hence, the results affirm that the new DRASTIC-LP model in this study is able to effectively identify the potential areas of Chiang Mai Province, Thailand that are more vulnerable to groundwater pollution.

Table 6. Analysis of groundwater vulnerability by the New DRASTIC-LP model, comparing the rainfall behavior and land-use pattern situations of the baseline (2020) and future 10-year periods (2030, 2040, 2050, 2060, and 2070).

Contaminate Class	Index Values	New DRASTIC-LP		MIROC-ESM-CHEM Model [1/]					
		Present (2020)		RCP8.5 Scenario (2030)			RCP8.5 Scenario (2040)		
		Area		Area		Change	Area		Change
		(km^2)	%	(km^2)	%	%	(km^2)	%	%
Very Low	<120.00	14,789.43	73.55	15,166.77	75.43	+1.88	15,679.55	77.98	+4.43
Low	120.00–140.00	2066.23	10.28	1708.12	8.50	−1.78	1260.91	6.27	−4.01
Moderate	140.01–160.00	1090.13	5.42	1025.93	5.10	−0.32	863.56	4.29	−1.13
High	160.01–180.00	1718.64	8.55	1818.32	9.04	+0.50	2031.15	10.10	+1.55
Very High	>180.00	442.63	2.20	387.91	1.93	−0.27	271.89	1.35	−0.85

Contaminate Class	Index Values	New DRASTIC-LP		MIROC-ESM-CHEM Model [1/]					
		Present (2020)		RCP8.5 Scenario (2050)			RCP8.5 Scenario (2060)		
		Area		Area		Change	Area		Change
		(km^2)	%	(km^2)	%	%	(km^2)	%	%
Very Low	<120.00	14,789.43	73.55	15,306.31	76.12	+2.57	15,300.11	76.09	+2.54
Low	120.00–140.00	2066.23	10.28	1597.81	7.95	−2.33	1545.01	7.68	−2.59
Moderate	140.01–160.00	1090.13	5.42	1025.26	5.10	−0.32	1089.43	5.42	−0.00
High	160.01–180.00	1718.64	8.55	1831.98	9.11	+0.56	1833.12	9.12	+0.57
Very High	>180.00	442.63	2.20	345.69	1.72	−0.48	339.39	1.69	−0.51

Contaminate Class	Index Values	New DRASTIC-LP		MIROC-ESM-CHEM Model [1/]		
		Present (2020)		RCP8.5 Scenario (2070)		
		Area		Area		Change
		(km^2)	%	(km^2)	%	%
Very Low	<120.00	14,789.43	73.55	14,900.39	74.11	+0.55
Low	120.00–140.00	2066.23	10.28	1890.64	9.40	−0.87
Moderate	140.01–160.00	1090.13	5.42	1136.32	5.65	+0.23
High	160.01–180.00	1718.64	8.55	1810.66	9.01	+0.46
Very High	>180.00	442.63	2.20	369.05	1.84	−0.37

Note: [1/] MIROC-ESM-CHEM Model can simulate rainfall behavior across the 50-year period (2021–2070).

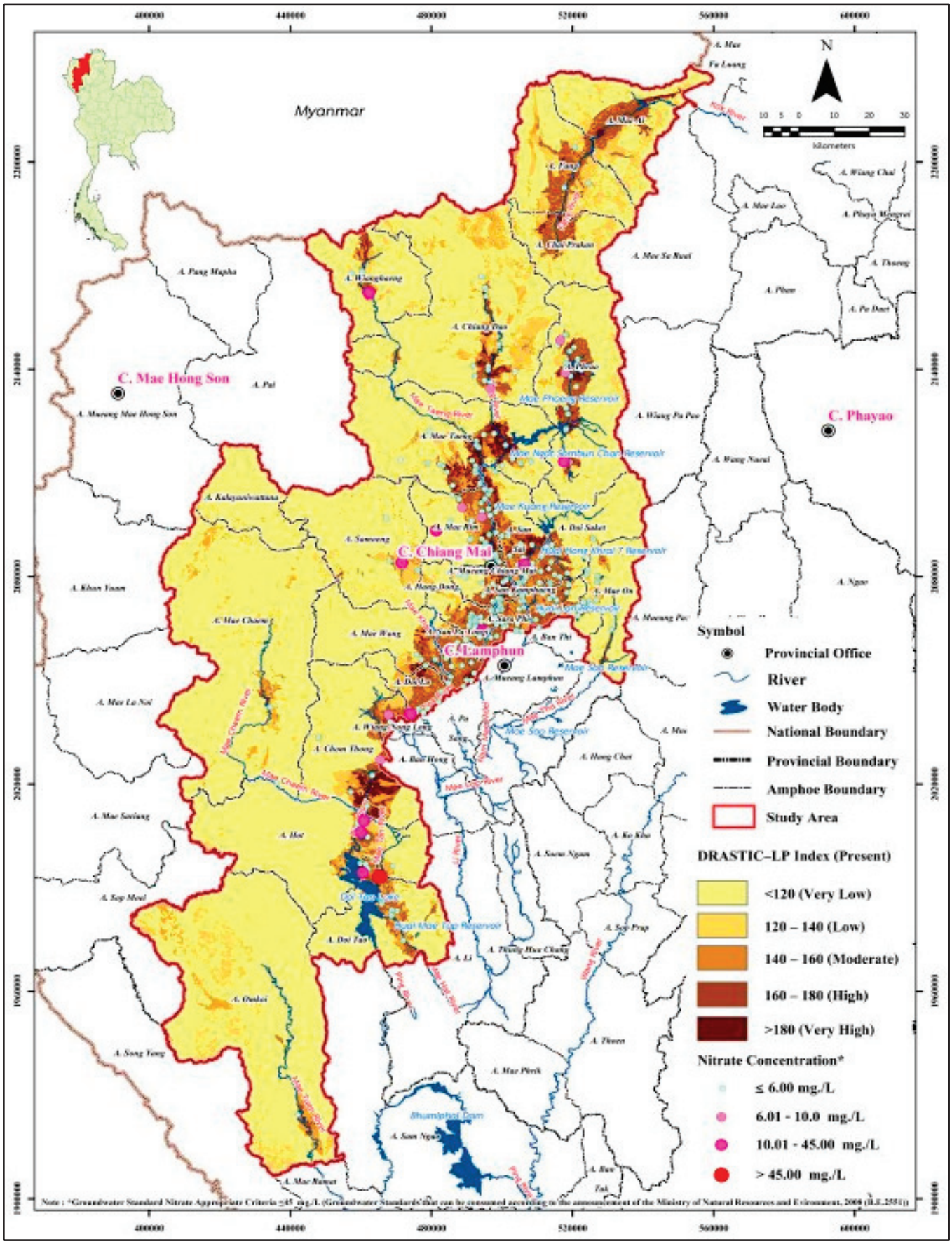

Figure 16. Nitrate (NO_3^-) calibration on baseline groundwater resource vulnerability (2020).

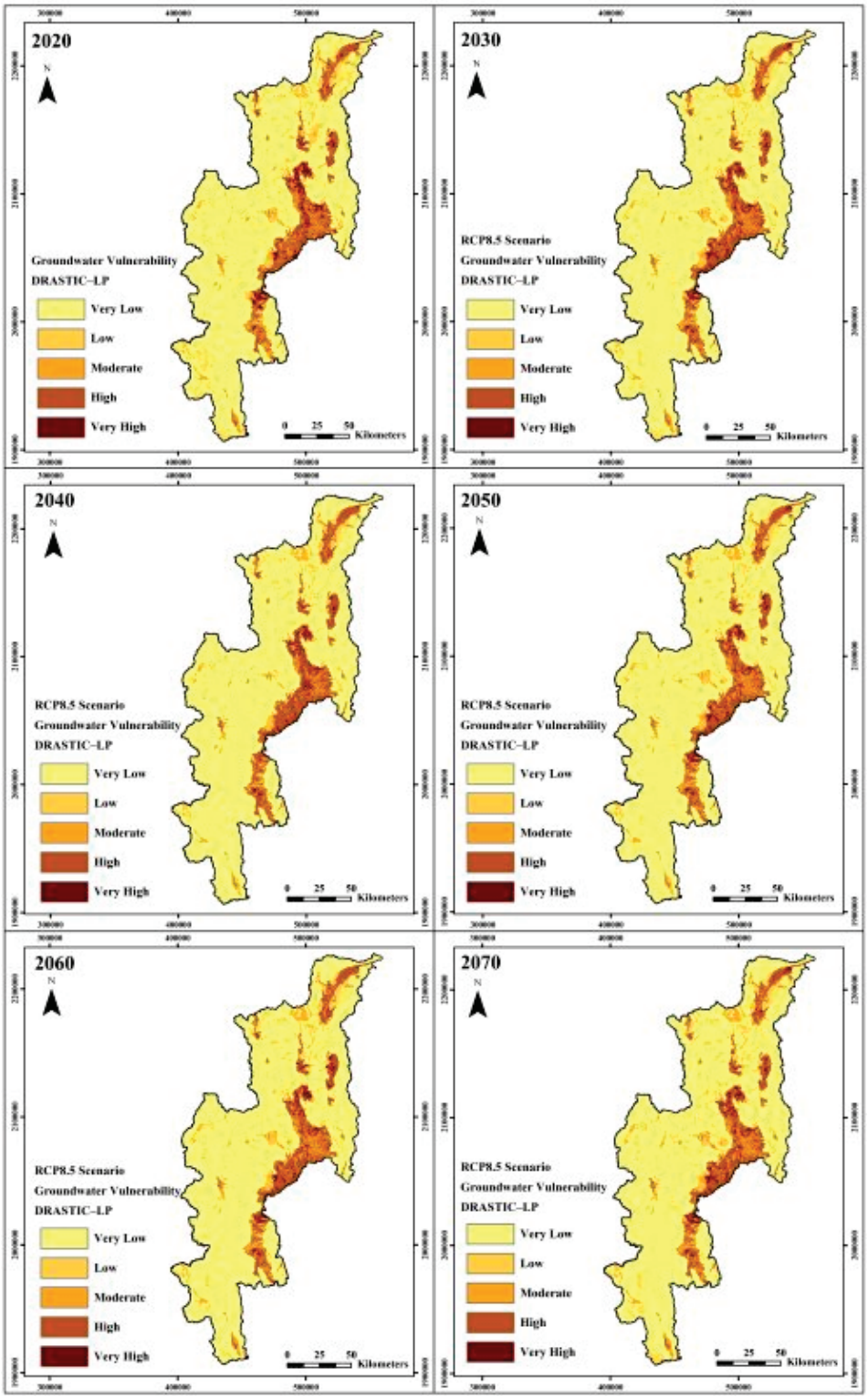

Figure 17. Groundwater resources vulnerability of the baseline period (2020) and for the future period (2021–2070), using the MIROC-ESM-CHEM model with the RCP8.5 scenario.

4. Groundwater Resource Risk Management

Normally, achieving the sustainable development of groundwater resources involves striking a balance between usage and demand, encompassing both aspects of quality and quantity. In Chiang Mai Province, it has become evident from historical to current contexts that effective groundwater resource management is imperative. Failure to regulate and mitigate groundwater usages can result in various short-term and long-term problems,

including groundwater deterioration, heavy metal contamination, other toxins, and even over-pumping. Consequently, managing groundwater resources is intricately linked to the overseeing groundwater user groups to attain equilibrium within the socio-economic system for national development and ensuring the sustainability of hydrogeological systems on the supply side. A risk management approach for the sustainable development of groundwater resources is proposed as follows:

1. Groundwater resource management for sustainable development is divided into three phases, as follows:

(a) Short-term or urgent phase (1–3 years):

i. Government agencies must thoroughly study and review existing laws and regulations related to groundwater protection, utilization, monitoring, remediation, as well as identify regulatory gaps and update needs.
ii. Establish a baseline database of the nation's groundwater quality, review the locations of monitoring stations and data gaps, and ensure that the collected data aligns with the requirements for monitoring and prediction models.
iii. Establish heavy metals baseline values in groundwater resources, review critical parameters, and set up a list of parameters to be tracked and modeled, including useful indicators like As, Pb, and NO_3^-, etc. Urgent mitigating measures should focus on controlling and reducing fertilizer use, including nitrate and pollution control, particularly wastewater from septic tanks in urban areas.
iv. Establish a general awareness campaign, including in schools, emphasizing the importance of properly managing this valuable natural resource. Encourage uncontrolled farmers who are conducting agricultural activities along the Mae Ping River to cooperate in reducing fertilizer use, including nitrate, especially in urban areas.

(b) Medium-term phase (3–10 years):

i Strengthen and focus on regulations for better the monitoring and control of groundwater resource usage.
ii Develop guidelines for planning, developing, remediating, and monitoring groundwater use, as well as treatment, rehabilitation, and damage assessment for heavy metal contamination in groundwater resources.
iii Authorize and expand the roles and responsibilities of relevant government agencies, especially the Department of Groundwater Resources (DGR), the Royal Irrigation Department (RID), the Department of Water Resources (DWR), and the Office of National Water Resources (ONWR).
iv Promote community education and involvement in groundwater management, as well as generate economic tools to offset damage to anthropogenic, natural resources, and the environmental aspects from heavy metal or toxic contamination in groundwater resources.

(c) Long-term phase (>10 years):

i. Concerned government agencies, especially the Department of Groundwater Resources (DGR), must be supported, and must cooperate with other local agencies and local communities for public participation in all sectors related to groundwater resources management. The participation cloud involves site selection, groundwater well drilling, well development, the design and installation of pumps, training, and well maintenance.
ii. Review the institutional structure for groundwater resource management and the roles of stakeholder departments at 10–year intervals for efficiency and relevance in order to adapt to changing conditions and needs.
iii. Periodically review regulations, guidelines, and standards every 10–15 years in order to ensure that they remain up to date with practices and tech-

nology. Harmonize water-related laws for both groundwater and surface water resources.

iv. Continuously educate and raise awareness in every sector, intermittently.

2. The action plan for sustainable groundwater resource management should be implemented in order to inspect and assess the conditions of groundwater resources, based on the study and analysis of main factors like groundwater vulnerability, vulnerability mapping, contamination risks, groundwater conditions, treatment plants, rehabilitation, groundwater damage assessment, and the roles and responsibilities of concerned government agencies. Thus, the action plan for sustainable groundwater resource management should involve the country, expanding the tool for local decision makers and assessing scenarios, such as new developments. Responsible government agencies include the Department of Groundwater Resources (DGR), the Department of Industrial Work (DIW), the Department of Local Administration (DLA), the Provincial Industry Office (PIO), the Environmental and Pollution Contral Office (EPCO), the Provincial Public Health Office (PPHO), and the Provincial Natural Resources and Environment Office (PNREO), etc. These action plans include the following:

(a) Establish a predictive vulnerability model for all regions.

(b) Develop the early warning system, disseminating information to local communities, decision makers, and stakeholder agencies at the central level. Responsible government agencies include the Department of Groundwater Resources (DGR), the Department of Industrial Work (DIW), the Department of Local Administration (DLA), the Provincial Industry Office (PIO), the Environmental and Pollution Control Office (EPCO), the Provincial Public Health Office (PPHO), and the Provincial Natural Resources and Environment Office (PNREO), etc.

(c) Implement a remote data collection, monitoring, and evaluation system for obtaining real-time data. Responsible agencies include the Department of Groundwater Resources (DGR), the Pollution Control Department (PCD), the Wastewater Management Authority (WMA), the Department of Industrial Works (DIW), the Provincial Industry Office (PIO), the Provincial Natural Resources and Environment Office (PNREO), and the Environmental and Pollution Control Office (EPCO), etc.

(d) Develop pollution source tracking and identification capabilities using the model to identify illegal polluters. Responsible government agencies include the Pollution Control Department (PCD), the Provincial Natural Resources and Environment Office (PNREO), and the Department of Groundwater Resources (DGR), etc.

(e) Set up an interface plan for water resource management, integrating groundwater and surface water resources. Responsible government agencies include the Department of Groundwater Resources (DGR), the Royal Irrigation Department (RID), the Office of the National Water Resources (ONWR), and the Department of Water Resources (DWR), etc.

(f) Determine guidelines for improving the law in order to enhance the roles and duties of officials under the Groundwater Act 1977, making them administrative officials or police officers, according to the criminal procedure law for more efficient law enforcement. Responsible government agencies include the Department of Groundwater Resources (DGR), the Secretariat of the House of Representatives (SHR), and the Secretariat of the Senate (SS), etc.

5. Discussion

The primary objective of groundwater resource protection is to safeguard both consolidated and unconsolidated aquifers, comprehensively. In addition, groundwater source protection aims to prevent the anthropogenic contamination of groundwater production wells, as opposed to natural contamination. While most groundwater vulnerability studies focus on groundwater resource protection, this research extends its scope to encompass all vulnerability studies related to groundwater resources or groundwater source protection. Previous studies have proposed various methods for assessing groundwater resource vulnerability over the past 35 years, as shown in Table 7. These various meth-

ods highlight diverse approaches undertaken globally, starting with the original DRASTIC model [11], and evolving through subsequent modifications, e.g., Sadat-Noori and Ebrahimi [14], Jenifer and Jha [16], Maqsoom et al. [17], Rahman [18], Shirazi et al. [19], Zghibi et al. [20], Abdeslama et al. [21], Rajput et al. [22], Mohammed et al. [23], Nurroh et al. [24], Bera et al. [25], Chilaue et al. [26], Zhang et al. [27], and Wei and Chi [28]. Some studies have applied the original DRASTIC model to the modified DRASTIC model, e.g., Lima et al. [12], Li and Merchant [13], Sadat-Noori and Ebrahimi [14], Huang et al. [15], Jenifer and Jha [16], Maqsoom et al. [17], Mkumbo et al. [30], and Zhang et al. [29], and Mkumbo et al. [30]. These reviews focus on index-based applied methods, considering land-use pattern changes and/or climate change, for both the current situation and the future scenarios when assessing groundwater resource vulnerability. Consequently, a comprehensive review of the literature, as shown in Table 1, reveals that past reviews had several gaps and lacked a coverage of studies that dealt with groundwater resource vulnerability under the influence of climate change and land-use pattern changes, and while using modern models. These limitations imply a narrow focus, necessitating an in-depth review, considering the state-of-the-art methods and approaches that consider the influence of climate change and land-use pattern changes, based on the current situation and the future scenarios, and using modern models.

This paper aims to assess the future risks of groundwater resource vulnerability patterns, based on climate change, projected by the MIROC-ESM-CHEM model under the RCP8.5 scenario (indicating very high greenhouse gas emissions), stemming from anthropogenic activities and changes in land-use patterns (using the CA_Markov Chain model). These risks span various spatial and temporal scales. This study integrates climate change, land-use pattern changes models, and a groundwater vulnerability model using GIS-based overlay techniques to produce a groundwater vulnerability map for the next 50 years (2021–2070) in Chiang Mai Province, Northern Thailand. The new DRASTIC-LP approach, modified by Aller et al. [11], effectively links groundwater resource vulnerability patterns with climate change and land-use pattern changes at the regional scale, with potential application in other areas of Thailand and even globally.

The results of the new DRASTIC-LP mapping indicate that groundwater resource vulnerability patterns in Chiang Mai Province will change over the next 50 years (2021–2070). The risk of groundwater resource vulnerability, centered around districts like Mueang Chiang Mai District, Mae Rim District, Saraphi District, Mae Taeng District, Hang Dong District, San Sai District, San Pa Tong District, San Kamphaeng District, Chom Thong District, Doi Tao District, Doi Lo District, Mae Ai District, Fang District, and Hot District, is expected to spread continuously to surrounding areas. The study emphasizes that the eastern areas of Chiang Mai Province, particularly recharge areas and low-lands along main rivers and tributaries, will be significantly affected by climate change and land-use pattern changes. Under the RCP8.5 scenario (very high greenhouse gas emissions) in the next 50 years (2021–2070), the new DRASTIC-LP modeling reveals an increased contamination risk in groundwater resources through nitrate (NO_3^-) compounds from chemical fertilizers and/or pesticide in intensive agricultural sectors and/or the processing of industrial areas, especially in the eastern part of Chiang Mai Province. The results indicate a notable rise in groundwater pollution risks under these scenarios, suggesting that the rapid development of Chiang Mai Province may not be sustainable in terms of the environment, social aspects, and quality of life. Recent field studies conducted during February to March 2020, May to June 2020, and November to December 2020 [51,52] further support these findings, showing a significant increase in nitrate (NO_3^-) concentrations in the shallow groundwater aquifer in eastern areas and lowlands along main rivers and tributaries. Furthermore, in the future, increasing risks of groundwater pollution will persist, driven by urbanization and the expansion of intensive agricultural areas, industrial processes, and anthropogenic activities. To address these concerns, effective site selection, the prioritization of monitoring areas, appropriate remedial measures, and the formulation of pollution protection and prevention strategies and policies are crucial, especially in high groundwater vulnerability areas.

Table 7. Summary of methodological comparisons between this paper and other DRASTIC techniques: (**a**) the Original DRASTIC model (Aller et al. [11]); and (**b**) the Modified DRASTIC model.

	Methodology of Assessing the Groundwater Resources Vulnerability	Modified DRASTIC Model								Original DRASTIC Model												
		This Paper	**[12]**	**[13]**	**[14] 1/+2/**	**[15]**	**[16] 2/**	**[17] 2/**	**[29] 1/+2/**	**[30]**	**[11]**	**[18]**	**[19]**	**[20]**	**[21]**	**[22]**	**[23]**	**[24]**	**[25]**	**[26]**	**[27]**	**[28]**
1.	Terms in Equation (Indexes)	**9**	8	7	7	8	9	8	11	8	7	7	7	7	7	7	7	7	7	7	7	7
2.	Components of Equation																					
2.1.	D (Depth to Water)	✓	✓	✓	✓	✓	✓	✓	✓	✓	✓	✓	✓	✓	✓	✓	✓	✓	✓	✓	✓	✓
2.2.	R (Net Recharge)	✓	✓	✓	✓	✓	✓	✓	✓	✓	✓	✓	✓	✓	✓	✓	✓	✓	✓	✓	✓	✓
2.3.	A (Aquifer Media)	✓	✓	✓	✓	✓	✓	✓	✓	✓	✓	✓	✓	✓	✓	✓	✓	✓	✓	✓	✓	✓
2.4.	S (Soil Media)	✓	✓	✓	✓	✓	✓	✓	✓	✓	✓	✓	✓	✓	✓	✓	✓	✓	✓	✓	✓	✓
2.5.	T (Topography)	✓	✓	✓	✓	✓	✓	✓	✓	✓	✓	✓	✓	✓	✓	✓	✓	✓	✓	✓	✓	✓
2.6.	I (Impact of Vadose Zone)	✓	✓	✓	✓	✓	✓	✓	✓	✓	✓	✓	✓	✓	✓	✓	✓	✓	✓	✓	✓	✓
2.7.	C (Hydraulic Conductivity)	✓	✓	x	✓	✓	✓	✓	✓	✓	✓	✓	✓	✓	✓	✓	✓	✓	✓	✓	✓	✓
2.8.	L/P/LU/LC (Land-Use Pattern)	✓	✓	✓	x	✓	✓	x	✓	✓	x	x	x	x	x	x	x	x	x	x	x	x
2.9.	P (Point Source Pollution) 3/	✓	x	x	x	x	x	x	x	x	x	x	x	x	x	x	x	x	x	x	x	x
2.10.	A'/LD (Anthropogenic Activities) 3/	✓	x	x	x	x	✓	✓	✓	x	x	x	x	x	x	x	x	x	x	x	x	x
2.11.	T' (Aquifer Thckness)	**x**	x	x	x	x	x	x	✓	x	x	x	x	x	x	x	x	x	x	x	x	x
2.12.	P' (Aquifer Water Potential)	**x**	x	x	x	x	x	x	✓	x	x	x	x	x	x	x	x	x	x	x	x	x
2.13.	D' (Pollution Sources Distance)	**x**	x	x	x	x	x	x	✓	x	x	x	x	x	x	x	x	x	x	x	x	x
3.	Climate Change Analysis																					
3.1.	MIROC-ESM-CHEM Model under RCP8.5 Scenario	✓	x	x	x	x	x	x	x	x	x	x	x	x	x	x	x	x	x	x	x	x
3.2.	GCMs Model under the B1, A1B, A2 Scenarios/RCP2.6, 4.5, 6.0, 8.5	✓	x	✓	x	✓	x	x	x	x	x	x	x	x	x	x	x	x	x	x	x	x
4.	Land-Use Patterns Change Analysis using CA_Markov Chain Model; LTMModel; or Dyna-CLUE Model	✓	✓	✓	x	✓	x	x	x	x	x	x	x	x	x	x	x	x	x	x	x	x
5.	Groundwater Risk Mapping																					
5.1.	GIS-based Techniques	✓	✓	✓	✓	✓	✓	✓	✓	✓	x	✓	✓	✓	✓	✓	✓	✓	✓	✓	✓	✓
5.2.	Overlay Techniques	✓	x	x	x	x	x	x	x	x	✓	x	x	x	x	x	x	x	x	x	x	x
6.	Predicting Future Groundwater Resources Vulnerability	✓	✓	✓	x	✓	x	x	x	x	x	x	x	x	x	x	x	x	x	x	x	x

Notes: 1/ = The modified DRASTIC model is used to calibrate and modify the original algorithm in order to obtain accurate results. 2/ = The original DRASTIC model is used to compare with the modified DRASTIC. 3/ = Point source pollutions are part of anthropogenic activities that affect the groundwater resources vulnerability. ✓ = yes; x = no.

6. Conclusions

In conclusion, the new approach model serves as a valuable planning and predictive tool for local and national decision makers involved in regional development. While this study focuses on Chiang Mai Province, its adaptability and applicability is evident, particularly in other regions of Thailand or even globally who are facing significant climate changes and rapid land-use pattern changes. Considering future climate changes when using the MIROC-ESM-CHEM Model under the RCP8.5 scenario (very high greenhouse gas emissions), alongside future land-use patterns by the CA_Markov Chain model, the simulation of groundwater vulnerability patterns for the next 50 years (2021–2070) emphasizes the necessity of formulating policies and strategies for sustainable groundwater resource development. The groundwater vulnerability map, derived from the new DRASTIC-LP model, can be used as a base for managing groundwater pollution in the future scenario, aiding decision makers in identifying potential vulnerabilities and taking early measures to protect and restore critical groundwater resources in Chiang Mai Province.

The contamination-risk management of sustainable groundwater resource development places emphasis on concerned government agencies. Standardizing and establishing heavy metal baseline values in groundwater resources, along with classifying groundwater quality, are imperative. Moreover, a thorough review and legislation of pertinent laws and regulations, accompanied by the authorization and expansion of roles and responsibilities of concerned government agencies, are necessary. The promotion and support of local communities in participating in the maintenance, selection of groundwater well sites, and well development, as well as fostering public participation across various sectors such as government, local scholars, academia, local communities, and industrial private sectors, etc., are essential actions. These efforts are particularly crucial for generating economic tools to address any environmental damage caused by anthropogenic activities, as well as the contamination of heavy metals or toxic wastes in groundwater resources. Consequently, an action plan for sustainable groundwater resource management must be implemented to inspect and assess the condition of groundwater resources. This action plan should be based on the results of studies and analyses addressing the following issues:

1. Groundwater resource vulnerability: Evaluate the susceptibility of groundwater resources to external influences, considering factors such as land-use patterns, anthropogenic activities, and point source pollutions.

2. Groundwater vulnerability map: Develop comprehensive groundwater resource vulnerability maps using advanced tools and GIS-based techniques, integrating data on climate change, land-use patterns, and hydrogeological conditions.

3. Groundwater risk: Identify and assess potential contamination risks associated with groundwater contamination, considering factors like point pollutant sources, aquifer characteristics, and human or anthropogenic activities.

4. Groundwater conditions: Analyze the present state of groundwater conditions, including water levels, quality, and natural variations, to understand the contamination baseline and potential deviations.

5. Treatment plan: Formulate plans for treating contaminated groundwater, outlining effective strategies for the removal of pollutants and the implementation of preventive measures.

6. Rehabilitation: Develop rehabilitation programs for every area affected by groundwater contamination and groundwater risks, including measures to restore aquifer health and mitigate long-term environmental damage.

7. Groundwater damage assessment: Conduct assessments to quantify and understand the extent of damage caused by anthropogenic/human activities, heavy metal contamination, or toxic waste in groundwater resources.

8. Roles and responsibilities of concerned government agencies: Clearly define and allocate roles and responsibilities among government agencies involved in groundwater management, such as the Department of Groundwater Resources (DWR), the Royal Irrigation Department (RID), and the Environmental and Pollution Control Office (EPCO).

By systematically addressing these issues in the action plan, effective and sustainable groundwater management can be achieved. The active involvement of local communities and collaboration across diverse sectors will play a pivotal role in mitigating environ-mental damage and ensuring the long-term health of groundwater resources.

The results of this study will be extended in future studies in mapping the risks of groundwater contamination under climate change, based on the RCP8.5 scenario and changes in land-use patterns for the 50-year period with numerical concept models, hydrogeological models, or (numerical) groundwater flow models (or called MODFLOW model) [59]. It predicts the possibility of spreading the risk of heavy metal contamination in groundwater resources from pollutant sources. Moreover, it is also used to predict the impacts of anthropogenic activities on the quality and quantity of groundwater resources.

Author Contributions: Conceptualization, C.I. and A.L.; methodology, C.I. and A.L.; software, C.I.; validation, C.I. and A.L.; formal analysis, C.I.; investigation, C.I. and A.L.; resources, C.I.; data curation, C.I.; Writing—Original draft preparation, C.I.; Writing—Review and editing, C.I. and A.L.; visualization, C.I.; supervision, A.L. All authors have read and agreed to the published version of the manuscript.

Funding: This research received no external funding.

Data Availability Statement: The behavior of temperature, rainfall conditions, land-use patterns, figures and tables of groundwater vulnerability, and groundwater contamination-risk maps, as well as simulation input files, are available upon request.

Acknowledgments: This research work was partially supported data by the Department of Groundwater Resources (DGR), the Royal Irrigation Department (RID), and the Thai Meteorological Department (TMD). The authors would also like to express their gratitude to company employee of Dhara Consultants Co., Ltd., in Sam Sern Nok, Huai Khwang, Bangkok, Thailand and Trans Asia Consultants Co., Ltd., in Sam Nok, Huai Khwang, Bangkok, Thailand who contributed to their support data for this academic research publication.

Conflicts of Interest: The authors declare that the research was conducted in the absence of any commercial or financial relationships that could be construed as a potential conflict of interest.

References

1. Thairath Newspaper. Underground Treasure Inscriptions: The Ministry of Natural Resources and Environment, "Groundwater maps" across the Country Solve the Repeated "Drought" Crisis. Available online: https://www.thairath.co.th/news/local/1701995 (accessed on 12 November 2023).
2. Department of Groundwater Resources (DGR). *Thailand's Conjunctive Groundwater and Surface Water Use Planning: Northern Thailand*; Final Report; Ministry of Natural Resources and Environment: Bangkok, Thailand, 2010.
3. Department of Groundwater Resources (DGR). *The State of Groundwater Annual Report: Thailand Groundwater Monitoring Networks Project*; Final Report; Ministry of Natural Resources and Environment: Bangkok, Thailand, 2018.
4. Zhao, X.; Wang, D.; Xu, H.; Ding, Z.; Shi, Y.; Lu, Z.; Cheng, Z. Groundwater pollution risk assessment based on groundwater vulnerability and pollution load on an isolated island. *J. Chemosphere* **2022**, *289*, 133134. [CrossRef] [PubMed]
5. National Research Council (NRC). *Groundwater Vulnerability Assessment: Predictive Relative Contamination Potential under Conditions of Uncertainty*; National Academy Press: Washington, DC, USA, 1993; 211p.
6. Machiwal, D.; Jha, M.K.; Singh, V.P.; Mohan, C. Assessment and mapping of groundwater vulnerability to pollution: Current status and challenges. *Earth-Sci. Rev.* **2018**, *185*, 901–927. [CrossRef]
7. Ducci, D. Influence of Climate Changes on Vulnerability Maps. In Proceedings of the First Conference and Workshop on "Groundwater and Climate Change", Norwich, UK, 4–6 April 2005.
8. Butscher, C.; Huggenberger, P. Modeling the temporal variability of karst groundwater vulnerability, with implications for climate change. *Environ. Sci. Technol.* **2009**, *43*, 1665–1669. [CrossRef]
9. Keilholz, P.; Disse, M.; Halik, U. Effects of land use and climate change on groundwater and ecosystems at the Middle Reaches of the Tarim River Using the MIKE SHE integrated hydrological model. *Water* **2015**, *7*, 3040–3056. [CrossRef]
10. Nistor, M.M. Vulnerability of groundwater resources under climate change in the Pannonian Basin. *Geo-Spat. Inf. Sci.* **2019**, *22*, 345–358. [CrossRef]
11. Aller, L.; Bennett, T.; Lehr, J.; Petty, R.J.; Hackett, G. *DRASTIC: A Standardized System for Evaluating Groundwater Pollution Potential using Hydrogeologic Settings*; NWW AIEPA Series; Robert, S., Ed.; US.EPA Report 600/2-87/035; Kerr Environmental Research Laboratory: Ada, OK, USA, 1987; 622p.

12. Lima, M.L.; Zelaya, K.; Massone, H. Groundwater vulnerability assessment combining the drastic and Dyna-Clue Model in the Argentine Pampas. *Environ. Manag.* **2011**, *47*, 828–839. [CrossRef]
13. Li, R.; Merchant, J.W. Modeling vulnerability of groundwater to pollution under future scenarios of climate change and biofuels-related land use change: A case study in North Dakota, U.S.A. *Sci. Total Environ.* **2013**, *447*, 32–45. [CrossRef]
14. Sadat-Noori, M.; Ebrahimi, K. Groundwater vulnerability assessment in agricultural areas using a modified DRASTIC model. *Environ. Monit. Assess.* **2016**, *188*, 19. [CrossRef]
15. Huang, L.; Zeng, G.; Liang, J.; Hua, S.; Yuan, Y.; Li, X.; Dong, H.; Liu, J.; Nie, S.; Liu, J. Combined Impacts of Land Use and Climate Change in the Modeling of Future Groundwater Vulnerability. *J. Hydrol. Eng.* **2017**, *22*. [CrossRef]
16. Jenifer, M.A.; Jha, M.K. Comparative evaluation of GIS-based models for mapping aquifer vulnerability in hard-rock terrains. *Environ. Earth Sci.* **2018**, *77*, 672. [CrossRef]
17. Maqsoom, A.; Aslam, B.; Khalil, U.; Ghorbanzadeh, O.; Ashraf, H.; Tufail, R.; Farooq, D.; Blaschke, T. A GIS-based DRASTIC Model and an adjusted DRASTIC Model (DRASTICA) for groundwater susceptibility assessment along the China-Pakistan Economic Corridor (CPEC) Route. *ISPRS Int. J. Geo-Inf.* **2020**, *9*, 332. [CrossRef]
18. Rahman, A. A GIS based DRASTIC model for assessing groundwater vulnerability in shallow aquifer in Aligarh, India. *Appl. Geogr.* **2008**, *28*, 32–53. [CrossRef]
19. Shirazi, S.M.; Imran, H.M.; Akib, S.; Yusop, Z.; Harun, Z.B. Groundwater vulnerability assessment in the Melaka State of Malaysia using DRASTIC and GIS techniques. *Environ. Earth Sci.* **2013**, *70*, 2293–2304. [CrossRef]
20. Zghibi, A.; Merzougui, A.; Chenini, I.; Ergaieg, K.; Zouhri, L.; Tarhouni, J. Groundwater vulnerability analysis of Tunisian coastal aquifer: An application of DRASTIC index method in GIS environment. *Int. Soc. Groundw. Sustain. Dev.* **2016**, *2–3*, 169–181. [CrossRef]
21. Abdeslama, I.; Fehdia, C.; Djabrib, L. Application of DRASTIC method for determining the vulnerability of an alluvial aquifer: Morsott-El Aouinet Northeast of Algeria: Using ArcGIS environment. In Proceedings of the International Conference on Technologies and Materials for Renewable Energy, Environment and Sustainability, TMREES17, Beirut, Lebanon, 21–24 April 2017.
22. Rajput, H.; Goyal, R.; Brighu, U. Modification and optimization of DRASTIC model for groundwater vulnerability and contamination risk assessment for Bhiwadi Region of Rajasthan, India. *Environ. Earth Sci.* **2020**, *79*, 136. [CrossRef]
23. Mohammed, S.H.A.; Nejad, R.A.; Hamamin, D.F. Vulnerability pesticide DRASTIC and risk intensity map for multi aquifer units: A case study from Basara basin, Iraqi Kurdistan Region. *Eurasia J. Biosci.* **2020**, *14*, 6119–6131.
24. Nurroh, S.; Gunawan, T.; Kurniawan, A. Assessment of groundwater pollution risk potential using DRASTIC Model in Yogyakarta City, Indonesia. *E3S Web Conf.* **2020**, *200*, 02002. [CrossRef]
25. Bera, A.; Mukhopadhyay, B.P.; Das, S. Groundwater vulnerability and contamination risk mapping of semi-arid Totko River Basin, India using GIS-based DRASTIC model and AHP techniques. *Chemosphere* **2022**, *307*, 135831. [CrossRef]
26. Chilaule, S.M.; Vélez-Nicolás, M.; Ruiz-Ortiz, V.; Sánchez-Bellón, Á.; García-López, S. Assessment of Intrinsic Vulnerability Using DRASTIC vs. Actual Nitrate Pollution: The Case of a Detrital Aquifer Impacted by Intensive Agriculture in Cádiz (Southern Spain). *Agriculture* **2023**, *13*, 1082. [CrossRef]
27. Zhang, Q.; Shan, Q.; Chen, F.; Liu, J.; Yuan, Y. Groundwater Vulnerability Assessment and Protection Strategy in the Coastal Area of China: A GIS-Based DRASTIC Model Approach. *Appl. Sci.* **2023**, *13*, 10781. [CrossRef]
28. Wei, Z.; Chi, Z. Groundwater Risk Assessment Based on DRASTIC and Special Vulnerability of Solidified/Stabilized Heavy-Metal-Contaminated Sites. *Sustainability* **2023**, *15*, 2997. [CrossRef]
29. Zhang, Y.; Qin, H.; An, G.; Huang, T. Vulnerability Assessment of Farmland Groundwater Pollution around Traditional Industrial Parks Based on the Improved DRASTIC Model-A Case Study in Shifang City, Sichuan Province, China. *Int. J. Environ. Res. Public Health* **2022**, *19*, 7600. [CrossRef] [PubMed]
30. Mkumbo, N.J.; Mussa, K.R.; Mariki, E.E.; Mjemah, I.C. The Use of the DRASTIC-LU/LC Model for Assessing Groundwater Vulnerability to Nitrate Contamination in Morogoro Municipality. *Tanzan. Earth* **2022**, *3*, 1161–1184. [CrossRef]
31. IPCC. *AR5 Synthesis Report: Climate Change 2014*; Mach, K.J., Planton, S., Stechow, C.V., Eds.; ANNEX II: Glossary; IPCC: Geneva, Switzerland, 2014.
32. Hyandye, C.; Lawence, W.M. A Markovian and cellular automata land-use change predictive model of the Usangu Catchment. *Int. J. Remote Sens.* **2017**, *38*, 64–81. [CrossRef]
33. Chiang Mai Provincial Office, Strategic and Information for Provincial Development Unit. *Briefing Information of Chiang Mai Province*; Chiang Mai Provincial Office: Chiang Mai, Thailand, 2020.
34. Royal Forest Department (RFD), Information and Communication Technology Center. *Statistical Book of the Royal Forest Department 2019*; Ministry of Natural Resources and Environment: Bangkok, Thailand, 2019.
35. Department of Groundwater Resources (DGR), Bureau of Groundwater Conservation and Restoration. *Activity No. 1 Report: Thailand Groundwater Situation Report, Project to Establish an Observation Network to Monitor the Situation of Groundwater, Fiscal Year 2015*; Department of Groundwater Resources: Bangkok, Thailand, 2015.
36. Jarurat, A. *Study of Hydrogeology and Aquifer Classification for Potential Analysis and Sustainable Groundwater Development in the Chiang Mai Basin*; Academic Report, No. BGCR.3/2008; Bureau of Groundwater Conservation and Restoration, Department of Groundwater Resources: Bangkok, Thailand, 2008.
37. Taweelarp, S.; Khebchareon, M.; Saenton, S. Evaluation of Groundwater Potential and Safe Yield of Heterogeneous Unconsolidated Aquifers in Chiang Mai Basin, Northern Thailand. *Water* **2021**, *13*, 558. [CrossRef]

38. Wattananikorn, K.; Beshir, J.A.; Nochaiwong, A. Gravity interpretation of Chiang Mai Basin, Northern Thailand: Concentrating on Ban Thung Sieo area. *J. Southeast Asian Earth Sci.* **1995**, *12*, 53–64. [CrossRef]
39. Asnachinda, P. Hydrogeochemistry of the Chiang Mai Basin, Northern Thailand. *J. Asian Earth Sci.* **1997**, *15*, 317–326. [CrossRef]
40. Ridd, M.R.; Barber, A.J.; Crow, M.J. *The Geology of Thailand*; Geological Society: London, UK, 2011.
41. Department of Groundwater Resources (DGR). *Groundwater Potential Map of Chiang Mai Province, Scale 1:100,000*; Ministry of Natural Resources and Environment: Bangkok, Thailand, 2017.
42. Department of Groundwater Resources (DGR). *Groundwater Resources Assessment of the Chiang Mai, Upper Chao Phraya, and Mae Klong Basins*; Final Report; Ministry of Natural Resources and Environment: Bangkok, Thailand, 2005.
43. Margane, A.; Tatong, T. Aspects of the hydrogeology of the Chiang Mai-Lamphun Basin, Thailand that are Important for the Groundwater Management. *Z. Angew. Geol.* **1999**, *45*, 188–197.
44. Kiwduangta, B. Hydrostratigraphic Model of the Shallow Aquifer in the Vicinity of the Northern Region Industrial Estate Area, Lamphun Province. Master's Thesis, Chiang Mai University, Chiang Mai, Thailand, 2012.
45. Losiri, C. Land use change model and urban area prediction in the future. *J. Soc. Sci. Srinakharinwirot Univ.* **2016**, *19*, 340–357.
46. Thai Meteorological Department (TMD). *Daily Temperature Data from the 30-Years Period (1991–2020) in Chiang Mai Province, Mae Hong Son Province, Lamphun Province, Lam Pang Province, and Chiang Rai Province*; Thai Meteorological Department: Bangkok, Thailand, 2021.
47. Thai Meteorological Department (TMD). *Daily Rainfall Data from the 30-Years Period (1991–2020) in Chiang Mai Province, and Its Influenced Areas*; Thai Meteorological Department: Bangkok, Thailand, 2021.
48. Royal Irrigation Department (RID). *Daily Rainfall Data from the 30-Years Period (1991–2020) in Chiang Mai Province, and Its Influenced Areas*; Royal Irrigation Department: Bangkok, Thailand, 2021.
49. Land Development Department (LDD). *Land Use Map (Level 1) in Chiang Mai Province (GIS), Scale of 1:25,000*; Land Development Department: Bangkok, Thailand, 2020.
50. Land Development Department (LDD). *Report on soil survey for agriculture in Chiang Mai Province, Scale of 1:25,000*; Academic Report No. 27/06/50; Land Development Department: Bangkok, Thailand, 2007.
51. Department of Groundwater Resources (DGR). *Final Report: The Study of Background Values of Heavy Metals in Groundwater, Chiang Mai and Lamphun Provinces*; Ministry of Natural Resources and Environment: Bangkok, Thailand, 2019.
52. Javadi, S.; Kardan Moghaddam, H.; Neshat, A. A new approach for vulnerability assessment of coastal aquifers using combined index. *Geocarto Int.* **2020**, *37*, 1681–1703. [CrossRef]
53. Moghaddama, K.H.; Mohsen Pourreza-Bilondib, M.; Masoud Bahreini Motlagh, B.M. Evaluation of Hierarchical Analysis Method in Calibration of DRASTIC-LU Vulnerability Index (Study Area: Birjand Aquifer). *Water Harvest. Res.* **2021**, *4*, 121–132.
54. Osborn, N.I.; Eckenstein, E.; Koon, K.Q. *Vulnerability Assessment of Twelve Major Aquifers in Oklahoma*; Technical Report 98-5; Oklahoma Water Resources Board: Oklahoma City, OK, USA, 1998; 29p.
55. Department of Groundwater Resources (DGR). *The Groundwater Quality Standard for Drinking Purpose According to the Notification of the Ministry of Natural Resources and Environment (2008)*; Ministry of Natural Resources and Environment: Bangkok, Thailand, 2008.
56. Barber, N.L. *Summary of Estimated Water Use in the United States in 2005*; USGS Publications Warehouse: Reston, VA, USA, 2010. [CrossRef]
57. Dubrovsky, N.M.; Burow, K.R.; Clark, G.M.; Gronberg, J.M.; Hamilton, P.A.; Hitt, K.J.; Mueller, D.K.; Munn, M.D.; Nolan, B.T.; Puckett, L.J.; et al. The Quality of our Nation's Waters-Nutrients in the Nation's Streams and Groundwater, 1992–2004. In *U.S. Geological Survey Circular 1350*; United States Geological Survey: Reston, VA, USA, 2010; p. 174. Available online: http://water.usgs.gov/nawqa/nutrients/pubs/circ1350 (accessed on 12 November 2023).
58. Madison, R.J.; Brunett, J.O. Overview of the occurrence of nitrate in groundwater of the U.S. National Water Summary 1984-Water Quality Issues. *U.S. Geol. Surv. Water-Supply Pap.* **1985**, *2275*, 93–105.
59. Condon, L.E.; Kollet, S.; Bierkens, M.F.P.; Fogg, G.E.; Maxwell, R.M.; Hill, M.C.; Fransen, H.-J.H.; Verhoef, A.; Van Loon, A.F.; Sulis, M.; et al. Global Groundwater Modeling and Monitoring: Opportunities and Challenges. *Water Resour. Res.* **2021**, *57*, e2020WR029500. [CrossRef]

Disclaimer/Publisher's Note: The statements, opinions and data contained in all publications are solely those of the individual author(s) and contributor(s) and not of MDPI and/or the editor(s). MDPI and/or the editor(s) disclaim responsibility for any injury to people or property resulting from any ideas, methods, instructions or products referred to in the content.

hydrology

MDPI

Article

A Conceptual Framework for Modeling Spatiotemporal Dynamics of Diesel Attenuation Capacity: A Case Study across Namyangju, South Korea

Livinia Saputra [1,2,†], Sang Hyun Kim [1,2,†], Kyung-Jin Lee [1], Seo Jin Ki [3], Ho Young Jo [4], Seunghak Lee [1,2,5,*] and Jaeshik Chung [1,2,*]

[1] Water Cycle Research Center, Korea Institute of Science and Technology (KIST), Seoul 02792, Republic of Korea; livinia@kist.re.kr (L.S.)
[2] Division of Energy and Environmental Technology, KIST School, Korea University of Science and Technology (UST), Seoul 02792, Republic of Korea
[3] Department of Environmental Engineering, Gyeongsang National University, Jinju 52725, Republic of Korea
[4] Department of Earth and Environmental Science, Korea University, Seoul 02841, Republic of Korea
[5] Graduate School of Energy and Environment (KU-KIST Green School), Seoul 20841, Republic of Korea
* Correspondence: seunglee@kist.re.kr (S.L.); jschung@kist.re.kr (J.C.)
† These authors contributed equally to this work.

Abstract: The vadose zone acts as a natural buffer against groundwater contamination, and thus, its attenuation capacity (AC) directly affects groundwater vulnerability to pollutants. A regression model from the previous study predicting the overall AC of soils against diesel was further expanded to the GIS-based overlay-index model. Among the six physicochemical parameters used in the regression model, saturation degree (SD) is notably susceptible to climatological and meteorological events. To accommodate the lack of soil SD historical data, a series of infiltration simulations were separately conducted using Phydrus code with moving boundary conditions (i.e., rainfall records). The temporal variation of SD and the resulting AC under transient conditions are captured by building a space–time cube using a temporal raster across the study area within the designated time frame (1997–2022). The emerging hot spot analysis (EHSA) tool, based on the Getis–Ord Gi* and Mann–Kendall statistics, is applied to further identify any existing pattern associated with both SD and AC in both space and time simultaneously. Under stationary conditions, AC decreases along depth and is relatively lower near water bodies. Similarly, AC cold spot trends also show up near water bodies under transient conditions. The result captures not only the trends across time but also shows the exact location where the changes happen. The proposed framework provides an efficient tool to look for locations that have a persistently low or a gradually decreasing ability to attenuate diesel over time, indicating the need for stricter management regulations from a long-term perspective.

Keywords: attenuation capacity; emerging hot spot analysis; GIS; groundwater vulnerability; overlay-index model

1. Introduction

Despite the numerous efforts [1–3] that have been taken to address the fate of various contaminants in the vadose zone, it is still inadequate to achieve a better understanding of natural attenuation therein due to the non-stationary nature. Process-based models (e.g., HYDRUS) are available for estimating the contaminant migration to the groundwater through a vadose zone, which solves Richard's equation to estimate the water flow under unsaturated conditions with accompanying contaminant transport [4]. However, it is difficult to extend their application to a large scale due to the heterogeneity in the subsurface properties and the computational cost. On the other hand, the GIS-based spatial model is

suitable for large-scale estimation and has been often used for groundwater vulnerability assessment. One of the most widely used models, DRASTIC [5] employs seven hydrogeological properties as the input parameters to assess the intrinsic groundwater vulnerability. Unfortunately, however, it failed to include the natural attenuation of contaminants in a vadose zone [6–8]. A previous study by Woo et al. (2022) addressed the effect of soil physicochemical properties on the overall attenuation capacity (AC) of a vadose zone soil against diesel, a type of refined petroleum product [9]. They found that six parameters consisting of two chemical properties and four physical properties, including soil moisture, play an essential role in soil's natural AC against diesel. Based on multiple linear regression analyses, an empirical relationship between the soil properties and the diesel AC of a vadose zone was suggested. Among those factors, however, the soil moisture is susceptible to temporally varying climatological and meteorological events.

The first few centimeters of surface soils have been reported to be affected mostly by climate change due to the complex interaction between the atmosphere and lithosphere near the ground surface, especially in relation to soil moisture [10–13]. The previous studies also mentioned the seasonal effects of meteorological events on the soil. Moreover, climate change should affect meteorological phenomena and alter global precipitation patterns, and thus, assessing its effect on AC along with the potential SD shifts might give a new understanding of the groundwater vulnerability to the contamination. However, soil SD data are not readily available. One way to obtain the SD is to simulate the soil water content on the basis of the climatological and meteorological data and calculate the SD on the basis of the soil properties. In this study, the spatiotemporal distribution of diesel AC in the city of South Korea (Namyangju city) was estimated with a focus on the variation of SD upon meteorological and climatological events.

Another problem is capturing the changes in SD and AC over time and space. Temporal changes are usually compared with snapshots between time snaps, e.g., forest coverage [14]. While comparing different periods can be useful, it may not capture the nuances of changes that occur between those periods. These in-between trends may not be fully captured by the comparison. It also cannot show where the areas are experiencing more or less changes over time. The emerging hot spot analysis (EHSA) tool in ArcGIS, developed by ESRI, provided a robust statistical assessment that simultaneously gives back the spatial and temporal hot and cold spot trend [15]. Even though EHSA has been applied in disease outbreaks [16,17], accident occurrence [18], flooding and drought [19–21], forest loss [22], and conservation monitoring [23,24], its application in soil vulnerability especially on vadose zone AC has not been recorded. Therefore, incorporating EHSA into the vulnerability study will provide a new way to assess and understand the dynamics of soil SD, AC, or other general vulnerability assessments.

The SD profile was obtained from the numerical simulation with moving boundary conditions, and subsequently, EHSA was performed to capture the temporal trends of both SD and AC within the designated time frame (1997–2022). However, we would like to note that the results we are presenting in this paper are solely for illustrative purposes regarding how incorporating temporal data with EHSA can enhance our understanding of environmental vulnerability.

2. Materials and Methods

2.1. Empirical Equation for Diesel Attenuation Capacity

Woo et al. (2022) developed an empirical relationship for determining the diesel attenuation capacity of a vadose zone with several soil properties [9]. Through laboratory experimentation and regression analysis, six parameters were identified as key factors affecting the attenuation capacity of a vadose zone to degrade diesel contamination therein. These parameters include soil organic matter content (OM), total phosphorus (TP), coefficient of uniformity (C_u), van Genuchten's n parameter (n), soil saturation degree (SD), and

the soil particle size at which 30% of the material is finer (D_{30}). The vadose zone attenuation capacity in this study was calculated using the equation below:

$$AC = OM_R + 2.70TP_R - 0.82D_{30R} + 0.93C_{uR} + 0.82n_R - 0.56SD_R \quad (1)$$

where the subscript R represents the rated value based on min–max data normalization followed by an evenly spaced binning of the data (Table 1). The OM in the soil is a significant factor that determines the biodegradation of organic contaminants such as diesel, which primarily consists of hydrophobic materials that can retain them as well; microbial growth and reproduction use those contaminants as a source of carbon and energy, leading to biodegradation of diesel in the soil [25]. Soils with higher OM have a greater capacity to retain and break down diesel. In addition, phosphorus is a crucial nutrient for microbial growth in soil, alongside carbon and nitrogen. Microorganisms use phosphorus to synthesize cellular components, such as nucleic acids [26].

Table 1. Parameter rating classification ranges.

Start	End	Rating
0.5	1.5	1
1.5	2.5	2
2.5	3.5	3
3.5	4.5	4
4.5	5.5	5

Soil grading is determined by the coefficient of uniformity (C_u), which is the ratio of D_{60} to D_{10}. A higher C_u means that the soil is better graded, with a more even composition of particles of different sizes. A uniform soil sample has particles with similar dimensions, resulting in a surface area that may be larger or smaller depending on the governing particle size. D_{30}, which represents the size of soil particles at which 30% of the soil (by weight) is finer than that size, supports the effect of soil particle size distribution on the overall AC. Soil with coarse particles and poor grading has a higher D_{30} value, which is closer to or within the range of sandy soil. Lower C_u paired with higher D_{30} indicates bigger pore sizes, which could promote the volatilization of diesel components. Bigger pores also provide less surface area for attachment and higher mobility for microbes to access substrates, electron donors/acceptors, and nutrients. D_{30} can therefore provide additional information about pore size and soil uniformity in the area under study.

A min–max data normalization was applied, as shown in Equation (2), and the normalized data were classified into five rating classes with equal intervals (Table 1). The minimum and maximum values used for each parameter were the global minimum and maximum values across the 100 cm soil depth at the area of interest considered in this study. The min–max values of each parameter can be found in the Supplementary Materials (Table S1).

$$X_i = \left(\frac{X - X_{min}}{X_{max} - X_{min}} \right) \times 5 + 0.5 \quad (2)$$

All these processes were performed in R studio [16], and the outputs are temporal SD and AC raster files with a spatial resolution of 100 m × 100 m. These raster files were then used as inputs in ArcGIS [27] for building space–time cubes and running EHSA (Section 2.3).

2.2. Parameter Estimation and Ratings

This study used publicly available data for the parameter estimation and ratings. The Korean Rural Development Administration (RDA) provides soil maps as vector and gridded data, which include information on soil series, soil texture, parent materials, and

more. The laboratory test data sheets, which show the soil physicochemical characteristics, like sand, silt, clay (SSC) distribution, soil organic carbon (SOC), bulk density, water content, and pH, are also provided. Table 2 summarizes the data used to create thematic layers in this study.

Table 2. Thematic layers used for attenuation capacity analyses.

Thematic Layers	Layer Information	Types	Publisher (Source)
Soil Series Map	South Korea RDA Database (upon request)	Vector	Korea RDA (http://soil.rda.go.kr/ (accessed on 9 June 2022))
Organic Matter Content	Estimated from Soil Organic Carbon Content	Tabular	
Total Phosphorous	Estimated from Soil Organic Carbon Content	Tabular	
Particle Size Distribution	South Korea RDA Database	Tabular	
van Genuchten's n	Estimated from Particle Size Distribution	Tabular	
Saturation Degree	Simulated using Phydrus	Tabular	-

Soil organic matter (OM) content was calculated by multiplying soil organic carbon (SOC) content and the van Bemmelen factor (Equation (3)) [28]. This conversion assumes that 58% of OM is in the form of SOC [28,29].

$$OM = 1.724 \times SOC \quad (3)$$

Total phosphorus in the soil was estimated on the basis of the relationship between TP and SOC described by Hou et al. (2018) for natural terrestrial ecosystems [30].

In the laboratory test data sheet published by Korea RDA, the particle size distribution of soil is divided into sand, silt, and clay. Sand is classified again as very fine, fine, medium, coarse, and very coarse. Silt and clay are divided again as fine and coarse. These subgroups are presented as the percent fraction of a particle size range. The particle size defining 10%, 30%, and 60% finer soil particles in a particle size distribution curve is represented as D_{10}, D_{30}, and D_{60}, respectively. Since the data range is a continuous scale from finest to coarsest, interpolation is used to find the values of D_{10}, D_{30}, and D_{60}. D_{30} is used directly in the attenuation capacity model, while D_{10} and D_{60} are part of uniformity estimation. The uniformity coefficient is a measure representing how well the soil is graded and can be obtained by the ratio of D_{60} to D_{10} (Equation (4)).

$$C_u = \frac{D_{60}}{D_{10}} \quad (4)$$

Rosetta is a software that adopts a hierarchical pedotransfer function (PTF), which allows the estimation of water retention parameters, including van Genuchten's (VG's) n [31–33]. HYDRUS-1D (Ver. 4.20) is a popular numerical simulator used in the field of soil physics that incorporated a simplified version of Rosetta in its module [34]. This study used Rosetta PTF in HYDRUS-1D to estimate the VG's n on the basis of the sand, silt, and clay content for each soil series. The usage of only SSC distribution for n estimation was mainly due to data limitations regarding bulk density and water content (soil field moisture), which were not available for the entire soil series.

2.3. Estimation of Temporal Changes in Soil Moisture and Resulting AC

In order to capture the temporal variation of the attenuation capacity according to the saturation degree, an infiltration simulation was conducted to obtain water content profiles using a Python-based HYDRUS-1D module, Phydrus [35], under moving boundary

conditions. Historical meteorological data in the model city for 26 years (1997–2022) were obtained from the KMA (Korea Meteorological Administration) (Figure S1). The input data for the simulation included precipitation, atmospheric temperature, and soil profile (lithology and thickness). The outputs were the daily water content data at ten different depths (each 10 cm intervals along 100 cm depth) for the 46-soil series considered in the study (Figure S2). SD can be calculated from soil water contents as follows (Equation (5)):

$$SD = \frac{\theta - \theta_r}{\theta_s - \theta_r} \quad (5)$$

where θ represents water content and θ_r and θ_s are the residual and saturated water contents, respectively. Upon the completion of the SD series, the temporal AC was then calculated using Equation (1), and raster files were built using R based on the SD data that were prepared. In this study, we focus on seasonal trends; thus the output raster is the averaged seasonal value of AC and SD for each year during the period 1997–2022.

2.4. Emerging Hot Spot Analysis

The process started with building space–time cubes (STCs), 3D visualizations of a geographical phenomenon. The horizontal plane of the cube represents the spatial context of the data (longitude and latitude), while the vertical axis represents time [17]. Each data point is treated as a bin and contains the attenuation capacity information for an exact location at a specific time. A *z*-score, *p*-value, and hot spot classification calculated on the basis of the Getis–Ord Gi* statistics will be added to each bin, which is then reanalyzed using Mann–Kendall statistics, which has been widely used in temporal trend analysis within hydrologic and climatological studies [36–40]. The outputs are the hot/cold spot trend over space and time. Within the context of this study, a hot spot is where an area has a significantly higher SD and AC compared to its surroundings, and vice versa for the cold spot. The spatial resolution applied in this study is 100 m × 100 m combined with various temporal resolutions. In addition to the AC, we also performed space–time pattern mining (STPM) for SD for further comparison and analysis. Figure 1 illustrates the overall workflow in this study.

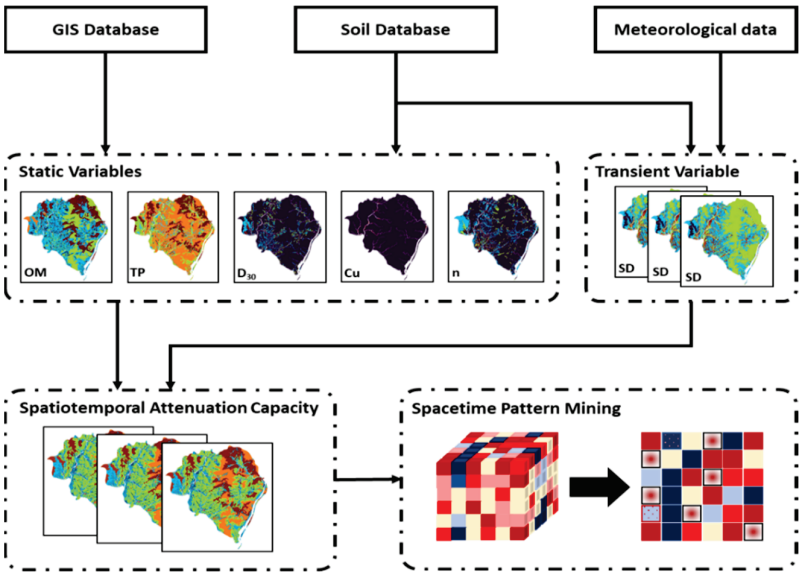

Figure 1. Methodological flow used in this study.

The site can be categorized into 17 patterns, namely persistent hot/cold spot, new hot/cold spot, consecutive hot/cold spot, intensifying hot/cold spot, diminishing hot/cold spot, sporadic hot/cold spot, oscillating hot/cold spot, historical hot/cold spot, and no pattern detected [17,19–21].

3. Results and Discussion

3.1. Soil Water Content Simulation and Saturation Degree Estimation

Several data collected from Korea RDA and KMA were prepared as inputs (precipitation, soil properties, soil profile, etc.) for the infiltration simulation using Phydrus. The output of the simulation is daily water content for the whole simulation period at ten different depths (10–100 cm in 10 cm increments). These data were used to calculate daily soil SD, which was then used to calculate temporal AC. It has to be noted that Phydrus also has its limitations in applying the HYDRUS-1D standard code. One notable setback is that Phydrus cannot handle the meteorological model yet; therefore, the simulation will only be influenced by precipitation and will disregard the effects of temperature and/or radiation. In addition, the HYDRUS-1D standard code itself does not support freezing and thawing processes, which should affect the water flow simulation results in late fall (as temperature drops), winter, and early spring (as temperature rises and induces thawing). For these reasons, as well as the previous reports on the different effects of meteorological events and climate change according to seasons, only the long-term trend of SD and AC in summers will be discussed.

3.2. SD and AC Distribution under the Stationary Conditions

Before conducting the temporal analysis, the equation for AC estimation (Equation (1)) was validated with the AC calculated from the six parameters of a random area of soil within the study area (text S1). Vulnerability studies are usually performed as a static parameter and ignore the fact that some stressors might constantly change over time. Originally, the AC estimation by Woo et al. (2022) is also designed to assess vadose zone vulnerability without considering the possible changes in AC due to SD changes as a parameter sensitive to meteorological dynamics [9]. By applying Equation (1) as it is in a GIS environment using a static one-value SD, the resulting spatial distributions at 10 cm, 50 cm, and 100 cm are presented in Figure 2.

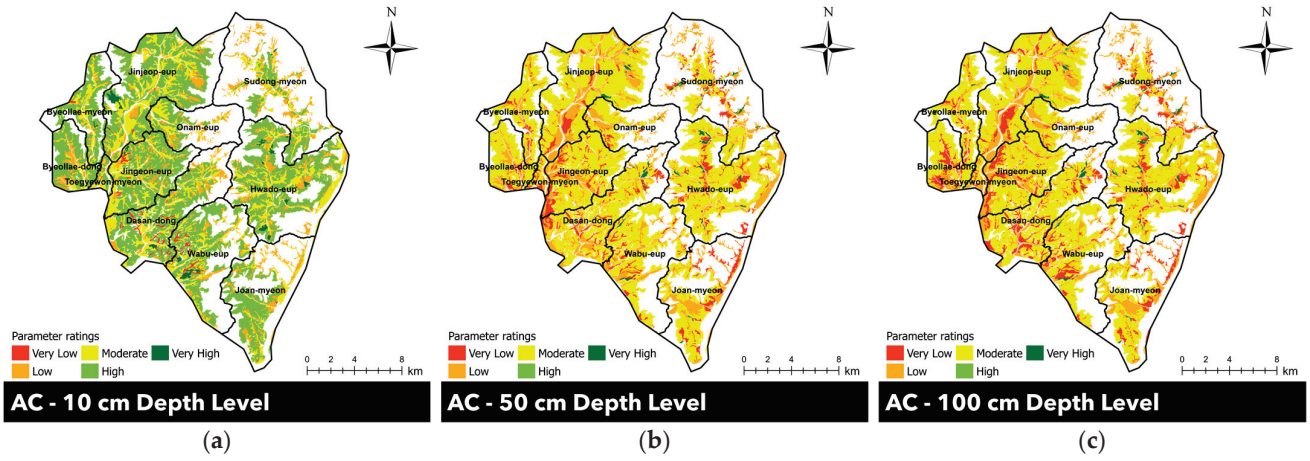

(**a**) (**b**) (**c**)

Figure 2. Spatial distribution of attenuation capacity (AC) in Namyangju at (**a**) 10 cm, (**b**) 50 cm, and (**c**) 100 cm.

Note that the AC maps show distinct patterns through the depth. In general, the topsoil showed higher AC than the one from the subsoils. In addition, ACs near water bodies were relatively low due to the uneven distribution of constituting parameters; OM and TP tend to have lower ratings near water bodies, while SD is higher. As both OM and TP have the highest weight in AC estimation, the lower value of these parameters results in a lower AC. In addition to that, SD has a negative effect on AC, and thus, a higher rating in SD will further decrease the resulting AC (Figure S3).

3.3. SD and AC Variation under Transient Conditions

As aforementioned, SD is a parameter that is constantly changing, which might also affect the overall AC in Namyangju. These changes can be assessed by comparing the SD and AC between time snaps, e.g., 1997 vs. 2022, January vs. June, etc. This kind of comparison is able to present the difference between time snaps, yet it is unable to incorporate the changes happening in between the time snaps and thus might yield a less accurate trend happening over time. By incorporating EHSA into the vulnerability analysis, such problems can be addressed. The end result of applying EHSA is that the overall relative trend of SD and AC in both space and time is obtained. Instead of comparing between time snaps (e.g., 1997 vs. 2022), EHSA considers the whole time period (e.g., 1997–2022) and reports back the trend happening over the time period.

The EHSA results of both SD and AC at 10 cm, 50 cm, and 100 cm are presented in Figure 3. A visual comparison between images in Figure 3 shows that at a depth of 100 cm, there seems to be a larger number of areas corresponding to persistent SD trends, especially for the cold spots. Contrary to the depth of 100 cm, the 50 cm depth has the least persistent SD trends. At both 10 cm and 50 cm, the pattern of SD is dominated by oscillating trends. However, EHSA results for AC show a more prominent persistent trend at 50 cm, while the 100 cm depth is dominated by oscillating and sporadic trends. Cold spots also seem to consistently show up near water bodies (southern part of Jinjeop-eup, eastern part of Toegyewon-myeon, and western part of Jingeon-eup), the western part of Namyangju (Byeollae-dong), and Sudong-myeon. Table 3 provides data on the percent area of each trend pattern at each depth for both SD and AC (based on Figure 3). Around 16% correspond to both persistent cold and hot spots at a 100 cm depth, while only ±10% and ±3% correspond to the persistent trends at the 10 and 50 cm depths, respectively. This result agrees with the general knowledge that water content is less transient at a deeper level. It is also shown that around 63% of the area at 10 cm and 62% of the area at 50 cm show transient oscillating and sporadic trends compared to only ±50% at 100 cm. However, it has to be highlighted that fewer areas with transient trends and a domination of persistent trends should be expected at a deeper level. The domination of resulting transient patterns most probably corresponds to the varying soil porosity along the depth.

Furthermore, we can investigate the effect of temporal changes of SD on AC in the summer season by comparing the overlapping areas of the same trend between SD and AC (Figure 3). The expected ideal relationship between SD and AC is a negative one, where the cold spot area in SD will return to a hot spot area in AC. Based on the overlapping area presented in Figure 4, only around 6%, 3%, and 13% of the areas return the ideal opposite relationship between SD and AC at depth of 10, 50, and 100 cm, respectively.

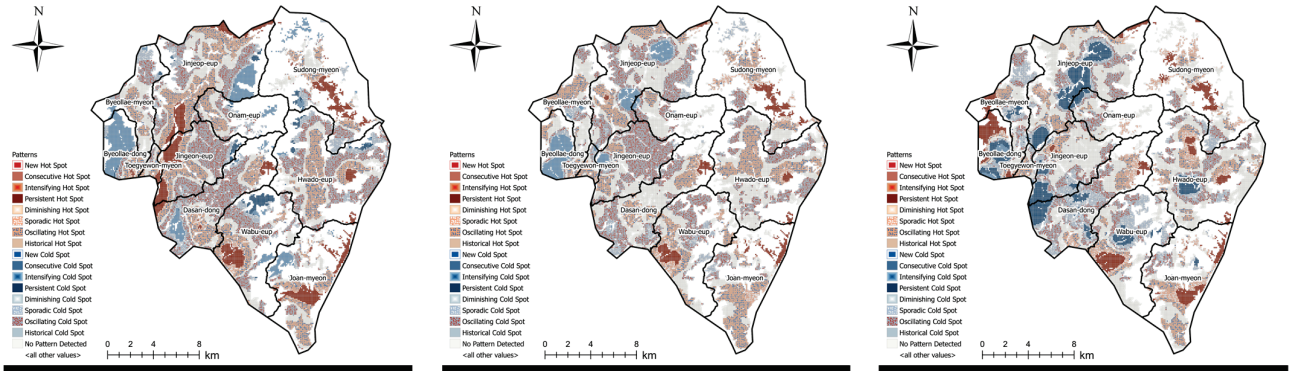

(**a1**) (**a2**) (**a3**)

Figure 3. *Cont.*

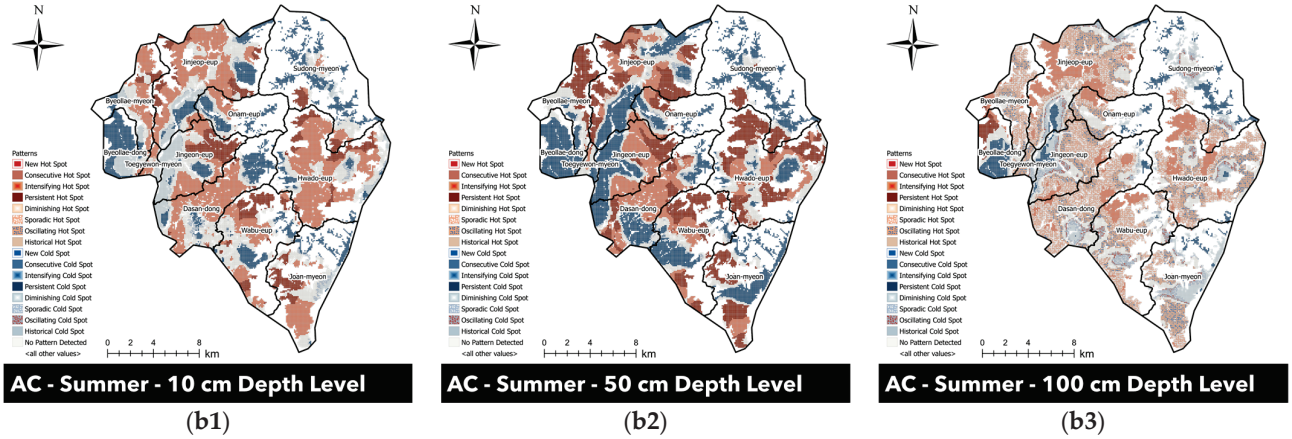

(**b1**) (**b2**) (**b3**)

Figure 3. Emerging hot spot analysis results for summer (**a1**–**a3**) saturation degree (SD) and (**b1**–**b3**) attenuation capacity (AC) in Namyangju at (**a1**,**b1**) 10 cm, (**a2**,**b2**) 50 cm, and (**a3**,**b3**) 100 cm.

Table 3. Area (%) of emerging hot spot (HS) and cold spot (CS) trends of saturation degree and attenuation capacity in summer at each depth.

Pattern	Saturation Degree			Attenuation Capacity		
	10 cm	50 cm	100 cm	10 cm	50 cm	100 cm
Oscillating CS	27.94	29.42	17.74			3.90
Sporadic CS	7.20	4.73	12.07	2.87	3.02	4.22
Diminishing CS				7.06	0.004	5.28
Persistent CS	1.81		9.62	18.25	32.09	7.13
Intensifying CS	7.52	4.42	0.50			
Intensifying HS				37.55	19.17	12.10
Persistent HS	8.90	3.37	6.80	11.61	27.51	1.03
Diminishing HS		0.03				
Sporadic HS	2.90	3.68	7.40	0.64	1.35	32.28
Oscillating HS	25.24	23.75	12.73			20.49

The ideal relationship here is when a persistent cold spot in SD returns as a persistent hot spot in AC or an intensifying hot spot in SD returns as an intensifying cold spot in AC, and so forth for the other trends. Despite that, the generally negative correlation between SD and AC still pertains to the overall cold spot and hot spot groups with 46%, 39%, and 42% area (at 10, 50, and 100 cm respectively), showing an overall trend where cold spot SD comes back as hot spot AC and vice versa. In addition, it is also shown that there is about 17% of the area at each depth level that denies the relationship between SD and AC. Although further investigation of the underlying reason for such trends is out of the scope of this study, it is most likely due to the other five governing factors in AC quantification overpowering the effect of SD in the final results.

In general, by incorporating both water flow simulation and EHSA, more insight into vadose zone vulnerability dynamics can be observed. If only a static or single value of SD is used as an input in the attenuation capacity of the vadose zone against diesel, a spatial distribution of areas with a relatively higher or lower AC might give some information and insight into where contamination mitigation and treatment strategies or stricter policies regarding diesel might be needed. Adding EHSA to such vulnerability studies provides an extra urgency factor, which helps in prioritizing areas with notable diminishing hot spots and/or intensifying cold spot trends, as both indicate a worsening vulnerability (to diesel) status over the period of study. EHSA will also help in determining which areas are improving (noted by an intensifying hot spot and diminishing cold spot), which areas require monitoring over time due to a persistent cold spot trend, and which areas are relatively more resilient to diesel contamination (persistent hot spot).

Saturation Degree	Attenuation Capacity: Oscillating CS	Sporadic CS	Diminishing CS	Persistent CS	Intensifying CS	Intensifying HS	Persistent HS	Diminishing HS	Sporadic HS	Oscillating HS
10 CM										
Oscillating CS		0.27	0.76	1.36		16.90	4.21		0.11	
Sporadic CS		0.03	0.09	1.01		2.48	2.73		0.03	
Diminishing CS										
Persistent CS			0.02	0.03		0.06	1.70			
Intensifying CS		0.004	0.22	4.62		0.75	1.15		0.004	
Intensifying HS										
Persistent HS		0.36	2.76	3.18		0.27	0.22			
Diminishing HS										
Sporadic HS		0.18	0.76	0.80		0.17	0.22		0.004	
Oscillating HS		1.40	1.91	4.72		8.41	0.68		0.30	
50 CM										
Oscillating CS		0.62		4.27		7.50	12.74		0.41	
Sporadic CS		0.28		1.88		0.48	1.25		0.03	
Diminishing CS										
Persistent CS										
Intensifying CS		0.11		3.91		0.01	0.05			
Intensifying HS										
Persistent HS				3.32			0.004		0.05	
Diminishing HS				0.03						
Sporadic HS		0.08		3.31			0.08		0.04	
Oscillating HS		1.04	0.004	8.86		3.43	4.20		0.31	
100 CM										
Oscillating CS	0.30	0.21	0.16	0.22		3.67			8.03	3.62
Sporadic CS	0.34	0.29	0.24	0.58		1.37			5.87	2.29
Diminishing CS										
Persistent CS	0.20	0.33	0.21	1.10		1.37			3.35	1.60
Intensifying CS		0.004	0.04	0.45						
Intensifying HS										
Persistent HS	0.31	0.48	1.76	1.45		0.48	1.02		0.31	0.28
Diminishing HS										
Sporadic HS	0.66	1.36	1.31	1.17		0.33	0.01		0.47	0.38
Oscillating HS	0.91	0.68	0.71	0.53		0.84			1.90	3.93

Figure 4. Overlapping area (%) of spatiotemporal hot spot (HS) and cold spot (CS) patterns of saturation degree and attenuation capacity in summer. The color scheme represents the percentage of the area from smallest (white) to largest (dark green).

4. Conclusions

This study applied an empirical model describing soil AC against diesel within a GIS environment. Six governing parameters, notably SOM, TP, D_{30}, C_u, n, and SD, were used to determine the spatial distribution of AC in Namyangju. Since SD is highly sensitive to meteorological and climatological changes, the temporal changes (and trends) of both SD and the resulting AC could be captured by incorporating EHSA into the designated time frame (1997–2022). For this purpose, infiltration simulation using Phydrus was performed to obtain simulated historical soil water content subsequently used in SD and AC estimations over time. By applying EHSA, the trends of SD and AC over space and time could be effectively identified. Areas with intensifying cold spots and diminishing hot spots that correspond to the decreasing AC might need stricter policies regarding diesel contamination prevention and mitigation strategies (e.g., areas near water bodies). On the other hand, areas with intensifying hot spots and diminishing cold spots that correspond

to the increasing AC might not need a policy that is as strict. The overlapping analysis between SD and AC revealed that the inherent negative correlation between SD and AC still pertains to the overall cold spot and hot spot groups with a small exception (ca. 17%) in which the SD and AC are proportional to each other, presumably due to the uneven distribution of the other five governing factors. Another limitation in this study is the difficulty of model calibration due to the fact that the AC is not directly measurable from the field. Due to this limitation, we focused more on proposing the conceptual framework in a way that incorporates EHSA in vulnerability studies to statistically analyze the vulnerability trend in space and time simultaneously and continuously.

Supplementary Materials: The following supporting information can be downloaded at: https://www.mdpi.com/article/10.3390/hydrology11020019/s1, Figure S1: Daily precipitation (mm) record in Namyangju from 1997–2022; Figure S2: 46 soil series in the studied area; Figure S3: Rated static parameter spatial distribution maps (a) OM, (b) TP, (c) D30, (d) Cu, (e) n in Namyangju at (1) 10 cm, (2) 50 cm, (3) 100 cm; Figure S4: left) Sampling point (red dot), right) Sampling process; Figure S5. The sampling point (red dot) shown in the AC map and the corresponding AC value generated from public data; Table S1: Minimum and maximum values for parameters and the attenuation capacity before normalization; Table S2: Parameter rating, weight, and AC of field sample; Text S1.

Author Contributions: The authors made fairly equal contributions to this manuscript. L.S. and J.C. conceived and conceptualized the study. L.S. and K.-J.L. collected and processed the data. L.S. and J.C. drafted the manuscript. J.C. provided supervision. S.J.K. contributed to methodology. H.Y.J. provided resources. S.H.K. and S.L. made revisions and improvements to the draft. All authors have read and agreed to the published version of the manuscript.

Funding: This work was supported by the Korea Environment Industry & Technology Institute (KEITI) through the Subsurface Environment Management (SEM) Project (2018002440006 and 202100 2470004), which is funded by the Korea Ministry of Environment (MOE). The authors also acknowledge support from the Future Research Program (2E33081) and K-Lab (Geo-SMaRT; 2E33084), which are funded by the Korea Institute of Science and Technology (KIST).

Data Availability Statement: The soil physicochemical data analyzed in this article are available on the Korea Rural Development Association (RDA) official website: http://soil.rda.go.kr/ (accessed on 9 June 2022). The meteorological data are available on the Korea Meteorological Administration (KMA) official website: https://data.kma.go.kr/ (accessed on 9 February 2023). The rest of the data presented in this study are available on request from the corresponding author.

Conflicts of Interest: The authors declare no conflicts of interest.

References

1. An, S.; Kim, K.; Woo, H.; Yun, S.T.; Chung, J.; Lee, S. Coupled Effect of Porous Network and Water Content on the Natural Attenuation of Diesel in Unsaturated Soils. *Chemosphere* **2022**, *302*, 134804. [CrossRef]
2. Bento, F.M.; Camargo, F.A.O.; Okeke, B.C.; Frankenberger, W.T. Comparative Bioremediation of Soils Contaminated with Diesel Oil by Natural Attenuation, Biostimulation and Bioaugmentation. *Bioresour. Technol.* **2005**, *96*, 1049–1055. [CrossRef]
3. Regadío, M.; Ruiz, A.I.; Rodríguez-Rastrero, M.; Cuevas, J. Containment and Attenuating Layers: An Affordable Strategy That Preserves Soil and Water from Landfill Pollution. *Waste Manag.* **2015**, *46*, 408–419. [CrossRef]
4. Šimůnek, J.; Šejna, M.A.; Saito, H.; Sakai, M.; Van Genuchten, M.T. *The HYDRUS-1D Software Package for Simulating the Movement of Water, Heat, and Multiple Solutes in Variably Saturated Media*; Version 4.17; Department of Environmental Sciences, University of California Riverside: Riverside, CA, USA.
5. Aller, L.; Bennett, T.; Lehr, J.H.; Petty, R.J.; Hackett, G. *DRASTIC: A Standardized Method for Evaluating Ground Water Pollution Potential Using Hydrogeologic Settings*; U.S. Environmental Protection Agency: Washington, DC, USA, 1987; p. 455.
6. Busico, G.; Alessandrino, L.; Mastrocicco, M. Denitrification in Intrinsic and Specific Groundwater Vulnerability Assessment: A Review. *Appl. Sci.* **2021**, *11*, 657. [CrossRef]
7. Douglas, S.H.; Dixon, B.; Griffin, D. Assessing the Abilities of Intrinsic and Specific Vulnerability Models to Indicate Groundwater Vulnerability to Groups of Similar Pesticides: A Comparative Study. *Phys. Geogr.* **2018**, *39*, 487–505. [CrossRef]
8. Andersen, L.J.; Gosk, E. Applicability of Vulnerability Maps. *Environ. Geol. Water Sci.* **1989**, *13*, 39–43. [CrossRef]
9. Woo, H.; An, S.; Kim, K.; Park, S.; Oh, S.; Kim, S.H.; Chung, J.; Lee, S. A New Evaluation Model for Natural Attenuation Capacity of Vadose Zone against Petroleum Contaminants. *J. Soil Groundw. Environ.* **2022**, *27*, 92–98. [CrossRef]

10. Chai, R.; Mao, J.; Chen, H.; Wang, Y.; Shi, X.; Jin, M.; Zhao, T.; Hoffman, F.M.; Ricciuto, D.M.; Wullschleger, S.D. Human-Caused Long-Term Changes in Global Aridity. *npj Clim. Atmos. Sci.* **2021**, *4*, 65. [CrossRef]
11. Lu, J.; Carbone, G.J.; Grego, J.M. Uncertainty and Hotspots in 21st Century Projections of Agricultural Drought from CMIP5 Models. *Sci. Rep.* **2019**, *9*, 4922. [CrossRef] [PubMed]
12. Wang, Y.; Mao, J.; Hoffman, F.M.; Bonfils, C.J.W.; Douville, H.; Jin, M.; Thornton, P.E.; Ricciuto, D.M.; Shi, X.; Chen, H.; et al. Quantification of Human Contribution to Soil Moisture-Based Terrestrial Aridity. *Nat. Commun.* **2022**, *13*, 6848. [CrossRef]
13. Lian, X.; Piao, S.; Chen, A.; Huntingford, C.; Fu, B.; Li, L.Z.X.; Huang, J.; Sheffield, J.; Berg, A.M.; Keenan, T.F.; et al. Multifaceted Characteristics of Dryland Aridity Changes in a Warming World. *Nat. Rev. Earth Environ.* **2021**, *2*, 232–250. [CrossRef]
14. Margono, B.A.; Potapov, P.V.; Turubanova, S.; Stolle, F.; Hansen, M.C. Primary Forest Cover Loss in Indonesia over 2000–2012. *Nat. Clim. Change* **2014**, *4*, 730–735. [CrossRef]
15. ESRI. *How Emerging Hot Spot Analysis Works*; Environmental Systems Research Institute: Redlands, CA, USA, 2023; Available online: https://pro.arcgis.com/en/pro-app/latest/tool-reference/space-time-pattern-mining/learnmoreemerging.htm (accessed on 14 November 2022).
16. Naqvi, S.A.A.; Sajjad, M.; Waseem, L.A.; Khalid, S.; Shaikh, S.; Kazmi, S.J.H. Integrating Spatial Modelling and Space–Time Pattern Mining Analytics for Vector Disease-Related Health Perspectives: A Case of Dengue Fever in Pakistan. *Int. J. Environ. Res. Public Health* **2021**, *18*, 12018. [CrossRef] [PubMed]
17. Purwanto, P.; Utaya, S.; Handoyo, B.; Bachri, S.; Astuti, I.S.; Sastro, K.; Utomo, B.; Aldianto, Y.E. Spatiotemporal Analysis of COVID-19 Spread with Emerging Hotspot Analysis and Space-Time Cube Models in East Java, Indonesia. *ISPRS Int. J. Geo Inf.* **2021**, *10*, 133. [CrossRef]
18. Kang, Y.; Cho, N.; Son, S. Spatiotemporal Characteristics of Elderly Population's Traffic Accidents in Seoul Using Space-Time Cube and Space-Time Kernel Density Estimation. *PLoS ONE* **2018**, *13*, e0196845. [CrossRef] [PubMed]
19. Xu, D.; Zhang, Q.; Ding, Y.; DE ZHANG, A. Spatiotemporal Pattern Mining of Drought in the Last 40 Years in China Based on the Spei and Space–Time Cube. *J. Appl. Meteorol. Climatol.* **2021**, *60*, 1219–1230. [CrossRef]
20. Lal, P.; Shekhar, A.; Gharun, M.; Das, N.N. Spatiotemporal Evolution of Global Long-Term Patterns of Soil Moisture. *Sci. Total Environ.* **2023**, *867*, 161470. [CrossRef] [PubMed]
21. Ahmadi, H.; Argany, M.; Ghanbari, A.; Ahmadi, M. Visualized Spatiotemporal Data Mining in Investigation of Urmia Lake Drought Effects on Increasing of PM10 in Tabriz Using Space-Time Cube (2004–2019). *Sustain. Cities Soc.* **2022**, *76*, 103399. [CrossRef]
22. Harris, N.L.; Goldman, E.; Gabris, C.; Nordling, J.; Minnemeyer, S.; Ansari, S.; Lippmann, M.; Bennett, L.; Raad, M.; Hansen, M.; et al. Using Spatial Statistics to Identify Emerging Hot Spots of Forest Loss. *Environ. Res. Lett.* **2017**, *12*, 024012. [CrossRef]
23. Betty, E.L.; Bollard, B.; Murphy, S.; Ogle, M.; Hendriks, H.; Orams, M.B.; Stockin, K.A. Using Emerging Hot Spot Analysis of Stranding Records to Inform Conservation Management of a Data-Poor Cetacean Species. *Biodivers. Conserv.* **2020**, *29*, 643–665. [CrossRef]
24. Cuba, N.; Sauls, L.A.; Bebbington, A.J.; Bebbington, D.H.; Chicchon, A.; Marimón, P.D.; Diaz, O.; Hecht, S.; Kandel, S.; Osborne, T.; et al. Emerging Hot Spot Analysis to Indicate Forest Conservation Priorities and Efficacy on Regional to Continental Scales: A Study of Forest Change in Selva Maya 2000–2020. *Environ. Res. Commun.* **2022**, *4*, 071004. [CrossRef]
25. Yang, M.; Yang, Y.S.; Du, X.; Cao, Y.; Lei, Y. Fate and Transport of Petroleum Hydrocarbons in Vadose Zone: Compound-Specific Natural Attenuation. *Water Air Soil Pollut.* **2013**, *224*, 1439. [CrossRef]
26. Mills, S.A.; Frankenberger, W.T. Evaluation of Phosphorus Sources Promoting Bioremediation of Diesel Fuel in Soil. *Bull. Environ. Contam. Toxicol.* **1994**, *53*, 280–284. [CrossRef] [PubMed]
27. R Core Team. *R: A Language and Environment for Statistical Computing*; R Foundation for Statistical Computing: Vienna, Austria, 2022.
28. Van Bemmelen, J. Über die Bestimmung des Wassers, des Humus, des Schwefels, der in den Colloïdalen Silikaten Gebundenen Kieselsäure, des Mangans usw im Ackerboden. *Landwirthschaftlichen Vers. Station.* **1890**, *37*, 279–290.
29. Pribyl, D.W. A Critical Review of the Conventional SOC to SOM Conversion Factor. *Geoderma* **2010**, *156*, 75–83. [CrossRef]
30. Hou, E.; Chen, C.; Luo, Y.; Zhou, G.; Kuang, Y.; Zhang, Y.; Heenan, M.; Lu, X.; Wen, D. Effects of Climate on Soil Phosphorus Cycle and Availability in Natural Terrestrial Ecosystems. *Glob. Change Biol.* **2018**, *24*, 3344–3356. [CrossRef]
31. Van Genuchten, M.T.; Schaap, M.G.; Leij, F.J. Rosetta: A Computer Program for Estimating Soil Hydraulic Parameters with Hierarchical Pedotransfer Functions. *J. Hydrol.* **2001**, *251*, 164–176.
32. Vereecken, H.; Weynants, M.; Javaux, M.; Pachepsky, Y.; Schaap, M.G.; van Genuchten, M.T. Using Pedotransfer Functions to Estimate the van Genuchten-Mualem Soil Hydraulic Properties: A Review. *Vadose Zone J.* **2010**, *9*, 795–820. [CrossRef]
33. Robinson, D.A.; Nemes, A.; Reinsch, S.; Radbourne, A.; Bentley, L.; Keith, A.M. Global Meta-Analysis of Soil Hydraulic Properties on the Same Soils with Differing Land Use. *Sci. Total Environ.* **2022**, *852*, 158506. [CrossRef] [PubMed]
34. Šimůnek, J.; van Genuchten, M.T.; Šejna, M. Development and Applications of the HYDRUS and STANMOD Software Packages and Related Codes. *Vadose Zone J.* **2008**, *7*, 587–600. [CrossRef]
35. Collenteur, R.; Vremec, M.; Brunetti, G. Interfacing FORTAN Code with Python: An Example for the Hydrus-1D Model. In Proceedings of the EGU General Assembly, Online, 3–8 May 2020.
36. Chen, Y.; Guan, Y.; Shao, G.; Zhang, D. Investigating Trends in Streamflow and Precipitation in Huangfuchuan Basin with Wavelet Analysis and the Mann-Kendall Test. *Water* **2016**, *8*, 77. [CrossRef]

37. Ali, R.; Kuriqi, A.; Abubaker, S.; Kisi, O. Long-Term Trends and Seasonality Detection of the Observed Flow in Yangtze River Using Mann-Kendall and Sen's Innovative Trend Method. *Water* **2019**, *11*, 1855. [CrossRef]
38. Baig, M.R.I.; Shahfahad; Naikoo, M.W.; Ansari, A.H.; Ahmad, S.; Rahman, A. Spatio-Temporal Analysis of Precipitation Pattern and Trend Using Standardized Precipitation Index and Mann–Kendall Test in Coastal Andhra Pradesh. *Model. Earth Syst. Environ.* **2022**, *8*, 2733–2752. [CrossRef]
39. Noori, R.; Woolway, R.I.; Saari, M.; Pulkkanen, M.; Kløve, B. Six Decades of Thermal Change in a Pristine Lake Situated North of the Arctic Circle. *Water Resour. Res.* **2022**, *58*, e2021WR031543. [CrossRef]
40. Noori, R.; Maghrebi, M.; Jessen, S.; Bateni, S.M.; Heggy, E.; Javadi, S.; Noury, M.; Pistre, S.; Abolfathi, S.; AghaKouchak, A. Decline in Iran's Groundwater Recharge. *Nat. Commun.* **2023**, *14*, 6674. [CrossRef]

Disclaimer/Publisher's Note: The statements, opinions and data contained in all publications are solely those of the individual author(s) and contributor(s) and not of MDPI and/or the editor(s). MDPI and/or the editor(s) disclaim responsibility for any injury to people or property resulting from any ideas, methods, instructions or products referred to in the content.

geosciences

MDPI

Article

Leachate Experiments to Evaluate Weathering of Waste Rock for Backfill Aquifers in Restored Coal Mine Pits, Powder River Basin, USA

Julianna Martin and Jeff B. Langman *

Department of Earth and Spatial Sciences, University of Idaho, Moscow, ID 83844, USA
* Correspondence: jlangman@uidaho.edu

Abstract: Restoration of open-pit mines may utilize waste rock for landscape reconstruction, which can include the construction of backfill aquifers. Weathering and contaminant transport may be different in backfill aquifers compared to the surrounding aquifer because of newly available mineral surfaces and transportable nano- to micro-scale particles generated during mining. Waste rock from the Cordero Rojo open-pit coal mine in the Powder River Basin was exposed to benchtop leachate experiments for 20 weeks at temperatures of 5 °C and 20 °C. Collected leachate was analyzed for Eh, pH, specific conductance, alkalinity, and cation and anion concentrations as unfiltered and 0.45-µm and 0.2-µm filtered concentrations. During the experiment, leachate Eh and pH substantially varied during the first 55 days, which corresponds to a period of high specific conductance (>1000 µS/cm) and alkalinity (>200 mg/L). Correspondingly, anion and cation concentrations were the largest during this early weathering stage, and the filter fractions indicated multiple forms of transported elements. After this early weathering stage, column leachate evolved towards a weathering equilibrium of neutral, oxidizing, and low solute conditions indicated by positive Eh values, pH near 7, and specific conductance <500 µS/cm. This evolution was reflected in the decline and stabilization or non-detection of metal(loid) concentrations reflective of a shift to primarily bulk aluminosilicate weathering when coal- and salt-associated elements, such as arsenic, cadmium, and selenium, were not detected or at minimal concentrations. Over the course of the experiment, the solute trend of certain elements indicated particular weathering processes—cadmium and nanoparticle transport, selenium and salt dissolution, and arsenic and pyrite oxidation. The mining of overburden formations and use of the waste rock for backfill aquifers as part of landscape reconstruction will create newly available mineral surfaces and nanoparticles that will weather to produce solute concentrations not typically found in groundwater associated with the original overburden.

Keywords: waste rock; backfill aquifer; leachate experiment; weathering evolution

1. Introduction

A backfill aquifer is produced from the filling of a mine pit with waste rock (e.g., overburden and interburden materials) and the return of groundwater from infiltrating precipitation or lateral inflow from the adjacent aquifer. As water percolates into the waste rock, a reaction front propagates through the aquifer as newly exposed mineral surfaces and small particles (e.g., nanoparticles) are exposed to weathering and transport processes [1,2]. Progression of the reaction front is visible in the temporal evolution of solute release until a new equilibrium of weathering is established [3–6]. The difficulty in predicting the potential water quality of backfill aquifers is not our lack of mineral weathering knowledge but our lack of understanding of the availability of potential sources contributing to solute release and transport in this modified aquifer matrix. The incomplete source identification for the prediction of solute release has resulted in the exceedance of water quality criteria for backfill aquifers when it was predicted that weathering of the waste rock would not result in groundwater contamination issues [7,8].

Backfill aquifers in the Powder River Basin (Figure 1), the largest coal mining district in the United States, have shown variable water quality and exceedance of water quality criteria for metal(loid) and nonmetal contaminants due to the waste rock used for landscape restoration. The blasting and transport of the waste rock produce a new aquifer matrix with the generation of new mineral surfaces and nanoparticles that can produce high weathering and solute transport rates [5,9–11]. A weathering or release rate is the rate at which primary minerals are congruently or incongruently transformed into secondary minerals with the release of dissolved reaction products (solutes) [9]. Predicting the release of solutes can be difficult because of coupled and sustained biogeochemical processes, but the identification of potential solute sources and associated reaction rates with the development of an applicable conceptual model is critical for estimating solute release and evaluating future water quality [12–14]. A governing physical property of weathering is the available surface area where smaller grain fractions typically undergo the greatest weathering and release of solutes [15–17]. The generation and transport of nanoparticles, materials with at least one dimension within the nanometer scale [18], can also contribute to the solute load through inclusion in the dissolved phase (<0.45-μm filtering) and will weather to produce additional solutes during transport [19]. Using waste rock from the Cordero Rojo Mine in the Powder River Basin (PRB), a leach column experiment was conducted to discriminate solute sources from newly created mineral surfaces and transportable particles to better understand solute release during early-stage weathering that can impact the water quality of backfill aquifers. Leachate data provided insight into the mineral sources of the solutes and the form of the solutes released with the weathering of the waste rock.

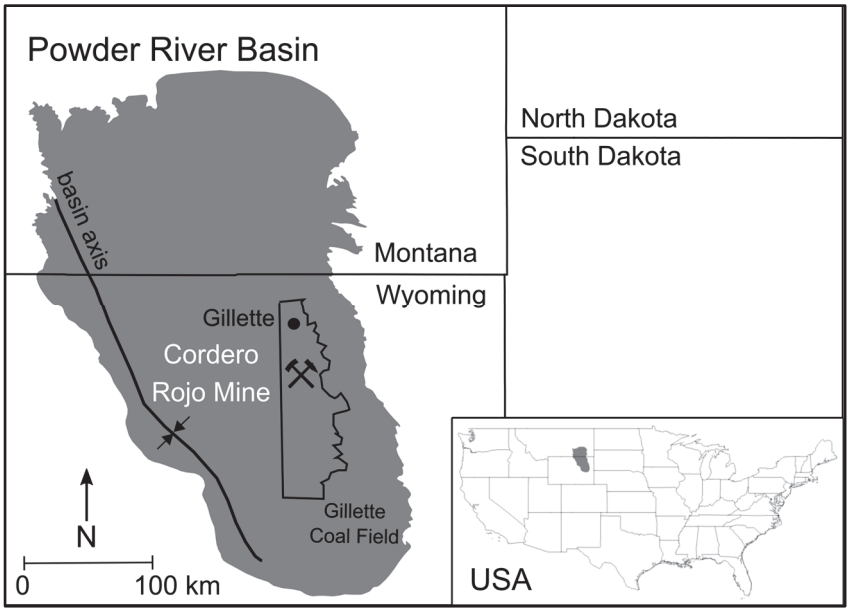

Figure 1. Location of the Cordero Rojo Mine near the town of Gillette in the Powder River Basin of Wyoming, USA (basin boundary from the U.S. Geological Survey).

1.1. Powder River Basin Geology

The PRB (Figure 1) is a north-northwest to south-southeast trending asymmetric syncline that accumulated marine, alluvial, fluvial, and lacustrine sediments [20]. The structural axis is located along the western part of the basin (Figure 1). The western limb of the PRB is characterized by steeply dipping (~20°) strata, and the eastern limb is characterized by gently dipping (2–5°) strata, including the coal-bearing rocks [21]. The Cordero Rojo Mine extracts its coal from the Wyodak-Anderson coal seam of the Tongue River member of the Fort Union Formation, which is overlain by upper units of the Paleocene Fort Union Formation and the near-surface Eocene Wasatch Formation [22] (Figure 2). Open-pit mining of the coal takes advantage of the near-surface coal deposits

along the basin's eastern margin and their gentle westward dip. A typical PRB mining operation consists of a westward-moving open pit, removal of overburden and coal, nearby storage of waste rock, and landscape restoration to the east of the active mine site (Figure 3).

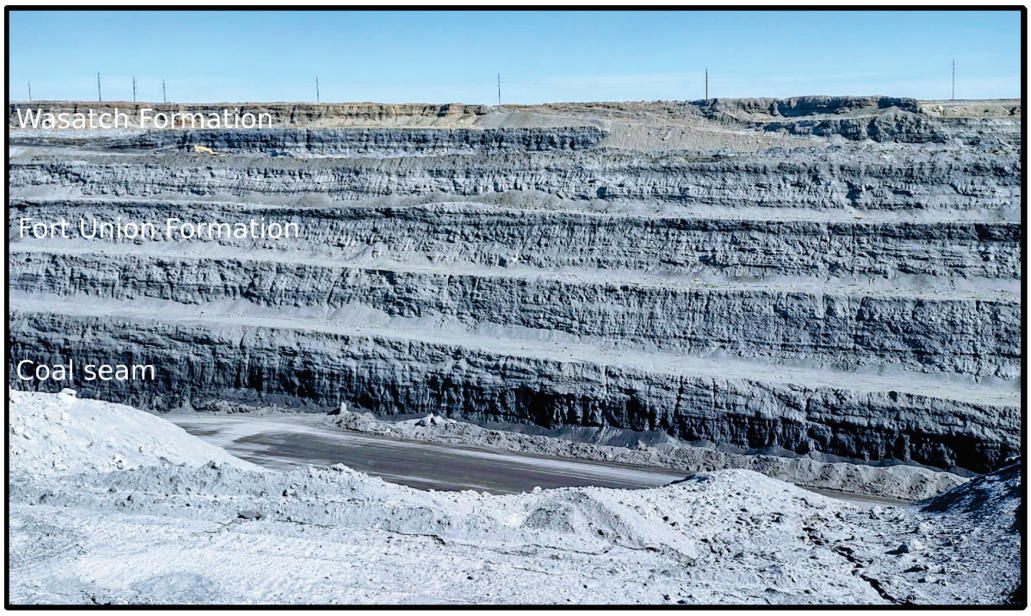

Figure 2. Overburden and coal seam at the Cordero Rojo Mine, Powder River Basin, Wyoming, USA.

Figure 3. Removal of overburden and waste rock generation during open-pit coal mining at the Cordero Rojo Mine, Powder River Basin, Wyoming, USA.

1.2. Powder River Basin Waste Rock and Groundwater Contaminants

Waste rock from the Cordero Rojo Mine in the PRB is derived from the Wasatch and Fort Union formations—sequences of interbedded fluvial, lacustrine, and palustrine deposits that compose the overburden [23–25]. The Wasatch Formation is composed of sandstones, mudstones, conglomerate lenses, and interbedded limestone and evaporites [26]. The Fort Union Formation is composed of non-sulfidic shales, mudstones, and concretionary sandstones [27,28] whose paleoenvironment also produced the interbedded

low-sulfur coal [29–31]. The PRB coal contains accessory minerals, such as arsenic-bearing pyrite [FeS_2], cadmium-bearing sphalerite [(Zn,Fe)S], and galena [PbS] [32]. Primary contaminants (exceedance of water quality criteria) detected in backfill aquifers of the PRB include arsenic [As], barium [Ba], manganese [Mn], and selenium [Se] [33]. Such contamination is not typically found in groundwater that has interacted with the Wasatch and Fort Union formations [34]. Therefore, it was hypothesized that production and disposal of the waste rock have incorporated small coal particles containing higher concentrations of the potential contaminants, exposed previously unavailable forms of the contaminants (e.g., bound salts), and/or produced contaminant-containing nanoparticles that are weathered and transported within the backfill aquifers. The goal of this study was to discriminate contaminant sources through the interpretation of solute trends indicative of weathering processes in the waste rock.

2. Study Methods

2.1. Waste Rock Collection

Wasatch and Fort Union waste rock were collected within two weeks of initial excavation from the Cordero Rojo Mine in August of 2021. The waste rock samples were collected from the most recent waste piles generated with mining of the overburden (nearest waste piles to the active mine site, as shown in Figure 3). Sample collection was completed according to the "clean hands" techniques as prescribed for field and laboratory experiments involving trace metals [35,36]. Wasatch and Fort Union waste rock were segregated during the mining process, and samples were collected separately per standard practice for sampling aggregates [37]. The samples were screened in the field to <6.3 mm to meet the criteria for kinetic columns [38,39]. The 300 kg of screened waste rock (86 kg Wasatch waste rock and 214 kg Fort Union waste rock) was sealed in 0.02 m^3 buckets and transported to the University of Idaho, where the waste rock was temporarily stored at 5 °C until dried at 125 °C for 48 h.

2.2. Waste Rock Characterization

To distinguish potential formation differences in contaminant sources, the dried Wasatch and Fort Union waste rock were evaluated for element composition (X-ray fluorescence (XRF)), grain size distribution, weathering resistance (slake durability test [40]), and surface area (Brunauer–Emmett–Teller (BET) analysis) prior to the start of the leach column experiment. Wasatch and Fort Union waste rock were submitted to the Washington State University GeoAnalytical Laboratory for XRF analysis (Advant'XP + sequential XRF, fused beads). Grain size distribution and slake durability tests were performed at the University of Idaho. Surface area was analyzed by a contract laboratory using a TriStar II Plus High Throughput Surface Area and Porosity Analyzer.

2.3. Leach Columns

A 20-week leach column experiment was conducted to evaluate the weathering processes responsible for controlling the release and transport of potential contaminants from the waste rock. Warm-room (20 °C ± 1 °C) and cold-room (5 °C ± 0.5 °C) PVC columns (0.6 m (H) × 0.1 m (W)) were loaded with 0.8 kg of dried Wasatch waste rock and 3.2 kg of dried Fort Union waste rock to mimic overburden distributions at the Cordero Rojo Mine, which is replicated with backfill aquifer construction. The base of each column contained a two-layer, 2.5-cm thick, non-reactive mesh filter for the retention of the waste rock material while allowing for the passage of <10-μm particles into the upper portion of the mesh and <4-μm particles in the lower portion of the mesh. This dual-layer mesh assisted in retaining bulk solids in the column while minimizing the clogging of the system with the movement of microparticles into the mesh.

The weathering cycle for each leach column consisted of a semiweekly schedule of the drip introduction of 1 L of deionized water and full saturation of the waste rock for 72 h followed by a 2 h drain period and a 6 h unsaturated period before resaturation of

the column. This is a modification of the standard humidity cell protocol [39] to simulate primarily saturated (e.g., aquifer) conditions and allow for the collection of sufficient water volume for analysis of environmental parameters and solutes. The twice-weekly collection of the leachate from each column was immediately analyzed for pH (±0.01 pH), Eh (±0.2 mV), and specific conductance (±0.01 µS/cm) with calibrated Orion 3-Star meters/probes followed by submission of samples to the University of Idaho Analytical Services Laboratory for analysis of anion (0.45-µm filtered) and cation (unfiltered (total), 0.45-µm filtered, and 0.2-µm filtered) concentrations. Additionally, alkalinity was determined by an OrionStarT940 auto-titrator using 0.1 N HCl (±0.1 mg/L as $CaCO_3$). Filtered anion (bromide [Br], chloride [Cl], fluoride [F], nitrate-nitrite [NO_3-NO_2 as N], ortho-phosphate [PO_4], and sulfate [SO_4]) concentrations were determined via ion chromatography (Dionex Aquion Ion Chromatograph). Cation (aluminum [Al], As, Ba, boron [B], Cd, calcium [Ca], chromium [Cr], copper [Cu], iron [Fe], lead [Pb], magnesium [Mg], Mn, molybdenum [Mo], nickel [Ni], potassium [K], Se, sodium [Na], zinc [Zn]) concentrations of unfiltered and filtered samples were determined via inductively coupled plasma optical emission spectrometry (ICP-OES) for larger concentrations (Perkin Elmer Optima 8300 ICP-OES) and inductively coupled plasma mass spectrometry (ICP-MS) for smaller concentrations (Agilent 7800 ICP-MS). Duplicate samples were randomly collected during each leachate collection period to assess laboratory analysis accuracy.

2.4. Data Analysis

The goal of the data analysis was the evaluation of the temporal trends, or variability with time, of the environmental parameters and of the release of solutes for the identification of substantive changes in weathering processes. The identification of changes in solute release from the waste rock assisted in discriminating contaminant sources and the weathering processes that released the solutes into solution. The temporal trends of the environmental parameters of pH, specific conductance, and alkalinity were smoothed using the moving window average (4-point window) technique to reduce the volatility of the data series and allow for an improved display of the data trends (all data in Supplementary Materials). Values of Eh were not smoothed to preserve reduction–oxidation (redox) conditions that widely varied during the experiment. A principal component analysis (PCA) was used to identify clusters of related metal(loid) solutes for discriminating potential weathering processes in warm and cold conditions and the unfiltered and filter fractions. Solute data sets that were predominantly (>80 %) below laboratory reporting limits were not included in the PCA.

A Spearman rank correlation analysis of Eh and redox-sensitive elements (As, Fe, Mn, and Mo) was performed to evaluate the oxidative dissolution of sulfide minerals, such as pyrite, that are present in the Fort Union Formation [32]. The Spearman test is a nonparametric measure of rank correlation (statistical dependence between the rankings of two variables) that produces a statistic (ρ) between +1 (perfect positive relation) and −1 (perfect negative relation). This correlation analysis was performed using only the warm-room unfiltered and filtered values because of substantial non-detection results for these elements in the cold-room leachate. A false discovery rate (q-value) was used in place of a *p*-value to minimize the presentation of false negatives. Additionally, the activation energy (E_a, Equation (1)) of the oxidative dissolution of pyrite was calculated to evaluate temporal changes in pyrite weathering that may indicate inhibition of sulfide weathering because of precipitate formation [41]. Arsenic was selected for the calculation of the activation energy because of its strong correlation with Eh and the presence of Fe and sulfur [S] in other mineral sources found in the waste rock [42]. The Arrhenius equation of a single temperature and rate constant (Equation (1)) was used to calculate E_a instead of the typical two-temperature/two-rate method because cold-room As concentrations decreased

below detection levels during the experiment. The one-temperature/rate method employs the geometric solution or slope (line of best fit) of the ln k-to-time relation for estimating E_a:

$$\ln(k) = \ln(A) - (E_a/RT) \quad (1)$$

where E_a is the activation energy ($J \cdot mol^{-1}$), R is the universal gas constant (8.314×10^{-3} $J \cdot mol^{-1} \cdot K^{-1}$), A is a pre-exponential factor (s^{-1}), and T is the temperature (K) at the respective times of the observed rate constant (k in $mol \cdot m^{-2} \cdot s^{-1}$).

3. Results and Discussion

3.1. Waste Rock Characterization

Large concentrations of Al and silicon (Si) were present in the Wasatch and Fort Union waste rock, reflective of the dominant aluminosilicate minerals that compose these fluvial and lacustrine deposits [20,26] (Figure 4). Larger concentrations of redox-sensitive elements of Fe and Mn were present in the Fort Union waste rock, which are indicative of the low-energy paleoenvironments associated with certain units of the Fort Union Formation [43,44]. The slake durability tests indicated stronger rock (93% durability index) from the Wasatch Formation compared to a durability index of 89% for rock from the Fort Union Formation. Such results align with the presence of substantial sandstone in the Wasatch Formation [26] compared to the higher content of shales and mudstones in the Fort Union Formation [44]. Correspondingly, the grain size distribution analysis indicated a greater fraction of clay-sized particles (7.6%) present in the Fort Union waste rock. The greater presence of smaller particles in the Fort Union waste rock also translated to a greater surface area of 14.2 m^2/g compared to the 5.1 m^2/g for the Wasatch sample.

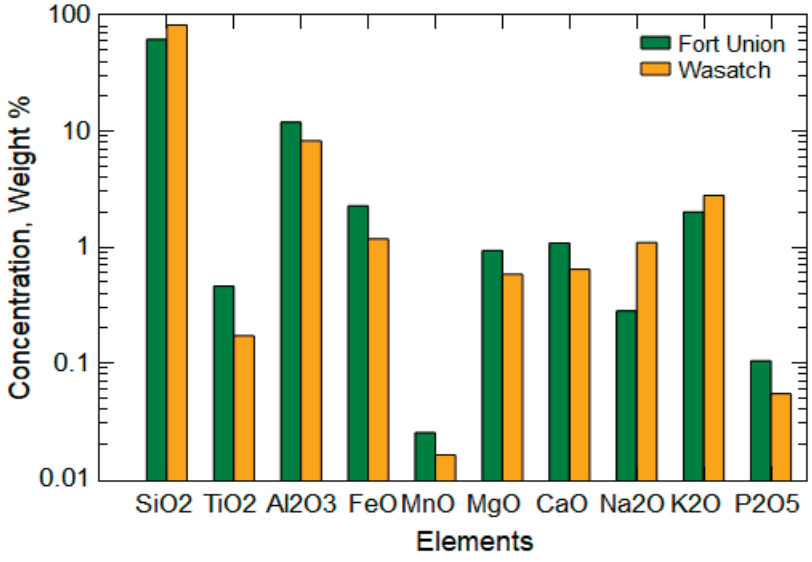

Figure 4. Element composition of the Fort Union and Wasatch waste rock from the Cordero Rojo Mine.

3.2. Leachate Environmental Conditions

The environmental parameters for warm- and cold-room leachates indicated high variability during the first 55 days of the experiment (Figure 5). Eh fluctuated between positive values (maximum of 142 mV for warm-room leachate and 154 mV for cold-room leachate) and negative values (minimum of −113 mV for the warm-room leachate and −118 mV for the cold-room leachate), indicating alternating oxidizing and reducing conditions with the greatest variability during the first 45 days. Specific conductance ranged from 6410 µS/cm to 315 µS/cm for the warm-room leachate and 6350 µS/cm to 271 µS/cm for cold-room leachate, and the specific conductance of leachate from both columns decreased sharply during the first 40 days of the experiment (Figure 5b). Values

of pH remained near neutral for the entire experiment, ranging from 6.05 to 7.03 for the warm-room leachate and 6.47 to 7.04 for the cold-room leachate (Figure 5c). However, comparison of the warm-room and cold-room pH trends indicated a greater difference in pH values during the first 55 days. Alkalinity ranged from 550 mg/L to 148 mg/L for the warm-room leachate and 613 mg/L to 139 mg/L for the cold-room leachate (Figure 5d) with a sharp decline in both alkalinities during the first 20 days and a slower decrease from day 20 to day 70.

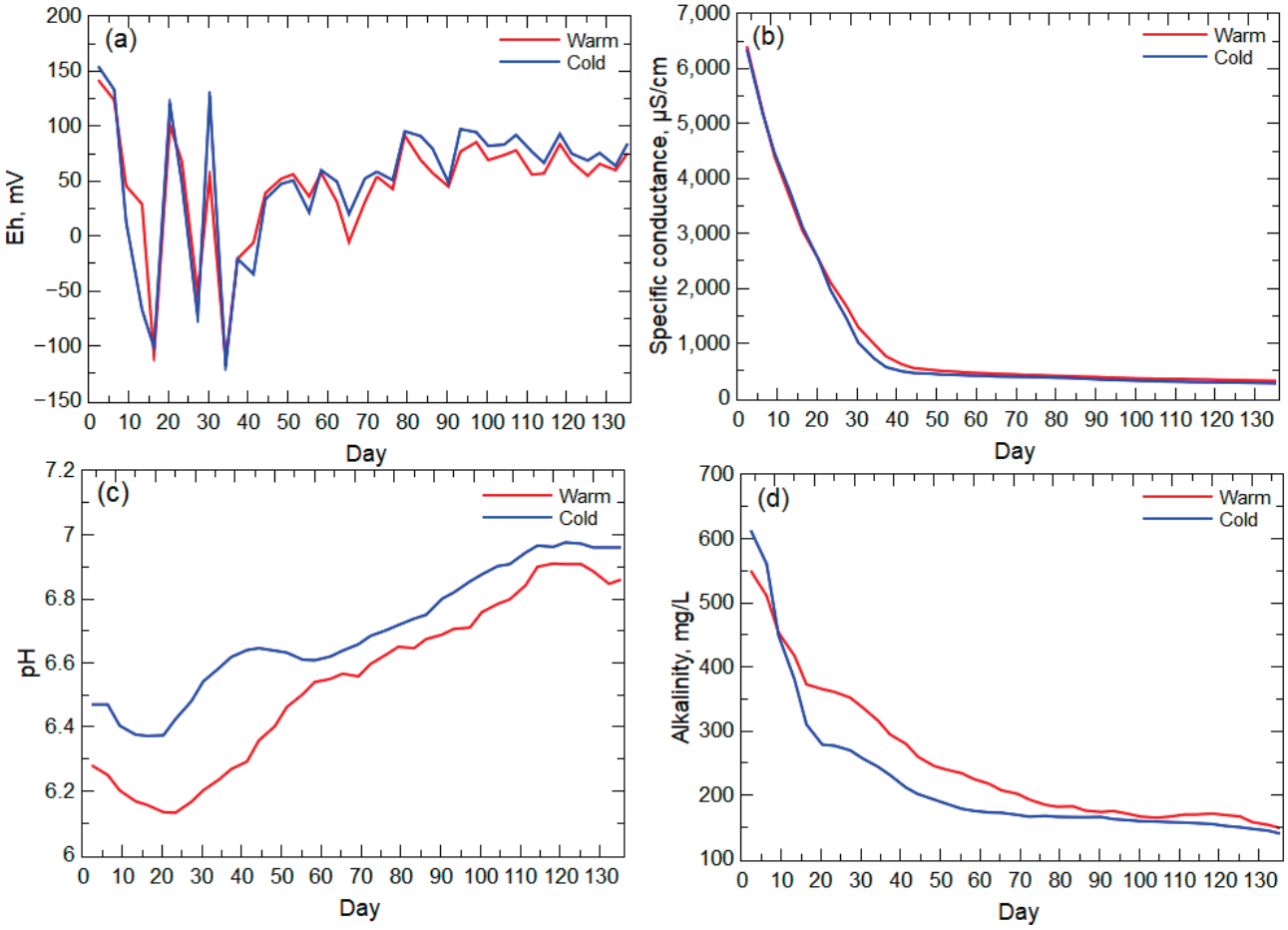

Figure 5. (**a**) Eh, (**b**) specific conductance, (**c**) pH, and (**d**) alkalinity for leachate from the warm- and cold-room columns. All trendlines have been smoothed using the moving window average (4-point window) technique except for Eh.

The high-solute-release period (early weathering stage) indicated by the leachate specific conductance likely is a result of the flushing of nano- to micro-scale particles and the influence of fast reaction weathering, such as sulfide oxidation [11,45], when the largest surface area of these minerals was available. This early weathering stage (day 3 to day 31, specific conductance >1000 µS/cm) also corresponds to sharp decreases and increases in Eh values and the period of maximum pH difference between the warm-room and cold-room leachates (Figure 5). These results indicate oxygen-consuming and acid-generating reactions, such as the oxidative dissolution of pyrite [46]. The lessening of the temperature effect on pH by day 55 corresponds to the stabilization of positive Eh values and the lessening of the decrease in the specific conductance trend (past the inflection point), which indicate a shift to weathering of less reactive minerals (e.g., aluminosilicates) and loss (consumption) of the more reactive sulfide minerals. Alkalinity values in the warm- and cold-room leachates remained elevated past this early weathering stage indicative of the relatively slower reactivity of available carbonate minerals [6,9,47], which have been identified in the Wasatch Formation [26,32].

3.3. Weathering Processes and Solute Trends

The first component (PC1, Table 1) of the PCA indicated an association (covariance of 0.14) of the major cations (Ca, Mg, and K) along with Mn, Ni, and Zn that is consistent in the unfiltered and filtered concentrations in warm- and cold-room conditions (Table 1, bold blue values). This association of the major cations indicates primarily bulk aluminosilicate and carbonate weathering throughout the experiment. The inclusion of Mn and Zn in this associated group likely reflects the presence of Mn and Zn-bearing carbonate species that have been identified in the Powder River Basin overburden formations [32]. Additionally, the Ni likely is from a clay source [32,48,49] that is weathered and transported during the experiment. The association of the redox-sensitive Mn with these elements likely is the result of the weathering of Mn oxides found in the Wasatch Formation [50], which is supported by the lack of correlation (Spearman ρ of −0.04 to −0.03, q-value of 0.84) between Eh and Mn concentrations (unfiltered or filtered) where a correlation would be expected if the Mn was being released with sulfide oxidation. The second component (PC2, Table 1) of the PCA indicated a correlation of As and Fe (stronger in filtered results) likely because of their association in sulfide minerals (e.g., As-bearing pyrite) found in the Wyodak-Anderson coal [48,51]. The second component also indicated an opposing correlation of Mo (positive) and Fe and As (negative) in the warm-room leachate (lack of detectable concentrations in the cold-room leachate), which may indicate the presence of Mo in the coal [52] that has a different mineral source than Fe and As. The association of Mo in PC2 likely is derived from the remaining organic carbon in the coal [32], which is supported by the strong, positive correlation (Spearman's ρ of 0.58 to 0.55, q-value of 0.0009) between Mo and Eh and suggestive of the oxidation of an organic source and release of Mo [53].

Table 1. Covariance matrix of the principal component analysis (two components: PC1 and PC2) for warm- and cold-room solute concentrations for each concentration fraction (total (unfiltered), 0.45-µm filtered, and 0.2 µm filtered). Noted associations in bold and colored fonts.

Element		Warm			Cold		
		Total	**0.45-µm**	**0.2-µm**	**Total**	**0.45-µm**	**0.2-µm**
As	PC1	0.02	0.03	0.03	0.09	0.13	0.13
	PC2	**−0.29**	**−0.26**	**−0.27**	−0.09	0.12	0.13
Ba	PC1	−0.13	−0.13	−0.13	−0.12	−0.13	−0.13
	PC2	0.09	0.09	0.09	0.14	0.14	0.14
B	PC1	0.11	0.14	0.14	0.09	0.14	0.14
	PC2	−0.05	0.01	0.01	0.06	−0.05	−0.05
Ca	PC1	**0.15**	**0.15**	**0.15**	**0.14**	**0.14**	**0.14**
	PC2	0.01	0.01	0.01	−0.03	−0.02	−0.02
Fe	PC1	0.11	0.06	0.07	0.03	−0.06	−0.06
	PC2	**−0.12**	**−0.27**	**−0.26**	0.14	−0.01	−0.01
Mg	PC1	**0.14**	**0.14**	**0.14**	**0.14**	**0.14**	**0.14**
	PC2	0.07	0.07	0.07	0.05	0.05	0.05
Mn	PC1	**0.14**	**0.14**	**0.14**	**0.14**	**0.14**	**0.14**
	PC2	−0.07	−0.07	−0.06	−0.04	−0.01	−0.01
Mo	PC1	−0.02	−0.02	−0.01	0.03	0.03	0.03
	PC2	0.26	0.25	0.27	0.23	0.26	0.26
Ni	PC1	**0.14**	**0.14**	**0.14**	**0.14**	**0.14**	**0.14**
	PC2	0.04	0.05	0.05	0.07	0.08	0.08
K	PC1	**0.14**	**0.14**	**0.14**	**0.14**	**0.14**	**0.14**
	PC2	0.04	0.05	0.05	0.03	0.03	0.03
Zn	PC1	**0.14**	**0.14**	**0.14**	**0.14**	**0.14**	**0.14**
	PC2	0.06	0.04	0.06	0.05	0.04	0.04

3.3.1. Salt Dissolution or Nanoparticle Flushing

The PCA did not include elements that were only detectable in the leachate during the first two weeks of the experiment, such as Cd and Se (Figure 6a,b). These elements

have an association with sulfide minerals in the PRB coal [42,54,55], but their concentration trends did not mimic a release indicative of the oxidative dissolution of pyrite, such as is seen with the As concentrations (Figure 6c). In the overburden formations, Se can be found in coal, coal-associated pyrite, water-leachable salts, and as sorbed particles (e.g., selenite [SeO_3]) [54]. Dreher and Finkelman [56] indicated that Se salts from past oxidation of pyrite may be the primary source of Se in the overburden, although they found seven different forms of Se with no discrimination between Wasatch and Fort Union formations. The quick release of Se and lack of difference between filter fraction concentrations and temperature conditions (Figure 6b) are indicative of a fast-dissolving salt and/or desorption and oxidation of Se particles, such as selenite. The incorporation of Se into gypsum ($CaSO_4$) can occur with the oxidation of pyrite/coal and the substitution of Se for S in gypsum [57,58]. Such processes are partially responsible for the significant presence of gypsum in Powder River Basin sedimentary formations [59–63]. Se-bearing salts can readily dissolve, but the dissolution of the salts may not contribute substantial soluble Se species (e.g., selenate (SeO_4^{2-})) if selenite is produced because of the preference of selenite to readily sorb to sediments [64–66]. The Se released into the leachate appears to be primarily particle release (early and large concentrations) with a contribution from Se salt dissolution that is more visible in the second week when the warm-room leachate indicated higher concentrations of Se.

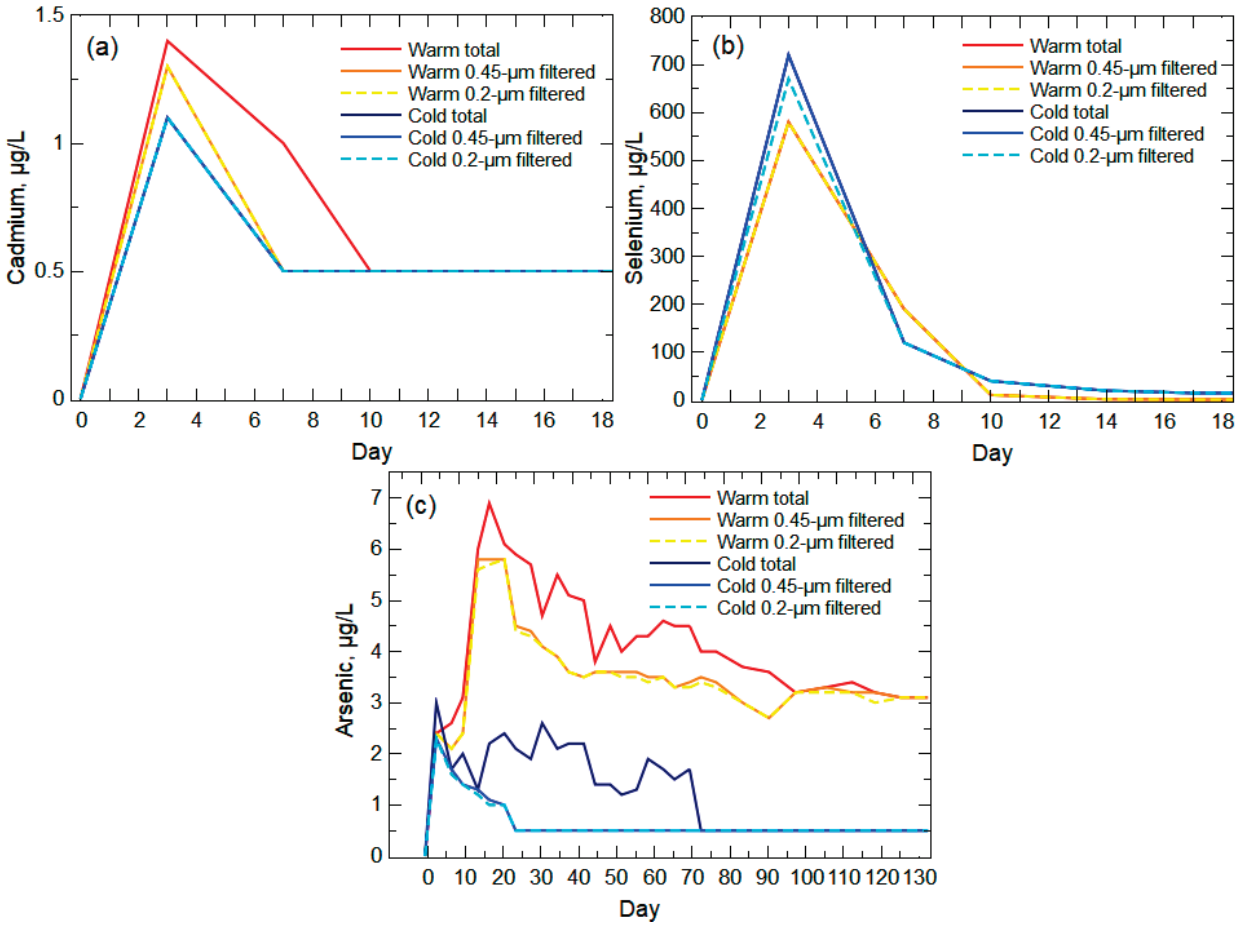

Figure 6. Unfiltered (total) and filtered concentrations in the warm-room and cold-room leachates for (**a**) cadmium and (**b**) selenium during the first 18 days of the experiment and (**c**) arsenic during the entire length of the experiment. All non-detect values were set to 0.5 µg/L, which is half the reporting limit for each of the analytes.

The leachate Cd trends indicate an early concentration peak that quickly decreased after day 3 for all filtered warm- and cold-room results and after day 7 for unfiltered warm-

room concentrations (Figure 6a). Cadmium has not been documented as a salt byproduct from the oxidation of sulfide minerals in the Fort Union Formation, but Cd is associated with sphalerite [(Fe, Zn)S] found in PRB coal [48]. Given the likely presence of Se salts from the oxidation of pyrite, it can be assumed that Cd was similarly released with sphalerite oxidation and deposited in the overburden formations. The introduction of leach water to the waste rock would not have a similar mobilizing effect on Cd compared to Se if both elements are contained in readily dissolvable salts since Cd is less soluble than Se [67]. This lower solubility of Cd is reflected in the much lower concentrations of Cd released from the waste rock compared to Se (Figure 6) even though there are equivalent amounts of Cd and Se in the Wyodak-Anderson coal seam [68]. With the lower solubility of Cd, it is assumed that the early release of Cd from the waste rock is because of the transport of Cd-bearing particles, primarily nanoparticles [69]. Not all of the Cd was present in nanoparticles given the greater release of Cd in the unfiltered warm-room leachate, which indicated a more torturous path of the release of larger particles being transported from the waste rock. Comparison of the pre-experiment Wasatch and Fort Union rock samples to post-experiment samples from the warm-room column indicated the loss of the smallest grains (<0.07 mm) from the Fort Union waste rock during the experiment indicative of the loss (e.g., transport, weathering) of small particles (Figure 7).

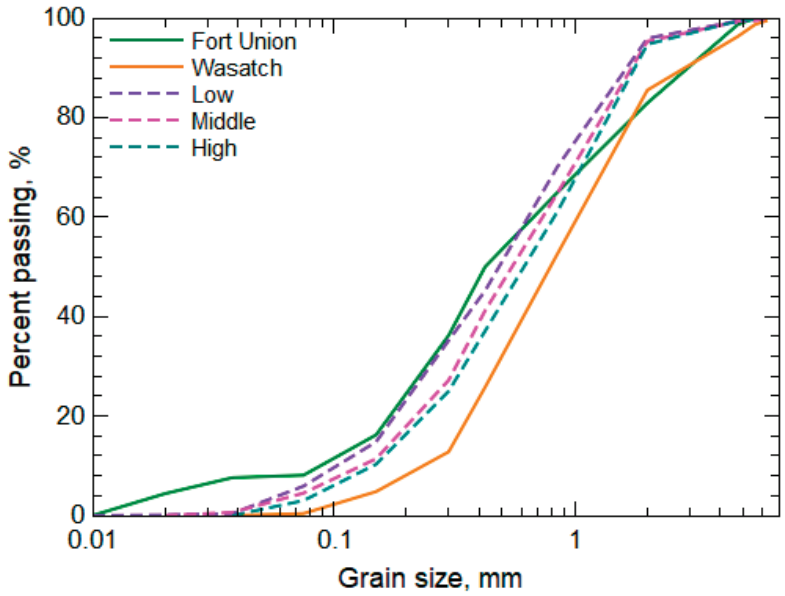

Figure 7. Grain size analysis of waste rock from the pre-experiment Fort Union and Wasatch samples and post-experimental waste rock sampled at three locations from the warm-room leach column (low, middle, and high).

3.3.2. Sulfide Oxidation

Arsenic concentrations were largest in warm-room and cold-room leachates during the early weathering stage when Eh varied between positive and negative values (Figure 6c), reflective of the likely consumption of oxygen with sulfide mineral weathering. The correlation analysis indicated a strong-to-moderate negative correlation (Spearman's ρ of −0.56 to −0.29, q-value of 0.0009 to 0.1) between As and Eh for the filtered and unfiltered concentrations. The majority of the As released in the warm-room leachate was present in the 0.2-µm filtered samples indicating ion release and/or small nanoparticles (Figure 6c). The larger As concentrations in unfiltered leachate from both temperature conditions indicate some release of As-bearing microparticles from the columns. The substantial difference in As concentrations between warm-room and cold-room leachates indicates a temperature effect for oxidative dissolution of As-bearing pyrite. However, the cold-room leachate continued to show the presence of As in the unfiltered solution following the loss of detectable As in the filtered fractions.

The release of As with weathering of As-bearing pyrite typically would result in an early peak concentration because of the dissolution of the source mineral(s) outer layer (rim or coating) followed by a moderated release according to the mass-to-volume ratio of the available mineral source and pH of the porewater solution [70,71]. The primary loss of As from the waste rock during the early weathering stage for the warm-room column is in the filtered samples and displays a concentration trend that peaks near day 17, followed by a moderate decreasing trend. The post-peak trend of As concentrations follows an expected element release trend for the oxidative dissolution of pyrite [72], which is indicative of the weathering of the As-bearing pyrite contained in the PRB coal that was incorporated into the waste rock. Calculation of the effective activation energy of pyrite weathering (Figure 8) from the filtered concentrations of As presents a typical energy trend of an initial energy barrier (oxidation of the mineral surface), an early drop in the energy barrier as the sulfide surface degrades, and a slow increase in the necessary energy for oxidation of the remaining sulfide mineral. This trend represents the oxidation of the unreacted sulfide surface (shrinking core model), which becomes controlled by the inward diffusion of oxygen given the pore-blocking effect of Fe and S precipitates on the unreacted sulfide surface [73]. This oxygen diffusion effect is more pronounced in neutral conditions, in which Fe is not solubilized and can form substantial Fe (oxyhydr)oxide precipitates [74–76]. The effective activation energy trend aligns with the evolution of activation energy necessary for the different bonding arrangements where the initial dissociation of oxygen at the sulfide surface typically requires an activation energy of 22.6 kJ/mol [77] (compared to our calculated 18.2 kJ/mol) followed by lower energy requirements with degradation of the mineral structure.

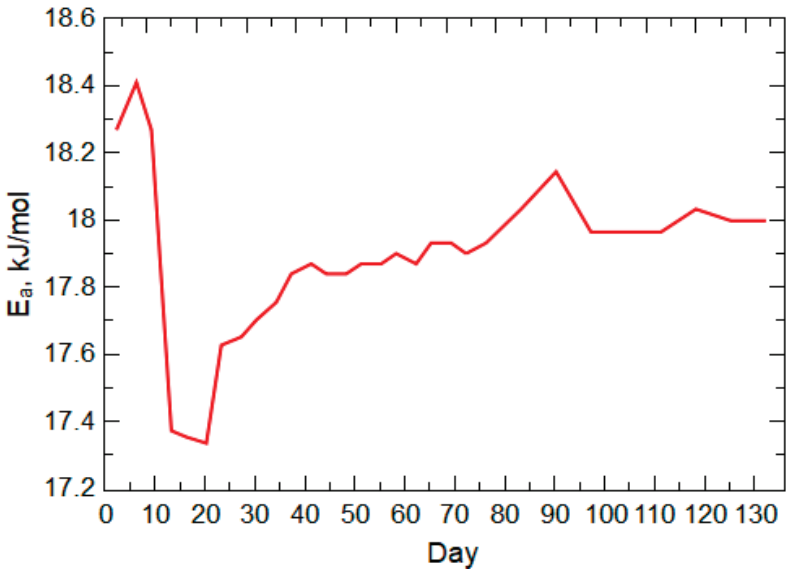

Figure 8. Activation energy (E_a) of pyrite weathering derived from warm-room leach column arsenic concentrations during the 20-week experiment.

3.3.3. Bulk Solid Weathering

With the identification of salt dissolution, particle transport, and pyrite oxidation contributing to the high solute release period, an additional weathering process is necessary to explain the large concentrations in most solutes during the early weathering stage and the following period of higher alkalinity (Figure 5). Transport of other nanoparticles and weathering of the bulk aluminosilicate and carbonate minerals likely explains the remaining contributions to the high solute and high alkalinity periods prior to the waste rock equilibrating to the low-solute weathering period (post-day 70). Carbonates typically weather at a higher rate compared to aluminosilicates [78], which may explain the higher Ca concentrations compared to K (Figure 9) even though there is greater K in the Wasatch and Fort Union waste rock (Figure 4). Carbonate weathering likely is responsible for the

pH moderation (>6.1) during pyrite oxidation early in the experiment and the increasing pH during the remainder of the experiment (Figure 5) as well as the longer period of high alkalinity compared to the high specific conductance period (Figure 5). The large, early concentrations for Ca and K suggest the release of Ca- and K-bearing nanoparticles [19], desorption (exchangeable ions) from larger particles [79], and/or loss from roughened surfaces [80], followed by a typical slow release of these elements with bulk aluminosilicate weathering [81,82]. Warm-room leachate shows higher initial concentrations than cold-room leachate for both Ca and K, which is the result of temperature and pH controls on desorption and mineral degradation [62–67].

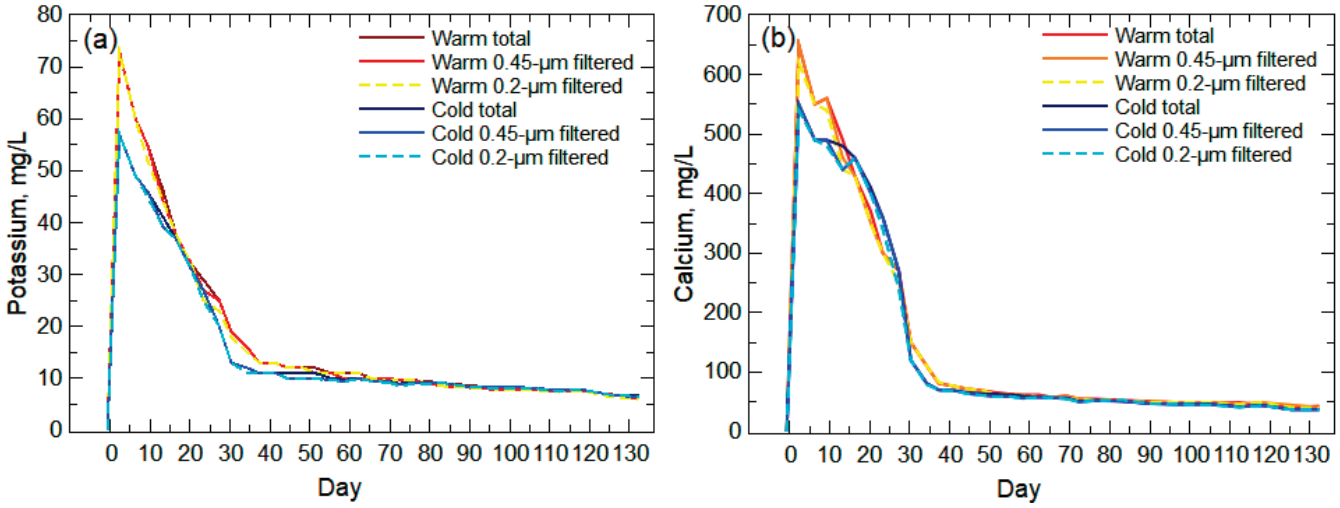

Figure 9. Potassium (**a**) and calcium (**b**) unfiltered (total) and filtered concentrations for the warm-room and cold-room leachates during the 20-week leach column experiment.

3.3.4. Multiple Source Weathering

Iron concentrations for warm- and cold-room leachates indicated multiple weathering processes causing the release of Fe over the course of the experiment (Figure 10). Iron content in the Wasatch and Fort Union waste rock is substantial (Figure 4) and has multiple mineral sources, including sulfides (pyrite) and aluminosilicates (feldspars and associated clays) along with sorbed Fe (oxyhydr)oxide particles. The relation of Fe and Eh was a moderate-to-weak negative correlation (Spearman's ρ of −0.31 for the filtered concentrations (q-value of 0.01) and −0.11 for the unfiltered concentrations (q-value of 0.7)), likely because of the variety of Fe sources and solubility controls on Fe. Given the low solubility of Fe^{3+} in oxidizing and near-neutral waters [83,84], Fe likely was released from the waste rock as desorbed Fe (oxyhydr)oxide particles early in the experiment, which accounts for the large total Fe concentration peak at day 3. The potential for mobile Fe forms is a complex interaction of environmental conditions and solute composition and concentrations that commonly results in the formation of nanoscale to colloidal Fe particles [85–89]. The much larger concentration of Fe in the warm-room leachate during this first week of the experiment is indicative of the effect of pH and temperature on Fe particle desorption and transport [90–92]. After the initial peak of Fe, there is a substantial release of Fe from the warm-room leachate with oxidation of the pyrite, which is limited under the cold-room conditions [93]. As Fe forms are mobilized and removed from the waste rock, along with the lessening of available sulfide surfaces, Fe starts to weather at a consistent and lower release rate at approximately day 65 (Figure 10), similar to the trends of Ca and K (Figure 9). This Fe trend likely is the result of the release of Fe (oxyhydr)oxides with weathering of the bulk solids and continued desorption and particle aggregation/deaggregation [94,95].

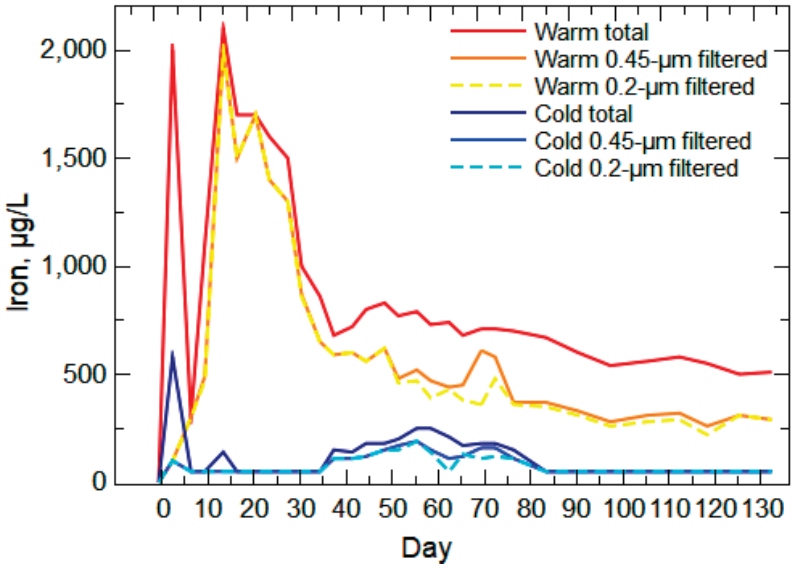

Figure 10. Iron unfiltered (total) and filtered concentrations for warm-room and cold-room leachates during the 20-week leach column experiment. Non-detect values were set to half the reporting limit (50 µg/L).

4. Conclusions

During mine site restoration, the construction and saturation of backfill aquifers may cause groundwater quality impacts because of freshly exposed mineral surfaces and the presence of newly created and transportable particles in the waste rock. Monitoring of groundwater in backfill aquifers of the Powder River Basin has indicated water quality impacts that were not expected given groundwater quality in aquifers contained in the original overburden/waste rock formations. A 20-week leach column experiment was conducted to characterize solute sources and weathering processes for recently generated waste rock from the Cordero Rojo Mine in the Powder River Basin. Analysis of the Eh, pH, specific conductance, alkalinity, and cation and anion concentrations of the leachate collected from warm-room and cold-room columns indicated an early weathering stage during the first 55 days of the experiment—indicated by Eh alternating between positive and negative values, pH < 6.5, specific conductance up to 6500 µS/cm, alkalinity > 500 mg/L, and the largest anion and cation concentrations during this period. After this early weathering period, alkalinity decreased but remained elevated at 200 to 300 mg/L and, along with elevated calcium values, indicated a transitional stage of additional carbonate weathering. Following this transitional weathering period, a low solute period representative of primarily aluminosilicate weathering occurred after day 70.

Multiple weathering processes were identified from leachate solute trends—particle transport, salt dissolution, sulfide oxidation, carbonate dissolution, and the weathering of the bulk aluminosilicate matrix. Certain elements indicated one or two weathering processes that were primarily responsible for the release of an element into solution: cadmium from particle transport during early flushing, selenium from particle transport and salt dissolution with early flushing and weathering of highly soluble minerals, arsenic from oxidation of pyrite found in the coal, calcium from particle transport and carbonate dissolution during and after the early weathering period, and potassium from particle transport and aluminosilicate weathering from early flushing through to equilibrium weathering. Elements with multiple mineral sources, such as iron, produced complex concentration trends because of concurrent and sequential weathering processes. The mining and landscape restoration process produces newly exposed mineral surfaces and nano- to micro-scale particles that may be weathered and transported in groundwater, creating water quality issues not expected given historical aquifer water quality in the regional geology of the Powder River Basin. Mining companies should expect an early weathering stage in back-

fill aquifers where contaminant concentrations may be higher unless actions are taken to minimize the presence or availability of newly accessible contaminant sources in the waste rock.

Supplementary Materials: The following supporting information can be downloaded at: https://www.mdpi.com/article/10.3390/geosciences14010004/s1.

Author Contributions: Conceptualization, J.B.L.; methodology, J.B.L.; validation, J.B.L. and J.M.; formal analysis, J.B.L. and J.M.; investigation, J.B.L. and J.M.; resources, J.B.L.; data curation, J.M.; writing—original draft preparation, J.B.L. and J.M.; writing—review and editing, J.B.L. and J.M.; visualization, J.B.L. and J.M.; supervision, J.B.L.; project administration, J.B.L.; funding acquisition, J.B.L. All authors have read and agreed to the published version of the manuscript.

Funding: This research received external funding from the U.S. Office of Surface Mining Reclamation and Enforcement under their Applied Science Program for Science and Technology Projects Related to Coal Mining and Reclamation (Grant# S21AC10037).

Data Availability Statement: All data analyzed as part of this study can be found in the attached Supplementary data file.

Acknowledgments: The authors wish to thank to the Office of Surface Mining Reclamation and Enforcement for their support and funding, Navajo Transitional Energy Company and Owen Tracy at the Cordero Rojo Mine for their collaboration and outreach, and the Geologic Society of America grant support for this project. The authors would also like to thank Gaige Swanson and Liam Knudson for their work on this project.

Conflicts of Interest: The authors declare no conflicts of interest.

References

1. Sharma, V.K.; Filip, J.; Zboril, R.; Varma, R.S. Natural Inorganic Nanoparticles—Formation, Fate, and Toxicity in the Environment. *Chem. Soc. Rev.* **2015**, *44*, 8410–8423. [CrossRef]
2. Jun, Y.-S.; Lee, B.; Waychunas, G.A. In Situ Observations of Nanoparticle Early Development Kinetics at Mineral−Water Interfaces. *Environ. Sci. Technol.* **2010**, *44*, 8182–8189. [CrossRef] [PubMed]
3. Acero, P.; Ayora, C.; Carrera, J.; Saaltink, M.W.; Olivella, S. Multiphase Flow and Reactive Transport Model in Vadose Tailings. *Appl. Geochem.* **2009**, *24*, 1238–1250. [CrossRef]
4. Blowes, D.W.; Jambor, J.L. The Pore-Water Geochemistry and the Mineralogy of the Vadose Zone of Sulfide Tailings, Waite Amulet, Quebec, Canada. *Appl. Geochem.* **1990**, *5*, 327–346. [CrossRef]
5. Dosseto, A.; Turner, S.P.; Chappell, J. The Evolution of Weathering Profiles through Time: New Insights from Uranium-Series Isotopes. *Earth Planet. Sci. Lett.* **2008**, *274*, 359–371. [CrossRef]
6. Yoo, K.; Mudd, S.M. Discrepancy between Mineral Residence Time and Soil Age: Implications for the Interpretation of Chemical Weathering Rates. *Geology* **2008**, *36*, 35–38. [CrossRef]
7. Slagle, S.E.; Lewis, B.D.; Lee, R.W. *Ground-Water Resources and Potential Hydrologic Effects of Surface Coal Mining in the Northern Powder River Basin, Southeastern Montana*; Water Supply Paper; U.S. Geological Survey: Reston, VA, USA, 1985. [CrossRef]
8. Bartos, T.T.; Ogle, K.M. *Water Quality and Environmental Isotopic Analyses of Ground-Water Samples Collected from the Wasatch and Fort Union Formations in Areas of Coalbed Methane Development: Implications to Recharge and Ground-Water Flow, Eastern Powder River Basin, Wyoming*; Water Resources Investigations Report 02-4045; U.S. Geological Survey: Reston, VA, USA, 2002. [CrossRef]
9. Colman, S.M. Rock-Weathering Rates as Functions of Time. *Quat. Res.* **1981**, *15*, 250–264. [CrossRef]
10. Drever, J.I.; Clow, D.W. Weathering Rates in Catchments. In *Reviews in Mineralogy and Geochemistry*; White, A.F., Brantley, S.L., Eds.; Mineralogical Society of America: Chantilly, VA, USA, 1995; Volume 31, pp. 463–483.
11. St-Arnault, M.; Vriens, B.; Blaskovich, R.; Aranda, C.; Klein, B.; Ulrich Mayer, K.; Beckie, R.D. Geochemical and Mineralogical Assessment of Reactivity in a Full-Scale Heterogeneous Waste-Rock Pile. *Miner. Eng.* **2020**, *145*, 106089. [CrossRef]
12. Futter, M.N.; Klaminder, J.; Lucas, R.W.; Laudon, H.; Köhler, S.J. Uncertainty in Silicate Mineral Weathering Rate Estimates: Source Partitioning and Policy Implications. *Environ. Res. Lett.* **2012**, *7*, 024025. [CrossRef]
13. Malmström, M.E.; Destouni, G.; Banwart, S.A.; Strömberg, B.H.E. Resolving the Scale-Dependence of Mineral Weathering Rates. *Environ. Sci. Technol.* **2000**, *34*, 1375–1378. [CrossRef]
14. Salmon, S.U.; Malmström, M.E. Quantification of Mineral Dissolution Rates and Applicability of Rate Laws: Laboratory Studies of Mill Tailings. *Appl. Geochem.* **2006**, *21*, 269–288. [CrossRef]
15. Banwart, S.A.; Evans, K.A.; Croxford, S. Predicting Mineral Weathering Rates at Field Scale for Mine Water Risk Assessment. *Geol. Soc. Lond. Spec. Publ.* **2002**, *198*, 137–157. [CrossRef]
16. Malmström, M.; Banwart, S. Biotite Dissolution at 25 °C: The pH Dependence of Dissolution Rate and Stoichiometry. *Geochim. Cosmochim. Acta* **1997**, *61*, 2779–2799. [CrossRef]

17. Stockwell, J.; Smith, L.; Jambor, J.L.; Beckie, R. The Relationship between Fluid Flow and Mineral Weathering in Heterogeneous Unsaturated Porous Media: A Physical and Geochemical Characterization of a Waste-Rock Pile. *Appl. Geochem.* **2006**, *21*, 1347–1361. [CrossRef]
18. Hochella, M.F., Jr.; Lower, S.K.; Maurice, P.A.; Penn, R.L.; Sahai, N.; Sparks, D.L.; Twining, B.S. Nanominerals, Mineral Nanoparticles, and Earth Systems. *Science* **2008**, *319*, 1631–1635. [CrossRef]
19. Hochella, M.F., Jr.; Mogk, D.W.; Ranville, J.; Allen, I.C.; Luther, G.W.; Marr, L.C.; McGrail, B.P.; Murayama, M.; Qafoku, N.P.; Rosso, K.M.; et al. Natural, Incidental, and Engineered Nanomaterials and Their Impacts on the Earth System. *Science* **2019**, *363*, eaau8299. [CrossRef]
20. Dolton, G.L.; Fox, J.E.; Clayton, J.L. *Petroleum Geology of the Powder River Basin, Wyoming and Montana*; Open-File Report, 88-450-P; U.S. Geological Survey: Reston, VA, USA, 1990. [CrossRef]
21. Flores, R.M. *Coalbed Methane in the Powder River Basin, Wyoming and Montana: An Assessment of the Tertiary-Upper Cretaceous Coalbed Methane Total Petroleum System*; Digital Data Series DDS–69–C; U.S. Geological Survey: Reston, VA, USA, 2004.
22. Fort Union Coal Assessment Team. *Resource Assessment of Selected Tertiary Coal Beds and Zones in the Northern Rocky Mountains and Great Plains Region*; Professional Paper 1625-A; U.S. Geological Survey: Reston, VA, USA, 1999. [CrossRef]
23. Yuretich, R.F.; Hickey, L.J.; Gregson, B.P.; Hsia, Y.L. Lacustrine Deposits in the Paleocene Fort Union Formation, Northern Bighorn Basin, Montana. *J. Sediment. Res.* **1984**, *54*, 836–852. [CrossRef]
24. Pocknall, D.T. Paleoenvironments and Age of the Wasatch Formation (Eocene), Powder River Basin, Wyoming. *PALAIOS* **1987**, *2*, 368–376. [CrossRef]
25. Lorenz, J.C.; Nadon, G.C. Braided-River Deposits in A Muddy Depositional Setting: The Molina Member of the Wasatch Formation (Paleogene), West-Central Colorado, U.S.A. *J. Sediment. Res.* **2002**, *72*, 376–385. [CrossRef]
26. Roehler, H.W. *Revised Stratigraphic Nomenclature for the Wasatch and Green River Formations of Eocene Age, Wyoming, Utah, and Colorado*; Professional Paper 1506-B; U.S. Geological Survey: Reston, VA, USA, 1991. [CrossRef]
27. Hoy, R.; Ogle, K.; Taylor, M. Evaluation of Water Quality Conditions in Coal Mine Backfill in the Powder River Basin of Wyoming. *J. Am. Soc. Min. Reclam.* **2003**, *2003*, 427–447. [CrossRef]
28. Belt, E.S.; Flores, R.M.; Warwick, P.D.; Conway, K.M.; Johnson, K.R.; Waskowitz, R.S. Relationship of Fluviodeltaic Facies to Coal Deposition in the Lower Fort Union Formation (Palaeocene), South-Western North Dakota. In *Sedimentology of Coal and Coal-Bearing Sequences*; Rahmani, R.A., Flores, R.M., Eds.; Wiley: Hoboken, NJ, USA, 1985. [CrossRef]
29. Ellis, M.S. *Quality of Economically Extractable Coal Beds in the Gillette Coal Field as Compared with Other Tertiary Coal Beds in the Powder River Basin, Wyoming and Montana*; Open-File Report 2002-174; U.S. Geological Survey: Reston, VA, USA, 2002. [CrossRef]
30. McClurg, J.E. Peat Forming Wetlands and the Thick Powder River Basin Coals; American Association of Petroleum Geologists, Eastern Powder River Basin—Black Hills. In Proceedings of the 39th Annual Field Conference Guidebook, Casper, WY, USA, 9–11 September 1988.
31. Moore, T.A. The Effects of Clastic Sedimentation on Organic Facies Development within a Tertiary Subbituminous Coal Bed, Powder River Basin, Montana, U.S.A. *Int. J. Coal Geol.* **1991**, *18*, 187–209. [CrossRef]
32. Palmer, C.A.; Mroczkowski, S.J.; Kolker, A.; Finkelman, R.B.; Bullock, J.H., Jr. *Chemical Analysis and Modes of Occurrence of Selected Trace Elements in a Powder River Basin Coal and Its Corresponding Simulated Cleaned Coal*; Open-File Report 2000-323; U.S. Geological Survey: Reston, VA, USA, 2001. [CrossRef]
33. Milligan, C.; Reddy, K. Monitoring of Groundwater Contamination by Trace Elements from CBNG Disposal Ponds Across the Powder River Basin, Wyoming. *J. Am. Soc. Min. Reclam.* **2007**, *2007*, 520–527. [CrossRef]
34. Wyoming State Engineer's Office. *Fort Union Formation Aquifer Monitoring Plan and Preliminary Aquifer Management Plan*; Wyoming Water Development Commission: Gillette, WY, USA, 1995; p. 73.
35. U.S. Environmental Protection Agency. *Method 1669, Sampling Ambient Water for Trace Metals at EPA Water Quality Criteria Levels*; USEPA Office of Water Engineering and Analysis Division: Washington, DC, USA, 1996; p. 35.
36. U.S. Geological Survey. National Field Manual for Collection of Water-Quality Data—Chapter A4. In *Collection of Water Samples*; U.S. Geological Survey: Reston, VA, USA, 2006; p. 231.
37. *ASTM D75/D75M-19*; Practice for Sampling Aggregates. ASTM International: West Conshohocken, PA, USA, 2019; p. 7. [CrossRef]
38. Lapakko, K.A.; White, W.W. Modification of the ASTM 5744-96 Kinetic Test. In Proceedings of the Fifth International Conference on Acid Rock Drainage; Society for Mining, Metallurgy, and Exploration: Littleton, CO, USA, 2000; pp. 631–639.
39. American Society for Testing and Materials. *Test Method for Laboratory Weathering of Solid Materials Using a Humidity Cell*; ASTM International: West Conshohocken, PA, USA, 2018; p. 24.
40. *ASTM D4644-04*; Test Method for Slake Durability of Shales and Similar Weak Rocks. ASTM International: West Conshohocken, PA, USA, 2010; p. 4. [CrossRef]
41. Fan, R.; Qian, G.; Li, Y.; Short, M.D.; Schumann, R.C.; Chen, M.; Smart, R.S.C.; Gerson, A.R. Evolution of Pyrite Oxidation from a 10-Year Kinetic Leach Study: Implications for Secondary Mineralisation in Acid Mine Drainage Control. *Chem. Geol.* **2022**, *588*, 120653. [CrossRef]
42. Kolker, A.; Palmer, C.A.; Bragg, L.J.; Bunnell, J.E. *Arsenic in Coal*; Fact Sheet 2005–3152; U.S. Geological Survey: Reston, VA, USA, 2005; p. 4.

43. Hagmaier, J.L. Groundwater Flow, Hydrochemistry, and Uranium Deposition in the Powder River Basin, Wyoming. Ph.D. Dissertation, University of North Dakota, Grand Forks, ND, USA, 1971.
44. Ayers, W.B., Jr. Lacustrine and Fluvial-Deltaic Depositional Systems, Fort Union Formation (Paleocene), Powder River Basin, Wyoming and Montana, American Association of Petroleum Geologists. *AAPG Bull.* **1986**, *70*, 1651–1673.
45. Harrison, A.L.; Dipple, G.M.; Song, W.; Power, I.M.; Mayer, K.U.; Beinlich, A.; Sinton, D. Changes in Mineral Reactivity Driven by Pore Fluid Mobility in Partially Wetted Porous Media. *Chem. Geol.* **2017**, *463*, 1–11. [CrossRef]
46. Nordstrom, D.K. Sulfide Mineral Oxidation. In *Encyclopedia of Geobiology*; Reitner, J., Thiel, V., Eds.; Encyclopedia of Earth Sciences Series; Springer: Dordrecht, The Netherlands, 2011; pp. 856–858. ISBN 978-1-4020-9211-4.
47. Carroll, D. *Rock Weathering*; Monographs in Geoscience; Springer: Greer, SC, USA, 1970; ISBN 978-1-4684-1796-8.
48. Finkelman, R.B.; Palmer, C.A.; Wang, P. Quantification of the Modes of Occurrence of 42 Elements in Coal. *Int. J. Coal Geol.* **2018**, *185*, 138–160. [CrossRef]
49. Finkelman, R. The Inorganic Geochemistry of Coal: A Scanning Electron Microscopy View. *Scanning Microsc.* **1987**, *21*, 9.
50. Sharp, W.N.; McKay, E.J.; McKeown, F.A.; White, A.M. *Geology and Uranium Deposits of the Pumpkin Buttes Area of the Powder River Basin, Wyoming*; Contributions to the Geology of Uranium; Bulletin 1107-H; U.S. Geological Survey: Reston, VA, USA, 1964. [CrossRef]
51. Luppens, J.A.; Scott, D.C.; Haacke, J.E.; Osmonson, L.M.; Rohrbacher, T.J.; Ellis, M.S. *Assessment of Coal Geology, Resources, and Reserves in the Gillette Coalfield, Powder River Basin, Wyoming*; Open-File Report 2008-1202; U.S. Geological Survey: Reston, VA, USA, 2008. [CrossRef]
52. Frascoli, F.; Hudson-Edwards, K.A. Geochemistry, Mineralogy and Microbiology of Molybdenum in Mining-Affected Environments. *Minerals* **2018**, *8*, 42. [CrossRef]
53. Horan, K. The Oxidative Weathering of Organic Matter and Its Carbon Dioxide Emissions: Insight from the Trace Elements Rhenium and Molybdenum. Ph.D. Dissertation, Durham University, Durham, UK, 2018.
54. Yudovich, Y.E.; Ketris, M.P. Selenium in Coal: A Review. *Int. J. Coal Geol.* **2006**, *67*, 112–126. [CrossRef]
55. Bao, Z.; Bain, J.; Saurette, E.; Zou Finfrock, Y.; Hu, Y.; Ptacek, C.J.; Blowes, D.W. Mineralogy-Dependent Sulfide Oxidation via Polysulfide and Thiosulfate Pathways during Weathering of Mixed-Sulfide Bearing Mine Waste Rock. *Geochim. Cosmochim. Acta* **2022**, *317*, 523–537. [CrossRef]
56. Dreher, G.B.; Finkelman, R.B. Selenium Mobilization in a Surface Coal Mine, Powder River Basin, Wyoming, U.S.A. *Environ. Geol. Water Sci.* **1992**, *19*, 155–167. [CrossRef]
57. Stillings, L.L.; Foster, A.L.; Koski, R.A.; Munk, L.; Shanks, W.C. Temporal Variation and the Effect of Rainfall on Metals Flux from the Historic Beatson Mine, Prince William Sound, Alaska, USA. *Appl. Geochem.* **2008**, *23*, 255–278. [CrossRef]
58. Wang, H.; Jiang, R.; Wang, B.; Yao, S. The Effect of Gypsum on the Fixation of Selenium in the Iron/Calcium-Selenium Coprecipitation Process. *Bull. Environ. Contam. Toxicol.* **2021**, *106*, 121–125. [CrossRef] [PubMed]
59. Lee, R.W. *Geochemistry of Water in the Fort Union Formation of the Northern Powder River Basin, Southeastern Montana*; Open-File Report; Open-File Report 80-336; U.S. Geological Survey: Reston, VA, USA, 1980. [CrossRef]
60. Huggins, F.E.; Huffman, G.P.; Lin, M.C. Observations on Low-Temperature Oxidation of Minerals in Bituminous Coals. *Int. J. Coal Geol.* **1983**, *3*, 157–182. [CrossRef]
61. See, R.B.; Reddy, K.J.; Vance, G.F.; Fadlelmawla, A.A.; Blaylock, M.J. *Geochemical Processes and the Effects of Natural Organic Solutes on the Solubility of Selenium in Coal-Mine Backfill Samples from the Powder River Basin, Wyoming*; Water-Resources Investigations Report 95-4200; U.S. Geological Survey: Reston, VA, USA, 1995. [CrossRef]
62. Healy, R.W.; Rice, C.A.; Bartos, T.T.; McKinley, M.P. Infiltration from an Impoundment for Coal-Bed Natural Gas, Powder River Basin, Wyoming: Evolution of Water and Sediment Chemistry. *Water Resour. Res.* **2008**, *44*. [CrossRef]
63. Rice, C.A.; Flores, R.M.; Stricker, G.D.; Ellis, M.S. Chemical and Stable Isotopic Evidence for Water/Rock Interaction and Biogenic Origin of Coalbed Methane, Fort Union Formation, Powder River Basin, Wyoming and Montana U.S.A. *Int. J. Coal Geol.* **2008**, *76*, 76–85. [CrossRef]
64. Elrashidi, M.A.; Adriano, D.C.; Workman, S.M.; Lindsay, W.L. Chemical Equilibria of Selenium in Soils: A Theoretical Development. *Soil Sci.* **1987**, *144*, 141–152. [CrossRef]
65. Paydary, P.; Schellenger, A.E.P.; Teli, M.; Jaisi, D.P.; Onnis-Hayden, A.; Larese-Casanova, P. Chemical Oxidation of Selenite to Selenate: Evaluation of Reactive Oxygen Species and O Transfer Pathways. *Chem. Geol.* **2021**, *575*, 120229. [CrossRef]
66. Torres, J.; Pintos, V.; Gonzatto, L.; Domínguez, S.; Kremer, C.; Kremer, E. Selenium Chemical Speciation in Natural Waters: Protonation and Complexation Behavior of Selenite and Selenate in the Presence of Environmentally Relevant Cations. *Chem. Geol.* **2011**, *288*, 32–38. [CrossRef]
67. Stoeppler, M. *Hazardous Metals in the Environment*; Techniques and Instrumentation in Analytical Chemistry; Elsevier Science: Amsterdam, The Netherlands, 1992; ISBN 978-0-08-087560-6.
68. Brownfield, M.E.; Cathcart, J.D.; Affolter, R.H.; Brownfield, I.K.; Rice, C.A.; O'Connor, J.T.; Zielinski, R.A.; Bullock, J.H.; Hower, J.C.; Meeker, G.P. *Characterization and Modes of Occurrence of Elements in Feed Coal and Coal Combustion Products from a Power Plant Utilizing Low-Sulfur Coal from the Powder River Basin, Wyoming*; Scientific Investigations Report 2004-5271; U.S. Geological Survey: Reston, VA, USA, 2005. [CrossRef]
69. Li, X.; Zhou, J.; Zhou, T.; Li, Z.; Hu, P.; Luo, Y.; Christie, P.; Wu, L. Potential Mobilization of Cadmium and Zinc in Soils Spiked with Smithsonite and Sphalerite under Different Water Management Regimes. *J. Environ. Manag.* **2022**, *324*, 116336. [CrossRef]

70. Acero, P.; Cama, J.; Ayora, C. Sphalerite Dissolution Kinetics in Acidic Environment. *Appl. Geochem.* **2007**, *22*, 1872–1883. [CrossRef]
71. Langman, J.B.; Moore, M.L.; Ptacek, C.J.; Smith, L.; Sego, D.; Blowes, D.W. Diavik Waste Rock Project: Evolution of Mineral Weathering, Element Release, and Acid Generation and Neutralization during a Five-Year Humidity Cell Experiment. *Minerals* **2014**, *4*, 257–278. [CrossRef]
72. Williamson, M.A.; Rimstidt, J.D. The Kinetics and Electrochemical Rate-Determining Step of Aqueous Pyrite Oxidation. *Geochim. Cosmochim. Acta* **1994**, *58*, 5443–5454. [CrossRef]
73. Hu, G.; Dam-Johansen, K.; Wedel, S.; Hansen, J.P. Decomposition and Oxidation of Pyrite. *Prog. Energy Combust. Sci.* **2006**, *32*, 295–314. [CrossRef]
74. Langman, J.B.; Blowes, D.W.; Veeramani, H.; Wilson, D.; Smith, L.; Sego, D.C.; Paktunc, D. The Mineral and Aqueous Phase Evolution of Sulfur and Nickel with Weathering of Pyrrhotite in a Low Sulfide, Granitic Waste Rock. *Chem. Geol.* **2015**, *401*, 169–179. [CrossRef]
75. Wunderly, M.D.; Blowes, D.W.; Frind, E.O.; Ptacek, C.J. Sulfide Mineral Oxidation and Subsequent Reactive Transport of Oxidation Products in Mine Tailings Impoundments: A Numerical Model. *Water Resour. Res.* **1996**, *32*, 3173–3187. [CrossRef]
76. Langman, J.B.; Ali, J.D.; Child, A.W.; Wilhelm, F.M.; Moberly, J.G. Sulfur Species, Bonding Environment, and Metal Mobilization in Mining-Impacted Lake Sediments: Column Experiments Replicating Seasonal Anoxia and Deposition of Algal Detritus. *Minerals* **2020**, *10*, 849. [CrossRef]
77. Dos Santos, E.C.; de Mendonça Silva, J.C.; Duarte, H.A. Pyrite Oxidation Mechanism by Oxygen in Aqueous Medium. *J. Phys. Chem. C* **2016**, *120*, 2760–2768. [CrossRef]
78. Lehmann, N.; Lantuit, H.; Böttcher, M.E.; Hartmann, J.; Eulenburg, A.; Thomas, H. Alkalinity Generation from Carbonate Weathering in a Silicate-Dominated Headwater Catchment at Iskorasfjellet, Northern Norway. *Biogeosciences* **2023**, *20*, 3459–3479. [CrossRef]
79. Agbenin, J.O.; van Raij, B. Rate Processes of Calcium, Magnesium and Potassium Desorption from Variable-Charge Soils by Mixed Ion-Exchange Resins. *Geoderma* **1999**, *93*, 141–157. [CrossRef]
80. White, A.F.; Blum, A.E.; Schulz, M.S.; Bullen, T.D.; Harden, J.W.; Peterson, M.L. Chemical Weathering Rates of a Soil Chronosequence on Granitic Alluvium: I. Quantification of Mineralogical and Surface Area Changes and Calculation of Primary Silicate Reaction Rates. *Geochim. Cosmochim. Acta* **1996**, *60*, 2533–2550. [CrossRef]
81. Skorina, T.; Allanore, A. Aqueous Alteration of Potassium-Bearing Aluminosilicate Minerals: From Mechanism to Processing. *Green Chem.* **2015**, *17*, 2123–2136. [CrossRef]
82. Sparks, D.L. Chemical Kinetics and Mass Transfer Processes in Soils and Soil Constituents. In *Transport Processes in Porous Media*; Bear, J., Corapcioglu, M.Y., Eds.; NATO ASI Series; Springer: Dordrecht, The Netherlands, 1991; pp. 583–637. ISBN 978-94-011-3628-0.
83. Hem, J.D.; Cropper, W.H. *Survey of Ferrous-Ferric Chemical Equilibria and Redox Potentials*; Water Supply Paper; Water Supply Paper 1459-A; U.S. Geological Survey: Reston, VA, USA, 1959. [CrossRef]
84. Schwertmann, U. Solubility and Dissolution of Iron Oxides. *Plant Soil* **1991**, *130*, 1–25. [CrossRef]
85. Liang, L.; Morgan, J.J. Chemical Aspects of Iron Oxide Coagulation in Water: Laboratory Studies and Implications for Natural Systems. *Aquat. Sci.* **1990**, *52*, 32–55. [CrossRef]
86. Davison, W. Iron and Manganese in Lakes. *Earth-Sci. Rev.* **1993**, *34*, 119–163. [CrossRef]
87. Perret, D.; Gaillard, J.-F.; Dominik, J.; Atteia, O. The Diversity of Natural Hydrous Iron Oxides. *Environ. Sci. Technol.* **2000**, *34*, 3540–3546. [CrossRef]
88. Gaffney, J.W.; White, K.N.; Boult, S. Oxidation State and Size of Fe Controlled by Organic Matter in Natural Waters. *Environ. Sci. Technol.* **2008**, *42*, 3575–3581. [CrossRef]
89. Hassellöv, M.; Kammer, F. von der Iron Oxides as Geochemical Nanovectors for Metal Transport in Soil-River Systems. *Elements* **2008**, *4*, 401–406. [CrossRef]
90. Weber, F.-A.; Hofacker, A.F.; Voegelin, A.; Kretzschmar, R. Temperature Dependence and Coupling of Iron and Arsenic Reduction and Release during Flooding of a Contaminated Soil. *Environ. Sci. Technol.* **2010**, *44*, 116–122. [CrossRef]
91. Hatje, V.; Payne, T.E.; Hill, D.M.; McOrist, G.; Birch, G.F.; Szymczak, R. Kinetics of Trace Element Uptake and Release by Particles in Estuarine Waters: Effects of pH, Salinity, and Particle Loading. *Environ. Int.* **2003**, *29*, 619–629. [CrossRef]
92. Possemiers, M.; Huysmans, M.; Anibas, C.; Batelaan, O.; Van Steenwinkel, J. Reactive Transport Modeling of Redox Processes to Assess $Fe(OH)_3$ Precipitation around Aquifer Thermal Energy Storage Wells in Phreatic Aquifers. *Environ. Earth Sci.* **2016**, *75*, 648. [CrossRef]
93. Sun, H.; Chen, M.; Zou, L.; Shu, R.; Ruan, R. Study of the Kinetics of Pyrite Oxidation under Controlled Redox Potential. *Hydrometallurgy* **2015**, *155*, 13–19. [CrossRef]
94. Journet, E.; Desboeufs, K.V.; Caquineau, S.; Colin, J.-L. Mineralogy as a Critical Factor of Dust Iron Solubility. *Geophys. Res. Lett.* **2008**, *35*. [CrossRef]
95. Wang, Z.; Li, R.; Cui, L.; Fu, H.; Lin, J.; Chen, J. Characterization and Acid-Mobilization Study for Typical Iron-Bearing Clay Mineral. *J. Environ. Sci.* **2018**, *71*, 222–232. [CrossRef]

Disclaimer/Publisher's Note: The statements, opinions and data contained in all publications are solely those of the individual author(s) and contributor(s) and not of MDPI and/or the editor(s). MDPI and/or the editor(s) disclaim responsibility for any injury to people or property resulting from any ideas, methods, instructions or products referred to in the content.

water

MDPI

Article

Geochemical Evidence Constraining Genesis and Mineral Scaling of the Yangbajing Geothermal Field, Southwestern China

Hu Yang [1], Xingcheng Yuan [2,*], Yongling Chen [1], Jiawei Liu [2], Chun Zhan [1], Guosen Lv [2], Junfeng Hu [1], Minglu Sun [3] and Yunhui Zhang [2]

[1] Research Center of Applied Geology, China Geological Survey, Chengdu 610036, China
[2] Yibin Research Institute, Southwest Jiaotong University, Yibin 644000, China
[3] College of Engineering, Tibet University, Lasa 850000, China
* Correspondence: yxc123456@my.swjtu.edu.cn

Abstract: The Yangbajing geothermal field, a renowned high-temperature geothermal resource in Tibet of southwestern China, has been utilized for power generation for several decades. To improve geothermal exploitation in the Yangbajing, genesis and mineral scaling have yet to be further revealed. In this study, hydrochemistry and D-O-Sr isotopy were employed for analyzing genesis and mineral scaling in the Yangbajing geothermal field. The geothermal waters were weakly alkaline and had a high TDS content (1400–2900 mg/L) with the Cl-Na, Cl·HCO_3-Na, and HCO_3·Cl-Na types. The dissolution of silicate minerals (sodium and potassium feldspars) and positive cation exchange controlled the hydrogeochemical process. The geothermal water was recharged from snow-melted water and meteoric water originating from the Nyainqentanglh Mountains and Tangshan Mountains. The geothermal waters possessed the highest reservoir temperature of 299 °C and the largest circulation depth of 2010 m according to various geothermometers. The geothermal waters can produce $CaCO_3$ and SiO_2 scaling during vertical and horizontal transport. These achievements can provide a scientific basis for the sustainable development and conservation of the high-temperature geothermal resources in Yangbajing and elsewhere.

Keywords: geothermal water; hydrogeochemical process; reservoir temperature; recharge source; genesis model; scaling trend

1. Introduction

The exploration of clean and renewable energy has become a significant research topic due to the energy crisis and environmental issues [1,2]. The tremendous potential of high-temperature geothermal resources for power generation has attracted substantial attention and research [3,4]. Revealing the genesis is the key for the development of a high-temperature geothermal system due to complicated physical–chemical processes. Recharge source, water–rock interaction, and reservoir temperature are the significant constituents of genesis analysis [5–8]. In addition, the scaling issue in geothermal wells has posed a serious limitation in the utilization of geothermal energy [9,10].

The application of hydrogeochemical approaches has played a significant role in tracing fluid sources, revealing water–rock interactions, estimating reservoir temperatures and hot/cold water mixing ratios, and predicting fluid fouling trends [10–12]. Stable isotopes (δD and $\delta^{18}O$) are widely used to trace the recharge source [13,14]. The correlation of ions and strontium isotopes ($^{87}Sr/^{86}Sr$) has been used to reveal the water–rock interaction characteristics of geothermal fluids during subsurface runoff and mixing with the parent geothermal fluids [15–17]. Reactive elements, such as Na, K, Mg, Ca, and SiO_2, have been used to assess the mineral equilibrium and estimate the reservoir temperature [18–21]. In

addition, the mineral saturation index (SI) can determine the dissolution equilibrium state of minerals and scaling tendency in geothermal fluids [22].

The Yangbajing area is a representative high-temperature geothermal field with great exploration potential in Tibet, southwestern China [23]. Numerous investigations have been conducted into the hydrochemical evolution of the Yangbajing geothermal field. These studies indicated that the geothermal water in this field was derived from the recharge of meteoric water and heated by subsurface magma [23–27]. Moreover, the characterization and sources of geothermal gases (He and CO_2) in the geothermal field were analyzed, and it was concluded that supercritical geothermal fluids did not exist in the geothermal field of the Yangbajing [2]. However, the reservoir temperature achieved in previous studies remained controversial with a wide range. And scarce knowledge of mineral scaling hampered geothermal exploitation.

The objective of this research is to constrain the genesis of the geothermal system in Yangbajing using hydrochemistry and D-O-Sr isotopy. (1) A correlation of hydrochemical parameters and Sr isotopy were used to reveal the factors dominating hydrochemistry. (2) Various geothermometers were applied to estimate the reservoir temperatures. (3) δD and $\delta^{18}O$ were applied to determine the recharge area. (4) Mineral scaling was quantitatively measured by Phreeqc modeling. The achievements of this study are expected to provide valuable knowledge for geothermal exploitation in the Yangbajing and similar high-temperature geothermal fields.

2. Geological and Geothermal Setting

The Yangbajing high-temperature geothermal field is located in the hinterland of the Qinghai-Tibetan Plateau, about 90 km northwest of Lhasa (Figure 1a). The geography exhibits a characteristic distribution of higher terrain in the northwest and lower terrain in the southeast, with the highest elevation area being Mount Nyainqentanglh (7162 m) [8]. The climate belongs to a semi-arid monsoon type with an average annual temperature of 2.5 °C and average annual rainfall of 382.8 mm. The Zangbuqu is the main river traversing the study area [24].

The collision of the Indian and Eurasian plates during the Cenozoic led to the uplift of the Tibetan Plateau. Subduction and thrusting of the Indian plate beneath the Tibetan Plateau resulted in the melting of the crustal contact zone, providing beneficial geological conditions for the formation of geothermal resources [28]. The Tibetan Plateau is divided from north to south into the Songpan-Ganzi Massif, the Qiangtang Massif, the Lhasa Massif, and the Himalayan Massif. These massifs are separated by the east–west trending Kunlun suture zone, the Jinshajiang suture zone, the Bangong-Nujiang suture zone, and the Indus-Yarluzangbo suture zone (Figure 1a) [28,29]. The Yangbajing geothermal field is located in the central part of the Yadong-Gulu rift system within the Lhasa Massif, sandwiched between the Nyainqentanglh Mountains in the northwest and the Tangshan Mountains in the southeast (Figure 1b) [2]. NNE–SSW and NE–SW extensional faults are distributed in front of the Nyainqentanglh Mountains and Tangshan Mountains, providing favorable space for the circulation of geothermal fluids (Figure 1b,c) [24].

The strata exposed in the geothermal field consist of Paleozoic gneisses and mélange in the northwestern part and Carboniferous-Permian slates and Upper Cretaceous breccias in the southeastern part (Figure 1b). The basement rocks of the geothermal field are composed of Late Yanshan-Himalayan granite which outcrops locally in the north [24,25]. The granite was formed by multistage magmatism from the Cretaceous to Neogene periods (K-Ar radiometric ages of 87.4 Ma and 8.1 Ma) [30]. The Yangbajing geothermal field has a substantial coverage of Quaternary sediments on its surface, including Holocene alluvial deposits, flood deposits, and glacial accumulations; Upper Pleistocene alluvial deposits, sinister, and glacial accumulations; and Middle Pleistocene glacial deposits (Figure 1d) [25].

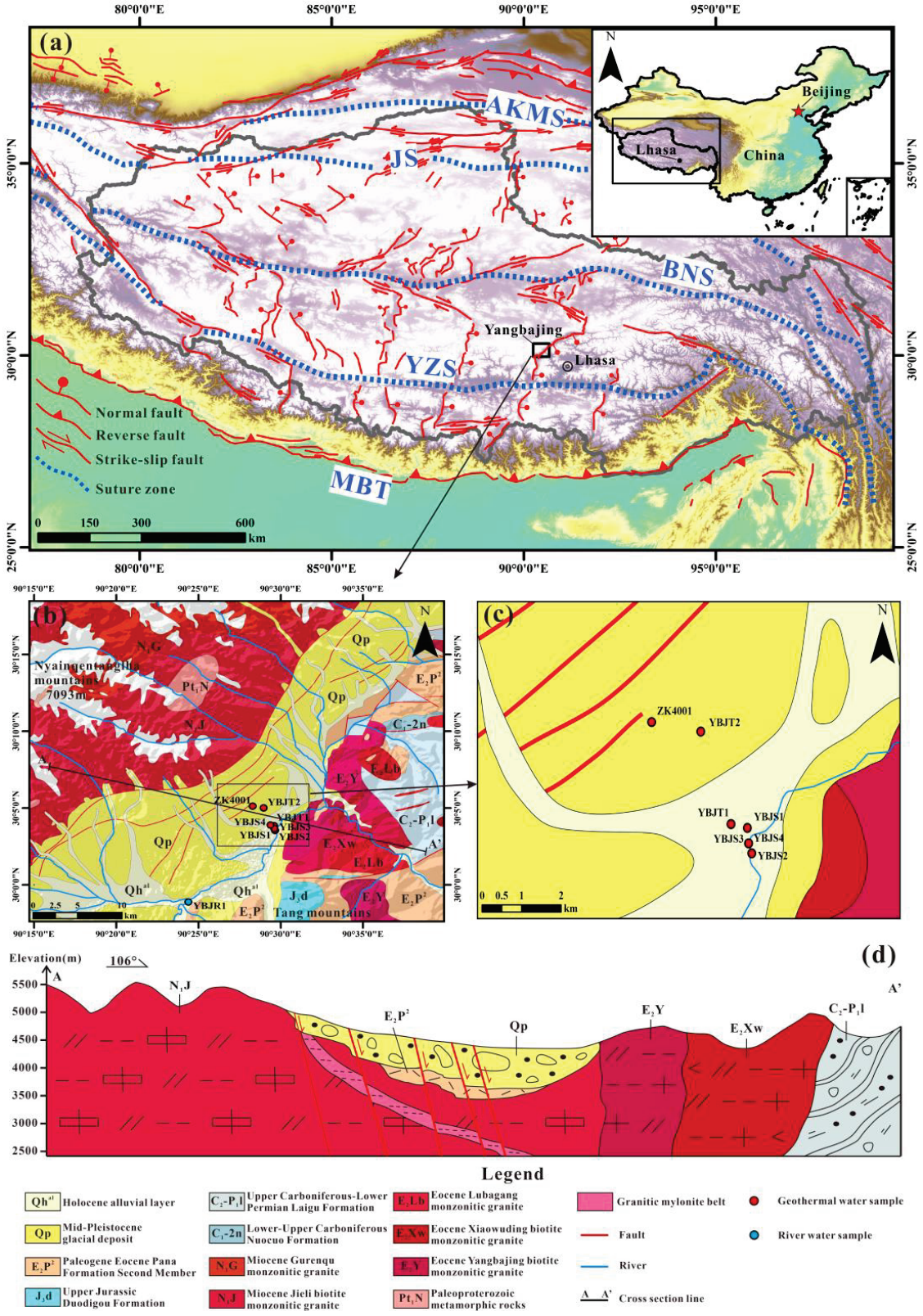

Figure 1. (**a**) Structural map of the Himalayan-Tibet orogenic belt (modified from refs. [31–33]). AKMS: Ayimaqin–Kunlun–Mutztagh suture; JS: Jinshajiang Suture; BNS: Bangong-Nujiang suture; YZS: YanglungZangbo suture; MBT: Main Boundary Thrust. (**b**) Regional geological map of Yangbajing geothermal field (reference [31]). (**c**) The sampling location of geothermal water and the phenomenon of typical geothermal water exposed to the surface. (**d**) Yangbajing geothermal field cross-section A-A'.

The findings of the INDEPTH (International Depth Profiling of Tibet and the Himalayas) project indicate that the magmatic melts present at a depth of 15–20 km provide a heat source for the geothermal system in the Yangbajing field [34–39]. During the field sampling conducted in June 2023, the temperature of the outcrop of the geothermal spring water was recorded to reach a maximum of 80 °C. Additionally, certain geothermal springs exhibited noticeable boiling phenomena, accompanied by the release of hot gas. The flow rate of these geothermal springs varied between approximately 1.5 L/s and 3.5 L/s (Figure 2). The geothermal field consists of two underlying geothermal reservoirs: (1) The shallow thermal reservoir is buried at a depth of 180–280 m. The northern region is primarily composed of eroded granite and Quaternary sandstone, while the southern region is predominantly comprised of Quaternary sediments. The reservoir temperature is 140–160 °C, and the geothermal fluids exhibit a characteristic of lateral replenishment in the NW–SE direction. (2) The deep thermal reservoir is buried at a depth of 950–1850 m. This reservoir is comprised of cranberries and fissures, while the surface is composed of very weathered cranes and dark clouds. The reservoir temperature is 250–278 °C [23,34].

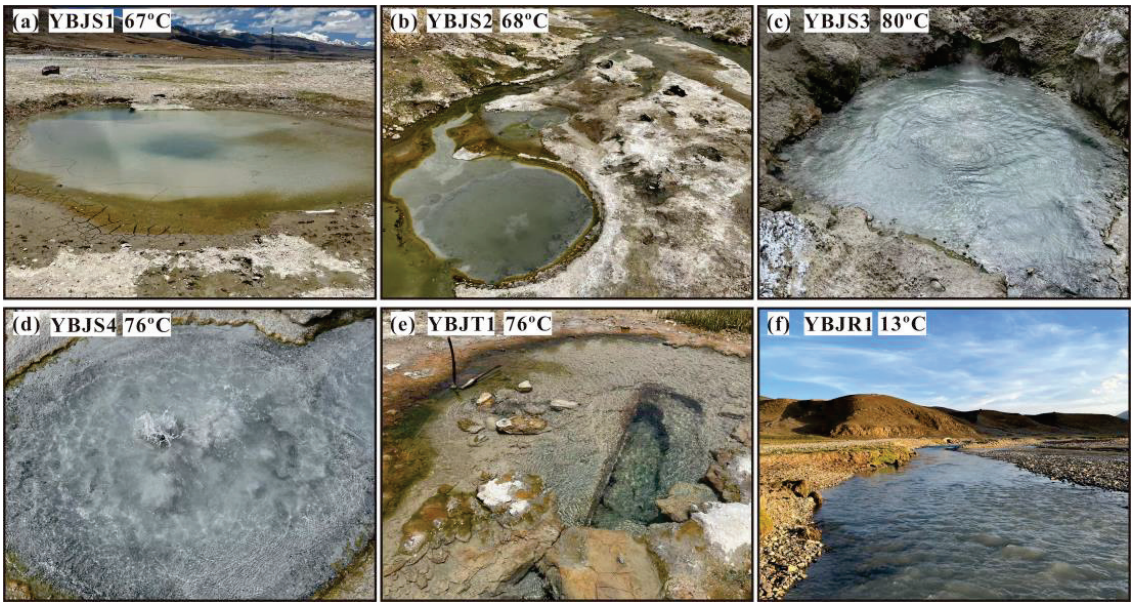

Figure 2. Photographs of geothermal water and river on site. (**a**) YBJS1, (**b**) YBJS2, (**c**) YBJS3, (**d**) YBJS4, (**e**) YBJT1, and (**f**) YBJR1. The temperatures marked in the figure were the exposure temperature of the site.

3. Methods

3.1. Sampling and Analysis

In June 2023, five sets of geothermal water samples (YBJS1–YBJS4, YBJT1) and one set of river water samples (YBJR1) were collected in the Yangbajing area of Tibet. Before sampling, temperature, pH, electrical conductivity (EC), oxidation reduction potential (ORP), and total dissolved solids (TDS) were measured using a German Multi3630IDS portable multiparameter water quality analyzer. HCO_3^- was determined via Gram titration. Prior to bottling, all water samples were filtered through 0.2 μm filter membranes and filled into 550 mL high-density polyethylene bottles. These bottles were washed and rinsed at least three times before sampling. In order to prevent precipitation of SiO_2 in the water, the geothermal water samples were diluted fivefold using deionized water prior to analysis for SiO_2 [6].

The collected samples were sent to Kehui Testing (Tianjin) Technology Co., Ltd. for hydrochemical and D-O-Sr isotope analyses. Major cations (K^+, Na^+, Ca^{2+}, and Mg^{2+}) were analyzed via inductively coupled plasma emission spectrometry (ICP-OES), while anions (Cl^-, SO_4^{2-}, and F^-) were analyzed via ion chromatography (Diona ICS-1100). Silicon and

other trace elements were detected by ICP-MS (7000C, Agilent). The ion charge balance was calculated to be less than ±10% for most samples (Table 1). Hydrogen and oxygen isotopes (δD and $\delta^{18}O$) were measured using the water balance hydroxide isotope analysis method (MAT251EM). The obtained data were subsequently standardized to Vienna Standard Mean Ocean Water (VSMOW) using the conventional δ (‰) expression. The accuracy of the detection of δD and $\delta^{18}O$ was ±0.5% and ±0.1%, respectively. Strontium isotopes ($^{87}Sr/^{86}Sr$) were tested via MC-ICP-MS using NIST SRM 987 Sr isotope standards as standards. In addition, this study also cited the sample data (YBJT2 and ZK4001) studied by references [24,25].

Table 1. Hydrochemical and isotopes results of geothermal water and river water samples.

NO.	Type	Elevation (m)	T(°C)	pH	TDS	Na^+	K^+	Mg^{2+}	Ca^{2+}	Cl^-	SO_4^{2-}
					mg/L						
YBJS1	HS	4291	67	8.34	1613	408.34	45.70	0.24	8.99	408.64	59.33
YBJS2		4280	68	9.14	1400	374.84	36.22	0.04	1.23	389.60	58.03
YBJS3		4280	80	9.12	1471	390.24	43.30	0.04	1.22	397.68	55.43
YBJS4		4280	76	9.19	1467	392.14	40.44	0.01	1.41	393.52	50.50
YBJT1	BW	4285	76	8.29	1599	410.04	50.87	0.51	10.59	435.92	53.19
YBJT2		4325	110	8.34	1700	300.20	38.60	0.23	4.70	514.00	58.40
ZK4001	DBW	4416	159	8.40	2900	709.00	135.00	0.13	2.10	1020.00	27.00
YBJR1	RW	4346	13	8.26	98	10.46	1.05	2.22	19.65	2.94	13.55

HCO_3^-	SiO_2	F	Sr	Li	B	$^{87}Sr/^{86}Sr$	δD (‰)	$\delta^{18}O$ (‰)	C.B. (%)	H.T.	R.E.(m)
		mg/L									
496.66	139.60	0.04	0.47	7.60	40.46	0.71219	−144.8	−16.88	3.71	Cl·HCO_3-Na	5229
90.61	157.60	0.15	0.60	6.91	40.01	0.71204	−148.5	−17.39	−11.67	Cl-Na	5372
160.58	165.00	0.02	0.46	7.36	40.20	0.71203	−150.7	−17.46	−9.51	Cl-Na	5458
761.62	170.60	0.02	0.46	7.32	38.93	0.71207	−149.2	−17.31	15.11	HCO_3·Cl-Na	5400
503.54	182.20	0.01	0.36	7.58	40.94	0.71205	−150.1	−17.33	4.69	Cl·HCO_3-Na	5435
163.60	165.80	19.60	0.21	6.40	58.70	0.71235	−142.1	−17.50	15.17	Cl-Na	5127
363.00	581.50	18.00	0.33	25.00	119.00	0.71259	−139.0	−16.00	2.54	Cl-Na	5008
80.29	12.80	0.02	0.10	0.11	0.32	0.70890	−121.8	−15.72	0.99	HCO_3-Ca·Na	–

Note: "−" means no calculation. ("HS" represents hot spring; "BW" represents borehole water; "DBW" represents deep borehole water; "RW" represents river water; "C.B." represents charge balance; "H.T." represents hydrochemical type; "R.E." represents recharge elevation; YBJT2 and ZK4001 (sampling depth was 1495 m) referring to [24,25].

3.2. Geochemical Calculations

The recharge sources of geothermal water were assessed using stable hydrogen (δD) and oxygen ($\delta^{18}O$) isotopes, including recharge elevation, recharge temperature, and the proportion of magma water contribution. The recharge sources were calculated based on correlation equations and isotope bivariate mixing models [40–42]. Reservoir temperatures have been assessed using a variety of geothermometers, including silica geothermometers (Equations (1) and (2)) [18], multimineral equilibria [43], and chloride–enthalpy diagrams [19]. In addition, the SI of various minerals in the geothermal water was calculated using the PHREEQC3.0 software to assess the mineral equilibrium state and scaling trends [44].

$$\text{Quartz geothermometer: } T\ (^\circ C) = 1309/(5.19 - \log(SiO_2)) - 273.15 \quad (1)$$

$$\text{Chalcedony geothermometer: } T\ (^\circ C) = 1032/(4.69 - \log(SiO_2)) - 273.15 \quad (2)$$

where SiO_2 is the chemical component in the geothermal water in mg/L.

A geothermometer is used to estimate reservoir temperature using the relationship between the content of specific chemical components in geothermal water and temperature. The basic basis is that the mineral and aqueous solutions in the deep thermal reservoir reach equilibrium. The temperature of geothermal water decreases during the rising process, but the chemical composition remains relatively stable, so as to estimate the reservoir temperature [45]. However, because most of the geothermal water exposed

on the surface has not reached the complete water–rock equilibrium state, the reservoir temperature estimated by the geothermometer is generally low and needs to meet the corresponding conditions [12]. The multimineral equilibrium method is to determine the equilibrium temperature by constructing the relationship between the log (Q/K) of the mineral component and the temperature. The temperature at the convergence of the mineral curve is the estimated reservoir temperature in the state of mineral equilibrium. The principle of this method is to correct the CO_2 degassing during the rise in geothermal water by adding equimolar components of HCO_3^- and H^+ to the file. In this study, all calculations were performed using the SOLVEQ-XPT program to calculate the SI change trend of a group of water-bearing minerals at different reservoir temperatures. The minerals selected were those present in the geothermal system. This method allows an accurate assessment of the temperature at which minerals in geothermal water reach equilibrium by correcting for the effects of boiling decompression cooling [6]. Since chlorine–enthalpy diagrams can indicate the cooling modes experienced by geothermal water during the ascent process, such as conduction cooling, adiabatic cooling, and mixing with cold groundwater, the estimated temperature is close to the highest geothermal reservoir temperature [14].

4. Results

4.1. Hydrochemical Characteristics

The characteristics of hydrochemical parameters are presented in Table 1. The pH value of the geothermal water in Yangbajing was weakly alkaline (8.29–9.19). The exposed temperature of the geothermal springs and borehole water were 67–80 °C and 76–159 °C. The boreholes had a higher exposed temperature than the geothermal springs. The TDS contents of the geothermal springs and borehole water were 1400–1613 mg/L and 1599–2900 mg/L (Figure 3). The main anions were Cl^- and HCO_3^-, and the main cation was Na^+ in geothermal springs. The main anion was Cl^- and the main cation was Na^+ in geothermal borehole waters. All geothermal waters showed higher concentrations of major elements (except Ca^{2+} and Mg^{2+}) and trace elements (SiO_2, F, Sr, Li, B) compared to river water (Table 1 and Figure 3). The hydrochemical characteristics of geothermal waters in the Yangbajing field were comparable with those in the Kangding [3] and Rehai [46] high-temperature geothermal systems in southwestern China. Hence, the Yangbajing field is possibly related to magma existence and fault activity as well.

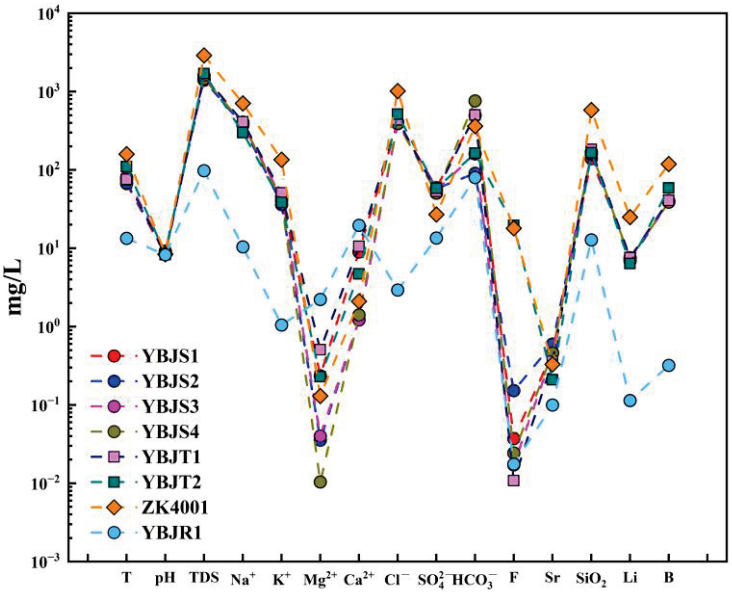

Figure 3. Schöoller diagram of all water samples in Yangbajing.

The Piper trilinear diagram showed that the hydrochemical types of geothermal water samples were predominantly of the Cl-Na, Cl·HCO_3-Na, and HCO_3·Cl-Na types (Table 1

and Figure 4). The hydrochemical type might be attributed to the reservoir lithology of the geothermal field being granite and sandstone (rich in silicate minerals) [34]. Interestingly, the process of mixing hot and cold water was indicated: Cl-Na-type water (deep reservoir) and HCO_3-Ca·Na-type water (shallow cold water) were mixed to form Cl-HCO_3·Na and HCO_3-Cl·Na-type water (shallow reservoir) (Figure 4). The shallow reservoir in Yangbajing was formed due to the upward flow of geothermal fluids from the deep reservoir into the Quaternary aquifer [24].

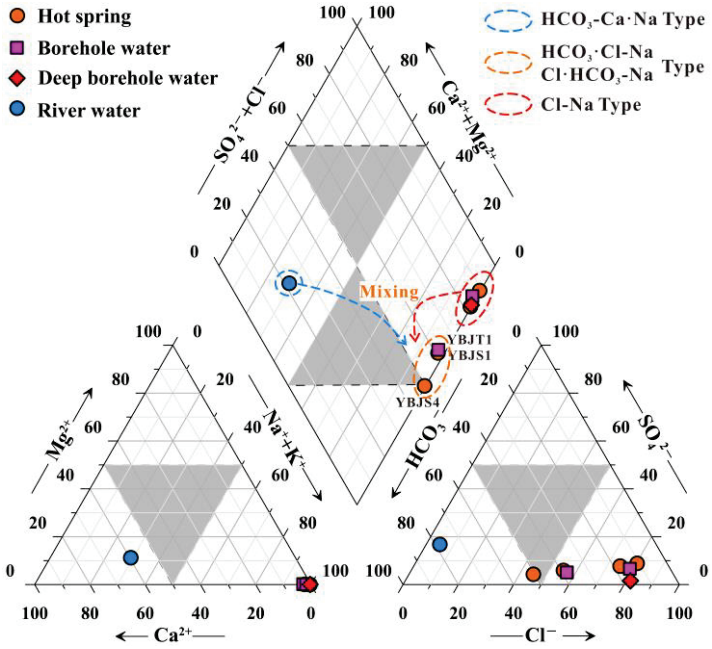

Figure 4. Piper trilinear diagram of all water samples from Yangbajing [47].

4.2. D-O-Sr Isotopes

The hydrogen (δD) and oxygen ($\delta^{18}O$) isotope ratios of geothermal water ranged from −150.7 ‰ to −139.0 ‰ and −17.50 ‰ to −16.00 ‰, respectively. River water was more enriched in hydrogen (δD) and oxygen ($\delta^{18}O$) than geothermal water (−121.8 ‰ and −15.72 ‰, respectively) (Table 1). The strontium isotope ($^{87}Sr/^{86}Sr$) ratios of geothermal water varied from 0.71203 to 0.71259; the strontium isotope ($^{87}Sr/^{86}Sr$) ratio of river water was lower than that of geothermal water, at 0.70890 (Table 1).

5. Discussion

5.1. Recharge Source by δD and $\delta^{18}O$

The stable hydrogen (δD) and oxygen ($\delta^{18}O$) isotopes of water samples followed the global meteoric water line (GMWL) [13] and the local meteoric water line (LMWL) [25], revealing the origin mainly from meteoric water (Figure 5a). The stable oxygen ($\delta^{18}O$) isotopic compositions of geothermal water (from −17.50 ‰ to −16.00 ‰) exhibited a notable positive isotopic shift compared to GMWL and LMWL, i.e., the "$\delta^{18}O$" drifting. This phenomenon could be attributed to oxygen isotopic exchange during the water–rock interaction [6].

The recharge source of geothermal water can be included in three end members: magmatic water (rectangle A, [48]), snow-melted water (rectangle B, [25]), and meteoric water (rectangle C, [3]) (Figure 5a). The river water was closer to end element C, suggesting its atmospheric recharge was dominant. Almost all geothermal waters fell in the straight line between snow-melted and magmatic water. The contribution of magmatic water in the geothermal water of Yangbajing was estimated to be between 15% and 23% using a bivariate isotopic mixing model.

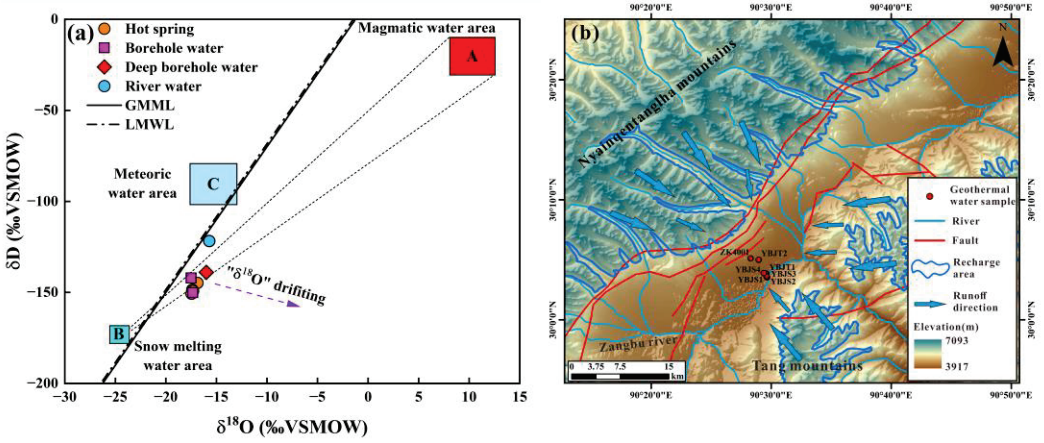

Figure 5. (**a**) The relationship between δD value and $\delta^{18}O$ value of all water samples in Yangbajing; (**b**) Yangbajing geothermal water recharge source area.

Due to the "$\delta^{18}O$" drift phenomenon, δD was more suitable for estimating the recharge elevation of geothermal water. According to the elevation gradient of δD on the Tibetan Plateau (–2.6%/100 m, [49]), the recharge elevations estimated by Equation (3) were between 5008 m and 5458 m (Table 1). In the study area, the Nyainqentanglh Mountains in the northwest and the Tangshan Mountains in the southeast were the recharge areas of geothermal water (Figure 5b). Based on the temperature effect of stable hydrogen isotopes (Equation (4)) [40], the recharge temperature of the geothermal water ranged from −20 °C to −16 °C.

$$H = (\delta R - \delta P)/K + h \quad (3)$$

where H (m) is the recharge elevation, δR (‰) is the δD of the geothermal water sample, δP (‰) is the δD of the river water sample, and h (m) is the elevation of the river.

$$\delta D = 3 \times T - 92 \quad (4)$$

where T (°C) is recharge temperature of the geothermal water.

5.2. Process Controlling Hydrochemical Compositions

5.2.1. Correlation of Hydrochemical Compositions

In this study, Pearson correlation analysis was performed to understand the correlation characteristics among the hydrochemical variables. As shown in Figure 6, the correlation between Cl^-, Na^+, K^+, SiO_2, Li, and B was very positive, with the correlation coefficients higher than 0.85, indicating that these variables might have the same source. However, Mg^{2+} and Ca^{2+} were negatively correlated with other ions, suggesting that there were other factors influencing the changes in Mg^{2+} and Ca^{2+} concentrations.

The relationships between Cl and other major ions are effective in tracing hydrogeochemical processes during the formation of geothermal water [12,50]. Among them, Cl correlated well with Na and K (R^2 = 0.87 and 0.94) (Figure 7a,b), and the ratio of Na/Cl was low, up to a maximum of only 1.0, indicating that the geothermal water circulation depth was shallow [51]. The negative correlation (R^2 = 0.80 and 0.57) between Cl and Ca and Mg in water samples (Figure 7c,d), along with their low concentrations of Ca and Mg, showed the absence of carbonate rocks in reservoir rocks. This conclusion aligned with the regional geological characteristics of the study area. The reason for the decrease in Ca^{2+} concentration might be the $CaCO_3$ scaling in the geothermal well [10,52]. Cl in the water samples correlated well with SO_4 (R^2 = 0.91), but there was little correlation with deep borehole water (Figure 7e). This occurred because the deep geothermal fluid is laden with H_2S gas. As it rises and experiences heat loss, a portion of it transforms into condensate water, which is subsequently leached out by the surrounding rocks and oxidized into SO_4 [27]. Consequently, the SO_4 concentration in the geothermal fluid increases during

ascent due to the oxidization of H_2S deep gas. A strong correlation of Cl between Li and B was observed for all water samples (R^2 = 0.92 and 0.99; Figure 7f,g), demonstrating that geothermal waters have a common primary geothermal fluid and have undergone mixing [53]. The favorable connection between Cl and SiO_2 in the geothermal water from Yangbajing (R^2 = 0.92; Figure 7h) was attributed to the strong association between the concentration of SiO_2 and temperature [18]. The poor correlation between Cl and F (R^2 = 0.48; Figure 7i) indicates that there were other geochemical processes affecting the concentration of F in shallow geothermal fluids.

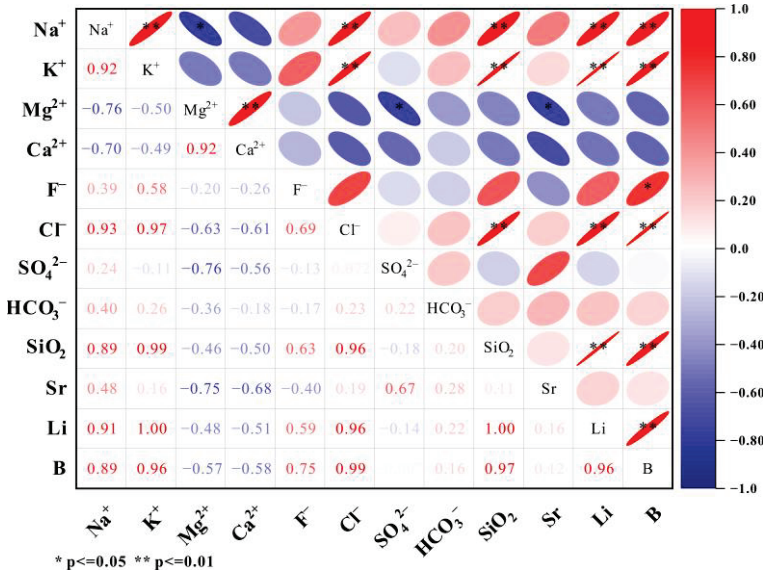

Figure 6. Pearson correlation of Yangbajing geothermal water. Red indicates positive correlation and blue indicates negative correlation.

In the study area, Cl-bearing minerals were not found in the strata. Consequently, the elevated concentration of Cl^- in geothermal water is attributed to magma, as magma has the capacity to supply a significant quantity of Cl^- to geothermal water [31,54]. Excess concentrations of Na^+ and K^+ relative to Cl^- might be derived from the dissolution of silicate minerals. Chemical activity diagrams of the Na_2O-Al_2O_3-SiO_2-H_2O and K_2O-Al_2O_3-SiO_2-H_2O systems can determine the dissolution process of silicate minerals [55]. The phase boundaries were plotted at 100 °C (black) and 200 °C (red) (Figure 8a,b). The dominant factors influencing the presence of Na^+ and K^+ in geothermal water appeared to be the dissolution of sodium feldspar and potassium feldspar, as seen in Equations (5) and (6) [6].

$$2NaAlSi_3O_8 + 3H_2O + 2CO_2 \rightarrow Al_2(SiO_5)(OH)_4 + 4SiO_2 + 2Na^+ + HCO_3^- \quad (5)$$

$$2KAlSi_3O_8 + 3H_2O + 2CO_2 \rightarrow Al_2(SiO_5)(OH)_4 + 4SiO_2 + 2K^+ + HCO_3^- \quad (6)$$

Moreover, ratio plots of $(Na^+ + K^+ - Cl^-)$ and $(Ca^{2+} + Mg^{2+}) - (SO_4^{2-} + HCO_3^-)$ can illustrate the effect of ion exchange on groundwater [56]. Schoeller indices CAI-I $(=(Cl^- - (Na^+ + K^+))/Cl^-)$ and CAI-II $(=(Cl^- - (Na^+ + K^+))/(HCO_3^- + SO_4^{2-} + CO_3^{2-} + NO_3^-))$ can further confirm the type of cation exchange [57]. The geothermal samples were distributed near the ion exchange line, and the CAI-I and CAI-II values were below zero (Figure 8c,d). This signifies that positive ion exchange occurred, i.e., Ca^{2+} in the geothermal water was replaced by Na^+ in the granite.

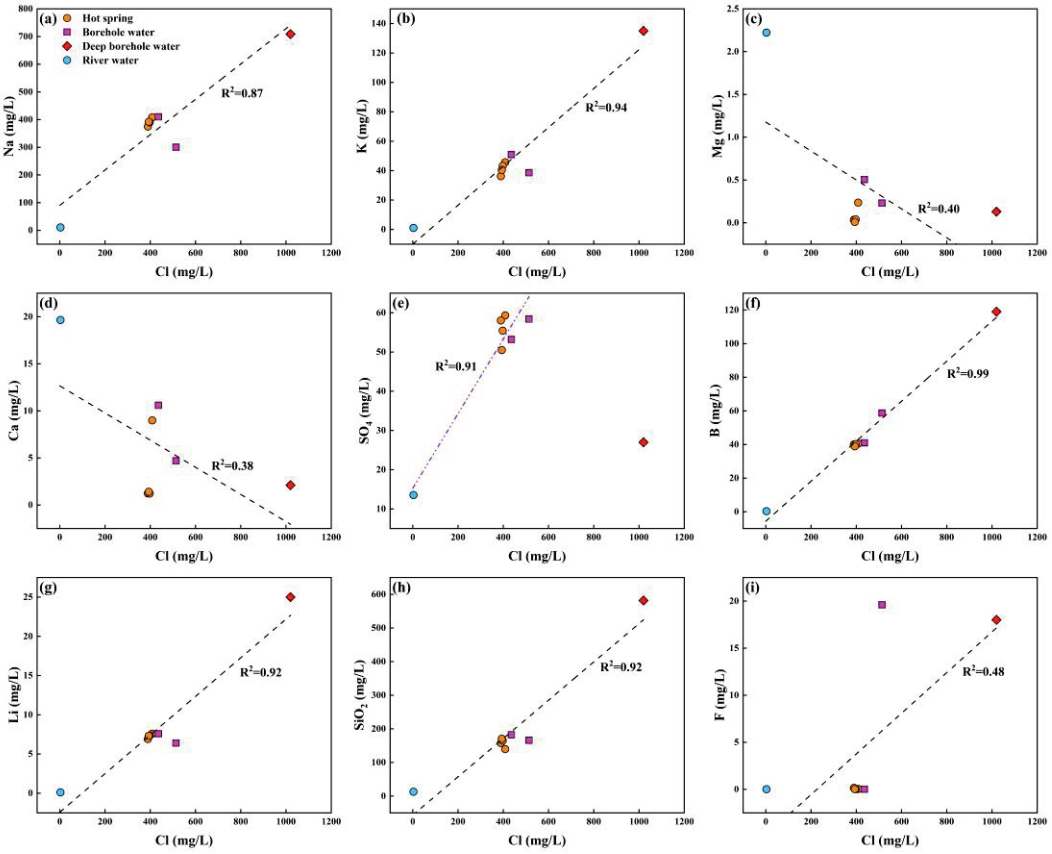

Figure 7. Relationship between Cl and hydrochemical parameters. (**a**) Na, (**b**) K, (**c**) Mg, (**d**) Ca, (**e**) SO_4, (**f**) B, (**g**) Li, (**h**) SiO_2, and (**i**) F. The black dotted line is the fitting line of all samples; the purple double-dotted line is the fitting line to remove the deep borehole water (ZK4001). The method used for fitting is divided into the least squares method.

5.2.2. Water–Rock Interactions Based on $^{87}Sr/^{86}Sr$ Ratio

The initial abundance of strontium isotopes ($^{87}Sr/^{86}Sr$) varies widely between rock types and can serve as a conservative tracer of water–rock interactions [58]. Previous studies showed that the $^{87}Sr/^{86}Sr$ ratios of silicate rocks in the Yangtze River Basin of China are typically >0.715 [59]. The $^{87}Sr/^{86}Sr$ ratios in marine carbonate rocks range from 0.707 to 0.709 [60]. In addition, the $^{87}Sr/^{86}Sr$ ratios in granites from the Yangbajing geothermal field in the study area were 0.710 to 0.718 [30]. The $^{87}Sr/^{86}Sr$ ratios of geothermal water consistently aligned with those of granite (Figure 9a), suggesting that the predominant source of strontium was the granite reservoir. The river water was located in the range of carbonate rocks, which could be related to the dissolution of carbonate rocks (Figure 1b). In addition, the negative correlation between Sr^{2+} and Ca^{2+} in geothermal water also confirmed that Sr^{2+} did not come from the dissolution of carbonate minerals (Figure 9b). Geothermal water leaches Sr^{2+} from silicate minerals during water–rock interactions, leading to an increase in Sr^{2+} concentration in geothermal water [61].

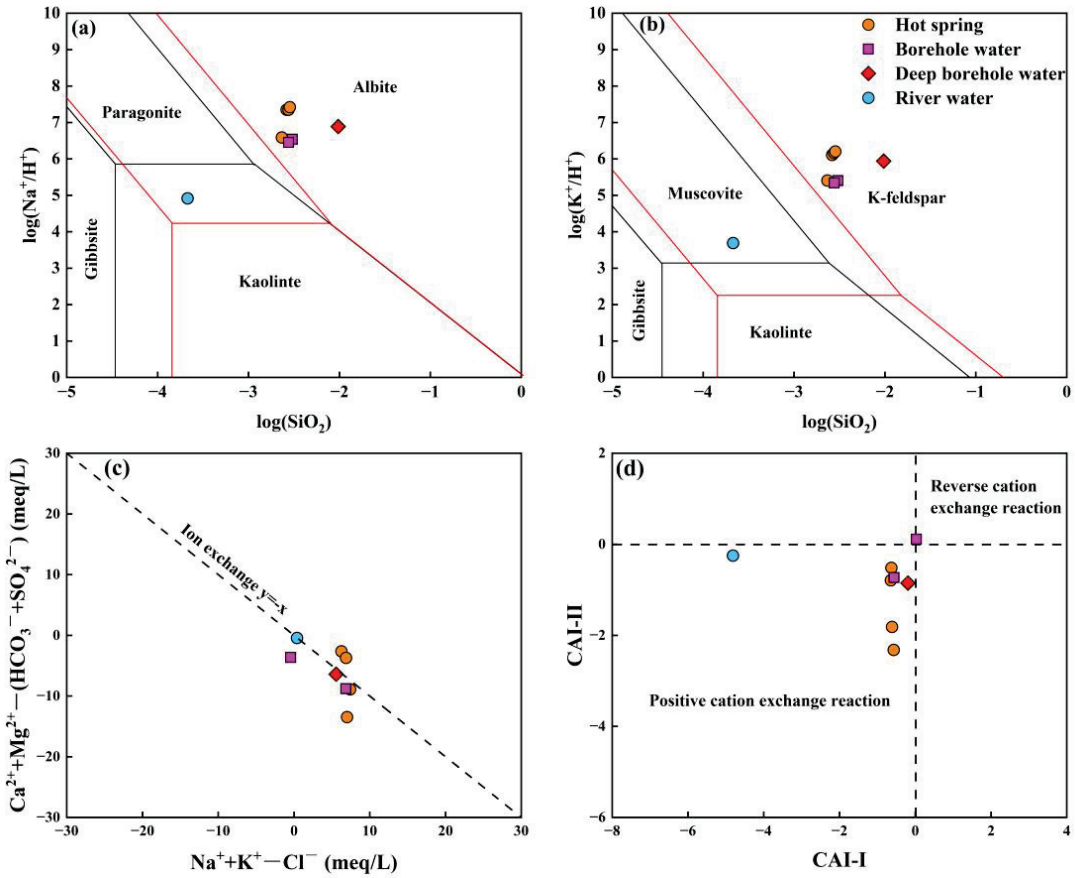

Figure 8. Hydrochemical analysis diagrams. (**a**) $\log(SiO_2)$ vs. $\log(Na^+/H^+)$, (**b**) $\log(SiO_2)$ vs. $\log(K^+/H^+)$, (**c**) $Na^+ + K^+ - Cl^-$ vs. $Ca^{2+} + Mg^{2+} - (HCO_3^- + SO_4^{2-})$, and (**d**) CAI-I vs. CAI-II.

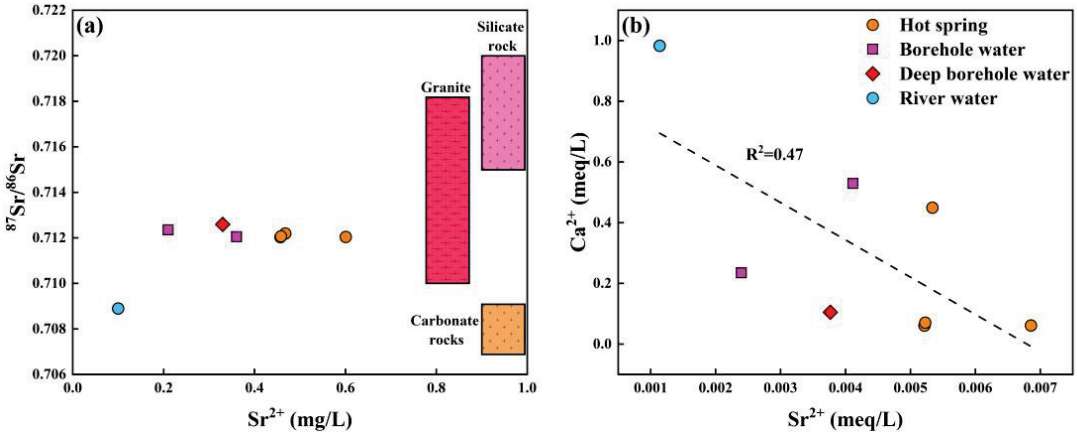

Figure 9. (**a**) Sr^{2+} vs. $^{87}Sr/^{86}Sr$, (**b**) Sr^{2+} vs. Ca^{2+}.

In conclusion, the geothermal water all came from the same primary geothermal fluid (stored in granite), which mixed with the cold water as it rose. The dissolution of silicate minerals (sodium and potassium feldspars) and positive cation exchange controlled the hydrochemical evolution, resulting in the formation of Cl-Na, Cl·HCO_3-Na, and HCO_3·Cl-Na types of geothermal water.

5.3. Geothermometry

5.3.1. Equilibrium State of Geothermal Waters

Geothermometers can estimate reservoir temperatures in geothermal systems, and the temperature-related water–rock equilibrium needs to be analyzed first [15]. The Na-K-Mg triangular diagram can classify waters as fully equilibrated waters, partially equilibrated or mixed waters, and immature waters [21]. It can be seen that the geothermal waters of Yangbajing were all located in partially equilibrated waters, with individual water samples close to the full equilibrium point (Figure 10). It indicates that the geothermal water of the Yangbajing geothermal field had reached a partial equilibrium state with the surrounding rocks, characteristic of partially equilibrated water. This occurrence was closely associated with the mixture of shallow cold water [6]. By comparing the data of Laoyulin and Rehai, we found that the samples in these three regions were not randomly distributed in the Na–K–Mg ternary diagram but linearly distributed along the isolines that tend to Na-K (Figure 10) [21]. Using Na-K geothermal thermometers, it was possible to estimate that deep reservoirs with temperatures as high as 240 °C, 282 °C, and 260 °C might exist beneath Yangbajing, Laoyulin, and Rehai. It was an interesting phenomenon that geothermal water from magmatic geothermal systems with higher Na^+ and K^+ concentrations did not change Na/K ratios during mixing with cold water, and thus, reservoir temperatures could be characterized intuitively in the Na–K–Mg ternary diagram. The deep borehole water ZK4001 in the Yangbajing geothermal system was located on the temperature line of 290 °C. The sample was collected at the depth of the borehole [24], indicating that the deep reservoir temperature in Yangbajing was actually higher.

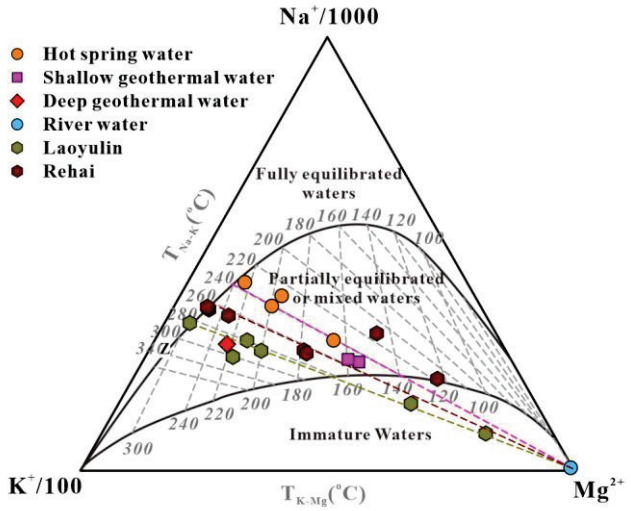

Figure 10. Na–K–Mg triangle diagram [21]. Laoyulin in Kangding and Rehai in Tengchong were from references [3,46].

5.3.2. Temperature and Depth of Geothermal Reservoir

The reservoir temperature of the geothermal water in Yangbajing was measured via the solute geothermometers, quartz and chalcedony [18,21], and the results are shown in Table 2. For geothermal springs and borehole water, the chalcedony geothermometer estimated temperatures at 132–152 °C; the quartz geothermometer estimated temperatures at 157–174 °C. The SI of quartz and chalcedony calculated by PHREEQC3.0 software was 0.03–0.44 and −0.20–0.15, respectively. It can be seen that the saturation degree of quartz in geothermal water is higher, so the temperature estimated by the quartz geothermometer was selected to represent the reservoir temperature. Most of the geothermal water in this study belonged to partially equilibrated water, and there was the influence of cold water mixing. Therefore, the solute thermometer could only reflect the shallow reservoir temperature after mixing with cold water. Additionally, research is necessary to investigate

the influence of various cooling mechanisms, including boiling depressurization cooling, adiabatic cooling, mixing with cold groundwater cooling, and conduction cooling [14].

Table 2. Calculations of reservoir temperature and cold water mixing ratio (a and b refer to [18]; c refers to [43]; d refers to [19]).

NO.	Quartz (a)	Chalcedony (b)	Multimineral Equilibria (c)	Chlorine–Enthalpy (d)	
			T	T	Mix
	(°C)		(°C)	(°C)	(%)
YBJS1	157	132	–	281	46
YBJS2	164	141	–	296	47
YBJS3	167	144	–	296	45
YBJS4	169	147	–	299	45
YBJT1	174	152	200–220	288	42
YBJT2	168	145	–	257	37
ZK4001	–	–	268–276	–	–

Note: "–" means no calculation.

During the process of boiling and depressurization, geothermal water undergoes the inevitable loss of some dissolved gases (e.g., CO_2). A corrective process for CO_2 degassing can be constructed using the multimineral equilibrium method so as to estimate the reservoir temperature under the influence of boiling decompression cooling. [43]. The SOLVEQ-XPT program was employed in this study to establish thermodynamic equilibrium between the minerals (Figure 11). Calculations were performed for two sample points, YBJT1 (from shallow reservoirs) and ZK4001 (from deep reservoirs), because in this study, these two points were the samples with the highest Cl concentration in the two reservoirs. The selected minerals began to converge in the temperature intervals of 200–220 °C and 268–276 °C, respectively, when 0.1 mol/L and 0.05 mol/L component species (H^+ and HCO_3^-) were added to these two places in the file to correct degassing (Figure 11). The multimineral equilibrium method estimated higher reservoir temperatures than the quartz geothermometer due to the correction for the effect of boiling decompression on temperature (Table 2). This suggests that the temperature estimated by the multimineral equilibrium method might be the reservoir temperature prior to cold water mixing. However, only the deep borehole sample ZK4001 had temperatures (268–276 °C) close to those estimated by the Na-K geothermometer in the Na–K–Mg ternary diagram (240 °C and 290 °C), whereas reservoir temperatures (200–220 °C) estimated by the shallow borehole sample YBJT1 were low. Geothermal water from the same parent geothermal fluid should have the same reservoir temperature. Therefore, it is necessary to continue to explore the difference in reservoir temperatures estimated for different types of geothermal water, that is, to consider the influence of other cooling mechanisms on the deep reservoir temperature estimation of shallow geothermal water.

There was a significant correlation (R^2 = 0.95) between Cl concentration and enthalpy for all water samples (Figure 12a). Therefore, in this study, a chlorine–enthalpy diagram [19] was used to analyze the effect of adiabatic cooling, conduction cooling, and cold water mixing on the temperature change in the geothermal water ascent process (Figure 12b). Drill hole ZK4001 was sampled at 1495 m below ground at temperatures up to 159.3 °C, with high Na^+ and Cl^- concentrations and low Ca^{2+} and Mg^{2+} concentrations (Table 1). Hence, adiabatic cooling was the main cooling method used to form the ZK4001 [14]. Most of the samples taken near the surface were below the local boiling temperature (85 °C), indicating that conduction cooling was experienced. We used the quartz-calculated temperatures to represent the transition point B between conduction cooling and cold water mixing; the line connecting the cold water point A and the transition point B as the cold water mixing line; and the intersection of the extension of A and B with the adiabatic cooling line, C, to represent the reservoir temperature (Figure 12b). The calculated deep reservoir temperatures were 257–299 °C for shallow geothermal water, and the cold water

mixing ratios were 37–47% (Table 2). It was inferred that reservoir one (299 °C) was the parent geothermal fluid in the deep reservoir of the Yangbajing geothermal field. Reservoir temperatures estimated from the geothermal water collected at shallow depths or at the surface were essentially the same as those estimated from the geothermal water collected deeper in the subsurface (ZK4001: 1459 m) due to consideration of the effects of a range of cooling mechanisms (Table 2).

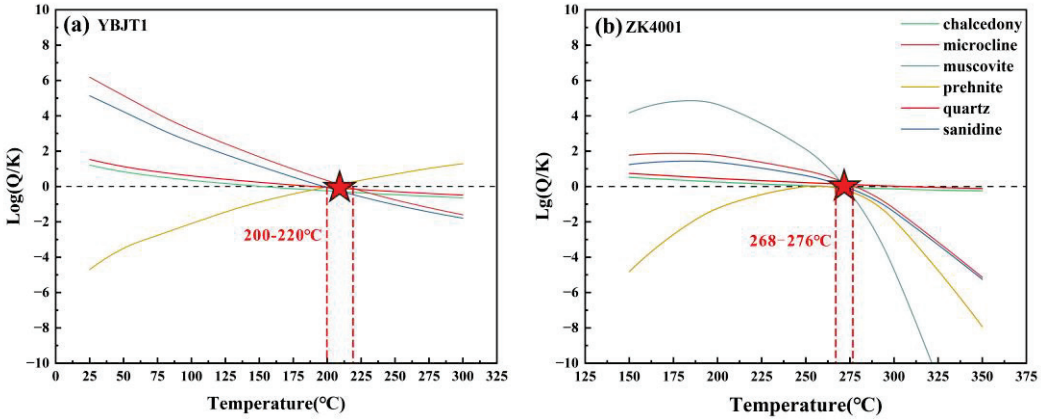

Figure 11. Results of estimation of shallow (**a**) and deep (**b**) geothermal reservoir temperatures via multivariate mineral–water equilibrium thermometers. The red star in the figure represents the position and corresponding temperature when the mineral group reaches equilibrium.

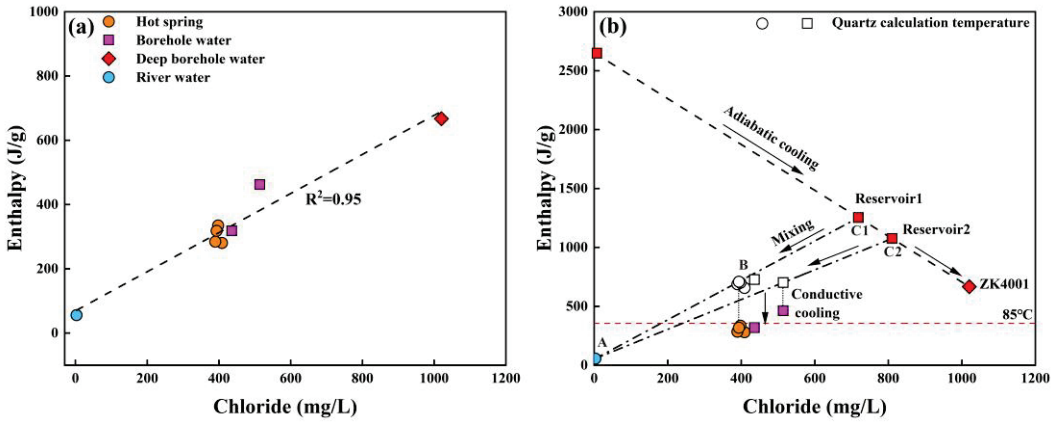

Figure 12. (**a**) The fitting relationship between chloride and enthalpy of Yangbajing water sample. (**b**) Chlorine–enthalpy diagram of Yangbajing water sample. The relationship between enthalpy and temperature is as follows: enthalpy = temperature × 4.1868; the unit is J/g.

In conclusion, the temperatures of the geothermal water in Yangbajing continued to decrease due to a series of effects during the cyclic rise. We synthesized the temperatures estimated by various methods and used the reservoir temperatures estimated by the chlorine–enthalpy diagram (257–299 °C) as the deep reservoir temperature; the reservoir temperatures estimated by the quartz geothermometer (157–174 °C) as the temperature of the shallow reservoir mixed with cold water; and the temperatures estimated by the multimineral equilibrium (YBJT1: 200–220 °C) as the temperatures between the deep and the shallow reservoirs, because the effects of a series of cooling mechanisms resulted in the differential temperature variations between the reservoirs. The shallow reservoir temperatures (157–174 °C) and deep reservoir temperatures (257–299 °C) estimated in the present study were basically consistent with the temperatures of geothermal water in underground boreholes measured by previous researchers (150–175 °C and 250–278 °C for shallow and deep boreholes, respectively) [23,34].

The geothermal gradient of Yangbajing is 6.67 m/°C [31]. According to the reservoir temperatures estimated in this study, the shallow reservoir depth was 1059–1172 m and the deep thermal reservoir depth was 1724–2010 m.

5.3.3. Conceptual Model of Geothermal System Genesis in Yangbajing

Based on the geological and topographic features (Figure 1b,d), this study proposed the genesis conceptual model of the geothermal system in Yangbajing (Figure 13). The geothermal water was recharged from snow-melted water and meteoric water originating from the Nyainqentanglh Mountains in the northwest and the Tangshan Mountains in the southeast, respectively. Further, the geothermal water was partially mixed with magmatic water. Recharged water rapidly infiltrated through fracture zones and fissures and circulated along geothermal water channels formed by faults and fracture systems. The minerals involved in water–rock interactions during circulation were mainly silicate minerals (sodium feldspar and potassium feldspar), while positive cation exchange occurred, resulting in the formation of weakly alkaline water of the Cl-Na, Cl·HCO_3-Na, and HCO_3·Cl-Na types. Cl, Li, and B in geothermal water all came from magmatic water at depth. During the ascent, the CO_2 and H_2S that accompany geothermal fluids brought out from the depths became condensate due to condensation and participated in water–rock interactions to form HCO_3^- and SO_4^{2-} [2,26]. Due to the high-temperature molten magma body beneath the Yangbajing [23], the heated high-temperature geothermal fluid rose along the interior of the pipe formed by the two sets of stretching normal faults, NNE–SSW and NE–SW. The temperature started to drop due to adiabatic cooling. A deep geothermal reservoir with high temperatures (257–299 °C) consisting of granitic mylonite and fissured granite was formed near a depth of 1724 m to 2010 m from the surface. Geothermal fluids continued to rise along the fracture pipe, and the temperature continued to fall due to conduction cooling. After mixing occurred with shallow cold water near the surface (1059–1172 m), a shallow reservoir with medium temperatures (157–174 °C) consisting of Quaternary sediments and sandstone was formed. The primary factor contributing to the presence of binary mixing relationships in geothermal water was the mixing with shallow cold water. The geothermal fluid in the shallow reservoir in the northwest continued to flow towards the southeast of the geothermal field through joint fissure channels, eventually overflowing to the surface to form hot springs.

5.4. Assessment of Scaling Trends in Geothermal Fluids

Scaling is one of the major problems in the utilization and production of geothermal fluids [62]. The change in hydrodynamic characteristics, gas partial pressure, and pH value will occur during the rising process of geothermal water, which will affect the change in scaling characteristics. In this research, the PHREEQC3.0 program was employed to model the alteration in equilibrium conditions of diverse minerals across a temperature range spanning from the wellhead temperature to 200 °C and the pH range of 4 to 10, respectively. Two samples, YBJS1 and YBJT1, were selected for simulation (Figure 14), because these two points had higher Ca^{2+} concentrations relative to the other samples (Table 1). Both samples exhibited supersaturation of aragonite and calcite across the entire temperature range (Figure 14a,b), indicating that intensive degassing of the geothermal water occurred during its ascent, resulting in a tendency for carbonate minerals to supersaturate and precipitate [6,10]. The carbonate minerals in the two samples gradually changed from an undersaturated state to a supersaturated state with the increase in the pH value (Figure 14c,d). This is because of the geothermal fluid flowing from the deep (high temperature and high pressure) to the shallow (low temperature and low pressure). During this transition, CO_2 degassing and the boiling of geothermal water occur, resulting in an increase in pH. Consequently, this promotes the precipitation of carbonate minerals [10,63]. It might be inferred that the occurrence of $CaCO_3$ scaling took place at a certain stage during the upward movement of geothermal water from the reservoir to the surface in the Yangbajing. Lei et al. analyzed the XRD of the scaling material from the wellheads

of Yangbajing and concluded that the volume share of $CaCO_3$ was more than 99% [52]. And by constructing a wellbore calcium carbonate scaling evaluation model, the maximum scaling rate of one well was simulated to be 0.067 mm/d, which occurred at a burial depth of 97.5 m.

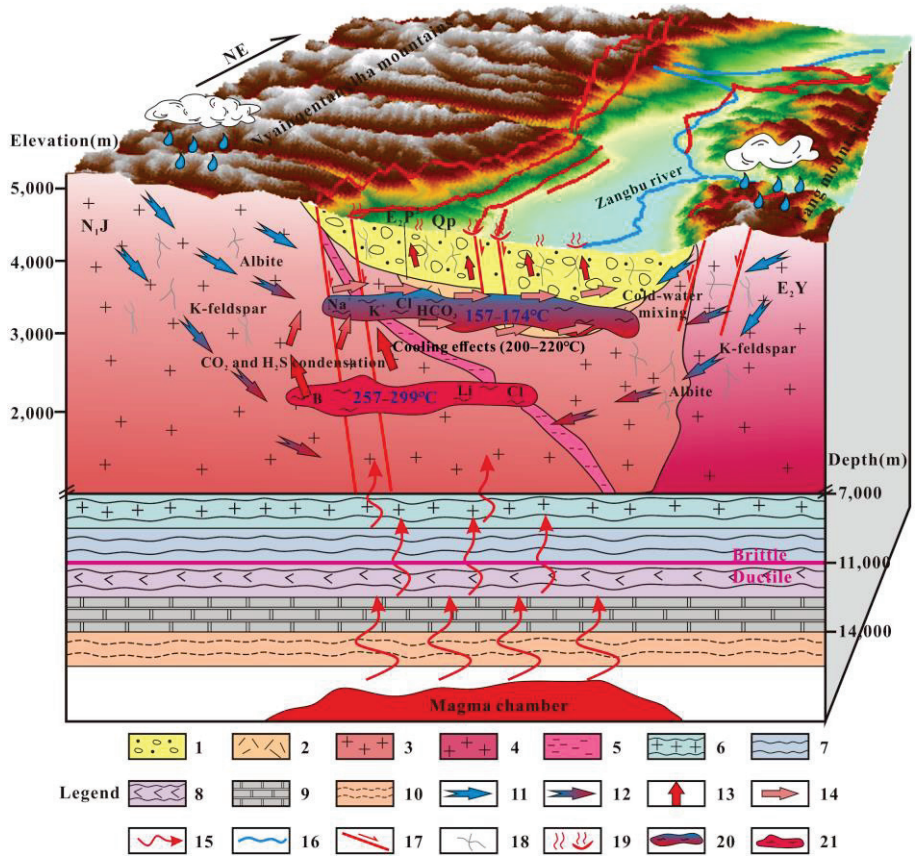

Figure 13. Conceptual model of genesis of Yangbajing geothermal system. The numbers in the figure are as follows: 1. Pleistocene glacial deposits in the Quaternary; 2. Paleogene Eocene Pana Formation trachyte and ignimbrite.; 3. Miocene Jieli medium–fine-grained biotite monzonitic granite; 4. fine-grained biotite monzonitic granite in the Eocene Yangbajingbingzhan; 5. granitic mylonite belt; 6. granitic gneiss; 7. gneiss; 8. granoamphibolite; 9. maritime carbonate rocks; 10. migmatite; 11. rainfall and snow melt infiltration recharge; 12. heating groundwater; 13. geothermal fluid rise; 14. geothermal fluid lateral flow; 15. deep-layer volatiles; 16. rivers; 17. normal fault; 18. joints and fissures; 19. steaming ground and geothermal spring; 20. shallow reservoirs; 21. deep reservoirs. This diagram is based on [2,23,24,31].

It was noteworthy that the silicate minerals in the geothermal water of Yangbajing basically reached a state of supersaturation as the temperature decreased and the pH did not exceed 9 (Figure 14). During the ascent, as the geothermal water mixed with the shallow cold water, there was a rapid decrease in temperature and pressure. The SiO_2 concentration in the shallow fluid surpassed the saturation point of quartz and chalcedony, triggering precipitation. Thus, the geothermal fluid slowly precipitated SiO_2 in the form of siliceous cementation in the transport channel, forming a self-enclosed cemented cap layer [8,27]. Sulfate minerals were undersaturated throughout the temperature and pH ranges (Figure 14), indicating that sulfate scaling did not occur in the geothermal waters of Yangbajing.

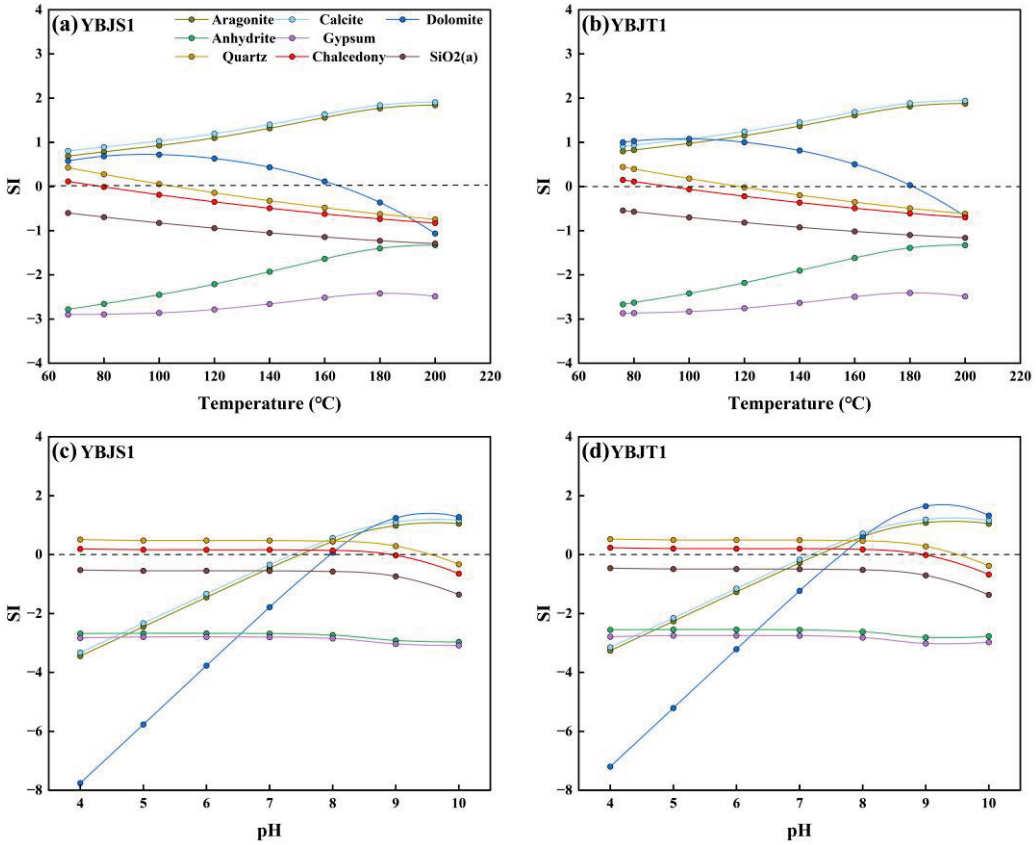

Figure 14. The saturation index of typical minerals in geothermal water changes at different temperatures and pH.

6. Conclusions

In this study, the following conclusions were drawn by investigating the hydrogeochemical characteristics, isotopic characteristics, and scaling characteristics of geothermal water in the Yangbajing geothermal field:

(1) The geothermal water was recharged from snow-melted water and local meteoric water located at higher altitudes on the Nyainqentanglha Mountains in the northwestern part and on the Tangshan Mountains in the southeastern part, and some of the magmatic water was mixed in the deep geothermal water.

(2) Weakly alkaline waters of the Cl-Na, Cl·HCO_3-Na, and HCO_3·Cl-Na types were identified in the Yangbajing geothermal field. The geothermal water all came from the same primary geothermal fluid in the granitic reservoir, which mixed with the cold water as it rose. The dissolution and positive cation exchange of silicate minerals (sodium and potassium feldspars) controlled the hydrochemical evolution.

(3) The temperature range of the shallow reservoir was between 157 °C and 174 °C, and the burial depth was 1059–1172 m; the temperature range of the deep reservoir was between 257 °C and 299 °C, and the burial depth of the reservoir was 1724–2010 m. The mixing ratio of geothermal water with cold water in the process of geothermal water ascension was about 37–47%. The geothermal water produced $CaCO_3$ and SiO_2 scaling during vertical and horizontal transport.

Author Contributions: Conceptualization, X.Y.; data curation, Y.C. and G.L.; formal analysis, J.L.; investigation, H.Y., X.Y., Y.C., C.Z., G.L. and M.S.; methodology, H.Y. and J.L.; software, Y.C., C.Z. and J.H.; supervision, Y.Z.; validation, J.L. and Y.Z.; writing—original draft, H.Y.; writing—review and editing, X.Y. All authors have read and agreed to the published version of the manuscript.

Funding: The Scientific Key R&D project of the Tibet Autonomous Region, grant number [XZ202201ZY0021G], the National Natural Science Foundation of China, grant number [42072313,

42102334], the Sichuan Provincial Department of Science and Technology Projects, grant number [2022NSFSC0413, 2023YFS0356], the Yibin Government Foundation, grant number [SWJTU2021020007, SWJTU2021020008].

Data Availability Statement: All of the research data have been provided in the paper.

Acknowledgments: We would like to thank the anonymous reviewers and editor for their constructive comments on this manuscript.

Conflicts of Interest: The authors declare no conflict of interest.

References

1. Capaccioni, B.; Vaselli, O.; Tassi, F.; Santo, A.P.; Huertas, A.D. Hydrogeochemistry of the thermal waters from the Sciacca Geothermal Field (Sicily, southern Italy). *J. Hydrol.* **2011**, *396*, 292–301. [CrossRef]
2. Wang, Y.; Li, L.; Wen, H.; Hao, Y. Geochemical evidence for the nonexistence of supercritical geothermal fluids at the Yangbajing geothermal field, southern Tibet. *J. Hydrol.* **2022**, *604*, 127243. [CrossRef]
3. Guo, Q.; Pang, Z.; Wang, Y.; Tian, J. Fluid geochemistry and geothermometry applications of the Kangding high-temperature geothermal system in eastern Himalayas. *Appl. Geochem.* **2017**, *81*, 63–75. [CrossRef]
4. Sanada, T.; Takamatsu, N.; Yoshiike, Y. Geochemical interpretation of long-term variations in rare earth element concentrations in acidic hot spring waters from the Tamagawa geothermal area, Japan. *Geothermics* **2006**, *35*, 141–155. [CrossRef]
5. Karaku, H. Helium and carbon isotope composition of gas discharges in the Simav Geothermal Field, Turkey: Implications for the heat source. *Geothermics* **2015**, *57*, 213–223. [CrossRef]
6. Tian, J.; Pang, Z.; Guo, Q.; Wang, Y.; Li, J.; Huang, T.; Kong, Y. Geochemistry of geothermal fluids with implications on the sources of water and heat recharge to the Rekeng high-temperature geothermal system in the Eastern Himalayan Syntax. *Geothermics* **2018**, *74*, 92–105. [CrossRef]
7. Criss, R.E. Use of Geochemical and Geophysical Techniques to Characterize and Prospect for Geothermal Resources and Hydrothermal Ore Deposits. *J. Earth Sci.* **2015**, *26*, 73–77. [CrossRef]
8. Zheng, X.; Duan, C.; Xia, B.; Jiang, Y.; Wen, J. Hydrogeochemical Modeling of the Shallow Thermal Water Evolution in Yangbajing Geothermal Field, Tibet. *J. Earth Sci.* **2018**, *30*, 870–878. [CrossRef]
9. Akın, T.; Kargı, H. Modeling the geochemical evolution of fluids in geothermal wells and its implication for sustainable energy production. *Geothermics* **2019**, *77*, 115–129. [CrossRef]
10. Li, Y.; Pang, Z.; Galeczka, I.M. Quantitative assessment of calcite scaling of a high temperature geothermal well in the Kangding geothermal field of Eastern Himalayan Syntax. *Geothermics* **2020**, *87*, 101844. [CrossRef]
11. Arnorsson, S. *Isotopic and Chemical Techniques in Geothermal Exploration, Development and Use*; International Atomic Energy Agency: Vienna, Austria, 2000.
12. Wang, Y.; Yuan, X.; Zhang, Y.; Zhang, X.; Xiao, Y.; Duo, J.; Huang, X.; Sun, M.; Lv, G. Hydrochemical, D–O–Sr isotopic and electromagnetic characteristics of geothermal waters from the Erdaoqiao area, SW China: Insights into genetic mechanism and scaling potential. *Ore Geol. Rev.* **2023**, *158*, 105486. [CrossRef]
13. Craig, H. Isotopic variations in meteoric waters. *Science* **1961**, *133*, 1702–1703. [CrossRef] [PubMed]
14. Li, X.; Qi, J.; Yi, L.; Xu, M.; Zhang, X.; Zhang, Q.; Tang, Y. Hydrochemical characteristics and evolution of geothermal waters in the eastern Himalayan syntaxis geothermal field, southern Tibet. *Geothermics* **2021**, *97*, 102233. [CrossRef]
15. Li, X.; Huang, X.; Liao, X.; Zhang, Y. Hydrogeochemical Characteristics and Conceptual Model of the Geothermal Waters in the Xianshuihe Fault Zone, Southwestern China. *Int. J. Environ. Res. Public Health* **2020**, *17*, 500. [CrossRef] [PubMed]
16. Yu, X.; Yuan, X.; Guo, H.; Zhang, Y.; Cao, H.; Luo, T.; Gong, Z.; Huang, H. Coupling Hydrochemistry and Stable Isotopes (δ2H, δ18O and 87Sr/86Sr) to Identify the Major Factors Affecting the Hydrochemical Process of Groundwater and Surface Water in the Lower Reaches of the Yarlung-Zangbo River, Southern Tibet, Southwestern China. *Water* **2022**, *14*, 3906. [CrossRef]
17. Zhang, Y.; He, Z.; Tian, H.; Huang, X.; Zhang, Z.; Liu, Y.; Xiao, Y.; Li, R. Hydrochemistry appraisal, quality assessment and health risk evaluation of shallow groundwater in the Mianyang area of Sichuan Basin, southwestern China. *Environ. Earth Sci.* **2021**, *80*, 576. [CrossRef]
18. Fournier, R.O. Chemical geothermometers and mixing models for geothermal systems. *Geothermics* **1977**, *5*, 41–50. [CrossRef]
19. Fournier, R.O. A Revised Equation for the Na/K Geothermometer. *Geotherm. Resour. Counc. Trans.* **1979**, *3*, 221–224.
20. Fournier, R.O.; Truesdell, A.H. Geochemical indicators of subsurface temperature. Part II. Estimation of temperature and fraction of hot water mixed with cold water. *J. Res. US Geol. Surv.* **1974**, *2*, 263–270.
21. Giggenbach, W.F. Geothermal solute equilibria. derivation of Na-K-Mg-Ca geoindicators. *Geochim. Cosmochim. Acta* **1988**, *52*, 2749–2765. [CrossRef]
22. Zhang, Y.; Xu, M.; Li, X.; Qi, J.; Zhang, Q.; Guo, J.; Yu, L.; Zhao, R. Hydrochemical Characteristics and Multivariate Statistical Analysis of Natural Water System: A Case Study in Kangding County, Southwestern China. *Water* **2018**, *10*, 80. [CrossRef]
23. Duo, J. The basic characteristics of the Yangbajing geothermal field—A typical high temperature geothermal system. *Eng. Sci.* **2003**, *5*, 42–47. (In Chinese)

24. Guo, Q.; Wang, Y.; Liu, W. Major hydrogeochemical processes in the two reservoirs of the Yangbajing geothermal field, Tibet, China. *J. Volcanol. Geotherm. Res.* **2007**, *166*, 255–268. [CrossRef]
25. Guo, Q.; Wang, Y.; Liu, W. O, H, and Sr isotope evidences of mixing processes in two geothermal fluid reservoirs at Yangbajing, Tibet, China. *Environ. Earth Sci.* **2010**, *59*, 1589–1597. [CrossRef]
26. Tong, W.; Zhu, M.; Chen, M. Sulfur-isotopic analysis and studies upon the Abyssal heat recharge of the Tibet's hydrothermal activities. *Acta Sci. Nat. Univ. Pekin.* **1982**, *18*, 79–85. (In Chinese)
27. Zhao, P.; Jin, J.; Zhang, H.Z.; Duo, J.; Liang, T.L. Chemical composition of thermal water in the Yangbajing geothermal field, Tibet. *Sci. Geol. Sin.* **1998**, *33*, 61–72. (In Chinese)
28. Elenga, H.I.; Tan, H.; Su, J.; Yang, J. Origin of the enrichment of B and alkali metal elements in the geothermal water in the Tibetan Plateau: Evidence from B and Sr isotopes. *Geochemistry* **2021**, *81*, 125797. [CrossRef]
29. Su, J.; Tan, H.; Chen, X. The groundwater deep circulation and large-scale geothermal deposition in response to the extension of the Yadong–Gulu rift, South Tibet, China. *J. Volcanol. Geotherm. Res.* **2020**, *395*, 106836. [CrossRef]
30. Zhao, P.; Dor, J.; Xie, E.J.; Jin, J. Strontium isotope data for thermal waters in selected high-temperature geothermal fields, China. *Acta Petrol. Sin.* **2003**, *19*, 569–576. (In Chinese)
31. Sun, M. *Hydrochemical Characteristics and Genetic Mechanism of Geothermal Resource in the Yangbajiang Area, Tibet*; Tibet University: Lhasa, China, 2023. (In Chinese)
32. Hou, Z.Q.; Li, Z.Q. Possible location for underthrusting front of the Indus Continent: Constraints from Helium isotope of the geothermal gas in southern Tibet and eastern Tibet. *Acta Geol. Sin.* **2004**, *78*, 482–493. (In Chinese)
33. Yin, A.; Harrison, T.M. Geologic Evolution of the Himalayan-Tibetan Orogen. *Annu. Rev. Earth Planet. Sci.* **2000**, *28*, 211–280. [CrossRef]
34. Guo, Q. Hydrogeochemistry of high-temperature geothermal systems in China: A review. *Appl. Geochem.* **2012**, *27*, 1887–1898. [CrossRef]
35. Brown, L.D.; Zhao, W.; Nelson, K.D.; Hauck, M.; Alsdorf, D.; Ross, A.; Cogan, M.; Clark, M.; Liu, X.; Che, J. Bright Spots, Structure, and Magmatism in Southern Tibet from INDEPTH Seismic Reflection Profiling. *Science* **1996**, *274*, 1688–1690. [CrossRef] [PubMed]
36. Chen, L.; Booker, J.; Jones, A.; Wu, N.; Unsworth, M.; Wei, W.; Tan, H. Electrically Conductive Crust in Southern Tibet from INDEPTH Magnetotelluric Surveying. *Science* **1996**, *274*, 1694–1696. [CrossRef] [PubMed]
37. Kind, R.; Ni, J.; Zhao, W.; Wu, J.; Yuan, X.; Zhao, L.; Sandvol, E.; Reese, C.; Nabelek, J.; Hearn, T. Evidence from Earthquake Data for a Partially Molten Crustal Layer in Southern Tibet. *Science* **1996**, *274*, 1692–1694. [CrossRef] [PubMed]
38. Makovsky, Y.; Klemperer, S.; Ratschbacher, L.; Brown, L.; Li, M.; Zhao, W.; Meng, F. INDEPTH Wide-Angle Reflection Observation of P-Wave-to-S-Wave Conversion from Crustal Bright Spots in Tibet. *Science* **1996**, *274*, 1690–1691. [CrossRef] [PubMed]
39. Nelson, K.D.; Zhao, W.; Brown, L.D.; Kuo, J.; Che, J.; Liu, X.; Klemperer, S.L.; Makovsky, Y.; Meissner, R.; Mechie, J.; et al. Partially Molten Middle Crust Beneath Southern Tibet: Synthesis of Project INDEPTH Results. *Science* **1996**, *274*, 1684–1688. [CrossRef]
40. Dansgaard, W. Stable Isotope in Precipitation. *Tellus* **1964**, *16*, 436–468. [CrossRef]
41. Pang, Z. pH dependant isotope variations in arc-type geothermal waters: New insights into their origins. *J. Geochem. Explor.* **2007**, *89*, 306–308. [CrossRef]
42. Ta, M.; Zhou, X.; Guo, J.; Wang, Y.; Wang, X.; Xu, Y. Hydrogeochemical characteristics and formation of the hot springs occurring in the plunging ends of an anticline in Chongqing, Eastern Sichuan Basin, China. *Environ. Earth Sci.* **2019**, *78*, 468. [CrossRef]
43. Pang, Z.; Reed, M. Theoretical Chemical Thermometry on Geothermal Waters: Problems and Methods. *Geochim. Et Cosmochim. Acta* **1998**, *62*, 1083–1091. [CrossRef]
44. Parkhurst, D.L.; Appelo, C.A.J. User's guide to PHREEQC (Version 2): A computer program for speciation, batch-reaction, one-dimensional transport, and inverse geochemical calculations. *Water-Resour. Investig. Rep.* **1999**, *99*, 312.
45. Zhou, X.; Jin, X.; Liang, S.; Shen, Y.; Zhang, H. *Special Topics on Groundwater Sciences*; Geological Publishing House: Beijing, China, 2017. (In Chinese)
46. Guo, Q.; Wang, Y. Geochemistry of hot springs in the Tengchong hydrothermal areas, Southwestern China. *J. Volcanol. Geotherm. Res.* **2012**, *215–216*, 61–73. [CrossRef]
47. Piper, A. A Graphic Procedure in the Geochemical Interpretation of Water-Analyses. *Eos Trans. Am. Geophys. Union* **1944**, *25*, 914–923.
48. Giggenbach, W.F. Isotopic shifts in waters from geothermal and volcanic systems along convergent plate boundaries and their origin. *Earth Planet. Sci. Lett.* **1992**, *113*, 495–510. [CrossRef]
49. Yu, J.; Zhang, H.; Yu, F.; Liu, D. Oxygen and hydrogen isotopic compositions of meteoric waters in the eastern part of Xizang. *Chin. J. Geochem.* **1984**, *13*, 93–101. [CrossRef]
50. Truesdell, A.H.; Nathenson, M.; Rye, R.O. The effects of subsurface boiling and dilution on the isotopic compositions of Yellowstone thermal waters. *J. Geophys. Res.* **1977**, *82*, 3694–3704. [CrossRef]
51. Alçiçek, H.; Bülbül, A.; Brogi, A.; Liotta, D.; Ruggieri, G.; Capezzuoli, E.; Meccheri, M.; Yavuzer, İ.; Alçiçek, M.C. Origin, evolution and geothermometry of thermal waters in the Gölemezli Geothermal Field, Denizli Basin (SW Anatolia, Turkey). *J. Volcanol. Geotherm. Res.* **2018**, *349*, 1–30. [CrossRef]

52. Lei, H.W.; Bai, B.; Cui, Y.X.; Xie, Y.C.; Li, J.; Hou, X.W. Quantitative Assessment of Calcite Scaling of a High Temperature Geothermal Production Well: Hydrogeochemistry —Application to the Yangbajing Geothermal Fields, Tibet. *Earth Sci.* **2023**, *48*, 935–945. (In Chinese)
53. Tassi, F.; Aguilera, F.; Darrah, T.; Vaselli, O.; Capaccioni, B.; Poreda, R.J.; Delgado Huertas, A. Fluid geochemistry of hydrothermal systems in the Arica-Parinacota, Tarapacá and Antofagasta regions (northern Chile). *J. Volcanol. Geotherm. Res.* **2010**, *192*, 1–15. [CrossRef]
54. Henley, R.W.; Ellis, A.J. Geothermal systems ancient and modern: A geochemical review. *Earth Sci. Rev.* **1983**, *19*, 1–50. [CrossRef]
55. Shvartsev, S.L.; Sun, Z.; Borzenko, S.V.; Gao, B.; Tokarenko, O.G.; Zippa, E.V. Geochemistry of the thermal waters in Jiangxi Province, China. *Appl. Geochem.* **2018**, *96*, 113–130. [CrossRef]
56. Sun, M.; Zhang, X.; Yuan, X.; Yu, Z.; Xiao, Y.; Wang, Y.; Zhang, Y. Hydrochemical Characteristics and Genetic Mechanism of Geothermal Springs in the Aba Area, Western Sichuan Province, China. *Sustainability* **2022**, *14*, 12824. [CrossRef]
57. Zhang, Y.; Li, X.; Luo, M.; Wei, C.; Huang, X.; Xiao, Y.; Qin, L.; Pei, Q. Hydrochemistry and Entropy-Based Groundwater Quality Assessment in the Suining Area, Southwestern China. *J. Chem.* **2021**, *2021*, 5591892. [CrossRef]
58. Blum, J.D.; Erel, Y.; Brown, K. 87Sr/86Sr ratios of sierra nevada stream waters: Implications for relative mineral weathering rates. *Geochim. Cosmochim. Acta* **1993**, *57*, 5019–5025. [CrossRef]
59. Wang, Z.L.; Zhang, J.; Liu, C.Q. Strontium isotopic compositions of dissolved and suspended loads from the main channel of the Yangtze River. *Chemosphere* **2007**, *69*, 1081–1088. [CrossRef] [PubMed]
60. Han, G.; Liu, C.Q. Strontium isotope and major ion chemistry of the rainwaters from Guiyang, Guizhou Province, China. *Sci. Total Environ.* **2006**, *364*, 165–174. [CrossRef]
61. Fan, Y.; Pang, Z.; Liao, D.; Tian, J.; Hao, Y.; Huang, T.; Li, Y. Hydrogeochemical Characteristics and Genesis of Geothermal Water from the Ganzi Geothermal Field, Eastern Tibetan Plateau. *Water* **2019**, *11*, 1631. [CrossRef]
62. Chauhan, V.; Saevarsdottir, G.; Tesfahunegn, Y.A.; Asbjornsson, E.; Gudjonsdottir, M. Computational study of two-phase flashing flow in a calcite scaled geothermal wellbore. *Geothermics* **2021**, *97*, 102239. [CrossRef]
63. Yuan, X.; Zhang, Y.; Wang, Y.; Huang, X.; Sun, M.; Lv, G. Geothermal water chemical characteristics and scaling analysis of Xianshuihe fault zone. *Sediment. Geol. Tethyan Geol.* **2023**, *43*, 357–372. (In Chinese)

Disclaimer/Publisher's Note: The statements, opinions and data contained in all publications are solely those of the individual author(s) and contributor(s) and not of MDPI and/or the editor(s). MDPI and/or the editor(s) disclaim responsibility for any injury to people or property resulting from any ideas, methods, instructions or products referred to in the content.

water

MDPI

Article

Transport of Oxygen-Doped Graphitic Carbon Nitride in Saturated Sand: Effects of Concentration, Grain Size, and Ionic Strength

Thanh-Tuan Nguyen [1], Do-Gun Kim [2,*] and Seok-Oh Ko [1,*]

[1] Department of Civil Engineering, Kyung Hee University, 1732, Deakyungdaero, Yongin 17104, Gyeonggi-do, Republic of Korea; nguyentuan@khu.ac.kr
[2] Department of Environmental Engineering, Sunchon National University, 255 Jungang-ro, Suncheon 57922, Jeollanam-do, Republic of Korea
* Correspondence: dgkim@scnu.ac.kr (D.-G.K.); soko@khu.ac.kr (S.-O.K.); Tel.: +82-61-750-3817 (D.-G.K.); +82-31-201-2999 (S.-O.K.); Fax: +82-61-750-3810 (D.-G.K.); +82-31-202-8854 (S.-O.K.)

Abstract: In this study, the characteristics and transport of oxygen-doped graphitic carbon nitride (OgCN) were investigated in comparison with multi-walled carbon nanotube (MWCNT), and the transport of OgCN was evaluated under various conditions. OgCN was superior to MWCNT in transport within a quartz sand layer with less attachment and more detachment than MWCNT, which is attributable to more diverse and abundant functional groups, charges, defects, and amorphous graphitic structures. OgCN transport was well described by a one-dimensional advection–dispersion–retention model. The coefficients of retention (S_{max}), attachment (k_a), and detachment (k_d) calculated by the model were not always well-correlated with OgCN concentration and the grain size of the medium, suggesting that the OgCN transport was affected by various factors such as attachment, detachment, and pore size. However, it was clearly and significantly inhibited by ionic strength, via improved aggregation of OgCN. It is believed that the results of this study contribute to establish proper sub-surface injection strategies of carbonaceous materials for in situ chemical oxidation.

Keywords: oxygen-doped graphitic carbon nitride; column experiment; breakthrough curves; transport modeling

1. Introduction

In situ chemical oxidation (ISCO), which uses various oxidants, including hydrogen peroxide (H_2O_2), peroxydisulfate ($S_2O_8^{2-}$, PDS), peroxymonosulfate (HSO_5^-, PMS), and permanganate (MnO_4^-, PM), is an efficient and economical option for the removal of organic pollutants from soil and groundwater via oxidative degradation, limiting the spread of pollutants and their associated risks [1–3]. The ISCO is based on the oxidative degradation of organic pollutants by the attack of radical and/or non-radical reactive species, such as $^{\bullet}OH$, $SO_2^{\bullet-}$, and $^1O_2$, via the activation of the oxidants [4,5]. The activation is carried out using various homogeneous and heterogeneous catalysts and activators.

Homogeneous activators and/or catalysts include transition metal ions, most frequently Fe^{2+}, heat, UV, and ultrasound [6–8]. However, those homogeneous processes have critical drawbacks in subsurface applications, such as high cost, limited large-scale applications, blockage of pores in aquifers via the formation of metal precipitates, and secondary pollution by the migration of metals to clean zones [9,10].

Therefore, the use of heterogeneous catalysts such as solid-phase zero-valence metals, metal (hydr)oxides, metal-free carbonaceous materials, and composites can be beneficial in ISCO. These heterogeneous catalysts and/or activators have a broader range of working pH, are easily recovered, can be regenerated, and have a wider application via modification

of the reactive sites on them [11,12]. Among the heterogeneous catalysts, metal-containing materials have the inherent disadvantage of metal leaching, which causes secondary pollution, pore blocking, and the deactivation of the catalysts via migration, as well as the formation and accumulation of less reactive metal species [13–17]. On the other hand, the risks of metal-containing materials are avoided by using metal-free carbonaceous materials, such as graphene oxide (GO), cubic mesoporous carbon, carbon nanotubes (CNTs), nanodiamonds, graphitic carbon nitride (gCN), and activated carbon (AC). They have excellent thermal and chemical stability, availability, and well-developed meso- and micro-pores, which can provide more surface-reactive sites [13]. Therefore, carbonaceous materials can be good options for use as catalysts in ISCO and have been the focus of recent research [14].

Other than the high potential of the carbonaceous materials as catalysts in ISCO, it must be noted that the transport of the materials in the subsurface environment is critical for their successful application in ISCO [2,11]. A catalyst and/or activator must be transported through the pores of soil layers and spread readily throughout the contaminated zone [2,11,17]. The transport is more difficult for solid materials than dissolved ions, such as Fe^{2+} [2,11]. However, limited numbers of publications have investigated the transport of heterogeneous catalytic materials through porous media, such as aquifers.

In this regard, the transport of a metal-free carbonaceous material, which is one of the good candidates for catalysts for ISCO, was investigated in this study to establish a proper strategy for its injection into subsurface-contaminated zones. Oxygen-doped gCN (OgCN) was selected as the catalyst. OgCN has a graphene-like layered structure and is prepared using cheap materials, such as urea and oxalic acid, via replacing N atoms in the amino groups in the heptazine units of gCN [18]. The high potential of the OgCN in ISCO can be justified by the remediation efficiency and safety.

Both gCN and OgCN are good photocatalysts [18–21]. However, OgCN demonstrates effective PMS activation, an effect that is negligiblein gCN [18,19]. It was suggested that the electron-rich O and the electron-poor C atoms near the O accelerated the electron transfer from organic pollutants (electron donor) to PMS (electron acceptor), and the generation of reactive species, such as $SO_2^{\bullet-}$ and $^1O_2$, eventually enhanced the oxidative degradation of the organic pollutants [14,18,19]. For example, OgCN was excellent in the degradation of bisphenol-A (BPA) and oxytetracycline via PMS activation to generate $^{\bullet}OH$, $SO_2^{\bullet-}$, and $^1O_2$ [18,19]. Moreover, OgCN is also an efficient photocatalyst for BPA degradation via improved charge-carriers separation and changing the positions of valance and conduction bands [20,21]. In addition, gCNs are non-toxic [18], so the residual OgCN after the operation of ISCO does not cause a risk in the underground environment. First, the properties and transport of OgCN in a porous medium were compared with those of multi-walled carbon nanotubes (MWCNT), to identify the effects of the material characteristics on transport. Then, the transport of OgCN was evaluated under various OgCN concentrations, grain sizes of the medium, and ionic strength (IS).

2. Materials and Methods

2.1. Materials

The OgCN was synthesized from a mixture of urea and oxalic acid via one-step thermal treatment [21]. In detail, 20 g of urea and 8 g of oxalic acid were mixed and ground for 30 min. Then, the mixture was heated in a box furnace at 550 °C for 4 h at a ramp rate of 3 °C/min. It was shown that the doped O substitutes the graphitic- and pyridinic-N to increase the electron-rich O atoms and the electron-poor C atoms near the O, in OgCN [18,21]. The obtained brown powders were cooled to room temperature, ground, and stored until use. MWCNTs and graphite flakes were purchased from Carbon Nano-material Technology Co., Ltd. (Pohang, Republic of Korea) and Alfa Aesar (Ward Hill, MA, USA), respectively. They were rinsed with de-ionized (DI) water 10 times before drying at 105 °C for 24 h.

Standard sand (ISO 679, SNL Corp., Leucate, France) was used as the porous media. It was separated into two size ranges, 0.25–0.6 mm and 0.6–1.0 mm, by sieving. They were treated sequentially with 0.1 M of H_2SO_4 to remove metal oxides, and then 5% of H_2O_2 to remove organic materials on the surfaces [22]. They were then rinsed with DI water until the pH was 7.0 ± 0.2 and dried in an oven at 105 °C for 24 h.

2.2. Characterization

The crystal structure of the materials was analyzed via X-ray diffraction (XRD) using an X-ray Diffractometer (D8 Advance, Bruker, Germany) at a 2θ range of 3° to 89.14° and scanning speed of 0.2°/min, using Cu Kα radiation. The Raman spectra were recorded with an inVia Raman microscope (Renishaw, UK). The excitation wavelength was 514 nm, the spectral resolution was 4 cm^{-1}, the exposure time was 10 s, and the total acquisitions was 20. Fourier-transform infrared spectroscopy (FTIR) spectra were obtained using the Spectrum One system (Perkin-Elmer, Shelton, CT, USA) to determine the surface functional groups. The pellet was prepared using the ground mixtures of 200 mg of KBr with 0.2 g of OgCN or MWCNT. The spectra were recorded for 8 successive scans at the wavelengths of 4000–400 cm^{-1}, with a resolution of 4 cm^{-1}. The element chemical states on the surfaces of the catalysts were obtained via X-ray photoelectron spectroscopy (XPS) with K-Alpha (Thermo Electron, Waltham, MA, USA). A monochromatic Al α-Alpha radiation source was used and the spot diameter was 400 μm. The high-resolution XPS spectra were recorded for C1s, N1S, and O1s for 10 scans (0.1 eV steps) and with 30 eV of pass energy. The particle size distribution (PSD) was determined via dynamic light scattering (DLS) using a Zetasizer nanoseries (Zen 3600 Zetasizer Nano ZS, Particle Size Analyzer, Malvern Instruments, Malvern, UK) and the zeta potential of OgCN at different ionic strength (IS) concentrations (0, 2, 5, and 10 mM, pH 7) was determined using a Zeta Potential Analyzer (Brookhaven Instruments Corporation, Holtsville, NY, USA). The 5 g/L suspensions of OgCN or MWCNT were prepared in 0.01 M KCl aqueous solution and the pH was in a range from 2 to 10.

2.3. Column Experiments

The aqueous suspension of OgCN, MWCNT, or graphite was prepared by mixing 500 mg of OgCN in 1 L of DI water (Aquapuri 5-Super Water Purification System, Youngin Chromass, Anyang, Republic of Korea), and sonicated for 60 min to avoid aggregation. The pH of the suspension was adjusted to 7.0 ± 0.2 with 0.1 M HCl and 0.1 M NaOH.

A glass column of 25 mm inner diameter and 145 mm length, equipped with two end plates with stainless steel screens, was filled with the ISO sands. The packing densities were 1.43 and 1.5 g/cm^2, the pore volumes were 23 and 24 mL, and the porosities were 0.38 and 0.44 when the column was filled with sands of 0.25–0.6 mm and 0.6–1.0 mm, respectively. The tracer breakthrough test was carried out using 1 M of KCl (Daejung Chemicals, Siheung, Republic of Korea) solution at a flow rate of 5 mL/min to estimate the longitudinal dispersity [22]. The concentration of KCl was determined with a conductivity meter (LabQuest 2, Vernier Software & Technology LLC, Beaverton, OR, USA).

The transport of OgCN was investigated via the pulse injection method. The sand-filled column was flushed with 40 pore volumes (PVs) of the DI water. Then, 4 PVs of the OgCN suspension were injected into the saturated column for 22 min. It was quickly switched into DI water, and the flow was maintained until no OgCN was detected. The suspension and the DI water were injected using a peristaltic pump (LeadFluid-BT301L, Baoding Lead Fluid Technology Co., Ltd., Baoding, China), at a constant flow rate of 5 mL/min.

The effluent from the column was collected at predetermined intervals. The concentration of the OgCN and graphite of the samples was measured using a UV-Vis spectrophotometer (UVmini-1240, Shimadzu Corporation, Kyoto, Japan) at a wavelength of 500 nm [23], while that of MWCNT was determined at 400 nm [22].

2.4. Modeling

The results of transport experiments, i.e., the concentration of OgCN or MWCNT in the effluents of the columns at a predetermined time, were analyzed using the HYDRUS 1D software package. HYDRUS 1D is based on the advection–dispersion equation (ADE) via breakthrough curves (BTCs) of OgCN or MWCNT at different conditions to model transport and retention in the column [24]. The governing equations in this simulation are provided in Equations (1)–(3) [25]:

$$\theta \frac{\partial C}{\partial t} = \theta D \frac{\partial^2 C}{\partial x^2} - q \frac{\partial C}{\partial x} - \rho \frac{\partial S}{\partial t} \quad (1)$$

$$\rho \frac{\partial S}{\partial t} = \theta k_a \Psi C - k_d \rho S \quad (2)$$

$$\Psi = \left(1 - \frac{S}{S_{max}}\right)\left(\frac{d_c + x}{d_c}\right)^{-\beta} \quad (3)$$

where C is the OgCN concentration in the influent (mg L^{-1}); S is the solid phase OgCN concentration trapped in the media (mg g^{-1}); t is the time passed (min); D is the dispersion coefficient (cm min^{-1}); x is the travel distance (cm); θ is the porosity; ρ is the bulk density of sand (g cm^{-3}); q is the Darcy velocity (cm min^{-1}); S_{max} is the maximum retention of OgCN concentration on sand (mg g^{-1}); k_a is the first-order attachment coefficient (min^{-1}); k_d is the first-order detachment coefficient (min^{-1}); d_c is the medium grain size (cm); Ψ is the dimensionless function; and β is an empirical factor (with 0.43 as an ideal value) [24].

3. Results and Discussion

3.1. Comparisons of OgCN and MWCNT

3.1.1. Transport

The transports of OgCN and MWCNT were compared first, to investigate the differences between OgCN and MWCNT in relation to their properties. Figure 1 shows that the transport of OgCN was much better than that of MWCNT. Their transport recovery percentages were 76% and 18%, respectively. The maximum retention (S_{max}) of OgCN was higher (3.3527 mg g^{-1}) than that of MWCNT (2.6913 mg g^{-1}), and the k_a of OgCN (0.1514 min^{-1}) was around 31% of that of MWCNT (0.4886 min^{-1}). However, the k_d of OgCN (0.0052 min^{-1}) was 4.7 times higher than that of MWCNT (0.0011 min^{-1}), suggesting that the better transport of OgCN, compared with MWCNT, was more attributable to its superior detachment rather than a decreased attachment. In addition, it was found in the experiments that MWCNT was readily aggregated into larger particles when it was pumped out from the tank of the suspension, which was mixed for the whole of the period of experiments; in other words, when the mixing was stopped. This result is probably because of the intrinsically high hydrophobicity, which caused the MWCNT to mostly accumulate near the inlet of the column.

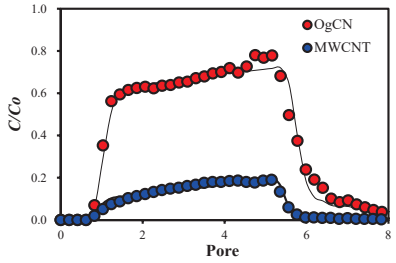

Figure 1. Experimental and modeling breakthrough curves of OgCN and MWCNT. [OgCN] = [MWCNT] = 50 mg L^{-1}, flow rate = 5 mL min^{-1}, pH = 7 ± 0.2, grain size = 0.6–1.0 mm.

3.1.2. Characteristics

The superior transport of OgCN relative to MWCNT was investigated further with respect to their properties. The FTIR spectra of OgCN and MWCNT showed common bands at ~3430, ~2917/2849, and ~1623 cm^{-1}, which can be assigned to the stretching vibrations of N–H/O–H, C–H, and aromatic C=C bonds, respectively. However, more bands were found for OgCN at 1418, 1318, and 1255 cm^{-1} representing C=O, C–N, and C–O in CN heterocycles, respectively [21,26]. In addition, a clear band was found at 810 cm^{-1}, which corresponds to the triazine units of gCNs [21] (Figure 2A).

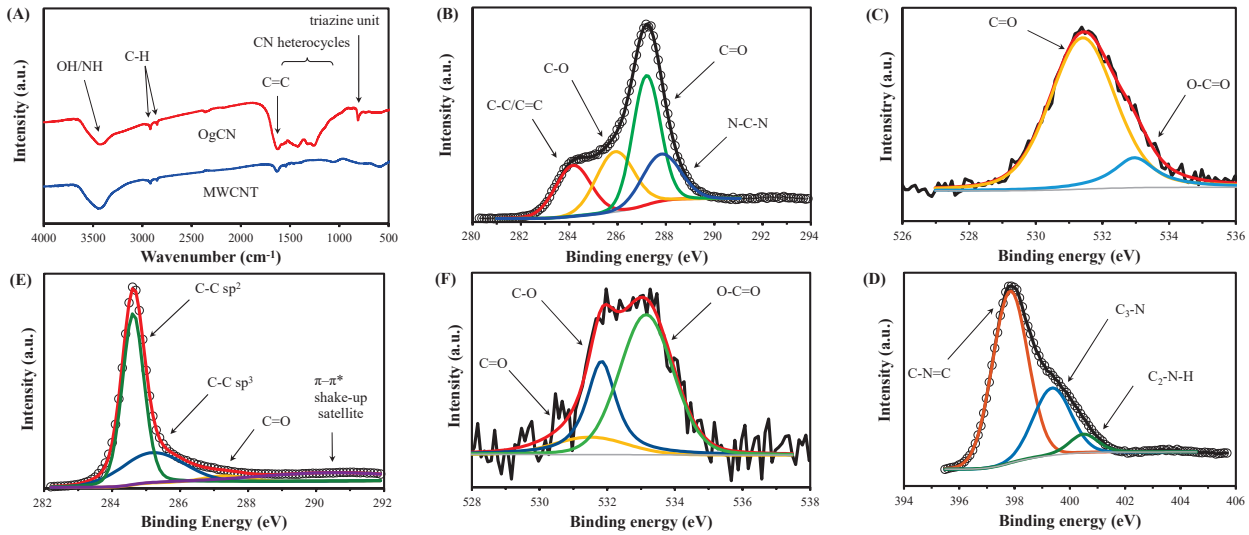

Figure 2. Results of (**A**) FTIR spectroscopy of OgCN and MWCNT; (**B**) C1s, (**C**) O1s, and (**D**) N1s XPS of OgCN; and (**E**) C1s and (**F**) O1s XPS of MWCNT.

The atomic fractions of C, N, and O were 47.2%, 49.06%, and 3.74%, respectively, for OgCN, while they were 98.89%, 0.26%, and 0.85%, respectively for MWCNT, demonstrating a CN structure and the successful doping of O in OgCN and the high purity of MWCNT, respectively. The (O + N)/C of OgCN (1.12) was much higher than that of MWCNT (0.01), indicating a greater hydrophilicity of OgCN than MWCNT. The high-resolution XPS spectra are presented in Figure 2B–F. The C1s, O1s, and N1s spectra were deconvoluted into characteristic peaks using XPS peak 4.1 software (Table 1) [27]. The C1s XPS spectrum of OgCN showed the peaks of graphitic C–C/C=C, C–O, C=O, and N–C–N at 284.2, 285.9, 287.2, and 287.8 eV, respectively, as assigned in previous works related to gCNs [28,29]. On the other hand, in the C1s XPS spectrum of MWCNT, the peaks of sp^2–C and sp^3–C, at 284.6 and 285.2 eV, respectively [28,29], were clearly separated, and the peaks of C–O and N–C–N were absent. The C=O peak was dominant in the O1s XPS spectrum of OgCN, while MWCNT's O1s XPS spectrum showed low-intensity peaks of C=O, C–O, and O–C=O [28]. The N1s spectrum of OgCN consisted of peaks corresponding to C–N=C, C_3–N, and C_2–N–H, at 397.8, 399.4, and 400.5 eV, respectively, as also reported in previous works about CNs [28,29].

Table 1. XPS results of OgCN and MWCNT.

		C1s							O1s			N1s		
		C–C/ C=C	C–C, sp^2	C–C sp^3	C–O	C=O	N–C–N	Π–Π* Shake-up Satellite	C=O	C–O	O–C=O	C–N=C	C_3–N	C_2–N–H
OgCN	Position (eV)	284.2			285.9	287.2	287.8		531.4		533.0	397.8	399.4	400.5
	Fraction (%)	9.2			11.2	17.9	8.8		3.2		0.6	32.7	13.3	3.1
	FWHM (eV)	1.7			1.9	1.3	1.9		2.3		1.5	1.5	1.6	1.2
MWCNT	Position (eV)		284.6	285.2		287.3		290.5	531.5	531.8	533.2	-	-	-
	Fraction (%)		53.3	25.3		3.3		17.0	0.1	0.3	0.5			
	FWHM (eV)		0.8	2.2		1.5		5.1	2.5	1.0	1.9	-	-	-

The XRD patterns of OgCN and MWCNT showed common peaks in the (100) plane for in-plane graphitic structures (13.4°) and in the (002) plane for inter-layer stacking [21] (Figure 3A). However, the diffraction angle of OgCN (27.6°) was higher than that of MWCNT (26.5°), indicating that the interlayer stacking was more severe in OgCN than in MWCNT [30]. This suggests that OgCN has a better tribological property, i.e., higher wear resistance and lower friction, than MWCNT, which would facilitate easier transport through the pores of a medium with less resistance [31].

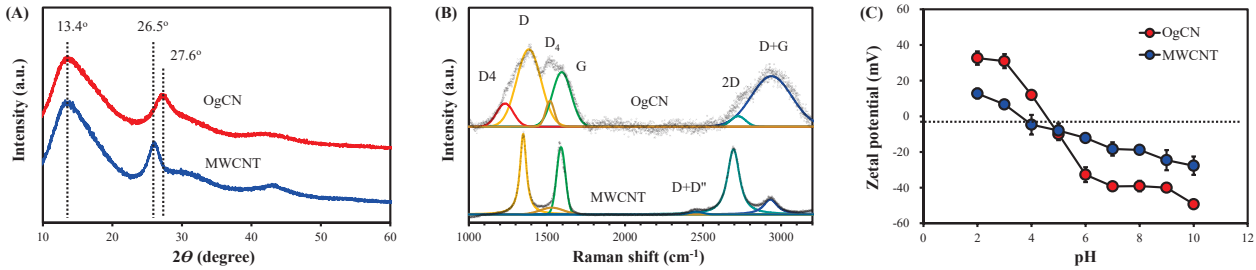

Figure 3. The (**A**) XRD patterns, (**B**) Raman spectra, and (**C**) zeta potential of OgCN and MWCNT.

The D4–, D–, D_4–, G–, 2D–, and D + G bands were found in the Raman spectrum of OgCN at 1232, 1384, 1519, 1595, 2724, and 2938 cm^{-1}, respectively (Figure 3B) (Table 2). The D4–band represents the disordered graphitic lattice, ionic impurities, and polyenes, while D–, D_4–, G–, 2D–, and D + G bands are associated with disordered structures such as defects and edges, amorphous carbon, ideal lattice of graphitic structures, single graphene-like layers, and a combination of the D and G bands, respectively [32,33]. The D4–band was not found, while a small D + D″–band was found at 2458 cm^{-1} in the Raman spectrum of MWCNT, which is assigned to the combination of the D–band and the D″–band representing amorphous carbon. On the other hand, the ratio of the intensity of the D–band to the G–band (I_D/I_G) represents the relative abundance of defects in graphitic structures, while the ratio of the intensity of the 2D–band to the G–band (I_{2D}/I_G) is indicative of the relative abundance of single-layer graphene and is inversely proportional to the degree of stacking of graphitic layers [32]. It was shown that I_D/I_G was higher for OgCN (1.83) than for MWCNT (1.81), while the I_{2D}/I_G was greatly larger for MWCNT than for OgCN. The results show that, compared with that in MWCNT, the graphitic structure in OgCN is characterized by more defects, either structural or by impurity, more amorphous structures, less ideal graphitic planes, less single-layer graphene-like structures, and a much greater degree of stacking, which is also suggested in XRD patterns (Figure 3A).

Table 2. Raman spectroscopy results of OgCN and MWCNT.

		D4	D	D_4	G	D + D″	2D	D + G	I_D/I_G	I_{2D}/I_G
OgCN	Center (cm^{-1})	1232	1384	1519	1595		2724	2938	1.83	0.15
	Area (%)	6.8	32.8	4.1	17.9		2.8	35.6		
	FWHM (cm^{-1})	127.2	182.9	65.8	141.4		113.1	304.1		
MWCNT	Center (cm^{-1})		1348	1531	1590	2458	2695	2932	1.31	1.89
	Area (%)		26.0	5.3	19.8	1.2	37.5	10.2		
	FWHM (cm^{-1})		48.9	175.7	64.9	94.4	91.6	106.8		

The zeta potential of OgCN and MWCNT are provided in Figure 3C. The points of zero charge (pH_{pzc}) were around 3.6 and 4.6 for MWCNT and OgCN, respectively. The absolute values of zeta potential were higher for OgCN than for MWCNT, at pHs of 2–4 and >5. This indicates that OgCN contains more acidic and/or basic functional groups than MWCNT [34]. This is also suggested by the FTIR spectra and XPS spectra, which show that OgCN was more abundant in O-, N-, and C-containing groups such as C=O, C–N, and C–O, than MWCNT (Figure 2).

Collectively, OgCN was less crystalline, more stacked, and more negatively charged at the pH of this study (7.0), richer in O- and/or N-containing functional groups, and more abundant in structural defects, than MWCNT. These properties are beneficial for transport in porous media, providing more charges and hydrophilicity. It was reported that a modified MWCNT, enriched with O-containing functional groups such as carboxylic groups via refluxing with HNO_3, showed enhanced transport relative to pristine MWCNT [35]. The enhanced transport of a material achieved by enriching functional groups was also demonstrated for single-wall CNTs (SWCNTs). The transport in quartz sand columns was better for humic-acid-modified SWCNTs than for oxidized SWCNTs because of more abundant functional groups, which provide more negative charges [36].

3.2. Transport of OgCN under Various Conditions

The transport of OgCN was investigated under varying OgCN concentrations, medium grain sizes, and IS. All results were analyzed using HYDRUS-1D (Equations (1)–(3)), which provided good fits to the experimental results, except for when IS was extremely high (10 mM KCl). The calculated parameters for each condition are presented in Table 3, and the results are discussed separately thereafter.

Table 3. Experimental conditions and parameters of HYDRUS-1D.

	Concentration (mg L^{-1})	**Grain Size (mm)**	**IS (mM KCl)**	**k_a (min^{-1})**	**k_d (min^{-1})**	**S_{max} (mg g^{-1})**	**r^2**
OgCN	10	0.25–0.6	0	0.1831	0.0029	2.76	0.950
	50	0.25–0.6	0	0.1920	0.0086	3.73	0.954
	100	0.25–0.6	0	0.3468	0.0033	4.30	0.916
	10	0.6–1.0	0	0.1850	0.0023	2.56	0.948
	50	0.6–1.0	0	0.1514	0.0052	3.35	0.973
	100	0.6–1.0	0	0.0936	0.0115	3.57	0.981
	50	0.6–1.0	2	0.2458	0.0001	3.81	0.933
	50	0.6–1.0	5	0.4160	0.0017	4.56	0.927
	50	0.6–1.0	10	0.6190	0.0005	5.74	0.885
MWCNT	50	0.6–1.0	0	0.4876	0.0023	2.69	0.975
	50	0.6–1.0	10	0.4886	0.0011	3.43	0.963

3.2.1. Effects of OgCN Concentration and the Grain Size of the Medium

Figure 4 shows the breakthrough curves of OgCN with respect to the passed pore volume at different OgCN concentrations and the grain size of the packed quartz sand. The k_a, k_d, and S_{max} are presented with respect to the OgCN concentrations in Figure 5.

The S_{max} increased with increasing OgCN concentration for both 0.25–0.6 and 0.6–1.0 mm sand, indicating that the retention is significantly affected by the influent amount. However, the increase in S_{max} was not as significant as the increase in OgCN concentration. The S_{max} was increased 1.56 (2.76 to 4.30 mg/g) and 1.40 (2.56 to 3.57 mg/g) times for the 0.25–0.6 mm and 0.6–1.0 mm sand columns, respectively, when the OgCN concentration was increased 10 times, i.e., from 10 mg/L to 100 mg/L. This suggests that not only the attachment, but also the detachment played an important role in the transport of OgCN, and that increased injection of OgCN is not necessarily followed by greater retention.

The k_a was decreased from 0.1850 to 0.0936 min^{-1}, while k_d was increased from 0.0023 to 0.0115 min^{-1}, as the OgCN concentration was increased in 0.6–1.0 mm sand, indicating that some of the OgCN retained in the quartz sand was detached. However, it is also shown that k_a and k_d were at their highest when OgCN concentrations were 100 and 50 mg/L, respectively, in 0.25–0.6 mm sand, having a lower porosity (0.38) than 0.6–1.0 mm sand (0.44). The different attachment and detachment values of OgCN indicate that they were significantly affected by the porosity, pore size, and factors such as the uniformity and size of the media, as recently revealed [37]. In addition, it is speculated that the retained

OgCN itself may form an unstable permeable network with varying holding capacity of particles [38].

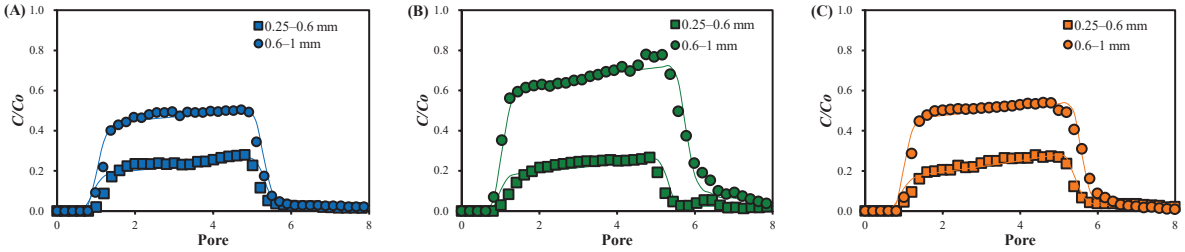

Figure 4. Experimental results and modeling breakthrough curves of the transport of OgCN of different concentrations in the column filled with quartz sands of different grain sizes: (**A**) 10 mg L^{-1}, (**B**) 50 mg L^{-1}, and (**C**) 100 mg L^{-1}. Flow rate = 5 mL min^{-1}, pH = 7 ± 0.2.

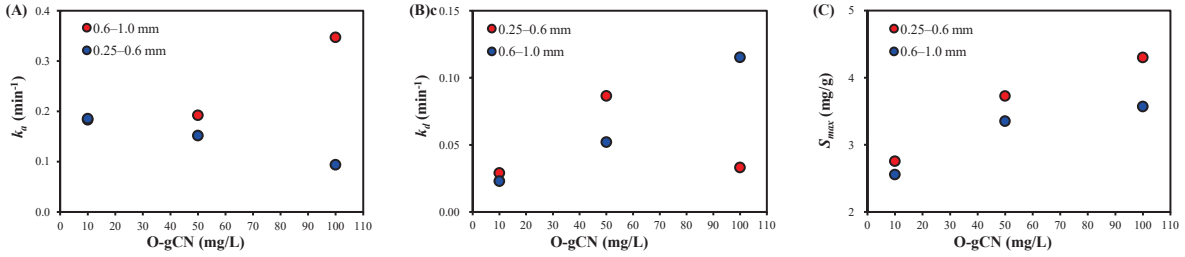

Figure 5. The correlations of OgCN concentration with (**A**) k_a, (**B**) k_d, and (**C**) S_{max} for 0.25–0.6 mm and 0.6–1.0 mm sand.

The S_{max} was similar for both sizes of sand when the OgCN concentration was 10 and 50 mg/L, with values of 2.56–2.76 and 3.35–3.73 mg/L, respectively, but it was higher in 0.25–0.6 mm sand (4.30 mg/g) than in 0.6–1.0 mm sand (3.57 mg/g), at 100 mg/L. This suggests that the attachment was improved while the detachment was suppressed in a medium of smaller pores above a certain input concentration of OgCN, i.e., 100 mg/L.

3.2.2. Effect of Ionic Strength

The breakthrough curves of OgCN at different IS are provided in Figure 6A, with the simulated curves, in relation to the volume of the O-gCN suspension passed through the column (V) divided by the pore volume of the column (V_0). The transport of OgCN was decreased as the IS was increased to 10 mM KCl. The parameters representing attachment (k_a) and retention (S_{max}) were increased, while the indicator of detachment (k_d) was decreased. The k_a and S_{max} were linearly correlated with IS (the concentration of KCl) with correlation coefficients (r^2) of 0.9917 and 0.9818, respectively. This strongly suggests that IS was directly correlated with the attachment and retention of OgCN in the medium in this study, i.e., quartz sand. On the other hand, the k_d was 0.0052 min^{-1} when no KCl was added, but was decreased greatly to 0.0001–0.0017 min^{-1} with 2–10 mM KCl. This indicates that the detachment of OgCN would be decreased dramatically under a low IS. Therefore, the increase in S_{max} with increasing IS was attributable to both enhanced attachment and suppressed detachment.

The enhanced attachment and suppressed detachment observed in the OgCN particles are associated with enhanced aggregation of OgCN particles and increased aggregate size. It was found that the zeta potential of OgCN was not notably affected at pHs of 2–5; however, it decreased significantly as the IS was increased at pHs of 6–7, where the experiments in this study were carried out (Figure 6B). The zeta potential was −39.28 ± 1.54 and −21.27 ± 6.58 mV when KCl concentrations were 0 (zero) and 10 mM, respectively. In addition, it was found via the PSD analysis of the aggregated OgCN particles in the suspensions at various IS, i.e., KCl concentration, that the average hydrodynamic diameter

of the OgCN increased gradually from 1484.7 ± 127.4 to 2035.0 ± 209.1 μm as the KCl concentration increased from 0 (zero) to 10 mM (Figure 6C). This is attributable to the compression of the electrical double layer on the surface of OgCN and the charge neutralization via the adsorption of ions with counter charge, which reduces the repulsion between OgCN particles [39,40], leading to increased retention of OgCN particles on the media as well as the aggregation of OgCN. The results in Figure 6 are compatible with Derjaguin–Landau–Verwey–Overbeek (DLVO) theory explanations, which proposed that electrostatic interactions played a detrimental role in regulating the transport of OgCN via controlling the colloidal stability and aggregation of OgCN [39,40].

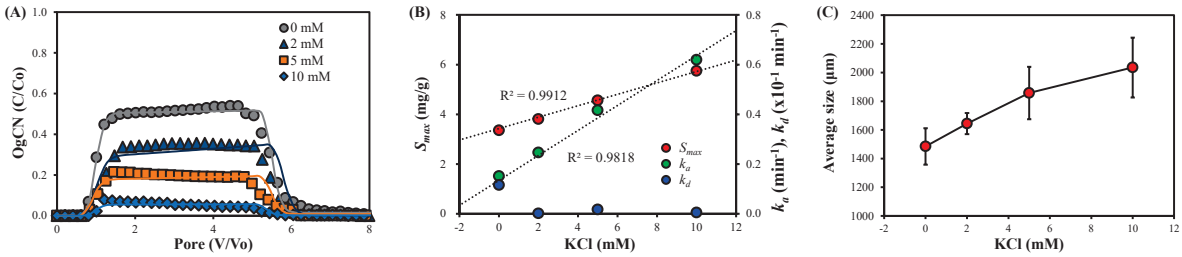

Figure 6. (**A**) Experimental and modeled breakthrough curves of OgCN with various IS and (**B**) the correlations of the parameters of the HYDRUS–1D model with IS. The flow rate was 5 mL min^{-1}, [OgCN] = 50 mg L^{-1}, pH = 7 ± 0.2. (**C**) The size of the OgCN aggregates with respect to IS (KCl concentration).

On the other hand, non-DLVO interactions, such as hydrogen bonding, would contribute to the results in Figure 6A [41]. It was reported that hydrogen bonding between the nitrogen lone pair electrons in gCN and Si-OH on quartz sand was promoted at high ISs. In addition, the deposited gCN provides new adsorption sites of gCN introduced later, via π–π conjugation [42]. It was also reported that the Debye length of gCN approaches the length of hydrogen bonds, i.e., 0.26–0.33 nm, with increasing IS, thus facilitating hydrogen bonding between quartz sand and gCN [42].

Meanwhile, the response of MWCNT to the raised IS was less sensitive compared with that of OgCN and differed from that of OgCN (Table 3). The S_{max} was increased from 2.69 to 3.43 mg/g when 10 mM KCl was used. However, the k_a did not show a notable change, while the k_d decreased greatly from 0.0023 to 0.0011 min^{-1}. These observations suggest that a decreased detachment, rather than increased attachment, was responsible for the enhanced retention of MWCNT, i.e., increased S_{max} is associated with increased IS.

4. Conclusions

In this study, OgCN and MWCNT were compared in terms of their characteristics and transport in porous media to identify the properties that would be beneficial for transport. Afterward, the transport of OgCN was investigated to evaluate the potential of its use in ISCO.

The transport of OgCN was much better than that of MWCNT, with less attachment and greater detachment. The OgCN contained more diverse and abundant O- and/or N-containing functional groups, such as graphitic C–C/C=C, C–O, C=O, N–C–N, C–N=C, and C_3–N, than MWCNT. In addition, OgCN contained more stacked, charged, disordered, defective, and amorphous graphitic structures than MWCNT. The transport of OgCN was well described using a 1-D ADR model (HYDRUS-1D), the parameters of which are provided. The S_{max} increased with increasing OgCN concentration, but the increase was not as significant as the increase in OgCN, and k_a and k_d were not always clearly dependent on the OgCN concentration and grain size of sand. These indicate that OgCN transport was influenced by a combination of attachment, detachment, and pore size. However, IS has clear and significant effects on transport via the reduction in zeta potential and the

associated increase in the size of OgCN aggregates. MWCNT showed similar responses to raised IS, but they were not as sensitive as OgCN.

The results of this study contribute substantially to efforts to prepare more readily transportable materials and to establish proper strategies for the subsurface injection of materials for ISCO.

Author Contributions: Data curation, D.-G.K.; analysis, D.-G.K. and T.-T.N.; funding acquisition, S.-O.K.; investigation, D.-G.K. and T.-T.N.; methodology, D.-G.K. and T.-T.N.; project administration, S.-O.K.; writing—original draft, D.-G.K. and T.-T.N.; and writing—review and editing, D.-G.K. and S.-O.K. All authors have read and agreed to the published version of the manuscript.

Funding: This work was supported by a National Research Foundation of Korea (NRF) grant funded by the Korean government (MSIT) (No. 2022R1A2B5B02001584).

Data Availability Statement: The data presented in this study are available on request from the corresponding author.

Conflicts of Interest: The authors declare no conflict of interest.

References

1. Yan, H.; Lai, C.; Wang, D.; Liu, S.; Li, X.; Zhou, X.; Yi, H.; Li, B.; Zhang, M.; Li, L. In Situ Chemical Oxidation: Peroxide or Persulfate Coupled with Membrane Technology for Wastewater Treatment. *J. Mater. Chem. A Mater.* **2021**, *9*, 11944–11960. [CrossRef]
2. Calenciuc, C.; Fdez-Sanromán, A.; Lama, G.; Annamalai, S.; Sanromán, A.; Pazos, M. Recent Developments in Advanced Oxidation Processes for Organics-Polluted Soil Reclamation. *Catalysts* **2022**, *12*, 64. [CrossRef]
3. Devi, P.; Das, U.; Dalai, A.K. In-Situ Chemical Oxidation: Principle and Applications of Peroxide and Persulfate Treatments in Wastewater Systems. *Sci. Total Environ.* **2016**, *571*, 643–657. [CrossRef] [PubMed]
4. Matthaiou, V.; Oulego, P.; Frontistis, Z.; Collado, S.; Hela, D.; Konstantinou, I.K.; Diaz, M.; Mantzavinos, D. Valorization of Steel Slag towards a Fenton-like Catalyst for the Degradation of Paraben by Activated Persulfate. *Chem. Eng. J.* **2019**, *360*, 728–739. [CrossRef]
5. Arellano, M.; Sanroman, M.A.; Pazos, M. Electro-Assisted Activation of Peroxymonosulfate by Iron-Based Minerals for the Degradation of 1-Butyl-1-Methylpyrrolidinium Chloride. *Sep. Purif. Technol.* **2019**, *208*, 34–41. [CrossRef]
6. Xiao, S.; Cheng, M.; Zhong, H.; Liu, Z.; Liu, Y.; Yang, X.; Liang, Q. Iron-Mediated Activation of Persulfate and Peroxymonosulfate in Both Homogeneous and Heterogeneous Ways: A Review. *Chem. Eng. J.* **2020**, *384*, 123265. [CrossRef]
7. Wang, J.; Wang, S. Activation of Persulfate (PS) and Peroxymonosulfate (PMS) and Application for the Degradation of Emerging Contaminants. *Chem. Eng. J.* **2018**, *334*, 1502–1517. [CrossRef]
8. Li, L.; Huang, J.; Hu, X.; Zhang, S.; Dai, Q.; Chai, H.; Gu, L. Activation of Sodium Percarbonate by Vanadium for the Degradation of Aniline in Water: Mechanism and Identification of Reactive Species. *Chemosphere* **2019**, *215*, 647–656. [CrossRef]
9. Ribeiro, A.R.; Nunes, O.C.; Pereira, M.F.R.; Silva, A.M.T. An Overview on the Advanced Oxidation Processes Applied for the Treatment of Water Pollutants Defined in the Recently Launched Directive 2013/39/EU. *Environ. Int.* **2015**, *75*, 33–51. [CrossRef]
10. Thomas, N.; Dionysiou, D.D.; Pillai, S.C. Heterogeneous Fenton Catalysts: A Review of Recent Advances. *J. Hazard. Mater.* **2021**, *404*, 124082. [CrossRef]
11. Chatterjee, R.; Bhanja, P.; Bhaumik, A. The Design and Synthesis of Heterogeneous Catalysts for Environmental Applications. *Dalton Trans.* **2021**, *50*, 4765–4771. [CrossRef] [PubMed]
12. Zhao, Q.; Mao, Q.; Zhou, Y.; Wei, J.; Liu, X.; Yang, J.; Luo, L.; Zhang, J.; Chen, H.; Chen, H. Metal-Free Carbon Materials-Catalyzed Sulfate Radical-Based Advanced Oxidation Processes: A Review on Heterogeneous Catalysts and Applications. *Chemosphere* **2017**, *189*, 224–238. [CrossRef] [PubMed]
13. Oyekunle, D.T.; Zhou, X.; Shahzad, A.; Chen, Z. Review on Carbonaceous Materials as Persulfate Activators: Structure–Performance Relationship, Mechanism and Future Perspectives on Water Treatment. *J. Mater. Chem. A Mater.* **2021**, *9*, 8012–8050. [CrossRef]
14. Zhu, K.; Shen, Y.; Hou, J.; Gao, J.; He, D.; Huang, J.; He, H.; Lei, L.; Chen, W. One-Step Synthesis of Nitrogen and Sulfur Co-Doped Mesoporous Graphite-like Carbon Nanosheets as a Bifunctional Material for Tetracycline Removal via Adsorption and Catalytic Degradation Processes: Performance and Mechanism. *Chem. Eng. J.* **2021**, *412*, 128521. [CrossRef]
15. Zhang, P.; Tan, X.; Liu, S.; Liu, Y.; Zeng, G.; Ye, S.; Yin, Z.; Hu, X.; Liu, N. Catalytic Degradation of Estrogen by Persulfate Activated with Iron-Doped Graphitic Biochar: Process Variables Effects and Matrix Effects. *Chem. Eng. J.* **2019**, *378*, 122141. [CrossRef]
16. Lin, K.-Y.A.; Zhang, Z.-Y.; Wi-Afedzi, T. Sulfur-Doped Carbon Nitride as a Non-Metal Heterogeneous Catalyst for Sulfate Radical-Based Advanced Oxidation Processes in the Absence of Light Irradiation. *J. Water Proc. Eng.* **2018**, *24*, 83–89. [CrossRef]
17. Kohantorabi, M.; Moussavi, G.; Giannakis, S. A Review of the Innovations in Metal-and Carbon-Based Catalysts Explored for Heterogeneous Peroxymonosulfate (PMS) Activation, with Focus on Radical vs. Non-Radical Degradation Pathways of Organic Contaminants. *Chem. Eng. J.* **2021**, *411*, 127957. [CrossRef]
18. Gao, Y.; Zhu, Y.; Lyu, L.; Zeng, Q.; Xing, X.; Hu, C. Electronic Structure Modulation of Graphitic Carbon Nitride by Oxygen Doping for Enhanced Catalytic Degradation of Organic Pollutants through Peroxymonosulfate Activation. *Environ. Sci. Technol.* **2018**, *52*, 14371–14380. [CrossRef]

19. Nguyen, T.T.; Kim, D.G.; Ko, S.O. Changes in the Catalytic Activity of Oxygen-Doped Graphitic Carbon Nitride for the Repeated Degradation of Oxytetracycline. *Chemosphere* **2022**, *307*, 135870. [CrossRef]
20. Tang, R.; Ding, R.; Xie, X. Preparation of Oxygen-Doped Graphitic Carbon Nitride and Its Visible-Light Photocatalytic Performance on Bisphenol A Degradation. *Water Sci. Technol.* **2018**, *78*, 1023–1033. [CrossRef]
21. Qiu, P.; Xu, C.; Chen, H.; Jiang, F.; Wang, X.; Lu, R.; Zhang, X. One Step Synthesis of Oxygen Doped Porous Graphitic Carbon Nitride with Remarkable Improvement of Photo-Oxidation Activity: Role of Oxygen on Visible Light Photocatalytic Activity. *Appl. Catal. B* **2017**, *206*, 319–327. [CrossRef]
22. O'Carroll, D.M.; Liu, X.; Mattison, N.T.; Petersen, E.J. Impact of Diameter on Carbon Nanotube Transport in Sand. *J. Colloid Interf. Sci.* **2013**, *390*, 96–104. [CrossRef] [PubMed]
23. Wang, J.; Zhang, L.; Long, F.; Wang, W.; Gu, Y.; Mo, S.; Zou, Z.; Fu, Z. Solvent-Free Catalytic Synthesis and Optical Properties of Super-Hard Phase Ultrafine Carbon Nitride Nanowires with Abundant Surface Active Sites. *RSC Adv.* **2016**, *6*, 23272–23278. [CrossRef]
24. Šimůnek, J.; Van Genuchten, M.T.; Šejna, M. The HYDRUS Software Package for Simulating Two-and Three-Dimensional Movement of Water, Heat, and Multiple Solutes in Variably-Saturated Media. *Tech. Man. Version* **2006**, *1*, 241.
25. Fan, W.; Jiang, X.; Lu, Y.; Huo, M.; Lin, S.; Geng, Z. Effects of Surfactants on Graphene Oxide Nanoparticles Transport in Saturated Porous Media. *J. Environ. Sci.* **2015**, *35*, 12–19. [CrossRef]
26. Zhou, X.-L.; Liu, Z.-M.; Kiss, J.; Sloan, D.W.; White, J.M. Surface Chemistry of Chloroiodomethane, Coadsorbed with H and O, on Pt(111). *J. Am. Chem. Soc.* **1995**, *117*, 3565–3592. [CrossRef]
27. Smith, M.; Scudiero, L.; Espinal, J.; McEwen, J.-S.; Garcia-Perez, M. Improving the deconvolution and interpretation of XPS spectra from chars by ab initio calculations. *Carbon* **2016**, *110*, 155–171. [CrossRef]
28. Meng, Y.; Li, Z.; Tan, J.; Li, J.; Wu, J.; Zhang, T.; Wang, X. Oxygen-Doped Porous Graphitic Carbon Nitride in Photocatalytic Peroxymonosulfate Activation for Enhanced Carbamazepine Removal: Performance, Influence Factors and Mechanisms. *Chem. Eng. J.* **2022**, *429*, 130860. [CrossRef]
29. Song, X.; Li, X.; Zhang, X.; Wu, Y.; Ma, C.; Huo, P.; Yan, Y. Fabricating C and O Co-Doped Carbon Nitride with Intramolecular Donor-Acceptor Systems for Efficient Photoreduction of CO_2 to CO. *Appl. Catal. B* **2020**, *268*, 118736. [CrossRef]
30. Majdoub, M.; Anfar, Z.; Amedlous, A. Emerging Chemical Functionalization of G-C3N4: Covalent/Noncovalent Modifications and Applications. *ACS Nano* **2020**, *14*, 12390–12469. [CrossRef]
31. Çelik, A.; Özer, H.Ö.; Tüzemen, Ş.M.; Yıldız, M.; Kovacı, H. Synthesis, characterization and tribological properties of solid lubricant graphite films produced by PECVD. *Mater. Today Comm.* **2023**, *36*, 106506. [CrossRef]
32. Jaworski, S.; Wierzbicki, M.; Sawosz, E.; Jung, A.; Gielerak, G.; Biernat, J.; Jaremek, H.; Łojkowski, W.; Woźniak, B.; Wojnarowicz, J. Graphene Oxide-Based Nanocomposites Decorated with Silver Nanoparticles as an Antibacterial Agent. *Nanoscale Res. Lett.* **2018**, *13*, 116. [CrossRef] [PubMed]
33. Sadezky, A.; Muckenhuber, H.; Grothe, H.; Niessner, R.; Pöschl, U. Raman Microspectroscopy of Soot and Related Carbonaceous Materials: Spectral Analysis and Structural Information. *Carbon NY* **2005**, *43*, 1731–1742. [CrossRef]
34. Kim, Y.; Choi, K.; Jung, J.; Park, S.; Kim, P.-G.; Park, J. Aquatic toxicity of acetaminophen, carbamazepine, cimetidine, diltiazem and six major sulfonamides, and their potential ecological risks in Korea. *Environ. Int.* **2007**, *33*, 370–375. [CrossRef] [PubMed]
35. Kasel, D.; Bradford, S.A.; Šimůnek, J.; Heggen, M.; Vereecken, H.; Klumpp, E. Transport and Retention of Multi-Walled Carbon Nanotubes in Saturated Porous Media: Effects of Input Concentration and Grain Size. *Water Res.* **2013**, *47*, 933–944. [CrossRef] [PubMed]
36. Tian, Y.; Gao, B.; Morales, V.L.; Wang, Y.; Wu, L. Effect of Surface Modification on Single-Walled Carbon Nanotube Retention and Transport in Saturated and Unsaturated Porous Media. *J. Hazard. Mater.* **2012**, *239*, 333–339. [CrossRef] [PubMed]
37. Hashemi, A.; Nguyen, C.; Loi, G.; Khazali, N.; Yang, Y.; Dang-Le, B.; Russell, T.; Bedrikovetsky, P. Colloidal Detachment in Porous Media: Stochastic Model and Upscaling. *Chem. Eng. J.* **2023**, *474*, 145436. [CrossRef]
38. Bradford, S.A.; Simunek, J.; Bettahar, M.; Van Genuchten, M.T.; Yates, S.R. Modeling Colloid Attachment, Straining, and Exclusion in Saturated Porous Media. *Environ. Sci. Technol.* **2003**, *37*, 2242–2250. [CrossRef]
39. Park, C.M.; Chu, K.H.; Heo, J.; Her, N.; Jang, M.; Son, A.; Yoon, Y. Environmental Behavior of Engineered Nanomaterials in Porous Media: A Review. *J. Hazard. Mater.* **2016**, *309*, 133–150. [CrossRef]
40. Sumanasekera, G.U.; Chen, G.; Takai, K.; Joly, J.; Kobayashi, N.; Enoki, T.; Eklund, P.C. Charge Transfer and Weak Chemisorption of Oxygen Molecules in Nanoporous Carbon Consisting of a Disordered Network of Nanographene Sheets. *J. Phys. Condens. Matter* **2010**, *22*, 334208. [CrossRef]
41. Zhang, M.; Bradford, S.A.; Klumpp, E.; Šimůnek, J.; Wang, S.; Wan, Q.; Jin, C.; Qiu, R. Significance of Non-DLVO Interactions on the Co-Transport of Functionalized Multiwalled Carbon Nanotubes and Soil Nanoparticles in Porous Media. *Environ. Sci. Technol.* **2022**, *56*, 10668–10680. [CrossRef] [PubMed]
42. Jiang, Y.; Guan, D.; Liu, Y.; Yin, X.; Zhou, S.; Zhang, G.; Wang, N.; Sun, H. The Transport of Graphitic Carbon Nitride in Saturated Porous Media: Effect of Hydrodynamic and Solution Chemistry. *Chemosphere* **2020**, *248*, 125973. [CrossRef] [PubMed]

Disclaimer/Publisher's Note: The statements, opinions and data contained in all publications are solely those of the individual author(s) and contributor(s) and not of MDPI and/or the editor(s). MDPI and/or the editor(s) disclaim responsibility for any injury to people or property resulting from any ideas, methods, instructions or products referred to in the content.

water

MDPI

Article

Health Risk Appraisal of Trace Elements in Groundwater in an Urban Area: A Case Study of Sichuan Basin, Southwest China

Zhongyou Yu [1,2], Rongwen Yao [3], Xun Huang [3] and Yuting Yan [3,*]

[1] Sichuan Hua Di Building Engineering Co., Ltd., Chengdu 610081, China
[2] Sichuan Province Engineering Technology Research Center of Geohazard Prevention, Chengdu 610081, China
[3] Yibin Research Institute, Southwest Jiaotong University, Yibin 644000, China
* Correspondence: ytyan2127@my.swjtu.edu.cn; Tel.: +86-18792530737

Abstract: Intense anthropogenic activities pose a serious threat to groundwater quality in urban areas. Assessing pollution levels and the health risks of trace elements within urban groundwater is crucial for protecting the groundwater environment. In this study, the heavy metal pollution index (HPI) and health risk assessment were conducted to analyze trace element pollution levels and the non-carcinogenic and carcinogenic risks of groundwater resources in Sichuan Basin, SW China, based on the hydrochemical results of 114 groundwater samples. The HPI results displayed that 14.92% of groundwater samples were contaminated, primarily attributed to anthropogenic influence. The health risk assessment indicated that children faced the highest non-carcinogenic risk while adults had the highest carcinogenic risk. The Monte Carlo simulation further enhanced the reliability of the health risk model. A sensitivity analysis indicated that Pb was the most sensitive element affecting both non-carcinogenic and carcinogenic risks. The achievements of this research would provide a basis for groundwater management in urban areas.

Keywords: health risk; uncertainty analysis; Sobol sensitivity analysis; heavy metal pollution; urban area

1. Introduction

Groundwater is regarded as one of the primary freshwater sources due to its wide distribution, safety, and clean properties [1,2]. Due to intense anthropogenic activities by increasing urbanization, groundwater quality is degrading worldwide [3]. Urban groundwater is often contaminated by industry and municipal sewage [4]. Heavy metals, such as Manganese (Mn), Copper (Cu), Zinc (Zn), and Lead (Pb), and toxic elements, such as Arsenic (As), are easily enriched in the groundwater of industrial areas, causing health diseases like poisoning, skin abnormalities, and cancer [5,6]. Hence, it is of great benefit to analyze the pollution level and health risks of contaminated groundwater in urban areas.

Trace elements are vital to human health in appropriate quantities but can be harmful to the body in excessive consumption [7]. Iron (Fe) is an important component of hemoglobin and is no danger to health [8]. Exposure to excessive Mn, Cu, Zn, As, and Pb contents will lead to serious health issues [9–13]. Ascertaining the quality of groundwater in terms of heavy metals is necessary for ensuring water security. The heavy metal pollution index (HPI) was usually used to calculate the collective pollution effect of heavy metals [14,15]. Nowadays, the health risk model proposed by the United States Environmental Protection Agency (USEPA) is a popular approach for health risk appraisal [16]. Increasing research has focused on assessing health risks caused by trace elements in groundwater [17–19]. Health risk evaluation is divided into non-carcinogenic risk and carcinogenic risk based on the toxicity of chemical elements. However, there is significant uncertainty due to large variations in age, weight, eating habits, and parameter selection among individuals and calculations. Ignoring uncertainty in health risk assessment will

lead to wrong results [3]. To solve this scientific problem, the Monte Carlo method was adopted to calculate uncertainty, making the risk model robust [20–22]. Monte Carlo simulation is a widely used method due to its flexibility and high efficiency. In addition, the sensitivity of health risk parameters was analyzed by the Sobol method [1,23,24]. This approach can deal with nonlinear data and provide a comprehensive analysis of global sensitivity [25].

The Sichuan Basin of southwestern China has flat terrain, fertile soil, and a large population. Research on the groundwater quality and health risks within the basin is of great significance to sustainable groundwater exploitation. However, existing studies mainly focused on nitrate pollution in the basin [26–29], and scarce studies focus on the contamination of trace elements. The objective of this research is to (1) clarify the pollution level and spatial distribution of trace elements; (2) evaluate the non-carcinogenic and carcinogenic risk for infants, children, and adults; and (3) analyze the uncertainty and sensitivity of the health risk model. The achievements of this study would make a vital contribution to groundwater management and protection in urban areas.

2. Materials and Methods

2.1. Study Area

The study area is situated in the northwest Sichuan basin, covering an area of 235.26 km^2 (Figure 1). In the study area. the annual average temperature is 16.43 °C and the annual average precipitation is 1485.1 mm. The topography of the study area is a valley, which is high on the northwest and southeast sides and low in the middle. The strata exposed in the study area include the Quaternary sediments and Jurassic to Cretaceous sandstone and mudstone. The aquifers consist of the Quaternary pore aquifer and Jurassic to Cretaceous pore and fissure aquifers. The groundwater level is shallow, with a depth of 5 to 20 m. Groundwater is recharged by atmospheric precipitation and discharged as springs in the local area. Agriculture is the primary industry of the study area, with rice fields covering 104 km^2. Residential areas, industrial parks, and other artificial surfaces are distributed, accounting for 16% of the total study area. Forests and grasslands are continuously distributed on both sides of the study area.

2.2. Sample Collection and Laboratory Testing

In the present study, a total of 114 groundwater samples were collected from 37 domestic wells in the study area in the wet, normal, and dry seasons of 2022. After 15 min of pumping wells, groundwater samples were bottled in pre-washed bottles. Meanwhile, the parameters of pH, total dissolved solids (TDS), and temperature were detected by a portable apparatus (WTW multi 3400i). The samples were finally measured by the laboratory of the Sichuan Bureau of Geology and Mineral Resources. Cation and anion contents were measured by ion chromatography (IC6100; Wayee, China). Each groundwater sample was tested three times to ensure accuracy. The precisions of laboratory testing for Mn, Fe, Cu, Zn, As, and Pb were 0.00012 mg/L, 0.00082 mg/L, 0.00008 mg/L, 0.00067 mg/L, 0.0003 mg/L, and 0.00009 mg/L. The charge balance was lower than 5%.

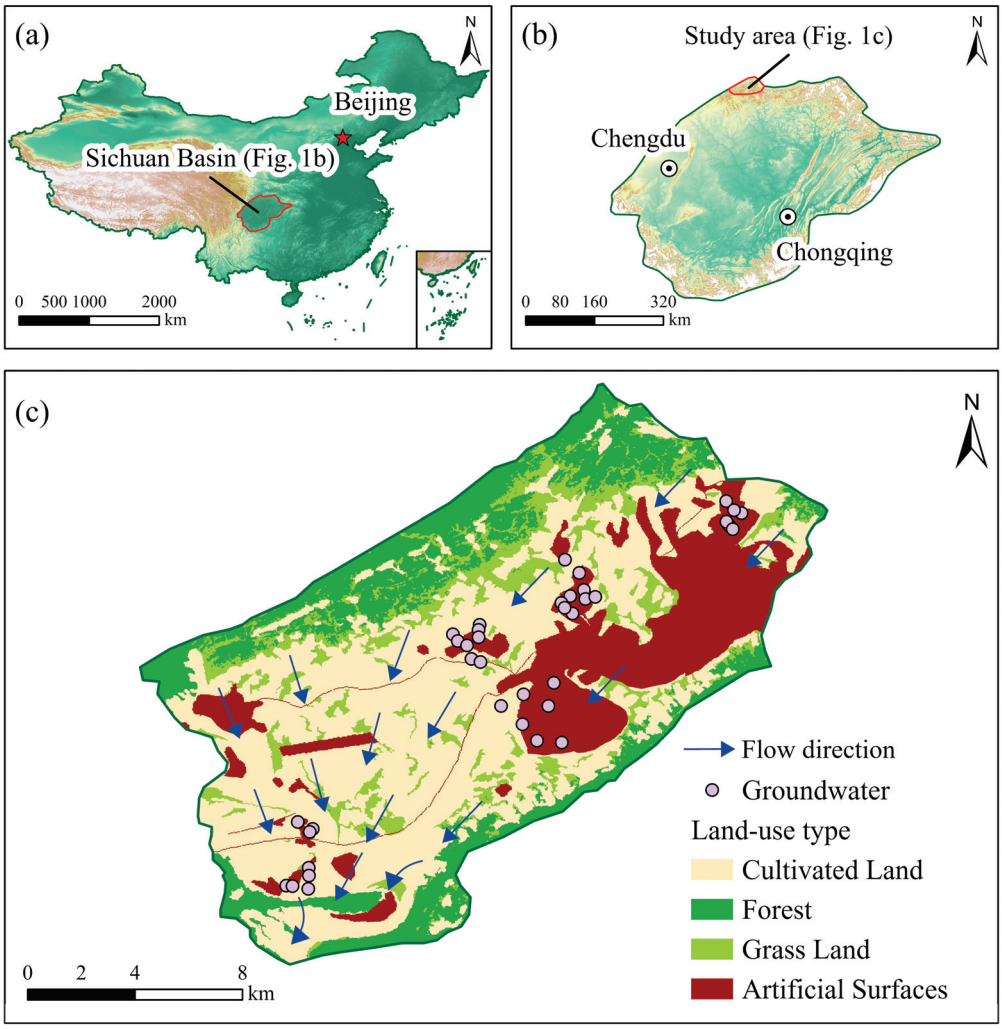

Figure 1. (**a**) The location of Sichuan Basin. (**b**) The position of study area in the Sichuan Basin. (**c**) The location of the study area with cover land-use types, including cultivated land, forest, grass land, artificial surfaces, and groundwater flow directions.

2.3. HPI

The heavy metal pollution index (*HPI*) was an effective method for evaluating heavy metal pollution [30]. The appraisal scores of the groundwater samples were calculated based on arithmetic weighted average value as Equation (1) [31]. The weight (W_i) of heavy metals is the inverse of the standard value S_i (Equation (2)). Class III in the Chinese standard [32] was determined to be S_i (Table 1). The quality level index (Q_i) is calculated from the measured concentration C_i and S_i (Equation (3)).

$$HPI = \frac{\sum_{i=1}^{n} W_i Q_i}{\sum_{i=1}^{n} W_i} \quad (1)$$

$$W_i = \frac{1}{S_i} \quad (2)$$

$$Q_i = \frac{C_i}{S_i} \times 100 \quad (3)$$

Table 1. The standard value, weight, and normalized weight of trace elements in the calculation of HPI.

Parameters	Unit	Standard Value	Weight	Normalized Weight
Mn	μg/L	100	0.01	0.087
Fe	μg/L	300	0.003333	0.029
Cu	μg/L	1000	0.001	0.009
Zn	μg/L	1000	0.001	0.009
Pb	μg/L	10	0.1	0.867

For the purpose of drinking, the samples with HPI values higher than 100 were considered to be polluted [33]. To carry out differentiated protection measures for groundwater, the HPI score was segmented into three grades: low (<15), medium (15–30), and high (>30) [30].

2.4. Health Risk Assessment

Heavy metals and toxic elements in groundwater can infiltrate the human body, causing harm to vital organs such as the brain, heart, and kidneys. A comprehensive model proposed by the USEPA has been applied to quantify human health risks [34]. The chronic daily intake (CDI) of trace elements for humans is determined by ion concentrations and various exposure parameters as Equation (4). The hazard quotient (HQ) is the risk caused by a single non-carcinogenic element (Mn, Cu, Zn, Pb, or As) (Equation (5)). The hazard index (HI) represents the total non-carcinogenic element (Equation (7)). The cancer risk (CR) resulting from lifetime exposure to Pb and As is calculated using Equation (6). Considering the physiological differences of various peoples, the population is categorized into three groups: infants (<6 months), children (6 months–17 years), and adults (>17 years) [35]. The exposure parameters for both the non-carcinogenic and carcinogenic models are presented in Tables 2 and 3.

$$\mathrm{CDI}_i = \frac{CW_i \times \mathrm{IR} \times \mathrm{EF} \times \mathrm{ED}}{\mathrm{BW} \times \mathrm{AT}} \tag{4}$$

$$\mathrm{HQ}_i = \frac{\mathrm{CDI}_i}{\mathrm{RfD}_i} \tag{5}$$

$$\mathrm{CR}_i = \mathrm{CDI}_i \times \mathrm{SF}_i \tag{6}$$

$$\mathrm{HI} = \mathrm{HQ}_{\mathrm{Mn}} + \mathrm{HQ}_{\mathrm{Cu}} + \mathrm{HQ}_{\mathrm{Zn}} + \mathrm{HQ}_{\mathrm{Pb}} + \mathrm{HQ}_{\mathrm{As}} \tag{7}$$

$$\mathrm{CR} = \mathrm{CR}_{\mathrm{As}} + \mathrm{CR}_{\mathrm{Pb}} \tag{8}$$

Table 2. The exposure parameters for infants, children, and adults.

Parameters	Definition	Units	Infants	Children	Adult
IR	Ingestion rate for water	L/day	0.65	1.5	2
EF	Exposure frequency for water	days/year	365	365	365
ED	Exposure duration for water	years	0.5	6	30
BW	Body weight	kg	6.94	25.9	65
AT non-cancer	Average time (ED × 365)	days	182.5	2190	10,950
AT cancer	Average time (365 × 70)	days	25,550	25,550	25,550

Table 3. The reference dose (RfD) of Mn, Cu, Zn, Pb, and As and the slope factor (SF) of Pb and As.

Parameter	Definition	Unit	Mn	Cu	Zn	Pb	As
RfD	Reference dose	mg/(kg·day)	0.06	1.6	0.06	0.002	0.0003
SF	Slope factor	kg·day/mg	–	–	–	0.055	1.5

According to the HI, groundwater samples were divided into 2 grades: suitable ($\leq$1) and not suitable (>1) for drinking water.

According to the CR, groundwater samples were divided into 5 grades: very suitable ($<10^{-6}$), suitable (1×10^{-6}–1×10^{-5}), should be considered as drinking water (1×10^{-5}–1×10^{-4}), safety measures should be taken (1×10^{-4}–1×10^{-3}), and not suitable ($>1 \times 10^{-3}$) for drinking water.

2.5. Monte Carlo Simulation

In traditional health risk assessment, hydrochemical data were gathered from a restricted number of sampling sites, which led to the uncertainty of the sampling process. In addition, exposure parameters were usually considered as fixed values, resulting in uncertainty in the parameter selection [1]. To address this uncertainty, the Monte Carlo approach was employed in the health risk model. In this study, the libraries of Numpy [36] and Scipy [37] in Python 3.10 were adopted to achieve Monte Carlo simulation. To assure precision, the simulation time was set to 10,000.

2.6. Sensitivity Analysis

Sobol's method, suggested by Sobol in 1993, was widely used to conduct the global sensitivity analysis [24]. This method is based on the variance decomposition methodology. The total variance was divided into the sum of the variance of a single parameter and the variance of multiple parameter interactions [38]. It has the ability to process nonlinear data. To implement Sobol's method, the SALib library in Python 3.10 was utilized [39].

3. Results

3.1. Statistical Results

The statistical results were presented in Table 4 and Figure 2, respectively. The pH exhibited a range of 6.81 to 8.63. The mean concentrations of trace elements, in descending order, were as follows: Mn (109.46 μg/L) > Fe (70.09 μg/L) > Zn (12.83 μg/L) > Cu (2.12 μg/L) > As (1.51 μg/L) > Pb (0.24 μg/L). Notably, 13.16% and 5.26% of groundwater samples exceeded the Chinese drinking water guidelines for Mn (n = 15) and Fe (n = 6), respectively. Furthermore, Mn and Fe exhibited high coefficients of variation (CV), suggesting that their concentrations were influenced by abnormal human activities or specific geological settings.

Table 4. Statistical results of pH and trace elements.

Parameters	Unit	Min	Max	Mean	Std.	CV (%)	Guideline for Drinking
pH	–	6.81	8.63	7.65	0.39	5.04	6.5–8.5
Mn	μg/L	0.13	2910.00	109.46	369.48	337.54	100
Fe	μg/L	0.82	1630.00	70.09	222.71	317.73	300
Cu	μg/L	0.08	26.10	2.12	3.21	151.27	1000
Zn	μg/L	0.67	220.00	12.83	23.46	182.78	1000
As	μg/L	0.30	8.90	1.51	2.18	144.44	10
Pb	μg/L	0.09	2.86	0.24	0.39	158.48	10

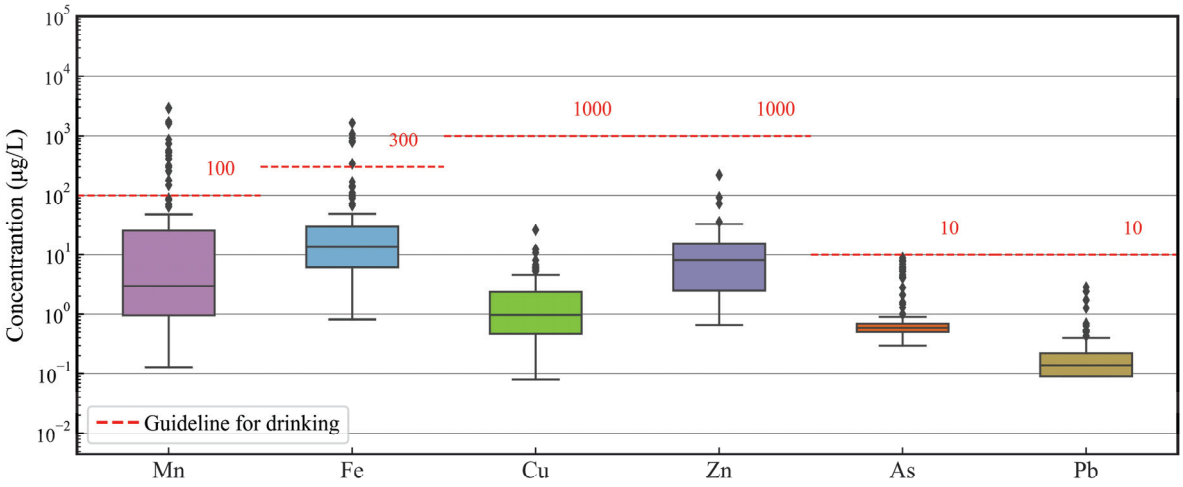

Figure 2. Box plot of trace elements concentrations with guidelines for drinking.

3.2. Distribution of Trace Elements

The Mn presented the highest concentration and CV value, which exceeded the Chinese limit of 100 μg/L. The samples with high Mn concentrations were situated in the northeastern part (Figure 3a), posing a significant potential risk to nearby residents. Following Mn, Fe concentrations exceeded the Chinese limit of 300 μg/L, respectively, ranked second in terms of concentration. Notably, high Fe concentrations were observed in the central and northeastern parts of the study area (Figure 3b).

The concentrations of Cu were all below the limit of 1000 μg/L. The relatively high values of Cu were located southeast of the study area (Figure 3c). Zn had minimal outliers (number = 4) and was slightly contaminated. The highest Zn content (220 μg/L) was distributed near the river (Figure 3d). The maximum As concentration was very close to the standard value. The distribution map of As presented that the samples situated near the city center had the highest concentrations (Figure 3e). Pb displayed the lowest concentration compared with other trace elements (Figure 3f). High Pb concentrations were distributed near the rivers.

The central and northeastern parts of the study area were mainly covered by artificial surfaces. The high levels of trace elements were distributed in the central and northeastern parts of the study area (Figure 3). This indicated that urban activities have led to an increase in the concentrations of chemical elements. For example, petrol contains lead, which can contaminate soil and groundwater. Industrial sewage increases the concentrations of heavy metals in groundwater.

High Mn concentrations harm the health status of the nervous system [9]. Exposure to excessive Cu content can affect cellular activities [10]. Exposure to high Zn concentrations will cause gastrointestinal disorders [11]. Long-term intake of arsenic will cause abnormal skin and can even cause skin cancer [12]. Excessive Pb will damage the central nervous system [13]. Therefore, knowing the pollution level and potential health risks of trace elements within groundwater is fundamental to developing pollution prevention policies and protecting human health.

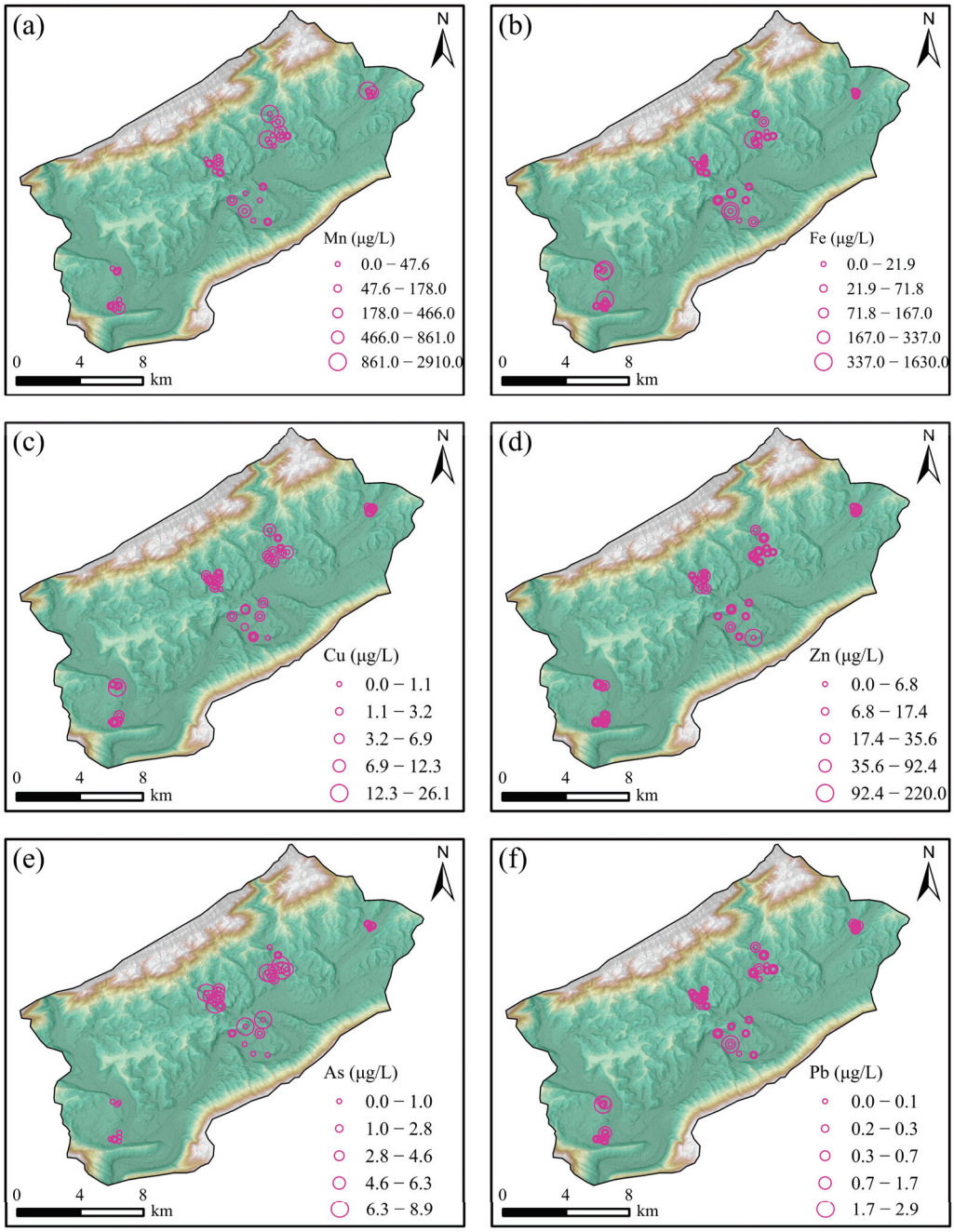

Figure 3. The distribution and concentration of trace elements in the study area. The spatial distribution of concentration for (**a**) Mn, (**b**) Fe, (**c**) Cu, (**d**) Zn, (**e**) As, and (**f**) Pb.

4. Discussion

4.1. Pollution Level

Compared with other trace elements, the weight and normalized weight of Pb were the highest in the HPI computation (Table 1). This is because Pb is a toxic chemical element. Even under low exposure levels, Pb would pose harmful effects on human health. The HPI values ranged from 0.80 to 253.49, with an average value of 12.30 (Figure 4a). A total of 85.69% of samples were categorized as low pollution, which was safe for humans to utilize and drink. A total of 5.26% of samples were medium pollution, which can be drunk after purification. A total of 9.65% of samples were high pollution, which was too seriously contaminated to be drunk by humans.

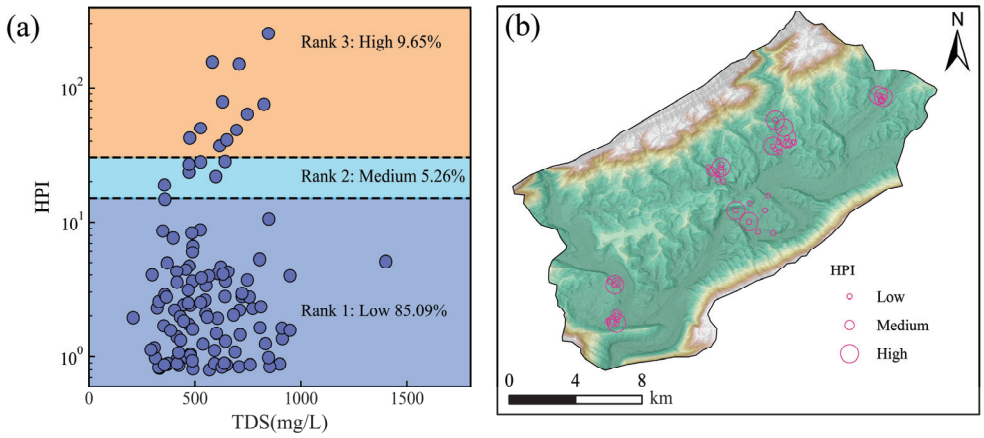

Figure 4. The heavy pollution index of trace elements in the study area. (**a**) HPI vs. TDS (**b**) Spatial distribution of the HPI values.

Most elevated pollution samples were distributed in the central and northeastern part of the study area (Figure 4b). Residual elevated pollution samples were situated southwest of the study area. The levels of heavy metal pollution in groundwater were closely related to the intensity of urban activities (Figure 1). More importantly, the groundwater flowed majorly from northeast to southwest (Figure 1). Therefore, the southwestern part is easily contaminated by heavily polluted groundwater in the central and northeastern parts. It is important to monitor groundwater in the central and northeastern parts.

4.2. Health Risk Evaluation

The ingestion of groundwater contaminated with trace elements poses significant threats to human health [40,41]. Elevated levels of Mn, Cu, Zn, As, and Pb can create non-carcinogenic risks, including central nervous effects, decreased blood enzymes, gastrointestinal system irritation, hyperpigmentation, keratosis, and possible vascular complications. Furthermore, exposure to As and Pb has been linked to the development of multiple internal organ cancers (respiratory system, liver, kidney, lung, and bladder). Therefore, this study conducted comprehensive assessments, encompassing both non-carcinogenic risk evaluation (for Mn, Cu, Zn, As, and Pb) and carcinogenic risk appraisal (specifically for As and Pb).

4.2.1. Non-Carcinogenic Risk

Generally, non-carcinogenic risks do not lead to cancer directly but are particularly capable of bringing toxicity to human health. The study identified significant distinctions in non-carcinogenic risks among their demographic groups (Figure 5a–c). On average, infants presented a greater health risk (0.66), adults exhibited the lowest health risk (0.41), and children fell in the middle (0.22). Additionally, the rate of exceedance (HI > 1) for infants, children, and adults was 15.79%, 5.26%, and 0%, respectively. These findings underscore the adverse effects of Mn, Cu, Zn, As, and Pb on both infants and children. Notably, infants presented the highest health risk based on both the average value and the rate of exceedance for the HI.

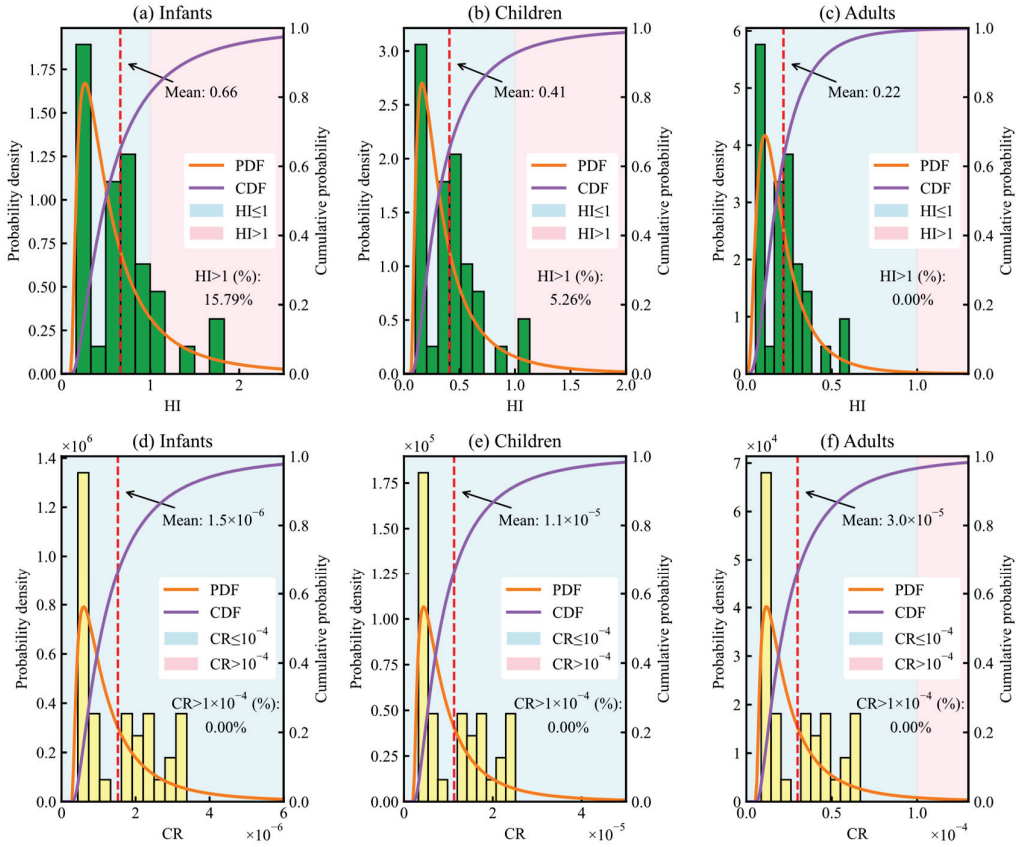

Figure 5. Cumulative permeability and probability density of HI and CR for infants, children, and adults. The PDF is defined as the probability density function. The CDF denotes the cumulative distribution function. (**a**) HI for infants, (**b**) HI for children, (**c**) HI for adults, (**d**) CR for infants, (**e**) CR for children, and (**f**) CR for adults.

It is well known that infants are lighter than children and adults in weight. Consequently, the enzyme metabolism ability in infants was extremely inadequate, leading to a diminished ability to process toxic substances effectively [27,42]. As a result, the infants had the worst HI values, which should be further examined. The areas that caused non-carcinogenic risks were mainly distributed in the central and northeastern parts. In particular, the city center posed more non-carcinogenic risks for infants. Hence, it is advisable to designate these areas as crucial monitoring targets.

4.2.2. Carcinogenic Risk

The CR of groundwater samples that were assessed for infants, children, and adults, were presented in Table 5 and Figure 5. For infants, the CR ranged from 4.4×10^{-7} to 3×10^{-6}, with an average value of 2×10^{-6}. Account for 47.37% of the samples had CR values below 10^{-6}, indicating a low risk. The remaining 52.63% fell within the range of 10^{-6}–10^{-5}. Therefore, the groundwater in the study area was considered safe for the infants, with a negligible cancer risk.

Table 5. The statistical results of HI and CR caused by hazardous substances for infants, children, and adults.

Parameter	Infants			Children			Adults		
	Min	Max	Mean	Min	Max	Mean	Min	Max	Mean
Mn	2.35×10^{-3}	1.52	0.171	1.45×10^{-3}	0.937	0.106	7.73×10^{-4}	0.498	5.61×10^{-2}
Cu	2.54×10^{-5}	5.22×10^{-4}	1.24×10^{-4}	1.57×10^{-5}	3.23×10^{-4}	7.69×10^{-5}	8.33×10^{-6}	1.72×10^{-4}	4.09×10^{-5}
Zn	7.19×10^{-3}	0.118	2.00×10^{-2}	4.45×10^{-3}	7.29×10^{-2}	1.24×10^{-2}	2.36×10^{-3}	3.87×10^{-2}	6.58×10^{-3}
As	0.135	1.05	0.47	8.37×10^{-2}	0.65	0.291	4.44×10^{-2}	0.345	0.155
Pb	4.21×10^{-3}	5.62×10^{-2}	1.15×10^{-2}	2.61×10^{-3}	3.47×10^{-2}	7.09×10^{-3}	1.38×10^{-3}	1.85×10^{-2}	3.77×10^{-3}
HI	0.16	1.83	0.66	0.10	1.13	0.41	0.05	0.6	0.22
As	4.35×10^{-7}	3.38×10^{-6}	1.51×10^{-6}	3.23×10^{-6}	2.51×10^{-5}	1.12×10^{-5}	8.57×10^{-6}	6.66×10^{-5}	2.98×10^{-5}
Pb	3.31×10^{-9}	4.42×10^{-8}	9.01×10^{-9}	2.46×10^{-8}	3.28×10^{-7}	6.69×10^{-8}	6.53×10^{-8}	8.7×10^{-7}	1.78×10^{-7}
CR	4.40×10^{-7}	3.00×10^{-6}	2.00×10^{-6}	3.26×10^{-6}	2.5×10^{-5}	1.1×10^{-5}	8.67×10^{-6}	6.7×10^{-5}	3×10^{-5}

For children, the range of the CR was 3.26×10^{-6}–2.5×10^{-5} with a mean value of 1.1×10^{-5}. 52.63% and 47.37% of possible exposure processes were classified as suitable to drink and categorized as "need caution", respectively. This suggests that approximately half of the samples, notably those located near the central part of the study area, warrant focus attention (Figure 6).

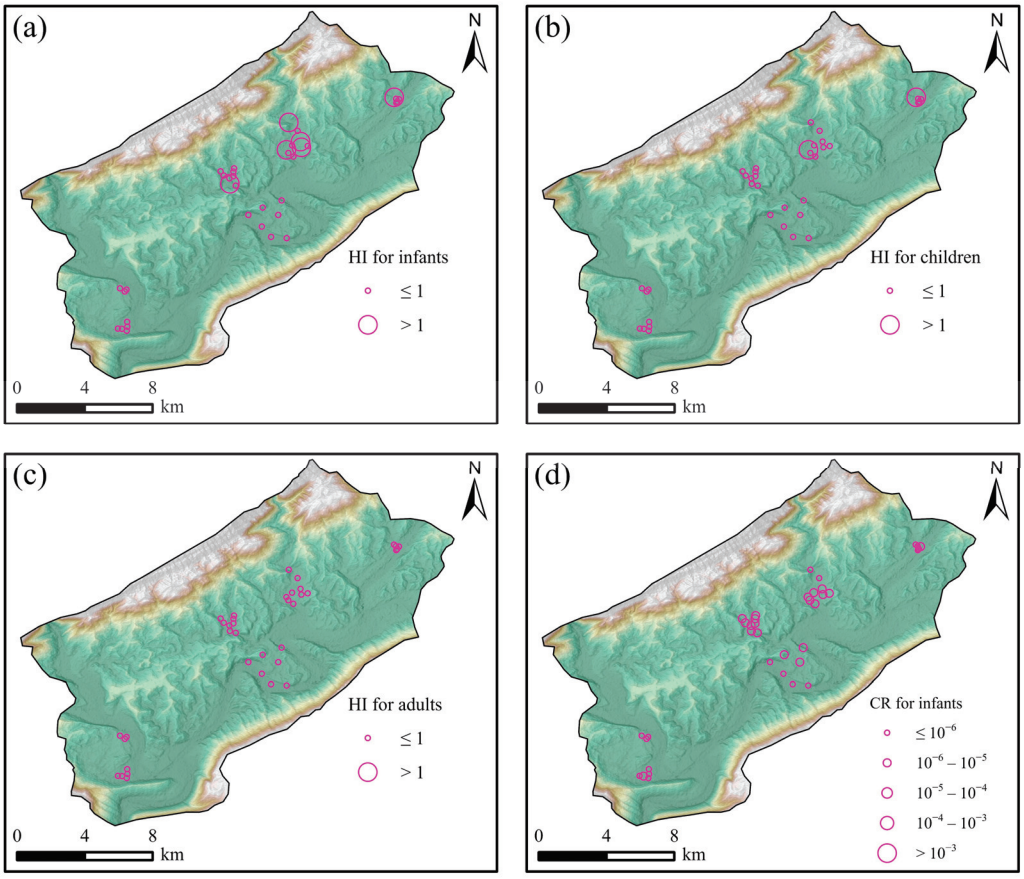

Figure 6. *Cont.*

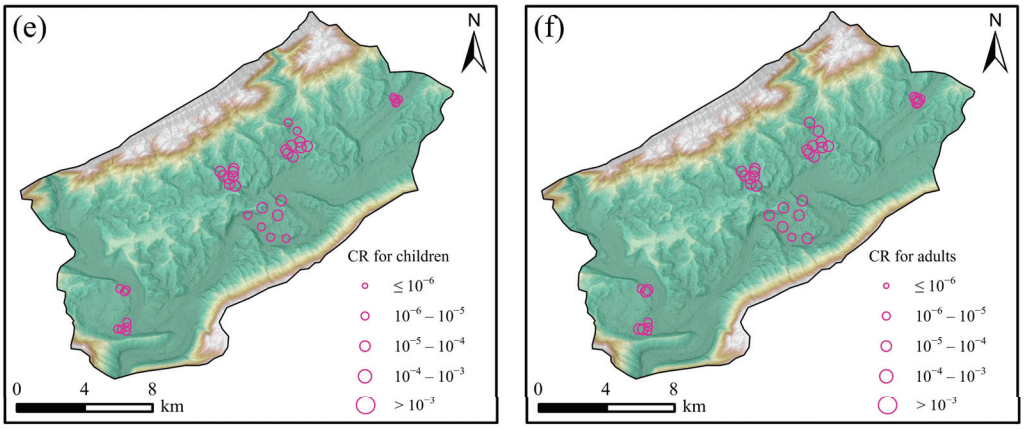

Figure 6. The distribution of HI and CR for infants, children, and adults in the study area. The distribution of (**a**) HI for infants, (**b**) HI for children, (**c**) HI for adults, (**d**) HI for infants, (**e**) CR for children, and (**f**) CR for adults.

For adults, the CR values ranged between 8.67×10^{-6} and 6.7×10^{-5}, with a mean value of 3×10^{-5}. Only 13.16% of samples were deemed suitable for drinking, while the remaining 86.74% of samples posed cancer risks, particularly those located near the central part (Figure 6). The automobile industry produces a lot of sewages containing Pb and As. The discharge of industrial sewages with Pb and As into groundwater may result in high Pb and As concentrations. The average order of CR for different age groups was adults (3×10^{-5}) > children (1.1×10^{-5}) > infants (1.5×10^{-6}). This order can be attributed to the long exposure duration of adults (ED = 30 years) to carcinogens compared to children (ED = 6 years) and infants (ED = 0.5 years).

4.3. Uncertainty Analysis

To assess the uncertainty associated with parameter selection and sampling in the process, Monte Carlo simulation was employed to simulate hazardous substances and their respective parameters using statistical parameters (Table 6). The distribution type of Mn, Cu, Zn, Pb, and As was examined through the K-S test in Python. Meanwhile, the distribution type of EF was referenced from a previous study [43].

Table 6. The distribution types and distribution parameters of Mn, Cu, Zn, Pb, As, and parameters.

Parameter	Distribution Type	Infants	Children	Adult
EF	Triangle	(180,345,365)	(180,345,365)	(180,345,365)
IR	Lognormal	(0.65, 0.065)	(1.5, 0.15)	(2, 0.2)
BW	Lognormal	(6.94, 0.694)	(25.9, 2.59)	(65, 6.5)
Mn	Lognormal	(3.54, 1.74)	(3.54, 1.74)	(3.54, 1.74)
Cu	Lognormal	(6.34, 0.62)	(6.34, 0.62)	(6.34, 0.62)
Zn	Lognormal	(4.55, 0.54)	(4.55, 0.54)	(4.55, 0.54)
Pb	Lognormal	(8.53, 0.59)	(8.53, 0.59)	(8.53, 0.59)
As	Lognormal	(6.74, 0.73)	(6.74, 0.73)	(6.74, 0.73)

The simulated health risk exhibited a conformity with lognormal distribution (Figure 7). Analysis of the HI revealed the percentage of simulated values exceeding 1 for infants, children, and adults at 15.29%, 8.05%, and 3.07%, respectively (Figure 7a–c). In comparison with the deterministic non-carcinogenic risk (Figure 6a–c), the mean of simulated HI, and the over-standard rate demonstrated a close alignment, indicating minimal uncertainty in the HI.

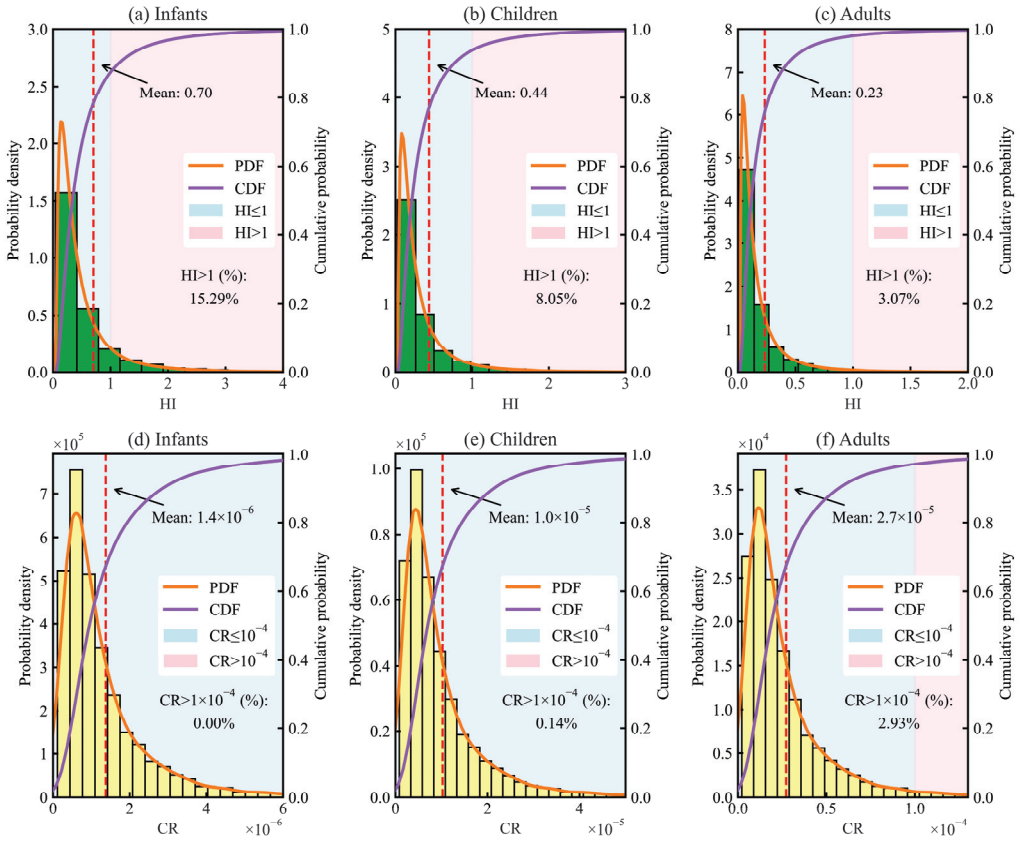

Figure 7. Cumulative permeability and probability density of HI and CR for infants, children, and adults based on Monte Carlo simulation. (**a**) HI for infants, (**b**) HI for children, (**c**) HI for adults, (**d**) HI for infants, (**e**) CR for children, and (**f**) CR for adults.

Examining the percentage of simulated carcinogenic risk (CR) exceeding 1 for infants, children, and adults (Figure 7d–f) yielded values of 0%, 0.14%, and 2.93%, respectively. Notably, the simulated CR values surpassed the actual values depicted in Figure 6d–f. This discrepancy can be attributed to the incorporation of uncertainties associated with health risks during groundwater sampling and parameter selection. The simulation process contributed to a more robust health risk analysis by capturing and integrating the inherent uncertainties in these phases.

4.4. Sobol Sensitivity Analysis

The Sobol method was used to identify the impact of dynamic parameters associated with health risk on HI and CR across diverse populations (Figure 8). Among the factors investigated, namely EF; IR; BW; and concentrations of Pb, As, Zn Cu, and Mn, it was observed that Pb concentration exerted the most substantial influence on both HI and CR. Additionally, EF contributed approximately 8% of the overall effect, followed by IR and BW.

The sensitivity analysis, when ordered by age group, revealed that the sensitivity of the HI was highest in infants, followed by children and adults. Conversely, the sensitivity order of CR exhibited a different pattern, with adults being the most sensitive, followed by children and infants. These findings underscore the significance of age-specific considerations in assessing health risks associated with groundwater contamination.

Pb concentration is a key factor affecting groundwater health. Addressing the source of Pb and reducing its concentration in groundwater could effectively mitigate health risks. Consequently, strategies aimed at minimizing the intake of groundwater contaminated by hazardous substances are crucial for safeguarding the health of the population in this region.

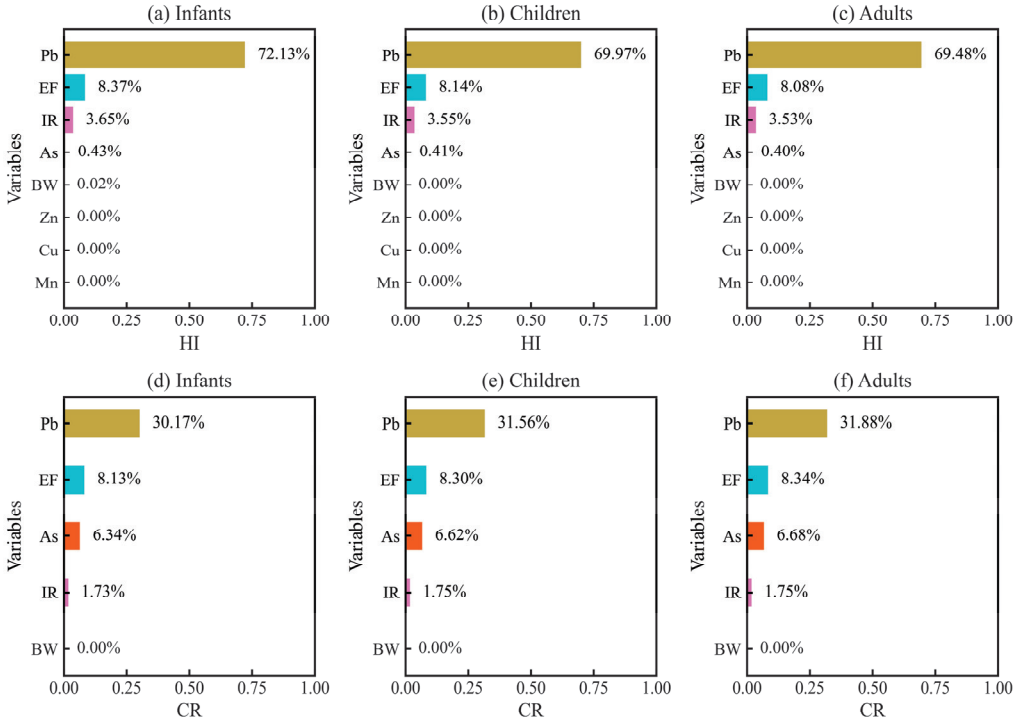

Figure 8. Sensitivity analysis of HI and CR for infants, children, and adults. (**a**) HI for infants, (**b**) HI for children, (**c**) HI for adults, (**d**) HI for infants, (**e**) CR for children, and (**f**) CR for adults.

4.5. Measures for the Security of Groundwater Quality

Based on the results of the health risks, the following recommendations are proposed:

(1) For industrial zones, it is advisable to establish focal monitoring sites and enhance surveillance of industrial wastewater, particularly for hazardous substances such as Pb and As.

(2) Considering the heightened susceptibility of individuals in lower age groups to non-carcinogenic risks, additional protective measures are suggested. These may include implementing safety restrictions in children's recreational areas to minimize their exposure to pollution sources.

(3) Residents are encouraged to consume purified drinking water to mitigate the accumulation of carcinogenic risks.

5. Conclusions

In this study, a comprehensive analysis of trace elements in 134 groundwater samples from a typical urban area was conducted, encompassing heavy metal pollution assessment, health risk evaluation, uncertainty analysis, and sensitivity analysis. The principal findings and conclusions are illustrated as follows:

(1) A substantial majority, specifically 85.09% of groundwater samples exhibited no signs of pollution. However, 5.26% and 9.65% of samples ranked as medium and high levels in the HPI, respectively. Areas with heavy contamination were identified in the central and northeastern regions of the study area. Highly contaminated groundwater should be paid more attention.

(2) The rates of HI exceeding 1 were observed in 15.97%, 5.26%, and 0% of cases for infants, children, and adults, respectively. The percentages of CR surpassing 1×10^{-4} were all 0% for infants, children, and adults. The health risk appraisal mean values indicated the highest non-carcinogenic risk to infants and notable carcinogenic risk to adults. More importantly, the uncertainty analyses revealed results that complemented the absence of risk in the actual risk assessments, thereby enhancing the robustness of the calculations.

(3) The Pb was the most influential indicator in health risk calculations. Small variations in lead levels were found to result in significant fluctuations in health risk outcomes. Following Pb, EF emerged as the second most sensitive indicator, reflecting the influence of dietary habits on health risks. Higher frequencies of intake were associated with elevated health risks.

Author Contributions: Conceptualization, Z.Y.; data curation, X.H.; formal analysis, R.Y.; investigation, Z.Y.; methodology, R.Y.; software, R.Y.; supervision, Y.Y.; validation, X.H. and Y.Y.; writing—original draft, Z.Y.; writing—review and editing, Y.Y. All authors have read and agreed to the published version of the manuscript.

Funding: This research was funded by the Yibin government, grant number SWJTU2021020007, SWJTU2021020008.

Data Availability Statement: The data presented in this study are available upon request from the corresponding author.

Conflicts of Interest: Author Zhongyou Yu was employed by the company Sichuan Hua Di Building Engineering Co., Ltd. The remaining authors declare that the research was conducted in the absence of any commercial or financial relationships that could be construed as a potential conflict of interest.

References

1. Gao, Y.; Qian, H.; Zhou, Y.; Chen, J.; Wang, H.; Ren, W.; Qu, W. Cumulative health risk assessment of multiple chemicals in groundwater based on deterministic and Monte Carlo models in a large semiarid basin. *J. Clean. Prod.* **2022**, *352*, 131567. [CrossRef]
2. Wang, Y.; Yuan, X.; Zhang, Y.; Zhang, X.; Xiao, Y.; Duo, J.; Huang, X.; Sun, M.; Lv, G. Hydrochemical, D–O–Sr isotopic and electromagnetic characteristics of geothermal waters from the Erdaoqiao area, SW China: Insights into genetic mechanism and scaling potential. *Ore Geol. Rev.* **2023**, *158*, 105486. [CrossRef]
3. Feng, B.; Ma, Y.; Qi, Y.; Zhong, Y.; Sha, X. Health risk assessment of groundwater nitrogen pollution in Yinchuan plain. *J. Contam. Hydrol.* **2022**, *249*, 104031. [CrossRef]
4. Marghade, D. Detailed geochemical assessment & indexing of shallow groundwater resources in metropolitan city of Nagpur (western Maharashtra, India) with potential health risk assessment of nitrate enriched groundwater for sustainable development. *Geochemistry* **2020**, *80*, 125627. [CrossRef]
5. Zhu, Y.; Yang, Q.; Wang, H.; Yang, J.; Zhang, X.; Li, Z.; Martín, J.D. A hydrochemical and isotopic approach for source identification and health risk assessment of groundwater arsenic pollution in the central Yinchuan basin. *Environ. Res.* **2023**, *231*, 116153. [CrossRef]
6. World Health Organization. *Guidelines for Drinking-Water Quality: Fourth Edition Incorporating the First Addendum*; World Health Organization: Geneva, Switzerland, 2017.
7. Li, P.; Wu, J.; Qian, H.; Lyu, X.; Liu, H. Origin and assessment of groundwater pollution and associated health risk: A case study in an industrial park, northwest China. *Environ. Geochem. Health* **2014**, *36*, 693–712. [CrossRef]
8. Podgorski, J.; Araya, D.; Berg, M. Geogenic manganese and iron in groundwater of Southeast Asia and Bangladesh—Machine learning spatial prediction modeling and comparison with arsenic. *Sci. Total Environ.* **2022**, *833*, 155131. [CrossRef]
9. Rushdi, M.I.; Basak, R.; Das, P.; Ahamed, T.; Bhattacharjee, S. Assessing the health risks associated with elevated manganese and iron in groundwater in Sreemangal and Moulvibazar Sadar, Bangladesh. *J. Hazard. Mater. Adv.* **2023**, *10*, 100287. [CrossRef]
10. Cai, L.-M.; Wang, Q.-S.; Luo, J.; Chen, L.-G.; Zhu, R.-L.; Wang, S.; Tang, C.-H. Heavy metal contamination and health risk assessment for children near a large Cu-smelter in central China. *Sci. Total Environ.* **2019**, *650*, 725–733. [CrossRef]
11. Traven, L.; Marinac-Pupavac, S.; Žurga, P.; Linšak, Ž.; Žeželj, S.P.; Glad, M.; Linšak, D.T.; Cenov, A. Arsenic (As), copper (Cu), zinc (Zn) and selenium (Se) in northwest Croatian seafood: A health risks assessment. *Toxicol. Rep.* **2023**, *11*, 413–419. [CrossRef]
12. Alarcón-Herrera, M.T.; Martin-Alarcon, D.A.; Gutiérrez, M.; Reynoso-Cuevas, L.; Martín-Domínguez, A.; Olmos-Márquez, M.A.; Bundschuh, J. Co-occurrence, possible origin, and health-risk assessment of arsenic and fluoride in drinking water sources in Mexico: Geographical data visualization. *Sci. Total Environ.* **2020**, *698*, 134168. [CrossRef]
13. Guan, Q.; Wang, F.; Xu, C.; Pan, N.; Lin, J.; Zhao, R.; Yang, Y.; Luo, H. Source apportionment of heavy metals in agricultural soil based on PMF: A case study in Hexi Corridor, northwest China. *Chemosphere* **2018**, *193*, 189–197. [CrossRef] [PubMed]
14. Zainudin, A.M.i.; Zulkefli, S.N.; Looi, L.J.; Aris, A.Z.; Sefie, A.; Isa, N.M. Spatial and temporal evaluation of groundwater hydrochemistry in an active phreatic zone of developed basin in selangor, Malaysia. *Appl. Geochem.* **2023**, *154*, 105656. [CrossRef]
15. Singh, K.K.; Tewari, G.; Kumar, S.; Busa, R.; Chaturvedi, A.; Rathore, S.S.; Singh, R.K.; Gangwar, A. Understanding urban groundwater pollution in the Upper Gangetic Alluvial Plains of northern India with multiple industries and their impact on drinking water quality and associated health risks. *Groundw. Sustain. Dev.* **2023**, *21*, 100902. [CrossRef]
16. USEPA. *Exposure Factors Handbook (2011 Edition)*; United States Environmental Protection Agency: Washington, DC, USA, 2011.

17. Vasseghian, Y.; Almomani, F.; Dragoi, E.-N. Health risk assessment induced by trace toxic metals in tap drinking water: Condorcet principle development. *Chemosphere* **2022**, *286*, 131821. [CrossRef]
18. Hossain, M.; Patra, P.K. Contamination zoning and health risk assessment of trace elements in groundwater through geostatistical modelling. *Ecotoxicol. Environ. Saf.* **2020**, *189*, 110038. [CrossRef]
19. Rashid, A.; Ayub, M.; Bundschuh, J.; Gao, X.; Ullah, Z.; Ali, L.; Li, C.; Ahmad, A.; Khan, S.; Rinklebe, J.; et al. Geochemical control, water quality indexing, source distribution, and potential health risk of fluoride and arsenic in groundwater: Occurrence, sources apportionment, and positive matrix factorization model. *J. Hazard. Mater.* **2023**, *460*, 132443. [CrossRef] [PubMed]
20. Nj, A.; Kh, B.; Am, C.; Hk, C.; Aam, D.; Goc, E. Non-carcinogenic risk assessment of exposure to heavy metals in underground water resources in Saraven, Iran: Spatial distribution, monte-carlo simulation, sensitive analysis. *Environ. Res.* **2021**, *204*, 112002.
21. Peng, S.; Xiao, X.; Zou, H.; Yang, Z.; Ahmad, U.M.; Zhao, Y.; Chen, H.; Li, G.; Liu, G.; Duan, X.; et al. Levels, origins and probabilistic health risk appraisal for trace elements in drinking water from Lhasa, Tibet. *Environ. Geochem. Health* **2022**, *45*, 3405–3421. [CrossRef]
22. Lei, M.; Li, K.; Guo, G.; Ju, T. Source-specific health risks apportionment of soil potential toxicity elements combining multiple receptor models with Monte Carlo simulation. *Sci. Total Environ.* **2022**, *817*, 152899. [CrossRef]
23. Wang, Y.; Cao, D.; Qin, J.; Zhao, S.; Lin, J.; Zhang, X.; Wang, J.; Zhu, M. Deterministic and Probabilistic Health Risk Assessment of Toxic Metals in the Daily Diets of Residents in Industrial Regions of Northern Ningxia, China. *Biol. Trace Elem. Res.* **2023**, *201*, 4334–4348. [CrossRef]
24. Sobol, I.M. Sensitivity estimates for nonlinear mathematical models. *Math. Model. Comput. Exp.* **1993**, *1*, 112–118.
25. Mukherjee, I.; Singh, U.K. Characterization of groundwater nitrate exposure using Monte Carlo and Sobol sensitivity approaches in the diverse aquifer systems of an agricultural semiarid region of Lower Ganga Basin, India. *Sci. Total Environ.* **2021**, *787*, 147657. [CrossRef]
26. Zhang, Y.; Li, X.; Luo, M.; Wei, C.; Huang, X.; Xiao, Y.; Qin, L.; Pei, Q.; Gao, X. Hydrochemistry and Entropy-Based Groundwater Quality Assessment in the Suining Area, Southwestern China. *J. Chem.* **2021**, *2021*, 5591892. [CrossRef]
27. Wang, Y.; Li, R.; Wu, X.; Yan, Y.; Wei, C.; Luo, M.; Xiao, Y.; Zhang, Y. Evaluation of Groundwater Quality for Drinking and Irrigation Purposes Using GIS-Based IWQI, EWQI and HHR Model. *Water* **2023**, *15*, 2233. [CrossRef]
28. Zhang, Y.; Dai, Y.; Wang, Y.; Huang, X.; Xiao, Y.; Pei, Q. Hydrochemistry, quality and potential health risk appraisal of nitrate enriched groundwater in the Nanchong area, southwestern China. *Sci. Total Environ.* **2021**, *784*, 147186. [CrossRef] [PubMed]
29. Zhang, H.; Xu, Y.; Cheng, S.; Li, Q.; Yu, H. Application of the dual-isotope approach and Bayesian isotope mixing model to identify nitrate in groundwater of a multiple land-use area in Chengdu Plain, China. *Sci. Total Environ.* **2020**, *717*, 137134. [CrossRef] [PubMed]
30. Pan, Y.; Peng, H.; Hou, Q.; Peng, K.; Shi, H.; Wang, S.; Zhang, W.; Zeng, M.; Huang, C.; Xu, L.; et al. Priority control factors for heavy metal groundwater contamination in peninsula regions based on source-oriented health risk assessment. *Sci. Total Environ.* **2023**, *894*, 165062. [CrossRef] [PubMed]
31. Sheng, D.; Meng, X.; Wen, X.; Wu, J.; Yu, H.; Wu, M. Contamination characteristics, source identification, and source-specific health risks of heavy metal(loid)s in groundwater of an arid oasis region in Northwest China. *Sci. Total Environ.* **2022**, *841*, 156733. [CrossRef]
32. *GB/T 14848-2017*; Standard for Groundwater Quality. AQSIQ: Beijing, China, 2017.
33. Prasad, B.; Kumari, P.; Bano, S.; Kumari, S. Ground water quality evaluation near mining area and development of heavy metal pollution index. *Appl. Water Sci.* **2014**, *4*, 11–17. [CrossRef]
34. USEPA. *Risk Assessment Guidance for Superfund Volume I Human Health Evaluation Manual (Part A)*; USEPA: Washington, DC, USA, 1989.
35. Zeng, Y.; Lu, H.; Zhou, J.; Zhou, Y.; Sun, Y.; Ma, C. Enrichment Mechanism and Health Risk Assessment of Fluoride in Groundwater in the Oasis Zone of the Tarim Basin in Xinjiang, China. *Expo. Health* **2023**, 1–16. [CrossRef]
36. Harris, C.R.; Millman, K.J.; Van Der Walt, S.J.; Gommers, R.; Virtanen, P.; Cournapeau, D.; Wieser, E.; Taylor, J.; Berg, S.; Smith, N.J.; et al. Array programming with NumPy. *Nature* **2020**, *585*, 357–362. [CrossRef]
37. Virtanen, P.; Gommers, R.; Oliphant, T.E.; Haberland, M.; Reddy, T.; Cournapeau, D.; Burovski, E.; Peterson, P.; Weckesser, W.; Bright, J.; et al. SciPy 1.0: Fundamental Algorithms for Scientific Computing in Python. *Nat. Methods* **2020**, *17*, 261–272. [CrossRef]
38. Mukherjee, I.; Singh, U.K. Environmental fate and health exposures of the geogenic and anthropogenic contaminants in potable groundwater of Lower Ganga Basin, India. *Geosci. Front.* **2022**, *13*, 101365. [CrossRef]
39. Iwanaga, T.; Usher, W.; Herman, J. Toward SALib 2.0: Advancing the accessibility and interpretability of global sensitivity analyses. *Socio-Environ. Syst. Model.* **2022**, *4*, 18155. [CrossRef]
40. Haghnazar, H.; Johannesson, K.H.; González-Pinzón, R.; Pourakbar, M.; Aghayani, E.; Rajabi, A.; Hashemi, A.A. Groundwater geochemistry, quality, and pollution of the largest lake basin in the Middle East: Comparison of PMF and PCA-MLR receptor models and application of the source-oriented HHRA approach. *Chemosphere* **2022**, *288*, 132489. [CrossRef]
41. Chen, R.; Chen, H.; Song, L.; Yao, Z.; Meng, F.; Teng, Y. Characterization and source apportionment of heavy metals in the sediments of Lake Tai (China) and its surrounding soils. *Sci. Total Environ.* **2019**, *694*, 133819. [CrossRef]

42. Adimalla, N.; Qian, H.; Li, P. Entropy water quality index and probabilistic health risk assessment from geochemistry of groundwaters in hard rock terrain of Nanganur County, South India. *Geochemistry* **2020**, *80*, 125544. [CrossRef]
43. Mukherjee, I.; Singh, U.K.; Singh, R.P.; Anshumali; Kumari, D.; Jha, P.K.; Mehta, P. Characterization of heavy metal pollution in an anthropogenically and geologically influenced semi-arid region of east India and assessment of ecological and human health risks. *Sci. Total Environ.* **2020**, *705*, 135801. [CrossRef]

Disclaimer/Publisher's Note: The statements, opinions and data contained in all publications are solely those of the individual author(s) and contributor(s) and not of MDPI and/or the editor(s). MDPI and/or the editor(s) disclaim responsibility for any injury to people or property resulting from any ideas, methods, instructions or products referred to in the content.

water

MDPI

Article

Development of Slow-Releasing Tablets Combined with Persulfate and Ferrous Iron for In Situ Chemical Oxidation in Trichloroethylene-Contaminated Aquifers

Geumhee Yun [1,†], Sunhwa Park [2,†], Young Kim [1] and Kyungjin Han [3,*]

[1] Department of Environmental Engineering, Korea University, Sejong 30019, Republic of Korea; rmal9292@korea.ac.kr (G.Y.); kimyo@korea.ac.kr (Y.K.)
[2] National Institute of Environmental Research, Incheon 22689, Republic of Korea; parksu@korea.kr
[3] Department of Environmental Engineering, Korea National University of Transportation, Chungju 27469, Republic of Korea
* Correspondence: rudwls1009@ut.ac.kr; Tel.: +82-43-841-5356
† These authors contributed equally to this work.

Abstract: Slow-releasing tablets combined with persulfate acting as an oxidant and ferrous iron acting as an activator were manufactured for in situ chemical oxidation. The trichloroethylene (TCE) removal efficiency according to the molar ratio of the oxidizer and activator in the 0, 0.5, 1, 1.5, 2, and 2.5 molar ratio (persulfate: ferrous iron) reactors were 15%, 89%, 90%, 82%, 71%, and 55%, respectively. In a batch reactor injected with an oxidation-activation combined tablet (OACT) and a liquid oxidizing/activator, the TCE removal efficiencies were 100% and 70%, respectively, showing that the tablet form had a high efficiency in contaminant removal. The evaluation of the dissolution characteristics and TCE removal efficiency of OACT 0.5 (tablet with a 1:0.5 molar ratio of persulfate to activator) and OACT 1.0 (tablet with a 1:1 molar ratio of persulfate to activator) under continuous flow conditions showed that the TCE removal efficiency of the OACT 1.0 column was approximately 1.4 times higher than that of OACT 0.5. The longevities of persulfate and ferrous iron of the OACT 1.0 tablet were 43.2 days and 41.7 days, respectively. Thus, OACT 1.0, which was manufactured effectively, was suitable for in situ slow-release chemical oxidation systems.

Keywords: chemical oxidation; slow-releasing tablet; oxidation-activation combined tablet; in situ slow-releasing chemical oxidation systems

1. Introduction

Conventionally, in situ groundwater chemical oxidation dissolves the oxidizing agent in an injection solution and supplies it to the groundwater in liquid form. Most in situ chemical oxidation processes target groundwater contaminated with petroleum and chlorinated aliphatic hydrocarbons (CAHs) by dissolving oxidizing agents, such as hydrogen peroxide and permanganate, in the liquid phase [1–5]. However, when a liquid-based oxidation process is applied in a contaminated aquifer, the concentration of contaminants may rebound. Hence, appropriate management strategies, such as periodic preparation and rejection of the oxidizing agent solution, are essential. Additionally, when applied for long-term operation, the removal efficiency and economic feasibility are reduced because of the tailing of the concentrated contaminants that may occur through back diffusion from the low-permeability layer in the latter half of the process application [6].

After injecting a liquid oxidizing agent into groundwater contaminated with CAHs, such as trichloroethylene (TCE), the contaminants have been reported to rebound after approximately 50 h, thus necessitating continuous injection [7]. Han et al. [8] applied a liquid-based management process to an aquifer contaminated with high nitrate concentrations, and a liquid was continuously injected in areas with rapid groundwater flow.

However, there are disadvantages, such as storing the liquid injection solution and the availability of spaces to occupy the site.

TCE, dichloroethylene, and vinyl chloride are often detected in the groundwater of large cities, such as Seoul, South Korea, which are characterized by high population densities. In this area, the risk of human exposure owing to contamination around subway stations with large floating populations is a concerning issue. Moreover, because the contaminated sites are located in a downtown area, the application of a large-scale remediation process is complex. Slow-release substances capable of controlled release allow the continuous supply of oxidizing agents for a long period with only one injection, minimizing the rebound and tailing of contaminant concentration and enabling efficient operation of the groundwater purification process [9]. Therefore, if an oxidation process using slow-release technology is applied, contaminated groundwater can be efficiently managed in urban areas. In a previous study, a candle-type, slow-release oxidizer combining permanganate and paraffin wax was developed and applied for groundwater remediation. However, this system exhibits several problems, such as insoluble paraffin by-products remaining in the well and the need for periodic removal of manganese dioxide scales from the candle surface [9–11].

Persulfate has the advantages of high solubility in water, high stability, and high oxidizing power. Moreover, it exhibits fewer problems with by-products generated during the reaction, which are disadvantages of permanganate, and can maintain a longer reaction time than hydrogen peroxide. In addition, the sulfate radical-based oxidation process is considered non-toxic, so it is an oxidation process that can effectively balance cost and environmental side effects compared to conventional hydroxyl radical-based oxidation processes [12–14]. Metals, such as ferrous iron, effectively promote this persulfate radical reaction [15,16]. Additionally, medicine-based, tablet-type, slow-releasing materials are environmentally friendly and produce no residual byproducts [6,17]. Therefore, in this study, we conducted an in situ groundwater remediation process using a tablet-based, slow-release oxidizer to manage hazardous contaminants in urban areas. To this end, we set up a tablet that combines persulfate, which can oxidize various organic substances, with ferrous iron as an activator to maximize radical reactions. The release and reduction characteristics of slow-release tablets were also evaluated.

2. Materials and Methods

2.1. Manufacture of Slow-Release Tablets

The slow-release tablets were based on microcrystalline cellulose (MCC) 101, hydroxypropyl methylcellulose 70 k (HPMC 70 k), and magnesium stearate, as reported by Han et al. [8] and were combined according to the ratios listed in Table 1. Sodium persulfate (Miwon Commercial Co., Ltd., Anyang, Republic of Korea) was used as an oxidizing agent for sustained-release tablets, and an aqueous ferrous iron [($FeSO_4 \cdot 7H_2O$($\pm$99%)] (Samchun, Seoul, Republic of Korea) was used as an activator. Specifically, the primary raw materials, persulfate or ferric iron, were mixed at approximately 60% of the total mass of the tablet. MCC 101 (BASF Chemical Co., Ltd., Ludwigshafen, Germany), HPMC 70 k (HPMC, Shin-Etsu Chemical Co., Ltd., Tokyo, Japan), and magnesium stearate (Namyoung Commercial Co., Ltd., Seoul, Republic of Korea) were mixed at 29%, 10%, and 1%, respectively, and then compressed into tablets using a Tablet Compression Machine (Good Price, Kimpo, Republic of Korea).

All materials were sieved with mesh #80 (nominal aperture 180 μm) and blended using a Turbular mixer (Turbular®, WAB, Muttenz, Switzerland) for 100 min. A hydraulic laboratory press (Carver® 3850, CARVER Inc., Wabash, IN, USA) tableted the mixture using a 10 mm rounded flat punch/die set under a tableting pressure of 2.0 tons. The physicochemical characterization of the manufactured tablets was evaluated through differential scanning calorimetry (DSC), X-ray diffraction (XRD), and Fourier transform infrared spectroscopy (FT-IR). The previous study described the detailed physicochemical characterization of the slow-releasing tablets [17].

Table 1. Component content in the prototype and combined tablets.

Component	Prototype Slow-Releasing Oxidation Tablets [SROT(p)]		Prototype Slow-Releasing Activator Tablets [SRAT(p)]		Oxidation-Activation Combined Tablet 1:0.5 [OACT(0.5)]		Oxidation-Activation Combined Tablet 1:1 [OACT(1.0)]	
	(mg/Tablet)	(Mass %)	(mg/Tablet)	(Mass %)	(mg/Tablet)	(Mass%)	(mg/Tablet)	(Mass%)
Sodium persulfate	600	60	N.I. [1]	N.A. [2]	270	37.9	200	27.7
Iron (II) sulfate heptahydrate	N.I.	N.A.	600	60	158	22.1	233	32.3
MCC 101	290	29	290	29	207	29.0	209	29.0
HPMC 70 k	100	10	100	10	71	10.0	72	10.0
Magnesium stearate	10	1	10	1	7	1.0	7	1.0
Total (mg)	1000	100	1000	100	713	100	721	100

Notes: [1] Not injected; [2] Not available.

A prototype slow-releasing oxidation tablet (SROT) and a slow-releasing activator tablet (SRAT) were manufactured according to the manufacturer's instructions. After evaluating SROT and SRAT, a tablet with a molar ratio of persulfate and activator of 1:0.5 [oxidation-activation combined tablet 1:0.5, OACT (0.5)] and a tablet with a molar ratio of persulfate and activator of 1:1 [oxidation-activation combined tablet 1:1, OACT (1.0)] were prepared.

2.2. Soil Column Setup

Three similar cylindrical soil columns (diameter 32 mm, length 80 mm, and total volume 64 cm^3) were constructed to evaluate the effects of OACT (0.5), OACT (1), and a control (OACT was not injected) on the chemical oxidation efficacy of TCE. Materials from an aquifer contaminated with CAHs, such as TCE, dichloroethylene, and vinyl chloride, were sieved through mesh #8 (nominal aperture 2.46 mm) to remove irregularly sized particles. Each column was packed with a sieved material to simulate the aquifer. The average bulk density and porosity were 1.55 g/mL and 0.31, respectively.

A continuously flowing cell was constructed with a serum bottle to mimic groundwater flow conditions in a well and to feed oxidants or activators released from SROA, SRAT, and OACT. An influent containing Br as a tracer was pumped from the reservoir into a continuously flowing cell at a 0.1 mL/min flow rate. The tablets were placed in a continuous-flow cell and the solution inside the cell was pumped into a soil column at a flow rate of 0.1 mL/min (Figure 1).

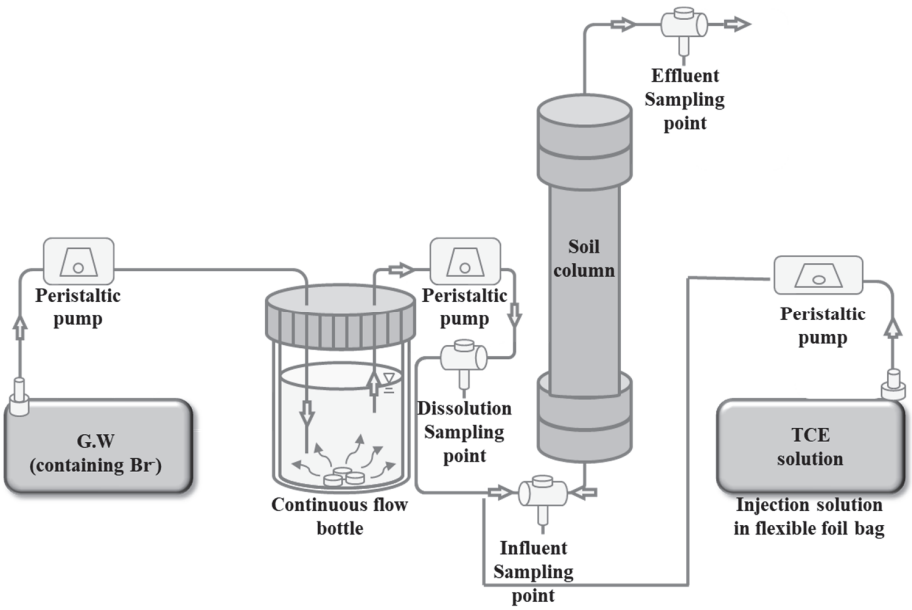

Figure 1. Schematic diagram of the column experiment.

2.3. Experiments Procedural

Experiments were conducted sequentially to evaluate the dissolution characteristics of slow-release tablets and the contaminant removal efficiency of the slow-release oxidation process under continuous-flow conditions simulating groundwater flow, as shown in Table 1. Using prototype tablets, a prototype tablet release test (PTRT) was performed to evaluate persulfate and ferrous release characteristics under continuous flow conditions. One tablet each of SROT and SRAT was injected into a continuous-flow vessel and distilled water was injected at a flow rate of 0.1 mL/mL. The prototype tablet batch test (PTBT) was performed to derive TCE removal efficacy by SROT and SRAT.

Theoretically, 1 mol of ferrous iron is required to activate 1 mol of persulfate radical reaction [18,19], as shown in Equation (1).

$$S_2O_8{}^{2-} + Fe^{2+} \rightarrow SO_4{}^{2-}\cdot + Fe^{3+} + SO_4{}^{2-} \quad (1)$$

Ferrous iron stimulates the activation of sulfate radicals during the oxidation reaction of persulfate. However, if present in excess, it can be used as a scavenger in radical consumption reactions [20,21]. Therefore, deriving an oxidizing agent and activator ratio is necessary to effectively promote radical reactions. Therefore, a combined tablet batch test (CTBT) was performed to optimize the mixing ratio of the oxidizer and activator in a batch reactor. In CTBT, we evaluated the oxidation characteristics of TCE under conditions of 0.5, 1, 1.5, 2, and 2.5 times the theoretical amount of ferrous iron required to activate persulfate. In this experiment, as shown in Equation (2), twice the amount of persulfate theoretically required to remove 10 mg/L of TCE was injected into all reactors. After deriving the optimal oxidizing agent to activator ratio, an OACT combining persulfate and ferrous iron was prepared using the manufacturing method described in Section 2.1.

$$3S_2O_8{}^{2-} + C_2HCl_3 + 4H_2O \rightarrow 6SO_4{}^{2-} + 2CO_2 + 9H^+ + 3Cl^- \quad (2)$$

A batch test was performed to evaluate the TCE removal efficiencies of SROT/SRAT, in which the oxidizing agent and activator were separated, and OACT, in which the two substances were mixed in one tablet. The experimental configurations are listed in Table 2. The amount of the tablet injection was designed such that each experimental group's total persulfate injection amount was the same.

Table 2. Composition of each experiment.

		Injected Tablet (Tablet)				**Flow Rate (mL/min)**	**Initial or Injected Solution Conc. (mg/L)**	
		SROT (P)	**SRAT (P)**	**OACT (0.5)**	**OACT (1.0)**		**Br-**	**TCE**
Prototype tablet release test (PTRT)	SROT	1	N.I. [1]	N.I.	N.I.	0.1	N.I.	N.I.
	SRAT	N.I.	1	N.I.	N.I.	0.1	N.I.	N.I.
Prototype tablet batch test (PTBT)	Control	N.I.	N.I.	N.I.	N.I.	N.A. [2]	N.I.	6.6 [3]
	SROT	1	N.I.	N.I.	N.I.	N.A.	N.I.	6.5
	SRAT	N.I.	1	N.I.	N.I.	N.A.	N.I.	6.4
	SROT + SRAT	1	1	N.I.	N.I.	N.A.	N.I.	6.6
Combined tablet batch test (CTBT)	Control	N.I.	N.I.	N.I.	N.I.	N.A.	N.I.	6.7
	SROT + SRAT	2	2	N.I.	N.I.	N.A.	N.I.	7.8
	OACT (0.5)	N.I.	N.I.	4	N.I.	N.A.	N.I.	8.5
	OACT (1.0)	N.I.	N.I.	N.I.	6	N.A.	N.I.	8.9
Combined tablet soil column test (CTST)	Control	N.I.	N.I.	N.I.	N.I.	0.1	34 ± 1.7 [3]	2.6 ± 0.2
	OACT (0.5)	N.I.	N.I.	3	N.I.	0.1	1075 ± 65.5	2.5 ± 0.2
	OACT (1.0)	N.I.	N.I.	N.I.	4	0.1	1120 ± 72.8	2.3 ± 0.2

Notes: [1] Not injected; [2] Not available; [3] Average value ± 95% confidence interval; TCE, trichloroethylene.

Finally, the combined tablet soil column test (CTST) was performed to evaluate the TCE removal efficacy of tablets containing combined persulfate and ferrous iron under continuous flow conditions. To equalize the amount of persulfate injected into the OACT (0.5) and OACT (1.0) columns, three OACT (0.5) tablets and four OACT (1.0) tablets were injected. The injection solution was designed to inject 10 mg/L of TCE, a contaminant, and 30 mg/L of Br^- as a tracer.

2.4. Data Analysis

The dissolution rate in the batch tests was determined using the Higuchi model (Equation (3)):

$$M_t = K_H \times t^{1/2} \tag{3}$$

where K_H ($T^{-1/2}$) is the Higuchi dissolution constant and *Mt* (M) is the quantity of solute released at time t (T).

The data obtained were plotted as the cumulative percentage of persulfate or ferrous iron released against the square root of time [22]. This equation describes the solute released from pharmaceutical dosage forms, such as matrix tablets with water-soluble materials [23].

Several equations, such as power functions [24] and first-order decay [25], have been reported to fit the release profiles of slow-release candles to estimate the longevity of these systems. These studies used organic crystalline matrices and paraffin wax to prepare slow-release materials and proposed equations to express the dissolution and diffusion processes owing to matrix pore bonding. However, they differ from the HPMC and MCC used in the present study.

Yeum et al. [17] performed a fitting using nonlinear regression on an empirical saturation-type equation of a three-parameter logistic function (Equation (4)) to acquire the best-fitting plot of the mass ratio of the cumulative mass of the released solute versus the initial mass of solute (M_r) over the release time (T). M_r versus t (T) plots were fitted using nonlinear regression with the SigmaPlot software (V. 12.0).

$$M_r = \frac{a}{1 + bt^c} \tag{4}$$

where *a*, *b*, and *c* are the constants. All constants in this function are dimensionless.

M_r was calculated by Equation (5):

$$M_r = \frac{Q\left(\frac{C_n + C_{n+1}}{2}\right)(t_{n+1} - t_n)}{M_i} \tag{5}$$

where M_r is the mass ratio of the cumulative mass of persulfate or ferrous iron released versus the initial mass of persulfate or ferrous iron in SROT or SRAT, *Mi* (M) is the initial mass of persulfate or ferrous iron in SROT or SRAT, Q (L3T-1) is the flow rate, C_{n+1} (ML-3) is the concentration of persulfate or ferrous iron in the effluent from a continuous flowing cell at time t_{n+1}, and C_n is the concentration of persulfate or ferrous iron in the effluent from a continuous flowing cell at time, t_n.

2.5. Analytical Methods

To measure the TCE concentrations, the samples were analyzed via headspace gas analysis using a Shimazu GC-17A (Kotyo, Japan) gas chromatograph (GC) equipped with a flame ionization detector. Further, 10 mL of the sample was removed from a 40 mL volatile organic acid vial, which was equilibrated in a shaking incubator at 20 °C. After equilibration, 200 µL of gas was sampled using a gastight syringe and injected into the GC. The specific operating conditions of the GC are described in Han et al. [8].

The Br^- concentration was measured using an ion chromatograph (IC) equipped with a conductivity detector. Samples were prefiltered using a 0.35 µm syringe filter and placed in a Dionex AS-DV autosampler (Dionex Co., Sunnyvale, CA, USA). The IC system was operated at 1.2 mL/min, and the mobile phase was composed of a mixture of 3.5 mM

Na_2CO_3 and 1.0 mM $NaHCO_3$. The samples were delivered to the loop at 4.0 mL/min, with a flush factor of 10. A current of 24 mA was applied to the detector. The chromatographic separation was performed using a Dionex IonPac AS14 column (Dionex Co., Sunnyvale, CA, USA). Analytical-grade potassium bromide (99%), sodium nitrate (99%), and sodium nitrite (98%) (Samchun Chemical Co., Ltd., Seoul, Republic of Korea) were used for the column experiments and laboratory analyses.

Persulfate was analyzed using the absorbance method. Using a persulfate–iodine reaction, a coloring reagent was prepared by mixing 5 g/L sodium bicarbonate and 100 g/L potassium iodide. Further, 10 mL of the prepared coloring reagent was mixed with 200 μL of the sample, and the mixed solution was analyzed for ferrous iron at 400 nm using a DR6000 UV-VIS spectrophotometer (Hach Company, Loveland, CO, USA).

Specifically, ferrous iron was analyzed using the 255 program of the spectrophotometer with a 103769 analytical reagent.

3. Results and Discussion

3.1. Persulfate and Ferrous Releasing Characteristics in PTRT

Measuring the persulfate and ferrous iron release profiles of SROT and SRAT under continuous flow conditions is essential for designing a slow-release tablet system for the chemical oxidation of organic contaminants. The persulfate and ferrous iron release profiles were measured by monitoring the persulfate and ferrous iron concentrations in a continuously flowing cell. Two completely different phases of change in the temporal solute concentrations were observed during the dissolution test (Figure 2a). At the beginning of the SROT-flowing cell, the persulfate concentration rapidly increased, reaching a peak value at 45 h; subsequently, the concentration decreased rapidly. SRAT also showed a similar trend, with ferrous iron showing a maximum concentration after 55 h and then decreasing rapidly. This change in concentration resulted from the difference between the solute dissolution rate from the tablet and the influent dilution rate into the flowing cell. In controlled-release systems, an agent (i.e., an oxidized or reduced compound) is released rapidly, followed by a slower release rate [10,17,26]. Therefore, the rapidly decreasing persulfate concentration after 45 h may be due to reduced release rates. In other words, this suggests that the release rate of persulfate from the tablet is slower than the rate of water flowing into the flowing cell. During the first phase of rapid growth, the release rate may be greater than the dilution rate.

During the release period, the average persulfate and ferrous ion concentrations released from SROT and SRAT were approximately 3.7 ± 1.3 and 3.4 ± 0.8 mmol/L, respectively. The average oxidizing agent and activator concentrations of the tablet are critical for the slow-release oxidation process. As described in Equation (1), the theoretical molar ratio of the oxidizer to the activator was 1:1. Additionally, many studies have reported that pollutant removal efficiency differs by more than two times depending on the presence or absence of ferrous iron, an activator [15,16,21]. A similar trend was observed in the experimental results for PTRT. Thus, the concentrations of solutes released from SROT and SRAT indicated that the contaminants can be effectively managed by the sulfate radical reaction in the tablet-based in situ oxidation process. Additionally, the release rates of persulfate and ferrous iron could be effectively controlled in prototype tablets produced using this manufacturing method.

The PTBT analysis conducted to evaluate TCE removal efficiency using the prototype tablets showed that there was no change in the TCE concentration in the control reactor injected with only TCE and reactor-injected SOAT (Figure 2b). This indicated that none of the reactors showed TCE decomposition due to physical mechanisms, such as volatilization and ferrous iron, an accelerator. In the reactor injected with SROT, an oxidizing agent, approximately 68% of 10 mg/L TCE decomposed in 9 h, whereas in the reactor simultaneously injected with SROT and SRAT, TCE was decomposed completely in 5 d. This indicated that the activator ferrous iron acted as a radical accelerator in the persulfate oxidation reaction and effectively decomposed pollutants. CO_2 is a by-product of the

chemical oxidation of organic substances such as TCE [27,28]. Therefore, we measured CO_2 as a by-product to prove that the TCE decreased due to a chemical reaction. CO_2 was at average 0.12 ± 0.04 mg/L, 0.51 ± 0.52 mg/L, 0.27 ± 0.12 mg/L, and 3.68 ± 4.78 mg/L in the four PTBT reactors, respectively (Figure 2c). Therefore, the TCE removal rate and CO_2 generation tended to be proportional, which suggests that TCE was mineralized into CO_2 through the oxidation reaction of persulfate.

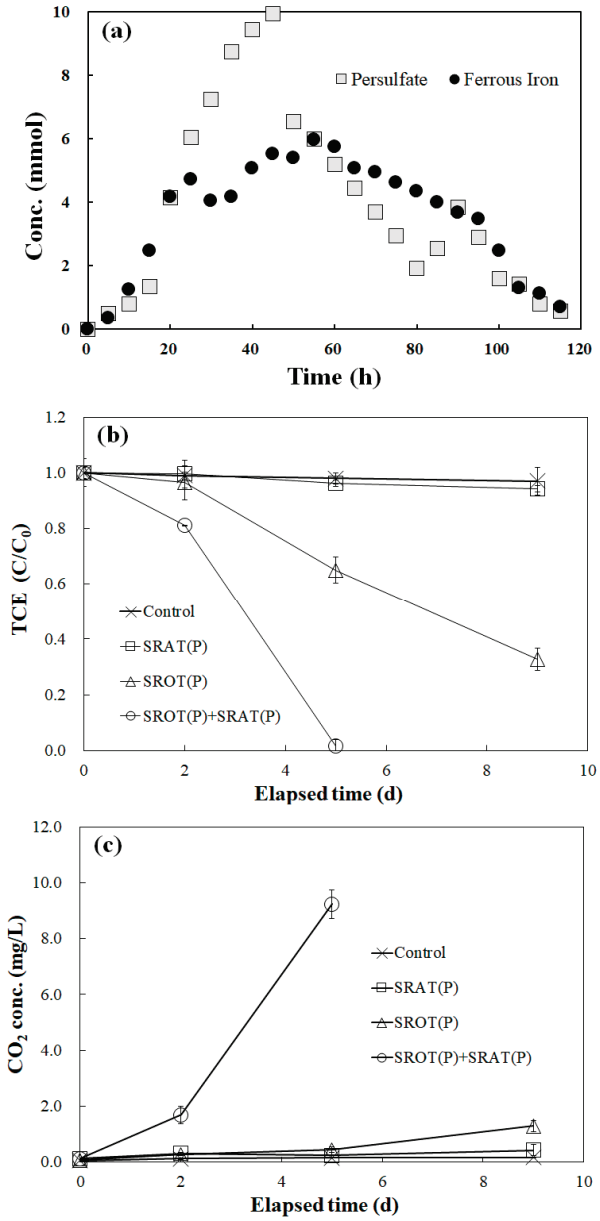

Figure 2. Release characteristics of prototypes SROT and SRAT under continuous flow conditions during the PTRT test (**a**) and TCE removal efficacy (**b**) and CO_2 concentrations (**c**) of prototype tablets in a batch reactor during the PTBT test.

3.2. Optimization Mixed Ratio of Oxidizer with Activator in CTBT

In the batch experiments conducted to evaluate the TCE removal efficiency using stoichiometric ratios of persulfate and the activator, the theoretical ferrous iron requirement according to Equation (2) was set to 0, 0.5, 1, 1.5, 2, and 2.5. After injecting the oxidizer and activator for 10 h, the TCE removal efficiencies at 0, 0.5, 1, 1.5, 2, and 2.5 molar ratio reactors were 15%, 89%, 90%, 82%, 71%, and 55%, respectively (Figure 3a). The low removal efficiency of TCE in the reactor without injecting ferrous iron as an activator resulted

from the direct chemical reaction of TCE with persulfate rather than a sulfate radical reaction [29,30]. Additionally, even when sufficient ferrous iron was injected, the TCE removal efficiency decreased, thus proving that sulfate radicals generated from persulfate through metal activity were consumed by excess ferrous iron. Therefore, these results suggested that the effective combination ratio of the oxidizing agent and activator would be 0.5–1 times the theoretical ratio of persulfate and ferrous iron. OACT (0.5) and OACT (1.0) tablets containing a combined oxidizing agent and activator were prepared according to the SROT and SRAT manufacturing methods.

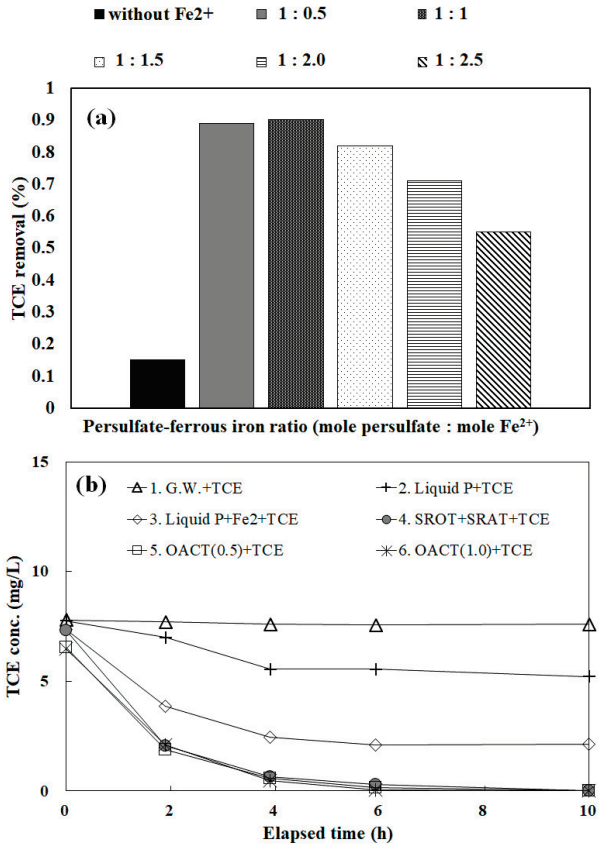

Figure 3. TCE degradation characteristics under various ferrous iron concentrations (**a**) and TCE degradation characteristics of prototype and combined tablets during the CTBT test (**b**).

A batch experiment was performed to evaluate the TCE removal efficiency of the OACT tablets. A reactor injected with a liquid oxidizing agent, oxidation tablet SROT, activator tablet SRAT, OACT (0.5), and OACT (1.0) were configured under the same conditions. The same mass of persulfate was injected into all reactors to accurately compare their efficiencies. In the control reactor, where only groundwater and TCE were present, the TCE concentration did not change for approximately 10 h, indicating no biochemical reactions of TCE due to dissolved substances present in groundwater (Figure 3b). In the reactor injected with only liquid persulfate, approximately 33% TCE was decomposed, whereas in the reactor injected with persulfate and ferrous iron simultaneously, the TCE removal efficiency was 71%. The injection of ferrous iron promoted the production of sulfate radicals in persulfate and was used to decompose pollutants. However, the oxidation reaction stopped after 6 h in both the liquid reactors.

This result presents a problem with the liquid injection method. Suppose that high oxidizing agent and activator concentrations are temporarily injected into the liquid. In such a case, they are not used efficiently to remove the target contaminants and can cause radical consumption and oxygen exchange rather than oxidation/promotion reactions. This indicates inefficient consumption of the activator through oxidation reactions with

oxygen. However, all three reactors into which the tablets were injected showed a similar trend, with 7 mg/L of TCE decomposed in approximately 6 h. This proved that the supply of oxidation/activators in the form of tablets in the in situ oxidation process to remove pollutants was more effective for decomposition than the conventional liquid injection method. Additionally, the results of injection did not differ through OACT, which is a combined oxidizer and activator, versus SROT with SRAT, suggesting that using combined tablets is efficient for the convenience of maintenance and production.

3.3. Evaluation of TCE Removal Efficacy in CTST

Soil column tests were performed to evaluate the oxidation efficacy of TCE using OACT (0.5) and OACT (1). The breakthrough curves of bromide (tracer) and TCE were obtained by measuring the effluent concentrations (Figure 4). For example, the same breakthrough curve C* (C_{Eff}/C_{inj}, effluent concentration divided by influent concentration) for Br and TCE indicated that TCE was not retarded (i.e., R = 1 for TCE). The lower C* of TCE compared with that of Br suggested that TCE may be adsorbed on the surface of the solid particles during transport through the column. The average C* of bromide in the three columns was 0.95 after approximately 2 d (two pore volumes), and 95% of the injected concentration was detected in the column effluent. The TCE_control column, in which only TCE was simultaneously injected, showed a C* value of 0.25, and only 25% of the injected concentration was detected at the outlet. Based on the calculation of the ratio of the 50% mass recovery time of TCE divided by the 50% mass recovery time of Br, the retardation factor of TCE was 1.49, indicating that TCE moves approximately 49% slower in the soil column via physical mechanisms, such as adsorption.

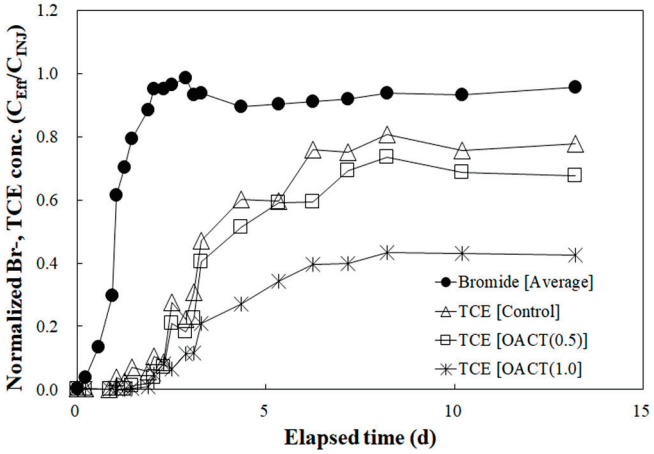

Figure 4. Normalized bromide and TCE concentrations in the soil column effluent during the CTST.

In the OACT (0.5) column, TCE showed a similar trend to the TCE_control column until approximately 4 d, but was detected to be approximately 0.1 times lower than that of the control column C*. C* in the OACT (1.0) column was significantly different from that in the other two columns after 3 d. The significantly lower C* value compared with that of the control column suggested that TCE degradation occurred through a chemical mechanism (oxidation) in addition to physical adsorption in the OACT (1.0) column. The mass recovery percentages of Br (average of 3 columns) and TCE in the control, OACT (0.5), and OACT (1.0) columns were calculated at 96% ± 2%, 61%, 50%, and 31%, respectively.

Significantly lower TCE C* values and mass recovery percentages of TCE compared to the tracer and control columns provided strong evidence of chemical oxidation induced by both the OACT (0.5) and OACT (1.0) columns. The lower removal efficiency of the column compared with that of the batch reactor suggested that the iron released from the OACT (0.5) tablet was likely consumed by oxygen or soil organic matter rather than by promoting sulfate radicals under the continuous injection of contaminated groundwater. However, in the case of the OACT (1.0) tablet, despite unnecessary consumption of ferrous iron, a

sufficient amount of activator was supplied for sulfate radical generation, and it would have shown a higher TCE removal efficiency compared to the OACT (0.5) column.

3.4. Estimating Longevity of OACT (1.0)

The longevity of persulfate and ferrous iron was confirmed using the results of OACT dissolution from the continuously flowing cell described in Section 3.3. In the flow cell, persulfate and ferrous iron showed maximum concentrations for approximately 2 d, similar to the release characteristics of the existing 3.1 prototype tablet, and the average concentrations at this time were 5.1 ± 2.3 mmol/L (Figure 5a) and 5.6 ± 3.4 mmol/L (Figure 5b), respectively. After 6 d, the concentrations of both solutes were maintained below 0.2 mmol/L, and the molar ratio of persulfate and ferrous iron was close to 1:1.

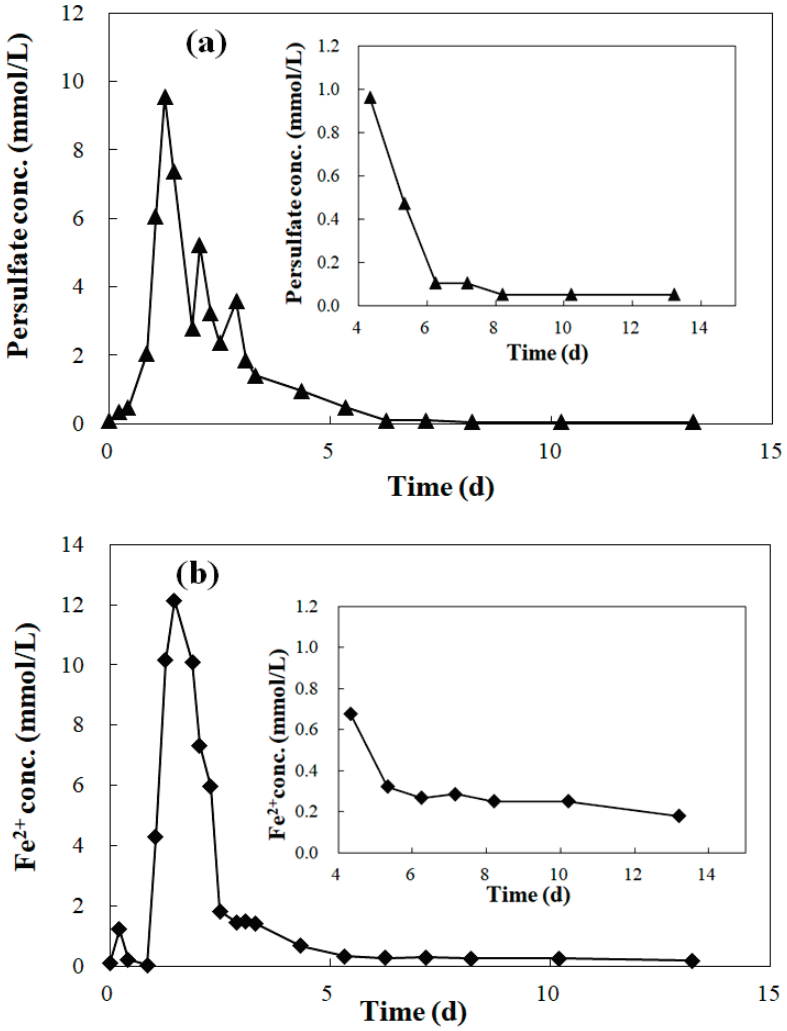

Figure 5. Release characteristics of the combined tablet of (**a**) OACT 1.0 PS and (**b**) ferrous iron under continuous flow during CTST.

For simplicity, previous studies defined the longevity of slow-release materials as the time taken to reach an Mr value of 0.80, as there was marginal change in Mr beyond 0.80. The predictions showed that OACT (1.0) persulfate and ferrous iron had 43.2 and 41.7 d of longevity, respectively (Figure 6). This study used small tablets (diameter 1.0 and height 0.6 cm), which have a shorter longevity than other large-scale release systems, and dissolution was found to last approximately 40 days. Considering that the longevity of slow-releasing material is generally dependent on size, the longevity is expected to increase if the tablet size is increased. The regression coefficient was >0.99 for all solutes.

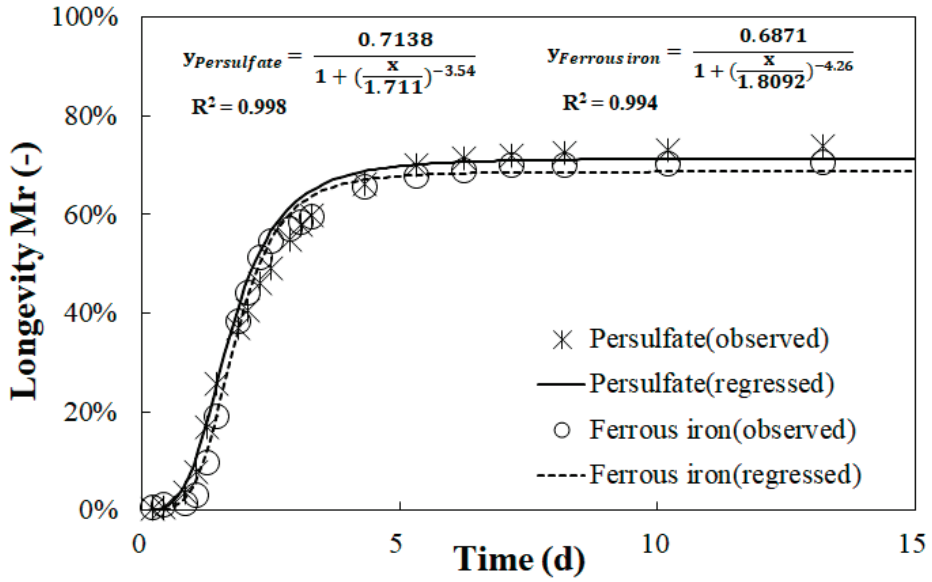

Figure 6. Observed and predicted M_r values for persulfate and ferrous iron during continuous flow cell release experiments of CTST at a 0.1 mL/min flow rate.

4. Conclusions

This study aimed to develop a slow-release tablet that combined persulfate as an oxidizing agent and ferrous iron as an activator. Various batch and column experimental results showed that the molar ratio of the oxidation activator optimized for pollutant removal was 1:1. The dissolution characteristics of OACT (1.0) were evaluated, and persulfate and ferrous iron showed average concentrations of approximately 5.1 ± 2.3 and 5.6 ± 3.4 mmol/L, respectively, during the release period. This was close to the ideal molar ratio of the oxidizer to the activator of 1:1. The longevity of the manufactured OACT (1.0) indicated that the cumulative released mass of persulfate and divalent iron reached 80% after 43.2 and 41.7 d, respectively. Therefore, OACT, which can remove pollutants for several to tens of days with a single injection, would effectively manage contaminated groundwater that cannot be actively remediated, such as in urban areas or industrial complexes. In the future, optimization of the slow-releasing in situ chemical oxidation process is necessary through long-term monitoring of the release characteristics and pollutant removal efficacy of slow-releasing tablets at contaminated sites.

Author Contributions: G.Y.: conceptualization, writing—original draft preparation, formal analysis; S.P.: writing—reviewing and editing; Y.K.: investigation, writing—reviewing and editing; K.H.: investigation, writing—reviewing and editing, Supervision. All authors have read and agreed to the published version of the manuscript.

Funding: This research was supported by the Korea Ministry of Environment and the Technology Institute (KEITI) as "The Subsurface Environmental Management (SEM) project (2018002480005 and 2021002470002)". This research was also supported by a grant from the National Institute of Environment Research (NIER), funded by the Ministry of Environment (MOE) of the Republic of Korea (NIER-RP2022-01-01-069). This research was also supported by Basic Science Research Program through the National Research Foundation of Korea funded by the Ministry of Education (2022R1F1A1068350 and 2020R1I1A1A0106806). This article has not been reviewed by these agencies, and no official endorsement should be inferred.

Data Availability Statement: Data are contained within the article.

Conflicts of Interest: The funders had no role in the design of the study; in the collection, analyses, or interpretation of data; in the writing of the manuscript; or in the decision to publish the results.

References

1. Greenberg, R.S.; Andrews, T.; Kakarla, P.K.; Watts, R.J. In-Situ Fenton-Like Oxidation of Volatile Organics: Laboratory, Pilot, and Full-Scale Demonstrations. *Remediation* **1998**, *8*, 29–42. [CrossRef]
2. Nelson, M.D.; Parker, B.L.; Al, T.A.; Cherry, J.A.; Loomer, D. Geochemical reactions resulting from in situ oxidation of PCE-DNAPL by KMnO4 in a sandy aquifer. *Environ. Sci. Technol.* **2001**, *35*, 1266–1275. [CrossRef] [PubMed]
3. Kakarla, P.K.; Andrews, T.; Greenberg, R.S.; Zervas, D.S. Modified Fenton's processes for effective in-situ chemical oxidation—Laboratory and field evaluation. *Remediation* **2002**, *12*, 23–36. [CrossRef]
4. Lowe, K.S.; Gardner, E.G.; Siegrist, R.L. Field evaluation of in situ chemical oxidation through vertical well-to-well recirculation of $NaMnO_4$. *Groundw. Monit. Remediat.* **2002**, *22*, 106–115. [CrossRef]
5. McGuire, T.M.; McDade, J.M.; Newell, C.J. Performance of DNAPL source depletion technologies at 59 chlorinated solvent-impacted sites. *Groundw. Monit. Remediat.* **2006**, *26*, 73–84. [CrossRef]
6. O'Connor, D.; Hou, D.; Ok, Y.S.; Song, Y.; Sarmah, A.K.; Li, X.; Tack, F.M. Sustainable in situ remediation of recalcitrant organic pollutants in groundwater with controlled release materials: A review. *J. Control. Release* **2018**, *283*, 200–213. [CrossRef] [PubMed]
7. Han, K.; Hong, U.; Park, S.; Lee, G.; Kwon, S.; Kim, Y. Long-term monitoring and evaluating biological activity of in situ anaerobic reductive dechlorination at a highly recharged and TCE-contaminated aquifer. *Desalination Water Treat.* **2016**, *57*, 24085–24095. [CrossRef]
8. Han, K.; Yoon, J.; Yeum, Y.; Park, S.; Kim, H.K.; Kim, M.; Chung, H.M.; Kwon, S.; Yun, S.-T.; Kim, Y. Efficacy of in situ well-based denitrification bio-barrier (WDB) remediating high nitrate flux in groundwater near a stock-raising complex. *J. Environ. Manag.* **2020**, *258*, 110004. [CrossRef]
9. Christenson, M.; Kambhu, A.; Reece, J.; Comfort, S.; Brunner, L. A five-year performance review of field-scale, slow-release permanganate candles with recommendations for second-generation improvements. *Chemosphere* **2016**, *150*, 239–247. [CrossRef]
10. Christenson, M.D.; Kambhu, A.; Comfort, S.D. Using slow-release permanganate candles to remove TCE from a low permeable aquifer at a former landfill. *Chemosphere* **2012**, *89*, 680–687. [CrossRef]
11. Kambhu, A.; Comfort, S.; Chokejaroenrat, C.; Sakulthaew, C. Developing slow-release persulfate candles to treat BTEX contaminated groundwater. *Chemosphere* **2012**, *89*, 656–664. [CrossRef] [PubMed]
12. Oh, W.D.; Dong, Z.L.; Lim, T.T. Generation of sulfate radicals through heterogeneous catalysis for organic contaminant removal:Current development, challenges, and prospects. *Appl. Catal. B Environ.* **2016**, *194*, 169–201. [CrossRef]
13. Ike, I.A.; Linden, K.G.; Orbell, J.D.; Duke, M. Critical review of the science and sustainability of persulphate advanced oxidation-processes. *Chem. Eng. J.* **2018**, *338*, 651–669. [CrossRef]
14. Waclawek, S.; Lutze, H.V.; Grubel, K.; Padil, V.V.T.; Cernik, M.; Dionysiou, D.D. Chemistry of persulfates in water andwastewater treatment: A review. *Chem. Eng. J.* **2017**, *330*, 44–62. [CrossRef]
15. Ghanbari, F.; Moradi, M. Application of peroxymonosulfateand its activation methods for degradation of environmental organicpollutants: Review. *Chem. Eng. J.* **2017**, *310*, 41–62. [CrossRef]
16. Iqbal, J.; Shah, N.S.; Khan, J.A.; Habila, M.A.; Boczkaj, G.; Shad, A.; Nazzal, Y.; Al-Taani, A.A.; Howari, F. Bimetallic Bi/Cu0-catalyzed persulfate-based advanced oxidation processes towards clofibric acid degradation in wastewater. *Water Resour. Ind.* **2023**, *30*, 100226. [CrossRef]
17. Yeum, Y.; Han, K.; Kang, J.H.; Kim, D.W.; Park, C.W.; Kwon, S.; Kim, Y. Production, characterization, and evaluation of two types of slow-releasing carbon source tablets for in-situ heterotrophic nitrate denitrification in aquifers. *Chemosphere* **2020**, *260*, 127478. [CrossRef]
18. Yu, Z.Y.; Wang, W.H.; Song, L.; Lu, L.Q.; Wang, Z.Y.; Jiang, X.F.; Dong, C.N.; Qiu, R.Y. Acceleration comparison between $Fe^{2+}/H_2O_2$and Co^{2+}/oxone for decolouration of azo dyes in homogeneoussystems. *Chem. Eng. J.* **2013**, *234*, 475–483.
19. Chen, Y.D.; Bai, S.; Li, R.; Su, G.; Duan, X.; Wang, S.; Ren, N.Q.; Ho, S.H. Magnetic biochar catalysts from anaerobic digested sludge: Production, application and environment impact. *Environ. Int.* **2019**, *126*, 302–308. [CrossRef]
20. Liu, H.; Bruton, T.A.; Doyle, F.M.; Sedlak, D.L. In situ chemical oxidation of contaminated groundwater by persulfate: Decomposition by Fe (III)-and Mn (IV)-containing oxides and aquifer materials. *Environ. Sci. Technol.* **2014**, *48*, 10330–10336. [CrossRef]
21. Zhang, Y.; Jiang, H.; Wang, H.; Wang, C. Separation of hazardous polyvinyl chloride from waste plastics by flotation assisted with surface modification of ammonium persulfate: Process and mechanism. *J. Hazard. Mater.* **2020**, *389*, 121918. [CrossRef] [PubMed]
22. Suriyaprakash, T.; Prabu, S.; Satyam, T. In-vitro studies of diclofenac sodium controlled-release dosage from biopolymeric hydrophilic matrices. *Ars. Pharm.* **2011**, *52*, 20–24.
23. Desai, S.; Simonelli, A.; Higuchi, W. Investigation of factors influencing release of solid drug dispersed in inert matrices. *J. Pharm. Sci.* **1965**, *54*, 1459–1464. [CrossRef] [PubMed]
24. Kang, N.; Hua, I.; Rao, P.S.C. Production and characterization of encapsulated potassium permanganate for sustained release as an in situ oxidant. *Ind. Eng. Chem. Res.* **2004**, *43*, 5187–5193. [CrossRef]
25. Lee, E.S.; Schwartz, F.W. Characteristics and applications of controlled–release KMnO4 for groundwater remediation. *Chemosphere* **2007**, *66*, 2058–2066. [CrossRef]
26. Chapelle, F.H.; Bradley, P.M.; Casey, C.C. Behavior of a chlorinated ethene plume following source-area treatment with Fenton's reagent. *Groundw. Monit. Remediat.* **2005**, *25*, 131–141. [CrossRef]

27. Chokejaroenrat, C.; Comfort, S.; Sakulthaew, C.; Dvorak, B. Improving the treatment of non-aqueous phase TCE in low permeability zones with permanganate. *J. Hazard. Mater.* **2014**, *268*, 177–184. [CrossRef]
28. Huang, K.C.; Hoag, G.E.; Chheda, P.; Woody, B.A.; Dobbs, G.M. Chemical oxidation of trichloroethylene with potassium permanganate in a porous medium. *Adv. Environ. Res.* **2002**, *7*, 217–229. [CrossRef]
29. Lin, D.; Fu, Y.; Li, X.; Wang, L.; Hou, M.; Hu, D.; Li, Q.; Zhang, Z.; Xu, C.; Qiu, S.; et al. Application of persulfate-based oxidation processes to address diverse sustainability challenges: A critical review. *J. Hazard. Mater.* **2022**, *440*, 129722. [CrossRef]
30. Tsitonaki, A.; Petri, B.; Crimi, M.; Mosbaek, H.A.N.S.; Siegrist, R.L.; Bjerg, P.L. In situ chemical oxidation of contaminated soil and groundwater using persulfate: A review. *Crit. Rev. Environ. Sci. Technol.* **2010**, *40*, 55–91. [CrossRef]

Disclaimer/Publisher's Note: The statements, opinions and data contained in all publications are solely those of the individual author(s) and contributor(s) and not of MDPI and/or the editor(s). MDPI and/or the editor(s) disclaim responsibility for any injury to people or property resulting from any ideas, methods, instructions or products referred to in the content.

water

MDPI

Article

Hydrochemical Appraisal and Driving Forces of Groundwater Quality and Potential Health Risks of Nitrate in Typical Agricultural Area of Southwestern China

Jiawei Liu [1,2], Chang Yang [3], Si Chen [3], Yangshuang Wang [1,2], Xingjun Zhang [3], Wulue Kang [3], Junyi Li [3], Ying Wang [1], Qili Hu [4] and Xingcheng Yuan [1,2,*]

[1] Yibin Research Institute, Southwest Jiaotong University, Yibin 644000, China
[2] Engineering Research Center of Groundwater Pollution Control and Remediation, Ministry of Education of China, Beijing Normal University, Beijing 100875, China
[3] Observation and Research Station of Ecological Restoration for Chongqing Typical Mining Areas, Ministry of Natural Resources, Chongqing Institute of Geology and Mineral Resources, Chongqing 401120, China; cs9605@tom.com (S.C.)
[4] State Environmental Protection Key Laboratory of Synergetic Control and Joint Remediation for Soil & Water Pollution, College of Ecology and Environment, Chengdu University of Technology, Chengdu 610059, China; huqili@cdut.edu.cn
* Correspondence: yxc123456@my.swjtu.edu.cn; Tel.: +86-182-2324-2939

Abstract: Elucidating the hydrogeochemical processes and quality assessment of groundwater holds significant importance for its sustainable development. In this paper, 53 groundwater samples were collected from a typical agricultural area in the northeastern Chongqing municipality in SW China. The integration of multivariate statistical analysis, ion ratio analysis, geomodelling analysis, the entropy water quality index, health risks assessment, and sensitivity analysis was carried out to explore the hydrochemical processes and quality assessment of groundwater in this study. The statistical results reveal that the cationic concentrations followed the order of $Ca^{2+} > Mg^{2+} > Na^{+} > K^{+}$, while the anionic components were in the order of $HCO_3^{-} > SO_4^{2-} > NO_3^{-} > Cl^{-}$. Based on the Piper trilinear diagram, the hydrochemical types were shown as Ca-HCO_3 and Ca-Mg-HCO_3 types. Hierarchical cluster analysis indicated that the groundwater samples could be categorized into three groups. The hydrochemical compositions were primarily influenced by water–rock interactions (e.g., carbonate dissolution and silicate weathering). In terms of irrigation suitability, the sodium adsorption ratios (SARs) ranged from 0.05 to 1.82, and the electrical conductivity (EC) varied from 116 to 1094 μs/cm, indicating that most groundwater samples were suitable for irrigation. The entropy-weighted water quality index ranged from 15 to 94, suggesting that the groundwater samples were suitable for drinking purposes. Non-carcinogenic human health risks followed the order of children > adult females > adult males, within the average values of 0.30, 0.21, and 0.18, respectively. Sensitivity analysis showed that the parameters had the weight order of NO_3 > body weight (BW) > ingestion rate (IR) > exposure frequency (EF). Hence, we recommend prioritizing the management of areas with high salinity levels, while avoiding the excessive use of nitrogen fertilizers, raising awareness among local residents about safe groundwater, and providing robust support for the sustainable development of groundwater in typical agricultural areas.

Keywords: multivariate statistical analysis; water–rock interaction; groundwater quality; human health risk; sensitivity analysis; agricultural area

1. Introduction

Groundwater is an indispensable natural resource, which serves as the primary cornerstone for human survival and societal progress [1]. It plays a crucial and irreplaceable function in facilitating economic expansion and preserving ecological balance [2]. The conflict

involving regional water supplies and groundwater environmental quality has emerged as a crucial development issue [3]. As the greatest developing nation internationally, the issue of China's water resource utilization deserves in-depth research. Groundwater accounts for 15.4% of the total water supply, but 77.3% of groundwater is deemed unsuitable for direct consumption [4,5]. In regions characterized by using nitrogen fertilizer in intense agricultural activity, nitrate contamination in groundwater often reaches elevated levels that pose a significant human health risk [6]. Prolonged ingestion of groundwater with elevated nitrate levels may lead to the development of diseases such as methemoglobinemia and gastric cancer [7,8]. Excessive agricultural activities contribute to an obvious deterioration in water quality, thereby posing a threat to drinking water safety for residents [9]. Meanwhile, timely monitoring of agricultural irrigation water quality stands as a vital measure in ensuring the efficient evolution of agricultural production [10].

The application of geography information systems (GISs) has become prevalent in the domain of groundwater monitoring and management [11]. The spatial distribution of hydrochemical parameters is indicated using a GIS [12]. Multivariate statistical analysis is a method that simultaneously examines and interprets the relationships between multiple variables, identifying primary correlations, trends, and variations within a dataset and providing valuable insights into the overall characteristics of groundwater systems [13]. Due to the numerous groundwater chemical parameters and their intricate interrelationships, along with the issue of inconsistent units among these parameters, directly discussing their multidimensional relationships becomes challenging. The principal component analysis (PCA) is a method used to simplify the complex relationships between various hydrochemical parameters, identify patterns of underlying trends, similarities, or differences in groundwater influenced by environmental factors, and aid in the assessment of interdependencies between arguments [14]. The objective of hierarchical cluster analysis (HCA) is to establish a methodology for classifying individual groundwater samples into distinct water quality categories, irrespective of factors such as the lithology of the aquifer, geological formations, and water–rock interactions [15]. Given that the inhabitants of the research area heavily rely on farming, coupled with the direct influence of groundwater quality on soil permeability and crop yield, appropriate hydrogeochemical parameters were selected to evaluate the applicability of agricultural irrigation purposes, such as the sodium adsorption ratio (SAR) and solute sodium percentage (%Na) [16]. The weighted water quality index (EWQI) surpasses the water quality index (WQI) by incorporating weighted factors, allowing for a more objective and comprehensive evaluation of groundwater quality that considers the relative importance of individual parameters [17]. The human health risk (HHR) model systematically assesses potential health risks linked to exposure to contaminated groundwater, considering factors such as contaminant concentrations, exposure pathways, and toxicity to estimate the likelihood and severity of adverse health effects on individuals exposed to the contaminated groundwater [18].

Northeastern Chongqing is a typical agricultural area with intense anthropogenic activity in southwestern China. Meanwhile, nitrate contamination has been identified in regional hydrogeological mapping, along with approximately 17% of groundwater samples exceeding the corresponding standard (20 mg/L). Nevertheless, groundwater quality assessment and the associated HHR in northeastern Chongqing have received relatively limited focus. Hence, it is imperative to enhance the knowledge of the groundwater's chemistry, quality, and health risks to ensure the sustainable management of groundwater resources in northeastern Chongqing. The primary objectives of this study were to (1) explore the hydrogeochemical characteristics of major ions in the groundwater, and (2) assess the potable and irrigation quality of the groundwater and potential human health risks. The findings of this study offer essential insights into the groundwater characteristics of northeastern Chongqing and give a vital reference for assessing water quality in an agricultural region.

2. Materials

2.1. Study Area

The study area is situated in the northeastern Chongqing municipality (109°45′20″–109°58′40″ E and 31°10′21″–31°19′52″ N), where agriculture constitutes the primary economic industry (Figure 1). The climate is categorized as being of the mid-subtropical and sub-mountainous northern subtropical types. The annual average temperature and annual average rainfall are 18.4 °C and 1049.3 mm. The terrain consists of low–middle mountains, low hills, and hilly plains [19]. In terms of land use types, the study region is characterized by agricultural land, which encompasses 46% of the total land area, with a focus on tobacco, corn, and wheat cultivation (Figure 1c). According to the data of the National Bureau of Statistics of China in 2019 [20], the amount of nitrogen fertilizer applied in Chongqing reached 441,000 tons, accounting for 48.4% of the total agricultural fertilizer; therefore, nitrogen fertilizer has been widely used.

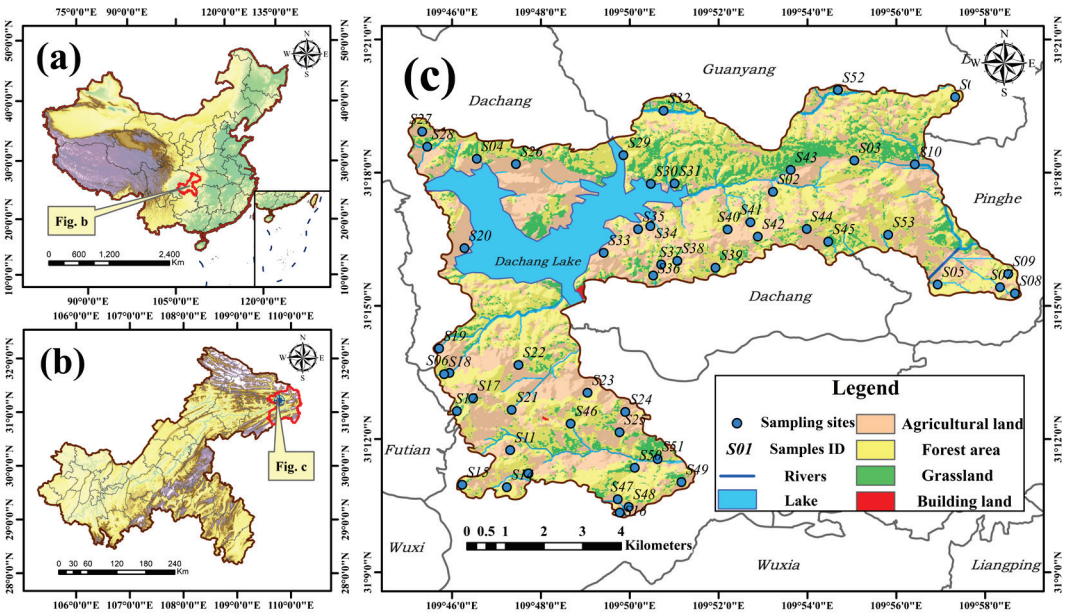

Figure 1. (**a**) Geographic location of Chongqing municipality in China. (**b**) The study area is located in the northeast of Chongqing municipality. (**c**) The distribution of groundwater sampling points and land use types in the study area, among which agricultural land occupies the largest proportion of 46%.

Geologically, the area is essentially located in the Daba Mountains. The strata consist of Triassic carbonate rocks (e.g., limestone and dolomite) and Permian clastic rocks (e.g., black shale, siliceous shale, interbedded gray-black thin–medium-bedded mudstone) [21,22]. Based on its hydrogeological characteristics, the groundwater is categorized into karst water (KW) in carbonate rocks and fissure water (FW) in clastic rocks [23,24]. KW is chiefly recharged via atmospheric precipitation, and surface water and is largely discharged in the form of springs. The flux in KW displays variation and ranges from 10 to 8640 m^3/d. FW, similarly recharged in the form of atmospheric precipitation and surface water, also receives lateral recharge from KW. The primary discharge mechanism for FW is via springs, while some groundwater flows through linear seepage into surface water systems. The flux is relatively stable, ranging from 250 to 1500 m^3/d.

2.2. Collection and Analysis of Groundwater Samples

In this paper, 53 groundwater samples were collected from different wells in January 2020 (Figure 1), and they were sent to the Chongqing Institute of Geology and Mineral Resources for experimental analysis in three days. The groundwater samples were all filtered

through a 0.45 μm filter and collected in sterilized plastic bottles (500 mL). Subsequently, all samples were hermetically sealed with parafilm, preserved in a 4 °C refrigerator and promptly transported for further experimental analysis.

The electrical conductivity (EC) and pH were determined using a portable multiparameter device (WTW-MultiLine Multi 3400i). The HCO_3^- concentration was determined using a Merck titration apparatus according to HNO_3^-. The remaining index testing methods were as follows: Na^+, K^+, Ca^{2+}, and Mg^{2+} concentrations were analyzed via ICP (ICP-OES) (Thermo Fisher ICAP-6300, Waltham, MA, USA); Cl^-, SO_4^{2-}, and NO_3^- concentrations were assessed using ion chromatography (ICS-2500, Dionex, Sunnyvale, CA, USA). The total dissolved solids (TDSs) were determined with the oven-drying method. The total hardness (TH) was titrated with EDTA-2Na.

The charge balance error (*CBE*) was utilized for accuracy confirmation (Equation (1)) [19]. The findings reveal that the *CBE* of major ions in the groundwater ranged from −2.7 to 5.4%, with an average of 1.4%.

$$CBE = \frac{\sum cations - \sum anions}{\sum cations + \sum anions} \times 100\% \quad (1)$$

3. Methods

3.1. Geochemical Modeling

Geochemical modeling with the PHREEQC (Version 3.3.9) program was utilized to determine the saturation indices (SIs) of minerals in the groundwater using Equation (2) [25]. When a mineral is in a supersaturated state, SI > 0; when a mineral is in an unsaturated state, SI < 0.

$$\mathrm{SI} = \log\left(\frac{\mathrm{IAP}}{\mathrm{K_{sp}}}\right) \quad (2)$$

3.2. Assessment of Groundwater Quality

Currently, there are a great number of indicators available for evaluating the appropriateness of groundwater in agricultural irrigation activities [26]. In this paper, essential indexes (the sodium adsorption ratio and sodium percentage) for irrigation groundwater quality were identified to assess the groundwater's suitability in agricultural applications.

The SAR [27] is calculated as follows in Equation (3).

$$\mathrm{SAR} = \frac{\mathrm{Na^+}}{\sqrt{\frac{(\mathrm{Ca^{2+}} + \mathrm{Mg^{2+}})}{2}}} \quad (3)$$

The SAR index is commonly utilized for assessing the quality of irrigation groundwater. The ion exchange process occurring in water yields a reduction in soil permeability, thereby impeding nutrient absorption by crops and consequently impacting crop growth [16].

The %Na [28] is calculated as follows in Equation (4).

$$\%\mathrm{Na} = \frac{\mathrm{Na^+} + \mathrm{K^+}}{(\mathrm{Ca^{2+}} + \mathrm{Mg^{2+}} + \mathrm{Na^+} + \mathrm{K^+})} \times 100\% \quad (4)$$

Ion concentration units were measured in Meq/L, and the suitability of groundwater irrigation was evaluated by plotting USSL and Wilcox diagrams.

Compared with the traditional WQI index, the EWQI gives a more objective evaluation [29]. By incorporating information entropy into the quantitative assessment of water quality indicators, the method mitigates the influence of human subjectivity on data analysis, thereby promoting objective quantification [30]. The calculation steps of the EWQI are outlined below:

(1) Determine the characteristic matrix X based on various parameters (Equation (5)).

$$X = \left(x_{ij}\right)_{m\times n} = \begin{bmatrix} x_{11} & \cdots & x_{1n} \\ \vdots & \ddots & \vdots \\ x_{m1} & \cdots & x_{mn} \end{bmatrix} \tag{5}$$

(2) In accordance with the natures of different parameters, determine the parameter types and normalize matrix X to derive the standardized matrix Y (Equations (6) and (7)).

$$y_{ij} = \begin{cases} \frac{x_{ij}-(x_{ij})_{\min}}{(x_{ij})_{\max}-(x_{ij})_{\min}} + 10^{-4} benefit \quad type \\ \frac{(x_{ij})_{\max}-x_{ij}}{(x_{ij})_{\max}-(x_{ij})_{\min}} + 10^{-4} cost \quad type \end{cases} \tag{6}$$

$$Y = \left(y_{ij}\right)_{m\times n} = \begin{bmatrix} y_{11} & \cdots & y_{1n} \\ \vdots & \ddots & \vdots \\ y_{m1} & \cdots & y_{mn} \end{bmatrix} \tag{7}$$

(3) Based on matrix Y, the information entropy (e_j) (Equations (8) and (9)) and entropy weight (w_j) (Equation (10)) are calculated.

$$P_{ij} = \frac{y_{ij}}{\sum_i^m y_{ij}} \tag{8}$$

$$e_j = -\frac{1}{\ln m}\sum_{i=1}^{m}\left(P_{ij}\times \ln P_{ij}\right) \tag{9}$$

$$w_j = \frac{1-e_j}{\sum_{i=1}^{n}\left(1-e_j\right)} \tag{10}$$

(4) Determine the qualitative rating scale (q_i) (Equation (11)) for each variable and calculate the EWQI (Equation (13)), where the pH is calculated separately (Equation (12)).

$$q_i = \frac{C_j}{S_j}\times 100 \tag{11}$$

$$q_{\mathrm{pH}} = \frac{\mathrm{pH}-7}{S_{\mathrm{pH}}-7}\times 100 \tag{12}$$

$$\mathrm{EWQI} = \sum_{j=1}^{m}\left(w_j \times q_j\right) \tag{13}$$

where m is the number of water samples, n is the evaluated hydrochemical indicator; P_{ij} is the jth parameter value of sample i; q_j is the quantitative rating scale of the hydrochemical parameter classification, calculated from the concentration C_j of hydrochemical parameter j; and S_j is the permissible limit from the Chinese standard for groundwater quality [31] for parameter j. The EWQI levels are clarified based on Table S1 [32].

3.3. Human Health Risk Assessment

Previous research has shown that the human health risk is mostly linked to the oral intake of groundwater [33]. Considering the concentrated nitrate concentration in the study area, this paper predominantly focused on evaluating the human non-carcinogenic health risks linked to oral intake [34]. The main parameters for the HHR model are presented in Table S2.

(1) The chronic daily intake (CDI) of contaminated groundwater ingested directly was calculated based on various physicochemical parameters [35] (Equation (14)).

$$\mathrm{CDI} = \frac{CW \times IR \times EF \times ED}{BW \times AT} \tag{14}$$

where *BW* is the average body weight; *AT* represents the average exposure time; *CW* is the groundwater contaminant concentration; *IR* is the daily oral ingestion rate; *EF* indicates the exposure frequency; and *ED* denotes the exposure duration.

(2) The human health hazard quotient (HQ_i) of contaminated groundwater is determined by utilizing Equation (15).

$$\mathrm{HQ}_i = \frac{\mathrm{CDI}}{\mathrm{RfD}_i} \tag{15}$$

where RfD_i represents the reference dose.

The hazard index (HI) is calculated as follows in Equation (16).

$$\mathrm{HI} = \mathrm{HQ}_1 + \mathrm{HQ}_2 + \cdots + \mathrm{HQ}_i \tag{16}$$

An HQ or HI of > 1 indicates pollutants may exist that pose potential harm to human health. On the contrary, if the HQ or HI is < 1, there are no hazards.

4. Results

4.1. Spatial Characteristics of Hydrochemistry

The spatial characteristics of hydrochemistry are displayed in Figure 2. The concentration of K^+ was relatively limited and prevalently dispersed in the southeastern area. Na^+ and Cl^- were predominantly concentrated in the southwest and eastern regions, indicating the possibility of a similar source. Ca^{2+} and HCO_3^- were predominantly distributed in the eastern and northwestern regions. Their extensive distribution and higher concentrations demonstrated that Ca^{2+} and HCO_3^- were the major controlling ions within the study area and originated from the same source. Mg^{2+} was primarily located in the southwestern, central, and eastern areas. SO_4^{2-} was concentrated in the southwestern region. The limited distribution characteristics and considerable differences in concentration expressed that sulfides within local coal-bearing seams may have exerted an impact on the concentration of SO_4^{2-}. The presence of NO_3^- serves as a toxicological indicator for human health in groundwater, and prolonged consumption of high levels of NO_3^- in groundwater might lead to severe harm to humans [36]. The NO_3^- was primarily in the southwest and east regions, suggesting that groundwater management should be significantly concentrated in those regions.

4.2. Hydrochemical Facies

Based on various hydrochemical parameters of groundwater samples, hierarchical cluster analysis (HCA) can be applied for hydrochemical classification [37]. The samples were associated and grouped using the average Euclidean distance, and a pedigree dendrogram was drawn using hierarchical cluster analysis [38,39]. Three groups (G1, G2, and G3) of 53 groundwater samples were recognized (Figure 3). The statistical analysis of hydrogeochemical components constitutes a general analytical method for characterizing the chemical composition of groundwater [40]. In this paper, box plots depict the basic characteristics of the groundwater chemical parameters (Figure 4; Table 1).

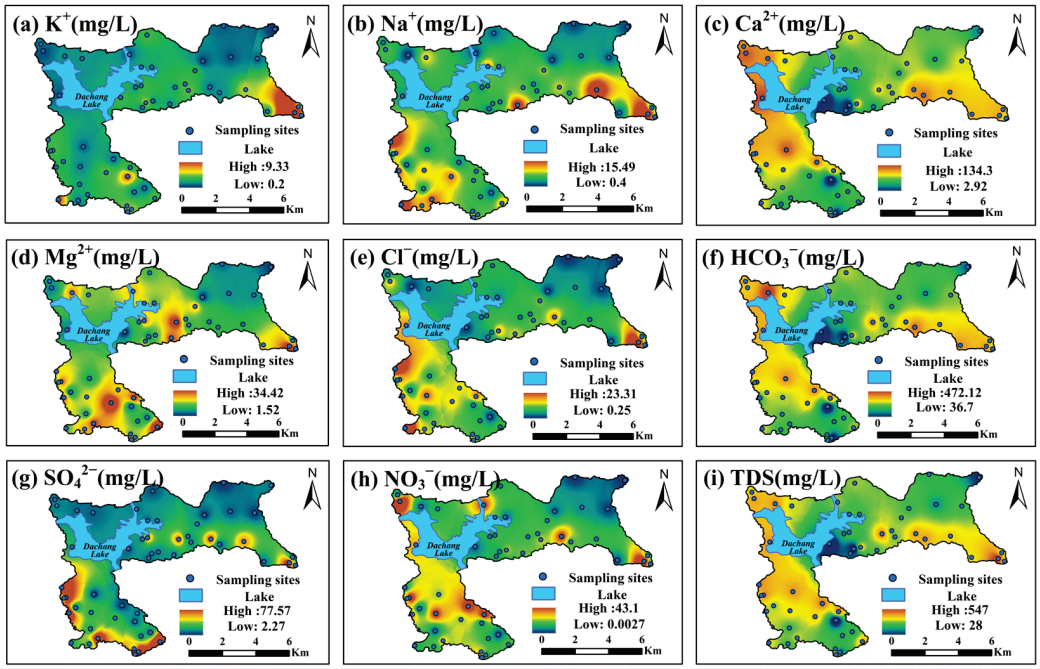

Figure 2. Distribution characteristics of different hydrochemical indicators in northeastern Chongqing municipality, China. (**a**) K^+, (**b**) Na^+, (**c**) Ca^{2+}, (**d**) Mg^{2+}, (**e**) Cl^-, (**f**) HCO_3^-, (**g**) SO_4^{2-}, (**h**) NO_3^-, and (**i**) TDS.

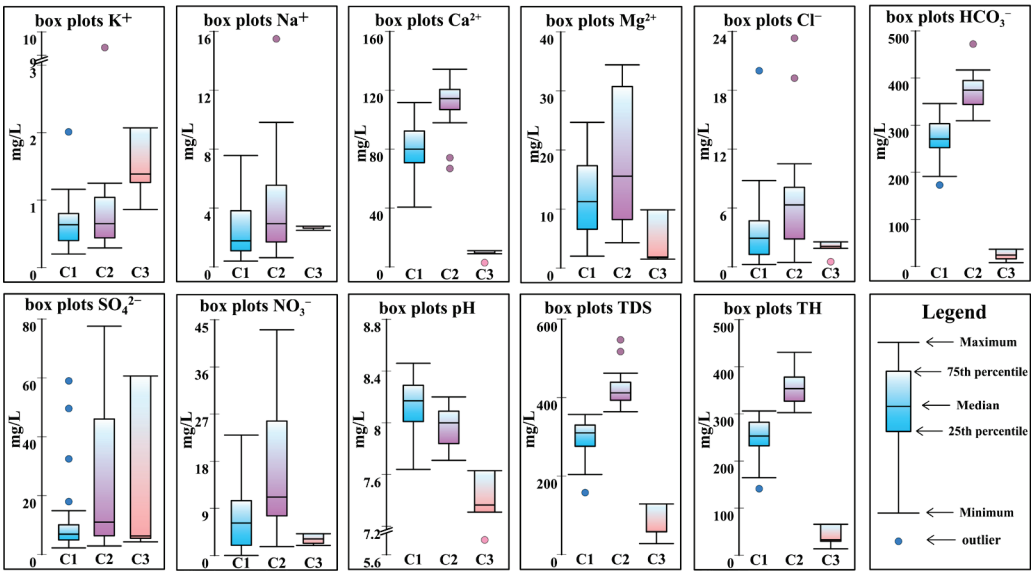

Figure 3. Box plots of groundwater chemical compositions in northeastern Chongqing municipality.

The number of G1 groundwater samples was 30. The pH values ranged from 7.64 to 8.46, with an average of 8.14, emphasizing a weakly alkaline nature. TDS is a crucial parameter in water chemistry analysis [42]. The values ranged from 158 to 357 mg·L^{-1}, with an average of 296 mg·L^{-1}, and were categorized as freshwater. The TH was typically proportional to the TDS and ranged from 141.15 to 306.26 mg·L^{-1}, with a mean of 248.20 mg·L^{-1}. The bulk of the samples were moderately hard water (150–300 mg·L^{-1}) and hard water (300–450 mg·L^{-1}). The cations principally included Ca^{2+} and Mg^{2+}, followed by Na^+ and K^+. The concentration of Ca^{2+} ranged from 40.63 to 111.68 mg·L^{-1}, with a mean of 79.95 mg·L^{-1}. The concentration of Mg^{2+} ranged from 2.02 to 24.68 mg·L^{-1}, with a mean of 11.72 mg·L^{-1}. In addition, anions mainly

included HCO_3^-, followed by SO_4^{2-} and NO_3^-. The concentration of HCO_3^- ranged from 172.98 to 345.95 mg·L^{-1}, with a mean of 272.42 mg·L^{-1}. The concentrations of SO_4^{2-} and NO_3^- ranged from 2.27 to 58.99 and 0.0027 to 22.99 mg·L^{-1}, with means of 11.05 and 6.94 mg·L^{-1}, respectively. The order of cation components followed the order of Ca^{2+} > Mg^{2+} > Na^+ > K^+, while the anionic components ranked as HCO_3^- > SO_4^{2-} > NO_3^- > Cl^-. The major anions and cations in G1 samples were Ca^{2+} and HCO_3^-, indicative of the Ca-HCO_3 hydrochemical type (Figure 5).

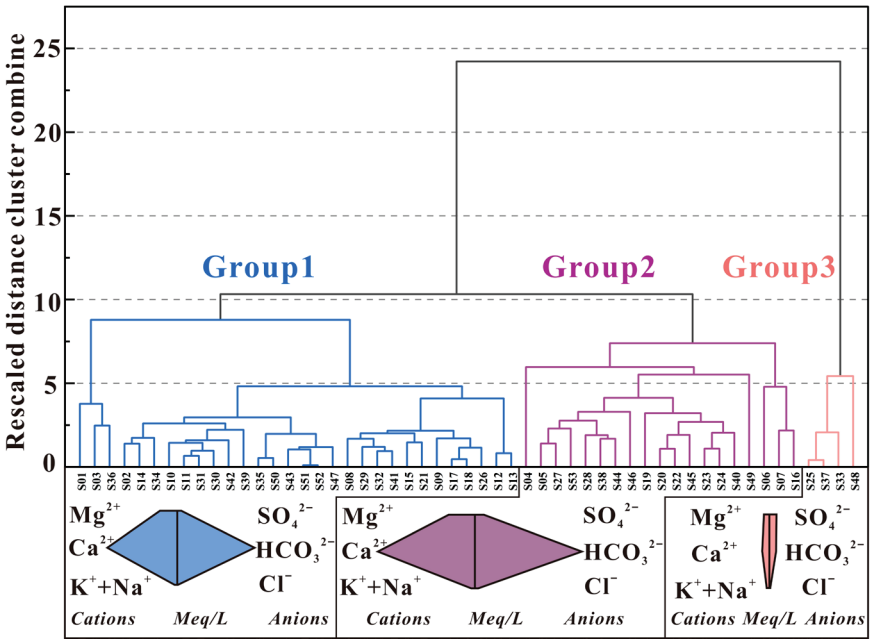

Figure 4. The dendrogram is used to depict the classification of water samples, while major ion concentrations are illustrated with the stiff diagram.

Table 1. Characteristics of diverse chemical indicators in the groundwater of northeastern Chongqing municipality, China.

Indicator	Maximum	Minimum	Mean	Standard Deviation	Coefficient of Variation (%)	Standard	Rate (%)
pH	8.46	5.76	7.99	0.39	5	6.5–8.5	0
TDS	547	28	323.96	103.89	32	1000	0
TH	430.74	13.54	270.26	90.89	34	450	0
EC	1094	116	659.31	192.71	29	-	-
K^+	9.33	0.2	0.90	1.23	137	-	-
Na^+	15.49	0.4	3.15	2.71	86	200	0
Ca^{2+}	134.3	2.92	85.95	30.95	36	200	0
Mg^{2+}	34.42	1.52	13.43	9.11	68	50	0
Cl^-	23.31	0.25	4.57	4.81	105	250	0
HCO_3^-	472.12	36.7	290.86	97.94	34	-	-
SO_4^{2-}	77.57	2.27	16.55	19.34	117	250	0
NO_3^-	43.1	0.0027	10.09	10.09	100	20	17

Notes: pH has no dimension, EC unit is μs/cm, TH–NO_3^- unit is mg/L; the standard (STD) derived from Chinese standard for groundwater quality [31] and World Health Organization [41]; rate is the proportion that exceeds the standard level.

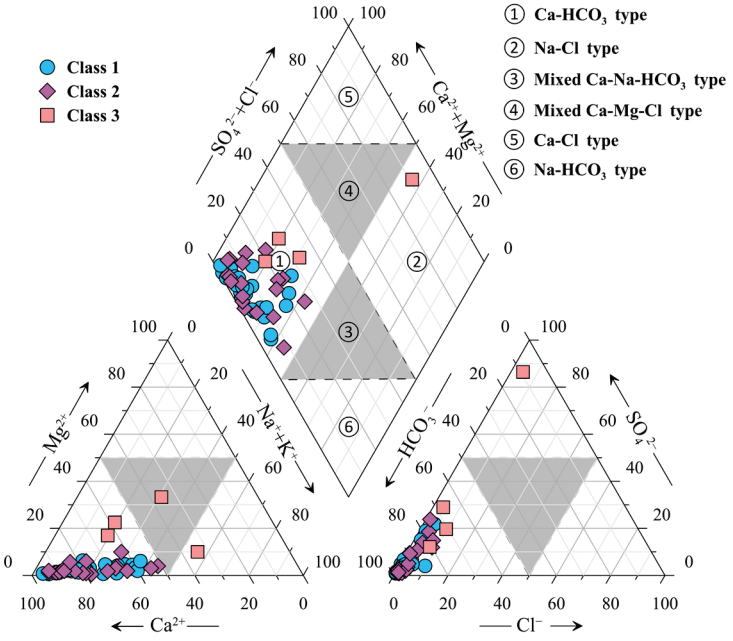

Figure 5. The hydrochemical types of the three groups (G1, G2, and G3) of groundwater in northeastern Chongqing were determined using a Piper trilinear diagram [43].

The number of G2 groundwater samples was 19. The pH values ranged between 7.71 and 8.20, with an average of 7.96, and paralleled those of G1. G2 had the highest TDS values, which ranged from 364 to 547 mg·L^{-1}, with an average of 422 mg·L^{-1}, and was classified as freshwater. Analogous to G1, the TH ranged from 302.61 to 430.74 mg·L^{-1}, with a mean of 354.37 mg·L^{-1}. The cations principally included Ca^{2+} and Mg^{2+}, followed by Na^+ and K^+. The anions mainly included HCO_3^-, followed by SO_4^{2-} and NO_3^-. The distributions of Na^+ and Cl^- were approximated, ranging from 0.63 to 15.49 and 0.46 to 23.31 mg·L^{-1}, with means of 4.21 and 6.93 mg·L^{-1}. Furthermore, the concentrations of Ca^{2+} and HCO_3^- ranged from 66.88 to 134.30 and 309.32 to 472.12 mg·L^{-1}, with means of 111.79 and 376.26 mg·L^{-1}. The order of cation components followed the order of Ca^{2+} > Mg^{2+} > Na^+ > K^+, while the anionic components ranked as HCO_3^- > SO_4^{2-} > NO_3^- > Cl^-. The major anion and cation in G2 samples were Ca^{2+} and HCO_3^-, indicative of the Ca-HCO_3 hydrochemical type (Figure 5).

The number of G3 samples was four. The pH values ranged from 7.63 to 5.76, with an average of 7.03. These samples had the lowest TDS values (28–129 mg·L^{-1}, with an average of 69 mg·L^{-1}) and were classified as freshwater. The TH ranged from 13.54 to 65.63 mg·L^{-1}, with a mean of 36.20 mg·L^{-1}, indicating extremely soft water throughout (TH < 75 mg·L^{-1}). The cations principally included Ca^{2+}, followed by Mg^{2+}. The anions principally comprised HCO_3^-, followed by SO_4^{2-}. The concentration of Ca^{2+} ranged from 2.92 to 11.04 mg·L^{-1}, with a mean of 8.23 mg·L^{-1}. The concentration of HCO_3^- ranged from 8.14 to 36.70 mg·L^{-1}, with a mean of 23.42 mg·L^{-1}. The order of cation components followed the order of Ca^{2+} > Mg^{2+} > Na^+ > K^+, while the anionic components ranked as HCO_3^- > SO_4^{2-} > NO_3^- > Cl^-. The major anion and cation in G2 samples were Ca^{2+} and HCO_3^-, indicative of Ca-HCO_3, Ca-Mg-SO_4, and Ca-Mg-Na-SO_4-HCO_3 hydrochemical types (Figure 5).

In summary, G1 groundwater samples accounted for 56.6% in total, followed by 35.85% for G2, and only 7.55% for G3. It is noted that the TDS and TH concentrations followed the order of G2 > G1 > G3. The higher TDS and TH concentrations were produced by longer flowing times and paths. The differences in the hydrochemical components of the three types of groundwater were mainly caused by different hydrogeochemical processes.

5. Discussion

5.1. Main Factors Dominating Hydrochemistry

The hierarchical cluster analysis showed that the groundwater was controlled by different effects in the study area. Among them, G1 and G2 groundwater samples exhibited higher TDS concentrations, with G2 showing the highest concentrations of NO_3^- and Cl^-. G3 samples, on the other hand, had the shortest runoff path and lower concentrations of various ions. However, the pivotal drivers behind the hydrochemical and geochemical variations within the region remain unclear, requiring further discussion.

5.1.1. Correlations between Hydrochemical Parameters

To investigate the relationship between each parameter and reduce the computational complexity, correlation analysis and PCA were combined to analyze the raw groundwater sample data [44]. The TDS and TH were typically regulated by major ions present in the groundwater, resulting in strong correlations between these parameters and major ions (Ca^{2+} and HCO_3^-) (Figure 6a) [45]. The high correlation coefficient between Ca^{2+} and HCO_3^- (0.934) suggests that they may be controlled by carbonate minerals.

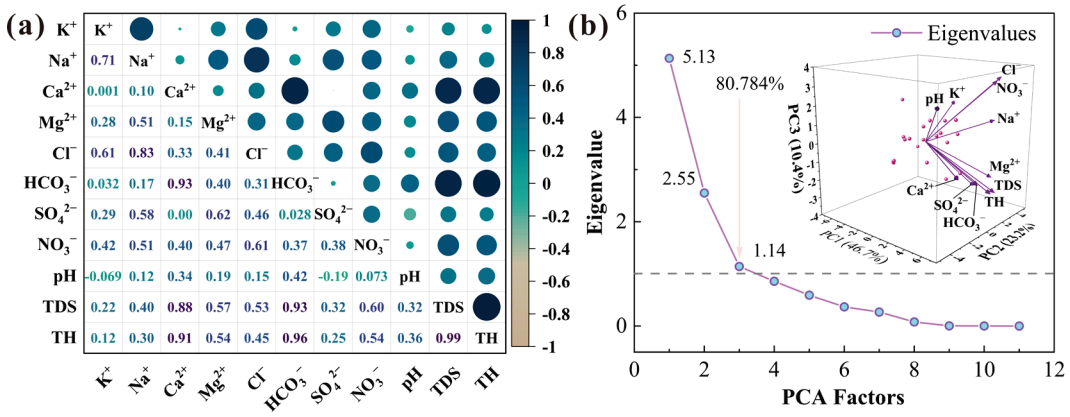

Figure 6. (**a**) Correlation analysis is primarily used to investigate the interrelationships and mutual influences among different parameters, aiming to ascertain whether there are associations or correlations between them. (**b**) The Scree plot illustrates the eigenvalues and cumulative variance, while the biplot (3D) depicts the relationships between various indicators.

PCA aims to decrease the dimensionality of multivariate data by extracting complex information and transforming it into a simplified dataset, thereby revealing the underlying structure of the original data [46]. The Kaiser–Meyer–Olkin (KMO) test is a method to assess the statistical significance of a dataset, and a value above 0.5 indicates acceptability, which helps determine the suitability of the research for PCA [47]. The KMO value (0.65) in this study suggested the PCA conclusions were statistically meaningful [48]. The eigenvalues and cumulative variances in PCA provide pivotal information about the data structure and distribution. Based on the Kaiser rule, principal components (PCs) with eigenvalues of greater than one can be retained, which helps to determine the number of PCs to achieve the purpose of data dimensionality reduction [49]. In this research, eigenvalues exceeding 1 were observed for three PCs (5.13, 2.55, and 1.14), which represented 80.784% of the variance (Table 2) (Figure 6b). Regarding the loading values, a value above 7.5 is considered strong, 5–7.5 is moderate, and 0.3–0.5 is weak [50]. PC1 accounted for 48.462% and exhibited strong loadings of Ca (0.746), Cl (0.729), HCO_3 (0.802), TDS (0.947), and TH (0.91), suggesting significant influences from natural processes such as mineral dissolution and precipitation (carbonate, silicate, or evaporite). Moreover, the notably positive NO_3 load (0.717) indicated the elevated NO_3 concentration in the study area. PC2 (23.072%) displayed relatively high loadings of Na (0.646) and K (0.633), highlighting that they have similar sources. The lower loadings of PC3 (9.25%) were attributed to the limited contribution of

this subset of samples to hydrochemical evolution, primarily because of their shorter flow path and the weaker geochemical interactions with the surrounding rock.

Table 2. Matrix of components for principal component analysis; each column contains the loading values for different indices, and the bold values indicate that the values are higher.

Variable Factor	PC1	PC2	PC3
Cumulative (%)	48.462	23.072	9.250
K	0.426	**0.633**	0.426
Na	0.64	**0.646**	0.23
Ca	**0.746**	−0.584	0.064
Mg	0.666	0.272	−0.424
Cl	**0.729**	0.455	0.301
HCO_3	**0.802**	−0.561	−0.016
SO_4	0.46	0.583	−0.545
NO_3	**0.717**	0.242	0.016
pH	0.339	−0.397	0.432
TDS	**0.947**	−0.28	−0.102
TH	**0.91**	−0.386	−0.12

5.1.2. Ion Ratio Analysis

In the analysis of the groundwater's chemical evolution, different ion ratios served as valuable indicators to enhance our understanding of the groundwater. The Gibbs diagrams were instrumental in deciding the geochemical processes affecting the groundwater composition, and the end-member diagrams assisted in determining the types of water–rock interactions, while other ion ratios helped clarify the principal sources of ions [17].

Three primary mechanisms govern the processes that hydrochemical components of groundwater undergo, as classified using Gibbs diagrams: precipitation, water–rock interactions, and evaporation [51]. Water–rock interactions describe chemical exchanges between groundwater and surrounding rocks, impacting the composition of the groundwater. All samples fell within the zone of water–rock interactions in this study (Figure 7a,b), indicating that the groundwater chemistry was primarily influenced by water–rock interactions and was not significantly affected by atmospheric precipitation or evaporation.

The primary types of water–rock interactions are silicate weathering, mineral evaporation, and carbonate dissolution, which can be determined by the Ca^{2+}/Na^{+}, and HCO_3^{-}/Na^{+}, Ca^{2+}/Na^{+}, and Mg^{2+}/Na^{+} ratios [52]. The G1 and G2 samples were closer to the carbonate dissolution area, indicating that carbonate dissolution dominated the water–rock interactions (Figure 7c,d). Additionally, G3 samples were closer to the silicate dissolution area, suggesting that silicate weathering dominated the water–rock interactions in G3 samples.

The G1 samples were not concentrated near the cation exchange reaction line, suggesting that the cation exchange reaction was not substantial (Figure 8a). In the Na^{+}/Cl^{-} ratio analysis, the majority of samples diverged from the $y = x$ line, signifying the improbability of halite dissolution (Figure 9a) [53]. In the Ca^{2+} vs. SO_4^{2-} diagram, the samples fell below the $y = x$ line, illustrating that the higher Ca^{2+} content contradicted the likelihood of gypsum dissolution (Figure 9c) [54]. Furthermore, the Ca^{2+} and HCO_3^{-} ratio could serve as an indicator of the origin of carbonate rocks. The points were distributed along the $y = x$ and $y = 2x$ dissolution lines, expressing that the Ca^{2+} and HCO_3^{-} primarily originated from calcite dissolution (Figure 9d) [17].

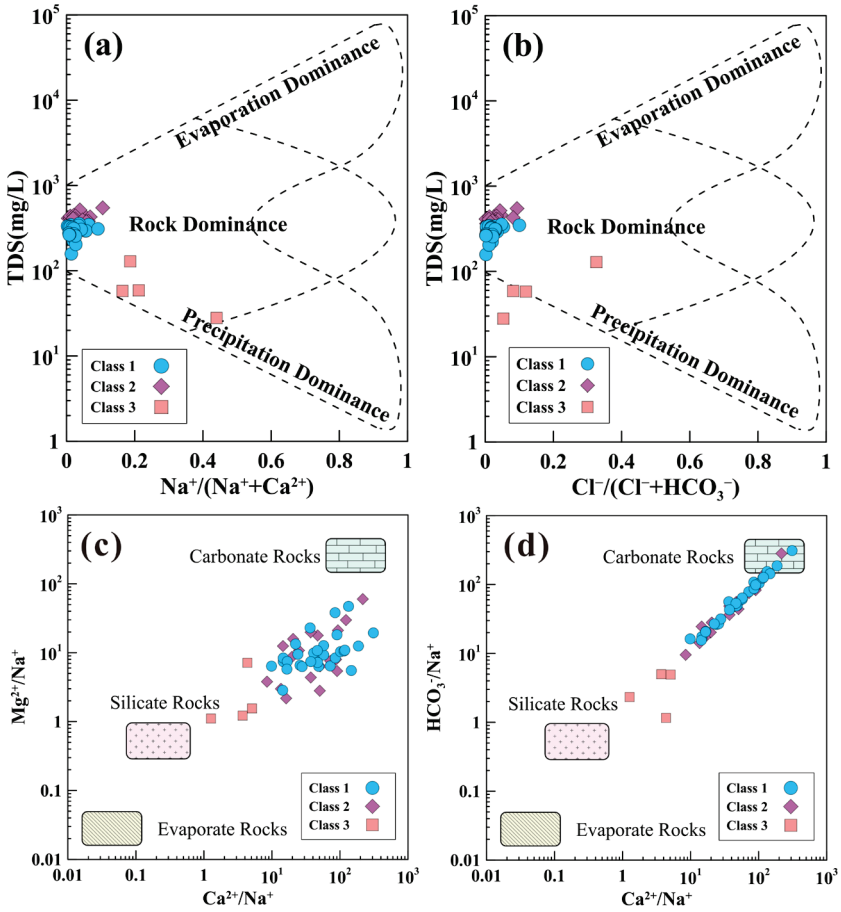

Figure 7. Gibbs distributions and end-member diagrams of groundwater samples. (**a**) $Na^+/(Na^+ + Ca^{2+})$ vs. TDS, (**b**) $Cl^-/(Cl^- + HCO_3^-)$ vs. TDS, (**c**) Ca^{2+}/Na^+ vs. Mg^{2+}/Na^+, and (**d**) Ca^{2+}/Na^+ vs. HCO_3^-/Na^+.

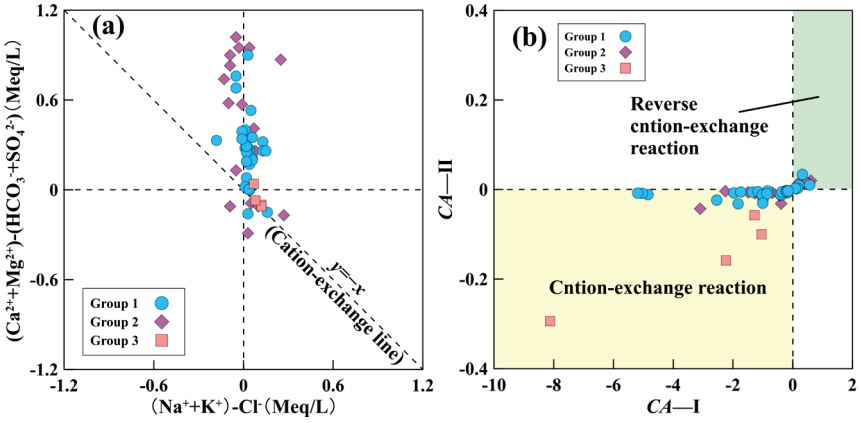

Figure 8. Diagrams of cation exchange reactions. (**a**) $(Na^+ + K^+ - Cl^-)$ vs. $(Ca^{2+} + Mg^{2+} - HCO_3^- - SO_4^{2-})$; (**b**) *CA*–I vs. *CA*–II.

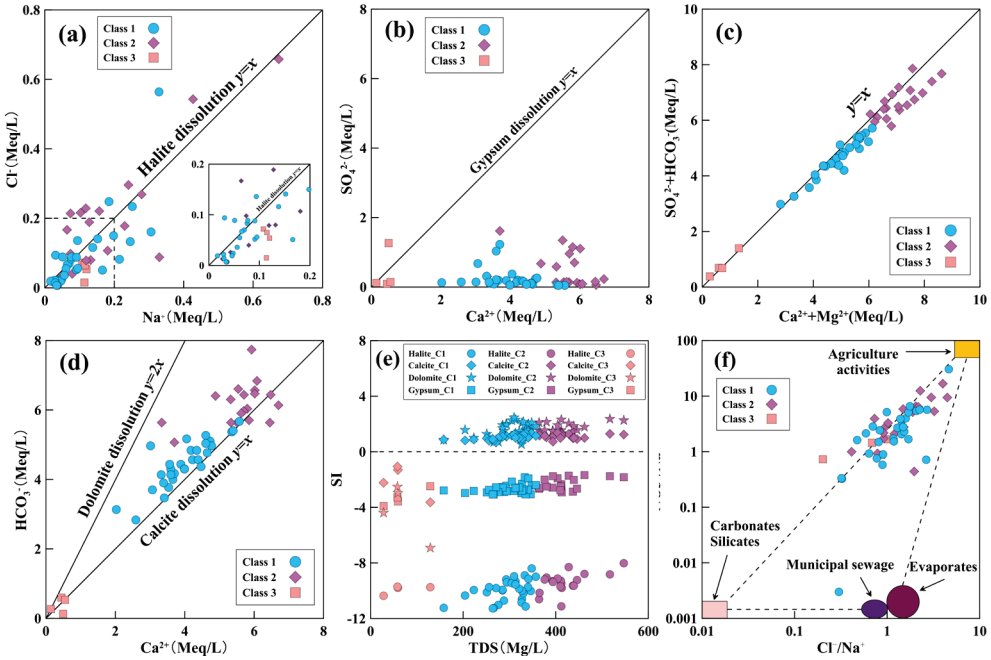

Figure 9. Ion ratio diagrams. (**a**) Na^+ vs. Cl^-, (**b**) Ca^{2+} + Mg^{2+} vs. $SO_4{}^{2-}$ + $HCO_3{}^-$, (**c**) Ca^{2+} vs. $SO_4{}^{2-}$, and (**d**) Ca^{2+} vs. $HCO_3{}^-$. (**e**) Scatter plot of mineral saturation indices and TDS values for groundwater. (**f**) Cl^-/Na^+ vs. $NO_3{}^-/Na^+$ to determine the $NO_3{}^-$ pollution sources for groundwater in northeastern Chongqing municipality.

In G2, most of the groundwater samples appeared near the $x = 0$ or $y = 0$ lines, indicating the reaction was insignificant (Figure 8b) [55]. Meanwhile, the rate of Na^+/Cl^- proved that halite dissolution was not the predominant process in G2 samples (Figure 9a). Most of the points (73.7%) fall below the $y = x$ line in Figure 9b, displaying that Ca^{2+} and Mg^{2+} were primarily derived from carbonate mineral dissolution. In the Ca^{2+} vs. $HCO_3{}^-$ diagram, the G2 samples cluster between the dolomite and calcite dissolution line, providing an explanation for the presence of calcite dissolution (Figure 9d).

In G3 samples, the presence of cation exchange reactions was substantiated by the ratios of $Na^+ + K^+ - Cl^-$ vs. $(Ca^{2+} + Mg^{2+}) - (HCO_3{}^- + SO_4{}^{2-})$ (Figure 8a). *CAI*−I ($[Cl^- - (Na^+ + K^+)]/Cl^-$) and *CAI*−II ($[Cl^- - (Na^+ + K^+)]/[HCO_3{}^- + SO_4{}^{2-} + CO_3{}^{2-} + NO_3{}^-]$) values can similarly serve to determine whether ion exchange has occurred in groundwater. Values of greater or less than zero indicate the occurrence of ion exchange; conversely, ion exchange is absent. In G3 samples, the *CAI*−I and *CAI*−II values were below zero, hence implying the existence of a cation exchange process (Figure 8b). The G3 samples were spread on the $y = x$ line, illustrating them being predominantly controlled by both carbonate dissolution and silicate weathering (Figure 9c).

To summarize, G1 and G2 groundwater samples were predominantly influenced by the dissolution of calcite minerals. G3 samples displayed evident cation exchange processes and were controlled by silicate weathering. Furthermore, the low ion contents showed that the runoff path of the G3 samples was relatively short, and the water–rock interactions were also limited.

5.1.3. Saturation Indices

The saturation index (SI) is a geochemical measure indicating whether a solution is oversaturated or undersaturated with respect to specific minerals, which provides vital insights into the potential for mineral precipitation or dissolution in the studied environment. On the other hand, the SI holds significant worth in comprehending the impacts on water quality. The systematic assessment of mineral saturation indices not only aids in the identification of potential water quality issues, such as changes resulting

from dissolution or precipitation processes but also establishes a scientific foundation for sustainable groundwater utilization and management.

The groundwater saturation index (SI) was primarily quantitatively determined through the use of PHREEQC (Figure 9e) [56]. In G1, the SI of calcite and dolomite exceeded 0, ranging from 0.68 to 1.33 and 0.53 to 2.46, with averages of 1.05 and 1.55, manifesting a state of supersaturation (Equations (17) and (18)). Inversely, gypsum and halite had concentrations of less than 0, with saturation coefficients ranging from −3.07 to −1.83 and −11.27 to −8.39, indicating that both minerals exist in a dissolved state while possessing some dissolution ability (Equations (19) and (20)).

The behavior of G2 samples was consistent with that of G1, where the ranges for calcite and dolomite were 0.73–1.36 and 1.2–2.36, respectively, and for gypsum and halite, the ranges were −2.92 to −1.68 and −11.12 to −8.02, respectively.

In G3 groundwater samples, the SI values of four minerals were all less than zero. The ranges of values for these coefficients were −3.63 to −1.06, −6.92 to −2.52, −3.91 to −2.48, and −10.36 to −9.71, demonstrating that the minerals in this type of sample were dissolved while also exhibiting some dissolution ability.

$$CaMg(CO_3)_2\ (\text{Dolomite}) + 2H^+ \longleftrightarrow Ca^{2+} + Mg^{2+} + 2HCO_3^- \quad (17)$$

$$CaCO_3\ (\text{Calcite}) + H^+ \longleftrightarrow Ca^{2+} + HCO_3^- \quad (18)$$

$$CaSO_4 \cdot 2H_2O\ (\text{Gypsum}) \longleftrightarrow Ca^{2+} + SO_4^{2-} + 2H_2O \quad (19)$$

$$NaCl\ (\text{Halite}) \longleftrightarrow Na^+ + Cl^- \quad (20)$$

Nitrate (NO_3^-) contamination is influenced by an array of artificial inputs [57]. Most of the points were situated in the upper right corner, illustrating a significant influence of agricultural activities on NO_3^- concentrations in the study area (Figure 9f). This conclusion is consistent with the current predominant use of land by residents.

5.2. Groundwater Suitability for Irrigation

Due to the heavy reliance on agriculture in northeastern Chongqing, appraising groundwater quality for agricultural irrigation purposes is imperative [16]. In general, increased groundwater salinity has a significant impact on soil salinization and crop yields. When hypersaline groundwater is used for irrigation, the soil forms crusts and hardens, thereby inhibiting crop growth [36]. The exchange of sodium ions in groundwater induces a reduction in soil permeability, adversely affecting nutrient absorption by crops [28].

The sodium absorption ratio (SAR) assesses the potential alkalinity hazard to the soil by comparing the concentrations of sodium, calcium, and magnesium in groundwater. Electrical conductivity (EC) is a crucial parameter in groundwater irrigation quality assessment, reflecting groundwater salinity [58]. The calculated SAR ranged from 0.05 to 1.82, with an average value of 0.49. The samples exhibited a range of EC values from 116 to 1094 μs/cm, with an average value of 674.9 μs/cm. The USSL and Wilcox diagrams serve as crucial tools in assessing the suitability of groundwater for irrigation, as they can depict the harmful effects of alkalinity and sodium in groundwater (Figure 10) [28].

The USSL diagram is partitioned into 16 water quality zones based on the appropriateness of the water for irrigation purposes (Figure 10a). Medium and low hazards indicate suitability for most types of soil in groundwater irrigation; a high hazard implies that certain management or treatment is needed before it is suitable for agricultural use; Very a high hazard indicates that the groundwater in this area is not suitable for agricultural irrigation. Table S3 shows the standard EC values. G1 groundwater samples were distributed in areas with medium salinity and low sodium hazards (C2S1), demonstrating that this portion of water is suitable for irrigation purposes on most soil types. G2 groundwater samples (approximately 32.1% of the total) were primarily deployed in regions with high

salinity and low sodium hazards (C3S1). High-salinity groundwater directly affects the absorption of water by plant roots. When soil permeability is feeble, the exchange of water and gas is influenced, leading to crop death [59]. Therefore, these samples were unsuitable for the irrigation of crops grown in poorly drained soils with restricted permeability. G3 samples were predominantly located in the safety zone (C1S1), showing that all water samples from this part of the site are suitable for irrigation purposes.

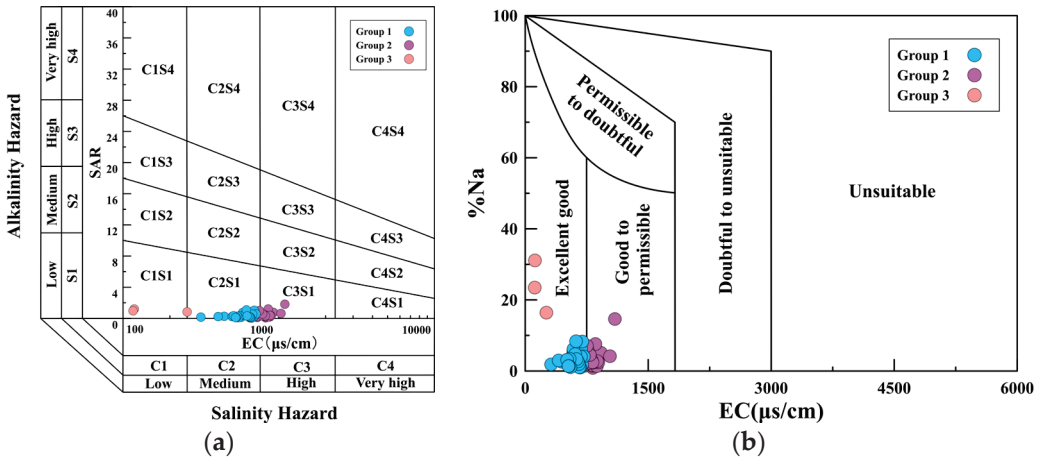

Figure 10. (**a**) The USSL diagram classifies groundwater samples into 16 categories based on alkalinity and salinity, subsequently determining their suitability for irrigation in the region; (**b**) the Wilcox diagram illustrates the groundwater irrigation quality based on EC and %Na.

The Wilcox diagram displays that the G1 groundwater samples were principally scattered in an excellent area, while the G2 samples were distributed in a good area (Figure 10b). G3 samples were distributed in an excellent area, but the %Na contents were slightly higher. Based on the correlation between conductivity and sodium content, it can be concluded that there are no irrigation groundwater quality hazards resulting from sodium exchange in the three types of samples within the study area.

The G1 groundwater samples were classified into areas of medium salt hazard and low sodium hazard (C2S1), while G2 samples were situated in regions with high salt hazard and low sodium hazard (C3S1). Hence, the salinity of groundwater should be managed with a focused approach, and sound water conservation facilities can be established to exclude soil salinity using natural water circulation. Measures such as the application of phosphogypsum to filter salts can be implemented if necessary to increase the active calcium cation content in the soil, mitigate crop damage caused by Na_2CO_3 and $NaHCO_3$, and lower pH.

5.3. Groundwater Suitability for Drinking

Given that nitrate contamination has been identified in regional hydrogeological mapping and approximately 17% of groundwater samples exceeding 20 mg/L, the EWQI was used to evaluate the suitability of the groundwater quality in the study area.

The EWQI is an efficient technique for the objective appraisal of drinking groundwater quality [17]. The evaluation results ranged from 15 to 94, with a mean value of 73. The groundwater quality varied from excellent (less than 50) to good (50–100). The groundwater quality index and TDS values were predominantly situated within the excellent and good zones (Figure 11a). The G1 and G2 water samples fell within the range of 50–100, while most of the G3 water samples were between 0 and 50. This indicates that the three groups of samples all conform to drinking water specifications.

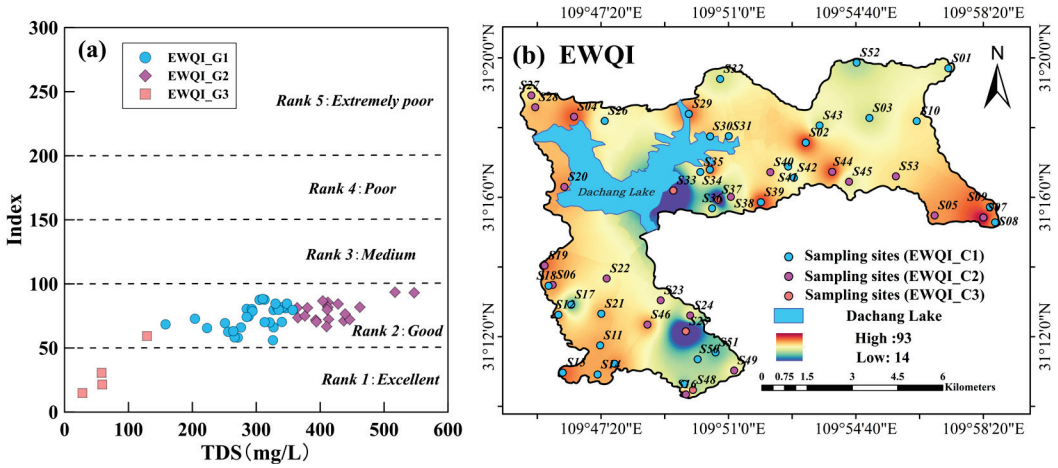

Figure 11. (**a**) The quality of drinking water is revealed through the use of EWQI and TDS; (**b**) the distribution of EWQIs among the three groups of samples within the study area.

The EWQI was widely distributed in a patchy pattern with higher water quality in the central region and relatively elevated water quality index values in both the western and eastern regions (Figure 11b). From the sample classification perspective, the G1 and G2 groundwater samples exhibit a more extensive distribution, with most samples located in relatively high EWQI regions, while all G3 samples are allocated in excellent EWQI locations. In a nutshell, the groundwater samples analyzed basically meet drinking water quality standards in this study.

5.4. Non-Carcinogenic Human Health Risks

The objective of this section is to quantify the potential impact of non-carcinogenic pollutants, specifically nitrates, on human health and to explore the sensitivity of different parameters.

Prolonged consumption of nitrate-contaminated groundwater may result in methemoglobinemia, leukemia, gastrointestinal cancer, and other illnesses [60]. Given the widespread distribution of NO_3^- in the area, along with approximately 17% of groundwater samples exceeding the corresponding standard (20 mg/L) for nitrate concentration (Figure 2h; Table 1), there is a potential for adverse effects on three different groups: children (CD), adult females (AFs), and adult males (AMs) [61] (Table S4).

The G1 groundwater samples' nitrate hazard quotient ($HQ_{Nitrate}$) values for the three groups had variations of 0.00–1.26 (mean = 0.36), 0.00–0.89 (mean = 0.25), and 0.00–0.76 (mean = 0.21). The G2 samples' $HQ_{Nitrate}$ value ranged from 0.06 to 0.67 with a mean of 0.24 for CD, 0.04 to 0.48 with a mean of 0.17 for AF, and 0.03 to 0.40 with a mean of 0.14 for AM. G3 samples' $HQ_{Nitrate}$ values ranged from 0.01 to 0.22 with a mean of 0.10 for CD, 0.01 to 0.16 with a mean of 0.07 for AF, and 0.01 to 0.13 with a mean of 0.01 for AM. Among these, only 10% of the G1 samples for CD exceeded one, indicating potential non-carcinogenic health risks related to nitrate. This denotes that CD were at greater risk and were more vulnerable to contaminated groundwater. Additionally, under nitrate contamination, AFs exhibited greater susceptibility compared with AM. To summarize, the analysis ranked the potential health hazards for distinct groups as follows: children > adult females > adult males. This observation stems from the fact that children ingest a greater proportion of water and food relative to their body weight [62].

Spatial distribution maps depicting non-carcinogenic risk levels were generated for different groups (Figure 12). The results of the HHR model reveal that regions with elevated risk for CD were primarily concentrated in the northwestern and eastern areas, but the scope of the high-risk range was limited to 5.66% of the total region. The high-risk range for AM and AF was not detected. Overall, the human health risk was low in most parts of the research region. Local areas with high health risks should be paid attention to with

monitoring techniques. Moreover, the authorities should implement measures such as avoiding excessive use of nitrogen fertilizers, raising awareness of safe water practices among local residents, prioritizing the use of high-quality regional groundwater, and employing targeted water treatment.

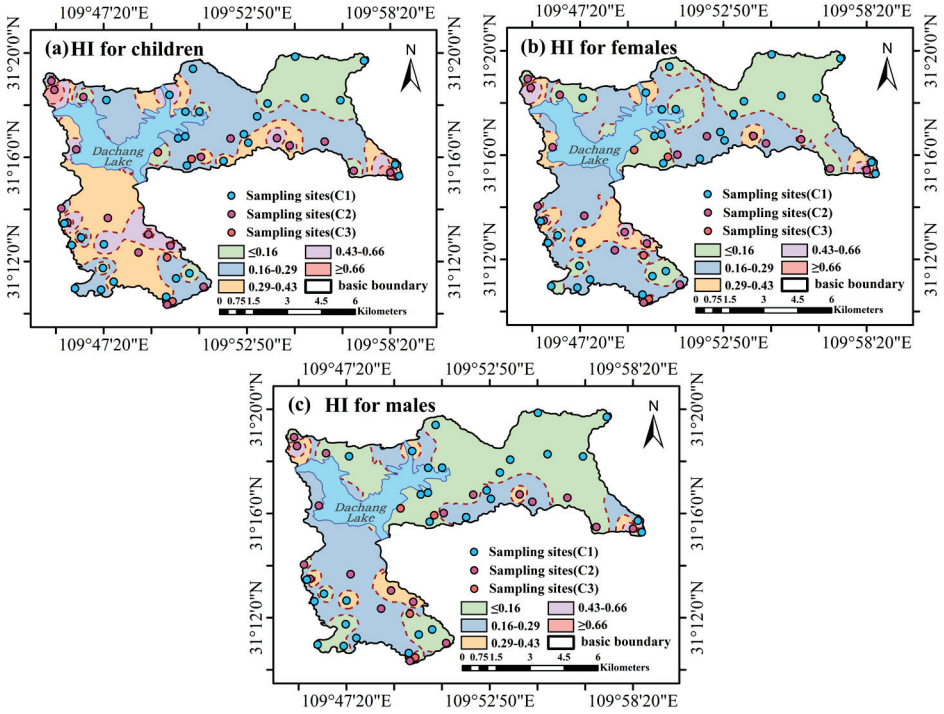

Figure 12. Spatial distribution diagrams of human non-carcinogenic risk assessment for different age groups: (**a**) children, (**b**) males, and (**c**) females.

Sensitivity analysis is a crucial part of the weight of different variables in the HHR model [26]. In this research, specific parameters were chosen for sensitivity analysis, including NO_3, BW, EF, and IR. The sensitivity of these parameters was determined using the Crystal Ball software (version 11.1; Oracle Inc., Austin, TX, USA) (Table 3). The NO_3 concentration exhibited the highest sensitivity, with values of 94.9% in children, 94.2% in adult males, and 93.2% in adult females. This clearly indicates that NO_3 was the primary influencing factor determining the level of human health risk. Consistently, the spatial distribution of high NO_3 concentrations closely resembled the distribution of low EWQIs and high HI values. In comparison, IR and EF demonstrated relatively lower sensitivities, with IR slightly exceeding EF. Negative sensitivity was detected for BW. Many scholars have come to similar conclusions, and the underlying reasons remain to be further studied [63–65]. In terms of the impact order in the sensitivity analysis, a ranking of NO_3 > BW > IR > EF was achieved.

Table 3. Sensitivity variance contributions of three groups to each parameter.

Parameter	HI_NO_3 for CD	HI_NO_3 for AFs	HI_NO_3 for AMs
BW	−1.8%	−2.8%	−4.5%
EF	0.9%	0.8%	0.6%
IR	2.4%	2.2%	1.7%
NO_3	94.9%	94.2%	93.2%

6. Conclusions

In this paper, 53 groundwater samples were collected from the northern part of Chongqing, SW China. The irrigation suitability using the physicochemical index was

calculated to evaluate its applicability in agricultural activities. Subsequently, the EWQI was computed for groundwater quality evaluation. Eventually, the human health risk assessment model was employed to determine the non-carcinogenic risk of nitrate in groundwater for children, adult females, and adult males. The primary discoveries are outlined as follows:

(1) Based on the HCA, three classes of groundwater samples were identified in the study region. The groundwater samples overall exhibited predominantly alkaline characteristics, with a predominance of hard water. The cationic components followed the order of $Ca^{2+} > Mg^{2+} > Na^{+} > K^{+}$, and the anionic components were relatively abundant in the order of $HCO_3^{-} > SO_4^{2-} > NO_3^{-} > Cl^{-}$. Among them, the hydrochemical types of G1 and G2 samples were mainly identified as Ca-HCO_3, while G3 samples exhibited Ca-HCO_3, Ca-Mg-SO_4, and Ca-Mg-Na-SO_4-HCO_3 types. The composition of groundwater is primarily influenced by water–rock interactions: carbonate dissolution for G1 and G2 samples, and carbonate dissolution and silicate weathering for G3 samples.

(2) The USSL and Wilcox diagrams revealed that the majority of the groundwater within the study area is deemed suitable for agricultural irrigation. However, 32.1% of the distributed groundwater is situated within high-salinity and low-sodium-hazard zones, signifying that these samples are unsuitable for crops grown in poorly drained soils with restricted permeability. The EWQI values demonstrated that all groundwater samples met the requirements for the basic potable standard.

(3) Groundwater nitrate contamination was ranked by age and gender as children > adult females > adult males. The sensitivity analysis expressed the NO_3 concentration as exhibiting the highest sensitivity (94.1%) and the influence sequence of each parameter as NO_3 > BW > IR > EF. Long-term use of groundwater in this region should give rise to human health risks (especially in children). Therefore, inhabitants who rely on water in these areas should seek alternative sources to fulfill their needs and mitigate the risks associated with nitrate contamination.

(4) The salinity of groundwater should be managed with a focused approach by authorities, and sound water conservation facilities can be established to exclude soil salinity using natural water circulation. Moreover, they should implement measures such as avoiding excessive use of nitrogen fertilizers, raising awareness of safe water practices among local residents, and employing targeted water treatment.

Supplementary Materials: The following supporting information can be downloaded at https://www.mdpi.com/article/10.3390/w15234095/s1. Table S1: Classification criteria of water quality based on EWQI; Table S2: Parameters for computing the health risks via oral intake and dermal contact exposure pathways; Table S3: Classification of salt hazards in irrigation groundwater; Table S4: Results of non-carcinogenic risk via drinking water intake and dermal contact.

Author Contributions: Methodology, J.L. (Jiawei Liu), C.Y. and J.L. (Junyi Li); Software, Y.W. (Yangshuang Wang), X.Z. and Q.H.; Formal analysis, C.Y. and Y.W. (Yangshuang Wang); Investigation, J.L. (Jiawei Liu), C.Y., S.C., X.Z., W.K., J.L. (Junyi Li) and X.Y.; Resources, W.K.; Data curation, C.Y. and Q.H.; Writing—original draft, J.L. (Jiawei Liu); Writing—review & editing, X.Y.; Supervision, S.C., Y.W. (Ying Wang) and X.Y.; Project administration, S.C.; Funding acquisition, Y.W. (Ying Wang) All authors have read and agreed to the published version of the manuscript.

Funding: This study was funded by the Yibin government (grant number: SWJTU2021020007; SWJTU2021020008), Natural Science Foundation of Chongqing (grant number: cstc2020jcyj-msmX1072; CSTB2022NSCQMSX0881), National Natural Science Foundation of China (grant number: 42072313), Natural Science Foundation of Sichuan Province (grant number: 2022NSFSC0413), the Open Project Program of Engineering Research Center of Groundwater Pollution Control and Remediation, the Ministry of Education of China (grant number: GW202213, GW202308), and the Scientific Key R&D project of the Tibet Autonomous Region (XZ202201ZY0021G).

Data Availability Statement: The data presented in this study are available upon request from the corresponding author.

Acknowledgments: We would like to thank the anonymous reviewers and editors for their constructive comments on this manuscript.

Conflicts of Interest: The authors declare no conflict of interest.

References

1. Li, P.; He, X.; Guo, W. Spatial groundwater quality and potential health risks due to nitrate ingestion through drinking water: A case study in Yan'an City on the Loess Plateau of northwest China. *Hum. Ecol. Risk Assess. Int. J.* **2019**, *25*, 11–31. [CrossRef]
2. Liu, M.; Xiao, C.; Liang, X.; Wei, H. Response of groundwater chemical characteristics to land use types and health risk assessment of nitrate in semi-arid areas: A case study of Shuangliao City, Northeast China. *Ecotoxicol. Environ. Saf.* **2022**, *236*, 113473. [CrossRef]
3. Jiang, W.; Sheng, Y.; Liu, H.; Ma, Z.; Song, Y.; Liu, F.; Chen, S. Groundwater quality assessment and hydrogeochemical processes in typical watersheds in Zhangjiakou region, northern China. *Environ. Sci. Pollut. Res. Int.* **2022**, *29*, 3521–3539. [CrossRef] [PubMed]
4. Ministry of Water Resources the People's Republic of China. *China Water Resources Bulletin 2020*; Ministry of Water Resources, PRC: Beijing, China, 2021. (In Chinese)
5. Ministry of Ecology and Environment the People's Republic of China. *Report on the State of the Ecology and Environment in China 2020*; Ministry of Ecology and Environment, PRC: Beijing, China, 2021. (In Chinese)
6. Li, Z.; Yang, Q.; Yang, Y.; Xie, C.; Ma, H. Hydrogeochemical controls on arsenic contamination potential and health threat in an intensive agricultural area, northern China. *Environ. Pollut.* **2020**, *256*, 113455. [CrossRef]
7. Fan, A.M.; Steinberg, V.E. Health Implications of Nitrate and Nitrite in Drinking Water: An Update on Methemoglobinemia Occurrence and Reproductive and Developmental Toxicity. *Regul. Toxicol. Pharmacol.* **1996**, *23*, 35–43. [CrossRef]
8. Forman, D.; Al-Dabbagh, S.; Doll, R. Nitrates, nitrites and gastric cancer in Great Britain. *Nature* **1985**, *313*, 620–625. [CrossRef] [PubMed]
9. Adimalla, N.; Qian, H. Groundwater quality evaluation using water quality index (WQI) for drinking purposes and human health risk (HHR) assessment in an agricultural region of Nanganur, south India. *Ecotoxicol. Environ. Saf.* **2019**, *176*, 153–161. [CrossRef]
10. Saraswat, A.; Ram, S.; Kouadri, S.; Raza, M.B.; Hombegowda, H.C.; Kumar, R.; Golui, D.; Maurya, P.K.; Ilić, P.; Rahman, M.M.; et al. Groundwater quality, fluoride health risk and geochemical modelling for drinking and irrigation water suitability assessment in Tundla block, Uttar Pradesh, India. *Groundw. Sustain. Dev.* **2023**, *23*, 100991. [CrossRef]
11. Ghosh, D.; Mandal, M.; Karmakar, M.; Banerjee, M.; Mandal, D. Application of geospatial technology for delineating groundwater potential zones in the Gandheswari watershed, West Bengal. *Sustain. Water Resour. Manag.* **2020**, *6*, 6–11. [CrossRef]
12. Chowdhury, P.; Mukhopadhyay, B.P.; Bera, A. Hydrochemical assessment of groundwater suitability for irrigation in the north-eastern blocks of Purulia district, India using GIS and AHP techniques. *Phys. Chem. Earth Parts A/B/C* **2022**, *126*, 103–108. [CrossRef]
13. Kim, K.-H.; Yun, S.-T.; Yu, S.; Choi, B.-Y.; Kim, M.-J.; Lee, K.-J. Geochemical pattern recognitions of deep thermal groundwater in South Korea using self-organizing map: Identified pathways of geochemical reaction and mixing. *J. Hydrol.* **2020**, *589*, 125202. [CrossRef]
14. Yang, W.; Zhao, Y.; Wang, D.; Wu, H.; Lin, A.; He, L. Using Principal Components Analysis and IDW Interpolation to Determine Spatial and Temporal Changes of Surface Water Quality of Xin'anjiang River in Huangshan, China. *Int. J. Environ. Res. Public Health* **2020**, *17*, 082942. [CrossRef]
15. Daughney, C.J.; Raiber, M.; Moreau-Fournier, M.; Morgenstern, U.; Raaij, R.v.d. Use of hierarchical cluster analysis to assess the representativeness of a baseline groundwater quality monitoring network: Comparison of New Zealand's national and regional groundwater monitoring programs. *Hydrogeol. J.* **2012**, *20*, 185–200. [CrossRef]
16. Zhao, X.; Guo, H.; Wang, Y.; Wang, G.; Wang, H.; Zang, X.; Zhu, J. Groundwater hydrogeochemical characteristics and quality suitability assessment for irrigation and drinking purposes in an agricultural region of the North China plain. *Environ. Earth Sci.* **2021**, *80*, 162. [CrossRef]
17. Zhang, Y.; Dai, Y.; Wang, Y.; Huang, X.; Xiao, Y.; Pei, Q. Hydrochemistry, quality and potential health risk appraisal of nitrate enriched groundwater in the Nanchong area, southwestern China. *Sci. Total Environ.* **2021**, *784*, 147186. [CrossRef]
18. Wang, Y.; Liu, J.; Yu, X.; Yan, Y.; Chen, Q.; Chen, S. Evaluation of groundwater quality and health risk assessment in southeastern Tibet, China. *Environ. Earth Sci.* **2023**, *82*, 455. [CrossRef]
19. Chen, S.; Tang, Z.; Wang, J.; Wu, J.; Yang, C.; Kang, W.; Huang, X. Multivariate Analysis and Geochemical Signatures of Shallow Groundwater in the Main Urban Area of Chongqing, Southwestern China. *Water* **2020**, *12*, 2833. [CrossRef]
20. NBS; PRC. *2020 China Statistical Yearbook*; China Statistical Press: Beijing, China, 2020. (In Chinese)
21. Pu, J.; Yuan, D.; Xiao, Q.; Zhao, H. Hydrogeochemical characteristics in karst subterranean streams: A case history from Chongqing, China. *Carbonates Evaporites* **2015**, *30*, 307–319. [CrossRef]
22. Zheng, D.; Liu, Y.; Luo, L.; Shahid, M.Z.; Hou, D. Spatial variation and health risk assessment of fluoride in drinking water in the Chongqing urban areas, China. *Environ. Geochem. Health* **2020**, *42*, 2925–2941. [CrossRef] [PubMed]

23. Yang, X.; Fu, J.; Han, X.; Zhang, C.; Pan, S.; Li, G.; Guo, Y.; PAn, J. Progress of geological hazards survey in the urban area from Wanzhou to Wushan in Three Gorges Reservoir. *Geol. Surv. China* **2021**, *8*, 97–107.
24. Pu, J.; Yuan, D.; Zhang, C.; Zhao, H. Hydrogeochemistry and possible sulfate sources in karst groundwater in Chongqing, China. *Environ. Earth Sci.* **2012**, *68*, 159–168. [CrossRef]
25. Yang, F.; Jia, C.; Yang, X.; Yang, H.; Chang, W. Probabilistic potential health risk quantification, hydrochemistry, driving forces of groundwater nitrate and fluoride in a typical irrigation district, Northern China. *J. Environ. Manag.* **2022**, *323*, 116171. [CrossRef] [PubMed]
26. Eldaw, E.; Huang, T.; Mohamed, A.K.; Mahama, Y. Classification of groundwater suitability for irrigation purposes using a comprehensive approach based on the AHP and GIS techniques in North Kurdufan Province, Sudan. *Appl. Water Sci.* **2021**, *11*, 126. [CrossRef]
27. Singh, A.K.; Tewary, B.K.; Sinha, A. Hydrochemistry and quality assessment of groundwater in part of Noida metropolitan city, Uttar Pradesh. *J. Geol. Soc. India* **2011**, *78*, 523–540. [CrossRef]
28. Bian, J.; Nie, S.; Wang, R.; Wan, H.; Liu, C. Hydrochemical characteristics and quality assessment of groundwater for irrigation use in central and eastern Songnen Plain, Northeast China. *Environ. Monit. Assess.* **2018**, *190*, 382. [CrossRef]
29. Gautam, U.; Tiwari, V.; Tripathi, V.K. Evaluation of groundwater quality of Prayagraj city using entropy water quality index (EWQI) and new integrated water quality index (IWQI). *Sustain. Water Resour. Manag.* **2022**, *8*, 57. [CrossRef]
30. Li, P.-Y.; Qian, H.; Wu, J.-H. Groundwater Quality Assessment Based on Improved Water Quality Index in Pengyang County, Ningxia, Northwest China. *E-J. Chem.* **2010**, *7*, S209–S216.
31. *GB/T 14848-2017*; GAQS (General Administration of Quality Supervision) and SAC (Standardization Administration of China): Standard for Groundwater Quality. Standardization Administration of the PRC: Beijing, China, 2017.
32. Li, X.; Huang, X.; Zhang, Y. Spatio-temporal analysis of groundwater chemistry, quality and potential human health risks in the Pinggu basin of North China Plain: Evidence from high-resolution monitoring dataset of 2015–2017. *Sci. Total Environ.* **2021**, *800*, 149568. [CrossRef]
33. Wang, Y.; Li, P. Appraisal of shallow groundwater quality with human health risk assessment in different seasons in rural areas of the Guanzhong Plain (China). *Environ. Res.* **2022**, *207*, 112210. [CrossRef]
34. Yuan, Y.; Liu, Y.; Luo, K.; Shahid, M.Z. Hydrochemical characteristics and a health risk assessment of the use of river water and groundwater as drinking sources in a rural area in Jiangjin District, China. *Environ. Earth Sci.* **2020**, *79*, 160. [CrossRef]
35. Li, Y.; Li, P.; Cui, X.; He, S. Groundwater quality, health risk, and major influencing factors in the lower Beiluo River watershed of northwest China. *Hum. Ecol. Risk Assess. Int. J.* **2021**, *27*, 1987–2013. [CrossRef]
36. Liu, J.; Gao, Z.; Wang, Z.; Xu, X.; Su, Q.; Wang, S.; Qu, W.; Xing, T. Hydrogeochemical processes and suitability assessment of groundwater in the Jiaodong Peninsula, China. *Environ. Monit. Assess.* **2020**, *192*, 384. [CrossRef] [PubMed]
37. Sharma, T.; Bajwa, B.S.; Kaur, I. Hydro-geochemical characteristics and quality appraisal of aquifers using multivariate statistics and associated risk assessment in Tarn-Taran district, Punjab, India. *Environ. Sci. Pollut. Res. Int.* **2022**, *29*, 54916–54938. [CrossRef]
38. Güler, C.; Thyne, G.D. Hydrologic and geologic factors controlling surface and groundwater chemistry in Indian Wells-Owens Valley area, southeastern California, USA. *J. Hydrol.* **2004**, *285*, 177–198. [CrossRef]
39. Wu, J.; Li, P.; Wang, D.; Ren, X.; Wei, M. Statistical and multivariate statistical techniques to trace the sources and affecting factors of groundwater pollution in a rapidly growing city on the Chinese Loess Plateau. *Hum. Ecol. Risk Assess. Int. J.* **2019**, *26*, 1603–1621. [CrossRef]
40. Feng, F.; Jia, Y.; Yang, Y.; Huan, H.; Lian, X.; Xu, X.; Xia, F.; Han, X.; Jiang, Y. Hydrogeochemical and statistical analysis of high fluoride groundwater in northern China. *Environ. Sci. Pollut. Res. Int.* **2020**, *27*, 34840–34861. [CrossRef] [PubMed]
41. WHO. *Guidelines for Drinking-Water Quality*, 4th ed.; World Health Organization: Geneva, Switzerland, 2017.
42. Geng, J.; Chen, J.; Zhang, S. Analysis of Hydro-Chemical Changes and Genesis of Major Ions in Upper Reach of Chishui River. *Juornal China Hydrol.* **2013**, *33*, 44–50.
43. Piper, A.M. A graphical procedure in the geochemical interpretation of water analysis. *Eos Trans. Am. Geophys. Union* **1944**, *25*, 914–928.
44. Dashora, M.; Kumar, A.; Kumar, S.; Kumar, P.; Kumar, A.; Singh, C.K. Geochemical assessment of groundwater in a desertic region of India using chemometric analysis and entropy water quality index (EWQI). *Nat. Hazards* **2022**, *112*, 747–782. [CrossRef]
45. Wu, H.; Xu, C.; Wang, J.; Xiang, Y.; Ren, M.; Qie, H.; Zhang, Y.; Yao, R.; Li, L.; Lin, A. Health risk assessment based on source identification of heavy metals: A case study of Beiyun River, China. *Ecotoxicol. Environ. Saf.* **2021**, *213*, 112046. [CrossRef]
46. Swain, S.; Sahoo, S.; Taloor, A.K. Groundwater quality assessment using geospatial and statistical approaches over Faridabad and Gurgaon districts of National Capital Region, India. *Appl. Water Sci.* **2022**, *12*, 75. [CrossRef]
47. Kaiser, H.F. An index of factorial simplicity. *Psychometrika* **1974**, *39*, 31–36. [CrossRef]
48. Zhang, H.; Cheng, S.; Li, H.; Fu, K.; Xu, Y. Groundwater pollution source identification and apportionment using PMF and PCA-APCA-MLR receptor models in a typical mixed land-use area in Southwestern China. *Sci. Total Environ.* **2020**, *741*, 140383. [CrossRef] [PubMed]
49. Gholizadeh, H.M.; Melesse, A.M.; Reddi, L. Water quality assessment and apportionment of pollution sources using APCS-MLR and PMF receptor modeling techniques in three major rivers of South Florida. *Sci. Total Environ.* **2016**, *566–567*, 1552–1567. [CrossRef] [PubMed]

50. Liu, C.W.; Lin, K.H.; Kuo, Y.M. Application of factor analysis in the assessment of groundwater quality in a blackfoot disease area in Taiwan. *Sci. Total Environ.* **2003**, *313*, 77–89. [CrossRef]
51. Gibbs, R.J. Mechanisms Controlling World Water Chemistry. *Science* **1970**, *170*, 1088–1090. [CrossRef]
52. Gaillardet, J.; Dupré, B.; Louvat, P.; Allègre, C. Global silicate weathering and CO_2 consumption rates deduced from the chemistry of large rivers. *Chem. Geol.* **1999**, *159*, 3–30. [CrossRef]
53. Wu, C.; Wu, X.; Qian, C.; Zhu, G. Hydrogeochemistry and groundwater quality assessment of high fluoride levels in the Yanchi endorheic region, northwest China. *Appl. Geochem.* **2018**, *98*, 404–417. [CrossRef]
54. Lv, G.; Zhang, X.; Wei, D.; Yu, Z.; Yuan, X.; Sun, M.; Kong, X.; Zhang, Y. Water—Rock Interactions, Genesis Mechanism, and Mineral Scaling of Geothermal Waters in Northwestern Sichuan, SW China. *Water* **2023**, *15*, 3730. [CrossRef]
55. Wang, Y.; Yuan, X.; Zhang, Y.; Zhang, X.; Xiao, Y.; Duo, J.; Huang, X.; Sun, M.; Lv, G. Hydrochemical, D–O–Sr isotopic and electromagnetic characteristics of geothermal waters from the Erdaoqiao area, SW China: Insights into genetic mechanism and scaling potential. *Ore Geol. Rev.* **2023**, *158*, 105486. [CrossRef]
56. Chen, K.; Liu, Q.; Yang, T.; Ju, Q.; Hou, X.; Gao, W.; Jiang, S. Groundwater pollution source identification and health risk assessment in the North Anhui Plain, eastern China: Insights from positive matrix factorization and Monte Carlo simulation. *Sci. Total Environ.* **2023**, *895*, 165186. [CrossRef]
57. Adimalla, N. Application of the Entropy Weighted Water Quality Index (EWQI) and the Pollution Index of Groundwater (PIG) to Assess Groundwater Quality for Drinking Purposes: A Case Study in a Rural Area of Telangana State, India. *Arch. Environ. Contam. Toxicol.* **2021**, *80*, 31–40. [CrossRef]
58. Richards, L.A. Diagnosis and Improvement of Saline and Alkali Soils. *Agric. Handb.* **1954**, *60*, 129–134. [CrossRef]
59. Oster, J.D.; Shainberg, I. Soil responses to sodicity and salinity: Challenges and opportunities. *Soil Res.* **2001**, *39*, 1219. [CrossRef]
60. Liu, Y.; Sheng, Y.; Feng, C.; Chen, N.; Liu, T. Distinct functional microbial communities mediating the heterotrophic denitrification in response to the excessive Fe (II) stress in groundwater under wheat-rice stone and rock phosphate amendments. *Environ. Res.* **2020**, *185*, 109391. [CrossRef] [PubMed]
61. Ju, Q.; Hu, Y.; Liu, Q.; Chai, H.; Chen, K.; Zhang, H.; Wu, Y. Source apportionment and ecological health risks assessment from major ions, metalloids and trace elements in multi-aquifer groundwater near the Sunan mine area, Eastern China. *Sci. Total Environ.* **2023**, *860*, 160454. [CrossRef] [PubMed]
62. Zhang, Y.; Li, X.; Luo, M.; Wei, C.; Huang, X.; Xiao, Y.; Qin, L.; Pei, Q.; Gao, X. Hydrochemistry and Entropy-Based Groundwater Quality Assessment in the Suining Area, Southwestern China. *J. Chem.* **2021**, *2021*, 5591892. [CrossRef]
63. Mukherjee, I.; Singh, U.K.; Singh, R.P.; Anshumali; Kumari, D.; Jha, P.K.; Mehta, P. Characterization of heavy metal pollution in an anthropogenically and geologically influenced semi-arid region of east India and assessment of ecological and human health risks. *Sci. Total Environ.* **2020**, *705*, 135801. [CrossRef]
64. Gao, B.; Gao, L.; Gao, J.; Xu, D.; Wang, Q.; Sun, K. Simultaneous evaluations of occurrence and probabilistic human health risk associated with trace elements in typical drinking water sources from major river basins in China. *Sci. Total Environ.* **2019**, *666*, 139–146. [CrossRef]
65. Meng, Y.; Wu, J.; Li, P. Distribution characteristics, source identification and health risk assessment of trace metals in the coastal groundwater of Taizhou City, China. *Environ. Res.* **2023**, *238*, 117085. [CrossRef]

Disclaimer/Publisher's Note: The statements, opinions and data contained in all publications are solely those of the individual author(s) and contributor(s) and not of MDPI and/or the editor(s). MDPI and/or the editor(s) disclaim responsibility for any injury to people or property resulting from any ideas, methods, instructions or products referred to in the content.

water

MDPI

Article

Microbiological and Physicochemical Quality of Groundwater and Risk Factors for Its Pollution in Ouagadougou, Burkina Faso

Oumar Traoré [1,2,*], Dissinviel Stéphane Kpoda [3], René Dembélé [1,2], Courage Kosi Setsoafia Saba [4], Johannes Cairns [5,6], Nicolas Barro [2] and Kaisa Haukka [7,*]

1 Unité de Formation et de Recherche en Sciences Appliquées et Technologies (UFR/SAT), Université de Dédougou, Dédougou BP 76, Burkina Faso; rene.dembele@univ-dedougou.bf
2 Laboratoire de Biologie Moléculaire d'Epidémiologie et de Surveillance des Bactéries et Virus Transmis par Les Aliments, CRSBAN/Département de Biochimie-Microbiologie, UFR/SVT-Université Joseph KI-ZERBO, Ouagadougou 03 BP 7021, Burkina Faso; barronicolas@yahoo.fr
3 Laboratoire de Microbiologie et de Biotechnologie Microbienne, Centre Universitaire Polytechnique de Ziniaré, Université Joseph KI-ZERBO, Ouagadougou 03 BP 7021, Burkina Faso; podadissin@yahoo.fr
4 Department of Microbiology, Faculty of Biosciences, University for Development Studies, Tamale P.O. Box TL 1882, Ghana; csetsoafia@uds.edu.gh
5 Department of Computer Science, Organismal and Evolutionary Biology Research Programme, University of Helsinki, 00014 Helsinki, Finland; johannes.cairns@helsinki.fi
6 Department of Biology, University of Turku, 20520 Turku, Finland
7 Department of Microbiology, University of Helsinki, P.O. Box 56, 00014 Helsinki, Finland
* Correspondence: marrou4@yahoo.fr or oumar.traore@univ-dedougou.bf (O.T.); kaisa.haukka@helsinki.fi (K.H.); Tel.: +226-70-78-42-66 (O.T.); +358-40-7494815 (K.H.)

Abstract: Ouagadougou is a city with three million inhabitants and an increasing demand for water of sufficient quality. New boreholes are drilled to match demand, but their protection from anthropogenic contamination is insufficient. To assess the quality of urban groundwater in Ouagadougou for the first time, a total of 32 borehole water samples were collected and assessed for bacteriological and physicochemical features using established methods. Health risk inspections and hazard assessments were undertaken at sampling sites to identify potential hazards and contributing factors. Statistical analysis was used to identify associations between risk factors and water pollution. The study revealed poor quality of groundwater in Ouagadougou with major nonconformities related to total coliforms, *Escherichia coli*, and turbidity. Water samples from 19 boreholes (59%) were contaminated with coliforms, and 11 (34%) with *E. coli*. Additionally, *Pseudomonas aeruginosa*, *Enterococcus*, and anaerobic sulphite-reducing bacterial spores were detected. Deviations from physicochemical quality requirements were observed for water turbidity, pH, nitrate, fluorine, and iron. Risk analysis showed the major high-risk practices to be sludge spreading or having a garbage heap, a latrine, a septic tank, or dirty water near a borehole. Based on these results, for public health protection, authorities must take strict measures to prohibit such practices around these important sources of drinking water in Ouagadougou.

Keywords: groundwater; boreholes; microbiological quality; physicochemical quality; risk factors; Africa

1. Introduction

The provision of clean and safe water is paramount to human health, and is considered a priority concern by the United Nations, featuring as Sustainable Development Goal (SDG) number six [1]. In developing countries, increases in human population size, animal farming, and industrialization exert an enormous pressure on the provision of safe drinking water [2]. Microbiologically contaminated water is a potential source of human enteric infections and indicates poor maintenance of hygiene-related infrastructure, as well as problems in the implementation of control measures [3]. Deficient basic sanitary practices

are often due to lack of awareness among the population. As a consequence, contaminated water is a major cause of diarrhoeal deaths and disease, especially for young children less than five years old, and other vulnerable populations [4].

In many areas in Africa, groundwater is the major source of drinking water for people, as groundwater is considered to be free from impurities and less susceptible to contamination, and more resilient to climate variability compared to surface water bodies [5–7]. However, groundwater quality is impacted by climate, slope, drainage conditions, water–rock interactions, and anthropogenic activities [8,9]. Factors such as storm water runoff, leakage of animal waste into the environment, agricultural practices, industry, energy production, mining, wastewater, and infiltration of inadequately treated domestic sewage can lead to deterioration of underground water sources [10–15].

In West Africa, particularly in rural areas, where access to safe drinking water can be limited, studies have been carried out to assess the risk that people are exposed to by consuming unsafe water. Previous studies in the region have reported microbiological pollution, high levels of mineralization, and much higher concentrations of nitrate and nitrite than the maximum limits set by WHO standards [16,17]. In Burkina Faso, previous studies carried out on the quality of groundwater have focused on heavy metal and chemical contamination in rural areas and the midwestern part of the country [18,19]. However, a recent study by Faye et al. [20] detected microbiological contamination as well as chemical deterioration in groundwater quality in the southwest part of the country. To date, no studies have been conducted on the microbiological and physicochemical quality of groundwater in the central region, including the capital city Ouagadougou. Therefore, we sought to assess water quality and analyze related sanitary risk factors in this area.

In Ouagadougou, many people use water from boreholes due to frequent ruptures in the public water supply system, and also due to the reputation of healthiness and good quality of groundwater. However, due to high population density (1025 inhabitants/km^2), boreholes are often constructed near pit latrines, and thus faecal matter from pit latrines can potentially contaminate groundwater [21,22]. Furthermore, some boreholes are deficiently protected, and penetration of surface water may cause transmission of animal waste or sewage to groundwater [23]. Therefore, the use of vulnerable groundwater aquifers without water purification or disinfection measures for drinking purposes poses a public health concern.

The objective of this work was to investigate the quality of groundwater and reveal its most important risk factors by examining water samples and the maintenance of selected borehole sites in Ouagadougou. The suitability of water for drinking from these groundwater sources was assessed by analyzing total coliforms, *Escherichia coli*, *Pseudomonas aeruginosa*, and enterococci that are commonly used as bacterial indicators in drinking water quality assessments. Additionally, detection of anaerobic sulphite-reducing bacterial spores was used to indicate faecal and/or soil contamination, since their presence indicates the failure of natural or artificial filtration measures [24]. In addition, physical and chemicals parameters including pH and electrical conductivity, turbidity, total hardness, total alkalinity, calcium and magnesium, chlorides, nitrite, nitrates, orthophosphate, sulfate, fluoride, and total iron were analyzed. This is the first study in the Ouagadougou region to consider both contamination risk levels based on sanitary inspection and physicochemical and microbiological parameters.

2. Materials and Methods

2.1. Study Area and Design

This study was conducted in Ouagadougou, the capital and largest city in Burkina Faso. It covers a total area of 600 square kilometers, with a population size of approximately 3,000,000 inhabitants (in 2020). The city has a tropical savannah climate, comprising dry and rainy seasons, and the weather is hot all year round. This study was conducted during the rainy season, extending from April to October, when rain characteristically falls in the form of thunderstorms. Sampling took place from July to September 2018. The study design is shown in Figure 1.

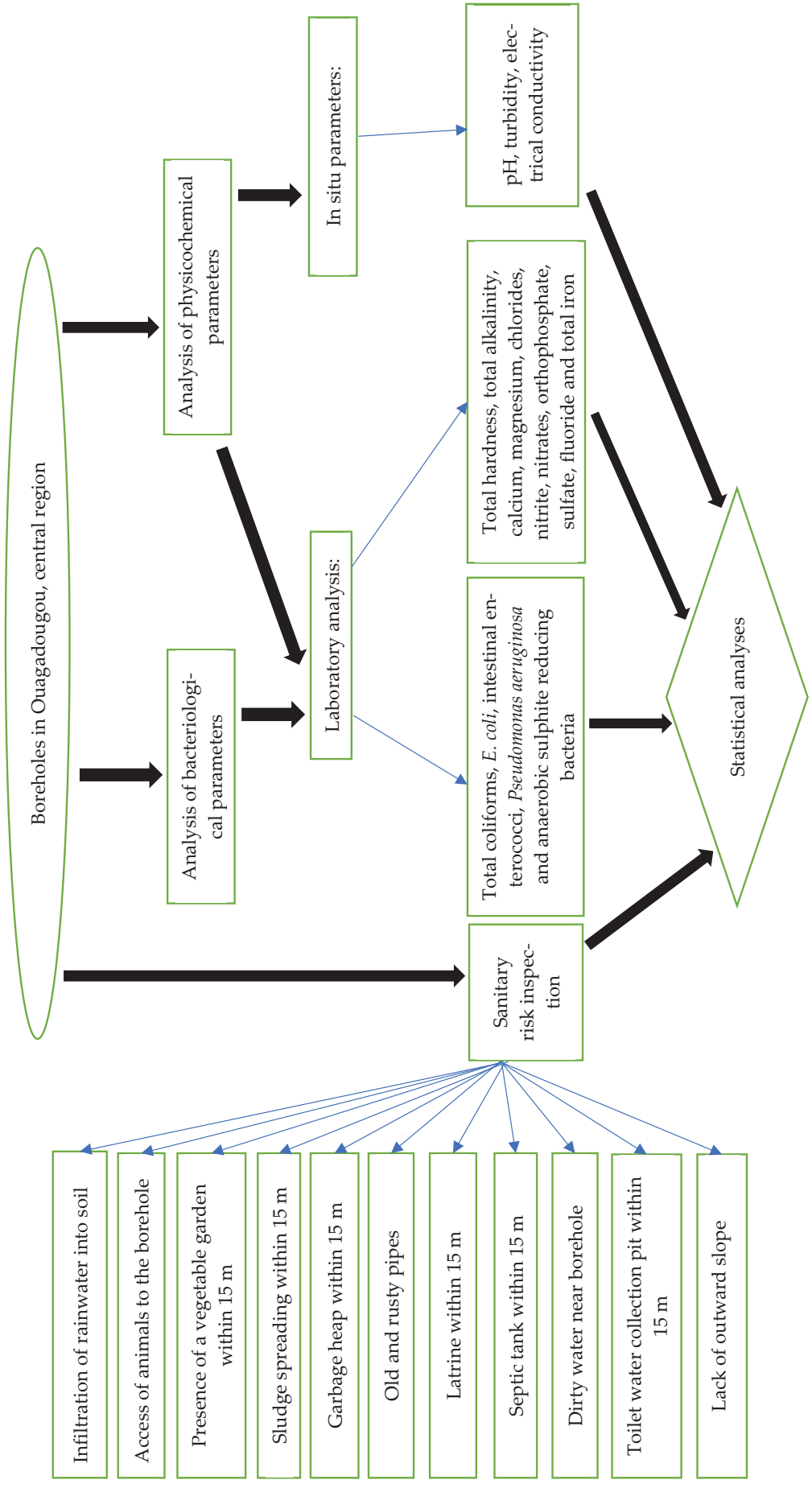

Figure 1. Flowchart for borehole sanitary risk inspection and water analyses.

Hydrogeologically, the study area consists mainly of granitoids intersected with NESW and NWSE oriented fractures. Most of the drilled boreholes are located directly above these fractures. Soil composition is key to determining the physicochemical features affecting water quality. The granitoids are covered with alterites composed of laterites, clayey, sandy, and granular arenas. These alterites have a high porosity of interstices, which provides them with good capacitive function, and are generally in hydraulic connection with underlying cracks and fractures [25].

Water from thirty-two (32) boreholes was sampled in Ouagadougou in a densely populated area with anthropogenic pressure (Figure 2). Boreholes were chosen according to their spatial distribution and frequency of use. The area is also subject to frequent flooding, resulting in poor hygienic conditions and sanitation.

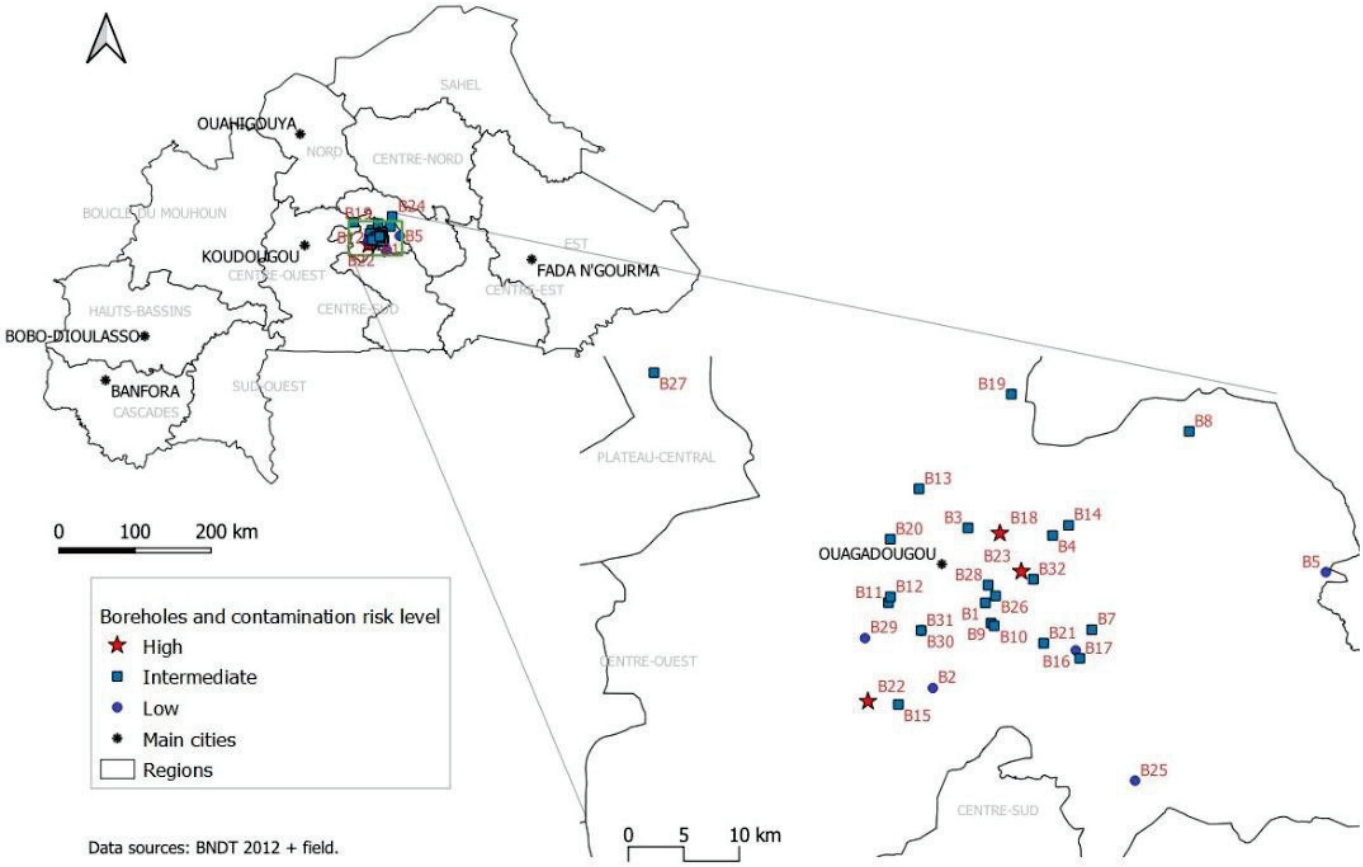

Figure 2. Contamination risk level for groundwater of 32 boreholes in Ouagadougou.

2.2. Sanitary Risk Inspection

At each site, during water sampling, a sanitary risk inspection involving the identification of potential point sources of microbial contamination was performed, as adapted from Lutterodt et al. [26]. The purpose was to collect data on drilled well maintenance and daily hygienic practices likely to protect or deteriorate the quality of groundwater.

Our procedure involved physical inspection of the boreholes, followed by inspection of the surrounding environment and recording their risk factors (Table 1). The parameters measured were: (1) infiltration of rainwater into soil (IRS), (2) access of animals to the borehole (AAB), (3) presence of a vegetable garden within 15 m (PVG), (4) sludge spreading within 15 m (SS), (5) garbage heap within 15 m (GH), (6) old and rusty pipes (POR), (7) latrine within 15 m (L), (8) septic tank within 15 m (ST), (9) dirty water near borehole (DWB), (10) toilet water collection pit within 15 m (TWCP), and (11) lack of outward slope (LOS) around the borehole.

Table 1. Contamination risk factors for groundwater of 32 boreholes in Ouagadougou.

Risk Factors for Borehole Water	Borehole Code	Number of Boreholes (%)
Infiltration of rain water into soil (IRS)	B04, B11, B15, B19, B21, B22, B23, B24, B26, B27, B28, B31, B32	13 (40.6)
Access of animals to borehole (AAB)	B03, B12, B13, B18, B22, B23, B29	7 (21.9)
Presence of vegetables garden within 15 m (PVG)	B04, B09, B10, B14	4 (12.5)
Sludge spreading within 15 m (SS)	B01, B18, B20	3 (9.4)
Garbage heap within 15 m (GH)	B03, B06, B07, B08, B12, B17, B18, B21, B22, B23, B24	11 (34.4)
Old and rusty pipe (POR)	B08, B11, B12, B19, B20, B22, B23	7 (21.9)
Latrine within 15 m (L)	B01, B02, B03, B05, B06, B07, B08, B12, B13, B16, B17, B18, B20, B22, B24, B26, B31, B32	18 (56.3)
Septic tank within 15 m (ST)	B04, B09, B10, B11, B14, B15, B19, B21, B23, B25, B27, B28, B29, B32	14 (43.8)
Dirty water near borehole (DWB)	B01, B02, B03, B06, B07, B08, B12, B13, B14, B17, B18, B20, B21, B22, B23, B24, B26	17 (53.1)
Toilet water collection pit within 15 m (TWCP)	None	0 (0)
Lack of outward slope (LOS)	B01, B03, B04, B06, B07, B08, B09, B10, B13, B14, B15, B17, B18, B19, B20, B21, B22, B23, B24, B25, B26, B27, B28, B31, B32	25 (78.1)

Inspection results were recorded as yes/no, with yes indicating the presence of a risk factor for contamination of the borehole, and no indicating the absence of risk for contamination. A final risk score was obtained on a scale of 1–11. A total score of 9–11 was considered very high-risk, 6–8 high-risk, 3–5 intermediate-risk, and 0–2 low-risk.

2.3. Water Sample Collection

After visual inspection of contamination factors, water samples were collected according to standard methods of the American Public Health Association [27]. In situ analyses of water samples were carried out by the measurement of pH, turbidity, and electrical conductivity. Samples were collected in borosilicate glass bottles for microbiological, and polypropylene bottles for physicochemical analyses. All samples were transported to the laboratory in a cooler box containing ice blocks for analysis conducted on the same day.

2.4. Microbiological Analyses

The water samples were analyzed for total coliforms (TC), *E. coli*, intestinal *enterococci* (IE), and *Pseudomonas aeruginosa* (colony-forming units, CFU/100 mL) by using a membrane filtration system. For each microbiological parameter, one blank sample (using sterilized water) was analyzed to verify that there was no contamination due to the handling process.

For enumeration of total coliforms and *E. coli*, water was filtered through nitrocellulose membrane filters with 0.45 µm pore size (Sigma Aldrich, St. Louis, MO, USA), after which filters were placed on Chromocult Coliform Agar Extra Selective CCAES plates (Merck, Darmstadt, Germany). After incubation at 37 °C for 24 h, colonies were counted using a colony counter. Dark blue to violet colonies were recorded as *E. coli*, and all pink, salmon, red, dark blue, or violet colonies were recorded as total coliforms.

For enumeration of intestinal *enterococci*, water was filtered through nitrocellulose membrane filters with 0.45 µm pore size (Sigma Aldrich, St. Louis, MO, USA), after which filters were placed on Slanetz and Bartley medium (Oxoid, Basingstoke, UK) and incubated at 37 °C for 48 h. If typical red/brown/pink colonies were observed after incubation, the membrane was transferred on a prewarmed (44 °C) plate of Bile Aesculina Azide agar

(Merck, Darmstadt, Germany), and incubated at 44 °C for 2 h. Typical black colonies were identified as intestinal *enterococci*.

For enumeration of *Pseudomonas aeruginosa*, 0.22 µm cellulose membrane filters were used, placed on Cetrimide agar (Liofilchem, Roseto degli Abruzzi, Italy), and incubated at 37 °C for 48 h. Blue/green colonies were considered to potentially be *P. aeruginosa*, regrown on Plate Count Agar (Liofilchem, Roseto degli Abruzzi, Italy) at 37 °C for 24 h, and confirmed by the presence of blue/green colonies on King A (SIGMA, Aldrich St. Louis, MO, USA) (poured into tubes with a slope) after 72 h of incubation at 22 °C.

For enumeration of anaerobic sulphite-reducing bacteria, the 50 mL water samples in flasks were placed in a water bath at 80 °C for 10 min. The samples were then cooled to 45–50 °C and filtered with pump vacuum through a 0.22 µm cellulose membrane filter. The membranes were placed inside meat liver (Oxoid, Basingstoke, UK) medium in a Petri dish before it had solidified. After solidification, the dishes were placed in a jar containing an anaerocult reagent (Merk, Darmstadt, Germany) generating an anaerobic atmosphere. The jar was incubated at 37 °C for 48 h. Black colonies were considered positive.

2.5. Physicochemical Analyses

All of the physicochemical parameters were determined by standard methods recommended by the American Public Health Association [21]. In situ physical parameters including pH and electrical conductivity (EC) were measured using a portable pH meter (WTW 3110) precalibrated with buffer solutions (pH 4 and 7), and a SCHOTT conductivity meter, respectively. The turbidity of the samples was determined using a portable 2100Q HACH turbidity meter.

Chemical parameters, including total hardness, total alkalinity (TA), the major cations calcium (Ca^{2+}) and magnesium (Mg^{2+}), and major anions such as chlorides (Cl^{-}), of borehole water samples were analyzed by titrimetric methods. Nitrite ($NO_2{}^{-}$), nitrates ($NO_3{}^{-}$), orthophosphate ($PO4^{3-}$), sulfate ($SO4^{2-}$), fluoride (F^{-}), and total iron (Fe^{2+}) were determined using a UV spectrophotometer (HACH).

2.6. Statistical Analyses

R 4.0.2. [28] was used to produce box plots depicting the physicochemical data and to perform principal component analysis (PCA) on 14 physicochemical and 5 microbiological parameters to determine relationships that may exist between these parameters.

R 4.2.1 [28] was used to analyze the risk factors in two stages. First, multivariate data analysis was performed to identify the environmental risk factors (11 factors and the combined risk score) significantly affecting water parameters. This was done using nonmetric multidimensional scaling (metaMDS function) and fitting environmental factors onto the NMDS ordination (envfitfunction with 999 permutations) with the vegan package [29]. Second, for the thus identified significant risk factors, separate binomial generalized linear models (GLMs) were constructed to detect the water parameters associated with the risk factor. For total risk score, linear regression was used. Prior to analyses, all bacterial count data were log (x + 1) transformed. In addition, one data point (B12) was removed as an outlier, as it had several parameter values a magnitude higher than the other samples and would have been too influential in the statistical analyses.

3. Results

3.1. Sanitary Inspection Results

Contamination risk factors for the 32 boreholes are shown in Table 1. The most common risk factors were the lack of outward slope that would allow surface water to run away from the well (25 boreholes), latrine within 15 m from the borehole (18), dirty water on the ground in the vicinity of the borehole (17), and a septic tank within 15 m from the borehole (14). Based on risk categorization of the 32 boreholes, three were in a high-risk, 23 in an intermediate risk, and 6 in a low-risk environment. None were in a very high-risk environment (Figure 2).

Microbiological Quality of Water Samples

Noncompliance of the borehole waters with microbiological and physicochemical quality criteria is shown in Table 2. Based on microbiological analyses, 19 (59.4%) borehole water samples were contaminated by coliforms, with three samples having a contamination level greater than 100 CFU/100 mL. *E. coli* was isolated from 11 samples, with maximum contamination of 33 CFU/100 mL in one sample. *Pseudomonas aeruginosa* was isolated from four samples, with maximum contamination exceeding 100 CFU/100 mL in one sample. *Enterococcus* was isolated from two samples, and anaerobic sulphite-reducing bacteria from one sample.

Table 2. Noncompliance of borehole water with microbiological and physicochemical quality criteria.

Parameters	**Microbiological Parameters**					**Physicochemical Parameters**				
	Total Coliforms	**EC**	**IE**	**PA**	**ASRBS**	**pH**	**Turbidity**	**Fluoride**	**Iron**	**Nitrate**
Units	CFU/100 mL	CFU/100 mL	CFU/100 mL	CFU/100 mL	CFU/100 mL	-	NTU	mg/L	mg/L	mg/L
Values	B01 (89), B02 (>100), B04 (14), B05 (>100), B06 (8), B07 (14), B08 (>100), B09 (10), B10 (9), B13 (92), B14 (68), B17 (66), B18 (88), B20 (56), B21 (57), B22 (69), B23 (87), B24 (6), B26 (69)	B01 (16), B08 (3), B13 (33), B14 (5), B17 (3), B18 (18), B20 (16), B21 (16), B22 (16), B23 (16), B26 (20)	B18 (3), B26 (1)	B03 (>100), B06 (75), B14 (66), B17 (56)	B18 (12)	B03 (6.2), B04 (6.4), B07 (6.4), B08 (6.3), B09 (6.4), B14 (6.3), B15 (6.3), B16 (6.4), B20 (6.4), B22 (6.4)	B08 (6.02), B12 (218), B14 (9.1), B18 (13.2), B20 (34.4), B22 (34.4), B24 (41) B32 (12.2)	B06 (3.5)	B08 (0.39)	B12 (469.9)
Total (%)	19 (59.4)	11(34.4)	2 (6.3)	4 (12.5)	1 (3.1)	10 (31.3)	7 (21.9)	1 (3.1)	1 (3.1)	1 (3.1)
WHO standards	0	0	0	0	0	6.5–8.5	5	≤1.5	≤0.3	≤50

TC = total coliforms; EC = *E. coli*; IE = intestinal enterococci; PA = *Pseudomonas aeruginosa*; ASRBS = anaerobic sulphite-reducing bacteria spores; CFU = colony-forming units; NTU = nephelometric turbidity unit. The CFU count for the microbiological parameters and the values for the physicochemical parameters are mentioned in parentheses.

In terms of microbiological quality, 62% of borehole water samples were noncompliant with WHO and national standards (0 CFU/100 mL) for containing total coliforms, *E. coli*, intestinal enterococci, *Pseudomonas aeruginosa*, or anaerobic sulphite-reducing bacteria spores (Table S1).

3.2. Physicochemical Quality of Water Samples

Major noncompliances of physicochemical water quality were related to turbidity, pH, nitrate, fluoride, and iron (Table S1). Box plots for the measured physicochemical parameters show the concentrations of each physicochemical parameter (Figure 3).

Turbidity values varied between 0.19 and 218 nephelometric turbidity units (NTUs). The national maximum value for drinking water is 5 NTUs, and it was exceeded in eight borehole water samples. An exceptionally high value was obtained for water from one borehole: the value was 43.6 times higher than the maximum value according to the national guideline.

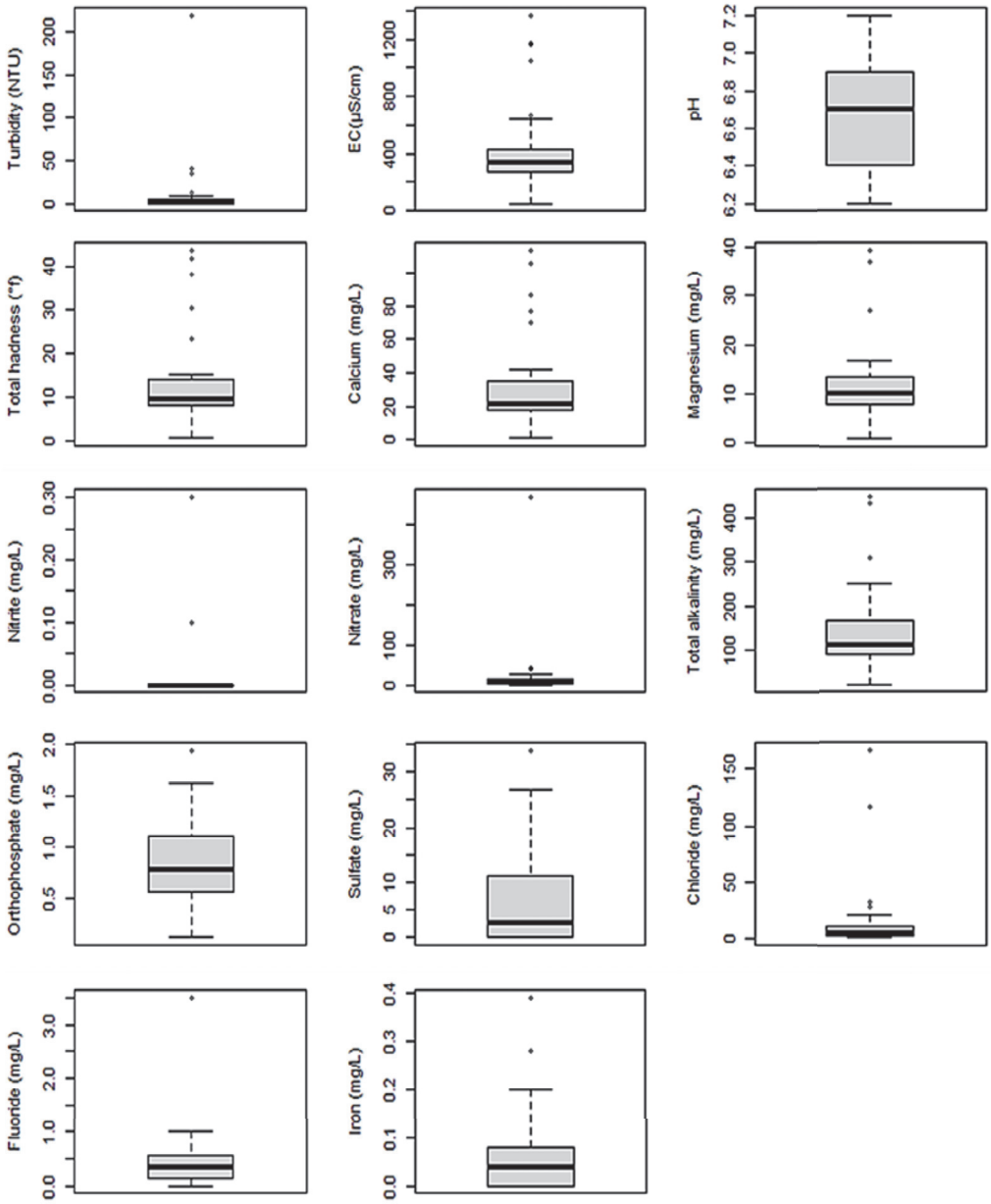

Figure 3. Box plots for physicochemical parameters quantified for 32 borehole water samples. The hinges represent the lower and upper quartiles, within which 50% of the data lie. The horizontal line within the box represents the median. The whiskers extend to the most extreme value within 1.5 interquartile range above or below the hinges, with dots beyond the whiskers indicating outliers. EC = electrical conductivity.

Electrical conductivity (EC) provided a general overview of the mineralization of borehole water in Ouagadougou. The values obtained varied between 50.1 and 1365 µS/cm, which are in compliance with the WHO guideline of ≤2500 µS/cm. There is no national standard for this parameter. EC represents total dissolved ions in groundwater samples, and impacts the taste of water. Low EC indicates a low amount of salt associated with good taste.

pH represents the concentration of hydrogen ions in a solution. Ten borehole water samples were not in the acceptable pH range, which is between 6.5 and 8.5 according to the national guideline.

The concentration of calcium varied from 0.9 to 114.2 mg/L, with the WHO guideline being ≤200 mg/L. The concentration of magnesium ranged from 0.9 to 39.5 mg/L, with

the WHO guideline being ≤50 mg/L. The total hardness of water is the sum of all calcium and magnesium salts present, carbonated and noncarbonated.

Nitrite and nitrate concentration ranged between 0 and 0.3 mg/L and 0 and 469.9 mg/L, respectively. According to national standards, nitrite and nitrate should not exceed 3 mg/L and 50 mg/L, respectively. Thus, the value of 469.9 mg/L for nitrate was much higher than the standard for drinking water.

Total alkalinity concentration ranged from 69.6 to 446.5 mg/L. Total alkalinity is a measure of the ability of water to resist changes in pH.

Orthophosphate concentration varied from 0.13 to 1.94 mg/L. There is no standard for this parameter, but orthophosphates are effective in limiting corrosion.

Sulfate concentration ranged from 0 to 34 mg/L, and was compliant with the national guideline which is ≤250 mg/L. High sulfate concentration in water can cause diarrhoea, leading to severe dehydration over the long term.

Chloride concentration varied between 0.7 and 166.9 mg/L. All the borehole water samples thus complied with the national guideline of ≤250 mg/L.

Fluoride values varied between 0 and 3.5 mg/L. The national guideline for drinking water is 1.5 mg/L, with only one borehole water sample exceeding this.

Iron concentration varied from 0 to 0.39 mg/L. The national guideline for drinking water is 0.3 mg/L, and only one borehole water exceeded this.

In conclusion, based on physicochemical parameters, 17 (53.1%) borehole water samples met the quality standards.

3.3. Overall Water Quality

Overall, 75% of the borehole water samples were not potable due to their noncompliance with the acceptable microbiological or physicochemical parameters or both. Most of the nonconformities were related to microbiology, as the microbiological and physicochemical noncompliance of the borehole waters were 62% and 44%, respectively.

Principal component analysis (PCA) was performed to detect possible correlations between the parameters measured (Figure 4, Tables S2–S4). Three main groups were formed: The first one included variables positively correlated with both axes (F1). It included chlorides (Cl^-, turbidity, nitrite ($NO_2{}^-$), and nitrate ($NO_3{}^-$). The second group was positioned positively on the x-axis (F1) and negatively on the y-axis (F2). It included calcium, magnesium, EC, TH, TA, pH, SO $SO_4{}^{2-}$, and F^-. The third group was positioned mainly on the negative side of the F1 axis, with a contribution of 42.7%. It included iron (Fe^{2+}) and orthophosphate ($PO4^{3-}$). The analysis showed that the biological factors are not correlated with any physical or chemical parameters.

3.4. Risk Factors for Borehole Contamination

According to multivariate data analysis (NMDS), water parameters were significantly affected by the environmental variables SS ($p = 0.026$), GH ($p = 0.038$), ST ($p = 0.029$), DWB ($p = 0.002$), and total risk score ($p = 0.010$).

Sludge spreading within 15 m (SS) was significantly associated with higher levels of ammonium and *E. coli* (ANOVA for binomial GLM: ammonium χ^2 (1.23) residual deviance RD = 2.8, $p = 0.002$; *E. coli* χ^2 (1.12) RD = 0.0, $p < 0.001$).

Garbage heap within 15 m (GH) was significantly associated with higher levels of ammonium, bicarbonate, and *P. aeruginosa*, and with lower levels of calcium (ANOVA for binomial GLM: ammonium χ^2 (1.23) RD = 24.1, $p = 0.03$; bicarbonate χ^2 (1.20) RD = 2.8, $p < 0.001$; *P. aeruginosa* χ^2 (1.11) RD = 144, $p < 0.001$; calcium χ^2 (1.25) RD 31.1, $p = 0.02$).

Presence of a septic tank within 15 m (ST) was significantly associated with higher levels of water hardness, nitrite, and nitrate, and with lower levels of ammonium (ANOVA for binomial GLM: water hardness χ^2 (1.26) RD = 32.6, $p = 0.01$; nitrite χ^2 (1.22) RD = 17.2, $p = 0.002$; nitrate χ^2 (1.21) RD = 0, $p < 0.001$; ammonium χ^2 (1.23) RD 27.0, $p = 0.048$).

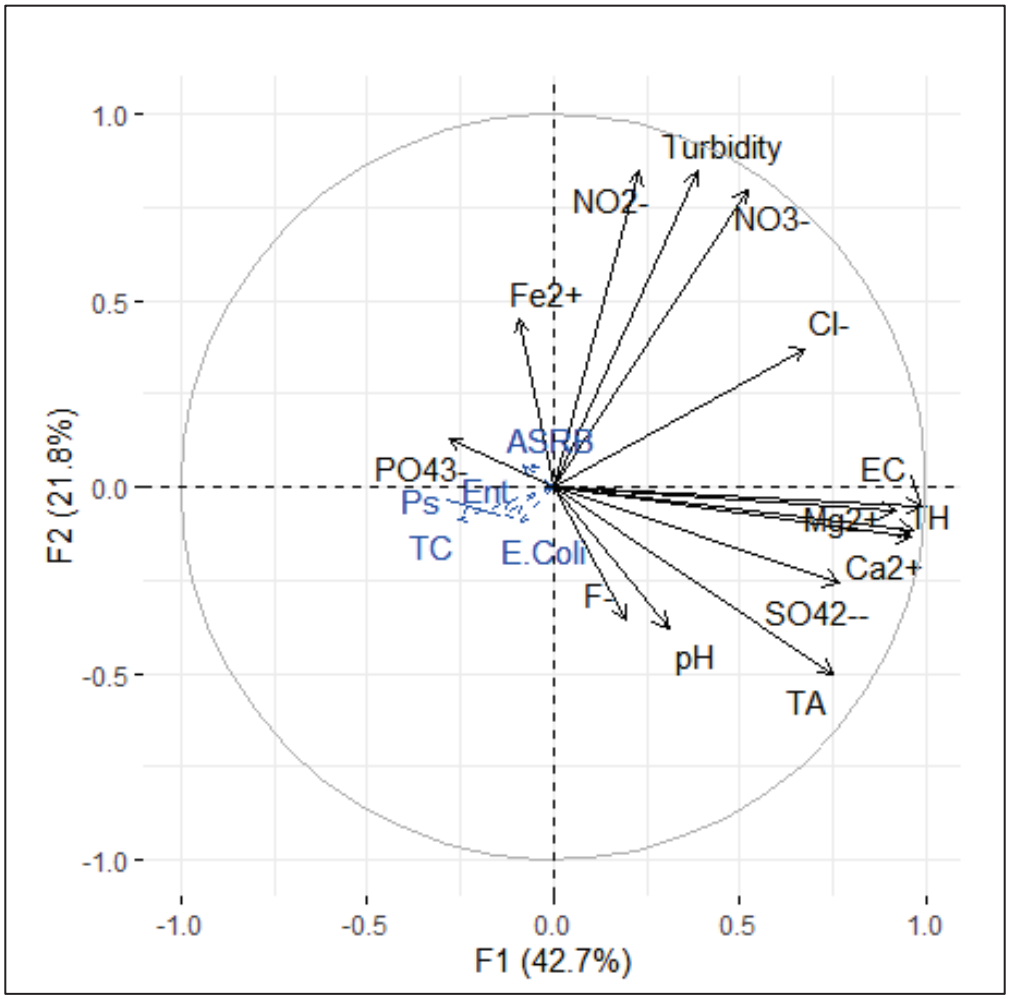

Figure 4. Correlation circle from principal component analysis (PCA) showing three main groupings for the physicochemical characteristics of the waters studied.

Dirty water near borehole (DWB) was significantly associated with higher levels of turbidity and sulphate, and with lower levels of nitrate (ANOVA for binomial GLM: water turbidity χ^2 (1.29) RD = 37.8, $p = 0.02$; sulphate χ^2 (1.18) RD = 0, $p = 0.001$; nitrate χ^2 (1.21) RD = 12.6, $p < 0.001$).

Total risk score was significantly associated with higher levels of turbidity, calcium, silica, total coliforms, and, marginally significantly, with *E. coli* (ANOVA for linear regression: turbidity F (1.29) = 27.7, $p < 0.001$; calcium F (1.25) = 41.2, $p = 0.003$; silica F (1.14) = 21.3, $p = 0.04$; total coliforms F (1.13) = 15.4, $p = 0.002$; *E. coli* F (1.12) = 9.2, $p = 0.05$).

4. Discussion

Thirty-two (32) boreholes were studied to assess their microbiological and physiological water quality and the anthropogenic risk factors correlated with water quality. The majority of the water samples (75%) did not comply with official sanitary requirements. Total coliforms and heterotrophic bacteria in water are indicators for poor hygienic quality, while *E. coli* and faecal coliforms indicate potential faecal contamination [30]. *E. coli* was detected in 34.4% of the borehole water samples. The standards set by the WHO or Burkinabe government for potable water require 0 CFU/100 mL for total coliforms, *E. coli*, intestinal enterococci, and *Pseudomonas aeruginosa*. However, many of the studied boreholes contained these bacteria. Of the anthropogenic risk factors observed, sludge spreading and a garbage heap within 15 m were significantly associated with high levels of *E. coli* and *P. aeruginosa.* The total risk score was significantly associated with higher

levels of total coliforms and, marginally significantly, with higher levels of *E. coli*. In other studies conducted in Africa, the presence of surface water and wastewater, potentially carrying harmful microorganisms, near boreholes was the greatest hazard identified as a source of groundwater contamination [10,31,32]. Connections between microbiological contamination and anthropogenic activities such as land application of wastewater biosolids, municipal solid waste landfills, agricultural operations, and poor sanitary practices have also been reported [32].

In the present study, intestinal enterococci and anaerobic sulphite-reducing bacterial spores were used as additional indicators for faecal contamination, as suggested previously [33]. They are more resistant than coliforms in the natural environment, and thus their presence in some of our borehole water samples can be due to past contamination.

In the present study, only one borehole water sample was noncompliant for nitrates, which seems rare compared to a previous study. Previously, in an analysis on the relationship between urban centers in sub-Saharan Africa and aquifer pollution risk for nitrate, Ouagadougou was shown to be at high risk for nitrate pollution [34]. High nitrate content is also frequently associated with a high number of faecal indicator bacteria, indicating faecal contamination of urban groundwater in Africa [35,36]. Generally, leaching of chemicals, agricultural fertilizers, animal manure, pollution from septic tanks, sewage discharge, atmospheric deposition, decomposition of plant and animal organisms, other wastewater and refuse released to the environment from domestic work are the main sources of nitrates and nitrite in water [10,31,33,37–40]. Long-term exposure to nitrate can result in adverse health effects such as headache, stomach cramps, vomiting, or increased heart rate [6]. Nitrate transformation into nitrites is more toxic and can potentially have a negative impact on health. In this study, the high content of nitrate in one borehole could be due to the presence of a septic tank nearby. The presence of a septic tank within 15 m was significantly associated with higher levels of water hardness, nitrite, and nitrate. However, this particular borehole is not the only one whose distance is less than 15 m from a septic tank, and thus other reasons such as the depth of the borehole, which was not taken into account in this study, should be considered. Only one borehole water sample was noncompliant for fluoride, although Burkina Faso is located in a region where relatively high geogenic fluoride concentration in groundwater has been predicted [41]. The main intake pathways of fluoride for humans are drinking water and food intake. Potential risks associated with high concentrations of fluorides ingestion include tooth damage and pronounced skeletal fluorosis following long-term exposure [13,41].

Water from one borehole was noncompliant for iron. Iron is known to cause an unpleasant metallic taste in water and a reddish colour, which could be linked to deoxygenation of water by organic activity in the soil and in the unsaturated zone [42]. Taste alteration is also the main impact of increased electrical conductivity in water [43]. Strongly correlated parameters such as Mg^{2+}, Ca^{2+}, total hardness, total alkalinity, and electrical conductivity were observed in the present study, similar to observations made in Niger by Amadou et al. [16].

Dirty water near a borehole can lead to the flow of runoff water into the borehole, and a consequent increase in turbidity affecting the acceptability of water to consumers [44]. Dirty water near a borehole was also found to be significantly associated with high levels of turbidity. Turbidity could also be due to the presence of suspended solids such as clay or silt, which give the water a cloudy appearance [45]. A significant association was not detected between turbidity and microbiological contamination in this study, although out of eight borehole water samples that did not comply with turbidity guidelines, six were also microbiologically noncompliant. A parameter not taken into account in our study was the depth of the boreholes. This can have an impact on the quality of the water, and several previous studies have indeed revealed shallow groundwaters to be polluted by chemicals and biological contaminants [31,46–48]. In addition to the depth of the borehole, seasonal variability and the number of people drawing water from each borehole were not considered in this study, but should be considered in subsequent studies. New methods

based on, for example, geographical information systems (GIS) and machine learning, have been utilized to improve surface water quality assessment [49,50]. Additionally, for groundwater quality assessment, new techniques including geoinformatics, remote sensing, and big data science are needed [7].

5. Implications

The common detection of deviations from water quality standards in groundwater samples indicates a need for continuous efforts by the government through the Ministry of Health and Public Hygiene to ensure the safety and quality of groundwater in Ouagadougou. By strengthening training programs, raising awareness, and implementing effective monitoring systems, the quality of borehole water can be maintained, safe-guarding public health. Moreover, there is need for regular surveillance of water quality and the environment surrounding boreholes.

6. Conclusions

This study showed that the groundwater in Ouagadougou is vulnerable to microbiological contamination due to anthropogenic activities. Most of the boreholes were in an intermediate-risk or a low-risk environment due to risks related to practices in the vicinity of the boreholes. Therefore, in order to prevent pollution, more attention must be paid to the maintenance of borehole surroundings. This requires both increased awareness among the population and enforcement of good practices by city authorities. Practices such as sludge spreading and having a garbage heap, a latrine, a septic tank, or dirty water near the borehole must be abolished. Outward slopes must be constructed around boreholes. Additional treatment measures such as filtration or disinfection of borehole water would also reduce the risks for public health. These changes can protect the boreholes as important sources of drinking water in Ouagadougou.

Supplementary Materials: The following supporting information can be downloaded at: https://www.mdpi.com/article/10.3390/w15213734/s1, Table S1: Physicochemical and microbiological parameters of borehole water; Table S2: Extraction Method, Principal Component Analysis; Table S3: Contribution of physicochemical parameters in the main components; Table S4: Correlation matrix between the microbiological and physicochemical parameters.

Author Contributions: Conceptualization, O.T.; methodology, O.T.; validation, O.T., D.S.K., R.D., C.K.S.S., J.C., K.H. and N.B.; statistical analysis, J.C. and O.T.; investigation, O.T.; resources, O.T.; data curation, O.T.; writing—original draft preparation, O.T.; writing—review and editing, O.T., K.H., J.C., C.K.S.S. and D.S.K.; supervision, N.B.; project administration, N.B. All authors have read and agreed to the published version of the manuscript.

Funding: The National Public Health Laboratory supported the study by providing the use of their technical equipment. Open access funding provided by University of Helsinki.

Data Availability Statement: Not applicable.

Conflicts of Interest: The authors declare no conflict of interest.

References

1. United Nations. *The Sustainable Development Goals Report*; United Nations: Geneva, Switzerland, 2022; p. 68.
2. Akoachere, J.T.K.A.; Omam, L.; Massalla, T.N. Assessment of the relationship between bacteriological quality of dug-wells, hygiene behaviour and well characteristics in two cholera endemic localities in Douala, Cameroon. *BMC Public Health* **2013**, *13*, 692–703. [CrossRef]
3. Baye, S.; Eshetie, M.; Denekew, T. Bacteriological and physicochemical quality of drinking water in Wegeda Town, Northwest Ethiopia. *J. Environ. Public Health* **2021**, *2021*, 6646269. [CrossRef]
4. Prüss-Ustün, A.; Bartram, J.; Clasen, T.; Colford, J.M., Jr.; Cumming, O.; Curtis, V.; Bonjour, V.; Dangour, A.D.; De France, J.; Fewtrell, L.; et al. Burden of disease from inadequate water, sanitation and hygiene in low- and middle-income settings: A retrospective analysis of data from 145 countries. *Trop. Med. Int. Health* **2014**, *19*, 894–905. [CrossRef]
5. MacDonald, A.M.; Bonsor, H.C.; O'Dochartaigh, B.E.O.; Taylor, R.G. Quantitative maps of groundwater resources in Africa. *Environ. Res. Lett.* **2012**, *7*, 024009. [CrossRef]

6. Lapworth, D.J.; MacDonald, A.M.; Tijani, M.N.; Darling, W.G.; Gooddy, D.C.; Bonsor, H.C.; Araguás-Araguás, L.J. Residence times of shallow groundwater in West Africa: Implications for hydrogeology and resilience to future changes in climate. *Hydrogeol. J.* **2013**, *21*, 673–686. [CrossRef]
7. Lapworth, D.; Boving, T.; Brauns, B.; Dottridge, J.; Hynds, P.; Kebede, S.; Kreamer, D.; Misstear, B.; Mukherjee, A.; Re, V.; et al. Groundwater quality: Global challenges, emerging threats and novel approaches. *Hydrogeol. J.* **2023**, *31*, 15–18. [CrossRef]
8. Rao, N.S. Seasonal variation of groundwater quality in a part of Guntur District, Andhra Pradesh, India. *Environ. Geol.* **2006**, *2006*, 413–429. [CrossRef]
9. Motlagh, A.M.; Yang, Z.; Saba, H. Groundwater quality. *Water Environ. Res.* **2020**, *92*, 1649–1658. [CrossRef]
10. Conboy, M.; Goss, M. Natural protection of groundwater against bacteria of fecal origin. *J. Contam. Hydrol.* **2000**, *43*, 1–24. [CrossRef]
11. Howard, G.; Pedley, S.; Barrett, M.; Nalubega, M.; Johal, K. Risk factors contributing to microbiological contamination of shallow groundwater in Kampala, Uganda. *Water Res.* **2003**, *37*, 3421–3429. [CrossRef]
12. Foppen, J.W.A.; van Herwerden, M.; Kebtie, M.; Noman, A.; Schijven, J.F.; Stuyfzand, P.J.; Uhlenbrook, S. Transport of *Escherichia coli* and solutes during waste water infiltration in an urban alluvial aquifer. *J. Contam. Hydrol.* **2008**, *95*, 1–16. [CrossRef] [PubMed]
13. Abdelkader, B.; Abdelhak, M.; Abdeslam, K.; Ahmed, M.; Brahim, Z. Estimation of pollution load of domestic sewage to Oued Bechar (SW Algeria) and its impact on the microbiological quality of groundwater. *Procedia Eng.* **2012**, *33*, 261–267. [CrossRef]
14. Odiyo, J.O.; Makungo, R. Chemical and microbial quality of groundwater in Siloam village, implications to human health and sources of contamination. *Int. J. Environ. Res. Public Health* **2018**, *15*, 317. [CrossRef] [PubMed]
15. DWA. *Groundwater Strategy*; Department of Water Affairs: Pretoria, South Africa, 2010; p. 64.
16. Raphael, O.; John, O.O.; Sandra, U.I.; Sunday, A.C. Assessment of borehole water quality consumed in Otukpo and its environs. *Int. J. Ecol. Sci. Environ. Eng.* **2018**, *5*, 71–78.
17. Adamou, H.; Ibrahim, B.; Salack, S.; Adamou, R.; Sanfo, S.; Liersch, S. Physico-chemical and bacteriological quality of groundwater in a rural area of Western Niger: A case study of Bonkoukou. *J. Water Health* **2020**, *18*, 77–90. [CrossRef]
18. Bretzler, A.; Lalanne, F.; Nikiema, J.; Podgorski, J.; Pfenninger, N.; Berg, M.; Schirmer, M. Groundwater arsenic contamination in Burkina Faso, West Africa: Predicting and verifying regions at risk. *Sci. Total Environ.* **2017**, *584–585*, 958–970. [CrossRef]
19. Sako, A.; Ouangaré, C.A.C. Hydrogeochemical characterization and natural background level determination of selected inorganic substances in groundwater from a semi-confined aquifer in Midwestern Burkina Faso, West Africa. *Environ. Monit. Assess.* **2023**, *195*, 519–545. [CrossRef]
20. Faye, M.D.; Kafando, M.B.; Sawadogo, B.; Panga, R.; Ouédraogo, S.; Yacouba, H. Groundwater Characteristics and Quality in the Cascades Region of Burkina Faso. *Resources* **2022**, *11*, 61. [CrossRef]
21. Lewis, W.J.; Foster, S.S.D.; Drasar, B.S. *The Risk of Groundwater Pollution by On-Site Sanitation in Developing Countries*; International Reference Centre for Waste Disposal: Duebendorf, Switzerland, 1982; p. 79.
22. Graham, J.P.; Matthew, L.P. Pit latrines and their impacts on groundwater quality: A systematic review. *Environ. Health Perspect.* **2013**, *121*, 521–530. [CrossRef]
23. Schijven, J.F.; Hassanizadeh, S.M.; Husman, A.M.D. Vulnerability of unconfined aquifers to virus contamination. *Water Res.* **2010**, *44*, 1170–1181. [CrossRef] [PubMed]
24. Rodier, J.; Legube, B. *L'analyse de L'eau, Contrôle et Interprétation*, 10th ed.; Dunod: Paris, France, 2016; p. 1759.
25. Castaing, C.; Billa, M.; Milesi, J.P.; Thieblemont, D.; Le Metour, J.; Egal, E.; Donzeau, M.; Guerrot, C.; Cocherie, A.; Chevremont, P.; et al. *Notice Explicative de la Carte Géologique et Minière à 1/1,000,000 du Burkina Faso*; Bureau de Recherches Géologiques et Minières: Orléans, France, 2003; p. 148.
26. Lutterodt, G.; Van de Vossenberg, J.; Hoiting, Y.; Kamara, A.K.; Oduro-Kwarteng, S.; Foppen, J.W.A. Microbial ground water quality status of hand-dug well and boreholes in the Dodowa area of Ghana. *Int. J. Environ. Res. Public Health* **2018**, *15*, 730. [CrossRef]
27. APHA; AWWA; WEF. *Standard Methods for Examination of Water and Wastewater*, 2nd ed.; American Public Health Association: Washington, DC, USA, 2012; p. 1360.
28. R Core Team. *R: A Language and Environment for Statistical Computing*; R Foundation for Statistical Computing: Vienna, Austria, 2020; Available online: https://www.R-project.org/ (accessed on 30 June 2022).
29. Oksanen, J.; Simpson, G.; Blanchet, F.; Kindt, R.; Legendre, P.; Minchin, P.; O'Hara, R.; Solymos, P.; Stevens, M.; Szoecs, E.; et al. Vegan: Community Ecology 2022, Package. R Package Version 2.6-4. Available online: https://CRAN.R-project.org/package=vegan (accessed on 30 June 2022).
30. Edberg, S.C.; Rice, E.W.; Karlin, R.J.; Allen, M.J. *Escherichia coli*: The best biological drinking water indicator for public health protection. *J. Appl. Microbiol.* **2000**, *88*, 106–116. [CrossRef]
31. Taonameso, S.; Mudau, L.S.; Traoré, A.N.; Potgetier, N. Borehole water: A potential health risk to rural communities in South Africa. *Water Supply* **2019**, *19*, 128–136. [CrossRef]
32. Pantaleo, P.A.; Komakech, H.C.; Mtei, K.M.; Njau, K.N. Contamination of groundwater sources in emerging African towns: The case of Babati town, Tanzania. *Water Pract. Technol.* **2018**, *13*, 980–990. [CrossRef]
33. Rice, E.W.; Covert, T.C.; Wild, D.K.; Berman, D.; Johnson, S.A.; Johnson, C.H. Comparative resistance of *Escherichia coli* and enterococci to chlorination. *J. Environ. Sci. Health A* **1996**, *28*, 89–97.

34. Kurwadkar, S.; Kanel, S.R.; Nakarmi, A. Groundwater pollution: Occurrence, detection, and remediation of organic and inorganic pollutants. *Water Environ. Res.* **2020**, *92*, 659–1668. [CrossRef]
35. Ouedraogo, I.; Defourny, P.; Vanclooster, M. Mapping the groundwater vulnerability for pollution at the pan African scale. *Sci. Total Environ.* **2016**, *544*, 939–953. [CrossRef] [PubMed]
36. Lapworth, D.J.; Nkhuwa, D.W.C.; Okotto-Okotto, J.; Pedley, S.; Stuart, M.E.; Tijani, M.N.; Wrigh, J. Urban groundwater quality in sub-Saharan Africa: Current status and implications for water security and public health. *Hydrogeol. J.* **2017**, *25*, 1093–1116. [CrossRef]
37. Sharma, B.; Parul; Verma, A.K.; Jain, U.; Yadav, J.K.; Singh, R.; Mishra, R. Occurrence of multidrug resistant *Escherichia coli* in groundwater of Brij region (UP) and its public health implications. *Vet. World* **2017**, *10*, 293–301. [CrossRef]
38. Razafitsiferana, T.; Bruno, R.; Mihasina, R.; Mahandrimanana, A. Analysis of the Physico-Chemical Parameters of the Water of the River of Mahavavy Situated in the District of Ambilobe, in the Region of Diana (DIEGO SUEREZ). *Resour. Environ.* **2017**, *7*, 168–175. [CrossRef]
39. Atekwana, E.A.; Geyer, C.J. Spatial and temporal variations in the geochemistry of shallow groundwater contaminated with nitrate at a residential site. *Environ. Sci. Pollut. Res. Int.* **2018**, *25*, 27155–27172. [CrossRef]
40. Huan, H.; Hu, L.; Yang, Y.; Jia, Y.; Lian, X.; Ma, X.; Jiang, Y.; Xi, B. Groundwater nitrate pollution risk assessment of the groundwater source field based on the integrated numerical simulations in the unsaturated zone and saturated aquifer. *Environ. Int.* **2020**, *137*, 105532–105541. [CrossRef] [PubMed]
41. World Water Quality Alliance. Assessing Groundwater Quality: A Global Perspective: Importance, Methods and Potential Data Sources; A Report by the Friends of Groundwater in the World Water Quality Alliance. In Proceedings of the 5th Session of the United Nations Environment Assembly, Nairobi, Kenya, 22–23 February 2021.
42. Goné, D.L.; Savané, I.; Yao, N.A.; Biémi, J. Analysis and Control of the Physicochemical Quality of Groundwater in the Chari Baguirmi Region in Chad. *Man. Sci. Nat.* **2005**, *11*, 85–94. [CrossRef]
43. CEAEQ. *Détermination de la Conductivité: Méthode Électrométrique, MA. 115–Cond. 1.1, rév. 1 (Determination of Conductivity: Electrometric Method, MA. 115–Cond. 1.1, rev. 1)*; Centre d'Expertise en Analyse Environnementale du Québec Ministère du Développement Durable, de l'Environnement et de la Lutte Contre les Changements Climatiques: Québec City, QC, Canada, 2020.
44. WHO. *Guidelines for Drinking-Water Quality, 4th ed*; World Health Organization: Geneva, Switzerland, 2011.
45. Bantin, A.B.; Wang, H.; Jun, X. Analysis and control of the physicochemical quality of groundwater in the Chari Baguirmi Region in Chad. *Water* **2020**, *12*, 2826. [CrossRef]
46. Masindi, V.; Foteinis, S. Groundwater contamination in sub-Saharan Africa: Implications for groundwater protection in developing countries. *Clean. Ing. Technol.* **2021**, *2*, 100038. [CrossRef]
47. Sorensen, J.; Lapworth, D.; Nkhuwa, D.; Stuart, M.; Gooddy, D.; Bell, R.; Chirwa, M.; Kabika, J.; Liemisa, M.; Chibesa, M.; et al. Emerging contaminants in urban groundwater Sources in Africa. *Water Res.* **2014**, *72*, 51–63. [CrossRef]
48. Nyenje, P.; Foppen, J.M.; Kulabako, R.; Muwanga, A.; Uhlenbrook, S. Nutrient pollution in shallow aquifers underlying pit latrines and domestic solid waste dumps in urban slums. *J. Environ. Manag.* **2013**, *122*, 15–24. [CrossRef] [PubMed]
49. Wong, Y.J.; Shimizu, Y.; He, K.; Sulaiman, N.M.N. Comparison among different ASEAN water quality indices for the assessment of the spatial variation of surface water quality in the Selangor river basin, Malaysia. *Environ. Monit. Assess.* **2020**, *192*, 644–659. [CrossRef]
50. Wong, Y.J.; Shimizu, Y.; Kamiya, A.; Maneechot, L.; Bharambe, K.P.; Fong, C.S.; Sulaiman, N.M.N. Application of artificial intelligence methods for monsoonal river classification in Selangor river basin, Malaysia. *Environ. Monit. Assess.* **2021**, *193*, 438–459. [CrossRef]

Disclaimer/Publisher's Note: The statements, opinions and data contained in all publications are solely those of the individual author(s) and contributor(s) and not of MDPI and/or the editor(s). MDPI and/or the editor(s) disclaim responsibility for any injury to people or property resulting from any ideas, methods, instructions or products referred to in the content.

water

MDPI

Article

Water–Rock Interactions, Genesis Mechanism, and Mineral Scaling of Geothermal Waters in Northwestern Sichuan, SW China

Guosen Lv [1,2], Xu Zhang [3,4,*], Denghui Wei [1], Zhongyou Yu [3,4], Xingcheng Yuan [1], Minglu Sun [5], Xiangxinyu Kong [5] and Yunhui Zhang [1,2,*]

1 Yibin Research Institute, Southwest Jiaotong University, Yibin 644000, China; yxcheng0722@163.com (X.Y.)
2 Engineering Research Center of Geothermal Resources Development Technology and Equipment, Ministry of Education, Jilin University, Changchun 130026, China
3 Sichuan Hua Di Building Engineering Co., Ltd., Chengdu 610081, China; yuzhongyou567@163.com
4 Sichuan Province Engineering Technology Research Center of Geohazard Prevention, Chengdu 610081, China
5 College of Engineering, Tibet University, Lasa 850000, China; 18638737150@163.com (X.K.)
* Correspondence: zhangxu1987613@163.com (X.Z.); zhangyunhui@swjtu.edu.cn (Y.Z.)

Abstract: Geothermal resources are the vital renewable energy for resolving energy crisis and environmental deterioration. Understanding hydrogeochemical processes, genesis mechanisms and scaling trends is crucial for securing the sustainable utilization of geothermal resources. In this study, fourteen geothermal waters were collected for hydrochemical and δ^2H–$\delta^{18}O$ isotopic analyses in northwestern Sichuan, SW China to clarify hydrogeochemical processes, genesis mechanisms, and scaling trends. Geothermal waters were recharged via atmospheric precipitation. Three different types of geothermal waters were identified using a piper diagram. Class 1 geothermal water with HCO_3–Na and HCO_3–SO_4–Na types formed in the contact zone with Yanshanian intrusions and heated by residual radioactive heat. The hydrochemical processes were sodium/potassium silicate dissolution and positive cation–exchange. Class 2 geothermal water with HCO_3–Ca and HCO_3–Ca–Mg type was carbonate–type and heated by geothermal gradient. The dissolution of carbonate minerals dominated the hydrochemical process. Class 3 geothermal water with the SO_4–Ca–Mg type was determined within deep faults. The dissolution of carbonatite and gypsum minerals and the oxidation of sulfides played a vital role in the hydrochemical process. The reservoir temperatures of geothermal waters followed the orders of Class 1 (74.9–137.6 °C) > Class 3 (85.9–100 °C) > Class 2 (38.7–93.5 °C). Calcium carbonate scaling should be paid attention to in Class1 and Class 3 geothermal water, and calcium sulfate scaling merely occurs in Class 3 geothermal water. This study provides vital information for geothermal exploitation in western Sichuan and other similar areas.

Keywords: western Sichuan; geothermal water; hydrogeochemical processes; geothermal reservoir; genesis model; scaling trends

1. Introduction

Because of energy shortage and environmental deterioration, the development and usage of clean energy have become a hot topic worldwide [1]. In the context of the "dual carbon" goal, geothermal energy, as a significant renewable energy, can effectively reduce carbon emissions and alleviate global warming [2–4]. Understanding the hydrogeochemical process and genesis mechanism of geothermal water is a prerequisite for the development and utilization of geothermal resources [5–8]. Meanwhile, the scaling of fluid components is a serious problem restricting the sustainable geothermal exploitation [9,10]. Therefore, the hydrogeochemical process, genesis mechanism, and scaling trends of geothermal waters play a vital role in geothermal study [11].

The hydrogeochemical properties in geothermal fluid provides insights into the ion source and reservoir temperature of geothermal water, which can reveal the genesis of

geothermal systems [5–8]. Correlation analysis can explore the relationship between hydrochemical components of geothermal fluid [12,13]. The reservoir temperature of the geothermal system is mainly based on mineral thermodynamics, such as SiO_2 geothermometer, silicon–enthalpy equations, cationic geothermometer, and the multi–mineral equilibrium [14]. δ^2H–$\delta^{18}O$ isotopes have emerged as a key technique for determining the recharge source of geothermal water [15,16]. Quantitative calculations have been widely used as a proven, inexpensive and effective method for identifying scaling trends of geothermal water [17].

Abundant geothermal resources had been investigated in the Ganzi and Aba areas of western Sichuan, SW China. However, significant imbalance exists in geothermal research between Ganzi and Aba areas. Great progress in geothermal exploitation has been achieved in Ganzi area of western Sichuan for decades, such as in hydrochemical processes, genesis mechanisms, and regional geological background of the geothermal resources in the Xianshuihe, Ganzi–Litang, and Jinshajiang fault zones of western Sichuan [18–21]. Little research has been carried out on geothermal resources in the Aba area compared to those in the Ganzi area. Knowledge of the hydrochemical processes and genesis mechanisms of geothermal waters have yet to be revealed in the Aba region. Additionally, the scaling of fluid components is a vital index in the exploitation of geothermal resources [9,10]. Therefore, 14 groups of geothermal water samples were collected in Aba area for hydrogeochemical and δ^2H–$\delta^{18}O$ isotopic analyses. The aims of this study were (1) identifying hydrochemical types and hydrochemical process of geothermal waters, (2) clarifying reservoir temperature, (3) analyzing recharge sources and elevation, and (4) estimating the scaling trend of geothermal water. These achievements would provide a significant reference for geothermal exploitation and utilization in western Sichuan and other similar areas.

2. Materials and Methods

2.1. Geological Setting

Western Sichuan is situated at the convergence of the Tibetan Plateau and the Sichuan Basin. Tectonically, it belongs to the southwest edge of the Songpan–Ganzi Indo–Chinese orogenic belt [7]. Because of the active neo–tectonic processes, amounts of geothermal resources were developed here [20,22]. The study area is situated in the north region of western Sichuan, with its longitude ranging between 100°30′ E and 104°30′ E and latitude between 30°35′ N and 34°20′ N. It is characterized by high mountain valleys with the highest elevation of 5588 m and the lowest elevation of 1640 m. The study area experiences a plateau monsoon climate, with an average annual temperature of 8.2 °C and an annual rainfall ranging from 500–830 mm [7,23]. The entire region is traversed by the Min River and its tributaries.

The Aba area experienced complex regional tectonics due to belonging to the Songpan–Ganzi fold belt [24]. The fold belt extends in a northeast–southwest direction, ranging from 40° to 50°. It is bounded by the Maqin–Lueyang deep fault zone in the north, the Minjiang fault zone in the east, and the Qinling trough fold system and the Yangzi platform to the east of the Maowen deep fault zone. Many faults were developed in the study area, including the NE–trending Maowen deep fault zone, the E–W–trending Maqin–Lueyang deep fault zone, the N–S–trending Minjiang–Huya fault zone, and other, smaller faults like the Maerkang fault and Miyaluo fault (Figure 1). The generation, storage, and circulation of geothermal fluid in the region are critically dependent on these faults. The fault's tensile fracture zones offer ideal passageways and heat reservoirs, and the wide feather–jointed fissures create water–conducting channels that allow the hot springs to be exposed. Intrusive rocks, such as Triassic granite, phyllite, and other types, are scattered in the south of the Aba area. The sedimentary strata—including Sinian and Silurian dolomite; Quaternary and Triassic sandstone; Triassic calcisilicarenite, slate, pebbly sandstone, and sandstone; Quaternary and Cambrian conglomerate; and a few crystallized chert—are widely distributed in the north of the study area.

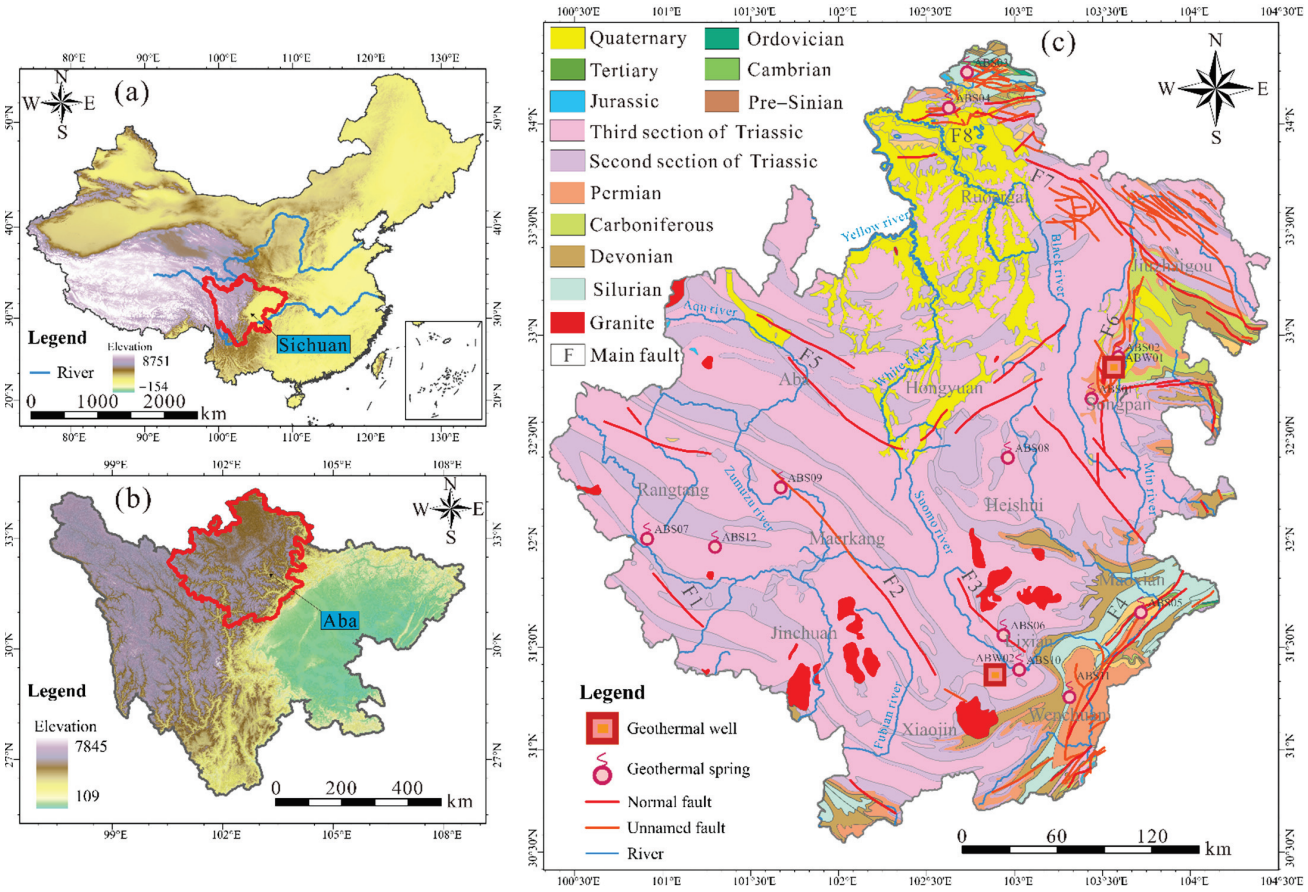

Figure 1. (**a**) China map; (**b**) Sichuan Province map; (**c**) regional geological map in the study area (F1: Jiaxuxiang–a secondary fault of the Seda fault zone; F2: Maerkang; F3: Miyaluo; F4: Maowen; F5: Aba; F6: Minjiang–Huya; F7: Maqu–Heye; F8: Maqin–Lueyang).

The geographical locations of geothermal water are mainly concentrated in Songpan county and Mao–Li–Wenchuan counties (Figure 1), and their exposed elevation range is 1703–3920 m [7]. The temperatures of the hot springs and geothermal wells ranges from 10.5 °C to 48 °C and from 38 °C to 65 °C, respectively. The Bipenggou geothermal well has the highest water temperature, reaching 65 °C (Figure 2a). The geothermal water flow rate varies between 2.4 L/s and 3.0 L/s. Sulfur odor smells are present in Jiyugou, Yuansanzi, Jiangzha, and Heta hot springs, and white calcified deposits are found at the mouth of the Yuansanzi hot spring (Figure 2b–e). Additionally, the Erdaohai hot spring is surrounded by a human–made hole to form a pool, with lumpy yellow sinter deposit at the bottom (Figure 2f). Similarly, the Guergou hot spring has been buried by a landslide, and it is now held downhill by a pipe and stored in a pool (Figure 2g,h). The Kejiu hot spring is artificially drilled water, the well is 46 m deep, and geothermal water which is acidic gushes out from the wellhead (Figure 2i).

Figure 2. Photos of part of the geothermal water exposed locations: (**a**) ABW02, (**b**) ABS02, (**c**) ABS03, (**d**) ABS04, (**e**) ABS05, (**f**) ABS01, (**g**,**h**) ABS06, and (**i**) ABS07.

2.2. Methods

2.2.1. Sampling and Analysis

The water samples were collected in 2019 and 2020. The initial determinations of temperature, acidity and alkalinity (pH), and total dissolved solids (TDS) were carried out in the field using a Multi3630IDS portable multiparameter water quality meter from Germany. Additionally, a Gran titration was conducted to determine the HCO_3 content using HNO_3. All water samples were initially filtered using a 0.45 μm filtration membrane. The 550 mL HDPE bottles were washed three times in the field before collecting the samples, which were then sealed with wax. The comprehensive analysis of the geothermal water samples was conducted by Sichuan Huadi New Energy Environmental Protection Technology Co. Ltd., while the δ^2H–$\delta^{18}O$ isotopic analysis was performed by the Institute of Hydrogeology and Environmental Geology, Chinese Academy of Geological Sciences. The concentrations of major cations (K^+, Na^+, Ca^{2+}, and Mg^{2+}) and major anions (Cl^- and $SO_4{}^{2-}$) in the samples were determined using inductively coupled plasma emission spectrometry (ICP–OES, testing precision 0.3–2.0%) and ion chromatography (Diona ICS–1100, testing precision 0.2%). The charge balance error was maintained below ±5%. δ^2H–$\delta^{18}O$ isotopes were measured using high–temperature thermal conversion element–isotope ratio mass spectrometry (HTC–IRMS) and Gasbench II isotope ratio mass spectrometry (Gasbench II–IRMS), respectively. The results were compared to the Vienna Standard Mean Ocean Water (VSMOW) as a standard, and the accuracies of δ^2H and $\delta^{18}O$ measurements were 1.0‰ and 0.2‰, respectively.

2.2.2. Geothermometer

The most–used geothermometer, the SiO_2 geothermometer, provides a reliable estimate of the geothermal reservoir temperature of geothermal water. The corresponding empirical equations of the quartz geothermometer are as follows [25]:

$$\text{No steam loss}: \ T(°C) = 1309/(5.19 - \log(SiO_2)) - 273.15 \quad (1)$$

$$\text{Maximum steam loss}: \ T(°C) = 1522/(5.75 - \log(SiO_2)) - 273.15 \quad (2)$$

where SiO_2 represents SiO_2 solubility in mg/L.

Geothermal water from the deep upward transport is frequently mixed to varying degrees with shallow cold water, so silica enthalpy equations and the silica enthalpy graphic methods are used to determine the initial temperature of geothermal water and the ratio of cold water mixing [7,8]. The involving equations are as follows [25]:

$$S_C X_1 + S_h(1 - X_1) = S_s \quad (3)$$

$$\rho C_{SiO2} X_2 + \rho H_{SiO2}(1 - X_2) = \rho S_{SiO2} \quad (4)$$

where S_c is the enthalpy of cold water (J/g); S_s is the final enthalpy of the hot spring (J/g, there is a certain relationship between the temperature and the enthalpy of geothermal water [25]); S_h is the initial enthalpy of the geothermal water (J/g); ρC_{SiO2} is the mass concentration of SiO_2 in the cold water (mg/L); ρS_{SiO2} is the mass concentration of SiO_2 in the spring water (mg/L); ρH_{SiO2} is the initial concentration of SiO_2 of the geothermal water (mg/L); X is the proportion of the cold water mixing.

2.2.3. Saturation Index

Saturation index (SI) is useful in understanding the mineral equilibrium in geothermal water [8,26]. In this study, we used the PHREEQC to calculate mineral saturation indices based on the equation [26]:

$$SI = \log(IAP/K) \quad (5)$$

where K is the equilibrium constant of the mineral dissolution reaction; IAP is the activity product of the relevant ions in the mineral dissolution reaction. When SI > 0, the mineral is oversaturated in the aqueous solution, and there is a tendency to precipitate; SI < 0, means that the mineral is not saturated in the aqueous solution; and when SI = 0, this suggests that the aqueous solution is exactly in equilibrium with the mineral.

2.2.4. Scaling Trend

Quantitative calculations are commonly employed as a reliable, cost–effective, and efficient approach to identifying scaling trends [17,27–29]. Thus, in this study, we have chosen quantitative calculations for predicting structural trends and analyzing corrosivity. The equations used for these calculations were presented in Table 1 and involve Larson's index, Ryzner's index, relative saturation index of gypsum ($CaSO_4$–$2H_2O$) ($R.S_{gypsum}$), and relative saturation of amorphous SiO_2 ($R.S_{SiO2}$).

Table 1. Quantitative calculation equations for scaling trends.

Method	Equation	No.	Reference
Larson Index (LI)	$LI = ([Cl^-] + [SO_4{}^{2-}])/[ALK]$	(6)	[17,27]
Ryzner Index (RI)	$RI = 2pH_1 - pH_2$	(7)	[17,28,29]
	$pH_1 = \log[Ca^{2+}] - \log[ALK] + Kc$	(8)	
	$pH_2 = \log[Ca^{2+}] - \log[ALK] + Ke$	(9)	
	$T(^\circ F) = 32 + 9/5 \times T$	(10)	
Relative saturation of gypsum ($R.S_{gypsum}$)	$R.S_{gypsum} = 10\hat{}(\log Ca^{2+} + \log SO_4{}^{2-} - \log K_{gypsum})$	(11)	[17]
Relative saturation of silica ($R.S_{SiO2}$)	$R.S_{SiO2} = SiO_2/(2.446 \times 10{,}000 \times e\hat{}(-1553/T_k))$	(12)	

3. Results

3.1. Hydrochemcial Facies

Table 2 shows that the study area's geothermal water samples are classified into three categories. The piper diagram in Figure 3 displays the scatter plots of cations (Ca^{2+}, Mg^{2+}, $Na^+ + K^+$) and anions ($HCO_3{}^-$, Cl^- and $SO_4{}^{2-}$) in water samples, allowing for the classification of hydrochemical properties [30].

Table 2. Statistics of basic hydrochemical parameters, main ions, and isotopes of geothermal springs and wells in the Aba area.

ID	Name	Class	Altitude (m)	T (°C)	pH	TDS (mg/L)	δ^2H	$\delta^{18}O$	Recharge Elevation (m)	No Steam Loss (°C)	Maximum Steam Loss (°C)	Reservoir Lithology
ABS06 [a]	Guergou	1	2583	48.0	9.1	68	−118.5	−16.6	4459	70.1	74.9	Granite
ABS07 [a]	Kejiu	1	3083	26.0	7.0	2190	−120.3	−16.1	4529	71.6	76.1	Sandstone
ABS08 [b]	Xiadagai	1	2369	35.0	9.1	229	−86.0	−12.1	3209	111.3	110.7	Calcisilicarenite
ABS09 [b]	Baoyan	1	2640	48.0	7.4	511	–	–	–	119.4	117.7	Slate/Phyllite
ABS10 [b]	Jiashikou	1	2925	44.0	9.3	384	–	–	–	117.0	115.6	Gravel–bearing sandstone
ABS11 [b]	Guanyinmiao	1	2612	32.0	7.5	2949	–	–	–	96.6	98.1	Limestone/Dolomite
ABS12 [d]	Youri	1	3920	23.0	9.5	227.4	−118.6	−16.4	4463	94.9	96.6	Sandstone
ABW02 [a]	Bipenggou	1	3067	65.0	8.1	258	−132.1	−18.1	4982	99.5	100.6	Granite
ABS01 [a]	Erdaohai	2	3430	18.3	6.5	1280	−99.4	−14.0	3725	29.8	38.7	Limestone
ABS02 [a]	Yuanshanzi	2	3081	10.5	6.6	2450	–	–	–	55.6	62.0	Limestone/Dolomite
ABS03 [a]	Jiangzha	2	3253	38.4	6.6	812	−102.5	−15.3	3844	83.0	86.2	Siliceous dolomite
ABS04 [a]	Heta	2	3360	30.5	7.3	305	−96.7	−14.3	3621	56.4	62.6	Conglomerate mixed with metamorphic limestone
ABW01 [c]	Chuanzhusi	2	3010	38.0	7.4	834	–	–	–	61.6	67.4	limestone
ABS05 [a]	Jiyugou	3	1703	31.9	7.2	2150	−86.7	−13.6	3236	82.6	85.9	Metamorphic dolomite

ID	Ca^{2+}	Mg^{2+}	Na^+	K^+	Cl^-	SO_4^{2-}	HCO_3^-	F^-	Li^+	Sr^{2+}	B^{3+}	SiO_2	Hydrochemical type
ABS06	0.6	0.1	19.7	1.5	3.2	18.2	24.5	1.5	0.03	0.01	0.1	23.8	HCO_3–SO_4–Na
ABS07	193.0	45.2	587.0	69.6	16.1	40.8	2339.0	2.5	6.7	1.8	13.8	24.7	HCO_3–Na
ABS08	1.0	0.4	55.2	1.0	6.0	23.7	96.1	8.4	0.1	0.01	0.1	60.9	HCO_3–Na
ABS09	18.0	3.7	94.2	5.3	1.6	12.3	297.0	6.3	0.8	0.1	0.1	71.7	HCO_3–Na
ABS10	0.5	0.4	97.9	1.4	14.7	14.0	243.0	3.3	0.1	136.0	0.1	68.3	HCO_3–Na
ABS11	43.5	41.7	615.0	62.4	49.9	9.0	2075.0	2.6	0.5	2.1	25.1	44.7	HCO_3–Na
ABS12	2.0	0.6	46.0	1.0	3.9	8.2	90.0	5.4	0.1	0.03	0.4	43.0	HCO_3–Na
ABW02	0.5	0.1	94.2	2.7	21.1	31.1	176.5	9.3	0.1	0.01	0.2	47.6	HCO_3–Na
ABS01	436.0	23.3	6.9	1.3	1.1	4.2	1514.0	0.4	0.03	0.4	0.3	7.4	HCO_3–Ca
ABS02	707.0	154.0	20.9	31.6	14.0	15.8	2863.0	1.7	0.3	0.7	6.1	16.2	HCO_3–Ca–Mg
ABS03	163.0	44.6	39.0	6.7	4.0	210.0	606.8	1.0	0.2	0.4	0.8	32.7	HCO_3–SO_4–Ca–Mg
ABS04	66.0	12.4	18.9	1.1	1.8	44.8	285.0	0.5	0.03	0.3	0.1	16.5	HCO_3–Ca
ABW01	146.3	68.1	73.1	2.4	12.8	84.0	854.3	0.6	0.01	4.6	2.5	19.1	HCO_3–Ca–Mg
ABS05	343.0	124.0	110.0	15.9	19.7	1360.0	301.6	3.0	0.2	4.8	0.7	32.4	SO_4–Ca–Mg
ABD01	59.9	10.4	17.1	1.5	1.8	55.3	221.9	0.1	0.1	0.3	0.1	8.5	HCO_3–Ca

Note(s): The units of ions and SiO_2 in the table are mg/L; [a]: taken in 2020; [b]: taken in 2019; [c]: taken in 2009; [d]: cite from [7]; ABD01: surface water; "–" indicates that the data was not obtained.

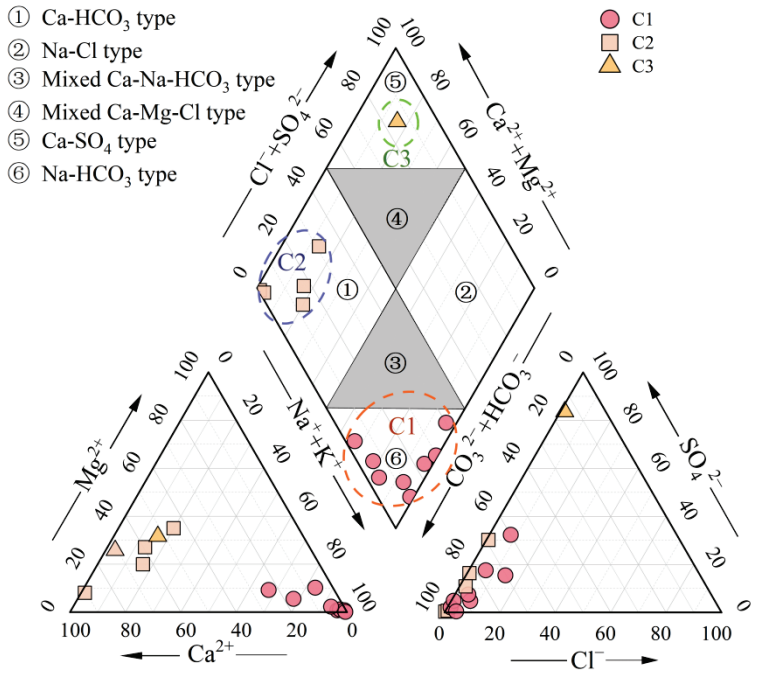

Figure 3. Piper trilinear diagram of geothermal water.

(1) Class 1 geothermal water

Class 1 geothermal waters are located in the southern Aba area. Most geothermal water samples of Class 1 were HCO_3–Na, while ABS06 had HCO_3–SO_4–Na. Low amounts of SO_4^{2-} and Cl^- were found in most samples. The temperature of geothermal waters ranged from 23 to 65 °C, with pH values ranging from 7.0 to 9.5. Except for ABS07 and ABS11, geothermal water TDS ranged from 68 mg/L to 511 m/L. ABS06, ABS08, ABS10, and ABW02 had significantly lower Ca^{2+} and Mg^{2+} concentrations (Figure 4). This geothermal water had a higher Li concentration than the other two, and other trace element (F, Sr, and B) contents were similar.

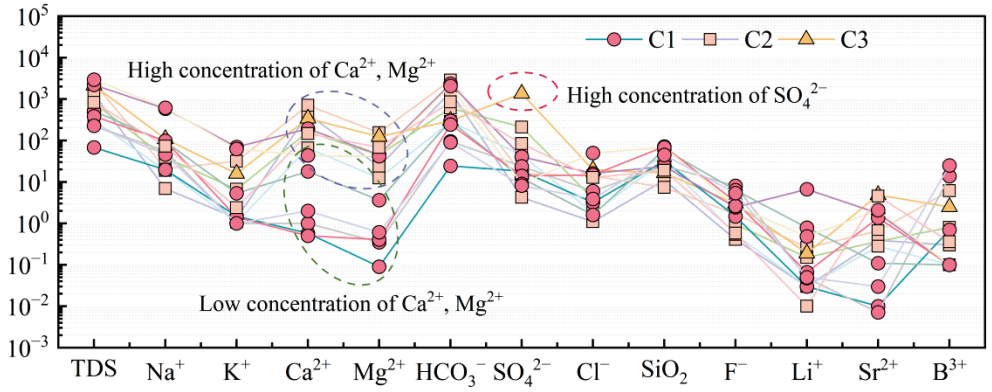

Figure 4. Schoeller diagram of major element components and trace element components of water samples.

(2) Class 2 geothermal water

Class 2 geothermal waters are scatted in the northern Aba area. Geothermal water samples can be divided into two groups according to anions: one with HCO_3^-, and the other with HCO_3^- and SO_4^{2-} (ABS03). All samples included mainly Ca^{2+} and Mg^{2+} or their combinations. Thus, geothermal waters from this hydrothermal field were HCO_3–Ca type, HCO_3–Ca–Mg type, and HCO_3–SO_4–Ca–Mg type. The Schoeller diagram (Figure 4)

demonstrated that these geothermal waters had more Ca^{2+} and Mg^{2+} than the southern area. TDS in geothermal water ranged from 305 mg/L to 1280 m/L at all sites, excepting ABS02 (2450 mg/L). It is worth noting that these geothermal waters had relatively lower temperatures (10.5 °C to 38.4 °C) and pH (6.5 to 7.4). Northern Aba geothermal waters had more diversified and complicated hydrochemical types than southern samples.

(3) Class 3 geothermal water

Class 3 geothermal water only had one sample (ABS05), located in the eastern of Aba area. Similarly to the northern geothermal field, Ca^{2+} and Mg^{2+} dominated. However, according to the Schoeller diagram (Figure 4), the ABS05 sample had a higher concentration of SO_4^{2-} (1360 mg/L) than the other two geothermal water samples, resulting in the SO_4–Ca–Mg type water. The geothermal water had a temperature of 31.9 °C and a TDS value of 2150 mg/L. This geothermal water sample contained 4.84 mg/L Sr, which was higher than the others. It is also worth noting that ABS05 sample altitude was 1703 m, significantly lower than the altitude of other sample locations.

3.2. Oxygen and Hydrogen Isotopes ($\delta^{18}O$ and $\delta^{2}H$)

A total of nine sets of δ^2H and $\delta^{18}O$ isotopes data were collected. The δ^2H and $\delta^{18}O$ values for Class 1 range from −132.1 to −86.0‰ and −18.1 to −12.1‰, respectively. The δ^2H and $\delta^{18}O$ values for Class 2 ranged from −102.5 to −96.7‰ and −15.3 to −14.0‰, respectively. The δ^2H and $\delta^{18}O$ values for Class 3 (ABS05) were −86.7‰ and −13.6‰.

4. Discussion

4.1. Ion Source Analysis

4.1.1. Correlation Analysis of Hydrochemical Parameters

Linear correlation between ions or indicators is frequently demonstrated using the Pearson correlation coefficient matrix [12,13]. Figure 5 showed strong positive relations between TDS, Ca^{2+}, Mg^{2+}, Na^+, K^+, Cl^-, HCO_3^-, and B, with coefficients above 0.6. This suggested a strong correlation between the concentration of TDS and Ca^{2+}, Mg^{2+}, Na^+, K^+, Cl^-, HCO_3^-, and B concentrations. Ca^{2+} and Mg^{2+} had a 0.8 correlation coefficient, indicating that carbonate mineral (such as dolomite) dissolution likely provided these elements, notably in Class 1 and Class 2 geothermal waters. Na^+, K^+, Cl^-, and HCO_3^- showed significant correlations with B (coefficients of 0.9, 0.9, and 0.8, respectively), suggesting that the origins of Na^+, K^+, Cl^-, and HCO_3^- may be similar to those of B.

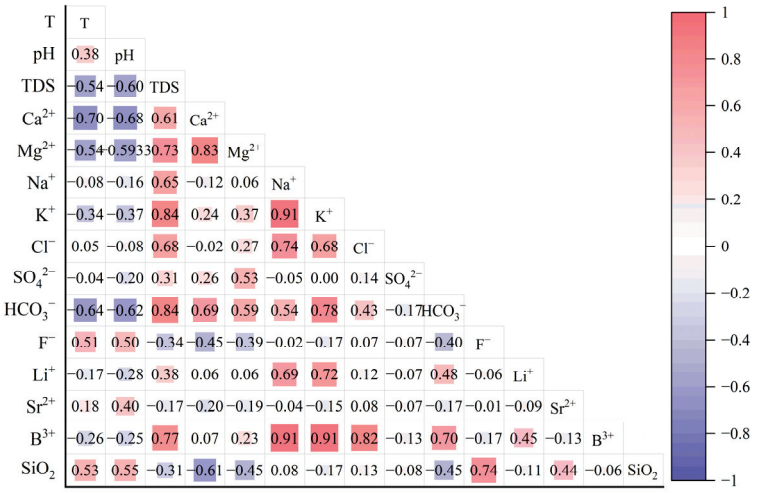

Figure 5. Pearson coefficient test correlation of hydrochemical parameters of geothermal waters (all parameter values for all 14 samples).

4.1.2. Ion Ratio Analysis

Cl^- is commonly utilized as a significant ion for tracking hydrogeochemical processes due to its minimal alteration through water–rock interactions during the rise of geothermal water and its resistance to adsorption by solid–phase mineral surfaces [31–33]. In Figure 6a–c, there were relatively obvious linear correlations between the concentration of Cl^- and the concentration of Na^+, K^+, and B compared to other ions, indicative of their similar source from deep fluids in Aba area's geothermal water. Additionally, the TDS was to some extent related to the concentration of Cl^- (Figure 6d), which was consistent with the Pearson correlation analysis results.

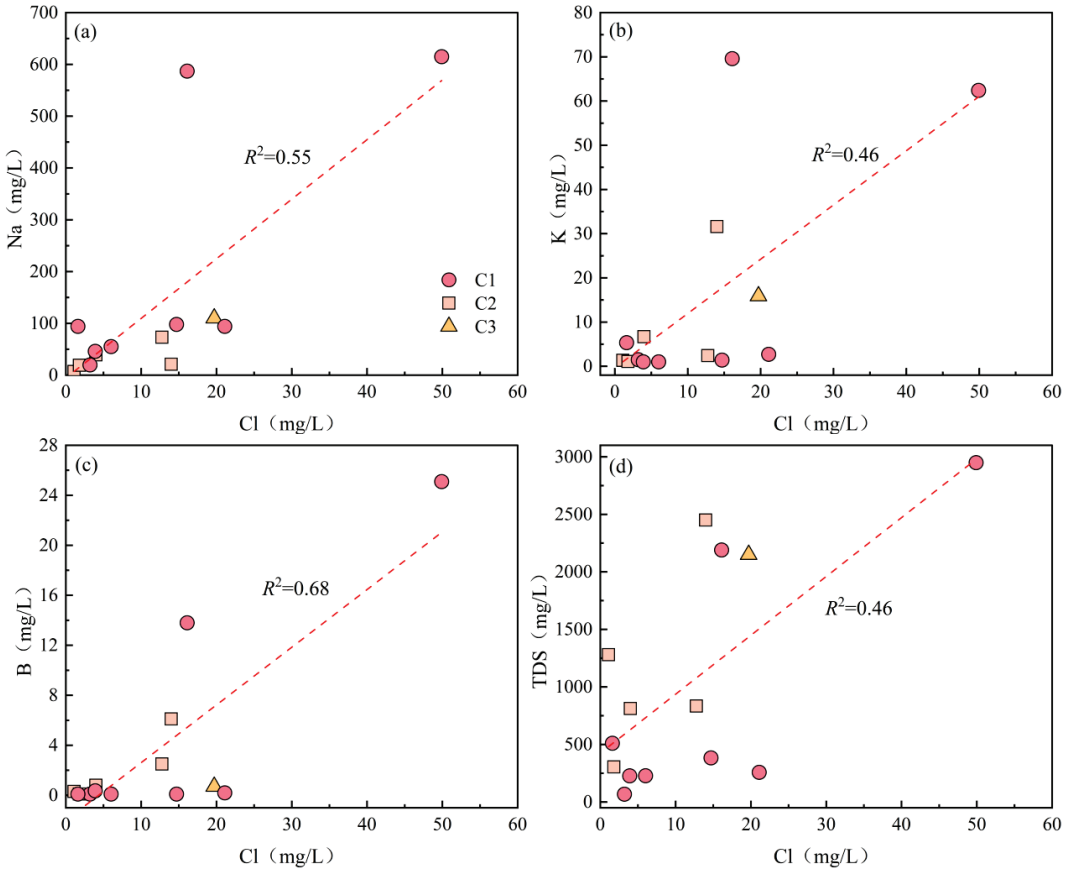

Figure 6. Relationship between Cl and some hydrochemical components: (**a**) Na; (**b**) K; (**c**) B; (**d**) TDS.

The major ion ratio of geothermal water can be used to determine the hydrochemical process [8,14,34]: Figure 7a indicates that the dissolution of salt rock minerals in the study area was very low.

Class 1 geothermal water: The relationship between Na^+, K^+, and HCO_3^- (Figure 7e) suggested that the elevated concentrations of HCO_3^- and Na^+ may be attributed to the reaction products of deep underground water, CO_2 and sodium/potassium silicate minerals—as shown in Equations (13) and (14) [34]. Additionally, the positive cation exchange (Equation (15)) was an important factor influencing the concentration of certain ions in this type geothermal water, especially in ABS07 and ABS11 hot springs (Figure 7f,g) [35]. Mover, the geothermal water points were located near the 100 °C equilibrium line (solid line) for kaolinite with muscovite, K–feldspar, paragonite, and albite. They were also located near the 200 °C equilibrium line (dashed line) for kaolinite with muscovite, paragonite, and gibbsite (Figure 7h,i) [36]. This suggested that the hydrothermal alteration provided Na^+ and K^+ sources for the geothermal water [14].

$$2NaAlSi_3O_8 + 3H_2O + CO_2 \rightarrow Al_2(Si_2O_5)(OH)_4 + 4SiO_2 + 2Na^+ + 2HCO_3^- \quad (13)$$

$$2KAlSi_3O_8 + 3H_2O + CO_2 \rightarrow Al_2(Si_2O_5)(OH)_4 + 4SiO_2 + 2K^+ + 2HCO_3^- \quad (14)$$

$$Ca^{2+}(Mg^{2+}) + 2NaX(solids) \rightarrow 2Na^+ + CaX_2(MgX_2)(solids) \quad (15)$$

Class 2 geothermal water: The relatively high concentrations of HCO_3^-, Ca^{2+}, and Mg^{2+} were a result of carbonate minerals dissolving, and sulfate mineral dissolution makes a negligible impact (Figure 7b,c) [34]. On the other hand, the geothermal water samples were observed to be in regions close to CAI–I = 0 and CAI–II = 0, suggesting a low degree of cation exchange reactions.

Class 3 geothermal water: The $HCO_3^-/(Ca^{2+} + Mg^{2+})$ ratio was less than 0.5 and the $(Ca^{2+} + Mg^{2+})/(HCO_3^- + SO_4^{2-})$ ratio was above 1 (Figure 7b,c), which suggested that the source of Ca^{2+} may also include sulfate minerals in addition to carbonates. Field investigation revealed that ABS05 hot spring outcrop was found alongside stone coals, indicating the presence of sulfide oxidation. This process results in the production of a significant amount of SO_4^{2-}, which is further supported by the higher concentration of SO_4^{2-} compared to Ca^{2+} in Class 3 geothermal water (Figure 7d).

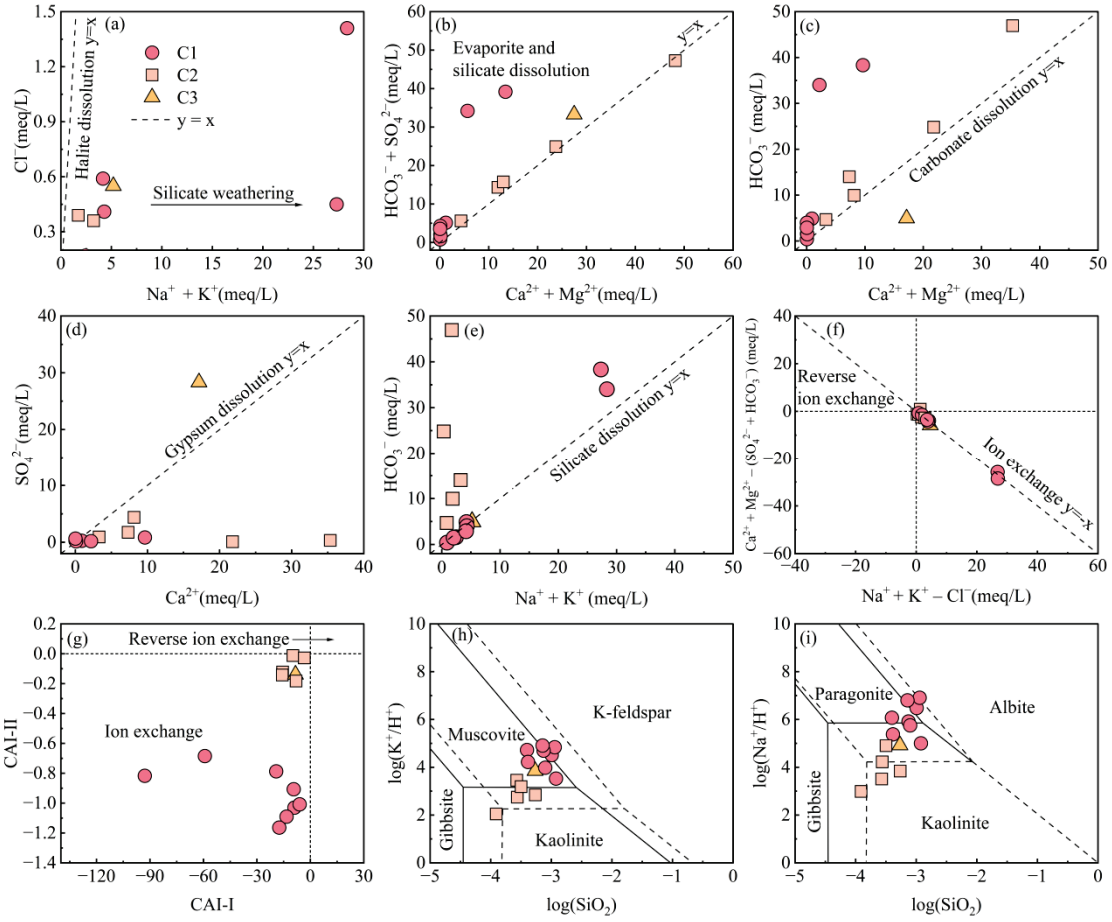

Figure 7. The relationship between the major ions of geothermal water: (**a**) Cl^- vs. $Na^+ + K^+$; (**b**) $HCO_3^- + SO_4^{2-}$ vs. $Ca^{2+} + Mg^{2+}$; (**c**) HCO_3^- vs. $Ca^{2+} + Mg^{2+}$; (**d**) SO_4^{2-} vs. Ca^{2+}; (**e**) HCO_3^- vs. $Na^+ + K^+$; (**f**) $(Ca^{2+} + Mg^{2+}) - (HCO_3^- + SO_4^{2-})$ vs. $Na^+ + K^+ - Cl^-$; (**g**) CAI–II vs. CAI–I (CAI–I = $(Cl^- - Na^+ - K^+)/Cl^-$; CAI–II = $(Cl^- - Na^+ - K^+)/(HCO_3^- + SO_4^{2-} + CO_3^{2-} + NO_3^-)$); (**h**) $\log(K^+/H^+)$ vs. $\log(SiO_2)$; (**i**) $\log(Na^+/H^+)$ vs. $\log(SiO_2)$.

4.2. Geothermal Reservoir Temperature

4.2.1. Water–Rock Equilibrium State

The Na–K–Mg ternary diagram illustrated that the geothermal water samples (excluding ABW02) were typical of immature water located in the lower–right corner of the triangular diagram [37] (Figure 8a). Furthermore, the Cl^-, $SO_4{}^{2-}$, and $HCO_3{}^-$ triangle diagram can be used to identify the mixing between hot and cold water [37,38]. In Figure 8b, it can be observed that the sample points were mainly distributed in the peripheral water region, indicative of the involvement of cold water or surface water. Hence, we can infer that geothermal water had not yet achieved a water–rock equilibrium state, and it was more suitable to utilize a SiO_2 geothermometer to calculate the reservoir temperature [7,14].

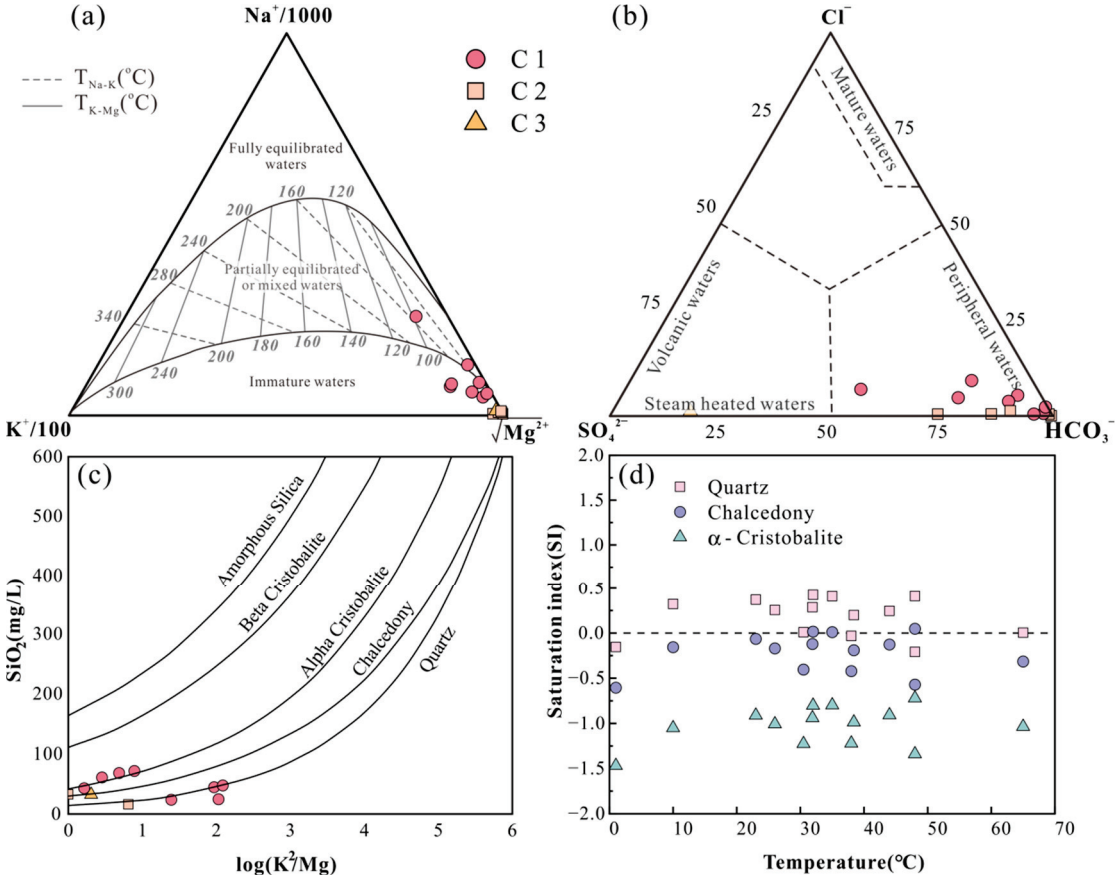

Figure 8. Identification of water–rock equilibrium and dissolution relationship of SiO_2 minerals: (**a**) Na–K–Mg diagram; (**b**) $Cl-SO_4-HCO_3$ triangle diagram; (**c**) SiO_2 vs. $\log(K^2/Mg)$; (**d**) mineral saturation index diagram.

4.2.2. SiO_2 Geothermometer

The SiO_2 geothermometer provides a reliable indication of the temperature based on the principle that the solubility of SiO_2 in the subsurface is influenced by temperature and pressure [8,33]. Various silica minerals were found naturally, including quartz, chalcedony, α–cristobalite, β–cristobalite, and amorphous silica. The $\log(K^2/Mg)$ vs. SiO_2 diagram and saturation index (SI) were employed to determine an appropriate silica geothermometer [39]. Figure 8c illustrated the distribution of geothermal samples in the study area were found to be present in quartz, chalcedony, and α–cristobalite. However, we noted that only the quartz was saturated (Figure 8d). Consequently, the quartz geothermometer was selected to calculate the reservoir temperature using Equations (1) and (2).

Because geothermal wells are considered semi–closed systems with minimal or no steam loss, the hot springs were assessed using the quartz steam loss equation, whereas the reservoir temperature for the geothermal wells was computed using the quartz no steam loss equation, yielding the results in Table 2. Class 1 geothermal water exhibited the highest geothermal reservoir temperature, ranging from 74.9–117.7 °C. Class 2 geothermal water had the lowest thermal reservoir temperature, ranging from 38.7–86.2 °C. Class 3 geothermal water had a thermal reservoir temperature of 85.9 °C.

4.2.3. Silicon Enthalpy Mixing Model

Representative samples of each type of geothermal water were selected to estimate the initial temperature and mixing ratio of cold water using silicon enthalpy equations (Equations (3) and (4)) [25]. The temperature and SiO_2 content of the cold water were obtained from ABD01, which recorded a temperature of 10.8 °C and a SiO_2 content of 8.5 mg/L. By substituting the enthalpy values of the geothermal water at different temperatures and the SiO_2 content of the spring water into the silicon enthalpy equations, the initial temperature was assumed to be between 50 °C and 300 °C. Different values of X_1 (Equation (3)) and X_2 (Equation (4)) were determined at various temperatures, and the resulting dot–line diagrams were used to establish the relationship between temperature and the cold water mixing ratio of the geothermal water (Figure 9a–c) [38].

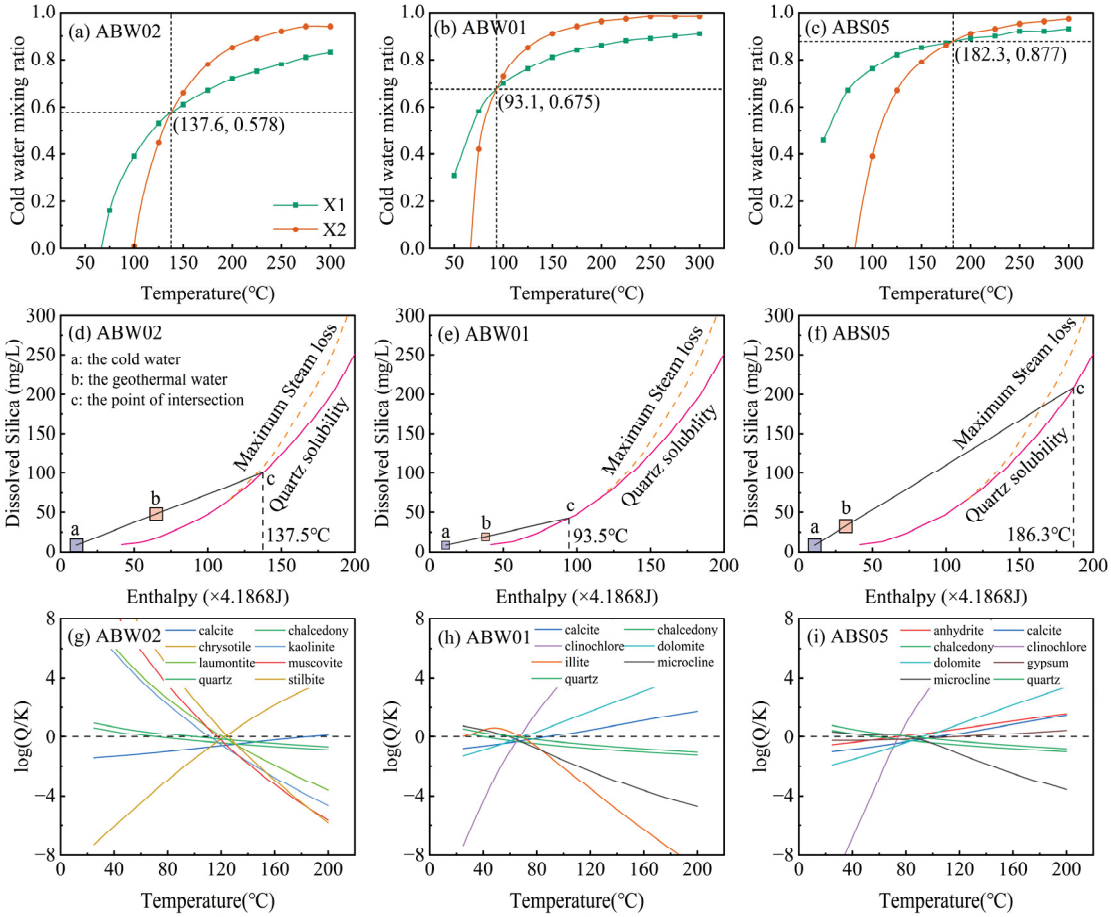

Figure 9. (**a**–**c**) Diagram of silicon–enthalpy equations (the left side of the is the initial reservoir temperature, the right side is the mixing ratio of cold water, and X_1 and X_2 are the proportion of the cold water mixing at different temperatures), (**d**–**f**) silicon–enthalpy graphical diagram and (**g**–**i**) the log(Q/K)–temperature diagrams of the main aluminosilicate minerals of geothermal water.

Moreover, a silicon–enthalpy graphical method has been conducted to estimate the reservoir temperature of mixing water [38,40]. It determined the enthalpy and SiO_2 content

of cold water as point a using the ABD01 sample as the reference, and the enthalpy and SiO_2 content of geothermal water samples were point b. By connecting points a and b and extending the line to intersect with the quartz solubilization curve at point c, the transverse coordinate of point c represented the initial temperature (Figure 9d–f). By combining the silicon–enthalpy equations and the silicon–enthalpy graphical method, the initial geothermal water temperatures range of ABW02, ABW01, and ABW01 were 137.5–137.6 °C, 93.1–93.5 °C, and 182.3–186.3 °C, respectively, while the mixing ratios of cold water were estimated to be 57.8%, 67.5%, and 87.7%, respectively.

4.2.4. Multi–Mineral Equilibrium Simulation

The equilibrium between multi–minerals and fluids plays a crucial role in studying hydrothermal–chemical processes and can also help in estimating thermal reservoir temperatures [34,41]. We used the SOLVEQ–XPT to calculate variations of the saturation indices of different minerals at a temperature step of 20 °C. The selection of minerals was based on thermal reservoir lithology [11,42]. In this study, we assumed that the concentration of Al is 0.05 mg/L [41]. Additionally, we took into account the degassing effect of CO_2 during the calculation process [11,34]. When adding equal amounts of HCO_3^- and H^+ of 0.01 mol/L, 0.05 mol/L and 0.1 mol/L, respectively, most of the selected minerals reached convergence. For CO_2 corrections, the convergence of the ABW02 geothermal water interval (Figure 9g) was observed between 120 and 140 °C. This result aligned with the temperature calculated using the silica enthalpy mixing model. Similarly, the convergence intervals for ABW01 geothermal water (Figure 9h) and ABS05 geothermal water (Figure 9i) were found to be between 60 and 80 °C and between 80 and 100 °C, respectively, which were consistent with the results obtained from the SiO_2 geothermometer.

Geographically (Figure 10), the geothermal waters in Li and Maerkang counties had higher outcrop temperatures (>40 °C), with the maximum recorded at the Bibenggou geothermal well (65 °C) (Figure 10a). In addition, most southern thermal reservoir temperatures are above 90 °C, unlike those in the north (Figure 10b). Magmatic intrusions are present near the Xianshuihe fault zone in the south of Aba area, which may explain this thermal reservoir temperature differential [16,43].

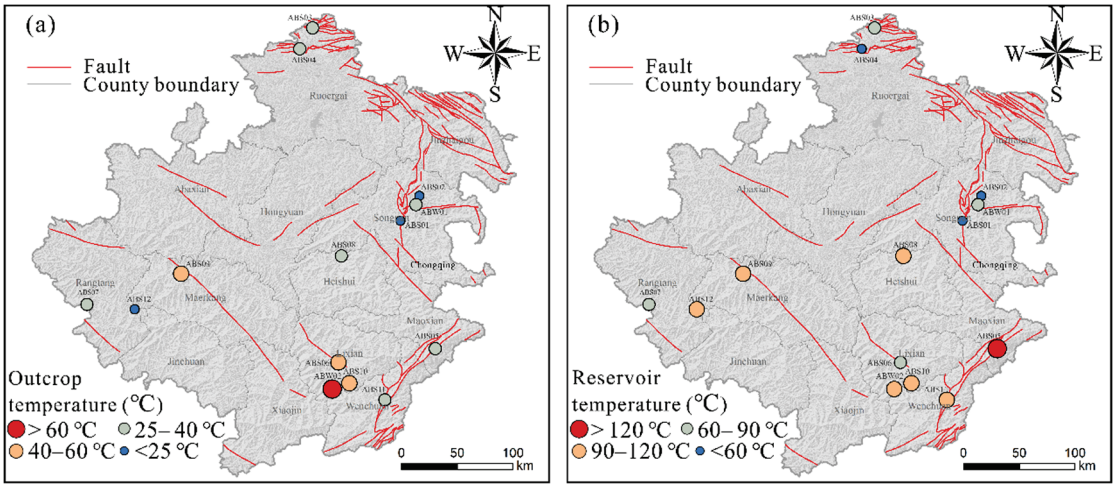

Figure 10. Spatial distribution of geothermal water in the Aba area: (**a**) outcrop temperature; (**b**) thermal reservoir temperature.

4.3. Recharge Sources Traced by δ^2H and $\delta^{18}O$

Changes in δ^2H and $\delta^{18}O$ isotopes can provide insights into the cycling process in various groundwater environments [44]. Craig observed a linear correlation between δ^2H and $\delta^{18}O$ isotopes and provided the global meteoric water line equation: $\delta^2H = 8\delta^{18}O + 10$ [45]. The global meteoric water line and the meteoric water line of the southwestern part of

China ($\delta^2H = 8.41\delta^{18}O + 16.72$) [46] were chosen to determine the source of geothermal water in this study. Figure 11 showed that geothermal samples were near meteoric water lines and far from mantle, magma, and metamorphic water sources. This indicated a tight link between Aba's geothermal fluids and meteoric water, which is the main recharge source.

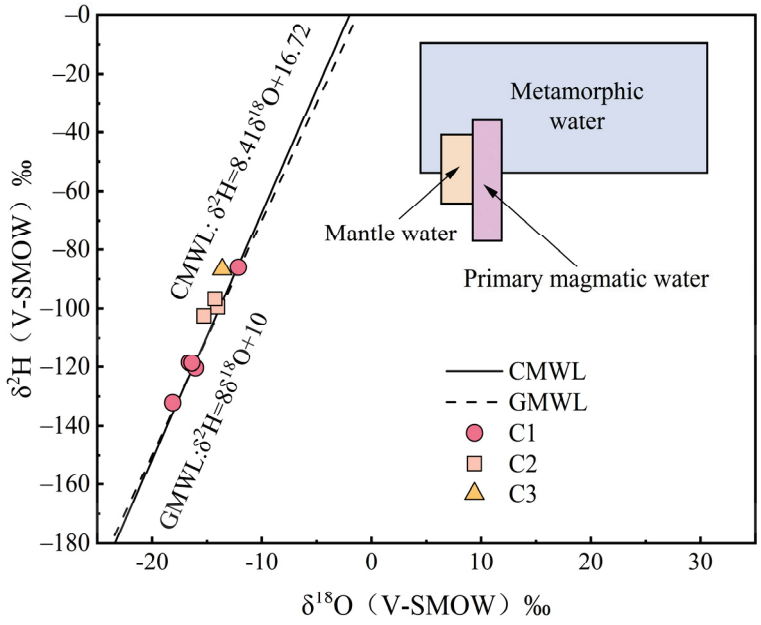

Figure 11. δ^2H–$\delta^{18}O$ for the geothermal waters in the Aba area (GMWL: global meteoric water line, CMWL: Chinese southwestern meteoric water line).

Because of the elevation effect of δ^2H and $\delta^{18}O$ isotopes in groundwater derived from meteoric water, they can be used to estimate the recharge elevation [47]. In geothermal circulation systems, water–rock interaction causes changes in $\delta^{18}O$ values in geothermal water, while δ^2H values are minimally affected by water–rock interaction and isotope exchange. Thus, the following equation was used to calculate the recharge elevation E [45]:

$$E = e + (\delta^2H - \delta^2H_0)/\Delta G \quad (16)$$

where the e was the reference point elevation (m) and δ^2H was the δ^2H value of geothermal water samples. δ^2H_0 was the δ^2H value of the reference point. The δ^2H_0 value (−94.7‰) and e value (3544 m) were determined in the Heishui county of the study area. The ΔG was the δ^2H elevation gradient of meteoric water in SW China (−2.6‰/100 m) [48]. Accordingly, the recharge elevations of three types of geothermal waters were calculated as 3209–4982 m, 3621–3824 m, and 3236 m (Table 2).

4.4. Genesis Model of Geothermal Water

Aba geothermal water genesis models can be divided into three different types. The intrusive zone contact type (Class 1 geothermal water) was dominated by magma residual heat and found in Li, Maerkang, and Rantang counties in southern Aba. The second type, carbonate type (Class 2 geothermal water), was controlled by deep and large carbonate fractures. Heishui and Ruoergai counties in northern Aba were its main locations. Third, the fracture type with high SO_4^{2-} content (Class 3 geothermal water) was influenced by the Maowen deep fault in eastern Aba.

4.4.1. Contact–Type of Intrusion Zone

This geothermal water was stored in sandstone–granite contact. The reservoir was heated because of the geothermal gradient, active deep faults, and granite radioactivity. Regional folding and fault tectonics affect geothermal water distribution. Bibenggou

geothermal well, Guergou hot spring, and Kejiu hot spring are examples. This study investigated the genesis model of this type of geothermal water from the Bibenggou well.

The 2400 m Bibenggou geothermal well was intentionally drilled. Sandstone dominated the strata, providing thermal reservoir cover and water insulation. The main recharge source was atmospheric precipitation, estimated at 4982 m (Table 2), indicating that snow water (about 4000 m snow line altitude) recharged underground geothermal water (Figure 12). Geothermal water originated when snow and meteoric water infiltrated fractures in granite–sandstone layers, heating to 99.5–137.6 °C due to geothermal gradient and residual heat from deep magma intrusive rocks. Geothermal water comprises abundant Na^+, K^+, and HCO_3^- due to the reaction between thermal water and surrounding sodium/potassium silicate minerals during circulation. By mixing geothermal water with deep increasing heat flow, CO_2 and trace elements like B and F were enhanced. After that, geothermal water rose along the fissures in the core of the inverted anticline, causing cation exchange processes in the shallow section and increasing Na^+ concentration. Ultimately, boreholes revealed HCO_3–Na type geothermal water.

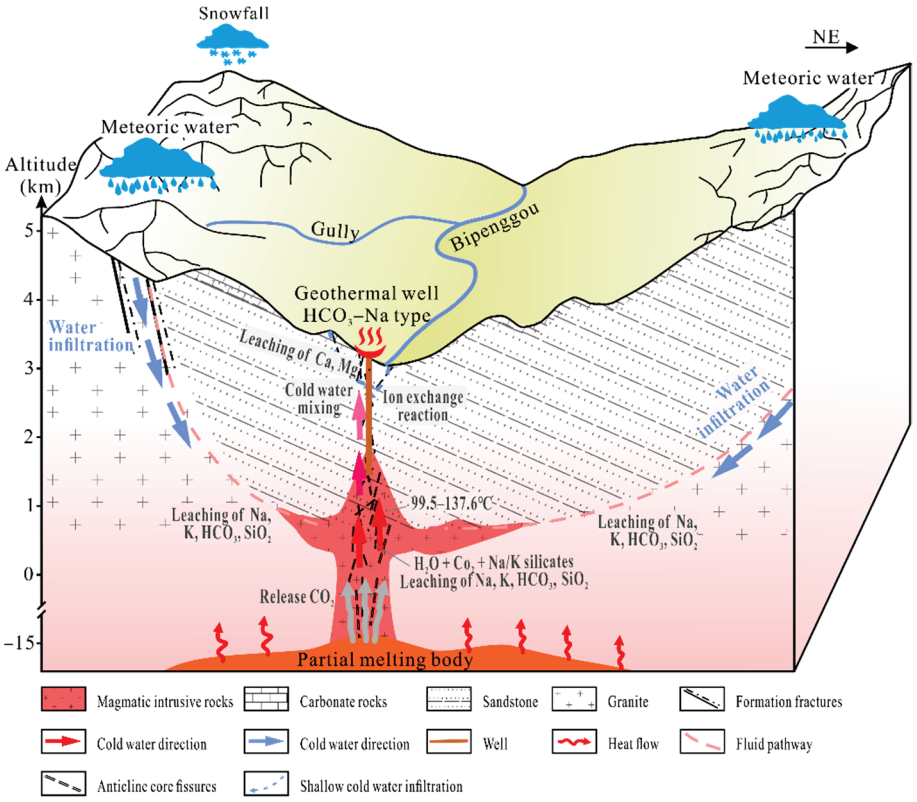

Figure 12. Genesis model of Bipenggou geothermal well.

4.4.2. Carbonate–Type in Carbonate ROCK Areas

This geothermal water reservoir was mostly carbonate rocks. The heat came from geothermal gradients. It had a low thermal reservoir temperature and little water–rock interaction. This group includes the Chuanzhusi geothermal well and Erdaohai hot spring, among others. This study investigated the genesis model of this type of geothermal water from the Chuanzhusi well.

The 122.8 m Chuanzhusi geothermal well was a self–spraying borehole. Permian and Carboniferous limestone comprise the reservoir. About 100 m of Quaternary sediments cover a 1680 m thick relative water–insulating layer above the reservoir layer. The covering protects the geothermal water reservoir from Min River water infiltration and provides thermal insulation. The Chuanzhusi geothermal wells were situated in a high geothermal area with a temperature gradient of 30–40 °C/km. At around 4200 m east of the Min

River, meteoric water infiltrated fault fractures (Figure 13). These fissures, solution cracks, and paleocarbonate channels led groundwater to depths of 1700–2000 m. It generated geothermal water when heated by the geothermal gradient, reaching temperatures between 61.6 °C to 93.5 °C. Over time, this water dissolved nearby rocks like calcite and dolomite, releasing Ca^{2+}, Mg^{2+}, and HCO_3^-. Trace elements like Sr and B were relatively abundant in the geothermal water. The intersection of the N–S–trending Min River fault zone and the W–trending minor cracks was where geothermal water was concentrated. The final drill holes found HCO_3–Ca–Mg geothermal water.

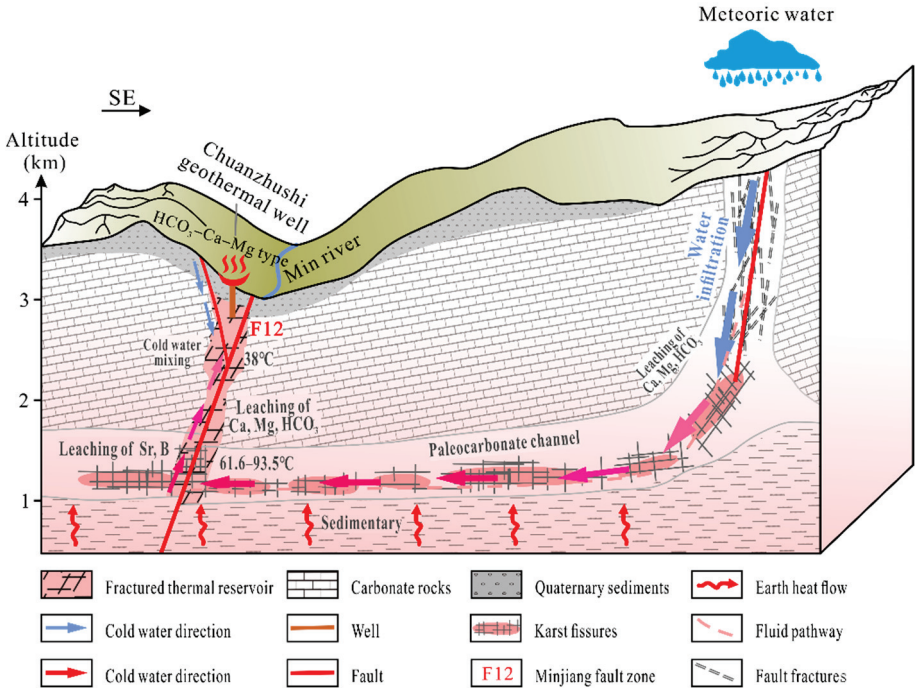

Figure 13. Genesis model of Chuanzhusi geothermal well.

4.4.3. Fracture–Type Controlled by Deep and Large Faults

This geothermal water concentrated in deep fault fissures. High SO_4^{2-} concentrations in these reservoirs came from deep H_2S and coal seams undergoing sulfide dissolution. Deep large fractures increased reservoir water storage and thermal conductivity. The geothermal display featured Jiyugou hot spring.

The geology of Jiyugou hot spring was complex due to its location in phyllite, argillaceous limestone, and fine sandstone strata with stone coal. Jiyugou hot spring had 106 to 142.2 Bq/L of radioactive radon gas, indicating a second heat source from radioactive decay. Mechanical frictional heat from Longmenshan active fractures and earthquakes also heats Jiyugou hot spring [49]. As shown in Figure 14, meteoric water infiltrated granite–dolomite fractures at 3200 m and was heated by geothermal gradient heating, crustal heat flow from radioactive element decay in the upper crust, and mechanical frictional heat from active faults and earthquakes. Geothermal water forms when its temperature rose to 85.9–100 °C. Geothermal water leached Ca^{2+} and Mg^{2+} from carbonate rocks during migration. The geothermal water had significant SO_4^{2-} concentrations due to paste salt, lenticular gypsum, and stone coal strata. Geothermal water followed fracture zones and fissures until it reached the Maowen fault zone and Jiyugou fracture, where it was discharged as SO_4–Ca–Mg geothermal water at topographically and tectonically helpful areas [49].

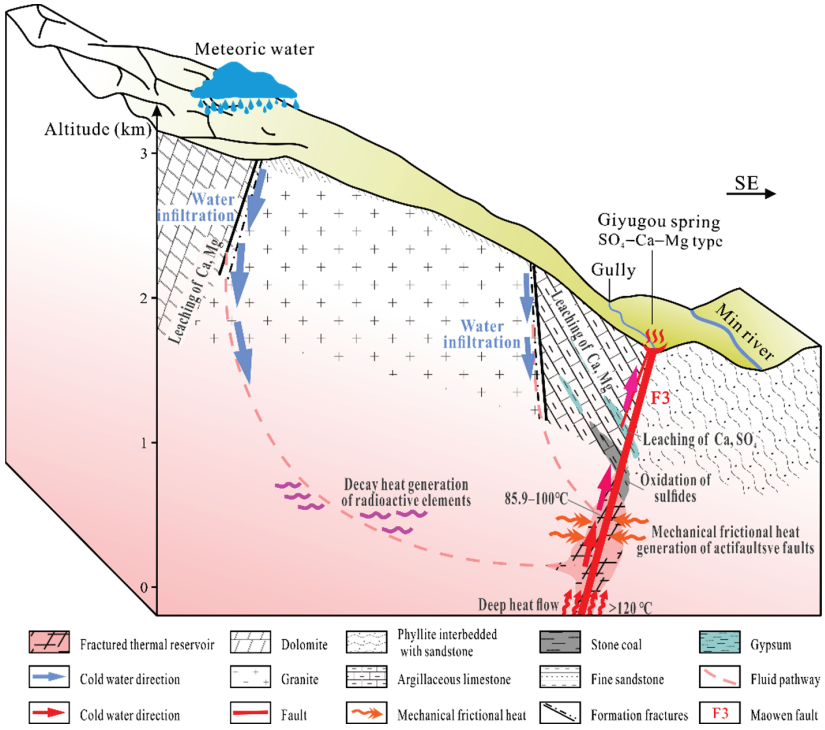

Figure 14. Genesis model of Jiyugou hot spring.

4.5. Prediction of Scaling Trends

Three types of scaling usually occur—carbonate scaling like calcium carbonate [50,51]; sulphate and heavy metal sulphide scaling, like calcium and iron sulphide [52,53]; and silicon and other siliceous components, like amorphous silica—depending on reservoir lithology, temperature, brine production, and utilization processes [54]. Silicon and calcium scaling are most common. High–temperature geothermal systems above 180 °C experience silicon scaling, while medium– and low–temperature systems (<150 °C) commonly have calcium scaling [10,55].

4.5.1. Scaling Trend of Calcium Carbonate

Upon rising, geothermal fluid rich in Ca^{2+} and HCO_3^- generates $Ca(HCO_3)_2$, which decomposes into $CaCO_3$. Decomposing calcium bicarbonate produces alkaline scaling, which forms bigger particles on the pipe wall by interacting and colliding with other components [56–59]. The chemical equations for $CaCO_3$ scaling reactions are as follows [10,58,59]:

$$H_2CO_3 \leftrightarrow CO_2(gas) + H_2O \quad (17)$$

$$HCO_3^- + H_2O \leftrightarrow H_2CO_3 + OH^- \quad (18)$$

$$Ca^{2+} + 2HCO_3^- \leftrightarrow CaCO_3(solid) + CO_2(gas) + H_2O \quad (19)$$

Qualitatively evaluating each geothermal water type's calcium carbonate scaling trend using the Larson Index (LI) and Ryzner Index (RI) is common [8,17,27–29]. When Cl ions are high (milligram equivalent percentage > 25%) in geothermal water, the Larson index approach is better for the calcium carbonate scaling trend (Equation (6)). When Cl ions are not high, the Ryzner index method is superior, as shown in Table 1 (Equations (7)–(10)). The pH_2 is the measured pH value of geothermal water (Table 2). Kc is usually determined graphically [60], and Ke is a constant with a TDS range of 200–6000 mg/L. Ke is 1.8 for temperatures above 100 °C, 2.6 for temperatures below 50 °C, and 2.6 − (2.6 − 1.8)/(100

− 50) × (t − 50) for temperatures between 50 and 100 °C [17,28,29]. After judging the Larson index, LI > 0.5 indicates no scaling but corrosivity, while LI < 0.5 indicates likely scaling and non–corrosivity [17,27]. Scaling severity is determined using the Ryzner index: RI < 4.0 indicates very severe scaling; 4.0 < RI < 5.0 indicates severe scaling; 5.0 < RI < 6.0 indicates moderate scaling; 6.0 < RI < 7.0 indicates slight scaling; and RI > 7.0 indicates no scaling [17,29].

Results are shown in Table 3. Calcium carbonate scaling trends in ABS01, ABS02, ABS07, and ABW01 were very severe; ABS03, ABS05, and ABS11 were severe; and ABS04 (average RI = 5.75) was moderate. ABS09 showed slight scaling (RI = 6.44). Finally, ABS06, ABS08, ABS10, ABS12, and ABW02 will not carbonate scale (RI > 7). The thermal reservoirs of ABS01–ABS05, ABS11, and ABW01 contained limestones and/or dolomites, which leached Ca^{2+} and $HCO_3{}^-$, causing Ca^{2+} and $HCO_3{}^-$ supersaturation and precipitation in geothermal water. In ABS07, CO_2 degassing produced excessive $HCO_3{}^-$ that reacted with Ca^{2+} to precipitate $CaCO_3$.

Table 3. Calculation results of scaling trends of calcium carbonate, sulfate, and silicate in three types of geothermal waters (RI^1 was calculated using Equations (7) and (8); RI^2 was calculated using Equations (7) and (9)).

ID	Class	Cl ion Milligram Equivalent Ratio	RI^1	RI^2	RI (Average)	Scaling Trend of Carbonate Minerals	$R.S_{gypsum}$	$R.S_{SiO2}$
ABS06	1	10.4%	9.2	10.5	9.9	No scaling	0.0001	0.1
ABS07	1	1.1%	3.1	3.7	3.4	Very severe	0.0194	0.2
ABS08	1	7.6%	8.0	8.9	8.5	No scaling	0.0002	0.4
ABS09	1	0.9%	5.8	7.1	6.4	Slight	0.0014	0.4
ABS10	1	8.8%	7.3	8.5	7.9	No scaling	0.0001	0.4
ABS11	1	4.0%	3.8	4.6	4.2	Severe	0.0008	0.3
ABS12	1	6.3%	7.5	8.0	7.7	No scaling	0.0001	0.3
ABW02	1	14.4%	8.0	9.5	8.8	No scaling	0.0001	0.2
ABS01	2	0.1%	3.5	3.8	3.7	Very severe	0.0039	0.1
ABS02	2	0.8%	2.8	2.8	2.8	Very severe	0.0454	0.2
ABS03	2	0.8%	4.4	5.4	4.9	Severe	0.1360	0.2
ABS04	2	0.9%	5.4	6.1	5.8	Moderate	0.0186	0.1
ABW01	2	2.2%	3.4	4.4	3.9	Very severe	0.0498	0.1
ABS05	3	1.6%	3.9	4.7	4.3	Severe	1.1424	0.2

4.5.2. Scaling Trend of Calcium Sulfate

Gypsum scaling has a major effect on geothermal fluids, followed by azurite and barite. Gypsum ($CaSO_4$–$2H_2O$) precipitates primarily if the geothermal fluid's temperature is below 100 °C, according to the precipitation equation [17,61]:

$$Ca^{2+} + 2SO_4{}^{2-} + 2H_2O \rightarrow CaSO_4 \cdot 2H_2O \quad (20)$$

Gypsum scaling can be qualitatively determined from relative saturation ($R.S_{gypsum}$). $\log K_{gypsum}$ is the solubility product of gypsum, which can be calculated using TDS and temperature in Equation (11) in Table 1 [17]. When $R.S_{gypsum} > 1$, gypsum is saturated and scaling may occur. The estimated results were in Table 3. $R.S_{gypsum} > 1$ for ABS05, showing gypsum scaling compatible with high $SO_4{}^{2-}$ content from sulfide dissolution and sulfide oxidation in ABS05 geothermal water. Other geothermal waters had $R.S_{gypsum}$ below 1, indicating no gypsum scaling.

4.5.3. Scaling Trend of Amorphous Silica

Using thermodynamics and kinetics, dissolved silica precipitates amorphously. Chemical sorption and polymerization precipitate silica. Chemical polymerization condenses

silica monomers into nanoscale polymer particles, while chemisorption deposits them directly on the surface. Silicon scaling chemical reaction equations are as follows [10,55]:

$$SiO_2 + 2H_2O \leftrightarrow Si(OH)_4 \quad (21)$$

$$Si(OH)_4 + OH^- \leftrightarrow (OH)_3Si^- + H_2O \quad (22)$$

$$Si(OH)_3{}^- + Si(OH)_4 \rightarrow (OH)_3Si\text{-}O\text{-}Si(OH)_3 + OH^- \quad (23)$$

$$2n(OH)_3Si\text{-}O\text{-}Si(OH)_3 \rightarrow \text{Cyclic/Colloidal silica} \rightarrow \text{Polymeric silica (scale)} \quad (24)$$

This study used the relative saturation of amorphous silica, $R.S_{SiO2}$, as in Table 1 (Equation (12)), where T_k is geothermal water's absolute temperature, to determine silica scaling. The scaling of amorphous silica is distinguished by $R.S_{SiO2} > 1$. The estimation results are shown in Table 3. Amorphous silica scaling was not present in Aba's geothermal water because none of the samples have $R.S_{SiO2}$ values greater than 1.

Figure 15 shows the study area's geothermal water scaling trend and geographic distribution. Scaling was more common in geothermal water near Aba border. First, all Class 2 geothermal water had calcium carbonate scaling, which ranged from severe to slight. Second, Class 1 geothermal water will be affected by extremely severe calcium carbonate scaling in ABS07, moderate in ABS09, and severe in ABS11. In contrast, ABS06, ABS08, ABS11, ABS12, and ABW02 do not scale. Finally, ABS05 will endure significant calcium carbonate and calcium sulfate scaling. Descaling methods like controlling CO_2 partial pressure, pH, or chemical additives are chosen based on scaling trends to choose effective preventive measures when developing and using regional geothermal water [10].

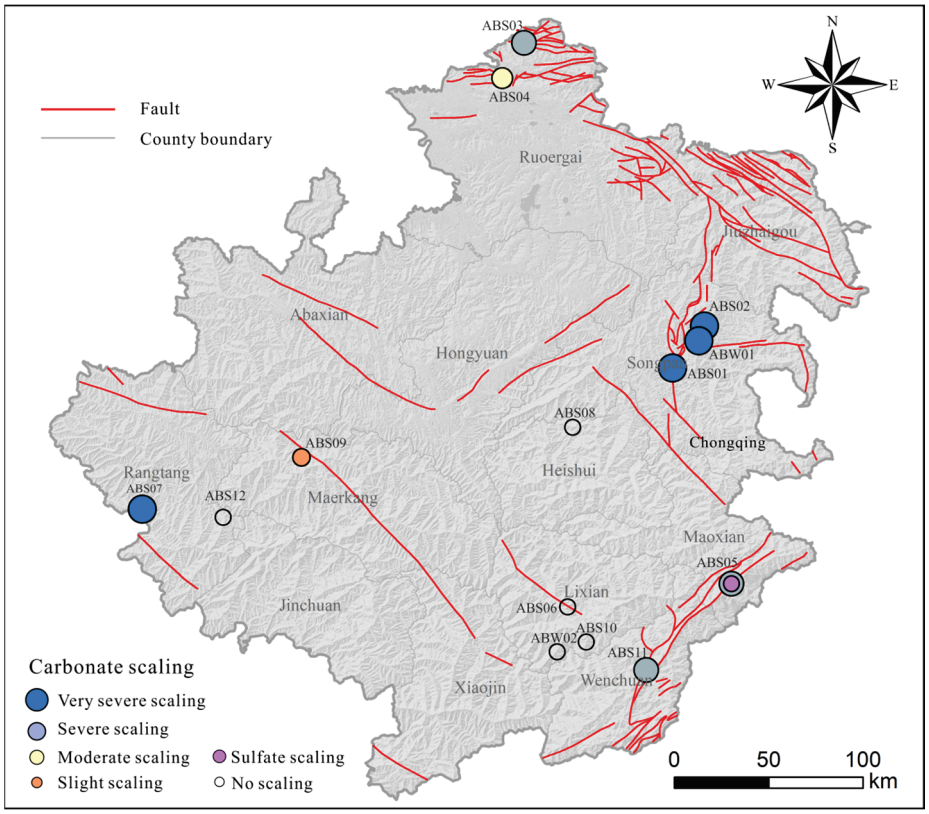

Figure 15. Spatial characteristics of scaling of geothermal water in Aba area.

5. Conclusions

To study hydrogeochemical processes, genesis mechanisms, and scaling trends in geothermal systems in northeastern Sichuan, we divided Aba geothermal water into three types. The conclusions achieved from hydrogeochemical and isotopic studies were listed below.

(1) Aba's geothermal water was recharged by atmospheric precipitation. Three types of geothermal waters recharge at 3209–4982 m, 3621–3824 m, 3236 m, respectively. Class 1 geothermal water was found across Aba area's southern region. Hydrochemistry types included HCO_3–Na and HCO_3–SO_4–Na. High concentrations of HCO_3^- and Na^+ were due to water, CO_2, and sodium silicate mineral reactions and positive cation exchange. Class 2 geothermal water in northern Aba contained both HCO_3–Ca and HCO_3–Ca–Mg types, which generated significant amounts of HCO_3^-, Ca^{2+}, and Mg^{2+} through carbonate mineral dissolution. Class 3 geothermal water in eastern Aba had a high SO_4^{2-} concentration due to oxidation of sulfides and gypsum mineral dissolution. It was SO_4–Ca–Mg type water.

(2) The geothermal reservoir temperature ranges for Class 1 geothermal water 74.9–137.6 °C, whereas Class 2 had lower temperature range at 38.7–93.5 °C. Geothermal water of Class 3 (ABS05) had a reservoir temperature of 85.9–100 °C and the initial temperature of up to 186.3 °C.

(3) The Aba geothermal water genesis model comprised three primary types: (1) the contact type, which was magma residual heat in Li, Maerkang, and Rantang counties' intrusive zones; (2) carbonate–type geothermal water controlled by deep and large fractures, which took geothermal gradient as the heat source and carbonates as the thermal reservoir; and (3) the fracture type with high SO_4^{2-} concentration, which was controlled by a deep, large fault and was generally found in the upper plate of the Maowen fault.

(4) ABS07, ABS09, and AB12 of Class 1 geothermal water will have slight to very serious calcium carbonate scaling, while ABS06, ABS08, ABS11, ABS12, and ABW02 will not. Class 2 geothermal water will have serious to very serious calcium carbonate scaling. Geothermal water in Class 3 will have severe calcium sulfate and calcium carbonate scaling.

Author Contributions: Writing—original draft preparation, investigation, methodology, G.L.; writing—review and editing, software, data curation, D.W., X.Y., M.S., Z.Y. and X.K.; review and editing, supervision, project administration, funding acquisition, Y.Z.; review and editing, resources, data curation, funding acquisition, X.Z. All authors have read and agreed to the published version of the manuscript.

Funding: This study was funded by National Natural Science Foundation of China grant number (42072313, 42102334), Sichuan Provincial Department of Science and Technology Projects grant number (2022NSFSC0413, 2023YFS0356), Sichuan Provincial Department of Natural Resources Research Project Funding grant number (KJ–2023–36), Open Fund of the Engineering Research Center of Geothermal Resources Development Technology and Equipment, Ministry of Education, Jilin University (22012).

Data Availability Statement: All the research data have been provided in the paper.

Acknowledgments: We would like to thank anonymous reviewers and editors for their constructive comments on this manuscript.

Conflicts of Interest: The authors declare no conflict of interest.

References

1. Capaccioni, B.; Vaselli, O.; Tassi, F.; Santo, A.P.; Huertas, A.D. Hydrogeochemistry of the thermal waters from the Sciacca Geothermal Field (Sicily, southern Italy). *J. Hydrol.* **2011**, *396*, 292–301. [CrossRef]
2. Craig, J.; Absar, A.; Bhat, G.; Cadel, G.; Hafiz, M.; Hakhoo, N.; Kashkari, R.; Moore, J.; Ricchiuto, T.E.; Thurow, J. Hot springs and the geothermal energy potential of Jammu & Kashmir State, N.W. Himalaya, India. *Earth-Sci. Rev.* **2013**, *126*, 156–177.

3. Lu, L.; Pang, Z.; Kong, Y.; Guo, Q.; Wang, Y.; Xu, C.; Gu, W.; Zhou, L.; Yu, D. Geochemical and isotopic evidence on the recharge and circulation of geothermal water in the Tangshan Geothermal System near Nanjing, China: Implications for sustainable development. *Hydrogeol. J.* **2018**, *26*, 1705–1719. [CrossRef]
4. Wang, C.; Zheng, M. Hydrochemical Characteristics and Evolution of Hot Fluids in the Gudui Geothermal Field in Comei County, Himalayas. *Geothermics* **2019**, *81*, 243–258. [CrossRef]
5. Asta, M.P.; Gimeno, M.J.; Auqué, L.F.; Gómez, J.; Acero, P.; Lapuente, P. Hydrochemistry and geothermometrical modeling of low-temperature Panticosa geothermal system (Spain). *J. Volcanol. Geotherm. Res.* **2012**, *235–236*, 84–95. [CrossRef]
6. Li, J.; Sagoe, G.; Yang, G.; Liu, D.; Li, Y. The application of geochemistry to bicarbonate thermal springs with high reservoir temperature: A case study of the Batang geothermal field, western Sichuan Province, China. *J. Volcanol. Geotherm. Res.* **2019**, *371*, 20–31. [CrossRef]
7. Sun, M.; Zhang, X.; Yuan, X.; Yu, Z.; Xiao, Y.; Wang, Y.; Zhang, Y. Hydrochemical Characteristics and Genetic Mechanism of Geothermal Springs in the Aba Area, Western Sichuan Province, China. *Sustainability* **2022**, *14*, 12824. [CrossRef]
8. Wang, Y.; Yuan, X.; Zhang, Y.; Zhang, X.; Xiao, Y.; Duo, J.; Huang, X.; Sun, M.; Lv, G. Hydrochemical, D–O–Sr isotopic and electromagnetic characteristics of geothermal waters from the Erdaoqiao area, SW China: Insights into genetic mechanism and scaling potential. *Ore Geol. Rev.* **2023**, *158*, 105486. [CrossRef]
9. Chauhan, V.; Saevarsdottir, G.; Tesfahunegn, Y.A.; Asbjornsson, E.; Gudjonsdottir, M. Computational study of two-phase flashing flow in a calcite scaled geothermal wellbore. *Geothermics* **2021**, *97*, 102239. [CrossRef]
10. Zhao, H.; Huang, Y.; Deng, S.; Wang, L.; Peng, H.; Shen, X.; Ling, D.; Liu, L.; Liu, Y. Research progress on scaling mechanism and anti-scaling technology of geothermal well system. *J. Dispers. Sci. Technol.* **2022**, *44*, 1657–1670. [CrossRef]
11. Tian, J.; Pang, Z.; Wang, Y.; Guo, Q. Fluid geochemistry of the Cuopu high temperature geothermal system in the eastern Himalayan syntaxis with implication on its genesis. *Appl. Geochem.* **2019**, *110*, 104422. [CrossRef]
12. Ahada, C.P.S.; Suthar, S. Hydrochemistry of groundwater in North Rajasthan, India: Chemical and multivariate analysis. *Environ. Earth Sci.* **2017**, *76*, 203. [CrossRef]
13. Xiao, Y.; Hao, Q.; Zhang, Y.; Zhu, Y.; Yin, S.; Qin, L.; Li, X. Investigating sources, driving forces and potential health risks of nitrate and fluoride in groundwater of a typical alluvial fan plain. *Sci. Total Environ.* **2022**, *802*, 149909. [CrossRef]
14. Zhang, X.; Deng, C.; Feng, T.; Zhang, Y. Geochemical Investigations of the Geothermal Waters in the Kangding Area, SW China: Constraints from Hydrochemistry and D-O-T Isotopy. *Water* **2023**, *15*, 2761. [CrossRef]
15. Chandrajith, R.; Barth, J.A.C.; Subasinghe, N.D.; Merten, D.; Dissanayake, C.B. Geochemical and isotope characterization of geothermal spring waters in Sri Lanka: Evidence for steeper than expected geothermal gradients. *J. Hydrol.* **2013**, *476*, 360–369. [CrossRef]
16. Li, X.; Huang, X.; Liao, X.; Zhang, Y. Hydrogeochemical Characteristics and Conceptual Model of the Geothermal Waters in the Xianshuihe Fault Zone, Southwestern China. *Int. J. Environ. Res. Public Health* **2020**, *17*, 500. [CrossRef]
17. Wei, M.; Tian, T.; Sun, Y.; Li, X. A study of the scaling trend of thermal groundwater in Kangding county of Sichuan. *Hydrogeol. Eng. Geol.* **2012**, *39*, 132–138. (In Chinese)
18. Liu, W.; Guan, L.; Liu, Y.; Xie, X.; Zhang, M.; Chen, B.; Xu, S.; Sano, Y. Fluid geochemistry and geothermal anomaly along the Yushu-Ganzi-Xianshuihe fault system, eastern Tibetan Plateau: Implications for regional seismic activity. *J. Hydrol.* **2022**, *607*, 127554. [CrossRef]
19. Qi, J.; Xu, M.; An, C.; Wu, M.; Zhang, Y.; Li, X.; Zhang, Q.; Lu, G. Characterizations of geothermal springs along the Moxi deep fault in the western Sichuan plateau, China. *Phys. Earth Planet. Inter.* **2017**, *263*, 12–22. [CrossRef]
20. Zhang, J.; Li, W.; Tang, X.; Tian, J.; Wang, Y.; Guo, Q.; Pang, Z. Geothermal data analysis at the high-temperature hydrothermal area in Western Sichuan. *Sci. China Earth Sci.* **2017**, *60*, 1507–1521. [CrossRef]
21. Zhang, W.; Wang, G.; Xing, L.; Li, T.; Zhao, J. Geochemical response of deep geothermal processes in the Litang region, Western Sichuan. *Energy Explor. Exploit.* **2019**, *37*, 626–645. [CrossRef]
22. Tang, X.; Zhang, J.; Pang, Z.; Hu, S.; Tian, J.; Bao, S. The eastern Tibetan Plateau geothermal belt, western China: Geology, geophysics, genesis, and hydrothermal system. *Tectonophysics* **2017**, *717*, 433–448. [CrossRef]
23. Zhang, X.; Liu, J.; Guo, B.; Wang, Z.; Li, Y. Temporal and spatial characteristics of snow cover in Aba, Sichuan from 2000 to 2015. *J. Arid Land Resour. Environ.* **2019**, *33*, 131–136.
24. Wang, E.; Meng, K.; Su, Z.; Meng, Q.; Chu, J.J.; Chen, Z.; Wang, G.; Shi, X.; Liang, X. Block rotation: Tectonic response of the Sichuan basin to the southeastward growth of the Tibetan Plateau along the Xianshuihe-Xiaojiang fault. *Tectonics* **2014**, *33*, 686–718. [CrossRef]
25. Fournier, R.O. Chemical geothermometers and mixing models for geothermal systems. *Geothermics* **1977**, *5*, 41–50. [CrossRef]
26. Singh, C.K.; Kumar, A.; Shashtri, S.; Kumar, A.; Kumar, P.; Mallick, J. Multivariate statistical analysis and geochemical modeling for geochemical assessment of groundwater of Delhi, India. *J. Geochem. Explor.* **2017**, *175*, 59–71. [CrossRef]
27. Klapper, H.S.a.; Bäßler, R.b.; Sobetzki, J.b.; Weidauer, K.b.; Stürzbecher, D.b. Corrosion resistance of different steel grades in the geothermal fluid of Molasse Basin (Article). *Mater. Corros.* **2013**, *64*, 764–771. [CrossRef]
28. Pátzay, G.; Stáhl, G.; Kármán, F.H.; Kálmán, E. Modeling of scale formation and corrosion from geothermal water. *Electrochim. Acta* **1998**, *43*, 137–147. [CrossRef]
29. Mundhenk, N.; Huttenloch, P.; Sanjuan, B.; Kohl, T.; Steger, H.; Zorn, R. Corrosion and scaling as interrelated phenomena in an operating geothermal power plant. *Corros. Sci.* **2013**, *70*, 17–28. [CrossRef]

30. Piper, A. A Graphic Procedure in the Geochemical Interpretation of Water-Analyses. *Eos Trans. Am. Geophys. Union* **1944**, *25*, 914–923. [CrossRef]
31. Arnórsson, S. The use of mixing models and chemical geothermometers for estimating underground temperatures in geothermal systems. *J. Volcanol. Geotherm. Res.* **1985**, *23*, 299–335. [CrossRef]
32. Arnórsson, S.; Andrésdóttir, A. Processes controlling the distribution of boron and chlorine in natural waters in Iceland. *Geochim. Cosmochim. Acta* **1995**, *59*, 4125–4146. [CrossRef]
33. Guo, Q.; Wang, Y. Geochemistry of hot springs in the Tengchong hydrothermal areas, Southwestern China. *J. Volcanol. Geotherm. Res.* **2012**, *215–216*, 61–73. [CrossRef]
34. Yi, L.; Qi, J.; Li, X.; Xu, M.; Zhang, X.; Zhang, Q.; Tang, Y. Geochemical characteristics and genesis of the high-temperature geothermal systems in the north section of the Sanjiang Orogenic belt in southeast Tibetan Plateau. *J. Volcanol. Geotherm. Res.* **2021**, *414*, 107244. [CrossRef]
35. Zhang, Y.; Dai, Y.; Wang, Y.; Huang, X.; Xiao, Y.; Pei, Q. Hydrochemistry, quality and potential health risk appraisal of nitrate enriched groundwater in the Nanchong area, southwestern China. *Sci. Total Environ.* **2021**, *784*, 147186. [CrossRef] [PubMed]
36. Holland, H.D. Solutions, minerals and equilibria: R. M. Garrels and C. L. Christ: Harper and Row, New York, 1965. 450 pp. $14.25. *Geochim. Cosmochim. Acta* **1966**, *30*, 457–458. [CrossRef]
37. Giggenbach, W.F. Geothermal solute equilibria. derivation of Na-K-Mg-Ca geoindicators. *Geochim. Cosmochim. Acta* **1988**, *52*, 2749–2765. [CrossRef]
38. Zhang, Y.; Xu, M.; Li, X.; Qi, J.; Zhang, Q.; Guo, J.; Yu, L.; Zhao, R. Hydrochemical Characteristics and Multivariate Statistical Analysis of Natural Water System: A Case Study in Kangding County, Southwestern China. *Water* **2018**, *10*, 80. [CrossRef]
39. Giggenbach, W.F.; Glover, R.B. Tectonic regime and major processes governing the chemistry of water and gas discharges from the rotorua geothermal field, New Zealand. *Geothermics* **1992**, *21*, 121–140. [CrossRef]
40. Giggenbach, W.F. Collection and analysis of geothermal and volcanic water and gas discharges. *Chem. Div. DSIR Rep.* **1989**, *2401*, 81.
41. Pang, Z.-H.; Reed, M. Theoretical Chemical Thermometry on Geothermal Waters: Problems and Methods. *Geochim. Cosmochim. Acta* **1998**, *62*, 1083–1091. [CrossRef]
42. Tian, J.; Pang, Z.; Guo, Q.; Wang, Y.; Li, J.; Huang, T.; Kong, Y. Geochemistry of geothermal fluids with implications on the sources of water and heat recharge to the Rekeng high-temperature geothermal system in the Eastern Himalayan Syntax. *Geothermics* **2018**, *74*, 92–105. [CrossRef]
43. Cheng, Y.; Pang, Z.; Kong, Y.; Chen, X.; Wang, G. Imaging the heat source of the Kangding high-temperature geothermal system on the Xianshuihe fault by magnetotelluric survey. *Geothermics* **2022**, *102*, 102386. [CrossRef]
44. Zhang, X.G. Application of isotopic geochemistry in geothermal exploration. *Hydrogeol. Eng. Geol.* **1988**, *1*, 28–31.
45. Craig, H. Isotopic variations in meteoric waters. *Science* **1961**, *133*, 1702–1703. [CrossRef]
46. Kong, Y.; Wang, K.; Li, J.; Pang, Z. Stable Isotopes of Precipitation in China: A Consideration of Moisture Sources. *Water* **2019**, *11*, 1239. [CrossRef]
47. Blasch, K.W.; Bryson, J.R. Distinguishing sources of ground water recharge by using δ2H and δ18O. *Groundwater* **2007**, *45*, 294–308. [CrossRef]
48. Yu, J.; Zhang, H.; Yu, F.; Liu, D. Oxygen and hydrogen isotopic compositions of meteoric waters in the eastern part of Xizang. *Chin. J. Geochem.* **1984**, *13*, 93–101. [CrossRef]
49. Ke, B.; Wu, Y.; Tian, M.; Li, C.; Song, P. Hydrogeochemical characteristics and formation mechanism of Jiyu Hot Spring in Sichuan. *Ground Water* **2022**, *44*, 7–10. (In Chinese)
50. Gabriella Stahl, E.K. Study of calcite scaling and corrosion processes in geothermal systems. *Geothermics* **2000**, *29*, 105–119. [CrossRef]
51. Bjørnstad, T.; Stamatakis, E. Mechanisms of mineral scaling in oil and geothermal wells studied in laboratory experiments by nuclear techniques. *Czechoslov. J. Phys.* **2006**, *56*, 405–416. [CrossRef]
52. Arthur, P.; Schmidt, F.A.H.; van Os, B.J.H.; Schuiling, R.D. Production of 210Pb from a Slochteren Sandstone gas reservoir. *Appl. Geochem.* **2000**, *15*, 1317–1329.
53. Holl, H.G.; Hurter, S.; Saadat, A.; Köhler, S.; Huenges, E. First-hand experience in a second-hand borehole: Hydraulic experiments and scaling in the geothermal well Groß Schönebeck after reopening. In Proceedings of the International Geothermal Conference, Reykjavík, Iceland, September, 2003. Available online: https://www.researchgate.net/profile/Markus-Wolfgramm/publication/266880623_First_hand_experience_in_a_second_hand_borehole_Hydraulic_experiments_and_scaling_in_the_geothermal_well_Gross_Schonebeck_after_reopening/links/5448b1b20cf22b3c14e318dc/First-hand-experience-in-a-second-hand-borehole-Hydraulic-experiments-and-scaling-in-the-geothermal-well-Gross-Schoenebeck-after-reopening.pdf (accessed on 24 September 2023).
54. Gunnarsson, I.; Arnórsson, S. Impact of silica scaling on the efficiency of heat extraction from high-temperature geothermal fluids. *Geothermics* **2005**, *34*, 320–329. [CrossRef]
55. Demir, M.M.; Baba, A.; Atilla, V.; Inanli, M. Types of the scaling in hyper saline geothermal system in northwest Turkey. *Geothermics* **2014**, *50*, 1–9. [CrossRef]
56. Jones, B. Review of aragonite and calcite crystal morphogenesis in thermal spring systems. *Sediment. Geol.* **2017**, *354*, 9–23. [CrossRef]

57. Wanner, C.; Eichinger, F.; Jahrfeld, T.; Diamond, L.W. Causes of abundant calcite scaling in geothermal wells in the Bavarian Molasse Basin, Southern Germany. *Geothermics* **2017**, *70*, 324–338. [CrossRef]
58. MacAdam, J.; Parsons, S.A. Calcium carbonate scale formation and control. *Rev. Environ. Sci. Biotechnol.* **2004**, *3*, 159–169. [CrossRef]
59. Alroomi, Y.M.; Hussain, K.F. Potential kinetic model for scaling and scale inhibition mechanism. *Desalination* **2016**, *393*, 186–195. [CrossRef]
60. Larson, T.E.; Sollo, F.W., Jr. Loss in Water Main Carrying Capacity. *J.-Am. Water Work. Assoc.* **1967**, *59*, 1565–1572. [CrossRef]
61. Zhang, H.; Hu, Y.; Yun, Z.; Qu, Z. Applying Hydro-Geochemistry Simulating Technology to Study Scaling of the High-Temperature Geothermal Well in Kangding County. *Adv. New Renew. Energy* **2016**, *4*, 111–117. (In Chinese) [CrossRef]

Disclaimer/Publisher's Note: The statements, opinions and data contained in all publications are solely those of the individual author(s) and contributor(s) and not of MDPI and/or the editor(s). MDPI and/or the editor(s) disclaim responsibility for any injury to people or property resulting from any ideas, methods, instructions or products referred to in the content.

hydrology

MDPI

Article

Hydrogeological Aspects of the Municipal Water Supply of Albania: Situation and Problems

Romeo Eftimi [1,*], Kastriot Shehu [2] and Franko Sara [3]

[1] Independent Researcher, Rr. Rreshit Çollaku, Pll. Kl. Konst., Nr. 43, 1000 Tirana, Albania
[2] Independent Researcher, HUK Projekt, Bulevardi Zogu 1, Pll.135, Nr. 9, 1000 Tirana, Albania; hukprojekt18@yahoo.com
[3] Hydrogeological Service of Albania, Rr. Kavaja, Nr. 153, 1000 Tirana, Albania; frankosara@yahoo.com
* Correspondence: eftimiromeo@gmail.com

Abstract: The municipal water supply, related mainly to the cities of Albania, began to develop in the second half of the 19th century and very intensively after 1945. Today, the reported mean water production for the cities, on average, is about 300 l/capita/d, including drinking and industrial water supplies. The territory of Albania has an uneven distribution of very heterogeneous aquifers conditioning often the difficulty of municipal water supply solutions. In this article, are analyzed and classified the hydrogeological aspects of the water supply sources of the settlements, which are summarized in five groups: (a) wells in alluvial intergranular aquifers; (b) karst springs; (c) wells in karst aquifers; (d) springs in fissured rocks; and (e) mixed water sources. For each group of the water supply sources, the main concerns regarding the quantity and quality problems are analyzed, facilitated by the description of a variety of representative examples of different situations. Based on the gained experience, important recommendations are given for the better understanding of hydrogeological aspects of water supply systems, related to the river water recharge areas, the seawater intrusion in coastal aquifers, and the high vulnerability of karst aquifers, as well as trans-boundary aquifers. However, the main problem of public water supply of Albania remains the poor management of water supply systems, which is reflected in the significant water losses, as well as the low public awareness of requests for sustainable use.

Keywords: municipal water supply; intergranular aquifers; karstic springs; groundwater contamination; Albania

1. Introduction

The construction of city water supply systems is a very ancient activity, testifying to the culture level and engineering knowledge of the early civilizations. A large part of these systems is still perfectly functioning nowadays, and there are uncounted examples, such as the water supply of ancient Rome. This consists of 11 aqueducts carrying more than 13 m^3/s of karst spring water to the city of old Rome from a distance of 16 to 91 km [1]. Generally, many cities continue to be supplied by karst springs today in the world, with diverse examples in south-eastern Europe, including Albania as well.

The Illyrians, the ancient people living in the territory of Albania, constructed the first cities during the IV–III centuries BC, and different contemporary techniques for that time were used for water supply [2]. The archaeological data testify to the high level of the ancient intake structures and water supply system of Apolonia [3], Durrahy (Durres), Buthrot (Butrinti) and Tepelena [2]; some are shown in Figure 1.

Albania's modern cities have no long history; they began to be built in the second half of the 19th century. Their water supply was initially based on the use of water resources within the settlement's territories, such as natural springs, or groundwater of the intergranular aquifers, captured by big-diameter dug wells. In some cases, such as in Gjirokaster City in South Albania, the population collected the rain water in "steras"

(cisterns), built in house cellars. The first modern water supply systems of Albania's cities began to be built after 1920. The end of World War II found Albania with seven water supply systems, five recharged by springs and two by diverted river waters, with a total capacity of 160 L/s. The population served by the water supply in 2010 was 2.65 million people, corresponding to 80.3% of the total population in the jurisdictional areas of all water utilities in Albania (3.31 million people). The first important hydrogeological investigation realized by the Albanian Hydrogeological Service (AHS), started after 1960, initially focused mainly on the intergranular aquifers. Later, it organized the hydrogeological prospecting of the entire territory of Albania, which was finalized with the Hydrogeological Map of Albania sc. 1:200,000 [4]. This map was the starting point for understanding all different aquifers of the country. At the same time, mass construction of the water works for the water supply of Albanian cities and industries began. The term "potable" was used for water distributed to the consumers through the water works, without distinction between water for drinking and that for other communal and industrial needs. As a result of the dynamic development of the cities and the growth of the economy, the water demands changed very often, making it difficult to manage the water supply problems. However, a great deal of experience was gained in solving water supply problems related to various hydrogeological situations.

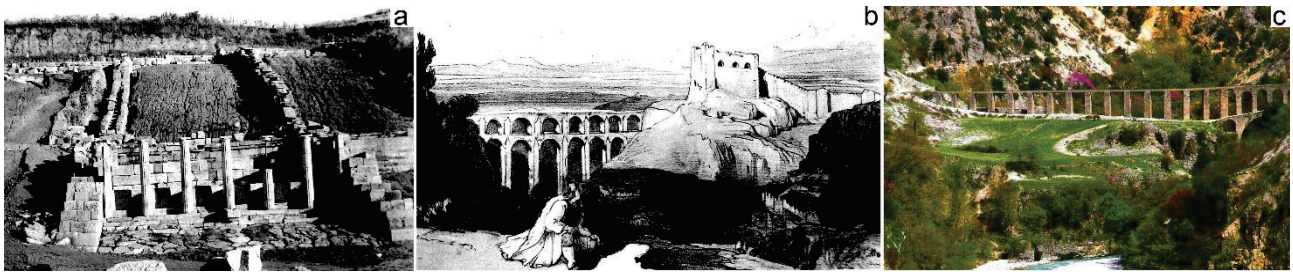

Figure 1. (**a**) The Monumental Fontana of Apolonia, IV century BC [3]; (**b**) aqueduct of Gjirokaster (gravure of XIX century); (**c**) aqueduct of the city of Tepelena (**b**,**c**), from [2].

The intergranular gravelly–sandy aquifers are situated mainly in the Near-Adriatic Plain and along the river valleys where the most important cities of Albania are situated. The location of the water supply wells in these aquifers should respect some contradictory principles [5]. Pumping wells should be placed near the recharge area in order to ensure sustainability and to increase the pumping capacity of the wells through induced infiltration [6–11]. However, near the recharge area, the pumped groundwater can be easily contaminated by polluted river water recharging the aquifer. Thus, a compromise between benefits and undesirable consequences should be respected when determining the location of the water wells [12–14]. Another concern for the intergranular aquifers is the polluting activities such as quarrying at the riverbed recharge areas [15], likely facilitating, in turn, seawater intrusion as a result of the decrease in aquifer hydraulic pressure [16]. Further, rapid and uncontrolled urbanization has a marked impact on groundwater quality too [17–19]. The hydrogeological investigations performed in Albania have already documented several examples of groundwater quality deterioration by pumping near the recharge areas of intergranular aquifers [20–24].

As in many Mediterranean countries [25–27], in Albania, the karst springs are also a very important source of potable water supply [4,28]. Experience in the use of karst springs as potable water sources has repeatedly demonstrated the problems of high variability of their discharge, often causing water shortages in the cities [25,29–31], and their easy pollution in areas of demographic growth and industrial development [32–37]. The main factors contributing to deterioration of the good quality in karst areas of Albania are, therefore: uncontrolled urban sewage, effluent and industrial discharges in lakes and rivers, quarrying in karst areas, use of karst landforms for illegal dumping and developing intensive agriculture activities in karst areas [15,38,39].

The magmatic rocks and molasses contain relatively restricted groundwater resources and are used for the water supply of small towns and villages. During the last 10 years, the increase in water demands for human and industrial water supplies has constricted the use of surface water. The available geological [40] and hydrogeological maps [4], and a variety of other data, have been collected and analyzed for this study. Most of these sources represent archive materials such as reports, chemical analyses and historical non-systematic monitoring by the AHS. The existing data have been compared to recent field observations by the authors. The article analyzes the hydrogeological aspects and experience of groundwater exploitation of different aquifers. To facilitate the analyses, the water supply sources of Albanian cities are classified into five groups, mainly related to the aquifers or to the applied solution of the problems. The analysis is illustrated with typical negative and positive examples of the solutions of the problems.

2. Hydrogeological Characteristics of Albania

Although geographically a small country, Albania has a great geological variety. Rocks vary in age from Ordovician to Quaternary, while, according to their origin, they are sedimentary, magmatic and metamorphic [40,41]. As seen in the simplified hydrogeological map of Albania (Figure 2a), due to uneven areal distribution of different rocks, the hydrogeological characteristics of the country's territory are highly variable also [4,10,28].

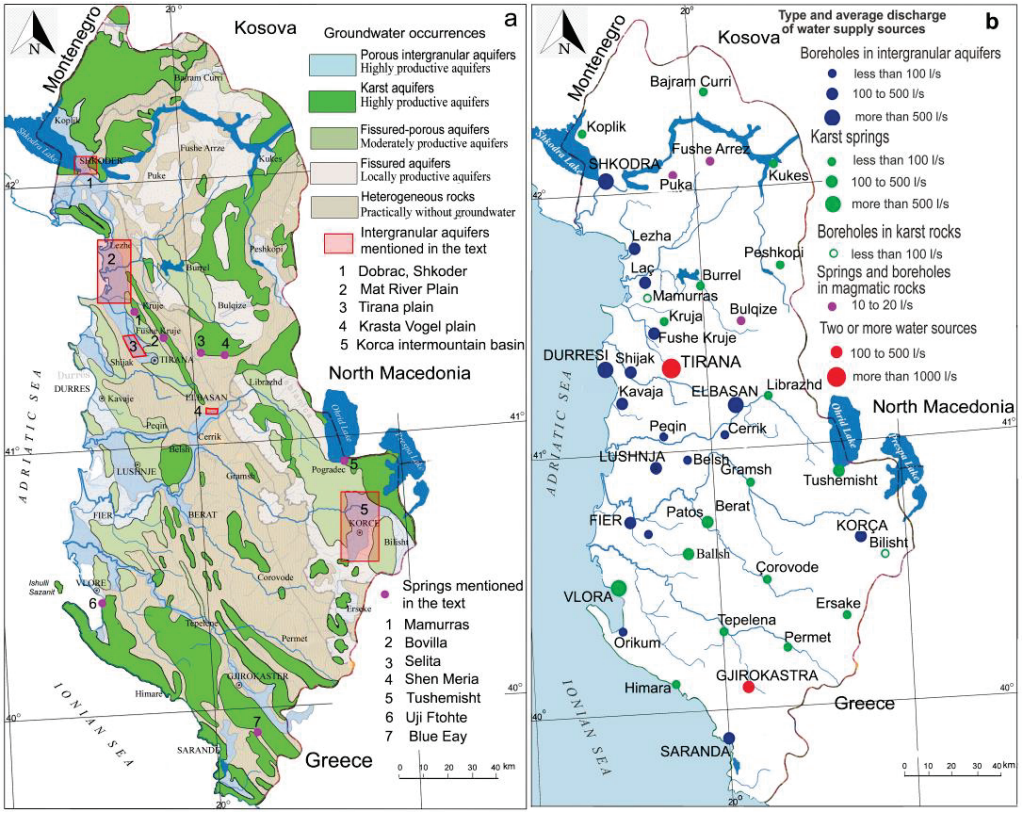

Figure 2. (**a**) Map of groundwater occurrences of Albania (modified from [42]), (**b**) map of water supply sources of the cities of Albania.

As shown in Figure 2, two different classes of rocks are the most abundant aquifers: (a) the porous, intergranular, mainly fluvial gravelly aquifers (blue color), exploitable mainly by drilling wells, and (b) the karstic aquifers (dark-green color), consisting usually of high-elevation carbonate structures recharging strong karst springs. The other fissured–porous aquifers, such as sandstone–conglomerate aquifers, and fissured magmatic rocks, are generally considered as moderate- to low-productive aquifers. The group of rocks, shown on the map with dark-brown color (Figure 2), occupies about 40% of

Albania's territory, consisting of low-productive to very low sedimentary and metamorphic rocks. This fact undoubtedly represents an aggravating factor for the water supply of the settlements and, in general, of the whole country. Table 1 shows the estimated total natural (renewable) and exploitable groundwater resources of Albania.

Table 1. Total natural and exploitable groundwater resources of Albania [28].

Aquifers Related to:	Natural Resources		Exploitable Resources	
	m^3/year	m^3/s	m^3/Year	m^3/s
Intergranular aquifers	0.47×10^9	15	0.945×10^9	30
Carbonate karst aquifer	7.15×10^9	227	2.84×10^9	90
Molasse rocks aquifers	0.45×10^9	14	0.22×10^9	7
Magmatic intrusive rocks aquifers	1.00×10^9	32	0.41×10^9	13
Total groundwater resources	9.07×10^9	288	4.4×10^9	140

The natural groundwater resources of Albania are estimated at about 288 m^3/s, while exploitable groundwater resources consist about 140 m^3/s, which, in most of the aquifers, corresponds to 50% of the total calculated natural groundwater resources. Exceptionally, in intergranular aquifers, the groundwater exploitable resources can be larger than the natural ones as a result of induced infiltration when pumping at the recharge areas. According to an approximate estimation, in Albania, urban and industrial water supply from the groundwater currently accounts for about 12 m^3/s, while rural water supply uses about 2.0 m^3/s, amounting to a total of about 14 m^3/s. Only Tirana has an additional water supply source of about 1.5–2 m^3/s, from the surface water of an artificial lake.

3. Hydrogeological Characteristics of the Water Supply of the Cities of Albania

Water supply sources of the Albanian cities can be summarized into five groups (Figure 2b):

- Drilling wells in intergranular aquifers;
- Karst springs;
- Drilling wells in karst aquifers;
- Drilling wells and springs in fissured rocks;
- Two or more different water supply sources, including surface water.

3.1. Water Supply from Intergranular Aquifers

The groundwater intake structures in intergranular aquifers of Albania consist mainly of pumped wells. As shown in Figure 2b, according to their total capacity, the groundwater intakes are classified in three groups: (a) less than 100 L/s, (b) from 100 to 500 L/s and (c) more than 500 L/s. Only in three cities (namely Shkoder, Durres and Elbasan) is the actual pumped capacity more than 500 L/s; in the others, the capacity is smaller.

The intergranular gravelly–sandy aquifers of Albania [4] generally consist of Quaternary fluvial deposits, with maximum thickness from about 50 to 200 m, representing mainly a multi-layered gravelly aquifer system.

The techniques of groundwater resource evaluation require an understanding of the concept of groundwater yield. The primary objective of most groundwater studies is the determination of the maximum possible pumping rates that are compatible with the hydrogeological environment from which the water will be taken. The known aquifer characteristics enable one to respect and harmonize two important principles when determining the location of pumping wells [5,12,13,43,44]: (a) the water supply wells preferably are located as close as possible to the recharge areas, thus ensuring sustainability of the groundwater flow and the possibility of increasing the pumping capacity of wells through induced infiltration [6,8–10], and (b) the water wells preferably are placed in areas with the highest aquifer transmissibility, ensuring higher pumping rates of the wells and, consequently, a reduction in their number.

The intergranular aquifers of Albania differ in their high filtration parameters; usually, the aquifer transmissibility varies from about 1000 to over 10,000 m^2/day, and, accordingly, the specific capacity of the pumped wells varies from 10 to more than 100 L/s/m [10,45], while, in some cases, the maximum total capacities of the wells exceed 200 L/s [24]. For evaluating the aquifer filtration parameters in Albania, the Thiem–Dupuit method for steady-state flow is widely used [46], together with different formulas representing the solution for non-steady-state flow. Special solutions are used for aquifers limited by one or more straight recharge boundaries [7–9].

In the following, four problematic examples of groundwater exploitation in intergranular aquifers of Albania are discussed: the Fushe Kuqe Plain, Krasta Vogel Plain, Shkodra Plain and Korça intermountain basin.

Fushe Kuqe Plain. This plain is situated south of the Mat River (Figure 3). It is one of the most abundant and most heavily pumped among the intergranular aquifers of Albania. The total surface of the Fushe Kuqe Plain is about 100 km^2 and is filled up by fluvial deposits of the Mat River with a maximum thickness of 200 m. Transmissivity of the gravel aquifer in the central area varies from about 4000 to 8000 m^2/day, and, accordingly, the specific capacity of the wells often exceeds 40 L/s/m [10,20]. The pumped groundwater is used for the water supply of the cities Durres, Lezhë, Milot and Laç, and for dozens of villages as well, with a total population of about 350,000 people (Figure 2).

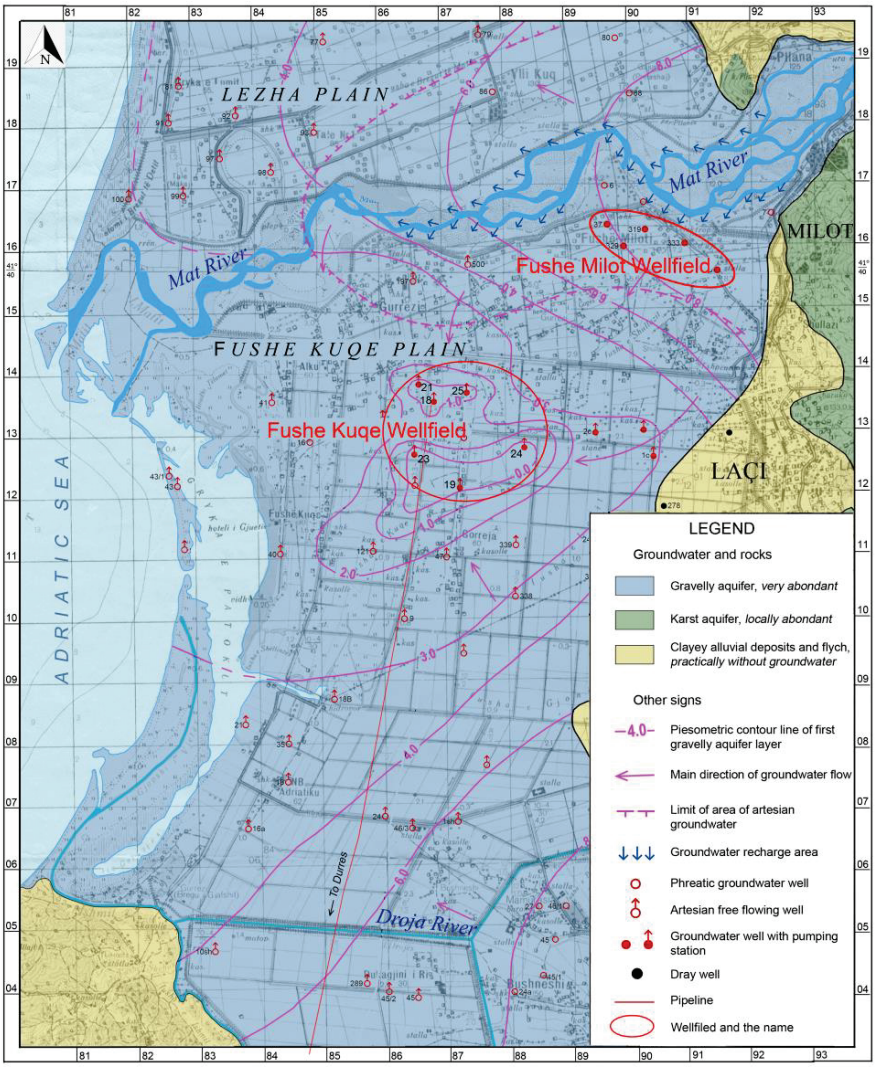

Figure 3. Hydrogeological map of intergranular alluvial aquifer of Mat River Plain, sc. 1:50,000 (modified from [20]).

The recharge source of this aquifer is the Mat River. The most important wellfields in this aquifer are those of Fushe Kuqe, with a capacity of 720 L/s, functioning since 1972, and Fushe Milot, with a capacity of 625 L/s, functioning since 2021 (Figure 3). Fushe Kuqe wellfield is located at similar distances from the Mat River (recharge area) and the Adriatic Sea (discharge area). Before starting intensive pumping of the groundwater (around 1972), the piezometric level in the wellfield area was stabilized about 4–5 m above the ground surface, corresponding to the absolute elevation of about 6 m. At present, the groundwater level is decreased and, in the center of the wellfield, is stabilized at an absolute elevation of around 0.0 m (Figure 3). This created a threat of sea water intrusion into the gravel aquifer.

As shown by environmental hydrochemical and isotope investigations, the occurrence of brackish water in the periphery areas is related to the exchange processes between the Ca^{2+} ions of the groundwater and the Na^{+} ions of clay intercalating layers, remnants of the Holocene Sea transgression [20,23,47].

Additionally, the hydrochemical observations [22] do not indicate a current risk of seawater intrusion in the studied aquifer. After more than 40 years of groundwater pumping in the Fushe Kuqe wellfield, the Cl and Na contents do not show any significant increase; marine water intrusion is thus still not yet considered a problem [5]. Nevertheless, the second big wellfield in Fushe Kuqe Plain, the Fushe Milot, is located near the Mat River recharging the aquifer (Figure 3). It has been calculated that the total influence of the pumping in the new wellfield of Fushe Milot should be less than 1 m in the center of the existing wellfield of Fushe Kuqe, and no intensification of the sea water intrusion will happen. This is supported by observation of the groundwater level and chemical analyses [20,23].

A big concern is the groundwater contamination by infiltration into the aquifer of polluted river water [5,12,48] since most of the Albanian rivers are polluted by untreated urban sewage waters discharged along the rivers [23]. In addition, the intensified quarrying at the riverbed recharge areas represents another serious concern [20,22]. The decrease in thickness of the gravel aquifers at the recharge areas causes reduction in the aquifer hydraulic pressure, which, in turn, facilitates seawater intrusion in the coastal areas [20,49].

Using the Ghyben–Herzberg equation, it is calculated that, actually, a groundwater level lowering of about 1 m at the upper part of the Mat riverbed recharge area causes an aquifer level lowering at the seashore of about 0.1 m, corresponding roughly to a 4 m increase in the freshwater–seawater interface. Nevertheless, the investigations have shown that there is no current risk of seawater intrusion since the wells close to the seashore are artesian [20]. In addition to this, the riverbed quarrying activities are also a source of groundwater contamination [50–52] by oil leakage from machineries, but, so far, no quantitative data on this issue are available.

Krasta Vogel Plain. Rapid urbanization has a profound effect on groundwater recharge and a marked impact on groundwater quality [17,18,33,53]. The intergranular aquifer of Krasta Vogel Plain, located near the eastern suburbs of the city of Elbasan, in Central Albania (Figure 2), testifies to this statement.

The small Krasta Vogel Plain aquifer located along the Shkumbin River is filled with high-permeability gravel deposits, hydraulically connected with the river (Figure 4). For the water supply of the city of Elbasan, three pumped wells, with a total capacity of 245 L/s, have been drilled at a distance of about 200 m from the riverbanks. As a result of the uncontrolled urban expansion of Krasta Vogel village without sewage water collection infrastructure, which started about 20 years ago, the groundwater pumped by wells nos. 2 and 3 was contaminated, and new wells were drilled upstream.

Dobraç wellfield. A similar example, but of a larger scale, is the Dobraç wellfield, near Shkodra Lake, in North Albania (Figure 5), initially developed in a peripheral, undeveloped area. Shkodra Plain is filled by a 60–70 m thick intergranular aquifer, covered by a thin-grained soil, with a thickness of 5–10 m. The groundwater is recharged by rainfall infiltration in the Shkodra Plain and moves westward to Shkodra Lake. The aquifer transmissivity in wide areas is higher than 8000 m^2/day, and the capacity of the wells is about 100–120 L/s. In Dobraç wellfield, about 800 L/s for the water supply of Shkodra City is

pumped, but the groundwater is threatened by infiltration of the untreated sewage water of the new urban area developed in the immediate vicinity of the pumped wells. Actually, two exploitable wells, the closest to the new urban area, each with a capacity of 100 L/s, are polluted and abandoned (Figure 5), and the same will likely happen in the future with the other pumping wells.

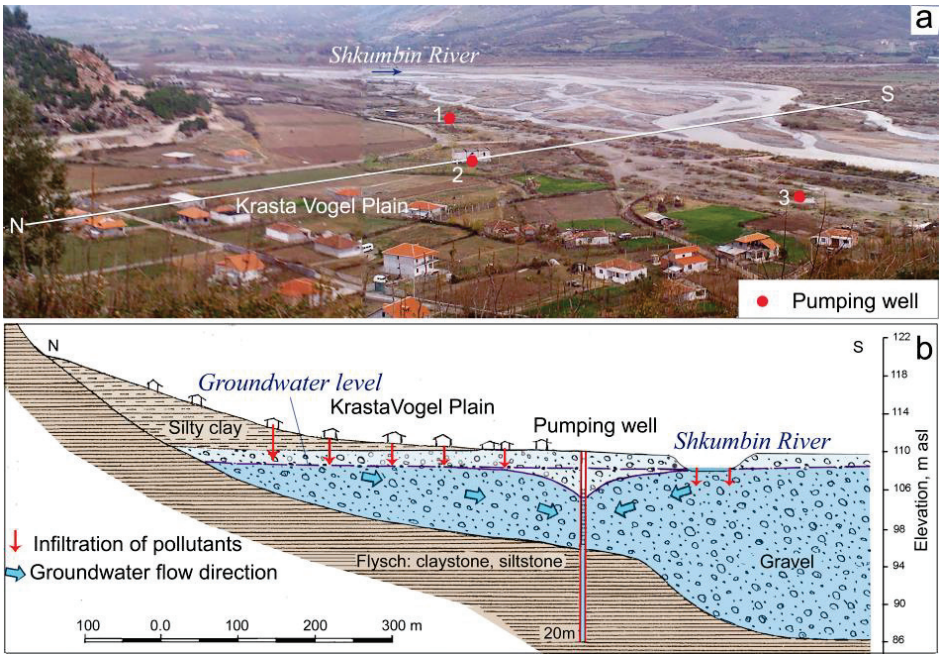

Figure 4. (**a**) General view of the intergranular aquifer in the Krasta Vogel Plain wellfield, (**b**) hydrogeological cross-section of the Krasta Vogel (modified from [24]).

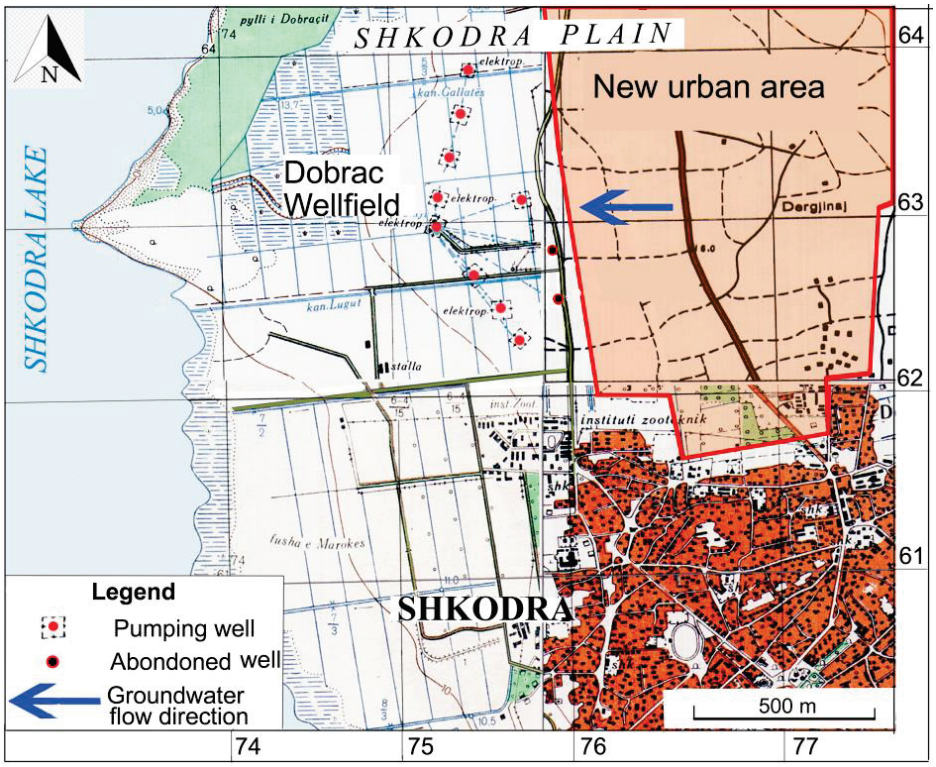

Figure 5. The new urban area is dividing threatening the Dobraç wellfield, with a capacity of about 800 L/s (improved from [10]).

Korça intermountain basin. This basin, located in south-eastern Albania (Figure 2), is the largest intermountain artesian basin of the country (Figure 6). It is filled with Pliocene–Holocene deposits (max. thickness of about 250 m), consisting of intercalation of the gravel intergranular aquifer with clayey layers. The main recharge sources of the basin are the small rivers flowing from the mountain gorges around the Korça plain. The intensive groundwater exploitation in the Korça basin started by the end of 1960s. The pumping intensification from the aquifers is always associated with the formation of a regional groundwater depression. Actually, in total, about 400 L/s is pumped in the Korça basin, used for the water supply of the city, creating in the center of the Turan wellfield a groundwater regional depression of about 14–16 m [45,54].

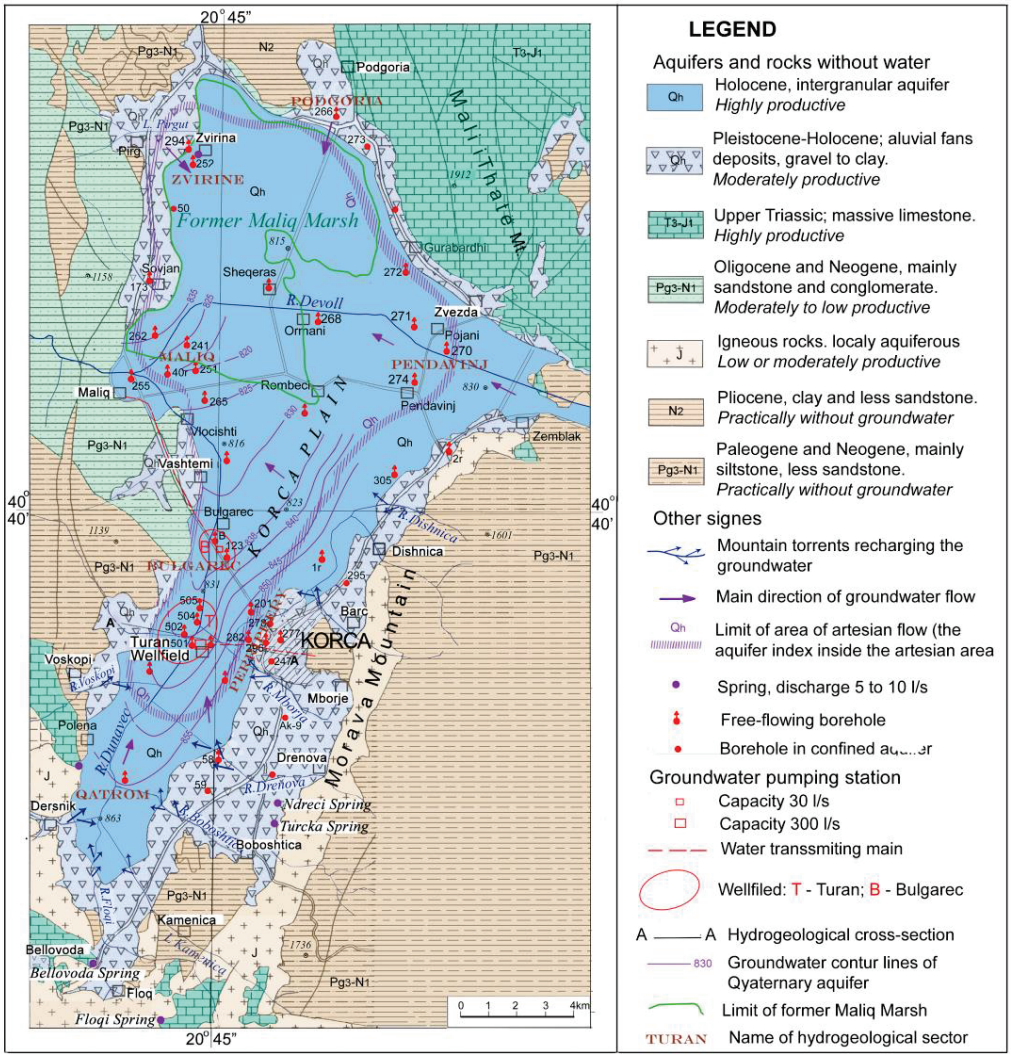

Figure 6. Hydrogeological map of Korça intermountain basin (modified from [45]).

The main problem regarding the intensification of the groundwater use in Korça basin is the sustainability which must be established between the quantity of pumped groundwater and eventual negative environmental impacts. Safe yield is traditionally defined as the attainment and maintenance of long-term balance between the amount of groundwater withdrawn annually and the annual amount of recharge [55]. However, the aquifer development, based upon the concept of safe yield, is not safe and sustainable [43,44,55–57]. If the groundwater pumping should be limited within the natural groundwater flow to respect the so-called "self-yield", it might be difficult, if not impossible, to face the constant increase in groundwater demands. Maybe it would be more appropriate to respect the "basin yield" concept, which can be sustained by the hydrogeological system of the ground-

water basin without causing unacceptable changes in any environmental components of the basin. Respecting the "basin yield" concept means sustainable groundwater management of the Korça basin, which must be necessarily accompanied by observations and control of the aquifer, water conservation measures, water quality monitoring and observation of the possible negative impacts such as the drying up of the rivers, pronounced changes in wetlands, including in their habitats, etc.

3.2. Water Supply from Karst Springs

Karst rocks occupy an area of 6750 km^2, or 24% of Albania's territory [4]. In Albania, 100 karst springs have an average discharge exceeding 100 L/s. Among them, 17 outflows discharge more than 1000 L/s, and Blue Eye Spring (Figure 2), the biggest spring of the country, reaches 18.4 m^3/s. Total renewable karst groundwater resources of Albania are estimated at about 227 m^3/s and account for about 80% of all groundwater resources in the country [28,58]. Based on climatic data and using empirical methods [59,60], the yearly efficient infiltration of the precipitations is calculated to be from 1500 to 2000 mm in the Albanian Alps, in the north of the country, 1100–1750 in the central and southern part and about 450 in south-eastern Albania [58]. Karst groundwater represents the main source of potable water supply in many countries, and particularly in coastal areas [25,27], where urbanization is growing fast. The experience of utilization of karst water resources encountered two main problems: (a) the spring discharge regime and (b) water quality deterioration.

Since the regime of the recharging karst springs rainfalls is highly variable (about 70% of them are concentrated during the period of November–April), their discharge regime is too. This is the reason why many cities face water shortages, especially during the summer–autumn months, when karst springs significantly reduce their flows [26,31,61]. Karst waters often show significant variations in their physic-chemical and bacteriological characteristics, and experience has shown that the variations in water quality are more pronounced when there are also variations in the output of karst springs [58,62].

In the following, experiences related to three big karst springs of Albania (Uji Ftohte, Bogova and Tushemisht) used for urban water supply are presented.

Uji Ftohte springs. This spring, the largest in the southern coastal area of Albania, 147 km long (Figure 2), issues from the Tragjas karst massif, consisting of Triassic dolomite and Jurassic to Eocene limestone and thin-bedded cherts. In the area of the Uji Ftoht springs, a transgressive contact between carbonate rocks and Neogene clayey formations is present [40,41], and the formations work as a barrier preventing the intrusion of seawater into the karst aquifer (Figure 7). Uji Ftoht Spring is used for the water supply of the city of Vlora, which has a population of about 170,000 inhabitants (Figure 7). This spring consists of 32 springs emerging at sea level along a 1.7 km long stretch. Three horizontal galleries parallel to the coastline, excavated at a distance of 60–70 m from the coast, at an elevation of 0.2–0.5 m asl, collect inside the rocks most of the discharges into the sea karst water [63]. The mean annual discharge of the three draining tunnels is about 2.0 m^3/s, while the mean water supply discharge for Vlora city varies by about 0.8 m^3/s. Based on non-systematic water quality analyses, the levels of some chemical parameters measured at drainage tunnels are as follows: conductivity 400–700 μS/cm, TDS 250–540 mg/L, pH 7.2–7.7, Cl 20–150 mg/L, Na 20–90 mg/L, HCO_3 50–60 mg/L, NO_2 missing, and water hydro-chemical type is HCO_3–Ca–Mg.

However, the situation in the catchment areas of the Uji Ftohte springs is undergoing rapid changes; instead of fruit trees, brushwood and meadows on outcropping rocks, an uncontrolled urban area without a centralized waste water system is under development above the water collecting at an elevation from 20 to 250 m (Figure 7). Bacteriological analyses, performed at least since 2009, confirm that Uji Ftohte springs are heavily polluted. The values of some bacteriological indexes confirm the groundwater pollution: total coliform, 10–20, faecal coliforms (Escherichia coli), 10–17, and *faecal streptococcus*, 2–4, which indicate the possible presence of various pathogens [64].

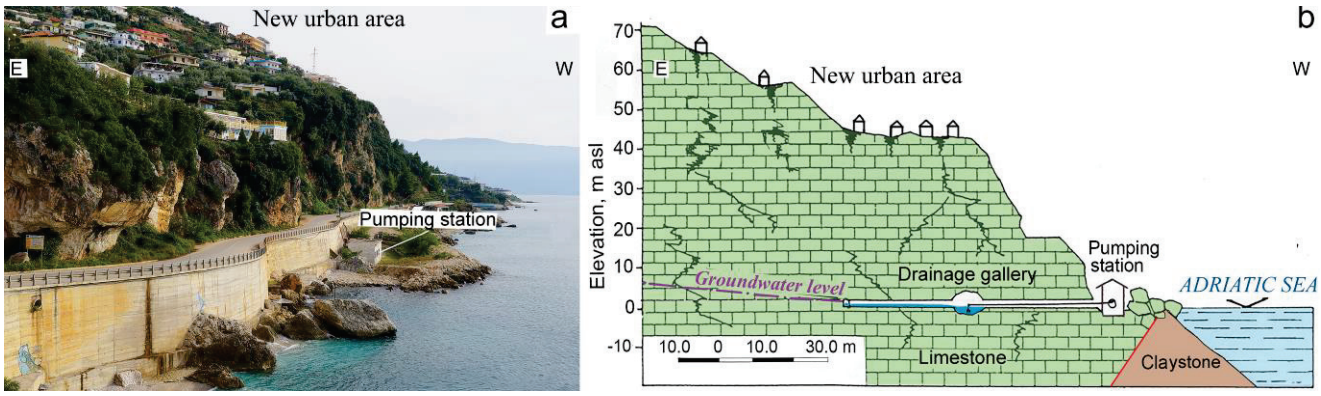

Figure 7. Uji Ftohte karst spring: (**a**) a new urban area is developing above the water collecting tunnels; (**b**) hydrogeological cross-section of the spring and the intake structure (modified from [38]).

With regard to the numerous possible hazards emanating from the urban area, the only mitigating element seems to be impervious "terra rossa" fillings of the cover sequences [32], which, in the Uji Ftohte spring area, have significant thickness. In case of a small thickness of the unsaturated zone, such as at Uji Ftohte, the purification process is also limited by the short time the water stays in the aquifer [65].

To protect the water quality of Uji Ftohte springs, the following measures are recommended: (a) to stop the development of the upstream urban area, (b) to ensure that water-impermeable septic tanks are constructed, (c) to construct the wastewater drainage system respecting the peculiar conditions in the considered area and (d) to monitor the water quality and establish protective areas of the groundwater catchment. So far, the only adopted measure is an increase in the dosage of chlorination.

Bogova Spring (Figure 2) is an example of the negative impact of limestone extraction through quarrying activity in a karst aquifer such as the mentioned similar examples [50–52,66]. The mentioned spring is one of three big karst springs issuing from Tomor karst massif, in Central Albania, and is located in its western part at 344 m asl. The water quality is excellent, the conductivity is about 224 μS/cm, the total hardness is 2.54 meq/L and the water type is HCO_3–Ca–Mg [38]. The average discharge of the spring is about 1350 L/s, and, by gravity, it is used for the water supply of the cities of Berat, Poliçan and Kuçove in Central Albania, with a total population of about 120,000 inhabitants.

The spring recharge area was a clean mountainous limestone area. This situation completely changed after 1995, when the quarrying activity accelerated, demanded by the construction industry. Quarrying is still particularly intensive upspring, at elevations of about 600–1000 m asl and distances of about 1.0–3.0 km north-east of the spring. This activity is responsible for the pollution of Bogova Spring, where, from time to time (mainly at the beginning of the rainy season), the spring water becomes turbid. The turbidity originates from the soil, favored by removal of the red clay in the subcutaneous zone [67], and rapidly spreads over large distances after every significant precipitation event, thus impacting the springs. Brief contamination episodes are interrupted by more or fewer long periods of clean spring water. In some events, the measured turbidity in the water distribution system of Berat varies from 2 to 4 NTU (nephelometric turbidity units), whilst the European guidelines indicate that turbidity values must not exceed 1.0 NTU [68]. The recommendation to stop quarrying within the spring's immediate protection area, with a 1 km buffer in the upstream direction, has not been respected.

Tushemisht spring. This spring is one of the St Naum–Tushemisht spring group, issuing from the Ohrid Lake coastal line, at the boundary between Albania and North Macedonia (Figure 2). The high karst mountain chain Mali Thatë–Galičica separates two lakes, Prespa Lake at elevation 849 m asl and the Ohrid Lake at elevation 693 m asl (Figure 8a). This massif is a transboundary karst aquifer shared by Albania, North Macedonia and Greece.

Water of Prespa Lake disappears in Zaver swallow hole and reappears at lower elevation as large karst springs along the Ohrid Lake coast [69]. The shorter transit water distance is about 17 km. The most important springs in the Ohrid Lake coastal line are the St Naum Spring, with an average discharge rate of 7.50 m^3/s issuing in North Macedonia, and Tushemisht spring, with an average discharge of 2.5 m^3/s, issuing in the Albanian territory (Figure 8a). As determined by the application of the environmental isotope methods, the total discharge of this spring group is recharged nearly 50% by the karst water of Mali Thatë–Galičica and about 50% by the Prespa Lake [38,70].

The city of Pogradec, located in the southern sector of Ohrid Lake (Figure 2), is an important, fast-developing tourist center in Albania. Since about 1980, Pogradec has been supplied with water by a gallery about 35 m long, excavated near the Tushemisht spring (Figure 8b). About 70 to 120 L/s water was pumped in a small collecting room. After detailed hydrogeological investigations in 2002, it was decided to enlarge the tapping structure, aimed at increasing the spring discharge to about 250 L/s. However, serious concerns have arisen about the possible pollution of the pumped karst water from the seepage of the eventually polluted Ohrid Lake water.

The practice of exploitation of karst springs offers many examples for the solution of similar problems, often consisting of the construction of special hydrotechnical structures, such as underground diaphragms [36,71,72]. Similarly, to avoid the infiltration of lake water into Tushemisht spring, a pumping shaft isolated by an impermeable diaphragm surrounding the waterworks was constructed (Figure 8b). The diaphragm consists of 74 alternated cemented and reinforced boring piles of diameter 600 mm and depth 5 to 10.5 m, tightly fixed on the karstified limestone basement. As proved by trace experiments, the concrete curtain is water tight, and even the groundwater level in the collecting room during the pumping of about 200 L/s is stabilized about 30 cm above the lake level.

Another important issue is the possibility of contamination of Tushemisht spring by the polluted Prespa Lake water recharging the spring. This is facilitated by large karst conduits separating the lakes [73], enabling high flow velocities, shortening the transit and reducing the necessary time for micro-organisms to die [32]. The main reason for pollution of the Prespa Lake area seems to be the rapid increase in population and tourism and the intensified agriculture, with village waste disposal sites scattered along the coastal line of Lake Prespa which discharge into the lake untreated waste water [38]. The situation becomes more problematic due to the catastrophic decrease of about 10.5 m in the level of Lake Prespa during the last 50 years as a result of the climate changes [74], corresponding to about 25–30% of the total lake volume [75]. The dramatic drop in lake level is accompanied by increased eutrophication [76]. Nevertheless, until now, no significant pollution of the Tushemisht spring has been reported.

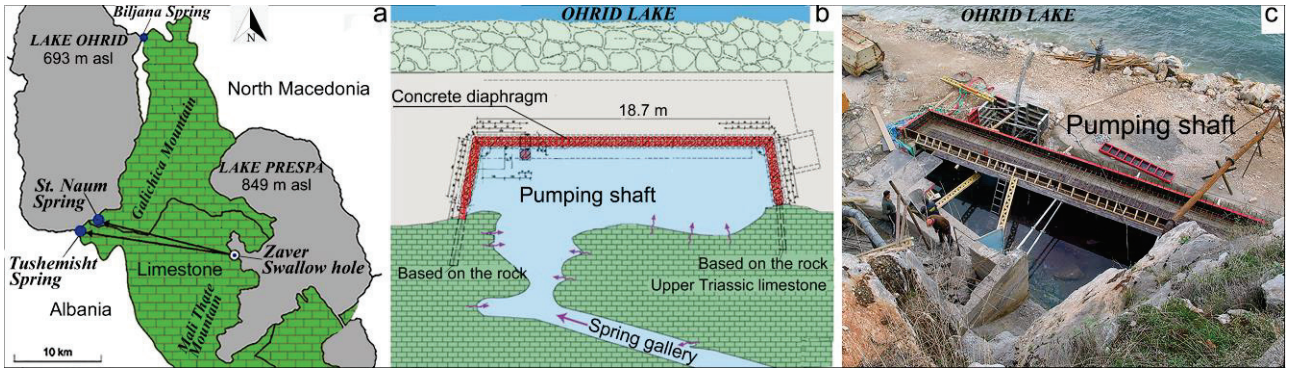

Figure 8. Tushemisht spring: (**a**) hydrogeological scheme of the transboundary karst aquifer Mali Thatë–Galičica, (modified from [76]), (**b**) sketch of isolation diaphragm, (**c**) pumping shaft during the construction ((**b**,**c**) from ILF Construction Company, Innsbruck, Austria).

For managing and protection of the karst aquifers, it is important to know their hydrogeological character, which can be established using the discharge and chemical variability data. Springs with high discharge variability can indicate a high degree of groundwater transport; there are at least two end-member types of groundwater flow in karst aquifers: conduit flow (fast flow) and diffuse flow (slow flow) [77]. The analyses of hydrograph separation constructing the master curve enable identification of the fast flow, slow flow and intermediate flow, enhancing the estimation of groundwater vulnerability [78,79]. The hardness variation was used by [80] to classify the springs into diffuse flow and conduit flow, but the list of chemical parameters used for this purpose was elongated by [81]. Both mentioned methods of interpretation were used to evaluate the karst flow character of the springs Selita and Blue Eye in Albania, and the result fully agreed. Selita spring has a prevailing conduit karst flow and high vulnerability in terms of groundwater quality, while Blue Eye Spring is characterized as a diffuse-flow spring and has lower sensitivity to potential pollution [58].

3.3. Water Supply from Drilling Wells in Karst Aquifers

As explained in the above paragraph, the main problem in water supply, related to karst springs, is the water shortage during the recession period [25,36,58,62,82,83]. The intake structures usually tap the natural discharge of the springs, despite the fact that dynamic water resources in karst often surpass undoubtedly the used karst water resources [84]. Based on groundwater monitoring, the ratio between the maximum and minimum discharges for karst springs of Albania vary mostly from 3 to more than 6, but there are also karst springs with maximum discharges higher than tenths of m^3/s that dry up totally [28,58].

To face the water shortage of the springs, the most appropriate type of water intake is through pumping dynamic karst water reserves by application of large-diameter wells [31,36]. The hydrogeological conditions must allow the drilling wells, sited in karst aquifers, to pump the static reserves in a short time, which should be replenished during the next wet season [25,27]. Usually, the drilling wells are located upstream in the catchment. The karst conduit system may be very heterogenous, and the boreholes at small distances may have very different productivity.

In the following, two examples of successful water supply by drilling wells near shortage springs are shortly described. The small city of Mamurras, located in Central Albania, was initially supplied by a karst spring discharging about 20 L/s, quite insufficient for the normal water supply of the increasing population of the city. The spring issues from Makaresh karst massif, consisting of Upper Cretaceous dolomite and limestone, with calculated water resources of about 400 L/s. During 2002, two wells, 50 m deep, were drilled near to the spring (Figure 9a). The pumping tests confirmed that both wells were abundant; the free flow of well 1 was nearly 50 L/s (Figure 9b), while the pumping capacity of well 2 was 60 L/s. Since 2002, the city of Mamurras has normally been supplied with about 50 L/s by one single well.

A similar example is the small city of Bilisht in south-eastern Albania (Figure 2). The city was supplied by an ascending karst spring issuing from Upper Eocene conglomerate limestone and discharging about 12 L/s. To improve the water supply of Bilisht during 2008, two wells were drilled upspring, 150 m deep. The pumping capacity of the new wells, individually, is about 35 L/s.

Using drilling wells for the capture and pumping of the renewable karst static water resources could be applied also in other places in Albania, such as around the cities of Koplik in North Albania and Permet and Gjirokaster in South Albania. There are cases of ascending vaucluse springs where the pumps are installed into the siphon channels of very big temporary springs, such as in Viroi and Goranxi, in South Albania, and of the perennial spring Syri Sheganit in Northern Albania. In each case, the pumping capacity is about 2 to 3 m^3/s, and the pumped water is used for irrigation.

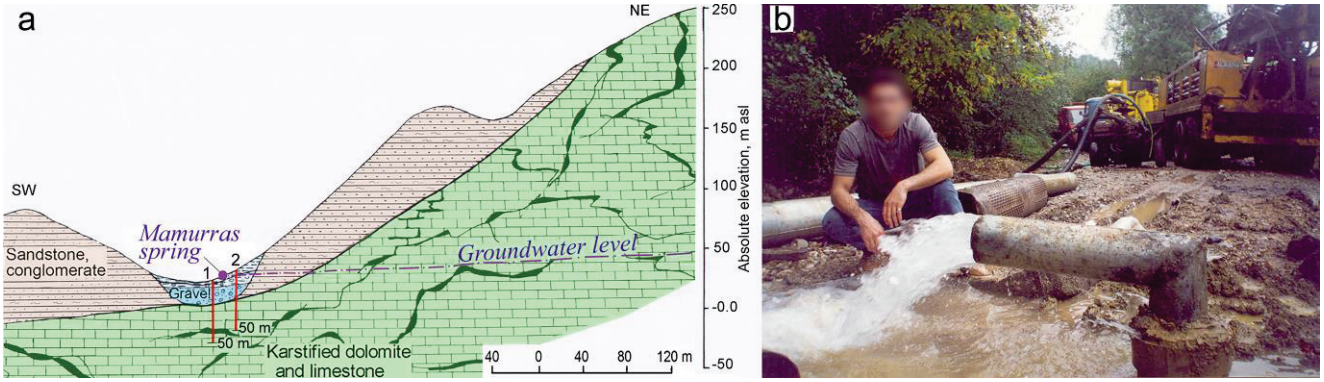

Figure 9. (**a**) Hydrogeological cross–section through two drilling wells used for Mamurras water supply; (**b**) drilling well no. 1, free flowing capacity of about 50 L/s.

3.4. Water Supply Wells in Fissured Rocks

There are two main fissured aquifers in Albania, one related to magmatic and the second to sandstone–conglomerate rocks (Figure 2a). The magmatic rocks crop out in inner Albania and occupy about 4200 km^2. They are mainly ultrabasic rocks, such as serpentine rocks, and less basic rocks such as gabbro. Generally, their water resources are related to two fissure zones distinguishable in the magmatic rocks [85]. The first zone develops close to the surface (down to about 30–40 m) and is represented by weathering joints, and the second is represented by faults. The groundwater of the first zone recharges small springs, usually discharging less than 1 L/s. The second zone, associated with faults, typically extends to a considerable depth of a hundred meters, or even more, containing usually pressurized (artesian) water. The drilling wells have a great diversity in output, reflecting the importance of the distribution of fracture systems and their frequency [28]. The free-flowing wells, tapping deep fault zones in intrusive rocks and placed at the low-elevation valley bottoms, vary from 1 to about 8 L/s. As for the ascending springs, related to well–developed fault zones, the maximum discharges vary from about 10 to 30 L/s.

Among the Albanian cities, only two small ones, Puka and Fushe-Arrza, are supplied with water from springs of magmatic rocks, their discharges varying in the range of 15–20 L/s. Since relatively larger springs issuing from magmatic rocks are missing, the increase in their water supply capacity still represents an unresolved problem. The encouraging results of the water wells drilled in magmatic rocks, mainly to investigate the mining hydrogeology of Albania [28,85], must serve as a support for intensifying the drilling of water supply wells for small cities located at such rocks.

The second fissured aquifer is of the sandstone–conglomerate (molasses) rocks, outcropping at about 4000 km^2 and consisting of intercalation of Neogene sandstone and clayey rocks; it has low permeability or is practically without water (Figure 2). The average transmissivity values and specific capacity of water wells are, respectively, about 3 to 15 m^2/day and about 0.03 to 0.2 L/s/m. The small groundwater resources of this aquifer are used only for family water supply. The Pliocene molasses deposits, represented by sandstone–conglomerate deposits known by the local name the Rrogozhina Formation, cover an area of 2300 km^2 and are located in the Near-Adriatic Plain. The average values of transmissivity and specific capacity have, respectively, values of about 80 m^2/day and about 0.4 L/s/m, while the maximum capacities of the wells are about 10 L/s [86]. The small cities of Kavaja and Roskovec, in Central Albania, are supplied from the Rrogozhina Formation aquifer with quantities of about 20 to 40 L/s. As the groundwater of this aquifer is usually hard, and the concentration of the iron often exceeds the drinking water limit of 0.3 mg/L, the use of this aquifer is constantly being reduced.

3.5. Water Supply from Two or More Different Water Supply Sources, Including Surface Waters

In Albania, only two cities, Tirana, the capital, and Gjirokaster, in Southern Albania, have mixed water supply systems consisting of two or more different water sources.

Tirana City. The water supply system of Tirana City consists of: (a) three karst springs; (b) four wellfields in intergranular aquifers; and (c) surface water of a reservoir (Figure 10).

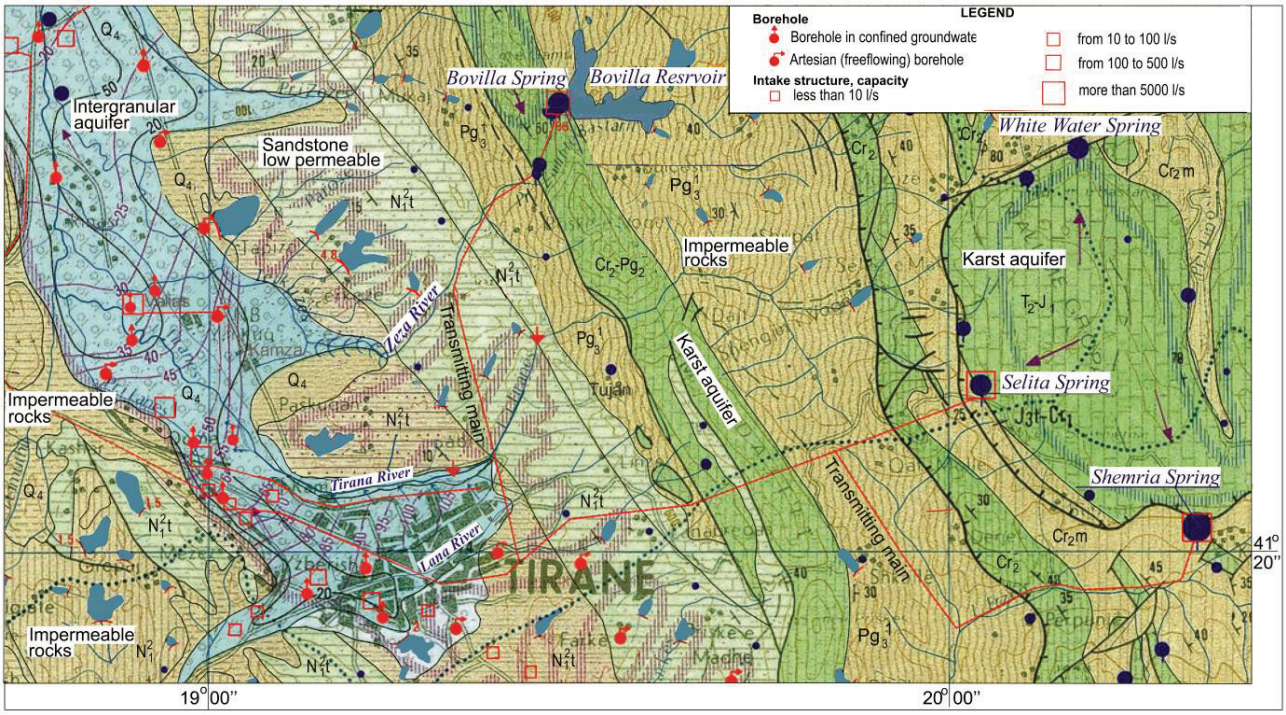

Figure 10. Hydrogeological map of Tirana area sc. 1:200,000 (modified from [4]).

The increase in water supply capacity for Tirana is related to the development of the city. The first centralized water supply system (capacity of 30 L/s) was constructed in 1940 and used the water of the Tirana River. In Tables 2 and 3 are summarized the main data of the karst springs and of water supply systems constructed after 1951 for Tirana water supply, also shown in Figure 10.

Table 2. Minimum, mean and maximum discharges of karst springs Selita, Shën Meria and Bovilla.

Spring	Qmin—L/s	Qmax—L/s	Qmean—L/s	Qmax/Qmin
Selita	230	1200	507	5.2
Shën Meria	613	>3000	894	>5.0
Bovilla	140	640	381	4.6
Total	983	>4840	1782	

Table 3. Average annual water quantity used for Tirana water supply.

Type of Water Resource	Water Supply System	Average Capacity of the Water Supply System, L/s
Karst springs	Selita Spring	439
	Shën Meria Spring	500
	Bovilla spring	381
Wellfields in the gravelly aquifer	Laknas, Berxull, Tirana	445
Surface	Bovilla Reservoir	2000–2500
Total		3765–4265

To balance the reduction in the spring's discharges during the summer–autumn season, as well as to face the necessity of additional water quantities during 1975–1990, some pumping wells, located in the Tirana plain, are included in the Tirana water supply system (Figure 10). The overall discharge of the pumped wells is about 300 L/s, a quantity that cannot satisfy but enables the water needs of the city. To face the needs of the high population increase in Tirana after the political changes of 1990, a large water supply system fed by the Bovilla Reservoir was constructed (Figure 10). Before the distribution, the water of the reservoir is treated physically and bacteriologically in a plant, initially constructed for the capacity 600–700 L/s and at present increased to about 2000 L/s.

Table 3 shows that the total water supply capacity of Tirana is equal to 4265 L/s. Unfortunately, performance of the water supply systems is deteriorated; the difference between System Input Volume and Billed Authorized Consumption, representing the water losses, is about 65%. In practice, the billed water quantity of Tirana is only 1493 L/s. Similarly to that of Tirana, the "water losses" in other urban water supply systems of Albania consist of about the same percentages.

Although different as regards the chemical composition, the quality of Tirana water sources respects the drinking water standard limit [21]. As concerns the bacteriological composition, there are constant problems, mostly with the groundwater pumped in the intergranular gravel aquifer of the Tirana plain. Generally, in these wellfields, the recommended groundwater protection measures are not respected; many buildings are constructed, even within the strong sanitary protection zone of the shallow pumped wells. Generally speaking, the rivers Lana and Tirana, representing the main recharge sources for the intergranular aquifer of Tirana, collect all the untreated sewages of the city and are heavily polluted [21]. Further, the water of Bovilla Reservoir is under constant threat of pollution by untreated sewerage of the rural centers (villages) situated in the lake watershed.

Gjirokaster city. Gjirokaster is the second city in Albania with a combined water supply system. Traditionally, the city was supplied with water from the "steras" (cisterns), situated in the cellars of the houses, where the rain water was collected, similarly to in other countries in the Mediterranean Basin [87–89]. The first centralized water supply system of the city was constructed in 1939, when the Tranoshisht karst spring water was diverted by gravity. The used capacity of this spring varied by about 15–40 L/s and soon was completely insufficient for the normal water supply of the city, particularly during the summer season. To compensate the summer water demands, during 1970, the water supply system of Hosi karst spring was built, with used capacity of about 40–60 L/s. However, the water quantity soon become problematic again, particularly during the summer. To compensate the needed water quantity demand, during 1985–1990, two big-diameter wells were drilled in the Drinos River valley, where 100 L/s is pumped from the intergranular aquifer filling the valley. As the hydraulic connection of the gravel aquifer with the Drinos River is very intensive and the distance from the recharging river to the pumped wells is only about 120 m, the contamination of the groundwater by the eventually polluted river water is a constant problem.

4. Discussion and Conclusions

Albania is a country rich in groundwater. The calculated renewable resources produce about 288 m^3/s, while the total exploitable resources produce about 140 m^3/s [28]. Groundwater in general is more desirable than the surface water as a water supply source for the following main reasons: (1) it is commonly free of pathogenic organisms; (2) temperature, color and chemical composition are nearly constant; (3) groundwater supplies are not seriously affected by short droughts; (4) the radiochemical and biological contamination of most groundwater is difficult [90]. Actually, the groundwater resources used for the water supply are estimated to produce about 14 m^3/s, consisting of only 10% of exploitable groundwater resources of Albania. Total capacity of the centralized water supply after 1944 was 160 L/s, of which about 63% was from karst springs and 37% from surface (river) water. In 2010, the total capacity of the centralized water supply systems was about 14 m^3/s and

served about 2.65 million people. According to the type of water sources, the population is supplied as follows: 54% from intergranular aquifers using water wells, 37% from karst water, and about 13% of the population is served by surface water. It seems the proportion of surface water use to total water use should rise significantly.

This work demonstrates that the water supply of the cities, or of the settlements in general, depends mainly on the type of the aquifer. There are two more important aquifers widely used for the water supply of Albania's settlements: the intergranular gravel–sandy aquifers and the limestone–dolomite karst aquifers.

The main problem related to the intergranular gravel–sandy aquifers is the location of the pumping wells. Locating them near the recharge areas ensures the sustainability of the groundwater flow [6,8–10,91]. However, this increases the hydraulic gradient of the groundwater flow, as well as the groundwater flow velocity, and, consequently, shortens the transit time of the groundwater flow from the recharge area (mainly the rivers) to the pumped wells. A similar situation is undesirable in terms of the quality of the pumped water, particularly when the transit time from the river to the pumping wells becomes shorter than 50 days, which is the necessary length of time for viruses to completely disappear. This is the reason why some legislations, such as in Germany, use 50 days of water travel time to determine the limit of the groundwater protection zone [92]. Therefore, this principle is not applied when dimensioning the groundwater protection zones in Albania. The common main pollutants of groundwater are the untreated domestic waste water and industrial waste water and the uncontrolled use of pesticides in agriculture [32,48], which, in Albania, are usually discharged directly into the rivers.

Gravel abstraction from the riverbeds for construction purposes is another important pollution source, with pollution coming from the hydrocarbons or fuels used by the operating machines. In addition to this, a negative impact of the riverbed quarrying is also the groundwater level lowering as a result of the thickness reduction in the gravel deposits in the recharge area. This is transmitted also in the decrease in the hydraulic pressure of freshwater flow in seaside areas, facilitating the seawater intrusion [16,49]. As explained above, this is one of the concerns arising from the intensification of the groundwater pumping in the Fushe Kuqe intergranular aquifer.

Although often problematic, karst aquifers represent the main source of potable water supply in many countries [25,27]. There are two important problems when karst aquifers are used as a water supply source: (a) the significant decrease in spring flow during the recession period, (b) easy contamination of karst aquifers by urbanized areas, agricultural activity and quarrying [36,37,39,51]. In addition, the fragility of the karst environment, and diffuse problems and degradation deriving from anthropogenic activities in the Albanian karst, has to be taken into account too [15,38].

One of the most important aspects of groundwater protection, in general, is the determination of the three groundwater protection zones, as foreseen in the Water Law of Albania, in accordance with the National Standard of the Potable Water [93]. Regarding the actual situation in Albania, it can be said that: (a) most of water supply sources are determined without performing the necessary detailed special hydrogeological investigations; (b) the recommended measures for different protection zones in many cases are not respected; (c) dimensioning of the groundwater protection zones does not take into consideration the fifty-days transit time principle, and often it is made arbitrary or empirically.

For sustainable water resources management in Albania, a reasonable equilibrium between groundwater intensive exploitation and its protection from depletion and pollution should be realized. This could be achieved mandatorily by intensive monitoring and control of aquifer and water conservation measures. The existing monitoring network in Albania is quite incomplete as concerns the number of observation points and the observed parameters.

To face the situation of municipality water supply in Albania, it appears necessary to urgently undertake the following measures: intensification of basin-wide hydrogeological investigations; establishment of a wide groundwater monitoring network including

hydrodynamic, hydrochemical and environmental isotopes; construction of detailed GIS hydrogeological maps at scale 1:25,000–1:50,000 and related mathematical models of the aquifers; compilation of the aquifer vulnerability maps; and establishment and respect of groundwater protection zones for each water supply source based on special hydrogeological investigation. Particularly, aimed at facing the problems dealing with transboundary aquifers, as a first step, there is the creation of active joint consultative bodies between transboundary countries for collecting, harmonizing and interchanging all available monitoring and geological–hydrogeological data. The sustainable water supply of settlements is linked with efficient governmental laws, with public education encouraging the maintenance of water supply systems and with a serious increase in the public interest in these problems, building up an environmental awareness in urban and rural areas.

Author Contributions: R.E.: conceptualization, methodology, data analyses and writing—original draft. K.S.: collecting and analyzing the data, methodology, supervision. F.S.: collection and analyzing the data, methodology, writing review and supervision. All authors have read and agreed to the published version of the manuscript.

Funding: This research received no external funding.

Institutional Review Board Statement: Not applicable.

Data Availability Statement: Readers can contact the authors for the available data and materials.

Acknowledgments: The authors are grateful to Zoran Stevanović and Mario Parise for their very helpful comments and advice that greatly improved this paper. The authors acknowledge four reviewers for their constructive comments and suggestions, which have been very helpful in improving the quality of the manuscript.

Conflicts of Interest: No conflict of interests are declared for this article.

References

1. Lombardi, L.; Corrazza, A. L'acqua e la cittá in epoca antica. In: La Geologia di Roma, dal centro storico all periferia, Part I, in Parise M, Apulian karst springs: A review. *J. Environ. Sci. Engng. Technol.* **2008**, *8*, 63–83.
2. Baçe, A.; Meksi, A.; Riza, E.; Karaiskaj, G.; Thomo, P. *The History of Albanian Architecture*; Ministria Kultures: Tirana, Albania, 1980. (In Albanian)
3. Ceka, N. *Apolonia e Ilirise*; Shtepia Botuese "8 Nentori": Tirana, Albania, 1982; p. 244.
4. Eftimi, R.; Bisha, G.; Tafilaj, I.; Sheganaku, X. *Hydrogeological Map of Albania, Scale 1:200,000*; Hamid Shijaku: Tirana, Albania, 1985. [CrossRef]
5. Noner, J.C. *Introduction to Hydrogeology*; CRC Press: Boca Raton, FL, USA, 2003; ISBN 9026519303.
6. Rorabaugh, M.I. *Groundwater in North-Eastern Louisville, Kentucky, with Reference to Induced Infiltration*; Geological Survey Water-Supply Paper 1360-B; US Government Printing Office: Washington, DC, USA, 1956.
7. Ferris, J.G.; Knowles, D.B.; Brown, R.H.; Stallman, R.W. *Theory of Aquifer Tests*; Ground-water hydraulics; Geological Survey Water-Supply Paper 1536-E; US Government Printing Office: Washington, DC, USA, 1962; p. 174.
8. Walton, W.C. Ground water resources evaluation: Mc Graw-Hill Book Company, 1970 Williams PW (1983) The role of subcutaneous zone in karst hydrology. *Int. J. Hydrol.* **1970**, *61*, 45–67.
9. Kruseman, G.P.; De Ridder, N.A. Analyses and evaluation of pumping test data. In *Intern. Inst. Land Reclamation and Improvement Bull. 11*; International Institute for Land Reclamation and Improvement: Wageningen, The Netherlands, 2000.
10. Eftimi, R. Hydraulic Parameters of the Intergranular Gravelly-Sandy Aquifers of the Western Lowland of Albania. Ph. D. Thesis, Geological Faculty, University of Tirana, Shtepia Botuese e Universitietit te Tiranes, Tirana, Albania, 1982; p. 177. (In Albanian)
11. Krešić, N. *Water in Karst: Management, Vulnerability and Restoration*; McGraw Hill: New York, NY, USA, 2013.
12. Freeze, R.A.; Cherry, J.A. *Groundwater*; Prentice-Hall, Inc.: Englewood Cliffs, NJ, USA, 1979; p. 605, ISBN 0-13-365312-9.
13. Bochever, F.M. *Vodozabori Podzemnih Vod*; Stroizdat: Moscow, Russia, 1979; 285p.
14. Anonymous, U.S. *Groundwater Manual. A Water Resources Technical Publication*; Department of the Interiors: Bureau of Reclamation, WA, USA, 1985; p. 480.
15. Parise, M.; Qiriazi, P.; Sala, S. Natural and anthropogenic hazards in karst areas of Albania. *Nat. Hazards Earth Syst. Sci.* **2004**, *4*, 569–581. [CrossRef]
16. Masciopinto, C.; Liso, I.S. Assessment of the impact of sea-level rise due to climate change on coastal groundwater discharge. *Sci. Total Environ.* **2016**, *569*, 672–680. [CrossRef]
17. Foster, S.; Morris, B.; Lawrence, A.; Chilton, J. Groundwater impact and issues in developing cities—An introductory review. In *Groundwater in the Urban Environment*; Chilton, J., Ed.; Balkema: Rotterdam, The Netherlands, 1999; pp. 3–16.

18. Suresh, T.S. Impact of urbanization on groundwater regime: A case study of Bangalore City, Kamataka, India. In *Groundwater in the Urban Environment*; Chilton, J., Ed.; An Introductory Review; Balkema: Rotterdam/Brrookfield, The Netherlands, 1999; pp. 251–258.
19. Vasileva, D. Urban impact on groundwater of Belgrade area. In *Groundwater in the Urban Environment*; Chilton, J., Ed.; Groundwater impact and issues in developing cities—An introductory review; Balkema: Rotterdam/Brrookfield, The Netherlands, 1999; pp. 259–262.
20. Eftimi, R. *Intensification of Groundwater Pumping in Fushe Kuqe Alluvial Basin for the Water Supply of Durres City in Albania, and the Possible implication of Seawater Intrusion*; Botimit: Tirana, Albania, 2012; p. 50.
21. Eftimi, R.; Shehu, K.; Leno, L. *Water Quality of Tirana Water Supply Systems*; ECAT: Tirana, Albania, 2000; p. 73. (In Albanian)
22. Gelaj, A.; Marku., S.; Puca, N. Evaluation and monitoring of groundwater of Albania Bul. Shk. Gjeol. 2. In Proceedings of XX CBGA Congress, Tirana, Albania, 24–26 September 2014; pp. 117–120.
23. Kumanova, X.; Marku, S.; Fröjdö, S.; Jacks, G. Recharge and sustainability of a coastal aquifer in northern Albania. *Hydrogeol. J.* **2014**, *22*, 883. [CrossRef]
24. Lako, A. Hydrogeological conditions of Shkumbin River valley of the area Labinot-Fushe Cerrik. *Përmb. Stud.* **1973**, *3*, 105–133. (In Albanian)
25. Bakalowicz, M. Karst groundwater: A challenge for new resources. *Hydrogeol. J.* **2005**, *13*, 148–160. [CrossRef]
26. Stevanović, Z.; Eftimi, R. Karstic sources of water supply for large consumers in South-Eastern Europe—Sustainability, disputes and advantages. *Geol. Croat.* **2010**, *63*, 179–185. [CrossRef]
27. Stevanović, Z. Karst water in potable water supply: A global scale overview. *Environ. Earth Sci.* **2019**, *78*, 662. [CrossRef]
28. Eftimi, R. Hydrogeological characteristics of Albania. *AQUAmundi* **2010**, *1*, 79–92.
29. Bonacci, O. Karst springs hydrographs as indicators of karst aquifers. *Hydrol. Sci. J.* **1993**, *38*, 51–62. [CrossRef]
30. Ford, D.; Wiliams, P. *Karst Hydrogeology and Geomorphology*; John Wiley & Sons: Hoboken, NJ, USA; Chichester, UK, 2007; p. 562.
31. Stevanović, Z.; Jemcov, I.; Milanović, S. Management of karst aquifers in Serbia for water supply. *Environ. Geol.* **2007**, *51*, 743–748. [CrossRef]
32. Drew, D.; Hötzl, H. (Eds.) *Karts Hydrogeology and Human Activities*; Balkema: Rotterdam, The Netherlans, 1999; p. 322.
33. De Waele, J.; Follesa, R. Human impact on karst: The example of Lusaka (Zambia). *Int. J. Speleol.* **2004**, *32*, 71–83.
34. Parise, M.; Gunn, J. (Eds.) *Natural and Anthropogenic Hazards in Karst Areas: Recognition, Analysis and Mitigation*; Special Publication 279; Geological Society: London, UK, 2007; 202p.
35. Parise, M.; Sammarco, M. The historical use of water resources in karst. *Environ. Earth Sci.* **2015**, *74*, 143–152. [CrossRef]
36. Parise, M.; Qiriazi, P.; Sala, S. Evaporite karst of Albania: Main features and cases of environmental degradation. *Environ. Geol.* **2008**, *53*, 967–974. [CrossRef]
37. Eftimi, R.; Zojer, H. Human impacts on karst aquifers of Albania. *Environ. Earth Sci.* **2015**, *74*, 57–70. [CrossRef]
38. Pisano, L.; Zumpano, V.; Pepe, M.; Liso, I.S.; Parise, M. Assessing Karst Landscape Degradation: A Case Study in Southern Italy. *Land* **2022**, *11*, 1842. [CrossRef]
39. Xhomo, A.; Kora, A.; Xhafa, Z.; Shallo, M. *Geology of Albania (Notes of the Geological Map of Albania, sc. 1:200000)*; Albanian Geological Service: Tirana, Albania, 2002.
40. Meço, N.; Aliaj, S. *Geology of Albania*; Gebrüder Bornatraeger: Stuttgart, Germany, 2000.
41. Eftimi, R.; Bisha, G.; Tafilaj, I.; Habilaj., L. *International Hydrogeological Map of Europe sc. 1:1.500.000, Sheet D6 Athina (Albanian Share)*; Bundesanstalt für Hanover Geowissenschaften und Rohstolfe/UNESCO: Hanover, Germany, 2009.
42. Bredehoeft, J.D. Safe yield and the water budget myth. *Groundw. Water* **1997**, *35*, 929. [CrossRef]
43. Sakiyan., J.; Yazicigil, H. Sustainable development and management of an aquifer system in western Turkey. *Hydrogeol. J.* **2004**, *12*, 66–80. [CrossRef]
44. Eftimi, R.; Sara, F. Quantity and quality of groundwater of intermountain basin of Korça in Albania and implication for sustainable management. *Geolagìčnij Žurnal* **2022**, *4*, 45–64.
45. Theis, C.V. The relation between the lowering of the piezometric surface and the rate and duration of discharge of a well using ground-water storage. *Eos Trans. Am. Geophys. Union* **1935**, *16*, 519–524. [CrossRef]
46. Eftimi, R. Hydrogeological overview of the Mat River alluvial plain. *Permb. Stud.* **1966**, *4*, 53–66. (In Albanian)
47. Chiesa, G. *Inquinamento delle Acque Sotterranee*; Hoepli-Milano: Milan, Italy, 1994; ISBN 88-203-2120-3.
48. Bear, J.; Verruijt, A. *Modelling Groundwater Flow and Pollution*; Theory and applications of transport in porous media; Riedel Publishing Company: Dordrecht, The Netherlands, 1994.
49. Gunn, J. The geomorphological impacts of limestone quarrying. *Catena* **1993**, *25*, 187–198.
50. Gunn, J. Quarrying of limestones. In *Encyclopaedia of Cave and Karst Science*; Gunn, J., Ed.; Routledge: London, UK, 2004; pp. 608–611.
51. Parise, M. Modern resource use and its impact in karst areas—Mining and quarrying. *Z. Geomorphol.* **2016**, *60*, 199–216. [CrossRef]
52. Mazzei, M.; Parise, M. On the implementation of environmental indices in karst. In *Karst Groundwater Contamination and Public Health*; White, W.B., Herman, J.S., Herman, E.K., Rutigliano, M., Eds.; Springer: Cham, Switzerland, 2018; pp. 245–247, ISBN 978-3-319-51069-9.

53. Eftimi, R. Hydraulic characteristics of the big capacity water supply wells of Korça City. In Proceedings of the XVIIIth Carpathian-Balkan Geological Association, Belgrade, Serbia, 3–6 September 2006; Sudar, M., Ercegovacm, M., Grubić, A., Eds.; pp. 118–122. (In Albania)
54. Sophocleus, M. Managing water resources systems: Why safe yield is not sustainable. *Ground Water* **1977**, *35*, 561. [CrossRef]
55. Sophocleus, M. From safe yield to sustainable development of water resources: The Kansas experience. *J. Hydrogeol.* **2000**, *235*, 27–43. [CrossRef]
56. Sophocleus, M. Interaction between groundwater and surface water: The state of the science. *Hydrogeol. J.* **2002**, *10*, 52–64. [CrossRef]
57. Eftimi, R.; Malik, P. Assessment of regional flow type and groundwater sensitivity to pollution using hydrograph analyses and hydrochemical data of the Selita and Blue Eye karst springs, Albania. *Hydrogeol. J.* **2019**, *27*, 2045–2059. [CrossRef]
58. Turc, L. The soil balance: Relations between rainfall, evaporation and flow. *Geogr. Rev.* **1954**, *38*, 6–44. (In French)
59. Kessler, H. Water balance investigations in the karst regions of Hungary. In *Actes du Colloque de Dubrovnik, Octobre 1965*; AIHS-UNESCO: Paris, France, 1967; pp. 91–105.
60. Parise, M.; Ravbar, N.; Živanovic, V.; Mikszewski, A.; Kresic, N.; Mádl-Szőnyi, J.; Kukuric, N. Hazards in Karst and Managing Water Resources Quality. In *Karst Aquifers—Characterization and Engineering. Professional Practice in Earth Sciences*; Stevanovic, Z., Ed.; Springer: Berlin/Heidelberg, Germany, 2015; Chapter 17; pp. 601–687. [CrossRef]
61. Zötl, J.G. An important factor for the drinking water supply in Austria. *Environ. Geol. Water Sci.* **1986**, *7*, 237–239. [CrossRef]
62. Tafilaj, I. *Hydrogeological Conditions of Uji Ftohte Springs, near Vlora*; AHS: Tirana, Albania, 1964.
63. Goldscheider, N. Delineation of spring protection zones. In *Groundwater Hydrology of Springs*; Kresić, N., Stevanović, Z., Eds.; Elsevier: Amsterdam, The Netherlands, 2010; pp. 305–338.
64. Carré, J.; Oller., G.; Mudry, J. How to protect groundwater catchments used for human consumption in karst areas? In Proceedings of the 9th Conference on Limestone Hydrogeology, Besancon, France, 1–3 September 2011; pp. 87–89.
65. Parise, M.; Closson, D.; Gutierrez, F.; Stevanović, Z. Anticipating and managing engineering problems in the complex karst environment. *Environ. Earth Sci.* **2015**, *74*, 7823–7835. [CrossRef]
66. Williams, P.W. The role of the epikarst in karst and cave hydrogeology: A review. *Int. J. Speleol.* **2008**, *37*, 1–10. [CrossRef]
67. Ministry of Health and Social Care of Albania. *National Strategy of Water Supply and Sewerage Services*; DoCM No 643, (14.09.2011); Ministry of Health and Social Care of Albania: Tirana, Albania, 2011; ISBN 978-9928-08-086-8.
68. Cvijić, J. *Fundamental of Geography and Geology of Macedonia and Serbia, Special Edition VIII*; Serbian Royal Academy: Belgrade, Serbia, 1906. (In Serbian)
69. Anovski, T.; Andonovski, B.; Minceva, B. Study of the hydrologic relationship between Ohrid and Prespa lakes. In Proceedings of the an IAEA International Symposium, Vienna, Italy, 11–15 March 1991; IAEA-SM-319/62p.
70. Cotecchia, V.; Micheletti, A.; Monterisi, L.; Salvemini, A. Caratteristiche tecniche delle opere per l'incremento di portata delle sorgente dell'Aggia (Alta Val d'Agri). *Geol. Appl. Idrogeol.* **1982**, *17*, 365–384.
71. Milanović, P.T. *Geological Engineering in Karst*; Zebra Publishing Ltd.: Belgrade, Serbia, 2010.
72. Amataj, S.; Anovski, T.; Eftimi, R.; Benishke, R.; Gourcy, L.; Kola, L.; Leontiadis, I.; Micevski, E.; Stamos, A.; Zoto, A. Tracer methods used to verify the hypothesis of Cvijić about the groundwater connection between Prespa and Ohrid lakes. *Environ. Geol.* **2007**, *51*, 749–755. [CrossRef]
73. Eftimi, E.; Stevanović, Z.; Stojev, V. Hydrogeology of Mali Thate-Galičica karst massif related to the catastrophic decrease of the level of Lake Prespa. *Environ. Earth Sci.* **2021**, *80*, 708. [CrossRef]
74. Popovska, C.; Bonacci, O. Basic data on hydrology of the Lakes Ohrid and Prespa. *Hydrol. Process.* **2007**, *21*, 658–664. [CrossRef]
75. Matzinger, A. Is the Anthropogenic Input Jeopardizing Unique Lake Ohrid?—Mass Flux Analyses and Management Consequences. Doctoral Dissertation, ETH Zurich, Zürich, Switzerland, 2006.
76. White, W.B. Conceptual models for carbonate aquifers. *Ground Water* **1969**, *7*, 15–21. [CrossRef]
77. Gregor, M.; Malik, P. Construction of master recession curve using genetic algorithms. *J. Hydrol. Hydromech.* **2012**, *60*, 3–15. [CrossRef]
78. Malik, P. Assessment of regional karstification degree and groundwater sensitivity to pollution using hydrograph analyses in the Velka Fatra Mts., Slovakia. *Environ. Geol.* **2007**, *51*, 707–711. [CrossRef]
79. Shuster, E.T.; White, W.B. Seasonal fluctuation in the chemistry of limestone springs: A possible means for characterising carbonate aquifers. *J. Hydrol.* **1971**, *14*, 93–128. [CrossRef]
80. Jacobson, R.I.; Langmuir, D. Controls on the quality variations of some carbonate spring water. *J. Hydrol.* **1974**, *23*, 247–265. [CrossRef]
81. Kresic, N.; Stevanovic, Z. (Eds.) *Hydrology of Springs: Engineering, Theory, Management and Sustainability*; Butterworth-heinemann: Oxford, UK, 2009; p. 736.
82. Liso, I.S.; Parise, M. Apulian karst springs: A review. *J. Environ. Sci. Eng. Technol.* **2020**, *8*, 63–83. [CrossRef]
83. Castany, G. *Prospection et Exploitation des Eaux Souterraines*; DUNOD: Paris, France, 1969; p. 717.
84. Tafilaj, I. Hydrogeological classification of mines of Albania. *Permb. Stud.* **1977**, 1–13. (In Albanian)
85. Eftimi, R. A comparative study of the hydraulic parameters and the yield of wells of some sedimentary rocks of Albania. In *Groundwater of Fractured Rocks*; Krásný, J., Ed.; IHP-Vi, Series on Groundwater No. 7; Sponsored by UNESCO: Prague, Czech Republic, 2003; ISBN 92-9220-002-X.

86. Laureano, P. Water atlas. In *Traditional Knowledge Sensitivity to e to Combat Desertification*; Bollati Boringhieri: Torino, Italy, 2001.
87. Mays, L.W.; Koutsoyiannis, D.; Angelakis, A.N. A brief history of urban water supply in the Antiquity. *Water Sci. Technol. Water Supply* **2007**, *7*, 1–12. [CrossRef]
88. Valipour, M.; Abdelkader, T.A.; Antoniou, G.P.; Sala, R.; Parise, M.; Salgot, M.; Sanaan Bensi, N.; Angelakis, A.N. Sustainability of underground hydro-technologies: From ancient to modern times and toward the future. *Sustainability* **2020**, *12*, 8983. [CrossRef]
89. Davis, S.N.; De Wiest, R.J.M. *Hydrogeology*; John Wiley and Sons: New York, NY, USA; Hoboken, NJ, USA, 1970; p. 463.
90. Bentall, R. Shortcuts and Special Problems in Aquifer Tests. In *Methods of Aquifer Tests*; Geological Survey Water-Supply Paper 1545-C; US Government Printing Office: Washington, DC, USA, 1963; p. 117.
91. Bentall, R. Methods of Determining permeability, Transmissibility and Drawdown. In *Groundwater Hydraulics*; Geological Survey Water-Supply Paper 1536-1; US Government Printing Office: Washington, DC, USA, 1963; pp. 245–341.
92. Goldscheider, N.; Pronk, M.; Zopfi, J. New insights into the transport of sediments and microorganisms in karts groundwater by continuous monitoring of particle-size distribution. *Geol. Croat.* **2010**, *63*, 137–142. [CrossRef]
93. *DoCM 145, (26.02.1998)*; National Standards, Based on the Potable Water Sanitation Rules, Designing, Establishment and Supervision of Water Supply Systems. Ministry of Health and of Public Care: Tirana, Albania, 1998.

Disclaimer/Publisher's Note: The statements, opinions and data contained in all publications are solely those of the individual author(s) and contributor(s) and not of MDPI and/or the editor(s). MDPI and/or the editor(s) disclaim responsibility for any injury to people or property resulting from any ideas, methods, instructions or products referred to in the content.

water

MDPI

Article

Geochemical Investigations of the Geothermal Waters in the Kangding Area, SW China: Constraints from Hydrochemistry and D-O-T Isotopy

Xialin Zhang [1,2], Chengdong Deng [1,3,*], Tao Feng [2] and Yunhui Zhang [1,3]

[1] Faculty of Geosciences and Environmental Engineering, Southwest Jiaotong University, Chengdu 611756, China
[2] China Railway Eryuan Engineering Group Co., Ltd., Chengdu 610031, China
[3] State Key Laboratory of Geohazard Prevention and Geoenvironment Protection, Chengdu University of Technology, Chengdu 610059, China
* Correspondence: dengcd927@163.com

Abstract: Geothermal resources, as a representative of clean energy, has been paid significant attention in the world. Due to active neotectonics and widespread magmatic rocks, the abundant geothermal waters in the Kangding area have been investigated. Hydrochemistry and D–O–T isotopy studies were carried out to clarify the genetic mechanism of geothermal waters. The hydrochemical types of geothermal waters are mainly Ca^{2+}–Na^{+}–HCO_3^{-} type, Na^{+}–Cl^{-}–HCO_3^{-} type, and Na^{+}–HCO_3^{-} type. Silicate dissolution and the cation exchange process are the water–rock interactions determining hydrochemical compositions. The recharge elevation of geothermal water was calculated to be 3034–3845 m, with an average of 3416 m. The reservoir temperatures of shallow and deep geothermal reservoirs vary from 50 to 115 °C and from 114 to 219 °C, respectively, and the mixing ratio of cold water is 0.56–0.89. These findings help to reveal the genetic mechanism of geothermal waters in the Kangding area.

Keywords: geothermal water; water–rock interaction; geothermal reservoir; recharge source; Kangding area

1. Introduction

The global geothermal resources are mainly distributed in tectonically active plate margins, which are manifested in four major high-temperature geothermal belts: the Pacific Rim, the Mediterranean–Himalayan, the Mid-Atlantic Ridge, and the Red Sea–Gulf of Aden–East African Rift Tropics [1]. In China, the Mediterranean–Himalayan geothermal belt consists of the Tibetan, the western Yunnan, and the western Sichuan geothermal belts [2]. In the context of the "double carbon" goal, the development and utilization of geothermal resources, as clean, green, and stable energy resources, has become a popular research topic globally [3–5]. The study of the geothermal genesis mechanism is an important prerequisite for geothermal resource development and utilization. The Earth is releasing energy outward all the time, but high-quality and high-temperature geothermal resources are often distributed in specific areas, which are closely related to the geological structure. Tectonically active volcanic–seismic–orogenic zones tend to form high-temperature geothermal resources, while tectonically gentle cratons tend to form low-to-moderate-temperature geothermal resources or even display no surface heat.

Geothermal fluids constitute a complete circulation of the recharge–runoff–discharge process in the geothermal system, so it is necessary to trace the flow process of geothermal water in the study area by hydrogeochemical signatures. Geothermal water lixiviates minerals during runoff. By analyzing hydrochemical compositions of geothermal waters, it is possible to assess the water–rock reactions experienced by geothermal water with the

corresponding hydrogeochemical diagrams [6,7] in the study area. Principal component analysis, a reduced-dimension algorithm, allows the integration of indicators in the spring to discern the main sources of ions [8,9]. The geothermal reservoir temperature is one of the important indicators used to determine the development and utilization of geothermal energy, and the calculation of the geothermal reservoir temperature of geothermal systems is mainly based on empirical formulas, such as SiO_2 geothermometer and cation geothermometer [10–15]. In addition, geothermal water is often mixed with cold water at the surface during the rising process, and the cold-water mixing ratio can be estimated using methods such as the SiO_2 equation.

The northern section of the Sanjiang orogenic belt is located in the southeastern part of the Tibetan Plateau, and is a transitional area between the high-temperature hydrothermal zone in southern Tibet and the high-temperature hydrothermal zone in western Sichuan. Its geothermal water chemistry types include the Na^+–HCO_3^- type, Na^+–Cl^- type, Ca^{2+} (Mg^{2+})–SO_4^{2-} type, and Ca^{2+} (Mg^{2+})–HCO_3^- type [16]. Researchers have investigated the deep thermal structure and crust–mantle heat flow ratio of the Batang–Litang–Kangding high-temperature hydrothermal region using a combination of gravity, magnetism, seism, and helium isotopes, and found that a low-velocity layer exists at a certain depth in the region, which provides the main heat source for the geothermal system [17]. The Xianshuihe Fault is a deep-seated fault. As a regional compression-torsional fracture in the deep crust, the Xianshuihe Fault plays a vital role in determining the hydrothermal activity of the Kangding geothermal area, which not only conducts the deep heat source [18], but also provides a channel for groundwater infiltration. Finally, for the geothermal reservoir temperature of the Kangding geothermal zone, previous studies have evaluated its development potential using the SiO_2 geothermometer, cation geothermometer, and chemical-thermodynamic geothermometer [19]. In summary, fruitful research results have been achieved in the Kangding geothermal area. However, due to the complexity of geothermal evolution in the Kangding geothermal area, the water–rock reactions need to be studied in depth and the genetic model has yet to be summarized [19–22].

Based on field work, hydrochemistry, and D-O-T isotopy, this study aimed to (1) explore the hydrogeochemical evolution; (2) identify the geothermal reservoir characteristics; (3) trace the recharge source and residential time; and (4) build the genetic model of the geothermal waters in the Kangding area. These achievements would provide a significant reference for geothermal exploitation and utilization.

2. Geothermal Geological Background

The study area belongs to the Ganzi Tibetan Autonomous Prefecture of Sichuan Province and is situated at the eastern margin of Tibetan Plateau (Figure 1). The climate is the sub-temperature plateau humid type with annual temperature of −14 to 29 °C and average annual rainfall of 664.4 to 974.8 mm. The terrain is typical of the alpine valley type with an elevation of 1390 to 7556 m. The elevation of the snow line in the area is 4800 m above sea level.

The exposed strata in the study area are mainly the Sinian, Silurian, Devonian, Permian, and Triassic carbonate and sandstone (Figure 2). The magmatic rocks exposed in the study area are mainly Neoproterozoic mafic rocks and Yanshanian to Himalayan granite, which indicates that two phases of magmatic intrusions developed in the study area. The zircon U-Pb dating results indicate that the latest phase of the Gonggarshan granite is a plagioclase formed at 15-4 Ma, which is a product of the recent rapid uplift of the Tibetan Plateau [23,24]. The Yanshanian to Himalayan granite is much younger than the Neoproterozoic Kangding mélange, and the heat generated by the decay of its radioactive elements provides a source of heat for the geothermal system in the region [25–28]. Due to active neotectonic activity, a number of faults and fractures have developed in the study area. At a regional scale, the Xianshuihe, Longmenshan, and Anninghe faults formed a giant "Y"-shaped tectonic system. The Xianshuihe fault is a strike slip fault, and the Kangding section controls the hydrothermal activity in the study area. The Xianshuihe fault provides a heat-conducting

channel for geothermal waters and acts as a water-blocking boundary. The secondary fractures play a role as a water-conducting channel for geothermal water. Geothermal springs are distributed along the faults and secondary fractures. The exposed temperature and flow are 30 to 88 °C and 0.3 to 10.0 L/s, respectively.

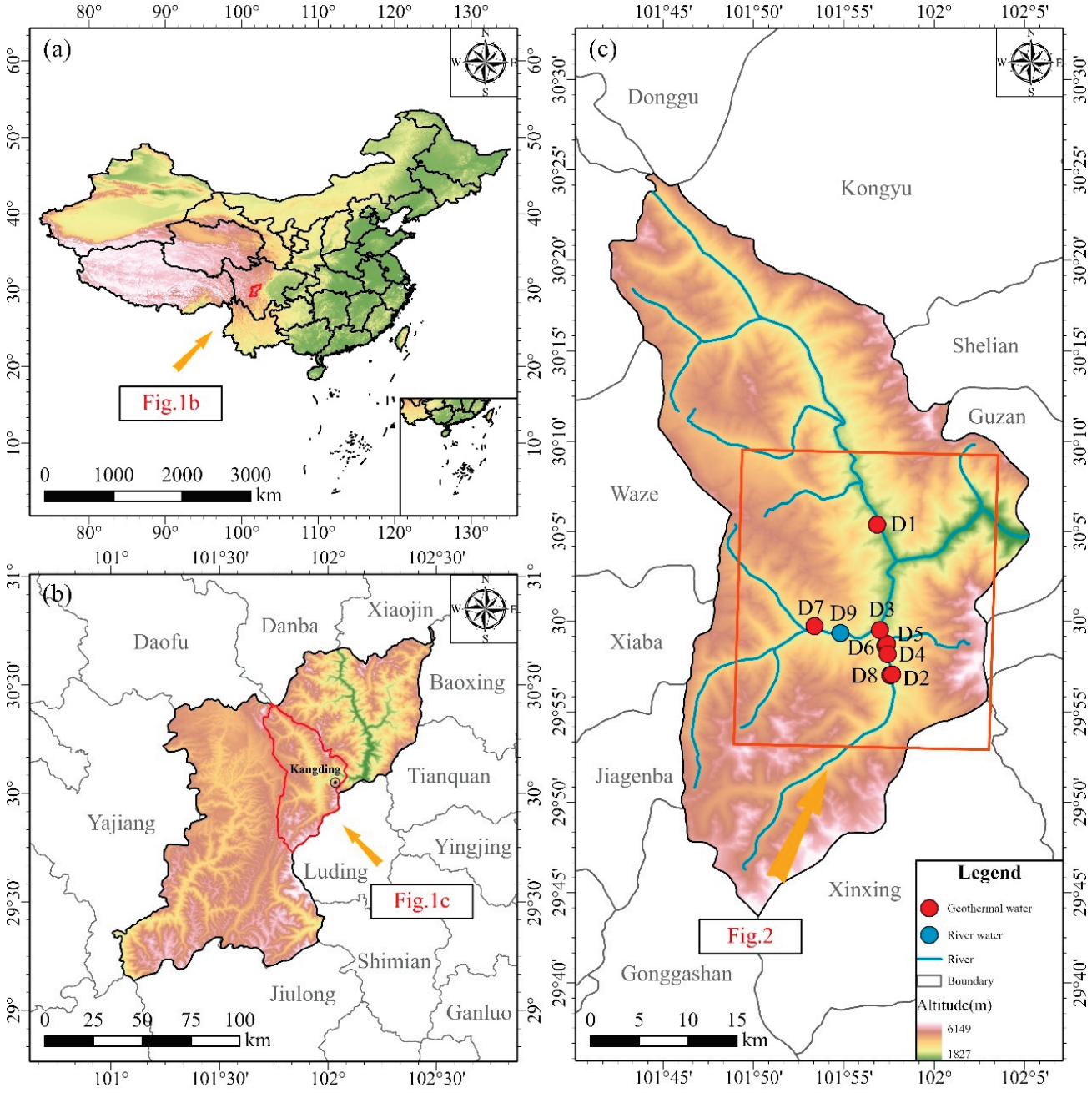

Figure 1. (**a**) Location of the Kangding county in China, (**b**) Location of the study are in the Kangding county, (**c**) Distribution of collected samples in the study area.

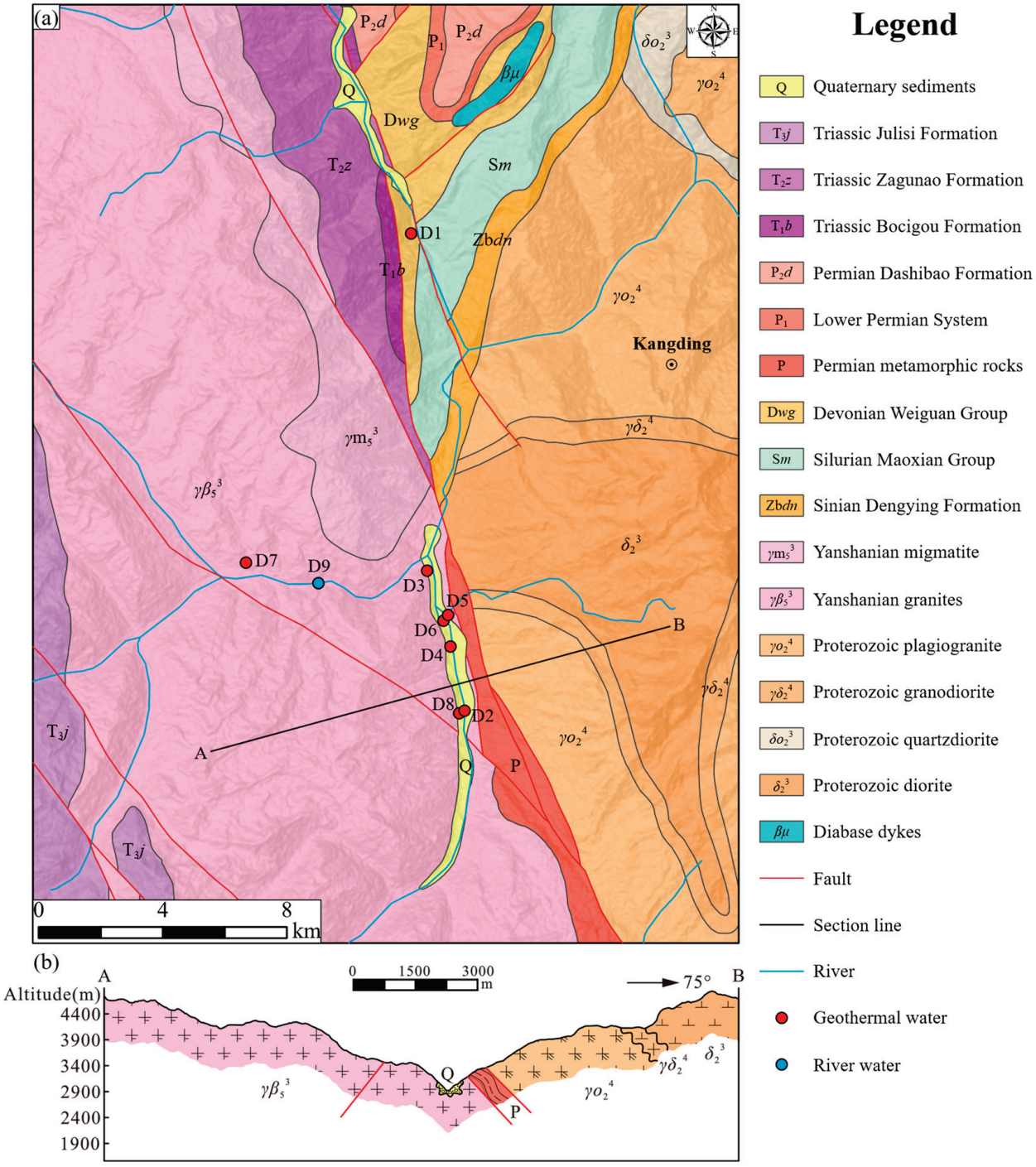

Figure 2. (**a**) Geological map of the study area, (**b**) Geological section A–B.

3. Sample Collection and Analytical Testing

Eight geothermal water samples and one river water sample were collected in the study area. The temperature and pH values were measured in situ by a portable device (WTW-MultiLine Multi 3310 IDS, Xylem Dewatering Solutions, Inc, Washington, DC, USA). The HCO_3^- concentration was determined by HNO_3 according to the standard titration in the field. All water samples were collected by polyethylene bottles after rinsing at least three times. Afterwards, water samples were sent to the laboratory for hydrochemical and isotopic analyses in the Tianjin Kehui Experimental Co., Ltd., Tianjin, China. The concentrations of the cations (Na^+, K^+, Ca^{2+}, Mg^{2+}, and H_2SiO_3) were determined by ICP-OES (ICAP6000, Thermo Fisher Scientific, Waltham, MA, USA). The anion concentrations

were analyzed by IC (Dionex ICS600, Thermo Fisher Scientific, Waltham, MA, USA). The detection limit for cations and anions was 1 mg/L, with precision better than 5%. The charge balance between major anions and cations was from −0.61% to +3.87%, within the permission range of ±5%. δD and $\delta^{18}O$ were measured using a laser absorption water isotope spectrometer analyzer. The results of δD and $\delta^{18}O$ were indicated following the VSMOW standard, with the precisions of 0.1‰ and 0.5‰, respectively. Tritium (^3H) were analyzed by the electrolytic enrichment method and presented as tritium units (TU).

4. Results and Discussion

4.1. Hydrochemical Characteristics

The concentration of cations and anions of geothermal waters followed the order of Na^+ (112.50–566.10 mg/L) > Ca^{2+} (3.21–296.59 mg/L) > K^+ (20.10–63.40 mg/L) > Mg^{2+} (0.49–34.05 mg/L), and HCO_3^- (317.30–1440.07 mg/L) > Cl^- (12.05–322.60 mg/L) > SO_4^{2-} (1.92–69.16 mg/L), respectively (Figure 3a). Hence, the major cations and anions of geothermal waters in the study area were Na^+ and HCO_3^-, respectively (Table 1). The hydrochemical types of geothermal water in the study area can be classified into three types: Ca^{2+}–Na^+–HCO_3^- (D1), Na^+–Cl^-–HCO_3^- (D2, D3, D6, D8), and Na^+–HCO_3^- (D3, D5. D7) (Figure 3b). The river sample was the hydrochemical type of Ca^{2+}–Mg^{2+}–HCO_3^- (D9).

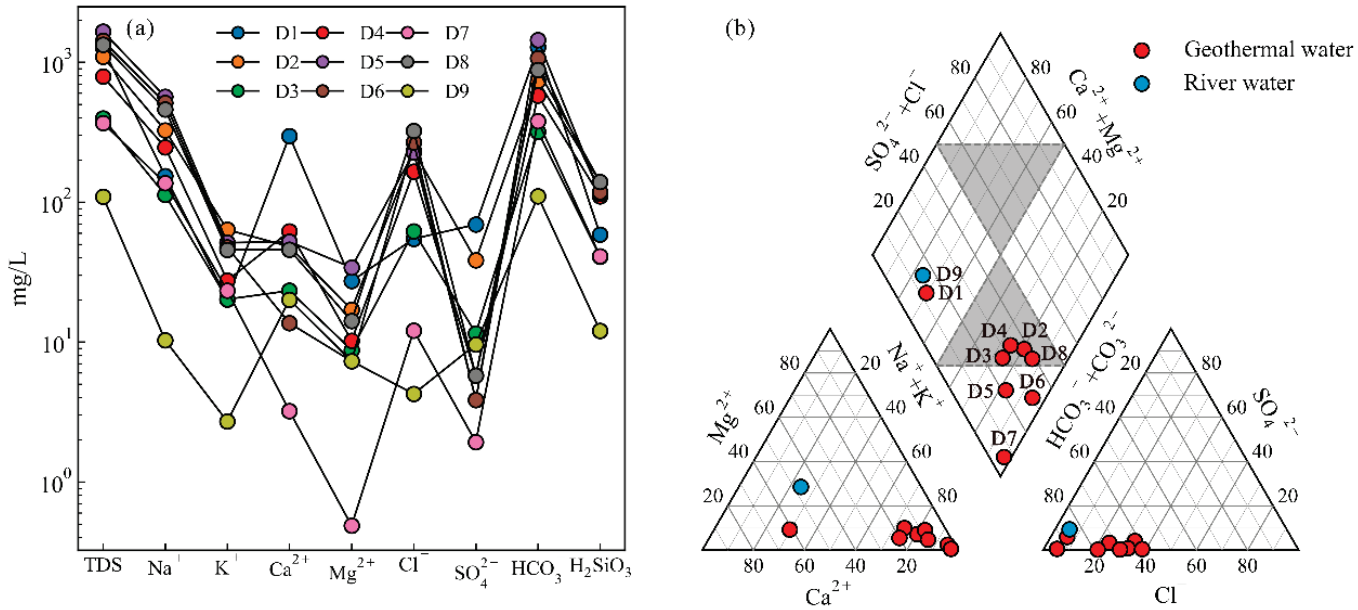

Figure 3. (**a**) Schöller diagram, (**b**) Piper trilinear diagram of geothermal waters.

4.2. Ion Source Analysis

4.2.1. Principal Component Analysis

Principal component analysis aims to transform multiple indicators into a few composite indicators (i.e., principal components) using the idea of dimensionality reduction, and each principal component is used to analyze and interpret the information contained in the original data indicators [8,9,29,30]. In order to identify the sources of major elements in geothermal fluids, the eight indicators of Ca^{2+}, Mg^{2+}, Na^+, K^+, Cl^-, SO_4^{2-}, HCO_3^-, and H_2SiO_3 of eight geothermal water samples were subjected to principal component analysis in this study. The Kaiser–Meyer–Olkin (KMO) index of 0.72 indicated the robustness of the PCA analysis. Two integrated indicators, PC1 and PC2, were obtained by scree plot (Figure 4a). PC1 included the hydrochemical components of Cl^-, K^+, Na^+, and H_2SiO_3, indicating the similar source from deep fluids. PC2 consisted of the hydrochemical components of Ca^{2+}, Mg^{2+}, SO_4^{2-}, and HCO_3^-, suggesting that they are determined by water–rock interactions in Equations (1)–(4) (Figure 4b).

Table 1. Hydrochemical and D-O-^{3}H isotopic results of geothermal water and river water samples.

Sample ID	Sample Type	Elevation (m)	Flow (L/s)	Discharge T (°C)	pH	TDS (mg/L)	Charge Balance (%)	Hydrochemical Type	Na^+ (mg/L)	K^+ (mg/L)
D1	Geothermal water	2600	10.0	42	6.2	1262	0.63	$Ca^{2+}\cdot Na^{+}–HCO_3^-$	153.50	20.10
D2		2970	2.0	88	7.1	1091	0.65	$Na^{+}–Cl^-\cdot HCO_3^-$	325.70	63.40
D3		2780	0.2	30	6.5	396	0.84	$Na^{+}–HCO_3^-$	112.50	20.20
D4		2920	1.0	65	6.4	788	3.87	$Na^{+}–Cl^-\cdot HCO_3^-$	246.50	27.50
D5		2912	1.0	72	7.1	1654	2.10	$Na^{+}–HCO_3^-$	566.10	51.20
D6		2860	2.0	85	7.2	1420	−0.61	$Na^{+}–Cl^-\cdot HCO_3^-$	512.10	47.40
D7		3296	1.0	54	7.6	366	1.14	$Na^{+}–HCO_3^-$	136.50	23.30
D8		2978	0.3	74	6.8	1332	2.07	$Na^{+}–Cl^-\cdot HCO_3^-$	459.60	45.50
D9	River water	2968	-	10	7.5	109	0.15	$Ca^{2+}\cdot Mg^{2+}–HCO_3^-$	10.30	2.70
Sample ID	Ca^{2+}	Mg^{2+}	Cl^-	SO_4^{2-}	HCO_3^-	H_2SiO_3	δD	$\delta^{18}O$	^{3}H	Recharge elevation
	mg/L	mg/L	mg/L	mg/L	mg/L	mg/L	‰VSMOW	‰VSMOW	TU	m
D1	296.59	27.24	54.59	69.16	1281.42	58.50	−113.2	−15.30	6.89	3034
D2	48.10	17.02	232.55	38.42	732.24	138.90	−118.0	−15.51	4.01	3076
D3	23.25	8.76	61.68	11.53	317.30	40.70	−112.1	−15.43	-	3261
D4	61.72	10.21	165.20	5.76	576.03	109.90	−118.9	−15.62	5.15	3296
D5	52.10	34.05	226.88	3.84	1440.07	114.80	−128.2	−16.03	3.14	3541
D6	13.63	7.30	266.58	3.84	1066.63	117.80	−127.5	−16.14	3.15	3626
D7	3.21	0.49	12.05	1.92	378.32	40.90	−133.2	−18.20	1.73	3652
D8	45.69	14.11	322.60	5.76	878.69	139.10	−125.3	−16.15	-	3845
D9	20.04	7.30	4.25	9.61	109.84	12.00	−110.4	−15.26	5.63	-

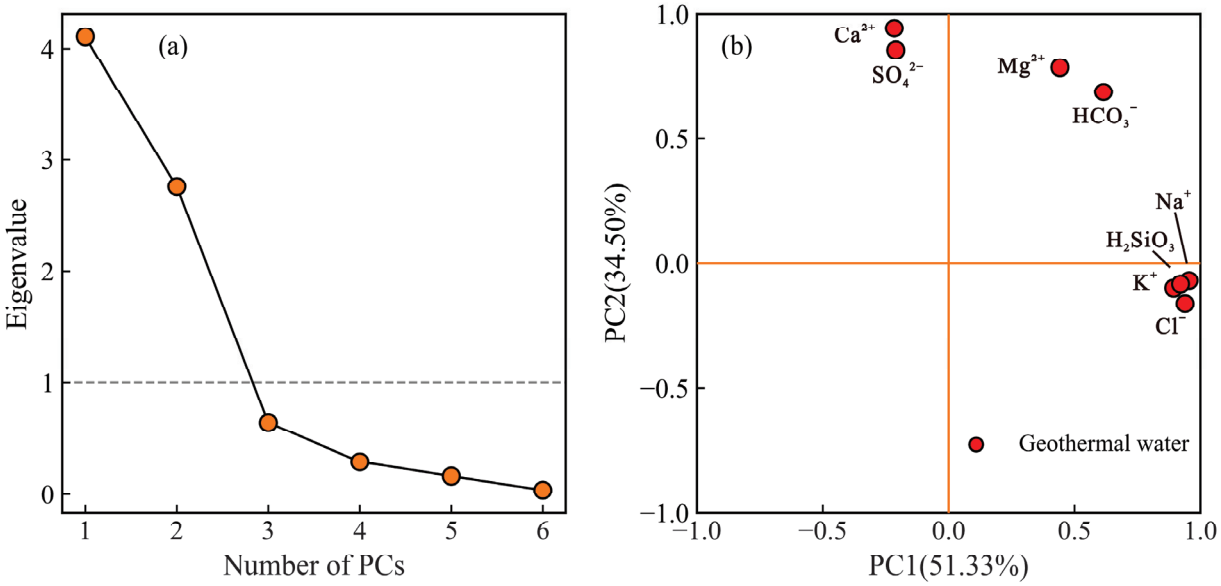

Figure 4. Principal component analysis of geothermal waters: (**a**) scree plot, (**b**) PC1 vs. PC2.

4.2.2. Cl^- Correlation Analysis

Cl^- is a conservative element in the hydrochemical process and is used to analyze the ion source [31–33]. In Figure 5, Cl^- is significantly positively correlated with Na^+, K^+, and H_2SiO_3, and the R^2 values are all above 0.65; it was assumed that they were derived from deep fluids. The linear correlation between Cl^- and HCO_3^- was slightly higher than that between Cl^- and Ca^{2+}, Mg^{2+}, and SO_4^{2-}, which may be due to the influence of mantle degassing and mixing of deep CO_2 [34,35]. The positive correlation between Cl^- and TDS also indicates that geothermal water was mixed with deep fluids. In contrast, the linear correlation between Cl^- and Ca^{2+}, Mg^{2+}, and SO_4^{2-} in the geothermal waters was very low, indicating that they had different sources, such as water–rock interaction.

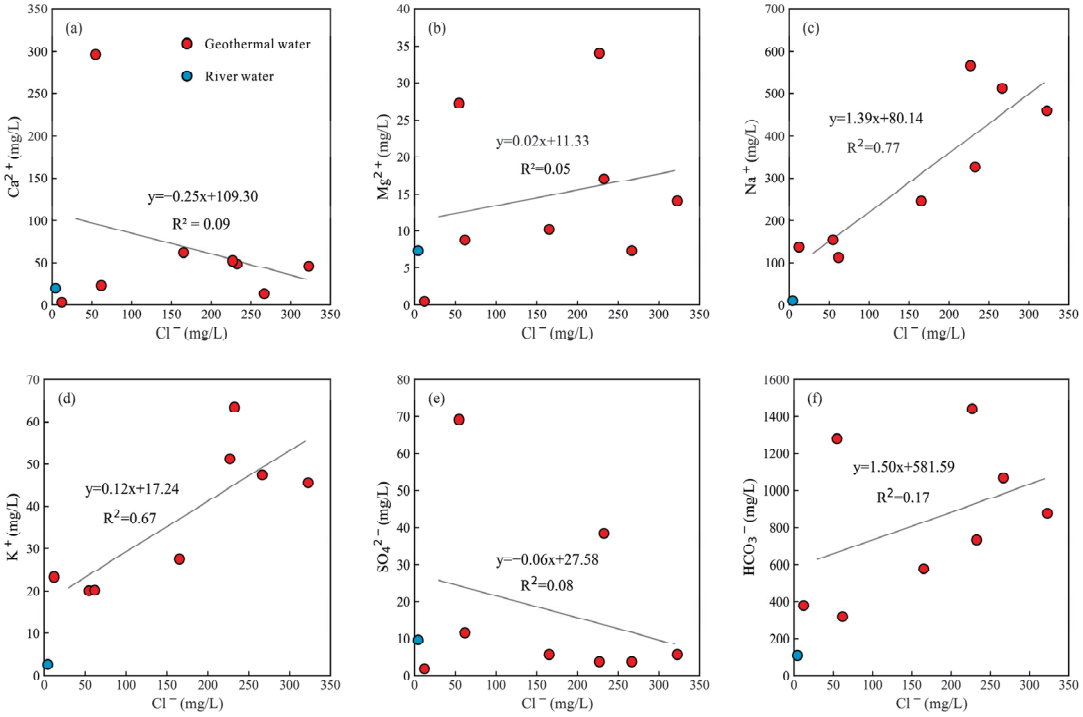

Figure 5. *Cont.*

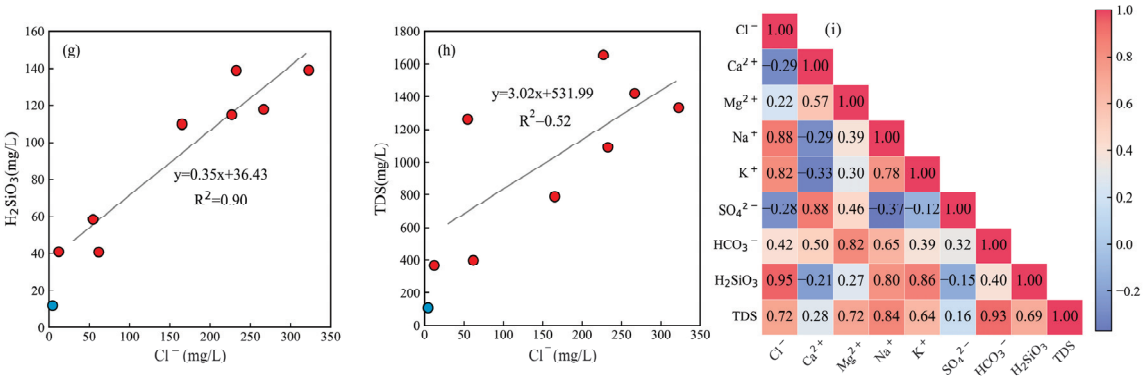

Figure 5. Relationship between Cl^- and hydrochemical parameters: (**a**) Ca^{2+}, (**b**) Mg^{2+}, (**c**) Na^+, (**d**) K^+, (**e**) $SO_4{}^{2-}$, (**f**) $HCO_3{}^-$, (**g**) H_2SiO_3, (**h**) TDS; (**i**) correlation matrix.

4.2.3. Ion Ratio Analysis

The molar ratio of $(Na^+ + K^+)/Cl^-$ is equal to 1 if halite dissolution exists [36]. In this study, the excess Na^+ and K^+ concentrations indicated they were possibly derived from silicate mineral dissolution (Figure 6a).

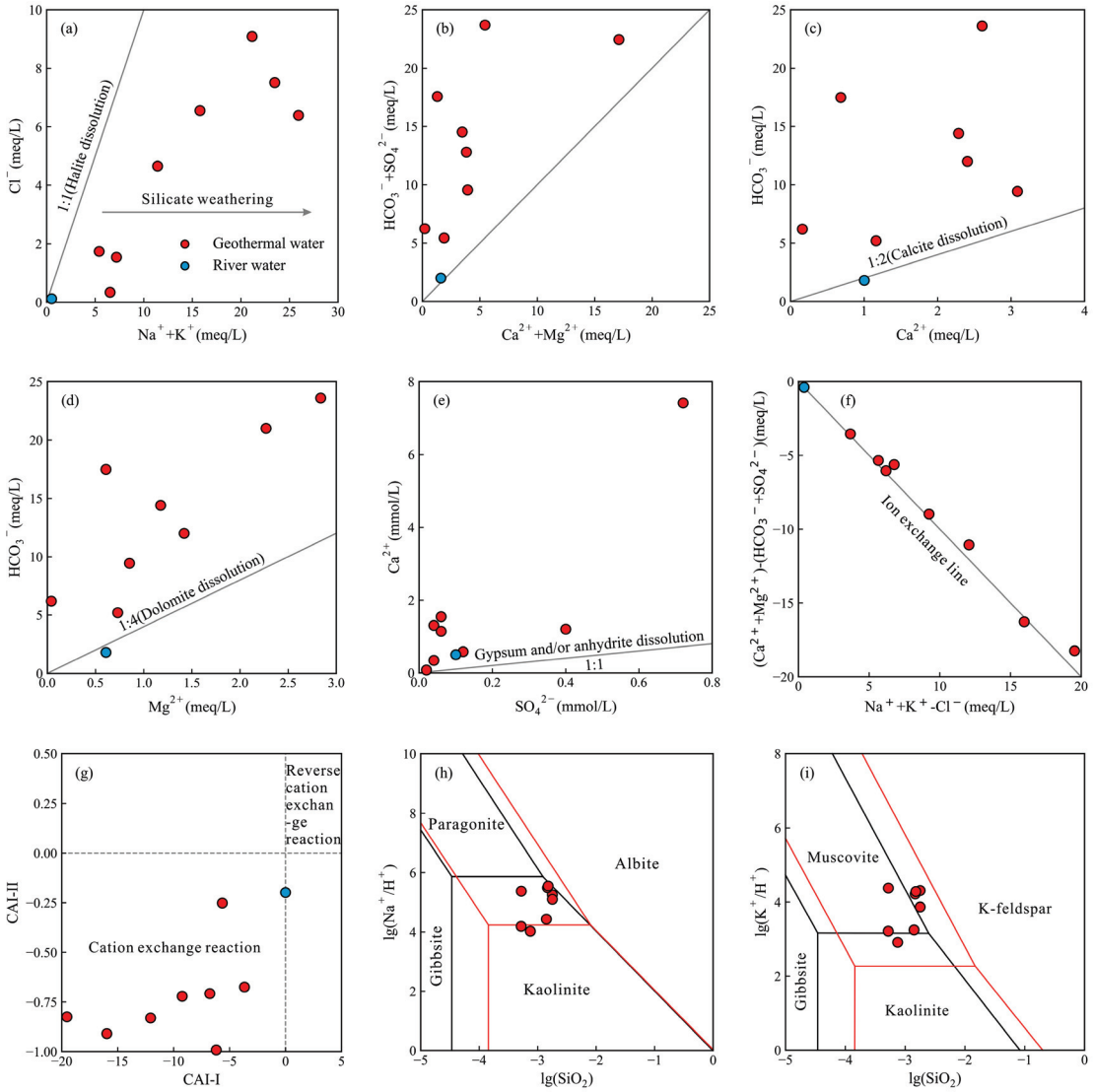

Figure 6. Hydrochemical analysis diagrams: (**a**) $Na^+ + K^+$ vs. Cl^-, (**b**) $Ca^{2+} + Mg^{2+}$ vs. $HCO_3{}^- + SO_4{}^{2-}$, (**c**) Ca^{2+} vs. $HCO_3{}^-$, (**d**) Mg^{2+} vs. $HCO_3{}^-$, (**e**) $SO_4{}^{2-}$ vs. Ca^{2+}, (**f**) $Na^+ + K^+$–Cl^- vs.

(Ca^{2+} + Mg^{2+})–(HCO_3^- + SO_4^{2-}), (**g**) CAI-I vs. CAI-II, (**h**) lg(SiO_2) vs. lg(Na^+/H^+), (**i**) lg(SiO_2) vs. lg(K^+/H^+).

When dissolution of carbonate minerals (calcite and dolomite) and gypsum occurs, the equivalence ratio of (Ca^{2+} + Mg^{2+})/(HCO_3^- + SO_4^{2-}) is 1:1 [37]. As shown in Figure 6b, the river water sample was located near the 1:1 line, while all geothermal water samples were distributed above the 1:1 line, which indicates that (Ca^{2+} + Mg^{2+}) was less than (HCO_3^- + SO_4^{2-}). This reveals that the dissolved Ca^{2+} and Mg^{2+} concentrations decreased during transport. The dissolution of calcite and dolomite is shown in Equations (1) and (2), respectively:

$$CO_2 + H_2O + CaCO_3 \rightarrow Ca^{2+} + 2HCO_3^- \quad (1)$$

$$CaMg(CO_2)_3 + 2CO_2 + 2H_2O \rightarrow Ca^{2+} + Mg^{2+} + 4HCO_3^- \quad (2)$$

The molar ratio of Ca^{2+} and HCO_3^- is 1:2 after calcite is dissolved, and the molar ratio of Mg^{2+} and HCO_3^- is 1:4 after dolomite is dissolved. As shown in Figure 6c,d, the river water sample is plotted near the calcite dissolution line and dolomite dissolution line, while the geothermal water samples are situated above the calcite dissolution line and dolomite dissolution line. The plots further prove that the dissolved Ca^{2+} and Mg^{2+} concentrations in calcite and dolomite are diluted during the transport. If geothermal water leaches gypsum (or hard gypsum), the molar ratio of Ca^{2+} to SO_4^{2-} is 1:1 (Equation (3)).

$$CaSO_4 - nH_2O \rightarrow Ca^{2+} + SO_4^{2-} + nH_2O \quad (3)$$

As shown in Figure 6e, all samples are located above the gypsum (or hard gypsum) dissolution line, which indicates that gypsum (or hard gypsum) was not dissolved in geothermal water. If evaporated sulfate minerals are dissolved in geothermal water, the following reaction would occur in solution according to the co-ion effect (Equation (4)):

$$2HCO_3^- + CaSO_4 - nH_2O \rightarrow CaCO_3 \downarrow + CO_2 \uparrow + SO_4^{2-} + (1 + n)H_2O \quad (4)$$

HCO_3^- and SO_4^{2-} would be negatively correlated. HCO_3^- and SO_4^{2-} did not show a significant negative correlation, which further indicates that the sulfate mineral gypsum (or hard gypsum) was not dissolved. The Na^+ concentration was higher than the Cl^- concentration, which may be due to the dissolution of sodium feldspar and other sodium-containing minerals. In addition, the influence of cation exchange and adsorption would cause the Na^+ and K^+ concentrations of rocks to be replaced by Ca^{2+} and Mg^{2+} of groundwater (Figure 6f). As shown in Figure 6g, the CAI-I and CAI-II values of geothermal water samples are below zero, which proves that the geothermal water underwent cation exchange reaction [38,39]. Hence, the geothermal waters were subject to cation exchange and adsorption, which caused changes in the chemical composition in geothermal water. As shown in Figure 6h, some geothermal water points are located near the 100 °C equilibrium line (black) of kaolinite and sodium feldspar, and some of the geothermal water points are located near the 200 °C equilibrium line (red) of kaolinite and sodium mica, which indicates that hydrothermal alteration was a source of Na^+ concentration in geothermal water. Figure 6i also illustrates that the K^+ concentration of geothermal water was derived from the dissolution of muscovite and kaolinite.

4.3. Recharge Source and Residential Time by D-O-T Isotopes

4.3.1. Recharge Source

Hydrogen and oxygen isotopes can be used to calculate the geothermal water recharge elevation, determine the source of geothermal water recharge, and estimate the intensity of geothermal water–rock interaction [19,40]. As shown in Figure 7, the geothermal water

samples and river water sample basically follow the global atmospheric precipitation line or the local atmospheric precipitation line. Compared with the river water sample, geothermal water samples deviate in a rightward direction (oxygen isotope drift). Since oxygen isotope exchange occurred between geothermal water and aquifer rock, the deuterium isotope was more suitable for estimating the recharge elevation of geothermal water in this study, and the calculation formula is shown in Equation (5):

$$H = \frac{R-R'}{\rho} \times 100 + h \quad (5)$$

where H is the recharge elevation (m), R is the δD isotopic value of geothermal water (‰), R′ is the δD isotopic value of atmospheric precipitation (‰), h is the elevation of atmospheric precipitation (m), and ρ is the δD isotope gradient value of atmospheric precipitation in the study area, which is taken as −2.6‰/100 m [41]. The recharge elevation of geothermal waters varied from 3034 m to 3845 m, with an average of 3416 m (Table 1). The results demonstrated the geothermal waters were recharged by atmospheric precipitation and snow melt water in the study area.

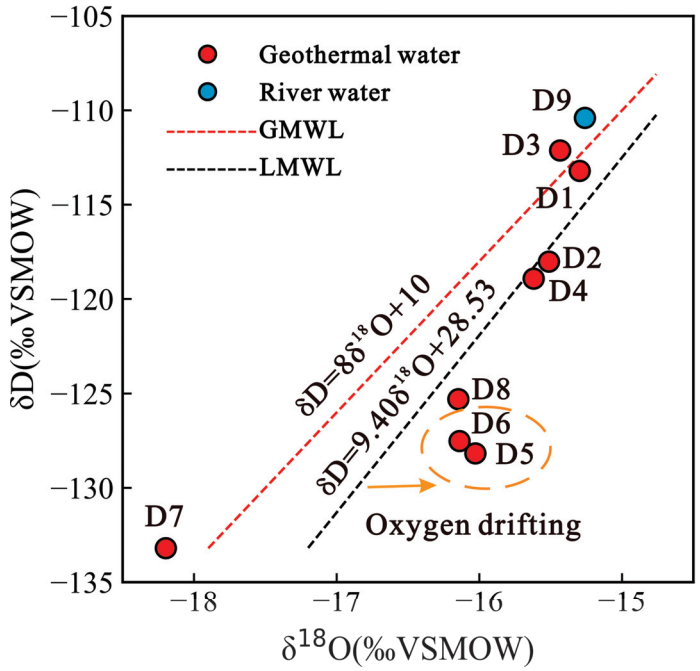

Figure 7. $\delta^{18}O$ vs. δD relationship diagram. GMWL: Global Meteoric Water Line [42]; LMOW: Local Meteoric Water Line [43].

4.3.2. Residential Time

In this study, the age range or average retention time of groundwater was estimated qualitatively by tritium; tritium content less than 1 TU in geothermal fluid is considered to be mainly due to recharge of sub-modern water before 1952 [44]. As shown in Figure 8a, the tritium contents of geothermal waters were greater than 1 TU, which indicates that geothermal water runoff was fast and easily renewed. Due to active local neotectonic activities, faults and fractures developed in the study area. In addition, the geomorphology of the study area was of the alpine canyon type, with a large terrain drop and strong hydrodynamic conditions. As the tritium isotope content increases in geothermal water, the $\delta^{18}O$ values increase in solution, the TDS content decreases, and the recharge elevation also tends to decrease (Figure 8b). On the one hand, the lower tritium content in geothermal water indicates that the longer the residential time of geothermal water and the stronger the water–rock interaction, the greater the solution TDS content. On the other hand, it was speculated that when geothermal water leached minerals, the lighter oxygen isotopes in minerals were easily carried to the aqueous solution, which made the solution $\delta^{18}O$ values

lower [45]. Finally, the geothermal water with higher recharge elevation has a larger water table, making it infiltrate to a deep level and increasing its circulation time (Figure 8c).

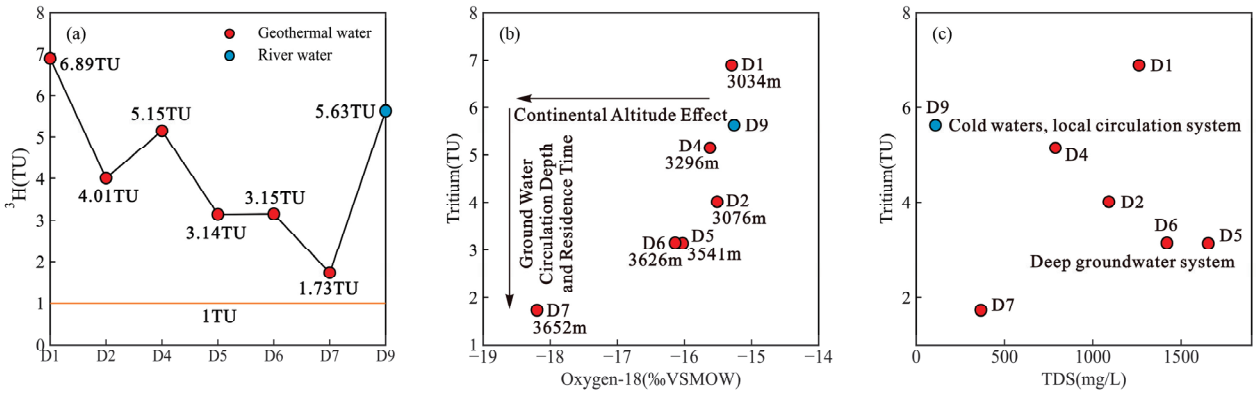

Figure 8. (**a**) The content of tritium and (**b**) $\delta^{18}O$ vs. tritium. Arrows indicate the increasing effects of altitude, depth of circulation, and residence time. (**c**) TDS vs. tritium diagram. Local circulation system indicates shallow circulation, short residence time, and rapid response to precipitation. Deep groundwater system indicates longer residence time and different depths.

4.4. Geothermal Reservoir

4.4.1. Water–Rock Equilibrium State

In the Na-K-Mg triangle diagram, the geothermal water samples are all located in the "immature water" area [46] (Figure 9). This indicates that the intensity of the geothermal water–rock interaction was not high in the study area, so this study was not suitable for calculating the geothermal reservoir temperature using the cation geothermometer.

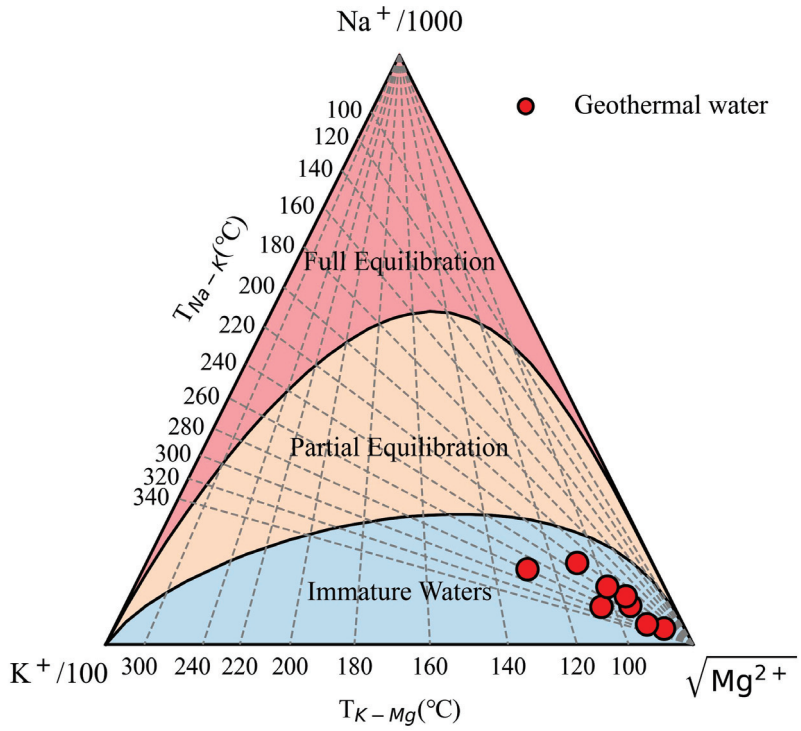

Figure 9. Na-K-Mg triangle in the geothermal water area.

The mineral saturation index (SI) of the geothermal waters was calculated using Phreeqc software with the database of phreeqc.dat, and the calculation results are shown in Table 2. The mineral saturation index was lower than zero, indicating the unsaturated

condition. Hard gypsum and gypsum were in unsaturated state, which may be due to the fact that there is no widely distributed paste salt layer in the study area, and the geothermal water did not fully dissolve and filter hard gypsum and gypsum in the runoff process. Calcite and dolomite were basically saturated, which was due to the extensive existence of carbonate rocks in the study area and the full dissolution and filtration of carbonate minerals by geothermal water in the runoff process. Quartz and chalcedony were basically in equilibrium, which provides a theoretical basis and data support for the calculation of the geothermal reservoir temperature by a SiO_2 geothermometer.

Table 2. Calculation results of mineral saturation index in the study area.

	Anhydrite	Calcite	Chalcedony	Dolomite	Gypsum	Quartz
D1	−1.62	0.39	−0.09	0.25	−1.49	0.29
D2	−1.98	0.85	−0.13	1.58	−2.29	0.13
D3	−3.23	−0.95	−0.12	−1.93	−2.98	0.3
D4	−2.87	−0.03	−0.04	−0.33	−2.97	0.28
D5	−3.28	0.91	−0.08	2.13	−3.45	0.22
D6	−3.6	0.49	−0.18	1.08	−3.88	0.09
D7	−4.57	−0.34	−0.37	−0.97	−4.56	−0.03
D8	−3.01	0.45	−0.01	0.85	−3.19	0.28

4.4.2. Geothermal Geothermometer

(1) SiO_2 geothermometer

The SiO_2 geothermometer is often used to calculate the temperature of geothermal reservoirs [47]. This study used quartz and chalcedony geothermometers for calculations and, after analysis, a suitable geothermometer was selected to represent the temperature of the shallow geothermal reservoir in the Kangding area. The equation for calculating the quartz geothermometer is shown as follows:

No steam loss:

$$T = 1309/(5.19 - \lg SiO_2) - 273.15 \quad (6)$$

Boiling flash steam:

$$T = 1522/(5.75 - \lg SiO_2) - 273.15 \quad (7)$$

The formula for calculating the chalcedony geothermometer is shown below:

$$T = 1032/(4.69 - \lg SiO_2) - 273.15 \quad (8)$$

The calculation results are shown in Table 3.

Table 3. Calculated results of quartz and chalcedony geothermal geothermometer in Kangding geothermal area (°C).

	Field Survey	Silica Geothermometer			Silicon Enthalpy Equation	
Sample ID	Discharge T	Quartz (No Vapor Loss)	Quartz (Maximum Vapor Loss)	Chalcedony	Cold Water Mixing Ratio	Reservoir Temperature
-	°C	°C	°C	°C	%	°C
D1	42	97	98	67	82	181
D2	88	141	136	115	58	194
D3	30	81	85	50	89	180
D4	65	128	125	100	73	205
D5	72	130	127	103	67	196
D6	85	132	128	104	56	178
D7	54	81	85	50	58	114
D8	74	141	136	115	70	219

The geothermal reservoir temperature range calculated by the quartz geothermometer without steam loss was 81–141 °C, and the average value was 116 °C; the geothermal reservoir temperature range calculated by the quartz boiling flash geothermometer was 85–136 °C, and the average value was 115 °C; the geothermal reservoir temperature range calculated by the chalcedony geothermometer was 50–115 °C, and the average value was 88 °C. The quartz geothermometer is suitable for high-temperature geothermal systems with geothermal reservoir temperature higher than 150 °C, and the geothermal reservoir temperature calculated by the quartz geothermometer was lower than 150 °C, so the chalcedony geothermometer was used to calculate the shallow geothermal reservoir temperature of the area. Hence, the shallow geothermal reservoir temperature of Kangding geothermal area was 50–115 °C.

In order to accurately calculate the initial temperature of geothermal water (deep geothermal reservoir temperature), as well as the cold water mixing ratio, this study used the silicon enthalpy equation method to analyze the geothermal water samples [48]. The silicon enthalpy equation method utilizes the following equations:

$$H_c X + H_h (1 - X) = H_s \quad (9)$$

$$Si_c X + Si_h (1 - X) = Si_s \quad (10)$$

where H_c, H_h, and H_s are the enthalpy of surface cold water, enthalpy of deep geothermal water, and enthalpy of hot spring water, respectively; Si_c, Si_h, and Si_s are the SiO_2 content of surface cold water, SiO_2 content of deep geothermal water, and SiO_2 content of hot spring water, respectively; X is the cold-water mixing ratio.

In this study, the river water in the Kangding geothermal area was used as the cold end of the surface, and the silicon enthalpy mixing curve of the study area was drawn as shown in Figure 10. As a result, the deep heat storage temperature range was 114–219 °C, and the shallow cold water mixing ratio was 0.56–0.89.

(2) Geochemical thermodynamic geothermometer

The geochemical thermodynamic geothermometer, i.e., the multi-mineral equilibrium graphical method, is a method used to calculate the geothermal reservoir temperature of the geothermal system based on the mineral saturation index (SI) [49]. It is based on the principle that the dissolved state of multiple minerals in water is considered a function of temperature; if a group of minerals approaches equilibrium at a specific temperature at the same time, the geothermal water can be judged to have reached equilibrium with this group of minerals, and the temperature at this time is the geothermal reservoir temperature. The calculation of the mineral saturation index is shown in Equation (11):

$$SI = \log Q/K = \log Q - \log K \quad (11)$$

where Q is the mineral activity product and K is the mineral equilibrium constant.

In this study, the point D2 with the highest surface outcrop temperatures was selected for geochemical thermodynamic geothermometer calculation, and the result is shown in Figure 11. The mineral saturation index of hot spring site D2 showed convergence around 200 °C, which further indicates that the deep geothermal reservoir temperature calculated in this study was reasonable, i.e., the deep geothermal reservoir in the Kangding geothermal area was about 200 °C.

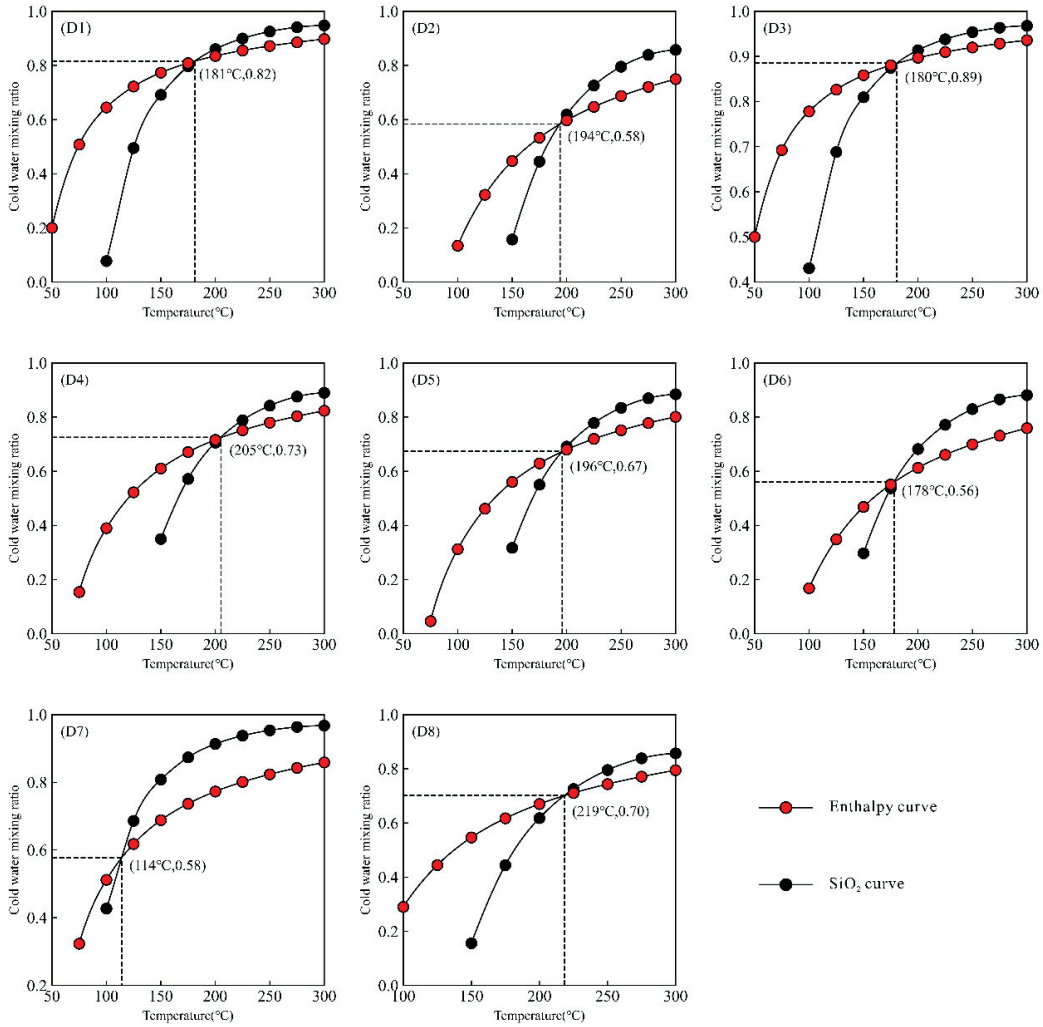

Figure 10. Relations between fraction of cold water and temperature in the mixing model. (Red curve = enthalpy, black curve = silica; the brackets at the intersection point show the initial geothermal temperature on the left and the mixing ratio of cold water on the right).

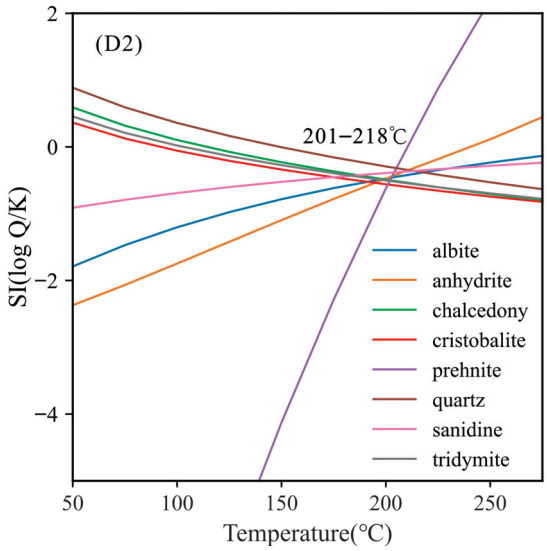

Figure 11. Mineral equilibria graph of D2 sample.

4.5. Genetic Model of Geothermal Waters in the Study Area

Comprehensive analysis of the above conceptual model of the geothermal system in the study area, as derived in this study, is shown in Figure 12. The study area is located in a region where a low-velocity, high-conductivity layer existed within the crust, which was considered to be a local melt. Ice melt water and atmospheric precipitation infiltrated along the tectonic fissures under great head pressure, and after heating by radioactive element decay in granite and heating by a deep local melt body, magma water was mixed in the deep thermal reservoir. Then, the geothermal fluid rose along the secondary water-conducting fractures of Xianshuihe fault and mixed with the infiltrated cold water in the shallow fissure thermal reservoir, and the cold-water mixing ratio was about 73%. After mixing, the geothermal water continued to rise along the dominant fractures and finally emerged as springs at the surface.

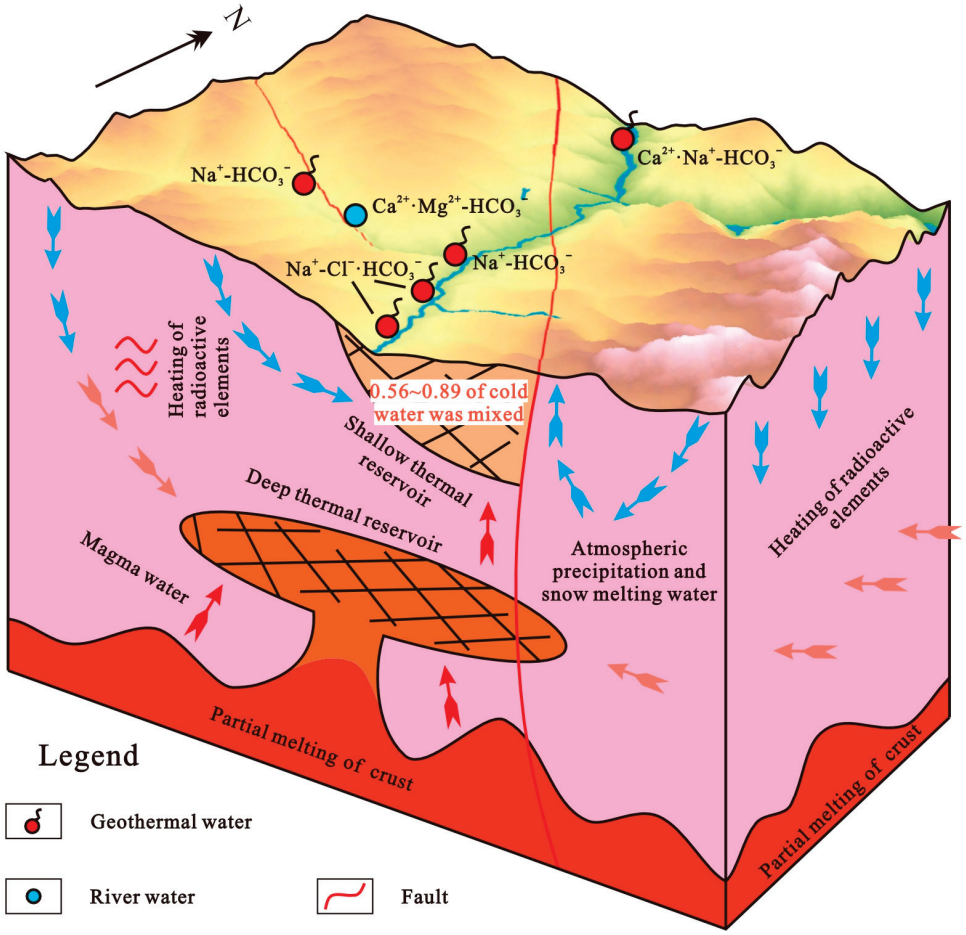

Figure 12. Conceptual model of the geothermal system in Kangding area.

5. Conclusions

By analyzing the geological and hydrogeochemical conditions of the study area, this study identified the water–rock interaction, determined the geothermal reservoir temperature of the geothermal system, and finally explored the genesis mode of the geothermal system in the Kangding geothermal area.

(1) The hydrochemical types of Kangding geothermal water were mainly Ca^{2+}–Na^{+}–HCO_3^- type, Na^{+}–$^-$–HCO_3^- type, and Na^{+}–HCO_3^- type. The hydrochemical characteristics of geothermal water were mainly influenced by deep fluid mixing and water–rock interactions in the Kangding geothermal area.

(2) The temperature of the deep geothermal reservoir was 114–219 °C, the temperature of the shallow geothermal reservoir was 50–115 °C, and the mixing ratio of cold water was 0.56–0.89.
(3) The geothermal water was affected by water–rock interactions in the study area, and there was a certain degree of the "oxygen isotope drift" phenomenon. In this study, the recharge elevation of geothermal water was calculated to be 3034–3845 m, with an average of 3416 m.
(4) The source of geothermal waters was atmospheric precipitation and high mountain ice and snow melt water in Kangding geothermal area. It was heated by a radioactive element decay in the granite and local melt body in the deep part, and mixed with magma water in the deep geothermal reservoir. Then, the geothermal fluid rose along the secondary fractures of Xianshui River, mixed with cold water in the shallow geothermal reservoir, and was exposed at the surface, thereby becoming springs.

Author Contributions: Writing—original draft preparation, investigation, methodology, X.Z.; writing—review and editing, software, data curation, C.D.; supervision, project administration, funding acquisition, T.F., resources, data curation, Y.Z. All authors have read and agreed to the published version of the manuscript.

Funding: This research was funded by National Natural Science Foundation of China grant number [42072313, 42102334], Sichuan Science and Technology Program grant number [2023YFS0356], Scientific Key R&D project of the Tibet Autonomous Region grant number [XZ202201ZY0021G], Opening fund of State Key Laboratory of Geohazard Prevention and Geoenvironment Protection (Chengdu University of Technology) grant number [SKLGP2022K017].

Data Availability Statement: All the research data has been provided in the paper.

Conflicts of Interest: The authors declare no conflict of interest.

References

1. Muffler, L.J.P. Tectonic and hydrologic control of the nature and distribution of geothermal resources. *Geo-Heat Cent. Q. Bull.* **1993**, *15*, 1–10.
2. Tang, X.; Zhang, J.; Pang, Z.; Hu, S.; Tian, J.; Bao, S. The eastern Tibetan Plateau geothermal belt, western China: Geology, geophysics, genesis, and hydrothermal system. *Tectonophysics* **2017**, *717*, 433–448. [CrossRef]
3. Guo, Q.; Planer-Friedrich, B.; Liu, M.; Yan, K.; Wu, G. Magmatic fluid input explaining the geochemical anomaly of very high arsenic in some southern Tibetan geothermal waters. *Chem. Geol.* **2019**, *513*, 32–43. [CrossRef]
4. Liu, M.; Guo, Q.; Wu, G.; Guo, W.; She, W.; Yan, W. Boron geochemistry of the geothermal waters from two typical hydrothermal systems in Southern Tibet (China): Daggyai and Quzhuomu. *Geothermics* **2019**, *82*, 190–202. [CrossRef]
5. Tian, J.; Pang, Z.; Wang, Y.; Guo, Q. Fluid geochemistry of the Cuopu high temperature geothermal system in the eastern Himalayan syntaxis with implication on its genesis. *Appl. Geochem.* **2019**, *110*, 104422. [CrossRef]
6. Apollaro, C.; Fuoco, I.; Gennaro, E.; Giuliani, L.; Iezzi, G.; Marini, L.; Radica, F.; Di Luccio, F.; Ventura, G.; Vespasiano, G. Advanced argillic alteration at Cave di Caolino, Lipari, Aeolian Islands (Italy): Implications for the mitigation of volcanic risks and the exploitation of geothermal resources. *Sci. Total Environ.* **2023**, *889*, 164333. [CrossRef]
7. Fuoco, I.; Figoli, A.; Criscuoli, A.; Brozzo, G.; De Rosa, R.; Gabriele, B.; Apollaro, C. Geochemical modeling of chromium release in natural waters and treatment by RO/NF membrane processes. *Chemosphere* **2020**, *254*, 126696. [CrossRef]
8. Griffiths, J.C. Statistics and Data Analysis in Geology. *Technometrics* **2005**, *47*, 526–527.
9. Zhang, X.; Guo, Q.; Liu, M.; Luo, J.; Yin, Z.; Zhang, C.; Zhu, M.; Guo, W.; Li, J.; Zhou, C. Hydrogeochemical processes occurring in the hydrothermal systems of the Gonghe–Guide basin, northwestern China: Critical insights from a principal components analysis (PCA). *Environ. Earth Sci.* **2016**, *75*, 1187. [CrossRef]
10. Cioni, R.; Marini, L. *A Thermodynamic Approach to Water Geothermometry*; Springer: Berlin/Heidelberg, Germany, 2020. [CrossRef]
11. Fournier, R.O.; Truesdell, A.H. An empirical Na K Ca geothermometer for natural waters. *Geochim. et Cosmochim. Acta* **1973**, *37*, 1255–1275. [CrossRef]
12. García-López, C.; Pandarinath, K.; Santoyo, E. Solute and gas geothermometry of geothermal wells: A geochemometrics study for evaluating the effectiveness of geothermometers to predict deep reservoir temperatures. *Int. Geol. Rev.* **2014**, *56*, 2015–2049. [CrossRef]
13. Santoyo, E.; Díaz-González, L. A New Improved Proposal of the Na/K Geothermometer to Estimate Deep Equilibrium Temperatures and their Uncertainties in Geothermal Systems. In Proceedings of the World Geothermal Congress, Bali, Indonesia, 1 November 2009.

14. Verma, S.P.; Pandarinath, K.; Santoyo, E. SolGeo: A new computer program for solute geothermometers and its application to Mexican geothermal fields. *Geothermics* **2008**, *37*, 597–621. [CrossRef]
15. Verma, S.P.; Santoyo, E. New improved equations for NaK, NaLi and SiO_2 geothermometers by outlier detection and rejection. *J. Volcanol. Geotherm. Res.* **1997**, *79*, 9–23. [CrossRef]
16. Yi, L.; Qi, J.; Li, X.; Xu, M.; Zhang, X.; Zhang, Q.; Tang, Y. Geochemical characteristics and genesis of the high-temperature geothermal systems in the north section of the Sanjiang Orogenic belt in southeast Tibetan Plateau. *J. Volcanol. Geotherm. Res.* **2021**, *414*, 107244. [CrossRef]
17. Zhang, J.; Li, W.; Tang, X.; Tian, J.; Wang, Y.; Guo, Q.; Pang, Z. Geothermal data analysis at the high-temperature hydrothermal area in Western Sichuan. *Sci. China Earth Sci.* **2017**, *60*, 1507–1521. [CrossRef]
18. Qi, J.; Xu, M.; An, C.; Wu, M.; Zhang, Y.; Li, X.; Zhang, Q.; Lu, G. Characterizations of geothermal springs along the Moxi deep fault in the western Sichuan plateau, China. *Phys. Earth Planet. Inter.* **2017**, *263*, 12–22. [CrossRef]
19. Luo, J.; Pang, Z.; Kong, Y.; Wang, Y. Geothermal potential evaluation and development prioritization based on geochemistry of geothermal waters from Kangding area, western Sichuan, China. *Environ. Earth Sci.* **2017**, *76*, 343. [CrossRef]
20. Guo, Q.; Pang, Z.; Wang, Y.; Tian, J. Fluid geochemistry and geothermometry applications of the Kangding high-temperature geothermal system in eastern Himalayas. *Appl. Geochem.* **2017**, *81*, 63–75. [CrossRef]
21. Li, X.; Huang, X.; Liao, X.; Zhang, Y. Hydrogeochemical Characteristics and Conceptual Model of the Geothermal Waters in the Xianshuihe Fault Zone, Southwestern China. *Int. J. Environ. Res. Public Health* **2020**, *17*, 500. [CrossRef]
22. Zhang, Y.; Xu, M.; Li, X.; Qi, J.; Zhang, Q.; Guo, J.; Yu, L.; Zhao, R. Hydrochemical Characteristics and Multivariate Statistical Analysis of Natural Water System: A Case Study in Kangding County, Southwestern China. *Water* **2018**, *10*, 80. [CrossRef]
23. Roberts, N.M.W.; Searle, M.P. Zircon U–Pb–Hf constraints from Gongga Shan granites on young crustal melting in eastern Tibet. *Geosci. Front.* **2019**, *10*, 885–894. [CrossRef]
24. Searle, M.P.; Roberts, N.M.W.; Chung, S.-L.; Lee, Y.-H.; Cook, K.L.; Elliott, J.R.; Weller, O.M.; St-Onge, M.R.; Xu, X.-W.; Tan, X.-B.; et al. Age and anatomy of the Gongga Shan batholith, eastern Tibetan Plateau, and its relationship to the active Xianshui-he fault. *Geosphere* **2016**, *12*, 948–970. [CrossRef]
25. Arevalo, R.; McDonough, W.F.; Luong, M. The K/U ratio of the silicate Earth: Insights into mantle composition, structure and thermal evolution. *Earth Planet. Sci. Lett.* **2009**, *278*, 361–369. [CrossRef]
26. de Sigoyer, J.; Vanderhaeghe, O.; Duchêne, S.; Billerot, A. Generation and emplacement of Triassic granitoids within the Songpan Ganze accretionary-orogenic wedge in a context of slab retreat accommodated by tear faulting, Eastern Tibetan plateau, China. *J. Asian Earth Sci.* **2014**, *88*, 192–216. [CrossRef]
27. Lai, S.-C.; Zhao, S.-W. Petrogenesis of the Zheduoshan Cenozoic granites in the eastern margin of Tibet: Constraints on the initial activity of the Xianshuihe Fault. *J. Geodyn.* **2018**, *117*, 49–59. [CrossRef]
28. Rybach, L. Radioactive heat production in rocks and its relation to other petrophysical parameters. *Pure Appl. Geophys.* **1976**, *114*, 309–317. [CrossRef]
29. Jiang, Y.; Guo, H.; Jia, Y.; Cao, Y.; Hu, C. Principal component analysis and hierarchical cluster analyses of arsenic groundwater geochemistry in the Hetao basin, Inner Mongolia. *Geochemistry* **2015**, *75*, 197–205. [CrossRef]
30. Seyedrahimi-Niaraq, M.; Mahdiyanfar, H.; Mokhtari, A.R. Integrating principal component analysis and U-statistics for mapping polluted areas in mining districts. *J. Geochem. Explor.* **2022**, *234*, 106924. [CrossRef]
31. Nyakairu, G.W.A.; Kasule, J.; Ouma, O.; Bahati, G. Origin and hydrogeochemical formation processes of geothermal fluids from the Kibiro area, Western Uganda. *Appl. Geochem.* **2023**, *152*, 105648. [CrossRef]
32. Wang, X.; Luo, Z.; Xu, C.; Lv, Y.; Cheng, L.; Zhang, Y. Formation mechanism of a carbonate geothermal system and calculation of the reservoir temperature under complex conditions. *Geothermics* **2022**, *99*, 102295. [CrossRef]
33. Wang, Y.; Li, L.; Wen, H.; Hao, Y. Geochemical evidence for the nonexistence of supercritical geothermal fluids at the Yangbajing geothermal field, southern Tibet. *J. Hydrol.* **2022**, *604*, 127243. [CrossRef]
34. Bärenbold, F.; Schmid, M.; Brennwald, M.S.; Kipfer, R. Missing atmospheric noble gases in a large, tropical lake: The case of Lake Kivu, East-Africa. *Chem. Geol.* **2020**, *532*, 119374. [CrossRef]
35. Stefánsson, A.; Sveinbjörnsdóttir, Á.E.; Heinemeier, J.; Arnórsson, S.; Kjartansdóttir, R.; Kristmannsdóttir, H. Mantle CO_2 degassing through the Icelandic crust: Evidence from carbon isotopes in groundwater. *Geochim. Cosmochim. Acta* **2016**, *191*, 300–319. [CrossRef]
36. Wang, Y.; Yuan, X.; Zhang, Y.; Zhang, X.; Xiao, Y.; Duo, J.; Huang, X.; Sun, M.; Lv, G. Hydrochemical, D–O–Sr isotopic and electromagnetic characteristics of geothermal waters from the Erdaoqiao area, SW China: Insights into genetic mechanism and scaling potential. *Ore Geol. Rev.* **2023**, *158*, 105486. [CrossRef]
37. Yang, P.; Luo, D.; Hong, A.; Ham, B.; Xie, S.; Ming, X.; Wang, Z.; Pang, Z. Hydrogeochemistry and geothermometry of the carbonate-evaporite aquifers controlled by deep-seated faults using major ions and environmental isotopes. *J. Hydrol.* **2019**, *579*, 124116. [CrossRef]
38. Carol, E.; Kruse, E.; Mas-Pla, J. Hydrochemical and isotopical evidence of ground water salinization processes on the coastal plain of Samborombón Bay, Argentina. *J. Hydrol.* **2009**, *365*, 335–345. [CrossRef]
39. Chen, L.; Wang, G.; Hu, F.; Wang, Y.; Liu, L. Groundwater hydrochemistry and isotope geochemistry in the Turpan Basin, northwestern China. *J. Arid Land* **2013**, *6*, 378–388. [CrossRef]

40. Wang, S.; Liu, Z.; Shao, J. Hydrochemistry and H-O-C-S Isotopic Geochemistry Characteristics of Geothermal Water in Nyemo-Nagqu, Tibet. *Acta Geol. Sin.-Engl. Ed.* **2017**, *91*, 644–657. [CrossRef]
41. Sun, M.; Zhang, X.; Yuan, X.; Yu, Z.; Xiao, Y.; Wang, Y.; Zhang, Y. Hydrochemical Characteristics and Genetic Mechanism of Geothermal Springs in the Aba Area, Western Sichuan Province, China. *Sustainability* **2022**, *14*, 12824. [CrossRef]
42. Craig, H. Isotopic Variations in Meteoric Waters. *Science* **1961**, *133*, 1702–1703. [CrossRef]
43. Xiangyang, S.; Genxu, W.; Juying, S.; Shouqin, S.; Zhaoyong, H.; Chunlin, S.; Shan, L. Contrasting water sources used by a coniferous forest in the high-altitude, southeastern Tibetan Plateau. *Sci. Total Environ.* **2022**, *849*, 157913. [CrossRef] [PubMed]
44. Thomas, M.A. The association of arsenic with redox conditions, depth, and ground-water age in the glacial aquifer system of the northern United States. In *Scientific Investigations Report*; US Geological Survey: Reston, VA, USA, 2007.
45. Pasvanoğlu, S. Geochemical Survey of low- temperature geothermal resource of the Reşadiye Spa (Tokat, Northern Turkey). *Geothermics* **2021**, *94*, 102088. [CrossRef]
46. Giggenbach, W.F. Geothermal solute equilibria. Derivation of Na-K-Mg-Ca geoindicators. *Geochim. Cosmochim. Acta* **1988**, *52*, 2749–2765. [CrossRef]
47. Fournier, R.O.; Berger, B.R.; Bethke, P.M. The Behavior of Silica in Hydrothermal Solutions. In *Geology and Geochemistry of Epithermal Systems*; Society of Economic Geologists: Littleton, CO, USA, 1985; Volume 2.
48. Fournier, R.O. Chemical geothermometers and mixing models for geothermal systems. *Geothermics* **1977**, *5*, 41–50. [CrossRef]
49. Reed, M.H. Calculation of multicomponent chemical equilibria and reaction processes in systems involving minerals, gases and an aqueous phase. *Geochim. Cosmochim. Acta* **1982**, *46*, 513–528. [CrossRef]

Disclaimer/Publisher's Note: The statements, opinions and data contained in all publications are solely those of the individual author(s) and contributor(s) and not of MDPI and/or the editor(s). MDPI and/or the editor(s) disclaim responsibility for any injury to people or property resulting from any ideas, methods, instructions or products referred to in the content.

water

MDPI

Article

Hydrochemical Characteristics and Formation Mechanism of Quaternary Groundwater in Baoshan Basin, Western Yunnan, China

Yi Xiao [1,2], Jiahui Zhang [3,*], Aihua Long [1,2,*], Shiguang Xu [4], Tingting Guo [3], Xinchen Gu [2,5], Xiaoya Deng [2] and Pei Zhang [2]

[1] College of Water Conservancy & Architectural Engineering, Shihezi University, Shihezi 832000, China; yam273021691@163.com
[2] State Key Laboratory of Simulation and Regulation of Water Cycle in River Basin, China Institute of Water Resources and Hydropower Research, Beijing 100044, China
[3] Department of Earth Sciences, Kunming University of Science and Technology, Kunming 650093, China
[4] Yunnan Geological and Mineral Engineering Survey Group Company, Kunming 650000, China
[5] State Key Laboratory of Hydraulic Engineering Simulation and Safety, School of Civil Engineering, Tianjin University, Tianjin 300072, China
* Correspondence: jiahuizhang2307@163.com (J.Z.); ahlong@iwhr.com (A.L.)

Abstract: The shallow groundwater of the quaternary system in the Baoshan basin, Yunnan Province is seriously polluted, threatening human health and restricting local socio-economic development; therefore, it is necessary to investigate the hydrochemical characteristics and formation mechanisms of the shallow groundwater of the quaternary system in the Baoshan basin. This study used EVS 2022 to establish a 3D visual geological model of the quaternary system in the basin and divided the shallow groundwater aquifers of the quaternary system into three groundwater systems, sampling 22, 9, and 4 groups in each groundwater system, respectively. Mathematical statistics, Piper's trilinear diagram, Gibbs plots, the Gaillardet model, the ion ratio method, groundwater saturation, and the PCA-APCS-MLR model were used to analyze the groundwater hydrochemical characteristics and genesis of the study area. The results show the following: (1) The types of groundwater chemicals are mainly HCO_3-Ca-Mg type and HCO_3-Ca, the causes of the water chemical characteristics are mainly influenced by water–rock interaction and alternate cation adsorption, and the rock types with which the groundwater exchanges substances are carbonate rocks and silicate rocks. (2) The Fe^{2+}, Mn^{2+}, and NH_3-N contents in groundwater systems I and II exceed the standard, which is the human activity area, and groundwater pollution is mainly affected by human activities. (3) Four main categories of factors were obtained according to the PCA-APCS-MLR model, namely dissolution filtration, migration and enrichment factors, geological and human activity factors, and environmental factors and pollution factors; the cumulative contribution of variance was 77.84%, and the groundwater chemical characteristics were jointly influenced by hydrogeological conditions and human activities. The results of this study provide a basis for groundwater protection and management in the Baoshan basin, where groundwater system I is the key area for pollution and should be strengthened for control.

Keywords: quaternary shallow groundwater; hydrochemical characteristics; water pollution; PCA-APCS-MLR model; Baoshan basin

1. Introduction

Groundwater has the characteristics of wide distribution, stable changes, good water quality, and easy application, making it an important resource indispensable for the long-term and stable development of human beings on Earth [1]. The current demand for groundwater resources has increased greatly, and unreasonable exploitation has caused

the deterioration of groundwater quality. Probing its groundwater chemical characteristics and causes can provide an important guarantee for groundwater quality monitoring and the sustainable development of socio-economic, industrial, agricultural, and ecological health [2–4].

Groundwater chemistry components are changing every moment due to the fact that groundwater exchanges substances with the external environment through flow, and the formation and evolution of groundwater during the water cycle are influenced by natural factors such as water–rock interaction [5–7], evaporation concentration [8–10], ion exchange [11,12], and redox [13]. Many scholars at home and abroad have conducted various studies on groundwater chemical characteristics and hydrochemical causes; the main research methods include statistical analysis [14,15], graphical methods [16,17], and ion proportionality [18,19], and the related research results are becoming increasingly fruitful. The impact of human activities such as industrialization and urbanization on groundwater is increasing [20,21], and many scholars have carried out risk assessment, pollution source identification, and wastewater treatment for heavy metals and organic matter contamination in groundwater [22]. However, traditional methods of water chemistry analysis encounter difficulty in quantitatively describing the complex evolution of groundwater chemistry under the conditions of human activities, and multivariate statistical models currently provide a more accurate and convenient method of groundwater chemistry characterization and pollution cause analysis [23,24].

The Baoshan basin is a typical quaternary fault basin in western Yunnan province, and quaternary groundwater is an important water supply source for resource production and the life of residents in the basin; however, groundwater indicators such as iron, manganese, and ammonia nitrogen seriously exceed the standard levels, which greatly threatens the productiveness of the region and safety of local people [25]. In order to ensure the long-term and stable utilization of quaternary groundwater resources in the Baoshan basin, it is urgent to understand the chemical characteristics of this groundwater and analyze the causes of pollution; however, few studies in this area have been reported in recent years. In this paper, we combine traditional hydrogeochemical methods and multivariate statistical methods to describe in detail the statistical characteristics of chemical indicators and groundwater chemical types in the quaternary groundwater of the Baoshan basin, determine the sources of groundwater ionic components, and analyze the causes of groundwater pollution, with the aim of providing a scientific basis for groundwater development, utilization, management, and protection in the Baoshan basin.

2. Materials and Methods

2.1. Study Area

The Baoshan basin in western Yunnan, with geographic coordinates of 98°08′ to 99°16′ E and 24°56′ to 25°14′ N, is located at the junction of China and Myanmar. The Baoshan basin is a lacustrine plain landscape surrounded by mountains and hills; the basin is oriented in the north–south direction [26] and is 15 km long and 7–10 km wide, with a total area of 230 km^2 (Figure 1). The Baoshan basin is located at low latitudes and high altitudes, with an average annual temperature of 14.7 °C. The average annual rainfall in Baoshan is about 1047.3 mm and the average annual evaporation is 1650.3 mm [27]. There are many rivers in the Baoshan basin, with the Donghe River being the main water system in the basin, flowing from the northern part of the basin; its tributaries on the east and west sides converge into the main river channel and then run off from north to south, finally discharging to the Nujiang River. The main stream of the Donghe River is 25.3 km long in the basin, which is the lowest erosion datum in the region.

The Baoshan basin is covered by quaternary sediments, and the surface outcrops are the quaternary holocene and quaternary pleistocene. The quaternary holocene sediments are mainly lacustrine deposits, which are gray and brown clay and pebble gravel layers mainly distributed in the center of the Baoshan basin and with a maximum thickness of 35.84 m [28,29]. Atmospheric precipitation is the main recharge term for groundwater in this

formation. In addition, agriculture and industry are mostly concentrated in the central part of the Baoshan basin, and agricultural irrigation water and domestic wastewater infiltrate into the aquifer in a facultative form. Due to the large hydraulic gradient, the bedrock fracture water and carbonate rocks in the surrounding mountains recharge the central part of the basin, and when the rainfall is high the river level rises rapidly, which locally causes the river to backcharge the groundwater [30]. The quaternary pleistocene consists of river and lake phase sediment of river alluvium, including clay, red clay, and gravel layers, which are mainly distributed at the edge of the Baoshan basin. The main source of groundwater recharge in this formation is atmospheric precipitation, and it is in contact with karst aquifers in the southern and northeastern part of the bedrock mountains; groundwater receives recharge from karst water and fissure water in the mountains. Groundwater in the region mainly runs toward the middle of the basin with a slow seepage rate, and eventually discharges to the Donghe River [28,29]. The surrounding mountainous areas are dominated by sedimentary clastic and carbonate rocks, and the main lithologies include limestones, argillaceous limestones, shales, and sandstones.

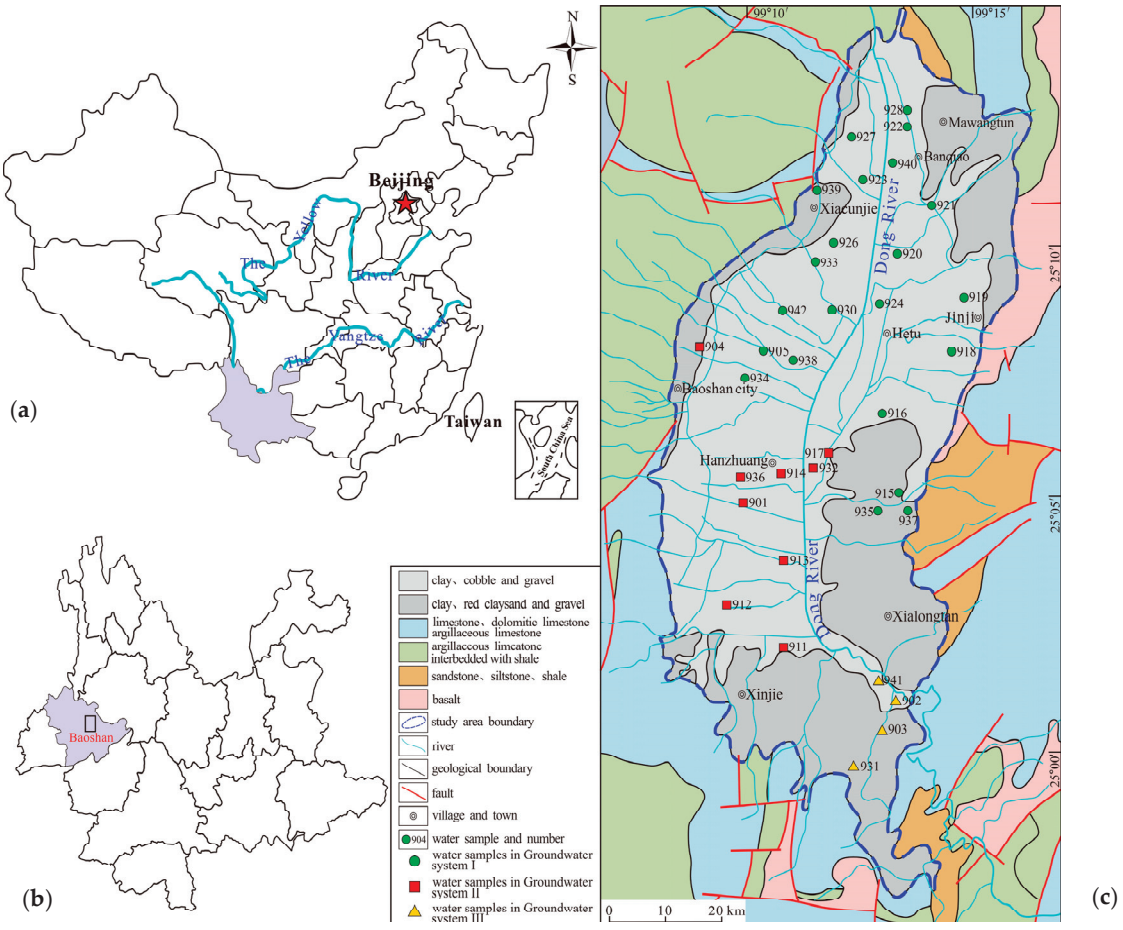

Figure 1. Distribution of regional hydrogeology and groundwater sampling points in the Baoshan basin, SW China: (**a**) location of Yunnan Province; (**b**) location of Baoshan basin; (**c**) regional hydrogeology of the Baoshan basin. The green points are the water samples in groundwater system I, the red points are the water samples in groundwater system II, and the yellow points are the water samples in groundwater system III.

2.2. Groundwater System

By collecting engineering geological borehole data, the quaternary strata in the basin can be generalized into seven layers according to the nature and water-richness of the geotechnical body: plain fill, clay, cobble and gravel, clay, sand and gravel, clay, and red

clay. The 3D geological modeling software Earth Volumetric Studio (EVS) [31] was used to establish a 3D geological model of the quaternary system in the Baoshan basin (Figure 2a) in order to visualize and analyze the quaternary strata in the Baoshan basin visually and clearly and then delineate the groundwater system, providing a basis for groundwater chemical characterization.

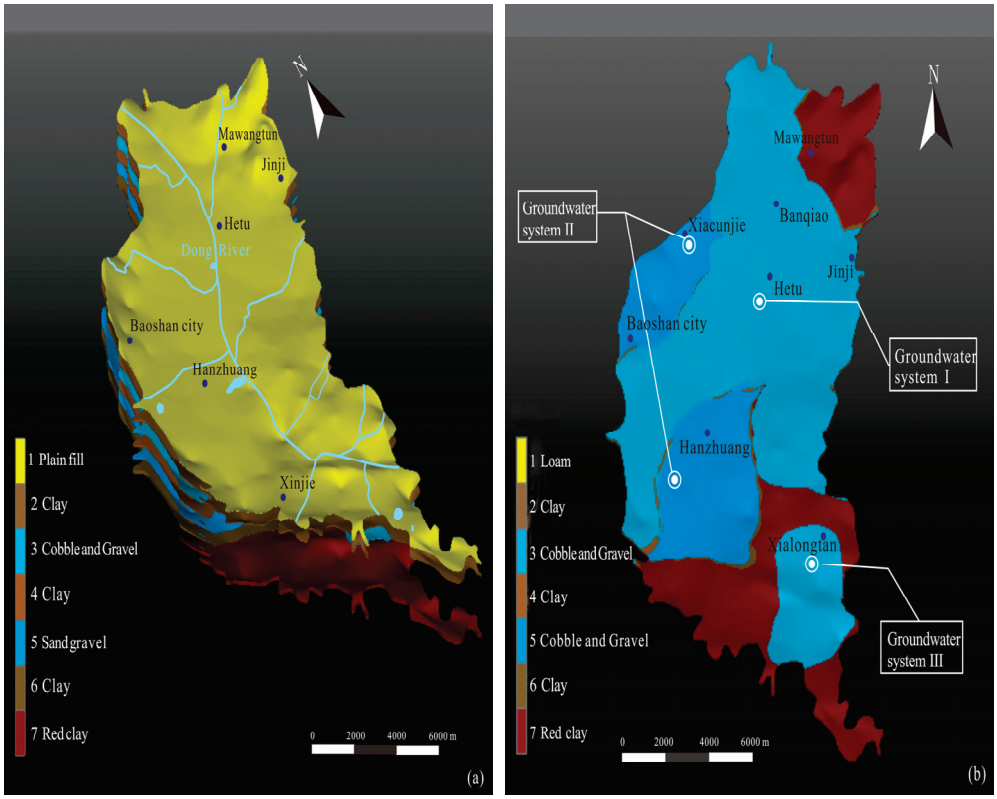

Figure 2. Three-dimensional geological model of quaternary system in Baoshan basin: (**a**) stratigraphic structure and (**b**) groundwater systems.

According to the hydrogeological conditions in the region, the Baoshan basin was divided into three groundwater systems, namely, groundwater system I, groundwater system II, and groundwater system III (Figure 2b).

2.3. Sample Collection and Testing

The groundwater samples were collected from residential wells and agricultural irrigation wells in 2019, and the sampling depths ranged from 0 to 20 m. The samples were all shallow groundwater. The groundwater system was used as the unit, with 22 groups of groundwater system I (green points in Figure 1c), 9 groups of groundwater system II (red points in Figure 1c), and 4 groups of groundwater system III (yellow points in Figure 1c), totaling 35 groups; the sampling points were labeled according to the sampling order.

A total of 28 indicators were selected for the water chemistry test, including pH, TDS, TH, seven major ions, organic substances, inorganic substances, and heavy metals. pH was measured on site using a PHS-3C pH meter, and the rest of the indicators in the groundwater samples were measured in the laboratory of Yunnan Sino-sci Testing Tech. Co, Ltd. (Shenzhen, China), HCO_3^-, Cl^-, and SO_4^{2-} were determined by acidity titration, the silver nitrate volumetric method, and the barium sulfate turbidimetric method, respectively; Ca^{2+} and Mg^{2+} were determined using the ASS method; Na^+, K^+, Fe^{2+}, and Mn^{2+} were determined via the FAAS method; and TDS, TH, COD, and NH_3-N were determined using the weighing method, EDTA method, CODMn method, and nano-reagent photometric method, respectively.

To ensure the reliability of the data, the anion and cation balance reliability test was performed on all the test results; the results showed that the relative error of anion and cation balance for all the water samples was between ±6% and that the test results were reliable. In this paper, ArcGIS 10.2, EVS 2022, Origin2021, PHREEQC 3.7.3, and SPSS 27 were used for water chemistry characterization, and the PCA-APCS-MLR model was used for groundwater pollution source analysis using SPSS software.

3. Results

3.1. Hydrochemical Characteristics

SPSS software was used to analyze 35 sets of water samples within the Baoshan basin and to count the parameter characteristic values of the water chemistry conventional components of the groundwater samples collected (Figure 3 and Table 1). The mean values reflect the overall situation of each conventional ion concentration index in the whole study area. The mean values of the cation concentration in each groundwater system of the shallow quaternary groundwater in the Baoshan basin are in the order of $Ca^{2+} > Na^{+} > Mg^{2+} > K^{+}$ from high to low, and Ca^{2+} is the most abundant cation in the shallow groundwater of the basin. The average values of anion concentrations from high to low are $HCO_3^{-} > Cl^{-} > SO_4^{2-}$, and HCO_3^{-} is the most abundant anion in the groundwater of the basin. For the three groundwater systems described separately, the TDS concentration values were in the range of 186.00–617.00 mg/L, 230.00–751.00 mg/L, and 247.00–320.00 mg/L, with mean values of 343.20 mg/L, 484.56 mg/L, and 293.73 mg/L, over all freshwater (TDS < 1000 mg/L). The TH concentration values were in the range of 117.00–446.00 mg/L, 135.00–442.00 mg/L, and 159.00–379.00 mg/L, with mean values of 278.86 mg/L, 278.00 mg/L, and 291.00 mg/L. One group of hard water (300 mg/L < TH < 450 mg/L) was found in each of groundwater system I and groundwater system II, while the rest were slightly hard water (150 mg/L < TH < 300 mg/L).

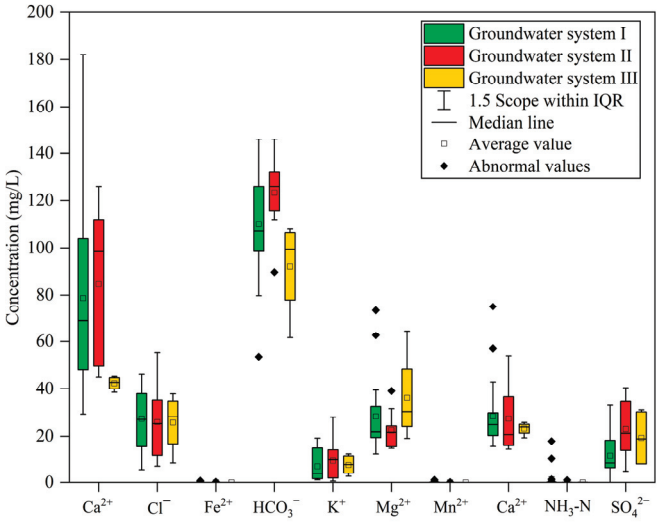

Figure 3. Box diagram of groundwater chemical composition in Baoshan basin.

The coefficient of variation was mainly used to compare the relationship between statistical indicators; a smaller coefficient of variation indicates that the variability of the variables is not significant, and a larger number of variances indicates that the chemical components of groundwater underwent a complex evolutionary process during its formation and evolution [32]. The pH intervals of the three groundwater systems were 6.17–8.27 mg/L, 7.22–8.29 mg/L, and 7.63–8.17 mg/L, with mean values of 7.81 mg/L, 7.96 mg/L, and 7.83 mg/L, respectively. The coefficients of variation were 0.07, 0.05, and 0.03, indicating that the spatial variability of the pH was not significant, and the groundwater was weakly alkaline in general. The coefficients of variation of Ca^{2+}, Mg^{2+}, Na^{+}, HCO_3^{-}, and Cl^{-} ranged from 0.19 to 0.52, indicating that the distribution of the above ions

was relatively stable in each groundwater system. The SO_4^{2-} concentration ranges were 0.00–33.22 mg/L, 5.10–40.40 mg/L, and 8.30–31.20 mg/L, with mean values of 11.66 mg/L, 22.98 mg/L, and 19.30 mg/L, respectively. The coefficient of variation was 0.90 in groundwater system I, 0.53 and 0.66 in groundwater system II and III, and the concentrations at water sample points 901 and 913 were 40.4 mg/L and 35.1 mg/L, respectively, which were more than twice the average value. It was speculated that the local ultra-high value of SO_4^{2-} in groundwater system I might be related to mixing with hot spring water. The K^+ concentration ranges were 1.11–19.20 mg/L, 0.58–28.00 mg/L, and 2.73–12.40 mg/L, with mean values of 7.22 mg/L, 9.65 mg/L, and 7.81 mg/L, respectively, in the groundwater systems. The coefficients of variation were 0.92 and 0.94 in groundwater systems I and II, respectively, and 0.58 in groundwater system III. The concentrations at water sample points 913, 921, and 922 were 28.00 mg/L, 18.50 mg/L, and 19.20 mg/L, respectively, indicating that K^+ is unevenly distributed in groundwater concentration values and is a sensitive factor susceptible to the groundwater environment and the local location of K^+. The very high value of K^+ may be closely related to local agricultural production. The coefficients of variation of Fe^{2+}, Mn^{2+}, and NH_3-N were greater than in groundwater systems I and II, and the coefficient of variation of COD was greater than in groundwater system I. In groundwater system III, Fe^{2+} and Mn^{2+} were not detected, and the coefficients of variation of NH_3-N and COD were 0.23 and 0.22, respectively; the above four indicators had obvious spatial variation, and represent the main pollutants in the groundwater of the Baoshan basin.

Table 1. Statistical results of the groundwater chemical parameters.

Indicators	Groundwater System I (n = 22)				Groundwater System II (n = 9)				Groundwater System III (n = 4)			
	Min	Max	Mean	Cv	Min	Max	Mean	Cv	Min	Max	Mean	Cv
pH	6.17	8.27	7.81	0.07	7.22	8.29	7.96	0.05	7.63	8.17	7.83	0.03
TDS	186.00	617.00	343.20	0.38	230.00	751.00	484.56	0.38	247.00	320.00	293.75	0.12
TH	117.00	446.00	278.86	0.32	135.00	442.00	278.00	0.41	159.00	379.00	291.00	0.33
Na^+	15.70	75.00	28.40	0.49	14.50	54.00	27.46	0.51	19.30	25.80	23.18	0.12
K^+	1.11	19.20	7.22	0.92	0.58	28.00	9.65	0.94	2.73	12.40	7.81	0.58
Ca^{2+}	29.30	182.00	78.79	0.46	45.00	126.00	84.67	0.37	38.60	45.30	42.33	0.07
Mg^{2+}	12.40	73.30	28.34	0.53	14.90	39.10	22.53	0.37	19.10	64.70	36.15	0.55
Cl^-	5.80	46.10	27.39	0.42	7.30	55.40	25.96	0.61	8.70	37.90	25.73	0.49
SO_4^{2-}	0.00	33.22	11.66	0.90	5.10	40.40	22.98	0.53	8.30	31.20	19.30	0.66
HCO_3^-	55.59	146.00	110.06	0.19	89.80	146.00	123.39	0.13	61.70	108.00	92.18	0.23
NH_3-N	0.00	1.40	0.15	2.55	0.00	19.90	2.62	2.48	0.00	0.70	0.23	1.47
Fe^{2+}	0.00	0.78	0.07	2.83	0.00	0.26	0.03	3.00	0.00	0.00	/	/
Mn^{2+}	0.00	1.14	0.15	2.12	0.00	0.17	0.02	2.66	0.00	0.00	/	/
COD	0.35	6.53	1.44	1.09	0.51	1.34	0.80	0.37	0.46	0.74	0.56	0.22

Notes: pH is dimensionless, the rest of the units are mg/L; "/" means there is no such calculation result.

By analyzing the relationship between the ratio of the molarity of ions to the molarity of the total dissolved ions and TDS, the contribution of the major ionic components to TDS in groundwater can be obtained (Figure 4). The contribution of HCO_3^- to TDS ranges from 19.8% to 60.8%; the contribution of Ca^{2+} to TDS ranges from 11.5% to 37.4%; and the contribution of Na^+ to TDS ranges from 4.9% to 19.8%. The anion with the highest contribution to TDS in all three groundwater systems was HCO_3^-, and the cations with high contribution were Ca^{2+} and Na^+. This shows that the highest content of HCO_3^-, Ca^{2+}, and Na^+ in the groundwater of the study area is consistent with the results of the statistical characteristic value analysis of water chemistry parameters.

3.2. Hydrochemical Types

The Piper trilinear diagram can reflect the main anions and cations in groundwater and their concentration ratios, and provides a classification basis for analyzing groundwater chemical types [33], which plays a very important role in revealing hydrogeochemical

laws. According to the analysis of the Piper diagram (Figure 5), the water sample points mainly fall in the 1/3/5 zone of the Piper diagram, indicating that the mass concentrations of alkaline earth metal ions in the samples all exceed the mass concentrations of alkali metal ions. Ca^{2+} was the dominant cation in the study area, with concentrations ranging from 25.16% to 70.81% milligram equivalent percent, followed by Mg^{2+} and Na^{+}, with concentrations ranging from 15.9% to 61.29% and 8.48% to 36.12% milligram equivalent percent, respectively. HCO_3^{-}, a weak acid ion, is the core anion in the study area, with the concentration of this ion ranging from 37.05% to 93.6% milligram equivalent percent, followed by Cl^{-}, with concentrations ranging from 6.4% to 46.11% milligram equivalent percent.

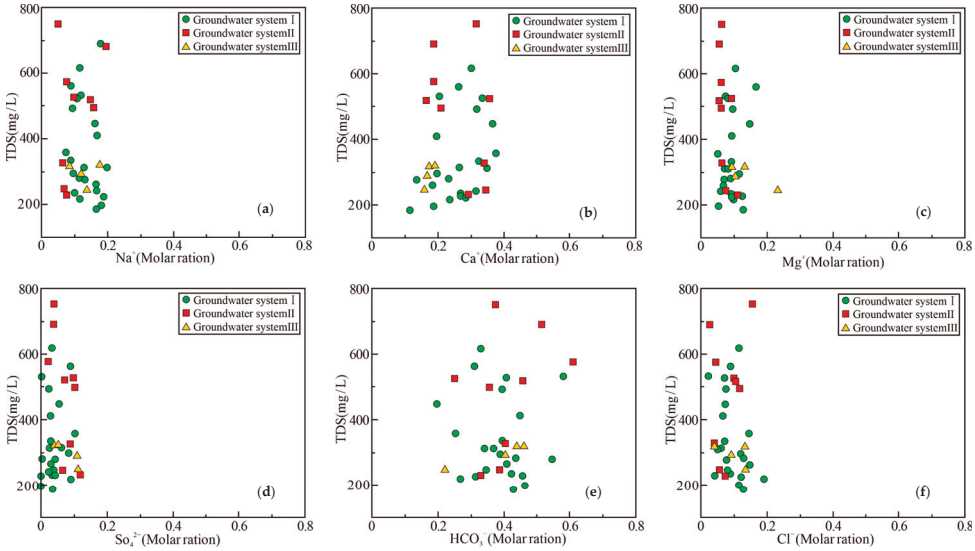

Figure 4. Contribution of major ions to TDS in groundwater: (**a**) contribution of Na^{+} to TDS; (**b**) contribution of Ca^{2+} to TDS; (**c**) contribution of Mg^{2+} to TDS; (**d**) contribution of SO_4^{2-} to TDS; (**e**) contribution of HCO_3^{-} to TDS; (**f**) contribution of Cl^{-} to TDS.

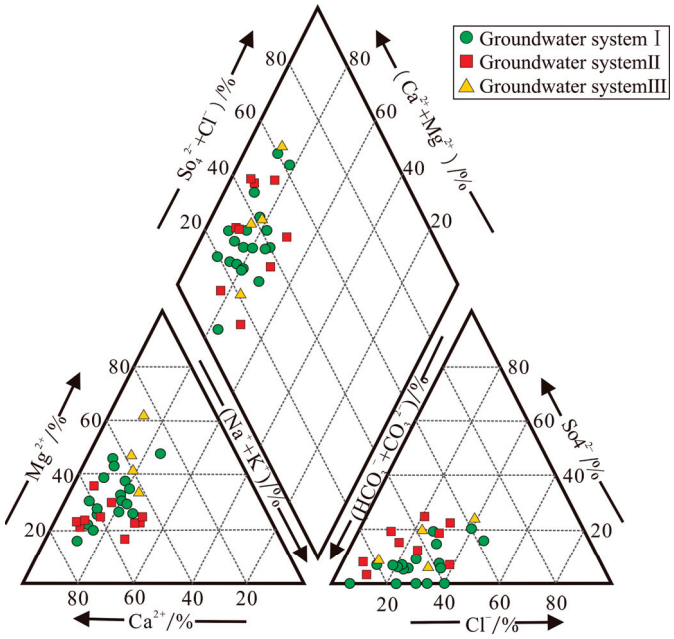

Figure 5. The Piper trilinear diagram for the groundwater samples.

The hydrochemical types in the study area include HCO_3-Ca, HCO_3-Ca-Na type, HCO_3-Ca-Mg type, HCO_3-Cl^-Ca type, Cl^-Ca type, HCO_3-Cl^-Ca-Na type, and HCO_3-Cl^-Ca-Mg type. The groundwater chemistry types at the groundwater sample sites in groundwater system III were all HCO_3-Ca-Mg types. Each hydrochemical type was distributed in groundwater system I and groundwater system II, and the HCO_3-Ca-Mg and HCO_3-Ca types were the main groundwater chemistry types in the study area.

Total salinity (TIS) is another important indicator used to characterize groundwater chemistry; it characterizes the sum of the concentrations of the major anions and cations. The major anions (SO_4^{2-} and HCO_3^-+Cl^-) in the water samples were selected as characteristic values [34] and the isosalinity contours were plotted (Figure 6). The water sample points of groundwater system I were distributed between 7 and 16 meq·L^{-1} salinity contours, the water sample points of groundwater system II were distributed between 9 and 16 meq·L^{-1} salinity contours, and the water sample points of groundwater system III were distributed between 7 and 11 salinity contours. The milligram equivalent concentration of SO_4^{2-} at each water sample site was less than 0.50 meq·L^{-1}, while the milligram equivalent concentration of HCO_3^-+Cl^- was greater than 1.75 meq·L^{-1}, indicating that the main anions in the groundwater of the Baoshan basin were HCO_3^-. Among the individual groundwaters, the groundwater of groundwater system II had the highest percentage of HCO_3^-+Cl^- while groundwater system III had the least.

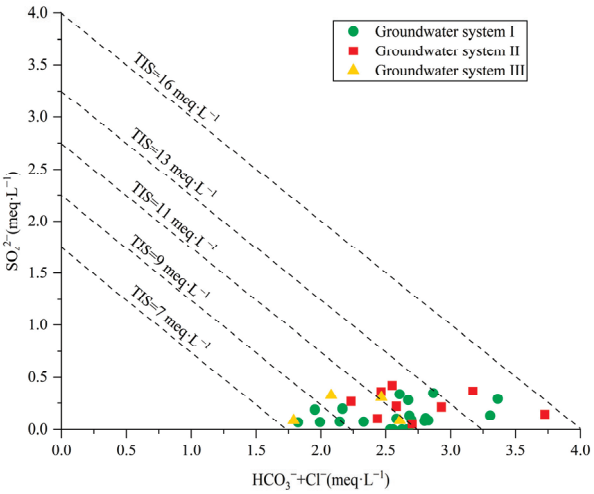

Figure 6. Correlation diagram of SO_4^{2-} and HCO_3^-+Cl^-.

3.3. Natural Sources of Groundwater Ion Fractions

3.3.1. Gibbs Plots

Gibbs plots can directly reflect the constraints and formation system of the main ions in the water column, including water–rock interaction, evaporation, and rainfall, which can lead to changes in the chemical composition of the groundwater column and changes in TDS [35].

The TDS values of the shallow groundwater of the quaternary system in the Baoshan basin ranged from 186 mg/L to 751 mg/L, $Na^+/(Na^+{+}Ca^{2+})$ from 0.12 to 0.52, and $Cl^-/(Cl^-{+}HCO_3^-)$ from 0.04 to 0.42. The groundwater sample points of the three groundwater systems were mostly scattered in the area where the $Na^+/(Na^+{+}Ca^{2+})$ and $Cl^-/(Cl^-{+}HCO_3^-)$ were less than 0.5 in the horizontal coordinate (Figure 7). The anions and cations in the groundwater mainly originated from the material exchange between the groundwater and the surrounding rock layers. The $Na^+/(Na^+{+}Ca^{2+})$ of individual water sample points in groundwater system I was greater than 0.5 and the water sample points were shifted to the upper right region, indicating that the groundwater at these water sample points is buried at a shallow depth and is affected by evaporation to an extent.

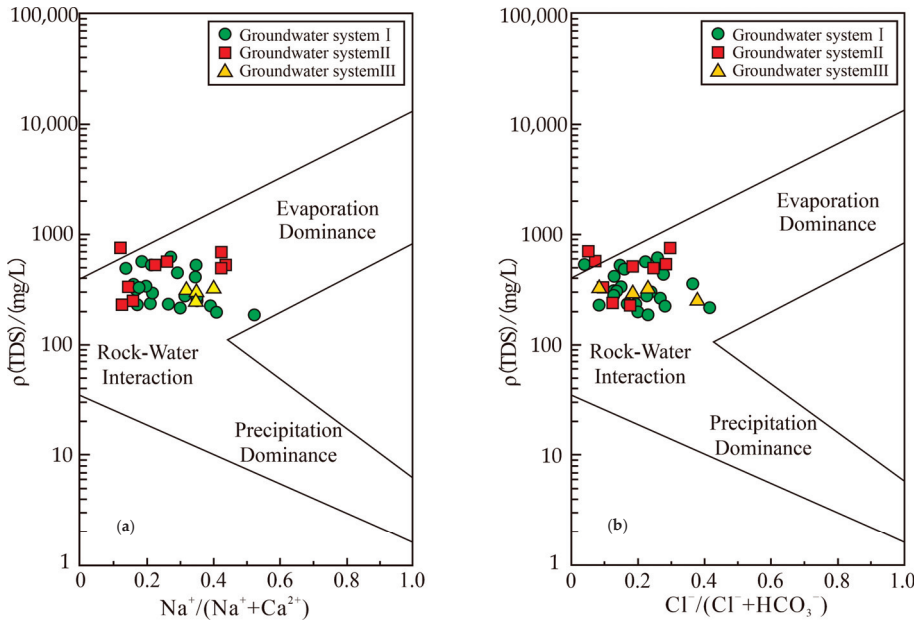

Figure 7. Gibbs plots of groundwater: (**a**) relationship between $Na^+/(Na^+ + Ca^{2+})$ and TDS and (**b**) relationship between $Cl^-/(Cl^- + HCO_3^-)$.

3.3.2. Dissolved Filtration of Rocks

The Gibbs plots allow a preliminary judgment to be made: the hydrochemical genesis of groundwater in the study area is closely related to water–rock interaction. To illustrate the specific water–rock interaction process, the Gaillardet model needs to be invoked for a further explanation of the water–rock process [36]. The model has three different units of water–rock interaction along the diagonal of the rectangle from the lower left to the upper right corner for evaporite, silicate, and carbonate rocks, in that order. The ratio of HCO_3^-/Na^+ to Ca^{2+}/Na^+ is calculated, and the position of this value in the model is the type of water–rock interaction. The Gaillardet model was established based on the test data of groundwater samples taken from the study area (Figure 8), from which it can be seen that the groundwater sample points in the study area are mainly located in the action interval of silicate and carbonate rocks, and far from the evaporite action interval. Combined with the types of geotechnical bodies in and around the basin, a preliminary conclusion can be drawn that the formation of groundwater chemical characteristics in the basin is mainly related to the dissolution and filtration of carbonate rocks and silicate rocks.

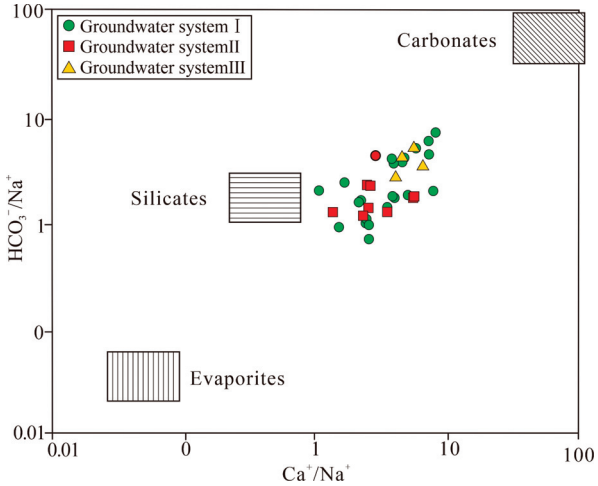

Figure 8. Gaillardet diagram based on the relationship between Ca^{2+}/Na^+ and HCO_3^-/Na^+.

3.3.3. Ion Proportionality Coefficient Characteristics

Through the Gaillardet model analysis, only the types of rocks that exchange material with groundwater in the basin can be known as carbonate rocks and silicate rocks. However, it is not possible to analyze which rock types exchange material with groundwater more strongly; thus, the ionic proportion coefficient method is needed in order to make any further judgment [37].

The ratio of Na^+ and Cl^- concentrations is called the groundwater genesis factor, a hydrogeochemical parameter characterizing the degree of Na^+ enrichment in groundwater [37]. If the value of Na^+/Cl^- in groundwater is close to 1, this indicates that Na^+ and Cl^- in groundwater mainly originate from the atmospheric precipitation or dissolution of rock salt; if the value is >1, this indicates that Na^+ and Cl^- may originate from cation exchange [37]. The Na^+/Cl^- ion ratio coefficient relationship (Figure 9) shows that most groundwater samples have a good correlation between sodium and chloride ions. There are 85.8% of groundwater sampling points with $Na^+/Cl^- > 1$, indicating that Na^+ and Cl^- are mainly subject to alternate cation adsorption. A total of 14.2% of groundwater sampling points with $Na^+/Cl^- < 1$ confirm that the source of Cl^- is not unique and that the possibility of groundwater contamination by human activities (domestic sewage and livestock manure effluent) is extremely high.

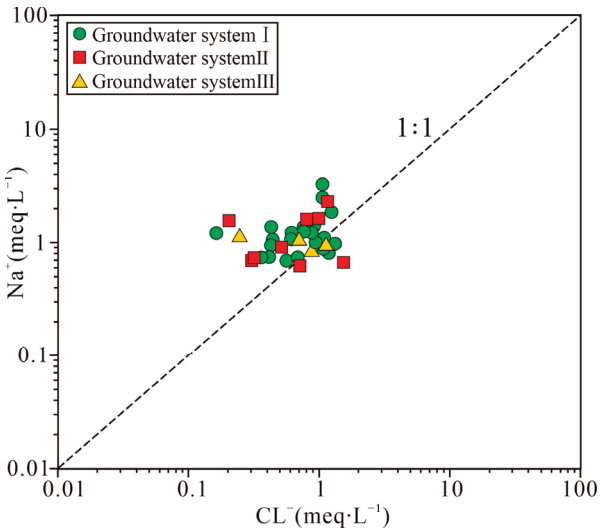

Figure 9. Relationship between Na^+ and Cl^-.

The contribution of the dissolution of other rock types to groundwater chemistry can be judged by the relationship of the ratio coefficient of $(Ca^{2+}+Mg^{2+})/(SO_4^{2-}+HCO_3^-)$. When the sample points are located above the 1:1 line, $Ca^{2+}+Mg^{2+}$ is more than $SO_4^{2-}+HCO_3^-$, implying that the water–rock interaction is dominated by the dissolution of carbonate rocks. When the sample points are located below the 1:1 line, this indicates that the water–rock interaction is dominated by weathering dissolution of silicate rocks. The groundwater sample points in all three groundwater systems are located above the 1:1 line (Figure 10), indicating that carbonate rocks are the main factors controlling the sources of Ca^{2+}, Mg^{2+}, SO_4^{2-}, and HCO_3^- in groundwater in the Baoshan basin. The dissolved amount of carbonate rocks in groundwater system I and groundwater system III is greater than that in groundwater system II.

According to the $(Cl^-+SO_4^{2-})/HCO_3^-$ ratio coefficient relationship (Figure 11), the water sample points in groundwater system III are all located below the 1:1 line, indicating that the groundwater components in this system mainly originate from carbonate rock dissolution in the mountains around the basin. Most of the water sample points in groundwater system I and groundwater system II are located below the 1:1 line, indicating that the groundwater components in the system mainly originate from carbonate rock dissolution. A small number of water sample points near Hanzhuang are located above the 1:1 line,

which is due to the poor runoff conditions in the area, which mainly dissolve materials in the loose quaternary rock layers. In general, most of the groundwater sample points in the study area are distributed below the 1:1 line and a small number of water sample points are distributed below the 1:1 line, indicating that the dissolution of carbonate rocks dominates in the groundwater of the study area.

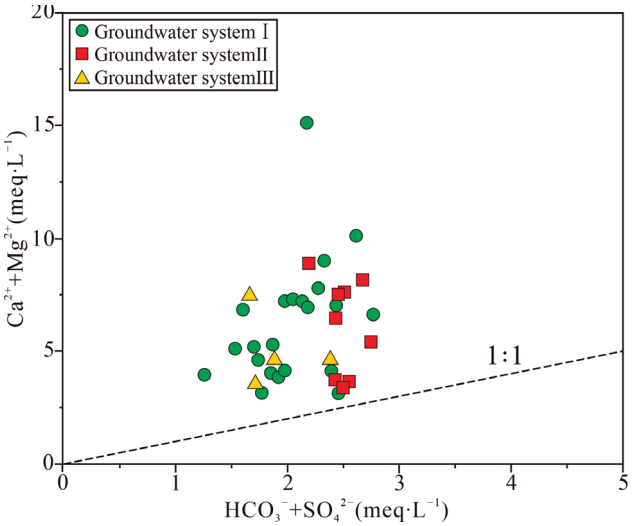

Figure 10. Relationship between ($Ca^{2+}+Mg^{2+}$) and ($SO_4^{2-}+HCO_3^-$).

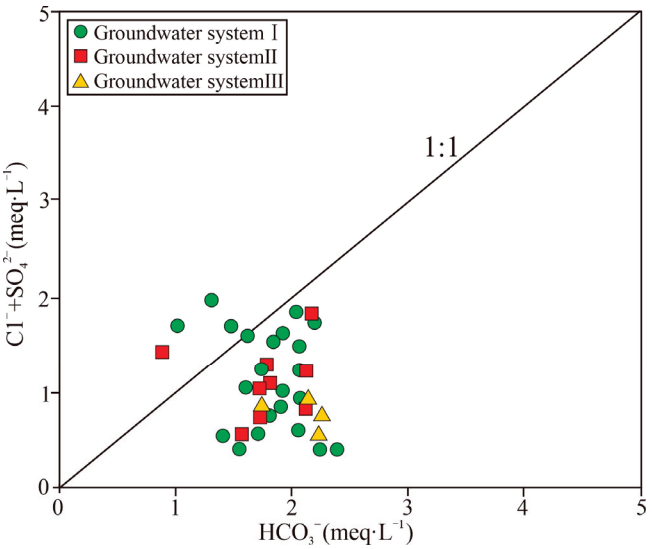

Figure 11. Relationship between ($Cl^-+SO_4^{2-}$) and HCO_3^-.

The cations in groundwater in the basin alternatively adsorb with the cations in the rock and soil bodies on the runoff pathway during the runoff process. The dissolution of atmospheric CO_2 in groundwater, which results in the production of HCO_3^- in groundwater, accelerates the dissolution rate of carbonate rocks following the following chemical equation:

$$CaCO_3+CO_2+H_2O \leftrightharpoons Ca^{2+}+2HCO_3^- \quad (1)$$

$$MgCO_3+CO_2+H_2O \leftrightharpoons Mg^{2+}+2HCO_3^- \quad (2)$$

$$CaMg(CO_3)_2+CO_2+H_2O \leftrightharpoons Ca^{2+}+Mg^{2+}+4HCO_3^- \quad (3)$$

The dissolution of limestones and argillaceous limestones leads to higher Ca^{2+} and Mg^{2+} concentrations in groundwater. The low mineralization of groundwater in the basin provides favorable conditions for the alternating cation adsorption of Ca^{2+} and Mg^{2+} in groundwater, with Na^+ and K^+ attached to the surface of rock and soil bodies. However, as the concentration of Na^+ and K^+ in groundwater increases, it may cause a reverse reaction. In this study, the chloride and alkali index was selected to analyze the specific exchange process of groundwater in the basin [38].

$$CAI1 = Cl^- - \left(Na^+ + K^+\right)/Cl^- \tag{4}$$

$$CAI2 = Cl^- - \left(Na^+ + K^+\right)/SO_4^{2-} + HCO_3^- + NO_3^- + CO_3^{2-} \tag{5}$$

The exchange of cations in groundwater can be divided in two ways: forward exchange and reverse exchange.

The positive cation exchange effect is

$$\begin{aligned}(Ca^{2+}\text{or } Mg^{2+})(\text{rock}) + 2Na^+(\text{groundwater}) \\ \rightarrow 2Na^+\text{rock} + (Ca^{2+}\text{or } Mg^{2+})(\text{groundwater})\end{aligned} \tag{6}$$

The reverse cation exchange interaction is

$$\begin{aligned}2Na^+\text{rock} + (Ca^{2+}\text{or } Mg^{2+})(\text{groundwater}) \\ \rightarrow (Ca^{2+}\text{or } Mg^{2+})(\text{rock}) + 2Na^+(\text{groundwater})\end{aligned} \tag{7}$$

According to the chlor-alkali index in the study area (Figure 12), the vast majority of water sample points in groundwater system III fall into the CAI1 < 0 and CAI2 < 0 regions, indicating that reverse exchange occurs in this groundwater system and that the Ca^{2+} and Mg^{2+} contents in groundwater are reduced. Most of the water sample points in groundwater system I and groundwater system II fall in the area of CAI1 < 0 and CAI2 < 0. Only in the area around Hanzhuang do the water sample points fall into the area of CAI1 > 0 and CAI2 > 0, indicating that the Ca^{2+} and Mg^{2+} contents are high in most areas of the two groundwater systems and that it is easy for reverse exchange to occur. In the area of Hanzhuang, positive exchange occurs due to the low Ca^{2+} and Mg^{2+} contents in the groundwater.

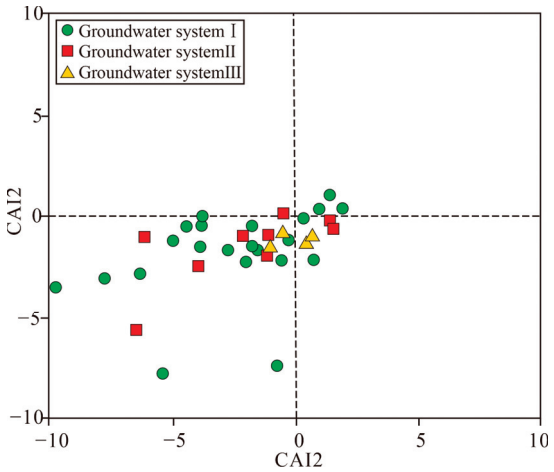

Figure 12. Chloro-alkaline indices diagram of groundwater.

3.3.4. Groundwater Saturation Index

To further understand the presence of possible mineral phases and the dissolution state in groundwater, the saturation index (SI) of minerals was calculated using PHREEQC software [39]. When SI < 0, this indicates that the mineral is in an unsaturated (dissolved)

state, while SI > 0 means that the mineral is in a saturated (precipitated) state and SI = 0 means that the aqueous solution is exactly in equilibrium with the mineral [39]. In the three groundwater systems, the average saturation indices were 0.12, 0.38, and −0.13 for calcite, 0.09, 0.49, and −0.34 for dolomite, and 0.01, 0.38, and −0.43 for aragonite, respectively, and the above minerals were basically in equilibrium in the groundwater (Figure 13). The average saturation indices of hard gypsum, gypsum, rock salt, and potassium salt in the three groundwater systems were less than 0, and the above minerals were in an unsaturated state in the groundwater. This indicates that the weathering dissolution of calcite and dolomite is the main controlling factor of the chemical composition in the groundwater, which is consistent with the results of the previous analysis.

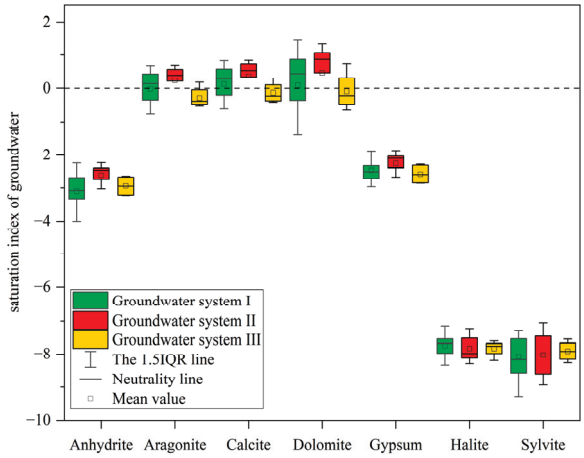

Figure 13. Box diagram of groundwater mineral saturation index in Baoshan basin.

3.4. Chemical Controlling Factors of Groundwater

The groundwater chemical characteristics of the study area are influenced by human activity factors in addition to hydrogeological conditions, water–rock interactions, and alternate cation adsorption. To further determine the degree of influence of each indicator on the chemical characteristics of the groundwater, a model was used to conduct a further analysis [40,41]. A total of fourteen indicators, including pH, K^+, Na^+, Ca^{2+}, Mg^{2+}, Cl^-, $SO_4{}^{2-}$, $HCO_3{}^-$, TDS, TH, Fe^{2+}, Mn^{2+}, NH_3-N, and COD, were selected for factor analysis considering both the detection rate and exceedance. The KMO-Bartlett sphericity test was performed for each index and the significance level was close to 0, indicating a strong correlation between the index variables that satisfied the test criteria. The Kaiser normalized maximum variance method was used to rotate the component matrix; four main factors (F1, F2, F3, and F4) were obtained, with a cumulative variance contribution of 77.84% (Table 2).

Table 2. Total variance interpretation for PCA analysis of groundwater samples.

Ingredients	Initial Eigenvalue			Extraction of the Sum of Squares of Loads			Sum of Squared Rotating Loads		
	Total	Variance (%)	Accumulation (%)	Total	Variance (%)	Accumulation (%)	Total	Variance (%)	Accumulation (%)
1	4.517	32.262	32.262	4.517	32.262	32.262	4.059	28.990	28.990
2	3.430	24.499	56.761	3.430	24.499	56.761	2.639	18.850	47.840
3	1.738	12.413	69.173	1.738	12.413	69.173	2.442	17.441	65.281
4	1.213	8.667	77.841	1.213	8.667	77.841	1.758	12.560	77.841

The main loads of dissolution filtration, migration, and enrichment factors (F1) are Ca^{2+}, Mg^{2+}, $SO_4{}^{2-}$, TDS, and TH (Table 3), with contributions of 64.56%, 84.72%, 76.14%, 86.52%, and 85.33%, respectively (Figure 14). The aquifer in the plain area has loose granular material, well-developed voids, and good runoff conditions, and the dissolution of carbonate and silicate rocks, such as tuffs, muddy tuffs, sedimentary clastic rocks, and clays, is the dominant factor in groundwater circulation. Meanwhile, the dissolution and enrichment of minerals during groundwater flow affects the changes in TDS and TH. During this process, the pore space of the aquifer is developed, the runoff is strong, the

hydraulic slope to the plain area gradually becomes slower, and the abundant carbonate rock and silicate rock minerals in the area are subject to the hydrogeochemical effect of dissolution–filtration–enrichment during the groundwater runoff process. As the local SO_4^{2-} concentration is high, there may be deep hot water recharge as well.

Table 3. Rotation factor loading matrix of groundwater indicators.

Water Chemistry Index	Ingredients			
	F1	**F2**	**F3**	**F4**
Zscore (pH)	0.273	−0.097	0.853	0.043
Zscore (Na^+)	0.036	0.818	−0.144	0.085
Zscore (K^+)	0.026	0.801	−0.326	0.061
Zscore (Ca^{2+})	0.754	0.271	0.232	−0.460
Zscore (Mg^{2+})	0.870	−0.067	0.061	−0.008
Zscore (Cl^-)	0.485	0.796	0.038	0.087
Zscore (SO_4^{2-})	0.725	−0.001	−0.139	−0.33
Zscore (HCO_3^-)	−0.178	−0.212	0.847	−0.143
Zscore (TDS)	0.977	0.087	0.025	−0.010
Zscore (TH)	0.978	0.103	0.032	−0.008
Zscore (Fe^{2+})	−0.417	0.451	0.247	0.817
Zscore (Mn^{2+})	0.043	−0.158	−0.148	0.859
Zscore (NH_3-N)	−0.216	0.556	0.103	0.720
Zscore (COD)	−0.083	0.488	−0.114	0.801

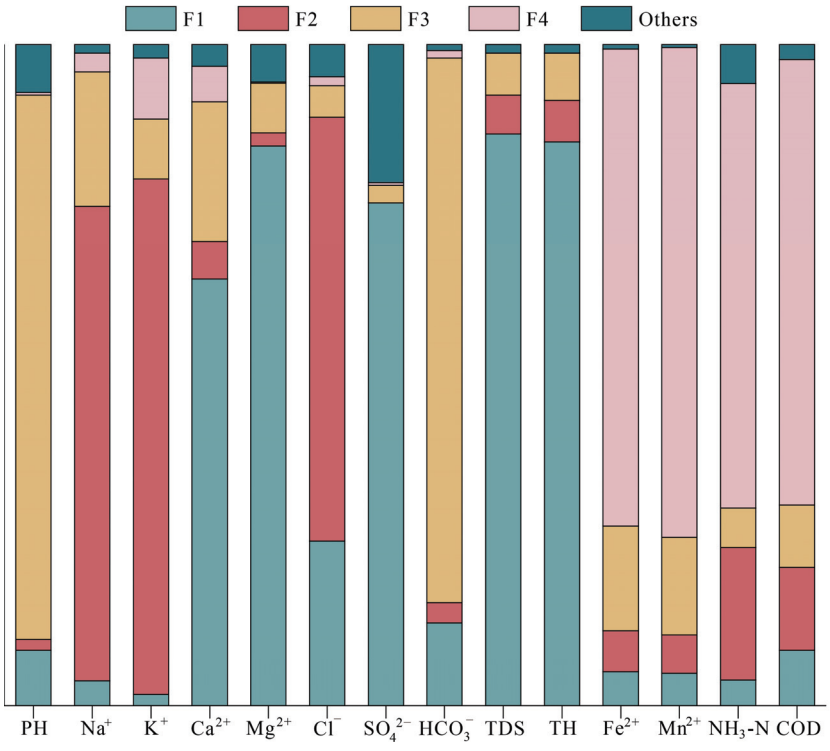

Figure 14. Contribution rate of index source for each factor.

The geological and anthropogenic factors (F2) are mainly loaded with Na^+, K^+, and Cl^- (Table 3), with contributions of 72.02%, 78.10%, and 64.19%, respectively (Figure 14). The center of the Baoshan basin is mainly deposited in the river and lake phase, and Na^+, K^+, and Cl^- are mainly derived from the cation exchange of groundwater in the basin. The center of the basin is densely inhabited and the rocks are highly permeable; thus, the groundwater is transported faster. Massive fertilization due to agriculture leads to

the transport of groundwater to the central part of the basin, while Na^+, K^+, and Cl^- in agricultural wastewater gather in the center of the basin.

The main loads of the environmental factors (F3) are pH and HCO_3^- (Table 3), with contribution rates of 82.36% and 82.38%, respectively (Figure 14). HCO_3^- in the region mainly derives from carbonate dissolution; the main lithologies in the area, such as Mawangtun in the northeastern part of the Baoshan basin and Hanzhuang in the western part, are tuffs and muddy tuffs; the groundwater runoff conditions in the pre-hill zone are strong, and carbonate weathering dissolution is strong and dominated by dissolution and filtration. Meanwhile, the shallow groundwater is mainly recharged by atmospheric precipitation, and the two together make HCO_3^- the main anion in groundwater.

The main loads of the pollution factors (F4) are Fe^{2+}, Mn^{2+}, NH_3-N, and COD (Table 3), with contributions of 72.24%, 73.44%, 64.31%, and 65.48%, respectively (Figure 14). The pleistocene quaternary in the Baoshan basin is rich in ilmenite, and the dissolution of water leads to Fe^{2+} and Mn^{2+} in the groundwater. The mineral layer contains pore pressurized water, and the top and bottom plates of the mineral layer are clay and red clay, which are poorly water-rich and have a relatively water-insulating effect, providing favorable conditions for the enrichment of Fe and Mn ions in the groundwater. The concentration of NH_3-N and COD increases due to livestock breeding, agricultural fertilization, and industrial wastewater. The high concentration of NH_3-N and COD in groundwater indicates the presence of organic matter pollution, and ammonia nitrogen dissolves in water, making the groundwater environment reductive, which in turn reduces the material in titaniferous sand ore to divalent free state Fe and Mn, causing the concentration of Fe^{2+} and Mn^{2+} in groundwater to increase.

4. Conclusions

Shallow groundwater chanting of the quaternary is widely used in the production and life of the inhabitants of the Baoshan basin. In this paper, the chemical evolution of groundwater and the causes of water contamination in the Baoshan basin are discussed using mathematical and statistical methods, the TIS diagram, Piper's trilinear diagram, Gibbs plots, the Gaillardet model, the ion scale factor, the saturation index, and the PCA-APCS-MLR model. The following conclusions can be drawn.

(1) The geochemical type of the shallow groundwater of the quaternary in the Baoshan basin is dominated by HCO_3-Ca-Mg and HCO_3-Ca. The main cations are Ca^{2+}, Na^+, and Mg^{2+}, and the main anions are HCO_3^- and Cl^-, among which Ca_{2+}, Na_+, and HCO_3^- have a high contribution to TDS, which is consistent with the results of the statistical eigenvalue analysis of water chemistry parameters. The total salinity (TIS) corroborates that HCO_3^- is the main anion in the region. Fe^{2+}, Mn^{2+}, and NH_3-N have variation coefficients greater than 1 in groundwater systems I and II, and are the main pollutants in the groundwater of the Baoshan basin.

(2) The genesis of water chemical characteristics is mainly influenced by water–rock interaction. The types of rocks with which material exchange with groundwater occurs are carbonate rocks (limestones, argillaceous limestones, red clay) and silicate rocks (sandstone, shale, clay), which are the main sources controlling Ca^{2+}, Mg^{2+}, SO_4^{2-}, and HCO_3^- in the groundwater of the Baoshan basin. Na^+, K^+, and Cl^- in groundwater mainly originate from alternate cation adsorption, and agricultural pollution is an important source as well. According to the results of the PHREEQC softwares calculation of groundwater mineral saturation, it is clear that the weathering dissolution of calcite and dolomite is the main controlling factor of chemical composition in the groundwater, which is consistent with the results of the previous analysis.

(3) Based on the calculation results of the PCA-APCS-MLR model, four main factors were obtained, namely, dissolved filtration, migration, and enrichment (F1), geological and human activity (F2), environmental factors (F3), and pollution factors (F4), with a cumulative variance contribution of 77.84%. F1 was mainly loaded with Ca^{2+},

Mg^{2+}, $SO_4{}^{2-}$, TDS, and TH; for F2, the main loads were Na^+, K^+, and Cl^-; for F3, the main loads were pH and $HCO_3{}^-$; and for F4, the main loads were Fe^{2+}, Mn^{2+}, NH_3-N, and COD. Pollution due to Fe^{2+} and Mn^{2+} mainly derives from the groundwater dissolved filtration of titaniferous sand ore in the quaternary strata and industrial wastewater discharge, while NH_3-N pollution mainly derives from the direct discharge of domestic and agricultural wastewater.

In view of the current situation that Fe^{2+}, Mn^{2+}, and NH_3-N exceed standards in the shallow groundwater of the quaternary in the Baoshan basin, the spatial distribution characteristics and migration pattern of pollutants should be further studied. Industrial wastewater and agricultural wastewater should be discharged after reaching the standards to prevent further pollution of the groundwater.

Author Contributions: Conceptualization, S.X.; methodology, T.G.; software, Y.X. and J.Z.; validation, S.X.; formal analysis, J.Z.; investigation, Y.X. and J.Z.; resources, A.L. and S.X.; data curation, Y.X.; writing—original draft preparation, Y.X.; writing—review and editing, A.L. and X.G.; visualization, J.Z.; supervision, X.D. and P.Z.; project administration, A.L.; funding acquisition, A.L. All authors have read and agreed to the published version of the manuscript.

Funding: This work was supported by the "Ten Thousand People Plan" of China for Science and Technology Innovation Leaders and the National Natural Science Foundation of China (Grant No. 52179028).

Data Availability Statement: The data presented in this study are available on request from the corresponding author.

Acknowledgments: The authors thank Yanhua Zhang, Jianhua Chai, Hongyi Fu, and Songtao Han for their fieldwork support. At the same time, the reviewers gave a lot of constructive comments. The editors were very efficient in handling the manuscript throughout the process. We would like to express our gratitude here.

Conflicts of Interest: The authors declare no conflict of interest.

References

1. Habibah, A.A.; Dahab, K.; Shabana, A.; Kamh, S.; Ibrahim, H. Assessment of the Hydrogeochemical Characteristics of Groundwater Resources at some Wadis in the East of El Minia Governorate, Eastern Desert, Egypt. *J. Acta Geol. Sin.* **2022**, *96*, 1082–1097. [CrossRef]
2. Gao, Y.; Chen, J.; Qian, H.; Wang, H.; Ren, W.; Qu, W. Hydrogeochemical characteristics and processes of groundwater in an over 2260 year irrigation district: A comparison between irrigated and nonirrigated areas. *J. Hydrol.* **2022**, *606*, 127437. [CrossRef]
3. Jabbo, J.N.; Isa, N.M.; Aris, A.Z.; Ramli, M.F.; Abubakar, M.B. Geochemometric approach to groundwater quality and health risk assessment of heavy metals of Yankari Game Reserve and its environs, Northeast Nigeria. *J. Clean. Prod.* **2022**, *330*, 129916. [CrossRef]
4. Jha, S.K.; Mishra, V.K.; Verma, C.L.; Sharma, N.; Sharma, B.R. Groundwater quality concern for wider adaptability of novel modes of managed aquifer recharge (MAR) in the Ganges Basin, India. *Agric. Water Manag.* **2021**, *246*, 106659. [CrossRef]
5. Takaya, K. Long-Term Reaction Characteristics of CO_2-Water-Rock Interaction: Insight into the Potential Groundwater Contamination Risk from Underground CO_2 Storage. *Resour. Geol.* **2018**, *68*, 93–100. [CrossRef]
6. Abdelgawad, A.M.; Watanabe, K.; Takeuchi, S. Water-rock interaction study on the occurrence of fluoride-rich groundwater at Mizunami area, Japan. *Environmentasia* **2009**, *2*, 20–29.
7. Jiang, J.; Fu, G.; Feng, Y.; Gu, X.; Jiang, P.; Shen, C.; Chen, Z. Characteristics and Causes of Coastal Water Chemistry in Qionghai City, China. *Appl. Sci.* **2023**, *13*, 5579. [CrossRef]
8. Chen, L.; Wang, G.; Hu, F.; Wang, Y.; Liu, L. Groundwater hydrochemistry and isotope geochemistry in the Turpan Basin, northwestern China. *J. Arid Land* **2014**, *6*, 378–388. [CrossRef]
9. Soboleva, E.B.; Tsypkin, G.G. Regimes of haline convection during the evaporation of groundwater containing a dissolved admixture. *Fluid Dyn.* **2016**, *51*, 364–371. [CrossRef]
10. Meredith, K.T.; Hollins, S.E.; Hughes, C.E.; Cendón, D.I.; Chisari, R.; Griffiths, A.; Crawford, J. Evaporation and concentration gradients created by episodic river recharge in a semi-arid zone aquifer: Insights from Cl−, δ18O, δ2H, and 3H. *J. Hydrol.* **2015**, *529*, 1070–1078. [CrossRef]
11. Kim, K.; Yun, S.T. Buffering of sodium concentration by cation exchange in the groundwater system of a sandy aquifer. *Geochem. J.* **2005**, *39*, 273–284. [CrossRef]

12. Xing, L.; Gao, H.; Zhan, Y. Groundwater hydrochemical characteristics and processes along flow paths in the North China Plain. *J. Asian Earth Sci.* **2013**, *S70–S71*, 250–264. [CrossRef]
13. Liu, Y.; Zhou, X.; Deng, Z.; Fang, B.; Tsutomu, Y.; Zhao, J.; Wang, X. Hydrochemical characteristics and genesis analysis of the Jifei hot spring in Yunnan, southwestern China. *Geothermics* **2015**, *53*, 38–45. [CrossRef]
14. Tian, X.; Fei, Y.-H.; Zhang, J.-L.; Li, Y.-S.; Dun, Y.; Guo, C.-Y. Analysis on hydrochemical characteristics of groundwater in strongly exploited area in Hutuo River Plain. *J. Groundw. Sci. Eng.* **2017**, *2*, 44–53.
15. Nathaniel, A.; Abigail, A. Comparative Analysis of the Hydrochemical Characteristics of Ground Water Sources Found within the Kassena Nankana East District of the Upper East Region of Ghana. *Am. J. Min. Met.* **2017**, *4*, 45–50.
16. Chotpantarat, S.; Thamrongsrisakul, J. Natural and anthropogenic factors influencing hydrochemical characteristics and heavy metals in groundwater surrounding a gold mine, Thailand. *J. Asian Earth Sci.* **2021**, *211*, 104692. [CrossRef]
17. Li, J.; Wang, W.; Wang, D.; Li, J.; Dong, J. Hydrochemical and Stable Isotope Characteristics of Lake Water and Groundwater in the Beiluhe Basin, Qinghai—Tibet Plateau. *Water* **2020**, *12*, 2269. [CrossRef]
18. Sivasubramanian, P.; Balasubramanian, N. Hydrochemical characteristics of coastal aquifers of Kadaladi, Ramanathapuram District, Tamilnadu, India. *Appl. Water Sci.* **2013**, *3*, 603–612. [CrossRef]
19. Pazand, K.; Khosravi, D.; Ghaderi, M.R.; Rezvaniyanzadeh, M.R. Identification of the hydrogeochemical processes and assessment of groundwater in a semi-arid region using major ion chemistry: A case study of Ardestan basin in Central Iran. *Groundw. Sustain. Dev.* **2018**, *6*, 245–254. [CrossRef]
20. Bouri, S.; Nsiri, M.; Brahim, F.B.; Khlifi, M. Assessment of the effects of anthropogenic activities on the El Arich groundwater using hydrogeochemistry, GIS and multivariate statistical techniques: A case study of the semi-arid Kasserine region, Tunisia. *Environ. Qual. Manag.* **2022**, *31*, 261–281.
21. Ren, K. Effects of Urbanization on Groundwater Quality of Laolongdong Watershed. In Proceedings of the First Joint Scientific Meeting of Geological Society of China (GS) Cand Geological Society of America (GSA) (Roof of the World), Chengdu, China, 17–19 June 2013; Volume 87, pp. 384–398.
22. Karunanidhi, D.; Subramani, T.; Roy, P.D.; Li, H. Impact of groundwater contamination on human health. *Environ. Geochem. Health* **2021**, *43*, 643–647. [CrossRef] [PubMed]
23. Meng, L.; Zuo, R.; Wang, J.S.; Yang, J.; Shi, R.T. Quantitative source apportionment of groundwater pollution based on PCA-APCS-MLR. *China Environ. Sci.* **2017**, *37*, 3773–3786.
24. Zhang, H.; Cheng, S.; Li, H.; Fu, K.; Xu, Y. Groundwater pollution source identification and apportionment using PMF and PCA-APCA-MLR receptor models in a typical mixed land-use area in Southwestern China. *Sci. Total Environ.* **2020**, *741*, 140383. [CrossRef]
25. Xiao, Y.; Zhang, J.; Guo, T. Evaluation of Quaternary Groundwater Quality Based on AHP-Entropy Weight Method in Baoshan Basin, Yunnan, China. *World Sci. Res. J.* **2021**, *7*, 76–82.
26. He, Y.; Li, N.; Wang, Z.; Wang, H.; Yang, G.; Xiao, L.; Wu, J.; Sun, B. Quercus yangyiensis sp. nov. from the late Pliocene of Baoshan, Yunnan and its paleoclimatic significance. *Acta Geol. Sin.* **2014**, *88*, 738–747. [CrossRef]
27. Yu, Y.; Wang, J.; Cheng, F.; Deng, H.; Chen, S. Drought monitoring in Yunnan Province based on a TRMM precipitation product. *Nat. Hazards* **2020**, *104*, 2369–2387. [CrossRef]
28. Bao, Z.Y. Hydrogeological Conditions and Searching for Groundwater in the Baoshan Region, Yunnan. *Acta Geol. Sichuan* **2012**, *32*, 87–91.
29. Han, Z.; Xiang, H.; Guo, S. Sinistral shear and extension of the northern section of Lijiang Basin in northwest Yunnan in Quaternary. *Chin. Sci. Bull.* **2005**, *50*, 452–459. [CrossRef]
30. Dai, S.; Liu, S.; Zhao, Y.; Zhao, Z.; Gao, F.; Wu, S.; Mou, F. The Formation and Evolution of the Baoshan Basin, Yunnan Province. *Pet. Geol. Exp.* **1998**, *S1*, 178–180.
31. Huang, H.; Liu, L. An Application of EVS Hybrid Modeling Method. *Soil Eng. Found.* **2022**, *36*, 208.
32. Green, C.T.; Bekins, B.A.; Kalkhoff, S.J.; Hirsch, R.M.; Liao, L.; Barnes, K.K. Decadal surface water quality trends under variable climate, land use, and hydrogeochemical setting in Iowa, USA. *Water Resour. Res.* **2014**, *50*, 2425–2443. [CrossRef]
33. Hoaghia, M.-A.; Roman, C.; Tanaselia, C.; Ristoiu, D. Groundwater chemistry rendering using Durov, Piper and ion balance diagrams. Study case: The northern part of Sibiu county. *Sud. Univ. Babeș-Bolyai Chem.* **2015**, *2*, 161–168.
34. Apollaro, C.; Tripodi, V.; Vespasiano, G.; De Rosa, R.; Dotsika, E.; Fuoco, I.; Critelli, S.; Muto, F.J.M.; Geology, P. Chemical, isotopic and geotectonic relations of the warm and cold waters of the Galatro and Antonimina thermal areas, southern Calabria, Italy. *Mar. Pet. Greol.* **2019**, *109*, 469–483. [CrossRef]
35. Marandi, A.; Shand, P. Groundwater chemistry and the Gibbs Diagram. *Appl. Geochem.* **2018**, *97*, 209–212. [CrossRef]
36. Wu, C.; Wu, X.; Lu, C.; Sun, Q.; He, X.; Yan, L.; Qin, T. Hydrogeochemical characterization and its seasonal changes of groundwater based on self-organizing maps. *Water* **2021**, *13*, 3065. [CrossRef]
37. Elumalai, V.; Rajmohan, N.; Sithole, B.; Li, P.; Uthandi, S.; van Tol, J. Geochemical evolution and the processes controlling groundwater chemistry using ionic ratios, geochemical modelling and chemometric analysis in uMhlathuze catchment, KwaZulu-Natal, South Africa. *Chemosphere* **2023**, *312*, 137179. [CrossRef]
38. Zhang, J.; Shi, Z.; Wang, G.; Jiang, J.; Yang, B. Hydrochemical characteristics and evolution of groundwater in the Dachaidan area, Qaidam Basin. *Earth Sci. Front.* **2021**, *28*, 194.

39. Apollaro, C.; Marini, L.; De Rosa, R. Use of reaction path modeling to predict the chemistry of stream water and groundwater: A case study from the Fiume Grande valley (Calabria, Italy). *Environ. Geol.* **2007**, *51*, 1133–1145. [CrossRef]
40. Li, W.; Wu, J.; Zhou, C.; Nsabimana, A. Groundwater pollution source identification and apportionment using PMF and PCA-APCS-MLR receptor models in Tongchuan City, China. *Arch. Environ. Contam. Toxicol.* **2021**, *81*, 397–413. [CrossRef]
41. Meng, L.; Zuo, R.; Wang, J.-S.; Yang, J.; Teng, Y.-G.; Shi, R.-T.; Zhai, Y.-Z. Apportionment and evolution of pollution sources in a typical riverside groundwater resource area using PCA-APCS-MLR model. *J. Contam. Hydrol.* **2018**, *218*, 70–83. [CrossRef]

Disclaimer/Publisher's Note: The statements, opinions and data contained in all publications are solely those of the individual author(s) and contributor(s) and not of MDPI and/or the editor(s). MDPI and/or the editor(s) disclaim responsibility for any injury to people or property resulting from any ideas, methods, instructions or products referred to in the content.

hydrology

MDPI

Article

How to Predict the Efficacy of Free-Product DNAPL Pool Extraction Using 3D High-Precision Numerical Simulations: An Interdisciplinary Test Study in South-Western Sicily (Italy)

Alessandra Feo [1], Federica Lo Medico [2,*], Pietro Rizzo [1], Maurizio Gasparo Morticelli [2], Riccardo Pinardi [1], Edoardo Rotigliano [2] and Fulvio Celico [1]

[1] Department of Chemistry, Life Sciences and Environmental Sustainability, University of Parma, 43124 Parma, Italy; alessandra.feo@unipr.it (A.F.); pietro.rizzo@unipr.it (P.R.); riccardo.pinardi@studenti.unipr.it (R.P.); fulvio.celico@unipr.it (F.C.)

[2] Department of Earth and Marine Sciences, University of Palermo, 90123 Palermo, Italy; maurizio.gasparo@unipa.it (M.G.M.); edoardo.rotigliano@unipa.it (E.R.)

* Correspondence: federica.lomedico@unipa.it

Abstract: Dense nonaqueous phase liquids (DNAPLs) are known to be denser than water and immiscible with other fluids. Once released into the environment, they migrate downward through the variably saturated zone, causing severe damage. For this reason, it is essential to properly develop a rapid response strategy, including predictions of contaminant migration trajectories from numerical simulations modeling. This paper presents a series of simulations of free-product DNAPL extraction by means of a purpose-designed pumping well. The objective is to minimize the environmental impact caused by DNAPL release in the subsurface, estimating the recoverable free-product DNAPL, depending on the hydraulic properties of the aquifer medium, and estimating the leaving residual DNAPL that could act as a long-term pollution source. Coupling the numerical simulations to the bacterial community characterization (through biomolecular analyses), it was verified that (i) the DNAPL recovery (mainly PCE at the study site) through a pumping well would be almost complete and (ii) the application of other remediation techniques (such as bioremediation) would not be necessary to remove the pollution source because (iii) a natural attenuation process is provided by the autochthonous bacterial community, which is characterized by genera (such as *Dechloromonas*, *Rhodoferax*, and *Desulfurivibrio*) that have metabolic pathways capable of favoring the degradation of chlorinated compounds.

Keywords: DNAPL; high-precision numerical simulations; free-product pumping

1. Introduction

Chlorinated organic compounds are widespread aquifer contaminants. They are referred to as dense nonaqueous-phase liquids (DNAPLs); therefore, they are denser than water, with very low water solubility, and capable of migrating under pressure and gravity forces through both unsaturated and saturated aquifer systems until reaching a bottom aquiclude (e.g., [1]). They are usually detected in industrial and urban areas due to their extensive application in chemical production, dry cleaning, and metal degreasing. These pollutants persist in the environment and are linked to toxic and sometimes carcinogenic effects (e.g., [2,3]). Several of these compounds are of great concern, as shown by the records of the Stockholm Convention on Persistent Organic Pollutants (POP).

The behavior and fate of chlorinated organic compounds in the subsurface have been studied since the early 1980s (e.g., [4–10]). Some numerical models, including models of migration [11,12] in fractured aquifers [13] and the remediation of alluvial aquifers [14] using MT3DMS numerical codes [15,16], have been written to simulate their migration in aquifer systems. There are numerous studies on contaminant transport resulting from

the dissolution of NAPL pools. Some examples of single-component pool dissolution studies include [17,18]. Some examples of multicomponent NAPL pool dissolution studies include [19,20]. Not only are numerical models available in the literature but numerous analytical models of contaminant transport from the dissolution of single-component NAPL pools in saturated porous media [21,22] and the dissolution of multicomponent DNAPL pools in an experimental aquifer [23] have been published.

The dynamics of spilled DNAPL migration in a variably saturated zones can be described using numerical simulations for the governing equations of immiscible-phase fluid flow in a porous medium. These equations are coupled conserved partial differential equations for each fluid flow, based on the Darcy equation, with the conservation of the mass and an equation of state. They are written as a function of each fluid flow's saturation, capillary pressure, density, viscosity, permeability, and porosity.

Since the capillary pressure and permeability of each phase is a function of the saturation, these equations are nonlinear, with a dominant hyperbolic advection term proportional to the gravity and pressure gradient. They are responsible for forming sharp front and rarefaction shocks, which can create significant errors in the output results if not treated with conservative numerical solutions. For example, recent results are available for contaminant transport modeling in porous media, including the presence of NAPLs [24,25], immiscible fluid flow in unsaturated zones [26], a high-resolution central upwind scheme for two-phase fluid flow [27], a finite-volume WENO scheme and discontinuous Galerkin methods [28], and a second-order accurate difference method for nonlinear conservation laws [29].

This study deals with a 3D numerical model implemented to simulate free-product DNAPL extraction in a synclinal aquifer using the method introduced by Feo and Celico [30,31]. It is based on the high-resolution shock-capturing (HRSC) flux conservation method [32–34] to follow sharp discontinuities accurately and the temporal dynamics of three-phase immiscible fluid flow in a porous medium. Several validation tests were performed in [30,31,35–38] to verify the accuracy of the HRSC method and the CactusHydro code. CactusHydro is based on the Cactus computational toolkit [39–41], an open-source software framework for developing high-performance parallel computing (HPC) simulation codes, and the data are evolved on a Cartesian mesh using Carpet [42,43].

The numerical model presented here simulates the free-product DNAPL extraction by means of a purpose-designed pumping well, with the aim of (i) minimizing the environmental impact caused by DNAPL release on the subsurface; (ii) estimating the recoverable free-product DNAPL, depending on the hydraulic properties of the aquifer medium; and (iii) estimating the residual DNAPL, which could act as a long-term pollution source. The numerical approach was coupled to biomolecular investigations to analyze the autochthonous bacterial community in ground- and spring waters and verify the existence of microorganisms potentially associated with chlorinated solvent biodegradation. The coupled experimental modeling approach was tested in south-western Sicily (Italy), where tetrachloroethylene (PCE) and trichloromethane (TCM) have been detected in spring waters fed by a synclinal evaporitic aquifer.

2. Study Area

The study area is located in south-western Sicily, between the small towns of Siculiana and Montallegro (Figure 1). From a hydrogeological point of view, the research area is situated inside the "Fosso delle Canne" stream basin. It geologically corresponds [44] to the south-to-southeast vergent Sicilian fold and thrust belt [45], bordered by the Gela thrust front and Kabilian–Calabrian thrust front. The whole area is characterized by the outcropping of neogenic deposits filling the syntectonic basin growing above the deformed substrate. In detail, lithotypes pertaining to the upper Messinian evaporitic succession (Gessoso–Solfifera series) consisting of limestone, gypsum, and salt, as well as numerous intercalations of clays, marls, and carbonates, overlie the Tripoli formation (TRP), constituted by diatomitic laminites and clay deposits of late Tortonian to Early Messinian

ages. These deposits are part of the Terravecchia and Licata formations, which will be referred to in the following as Argille di base (AB). The succession is overlain by Pliocene marly calcilutites (Trubi Fm.: TRB). Finally, the more recent units are represented by sandy clays and arenites (Montallegro Fm.: MNT) of Pleistocene ages. Large sectors of the studied area are covered by recent debris covers of alluvial, eluvial, and colluvial origin.

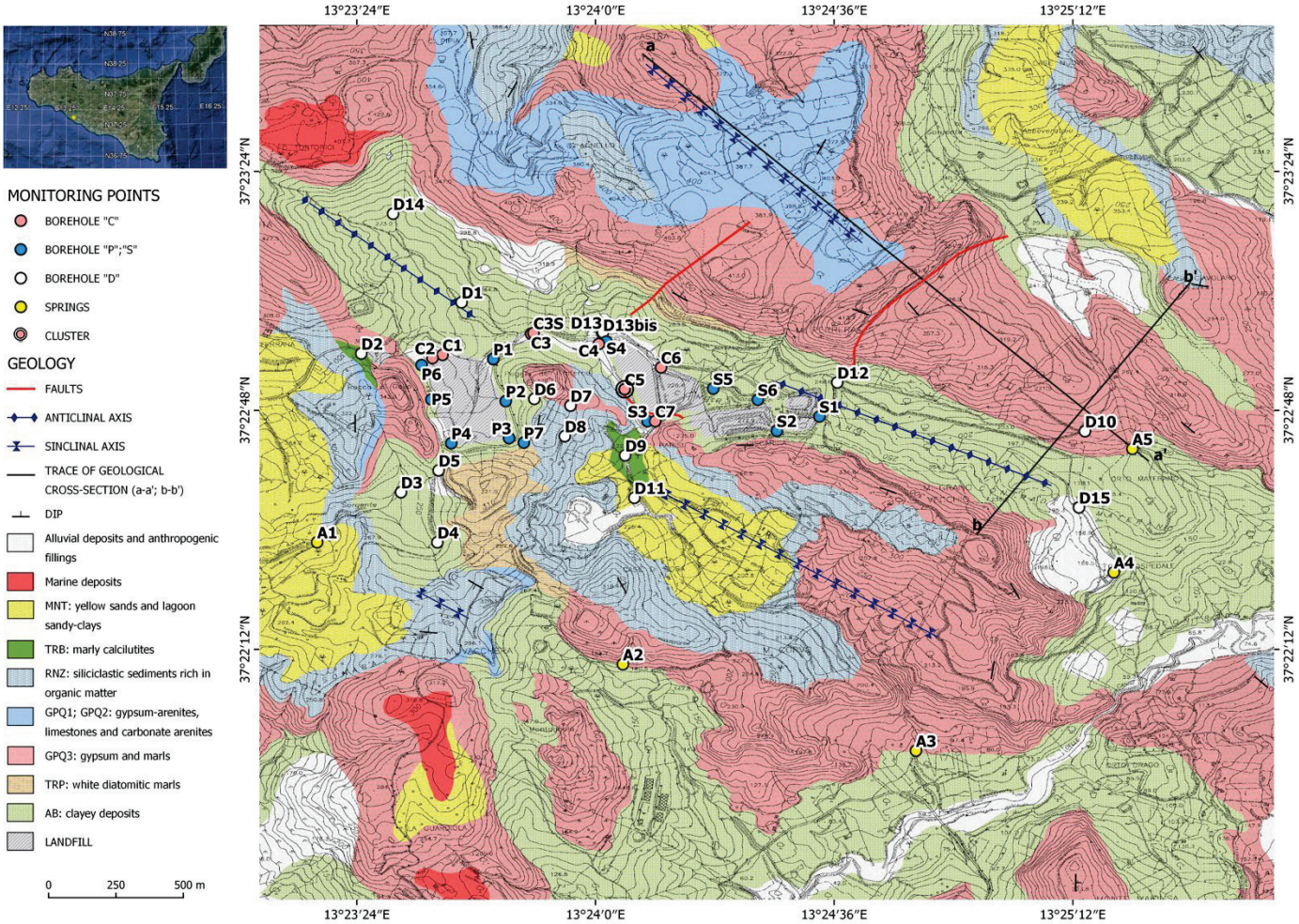

Figure 1. Geological map.

The geomorphological setting of the area is marked by a series of fluvial terraces, frequently found in long gullies and V-shaped valleys. In particular, different lithologies have produced different landforms, with gypsum lithologies affected by karst processes, resulting in a great variety of forms, such as poljes and karren. At the same time, on the clayey slopes, morphogenetic processes have produced landforms such as shallow landslides, rills, and gullies [46].

The geological structure of this sector of Sicily is marked by a poliarmonic fold system with an NW-SE trend axis that runs parallel to the trend of the Sicilian fold and thrust belt. The drainage network's shape is influenced by this setting and the existence of lithologies prone to karst processes and erosion. Moreover, there are numerous relief inversions caused by differential erosion events.

3. Materials and Methods

3.1. Geological and Hydrogeological Investigations

To reconstruct the local geology, the stratigraphic logs of 40 geognostic boreholes were considered (Figure 1). In total, 22 out of 40 boreholes were then equipped as piezometers.

The 2D interpretations were uploaded to the three-dimensional geologic modeling software (Move by Petroleum Experts Limited and LeapfrogGeo by Sequent) and the modeling processes allowed the 3D reconstruction of the main geological surface of interest of this work; that is to say, the aquifer bottom. In addition, it was also possible to reconstruct the topographic elevation through official regional cartography and the expected groundwater surface. The latter was obtained by interpolating the location of spring A5 and the hydraulic head measured in observation well D10, thereby estimating the local hydraulic gradient.

Within this study process, the aquifer bottom's morphology was a nodal issue, considering the need to identify the more probable locations of DNAPL pools. For this reason, once a marked localized depression was clearly identified, a square area of about 50 × 50 m was selected to simulate the DNAPL extraction through pumping, with a grid spacing of 0.1 m.

From November 2021 to May 2022, hydraulic head measurements were carried out monthly using a water level meter. Within the present study, the main aim was to reconstruct the groundwater flow net related to the low-permeability medium outcropping south of the evaporitic aquifer that feeds spring A5 to check possible hydraulic interactions between the two media and then acquire useful information about the origin of the DNAPLs. Therefore, this groundwater flow net was reconstructed using the hydraulic head measured in the only piezometers drilled and screened within the clayey deposits (D12, D13, D13bis, D15, S1, S2, S3, S4, S5, S6, C4, C5, C6, and C7 in Figure 1).

Moreover, taking into account the detection of chlorinated solvents in A5 spring waters during the first observation year, it was decided to continuously measure the hydraulic head fluctuations in piezometer D10 (drilled and screened within the evaporitic aquifer feeding spring A5) during rainfall events, so as to quantify the time lag between precipitation and head rise in a such aquifer. In more detail, he D10 is 36 m deep and was screened between 5 and 35 m below ground. Therefore, in early 2023, a pressure transducer was installed at the bottom of the well in D10, and the hydraulic head was measured on an hourly basis. Contextually, the rainfall was measured in a meteorological station located at the study site hourly.

3.2. Hydrochemical Analyses

Both spring and groundwater samples were collected (at A5 and P10, respectively) from November 2021 to May 2022 on a seasonal basis.

Since a preliminary hydraulic test in D10 suggested low local permeability of the aquifer medium, groundwater sampling was planned to collect samples through a bailer (before purging) and (when possible) through the usual low-flow purging procedure. As a matter of fact, it was possible to collect groundwater samples through the low-flow purging procedure only twice (November 2021 and February 2022). All samples were analyzed in order to acquire information throughout the observation period.

The chemical analyses were carried out by C.A.D.A. s.n.c. (Chimica Applicata Depurazione Acque, società in nome collettivo), a laboratory with ISO 9001:2015, ISO 14001:2015, and ISO 45001:2018 accreditations recognized by the Italian Accreditation Committee (ACCREDIA; accreditation number 0439L).

3.3. Microbiological Analyses: 16S Ribosomal RNA Gene Next-Generation Sequencing (NGS)

The microbiological survey was carried out in November 2021. Water samples (1 L) were filtered through sterile mixed esters of cellulose filters (S-PakTM membrane filters, 47 mm diameter, 0.22 μm pore size; Millipore Corporation, Billerica, MA, USA) within 24 h of collection. The bacterial DNA extraction from the sample filters was performed using the commercial FastDNA SPIN Kit for soil (MP Biomedicals, LLC, Solon, OH, USA) and the FastPrep®Instrument (MP Biomedicals, LLC, Solon, OH, USA). Once the DNA extraction was complete, the quantity and integrity of the DNA were evaluated by electrophoresis in 0.8% agarose gel containing 1 μg/mL of Gel-RedTM (Biotium, Inc., Fremont, CA, USA), in

TAE 1X running buffer (40 mM tris base, 20 mM acetic acid, and 1 mM EDTA pH 8), and the amplification reactions were performed by polymerase chain reaction (PCR). The 16S rDNA profiles of the bacterial communities in the samples were obtained using NGS technologies at the Genprobio Srl Laboratory (Parma, Italy). Partial 16S rRNA gene sequences were obtained from the extracted DNA by PCR, using the primer pair of Probio_Uni and/Probio_Rev, which targets the V3 region of the bacterial 16S rRNA gene sequence [38]. The amplifications were carried out using a Verity Thermocycler (Applied Biosystems, Foster City, CA, USA), and the PCR products were purified by magnetic purification using Agencourt AMPure XP DNA purification beads (Beckman Coulter Genomics GmbH, Bernried, Germany) to remove the primer dimers. Amplicon checks were carried out as previously described [47]. The sequencing was performed using an Illumina MiSeq sequencer (Illumina, Hayward, CA, USA) with MiSeq Reagent Kit v3 chemicals. The fastq files were processed using a custom script based on the QIIME software suite [48]. The quality control process retained sequences with lengths between 140 and 400 bp, meaning sequence quality scores >20, whereas sequences with homopolymers >7 bp and mismatched primers were omitted. To calculate downstream diversity measures, operational taxonomic units (OTUs) were defined at 100% sequence homology using DADA2 [49]; OTUs not encompassing at least two sequences of the same sample were removed. All reads were classified to the lowest possible taxonomic rank using QIIME2 [47,50] and a reference dataset from the SILVA database v132 [51].

3.4. Hydrogeological Parameters of the Numerical Model Using CactusHydro

A 3D numerical model was set up using the numerical code CactusHydro, introduced in [CF nature, CF plosone]. CactusHydro resolves the governing partial differential equations that describe the migration of an immiscible phase fluid flow in a porous medium composed of a nonaqueous phase (n), water (w), and air (a) and a variably saturated zone. In particular, the spilled DNAPL is considered immiscible, and the effects of the volatilization, biodegradation, or dissolution are not considered. CactusHydro treats the vertical and horizontal movements of the contaminant in the variably saturated zone, which is numerically resolved as a unique zone, together (not separating the vertical movement from the horizontal one, since the flow equation includes both zones). Recent applications of the code can be found in [30,31,35–37].

Tables 1 and 2 show the DNAPL (PCE) phase properties, such as the density, viscosity, porosity, and hydrogeological parameters used in the numerical simulations. In particular, the density of the DNAPL contaminant is $\rho_n = 1643$ kg/m^3, which is denser than the water, while its viscosity is $\mu_n = 0.844 \times 10^{-3}$ kg/(ms). The simulations were carried out using the PCE as the reference DNAPL because it was the chlorinated organic compound detected at spring A5 with the highest concentration.

Here, we investigate a range of values for the permeability, porosity, and irreducible wetting phase saturation. For the permeability, we choose a range of values for the hydraulic conductivity between $K = \left[10^{-2}, 10^{-6}\right]$ m/s, which corresponds to a minimum value of 1.020×10^{-13} m^2, and a maximum value of 1.020×10^{-9} m^2 for the permeability in fissured and karstified aquifer media [52]. See Tables 1 and 2 and the relations between the hydraulic conductivity and permeability and the density and viscosity of water, $k = \frac{K\,\mu_w}{\rho_w\,g}$.

The porosity range is $[0.05, 0.50]$ [52]. The irreducible wetting phase saturation range is $[0.01, 0.03]$. These are typical values for a residual fracture together with the van Genuchten [53] parameters [54]. See Tables 1 and 2.

For a three-phase fluid flow, we need two capillary pressures. In our formulation [30,31], we use the air–water phase, $p_{caw} = (p_a - p_w)$, and the capillary pressure for the air–nonaqueous phase $p_{can} = (p_a - p_n)$. Then, the nonaqueous liquid–water capillary pressure is given by $p_{cnw} = (p_n - p_w) = (p_{caw} - p_{can})$. The relative permeabilities k_{rw}, k_{rn}, and k_{ra} and the capillary pressures are a function of the saturations, $k_{r\alpha} = k_{r\alpha}(S_a, S_n, S_w)$, $p_{can} = p_{can}(S_a, S_n, S_w)$, and $p_{caw} = p_{caw}(S_a, S_n, S_w)$. The three

phases are extended from the two-phase expressions [46] (see [30,31]). For the capillary pressure instead, we use the van Genuchten model [53] (see [30,31]).

Table 1. Definitions of the parameters used in the numerical simulations of DNAPL (PCE) migration and the values of three parameters (maximum absolute permeability, maximum porosity, and minimal irreducible water phase saturation).

Parameter	Symbol	Value
Absolute permeability (max)	k_{max}	1.020×10^{-9} m^2
Rock compressibility	c_R	4.35×10^{-7}Pa^{-1}
Porosity (max)	$\phi_{0,max}$	0.50
Water viscosity	μ_w	10^{-3} kg/(ms)
Water density	ρ_w	10^3 kg/m^3
DNAPL viscosity	μ_n	0.844×10^{-3} kg/(ms)
DNAPL density	ρ_n	1643 kg/m^3
Air viscosity	μ_a	1.8×10^{-5}kg/(ms)
Air density	ρ_a	1.225 kg/m^3
Van Genuchten	(n, m)	$\left(2.57, 1 - \frac{1}{2.57}\right)$
Irreducible wetting phase saturation (min)	$S_{wir,min}$	0.010
Surface tension of air–water	σ_{aw}	7.199×10^{-2} N/m
Interfacial tension nonaqueous water	σ_{nw}	4.44×10^{-2} N/m
Capillary pressure of air–water at zero saturation	p_{caw0}	676.55 Pa
Capillary pressure of air–nonaqueous phase at zero saturation	p_{can0}	259.83 Pa

Table 2. Definitions of the parameters used in the numerical simulations of DNAPL (PCE) migration and the values of three parameters (minimal absolute permeability, minimal porosity, and maximum irreducible water phase saturation).

Parameter	Symbol	Value
Absolute permeability (min)	k_{min}	1.020×10^{-13} m^2
Rock compressibility	c_R	4.35×10^{-7} Pa^{-1}
Porosity (min)	$\phi_{0,min}$	0.05
Water viscosity	μ_w	10^{-3} kg/(ms)
Water density	ρ_w	10^3 kg/m^3
DNAPL viscosity	μ_n	0.844×10^{-3} kg/(ms)
DNAPL density	ρ_n	1643 kg/m^3
Air viscosity	μ_a	1.8×10^{-5} kg/(ms)
Air density	ρ_a	1.225 kg/m^3
Van Genuchten	(n, m)	$\left(2.57, 1 - \frac{1}{2.57}\right)$
Irreducible wetting phase saturation (max)	$S_{wir,max}$	0.030
Surface tension of air–water	σ_{aw}	7.199×10^{-2} N/m
Interfacial tension nonaqueous water	σ_{nw}	4.44×10^{-2} N/m
Capillary pressure of air–water at zero saturation	p_{caw0}	676.55 Pa
Capillary pressure of air–nonaqueous phase at zero saturation	p_{can0}	259.83 Pa

The van Genuchten parameter is $\alpha = \left(\frac{p_c}{\rho_w g}\right)^{-1}$, where p_c is the capillary pressure head. For "sand", the value is $\alpha = 0.145$ cm$^{-1} = 14.5$ m^{-1}, and the capillary pressure between the air and water at zero saturation gives $p_{caw} = \frac{\rho_w g}{\alpha} = \frac{10^3 \text{kg/m}^3 9.81 \text{ m/s}^2}{14.5 \text{ m}^{-1}} = 676.55$ Pa.

Using the value of the interfacial tension $\sigma_{nw} = 4.44 \times 10^{-2}$ N/m and $\sigma_{aw} = 7.199 \times 10^{-2}$ N/m, we get $\beta_{nw} = \frac{\sigma_{aw}}{\sigma_{nw}} = 1.62$ and $p_{cnw}(S_w) = \frac{p_{caw}}{\beta_{nw}} = 417.62$ Pa. Then, the capillary pressure at zero saturation is $p_{can} = p_{caw} - p_{cnw} = 259.83$ Pa.

4. Results

4.1. Morphology of the Bottom Aquitard

Based on the available stratigraphic data and available geologic outcrops, two interpretative profiles extending NW–SE and SW–NE were drawn (Figure 2a,b).

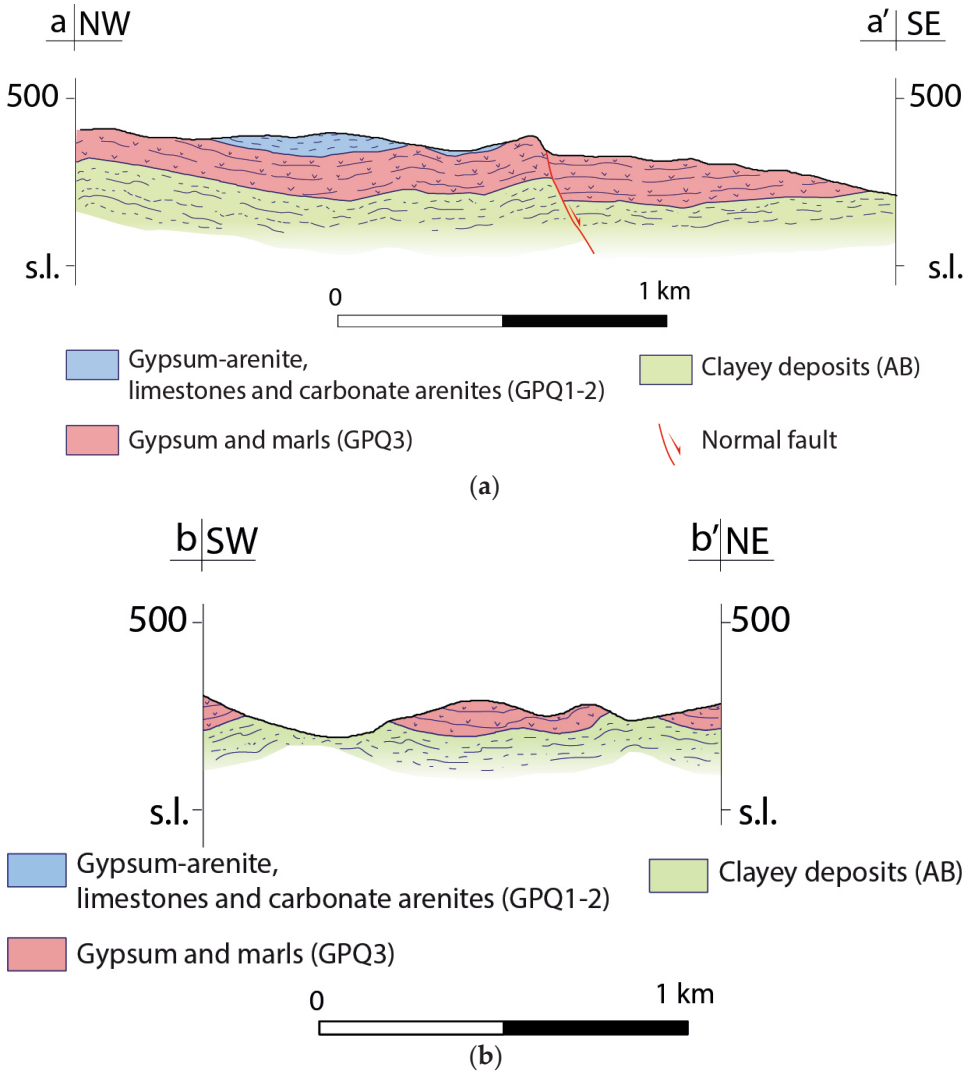

Figure 2. (**a**) Geological section oriented NW–SE (see location in Figure 1) (**b**). Geological section oriented SW–NE (see location in Figure 1).

The resulting morphology of the aquifer bottom showed a general SE-ward slope in accordance with the topography trend. In addition to this general arrangement, hectometric elevation changes were recognized in this surface, producing a localized depression toward the hill's central axis from NW to SE. Inside this central, more depressed area, we recognized a localized further low-relief area, which generated a closed underground basin suitable for a DNAPL pool (Figure 3).

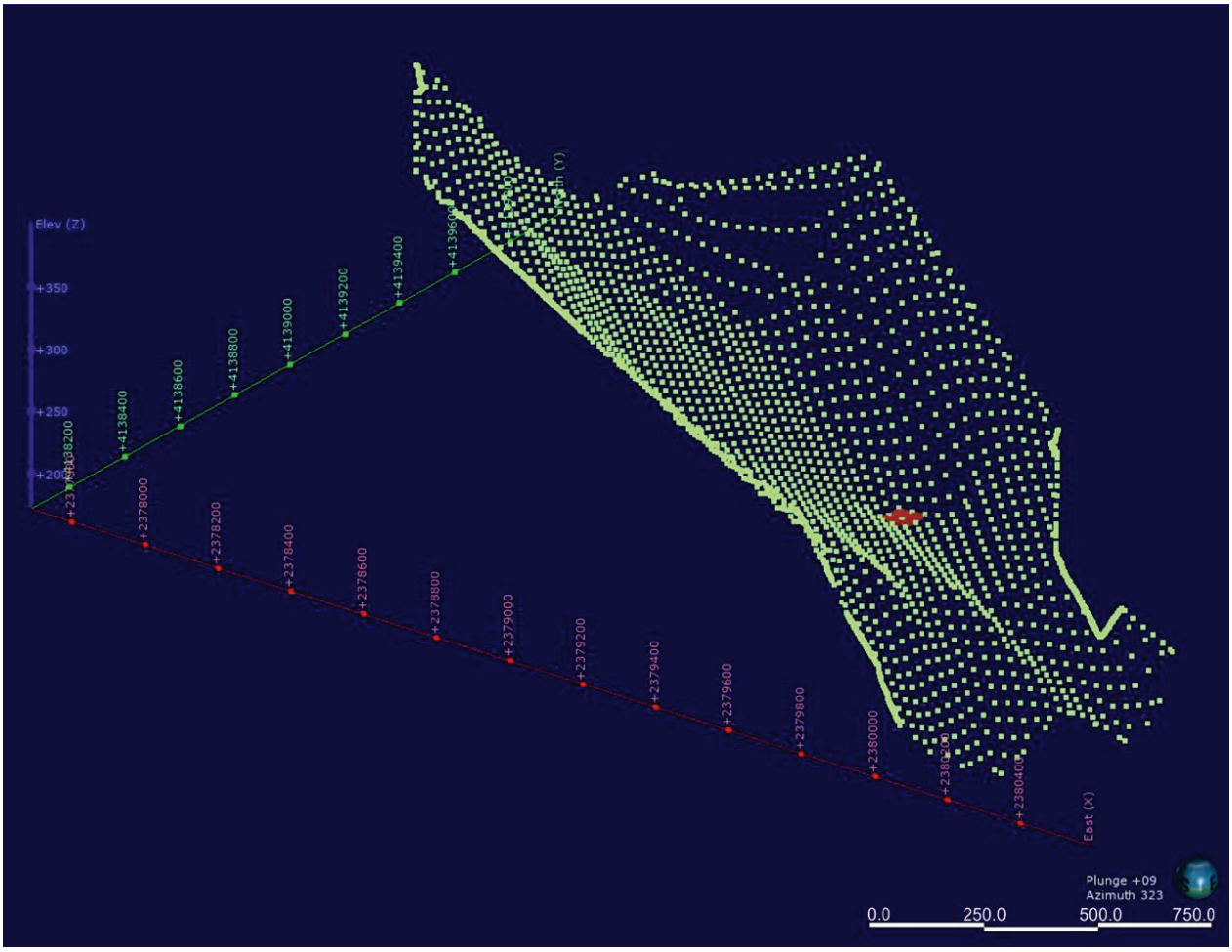

Figure 3. Morphology of the evaporitic aquifer bottom (green dots: bottom of the evaporitic aquifer; red polygon: localized depression in the bottom of the aquifer, utilized for the numerical model; Y-axis green line: NS axis with coordinates in the reference system Rome_1940_Gauss_Boaga; X-axis red line: EW axis with coordinates in the reference system Rome_1940_Gauss_Boaga; Z-axis blue line: elevations in m asl). The view is from the SE, as indicated by the reference globe above the scale. Vertical exaggeration = 3×. Images generated by LeapfrogGeo version 2021.1.3.

4.2. Hydrogeological Model

As per the low-permeability medium outcropping south of the evaporitic aquifer that feeds spring A5, Figure 4 clearly shows that the local groundwater does not flow toward the evaporites. The SW–NE groundwater divide separates (i) a western subsystem of the clayey medium where the groundwater flows from east to west and then to the south (towards S3) and (ii) an eastern subsystem where the groundwater flows from north-west to the south-east (towards D15). Overall, this groundwater pathway agrees with that reconstructed by Rizzo et al. (2020) [55].

Conversely, within the evaporitic aquifer, the groundwater flows north-west to south-east towards spring A5. This spring is then fed by the effective infiltration within the evaporitic rocks and the surface runoff infiltrating into swallow holes located north of the spring (the red triangle in Figure 4 shows the largest one).

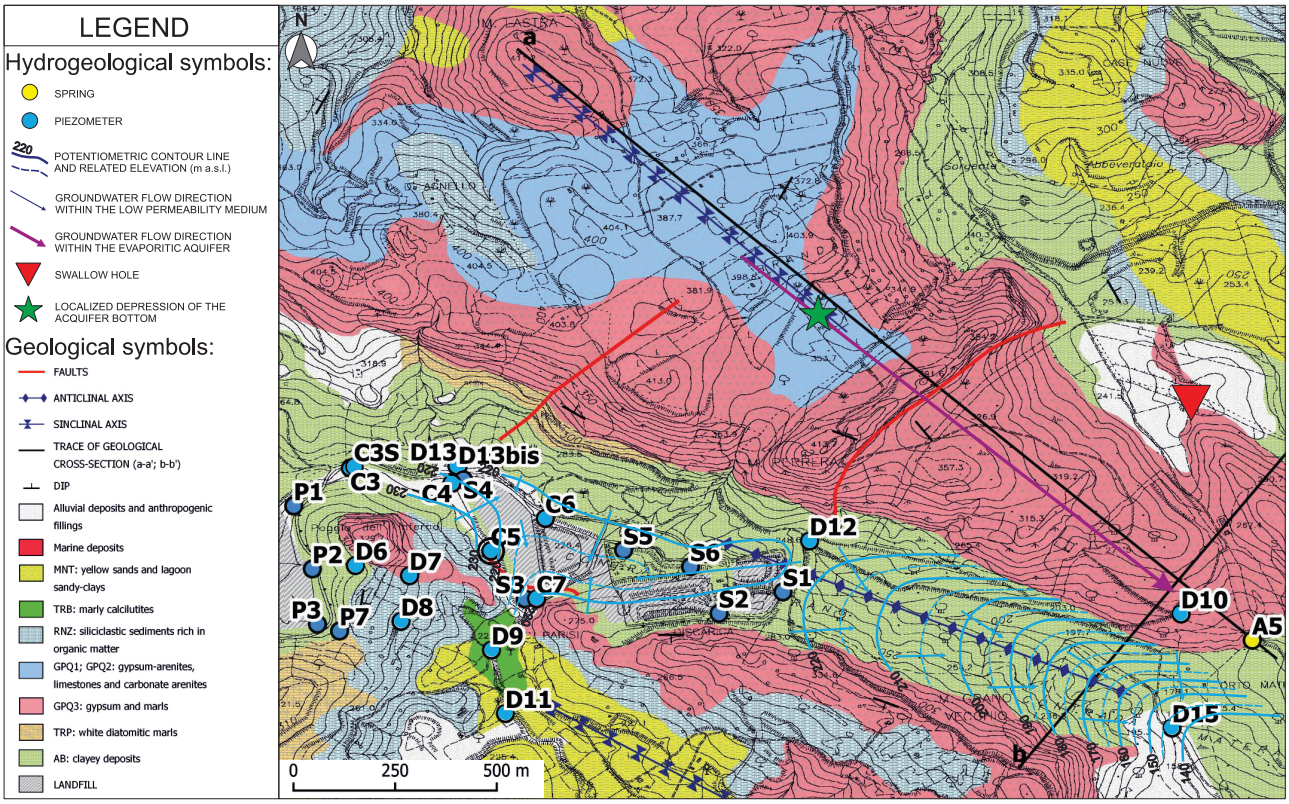

Figure 4. Hydrogeological sketch.

4.3. Hydrochemical Features

Table 3 shows the descriptive statistics results for the physicochemical parameters measured in A5 and D10.

Table 3. Physicochemical parameters of spring (A5) and groundwaters (D10) (Min is the minimum value; Max is the maximum value; D.ST. is the standard deviation; 25Q is the 1st quartile; 75Q is the 3rd quartile; 10P is the 10th percentile; 90P is the 90th percentile; C.V. is the coefficient of variation).

		Average	Median	Min	Max	D.ST.	25Q	75Q	10P	90P	C.V
A5	**T**	20.16	20.8	16.50	23.2	2.07	19.2	21.20	17.30	21.68	971.67
	pH	6.97	7.24	6.18	7.48	0.49	6.44	7.32	6.37	7.36	1426.26
	Eh	312.67	189	46.90	1572	479.08	100	239.10	55.22	522.24	65.26
	Ec	3.50	2.364	0.70	9.937	2.82	1.63	4.03	1.42	6.36	124.06
D10	**T**	19.88	20.1	16.10	22.8	1.75	19.8	20.50	18.42	20.96	1133.66
	pH	7.26	7.06	6.68	8.34	0.54	6.99	7.32	6.87	7.97	1334.70
	Eh	254.28	130.9	51.00	522.5	188.34	109.1	427.60	70.28	451.22	135.01
	Ec	3.37	3.50	1.82	5.308	1.04	2.68	3.73	2.36	4.26	322.92

The Langelier–Ludwig diagram indicates that both the spring and groundwater samples belong to the chloride sulfate alkaline earth water type, even if a slight variation can be observed over time (Figure 5). As expected, no significant differences can be observed between the spring and groundwater samples. Moreover, very similar results were obtained for the groundwater samples collected twice in static conditions (through a bailer) and through the usual low-flow purging procedure.

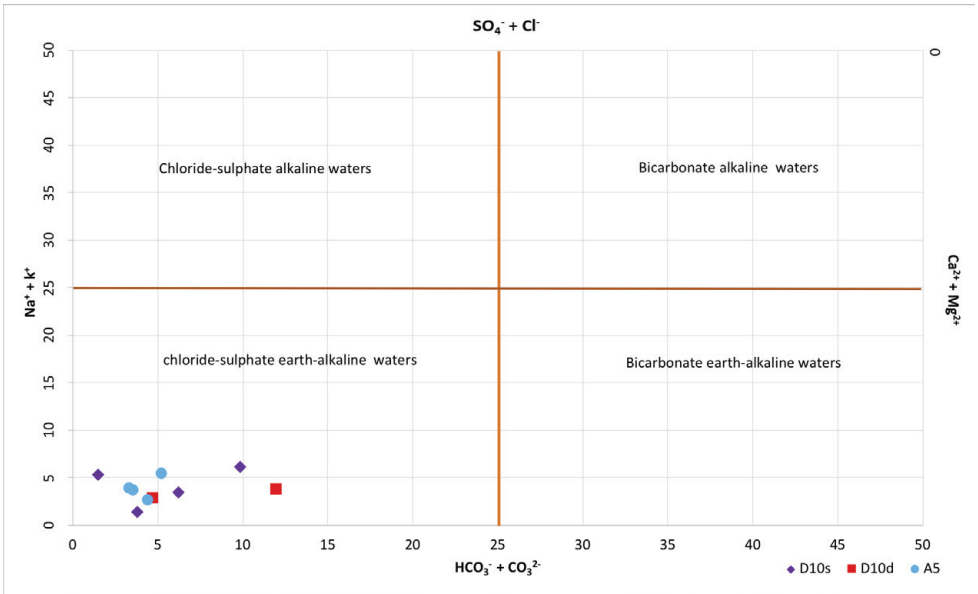

Figure 5. Lamgelier–Ludwig diagram.

As per the chlorinated organic compounds, slight contamination (tetrachloroethylene [PCE] = 7.9 µg/L; trichloromethane [TCM] = 0.73 µg/L) was detected only in November 2021 at spring A5, close to a heavy precipitation period (cumulative rainfall of 210 mm during the previous 15 days). Conversely, chlorinated organic compounds were never detected in D10 groundwaters during the observation period.

4.4. Microbial Communities

The biomolecular analysis results for the 16S rRNA were deposited in the National Center for Biotechnology Information (NCBI) Sequence Read Archive (SRA) with the project accession number PRJNA967144. Proteobacteria, Firmicutes, and Bacteroidetes represented the three major phyla in the groundwater samples, accounting for, on average, 52%, 22%, and 17% in A5 and 58%, 22%, and 14% in D10, respectively. This abundance was also confirmed at the genus taxonomic level, where genera belonging to these phyla, such as Rhodoferax, Bacteroides, Pseudomonas, and Faecalibacterium, emerged.

Starting from the analysis of the microbial community at the genus level, in both samples, various microbial communities can be observed to which both aerobic and anaerobic or facultative anaerobic bacterial genera belong. Generally, both communities are characterized by mesophilic microorganisms, with some genera characterized by halophilic or halotolerant capacities found in sample D10 or by sulfur-reducing capacities in sample A5. In addition, a large presence of fecal bacteria can also be observed, which appear to be abundant both in the sample of the A5 spring and in the D10 piezometer.

The analysis reveals the presence of bacterial genera that could have metabolic pathways capable of favoring the degradation of chlorinated compounds, such as Rhodoferax and Desulfurivibrio [56,57]. Moreover, from the analysis at the taxonomic species level, the presence of the species Dechloromonas hortensis can be observed, which is associated with the dehalogenation of chlorinated compounds such as PCE [58].

4.5. 3D High-Precision Numerical Simulations Results

The 3D numerical model developed in this study was based on the conceptual model explained in the previous section. It describes the scenario in which a free-product PCE pool lies at the bottom of an aquifer and remains fixed in that position, although there is a hydraulic gradient. It then numerically simulates the pumping extraction through a well using an HRSC conservative flux method and the CactusHydro code introduced in [30,31], with the addition of a module that allows the contaminant's extraction within

a time interval. It is based on the reconstruction through interpolation of the points of two surfaces, the aquifer's bottom surface (impermeable) and the upper-level surface (ground surface). A third surface located between the previous ones is the groundwater table that separates the unsaturated zone from the saturated aquifer zone. Figure 6a shows these three surfaces, where the green mesh is the ground surface and the blue mesh is the groundwater table surface. The red mesh is the aquifer's bottom surface, while the larger image of the aquifer's bottom surface highlights a depression in the aquifer's base, using the georeferenced coordinates and a grid spacing of 0.1 m.

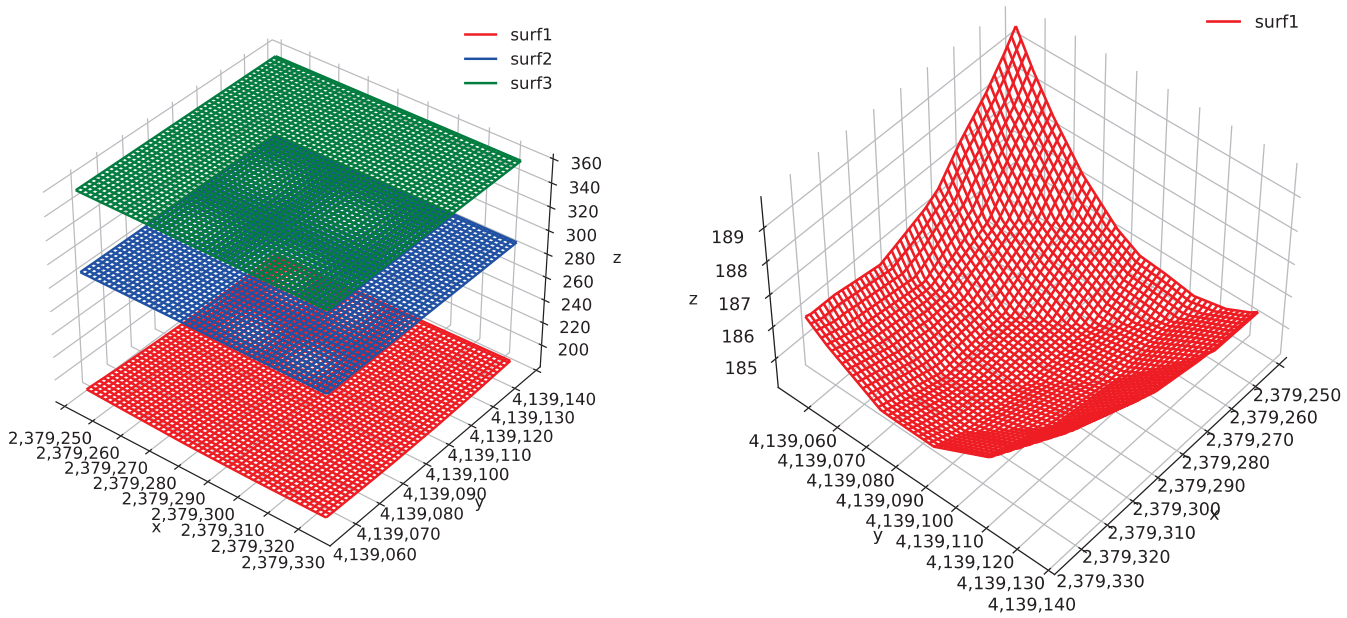

(**a**) (**b**)

Figure 6. The three surfaces with georeferenced coordinates: (**a**) the three surfaces, i.e., the aquifer's bottom surface (surf2-red), the upper-level topographic surface (surf1-green), and the groundwater table surface (surf3-blue); (**b**) a larger image of the aquifer's bottom surface that highlights a depression in the impermeable base with the contaminant's location.

Initially, we consider a fixed volume for the DNAPL pool (PCE; density $\rho_n = 1643\,\mathrm{kg/m^3}$) positioned in the impermeable aquifer bottom. The contaminant remains located in a single depression in the saturated zone (see Figure 6b). Figure 7 shows the three-dimensional interpolating cubic grid geometry used in this paper. We assume a variably saturated zone to be a parallelepiped measuring 44.0 m long from $x = [-20.0, 20.0]$ m (left-hand side), 40.0 m wide from $y = [-20.0, 20.0]$ m (right-hand side), and 179.0 m deep from $z = [181.0, 360.0]$ m, for two different times (Figure 7a: t = 0 s; Figure 7b: t = 1 day and 5.0 h). We use a spatial resolution of $dx = dy = dz = 1.0$ m and a time step size of $dt = 0.01$ s. We use a three-phase fluid flow (water + DNAPL + air) and the hydrogeological parameters from Table 1. The DNAPL is positioned at $(x, y, z) = (0, 0, 185.0)$ m. The extraction pump is situated at $(x, y, z) = (2, 0, 185.0)$ m. The aquifer medium is composed of a dry zone (and indeed an unsaturated part with $S_w = 0$), namely the one depicted in white in Figure 7, and a saturated one, namely the one depicted in blue, separated by a groundwater table surface with a hydraulic gradient of 7.1% towards SE. The green color at the bottom represents the base of the aquifer. The green color on the upper side represents the atmosphere.

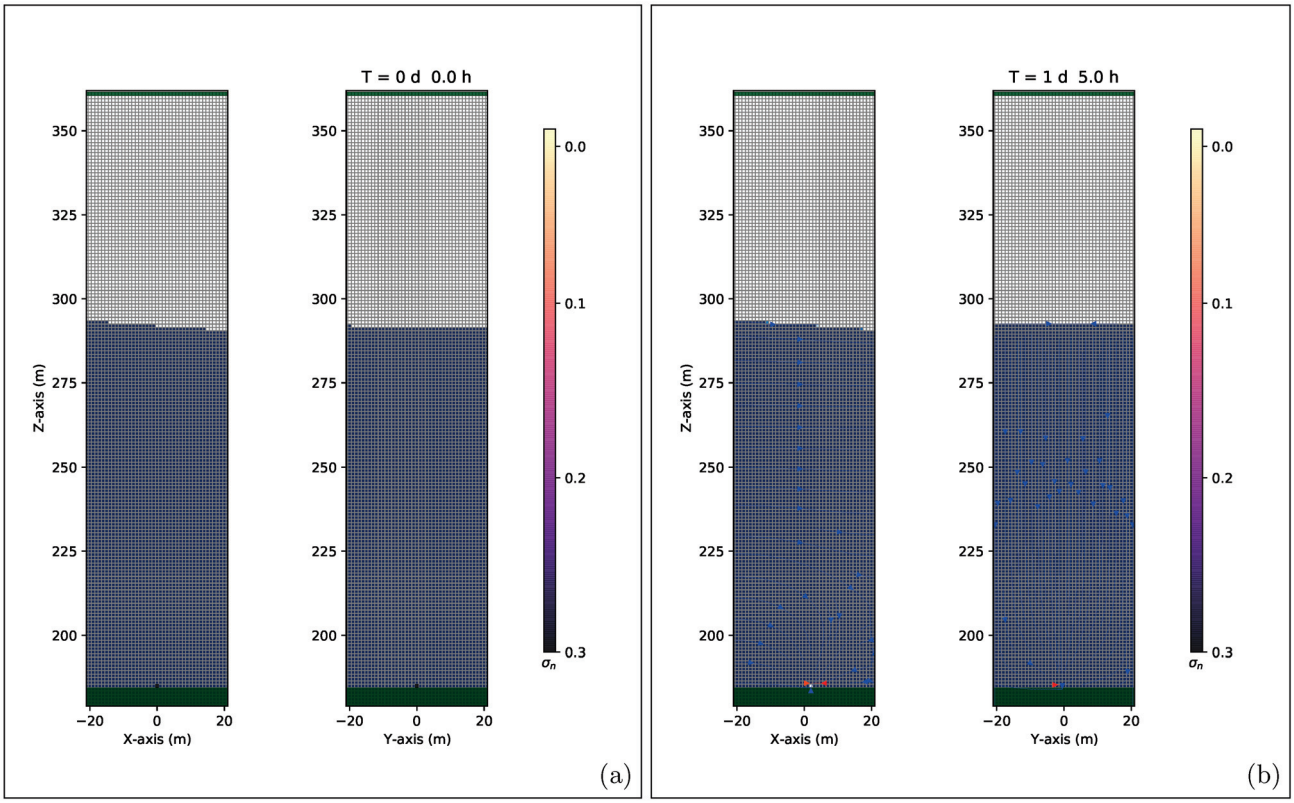

Figure 7. The three-dimensional interpolated grid geometry used in the numerical simulation of a three-phase fluid flow (water + DNAPL + air) and the hydrogeological parameters of Table 1, with a spatial grid resolution of 1.0 m and grid dimensions of 40 $\times$ 40 $\times$ 179 m, for two different times: (**a**) t = 0 s; (**b**) t = 1 day and 5.0 h. The immiscible contaminant is situated at the bottom of the interpolating cubic grid (see the $z - x$ and $z - y$ plane views). The green color in the bottom zone represents the aquifer base. The green line in the upper area represents the atmosphere. The white color is the unsaturated zone. The blue color is the saturated aquifer.

The left-hand side of this figure shows the $z - x$ plane view (Figure 7a) and the right-hand side shows the $z - y$ plane view. The green color on the bottom zone represents the aquifer base. The green line in the upper area represents the atmosphere. The white color is the unsaturated aquifer. The saturated aquifer is colored blue. The scale indicates the values of the saturation contours ($\sigma_n = S_n\phi$), where S_n is the saturation of the nonaqueous phase and ϕ is the porosity (whose initial value is given in Table 1).

Figure 7a shows the initial contaminant, which after more than 24 h is completely extracted from the pumping well (Figure 7b).

Since we want to pay attention to the extraction pump, we show a zoomed-in view of Figure 7 of the fate of the DNAPL using the data from Table 1. Figure 8 shows the numerical results of the saturation contours ($\sigma_n = S_n\phi$) at different times (Figure 7a: t = 0 s; Figure 7b: t 0.1 h; Figure 7c: t = 0.2 h; Figure 7d: t = 1.1 h.

At t = 0 s (see Figure 8a), there is a cubic volume for the PCE (with the values given in Table 1) and a saturation of $S_n = 1$. The quantity of the mass at the bottom is equal to 1643 kg/m^3 $\times$ (40 $\times$ 40 $\times$ 179) m^3 $\times$ 2.15587709497209 $\times$ 10^{-6} = 1014.5 kg. The extraction pump is situated two meters away in the x-coordinates, so the contaminant starts to move on the right-hand side (see Figure 8b,c) until time t = 1.1 h (panel (d)), where the mass that remains is practically zero. In Figure 8d, the white cube indicates the position of the well and the absence of contaminant.

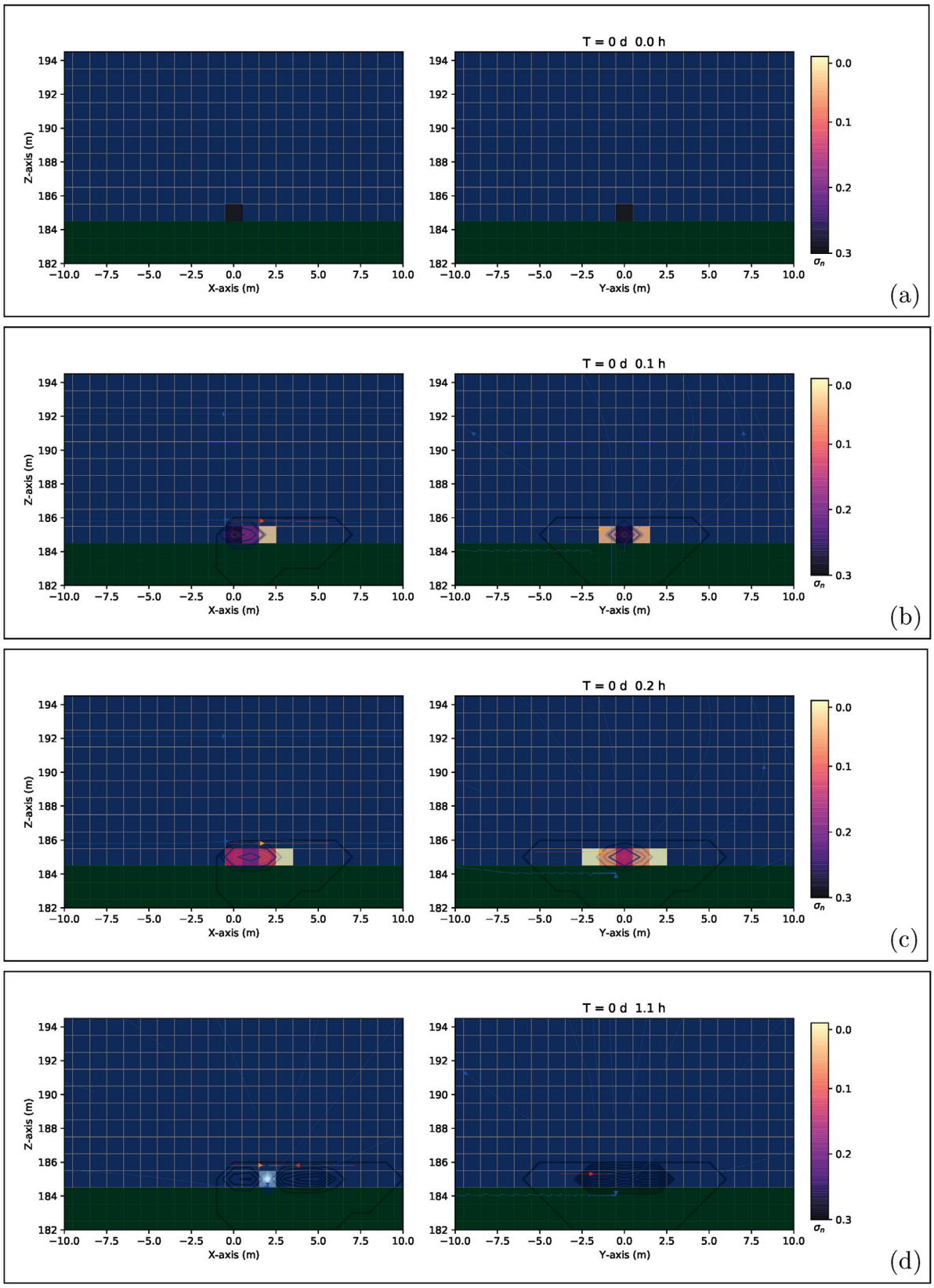

Figure 8. Three-dimensional numerical results of the saturation contours ($\sigma_n = S_n\phi$) of the DNAPL using the hydrogeological parameters from Table 1 at different times: (**a**) t = 0 s; (**b**) t 0.1 h; (**c**) t = 0.2 h; (**d**) t = 1.1 h. The red and blue arrows denote the flow direction of σ_n and σ_w, respectively.

The pumping rate of the extraction process (contaminant and water) is $Q_T = -0.000407\ \mathrm{m}^3/\mathrm{s} = -0.407\ \mathrm{L/s}$. Before starting the pumping process, the value of the saturation multiplied by the porosity is $\sigma_n = 2.15587709497209 \times 10^{-6}$. After 104611.8 s, the value is $\sigma_n = 7.36016960716937 \times 10^{-11}$. Its ratio is 3.41×10^{-5}, meaning very few contaminants are left at the bottom of the aquifer.

We also analyzed the numerical case shown in Figure 9, in which the grid geometry is similar to the previous case but the hydrogeological parameters are those from Table 2. We use a spatial resolution of $dx = dy = dz = 1.0$ m and a time step size of $dt = 0.1$ s. Since the irreducible wetting saturation is 0.03 (greater than the previous case of 0.01) and the porosity is 0.05 (as the absolute permeability is also four orders of magnitude smaller than in the previous case; compare Table 2 with Table 1), we expect that it will take longer to remove the contaminant.

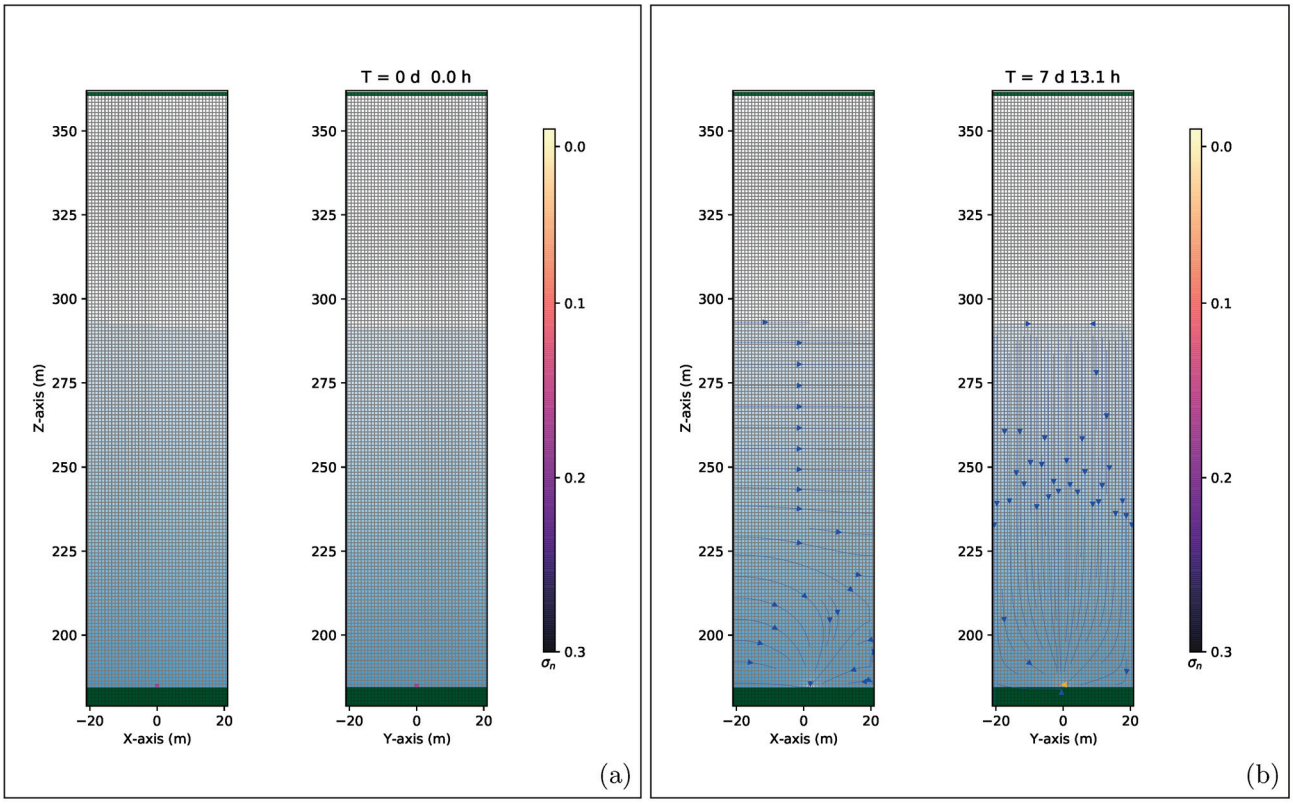

Figure 9. The three-dimensional interpolated grid geometry used in the numerical simulation of a three-phase fluid flow (water + DNAPL + air) and the hydrogeological parameters from Table 2, with a spatial grid resolution of 1.0 m and a grid dimension of 40 × 40 × 179 m for two different times: (**a**) t = 0 s; (**b**) t = 7 days and 13.1 h. The immiscible contaminant is situated at the bottom of the interpolating cubic grid (see the $z - x$ and $z - y$ plane views). The green color in the bottom zone represents the aquifer base. The green line in the upper area represents the atmosphere. The white color is the unsaturated zone. The blue color the saturated aquifer.

Figure 10 shows a zoomed-in view of the grid in the region of interest at different times (Figure 10a: t = 0 s.; Figure 10b: t =1.1 h; Figure 10c: t = 2.3 h; Figure 10d: t = 2 days and 8.9 h. Indeed, the pumping rate for the extraction process (contaminant and water) is $Q_T = -0.000095\ \mathrm{m}^3/\mathrm{s} = -0.095\ \mathrm{L/s}$. Compared with the previous case, the flow rate in this case is smaller and it takes longer to extract the contaminant. Before pumping, the value of the saturation multiplied by the porosity is $\sigma_n = 5.84648044692737 \times 10^{-7}$. After 652902.4 s, the value is $\sigma_n = 1.30456707252625 \times 10^{-9}$. Its ratio is 2.23×10^{-3}, which is still very small but bigger than the previous case.

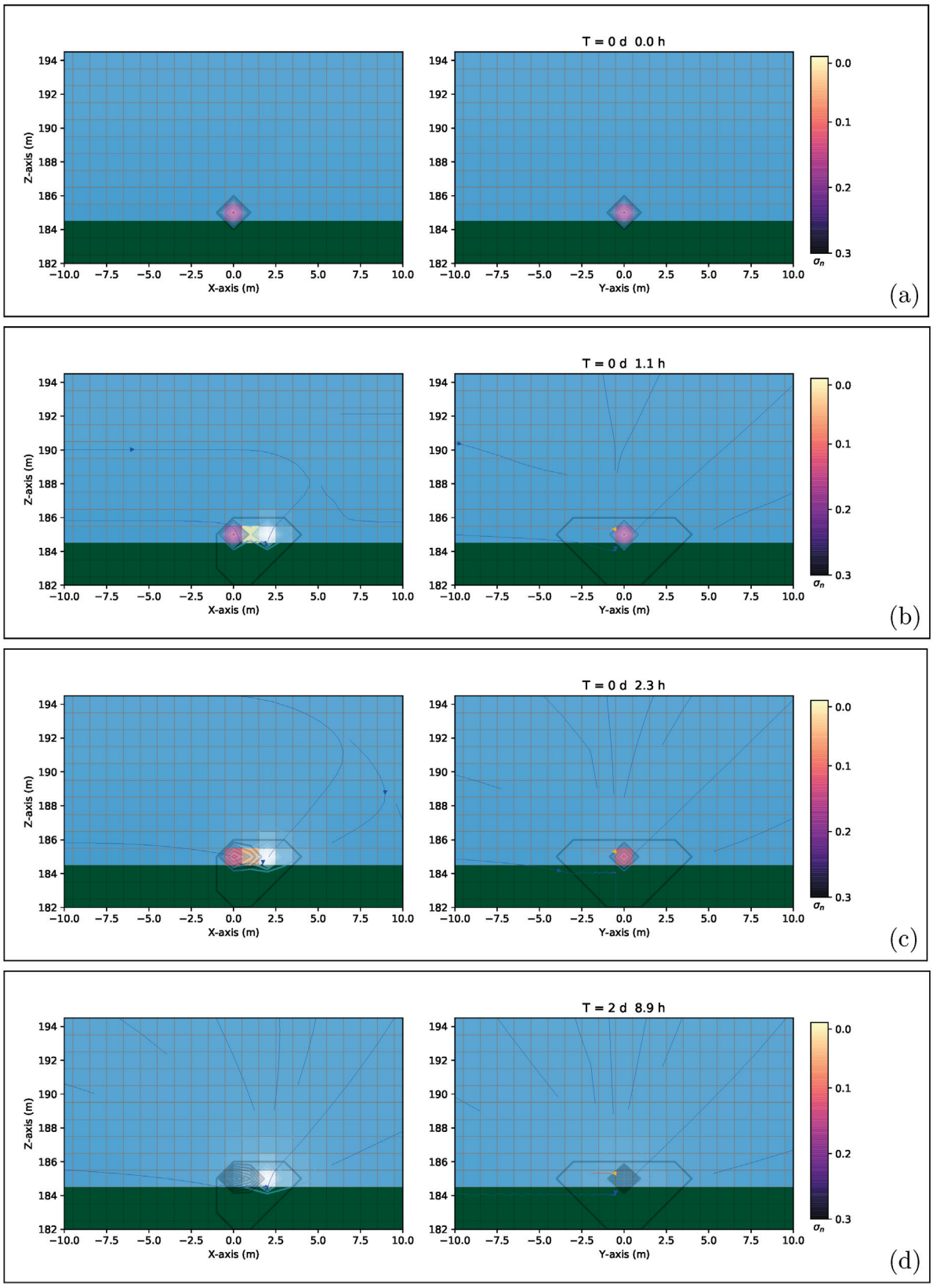

Figure 10. Three-dimensional numerical results for the saturation contours ($\sigma_n = S_n\phi$) of the DNAPL using the hydrogeological parameters from Table 2 at different times: (**a**) t = 0 s; (**b**) t = 1.1 h; (**c**) t = 2.3 h; (**d**) t = 2 days and 8.9 h.

5. Discussion and Conclusions

A slightly chlorinated organic compound (mainly PCE, subordinately TCM) was detected once at the test site in spring waters during the observation period. Conversely, no pollution was contextually detected in groundwater samples collected in observation well D10 drilled in the feeding aquifer. The episodic detection of PCE and TCM (as a consequence of heavy rainfall), as well as the apparent discrepancy between the spring and groundwater samples in terms of contamination, are congruent with the following scenario: (i) one or more DNAPLs pools lie at the bottom of the investigated aquifer, representing long-term ground and spring water pollution sources; (ii) the plume that originated within the saturated aquifer was not intercepted by the observation well D10; (iii) both the PCE and TCM were detected in spring water but were associated only with huge precipitation; (iv) the magnitude of the pressure head increase at the aquifer bottom consequent to an unusual recharge event (210 mm in 15 days) was able to cause the significantly increased mobilization and flow of deep (contaminated) groundwater towards the spring; (v) as a result, an unusually high volume of deep (contaminated) groundwater temporarily flowed out at spring A5, high enough to be detected.

The effectiveness of this interpretation was further supported by analyzing the hydraulic head rise on an hourly basis in D10 in early 2023. As shown in Figure 11, (i) the 23.8 mm of rainfall in 12 h between 9 February 2023 and 10 February 2023 caused a fast (about 7 h of time lag) rise (about 0.4 m) in the groundwater head, while (ii) the 28.4 mm of rainfall in 3 h on 3 March 2023 caused a rapid (about 8 h of time lag) rise (about 0.5 m) in the hydraulic head. Based on these data and supposing a linear relationship between the data, the 210 mm precipitation event that preceded the only PCE and TCM detection instance in spring waters during the observation period should have caused an unusual and huge head rise in the order of several meters at D10.

Considering the conceptual model described before, three-dimensional numerical modeling was successfully implemented to predict the efficacy of free-product PCE extraction through a pumping well in the test aquifer. We followed the numerical results based on the saturation contours of the three-phase immiscible fluid flow formed by water, DNAPL, and air in dry soil at different times, using the CactusHydro [30,31] conservative HRSC method, which precisely follows the advective part of the fluid flow and resolves the hyperbolic part of the nonlinear governing coupled equations of a three-phase immiscible fluid flow.

Taking into consideration the morphology of the bottom aquiclude (purposely reconstructed through a detailed geological characterization of the test site) and the existence of a unique depression where the DNAPL pool could be located, the numerical model was not used to simulate the DNAPL's migration to the subsurface once released in the environment. Instead, we simulated the effects of the pumping well screened at the bottom of the pool to recover the contaminant. The results indicated that CactusHydro can precisely follow the contaminant's fate and its recovery using a pumping well. Moreover, the simulation model showed that the free-product pumping recovered almost the whole DNAPL pool, even though a slight difference in the recovery percentages can be expected depending on the hydraulic features of the aquifer medium.

Taking into consideration the results of the numerical simulation, the pumping solution could avoid a significant volume of free product acting as a long-term pollution source. At the same time, the existence of an autochthonous microbial community able to degrade chlorinated solvents will promote natural attenuation processes within the groundwater matrix.

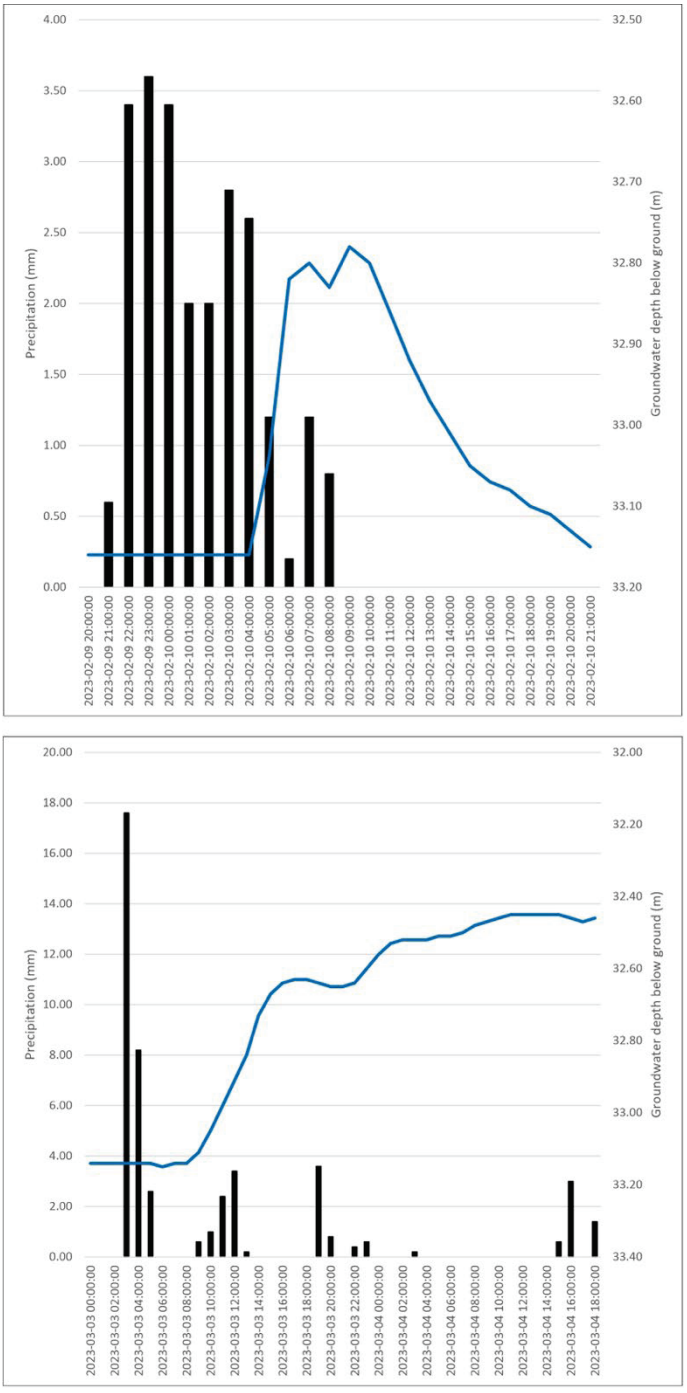

Figure 11. Hydraulic head in D10 (blue line) vs. rainfall (black bars) on an hourly basis (dates are given in year-month-day-hour).

The limitations of the numerical model are that at this stage (i) we consider these fluids (groundwater and PCE) immiscible, and the process of volatilization or dissolution was not considered, while (ii) the hydraulic parameters of the aquifer medium (permeability, porosity, irreducible water saturation) did not refer to the specific test site but were taken from the scientific literature. However, both limitations are acceptable at the planning stage of this type of research on heterogeneous aquifer media because they are normally finalized to optimize the interdisciplinary approach in order to respond to some basic questions: (i) Do we expect that hydraulic heterogeneities to significantly influence the free-product DNAPL extraction? (ii) If so, that is the expected range of free-product DNAPL recovery

rates as a function of the expected aquifer heterogeneity? (iii) Is it necessary to design and apply bioremediation techniques associated with free-product extraction or can the natural attenuation provided by the autochthonous microbial community be considered enough to efficaciously remove the pollution source? Additionally, the field site is contaminated with both PCE and TCM and the numerical model used here does not differentiate between single-component and multicomponent DNAPLs. We plane to include more than one nonaqueous phase liquid in the future.

As per the last issue, coupling the numerical simulations of the study site to the bacterial community characterization, we were effectively able to predict that (i) the PCE recovery through a pumping well will be almost completed and (ii) the application of other remediation techniques (such as bioremediation) is not necessary to remove the pollution source because (iii) a natural attenuation process is provided by the autochthonous bacterial community, which is characterized by genera (such as *Dechloromonas*, *Rhodoferax*, and *Desulfurivibrio*) that could have metabolic pathways capable of favoring the degradation of chlorinated compounds.

In a wider context, this study demonstrates that a coupled experimental modeling approach, based on results obtained from an interdisciplinary perspective, is an effective way to synergically plan and design both short- (pumping well) and medium-term (e.g., natural attenuation) solutions to remove DNAPL pools from aquifer systems efficaciously.

Author Contributions: Conceptualization, A.F., E.R., and F.C.; methodology, A.F., F.L.M., P.R., M.G.M., R.P., E.R. and F.C.; software, F.L.M., M.G.M. and R.P..; validation, A.F., E.R. and F.C.; formal analysis, A.F., F.L.M., P.R., M.G.M., R.P., E.R. and F.C.; investigation, F.L, P.R. and M.G.M.; resources, F.L.M., P.R., M.G.M. and R.P.; data curation, F.L.M., P.R., M.G.M. and R.P.; writing—original draft preparation, A.F., F.L.M., P.R., M.G.M., R.P., E.R. and F.C.; writing—review and editing, A.F., F.L.M., E.R. and F.C.; visualization, A.F., F.L.M., M.G.M. and R.P.; supervision, E.R. and F.C.; project administration, E.R. and F.C.; funding acquisition, E.R. and F.C. All authors have read and agreed to the published version of the manuscript.

Funding: This research was funded by Catanzaro Costruzioni S.r.l. (Heads of Funds: E. Rotigliano, F. Celico).

Data Availability Statement: The data are contained within the article.

Acknowledgments: We warmly acknowledge Fabio Catanzaro, Salvatore Accardo, and Rosario Varsalona for their useful discussions. This work used high-performance-computing resources at the University of Parma (https://www.hpc.unipr.it) accessed on 1 January 2023. This work benefited from the equipment and framework of the COMP-R Initiative, funded by the 'Departments of Excellence' program of the Italian Ministry for Education, University, and Research (MIUR, 2023–2027). A.F. and F.C. acknowledge the financial support from the PNRR MUR project ECS_00000033_ECOSISTER. We also thank the two anonymous reviewers for their valuable comments and questions.

Conflicts of Interest: The authors declare no conflict of interest.

References

1. Mercer, J.W.; Cohen, R.M. A review of immiscible fluids in the subsurface: Properties, models, characterization and remediation. *J. Contam. Hydrol.* **1990**, *6*, 107–163. [CrossRef]
2. Henschler, D. Toxicity of chlorinated organic compounds: Effects of the introduction of chlorine in organic molecules. *Angew. Chem.* **1994**, *33*, 1920–1935. [CrossRef]
3. Volpe, A.; Del Moro, G.; Rossetti, S.; Tandoi, V.; Lopez, A. Remediation of PCE-contaminated groundwater from an industrial site in southern Italy: A laboratory-scale study. *Process Biochem.* **2007**, *42*, 1498–1505. [CrossRef]
4. Lyman, W.; Reehl, W.; Rosenblatt, D. *Handbook of Chemical Properties Estimation Methods-Environmental Behavior of Organic Compound*; McGraw-Hill: New York, NY, USA, 1982.
5. Mackay, D.; Roberts, P.; Cherry, J. Transport of organic contaminants in groundwater. *Environ. Sci. Technol.* **1985**, *19*, 384–392. [CrossRef] [PubMed]
6. Parker, J.C.; Lenhard, R.J.; Kuppusamy, T. A parametric model for constitutive properties governing multi-phase flow in porous media. *Water Resour Res.* **1987**, *23*, 618–624. [CrossRef]
7. Kueper, B.; Frind, E. An overview of immiscible fingering in porous media. *J. Contam. Hydrol.* **1988**, *2*, 95–110. [CrossRef]
8. Kueper, B.; Abbott, W.; Farquhar, G. Experimental observations of multiphase flow in heterogeneous porous media. *J. Contam. Hydrol.* **1989**, *5*, 83–95. [CrossRef]

9. Kueper, B.; Frind, E.O. Two-phase flow in heterogeneous porous media: 2. Model application. *Water Resour. Res.* **1991**, *27*, 1059–1070. [CrossRef]
10. Parker, J. Multiphase flow and transport in porous media. *Rev. Geophys.* **1989**, *27*, 311–328. [CrossRef]
11. Hirata, T.; Muraoka, K. Vertical migration of chlorinated organic compounds in porous media. *Water Res.* **1988**, *22*, 481–484. [CrossRef]
12. Ahmadi, H.; Kilanehei, F.; Nazari-Sharabian, M. Impact of Pumping Rate on Contaminant Transport in Groundwater—A Numerical Study. *Hydrology* **2021**, *8*, 103. [CrossRef]
13. McLaren, R.G.; Sudicky, E.A.; Park, Y.-J.; Illman, W.A. Numerical simulation of DNAPL emissions and remediation in a fractured dolomitic aquifer. *J. Contam. Hydrol.* **2012**, *136*, 56–71. [CrossRef] [PubMed]
14. Guadaño, J.; Gómez, J.; Fernández, J.; Lorenzo, D.; Domínguez, C.M.; Cotillas, S.; García-Cervilla, R.; Santos, A. Remediation of the Alluvial Aquifer of the Sardas Landfill (Sabiñánigo, Huesca) by Surfactant Application. *Sustainability* **2022**, *14*, 16576. [CrossRef]
15. Zhou, J.; Song, B.; Yu, L.; Xie, W.; Lu, X.; Jiang, D.; Kong, L.; Deng, S.; Song, M. Numerical Research on Migration Law of Typical Chlorinated Organic Matter in Shallow Groundwater of Yangtze Delta Region. *Water* **2023**, *15*, 1381. [CrossRef]
16. Zheng, C.; Wang, P.P. MT3DMS: A Modular Three-Dimensional Multispe-cies Transport Model for Simulation of Advection, Dispersion, and Chemical Reactions of Contaminants in Groundwater Systems. In *Documentation and User's Guide*; No. SERDP-99-1; U.S. Army Engineer Research and Development Center: Vicksburg, MS, USA, 1999.
17. Anderson, M.R.; Johnson, R.L.; Pankow, J.K. Dissolution of Dense Chlorinated Solvents into Groundwater. 3. Modeling Contaminant Plumes from Fingers and Pools of Solvent. *Environ. Sci. Technol.* **1992**, *26*, 901–908. [CrossRef]
18. Johnson, R.L.; Pankov, J.F. Dissolution of Dense Chlorinated Solvents into Groundwater. 2. Source Functions for Pools of Solvent. *Environ. Sci. Technol.* **1992**, *26*, 896–901. [CrossRef]
19. Roy, J.W.; Smith, J.E.; Gillham, R.W. Laboratory evidence of natural remobilization of multicomponent DNAPL pools due to dissolution. *J. Contam. Hydrol.* **2004**, *74*, 145–161. [CrossRef]
20. Seagren, E.A.; Rittmann, B.E.; Valocchi, A.J. An experimental investigation of NAPL pool dissolution enhancement by flushing. *J. Contam. Hydrol.* **1999**, *37*, 111. [CrossRef]
21. Chrysikopoulos, C.V.; Voudrias, E.A.; Fyrillas, M.M. Modeling of contaminant transport resulting from dissolution of nonaqueous phase liquid pools in saturated porous media. *Transp. Porous Med.* **1994**, *16*, 125–145. [CrossRef]
22. Chrysikopoulos, C.V. Three-dimensional analytical models of contaminant transport from nonaqueous phase liquid pool dissolution in saturated subsurface formation. *Water Resour. Res.* **1995**, *31*, 1137–1145. [CrossRef]
23. Kenneth, Y.L.; Chrysikopoulos, C.V. Dissolution of a multicomponent of DNAPL pool in an experimental aquifer. *J. Hazard. Mater.* **2006**, *B128*, 218–226.
24. Soga, K.; Page, J.W.E.; Illangasekare, T.H. A review of NAPL source zone remediation efficiency and the mass flux approach. *J. Hazard. Mater.* **2014**, *110*, 13–27. [CrossRef] [PubMed]
25. Essaid, H.; Bekins, B.A.; Cozzarelli, I.M. Organic contaminant transport and fate in the subsurface: Evolution of knowledge and understanding. *Water Resour. Res.* **2015**, *51*, 4861–4902. [CrossRef]
26. Praseeja, A.V.; Sajikumar, N. A review on the study of immiscible fluid flow in unsaturated porous media: Modeling and remediation. *J. Porous Media* **2019**, *22*, 889–922. [CrossRef]
27. Ahmed, M.; Saleem, M.R.; Zia, S.; Qamar, S. Central Upwind Scheme for a Compressible Two-Phase Flow Model. *PLoS ONE* **2015**, *10*, e0126273. [CrossRef] [PubMed]
28. Pandare, A.K.; Waltz, J.; Bakosi, J. A reconstructed discontinuous Galerkin method for multi-material hydrodynamics with sharp interfaces. *Int. J. Numer. Methods Fluids* **2020**, *92*, 874–889. [CrossRef]
29. Kuchařík, M.; Liska, R.; Steinberg, S.; Wendroff, B. Optimally-stable second-order accurate difference schemes for non-linear conservation laws in 3D. *Appl. Numer. Math.* **2006**, *56*, 589–607. [CrossRef]
30. Feo, A.; Celico, F. High-resolution shock-capturing numerical simulations of three-phase immiscible fluids from the unsaturated to the saturated zone. *Sci. Rep.* **2021**, *11*, 5212. [CrossRef]
31. Feo, A.; Celico, F. Investigating the migration of immiscible contaminant fluid flow in homogeneous and heterogeneous aquifers with high-precision numerical simulations. *PLoS ONE* **2022**, *17*, e0266486. [CrossRef]
32. Kurganov, A.; Tadmor, E. New high-resolution central scheme for non-linear conservation laws and convection-diffusion equations. *J. Comput. Phys.* **2000**, *160*, 241–282. [CrossRef]
33. Lax, P.; Wendroff, B. Systems of conservation laws. *Commun. Pure Appl. Math.* **1960**, *3*, 217–237. [CrossRef]
34. Hou, T.Y.; LeFloch, P.G. Why nonconservative schemes converge to wrong solutions: Error analysis. *Math. Comp.* **1994**, *62*, 497–530. [CrossRef]
35. Feo, A.; Celico, F.; Zanini, A. Migration of DNAPL in Saturated Porous Media: Validation of High-Resolution Shock-Capturing Numerical Simulations through a Sandbox Experiment. *Water* **2023**, *15*, 1471. [CrossRef]
36. Feo, A.; Pinardi, R.; Scanferla, E.; Celico, F. How to Minimize the Environmental Contamination Caused by Hydrocarbon Releases by Onshore Pipelines: The Key Role of a Three-Dimensional Three-Phase Fluid Flow Numerical Model. *Water* **2023**, *15*, 1900. [CrossRef]

37. Feo, A.; Pinardi, R.; Artoni, A.; Celico, F. Three-Dimensional High-Precision Numerical Simulations of Free-Product DNAPL Extraction in Potential Emergency Scenarios: A Test Study in a PCE-Contaminated Alluvial Aquifer (Parma, Northern Italy). *Sustainability* **2023**, *15*, 9166. [CrossRef]
38. Pinardi, R.; Feo, A.; Ruffini, A.; Celico, F. Purpose-Designed Hydrogeological Maps for Wide Interconnected Surface–Groundwater Systems: The Test Example of Parma Alluvial Aquifer and Taro River Basin (Northern Italy). *Hydrology* **2023**, *10*, 127. [CrossRef]
39. Allen, G.; Goodale, T.; Lanfermann, G.; Radke, T.; Rideout, D.; Thornburg, J. Cactus Users' Guide. 2011. Available online: http://www.cactuscode.org/documentation/UsersGuide.pdf (accessed on 1 January 2023).
40. Cactus Developers. Cactus Computational Toolkit. Available online: http://www.cactuscode.org (accessed on 1 January 2023).
41. Goodale, T.; Allen, G.; Lanfermann, G.; Massó, J.; Radke, T.; Seidel, E.; Shalf, J. The Cactus Framework and Toolkit: Design and Applications. In *Vector and Parallel Processing—VECPAR'2002, Proceedings of the 5th International Converence, Porto, Portugal, 26–28 June 2002*; Lecture Notes in Computer Science; Springer: Berlin, Germany, 2003; Available online: http://edoc.mpg.de/3341 (accessed on 1 January 2023).
42. Schnetter, E.; Hawley, S.H.; Hawke, I. Evolutions in 3D numerical relativity using fixed mesh refinement. *Class. Quantum Gravity* **2004**, *21*, 1465–1488. [CrossRef]
43. Schnetter, E.; Diener, P.; Dorband, E.N.; Tiglio, M. A multi-block infrastructure for three-dimensional time-dependent numerical relativity. *Class. Quantum Gravity* **2006**, *23*, S553. [CrossRef]
44. Gugliotta, C.; Gasparo Morticelli, M.; Avellone, G.; Agate, M.; Barchi, M.R.; Albanese, C.; Valenti, V.; Catalano, R. Middle Miocene—Early Pliocene wedge-top basins of North-Western Sicily (Italy). Constraints for the tectonic evolution of a "non-conventional" thrust belt, affected by transpression. *J. Geol. Soc. Lond.* **2014**, *171*, 211–226. [CrossRef]
45. Catalano, R.; Valenti, V.; Albanese, C.; Accaino, F.; Sulli, A.; Tinivella, U.; Gasparo Morticelli, M.; Zanolla, C.; Giustiniani, M. Sicily's fold/thrust belt and slab rollback: The SI. *RI.PRO. seismic crustal transect. J. Geol. Soc. Lond.* **2013**, *170*, 451–464.
46. Cappadonia, C.; Coratza, P.; Agnesi, V.; Soldati, M. Malta and Sicily joined by geoheritage enhancement and geotourism within the framework of land management and development. *Swiss. J. Geosci.* **2018**, *8*, 253. [CrossRef]
47. Milani, C.; Hevia, A.; Foroni, E.; Duranti, S.; Turroni, F.; Lugli, G.A.; Sanchez, B.; Martín, R.; Gueimonde, M.; van Sinderen, D.; et al. Assessing the Fecal Microbiota: An Optimized Ion Torrent 16S rRNA Gene-Based Analysis Protocol. *PLoS ONE* **2013**, *8*, e68739. [CrossRef]
48. Caporaso, J.G.; Kuczynski, J.; Stombaugh, J.; Bittinger, K.; Bushman, F.D.; Costello, E.K.; Fierer, N.; Gonzalez Peña, A.; Goodrich, J.K.; Gordon, J.I.; et al. QIIME allows analysis of high-throughput community sequencing data. *Nat. Methods* **2010**, *7*, 335–336. [CrossRef]
49. Callahan, B.J.; McMurdie, P.J.; Rosen, M.J.; Han, A.W.; Johnson, A.J.; Holmes, S.P. DADA2: High-resolution sample inference from Illumina amplicon data. *Nat. Methods* **2016**, *13*, 581–583. [CrossRef]
50. Bokulich, N.A.; Kaehler, B.D.; Rideout, J.R.; Dillon, M.; Bolyen, E.; Knight, R.; Huttley, G.A.; Caporaso, G.J. Optimizing taxonomic classification of marker-gene amplicon sequences with QIIME 2′s q2-feature-classifier plugin. *Microbiome* **2018**, *6*, 90. [CrossRef]
51. Quast, C.; Pruesse, E.; Yilmaz, P.; Gerken, J.; Schweer, T.; Yarza, P.; Peplies, J.; Glöckner, F.O. The SILVA ribosomal RNA gene database project: Improved data processing and web-based tools. *Nucleic Acids Res.* **2012**, *41*, 590–596. [CrossRef] [PubMed]
52. Freeze, R.A.; Cherry, J.A. *Groundwater Book*; Prentice-Hall Inc.: Englewood Cliffs, NJ, USA, 1979.
53. Van Genuchten, M.T. A closed form equation for predicting the hydraulic conductivity of unsaturated soils. *Soil Sci. Soc. Am. J.* **1980**, *44*, 892–898. [CrossRef]
54. Yu-Shu, W. *Multiphase Fluid Flow in Porous and Fractured Reservoirs*; Elsevier: Oxford, UK, 2015; p. 243.
55. Rizzo, P.; Cappadonia, C.; Rotigliano, E.; Iacumin, P.; Sanangelantoni, A.M.; Zerbini, G.; Celico, F. Hydrogeological behaviour and geochemical features of waters in evaporite-bearing low-permeability successions: A case study in Southern Italy. *Appl. Sci.* **2020**, *10*, 8177. [CrossRef]
56. Zaa, C.L.Y.; McLean, J.E.; Dupont, R.R.; Norton, J.M.; Sorensen, D.L. Dechlorinating and iron reducing bacteria distribution in a TCE-contaminated aquifer. *Groundw. Monit. Remediat.* **2010**, *30*, 46–57. [CrossRef]
57. Della-Negra, O.; Chaussonnerie, S.; Fonknechten, N.; Barbance, A.; Muselet, D.; Martin, D.E.; Fouteau, S.; Fischer, C.; Saaidi, P.-L.; Le Paslier, D. Transformation of the recalcitrant pesticide chlordecone by *Desulfovibrio* sp. 86 with a switch from ring-opening dechlorination to reductive sulfidation activity. *Sci. Rep.* **2020**, *10*, 13545. [CrossRef]
58. Wolterink, A.; Kim, S.; Muusse, M.; Kim, I.S.; Roholl, P.J.; van Ginkel, C.G.; Stams, A.J.M.; Kengen, S.W. Dechloromonas hortensis sp. nov. and strain ASK-1, two novel (per) chlorate-reducing bacteria, and taxonomic description of strain GR-1. *Int. J. Syst. Evol. Microbiol.* **2005**, *55*, 2063–2068. [CrossRef] [PubMed]

Disclaimer/Publisher's Note: The statements, opinions and data contained in all publications are solely those of the individual author(s) and contributor(s) and not of MDPI and/or the editor(s). MDPI and/or the editor(s) disclaim responsibility for any injury to people or property resulting from any ideas, methods, instructions or products referred to in the content.

geosciences

MDPI

Article

Groundwater Quality Variations in Multiple Aquifers: A Comprehensive Evaluation for Public Health and Agricultural Use

Jeerapong Laonamsai [1,2,*], Veeraphat Pawana [1], Phupha Chipthamlong [1], Phornsuda Chomcheawchan [1], Kiattipong Kamdee [3], Bounhome Kimmany [4] and Phongthorn Julphunthong [1,5]

1 Department of Civil Engineering, Faculty of Engineering, Naresuan University, Phitsanulok 65000, Thailand
2 Water Resources Research Center, Faculty of Engineering, Naresuan University, Phitsanulok 65000, Thailand
3 Thailand Institute of Nuclear Technology, Nakonnayok 26120, Thailand
4 Department of Meteorology and Hydrology, Faculty of Water Resources, National University of Laos, Vientiane 01010, Laos
5 Research Center for Academic Excellence in Applied Physics, Faculty of Science, Naresuan University, Phitsanulok 65000, Thailand
* Correspondence: jeerapongl@nu.ac.th

Abstract: Understanding hydrological and hydrochemical processes is crucial for the effective management and protection of groundwater resources. This study conducted a comprehensive investigation into hydrochemical processes and variations in groundwater quality across five distinct aquifers in Phra Nakhon Si Ayutthaya, Thailand: Bangkok (BKK), Phra Pradaeng (PPD), Nakhon Luang (NKL), Nonthaburi (NTB), and Sam Khok (SK). Utilizing various diagrams, the findings revealed that high levels of sodium and salinity in shallow aquifers (BKK and PPD) were found which can impede soil permeability and have potential consequences on crop yields. The presence of four distinct types of groundwater—Na-Cl, Na-HCO_3, Ca-Cl, and Ca-HCO_3—suggests the influence of rock weathering, mineral dissolution, and ion exchange reactions with the surrounding geological formations, controlling the chemistry in the groundwater basin. The research also highlights concerns regarding groundwater quality, particularly elevated concentrations of heavy metals (e.g., Zn, Hg, Pd, Fe, and Mn) exceeding safe drinking water guidelines established by the World Health Organization (WHO) in certain samples. The evaluation of water suitability for consumption and irrigation using the Water Quality Index (WQI) and Wilcox diagram reveals a predominance of "poor" or "unsuitable" categorizations. Untreated sewage discharge and fertilizer usage were identified as the primary anthropogenic activities affecting hydrochemical processes in groundwater. These findings emphasize the need for continuous monitoring, appropriate management, and remediation efforts to mitigate potential hazards.

Keywords: groundwater quality; heavy metal; hydrogeology; groundwater contamination; hydrochemistry

1. Introduction

Groundwater is particularly valued for its relatively pure nature compared to surface water [1,2]. This water resource plays a crucial role in the domestic, agricultural, and industrial sectors [3,4], especially during the post-monsoon season. However, aquifers are increasingly facing threats of contamination as a result of factors such as industrial growth and urbanization, leading to health risks [5–9]. Given these threats, it is imperative to establish regular processes for monitoring water quality. Consequently, the identification and mitigation of associated health risks become urgent tasks for environmental and medical geochemists [7,10,11].

Geogenic sources, such as rock leaching and weathering, and anthropogenic activities, like metal mining, smelting, fossil fuel combustion, pesticide use, and sewage sludge, have

led to the accumulation of heavy metals in the soil and groundwater, including arsenic and lead [12–14]. Prolonged exposure to these metals through drinking water can result in various health issues, such as cancer, neurological disorders, developmental problems, and organ damage. Additionally, certain geological formations may contain radioactive elements like uranium or radon, which can seep into groundwater, increasing the risk of cancer and radiation-related health problems [15]. Natural pollutants, like fluoride, can also be present in groundwater due to chemical processes along its hydrogeological path [13]. Elevated fluoride levels in groundwater can cause dental and skeletal fluorosis. Geogenic pollutants can increase the salinity and mineral content of groundwater, negatively impacting plant growth and crop yield. Excessive salts, boron, selenium, and heavy metals can be toxic to plants, inhibiting nutrient uptake, photosynthesis, and causing cellular damage, ultimately leading to stunted growth, reduced crop quality, and crop failure [16].

Industrial processes and waste disposal are significant sources of heavy metal release into the environment [17–20]. Areas with high industrial concentrations often face water pollution as heavy-metal-containing wastewater infiltrates aquifers [21]. Health risks associated with heavy metal exposure include growth retardation and cancer development [22,23]. Ingestion or inhalation of lead-contaminated water or soil can cause neurological damage, developmental issues, anemia, and impaired kidney function [24]. Prolonged exposure to cadmium-contaminated water or crops can result in kidney damage, lung disease, and an increased risk of cancer [24]. Consumption of mercury-contaminated water or fish can lead to neurological damage, impaired cognitive function, and developmental issues in children. Chromium (Cr), released by metal plating, tanneries, and stainless-steel production, poses particular harm, increasing the risk of lung cancer, respiratory issues, liver damage, and skin problems [25,26]. Arsenic in groundwater poses health risks, including skin lesions, cardiovascular diseases, neurological effects, and an increased risk of cancer [7,10,24]. Arsenic accumulation in crops hampers growth, reduces yield, and poses a food safety risk [25].

In Phra Nakhon Si Ayutthaya, Thailand, there is significant concern regarding industrial and agricultural pollution. As a major rice-producing area, intensive agriculture in this region can result in the leaching of agrochemicals, such as pesticides and fertilizers, into groundwater, leading to water contamination and elevated nitrate levels, which pose risks to human health and the environment [27,28]. Industrial activities and urban development also contribute to groundwater pollution, with industrial effluents often containing heavy metals and other hazardous substances, while urban runoff carries pollutants such as oils, heavy metals, and chemicals into groundwater sources. Additionally, naturally occurring geogenic contaminants, such as arsenic or fluoride, can be present in elevated levels in groundwater [14], posing health risks if consumed. Therefore, a large population in the area is at risk of consuming contaminated water. Monitoring environmental hazards over time is crucial for understanding changes in contamination levels.

The objective of this study is to assess the impact of industrialization and agricultural practices, particularly fertilizer use, on groundwater quality in rapidly developing industrial regions. The research aims to answer the following question: What are the main hydrochemical characteristics and variations in groundwater quality across multiple aquifers in Phra Nakhon Si Ayutthaya, Thailand, and how do these variations affect public health and agricultural use? The central focus of this investigation is to examine the pressure exerted on the region's geological resources, specifically groundwater, due to the increasing use of fertilizers and the expansion of industrial zones. Various industries are assumed to gradually introduce pollutants into the environment, significantly affecting groundwater quality. The assumption is that these harmful substances can permeate into groundwater and contaminate the food chain, potentially leading to health complications if the water is consumed without treatment. This research aims to thoroughly analyze pollution levels and identify the most critical contaminants as a starting point. The study's objectives include raising awareness and implementing proactive measures to mitigate potential health risks based on the continuous assessment of pollution impacts.

2. Materials and Methods

2.1. Study Area and Climate Conditions

The study area is located in Phra Nakhon Si Ayutthaya Province (Figure 1a), situated in the quaternary floodplains (Qfd) of central Thailand (Figure 1b), approximately 76 km north of the coast. The province lies between longitudes 100.2° E and 100.8° E and latitudes 14.1° N and 14.7° N, sharing its borders with several other provinces.

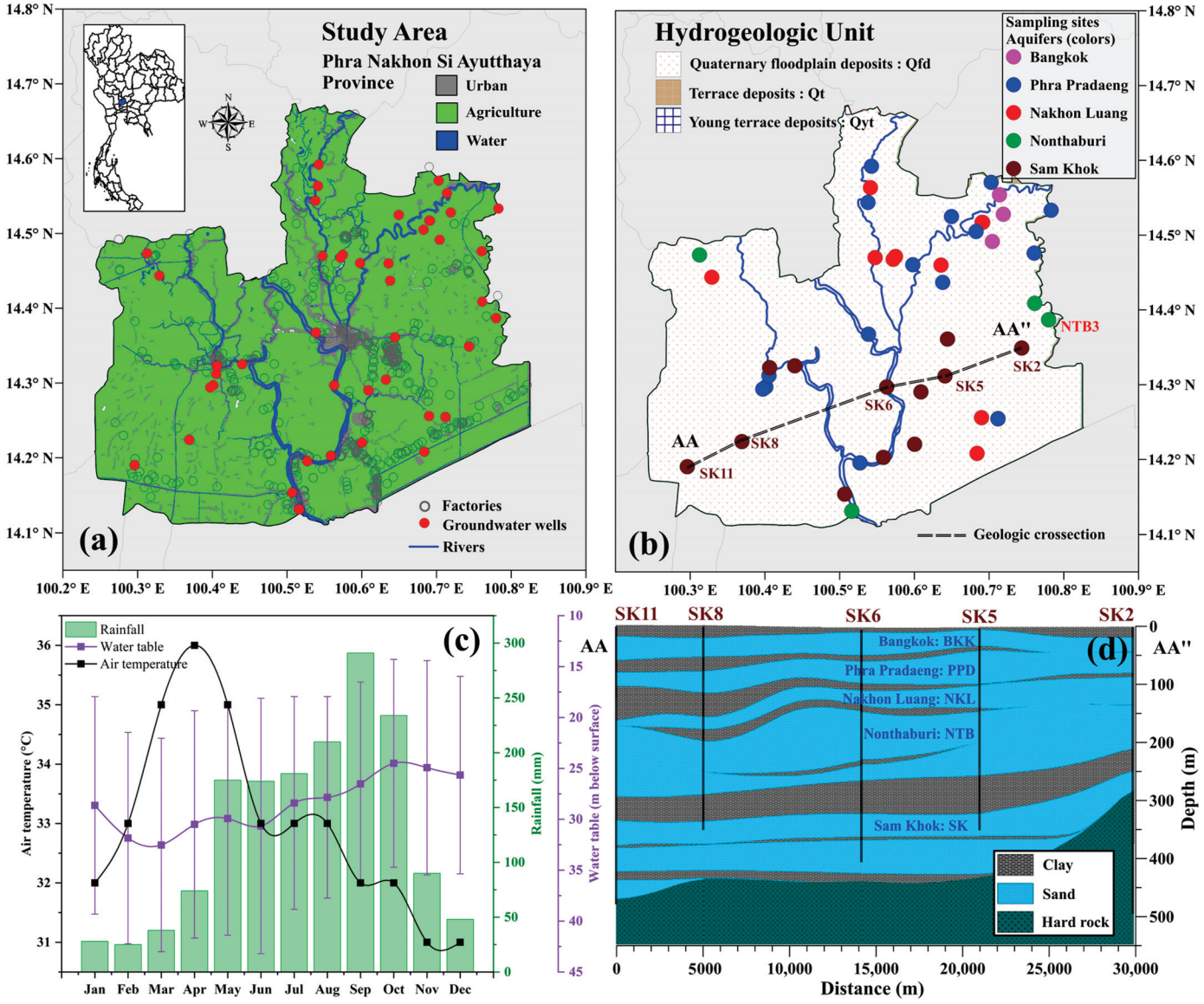

Figure 1. (**a**) Study area representing land use (source: LULC 2020 [29]). (**b**) Site samplings from various aquifers (e.g., Bangkok aquifer (BKK, 0–50 m depth), Phra Pradaeng aquifer (PPD, 51–100 m depth), Nakhon Luang aquifer (NKL, 101–150 m depth), Nonthaburi aquifer (NTB, 151–200 m depth), and Sam Khok aquifer (SK, 201–350 m depth)). (**c**) Mean monthly (1993–2022) rainfall (mm), mean monthly (1993–2022) air temperature (°C), and mean monthly (2013–2022) water table (m below earth surface) provided by the Thailand Department of Groundwater and the Department of Water Resources. (**d**) Geological cross section surveyed by the Thailand Department of Groundwater in 2022.

A total of 92 wells distributed over the area were observed. It covers an area of approximately 2501 km^2. Phra Nakhon Si Ayutthaya, like much of Thailand, experiences a tropical monsoon climate [30,31]. The region has three primary seasons: summer from

March to May, the rainy season from June to October, and winter from November to February. Summer temperatures can reach up to 35–40 °C, while during the winter, they typically range between 20 and 30 °C. The average annual rainfall (1993–2022) is approximately 1215 to 1432 mm, with heavy rain falling during the monsoon season, peaking around September (Figure 1c). Monthly rainfall can significantly vary, with minimal precipitation in summer and potentially over 200 mm per month at the height of the rainy season. Groundwater levels in the region are typically high (averaging 26.51 ± 9.77 m below the earth's surface) due to the flat topography and abundant rainfall. However, these levels can fluctuate throughout the year in response to rainfall patterns, with a one-month lag time [27], and extraction for irrigation and other uses. The water table tends to be at its highest at the end of the rainy season and gradually declines through summer until it is recharged by the rains again.

This study area, predominantly flat, is characterized by the central river basin of the Chao Phraya River, a significant waterway for both transportation and irrigation. Numerous smaller rivers and canals branching off from the Chao Phraya River have created a fertile, well-irrigated area, ideal for agriculture. The region's alluvial soils, combined with its tropical monsoon climate, support a variety of agricultural activities, with rice and coconut farming being the most prevalent. This area is also a vital hub of industry. Major industrial estates include the Rojana Industrial Park, Hi-Tech Industrial Estate, and Bang Pa-In Industrial Estate, hosting a variety of manufacturing units ranging from automotive, electronics, leather, and textile industries to food processing and packaging units. While the province is extensively utilized for agriculture (64%) and industry, there is also a significant amount of land used for residential areas, especially in and around urban centers. However, the province faces environmental challenges related to land use and industrialization, such as water pollution due to untreated industrial waste, soil degradation, and urban encroachment onto agricultural and natural lands [32].

2.2. Hydrogeological Settings

The hydrogeology of Phra Nakhon Si Ayutthaya, situated within the floodplain deposits of the Chao Phraya River basin, comprises a complex and distinct layered aquifer system (Figure 1d). This system consists of vertically arranged aquifers, each with its own unique properties and varying degrees of hydraulic interconnectivity [33]. The shallowest layer, known as the Bangkok aquifer (BKK), extends up to 50 m and primarily consists of alluvial deposits from the Holocene age. The BKK aquifer serves as the primary source of groundwater for domestic and agricultural purposes [34]. Below the BKK aquifer lies the Phra Pradaeng aquifer (PPD), situated between 51 and 100 m. Composed of older alluvial deposits from the Pleistocene age, the PPD aquifer functions as a significant water storage unit [34,35]. The Nakhon Luang aquifer (NKL), which extends from 101 to 150 m, consists of Tertiary sediments, both marine and non-marine, and is typically confined due to overlying impermeable layers [36]. The Nonthaburi aquifer (NTB) follows, ranging from 151 to 200 m and composed of late Pleistocene age sand and clay layers [36]. The hydrological characteristics of the NTB aquifer can vary widely. Lastly, the deepest layer is the Sam Khok aquifer (SK), stretching from 201 to 350 m and composed of early Tertiary marine sediments [36]. These aquifers receive recharge from rainfall and river infiltration, and they discharge into the rivers and canals [3]. Groundwater flow generally follows the surface topography, moving from the north and northeast toward the Chao Phraya River [37].

2.3. Sampling Collection

Water quality testing is a complex process involving multiple steps. Any missed or incorrectly executed step can compromise the entire test, making careful planning and understanding of the test's specific objectives essential [38]. This study conforms to the standard procedures delineated by the American Public Health Association (APHA) [39] and the United States Salinity Laboratory (USSL) [40], ensuring precise groundwater

sampling and analysis. In this specific study, the research involved collecting groundwater samples from hand-dug wells and boreholes dispersed across the province's industrial areas. During the dry season (November 2022), a total of 92 samples were gathered from these industrial estates, supplemented by additional samples from agricultural regions within the same surrounding area (Figure 1a,b). Borehole distribution across each aquifer of the study area encompasses eighteen boreholes (20% of total boreholes) in the BKK aquifer, nineteen boreholes (21% of total boreholes) in the PPD aquifer, fifteen boreholes (16% of total boreholes) in the NTB aquifer, twenty-three boreholes (25% of total boreholes) in the NKL aquifer, and seventeen boreholes (18% of total boreholes) in the SK aquifer. Physical and chemical analysis samples were collected using a 2.5 L low-density polyethylene bottle. A separate 1 L container, immediately supplemented with 2 mL of concentrated HNO_3 on-site, was utilized for metal content analysis. Prior to use, the containers designated for sampling underwent meticulous cleaning, rinsed five times with distilled water. The entire process employed chemicals of analytical grade.

2.4. Hydrogeochemical Analyses

On-site, immediate measurements were captured for appearance, pH, temperature (°C), electrical conductivity (μS/cm), and total dissolved solids (mg/L) of the water. Every sample received an accurate label, preparing it for subsequent laboratory analysis. Rigorous precautions were instituted to avoid contamination during the collection process. For instance, pH meter calibration using distilled water secured trustworthy readings. Likewise, sample bottles underwent meticulous rinsing, initially with distilled water, then with the water sample itself before collection.

A comprehensive assessment of water quality involved evaluating a wide range of parameters. These parameters included pH, temperature, electrical conductivity (EC), chloride (Cl), fluoride (F), total dissolved solids (TDS), nitrate (NO_3), sulfate (SO_4), phosphate (PO_4), carbonate (CO_3), bicarbonate (HCO_3), calcium (Ca), magnesium (Mg), sodium (Na), potassium (K), and several heavy metals such as arsenic (As), cadmium (Cd), nickel (Ni), lead (Pb), selenium (Se), chromium (Cr), zinc (Zn), mercury (Hg), iron (Fe), and manganese (Mn). Established instrumental techniques and standard analytical methods were employed to identify and measure these physical and chemical parameters [39]. Ion chromatography mass spectrometry (IC) was used to analyze primary ions, while an atomic absorption spectrophotometer (AAS) was utilized for trace and heavy metal evaluation. The analytical error for both methods was kept below 5% and 10%, respectively. The data collected on various water quality parameters and heavy metals were then compared against the drinking water quality guidelines set by the World Health Organization (WHO) to ensure compliance [41].

Numerous scientific studies have documented various methodologies for evaluating groundwater quality [42–44]. These methodologies utilize the physical and chemical characteristics of water and have been applied in different settings to determine its suitability for drinking. The Water Quality Index (WQI) method, which employs a weighted arithmetic index, has been widely used in many studies to assess water potability [42–45]. This investigation followed a similar approach, integrating the weighted arithmetic index method along with traditional graphical methods such as Stiff [46], Durov [47], Wilcox [48], and USSL diagrams [40].

Additionally, a ternary plot was conducted to analyze the chemical properties of groundwater. This plot illustrates the distribution of major cations (Na, K, and Ca) and anions (Cl, SO_4, and carbonate alkalinity) [49,50]. Carbonate alkalinity (Alk_c, meq/L) represents the combined concentration of CO_3 and HCO_3 ions. Furthermore, a binary diagram of Cl and SO_4+Alk_C was utilized to provide information about the total ionic salinity (TIS, Σmeq/L). By comparing the position of each groundwater sample with the iso-Σmeq/L lines (lines with a slope of -1), the TIS value could be observed [51].

The World Health Organization's guidelines for drinking water [41] served as a reference point against which the computed WQIs were measured. The WQI offers a

simplified summary of water quality based on various chemical parameters and can be calculated using the following equation:

$$WQI = \Sigma (W_i \times q_i) \quad (1)$$

In this formula, "W_i" represents the relative weight of each parameter, and "q_i" denotes the sub-index for each parameter (Table 1). The W_i is usually assigned based on the perceived importance ($w_i/\Sigma w_i$, Table 1) of each parameter for water quality. The assigned weight (w_i) to each parameter (between 1 and 5) was considered based on its relative importance to the overall quality of groundwater [52].

Table 1. Standards, weights, and relative weights used for WQI computation.

Parameters	WHO (2022) Standard (S_i, mg/L)	Weight (w_i, mg/L)	Relative Weight (W_i, mg/L)
pH	8.5	4	0.0533
TDS	1000	4	0.0533
Ca	100	2	0.0267
Mg	50	2	0.0267
Na	200	3	0.0400
K	20	2	0.0267
HCO_3	350	2	0.0267
SO_4	250	3	0.0400
Cl	250	3	0.0400
NO_3	50	2	0.0267
PO_4	5	4	0.0533
F	1	5	0.0667
As	0.01	5	0.0667
Zn	5	2	0.0267
Pb	0.01	5	0.0667
Hg	0.006	5	0.0667
Fe	0.3	3	0.0400
Mn	0.4	4	0.0533
Cr	0.05	5	0.0667
Cd	0.003	5	0.0667
Ni	0.02	5	0.0667
Total		75	1

The sub-index or q_i is typically computed by comparing the measured value (C_i) for each parameter with its respective guideline or standard (S_i). Each q_i was calculated using the following equation:

$$q_i = (C_i/S_i) \times 100 \quad (2)$$

where C_i is the observed concentration (mg/L) of each parameter in the groundwater sample, and S_i is the standard guideline value (mg/L) for that parameter as set by a recognized authority, such as the World Health Organization (WHO) [41]. The resulting q_i values are then scaled and summed to obtain the overall WQI. A WQI exceeding 300 indicates that the water is unsuitable for drinking [53].

Groundwater quality for irrigation applications was evaluated using various tools. The methodologies incorporated the United States Salinity Laboratory (USSL) diagram [40], the Wilcox diagram [48], and electrical conductivity (EC) values. Additionally, the calculation of essential agricultural indices, namely the sodium adsorption ratio (SAR) [40] and the sodium percentage (%Na) [54], was carried out. The SAR was calculated using the following equation:

$$SAR = [Na^+]/\sqrt{([Ca^{2+}] + [Mg^{2+}])/2} \quad (3)$$

Here, the concentrations of sodium (Na^+), calcium (Ca^{2+}), and magnesium (Mg^{2+}) are measured in milliequivalents per liter (meq/L). The sodium percentage (%Na) was computed using the following formula:

$$\%Na = [Na+] \times 100/([Ca^{2+}] + [Mg^{2+}] + [Na^+] + [K^+]) \quad (4)$$

In this formula, potassium (K+) concentration is also considered, with all ion concentrations measured in meq/L. These methods, incorporated in the study for determining the suitability of water for irrigation, have been regarded as effective strategies in assessing the aptness of water for irrigation applications [54].

3. Results and Discussion

3.1. Hydrochemical Facies in Groundwater

Groundwater levels, influenced by aquifer type and geographic location, can vary from a few meters to over 40 m below the surface (Figure 2a). The Sam Khok (SK) aquifer typically exhibited deeper groundwater depths (ranging from 3.50 m to 41.38 m below the earth's surface, with an average of 27.59 ± 11.56 m), suggesting the presence of elevated bedrock or less permeable soil layers [55]. The Nakhon Luang (NKL) aquifer showed profound levels, but certain areas had shallower readings (with an average of 21.44 ± 8.06 m), indicating varying geological conditions or recharge rates. The Phra Pradaeng (PPD) aquifer displayed a spectrum of water levels (ranging from 4.04 m to 44.77 m, with an average of 17.81 ± 12.03 m), hinting at diverse geological situations. Conversely, the Nonthaburi (NTB) and Bangkok (BKK) aquifers predominantly revealed shallower groundwater depths. The NTB aquifer presented a range of levels (from 5.06–34.76 m, with an average of 21.44 ± 8.06 m) but trended toward deeper ones in certain locations (Figure 2a), while the BKK aquifer consistently reflects shallower levels (averaging 13.85 ± 11.99 m), implying regions of high permeability or superior recharge rates [35].

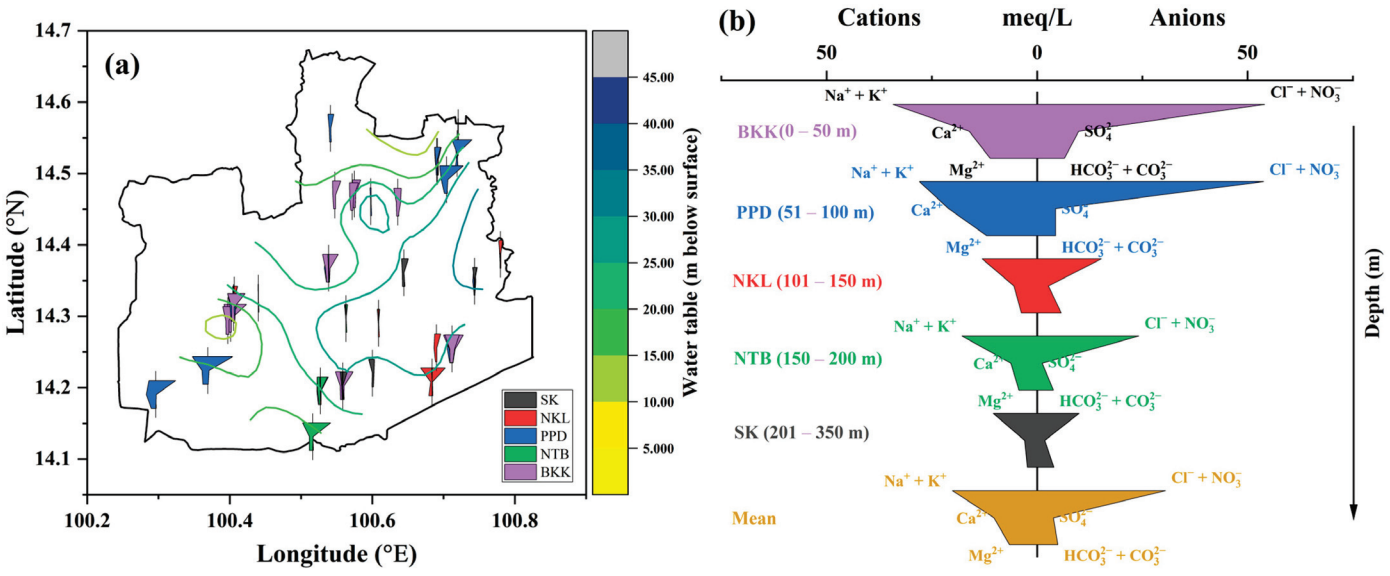

Figure 2. (**a**) Stiff diagram map (in meq/L unit) showing the spatial distribution of main cations ($Na^+ + K^+$, Ca^{2+}, and Mg^{2+}) and anions ($Cl^- + NO^{3-}$, $SO_4{}^{2-}$, and $HCO_3{}^- + CO_3{}^{2-}$) in groundwater in 2022. Colors represent groundwater aquifers. Contour lines show average water table during 2013–2022. (**b**) Stiff diagram for mean main ions (meq/L) in each aquifer and for overall groundwater samples. Colors in Stiff indicate groundwater aquifers (e.g., Bangkok aquifer (BKK, 0–50 m depth), Phra Pradaeng aquifer (PPD, 51–100 m depth), Nakhon Luang aquifer (NKL, 101–150 m depth), Nonthaburi aquifer (NTB, 151–200 m depth), and Sam Khok aquifer (SK, 201–350 m depth)).

Geographic location, such as longitude 100.64° E and latitude 14.46° N, also plays a significant role, as different aquifers exhibited varied water levels (Figure 2b), indicating complex geological settings. However, it is important to note that these observations are general, and specific geological factors, hydrological conditions, and human interventions can greatly influence groundwater levels [37]. Differences in extraction rates, aquifer characteristics (permeability and porosity), and rainfall patterns and evaporation can contribute to variations in groundwater depths between aquifers [56].

The physical properties of groundwater showed variations across different aquifers. The BKK aquifer showed variability in electrical conductivity (EC), ranging from 712.46 to 11,266.21 μS/cm (averaging 7398.31 ± 3523.96 μS/cm), with some wells recording high levels of total dissolved solids (TDS, maximum 7323.04 mg/L). The PPD aquifer also showed high TDS levels at certain sites (12,275.90 mg/L), potentially indicating pollution or high mineral content. The NKL aquifer exhibited considerable variations in pH levels (5.99–9.77 with an average of 8.01 ± 0.88), suggesting diverse water quality. The NTB aquifer had a low pH value in one site (3.1), indicating a more acidic environment influenced by local soil composition or biological activities. Lastly, the SK aquifer demonstrated varied EC values, ranging from 572.91 to 3778 μS/cm with a mean of 1536.22 ± 1142.50 μS/cm.

There was a significant variation in calcium (Ca) concentration, ranging from very low to high values across different aquifers (Figure 2b). The Ca ranged between 1.0 mg/L (NTB aquifer) and 1640.0 mg/L (BKK aquifer) with an average value of 175.84 ± 258.08 mg/L (Table 2). A wide variation was also found for magnesium (Mg) concentration (0.7–487.78 mg/L). The overall average Mg was 53.55 ± 101.52 mg/L. The maximum Mg was observed at the PPD aquifer (487.78 mg/L), while the minimum value was found at the NTB aquifer (0.7 mg/L). Higher concentrations of Ca and Mg ions usually indicate the presence of limestone and dolomite in the geological substrate [57]. This could be the case for the samples from the PPD aquifer, which show very high concentrations of both calcium and magnesium. These ions are also important indicators of water hardness [58], with higher concentrations leading to harder water.

Table 2. Concentration of cations and anions in groundwater across different aquifers.

Ions	Concentration (mg/L)			
	Maximum (Aquifer)	**Minimum (Aquifer)**	**Average**	**Standard Deviation**
Ca	1640.0 (BKK)	1.0 (PPD)	219.53	258.08
Mg	487.78 (PPD)	0.7 (SK)	46.97	101.52
Na	2888.89 (PPD)	26.0 (BKK)	590.62	507.81
K	60.0 (NKL)	1.0 (PPD)	10.94	10.99
Cl	9548.8 (BKK)	7.2 (NTB)	834.17	1463.07
SO_4	1109.33 (BKK)	0.0 (PPD)	343.88	254.79
HCO_3	788.0 (SK)	0.0 (PPD)	309.47	142.52
CO_3	370.25 (NKL)	0.0 (PPD)	216.83	11.10
NO_3	21.5 (BKK)	0.0 (NTB and SK)	2.68	11.69

Bangkok aquifer (BKK, 0–50 m depth), Phra Pradaeng aquifer (PPD, 51–100 m depth), Nakhon Luang aquifer (NKL, 101–150 m depth), Nonthaburi aquifer (NTB, 151–200 m depth), and Sam Khok aquifer (SK, 201–350 m depth).

The sodium (Na) concentration varied significantly between aquifers (Figure 2b), with an average of 446.78 ± 507.81 mg/L. The maximum was found in the PPD aquifer (2888.89 mg/L), while the BKK aquifer had the minimum Na concentration (26.0 mg/L), reflecting differences in the composition and sources of groundwater [59]. Variations in mineralization were also observed in groundwater, as indicated by distinct potassium (K) levels (Table 2). The maximum K was 60.0 mg/L (NKL), and the minimum K was 1.0 mg/L, found at the PPD aquifer. The Na and K ions are commonly found in igneous and metamorphic rocks, as well as in clays [60]. High concentrations of Na ion, such as in some samples from PPD, could also signify a large input from such rocks or from seawater intrusion.

Chloride (Cl) concentration showed a broad variation, ranging from 7.2 mg/L (NKL aquifer) to 9548.8 mg/L (BKK aquifer), indicating different levels of salinity and potential sources such as seawater intrusion or anthropogenic activities [35]. Furthermore, there was also a significant variation in sulfate (SO_4) concentration (0.0–1109.33 mg/L, Table 2), reflecting differences in geological formations and groundwater flow patterns. Extremely high levels of Cl and SO_4, like those found in the samples from PPD and BKK, could suggest contamination from industrial effluents, sewage, or possible seawater intrusion [61].

Moreover, the bicarbonate (HCO_3) concentration varied from zero to 788.0 mg/L in the SK aquifer, which can be influenced by factors such as carbonate rock dissolution and groundwater recharge [62]. Different hydrochemical conditions can also result in varying carbonate (CO_3) concentrations (0.0–219.67 mg/L), but these were generally low (Figure 2b). The HCO_3 and CO_3 ions are associated with limestone and are a significant component of temporary hardness in water [58]. Therefore, high HCO_3 and CO_3 levels, such as in the samples from the NKL aquifer, could indicate the presence of limestone in the aquifer. Additionally, high nitrate (NO_3) concentration indicates potential sources such as agricultural activities or contamination in the BKK aquifer (21.5 mg/L) (Table 2 and Figure 2b). NO_3 is also associated with agricultural runoff, especially from fertilizer use and wastewater treatment plants [63]. Higher concentrations, as seen in some samples from PPD and BKK, could suggest contamination from these sources. Long-term exposure to high levels of nitrates is harmful to human health, particularly for infants and pregnant women [63]. Conversely, it was not found in the deeper aquifers (NTB and SK).

3.2. Groundwater Characterization

To interpret and identify the prominent ionic elements and water mixtures in the local aquifer, the results relied on a series of traditional graphical presentations of the hydrochemical data. A well-recognized methodology to categorize groundwater types according to their ionic constituents comes from Durov [47] (Figure 3). The Durov diagram shows all 58 samples lying in Zone 1, implying a Na predominance among the cations and Cl and HCO_3 predominance in Zone 5 and Zone 7, respectively, for the anions. The high percentages of Na + K could suggest the influence of saltwater intrusion or water–rock interactions [60,61]. However, there was no correlation between TDS and Na+K, and the pH in groundwater did not vary based on Cl ions. A high concentration of Cl suggests the influence of evaporation, sewage pollution, or saltwater intrusion [35]. Additionally, many samples showed CO_3+HCO_3 as the dominant anion. High bicarbonate can indicate groundwater that is influenced by carbonate minerals and is common in groundwater, which can be further affected by soil CO_2 [64]. In addition to saltwater intrusion, a suggestion from the Durov plot is that calcite and gypsum dissolution (Zone D, Figure 3) and cation exchange serve as the principal hydrochemical processes affecting groundwater chemistry in the area under study. This could also be due to the infiltration of water from bicarbonate minerals (Zone G, Figure 3) [47].

The hydrochemical aspects presented by the Durov diagram are confirmed in the ternary plots of cations and anions (Figure 4). Displayed in the cation field (Figure 4a) is an enrichment in Na (average 68.72 $\pm$ 16.08 eq%) and Ca (average 30.50 $\pm$ 15.99 eq%), with Cl (average 58.82 $\pm$ 29.81 eq%) and HCO_3 (average 30.97 $\pm$ 27.87 eq%) prevailing in the anion field (Figure 4b). Four types of groundwater can be discerned: the Na-Cl type, represented by 50 samples; the Na-HCO_3 type, represented by 8 samples; the Ca-Cl type, represented by 7 samples; and a mixed type, represented by only 17 samples. The Na-Cl type was the most common type of groundwater in the investigated area, which signifies a high sodium and chloride concentration. Sodium and chloride can occur naturally in groundwater from the dissolution of salt deposits and the weathering of rocks containing sodium-bearing minerals [60]. However, high Na and Cl levels might be indicative of anthropogenic influences such as wastewater, septic system, or agricultural effluents, especially in coastal regions where seawater intrusion may be a factor [65]. The Na-HCO_3 groundwater type indicates a longer residence time with more water–rock interactions [66],

which can lead to an increase in sodium and bicarbonate ions. This type was also associated with more alkaline conditions [67], and the weathering of silicate minerals like feldspar or clay minerals lead to the Na-HCO_3 type of groundwater [68]. The industrial effects could be found in the Ca-Cl type. In addition to the dissolution of minerals like gypsum and anhydrite (for calcium) and halite (for chloride), anthropogenic factors like industrial effluents or agricultural runoff contribute to the calcium or chloride levels in this type of groundwater [69]. The last group is the fresh water type dominated by Ca-HCO_3 composition (Figures 3 and 4) suggesting the dissolution of Ca-rich phases and ionic exchange controlling the geochemical processes, particularly occurring in metabasaltic and carbonatic rocks [20,70].

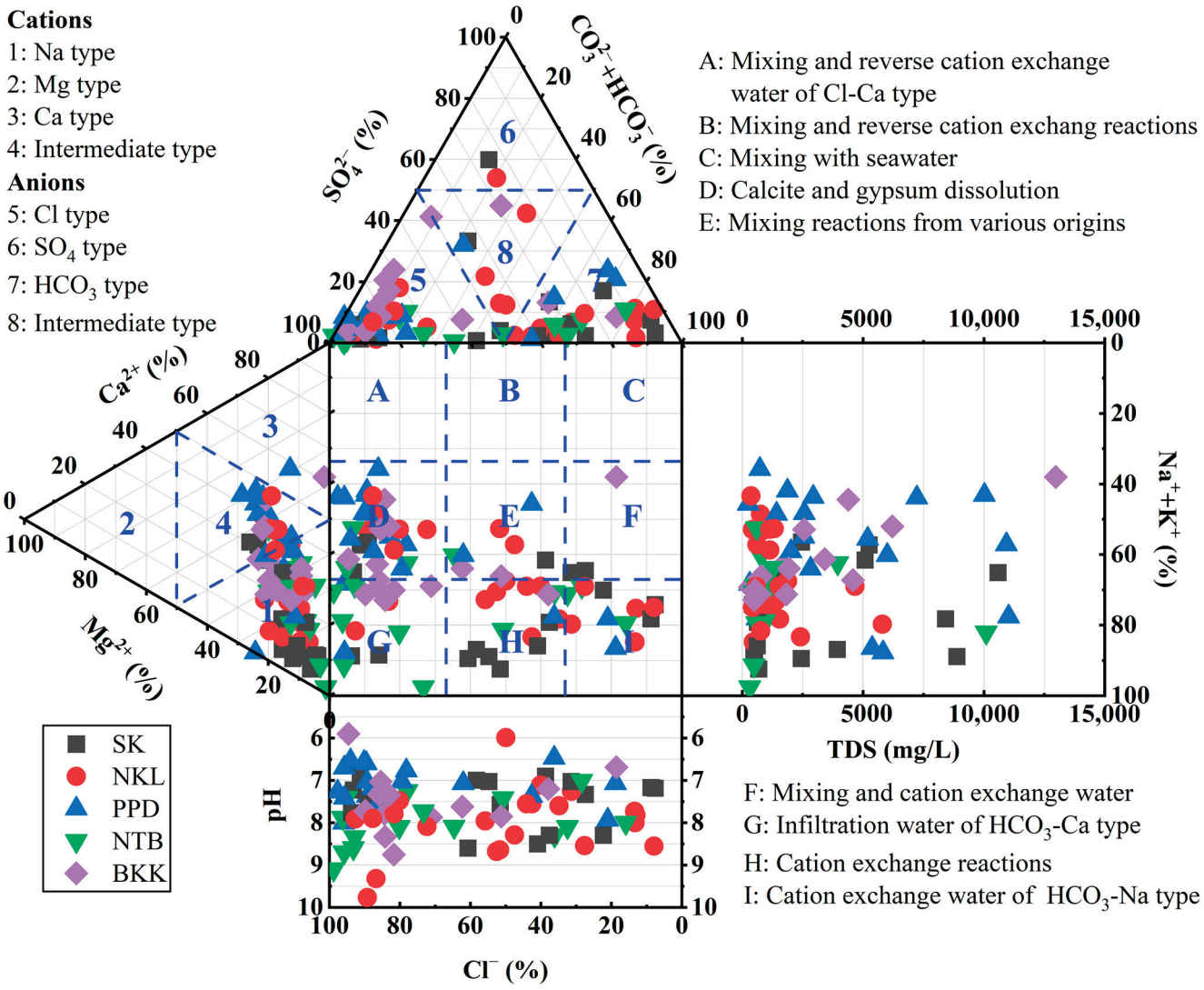

Figure 3. Durov diagram showing hydrogeological processes in Phra Nakhon Si Ayutthaya Province in 2022. Colors indicate groundwater aquifers (e.g., Bangkok aquifer (BKK, 0–50 m depth), Phra Pradaeng aquifer (PPD, 51–100 m depth), Nakhon Luang aquifer (NKL, 101–150 m depth), Nonthaburi aquifer (NTB, 151–200 m depth), and Sam Khok aquifer (SK, 201–350 m depth)).

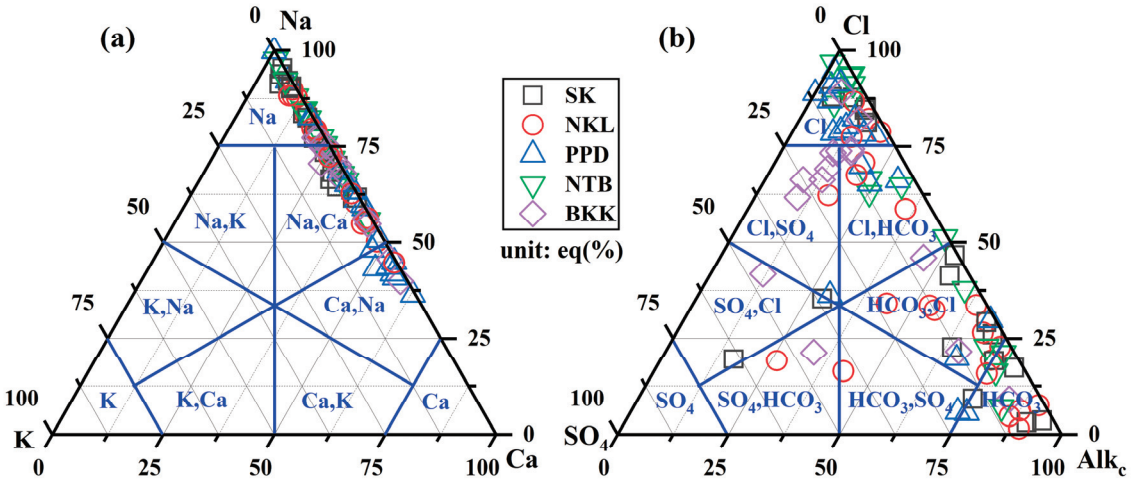

Figure 4. Ternary diagram for (**a**) cations (Na, K, and Ca) and (**b**) anions (SO_4, Cl, and Alkalinity). Colors indicate groundwater aquifers (e.g., Bangkok aquifer (BKK, 0–50 m depth), Phra Pradaeng aquifer (PPD, 51–100 m depth), Nakhon Luang aquifer (NKL, 101–150 m depth), Nonthaburi aquifer (NTB, 151–200 m depth), and Sam Khok aquifer (SK, 201–350 m depth)).

Furthermore, the groundwater type differs between aquifers (BKK, PPD, NKL, NTB, and SK) and shows different dominant ions, indicating diverse geological formations and sources of the water, as well as different levels of interaction with rocks and soil. These findings should be validated by other potentially comprehensive hydrogeochemical analyses (e.g., stable isotopes, trace elements) to confirm the sources of major ions.

When considering the salinity, the water samples were plotted on total ionic salinity (TIS, meq/L) (Figure 5). A TIS between 5 and 100 meq/L is observed. The binary diagram of Cl versus SO_4+Alk_C shows that the groundwater in the BKK and PPD aquifers had high salinity greater than 60 meq/L with an average value of 70.26 ± 41.38 meq/L for BKK and 62.32 ± 60.66 meq/L for PPD. This high salinity in shallow groundwater indicates the salinization from sea water flowing upstream along the Chao Phraya River. Conversely, salinity was generally low (<30 meq/L) in the deeper groundwater aquifers (deeper than 100 m depth) such as NKL, NTB, and SK. In addition to variation in depth, TIS also differed between groundwater basins in Thailand. The groundwater in southern Thailand has reported that their TIS was between 0.007 and 0.12 meq/L depending on the geological and geographical settings [71]. Compared to other regions, a TIS of 20–80 meq/L was reported for the groundwater in the industrial areas of Shaying River Basin, China [72]. The high salinity of groundwater is also the result of natural processes such as the interaction with soluble evaporite. Conversely, lower-TIS groundwater (<45 meq/kg) was observed in Mozambique [50]. Their groundwater was not mixed with saline water.

3.3. Groundwater Quality for Human Consumption

The heavy metal concentration (mg/L) varied between aquifers across the study area (Figure 6). Compared to the World Health Organization's (WHO) drinking water standards [41] (Table 1), the concentrations of several heavy metals (as shown in Appendix A, Table A1), notably zinc (0–140 mg/L, averaged 8.01 ± 22.20 mg/L), mercury (0–1.02 mg/L, averaged 0.17 ± 0.29 mg/L), lead (0–0.159 mg/L, averaged 0.0031 ± 0.017 mg/L), manganese (0–830 mg/L, averaged 132.59 ± 186.02 mg/L), and iron (0–580 mg/L, averaged 27.70 ± 91.13 mg/L) in certain groundwater samples, significantly exceed the WHO's standard [41] for safe drinking water (Figure 6). These findings indicate potential public health risks if the water is consumed without proper treatment. However, the contaminants might come from various sources, including agricultural runoff, industrial waste, and natural mineral deposits [73]. It is also worth noting the wide range of concentrations for each metal across different locations (Figure 6). This suggests significant spatial variability in the

groundwater's heavy metal contamination, which could be due to variations in local geology, the influence of human activities such as agricultural and industrial activities [17,21], or both.

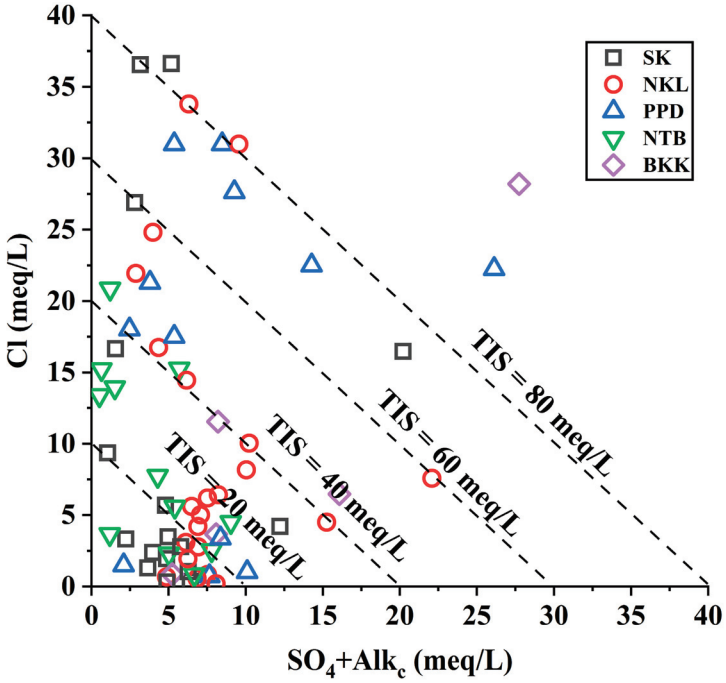

Figure 5. Total ionic salinity (TIS) diagram. Colors indicate groundwater aquifers (e.g., Bangkok aquifer (BKK, 0–50 m depth), Phra Pradaeng aquifer (PPD, 51–100 m depth), Nakhon Luang aquifer (NKL, 101–150 m depth), Nonthaburi aquifer (NTB, 151–200 m depth), and Sam Khok aquifer (SK, 201–350 m depth)).

Natural sources of zinc (Zn) in groundwater include the dissolution and weathering of Zn-containing rocks and minerals present in the Earth's crust [11,74]. In groundwater, the Zn concentration is usually below 0.010–0.040 mg/L [74,75]. Extremely high Zn in the study area might be released from the use of Zn-containing materials like rubber tires in vehicle industries [11]. The presence of Zn in groundwater can have implications for both human health and crop production [76]. Zn is an essential micronutrient for human health, and its deficiency can lead to various health problems [77,78]. Conversely, excessive Zn intake can also be harmful [26,77,79]. In terms of crop production, Zn plays a vital role in several plant physiological functions and is necessary for optimal growth and development. Zn deficiency in soil–crop systems is widespread globally, particularly in calcareous, high-pH, eroded, and land-leveled soils [76]. The findings suggest reducing groundwater use or using iron oxide [80] and zeolite [81] in situ adsorption barriers. Concentrations of dissolved zinc were strongly reduced due to inserting the iron oxide or zeolite permeable barriers.

Industrial activities like leather manufacturing, mining, and chemical manufacturing can release mercury (Hg) into the environment [11,82]. The Hg can transform into methylmercury, a highly toxic form that can accumulate in fish and contaminate water bodies [83]. Consuming Hg-contaminated water or fish can cause neurological damage, impaired cognitive function, and developmental issues in children [82,84]. To reduce Hg below standard limits [41], the use of synthetic chelating ligands such as K_2BDET could reduce mercury concentrations [85]. Ingesting or inhaling lead (Pb)-contaminated water or soil released from battery manufacturing and paint production can lead to neurological damage, developmental issues in children, anemia, and impaired kidney function [24]. Lead can also accumulate in crops, affecting their growth and quality [86]. According to

the literature report, the 5 g/L of kaolin-supported nanoscale zero-valent iron can remove Pb from wastewater within 60 min [87,88].

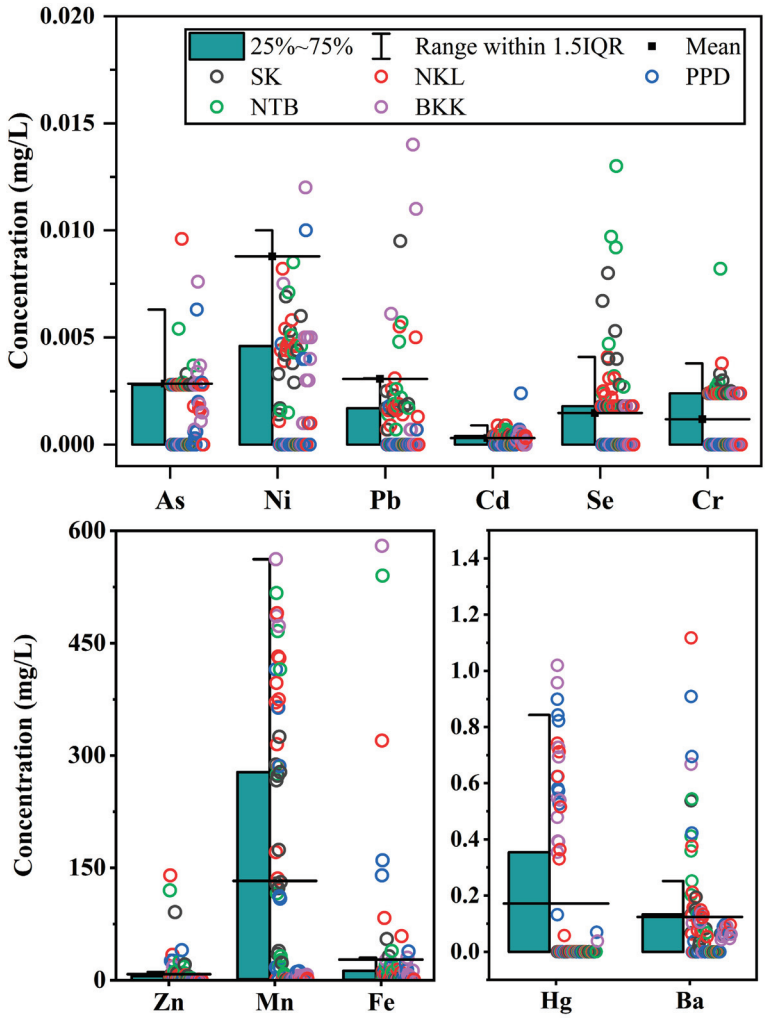

Figure 6. Heavy metal concentration in milligrams per liter (mg/L) of groundwater in various aquifers in Phra Nakhon Si Ayutthaya, Thailand, in 2022. Colors indicate groundwater aquifers (e.g., Bangkok aquifer (BKK, 0–50 m depth), Phra Pradaeng aquifer (PPD, 51–100 m depth), Nakhon Luang aquifer (NKL, 101–150 m depth), Nonthaburi aquifer (NTB, 151–200 m depth), and Sam Khok aquifer (SK, 201–350 m depth)).

The manufacturing can also introduce manganese (Mn) and iron (Fe) into the environment through wastewater discharges [89]. High levels of Mn in drinking water can lead to health issues such as neurological effects, including cognitive and behavioral changes [90]. It can also cause manganism, a condition similar to Parkinson's disease, characterized by movement disorders. High concentrations of Mn in groundwater can also lead to a condition called manganese toxicity, which affects various crops, including rice, soybeans, and wheat [91]. Symptoms of manganese toxicity in plants include leaf chlorosis, stunted growth, and reduced crop yield [25,92]. In general, Fe is an essential nutrient for the human body, but excessive iron concentrations in drinking water can pose health risks. High Fe levels may cause gastrointestinal issues, such as stomach pain, nausea, and diarrhea [91]. Additionally, Fe can affect the taste, odor, and appearance of water, making it less appealing for consumption [25]. However, Fe and Mn can be removed from groundwater by a process that combines oxidation and microfiltration [93,94]. Furthermore, industries such as mining, metal smelting, and wood preservation might cause arsenic (As) contamination in groundwater [14], posing significant health risks. Prolonged exposure to arsenic can

lead to skin lesions, cardiovascular diseases, and neurological effects [7,25,63]. Previous research has documented that using coconut husk carbon can remove As concentration with a metal adsorption capacity of 159 mg/g [95].

Hydrochemical characterization, being the initial phase in assessing water quality, identified the concentration of individual parameters in this study (Figures 2–6). It also evaluated groundwater quality by comparing the results to WHO guidelines [41] (Table 1). The Water Quality Index (WQI), however, takes on a critical role in assessing the overall groundwater quality. It provides a comprehensive view of the influence of groundwater's chemical parameters on its quality. Using the water quality classification model [53], the general evaluation of groundwater for drinking purposes was derived (Table 3). The result revealed that none of the samples fell into the "excellent water (WQI < 50)" or "good water (51 < WQI < 100)" categories. A significant proportion of samples, notably all from all aquifers, displayed WQI values that would categorize them as "poor water (101 < WQI < 200)" and even beyond (Table 3). In fact, many values exceeded 300 (84% of all samples), indicating that they could be classified as "unsuitable water" for drinking. A few samples showed WQI values that were close to or within the lower end of the "poor water" category, or in a few isolated cases, below 100 (13% of all samples). However, the majority of samples are not classified as suitable for drinking according to the classification scheme by Sahu and Sikdar [53]. The spatial distribution of these groundwater types (Figure 2a) as depicted by the WQI values (Table 3) suggests that groundwater quality varies significantly within the study area, with many areas posing potential health risks if the water is consumed. Although some samples contained heavy metals below the WHO standard limits (Figure 6), continuous monitoring and mitigation measures are recommended due to the harmful effects of long-term low-concentration exposure. The local health and environment authorities should investigate further to identify the sources of these heavy metals and consider appropriate treatment and remediation measures. The result suggests that the use of nanoscale zero-valent iron and in situ permeable barriers such as iron oxide, zeolite, chelation, and microfiltration is necessary to improve water quality before consumption [80,81,87,88,96].

Table 3. Water Quality Index (WQI).

Aquifers	Water Quality Index (WQI)		
	Max	Min	Mean
BKK	14,314	28	2590
PPD	5752	22	1659
NKL	9251	55	2761
NTB	11,443	23	3314
SK	4414	26	1775
Average	9035	31	2419

Bangkok aquifer (BKK, 0–50 m depth), Phra Pradaeng aquifer (PPD, 51–100 m depth), Nakhon Luang aquifer (NKL, 101–150 m depth), Nonthaburi aquifer (NTB, 151–200 m depth), and Sam Khok aquifer (SK, 201–350 m depth). Excellent water (WQI < 50), good water (51 < WQI < 100), poor water (101 < WQI < 200), unsuitable water for drinking (WQI > 300) [53].

3.4. Groundwater Quality for Irrigation Purposes

The sodium adsorption ratio (SAR) is a measure of the suitability of water for use in agricultural irrigation, as determined by the concentrations of solids dissolved in the water [40]. The results for the SAR were plotted with the EC value, ranging from 391 μS/cm to 19,181 μS/cm. EC, or electrical conductivity, is a measure of the water's ability to conduct electricity, which indicates the number of dissolved salts or substances in the water [86] (Figure 7a). High values of EC denote high salinity, which is not favorable for most crops [86]. Irrigation with high-salinity water can result in salt accumulation in the root zone, impacting plant growth and yield. Crops vary in their tolerance to salinity [16]. In Phra Nakhon Si Ayutthaya Province, most agricultural crops consist of rice and coconut.

Both rice and coconut trees have moderate salinity tolerance. For rice, the threshold EC is about 3000 µS/cm, and for coconut, it is slightly higher [16].

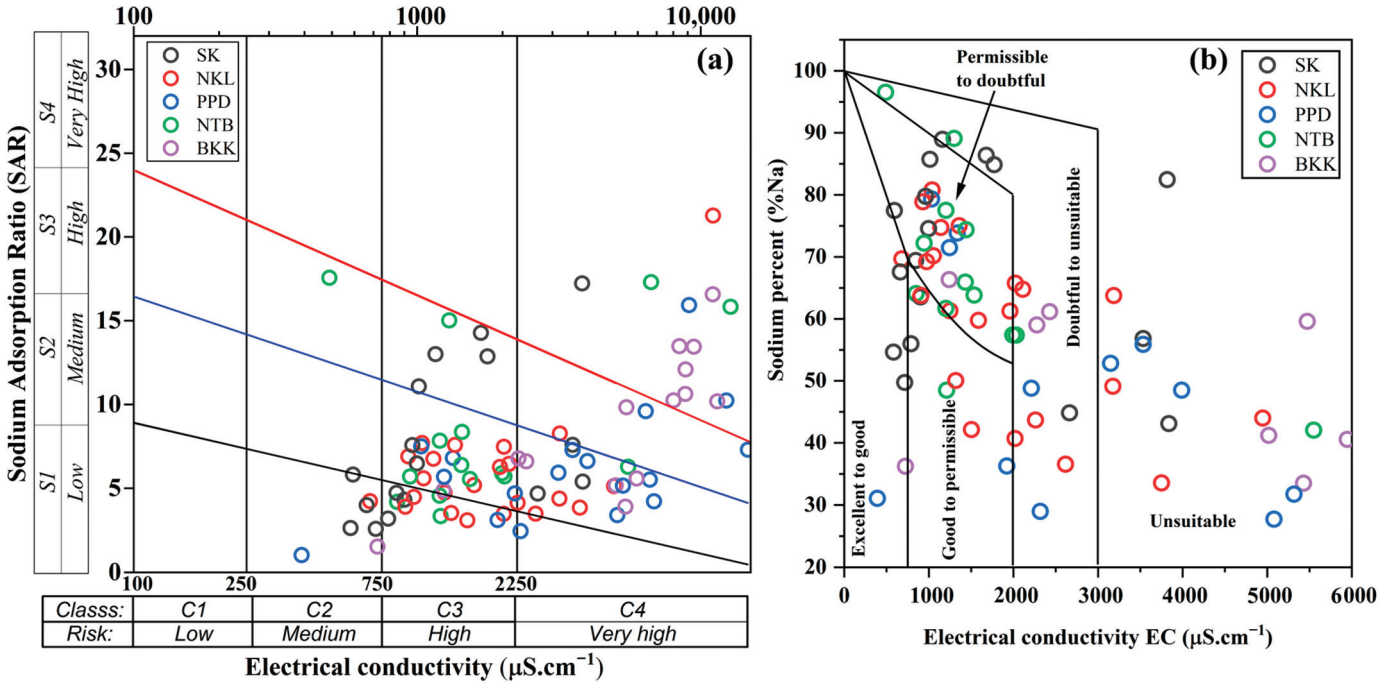

Figure 7. (**a**) USSL diagram showing sodium adsorption ratio (SAR) and electrical conductivity (EC, µS/cm) at sampling stations. (**b**) Wilcox diagram showing sodium percent (%Na) and electrical conductivity (EC, µS/cm) at sampling stations. Colors in plots indicate groundwater aquifers (e.g., Bangkok aquifer (BKK, 0–50 m depth), Phra Pradaeng aquifer (PPD, 51–100 m depth), Nakhon Luang aquifer (NKL, 101–150 m depth), Nonthaburi aquifer (NTB, 151–200 m depth), and Sam Khok aquifer (SK, 201–350 m depth)).

The SAR values fell in the range of 1.03–21.28 (averaged 7.38 ± 4.36) for all the samples and were typically found to be in the range of 1.03–5.92 for the groundwater deeper than 100 m (NKL, NTB, and SK aquifers). This indicates a sodium hazard class of S1 (Figure 7a) and excellent water quality [97]. Groundwater with SAR values greater than 6 is observed to have permeability problems [40,98], indicating that sodium salts dominate, which can result in soil swelling and decreased permeability [66,97], impeding the uptake of water by crops.

Furthermore, the samples were also assessed for sodium hazard or sodium percent (%Na) [54] (Figure 7b). It represents the sodium content of the water as a percentage. High sodium content in irrigation water can cause degradation of soil structure, resulting in reduced water infiltration capacity [54,65]. This could further lead to lower yields due to waterlogging and decreased aeration [98]. The %Na ranged between 27.72 and 96.53 with an average value of 59.04 ± 16.25 for all samples (Figure 7b). Values less than 20% indicate excellent water quality. In this study, only 12 sites fell within the standard range of 20–40%, classifying the samples as good-quality water [48]. When the sodium range is high, Na can be absorbed by clay particles and displace Mg and Ca ions [99]. When Na in water is displaced with Mg and Ca ions in the soil, it can reduce soil permeability and result in poor internal soil drainage. This can restrict the movement of air and water in the soils and such soils generally become hard when dry [98].

For groundwater shallower than 200 m depth (BKK, PPD, NKL, and NTB aquifers), these aquifers showed relatively high variability in EC, SAR, and %Na. Some of the values were quite high, particularly in the BKK and PPD aquifers, suggesting that irrigation water from these aquifers could have significant impacts on soil properties and crop yields [86]. The high salinity (EC) and sodium content (%Na) could contribute to soil degradation [48], while high SAR values could cause problems with soil structure and water uptake [40]. It

appears that the groundwater in many of these aquifers may not be suitable for irrigation without some form of treatment or management, especially for salt-sensitive crops. The high salinity and sodicity could negatively affect soil health and, as a consequence, crop health and productivity, including rice and coconut. However, for the deeper groundwater (SK aquifer), this aquifer had generally lower values of EC, SAR, and %Na. Irrigation water from this aquifer might have less severe impacts on soil properties and crop yields, although some measurements still suggest potential issues, especially regarding the SAR and %Na. Furthermore, the actual impact would also depend on other factors such as the specific crop variety, the soil type, the extent of rainfall (which can help leach salts), and the farmers' management practices [86].

Several studies have examined the impact of nitrogen (N), phosphorus (P), and potassium (K) fertilizers, also known as NPK, on soil and groundwater quality. These nutrients are essential for crop growth, but their leaching into groundwater can disrupt ecosystems and agriculture. In the study area, the concentrations of nitrate (NO_3), a component of N, in groundwater compared to phosphates (PO_4) and potassium (K) were observed due to their mobility and abundance. A study proposed a diagram illustrating the correlation between these ions in the groundwater (Figure 8). The plot highlighted areas with varying degrees of contamination, revealing that factors such as the source and amount of fertilizer, the relative proportion of NPK, and aquifer properties can influence contamination levels.

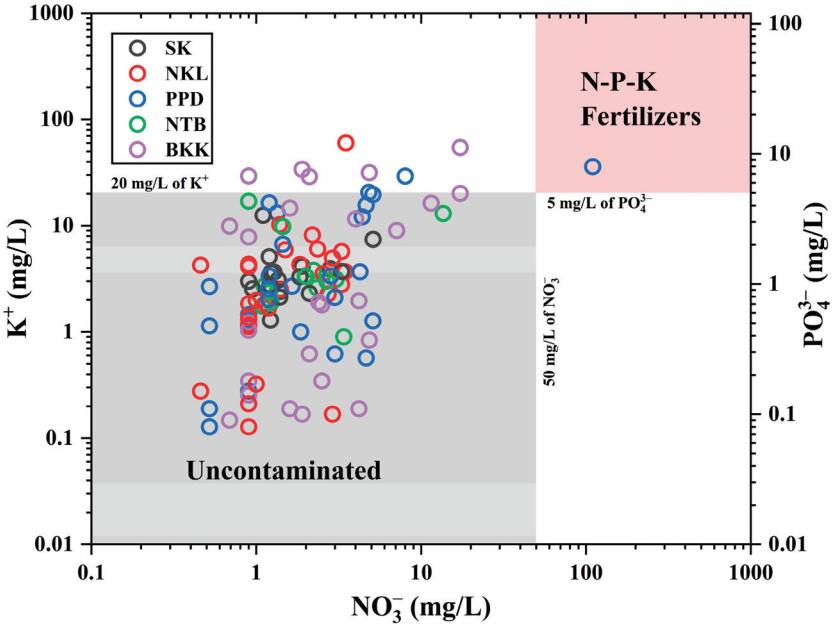

Figure 8. Bivariate plot between NO_3^- and K^+ and PO_4^{3-} showing the influence of fertilizer on the groundwater quality of the study area aquifer [41]. Colors indicate groundwater aquifers (e.g., Bangkok aquifer (BKK, 0–50 m depth), Phra Pradaeng aquifer (PPD, 51–100 m depth), Nakhon Luang aquifer (NKL, 101–150 m depth), Nonthaburi aquifer (NTB, 151–200 m depth), and Sam Khok aquifer (SK, 201–350 m depth)).

Nonlinear patterns were observed in specific samples (Figure 8), pointing to several agricultural areas or watersheds impacted by fertilizer pollution. The slope of this line can change based on the origin of the fertilizer, the quantity applied, and the relative NPK composition. The composition of recharged water moving through the vadose zone was found to vary depending on fertilizer application, linked to diverse cropping patterns. Shifts in farming methods and the varied properties of aquifers could influence NO_3 distribution in agricultural watersheds [63]. The slope might also indicate a variation in nitrate levels corresponding to minor increases in potash or phosphate values. It is noteworthy that highly soluble nitrate and nitrite (NO_2) have greater mobility and form weaker bonds with soil particles [100]. NO_3 originates from the oxidation of ammonia,

which increases due to nitrogen fertilizer application [63,100,101]. The oxidation process depletes oxygen levels, hastening the migration of nitrogen compounds to the water table through the vadose layer [102]. The groundwater's vulnerability to fertilizers was particularly evident in Phra Nakhon Si Ayutthaya due to its shallow water table and sedimentary formations. Sixty-four percent of the area is being cultivated more than once, primarily during the Ayutthaya one rice season in August. Therefore, nitrate, phosphate, and potassium impacts are still significant in the BKK aquifer (Figure 8) during the sampling period in January 2022.

Comparison with other regions revealed that aquifer properties, cropping patterns, and fertilizer use affect irrigation suitability [38,46,97,103]. For instance, groundwater from confined aquifers (SK aquifer) demonstrated better irrigation properties than unconfined aquifers (BKK and PPD aquifers). This suggests a higher contamination risk in unconfined aquifers. High sodium absorption ratio (SAR) values in the BKK aquifer (Figure 7a) are associated with the overexploitation of groundwater, excessive agrochemical use, and greater evapotranspiration during dry seasons, resulting in high salinity, deeming the water unsuitable for irrigation [38,97]. Other contributing factors to water quality for irrigation include natural weathering, bedrock leaching, and climate variability [104].

4. Conclusions

This research explores the hydrochemical facies and characteristics of groundwater from five distinct aquifers. Groundwater physical and chemical properties, such as electrical conductivity (EC), pH, and total dissolved solids (TDS), exhibit remarkable differences across aquifers, hinting at diverse water quality and potential pollution or high mineral content. The varying concentration of elements like Ca, Mg, Na, K, Cl, SO_4, HCO_3, CO_3, NO_3, and heavy metals in the groundwater reveals different geological and hydrological conditions, potential contamination sources, and water hardness levels. Furthermore, the quality of groundwater was evaluated for human consumption and agricultural irrigation purposes. Notably, heavy metal concentrations, such as zinc, mercury, lead, manganese, and iron, significantly exceeded the World Health Organization's (WHO) standards for safe drinking water in certain groundwater samples, signaling potential public health risks. Most samples were classified as "poor" or "unsuitable" for drinking, according to the Water Quality Index (WQI), indicating considerable groundwater quality variability within the study area. The likely sources of contamination include agricultural runoff, industrial waste, and natural mineral deposits. The research emphasizes the importance of continuous monitoring and remediation measures to ensure water safety. The treatment technologies such as nanoscale zero-valent iron and in situ permeable reactive barriers such as iron oxide, zeolite, chelation, and microfiltration should be employed for pollutant removal before consumption. The findings conclude that continuous monitoring, effective management practices, and treatment measures are critical for preserving groundwater quality. This work thus provides a comprehensive understanding of groundwater quality across diverse aquifers, emphasizing the need for strategic measures to safeguard water safety and sustainability.

Author Contributions: Conceptualization, J.L., P.J. and V.P.; methodology, J.L., P.C. (Phupha Chipthamlong) and B.K.; software, V.P. and P.J.; validation, J.L., P.C. (Phornsuda Chomcheawchan) and K.K.; formal analysis, K.K. and B.K.; investigation, J.L. and B.K.; resources, J.L., P.J. and K.K.; data curation, V.P. and P.C. (Phupha Chipthamlong); original manuscript writing, J.L. and P.C. (Phornsuda Chomcheawchan); manuscript review and editing, K.K., P.J. and P.C. (Phornsuda Chomcheawchan); visualization, V.P. and P.C. (Phupha Chipthamlong); supervision, B.K.; project administration, B.K.; funding acquisition, J.L. and P.J. All authors have read and agreed to the published version of the manuscript.

Funding: This research was funded by Naresuan University, Grant Number: R2566C003.

Data Availability Statement: Not applicable.

Acknowledgments: The authors acknowledge the Department of Groundwater Resources and the Royal Irrigation Department for supporting the hydrogeological data and their technical support.

Conflicts of Interest: The authors declare no conflict of interest.

Appendix A

Table A1. Heavy metal concentration (mg/L) in groundwater across different aquifers in Phra Nakhon Si Ayutthaya collected in November 2022.

Elements	Values (mg/L)	Aquifers					
		BKK	PPD	NKL	NTB	SK	Overall
As	Max	0.0158	0.0253	0.0329	0.0054	0.0033	0.0329
	Min	0.0000	0.0000	0.0000	0.0000	0.0000	0.0000
	Mean	0.0028	0.0021	0.0047	0.0019	0.0017	0.0028
	StdDev	0.0040	0.0058	0.0083	0.0017	0.0014	0.0053
Zn	Max	18.0000	40.0000	140.0000	120.0000	91.0000	140.0000
	Min	0.0000	0.0000	0.0000	0.0000	0.0000	0.0000
	Mean	1.4549	5.3316	9.7915	12.7844	9.1000	7.8058
	StdDev	4.4426	11.6740	29.2966	29.4649	21.1045	21.8650
Hg	Max	1.0200	0.8990	0.7430	0.0002	0.0003	1.0200
	Min	0.0000	0.0000	0.0000	0.0000	0.0000	0.0000
	Mean	0.3840	0.2669	0.1773	0.0001	0.0001	0.1663
	StdDev	0.3527	0.3493	0.2834	0.0001	0.0001	0.2913
Ni	Max	0.0120	0.0100	0.5160	0.0425	0.0069	0.5160
	Min	0.0000	0.0000	0.0000	0.0000	0.0000	0.0000
	Mean	0.0032	0.0015	0.0252	0.0051	0.0025	0.0085
	StdDev	0.0033	0.0027	0.1070	0.0103	0.0024	0.0537
Pb	Max	0.0140	0.0018	0.0055	0.0057	0.1590	0.1590
	Min	0.0000	0.0000	0.0000	0.0000	0.0000	0.0000
	Mean	0.0021	0.0001	0.0014	0.0015	0.0103	0.0030
	StdDev	0.0044	0.0004	0.0015	0.0017	0.0372	0.0166
Mn	Max	562.0000	415.0000	490.0000	830.0000	325.0000	830.0000
	Min	0.1910	0.1000	0.2000	0.0000	0.1000	0.0000
	Mean	98.1132	72.0928	164.5378	187.4125	115.9472	128.3652
	StdDev	203.6324	131.9233	189.1197	252.4662	121.7922	184.3860
Cd	Max	0.0006	0.0024	0.0009	0.0007	0.0009	0.0024
	Min	0.0000	0.0000	0.0000	0.0000	0.0000	0.0000
	Mean	0.0002	0.0003	0.0004	0.0003	0.0003	0.0003
	StdDev	0.0002	0.0006	0.0003	0.0003	0.0003	0.0003
Fe	Max	580.0000	160.0000	320.0000	540.0000	55.0000	580.0000
	Min	0.5000	0.0000	0.0460	0.1000	0.2000	0.0000
	Mean	61.7444	22.5959	23.3658	42.1406	6.6250	29.8712
	StdDev	153.3979	46.0680	67.7370	133.2024	14.1562	93.2930
Ba	Max	0.6680	0.9090	1.1176	0.5436	0.5375	1.1176
	Min	0.0000	0.0000	0.0000	0.0000	0.0000	0.0000
	Mean	0.1005	0.1382	0.1477	0.1420	0.0796	0.1232
	StdDev	0.1564	0.2563	0.2279	0.1715	0.1305	0.1958
Se	Max	0.0018	0.0018	0.0041	0.0130	0.0080	0.0130
	Min	0.0000	0.0000	0.0000	0.0000	0.0000	0.0000
	Mean	0.0004	0.0002	0.0015	0.0031	0.0022	0.0014
	StdDev	0.0007	0.0006	0.0012	0.0041	0.0025	0.0024
Cr	Max	0.0024	0.0024	0.0038	0.0082	0.0033	0.0082
	Min	0.0000	0.0000	0.0000	0.0000	0.0000	0.0000
	Mean	0.0005	0.0003	0.0016	0.0018	0.0016	0.0012
	StdDev	0.0010	0.0008	0.0013	0.0021	0.0013	0.0014

Note: Bangkok aquifer (BKK, 0–50 m depth), Phra Pradaeng aquifer (PPD, 51–100 m depth), Nakhon Luang aquifer (NKL, 101–150 m depth), Nonthaburi aquifer (NTB, 151–200 m depth), and Sam Khok aquifer (SK, 201–350 m depth).

References

1. Arya, S.; Kumar, V.; Sharma, S. Analysis of water quality parameters of groundwater in and around Diamond Cement Industry, Jhansi, Central India. *Int. J. Curr. Res.* **2012**, *4*, 75–77.
2. Kaviarasan, M.; Geetha, P.; Soman, K.P. GIS-based ground water quality monitoring in Thiruvannamalai District, Tamil Nadu, India. In Proceedings of the International Conference on Soft Computing Systems: ICSCS 2015, Chennai, India, 20–21 April 2015; pp. 685–700.
3. Putthividhya, A.; Laonamsai, J. Assessment of Surface and Ground-water Interactions using Stable Isotope Fingerprinting Technique in Thailand. In Proceedings of the World Environmental and Water Resources Congress, Austin, TX, USA, 17–21 May 2015; pp. 464–474.
4. Babiker, I.S.; Mohamed, M.A.A.; Hiyama, T. Assessing groundwater quality using GIS. *Water Resour. Manag.* **2007**, *21*, 699–715. [CrossRef]
5. Zhang, Y.; Wu, J.; Xu, B. Human health risk assessment of groundwater nitrogen pollution in Jinghui canal irrigation area of the loess region, northwest China. *Environ. Earth Sci.* **2018**, *77*, 273. [CrossRef]
6. Raza, M.; Hussain, F.; Lee, J.-Y.; Shakoor, M.B.; Kwon, K.D. Groundwater status in Pakistan: A review of contamination, health risks, and potential needs. *Crit. Rev. Environ. Sci. Technol.* **2017**, *47*, 1713–1762. [CrossRef]
7. Shankar, S.; Shanker, U. Arsenic contamination of groundwater: A review of sources, prevalence, health risks, and strategies for mitigation. *Sci. World J.* **2014**, *2014*, 304524. [CrossRef]
8. Ullah, R.; Malik, R.N.; Qadir, A. Assessment of groundwater contamination in an industrial city, Sialkot, Pakistan. *Afr. J. Environ. Sci. Technol.* **2009**, *3*, 429–446.
9. Dawood, F.; Akhtar, M.M.; Ehsan, M. Evaluating urbanization impact on stressed aquifer of Quetta Valley, Pakistan. *Desalin. Water Treat.* **2021**, *222*, 103–113. [CrossRef]
10. Rapant, S.; Krčmová, K. Health risk assessment maps for arsenic groundwater content: Application of national geochemical databases. *Environ. Geochem. Health* **2007**, *29*, 131–141. [CrossRef]
11. Li, P.; Karunanidhi, D.; Subramani, T.; Srinivasamoorthy, K. Sources and consequences of groundwater contamination. *Arch. Environ. Contam. Toxicol.* **2021**, *80*, 1–10. [CrossRef] [PubMed]
12. Kumar, M.; Borah, P.; Devi, P. Priority and emerging pollutants in water. In *Inorganic Pollutants in Water*; Elsevier: Amsterdam, The Netherlands, 2020; pp. 33–49.
13. Fuoco, I.; Marini, L.; De Rosa, R.; Figoli, A.; Gabriele, B.; Apollaro, C. Use of reaction path modelling to investigate the evolution of water chemistry in shallow to deep crystalline aquifers with a special focus on fluoride. *Sci. Total Environ.* **2022**, *830*, 154566. [CrossRef]
14. Alarcón-Herrera, M.T.; Gutiérrez, M. Geogenic arsenic in groundwater: Challenges, gaps, and future directions. *Curr. Opin. Environ. Sci. Health* **2022**, *27*, 100349. [CrossRef]
15. Cho, B.W.; Choo, C.O. Geochemical behavior of uranium and radon in groundwater of Jurassic granite area, Icheon, Middle Korea. *Water* **2019**, *11*, 1278. [CrossRef]
16. Shannon, M.C.; Grieve, C.M. Tolerance of vegetable crops to salinity. *Sci. Hortic.* **1998**, *78*, 5–38. [CrossRef]
17. Barakat, M.A. New trends in removing heavy metals from industrial wastewater. *Arab. J. Chem.* **2011**, *4*, 361–377. [CrossRef]
18. Fu, Z.; Xi, S. The effects of heavy metals on human metabolism. *Toxicol. Mech. Methods* **2020**, *30*, 167–176. [CrossRef]
19. Mohankumar, K.; Hariharan, V.; Rao, N.P. Heavy metal contamination in groundwater around industrial estate vs residential areas in Coimbatore, India. *J. Clin. Diagn. Res. JCDR* **2016**, *10*, BC05. [CrossRef]
20. Mehmood, A.; Qadir, A.; Ehsan, M.; Ali, A.; Raza, D.; Aziz, H. Hydrogeological studies and evaluation of surface and groundwater quality of Khyber Pakhtunkhwa, Pakistan. *Desalin. Water Treat.* **2021**, *244*, 41–54. [CrossRef]
21. Bhutiani, R.; Kulkarni, D.B.; Khanna, D.R.; Gautam, A. Geochemical distribution and environmental risk assessment of heavy metals in groundwater of an industrial area and its surroundings, Haridwar, India. *Energy Ecol. Environ.* **2017**, *2*, 155–167. [CrossRef]
22. Chanpiwat, P.; Lee, B.-T.; Kim, K.-W.; Sthiannopkao, S. Human health risk assessment for ingestion exposure to groundwater contaminated by naturally occurring mixtures of toxic heavy metals in the Lao PDR. *Environ. Monit. Assess.* **2014**, *186*, 4905–4923. [CrossRef]
23. Rehman, K.; Fatima, F.; Waheed, I.; Akash, M.S.H. Prevalence of exposure of heavy metals and their impact on health consequences. *J. Cell. Biochem.* **2018**, *119*, 157–184. [CrossRef]
24. Rezaei, H.; Zarei, A.; Kamarehie, B.; Jafari, A.; Fakhri, Y.; Bidarpoor, F.; Karami, M.A.; Farhang, M.; Ghaderpoori, M.; Sadeghi, H. Levels, distributions and health risk assessment of lead, cadmium and arsenic found in drinking groundwater of Dehgolan's villages, Iran. *Toxicol. Environ. Health Sci.* **2019**, *11*, 54–62. [CrossRef]
25. Ghosh, G.C.; Khan, M.J.H.; Chakraborty, T.K.; Zaman, S.; Kabir, A.H.M.E.; Tanaka, H. Human health risk assessment of elevated and variable iron and manganese intake with arsenic-safe groundwater in Jashore, Bangladesh. *Sci. Rep.* **2020**, *10*, 5206. [CrossRef]
26. Batayneh, A.T. Toxic (aluminum, beryllium, boron, chromium and zinc) in groundwater: Health risk assessment. *Int. J. Environ. Sci. Technol.* **2012**, *9*, 153–162. [CrossRef]
27. Laonamsai, J.; Ichiyanagi, K.; Patsinghasanee, S. Isotopic temporal and spatial variations of tropical rivers in Thailand reflect monsoon precipitation signals. *Hydrol. Process.* **2021**, *35*, e14068. [CrossRef]

28. Laonamsai, J.; Putthividhya, A. Preliminary assessment of groundwater and surface water characteristics in the upper Chao Phraya River Basin land using a stable isotope fingerprinting technique. In Proceedings of the World Environmental and Water Resources Congress, West Palm Beach, FL, USA, 22–26 May 2016; pp. 367–386.
29. Venter, Z.S.; Barton, D.N.; Chakraborty, T.; Simensen, T.; Singh, G. Global 10 m Land Use Land Cover Datasets: A Comparison of Dynamic World, World Cover and Esri Land Cover. *Remote Sens.* **2022**, *14*, 4101. [CrossRef]
30. Peel, M.C.; Finlayson, B.L.; McMahon, T.A. Updated world map of the Köppen-Geiger climate classification. *Hydrol. Earth Syst. Sci.* **2007**, *11*, 1633–1644. [CrossRef]
31. Laonamsai, J.; Ichiyanagi, K.; Kamdee, K.; Putthividhya, A.; Tanoue, M. Spatial and temporal distributions of stable isotopes in precipitation over Thailand. *Hydrol. Process.* **2021**, *35*, e13995. [CrossRef]
32. Tevapitak, K.; Helmsing, A.H.J.B. The interaction between local governments and stakeholders in environmental management: The case of water pollution by SMEs in Thailand. *J. Environ. Manag.* **2019**, *247*, 840–848. [CrossRef] [PubMed]
33. Phien-wej, N.; Giao, P.H.; Nutalaya, P. Land subsidence in bangkok, Thailand. *Eng. Geol.* **2006**, *82*, 187–201. [CrossRef]
34. Stoecker, F.; Babel, M.S.; Gupta, A.D.; Rivas, A.A.; Evers, M.; Kazama, F.; Nakamura, T. Hydrogeochemical and isotopic characterization of groundwater salinization in the Bangkok aquifer system, Thailand. *Environ. Earth Sci.* **2013**, *68*, 749–763. [CrossRef]
35. Gupta, A.D. Simulated Salt-Water Movement in the Nakhon Luang Aquifer, Bangkok, Thailand. *Groundwater* **1985**, *23*, 512–522. [CrossRef]
36. Nutalaya, P.; Yong, R.N.; Chumnankit, T.; Buapeng, S. Land subsidence in Bangkok during 1978–1988. *Sea-Level Rise Coast. Subsid. Causes Conseq. Strateg.* **1996**, *2*, 105–130.
37. Putthividhya, A.; Laonamsai, J. SWAT and MODFLOW modeling of spatio-temporal runoff and groundwater recharge distribution. In Proceedings of the World Environmental and Water Resources Congress, Sacramento, CA, USA, 21–25 May 2017; pp. 51–65.
38. Deborah, C. *Water Quality Assessments: A Guide to Use of Biota, Sediments and Water in Environmental Monitoring*; UNESCO/WHO/UNEP: Cambridge, UK, 1996.
39. Miner, G. Standard methods for the examination of water and wastewater. *Am. Water Work. Assoc. J.* **2006**, *98*, 130. [CrossRef]
40. Richards, L.A. *Diagnosis and Improvement of Saline and Alkali Soils*; LWW: Philadelphia, PA, USA, 1954; Volume 78.
41. World Health Organization. *Guidelines for Drinking-Water Quality: Incorporating the First and Second Addenda*; World Health Organization: Geneva, Switzerland, 2022.
42. Rabeiy, R.E. Assessment and modeling of groundwater quality using WQI and GIS in Upper Egypt area. *Environ. Sci. Pollut. Res.* **2018**, *25*, 30808–30817. [CrossRef] [PubMed]
43. Magesh, N.S.; Chandrasekar, N. Evaluation of spatial variations in groundwater quality by WQI and GIS technique: A case study of Virudunagar District, Tamil Nadu, India. *Arab. J. Geosci.* **2013**, *6*, 1883–1898. [CrossRef]
44. Unigwe, C.O.; Egbueri, J.C. Drinking water quality assessment based on statistical analysis and three water quality indices (MWQI, IWQI and EWQI): A case study. *Environ. Dev. Sustain.* **2023**, *25*, 686–707. [CrossRef]
45. Ram, A.; Tiwari, S.K.; Pandey, H.K.; Chaurasia, A.K.; Singh, S.; Singh, Y.V. Groundwater quality assessment using water quality index (WQI) under GIS framework. *Appl. Water Sci.* **2021**, *11*, 46. [CrossRef]
46. Loh, Y.S.A.; Akurugu, B.A.; Manu, E.; Aliou, A.-S. Assessment of groundwater quality and the main controls on its hydrochemistry in some Voltaian and basement aquifers, northern Ghana. *Groundw. Sustain. Dev.* **2020**, *10*, 100296. [CrossRef]
47. Ravikumar, P.; Somashekar, R.K.; Prakash, K.L. A comparative study on usage of Durov and Piper diagrams to interpret hydrochemical processes in groundwater from SRLIS river basin, Karnataka, India. *Elixir Earth Sci* **2015**, *80*, 31073–31077.
48. Wilcox, L. *Classification and Use of Irrigation Waters*; US Department of Agriculture: Washington, DC, USA, 1955.
49. Cioni, R.; Marini, L. *A Thermodynamic Approach to Water Geothermometry*; Springer: Berlin/Heidelberg, Germany, 2020.
50. Procesi, M.; Marini, L.; Cinti, D.; Sciarra, A.; Basile, P.; Mazzoni, T.; Zarlenga, F. Preliminary fluid geochemical survey in Tete Province and prospective development of geothermics in Mozambique. *Geotherm. Energy* **2022**, *10*, 2. [CrossRef]
51. Tonani, F.B.; Nagao, K.; Moore, J.; Natale, G.; Sperry, T. Water and gas geochemistry of the Cove-Fort Sulphurdale geothermal system. In Proceedings of the Twenty-Third Workshop on Geothermal Reservoir Engineering, Stanford, CA, USA, 26–28 January 1998; pp. 26–28.
52. Chegbeleh, L.P.; Aklika, D.K.; Akurugu, B.A. Hydrochemical characterization and suitability assessment of groundwater quality in the Saboba and Chereponi Districts, Ghana. *Hydrology* **2020**, *7*, 53. [CrossRef]
53. Sahu, P.; Sikdar, P.K. Hydrochemical framework of the aquifer in and around East Kolkata Wetlands, West Bengal, India. *Environ. Geol.* **2008**, *55*, 823–835. [CrossRef]
54. Sadashivaiah, C.; Ramakrishnaiah, C.R.; Ranganna, G. Hydrochemical analysis and evaluation of groundwater quality in Tumkur Taluk, Karnataka State, India. *Int. J. Environ. Res. Public Health* **2008**, *5*, 158–164. [CrossRef] [PubMed]
55. Sinsakul, S. Late quaternary geology of the lower central plain, Thailand. *J. Asian Earth Sci.* **2000**, *18*, 415–426. [CrossRef]
56. Laonamsai, J.; Ichiyanagi, K.; Patsinghasanee, S.; Kamdee, K.; Tomun, N. Application of Stable Isotopic Compositions of Rainfall Runoff for Evaporation Estimation in Thailand Mekong River Basin. *Water* **2022**, *14*, 2803. [CrossRef]
57. Stanienda, K.J. Carbonate phases rich in magnesium in the Triassic limestones of the eastern part of the Germanic Basin. *Carb. Evaporites* **2016**, *31*, 387–405. [CrossRef]

58. Krawczyk, W.E.; Ford, D.C. Correlating specific conductivity with total hardness in limestone and dolomite karst waters. *Earth Surf. Process. Landf.* **2006**, *31*, 221–234. [CrossRef]
59. Ahmed, A.A.; Shabana, A.R.; Saleh, A.A. Using hydrochemical and isotopic data to determine sources of recharge and groundwater evolution in arid region from Eastern Desert, Egypt. *J. Afr. Earth Sci.* **2019**, *151*, 36–46. [CrossRef]
60. Bucher, K.; Grapes, R. *Petrogenesis of Metamorphic Rocks*; Springer Science & Business Media: Berlin/Heidelberg, Germany, 2011.
61. Park, S.-C.; Yun, S.-T.; Chae, G.-T.; Yoo, I.-S.; Shin, K.-S.; Heo, C.-H.; Lee, S.-K. Regional hydrochemical study on salinization of coastal aquifers, western coastal area of South Korea. *J. Hydrol.* **2005**, *313*, 182–194. [CrossRef]
62. Li, P.; Qian, H.; Wu, J.; Zhang, Y.; Zhang, H. Major ion chemistry of shallow groundwater in the Dongsheng Coalfield, Ordos Basin, China. *Mine Water Environ.* **2013**, *32*, 195. [CrossRef]
63. Hosono, T.; Nakano, T.; Shimizu, Y.; Onodera, S.i.; Taniguchi, M. Hydrogeological constraint on nitrate and arsenic contamination in Asian metropolitan groundwater. *Hydrol. Process.* **2011**, *25*, 2742–2754. [CrossRef]
64. Lucena, J.J. Effects of bicarbonate, nitrate and other environmental factors on iron deficiency chlorosis. A review. *J. Plant Nutr.* **2000**, *23*, 1591–1606. [CrossRef]
65. Ebrahimi, M.; Kazemi, H.; Ehtashemi, M.; Rockaway, T.D. Assessment of groundwater quantity and quality and saltwater intrusion in the Damghan basin, Iran. *Geochemistry* **2016**, *76*, 227–241. [CrossRef]
66. Chae, G.-T.; Yun, S.-T.; Kim, K.; Mayer, B. Hydrogeochemistry of sodium-bicarbonate type bedrock groundwater in the Pocheon spa area, South Korea: Water–rock interaction and hydrologic mixing. *J. Hydrol.* **2006**, *321*, 326–343. [CrossRef]
67. Schofield, S.; Jankowski, J. Hydrochemistry and isotopic composition of Na–HCO3-rich groundwaters from the Ballimore region, central New South Wales, Australia. *Chem. Geol.* **2004**, *211*, 111–134. [CrossRef]
68. Chidambaram, S.; Karmegam, U.; Sasidhar, P.; Prasanna, M.V.; Manivannan, R.; Arunachalam, S.; Manikandan, S.; Anandhan, P. Significance of saturation index of certain clay minerals in shallow coastal groundwater, in and around Kalpakkam, Tamil Nadu, India. *J. Earth Syst. Sci.* **2011**, *120*, 897. [CrossRef]
69. Nihalani, S.A.; Behede, S.N.; Meeruty, A.R. Groundwater suitability determination near solid waste dump site at Pune. *Sustain. Water Resour. Manag.* **2022**, *8*, 64. [CrossRef]
70. Vespasiano, G.; Muto, F.; Apollaro, C. Geochemical, geological and groundwater quality characterization of a complex geological framework: The case study of the Coreca area (Calabria, South Italy). *Geosciences* **2021**, *11*, 121. [CrossRef]
71. Williams, M.; Fordyce, F.; Paijitprapapon, A.; Charoenchaisri, P. Arsenic contamination in surface drainage and groundwater in part of the southeast Asian tin belt, Nakhon Si Thammarat Province, southern Thailand. *Environ. Geol.* **1996**, *27*, 16–33. [CrossRef]
72. Li, B.; Song, X.; Yang, L.; Yao, D.; Xu, Y. Insights onto Hydrologic and Hydro-Chemical Processes of Riparian Groundwater Using Environmental Tracers in the Highly Disturbed Shaying River Basin, China. *Water* **2020**, *12*, 1939. [CrossRef]
73. Alloway, B.J. Sources of heavy metals and metalloids in soils. *Heavy Met. Soils Trace Met. Met. Soils Bioavailab.* **2013**, *22*, 11–50.
74. Nriagu, J.O. *Zinc in the Environment. Part I: Ecological Sycling*; John Wiley & Sons: New York, NY, USA, 1980.
75. Nordberg, G.F.; Nordberg, M.; Costa, M. Toxicology of metals: Overview, definitions, concepts, and trends. *Handb. Toxicol. Met.* **2022**, 1–14. [CrossRef]
76. Das, S.; Green, A. Zinc in Crops and Human Health. In *Biofortification of Food Crops*; Singh, U., Praharaj, C.S., Singh, S.S., Singh, N.P., Eds.; Springer India: New Delhi, India, 2016; pp. 31–40.
77. Wagner, S.E.; Burch, J.B.; Hussey, J.; Temples, T.; Bolick-Aldrich, S.; Mosley-Broughton, C.; Liu, Y.; Hebert, J.R. Soil zinc content, groundwater usage, and prostate cancer incidence in South Carolina. *Cancer Causes Control* **2009**, *20*, 345–353. [CrossRef]
78. Haglund, B.; Ryckenberg, K.; Selinus, O.; Dahlquist, G. Evidence of a Relationship Between Childhood-Onset Type I Diabetes and Low Groundwater Concentration of Zinc. *Diabetes Care* **1996**, *19*, 873–875. [CrossRef]
79. Nriagu, J.O. *Zinc in the Environment. Part II: Health Effects*; John Wiley & Sons: New York, NY, USA, 1980.
80. Krok, B.; Mohammadian, S.; Noll, H.M.; Surau, C.; Markwort, S.; Fritzsche, A.; Nachev, M.; Sures, B.; Meckenstock, R.U. Remediation of zinc-contaminated groundwater by iron oxide in situ adsorption barriers—From lab to the field. *Sci. Total Environ.* **2022**, *807*, 151066. [CrossRef]
81. Vukojević Medvidović, N.; Nuić, I.; Ugrina, M.; Trgo, M. Evaluation of Natural Zeolite as a Material for Permeable Reactive Barrier for Remediation of Zinc-Contaminated Groundwater Based on Column Study. *Water Air Soil Pollut.* **2018**, *229*, 367. [CrossRef]
82. Ghezzi, L.; Arrighi, S.; Giannecchini, R.; Bini, M.; Valerio, M.; Petrini, R. The legacy of mercury contamination from a past leather manufacturer and health risk assessment in an urban area (Pisa Municipality, Italy). *Sustainability* **2022**, *14*, 4367. [CrossRef]
83. González-Fernández, B.; Menéndez-Casares, E.; Meléndez-Asensio, M.; Fernández-Menéndez, S.; Ramos-Muñiz, F.; Cruz-Hernández, P.; González-Quirós, A. Sources of mercury in groundwater and soils of west Gijón (Asturias, NW Spain). *Sci. Total Environ.* **2014**, *481*, 217–231. [CrossRef]
84. Khattak, S.A.; Rashid, A.; Tariq, M.; Ali, L.; Gao, X.; Ayub, M.; Javed, A. Potential risk and source distribution of groundwater contamination by mercury in district Swabi, Pakistan: Application of multivariate study. *Environ. Dev. Sustain.* **2021**, *23*, 2279–2297. [CrossRef]
85. Blue, L.Y.; Van Aelstyn, M.A.; Matlock, M.; Atwood, D.A. Low-level mercury removal from groundwater using a synthetic chelating ligand. *Water Res.* **2008**, *42*, 2025–2028. [CrossRef]
86. Shalhevet, J. Using water of marginal quality for crop production: Major issues. *Agric. Water Manag.* **1994**, *25*, 233–269. [CrossRef]

87. Fu, F.; Dionysiou, D.D.; Liu, H. The use of zero-valent iron for groundwater remediation and wastewater treatment: A review. *J. Hazard. Mater.* **2014**, *267*, 194–205. [CrossRef] [PubMed]
88. Zhang, X.; Lin, S.; Lu, X.-Q.; Chen, Z.-l. Removal of Pb(II) from water using synthesized kaolin supported nanoscale zero-valent iron. *Chem. Eng. J.* **2010**, *163*, 243–248. [CrossRef]
89. Ahmad, W.; Alharthy, R.D.; Zubair, M.; Ahmed, M.; Hameed, A.; Rafique, S. Toxic and heavy metals contamination assessment in soil and water to evaluate human health risk. *Sci. Rep.* **2021**, *11*, 17006. [CrossRef]
90. Levy, B.S.; Nassetta, W.J. Neurologic effects of manganese in humans: A review. *Int. J. Occup. Environ. Health* **2003**, *9*, 153–163. [CrossRef]
91. Rajmohan, N.; Elango, L. Distribution of iron, manganese, zinc and atrazine in groundwater in parts of Palar and Cheyyar river basins, South India. *Environ. Monit. Assess.* **2005**, *107*, 115–131. [CrossRef]
92. Podgorski, J.; Araya, D.; Berg, M. Geogenic manganese and iron in groundwater of Southeast Asia and Bangladesh—Machine learning spatial prediction modeling and comparison with arsenic. *Sci. Total Environ.* **2022**, *833*, 155131. [CrossRef] [PubMed]
93. Guo, Y.; Huang, T.; Wen, G.; Cao, X. The simultaneous removal of ammonium and manganese from groundwater by iron-manganese co-oxide filter film: The role of chemical catalytic oxidation for ammonium removal. *Chem. Eng. J.* **2017**, *308*, 322–329. [CrossRef]
94. Ellis, D.; Bouchard, C.; Lantagne, G. Removal of iron and manganese from groundwater by oxidation and microfiltration. *Desalination* **2000**, *130*, 255–264. [CrossRef]
95. Babel, S.; Kurniawan, T.A. Various treatment technologies to remove arsenic and mercury from contaminated groundwater: An overview. *Proc. Southeast Asian Water Environ.* **2005**, *1*. [CrossRef]
96. Hashim, M.A.; Mukhopadhyay, S.; Sahu, J.N.; Sengupta, B. Remediation technologies for heavy metal contaminated groundwater. *J. Environ. Manag.* **2011**, *92*, 2355–2388. [CrossRef] [PubMed]
97. Kumar, S.K.; Rammohan, V.; Sahayam, J.D.; Jeevanandam, M. Assessment of groundwater quality and hydrogeochemistry of Manimuktha River basin, Tamil Nadu, India. *Environ. Monit. Assess.* **2009**, *159*, 341–351. [CrossRef] [PubMed]
98. Saleh, A.; Al-Ruwaih, F.; Shehata, M. Hydrogeochemical processes operating within the main aquifers of Kuwait. *J. Arid Environ.* **1999**, *42*, 195–209. [CrossRef]
99. Anandakumar, S.; Subramani, T.; Elango, L. Major ion groundwater chemistry of Lower Bhavani River Basin, Tamil Nadu, India. *J. Appl. Geochem.* **2009**, *11*, 92–101.
100. Kaçaroğlu, F.; Günay, G. Groundwater nitrate pollution in an alluvium aquifer, Eskişehir urban area and its vicinity, Turkey. *Environ. Geol.* **1997**, *31*, 178–184. [CrossRef]
101. Srivastav, A.L. Chemical fertilizers and pesticides: Role in groundwater contamination. In *Agrochemicals Detection, Treatment and Remediation*; Elsevier: Amsterdam, The Netherlands, 2020; pp. 143–159.
102. Squillace, P.J.; Scott, J.C.; Moran, M.J.; Nolan, B.T.; Kolpin, D.W. VOCs, pesticides, nitrate, and their mixtures in groundwater used for drinking water in the United States. *Environ. Sci. Technol.* **2002**, *36*, 1923–1930. [CrossRef]
103. Boateng, T.K.; Opoku, F.; Acquaah, S.O.; Akoto, O. Groundwater quality assessment using statistical approach and water quality index in Ejisu-Juaben Municipality, Ghana. *Environ. Earth Sci.* **2016**, *75*, 489. [CrossRef]
104. Czarnecki, S.; Düring, R.A. Influence of long-term mineral fertilization on metal contents and properties of soil samples taken from different locations in Hesse, Germany. *Soil* **2015**, *1*, 23–33. [CrossRef]

Disclaimer/Publisher's Note: The statements, opinions and data contained in all publications are solely those of the individual author(s) and contributor(s) and not of MDPI and/or the editor(s). MDPI and/or the editor(s) disclaim responsibility for any injury to people or property resulting from any ideas, methods, instructions or products referred to in the content.

hydrology

MDPI

Article

The Characterization of Groundwater Quality for Safe Drinking Water Wells via Disinfection and Sterilization in Jordan: A Case Study

Mehaysen Al-Mahasneh, Abeer Al Bsoul *, Nada Al-Ananzeh *, Hussam Elddin Al-Khasawane *, Marwan Al-Mahasneh and Raeda Tashtoush

Chemical Engineering Department, Al-Huson University College, Al-Balqa' Applied University, Al-Salt P.O. Box 19117, Jordan; m.mahasneh@bau.edu.jo (M.A.-M.); 32119119027@std.bau.edu.jo (M.A.-M.); rtashtoush@bau.edu.jo (R.T.)

* Correspondence: dr.abeeralbsoul@bau.edu.jo (A.A.B.); nadaalananzeh@bau.edu.jo (N.A.-A.); h.khasawneh@bau.edu.jo (H.E.A.-K.); Tel.: +962-790943606 (A.A.B.); +962-775613021 (N.A.-A.); +962-776844853 (H.E.A.-K.)

Abstract: This work aims to evaluate the quality of drinking water in the Disi aquifer in Jordan. Several water quality parameters are included in the mathematical equation to evaluate the average water quality and establish the suitability of water for drinking purposes. Water sampling zones from three wells were used to calculate the water quality indices (WQI). The water samples were analyzed for several physicochemical parameters, including pH, turbidity, total dissolved solids, Na^+, Ca^{2+}, Mg^{2+}, Na^+, K^+, HCO^{3-}, $SO_4{}^{2-}$, Cl^-, $NO_3{}^-$, total hardness, electrical conductivity (EC) and other elements (Fe^{2+}, Zn^{2+}, Mn^{2+}, Cd^{2+}, As^{2-}, Pb^{4+} and Cu^{2+}), in the groundwater wells. Biological parameters, such as faecal coliform, were also tested. The Weighted Arithmetic WQI indicated that most of the wells were of good to excellent quality. These determined indices support decision making and are beneficial to monitoring the groundwater quality in the Disi aquifer. The relative weight is specific to each parameter and ranges from 1 to 5; it establishes the importance of the water quality parameters for domestic purposes. The WQI analysis rates the water quality between 75 to 65 from good to medium. The water quality of the Disi aquifer for potable drinking water was compared with the guidelines of the World Health Organization (2011) and the Jordan Drinking Standard (JS286); the results indicated that water in the Disi aquifer was of high quality and was fit for drinking.

Keywords: disinfection; drinking water; hypochlorite; Rum group; physiochemical parameter; Jordan

1. Introduction

The decline in the quality of water from springs, boreholes, sealed wells, hand-dug wells, streams, rivers and lakes is caused by the presence of microbes, nutrients, heavy metals, organic chemicals and sediments. Boreholes, which are wells drilled using a drilling rig, draw water from isolated groundwater sources that are filtered through layers of soil and rock before reaching the surface. These sources may contain minerals and have an unpleasant colour or odour, but they are mostly free of contamination and do not require disinfection. Sealed wells are shallow wells that have been sealed, with cement around a pump, to prevent contamination. However, contamination is a possibility, and therefore, chlorine is frequently used to treat sealed wells.

This research paper discusses the methods used to disinfect the public water supply system, which includes submersible pump and related water distribution systems. Disinfection kills or reduces harmful microorganisms like viruses, bacteria and other microorganisms present in drinking water. Controlling microorganisms in a well and the

distribution system is achieved via disinfection. From the earliest records to the twentieth century, the history of water purification can be broken down as follows: the pursuit of clean water [1]. From 1902 to 1921, a mixture of iron chloride and lime chloride was used to chlorinate a highly-coloured water supply [2]. Four WQIs and FL, based on in situ measurements at nine different wells along the study area in Jouamaa Hakama Region (North of Morocco), were used and compared, alongside twelve bacteriological and physical–chemical parameters [3]. The use of chlorine gas largely replaced the use of lime chloride in disinfecting drinking water [4].

The process of flushing the well and water system with a chlorine solution, to kill bacteria and other microorganisms, is known as chlorination or 'shock chlorination' [5].

Free chlorine residual comprises two main compounds: hypochlorous acid (HOCl) and hypochlorite ion (OCl^-). Hypochlorous acid is more effective in killing pathogens than the hypochlorite ion [6].

Calcium hypochlorite Ca $(ClO)_2$, chloride (Cl), hypochlorous acid (HOCL) and water (H_2O) are involved.

When chlorine is added to water, the following chemical reaction occurs:

$$Ca(ClO)_2 + H_2O \Rightarrow Ca^{2+}(aq) + ClO_2(aq) \Rightarrow Cl + 2O + 2H \quad (1)$$

Chlorine, when added to water, reacts with hypochlorous acid and hydrochloride acid to form a pH-dependent equilibrium mixture.

$$CL_2 + H_2O \rightarrow HOCL + HCL \quad (2)$$

Hypochlorous acid partially dissociates into hydrogen and hypochlorite ions based on the pH:

$$HOCL \rightarrow H^+ + CLO^- \quad (3)$$

Chlorinated water recirculation helps to distribute the chlorine, thoroughly mix the water column and wash down the well casing's sidewalls [7].

Groundwater is water that is found below the surface. It is the source of water for wells and springs and helps to sustain water flow in surface water bodies such as lakes and streams. It is a valuable resource because it supplies many residents and businesses with water and contributes to the health and integrity of our aquatic ecosystems [8]. Many groundwater sources and water from lakes, rivers, or streams contain 'germs' that can spread diseases. Pathogens are germs that cause water-borne infections, which can result in serious reactions and complications, including death. They include parasites, viruses, and bacteria. These pathogens, which are present in human or animal faeces, increase in number when they enter drinking water sources [9].

Well disinfection helps to get rid of or reduce harmful bacteria and viruses, as well as harmless bacteria that cause a bad taste and smell [10].

Although shock chlorination is necessary for the maintenance of wells and disease prevention, it does not guarantee safe drinking water. Safe drinking water can be ensured by incorporating shock chlorination into a well management strategy that includes the responsible decommissioning of abandoned wells, adequate well protection and the maintenance of a water monitoring program. Groundwater from private wells supports 5 million people across Canada [11].

The aims of this study are as follows:

- To investigate the physicochemical parameters and bacterial microbes in groundwater.
- To study the effect of the disinfection and sterilization of water wells, by calcium hypochlorite, on groundwater geochemical variables and microbes.
- To calculate the volume of disinfection and sterilization using a pumping test.
- To compare the quality of Jordanian water wells, using Jordanian Drinking Water Standards, before and after the disinfection.

The microbial population, in a well, is divided into "nuisance" and "pathogenic" bacteria. The most prevalent pathogens are iron bacteria and sulphate-reducing bacteria (SRB) [12]. Although these bacteria are not harmful, they pose a health risk as they form biofilms that protect against pathogens and hinder faecal coliform testing [13]. There are pathogenic microbes, protozoa, and infections that make up unsafe microorganisms. The majority of microorganisms reside in various aggregates called 'biofilms'. Biofilms are commonplace and symbolize the most prosperous way of life. They carry the potential for self-cleaning in soils, sediments, and water, and are the active ingredient in biofiltration [14]. About half of all drinking water wells in the US, tested in recent studies, have evidence of faecal contamination. Groundwater is significantly associated with outbreaks of waterborne diseases; many pathogens have been found in groundwater [15,16].

This study aims to compare the quality of Jordanian water wells before and after the chlorination treatment. The quality parameters were compared to the Jordanian Drinking Water Standards and WHO (2011) to ensure that they adhere to the guidelines of the Drinking Water Standard. The proper regulation of the water supply includes the completion of a water well, the cleaning of existing wells, the proper development of new wells by flushing the water supply, remediation with a properly prepared chlorine solution and the collection and analysis of water samples. The limitations of the study are due to constraints on research design, methodology and materials.

2. Materials and Methods

2.1. The Study Area

The area of study is the Disi region in South Jordan. The Disi aquifer is a groundwater resource in South Jordan that serves as the primary source of water for the Mudawara Region (Figure 1). It is one of Jordan's most permeable and productive sandstone aquifers. It is an important source of water in the region for agricultural domestic and industrial use. The aquifer is made up of rock units, which overlay the basement complex of the Precambrian era. They are divided into two groups: the upper Khreim group and the lower Rum group. These are formations called Saleb, Burj, Umm Ishrin, Disi and Umm Sahm. The rock formations of the Rum group comprise the Rum aquifer system, which dominates the freshwater aquifer system in South Jordan, and the rock formations of the Khreim group represent the confining layer, in which the Sahl Suwaan formation occurs. The Khreim group consists of more silty sandstone and mudstone, and includes the Dubaydib and Hiswa formations. They have a depth of 0–158 m.

The other group is the Rum group, which includes the Umm Sahm formation; it is comparable to clean sandstone and is found at depths ranging from 158 m to the borehole's total depth of 550 m.

2.2. Hydrogeology of Disi Aquifer

The Rum aquifer is situated in the northeastern section of the Disi region in the lower part of the Hiswa Formation (Khreim Group). The aquifer is unconfined to the west and southwest, where there are outcrops of the Umm Sahm Formation; from its western limit, the aquifer extends more than 1000 m eastwards. Water was pumped from both the unconfined aquifer, in the Disi–Sahl Suwaan area, and the confined aquifer, in the Mudawarra area, in the Disi–Mudawarra area. Figure 1 depicts the typical flow direction of groundwater to the northeast. The project area's piezometric surface is between 720–740 m above mean sea level (AMSL) and corresponds to water levels of 100 to 200 m below ground level. The hydraulic conductivity ranges between 1 and 4 m/day. The groundwater quality is generally acceptable, with total dissolved solids (TDSs) levels ranging from 200 to 300 mg/L, electrical conductivity (EC) values ranging from 350 to 400 S/cm and pH values ranging from 7 to 8.

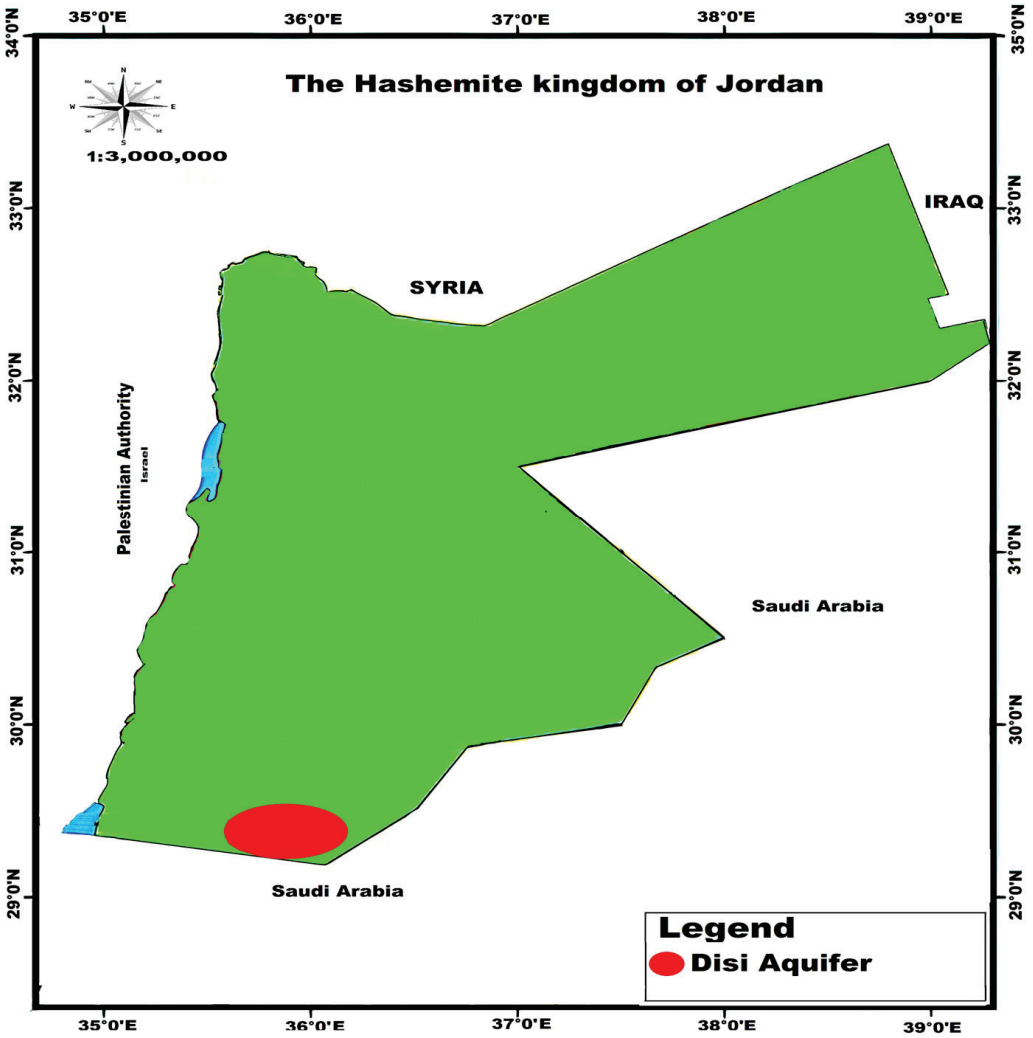

Figure 1. Disi Aquifer, the study area.

2.3. Water Sampling and Physicochemical Analyses

Several water wells in the study area were used to collect water samples for this study. Water investigations were realized considering the nature of water, as per standard techniques, to decide the physicochemical examinations and bacteriological boundaries to be used in sanitization. Figure 2 depicts the methodology layout used to define and estimate the study area's water quality using a flowchart. The process of gathering data is an essential part of any research. Major, minor, and trace element analyses were carried out in the laboratories. These examinations were meant to decide the convergence of cations (Ca^{2+}, Mg^{2+}, Na^{+}, K^{+}), anions (HCO_3^{-}, SO_4^{2-}, Cl^{-}), nitrate (NO_3^{-}), pH, TDSs and turbidity, with standing complete hardness and minor components (Fe^{2+}, Zn^{2+}, fn^{2+}, Cd^{2+}, As^{2-} and Cu^{2+}) in the wells.

2.4. Analytical Methods

Water chemical analyses were conducted to identify the quality of water, according to standard methods, to determine the physicochemical analyses and bacteriological parameters before and after sterilization. The pH was measured using a pH meter and turbidity was measured using a turbidity meter. The total dissolved solids (TDSs) and EC were measured, in the field, after collecting samples.

The cations and anions were measured in all groundwater samples from the Disi aquifer in the laboratory. The cations (Ca^{2+}, Na^{+}, Mg^{2+}, K^{+}) and anions (Cl^{-}, HCO_3^{-}, SO_4^{2-}, NO_3^{-}) were analysed via ion chromatography and the water quality sector. The bac-

teria species/aerobic bacteria were analysed using 'Vitek2 compact 15', by the bioMérieux, Inc. Durham, USA. The alkalinity titration method used was SM 2320B. The total hardness was analysed using EDTA Titrimetric and the EC was analysed using the laboratory method (Ref. CHI-EC -R007).

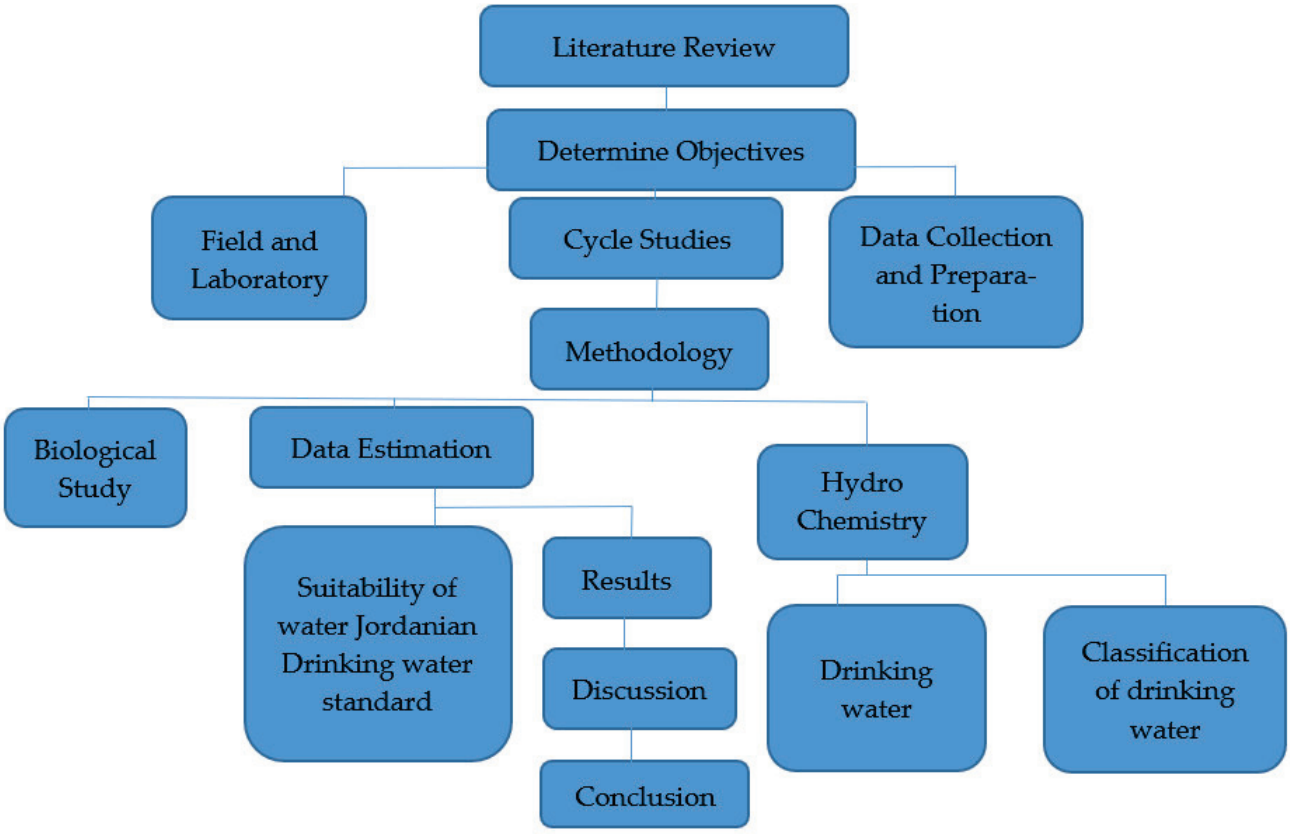

Figure 2. Flowchart illustrating the research steps.

2.5. Pursuit of Hygienic Drilling

Perfect general sanitation can reduce the introduction of microbial contaminants into newly constructed or restored wells during the storage, transportation, handling and assembly of well components. Adequate sanitation, during the construction or repair of a water supply system, refers to cleaning and taking precautions to prevent disease by preventing the introduction of bacteria and other contaminants. The drilling contractor should take precautions to keep contaminants from entering the well. This can be achieved using continuous sterilization methods, which are required to ensure the safety of the water supply.

2.6. Chlorine Procedure

In practice, according to Schnieders, chlorine concentrations should be kept between 50 and 200 parts per million (ppm), and the standard recommended concentration should be no less than 50 mg/L and no more than 200 mg/L whenever disinfection is desired [17]. Calcium hypochlorite is a white granular compound containing about 60 to 70 per cent of available chlorine.

The volume of water in the well and the quantity of chlorine required were calculated before well construction or pump installation. The actual pump rate, expressed in gallons per minute, was used to determine the rate at which the solution was introduced into the system, rather than the typical 24 h consumption.

2.7. Well Disinfection

After building or repairing a well or pump, the complete well and pumping system must be disinfected to kill harmful microorganisms (germs and bacteria) on the well casing, gravel, soil, rising main, and pumping rod, or in the water.

The pumping rod and riser pipe were installed in a live, recently drilled water well of a depth of 550 m. Before the well was sealed, it was disinfected. The water level in the well was 99.81 m below the surface.

Table 1 shows the properties of the well for disinfection: the total depth was 550 m, the water level was 99.81 m, the casing was $18^5/_8''$ (0.473 m) and the screen was $10^3/_4''$ (0.273 m).

Table 1. Features of the well that was to be disinfected.

Water level (m) 99.81	Screen OD $10^3/_4''$	Length, 170.40 m
Total depth (m) 550	Casing OD $10^3/_4''$	Length, 90.15 m
	Casing OD $18^5/_8''$	Length, 183.40 m
Total gravel pack volume	46 m^3	

Table 2 shows the procedures for disinfecting this well, as well as the volume of the added hypochlorite, were calculated as follows:

Table 2. Calculation of volumes for disinfection.

The volume inside the casing $18^5/_8''$ OD	29.280 m^3
The volume inside the $10^3/_4''$ OD screen	9.970 m^3
The volume inside the $10^3/_4''$ ID casing	4.530 m^3
The volume inside the gravel pack (volume × Porosity %)	13.800 m^3
Total volumes	57.580 m^3

Table 3 shows that the concentration of the free chlorine residual, after 30 min of pumping water out of the well, was 10 mg/L. After one hour of pumping, it became 4 mg/L and the pumping was continued by airlifting the well water out until the chlorine concentration in the water reached 0 mg/L after a reaction time of approximately 12 h.

Table 3. Analysis of the concentration of control chlorine (mg/L CL_2).

Analyses	**Concentration (mg/L)**	**Time (min)**	**Event**
Inspection	10.00	8:30	30 min after the beginning of airlift pumping
2	4:00	9:00	60 min after the beginning of airlift pumping
3	0:00	10:30	150 min after the beginning of airlift pumping
4	0:00	12:10	Inspection 240 min after the beginning of airlift pumping

The chlorine concentration, for disinfection, was no less than 50 mg/L and no more than 200 mg/L. The total volume and the quantity of calcium hypochlorite required for a 100 ppm free chlorine dosage in the screen and casing sections are shown in Table 4. Here, (57.580 m^3) is divided by 0.080 kg/m^3 or 4.606 kg, with an excess of 10%, equalling 5.3 kg. The pumping steps were conducted using 8.57 m^3 of solution, mixed water (66.2 m^3) and hypochlorite (5.3 kg).

Table 4. Test of sterilization using pumping.

Mixed water	66.2 m^3	**Calcium Hypochlorite**	5.3 kg
1st step	8.57 m^3 at 525 m	5th step	8.57 m^3 at 327 m
2nd step	8.57 m^3 at 459 m	6th step	8.57 m^3 at 261 m
3rd step	8.57 m^3 at 417 m	7th step	8.57 m^3 at 219 m
4th step	8.57 m^3 at 375 m	8th step	0-m^3
Dead volume 6.2 m^3			

Table 4 shows that 100 ppm of Ca–hypochlorite solution was injected through the drill pipes to sterilize the well. Then, 5.30 kg of Ca–hypochlorite and 66.20 m^3 of water were mixed for this purpose and pumped through the drill pipes and the washing tool, at seven different depths, from 219 m below the reference point (bRP), which is the top of the screen, to 525 m bRP, which is the end of the screen. Then, 8.57 m^3 of the solution was injected at each level. Figure 3 shows the stages of well disinfection. It was found that the pH of the chlorine solution in the well should be between 6 and 7 in order to keep the chlorine in the anon oxidative state (hypochlorous acid) after a reaction time of approximately 4 to 12 h, for effective increased contact time.

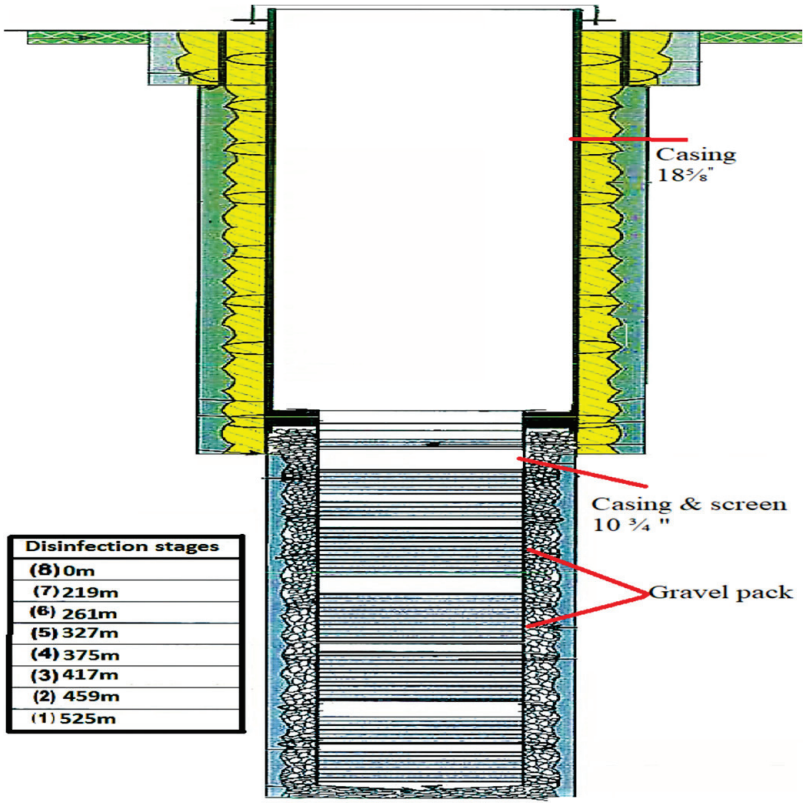

Figure 3. Well profile with disinfection stages.

The well was cleaned of the sterilization solution via airlifting until the chlorine concentration in the water reached 0 mg/L; at this point, the raised contact time became effective. This controlled organic growth produced a minimal taste and smell of chlorine. The force domain of calcium hypochlorite ranges from 30% to 75% for available chlorine, with 70% combined chlorine.

Chlorine is an extremely reactive substance. When it is added to a well, it first combines with inorganic components like hydrogen, ferrous iron, and manganese. No

disinfection occurs at this stage. The chlorine residue reacts with organic matter (algae, phenols and slime growth) after these components are reduced.

Chlorine will combine with nitrogen compounds (primarily ammonia) to form chloramines once the demand request, extended by inorganic and organic compounds, has been met. This combined chlorine form disinfects for a longer period. Chlorine concentrations of 50 ppm or less should be used if pH control is not used during times of prolonged contact [18].

3. Water Quality

3.1. Hydrochemistry in the Field and Water Sampling

A Steady-Rate Pumping Test (SRPT) was used to collect water samples from the sampling tap for chemical analyses. The samples were taken after the disinfection of the wells. Master and secondary ions, as well as physical parameters, were examined in both samples. The bacteriological parameters of the second sample were also investigated. The Water Quality Sector and the laboratories received three samples, respectively. The physical parameters, measured on-site, are shown in Table 5.

Table 5. The measurements of physical and chemical parameters on the spot during SRPT.

Parameters	Unit	Sample 1	Sample 2
Temperature	[°C]	32.10	32.00
Electrical Conductivity	[μS/cm]	384	382
pH	-	8.06	8.00
eH—ORP	[mV]	−62	−60.00
Turbidity	[NTU]	0.5	1.51
Dissolved Oxygen—O_2	[mg/L]	2.31	2.26
Hydrogen Sulphide—H_2S	[mg/L]	0.564	0.510
Carbon Dioxide—CO_2	[mg/L]	119.0	105.00

Table 6 shows the three water samples that were taken for physical, chemical, and bacteriological analyses. Table 6 shows the parameters measured using the analytical methods and Jordanian standards during the analyses, and the interpretation of the results. Water chemical analyses were conducted to identify the quality of water, according to standard methods, and the laboratory results were compared with the respective threshold values of the aforementioned standards.

3.2. Water Quality Index

Groundwater synthetic examinations were used to ascertain the values of the water quality record. The Jordanian drinking water guidelines, for 2008, were consulted while calculating WQI, as displayed in Table 7. In the first step, the weight (wi) of each chemical parameter was determined based on its relative importance to the quality of drinking water, as shown in Table 8. A maximum weight of five is given to chemical parameters of great importance in the evaluation of water quality, while a minimum weight of one is given to chemical parameters that have no impact on the overall quality of water [19].

$$\mathrm{Wi} = \frac{\mathrm{wi}}{\sum_{i=1} \mathrm{wi}} \tag{4}$$

where Wi is the relative weight, wi is the weight of each parameter and n is the number of parameters. In the third step, the quality rating scale (qi) was calculated, according to equation number (5), by dividing each chemical parameter concentration (Ci), in each

water sample, by its respective Jordanian Standards for Drinking Water (Si), as shown in Table 8; the result is multiplied by 100.

$$qi = \left(\frac{Ci}{Si}\right) * 100 \quad (5)$$

Table 6. The outcomes of the lab analyses of water samples.

Parameter	Unit	1st Sample	2nd Sample	3rd Sample	Jordanian Drinking Water Standard 2008	EU Drinking Water Standard 1998
Electrical Conductivity	µS/cm	372	376	383	--	2500
pH	--	8.02	7.96	7.66	6.5–8.5	--
Colour	CU	<15	<15	--	15	Acceptable
Turbidity	NTU	1.72	0.76	2.35	5	Acceptable
TDS	mg/L	207	208	212	1000	--
Hardness	mg/L	123	125	130	500	--
Alkalinity	mg/L	82.5	85.5	102.50	--	--
Calcium	mg/L	37.44	37.40	37.20	--	--
Magnesium	mg/L	6.34	6.27	6.12	--	--
Sodium	mg/L	28.64	28.69	27.60	200	200
Potassium	mg/L	1.62	1.52	1.48	--	--
Chloride	mg/L	40.19	39.44	39.76	500	250
Sulphate	mg/L	31.18	29.10	30.12	500	250
Bicarbonate	mg/L	-	-	--	--	--
Nitrate	mg/L	7.83	7.88	8.23	50	50
Ammonium	mg/L	<0.10	<0.10	<0.10	0.2	0.5
Ortho Phosphate	mg/L	0.04	0.06	0.05	--	--
Sulphur	mg/L	<0.20	<0.20	<0.20	--	--
Iron	mg/L	0.18	0.11	0.25	1.0	0.2
Manganese	mg/L	<0.01	0.01	<0.01	0.1	0.05
Fluoride	mg/L	<0.20	<0.20	<0.20	1.5	1.5
Aluminium	mg/L	<0.01	<0.01	<0.01	0.1	0.2
Lead	mg/L	<0.01	<0.01	<0.01	0.01	0.01
Cadmium	mg/L	<0.003	<0.003	<0.003	0.003	0.005
Arsenic	mg/L	<0.005	<0.005	<0.005	0.01	0.01
Iron Bacteria	Per Volume	-	Not seen	Not seen/20 mL	--	--
Sulphate- reducing Bacteria	Per Volume	-	+ve/100 mL	+ve/100 mL	--	--
Sulphur Oxidizing bacteria	MPN/100 ml	-	<1.8	<1.8	--	--

In the fourth step, the sub-index of the parameter (SLi) was calculated for each chemical parameter, using the following relationship:

$$SLi = Wi.qi \quad (6)$$

Finally, the WQI was computed using the following relationship:

$$WQI = \sum SLi \quad (7)$$

The method employed to calculate the water quality index, using the Jordanian Standards of Drinking Water Quality (2008), is explained in detail in Table 7 [20].

Table 8 shows the weights assigned to parameters. The overall suitability of drinking water was estimated using a combined measure of WQI. The water quality index (WQI) was calculated to estimate the influence of natural and anthropogenic activities based on several key parameters of drinking water chemistry. To calculate the WQI, the weight was

assigned specifically regarding the physicochemical parameters' conformity to their relative importance in the overall quality of water for drinking water purposes. The determined weight ranges from one to five. The maximum weight of five was assigned for NO_3; a weight of four was given to pH, TDS and SO_4; a weight of three was assigned to HCO_3 and Cl; a weight of two was given to Ca, Mg, Na and K, and a weight of one was assigned to PO_4^{3-}.

Table 7. Drinking Water Quality Jordanian Standards (2008).

Parameters	Unit	Jordanian Standard for Drinking Water	WHO Guidelines (2011)
TDS	mg/L	1000	500
PH		6.5–8.5	6.5–8.5
Ca^{2+}	mg/L	200	75–200
Mg^{2+}	mg/L	150	50–150
Na^{+}	mg/L	200	200
K^{+}	mg/L	200	10–50
Cl^{-}	mg/L	500	250
HCO_3^{-}	mg/L	200	500
SO_4^{2-}	mg/L	500	250
NO_3^{-}	mg/L	50	45

Table 8. Weights are assigned to parameters [19].

Parameters	Weight (wi) *
pH	4
T	4
TDS	5
Ca^{2+}	2
Mg^{2+}	2
Na^{+}	2
K^{+}	2
Cl^{-}	3
HCO_3^{-}	3
SO_4^{2-}	4
NO_3^{-}	5
PO_4^{3-}	1

* Each criterion is assigned a weight (Wi) ranging from 1 (lowest impact on water quality) to 5 (greatest impact).

Here, Wi is the relative weight and Qi is the scale rating of the parameter. pH, T, TDS, Ca^{2+}, Mg^{2+}, Na^{+}, K^{+}, Cl^{-}, HCO_3^{-}, SO_4^{2-}, NO_3^{-}, PO_4^{3-} are the variables included in the calculations. Each variable received a rating that was calculated using the arithmetic mean, and the ratings were then changed to temporary weights. The final weight was then calculated by dividing each temporary weight by the total number of temporary weights [21–25].

Table 9 shows a colour spectrum was used to show the range in the water quality of each area [26], with dark red signifying very poor water quality (WQI = 0–10), a narrow strip of yellow showing average quality (50 WQI), and dark blue signifying excellent water quality (WQI = 90–100).

Table 9. Classification of water quality [25,27,28].

WQI Value	Class
Excellent water	<50
Good water	50–100
Poor water	100–200
Very poor water	200–300
Unsuitable for drinking	>300

Tables 5, 6 and 10 show the permissible limits of physical–chemical and bacterio-logical parameters confirmed using the Jordanian standards for drinking water [20].

Table 10. Calculating the water quality index (WQI) of wells.

Chemical Parameters	Si	Weight (wi)	Relative Weight (Wi)	Ci	qi	SLi
TDS	1000	4	0.13	210	21	2.73
pH	6.5–8.5	4	0.13	7.81	91.88	11.94
Ca^{2+}	200	2	0.06	37.80	18.60	1.11
Mg^{2+}	150	2	0.06	6.14	4.09	0.25
Na^{+}	200	2	0.06	28.50	14.25	0.85
K^{+}	12	2	0.06	1.5	12.50	0.75
Cl^{-}	500	3	0.10	39.50	7.9	0.79
$HCO_3{}^{-}$	200	3	0.10	98	136	13.60
$SO_4{}^{2-}$	500	4	0.13	30.50	6.10	0.79
$NO_3{}^{-}$	50	5	0.16	7.75	15.50	0.48

If T is 'medium', pH is 'medium', EC is 'high', TDSs is 'very low', DO is 'high', NO_3 is 'very low', NH_4 is 'very low', PO_4 is 'very low', TURB is 'low' and FC is 'very low', then the quality is 'excellent'.

If (T is 'very high' or T is 'low' or T is 'medium' or T is 'high'), (pH is 'low' or pH is 'medium' or pH is 'high' or pH is 'very high'), (EC is 'very low' or EC is 'low' or EC is 'medium' or EC is 'high'), (TDSs is 'very low' or TDSs is 'low' or TDSs is 'medium' or TDSs is 'high'), (DO is 'low' or DO is 'medium' or DO is 'high'), (NO_3 is 'very low' or NO_3 is 'low' or NO_3 is 'medium' and NH_4 is 'very low' or NH_4 is 'low' or NH_4 is 'medium'), (PO_4 is 'very low' or PO_4 is 'low' or PO_4 is 'medium, and TURB is 'very low' or TURB is 'low' or TURB is 'medium' or TURB is 'high') and (FC is 'very low' or FC is 'low'), then the quality is 'acceptable'.

If T is 'very high' or pH is 'very low', EC is 'very high' or TDSs is 'very high', DO is 'very low' or NO_3 is 'high' or NO_3 is 'very high' or NH_4 is 'high' or NH_4 is 'very high' or PO_4 is 'high' or PO_4 is 'very high' or TURB is 'very high' or FC is 'very high', then the quality is 'poor'.

Table 11 shows that the WQI in the Disi aquifer groundwater varies from 75 to 65. According to Jordan's water standards 2008, the EU drinking water standards 1998 and the WHO standards 2011, the results of the water sample analysis show that the water quality is good and suitable for consumption. This study could serve as a foundation on which the authorities could develop a groundwater management plan in the study area in the future.

Table 11. Well test values for the Disi aquifer well with WQI values.

Well	WQI	Ec µs/cm	PH	Ca mg/L	Mg mg/L	Na mg/L	K mg/L	CL mg/L	HCO_3 mg/L	SO_4 mg/L	NO_3 mg/L	TDS mg/L
A	75	372	8.02	37.44	6.34	28.64	1.62	40.19	113	31.18	7.83	207
B	66	376	7.96	37.40	6.27	28.69	1.52	39.44	109	29.10	7.88	208
C	65	383	7.66	37.20	6.12	27.60	1.48	39.76	115	30.12	8.23	212

4. Results

4.1. A Physical-Chemical Metric

Tables 5 and 6 display the physicochemical properties of water quality. The pH values of the three samples were 7.96, 8.02 and 7.66, respectively. The temperatures of the groundwater were 30 °C, 32.01 °C and 29.5 °C, respectively, and the highest value in the mean was 32.01 °C. Sample 1 had a mean temperature of 32.01 °C, sample 2 had a mean temperature of 30 °C and the minimum value had a mean temperature of 29.5 °C. The turbidity of the water ranged between 0.76 NTU, 1.72 NTU and 2.37 NTU, with samples 3 showing the highest value and sample 1 showing the lowest value. The total dissolved solids were between 207, 208 and 212 mg/L. The electrical conductivity of samples 1 and 2 ranged between 372, 376 and 383 µS/cm, respectively. Water samples contained a free residual chlorine value of 0.00 mg/L.

4.2. Bacteriological Investigations

Bacteriological investigations, after 23 h of steady pumping, revealed the presence of the aerobic bacteria called *Acinetobacter haemoliticus*. Sulphate-reducing bacteria, *Sphingomonas pauciummobitis* (an aerobic bacteria), and coliforms were found in the water after the final disinfection. After the well was sterilized, the total number of coliform bacteria was 1.8 MPN/100 mL, which was higher than the threshold (0/100 mL). Sulphate-oxidizing bacteria were present at a rate of less than 1.8 MPN/100 mL, and the total coliform count was 1.8 MPN/100 mL. Iron bacteria were not observed, as shown in Table 6.

5. Discussion

The World Health Organization's standards serve as the foundation for laboratory analyses of the Jordanian drinking water standards [29]. The EU guidelines from 1998 [30], which serve as a reference for the Jordanian standards, could not recode the threshold values for some parameters [29,30].

The impact of pH: pH is a proportion of the acidic or basic states of water. As the human body is made up of 50–60 percent water, the pH of drinking water can significantly impact body chemistry and health. The study found that the pH of the water samples ranged from 7.96 to 8.02, which indicates that the water from the aquifer was alkaline in nature, as shown in Tables 5 and 6. The pH of the water was in the range of 6.5–8.5, which was in tune with the guidelines established by WHO [31] for the quality of drinking water. According to WHO recommendations, the pH may range from 6.5 to 9.5.

As defined by Adegboyega et al., the temperature that defines the value of the chemical reaction in water ranges from 30 to 32.01 °C [32].

The turbidity, which ranged from 0.5 to 1.51 NTU, was also within WHO's [31] permissible limits of 5 NTU, i.e., the drinking water supply was of high quality, according to Jordanian standards, as shown in Table 6.

Dissolved oxygen (DO), the maximum oxygen concentration that can dissolve in water, is determined by the temperature of the water, and it can vary from location to location and from time to time. The DO, in the range of 2.26 to 2.31, thus falls within permissible limits given by WHO (2017) [33].

This study's findings demonstrate that low bacterial counts were correlated with low turbidity values. The reports by Oparaocha et al. [34], as well as the findings of Agbabiaka et al. [35], also support these findings.

The total concentration of dissolved substances in groundwater is measured by TDSs, which is an important parameter for evaluating the quality of groundwater and drinking water. According to Anbazhagan and Nair [36], TDSs refers to fully dissolved minerals in groundwater, such as calcium, chlorides, carbonates, bicarbonates, magnesium, silica, and sodium. According to Adesoji and Ogunjobi [37], who conducted a similar experiment in which the water also exceeded the [38] permissible limits of 500 mg/L recommended by the WHO (2010), the TDS values were 207, 208 and 212 mg/L, respectively, thus within the Jordanian standards [20,31].

The samples had total hardness values of 123, 125 and 130 mg/L, respectively. The reports regarding the recommended permissible limits of 500 mg/L also support these findings. The electrical conductivity of the water samples ranged from 700 to 900 μS/cm, and the average rates were recorded. Water had a higher electrical conductivity due to the dissolved salts.

The EC can be measured indirectly to the determine TDSs. The treated water samples, which were taken after treatment, were found to have the lowest EC values of 372, 376 and 383 μS /cm, respectively, which is a sign of a decrease in the dissolved salts. The electrical conductivity fell within the WHO's acceptable range of 0–1000 μS /cm [38].

On the one hand, the measurement of pollution indicator parameters, like ammonia and nitrate, demonstrated that all readings were within acceptable ranges (Tables 2–4). Additionally, Figure 7 shows that there was a strong correlation between ammonia and the iron concentration in various sampling methods.

The effect of nitrate nitrogen can over stimulate the growth of aquatic plants and algae and result in the eutrophication of surface waters. It can even 'kill' a lake by depriving it of oxygen, which can lead to anaerobic conditions in the water bodies and fish deaths. Extremely high levels of nitrate nitrogen can make it harder for fish and other aquatic invertebrates to breathe, which can reduce the diversity of animals and plants in the environment.

The water's nitrate (NO_3^-) contents, which were 7.83, 7.88 and 8.23 mg/L, respectively, were low enough to not pose any health hazard to the consumers. In the presence of microbial contamination, a high nitrate content can result in thaemoglobinaemia, or blue baby syndrome, in bottle-fed infants [32]. Therefore, water with a nitrate standard greater than 100 mg/L is not suitable for use in infants. Nitrate is a significant plant nutrient and is a naturally occurring component in the environment. The nitrate standard, given in this study, indicates that the water is less exposed to inorganic components in the auriferous materials. As the nitrate level is within the standard for drinking water, there is no health risk to consumers.

The magnesium ion (Mg^{2+}) was monitored with values of 6.27, 6.34 and 6.12 mg/L for the minimum and maximum levels. These levels did not go above the recommended limit of 30 mg/L for use in drinking water. The overall goal is to use the water quality index (WQI), for drinking water, to evaluate the quality of the groundwater in the Al-Zaatari camp, in Jordan, using the major cations and anions that could be harmful to humans [39]. The WHO-permitted limit for fluoride concentrations is 1.5 mg/L. Therefore, the groundwater can be used for drinking, as it has fluoride concentrations of 0.2 mg/L. The water samples also contain iron, a vital mineral, in its naturally occurring form.

The quartzite rocks of Sheikhpura are an geogenic source of iron in groundwater in India. The literature mentions a similar geogenic source of iron in groundwater [40,41]. According to WHO and BIS drinking-related standards [42], the ideal level of iron is less

than 0.1 mg/L and 0.3 mg/L [43]. A comparison of the laboratory results, with the respective threshold values of the aforementioned standard, is shown in Table 6. It also contains the results of the laboratory analyses of the samples. The concentration of manganese ranges from <0.01 to 0.01 mg/L, which is under the permissible limit of 0.1–0.05 mg/L, as recommended by [29,30,32]. Table 6 demonstrates that all other elements are present at concentrations below the permissible limit. The iron concentration ranges from 0.11 to 0.18 mg/L, which is under the permissible limit of 1.0 mg/L, as recommended by WHO. Table 6 shows a comparison of the laboratory results, with the respective threshold values of the aforementioned standards. Table 6 shows that all other elements are present at concentrations below their particular threshold values. The turbidity, sand content, pH, temperature and electrical conductivity were all measured during airlifting and backwashing. The sand content, turbidity, pH, temperature and electrical conductivity were all measured in the well water, which has very low turbidity. Figure 4 depicts the sand content in conjunction with the electrical conductivity. Each screen section met the acceptance criteria, with a sand content of fewer than 50 parts per million and an electrical conductivity of 900 µS/cm. Water with a high salt content and a high sand content, as shown in Figure 4, will have a high electrical conductivity; it will show a high level of impurity in this phase.

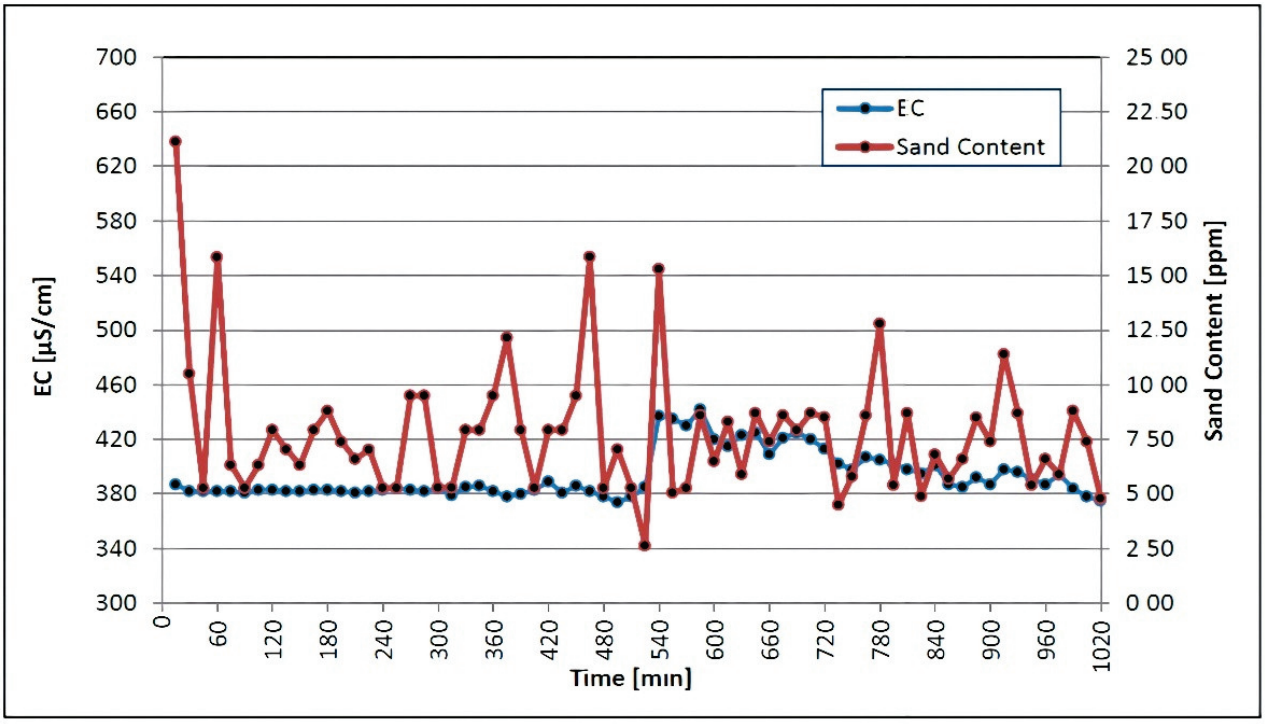

Figure 4. Electrical conductivity and sand content were measured during backwashing and airlifting.

The swabbing, airlifting and water jetting of the isolated screen sections were simultaneously carried out after the airlift pumping and backwashing procedures. The swabbing tool was moved up and down, in each screen section, until the EC of 700 µS/cm and the sand content of 10 ppm met the EU standards [30]. Figure 5 depicts plots of the sand content and electrical conductivity, which were decreased during the disinfection treatment and the other operation, following the jetting of each screen section; these values were 372 µS/cm, 376 µS/cm, and 383 µS/cm, respectively. The swabbing tool was used in three consecutive steps, with the pressure of the injected water increasing from 7 bar to 14 bar to 20 bar during each step.

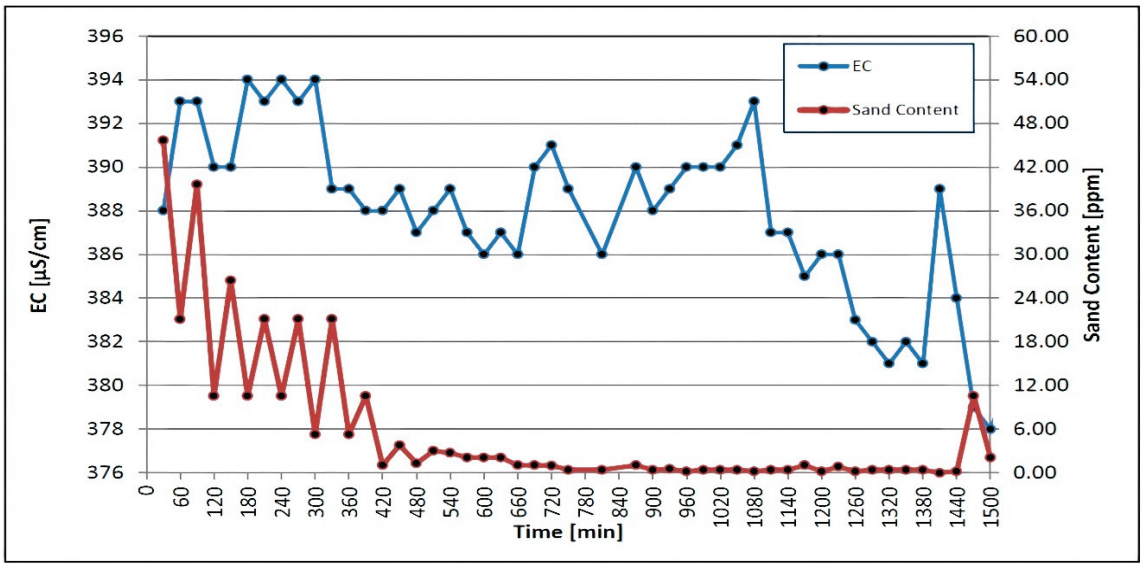

Figure 5. Electrical conductivity and sand content were measured during airlifting and swabbing.

The second run of swabbing and airlifting followed in the same manner as the first. A high rate of pumping and backwashing occurred at discharge rates of 60.27, 80.22 and 99.83 L/s, respectively. Each step was carried out until the turbidity and sand content was below 5 NTU and 2 ppm, respectively. As depicted in Figure 6, the turbidity and sand content of the discharged water continuously decreased throughout the third step. Proper well development makes it easier to remove turbidity and sand content, which increases the success rate of the disinfection. According to Lechevallier et al., the suspended particles in cloudy water hinder the chlorine's efforts to kill microorganisms [44].

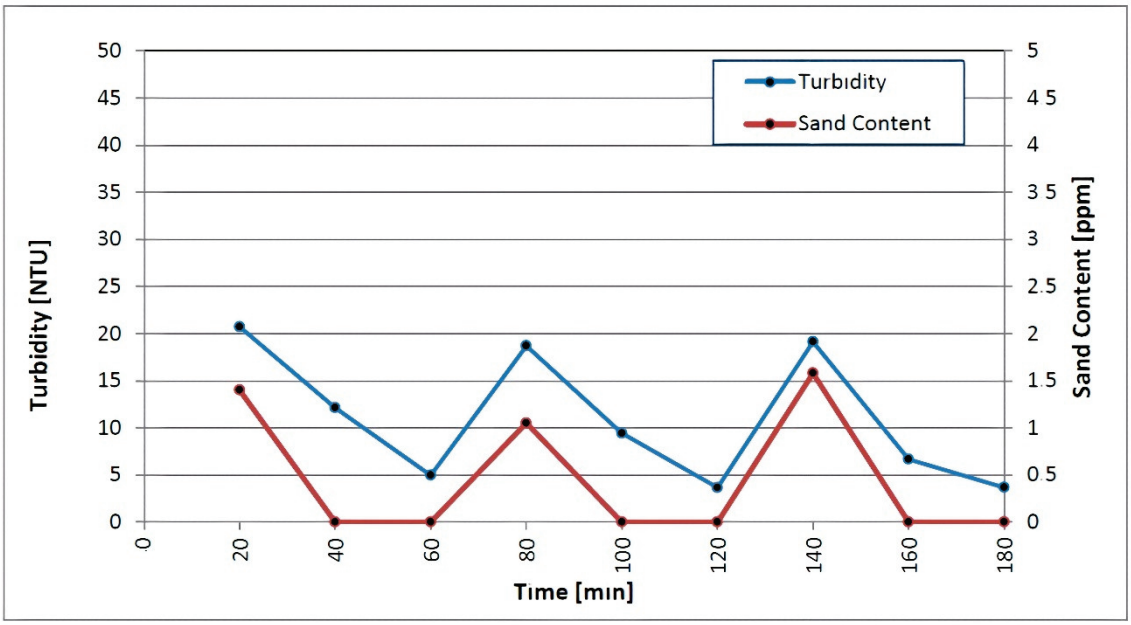

Figure 6. Measurements of turbidity and sand content during backwashing and high-rate pumping.

The authors concluded that the low removal of turbidity was due to the presence of fine clay particles in raw water, which penetrated the filter [45]. In a full-scale study, turbidity removal was between 0% and 63%, due to the fine particles present in the raw water and the large fraction (4% by weight) of fines in the new sand media used in the study [46]. Turbidity may not be a suitable surrogate for evaluating the removal of pathogens via slow

sand filtration because it can achieve the effective removal of microbial pathogens without necessarily reducing turbidity. Table 6 shows that the effect of chlorine on the minerals in the water can cause water from a chlorine-treated water supply system to be turbid. After steady-rate pumping, bacteriological analyses revealed the presence of the aerobic bacteria *Acinetobacter haemoliticus* and a matching total bacterial count [47].

This higher bacterial count is a clear sign of bacterial regrowth and post-treatment failure or contamination. The total coliform counts did not meet the WHO's requirement of zero coliform counts in a 100 mL sample. This was a clear indication of contamination and inadequate water infrastructure. Sulphate-reducing bacteria, aerobic bacteria like *Sphingomonas pauciummobitis*, and coliforms could be found in the treated water. After well sterilization, the total coliform bacteria content was 1.8 MPN/100 mL, which was higher than the threshold (0/100 mL).

The growth of bacteria and the occurrence of coliforms depend on a complex interaction of many factors including temperature, disinfectant type and residual, pipe material, corrosion and other engineering and operational parameters [48–51]. Recent research has indicated that various disinfectants differ in their ability to interact with biofilm bacteria.

Monochloramine, although a much less reactive disinfectant than free chlorine, is more specific in the type of compounds that it will react with [52]. Therefore, monochloramine can be more effective than free chlorine at penetrating and inactivating certain types of biofilms, particularly those containing corrosion products [53,54].

A study of 30 distribution systems, using free chlorine and chloramines, showed a difference in the density and occurrence of coliform bacteria between systems [51]. Modelling indicates that the penetration of free chlorine into a biofilm is limited by its fast reaction rate [52]. Free chlorine is essentially consumed before it can react with the bacterial components of the film [55]. Chloramines, on the other hand, are slow reacting; they diffuse into the biofilm and eventually inactivate attached bacteria. This is a mechanism that has been demonstrated using an alginate bead model [55,56]. The study showed that free chlorine did not effectively penetrate alginate beads containing bacterial cells, but chloramines penetrated the alginate material and reduced bacterial levels by nearly one million-fold over a 60 min interval (2.5 mg/L chloramines, pH 8.9) [57]. It also reported that hospitals supplied with water containing a chloramine residual were 10 times less likely to experience water-associated legionella infections. Similarly [58], in a study of 166 hospitals, it was found that nosocomial legionellosis was five times less likely to occur in hospitals served with chloraminated water. The authors attributed the effectiveness of chloramines, for legionella control, to the ability of the disinfectant to penetrate biofilms.

In addition to the type of disinfectant used, the residual maintained at the end of the distribution system was also related to coliform occurrences [51]. Systems that maintained dead-end free chlorine levels of less than 0.2 mg/L or monochloramine levels of less than 0.5 mg/L had substantially more coliform occurrences than systems maintaining higher disinfectant residual systems with highly assimilable organic carbon (AOC) levels. Therefore, the maintenance of a disinfectant residual alone does not ensure that treated waters will be free of coliform bacteria.

After well sterilization, the total coliform bacteria content was 1.8, which is also above the threshold (0/100 mL). The authors attributed this effect to the rapid reaction rate of free chlorine and its limited ability to penetrate a biofilm [55]. Free chlorine is consumed before reacting with the film's bacterial components [55]. On the other hand, chloramines react more slowly; they can diffuse into the biofilm and ultimately inactivate connected microorganisms; this is a system that has been shown utilizing an alginate dot model [55,56]. Free chlorine, according to the study, was unable to penetrate bacterial-filled alginate beads. The concentrations of all the other elements were below their respective thresholds.

The status of the borehole was checked through a closed-circuit television logging unit (CCTV) survey before the assembly of the lasting pump. After well A was completed, from a depth of 284 m to a depth of 545 m, wells B and C were completed, respectively. The first CCTV survey was used for the final check. Some areas, including the dislocate pattern

shown in Figure 7, had small biofouling. It was confirmed, via the final CCTV survey and bacteriological laboratory results of the collected water samples, that the ongoing processes of biofouling and corrosion in wells may not affect their productivity or safety. The test results for the water samples taken from sterilized and disinfected wells revealed that neither iron bacteria nor bacteria species/anaerobic bacteria were present in the wells [59].

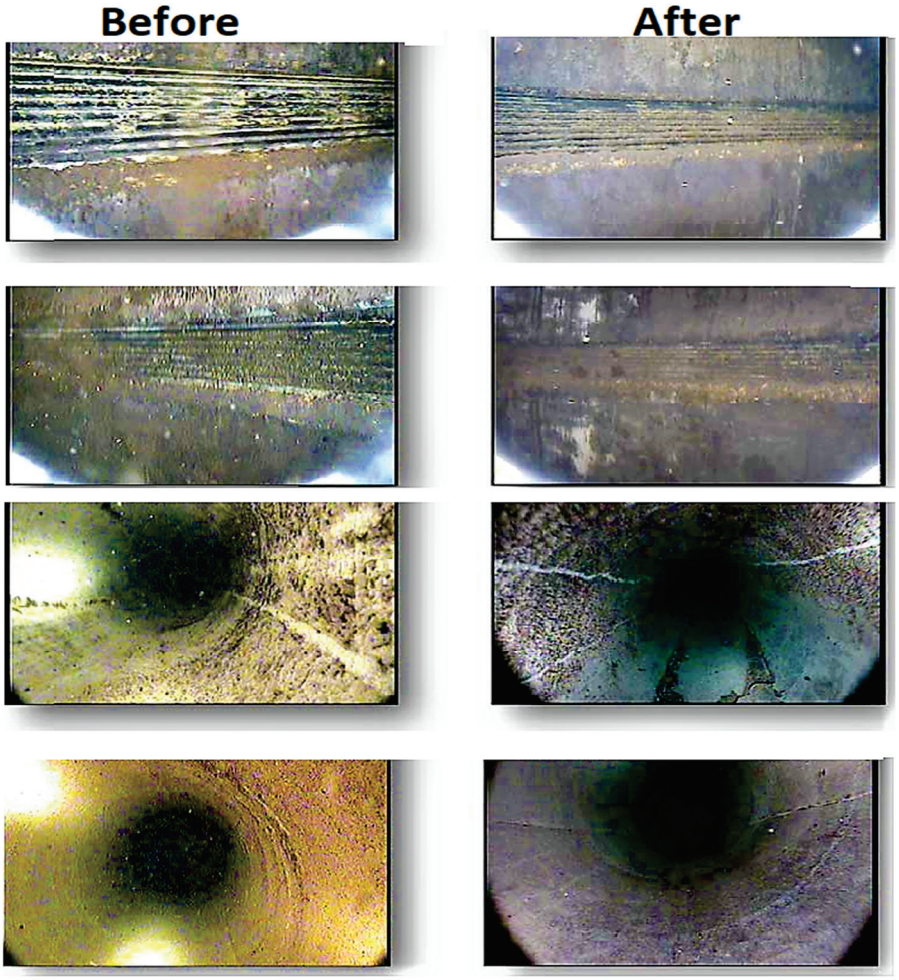

Figure 7. CCTV images showing the comparison of well cleaning before and after disinfection [59].

The content of total coliform bacteria after well sterilization was <1.8, which is also above the threshold value (0/100 mL). The authors attributed this effect to the fact that the penetration of free chlorine into a biofilm is limited by its fast reaction rate [52]. Free chlorine is essentially consumed before it can react with the bacterial components of the film [55]. Chloramines, on the other hand, react slowly; they can diffuse into the biofilm and eventually inactivate attached bacteria; this is a mechanism that has been demonstrated using an alginate bead model [55,56]. The study showed that free chlorine did not effectively penetrate alginate beads containing bacterial cells. The concentrations of all other elements were below their respective threshold values. According to Tables 5, 6 and 10, the permissible limits of physical–chemical and bacterio-logical parameters are confirmed by the Jordanian standards for drinking water and WHO [20,31].

6. Conclusions

Groundwater quality analysis, drilling, monitoring, the completion of wells and their management benefit from effective decision making that incorporates fulfilment techniques, geostatistical systems and retreating analysis. The solution to this problem was found using a methodology that was defined according to the following objectives:

- Identification of the analytical methods for the determined physicochemical and bacteriological analysis.
- The water tests were investigated and different arrangements of physicochemical parameters, such as the pH, turbidity, total dissolved solids, sodium, potassium, calcium, magnesium, chloride, sulphate, bicarbonate, complete hardness, and nitrate, and different components were shown as medium fixation and as not surpassing the Jordanian Principles of Drinking, which was viewed as being under the permissible limits.
- The acceptable quality of groundwater wells was demonstrated in this case study, conducted to support decision makers in the south of Jordan (Water Authority), by testing the performance of groundwater quality determinations using WQIs. Based on Jordanian standards, the findings suggest that the groundwater is within the permissible limits for human consumption.
- The sterilization solution was pumped via airlifting until the chlorine concentration in the water reached 0 mg/L after a reaction time of approximately 12 h.
- After steady-rate pumping, bacteriological analyses revealed the presence of the aerobic bacteria *Acinetobacter haemoliticus*. After the final disinfection, sulfate-reducing bacteria, *Sphingomonas pauciummobitis* (aerobic bacteria), and coliforms could not be found in the water.

Author Contributions: Conceptualization, N.A.-A.; Data curation, H.E.A.-K. and R.T.; Formal analysis, N.A.-A., H.E.A.-K. and M.A.-M. (Marwan Al-Mahasneh); Investigation, M.A.-M. (Mehaysen Al-Mahasneh) and A.A.B.; Methodology, M.A.-M. (Mehaysen Al-Mahasneh), A.A.B. and H.E.A.-K.; Project administration, M.A.-M. (Mehaysen Al-Mahasneh) and H.E.A.-K.; Resources, M.A.-M. (Mehaysen Al-Mahasneh); Software, M.A.-M. (Marwan Al-Mahasneh) and R.T.; Validation, N.A.-A.; Writing—original draft, M.A.-M. (Mehaysen Al-Mahasneh); Writing—review & editing, A.A.B., M.A.-M. (Marwan Al-Mahasneh) and R.T. All authors have read and agreed to the published version of the manuscript.

Funding: This research received no external funding.

Data Availability Statement: Not applicable.

Conflicts of Interest: The authors declare no conflict of interest.

Abbreviations

CFU	Colony-Forming Unit.
NTU	Nephelometric Turbidity Unit.
MPN	Most Probable Number technique.
LRV	Lowest Reported Value.
μS/cm	Electrical conductivity of water

References

1. Baker, M.N. *The Quest for Pure Water, the History of Water Purification from the Earliest Records to the Twentieth Century*, 2nd ed.; American Water Works Association: Denver, CO, USA, 1981; pp. 258–276.
2. Whipple, G.C. Disinfection as a Means of Water Purification. In Proceedings of the American Water Works Association, Boston, MA, USA, 26–30 June 1906; pp. 266–280.
3. Azzirgue, E.M.; Cherif, E.K.; Tchakoucht, T.A.; El Azhari, H.; Salmoun, F. Testing Groundwater Quality in Jouamaa Hakama Region (North of Morocco) Using Water Quality Indices (WQIs) and Fuzzy Logic Method: An Exploratory Study. *Water* **2022**, *14*, 3028. [CrossRef]
4. Hodges, L. *Environmental Pollution*, 2nd ed.; Rinehart and Winston: New York, NY, USA, 1977; p. 189.
5. Nova Scotia Canada, Environment and Labour. Disinfection of Water Wells by Chlorination. Available online: www.gov.ns.ca/nse/water (accessed on 8 September 2005).
6. Fair, G.M.; Corris, J.; Chang, S.L.; Weil, I.; Burden, R.P. The Behavior of Chlorine as a Water Disinfectant. *J. Am. Water Works Assoc.* **1948**, *40*, 1051–1061. [CrossRef]
7. Kyra, M. Well and Water System Disinfection for Public Drinking Water Systems. PUB2476. 7 January 2013.
8. Nova Scotia Canada, Environment and Climate Change. The Nova Scotia Groundwater Levels Timeline Map. Available online: www.gov.ns.ca/nse/water (accessed on 16 October 2018).

9. British Columbia, Health Link BC, Disinfecting Drinking Water, 2021 Water Quality Annual Report; July 2021; No 49b. Available online: https://www.healthlinkbc.ca/sites/default/files/documents/healthfiles/hfile49b.pdf (accessed on 8 September 2005).
10. British Columbia, Health Link BC, Well Water Testing Last Updated: 1 June 2021; No 05b. Available online: https://www.healthlinkbc.ca/sites/default/files/documents/hfile05b.pdf (accessed on 31 March 2013).
11. Indiana Department of Environmental Management. Annual Compliance Report for Indiana Public Water Supply Systems. Available online: https://www.in.gov/idem/cleanwater/files/dw_compliance_report_2019.pdf (accessed on 8 July 2020).
12. Environment Canada. Groundwater. Ottawa ON: Environment Canada. Available online: https://www.ec.gc.ca/Content/B/3/F/B3F88B37-1223-4B6E-9673-68C356740E90/131101_English_DOE_DPR.pdf (accessed on 31 March 2013).
13. Eykelbosh, A.J. Review of Guidelines for Shock Chlorination in Private Wells; the National Collaborating Centre for Environmental Health at the British Columbia Centre for Disease Control; November 2013. Available online: https://www.ncceh.ca/sites/default/files/Shock_Chlorination_Wells_Nov_2013.pdf (accessed on 31 March 2013).
14. Cullimore, D.R.; McCann, A.E. *The Identification, Cultivation and Control of Iron Bacteria in Groundwater*; Academic Press, Inc.: London, UK; Skinner, F.A., Shewan, J.M., Eds.; 1977; pp. 219–261. Available online: https://www.dbi.ca/Books/PDFs/Water-Paper.PDF (accessed on 31 March 2013).
15. Wingender, J.; Flemming, H.C. Biofilms in drinking water and their role as reservoirs for pathogens. *Int. J. Hyg. Environ. Health* **2011**, *214*, 417–423. [CrossRef] [PubMed]
16. Macler, B.A.; Merkle, J.C. Current knowledge of groundwater microbial pathogens and their control. *Hydrogeol. J.* **2000**, *8*, 29–40. Available online: https://link.springer.com/content/pdf/10.1007/PL00010972.pdf?pdf=inline%20link (accessed on 31 March 2013).
17. Schnieders, J.H. Coliforms and Disinfection of Water Well. *Water Well J.* **2001**, *55*, 14–15.
18. Schnieders, J.H. Well Chlorination. *Water Well J.* **1998**, *52*, 25–26.
19. Kachroud, M.; Trolard, F.; Kefi, M.; Jebari, S.; Bourrié, G. Water Quality Indices: Challenges and Application Limits in the Literature. *Water* **2019**, *11*, 361. [CrossRef]
20. Jordanian Institute for Standards and Metrology (JISM). *Jordan Water Quality Standards (JWQS)*; JISM: Amman, Jodan, 2015.
21. Tyagi, S.; Sharma, B.; Singh, P.; Dobhal, R. Water Quality Assessment in Terms of Water Quality Index. *Am. J. Water ResourcesWater Resour.* **2013**, *1*, 34–38. [CrossRef]
22. Effendi, H.; Romanto; Wardiatno, Y. Water Quality Status of Ciambulawung River, Banten Province, Based on Pollution Index and NSF-WQI. *Proc. Environ. Sci.* **2015**, *24*, 228–237. [CrossRef]
23. Zeinalzadeh, K.; Rezaei, E. Determining Spatial and Temporal Changes of Surface Water Quality Using Principal Component Analysis. *J. Hydrol. Reg. Stud.* **2017**, *13*, 1–10. [CrossRef]
24. Matta, G.; Nayak, A.; Kumar, A.; Kumar, P. Water Quality Assessment Using NSFWQI, OIP and Multivariate Techniques of Ganga River System, Uttarakhand, India. *Appl. Water Sci.* **2020**, *10*, 206. [CrossRef]
25. Abbasnia, A.; Alimohammadi, M.; Mahvi, A.H.; Nabizadeh, R.; Yousefi, M.; Mohammadi, A.A.; Pasalari, H.; Mirzabeigi, M. Assessment of Groundwater Quality and Evaluation of Scaling and Corrosiveness Potential of Drinking Water Samples in Villages of Chabahr City, Sistan and Baluchistan Province in Iran. *Data Brief* **2018**, *16*, 182–192. [CrossRef] [PubMed]
26. Brown, R.M.; McClelland, N.I.; Deininger, R.A.; Landwehr, J.M. Validating the WQI. In Proceedings of the National Meeting of American Society of Civil Engineers on Water Resources Engineering, Washington, DC, USA, 29 January–2 February 1973; Volume 29.
27. Nabizadeh, R.; Valadi, A.M.; Alimohammadi, M.; Naddafi, K.; Mahvi, A.H.; Yousef, Z.S. Development of Innovative Computer Software to Facilitate the Setup and Computation of Water Quality Index. *J. Environ. Health Sci. Eng.* **2013**, *11*, 1. [CrossRef] [PubMed]
28. Paun, I.; Cruceru, L.V.; Chiriac, F.L.; Niculescu, M.; Vasile, G.G.; Marin, N.M. *Water Quality Indices—Methods for Evaluating the Quality Of Drinking Water, Incd Ecoind—International Symposium—"The Environment And The Industry"*; INCD Ecoind: Bucuresti, Romania, 2016; pp. 395–402.
29. European Council. Council Directive 98/83/EC on the Quality of Water Intended for Human Consumption as Amended by Regulations 1882/2003/EC and 596/2009/EC—OJ L330 of 05/12/1998—23 p. 1998. Available online: https://eur-lex.europa.eu/legal-content/EN/TXT/PDF/?uri=CELEX:01998L0083-20151027&from=EN (accessed on 31 March 2013).
30. World Health Organization (WHO). *International Standards for Drinking Water*, 3rd ed.; WHO: Geneva, Switzerland, 2006; pp. 10–15.
31. WHO. *Guidelines for Drinking-Water Quality*, 4th ed.; Incorporating the 1st Addendum; WHO: Geneva, Switzerland, 2017.
32. Adegboyega, A.M.; Olalude, C.B.; Odunola, O.A. Physicochemical and bacteriological analysis of water samples used for domestic purposes in Idi Ayunre, Oyo State, Southwestern Nigeria. *IOSR J. Appl. Chem.* **2010**, *8*, 46–50.
33. Hyarat, T.; Al Kuisi, M. Comparison between Weighted Arithmetic and Canadian Council of Ministers of the Environment Water Quality Indices performance in Amman-Zarqa Area, Jordan. *Jordan J. Earth Environ. Sci.* **2021**, *12*, 295–305.
34. Oparaocha, E.T.; Iroegbu, O.C.; Obi, R.K. Assessment of quality of drinking water sources in the Federal University of Technology, Owerri, Imo state, Nigeria. *J. Appl. Biosci.* **2010**, *32*, 1964–1976.
35. Agbabiaka, T.O.; Sule, I.O.; Oyeyiola, G.P. Spatial assessment of public water supplies in densely populated areas of Ilorin Metropolis, Kwara State, Nigeria. *Fountain J. Natural Appl. Sci.* **2014**, *3*, 20–28.
36. Anbazhagan, S.; Nair, A.M. Geographic information system and groundwater quality mapping in Panvel Basin, Maharashtra, India. *Environ. Geol.* **2004**, *45*, 753–761. [CrossRef]

37. Adesoji, A.T.; Ogunjobi, A.A. Occurrence of multidrug-resistant bacteria in selected water distribution systems in Oyo State, Nigeria. *Glob. Vet.* **2013**, *11*, 214–224.
38. WHO. *Guidelines for Drinking Water Quality*, 3rd ed.; World Health Organization: Geneva, Switzerland, 2010.
39. Obeidat, M.; Awawdeh, M. Assessment of groundwater quality in the area surrounding Al-Zaatari Camp, Jordan, using cluster analysis and water quality index (WQI). *Jordan J. Earth Environ. Sci.* **2021**, *12*, 187–197.
40. Rao, N.S. Iron content in groundwaters of Visakhapatnam environs, Andhra Pradesh, India. *Environ. Monit. Assess.* **2008**, *136*, 437–447. [CrossRef]
41. Amanambu, A.C. Geogenic contamination: Hydrogeochemical processes and relationships in Shallow Aquifers of Ibadan, South-West Nigeria. *Bull. Geogr. Phys. Geogr. Ser.* **2015**, *9*, 5–20. [CrossRef]
42. World Health Organization. *Guidelines for Drinking-Water Quality*, 4th ed.; World Health Organization: Geneva, Switzerland, 2011; 564p.
43. *Specification IS 10500*; Indian Standard Drinking Water. Bureau of Indian Standards: New Delhi, India, 2012.
44. LeChevallier, W.M.; Au, K.-K. *Water Treatment and Pathogen Control: Process Efficiency in Achieving Safe Drinking Water*; Iwa Publishing: London, UK, 2004.
45. World Health Organization (WHO). Health Criteria and Other Supporting Information. In *Guidelines for Drinking-Water Quality*, 2nd ed.; WHO: Geneva, Switzerland, 1996; Volume 2.
46. Ongerth, J.E. Evaluation of Treatment for Removing Giardia Cysts. *J. AWWA* **1990**, *82*, 85–96. [CrossRef]
47. Eniola, K.I.; Odaibo, A.D.; Olayemi, A.B.; Ajiboye, T.O. Bacteriological assessment of treated piped water in parts of Ilorin Metropolis. *Niger. J. Microbiol.* **2015**, *28*, 2797–2803.
48. Berger, P.S.; LeChevallier, M.W.; Reasoner, D.J. *Control of Biofilm Growth in Drinking Water Distribution Systems*; Office of Research and Development: Washington, DC, USA, 1992.
49. LeChevallier, M.W. *Biocides and the Current Status of Biofouling Control in Water Systems*; Springer: Berlin, Germany, 1991; pp. 113–132.
50. LeChevallier, M.W.; Schulz, W.; Lee, R.G. Bacterial nutrients in drinking water. *Appl. Environ. Microbiol.* **1991**, *57*, 857–862. [CrossRef] [PubMed]
51. LeChevallier, M.W.; Welch, N.J.; Smith, D.B. Full-scale studies of factors related to coliform regrowth in drinking water. *Appl. Environ. Microbiol.* **1996**, *62*, 2201–2211. [CrossRef]
52. De Beer, D.; Srinivasan, R.; Stewart, P.S. Direct measurement of chlorine penetration into biofilms during disinfection. *Appl. Environ. Microbiol.* **1994**, *60*, 4339–4344. [CrossRef]
53. LeChevallier, M.W.; Lowry, C.D.; Lee, R.G. Disinfection of biofilms in a model distribution system. *J. Am. Water Works Assoc.* **1990**, *82*, 87–99. [CrossRef]
54. Norton, C.D.; LeChevallier, M.W. Chloramination: Its effect on distribution system water quality. *J. Am. Water Works Assoc.* **1997**, *89*, 66–77. [CrossRef]
55. Chen, X.; Stewart, P.S. Chlorine penetration into artificial biofilm is limited by a reaction-diffusion interaction. *Environ. Sci. Technol.* **1996**, *30*, 2078–2083. [CrossRef]
56. Stewart, P.S.; McFeters, G.A.; Huang, C.T. *Biofilm Control by Antimicrobial Agents*; Bryers, J.D., Ed.; John Wiley & Sons: New York, NY, USA, 2000.
57. Kool, J.C.; Carpenter, J.C.; Fields, B.S. Effect of monochloramine disinfection of municipal drinking water on risk of nosocomial Legionnaires' disease. *Lancet* **1999**, *353*, 272–277. [CrossRef]
58. Heffelfinger, J.D.; Kool, J.L.; Fridkin, S.; Fraser, V.J.; Hageman, J.; Carpenter, J.; Whitney, C.G.; Society for Healthcare Epidemiology of America. Risk of hospital-acquired Legionnaires' disease in cities using monochloramine versus other water disinfectants. *Infect. Control Hosp. Epidemiol.* **2003**, *24*, 569–574. [CrossRef] [PubMed]
59. Manasneh, M.A. Disinfection Water Wells and Sterilization. *Comput. Water Energy Environ. Eng.* **2016**, *5*, 38–46. [CrossRef]

Disclaimer/Publisher's Note: The statements, opinions and data contained in all publications are solely those of the individual author(s) and contributor(s) and not of MDPI and/or the editor(s). MDPI and/or the editor(s) disclaim responsibility for any injury to people or property resulting from any ideas, methods, instructions or products referred to in the content.

International Journal of
Environmental Research and Public Health

MDPI

Article

Anthropogenic Contamination in the Free Aquifer of the San Luis Potosí Valley

Sonia Torres-Rivera [1], José Ramón Torres-Hernández [1], Simón Eduardo Carranco-Lozada [2,*], María Elena García-Arreola [1], Rubén Alfonso López-Doncel [1] and Jesús Anibal Montenegro-Ríos [1]

[1] Instituto de Geología, Facultad de Ingeniería, Universidad Autónoma de San Luis Potosí (UASLP), Manuel Nava No. 5, Zona Universitaria Poniente, San Luis Potosí 78290, Mexico; sonia.rivera@uaslp.mx (S.T.-R.); jrtorres@uaslp.mx (J.R.T.-H.); maria.garcia@uaslp.mx (M.E.G.-A.); rlopez@uaslp.mx (R.A.L.-D.); anibal.montenegro@uaslp.mx (J.A.M.-R.)

[2] Instituto Politécnico Nacional, CECyT 15 Diodoro Antunez Echegaray, Dr. Gastón Melo 41, Tenantitla, Milpa Alta, San Antonio Tecómitl 12100, Mexico

* Correspondence: scarrancol@ipn.mx; Tel.: +52-4771-574-603

Abstract: The San Luis Potosí valley is an endorheic basin that contains three aquifers: a shallow unconfined aquifer of alluvial material and two deep aquifers, free and confined. The groundwater contamination documented for the shallow aquifer generates contamination of the deep unconfined type aquifer, from which part of the population's drinking water needs are met. This study records incipient anthropogenic contamination of two types: biogenic and potentially toxic trace elements. The studied contaminants include fecal coliform bacteria, total coliform, nitrate, and potentially toxic elements such as: manganese (*Mn*), mercury (*Hg*), arsenic (*As*), and cadmium (*Cd*). This contamination in some locations exceeds the permissible limit for human consumption. Some major consequences to health, including severe illness, may be caused by the trace elements. The present results give a first signal about the contamination of the deep unconfined type aquifer due to anthropogenic activity in the valley. This is a priority issue because this aquifer supplies drinking water, and in the short or medium term it will have an effect on public health.

Keywords: human health; contamination; aquifer; land settlements

1. Introduction

Groundwater is of essential importance to our civilization because it is the largest reservoir of drinking water in the regions inhabited by humans [1]. Although drinking water can be found on the surface in streams or can be extracted from wells, groundwater is preferred because it does not tend to be contaminated with waste or microorganisms. Although groundwater is less polluted than surface water, increasing and diverse human activity due to urban development has gradually accelerated the quantity and diversity of pollutants in wastewater. Contamination sources include urban, mining, and industrial operations. Often, pollutants are beyond the capacity of treatment plants, so untreated water can become contaminated. Contaminated groundwater has thus become a top priority in industrialized countries and must be taken care of [2]. For example, Mushak [3] commented that human beings exposed to chemical and organic pollutants contained in groundwater may be more susceptible to cancer, stomach disease, or malformations in babies. Wang [4] documents that in China, more than 400 cities exploit groundwater—using more than 1/3 of the total water resources—as the only source of water supply, so a series of problems with groundwater utilization has gradually arisen. One of the best-known examples is the contamination with organic solvents and dioxins of the "Love Canal" in New York in 1978, to which high rates of cancer and an alarming number of birth defects have been attributed [5]. In Mexico, agriculture is the human activity that pollutes water the most, but the greatest damage is caused by urban and industrial waste [6]. Some 30 million

tons of garbage buried in eastern Mexico City contaminate the region's groundwater [7]. Diarrhea is the fifth-leading cause of infant death in Mexico and is associated with the water consumed [7]. In the future, it is expected that groundwater sources will increasingly become the only source of additional water for community development, particularly in more remote areas. However, the quality and quantity of these resources are constantly threatened by the activities inherent to the growth and development of urban centers. In the San Luis Potosí Valley (VSLP), recent water quality studies documented that the water contains high concentrations of fluoride (attributed to the substrate draining surface water and water–rock interaction) and *As* (assigned to mining activity [8]) in addition to other elements derived from anthropogenic activity. Currently, anthropogenic activities have a high impact on the quality of groundwater in the VSLP (housed in three aquifers—one unconfined and two deep aquifers) with the increase in population, change in land use, and expansion of industrial and mining activities. These factors were responsible for the contamination of the unconfined aquifer with heavy metals, major ions, nitrates, fats, oils, grease, and bacteriological contamination. The low average annual precipitation does not contribute substantially to surface water recharge, but it is considered that in times of rain, the contribution is by infiltration in the margins of the valley that mainly feed the unconfined aquifer and the deep unconfined type [9] (Figure 1b). Aguirre and Martinez [10] determined the areas of the valley where pronounced depletion cones are manifested by the pumping of deep wells, and they point out that this highlights the over-exploitation of this aquifer. Another important factor to examine is the subsurface geology of the valley. Aguirre [11], based on the information of lithological sections from deep wells, documents the structural and geological situation of the subsoil of the VSLP and Villa de Reyes (Figure 1a). With this, the author verified the existence of basement blocks delimited by staggered faults along with their course and range of settlement, thicknesses, and continuity of the lithological units of the subsoil, which are fundamental data to define the dimensions and real geometry of the deep aquifer of that valley. The "Atlas de riesgo" for the municipalities of San Luis Potosí (capital) and Soledad de Graciano Sanchez documents land settlements (Figure 1a) that coincide with the limits of some of the basement blocks in the subsoil reported by [11], suggesting that the settlements are controlled by these structures. The water-quality records where contamination was detected in the shallow aquifer (unconfined type) coincide with the surface areas where ground settlements and faulting (with rupture of the hardened soil substrate or tepetate that supports it) have been reported in the Valley of San Luis Potosí [12]. This paper argues that the widely documented anthropogenic contamination of the shallow aquifer [8,9,13] is manifesting, incipiently, in one of the two deep aquifers (unconfined type) and is linked to the possible deterioration and rupture of drainage pipes (especially old drainage pipes) because the settlement and faulting of the valley terrain are creating conduits for percolation of contaminated water into the deep unconfined aquifer. The importance of these studies is that a large part of the population of the municipalities of San Luis Potosí capital; Soledad of Graciano Sanchez, S.L.P.; and Mezquitic de Carmona, S.L.P.; receive water for human consumption from the aquifer examined here, so it is a priority to evaluate the risks that this implies for the health of the population and to take the necessary measures to prevent them. As Espinoza [14] suggests, the infiltration of contaminated water can significantly affect changes in the chemical composition and can cause extreme cases of remediation costs in the drainage network, treatment plants, etc.

This work documents that contamination by trace elements—with potentially harmful effects on health—have percolated from the contaminated shallow aquifer to the deep unconfined type. This process is assumed to be of a temporary and recent nature due to ground settlement processes and fracturing of the tepetate layer that supports the shallow aquifer.

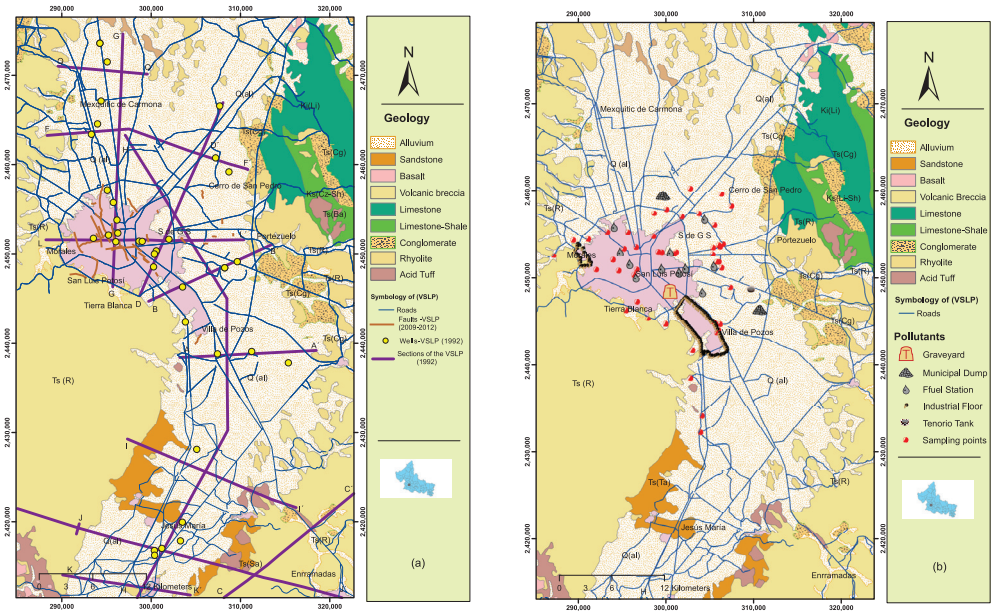

Figure 1. (**a**) Locations of subsurface geology sections based on lithologic columns from deep wells drilled in the valley (according to [11]) and faults (brown). These structures control land settlement in the valley and generally delineate the tectonic blocks covered by the alluvial fill (according to the "Atlas de riesgo of the municipalities of San Luis Potosí and Soledad de Graciano Sanchez 2018"). (**b**) Location of water samples from the unconfined aquifer reported by [9], wherein the water quality is documented based on its degree of contamination. (Arc map and surfer programs were used to create the images.)

2. Materials and Methods

According to the topography of the study area, the recharge and discharge zones were identified and selection of the points of wells and waterwheels was carried out. The samples of wells that correspond to the deep unconfined type have an average depth of 260 m. In the shallow aquifer, wells have a depth of approximately 40 m [9]. Sample bottles were washed with 10% hydrochloric acid (*HCl*) and phosphate-free detergent, rinsed more than three times with distilled water, and allowed to dry. In the hydrogeochemical sampling campaign, 29 groundwater samples were taken from 22 wells and 7 waterwheels. Each sample was taken using a peristaltic pump with a hose with two ends; the sample was passed through one end, and the other end was passed through a 0.45 µm filter and deposited into the duly labeled polyethylene container. In situ physical parameters such as pH, T (temperature), EC (electrical conductivity), DO (dissolved oxygen), ORP (oxide reduction potential), and total dissolved solids (TDS) were measured with a Hanna HI 9829 multiparameter, and sample alkalinity was tested with an HI3811 test kit with a 10 mL phenolphthalein indicator, 10 mL bromophenol blue indicator, and 120 mL alkalinity titrator. Samples taken for cation and trace element testing were preserved with ultra-pure concentrated nitric acid and kept in a cooler for transfer to the laboratory [15,16].

2.1. Location

The state of San Luis Potosí is located north of the Central Plateau in the central–eastern part of Mexico between the parallels 21°09′35″ and 24°33′09″ north latitude and the meridians 98°19′52‴ and 102°17′51″ west of Greenwich (Figure 2). It is divided into four natural regions: Altiplano, Centro, Zona Media, and Huasteca [17]. It is divided into two contrasting hydrogeological regions: The Salado region, located in the north–central portion of the state and with an area of 35,164.19 km^2, presents a dendritic endorheic hydrological pattern where surface water currents are intermittent, scarce, and with little flow—flowing only during the rainy season in summer and occasionally in winter. The second is the Pánuco region, located in the south–southeast portion of the state and has

an area of 27,140.55 km^2 and a dense fluvial network of perennial streams that form some rivers that flow into the Gulf of Mexico [18]. The San Luis Potosí aquifer is defined with the code 2411 in the Geographic Information System for Groundwater Management (SIGMAS) of the CONAGUA [19] (Figure 2).

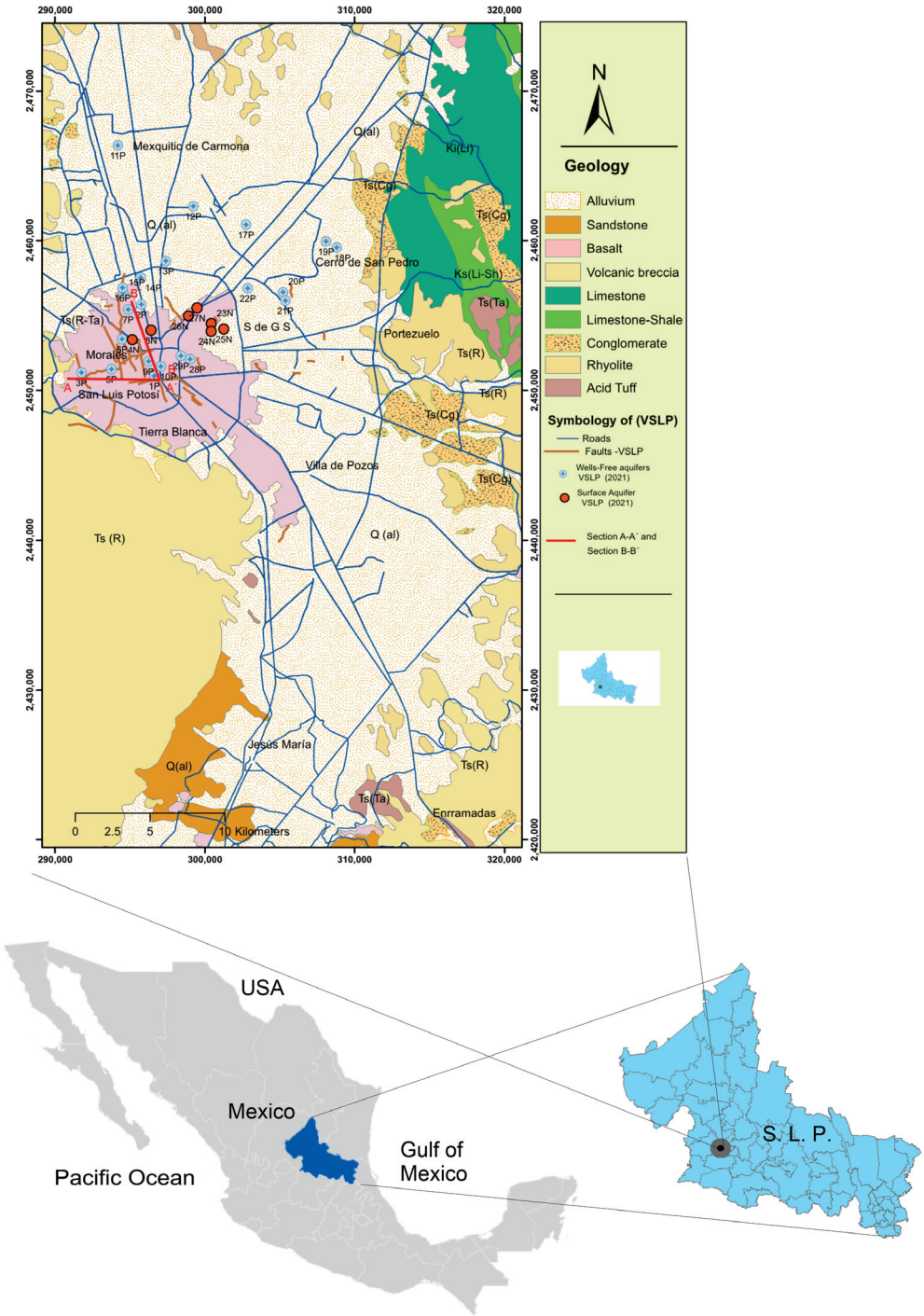

Figure 2. The San Luis Potosí aquifer is located in the central–western portion of the state of San Luis Potosí, has an area of about 1980 km^2, and is between the municipalities of San Luis Potosí and Soledad de Graciano Sanchez in the state of San Luis Potosí. It is orographically limited to the north by a group of hills called "Alto La Melada", to the west–south by the Sierra de San Miguelito, and to the east by the Sierra de Álvarez. (The arc map program was used to create the image).

There are three aquifers in the San Luis Potosí Valley (VSLP). One is of the unconfined type and has a shallow depth of only approximately 40 m [19] and a stratum of low hydraulic conductivity; it is recharged from precipitation in the valley, and its behavior is very dynamic. It has diffuse induced recharge (occasionally by drinking water and/or drainage leaks) and by irrigation water returns [9]. Irrigation return flows are responsible for the deterioration of groundwater quality in a large number of countries, particularly in semiarid and arid regions [20]. Several studies have detected the presence of organic and bacteriological contaminants in the water captured by this aquifer, which has been attributed to the shallow depth at which it is located and the fact that most of the crops are irrigated with untreated municipal sewage; in addition, contamination by some metals can be linked to anthropogenic activities [13,21–23]. The aquifer material has textural variations that influence its characteristics as an aquifer. Towards the Sierra de San Miguelito (SSM), conglomerates immersed in a sandy-clay matrix predominate, and towards the northeast of the east valley, silts and sands predominate. The direction of flow of the unconfined aquifer is from southwest to northeast [24], and its recharge depends on conditions such as precipitation, evapotranspiration, runoff, vegetation, presence of soil layer, the slope of the terrain, and permeability of the material. The main recharge in the aquifer takes place in the southwestern and western flank of the VSLP from the streams that flow down from the SSM towards the valley [25]. In this region, the boundary of the unconfined aquifer is located towards the La Palma locality, where the granular material is wedged and its contact with the fractured volcanic material is closer. The aquifer of the granular medium feeds the wells and rests on the hardened soil or "tepetate". The other unconfined type (and deeper) aquifer, which is hosted in the granular alluvial material that fills the tectonic trenches that are now buried by the valley fill, has been the most exploited. Geological structures such as faults control the distribution and thickness of this aquifer unit, which is composed mainly of Paleogene and Quaternary clastic materials. The aquifer is currently exploited by wells that reach depths of up to 350 m of sedimentary material. Its upper limit is approximately 100 to 150 m deep. It is confined in the center of the valley by a sedimentary layer that is not very permeable. Its thickness ranges from 100 to 200 m [23]. Another aquifer of the confined and deeper type is hosted in alluvial material that was covered by a pyroclastic unit (an ignimbrite) that constitutes its seal and separates it from the unconfined type. Most of the wells drilled in this aquifer have depths of 350–450 m, although there are some that are 800–1000 m [25]. The depth of the potentiometric surface is greater than 150 m depending on the location within the valley.

2.2. Geology

The aquifer studied is located in an endorheic tectonic valley whose lowest topographic parts are in its northeastern part. The various studies carried out to date [11,25,26] have fully established the geology around the valley, which is outlined below. The basement is a sequence of calcareous and calcareous–marine clay–calcareous rocks (basin and platform) of Mesozoic age, outcropping in the Sierras of Alvarez and El Coro, which limit the valley in the eastern and northeastern parts. The north, west, and southwest limits are: La Melada and San Miguelito mountains (respectively), which are formed of Paleogene (Oligocene–Miocene) volcanic rocks of rhyolitic and dacitic composition. The valley was formed by extensional faults in two main systems, those of NW-SE orientation (north and southwest limits of the valley) and those of N-S orientation in the other limits. Geological events that shaped the valley generated a series of tectonic blocks that remained under the alluvial fill and have been determined by the coincidence of lithological columns cut by numerous wells at different depths and evidenced by magnetometry geophysical studies [27]. Thus, the aquifers have been documented: the deep confined in clastic deposits between the Mesozoic basement and pyroclastic deposits (ignimbrites) from the middle Oligocene that outcrop regionally; intermediate in the fill of alluvial material deposited on the ignimbrites; and upper "pendant" (5–30 m higher) that has its base on the hardened layer called "tepetate", which is typical of the arid and semi-arid regions of Mexico. Due

to its characteristics, this shallow aquifer is the most susceptible to being impacted by anthropic activity and is the object of this research study, especially with respect to its influence on the incipient contamination of the deep unconfined type.

2.3. Sample Analysis

The analysis of the samples was carried out at the geochemistry laboratory of the Geology Institute, Universidad Autonoma of San Luis Potosí. The analysis consisted of determining the concentrations of the major ions sodium (Na^+), potassium (K^+), calcium (Ca^{+2}), and magnesium (Mg^{+2})] using an optical emission spectrophotometer with plasma coupled to atomic absorption induction (ICO-OES). Induction-coupled plasma–inductively coupled mass spectrometer (ICP-MS) was used to determine trace elements such as mercury (*Hg*), barium (*Ba*), strontium (*Sr*), cadmium (*Cd*), lead (*Pb*), silver (*Ag*), rubidium (*Rb*), cobalt (*Co*), copper (*Cu*), iron (*Fe*), arsenic (*As*), lithium (*Li*), nickel (*Ni*), manganese (*Mn*), chromium (*Cr*), zinc (*Zn*), and aluminum (*Al*). The UV-Vis method with HACH DR/2000 equipment was used for the analysis of nitrates ($N - NO_3$), sulfates ($SO_4{}^{-2}$), and fluorine (F^-); the volumetric method tested for bicarbonates ($HCO_3{}^-$) and carbonates ($CO_3{}^{-2}$); the argentometric method tested for chlorides (Cl^-); the analysis of pH, electrical conductivity, alkalinity, total dissolved solids, fats and oils (GA), total coliforms (CT), and fecal coliforms (CF) was performed in the groundwater laboratory of the Faculty of Engineering of the UASLP.

3. Results

In February 2020, the sampling campaign of the VSLP was carried out in order to obtain its physicochemical parameters in situ (Table 1), and, in addition, the characterization of the chemical composition of the groundwater of the valley was carried out in Table 2. These parameters are expressed for a 10.57 km physicochemical section (Figure 3 of the VSLP. It begins in the southwestern part of the valley with sample 3P located along Hernán Cortés avenue; crosses the valley towards the center of the city with samples 1P, 10P, and 9P; heads north of the valley for 4N, 6P, 8N, and 7P; and at the end of the stretch is sample 2P—this development is the furthest from the VSLP, with the volcanic rocks at the base of this aquifer approximately 360 m deep. The pH at the beginning in the 3P sample was 7.7; it increases and reaches values of 8 in 5P and maintains little variation until Tangamanga park; however, in the end, values of 8.54 are reached in 2P (Figure 3 and Table 1). The temperature starts at 38 °C, and throughout the section, the temperature is discontinuous and decreases gradually until reaching 26 °C at the end of the section in the El Saucito 2P sample (Figure 3 and Table 1). The average electrical conductivity in the water is 488 µS/cm in the entire section. It starts low at 3P (769 µS/cm); the highest points are located almost in the center of the section in the valley at 4N (808 µS/cm) and 8N (930 µS/cm) due to the chemical components dissolved in the water; the value decreases at the end of the section in the 2P samples, which suggests that the waters interact with volcanic rocks (Figure 3 and Table 1). Alkalinity starts with values of 156 mg/L at 3P, increases slightly towards the center of the valley to 210 mg/L at 9P and 10P, and increases to 348 mg/L at 4N and 8N; this increase is associated with the interaction of water with carbonates in the sands and silts of the fill material (Figure 3 and Table 1). Regarding the total dissolved solids (TDS), this value begins with a concentration in 3P of 206 mg/L, increases towards the center of the valley in 1P (391 mg/L), 4N (403 mg/L), and 8N (465 mg/L), and decreases at the end. The concentration changes in 4N and 8N that are in the shallow aquifer reflect the contamination of the shallow aquifer; added to the above, this is consistent with the CE ion network and the salts, minerals, metals and any other organic or inorganic compounds (Figure 3 and Table 1).

Table 1. Physicochemical parameters of the in situ VSLP taken from the groundwater samples collected.

			UTM		Field Parameters							
					Ta	Ts	pH	EC	DO	TDS	Alk	ORP
Sample	Location	Sampling Point	Lat	Long	°C	°C		µS/cm	%	ppm		mV
1P	Alameda	well	296,631	2,450,966	23.0	22.8	8.0	769	24.0	391	189	118.6
2P	Saucito	well	295,751	2,455,752	23.0	26.0	8.5	377	31.7	183	119	132.0
3P	Parque Morales	well	291,769	2,451,178	31.0	37.7	7.7	410	-	206	156	209.0
4N	La Venadita	waterwheel	295,163	2,453,378	19.0	22.0	7.4	808	-	403	348	210.0
5P	Muñoz	well	293,763	2,451,413	33.0	38.2	7.0	395	15.4	197	150	284.0
6P	Tangamanga 2	well	294,471	2,453,418	30.0	33.9	7.4	347	32.5	173	105	295.5
7P	CNA-27	well	294,881	2,455,405	15.7	26.3	7.5	230	28.9	115	75	273.2
8N	3a.Chica	waterwheel	296,410	2,454,010	16.5	22.6	7.2	930	4.4	465	270	311.8
9P	República	well	296,244	2,451,936	20.0	26.4	7.0	253	32.5	127	210	312.0
10P	Montesillo	well	297,060	2,451,589	20.2	35.3	7.5	369	27.5	185	210	275.2
11P	Tierra Rajada	well	294,195	2,466,356	27.0	24.7	8.2	320	20.0	160	153	56.0
12P	Rinconada	well	299,229	2,462,282	27.0	26.0	7.8	335	60.0	162	165	140.0
13P	Milpillas	well	297,401	2,458,626	19.0	26.1	7.8	473	38.9	237	213	198.0
14P	Compostela	well	295,723	2,457,515	23.7	29.7	7.6	467	46.3	183	192	127.7
15P	Ponciano	well	294553	2456510	23.1	33.5	7.4	333	38.6	166	174	183.0
16P	Ponciano 1	well	294,510	2,456,843	25.0	31.5	7.5	306	41.5	153	153	183.5
17P	El Ranchito	well	302,757	2,461,064	22.7	23.5	7.0	298	57.2	145	129	93.9
18P	Well 2 Agronomia	well	308,813	2,459,533	25.0	23.5	6.7	1112	60.0	556	195	190.0
19P	Well 3 Agronomia	well	308,094	2,459,937	20.0	24.4	7.1	568	53.2	283	153	228.8
20P	Valle de la Palma	well	305,225	2,456,570	21.7	20.8	6.7	862	55.3	429	171	206.0
21P	El Diamante	well	305,381	2,456,010	18.4	20.4	6.6	1088	52.7	536	243	208.5
22P	El Zapote	well	302,858	2,456,810	18.0	20.5	6.9	1518	38.6	759	360	191.8
23N	Soledad 1	waterwheel	300,442	2,454,448	21.8	21.1	6.9	2156	8.2	1077	450	105.1
24N	Soledad 2	waterwheel	300,438	2,453,941	23.4	20.0	7.1	1914	12.2	944	390	76.5
25N	Soledad 3	waterwheel	301,278	2,454,092	24.5	20.5	7.1	1790	15.5	894	480	105.6
26N	Potrero de adentro	waterwheel	298,923	2,454,963	24.9	21.3	6.7	909	0.0	456	252	133.4
27N	Soledad 4	waterwheel	299,490	2,455,503	22.3	20.1	6.7	1028	5.1	514	393	142.4
28P	Well Praderas	well	299,024	2,452,087	22.9	33.2	7.3	279	30.0	138	162	139.7
29P	Well Las Palmas	well	298,407	2,452,303	25.4	34.8	7.5	297	30.3	149	138	128.0

Ambient temperature °C (TA), sample temperature °C (Ts), hydrogen potential (pH), electric conductivity (EC), dissolved oxygen (DO), total dissolved solids (TDS), alkalinity (Alk), and oxidation reduction potential (ORP).

The oxidation/reduction potential in units of milliVolts (mV) starts low at 3P (209 mV), the high values are represented at 5P (284 mV), 4N (210 mV), and 8N (312 mV), and the last point concludes with a low concentration in 2P (132 mV) (Figure 3 and Table 1). The samples analyzed in the laboratory must comply with the principle of electroneutrality: the sum of the charges of all the cations must be equal to the sum of the charges of all the anions and they must be electrically neutral [28]. To check the accuracy of the analysis of the majority ions, ionic balance is performed (Equation (1)).

$$\%Electroneutralidad = \frac{\sum Cations - \sum Anions}{\sum Cations + \sum Anions} \times 100 \quad (1)$$

Cations and anions are expressed in meq/L [29]. For the analysis of a sample to be valid, the amplitude of variation of the electroneutrality percentage must be ±5%, although an amplitude of up to ±10% can be accepted [30]. In this case, the interval ±10% was considered (Table 2). The predominant water family of the analyzed samples presents 55.2% of bicarbonate-calcium composition ($Ca - HCO_3^-$), bicarbonate-sodium ($Na - HCO_3^-$) is second place and represents 37.9% of the total samples, and 6.89% were of chloride-calcium composition ($Ca - Cl^-$) (Table 2) in coherence with the nature of the fractured and carbonate volcanic rock of the main permeable materials existing in the center of the VSLP.

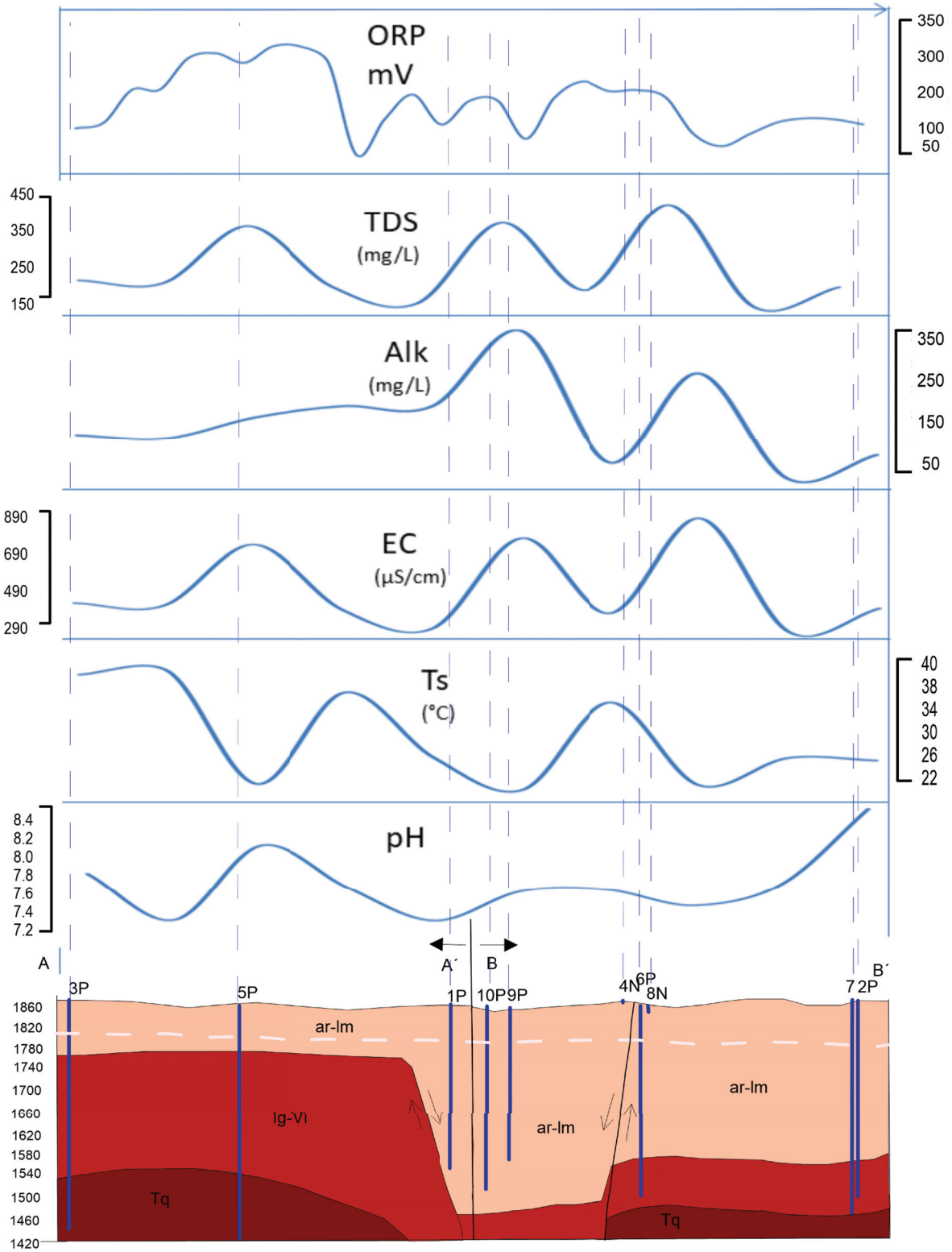

Figure 3. Schematic geological section of the San Luis Potosí Valley (VSLP). (Grapher 11 was used to create the image).

Table 2. Main characteristics of major elements and chemical families of groundwater.

	Laboratory mg/L										
Sample	Na^+	K^+	Ca^{+2}	Mg^{+2}	CO_3^{-2}	HCO_3^-	Cl^-	SO_4^{-2}	$N-NO_3^-$	F^-	**%Error**
1P	49.8	44.6	59.4	9.9	0.0	212.4	60.9	92.0	7.8	0.0	−3.9
2P	29.6	8.6	36.4	1.7	0.0	146.0	30.5	11.0	4.2	0.1	−4.4
3P	61.0	3.4	24.6	3.7	0.0	186.7	10.2	55.0	2.5	0.5	−4.7
4N	50.0	5.4	99.8	9.3	0.0	340.4	45.7	60.0	7.6	0.6	−3.7
5P	60.0	2.6	20.0	1.9	0.0	153.7	30.5	25.0	2.4	2.1	−4.4
6P	39.0	4.5	27.6	3.7	0.0	142.7	25.4	19.0	2.5	1.7	−3.0
7P	27.0	19.2	33.8	2.8	0.0	164.7	20.3	7.0	3.0	0.7	−1.1
8N	196.0	35.6	52.2	4.7	0.0	318.4	116.8	105.0	15.0	1.0	2.5
9P	24.0	5.4	24.6	2.8	0.0	65.9	40.6	16.0	3.1	1.9	−4.3
10P	53.0	8.2	23.0	1.9	0.0	142.7	30.5	27.0	2.7	1.3	−2.6
11P	37.5	11.2	53.4	1.9	0.0	151.3	67.5	14.4	2.1	0.6	−1.3
12P	24.8	7.5	68.3	2.0	0.0	156.2	49.6	22.5	0.5	0.6	3.8
13P	41.2	16.6	48.7	2.1	0.0	190.3	49.6	25.0	0.7	0.7	−3.0
14P	44.3	9.3	47.4	1.4	0.0	200.1	41.7	20.0	0.3	1.2	−3.2
15P	57.4	5.4	35.0	1.0	0.0	146.4	53.6	35.0	1.7	2.2	−4.4
16P	16.6	13.4	65.3	5.2	0.0	161.0	39.7	27.5	1.9	2.2	1.8
17P	57.5	5.3	36.7	0.5	0.0	151.3	33.8	55.0	1.8	0.4	−2.3
18P	65.7	22.2	115.8	15.0	0.0	185.4	210.4	87.5	5.0	0.5	−3.4
19P	25.6	12.7	86.1	16.0	0.0	151.3	111.2	45.0	0.0	0.6	3.5
20P	41.7	26.5	93.5	15.1	0.0	195.2	95.3	90.0	5.0	0.4	1.7
21P	53.2	29.7	137.9	19.2	0.0	224.5	123.1	175.0	5.0	0.4	1.6
22P	267.9	0.2	31.1	0.1	0.0	258.6	200.5	200.0	5.0	0.6	−4.4
23N	208.6	41.4	182.7	26.1	0.0	463.6	234.3	300.0	5.0	0.6	1.4
24N	194.3	37.7	161.2	24.3	0.0	453.8	95.3	365.0	5.0	0.0	3.7
25N	172.7	31.1	146.9	22.5	0.0	400.2	152.9	250.0	5.0	0.0	3.2
26N	72.1	34.4	76.1	16.4	0.0	278.2	43.7	112.5	5.0	2.0	3.2
27N	89.9	36.8	81.1	18.3	0.0	258.6	85.4	175.0	5.0	2.0	−1.6
28P	47.5	6.2	25.6	1.6	0.0	180.6	23.8	7.0	0.6	1.2	−3.3
29P	42.2	3.6	22.2	0.6	0.0	151.3	13.9	8.0	0.5	1.4	−1.0

The aforementioned water families reflect that the main supply corresponds to the Santiago River, and the salt content corresponds to the interaction of bicarbonate-sodium water where the water movement is in contact with the fractured volcanic material, sand, and silt; so the flow of this may have hydraulic communication with the aquifer of the granular medium that feeds the wells and rests on the hardened soil or "tepetate". The bicarbonate-calcium family may represent the interaction of the water with the granular material that filled the tectonic pits, and the chloride-calcium family may be due to the agricultural activity developed in that area. The chemical composition of groundwater is the result of continuous processes of interaction between the meteoric water that infiltrates the ground and circulates through the different subsoil materials. Chemical analyses of water samples taken directly from the wells—plotted on a Piper diagram [31]—define different (types of) water families (Figure 4). The bicarbonate-calcium family is represented by the pink diamond, is located in the east and center of the VSLP, and indicates samples that passed through carbonate rocks (1P, 2P, 3P, 7P, 11P, 12P, 13P, 14P, 16P, 19P, 20P, 21P, and 22P); 4N, 23N, 26N and 27N are the result of processes of water mixtures found in the center of the diamond, and samples with a direction towards the south of the gray diamond are also observed: this represents an ion exchange corresponding to samples 3P, 5P, 6P, 10P,15P, 17P, 28P, and 29P; 8N, 24N and 25N are from deep wells, and only two chloride-calcium samples were found (9P and 18P), which correspond, respectively, to 280 m and 350 m depths that cut through granular material that filled the valley; well 9P is located in the center of the city of San Luis Potosí, and well 18P is to the NE of the valley in the Agronomy School (Figure 4).

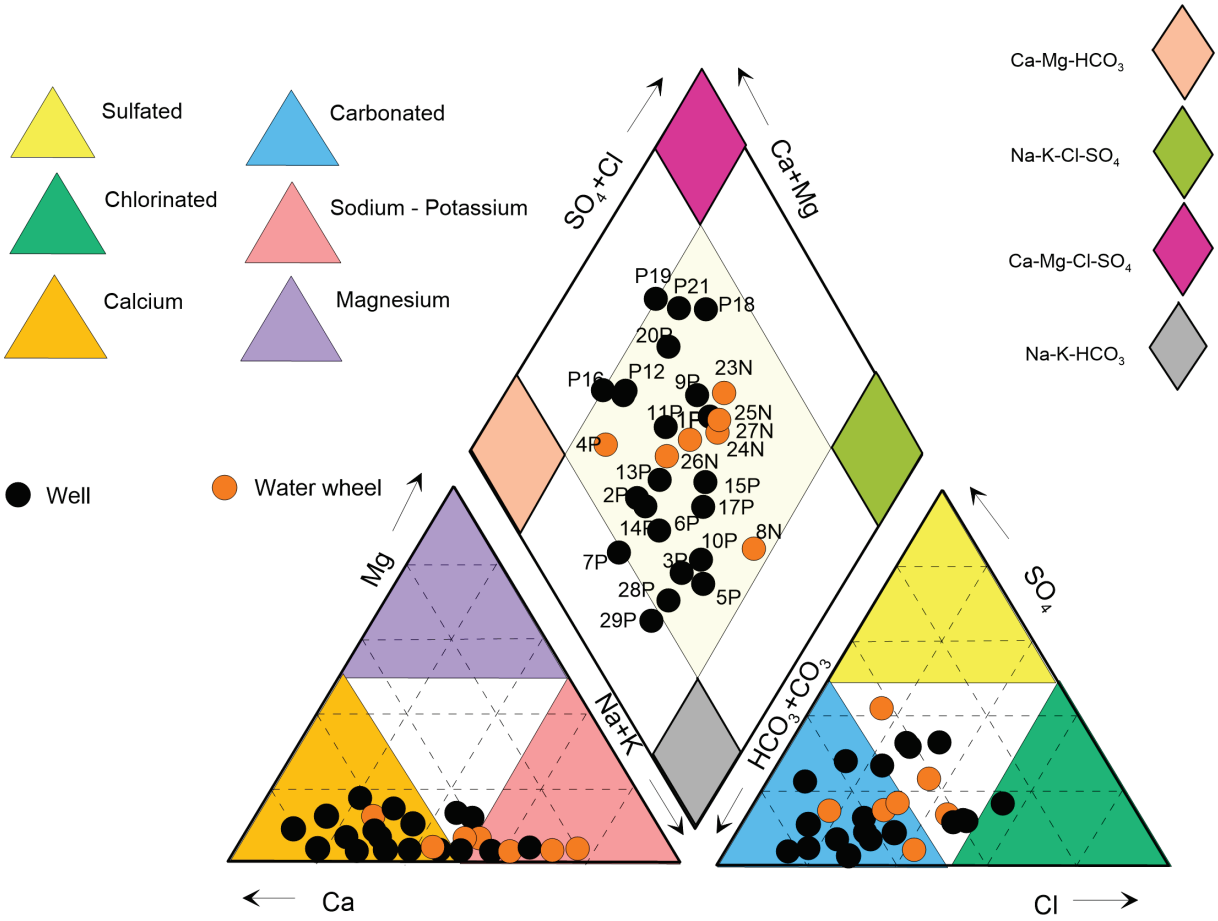

Figure 4. Piper diagram modified from [31] shows families of water. (Surfer was used to create the image).

Ionic ratios are used to support the identification of possible groundwater origins or mixing processes occurring in the subsurface; the $Na^{+2}K^{+}$ vs. $Cl^{-} + SO_4^{-2}$ ratio is proposed by [32] to identify the presence of regional flows as well as in the characterization of some evolutionary processes of geogenic or anthropogenic origin. Thus, it was used in the identification of these for the study area (Figure 5). In this study, most of the samples were found in the local flow area, and five were found in the intermediate flow, which means that the water is of recent infiltration and that it has had little chemical evolution and water–rock interaction.

Table 3 shows the results of nitrogen and phosphorus contents of the sampled works (wells and waterwheels) and localities referred to in the maps. Table 4 shows the results of bacteriological contents, and Tables 5 and 6 show the contents of trace elements and metals, respectively.

3.1. Nitrogen and Phosphorus Content

Sample 8N (Table 3) is the only one with anomalous nitrogen content and belongs to a 3 m deep private well located in settlement 3a Chica in the El Saucito zone north of the VSLP. It presents a concentration of 15 mg/L of nitrate nitrogen ($N - NO_3^{-}$), which exceeds the maximum allowable limit of 10 mg/L set by NOM-127-SSA1-1994 [33].

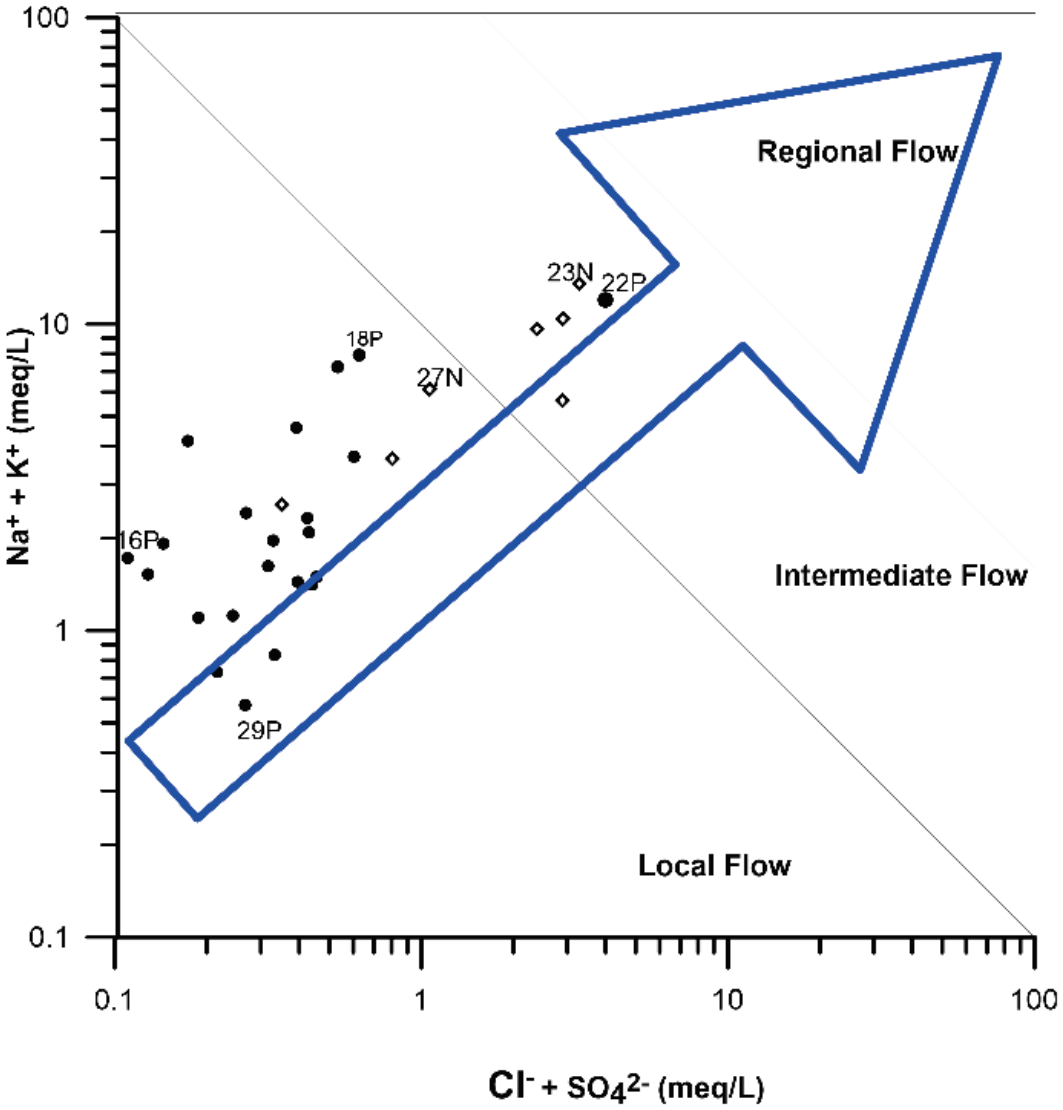

Figure 5. The Mifflin [32] diagram shows two different water flows, one local and one intermediate. (Grapher was used to create the image).

Table 3. The results of nitrate nitrogen ($N - NO_3^-$) and phosphorus (P).

	Laboratory	
Sample	$N - NO_3^-$ mg/L	P mg/L
1P	7.8	0.216
2P	4.2	<0.01
3P	2.5	0.002
4N	7.6	0.131
5P	2.4	0.003
6P	2.5	0.019
7P	3	0.085
8N	15	0.449
9P	3.1	0.261
10P	2.7	0.007

Table 3. *Cont.*

	Laboratory	
Sample	$N-NO_3^-$ mg/L	P mg/L
11P	2.1	<0.01
12P	0.5	<0.01
13P	0.70	<0.01
14P	0.30	<0.01
15P	1.7	<0.01
16P	1.9	<0.01
17P	1.8	<0.01
18P	5	0.015
19P	0	<0.01
20P	5	<0.01
21P	5	<0.01
22P	5	0.087
23N	5	<0.01
24N	5	0.158
25N	5	0.011
26N	5	<0.01
27N	5	0.069
28P	0.6	<0.01
29P	0.5	<0.01

Maximum permissible limits: nitrogen from nitrates $N-NO_3^- = 10$ mg/L, NOM-127-SSA1-1994; phosphorus of phosphates $PO_4 = 0.1$ mg/L, WHO-2004; and total phosphorus PT = 5 mg/L, NOM-001-SSA1-1996.

3.2. Bacteriological Results

Regarding the biogenic content in the sampled waters related to anthropogenic activity, the results are shown in Table 4. Of the seven wells sampled, only three show high biogenic contents related to anthropogenic activity. These are noria 4N, with a concentration of 2 NMP/100, and norias 24N and 27N, with concentrations of 11 NMP/100 and 5NMP/100, respectively. Concerning the wells, the presence of fecal coliforms is documented in wells of the deep unconfined type of the VSLP. Of the 29 wells studied (100%), 12 samples (41%) were found to be out of the norm. These are: well 2P with a concentration of 3 NMP/100 (most probable number per 100 mL); well 3P with a concentration of 8 NMP/100 (from Morales Park); well 12P with a concentration of 11 NMP/100; wells 15P and 16P with concentrations of 11 NMP/100; well 17P with a concentration of 14 NMP/100; wells 18P and 19P with concentrations of 5 NMP/100 and 17 NMP/100, respectively; well 20P with a concentration of 11 NMP/100; well 22P with a concentration of 5 NMP/100; and well 28P with a concentration of 11 NMP/100.

3.3. Fats and Oils

The measurement of fats and oils does not measure a specific substance but a group of substances with the same physicochemical characteristics (solubility). Therefore, the measurement of fats and oils includes fatty acids, soaps, fats, waxes, hydrocarbons, oils, and any other substance that can be extracted with hexane, and its permissible limit is 26 mg/L according to NOM-002- SEMARNAT-1996 [34]. Therefore, almost all the samples show low concentrations of fats and oils, although they present small amounts.

Table 4. Bacteriological concentrations: permissible limit for Fecal Col. = 0 most probable number per 100 (0 NMP/100) not detectable, NOM-127; permissible limit for Total Col. = (2NMP/100), NOM-127; and permissible limit for Fats and Oils (G and A) = (21 mg/L), NOM-002.

Sample	Fecal Coliforms	Total Coliforms	Fats and Oils (mg/L)	Depth (m)
1P	<3	<3	6.63	300
2P	<3	150	2.65	360
3P	8	8	5.1	420
4N	<3	<3	3.7	3
5P	<3	<3	2.9	200
6P	<3	<3	6.8	418
7P	<3	<3	4.4	400
8N	<3	<3	6.8	5
9P	<3	<3	7.7	280
10P	<3	<3	7.7	700
11P	<3	<3	-	200
12P	11	13	-	350
13P	<3	7	-	250
14P	<3	<3	-	360
15P	11	11	-	360
16P	11	16	-	400
17P	14	14	-	350
18P	5	10	-	350
19P	17	17	-	222
20P	11	16	-	70
21P	<3	<3	-	60
22P	5	7	-	1180
23N	<3	<3	-	8
24N	11	11	-	10
25N	<3	<3	-	7
26N	<3	<3	-	5
27N	5	5	-	10
28P	11	11	-	600
29P	<3	<3	-	300

Permissible limits of fecal coliforms = no detectables (0 NMP/100 mL), NOM-127; permissible limits of total coliforms = (2 NMP/100 mL), NOM-127; and permissible limits of fats and oil = (21 mg/L), NOM-001.

3.4. Metals and Trace Elements

Tables 5 and 6, respectively, document the contents of metals and trace elements measured in the samples studied. In these tables, we highlight that the out-of-range samples correspond to *Mg*, *As*, *Cd*, and *Hg*. For *Mg*, only one sample exceeds this permissible limit: well 18P with a concentration of 0.84 mg/L. For *As*, wells 24N (in Soledad) with a concentration of 0.05 mg/L, 12P with a concentration of 0.126 mg/L, and 18P with a concentration of 0.09 mg/L are the ones with contents that exceed the permitted levels (Figure 6a).

For *Cd*, the samples that exceed the limit are: wells 24N and 26N with concentrations of 0.0067 mg/L and 0.0119 mg/L, respectively; 11P with a concentration of 0.0169 mg/L; 12P with a concentration of 0.0206 mg/L; P14 with a concentration of 0.005 mg/L; 17P with a concentration of 0.0085 mg/L; 20P with a concentration of 0.01068 mg/L; and 29P with a concentration of 0.00524 mg/L (Figure 6b). For *Hg*, the samples that fall outside the norm are: wells 23N with a concentration of 0.004 mg/L; 25N with a concentration of 0.002 mg/L;

11P with a contraction of 0.002 mg/L; 18P with a concentration of 0.0015 mg/L; 20P with a concentration of 0.002 mg/L; and 22P with a concentration of 0.0012 mg/L (Figure 6c).

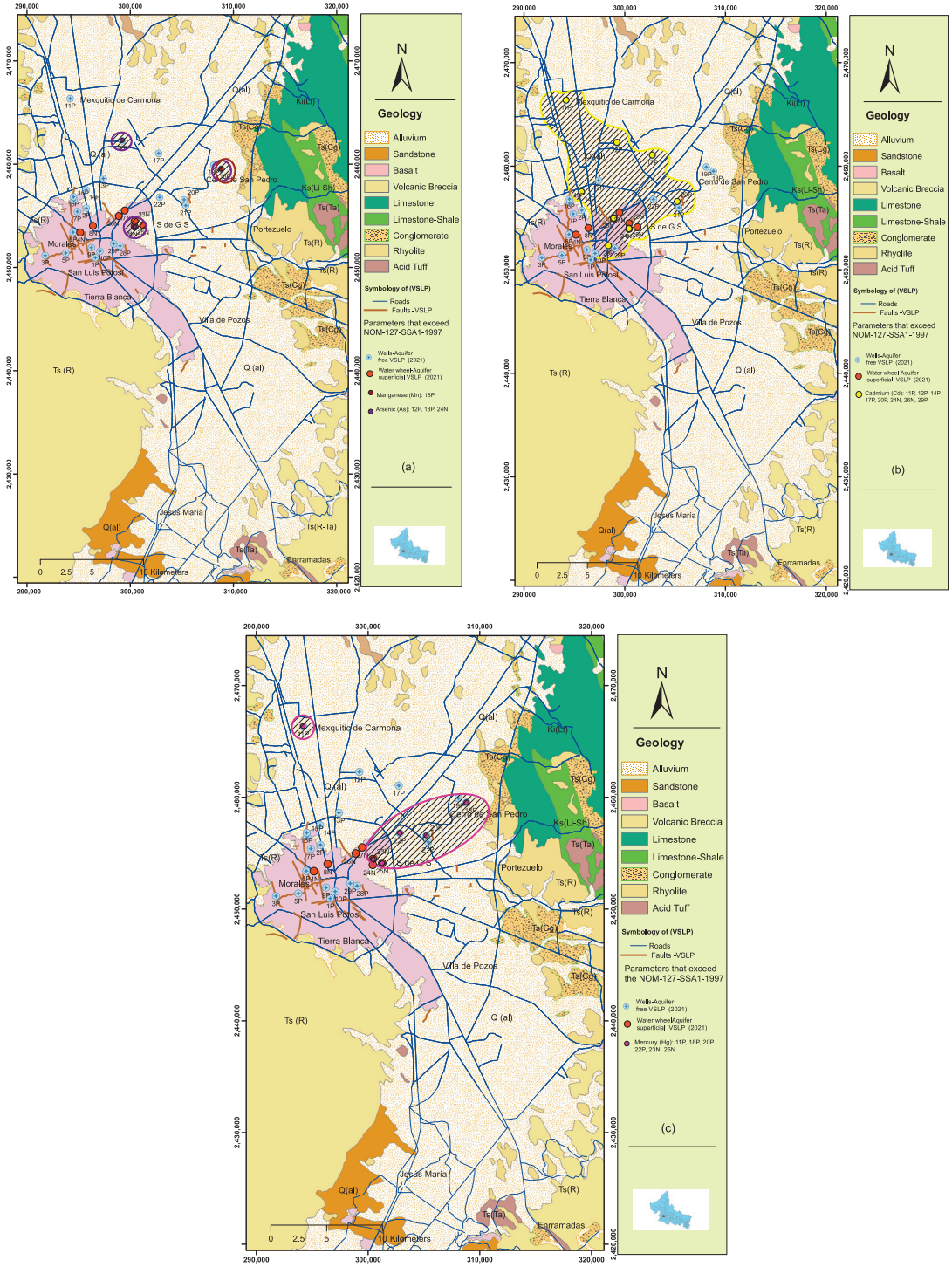

Figure 6. The shaded maps represent trace elements that exceed the allowable limits of the NOM-127-SSA1 [33] standard. Concentrations are indicated in (mg/L): (**a**) arsenic (*As*) concentration, (**b**) Cadmium (*Cd*) concentration, and (**c**) mercury (*Hg*) concentration. (Arc map software was used to create the image).

Table 5. Concentrations of heavy metals and trace element analysis. Permissible limit in (mg/L or ppm) of: aluminum (*Al*) = 0.2, chromium (*Cr*) = 0.05, manganese (*Mn*) = 0.15, iron (*Fe*) = 0.3, copper (*Cu*) = 2, zinc (*Zn*) = 5, and arsenic (*As*), cadmium (*Cd*), and mercury (*Hg*) = 0.001 according to NOM-127-SSA1-1994.

Sample	Li ppm	B ppm	Al ppm	P ppm	Sc ppm	Ti ppm	V ppm	Cr ppm	Mn ppm	Fe ppm	Ni ppm	Cu ppm	Zn ppm	Ga ppm	Ge ppm
1P	0.00	0.14	0.004	0.216	0.006	0.004	0.008	0.0002	0.026	<0.01	0.0007	<0.01	0.01	0.002	<0.01
2P	0.07	0.09	0.021	<0.01	0.009	0.005	0.005	<0.01	0.065	<0.01	<0.01	<0.01	<0.01	0.002	<0.01
3P	0.26	0.24	<1.0	0.002	0.005	0.002	0.000	<0.01	<0.01	0.009	<0.01	<0.01	<0.01	<0.01	0.002
4N	0.01	0.22	0.062	0.13	0.010	0.006	0.016	0.0005	<0.01	0.005	<0.01	<0.01	0.00	0.002	<0.01
5P	0.27	0.26	<1.0	0.00	0.005	0.002	0.000	<0.01	<0.01	0.000	<0.01	<0.01	<0.01	<0.01	0.002
6P	0.17	0.17	0.031	0.02	0.007	0.004	0.002	<0.01	<0.01	0.016	<0.01	<0.01	<0.01	<0.01	0.001
7P	0.03	0.07	<1.0	0.09	0.009	0.006	0.005	<0.01	<0.01	0.001	<0.01	<0.01	<0.01	0.000	<0.01
8N	0.01	0.24	0.009	0.45	0.010	0.006	0.012	0.003	0.011	0.006	<0.01	0.0003	0.00	0.001	<0.01
9P	0.02	0.07	<1.0	0.26	0.010	0.006	0.005	<0.01	<0.01	<0.01	<0.01	<0.01	<0.01	0.001	<0.01
10P	0.00	0.21	<1.0	0.007	0.005	0.002	0.001	<0.01	<0.01	<0.01	<0.01	0.0001	0.00	<0.01	0.001
11P	0.07	0.14	0.075	<0.01	0.006	0.004	0.008	0.002	0.015	0.114	0.008	0.017	0.21	<0.01	<0.01
12P	0.26	0.09	0.024	<0.01	0.009	0.005	0.005	0.008	0.003	0.099	0.009	0.001	0.13	<0.01	<0.01
13P	0.01	0.24	0.027	<0.01	0.005	0.002	0.000	0.004	0.002	0.172	0.001	<0.01	0.17	<0.01	<0.01
14P	0.27	0.22	0.028	<0.01	0.010	0.006	0.016	0.001	<0.01	0.052	0.000	0.012	0.21	<0.01	<0.01
15P	0.17	0.26	0.002	<0.01	0.005	0.002	0.000	<0.01	< 0.01	0.025	<0.01	<0.01	0.13	<0.01	<0.01
16P	0.03	0.17	0.027	<0.01	0.007	0.004	0.002	<0.01	0.007	0.261	0.002	0.010	0.17	<0.01	<0.01
17P	0.01	0.07	0.016	<0.01	0.009	0.006	0.005	0.005	0.002	0.061	0.006	<0.01	0.21	<0.01	<0.01
18P	0.02	0.24	0.057	0.015	0.010	0.006	0.012	0.003	0.841	0.233	0.016	0.005	0.13	<0.01	<0.01
19P	0.00	0.07	0.044	<0.01	0.010	0.006	0.005	0.000	0.001	0.048	0.003	<0.01	0.17	<0.01	<0.01
20P	0.07	0.21	0.031	<0.01	0.005	0.002	0.001	0.000	0.006	0.059	0.003	0.017	0.21	<0.01	<0.01
21P	0.26	0.14	0.005	<0.01	0.006	0.004	0.008	0.003	<0.01	0.063	0.008	<0.01	0.13	<0.01	<0.01
22P	0.01	0.09	0.009	0.087	0.009	0.005	0.005	0.001	<0.01	0.097	0.009	<0.01	0.17	<0.01	<0.01
23N	0.27	0.24	0.067	<0.01	0.005	0.002	0.000	0.001	0.012	0.156	0.008	<0.01	0.21	<0.01	<0.01
24N	0.17	0.22	0.008	0.158	0.010	0.006	0.016	0.004	0.000	0.066	0.011	<0.01	0.13	<0.01	<0.01
25N	0.03	0.26	0.000	0.011	0.005	0.002	0.000	<0.01	0.001	0.042	0.006	<0.01	0.17	<0.01	<0.01
26N	0.01	0.17	0.028	<0.01	0.007	0.004	0.002	<0.01	<0.01	0.032	0.002	<0.01	0.21	<0.01	<0.01
27N	0.02	0.07	0.054	0.069	0.009	0.006	0.005	0.0001	0.006	0.067	0.003	<0.01	0.13	<0.01	<0.01
28P	0.00	0.24	0.022	<0.01	0.010	0.006	0.012	0.0018	<0.01	0.030	0.002	<0.01	0.17	<0.01	<0.01
29P	0.07	0.07	0.033	<0.01	0.010	0.006	0.005	0.0026	0.001	0.055	0.003	<0.01	0.21	<0.01	<0.01
Limit *				0.2					0.05	0.15	0.3		2	5	

* Maximum allowable limit according to NOM-127-SSA1-1994 [33].

Table 6. Concentrations of heavy metals and trace element analysis. Permissible limit in (mg/L or ppm) of: aluminum (*Al*) = 0.2, chromium (*Cr*) = 0.05, manganese (*Mn*) = 0.15, iron (*Fe*) = 0.3, copper (*Cu*) = 2, zinc (*Zn*) = 5, and arsenic (*As*), cadmium (*Cd*), and mercury (*Hg*) = 0.001 according to NOM-127-SSA1-1994.

Sample	As ppm	Se ppm	Br ppm	Rb ppm	Sr ppm	Mo ppm	Ag ppm	Cd ppm	I ppm	Cs ppm	Ba ppm	U ppm	W ppm	Hg ppm
1P	0.03	0.001	0.207	0.116	0.580	0.005	<0.01	<0.01	0.063	0.001	0.150	0.009	<0.01	<0.01
2P	0.01	0.000	0.124	0.029	0.244	0.000	<0.01	<0.01	0.052	0.011	0.139	0.010	<0.01	<0.01
3P	0.02	0.002	0.213	0.036	0.067	0.001	<0.01	<0.01	0.050	0.025	0.006	0.008	<0.01	<0.01
4N	0.03	0.004	0.206	0.128	0.601	0.001	<0.01	<0.01	0.065	<0.01	0.147	0.012	<0.01	<0.01
5P	0.03	0.002	0.209	0.031	0.071	0.001	<0.01	<0.01	0.050	0.027	0.010	0.007	<0.01	<0.01
6P	0.02	0.002	0.165	0.033	0.090	0.000	<0.01	<0.01	0.046	0.018	0.019	0.005	<0.01	<0.01
7P	0.01	0.001	0.112	0.029	0.122	0.000	<0.01	<0.01	0.025	0.012	0.055	0.000	<0.01	<0.01
8N	0.03	0.007	0.423	0.104	0.404	0.002	<0.01	<0.01	0.070	<0.01	0.089	0.019	<0.01	<0.01
9P	0.01	0.002	0.134	0.051	0.168	0.000	<0.01	<0.01	0.033	0.014	0.106	0.001	<0.01	<0.01
10P	0.02	0.002	0.195	0.027	0.069	0.001	<0.01	<0.01	0.045	0.018	0.005	0.007	<0.01	<0.01
11P	0.02	0.001	0.207	0.116	0.580	0.617	<0.01	0.017	0.063	1.252	84.0	0.010	0.000	0.002
12P	0.13	0.000	0.124	0.029	0.244	<0.01	<0.01	0.021	0.052	5.407	24.7	0.008	0.000	0.001
13P	0.01	0.002	0.213	0.036	0.067	<0.01	<0.01	0.003	0.050	<0.01	95.0	0.012	0.000	0.001
14P	0.03	0.004	0.206	0.128	0.601	0.000	<0.01	0.006	0.065	9.081	57.8	0.007	0.000	0.001
15P	0.03	0.002	0.209	0.031	0.071	0.001	<0.01	<0.01	0.050	10.835	20.2	0.005	0.000	0.001
16P	0.03	0.002	0.165	0.033	0.090	<0.01	<0.01	0.001	0.046	<0.01	69.4	0.000	0.000	0.002
17P	0.03	0.001	0.112	0.029	0.122	0.000	<0.01	0.009	0.025	9.706	11.6	0.019	0.000	0.001
18P	0.09	0.007	0.423	0.104	0.404	<0.01	<0.01	0.005	0.070	<0.01	101.6	0.001	0.000	0.0015
19P	0.02	0.002	0.134	0.051	0.168	<0.01	<0.01	0.003	0.033	<0.01	52.7	0.007	0.000	0.001
20P	0.01	0.002	0.195	0.027	0.069	<0.01	<0.01	0.011	0.045	<0.01	75.2	0.010	0.000	0.002
21P	0.03	0.001	0.207	0.116	0.580	<0.01	<0.01	0.005	0.063	<0.01	49.7	0.008	0.000	0.001
22P	0.03	0.000	0.124	0.029	0.244	<0.01	<0.01	0.002	0.052	<0.01	81.9	0.012	0.000	0.0012
23N	0.02	0.002	0.213	0.036	0.067	<0.01	<0.01	0.004	0.050	<0.01	30.2	0.007	0.000	0.004
24N	0.05	0.004	0.206	0.128	0.601	<0.01	<0.01	0.007	0.065	<0.01	28.0	0.005	0.000	0.001
25N	0.03	0.002	0.209	0.031	0.071	<0.01	<0.01	0.003	0.050	<0.01	27.9	0.000	0.000	0.002
26N	0.01	0.002	0.165	0.033	0.090	0.002	<0.01	0.012	0.046	<0.01	44.6	0.019	0.000	0.001
27N	0.02	0.001	0.112	0.029	0.122	0.004	<0.01	0.003	0.025	<0.01	56.5	0.001	0.000	0.001
28P	0.03	0.007	0.423	0.104	0.404	0.002	<0.01	0.003	0.070	9.252	5.8	0.007	0.000	0.001
29P	0.03	0.002	0.134	0.051	0.168	0.004	<0.01	0.005	0.033	7.538	13.1	0.010	0.000	0.001
Limit *	0.05							0.005			0.7			0.001

* Maximum allowable limit according to NOM-127-SSA1-1994 [33].

4. Discussion

Moran [13] and Lopez [9] studied water quality in this shallow (unconfined) aquifer and detected, in general, significant levels of nitrates, sulfates, chlorides, and, in the urban zone, punctual anomalies of heavy metals (mercury, barium, strontium, cadmium, lead, phosphorus, and silver). These authors report the highest anomalies in heavy metals for the industrial zone and in places where irrigation is done with recycled water from a water storage tank from the industrial zone. The distribution of the wells sampled in these studies coincides, roughly, with the distribution of the ground settlement faults that have been documented in the valley [12], which suggests that if the lower boundary of this aquifer has been fractured, water contaminated with these heavy metals is possibly infiltrating into the deep unconfined type housed in the granular medium that fills the valley. The results of the sampling and analysis of water from 22 wells and 7 waterwheels in this study show anthropogenic contamination. The anthropogenic contaminants (fecal coliforms, total coliforms, and trace elements) have a direct relationship to the drainage systems, and the sites where contents exceeding the permissible limits for human consumption set by NOM-127-SSA1-1994 [33] and NOM-002-ECOL [34] were detected in groundwater may indicate areas where there is advanced deterioration of the drainage pipes and which also have conduits for percolation to depth. In the El Saucito area, one of the settlement structures that has been tracked for nearly 30 years affects a large number of settlements north of the city, some of which have been urbanized by the use of very sensitive drainage materials. Faults in the event of subsidence are a serious source of contamination of shallow suspended aquifers, and, according to these results, cause infiltration of deep aquifers without limits. On the other hand, the Santiago River, with a distance of about 12.7 km [35], is the natural bed of the city and historically represents the natural edge that limited the growth of the urban sprawl; since flooding causes road safety and environmental health problems, the fracturing of the land within this river plays an important role during flooding. During the rainy season, part of the water infiltrates into the San Miguelito mountain range, and other surface water flows down and feeds the Santiago River as it follows its course from east to northeast, connecting with the rest of the territory and the wastewater treatment plant of the Tenorio Tank located in the industrial zone, then joining in a single flow to the northeast, passing by the side of the Agronomy School where well 19P and well 18P are located. These wells are contaminated with fecal coliforms and total coliforms, and the wells located in Soledad also have anthropogenic contamination. It is safe to assume that both factors—land settlement and the rupture of old drainage systems—may be contributing to the contamination of two aquifers in the San Luis Potosí Valley. In this case, the ground settlement structures that fracture the cemented and hardened material that supports the shallow unconfined aquifer are more towards the central–eastern part of the valley, which could facilitate the infiltration of contaminated water towards depth.

Nitrogen and Phosphorus

Nitrate and nitrite ions occur in soils and water as part of the nitrogen cycle in the earth. Nitrate constitutes the major total amount of nitrogen available in surface waters. Nitrogen occurs naturally in soils and is typically bound to organic and mineral matter in the soil. Life depends, among other things, on the proportion of nitrogen (N) and phosphorus (P) that is available in the medium. Normally, there is much more nitrogen than phosphorus [36]. However, at concentrations that exceed the norm of nitrates, they can cause methemoglobin, that is, oxygen deficiency in the blood, causing death. In this study area, only one sample (8N) presented a concentration of 15 mg/L, as shown in Table 3. Biogenic contaminants have a clear relationship with human wastes that are normally channeled through the drainage system and are driven to their dispersion towards the NE part of the VSLP in the cultivated areas in that sector of the valley. In this sense, the dispersion of organic pollutants should be preferentially manifested towards that part; nevertheless, the locations and the values found in the wells of the central part—where most of the population and commercial activity is concentrated—allow us to suppose that there is also percolation of drainage wastes towards

the unconfined aquifer, and that this occurs due to rupture of the drainage pipes. A major problem with this situation lies in the possibility that this biogenic contamination penetrates the deep unconfined type because part of the distribution of drinking water comes from that aquifer. This possibility has been confirmed in this study in at least one of the wells (2P), which contains a high concentration of total coliforms (up to 150 NMP/100), and, according to NOM-127-SSA1-1994 [33], the permissible limit for total coliform organisms in water for human consumption is 2 NMP/100 (most probable number per 100 mL); however, most of the wells sampled have contents of <3 NMP/100. This contamination is already reflected as increasing in 13 more wells (values between 5 and 16 NMP/100; see Table 4) covering a very wide area. The contrast of the area where this type of contamination with a clear anthropomorphic relationship is detected with the system of ground settlement faults in the VSLP suggests that both phenomena have a connection, given that this differential subsidence is linked to rupture of the "tepetate" layer that supports the shallow unconfined type aquifer that is known to be contaminated [9,13]. The percolation conduits to the deep aquifer are constituted by these faults. The well with a high value of these contaminants is located in an area where the greatest development of ground settlement has been detected: the most representative evolution of which is the Aeropuerto fault, which has been monitored for more than 20 years. Table 4 presents the results of total coliforms in the wells and waterwheels studied in the VSLP. However, 13 more samples (44%) have concentrations between 5 and 16; 8 of these (wells 15P, 16P, 17P, 18P, 19P, 20P, and 22P) have concentrations between 11 and 17 NMP/100. The other 15 samples have <3 NMP/100. The bacteriological results of the studied samples reflect the low quality of water for supplying the population in the valley. As for the wells, well 24N has a concentration of 11 NMP/100, and well 27N has a concentration of 5NMP/100; both are located in Soledad. PExceeding the allowable limit of fecal coliforms with no detectable NMP/100 mL, for example, in well 3P with a concentration of 8 NMP/100,are exceeded, for example, in well 3P with a concentration of 8 NMP/100, well 12P with a concentration of 13 NMP/100, wells 15P and 16P with concentrations of 11 NMP/100 and 16 NMP/100, respectively, well 17P with a concentration of 14 NMP/100, well 18P with a concentration 10 NMP/100, well 19P with a concentration of 17 NMP/100, well 20P with a concentration 16 NMP/100, well 22P with a concentration of 7 NMP/100, and well 28P with a concentration of 11 NMP/100. (Table 4). The other 15 samples have <3 NMP/100. The bacteriological results reflect the low quality of water for supplying the population in the valley. The noria 24N has a concentration of 11 NMP/100, and the noria 27N has a concentration of 5NMP/100. Concerning fats and oils, their detected content varies in value from 2.65 to 7.7, and the concentration increases in the wells towards the center of the valley following the direction of the subway flow. Of the eight wells where fats and oils were detected in the water, all have low concentrations (between 2.65 and 7.70 mg/L) with regard to the NOM-002-SEMARNAT-1996 [34] standard, which establishes 26 mg/L as the permissible limit. Only four of the water samples have concentrations above 6.2 mg/L, but all of them show contamination in the process; because fats and oils are a product of anthropogenic activity, the fact that they are present in the wells reveals that they have percolated into the deep aquifer. This is supported by two important factors: (1) The central zone of the VSLP has the highest concentration of ground settlement faults. This is logical since in the center of the city of San Luis Potosí there are restaurants, hotels, public bathrooms, the train station, etc. (2) The concentration increases towards the wells in the center following the direction of the subway flow. Another factor to consider is the presence of trace elements (with some heavy metals) in the wells of the deep unconfined type. The values detected are presented in Tables 5 and 6. Manganese (*Mn*) is considered a mineral associated with igneous and metamorphic rocks containing divalent *Mn* as a minor constituent; in particular, it is significant in basalt due to its dominant mineralogy of olivines, pyroxene, and amphibole. Small amounts are present in dolomites and limestones in place of calcium [37]. The previous source is mainly responsible for the contribution of *Mn* in the study area. This element is normally found in organisms as an activator of certain enzymes. When ingested in large doses, it is a poison that mainly affects the central nervous system; in appreciable quantities,

it produces an unpleasant taste in the water, which makes its presence noticeable when drinking and its toxic action more easily avoided [37]. The permissible limit for human consumption according to NOM-127 is 0.15 mg/L; one sample exceeds this permissible limit: well 18P with a concentration of 0.84 mg/L (Figure 6a). Arsenic is important in water chemistry, especially since the modern use of pesticides has become widespread and these products contain this element. *As* is found free in nature as a steel-gray, brittle solid [38]. High concentrations of arsenic are commonly associated with sediments that are partially derived from volcanic rocks of acidic or intermediate composition [29]. The presence of this element is most likely due to the occasional input of arsenic-containing fertilizers; however, it may also be due to the dissolution of arsenic-bearing volcanic rocks within the study area. Long-term exposure to *As* via drinking water at concentrations of 0.05 mg/L and even lower causes skin, lung, bladder, and kidney cancer and skin alterations such as pigmentation changes and thinning of the skin. Immediate symptoms of acute poisoning include vomiting, abdominal pain, and hemorrhagic diarrhea [39]. The permissible limit established for arsenic (As) by NOM-127-SSA1-1994 [33] is 0.05 mg/L. The out-of-range samples are: the 24N Soledad waterwheel with a concentration of 0.05 mg/L and wells 12P with a concentration of 0.126 mg/L and 18P with a concentration of 0.09 mg/L (Figure 6a). Cadmium is considered, biologically, neither beneficial nor essential for man, but it is a toxicant that acts on the kidneys and liver and produces nausea and vomiting. Cadmium poisoning produces arterial hypertension, and it is a proven carcinogen [38]. As for its presence in groundwater, its probable source is of external origin, and it is not so much associated with the dissolution of minerals containing cadmium in their composition. Water contaminated by cadmium generates corrosion of the pipes used because cadmium is a contaminant of galvanized iron and zinc [38]. The permissible limit for cadmium (*Cd*) in human consumption is 0.005 mg/L according to NOM-127-SSA1-1994 [33]; the samples that exceed the limit are the waterwheels 24N with a concentration of 0.0067 mg/L and 26N with a concentration of 0.0119 mg/L and wells 11P with a concentration of 0.0169 mg/L, 12P with a concentration of 0.0206 mg/L, 14P with a concentration of 0.005 mg/L, 17P El Ranchito with a concentration of 0.0085 mg/L, 20P with a concentration of 0.01068 mg/L, and 29P with a concentration of 0.00524 mg/L (Figure 6b). These values indicate that for the shallow aquifer—the zone where the 24N well are located—contamination by this metal is only slightly higher than the standard (0.0067 mg/L), while for 26N it is double this value (0.0119 mg/L). Wells 14P and 29P show incipient values, or rather, values at the limit of the standard (0.005 and 0.00524 mg/L, respectively). Wells 11P, 12P, and 20P show values two to four times the norm (0.01068, 0.01690, and 0.02060 mg/L, respectively), which is highly worrisome. Mercury is one of the most widely distributed metals in the environment and is known for its high toxicity (mainly methylmercury); it is harmful to the environment and can bioaccumulate. It can come from both natural and anthropogenic sources. It is released naturally by mobilization generated in the earth's crust, by volcanic activity, and by rock erosion. Anthropogenic sources are associated with the use of fossil fuels and the mining industry. An important source is currently represented by the remobilization and release of waste deposited in soils, sediments, water bodies, and garbage dumps; the incineration of municipal, medical and hazardous waste; and cremations and releases to the ground in cemeteries [40]. The maximum allowable limit for mercury (*Hg*) is 0.001 mg/L. The samples that exceed this limit are waterwheels 23N with a concentration of 0.004 mg/L and 25N with a concentration of 0.002 mg/L and wells 11P with a contraction of 0.002 mg/L, 18P with a concentration of 0.0015 mg/L, 20P with a concentration of 0.002 mg/L, and 22P with a concentration of 0.0012 mg/L (Figure 6c). From the distribution of the wells and waterwheels and the values recorded for these trace elements in the sampled waters reported here, it is inferred that they come from the leaching of sediments derived from the historical metallurgical processes of mining in Cerro de San Pedro due to the distribution of elements (*Mn*, *As*, *Cd*, and *Hg*) that were detected in this area. In the "Atlas de riesgo" for the municipalities of San Luis Potosí and Soledad de Graciano Sanchez (the northeastern part of the valley), a series of ground settlement fault segments are recorded, which may

represent infiltration conduits for water into the deep aquifer. Given that the maximum concentration detected (0.004 mg/L) is from well 23N, and that well 20P located in the same area of the valley has a concentration of 0.002 mg/L (double that allowed by the standard), it can be argued that there is infiltration of this element from the shallow aquifer to the deep aquifer. However, for well 11P located in the NW of the VSLP, which is outside the influence of the zone of influence mentioned here, the possible contamination factor is the Peñazco municipal dump located in that sector given that land settlements also occur in that area, which is why it is known as the "Tierra Rajada" site (to NW of the valley). The most common damages occur in: the nervous system, affecting brain functions, which can cause degradation of the ability to learn, personality changes, tremors, vision changes, deafness, muscle incoordination, and memory loss; DNA and chromosomes; allergic reactions, skin irritation; tiredness; and headache; and negative effects on reproduction, with changes in sperm, birth defects, and miscarriage [40]. The detected values of the aforementioned trace elements represent contamination levels because they exceed the permissible limits of the NOM-127-SSA1-1994 [33] standard; these trace elements represent a danger to groundwater, nitrates, fecal coliforms, and total coliforms at concentrations lower than those reported [9,13]. In the superficial aquifer, there is evidence of infiltration of water from the unconfined aquifer into the deep free aquifer. These results corroborate that part of the nitrate, fecal coliform, and total and trace coliform that contaminated waters in the shallow unconfined aquifer as reported in previous studies [9,13] are infiltrating into the shallow unconfined type through the lattice of ground settlement faults in the valley. Extensive study of the waters of the deep aquifer wells allowed us to verify that the waters of the intermediate unconfined type are showing signs of anthropogenic, biogenic, and heavy metal contamination. This is of great importance, especially if the water from these wells is used for human consumption. The trace elements in the sampled waters reported here are inferred to come from the leaching of sediments derived from the historical metallurgical processes of mining in Cerro de San Pedro due to the distribution of elements (Mn, As, Cd, and Hg) detected in this area. It is assumed that there may be natural recharge of the deep aquifer in the northeastern margin of the valley, but the record of recent settlements that have been documented allows us to suppose that this process may also be recent or that its dilutional effect may be added if the first possibility has been active. That will require other studies not carried out here, which we can assume soon.

5. Conclusions

The current study reveals evidence of contamination resulting from anthropogenic activities in the deep unconfined type of the San Luis Potosí valley.

- The deep aquifer has been infiltrated by organic contaminants, E. coli, and total coliforms that are commonly found in the shallow aquifer. This contamination is especially prevalent in well 2P, which is situated in the area with the longest history of land settlement in the valley.
- Fats and oils, which are directly derived from anthropogenic activities and widely present in the shallow aquifer, have also been detected in the wells, suggesting that their infiltration into the deep aquifer is already underway.
- The nitrate levels in drinking water are due to contamination from animal waste or water spills from dairies or livestock, excessive use of fertilizers, and/or infiltration of human sewage from septic tanks.
- The presence of incipient and localized manganese (Mn) contamination in groundwater is caused by rainwater drainage in the limestone and dolomite that outcrop extensively in the Sierra de Alvarez, which borders the valley on its eastern side.
- Arsenic (As) in groundwater may be contributed by arsenic residues in the "Jales" derived from mining activity or occasional contributions of fertilizers containing arsenic.
- Three of the samples taken from the wells (11P, 12P, and 20P) showed cadmium levels two to four times higher than the allowable limit of the standard, which poses a high risk to human health.

- Mercury (*Hg*) concentrations in the wells suggests that contamination by this element comes from the leaching of sediments derived from historical metallurgical processes of mining in Cerro de San Pedro due to the distribution of elements *Mn*, *As*, *Cd*, and *Hg* (Figure 7).

The study suggests that there could be infiltration of contaminated water from the shallow aquifer into the deep aquifer through numerous subsurface faults in the central part of the valley. Initially considered unclear or insignificant, this issue is now proposed as a top priority due to its potential implications for both the population's drinking water supply and public health in the short and long term. A more comprehensive investigation of the latter aquifer is deemed necessary to provide more thorough documentation of the reported findings.

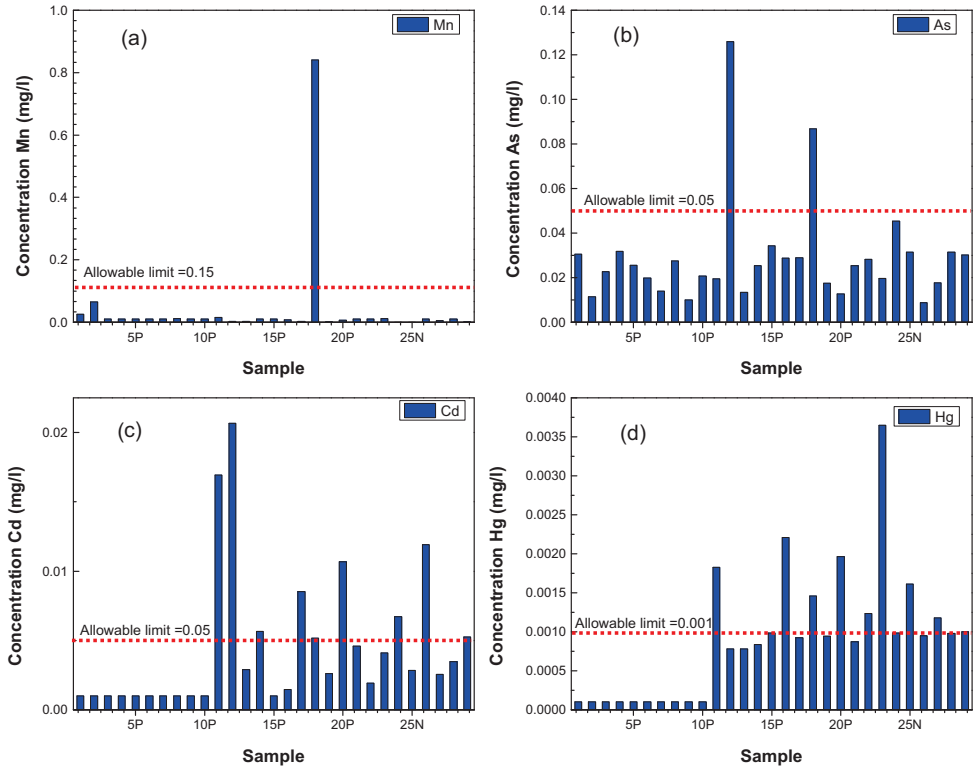

Figure 7. Concentrations of elements that exceed the allowable limits set by NOM-127-SSA1: (**a**) manganese (*Mn*) concentration, (**b**) arsenic (*As*) concentration, (**c**) cadmium (*Cd*) concentration, and (**d**) mercury (*Hg*) concentration. (Arc map program was used to create the image).

Author Contributions: Conceptualization, S.T.-R., J.R.T.-H. and R.A.L.-D.; methodology, S.T.-R. and J.R.T.-H.; software, S.E.C.-L. and J.A.M.-R.; validation, S.T.-R. and J.R.T.-H.; formal analysis, S.T.-R., J.R.T.-H. and M.E.G.-A.; investigation, S.T.-R., J.R.T.-H. and M.E.G.-A.; resources, S.T.-R., J.R.T.-H. and M.E.G.-A.; data curation, S.T.-R., M.E.G.-A. and J.R.T.-H.; writing—original draft preparation, S.T.-R., R.A.L.-D. and J.A.M.-R.; writing—review and editing, S.E.C.-L., R.A.L.-D. and J.A.M.-R.; visualization, S.E.C.-L.; supervision, R.A.L.-D.; project administration, S.T.-R. and J.R.T.-H.; funding acquisition, S.T.-R. and J.R.T.-H. All authors have read and agreed to the published version of the manuscript.

Funding: Consejo Nacional de Humanidades Ciencias y Tecnologias. CVU: 386957 and 210817.

Institutional Review Board Statement: Not applicable.

Informed Consent Statement: Not applicable.

Data Availability Statement: The data generated in this study are presented in the tables and maps in this manuscript.

Acknowledgments: We would like to thank CONAHCYT for the postdoctoral fellowship for this project; the Engineering Groundwater Laboratory where the major elements were analyzed; and chemistry graduate Miguel Ángel Cortina Rangel, who was in charge of the physical Geochemistry laboratory, for his support in the analysis of trace elements. Both laboratories belong to the Faculty of Engineering of the UASLP. The CONACYT scholarship was received as support during the preparation of this manuscript (CVU: 386957 and 210817).

Conflicts of Interest: The authors declare no conflict of interest.

Abbreviations

The following abbreviations are used in this manuscript:

CONAGUA	Comisiona Nacional del Agua
CRM	Consejo de Recursos Minerales
INEGI	Instituto Nacional de Estadistica, Geografía e Informatica
IPICYT	Instituto Potosino de Investigacion Cientifica y Tecnologica
SEMARNAT	Secretaría de Medio Ambiente y Recursos Naturales
SIGMAS	System for Groundwater Management
UASLP	Universidad Autonoma de San Luis Potosí
UNESCO	United Nations Educational, Scientific and Cultural Organization
UTM	Universal Transverse Mercator
VSLP	Valley of San Luis Potosí

References

1. Schmoll, O.; Howard, G.; Chilton, J.; Chorus, I. *Protecting Groundwater for Health: Managing the Quality of Drinking-Water Sources*; World Health Organization: Geneva, Switzerland, 2006.
2. Yuan, L.; Fei, W.; Jia, F.; Junping, L.; Qi, L.; Fangru, N.; Shulian, X. Increased health threats from land use change caused by anthropogenic activity in an endemic fluorosis and arsenicosis area. *Environ. Pollut.* **2020**, *261*, 114130. [CrossRef] [PubMed]
3. Mushak, E.W.; Piver, W.T. Agricultural chemical utilization and human health. *Environ. Health Perspect.* **1992**, *97*, 269–274. [CrossRef] [PubMed]
4. Wang, H.; Liu, S.; Du, S. The investigation and assessment on groundwater organic pollution. *Org. Pollut. Monit. Risk Treat* **2013**, 87–95. [CrossRef]
5. Rodríguez, G.A. Environmental Conflicts threaten the health of the population and the world's biodiversity. *Rev. Derecho* **2007**, 329–347.
6. Shortle, J.S.; Dunn, J.W. The relative efficiency of agricultural source water pollution control policies. *Am. J. Agric. Econ.* **1986**, *68*, 668–677. [CrossRef]
7. Pacheco, J.; Marín, L.; Cabrera, A.; Steinich, B.; Escolero, O. Nitrate temporal and spatial patterns in 12 water-supply wells, Yucatan, Mexico. *Environ. Geol.* **2001**, *40*, 708–715. [CrossRef]
8. Estrada-Perez, F. El agua de San Luis Potosí, Contaminación y Saneamiento. Bachelor's Thesis, Facultad de Agronomía y Veterinaria, Universidad Autónoma de San Luis Potosí, San Luis Potosí, Mexico, 2013.
9. López-Álvarez, B.; Ramos-Leal, J.A.; Moran-Ramírez, J.; Cardona Benavides, A.; Hernández Garcia, G. Origin of water quality of the unconfined aquifer and its relation with changes in land use in the San Luis Potosí valley. *Bol. Soc. Geol. Mex.* **2013**, *65*, 9–26.
10. Aguirre Hernandez, M.A.; Martínez Ruiz, V.J. Comportamiento del nivel estático del acuífero profundo de la cuenca de San Luis Potosí. *Univ. Autónoma San Luis Potosí Inst. Geol. Metal.* **1984**, *96*, 16.
11. Aguirre Hernández, M.A. Geología del subsuelo de las cuencas geohidrológicas del valle de San Luis Potosí y de villa de reyes, en el Edo. de San Luis Potosí. *Univ. Autónoma San Luis Potosí Inst. Geol. Metal.* **1992**, *116*, 46.
12. Potosí, H.A.D.S.L. Actualización del Atlas de Riesgo para el Municipio de San Luis Potosí y. Su Zona Conurbada. Instituto de Geologia, Universidad Autonoma de San Luis Potosi, San Luis Potosi. Mexico. Available online: https://sanluisimplan.gob.mx/atlas-de-riesgo-para-el-municipio-de-san-luis-potosi/ (accessed on 31 March 2018)
13. Moran, R.J. Evaluación de la calidad química del agua en el acuífero somero de San Luis Potosí: San Luis Potosí, S.L.P. Bachelor's Thesis, Área de Ciencias Químico Biológicas, Universidad del Noreste, Tampico, Mexico, 2010.
14. Espinosa Gutiérrez, G.; Mareike Evers, P.; Otterpohl, R.; Paredes Limas, J.C.; Zambrano Cárdenas, R.M.; González Torres, L. Evaluación de las infiltraciones al sistema de drenaje mediante análisis comparativo de la concentración de contaminantes en agua residual: Caso de estudio en Tepic, México. *Rev. Int. Contam. Ambient* **2015**, *31*, 89–98.
15. Liang, B.; Han, G.; Liu, M.; Yang, K.; Li, X.; Liu, J. Distribution, sources, and water quality assessment of dissolved heavy metals in the Jiulongjiang River water, Southeast China. *Int. J. Environ. Res. Public Health* **2018**, *15*, 2752. [CrossRef] [PubMed]
16. Forrest, B.J. Collecting Water-Quality Samples for Dissolved Metals-in-Water. In *Water Quality Handbook*, 2nd ed.; U.S. Environmental Protection Agency: Washington, DC, USA, 2000.
17. INEGI. Estadísticas censales a escalas geoelectorales, II Conteo de Población y Vivienda 2005. *Inst. Nac. Estad. Geogr. Inform.* **2009**.

18. Monografıa geologica-minera del Estado de Sonora. In *Secretarıa de Energıa Minas e Industria Paraestatal*; Consejo de Recursos Minerales: Hidalgo, Mexico, 1992.
19. CONAGUA. Determinación de la disponibilidad de agua en el acuífero Cerritos-Villa Juárez (2414). In *Estado de San Luis Potosí México D.F. Comisión Nacional del Agua Subdirección General Técnica Manejo de Aguas Subterráneas Subgerencia de Evaluación y Manejo de Acuíferos*; Comisión Nacional del Agua: Mexico City, Mexico, 2020.
20. Zaporozec, A. Groundwater contamination inventory: A methodological guide with a model legend for groundwater contamination inventory and risk maps. In *IHP-VI, Series on Groundwater, 2*; UNESCO: Paris, France, 2004; Volume 2.
21. Carrillo-Rivera, J.J.; Armienta, M.A. Diferenciación de la contaminación inorgánica en las aguas subterráneas del valle de la ciudad de San Luis Potosí, S.L.P. Mexico. *Geofis. Int.* **1989**, *28*, 763–783.
22. Carrillo, R.J.J.; Cardona, B.A.; Huizar, A.R.; Graniel, C.E. Response of the interaction between groundwater and other components of the environment in Mexico. *Environ. Geol.* **2008**, *55*, 303–319. [CrossRef]
23. IPICYT. Instituto Potosino de Investigación Científica y Tecnológica. Estudio hidrogeológico de la porción oriental del Valle de San Luis Potosí. In *Reporte Técnico Elaborado Para el Gobierno del Estado de San Luis Potosí*; IPICYT: San Luis, Mexico, 2007.
24. Ramos-Leal, J.A.; Lopez-Loera, H.; Martínez Ruiz, V.J.; Aranda-Gómez, J.J. Event succession and geometry of the central part of the Villa de Reyes aquifer (San Luis Potosí, Mexico) inferred from geoelectric data. *Rev. Mex. Cienc. Geol.* **2007**, *24*, 31–46.
25. Cardona-Benavides, A. Hidrogeoquímica de Sistemas de Flujo, Regional, Intermedio y Local Resultado del Marco Geológico en la Mesa Central: Reacciones, Procesos y Contaminacion. Ph.D. Thesis, Instituto de Geofísica, Universidad Nacional Autónoma de México, Mexico City, Mexico, 2007.
26. Labarthe-Hernández, G.; Tristán-González, M.; Aranda-Gómez, J.J. Revisión estratigráfica del cenozoico de la parte central del edo. de San Luis Potosí. *Univ. Autónoma San Luis Potosí. Inst. Geol.* **1982**, *85*, 208.
27. López-Loera, H.; Tristán-González, M. Geology and magnetometry of the Villa de Reyes graben, San Luis Potosí, Mesa Central, Mexico: Tectonic implications. *Bol. Soc. Geol. Mex.* **2013**, *65*, 137–156. [CrossRef]
28. Fitts, C.R. *Groundwater Science*; Elsevier: Amsterdam, The Netherlands, 2002.
29. Appelo, C.A.J.; Postma, D. *Geochemistry, Groundwater and Pollution*; CRC Press: Boca Raton, FL, USA, 2004.
30. Freeze, R.A.; Cherry, J.A. *Groundwater*; Prentice-Hall Inc.: Eaglewood Cliffs, NJ, USA, 1979.
31. Piper, A.M. A graphic procedure in the geochemical interpretation of water-analyses. *Eos Trans. Am. Geophys. Union* **2001**, *25*, 914–928. [CrossRef]
32. Mifflin, M.D. Region 5, Great Basin. In *Hydrogeology*; Geological Society of America: Boulder, CO, USA, 1988.
33. NOM-127-SSA1-1994. NORMA Oficial Mexicana. SEMARNAT. Salud Ambiental, Agua Para Uso Y Consumo Humano-Limites Permisibles De Calidad Y Tratamientos A Que Debe Someterse El Agua Para Su potabilización. Diario Oficial de la Federación el 18 de Febrero de 1996. México. Available online: http://www.salud.gob.mx/unidades/cdi/nom/127ssa14.html (accessed on 20 April 2023).
34. NORMA Oficial Mexicana NOM-002-ECOL-1996. SEMARNAT. Que Establece los Límites Máximos Permisibles de Contaminantes en las Descargas de Aguas Residuales a los Sistemas de Alcantarillado Urbano o Municipal. Available online: https://www.profepa.gob.mx/innovaportal/file/3295/1/nom-002-semarnat-1996.pdf (accessed on 20 April 2023).
35. SGG. Secretaria General de Gobierno. Plan de San Luis. Periódico Oficial del Gobierno del estado. Decreto 191.- Plan Estatal de Desarrollo 2015–2021. Mexico. 2016. Available online: https://slp.gob.mx/secult/pdf/Plan-Estatal-de-Desarrollo-2015-2021-(23-MAR-2016).pdf (accessed on 20 April 2023).
36. Yang, Y.; Gao, B.; Hao, H.; Zhou, H.; Lu, J. Nitrogen and phosphorus in sediments in China: A national-scale assessment and review. *Sci. Total Environ.* **2017**, *576*, 840–849. [CrossRef] [PubMed]
37. Hem, J.D. Study and interpretation of the chemical characteristics of natural water. In *USGS Numbered Series*; US Geological Survey: Reston, VA, USA, 1959; Number 1473.
38. Catalan Lafuente, J.G. *Química del Agua*, 2nd ed.; Bellisco: Madrid, Spain, 1981; p. 423.
39. Calvo, C.; Alvarez-Benedí, J.; Andrade, M.; Marinero, P.; Bolado, S. arsenic contamination in groundwater in the Province of Valladolid: Seasonal Variations. *Stud. Vadose Zone* **2003**, *6*, 91–98.
40. Zambrano Cárdenas, R. González Torres, L.; Arangure Zuñiga, F.J.; Ortega Aguirre, J.; Paredes Lima, J.C.; Espinosa Rodríguez, M.A. El mercurio y sus consecuencias en la salud. In *Revista Fuente Nueva Epoca*; 2014. Available online: http://dspace.uan.mx:8080/jspui/handle/123456789/287 (accessed on 5 May 2023).

Disclaimer/Publisher's Note: The statements, opinions and data contained in all publications are solely those of the individual author(s) and contributor(s) and not of MDPI and/or the editor(s). MDPI and/or the editor(s) disclaim responsibility for any injury to people or property resulting from any ideas, methods, instructions or products referred to in the content.

water

MDPI

Article

Evaluation of Groundwater Quality for Drinking and Irrigation Purposes Using GIS-Based IWQI, EWQI and HHR Model

Ying Wang [1], Rui Li [1,2], Xiangchuan Wu [1,2], Yuting Yan [2], Changli Wei [3], Ming Luo [3], Yong Xiao [2] and Yunhui Zhang [1,2,*]

[1] Yibin Research Institute, Southwest Jiaotong University, Yibin 644000, China
[2] Faculty of Geosciences and Environmental Engineering, Southwest Jiaotong University, Chengdu 611756, China
[3] Sichuan Institute of Geological Survey, Chengdu 610081, China
* Correspondence: zhangyunhui@swjtu.edu.cn

Abstract: Groundwater pollution has emerged as a significant water crisis in various regions around the globe. Groundwater serves as a crucial source of water for human consumption and agricultural activities in the Sichuan Basin where groundwater quality has yet to be concentrated. A total of 41 groundwater samples were collected from domestic wells in Suining city of the Sichuan Basin, which were used for analyzing the hydrogeochemical processes and suitability for irrigation and drinking purposes. In the study area, groundwater samples belonged to the HCO_3-Ca type. Hydrochemical compositions were dominated by carbonate and silicate mineral dissolution with positive cation exchange. Agricultural activities and urban sewage were the primary sources of NO_3^- pollution. The irrigation water quality index (IWQI) was calculated using electronic conductivity (EC), Na^+, Cl^-, HCO_3^-, and sodium adsorption ratio (SAR). The IWQI values showed that the suitability of groundwater irrigation was generally good and presented the decreasing trend southeastwardly. According to the entropy-weighted water quality index (EWQI), the groundwater quality for drinking purposes was generally good. However, there were some local areas with poor water quality concentrated in the southeast part. According to the human health risk (HHR) model, the groundwater was deemed safe for adults and children. However, for infants, the nitrate level in the groundwater remained high and posed potential health risks. The combined IWQI and EWQI evaluation served as a valuable reference for the utilization of the groundwater resource in the Sichuan Basin, as well as other comparable regions worldwide.

Keywords: hydrochemistry; GIS; groundwater quality; health risk assessment; Sichuan Basin

1. Introduction

Groundwater is a valuable natural resource that is crucial to numerous human activities [1]. Groundwater has become the primary water source for industry and agriculture in the world, due to its extensive coverage area, large storage capacity, excellent water quality, stable flow, and strong resistance to external pollution factors [2–7]. The world's population has been growing exponentially in recent years, posing a significant threat to the quality of groundwater worldwide [8–11]. The occurrence of many serious water pollution incidents around the world has caused major environmental and health problems [12,13]. In situations where groundwater pollution is extensive, the agricultural industry's continued use of low-quality groundwater for irrigation can result in soil pollution. This can cause deterioration to the soil's physical and chemical properties, ultimately leading to a reduction in its fertility [14]. Contaminated groundwater used for domestic and drinking purposes will generate both carcinogenic and non-carcinogenic health risks to humans [15]. Thus far, nitrate, arsenic, and fluoride have been the primary pollutants responsible for groundwater contamination [16].

The suitability of groundwater for irrigation is determined by the mineral elements present in the water and their impact on the soil and crops [17,18]. The quality of groundwater for irrigation is evaluated based on the concentration of anions and cations. Common indicators for evaluating groundwater irrigation quality include the sodium adsorption ratio (SAR), sodium percentage (Na%), permeability index (PI), and residual sodium carbonate (RSC) [19–23]. The irrigation water quality index (IWQI) is a crucial and unique model for evaluating the suitability of groundwater for agricultural irrigation [24]. However, since each groundwater index has different dimensions and magnitudes, principal component analysis (PCA) is often used to simplify IWQI calculations by reducing dimensionality [25]. The entropy-weighted water quality index (EWQI) is a crucial tool for assessing the suitability of groundwater for drinking purposes. It assigns varying weights to different water chemistry parameters based on their characteristics, reducing the impact of subjective weight assignments on calculation results. This improves the accuracy of the evaluation and makes it more objective [26,27]. Nitrate pollution in drinking water has severe implications on human health. Long-term consumption of groundwater with excessive nitrate content can result in methemoglobinemia, digestive cancer, and blue baby syndrome [28]. To validate the sustainable utilization of groundwater resource, it is necessary to assess the groundwater quality for irrigation and drinking purposes.

The Sichuan Basin, located in southwestern China, possesses abundant groundwater resources. The Sichuan Provincial Government has prioritized the management and utilization of these resources. In recent years, numerous scholars have conducted groundwater surveys and evaluations of groundwater quality in the Sichuan Basin and its surrounding areas [24,29,30]. Despite the importance of groundwater resources for agricultural irrigation, studies analyzing and investigating these resources within the Sichuan Basin are scarce. Additionally, the long-time high-dosage nitrogen fertilizer uses and heavy reliance on agricultural fertilizers in the region has led to high levels of nitrate contamination in many areas [31–34]. This study aims to analyze the hydrochemical characteristics of groundwater and identify the factors dominating hydrochemistry in the Sichuan Basin. Additionally, the study will assess the suitability of groundwater for agricultural irrigation by utilizing the basic irrigation index and IWQI and evaluate the quality of groundwater for drinking purposes and health risk analysis (Figure 1). The findings of this evaluation can serve as a guide for similar areas, while also helping to prevent and manage groundwater resource pollution in the Sichuan Basin.

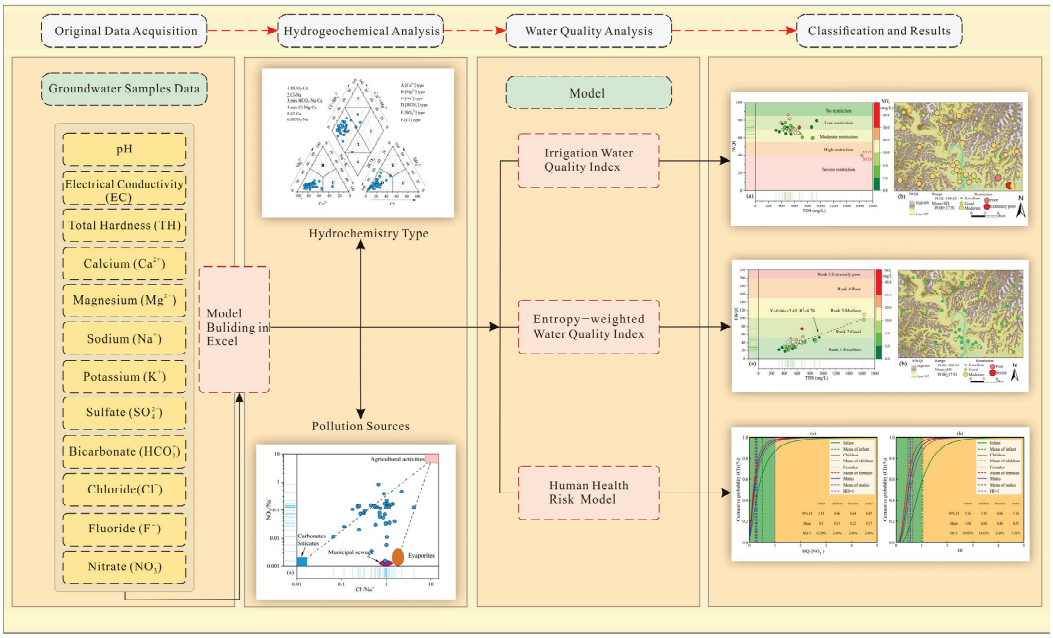

Figure 1. The flowchart of the workflows in this study.

2. Materials and Methods

2.1. Study Area

The study area belongs to Suining city and is located in the central region of the Sichuan Basin, within the longitude of 105°10′–105°39′ E and the latitude of 30°40′–31°10′ N (Figure 2a,b). It is located in the transitional zone between the low mountains in the north and the hilly terrain in the south of Sichuan and is characterized by a typical low mountain and hilly terrain. The study area has higher elevations in the north and lower elevations in the south, with elevations of 291 to 652 m. The mountainous and hilly area within the county covers over 85% of the total land area, making it a major agricultural area [35]. The study area has a subtropical monsoon climate with an annual average temperature of 17.2 °C. The maximum temperature is 37.2 °C and the minimum temperature is −2.4 °C. The annual average precipitation is 887.3 mm, with a minimum of 660.7 mm and a maximum of 1389.2 mm. Abundant rainfall has resulted in the development of well-connected rivers and streams due to the low mountain and hilly terrain. This has led to a high overall river network density. The study area is primarily composed of sandstones and mudstones from the Jurassic and Cretaceous periods, with some areas of Quaternary sediments [36]. These sandstones and mudstones are mostly interbedded and include calcareous and feldspathic sandstones. Precipitation infiltration is the primary mode of groundwater recharge in the area, which is facilitated by the abundant precipitation.

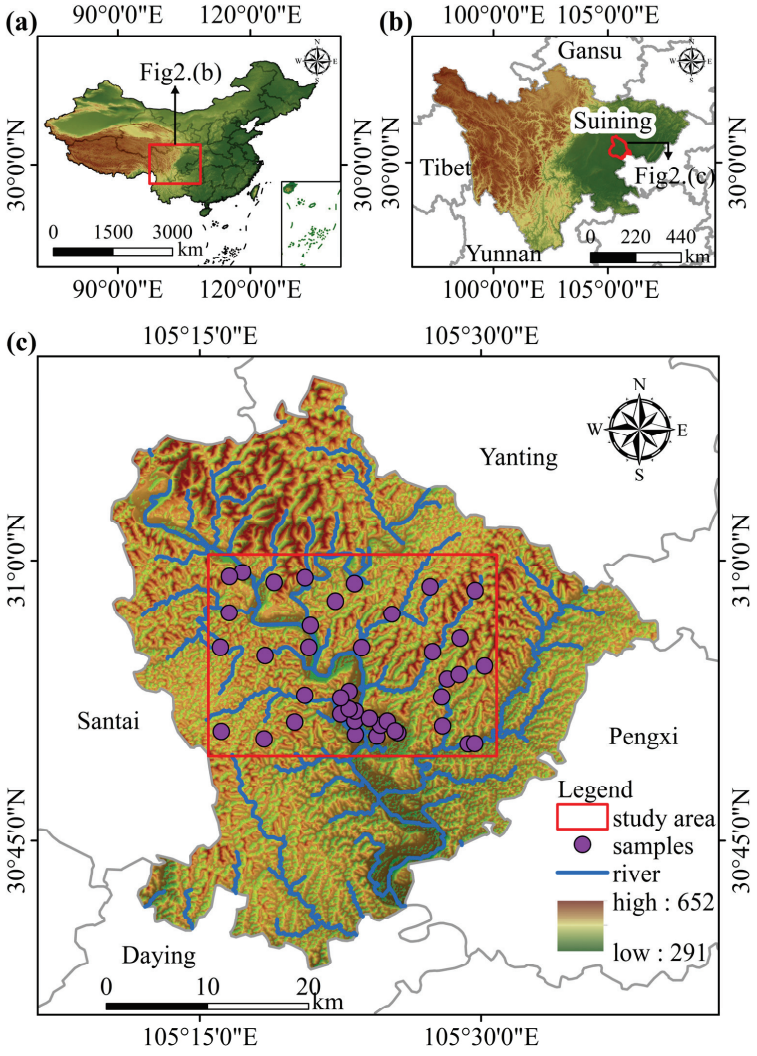

Figure 2. Overview of the study area. (**a**,**b**) indicate the relative location of the study area, while (**c**) provides an overview of the area and displays the distribution of the 41 sampling sites.

The study area has a variety of soil types, such as purple soil, alluvial soil, yellow soil, and paddy soil. Among these, purple soil covers the largest portion of the mountainous hilly area, accounting for approximately 86.3% of the total land area [37]. This type of soil is mainly composed of purple clay and purple sandy soils with gravels, sands, and clays. However, it has poor water-holding capacity and weathering resistance. Although purple soils exhibit higher pH values and have a greater fertility status, their fertility primarily results from the extensive use of chemical fertilizers in the past. Nitrogen, potassium, and phosphorus fertilizers have been utilized to stabilize the soil's nutrient content, while organic fertilizers and boron and zinc fertilizers can enhance soil fertility. Unfortunately, the excessive use of agricultural fertilizers and the illegal disposal of sludge in the name of "soil improvement" in the study area have seriously polluted the surrounding environment and led to serious groundwater contamination [34,38]. In addition to agriculture, the study area has experienced significant industrial growth in recent years. The factories are primarily located in the southern part of the study area, where the population is concentrated, as well as in the new industrial area in the southeast.

2.2. Methodology

2.2.1. Sampling and Analysis Methods

The study collected 41 groundwater samples from domestic tube wells and public water supply wells located in the central Sichuan Basin. The sampling points were illustrated in Figure 2c. The sampling depths were varied from 50 m to 100 m. To mitigate the potential impact of stagnant water in the pipeline during sampling, this study employed a technique of pumping more than three times the volume of the wells in each borehole. Prior to collecting the samples, the sampling bottles were thoroughly rinsed with the target water samples at least 3–5 times. The study measured geophysical–chemical parameters, such as pH, TDS, TH, and the concentration of major anions and cations. Sampling involved measuring physical and chemical properties in situ using a portable multimeter device (WTW multi 3400i), including pH, TDS, TH, and temperature. Groundwater samples were collected and sent to the Sichuan Geological Survey Institute for hydrochemical analysis. Anion content was determined using ion chromatography, while cation content was measured using atomic absorption spectrophotometry. To confirm the reliability of the chemical analysis of each sample, groundwater ion balance tests were performed using Equation (1) after excluding other ions below the test line. The calculated results were accurate as the water sample error was within the acceptable range of ±5% [39].

$$\mathrm{CBE} = \frac{\sum\left(\mathrm{Mg^{2+}} + \mathrm{Ca^{2+}} + \mathrm{Na^{+}} + \mathrm{K^{+}}\right) - \sum\left(\mathrm{HCO_3^{-}} + \mathrm{SO_4^{2-}} + \mathrm{NO_3^{-}} + \mathrm{Cl^{-}} + \mathrm{F^{-}}\right)}{\sum\left(\mathrm{Mg^{2+}} + \mathrm{Ca^{2+}} + \mathrm{Na^{+}} + \mathrm{K^{+}}\right) + \sum\left(\mathrm{HCO_3^{-}} + \mathrm{SO_4^{2-}} + \mathrm{NO_3^{-}} + \mathrm{Cl^{-}} + \mathrm{F^{-}}\right)} \quad (1)$$

2.2.2. Principal Component Analysis (PCA)

Principal component analysis (PCA) is a multivariate statistical method that effectively identifies the factors controlling the hydrogeochemical compositions [40–42]. PCA on hydrogeochemical parameters can simplify intricate analytical metrics, reducing the dimensionality of the analysis and allowing for the preliminary identification of contaminant sources in groundwater [43,44]. To ensure comparability between the different indicators, z-score normalization was performed prior to conducting PCA. To determine the suitability of the dataset for PCA, KMO (Kaiser–Meyer–Olkin), and Bartlett tests were conducted. KMO measures the bias correlation between variables and indicators, and a value greater than 0.5 indicates that the data are suitable for factor analysis processing. Bartlett's sphericity test measures the degree of correlation between each indicator variable, and a significance level ρ less than 0.05 indicates relevance between each variable indicator [45]. Only principal components with eigenvalues greater than 1 were included in the analysis. The PCA calculation was carried out using SPSS25.0 software.

2.2.3. Nitrate Pollution Index (NPI)

Nitrate pollution is a major contributor to groundwater contamination on a global scale. To quantify the extent of nitrate contamination in groundwater, a straightforward nitrate pollution index (NPI) is utilized. The value of NPI is calculated using Equation (2) [46]:

$$\mathrm{NPI} = \frac{C_m - C_s}{C_s} \quad (2)$$

The equation for determining NPI involves measuring the nitrate concentration (C_m) of water samples and comparing it to the threshold value (C_s) induced by human activities, which is recommended to be 10 mg/L [47]. The resulting NPI can then be classified into one of five levels [48], each with its corresponding grading as listed in Table 1.

Table 1. Study area water quality evaluation index classification and results statistics.

Indices	Range	Classification	Distribution%
Electrical conductivity (EC)	<250	Excellent	0.00%
	250–750	Good	36.58%
	750–2000	Doubtful	58.54%
	>2000	Unsuitable	4.88%
Sodium adsorption ratio (SAR)	<10	Excellent	100.00%
	10–18	Good	0.00%
	18–26	Doubtful	0.00%
	>26	Unsuitable	0.00%
Residual sodium carbonate (RSC)	<1.25	Good	97.56%
	1.25–2.5	Doubtful	2.44%
	>2.5	Unsuitable	0.00%
Permeability index (PI)	Class I (>75%)	Excellent	7.32%
	Class II (25–75%)	Good	92.68%
	Class III (<25%)	Poor	0.00%
Irrigation water quality index (IWQI)	[85, 100]	No restriction	2.44%
	[70, 85]	Low restriction	39.02%
	[55, 70]	Moderate restriction	53.66%
	[40, 55]	High restriction	2.44%
	[0, 40]	Severe restriction	2.44%
Nitrate Pollution Index (NPI)	<0	No pollution	68.30%
	[0, 1]	Light pollution	21.95%
	[1, 2]	Moderate pollution	7.32%
	[2, 3]	Significant pollution	0.00%
	>3	Very significant pollution	2.44%
Entropy-weighted Water Quality index (EWQI)	<50	Excellent	87.80%
	50–100	Good	9.76%
	100–150	Medium	2.44%
	150–200	Poor	0.00%
	>200	Extremely poor	0.00%

2.2.4. Evaluation of Irrigation Water Quality Based on Hydrogeochemical Indexes

To ensure a comprehensive evaluation of irrigation water quality, it is crucial to utilize multiple indicators. This study specifically selected four indicators, including SAR, Na%, RSC, and PI, to fully interpret and evaluate the chemical properties of the water.

The SAR is an important measure of the concentration of Na^+ in groundwater. A higher SAR value indicates a greater adsorption effect on Na^+, which can alter the structure of soil agglomerates and reduce infiltration performance, ultimately leading to decreased drainage performance. These problems arise due to the replacement of exchangeable Ca^{2+} and Mg^{2+} ions in soil with Na^+ ions, which leads to the dispersion of soil particles and the breakdown of soil structure. High SAR conditions lead to dry, compact, and hard soil,

which in turn reduces air and water infiltration rates. This problem is influenced by various factors, such as soil type and salinity ratio. Therefore, it is essential to calculate SAR values before using water for agricultural irrigation. Wilcox proposed a calculation formula for SAR values, as shown in Equation (3) [22,46].

$$\mathrm{SAR} = \frac{\mathrm{Na}^+}{\sqrt{(\mathrm{Ca}^{2+} + \mathrm{Mg}^{2+})/2}} \tag{3}$$

The %Na is a crucial factor in evaluating the appropriateness of irrigation water. If water contains high levels of sodium, it can react with carbonates and cause soil alkalinity to rise. Additionally, excessive amounts of sodium chloride can lead to soil salinization, which decreases soil permeability and hinders water flow through the soil, ultimately affecting crop growth. The formula for calculating the sodium percentage is presented in Equation (4) [19,49].

$$\%\mathrm{Na}^+ = \frac{\mathrm{Na}^+}{\mathrm{Ca}^{2+} + \mathrm{Mg}^{2+} + \mathrm{Na}^+ + \mathrm{K}^+} \times 100\% \tag{4}$$

The suitability of irrigation water quality is evaluated based on the RSC parameter, which indicates the relationship between weak acids and alkaline earth minerals present in groundwater. RSC values can be calculated using Equation (5) [50]. High RSC values in irrigation water can negatively impact crop yields and cause severe alkali damage if used for prolonged periods. Therefore, it is important to consider RSC values when selecting water for agricultural irrigation.

$$\mathrm{RSC} = \left(\mathrm{HCO}_3^- + \mathrm{CO}_3^{2-}\right) - \left(\mathrm{Ca}^{2+} + \mathrm{Mg}^{2+}\right) \tag{5}$$

The soil structure is significantly influenced by the PI parameter, which can also be utilized to evaluate if groundwater is appropriate for irrigation. The PI is determined by the correlation between cations and bases present in water. When specific ions, such as calcium, magnesium, sodium, and bicarbonate ions, are excessively present, they can harm the soil structure and decrease its permeability. This reduction in soil permeability can negatively affect the absorption of nutrients and crop growth. The PI can be calculated using Equation (6).

$$\mathrm{PI} = \frac{\mathrm{Na}^+ + \sqrt{\mathrm{HCO}_3^-}}{\mathrm{Ca}^{2+} + \mathrm{Mg}^{2+} + \mathrm{Na}^+} \times 100\% \tag{6}$$

The ion units involved in the above formula are all meq/L.

2.2.5. Irrigation Water Quality Assessment Based on the IWQI

In order to determine the most influential factors affecting irrigation water quality, a PCA was conducted. The results of this analysis were used to select key parameters for calculating the IWQI using Equation (7) [22,51].

$$\mathrm{IWQI} = \sum_{i=1}^{\mathrm{n}} q_i w_i \tag{7}$$

To calculate the IWQI, Equation (7) uses the variable n, which represents the number of parameters affecting the WIQI, as determined through PCA. The value of the *i*th parameter is indicated by q_i, as calculated using Equation (8), while the weight of the *i*th parameter in the IWQI calculation is represented by w_i, also calculated using Equation (9).

Table 2 provides the recommended water quality parameters by the UCCC, along with the evaluation criteria established by Ayers and Westcot [52] for each parameter.

$$q_i = (q_i)_{\max} - \left[\left(x_{ij} - x_{inf} \right) \times \frac{(q_i)_{amp}}{x_{amp}} \right] \tag{8}$$

Table 2. Parameter limiting values for quality measurement (q_i) calculation.

q_i	EC (μS/m)	SAR (meq/L)$^{0.5}$	rNa^+	rCl^-	$rHCO_3{}^-$
85–100	[200, 750)	[0, 3)	[2, 3)	[0, 4)	[1.0, 1.5)
60–85	[750, 1500)	[3, 6)	[3, 6)	[4, 7)	[1.5, 4.5)
35–60	[1500, 3000)	[6, 12)	[6, 9)	[7, 10)	[4.5, 8.5)
0–35	EC < 200 or EC > 3000	SAR ≥ 12	$rNa^+ < 2$ or $rNa^+ \geq 9$	$rCl^- \geq 10$	$rHCO_3{}^- < 1$ or $rHCO_3{}^- \geq 8.5$

Note: EC unit is μS/m, SAR unit is (meq/L)$^{0.5}$, and other units are meq/L.

In Equation (8), $(q_i)_{\max}$ represents the highest value of q_i within the grading range assigned to the *i*th parameter. The variable x_{ij} is the measured value of the *j*th sample for the *i*th parameter, and x_{inf} represents the lower limit of the grading range assigned to the *i*th parameter. The term $(q_i)_{amp}$ refers to the range of qi for the *i*th parameter, which is calculated as the difference between the highest and lowest values of q_i within the grading range for that parameter. x_{amp} is a term used to refer to the grading range for the *i*th parameter in x_{amp}. It is calculated as the difference between the upper and lower limits of that grading range. However, if x_{ij} exceeds the maximum graded upper limit, x_{amp} is computed as the difference between x_{ij} and the maximum graded upper limit.

$$w_i = \sum_{j=1}^{k} \left(F_j \times \left| A_{ij} \right| \right) / \sum_{j=1}^{k} \sum_{m=1}^{n} \left(F_j \times \left| A_{mj} \right| \right) \tag{9}$$

In Equation (9), F_j represents the eigenvalue of the *j*th principal component, while A_{ij} represents the eigenvector of the *j*th principal component corresponding to the *i*th parameter. The total number of principal components selected by PCA is denoted by k, and n represents the number of parameters used to calculate IWQI.

2.2.6. Entropy-Weighted Water Quality Index (EWQI)

The EWQI is a method of evaluating regional water quality by using the test results of multiple water quality parameters to represent it in a dimensionless value. The calculation of EWQI involves using entropy weight calculation to minimize the impact of subjective factors and improve the objective accuracy of the index. The following steps outline the calculation of EWQI [23,24]:

The first step in calculating the EWQI is to create an initial matrix that represents the water quality values. This is done by consolidating and displaying the data that has been sampled and monitored in the form of a matrix, as shown in Equation (10). The number of samples is denoted by m and the number of parameters by n, resulting in an initial matrix of water quality values denoted by X. Within the water quality matrix X, the measurement value of the *j*th evaluation index for the *i*th water sample is represented by X_{ij}.

$$X = \begin{bmatrix} x_{11} & x_{12} & \cdots & x_{1n} \\ x_{21} & x_{22} & \cdots & x_{2n} \\ \vdots & \vdots & \ddots & \vdots \\ x_{m1} & x_{m2} & \cdots & x_{mn} \end{bmatrix} \tag{10}$$

The second step involves the standardization of water quality data to account for differences in the scale and dimensions of the values for each evaluation index. This step helps to reduce the impact of human subjective factors. The standardization process is

carried out using Equations (11) and (12), where $(x_{ij})_{max}$ and $(x_{ij})_{min}$ represent the maximum and minimum values of the evaluation variables in column j of the initial water quality numerical matrix, respectively. The resulting matrix, Y, is the standardized water quality numerical matrix.

$$y_{ij} = \frac{x_{ij} - (x_{ij})_{min}}{(x_{ij})_{max} - (x_{ij})_{min}} \tag{11}$$

$$\mathrm{Y} = \begin{bmatrix} y_{11} & y_{12} & \cdots & y_{1n} \\ y_{21} & y_{22} & \cdots & y_{2n} \\ \vdots & \vdots & \ddots & \vdots \\ y_{m1} & y_{m2} & \cdots & y_{mn} \end{bmatrix} \tag{12}$$

The third step is to determine the weight of each evaluation factor. To reduce the impact of subjective factors and improve the objectivity of the results, the entropy weighting method is employed to determine the weights of each evaluation factor. The entropy weight of the jth evaluation factor, denoted by w_j, is calculated using Equations (13)–(15). Here, m represents the number of samples to be evaluated for water quality, and n represents the number of evaluation factors. P_{ij} is the ratio of y_{ij} in the standardized water quality value matrix to the sum of the index values in the column while e_j represents the information entropy of the jth evaluation factor. Finally, w_j is the weight of the jth evaluation factor in the study.

$$p_{ij} = \frac{y_{ij}}{\sum_{i=1}^{\mathrm{m}} y_{ij}} \tag{13}$$

$$e_j = -\frac{1}{\ln m} \sum_{i=1}^{m} P_{ij} \ln P_{ij} \tag{14}$$

$$w_j = \frac{1 - e_j}{\sum_{j=1}^{\mathrm{n}} (1 - e_j)} \tag{15}$$

The fourth step is to calculate the water quality ratio according to the evaluation criteria of each evaluation factor, as shown in Equations (16) and (17). Among them, C_{ij} indicates the measured concentration value of the ith parameter in the data corresponding to the j evaluation factor, and S_j corresponds to the groundwater quality evaluation standard of the j evaluation factor.

$$q_{ij} = \frac{C_{ij}}{S_j} \times 100 \tag{16}$$

$$q_{\mathrm{pH}} = \begin{cases} \frac{\mathrm{C_{pH}} - 7}{8.5 - 7} \times 100 & \mathrm{C_{pH}} > 7 \\ \frac{7 - \mathrm{C_{pH}}}{7 - 6.5} \times 100 & \mathrm{C_{pH}} < 7 \end{cases} \tag{17}$$

The fifth step is to calculate and classify the water quality index. After obtaining the weight w_j of the jth indicator in the study and the water quality proportion q_{ij}, the water quality index (WQI) can be calculated, as shown in Equation (18). According to the calculated EWQI, groundwater can be classified into five groundwater categories (Table 1) [23,24,53].

$$\mathrm{EWQI} = \sum_{j=1}^{\mathrm{n}} w_j q_{ij} \tag{18}$$

2.2.7. Human Health Risk Assessment

The methodology utilized for analyzing health risks is based on the health risk assessment model proposed by USEPA [54], which has been widely accepted and utilized by the academic community. The two primary pathways of human exposure to groundwater pollutants are through skin contact and oral ingestion. Previous studies have indicated that the main human health hazards arise from the oral ingestion of groundwater pollutants, rather than from dermal contact [55–57]. The study categorized the population into four

groups based on age and gender: infants aged 0–6 months, children aged 7 months to 18 years, adult males over 18 years, and adult females over 18 years. The assessment methods and calculations used are presented in Equations (19)–(22). The study defined hazard index (HI) and hazard quotient (HQ_i) as measures of the potential non-carcinogenic risk posed by various groundwater contaminants and pollutants. The CDI refers to the daily exposure dose ($mg \cdot kg^{-1} \cdot d^{-1}$) when taken orally, while RfD pertains to the reference dose ($mg \cdot kg^{-1} \cdot d^{-1}$) of the corresponding contaminant when taken orally. Ci stands for the measured concentration of contaminant i in groundwater, IR represents the average daily drinking volume ($L \cdot d^{-1}$), EF and ED denote the exposure frequency ($d \cdot a^{-1}$) and annual exposure duration (a), respectively. BW is the average body weight of the inhabitants (kg), and AT is the average time (d).

$$HQ_i = \frac{CDI_i}{RfD_i} \tag{19}$$

$$HI = HQ_1 + HQ_2 + \cdots + HQ_i \tag{20}$$

$$CDI_i \cdot = \frac{C_i \times IR \times EF \times ED}{BW \times AT} \tag{21}$$

$$AT = ED \times 365 \tag{22}$$

The hazard index (HI) is used to evaluate and grade the potential risk of groundwater pollution. If the HI is less than 1, the potential risk is considered negligible. If HI falls between 1 and 4, the potential risk is moderate and requires groundwater pollution treatment based on the actual situation. If HI exceeds 4, the potential risk is high, and further groundwater treatment and control are necessary.

3. Results

3.1. General Hydrogeochemical Characteristics

This study utilized quantitative analysis of various physical and chemical parameters to gain a better understanding of groundwater formation and its water quality. The hydrochemical data were analyzed using SPSS 25.0. Descriptive statistical analysis was conducted, including mean, minimum, maximum, standard deviation, and coefficient of variation. Table 3 presents the statistical analysis results of the exceedances of each component based on the standards set by the World Health Organization (WHO) [58] and the current situation in China [59] for drinking water purposes. Figure 3 presents a combination of a box plot and a normal distribution curve. This visual representation not only showcases the maximum value, mean, standard deviation, median, upper quartile, and lower quartile included in the box plot but also provides insight into the overall distribution of the data. The pH values of the sampled groundwater ranged from 7.2 to 8.1, while the TDS ranged from 316 to 1636 mg/L. It is worth noting that only two groundwater samples had TDS values higher than the permissible limit for drinking water (1000 mg/L). Based on the pH and TDS values, the study area can be inferred to have weak alkaline groundwater with low to medium mineralization. The groundwater hardness ranged from 208.94 to 887.63 mg/L, with an average of 435.96 mg/L. The study found that approximately 30% of water samples had exceeded the standard for hardness, indicating that the overall water quality is hard. The high total hardness (TH) values observed were attributed to the presence of Ca^{2+} and Mg^{2+} ions in the water [43], which are commonly associated with rocks rich in minerals such as calcite and dolomite found in the aquifers of the study area.

Table 3. Statistical analysis of hydro-chemical parameters of groundwater samples (units of all parameters are mg/L, except pH).

Parameters	Max	Min	Mean	SD	CV	Limit	% of SEL
pH	8.10	7.20	7.64	0.22	3.00%	6.5–8.5 *	0.00
TDS	1636.00	316.00	617.47	272.80	44.00%	1000.00 *	4.88
TH	887.63	208.94	435.96	134.29	31.00%	450.00 *	29.27
K^+	44.47	0.62	5.09	8.64	170%	-	-
Na^+	219.34	7.31	41.38	44.88	108%	200.00 *	7.32
Ca^{2+}	272.83	40.28	132.08	46.57	35%	200.00 *	9.76
Mg^{2+}	50.10	9.75	24.59	8.84	36%	150.00 *	0.00
Cl^-	351.50	3.05	54.69	72.50	133%	250.00 *	4.88
$SO_4{}^{2-}$	449.40	23.83	96.52	89.66	93%	250.00 *	7.32
$HCO_3{}^-$	644.86	144.29	400.68	87.87	22%	-	-
$NO_3{}^-$	49.70	0.02	8.57	8.90	104%	10.00 **	31.71
F^-	0.80	0.12	0.35	0.14	40%	1.00 *	0.00

Note: SD, standard deviation; CV (%), coefficient of variation; % of SEL.% of samples exceeding acceptable limit; * WHO guideline; ** Chinese guideline.

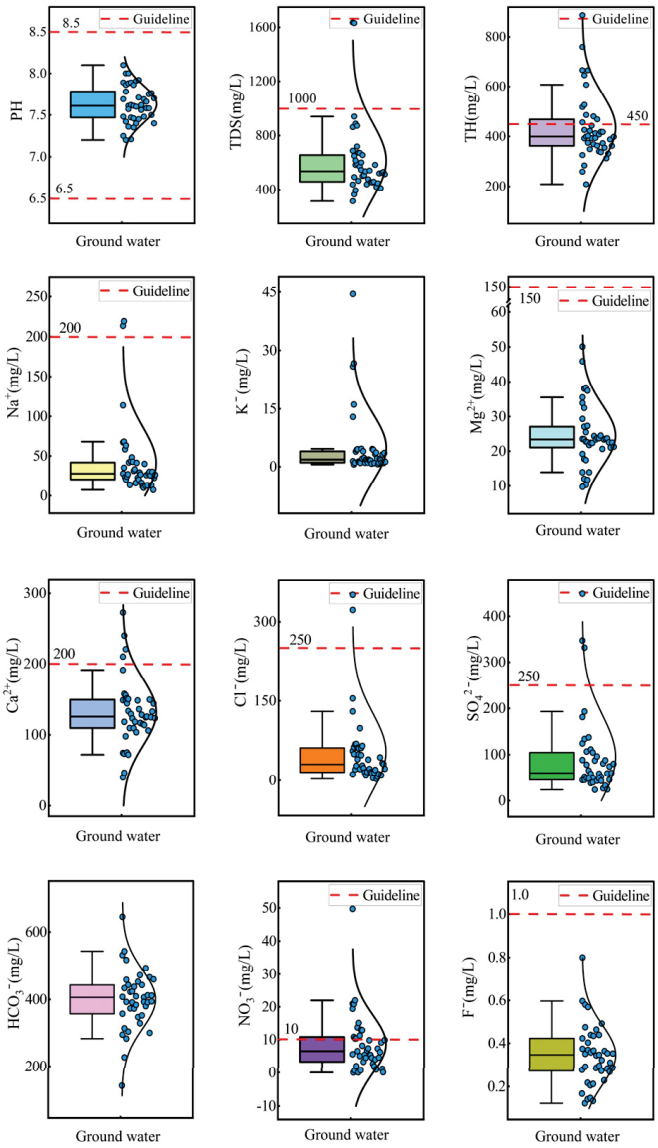

Figure 3. Distribution and exceedance of each physicochemical parameter in groundwater samples.

The study area exhibited a range of K^+ concentration, from 0.62 to 44.47 mg/L, with an average value of 5.54 mg/L. The southwest region had higher K^+ levels. This is possibly due to a significant amount of potassium feldspar sandstone. The study area's soil is mainly purple soil, and the parent rocks of the soil have a relatively high K^+ content. The samples had Na^+ concentrations ranging from 7.31 to 219.34 mg/L, with an average value of 41.38 mg/L. Similarly, the Cl^- concentrations ranged from 3.05 to 351.50 mg/L, with an average value of 54.69 mg/L. The distribution of Cl^- concentration was found to be similar to that of Na^+, indicating the presence of salt rock distribution in the study area. The study area exhibited a range of Ca^{2+} concentration from 40.28 to 272.83 mg/L, with an average of 132.08 mg/L. The Mg^{2+} concentration ranged from 9.75 to 50.10 mg/L, with an average of 24.59 mg/L. Additionally, the HCO_3^- concentration ranged from 144.29 to 644.86 mg/L, with an average of 400.68 mg/L. The Ca^{2+}, Mg^{2+}, and HCO_3^- concentrations are a result of carbonate mineral dissolution. The study found that the concentration of SO_4^{2-} in the sampled water ranged from 28.83 to 449.40 mg/L, with an average of 83.52 mg/L. It was observed that the samples with high concentrations of SO_4^{2-} also had high concentrations of Ca^{2+}. This suggests a possible relationship between the dissolution of gypsum layers in the geological formations of the study area and the high levels of SO_4^{2-} and Ca^{2+} found in the water samples. The concentration of NO_3^- in the water samples ranged from 0.02 to 49.70 mg/L, with 31.71% of the samples exceeding the allowable drinking limit of 10 mg/L. On the other hand, the concentration of F^- ranged from 0.12 to 0.80 mg/L, which is well below the recommended limit of 1 mg/L.

Based on the results presented in Table 3, it is evident that the major cations and anions exhibit a coefficient of variation greater than 10%, indicating significant spatial variability and heterogeneity in their distribution. Among the major cations and anions, K^+, Cl^-, and Na^+ show the most significant variation. On average, the cation content is highest for Ca^{2+}, followed by Na^+, Mg^{2+}, and K^+. Similarly, the anion content is highest for HCO_3^-, followed by SO_4^{2-}, Cl^-, NO_3^-, and F^-. The water chemistry type of the sampled groundwater can be determined by using Piper's trilinear diagram [24,30,60], which also reflects the relative content of major ions and general water chemistry characteristics in groundwater. The study found that the groundwater sampled was primarily of the HCO_3^- Ca type, as indicated in Figure 4. This is in line with the observation that Ca^{2+} and HCO_3^- are the dominant cations and anions in the region. However, some high salinity groundwater types, such as mix HCO_3-Na·Ca and mix Cl-Mg·Ca, may be attributed to water–rock interactions in the study area. Based on the analysis of Table 3, it can be concluded that apart from TH and NO_3^-, all other water chemistry parameters of the samples are within the permissible limits for drinking water. This suggests that the groundwater in the study area is a viable source of high-quality drinking water.

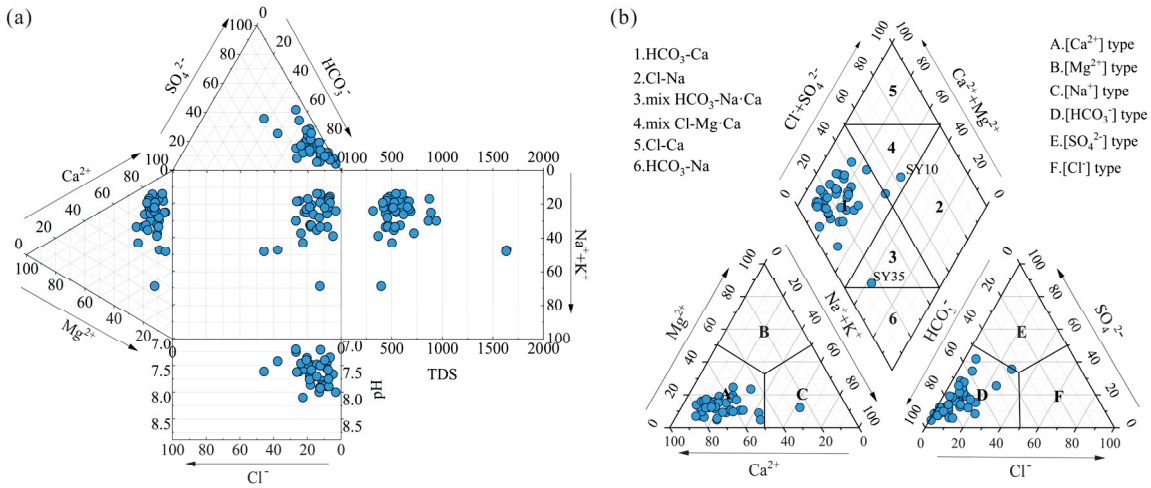

Figure 4. (**a**) Durov diagram, (**b**) Piper trilinear diagram of samples in the study area.

3.2. Principal Component Analysis (PCA)

This study utilized the PCA method to identify the main factors that influence the hydrochemical composition of groundwater in the study area. The data types included major ions such as K^+, Na^+, Ca^{2+}, Mg^{2+}, Cl^-, SO_4^{2-}, HCO_3^-, NO_3^-, F^-, as well as pH, EC, and SAR. Prior to importing the hydrochemical parameters into SPSS 25 software for PCA, Z-score standardization was performed. PCA was utilized to reduce the dimensionality of the twelve parameters and expose their relationships. The KOM (KMO = 0.586 > 0.5) and Bartlett tests (ρ = 0.000 < 0.05) in this study showed that the above data were suitable for analysis using PCA. The findings of PCA are presented in both Table 4 and Figure 5.

Table 4. Factor loading matrix and EWQI weights for each parameter of PCA.

Parameters	PC1	PC2	PC3	PC4	Communality	W_i
EC	0.921	0.021	−0.099	−0.205	0.900	0.204
pH	−0.372	0.181	−0.449	0.651	0.796	-
Ca^{2+}	0.833	−0.136	0.281	−0.223	0.842	-
Mg^{2+}	0.481	0.456	0.317	0.297	0.628	-
Na^+	0.907	0.109	−0.289	0.191	0.954	0.215
K^+	0.305	−0.324	0.338	0.325	0.418	-
HCO_3^-	0.629	−0.112	0.577	0.321	0.843	0.178
SO_4^{2-}	0.856	−0.162	−0.187	−0.260	0.861	-
Cl^-	0.932	0.065	−0.176	0.024	0.904	0.205
NO_3^-	0.047	0.745	−0.098	−0.415	0.740	-
F^-	−0.062	0.749	0.389	0.091	0.725	-
SAR	0.766	0.133	−0.409	0.294	0.858	0.198
Eigenvalue	5.417	1.554	1.315	1.184	-	-
Cumulative	45.144	58.092	69.046	78.911	-	1

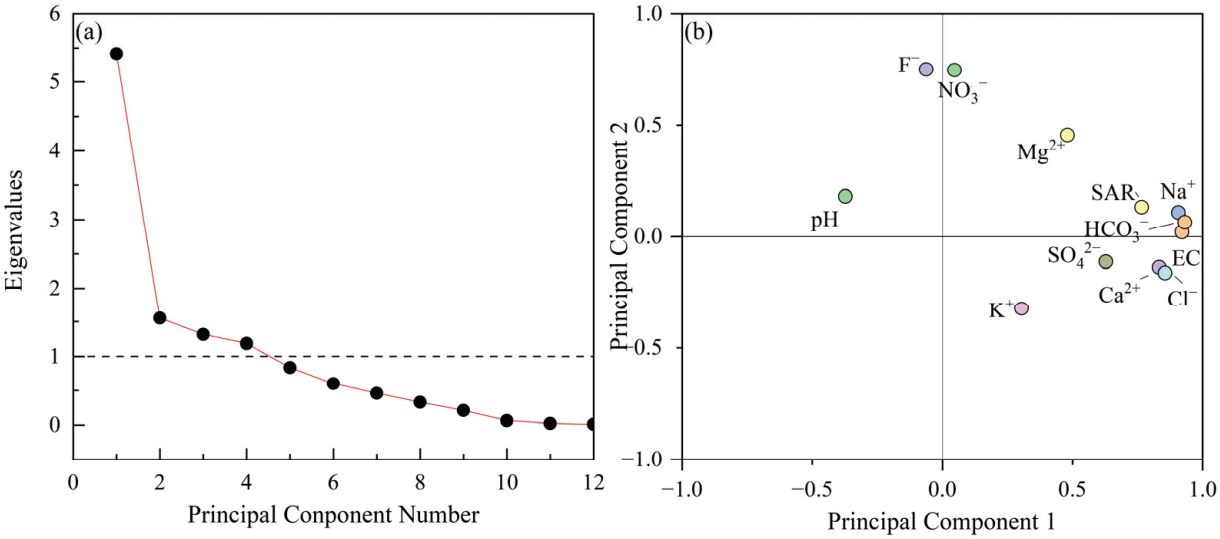

Figure 5. Results of principal component analysis. (**a**) Scree plot; (**b**) Factor loadings for PC1 and PC2.

Table 4 showcases the contribution of various parameters to the four principal components. The selected principal components, which had eigenvalues greater than 1, accounted for 78.91% of the total variance. PC1 had the highest percentage of variance, at 45.14%, and showed a strong load of EC, Ca^{2+}, Na^+, Cl^-, SO_4^{2-}, and SAR. This suggests that natural mineral dissolution and precipitation processes have a dominant effect on these parameters. PC2 contributed to 12.95% of the total variance and exhibited strong loads of F^- and NO_3^-. The absence of fluoride-containing minerals, such as fluorite, in the study area suggests that the F^- is likely a result of human activities. The presence of excessive NO_3^- in the study area may be attributed to human activities such as the construction of industrial

parks and a prolonged history of agriculture. In order to identify the key parameters for the IWQI analysis, parameters with loadings greater than 0.35, such as EC, Na^+, Cl^-, HCO_3^-, and SAR, were selected as potential candidates [61,62].

3.3. Ion Source Analysis

The Gibbs diagram is a useful tool for understanding the correlation between aquifer lithology and water composition [63]. It is divided into three distinct fields, namely evaporation-dominated, water–rock interaction-dominated, and precipitation-dominated. Figure 6 illustrates the Gibbs diagram of water samples from the study area. Upon plotting the Gibbs diagram points in Microsoft Excel, it is apparent that the total dissolved solids (TDSs) of the water samples fall mostly between the range of 100 and 1000 mg/L. Additionally, the ratios of $Na^+/(Na^+ + Ca^{2+})$ and $Cl^-/(Cl^- + HCO_3^-)$ are observed to be predominantly within the range of 0–0.4. The Gibbs diagram suggests that water–rock interaction is the primary factor contributing to the formation of groundwater chemistry in the study area. The increasing trend of the cation weight ratio $Na^+/(Na^+ + Ca^{2+})$ in Figure 6b indicates that cation exchange also plays a role in the hydrogeochemical composition.

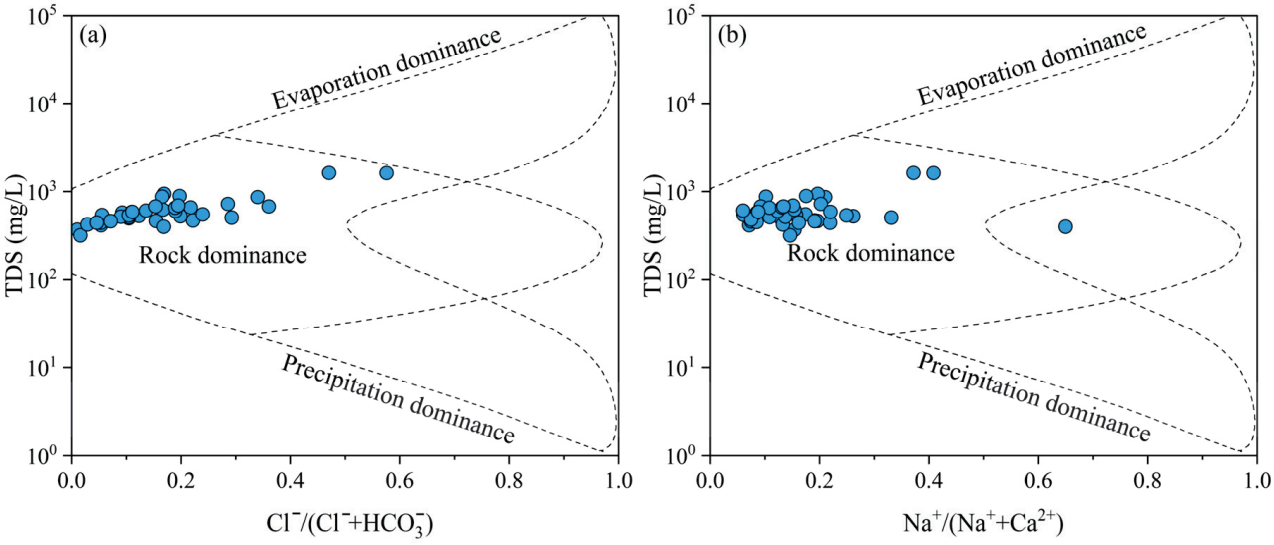

Figure 6. Hydrogeochemical processes based on Gibbs diagrams for (**a**) anions and (**b**) cations.

Prior research has demonstrated that examining the proportion of major ions present in groundwater can be a valuable technique for detecting potential water–rock interactions within groundwater systems [24,30]. In relation to Figure 7a, if the concentrations of Na^+ and Cl^- are obtained from salt dissolution, the molar ratio of Na^+/Cl^- will be equivalent to 1, as indicated in chemical Equation (23). This study found that groundwater samples in the study area are distributed evenly around the y = x line, with the presence of salt rock in the aquifer, indicating that the Na^+ and Cl^- concentrations are primarily derived from salt dissolution. The results also showed that some samples had higher Na^+ concentrations, which could be attributed to cation exchange during groundwater runoff processes. This occurs when groundwater interacts with feldspar minerals in sandstone, leading to the dissolution of Na^+ in minerals and its accumulation in groundwater. During runoff processes, Ca^{2+} in groundwater can undergo positive cation exchange with Na^+ in surrounding soil, resulting in the distribution of groundwater samples on both sides of the y = x line.

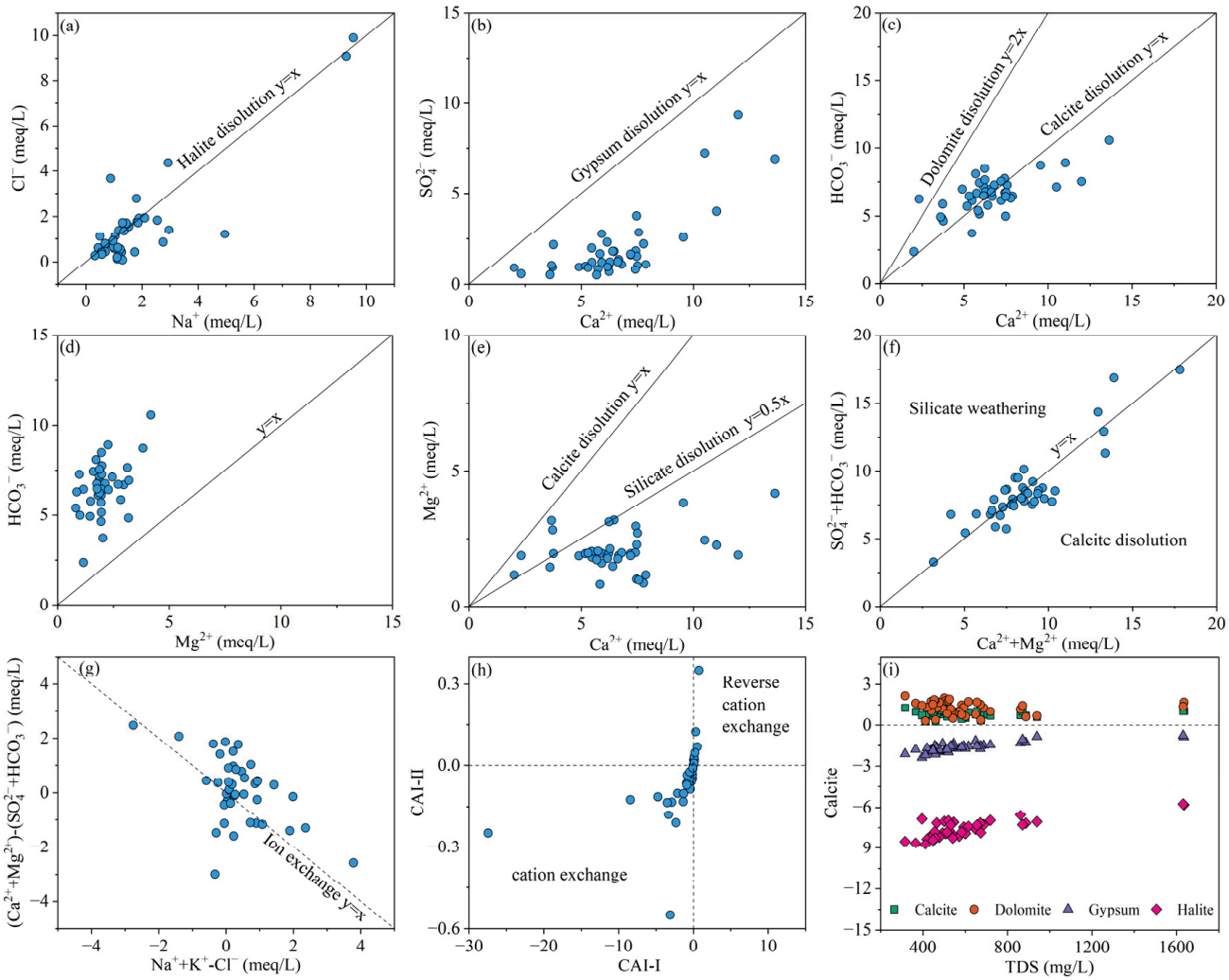

Figure 7. Scatter plots of (**a**) Cl^- vs. Na^+; (**b**) $SO_4{}^{2-}$ vs. Ca^{2+}; (**c**) $HCO_3{}^-$ vs. Ca^{2+}; (**d**) $HCO_3{}^-$ vs. Mg^{2+}; (**e**) Mg^{2+} vs. Ca^{2+}; (**f**) ($HCO_3{}^-$ + $SO_4{}^{2-}$) vs. (Ca^{2+} + Mg^{2+}); (**g**) (Ca^{2+} + Mg^{2+}) − ($HCO_3{}^-$ + $SO_4{}^{2-}$) vs. Na^+ + K^+ − Cl^-; (**h**) chloro alkaline indices CAI-I and CAI-II; (**i**) Saturation index of calcite, dolomite, gypsum, and halite.

In Figure 7b, it can be observed that gypsum dissolution releases equimolar amounts of Ca^{2+} and $SO_4{}^{2-}$ in groundwater, as shown in chemical Equation (24). The study area has gypsum thin layers in the aquifer. However, the ratio of $SO_4{}^{2-}/Ca^{2+}$ in the water samples is mostly less than 1, which suggests that the presence of Ca^{2+} in the water is not solely due to gypsum dissolution. It could also be a result of the dissolution of other carbonate minerals, such as calcite and dolomite. To determine the source of Ca^{2+} in the study area, Figure 7c,d were plotted. The $Ca^{2+}/HCO_3{}^-$ ratios for the dissolution of dolomite and calcite are 1:1 and 1:2, respectively. The findings from Figure 7c reveal that most of the samples in the study area are positioned between the y = x and y = 2x lines, indicating the presence of both dolomite and calcite dissolution. However, several samples fall below the y = x contour, implying the existence of other Ca^{2+} sources besides these two. This further supports the earlier mentioned source of gypsum dissolution. The results presented in Figure 7d indicate that all sample points are situated above the 1:1 $HCO_3{}^-$ to Mg^{2+} ratio line, which confirms the occurrence of both calcite and dolomite dissolution. Additionally, the excess $HCO_3{}^-$ is compensated for by other cations. Equations (25) and (26) represent the chemical equations for the dissolution of calcite and dolomite, respectively. The Ca^{2+}/Mg^{2+} ratio depicted in Figure 7e is frequently utilized to distinguish between the dissolution of carbonate minerals and silicate minerals as sources of ions in groundwater. A Ca^{2+}/Mg^{2+} ratio greater than

2 indicates silicate mineral dissolution, while a ratio between 1 and 2 suggests calcite dissolution. Dolomite dissolution results in a Ca^{2+}/Mg^{2+} ratio of 1. The hydrochemical composition of groundwater in the study area is influenced by both carbonate and silicate mineral dissolution, as indicated by Ca^{2+}/Mg^{2+} values greater than 1 in most groundwater samples, as shown in Figure 7e. The ratio shown in Figure 7f provides an explanation for the source of Ca^{2+} and Mg^{2+}. As observed in the (Ca^{2+} + Mg^{2+}) and ($HCO_3{}^-$ + $SO_4{}^{2-}$) binary diagram, the groundwater samples in Figure 7f are near the y = x line. This indicates that the primary source of ions in groundwater is due to the dissolution of calcite and silicate minerals.

$$NaCl \rightarrow Na^+ + Cl^- \quad (23)$$

$$CaSO_4 \cdot 2H_2O \rightleftharpoons Ca^{2+} + SO_4^{2-} + 2H_2O \quad (24)$$

$$CaCO_3(Calcite) + H_2CO_3 \rightarrow Ca^{2+} + 2HCO_3^- \quad (25)$$

$$CaMg(CO_3)_2(Dolomite) + 2H_2CO_3 \rightarrow Ca^{2+} + Mg^{2+} + 4HCO_3^- \quad (26)$$

The occurrence of ion exchange reactions between groundwater and aquifers is commonly assessed by examining the relationship between the concentrations of Na^+, K^+, and Cl^- versus Ca^{2+}, Mg^{2+}, $HCO_3{}^-$, and $SO_4{}^{2-}$ [64]. The distribution of groundwater samples above the y = x line suggests that major ions' relative concentration in the groundwater system is affected by cation exchange reactions. Furthermore, the chloro alkaline indices index (CAI-I and CAI-II) can determine whether the cation exchange process is forward or reverse [65]. These indices are calculated using Equations (27) and (28), which involve ion concentrations expressed in meq/L. In Figure 7g,h, it can be observed that most groundwater samples exhibit negative CAI-I and CAI-II values. This suggests that forward cation exchange reactions are taking place, wherein Ca^{2+} and Mg^{2+} ions in the groundwater are being replaced by K^+ and Na^+ ions in the aquifer. In Figure 7i, the saturation indices (SI) of specific minerals (calcite, dolomite, gypsum, and halite) in the groundwater system were calculated using PHREEQC (Version 3) software to further determine their status. The presence of positive SI values in carbonate minerals (such as calcite and dolomite) suggests that the groundwater's ion composition is linked to the dissolution of these minerals. On the other hand, the negative SI values observed in gypsum and halite indicate that these minerals are not in a saturated state in the groundwater system and therefore dissolve less in this area.

$$\text{CAI-I} = \left(Cl^- - \left(Na^+ + K^+\right)\right)/Cl^- \quad (27)$$

$$\text{CAI-II} = \left(Cl^- - \left(Na^+ + K^+\right)\right)/\left(HCO_3^- + SO_4^{2-} + CO_3^{2-} + NO_3^-\right) \quad (28)$$

3.4. Nitrate Pollution Analysis

As mentioned in the previous section, the study area is mainly affected by excessive $NO_3{}^-$ ions, which accounts for 31.71% of the total samples (Table 3). This section aims to analyze the sources of nitrate pollution. It has been established that human activities, including agricultural and industrial practices, as well as municipal wastewater, contribute significantly to $NO_3{}^-$ pollution [58,59]. As depicted in Figure 8, the samples that surpass the acceptable limit are dispersed throughout agricultural and residential areas, providing evidence that the surplus of $NO_3{}^-$ is predominantly a result of human activities.

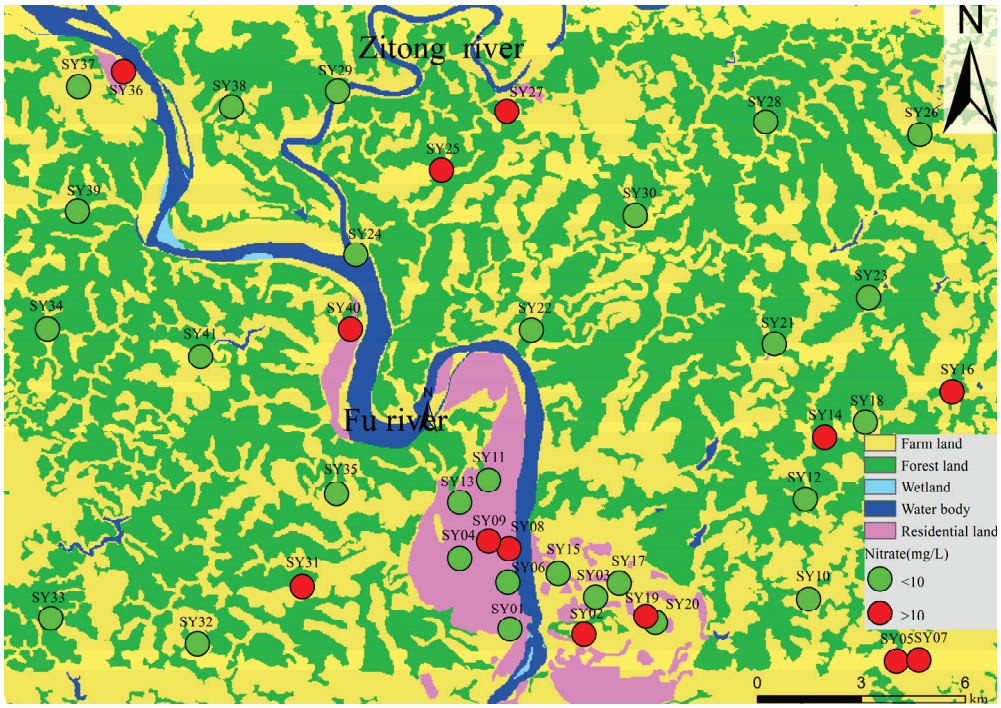

Figure 8. The different types of land use in the study area and the distribution of samples that have nitrate exceedances. It provides a visual representation of the relationship between land use and nitrate levels in the samples collected.

The data presented in Figure 9a clearly shows that the NO_3^- content in a significant number of groundwater samples exceeded the natural limit of 10 mg/L, indicating that nitrate pollution is likely due to human activities. To better understand the extent of this pollution, the NPI was introduced, and further analysis was conducted on the groundwater samples in the study area. The NPI–TDS relationship graph (Figure 9b) illustrates that the groundwater samples collected from the study area exhibit a range of nitrate pollution levels, with some showing no pollution while others exhibit severe pollution. Mild pollution was detected in 21.95% of the samples, while highly polluted water samples (SY20, SY14, SY02) were found in areas where human habitation and agriculture are prevalent. This confirms that the excessive nitrate levels are primarily caused by human activities. The study found that areas with high nitrate concentrations also had higher concentrations of TDS, Ca^{2+}, Mg^{2+}, HCO_3^-, Cl^-, and SO_4^{2-}. This suggests that anthropogenic influences not only increase nitrate concentration, but also increase groundwater salinity.

Under natural conditions, the NO_3^- to Cl^- ratio in groundwater is generally small. However, human activities such as agricultural, household, and municipal pollutant inputs can influence this ratio [66,67]. The NO_3^- to Cl^- ratio in naturally sampled groundwater with no human influence typically falls between 0.05 and 0.22. The study revealed that the NO_3^-/Cl^- ratio of groundwater ranged from 0.00 to 1.22, with 29.26% of the groundwater samples exceeding the natural upper limit of 0.22, accounting for 12 samples. This suggests that human activities in the area have a significant impact on the groundwater chemistry.

To better understand the sources of anthropogenic pollution that affect groundwater chemistry, correlations between Cl^-/Na^+ and NO_3^-/Na^+ as well as between NO_3^-/Cl^- and Cl^- were investigated. In Figure 10a, most groundwater samples were plotted near or on the y = x line, suggesting that the concentration of NO_3^- was influenced to some extent by agricultural activities and domestic wastewater. Figure 10b, on the other hand, shows that groundwater samples were primarily situated in areas where household/municipal inputs were dominant, with agricultural activities being a secondary factor contributing to NO_3^- levels exceeding the standard in the study area. According to Figures 9b and 10a, the high levels of NO_3^- in the study area are primarily a result of urban wastewater

discharge and, to a lesser extent, agricultural activities. This finding is consistent with the spatial distribution of nitrate-exceeding groundwater, which is mainly concentrated in the residential and agricultural areas of the study area, as shown in Figure 9. Thus, anthropogenic factors, such as urban sewage discharge and agricultural activities, are the main contributors to the excessive NO_3^- levels in the groundwater of the study area.

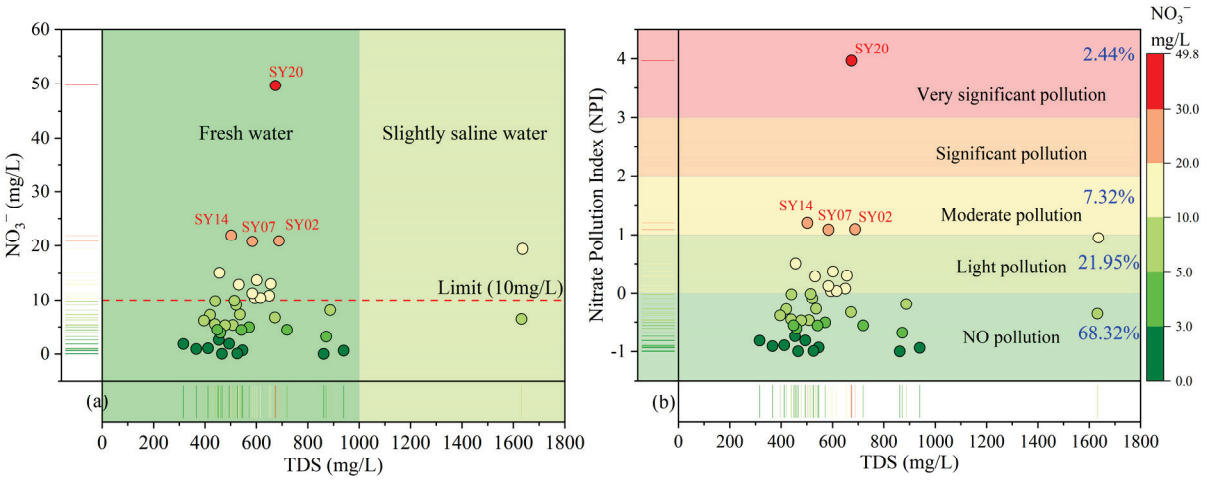

Figure 9. Scatter plots of (**a**) NO_3^- versus TDS, and (**b**) nitrate pollution index versus TDS.

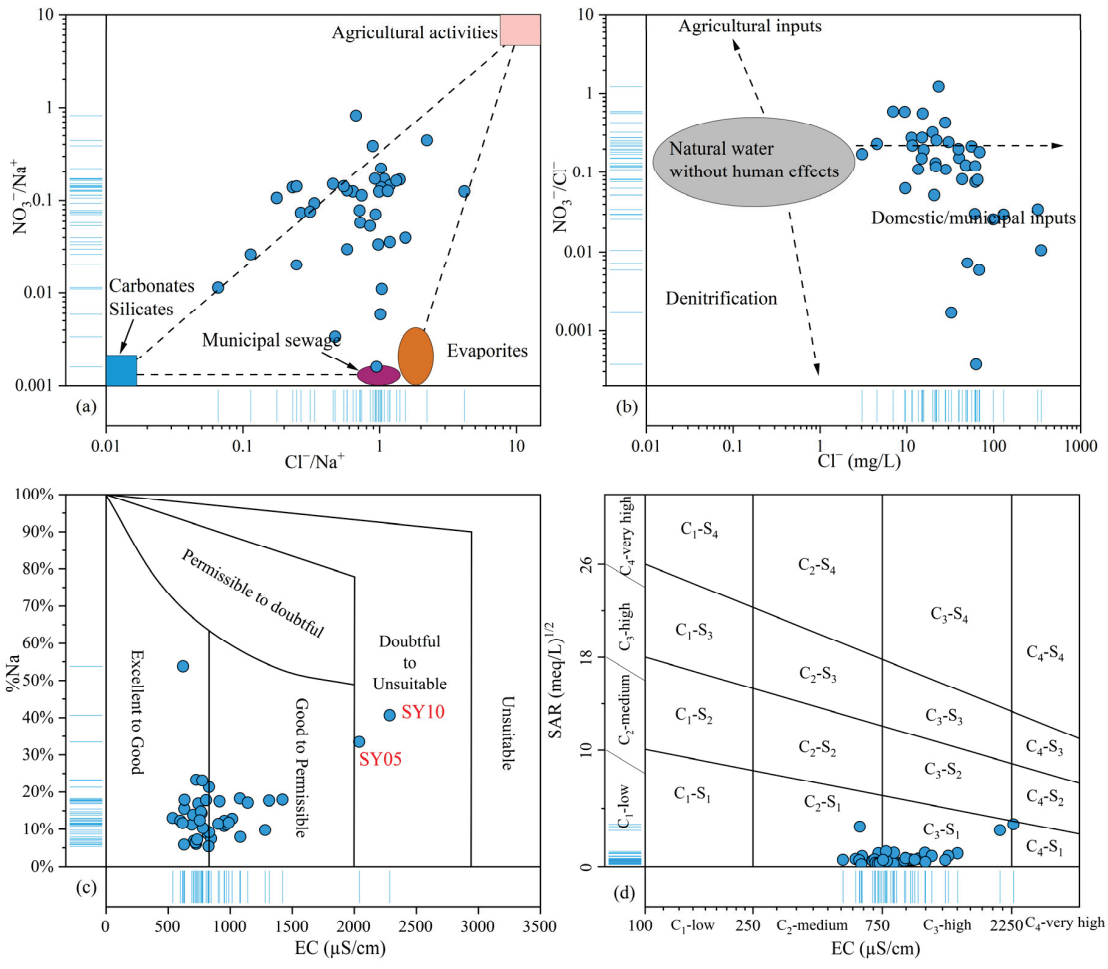

Figure 10. Scatter plots of (**a**) NO_3^-/Na^+ varus. Cl^-/Na^+; (**b**) NO_3^-/Cl^- varus. Cl^-; (**c**) Wilcox diagram (**d**) USSL diagram.

3.5. Evaluation of Irrigation Water Quality by Basic Hydrogeochemical Indexes

In this study, the suitability of groundwater for agricultural irrigation is determined by comparing the results of different indicator analyses with the corresponding irrigation water classification parameters provided in Table 1.

3.5.1. Salinity Hazard

Salinity is a crucial factor in determining the suitability of irrigation water, and it can be measured through conductivity (EC) or total dissolved solids (TDS). EC is an indicator of water conductivity and can reveal the harmful effects of salts on crops. In the study area, the EC values of groundwater samples ranged from 537 to 2286 μS/cm (with a mean of 906.27 μS/cm), as illustrated in Figure 11b. The salinity of groundwater in the study area increases from northwest to southeast. Only 36.58% of groundwater samples are suitable for irrigation without affecting crops. The irrigation suitability of 58.54% of groundwater samples is questionable, with EC values of two sample points exceeding 2000 μS/cm. If saline water is used for irrigation, the concentration of salts in the soil may rise to a harmful level and adversely affect the crops. The nutritional uptake and water retention of agricultural crops rely on the salt content in water, which means that each crop has a specific salinity limit. As a result, it is crucial to regulate the salinity of irrigation water when using groundwater for irrigation. In the southeast of the study area, groundwater can be utilized to irrigate crops that can tolerate high salinity levels, such as sunflowers, rye, wheat, and olives.

3.5.2. Sodium Hazard

The sodium adsorption ratio (SAR) is a useful indicator of sodium hazards in irrigation water. It is calculated by comparing the concentrations of Na^+ to Ca^{2+} and Mg^{2+} [68]. SAR is related to salt absorption on soil surfaces and can be used to evaluate the extent of damage caused by Na+ in irrigation water. Additionally, Na+ in irrigation water can replace Ca^{2+} and Mg^{2+} in the soil, which can reduce soil permeability. The SAR values of all samples range from 0.20 to 3.62 meq/L. According to Table 1, all samples fall under the excellent category in the SAR classification of irrigation water. This suggests that the groundwater in the study area is appropriate for irrigating all soil types as long as the SAR is used as the evaluation index (Figure 11d).

3.5.3. Residual Sodium Carbonate (RSC)

RSC is a useful tool for assessing the negative impact of carbonate (CO_3^{2-}) and bicarbonate (HCO_3^-) on the quality of agricultural irrigation water. When the concentrations of CO_3^{2-} and HCO_3^- ions in groundwater are higher than those of the Ca^{2+} and Mg^{2+} ions, the precipitation of Ca^{2+} and Mg^{2+} can occur. This can negatively affect soil permeability, cause soil compaction, and harm crop growth, rendering the groundwater unsuitable for irrigation purposes. Based on the guidelines provided by the US Salinity Laboratory, irrigation water quality can be categorized into three groups. Water sample with an RSC value of less than 1.25 meq/L is considered appropriate for irrigation. However, water with RSC values ranging from 1.25 to 2.5 meq/L may not be suitable for irrigation and requires further investigation. Water with RSC values exceeding 2.5 meq/L is deemed unsuitable for irrigation purposes. Figure 11f displays the RSC classification of irrigation water, indicating RSC values that range from −7.25 to 2.03 and an average value of −2.07. The Table 1 shows that 97.56% of groundwater samples were classified as suitable for irrigation, with only one sample being of doubtful suitability.

3.5.4. Permeability Index (PI)

The long-term use of irrigation water containing high levels of Na^+, Mg^{2+}, Ca^{2+}, and HCO_3^- can have a significant impact on soil permeability. To assess the suitability of groundwater for irrigation, this study utilized the permeability index (PI). The PI was used to establish a correlation between the total ion concentration and irrigation water quality,

which was categorized into three groups: excellent for PI > 75%, good for 25% < PI < 75%, and poor for PI < 25%. Based on the analysis and calculation of the permeability index of the samples, it was found that approximately 7.23% of the groundwater was of excellent quality for irrigation purposes, while approximately 92.86% of the groundwater was considered good for irrigation (Table 1). These findings suggest that the impact of irrigation water on soil properties is minimal. However, it is still recommended to monitor the long-term effects of groundwater and surface water irrigation on soil permeability in the study area.

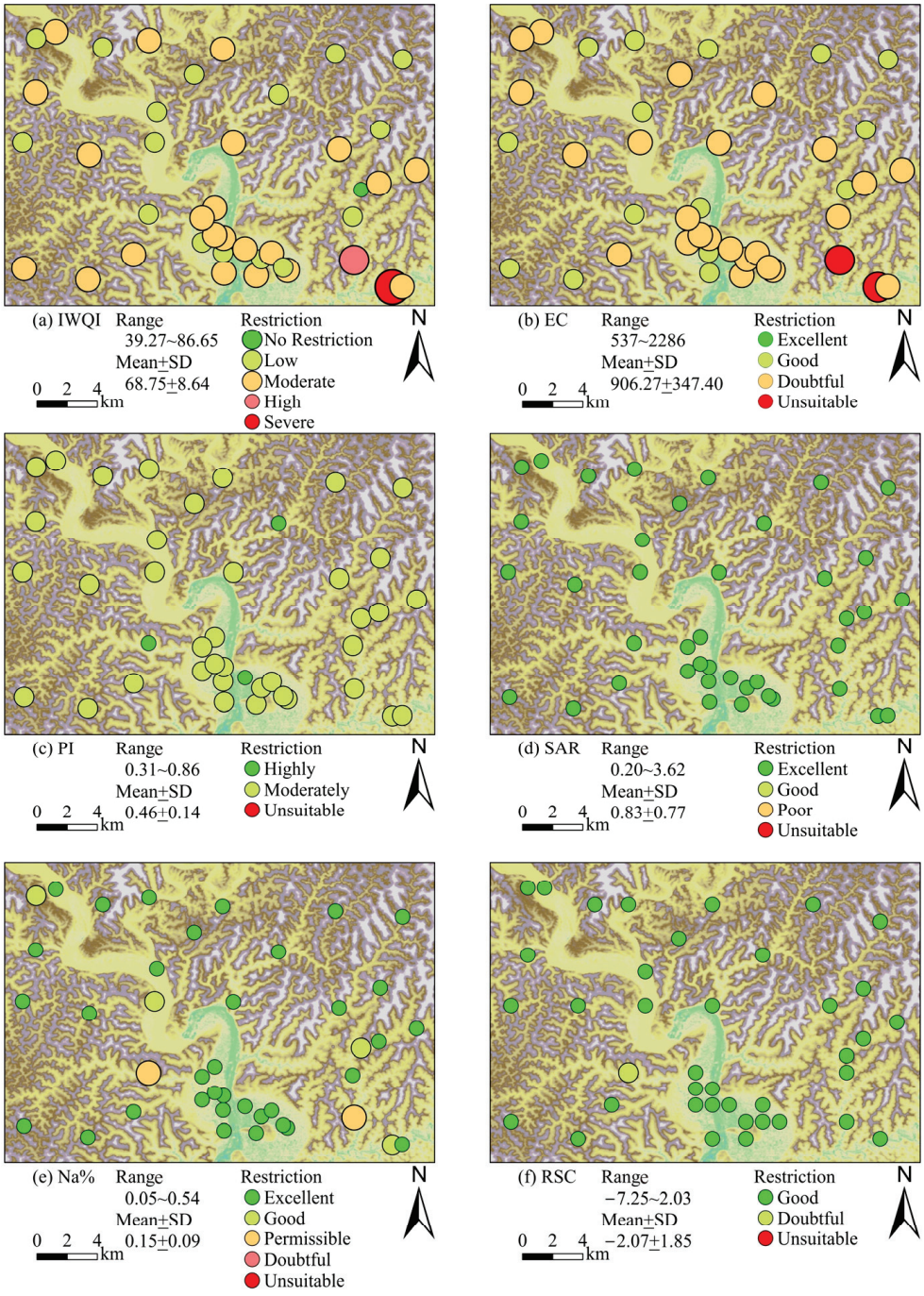

Figure 11. The overall decreasing suitability of groundwater indicators for irrigation from northwest to southeast, and their spatial distribution pattern: (**a**) IWQI, (**b**) EC, (**c**) PI, (**d**) SAR, (**e**) Na% and (**f**) RSC.

3.5.5. Percentage of Sodium (%Na)

The %Na is a useful indicator for evaluating the potential damage of sodium to soil structure. The %Na is used to classify irrigation water quality into five categories. According to the sodium content, irrigation water quality can be categorized as excellent if %Na is less than 20, good if it falls between 20 and 40%, usable for irrigation when %Na is between 40 and 60, questionable if %Na ranges between 60 and 80, and not suitable for irrigation if the %Na is greater than 80. Therefore, for long-term agricultural irrigation, water with sodium content below 60% is considered suitable. Water with a sodium content higher than 60% is unsuitable for use as irrigation water as it can cause sodium hazards to the soil through long-term irrigation practices. In the study area, the sodium content of water samples ranged from 5.36% to 53.79%. The groundwater in the study area is suitable for irrigation as the %Na is below 60%. Further exploration was conducted to determine its suitability for irrigation based on the relationship between the EC and %Na ratio, as shown in Figure 10c.

3.5.6. Wilcox Diagram

The Wilcox diagram is a tool that can be used to assess the quality of irrigation water based on both %Na and EC [69]. By plotting water samples on a graph with EC as the horizontal axis and %Na as the vertical axis, the diagram can classify irrigation water quality into five categories: excellent, good, permissible, doubtful, and unsuitable. Water samples that fall within the excellent or good regions are deemed suitable for agricultural irrigation. However, if they fall within the usable region, there is a potential risk of alkali damage when utilized for irrigation. This risk, although relatively small, can be mitigated by implementing appropriate measures. Water located in the marginally usable region for irrigation presents a risk of both salt and alkali damage. Conversely, water located in the unsuitable region is not appropriate for irrigation and can cause severe salt and alkali damage. In this study, water samples were plotted on the Wilcox diagram (Figure 10c) to determine their suitability for irrigation.

Of all the groundwater samples analyzed, only two fell within the marginally usable range, while the remaining samples were categorized as either excellent or good. This indicates that most of the samples are suitable for irrigation purposes. Based on the findings presented in Figure 11b, it is evident that groundwater samples with electrical conductivity (EC) values exceeding 2000 μS/cm are predominantly located in the southeastern region of the study area. This can be attributed to the construction of the industrial zone in the area. As a result, it is recommended that groundwater from the southeastern area should be avoided when selecting water sources for irrigation purposes.

3.5.7. USSL Diagram

The U.S. Salinity Laboratory's diagram (USSL diagram) was utilized to evaluate the groundwater's suitability for irrigation by assessing its water quality in greater detail [70]. The irrigation water was classified into four categories (C1, C2, C3, and C4) based on the degree of salinization harm. These categories were determined by the water's electrical conductivity, with ranges of less than 250, 250–750, 750–2250, and greater than 2250 μS/cm, respectively. The water was classified into four categories based on the degree of sodium (alkaline) hazard, namely S1 (low degree of alkaline hazard), S2 (moderate degree of alkaline hazard), S3 (high degree of alkaline hazard), and S4 (very high degree of alkaline hazard). These categories were determined based on the sodium adsorption ratio, with the ranges being <10, 10–18, 18–26, and >26, respectively. The USSL classification system can be used to categorize irrigation water into sixteen different categories. The groundwater samples in the study area were projected onto the USSL diagram and the results are displayed in Figure 10d.

The collected water samples are classified as S1 low-alkali damage water and are primarily found in the C2–S1 and C3–S1 areas, which are characterized by medium to high salinity and low-alkali damage water. The C3–S1 region has water samples with

high salinity but relatively low alkali content, making it conducive to the growth of most salt-tolerant crops. On the other hand, the C2–S1 region has water samples with moderate salinity and low alkali content, making it suitable for the growth of all moderately salt-tolerant crops.

According to data from the USSL chart, groundwater samples collected from the Shehong area have been categorized as having medium to high salinity and low sodium hazard. As a result, the groundwater in this area is suitable for irrigating most soils, with the exception of those with a low salt tolerance. This makes it relatively harmless. However, it may require special management of the groundwater salinity, and salt-tolerant crops should be selected for cultivation.

4. Discussion

4.1. Irrigation Water Quality Index (IWQI)

After conducting PCA on a set of physicochemical parameters, four principal components were obtained. The components with relatively high loadings were EC, Na^+, Cl^-, $HCO_3{}^-$, and SAR, indicating their importance in water quality assessment. Therefore, these five parameters were selected as the main parameters for calculating the IWQI. Table 2, established by Ayers and Westcot [71], defines key parameters for irrigation water, which have been identified by UCCC [61]. Table 4 lists the normalized weights for these selected parameters.

The results presented in Table 1 and Figure 12a show that the use of groundwater for irrigation in the study area has negative impacts on soil and crops at all levels. Moderate restriction was found in most groundwater samples (53.66%), while one sample showed high restriction, and another showed severe restriction.

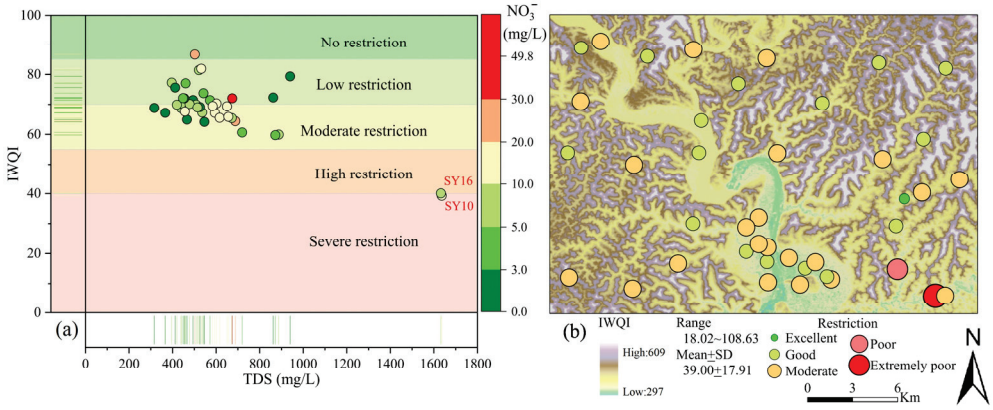

Figure 12. (**a**) Scatter plot of irrigation water quality index (IWQI) versus TDS. (**b**) Spatial distribution of groundwater quality for irrigation purposes based on IWQI.

According to Figure 11b, only 2.44% of the groundwater in the study area is categorized as unrestricted, meaning it can be used for most plants or crops without significant issues of alkali or salt damage to soils (as shown in Figure 10b,d). Approximately 39.02% of the groundwater is categorized as low-restriction irrigation water, suitable for use in irrigating soils with predominantly sandy texture and moderate permeability. However, it is not recommended to use this type of water for soils with heavy texture and high clay content as it may result in alkali damage. The predominant soil type in the study area is light-textured calcareous purple soil, which makes the groundwater suitable for irrigation without much concern about alkali damage. However, salt-sensitive plants are at an increased risk when using this water for irrigation. Approximately 53.66% of the groundwater samples are classified as moderately restricted irrigation water, making moderately salt-tolerant plants more suitable for cultivation in this region. In soils with favorable leaching conditions and moderate to high permeability, utilizing groundwater for irrigation is advised to prevent soil alkalinity from rising. Additionally, it is recommended to flush out soil salts when

using this groundwater for irrigation to avoid soil degradation. The study found that 4.88% of the groundwater in the area is classified as high-restriction irrigation groundwater due to the presence of one sample each of high and severe restriction types. This type of groundwater can only be used for soils with high permeability and no dense layer and is suitable only for plants with moderate to high salt tolerance.

The study reveals a decline in groundwater irrigation quality from the northwest to the southeast, which could be attributed to the topographical variation across the study area. The higher terrain in the northwest and lower terrain in the southeast may have led to the accumulation of salt and pollutants in the groundwater discharge region in the southeastern part of the study area. In addition, the study area includes the main urban area and industrial park of the study area, situated in the southern and southeastern parts, respectively. This may be a contributing factor to the observed trend of groundwater suitability for irrigation.

4.2. Irrigation Water Quality Assessment and Comments

This study utilized various indicators such as EC, SAR, Na%, RSC, PI, and IWQI to assess the appropriateness of groundwater in the study area of the Sichuan Basin as a source of irrigation water. The numerical values of each indicator were inputted into ArcGIS (10.8) software and the results were visualized through color-coded classifications for each sample, as shown in Figure 12. The study found that most of the groundwater in the area was suitable for irrigation when evaluated using SAR, Na%, RSC, and PI indicators. However, when EC and IWQI indicators were used, the quality of irrigation water decreased from northwest to southeast. The study found that groundwater in the northwest of the area was suitable for the irrigation of any crop and soil type. However, in the southeast, the groundwater was only suitable for crops with moderate to high salt tolerance and could only be used for soils with high permeability.

Therefore, rainwater collection systems can be constructed for agricultural irrigation to enhance crop productivity and prevent soil degradation in the study area. Additionally, it is suggested that artificial recharge techniques be implemented to combat high salinity and alkalinity in the region. When choosing an area for well irrigation, it is important to exercise caution and select an appropriate location. It is recommended to conduct groundwater extraction in the discharge area to improve the hydraulic gradient of groundwater and prevent salt accumulation. This can help to enhance the flow conditions of groundwater and ensure the success of the irrigation process [33,34,38,72]. To prevent soil degradation, it is essential to take measures to strengthen sewage treatment and reduce pollutant levels in the groundwater environment caused by human activities. Another important step is to adopt advanced irrigation methods such as sprinkler, micro-irrigation, and drip irrigation to minimize the impact of groundwater chemistry on soil. Lowering irrigation water pollution and soil degradation has the potential to improve crop yields and promote local economic development. To ensure the successful implementation of these methods, it is recommended to conduct an economic feasibility analysis within the current research field.

4.3. Entropy-Weighted Water Quality Index (EWQI)

In order to fully assess the quality of drinking water in the study area, 12 components, including cations, such as K^+, Na^+, Ca^{2+}, Mg^{2+}, and anions, such as Cl^-, $SO_4{}^{2-}$, $HCO_3{}^-$, $NO_3{}^-$, F^-, as well as pH, TDS, and TH (expressed as $CaCO_3$), were calculated using Equations (10)–(18) to obtain the EWQI. The study results, depicted in Figure 13, reveal that the groundwater quality in the area under investigation ranges from excellent to moderate. Notably, none of the samples indicated poor quality. A total of 97.56% of all samples (41 samples) were classified as level 1 or 2 (EWQI value < 100), and only one sample (SY05) was classified as level 3. The study found that the groundwater samples in levels 1 and 2 were safe for drinking, while the only the one remaining sample was not suitable [66,73]. However, it is worth noting that most of the groundwater samples analyzed in this study meet the quality requirements for drinking water.

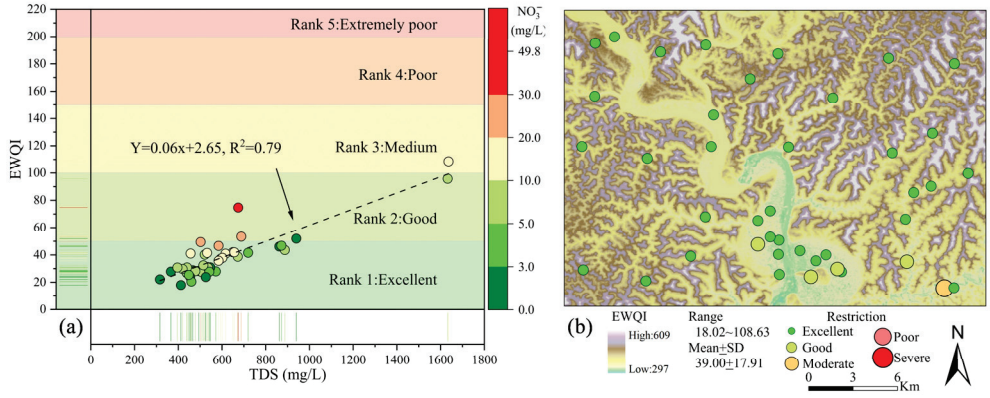

Figure 13. (**a**) Scatter plot of entropy-weighted water quality index (EWQI) versus TDS. (**b**) Spatial distribution of groundwater quality for drinking purposes based on EWQI.

In this study, the EWQI value and grade of groundwater samples in the study area were visualized using the interpolation method of geographic information system (GIS) and presented in Figure 13b. The figure shows that the quality of groundwater for drinking decreases from northwest to southeast in the study area. The study area depicts a decrease in groundwater quality for drinking from northwest to southeast. As a result, the groundwater in all regions except the southeast of the study area is suitable for direct use as a drinking water source. Nevertheless, it is imperative to focus on the industrial park of the study area, which is located in the southeast of the study area and improve the groundwater quality to ensure the well-being of local residents. The southeastern region has relatively high concentrations of NO_3^- and TDS, which contribute to high EWQI values. Figure 13a shows a strong positive correlation between TDS and EWQI values (Pearson correlation coefficient $R^2 = 0.79$). Additionally, higher nitrate concentrations are associated with higher EWQI values, as indicated by the point colors. Therefore, it can be concluded that the levels of NO_3^- and TDS have a significant impact on the EWQI values in the area. While the overall water quality in the study area is good, there are certain locations with poor quality drinking water. However, the severity of the situation is not alarming. Proper management and the treatment of groundwater can lead to significant improvements in the water quality of the area.

4.4. Potential Health Risk Assessment

The USEPA's health risk assessment model is commonly utilized to evaluate potential hazards [24,30]. In this study, nitrate pollution was chosen for a non-carcinogenic health risk assessment due to the prevalence of excessive nitrate concentrations in the study area's groundwater. Long-term ingestion of groundwater with high nitrate concentrations can pose several health risks to humans, such as methemoglobinemia or blue baby syndrome, esophageal and stomach cancers, and thyroid hypertrophy [24,30,41,74]. To evaluate the non-carcinogenic health hazards for various groups, including adults, children, and infants, hazard quotient (HQ) values were computed. Table 5 illustrates the statistical features of $HQ_{Nitrate}$ and cumulative non-carcinogenic risk (HI_{Total}) for each population group.

The HQ < 1 indicates that there is no potential non-carcinogenic health risk to humans [75]. Statistical analysis shows that the range of $HQ_{Nitrate}$ is between 0.00 and 1.29 and 0.00 and 1.54 for adult females and adult males, respectively. For children and infants, the range is between 0.00 and 1.80 and 0.00 and 2.91, respectively. The average $HQ_{Nitrate}$ values for adult females, adult males, children, and infants are 0.18, 0.22, 0.26, and 0.42, respectively. Notably, infants have the highest $HQ_{Nitrate}$ value among the four populations. In this study, the cumulative non-carcinogenic risks were found to range from 0.13 to 1.69 for adult females, 0.16 to 2.01 for adult males, 0.18 to 2.35 for children, and 0.30 to 3.8 for infants, with mean values of 0.42, 0.50, 0.58, and 0.94, respectively. Infants were found to have the highest health risk levels due to their sensitivity to nitrate poisoning and less

developed enzyme metabolism, making them more susceptible to the harmful effects of nitrates from external sources [41,76].

Table 5. Statistics of health risks assessment results through drinking water intake.

Classification	Population	Max	Min	Mean	SD
$HQ_{Nitrate}$	Infants	2.91	0.00	0.42	0.49
	Children	1.80	0.00	0.26	0.31
	Females	1.29	0.00	0.18	0.22
	Males	1.54	0.00	0.22	0.26
HI_{Total}	Infants	3.80	0.30	0.94	0.60
	Children	2.35	0.18	0.58	0.37
	Females	1.69	0.13	0.42	0.27
	Males	2.01	0.16	0.50	0.32

Note: SD standard deviation.

This study utilized Monte Carlo simulation methods to evaluate the potential non-carcinogenic health hazards associated with drinking water in the area under investigation for various population groups, including infants, children, adult males, and adult females. Figure 14 displays the cumulative probability distribution of the potential non-cancerous health risks. Moreover, the 95th percentile is commonly used to ascertain whether the health risk of the indicator surpasses the acceptable limit for different populations, with the aim of mitigating the impact of extreme values on the assessment [76].

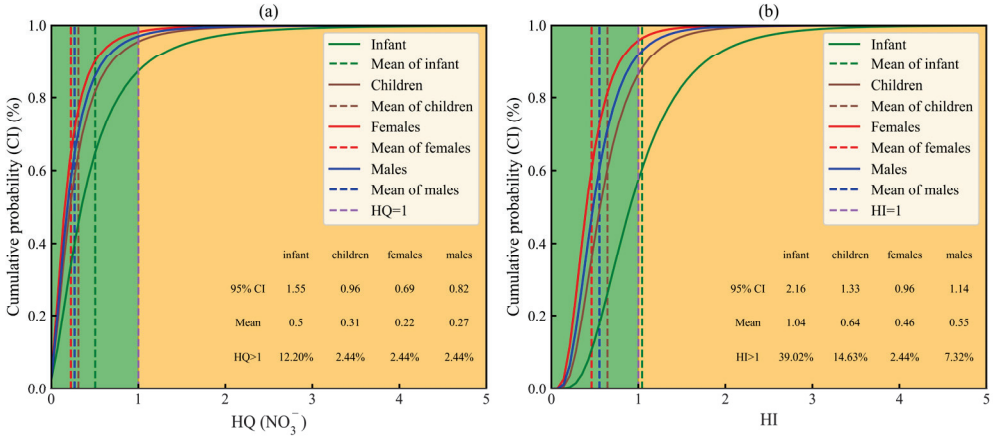

Figure 14. Cumulative probability distribution curves: (**a**) Non-carcinogenic health risk of nitrate, $HQ_{Nitrate}$; (**b**) Cumulative non-carcinogenic health risk, HI_{Total}; Vertical dashed lines indicate mean.

According to Figure 14, the 95% confidence interval for $HQ_{Nitrate}$ is greater than 1 for infants at 1.55. However, for children, adult males, and adult females, the 95% confidence interval for $HQ_{Nitrate}$ is less than 1 at 0.96, 0.82, and 0.69, respectively. The study found that NO_3^- poses the greatest non-carcinogenic health risk to infants in the area, with decreasing effects observed in children, adult males, and adult females. The cumulative non-carcinogenic health risks across the four populations followed a similar pattern to that of NO_3^-.

To better comprehend the distribution of non-carcinogenic health hazards among various populations in the study area, the cumulative non-carcinogenic health risks were interpolated and presented in Figure 15. The sample points in the study area were categorized into different colors based on whether the HI_{Total} of different groups exceeded 1. The red color in the figure indicates a higher level of health risk.

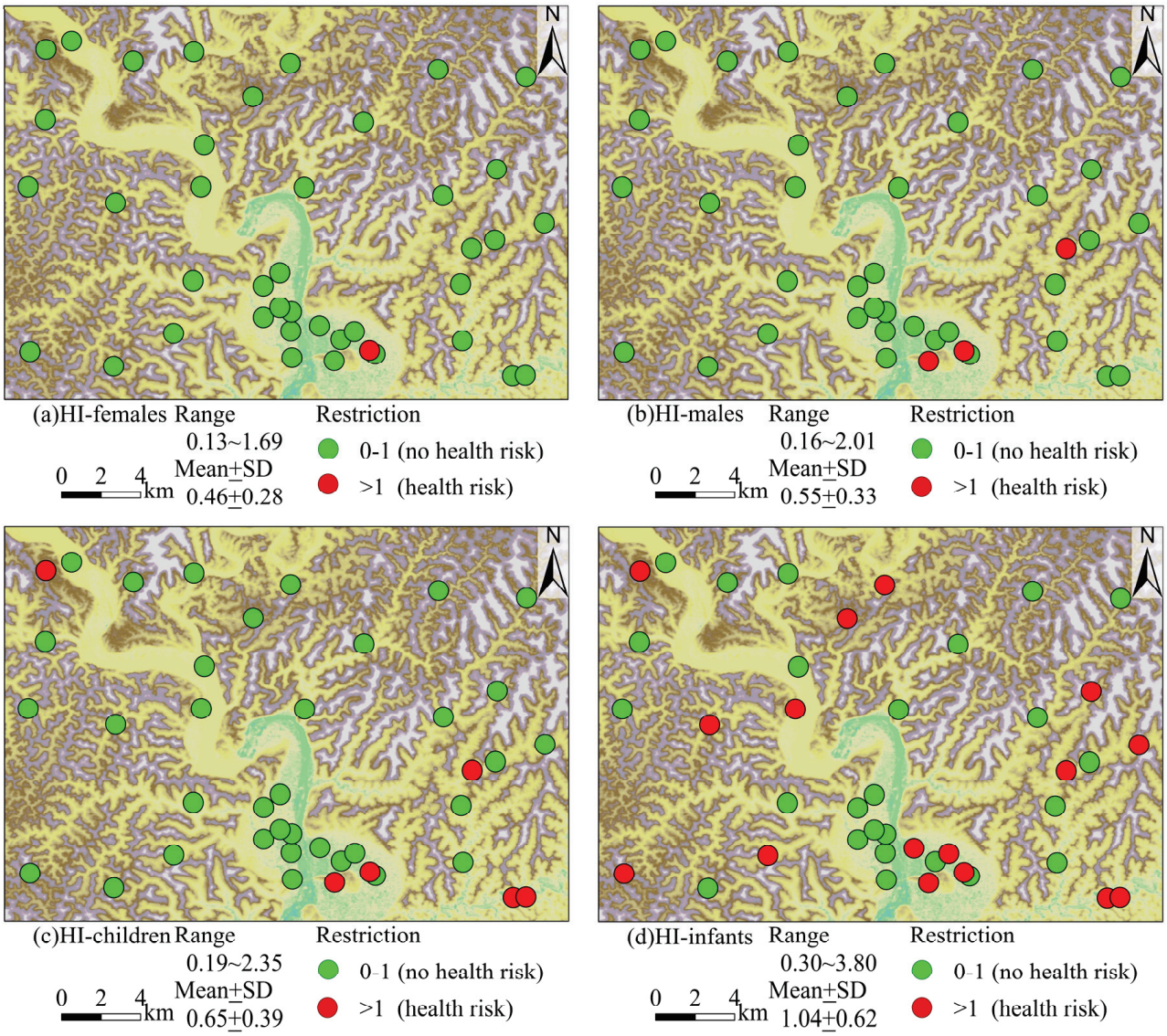

Figure 15. Spatial distribution of the HI_{Total} of noncarcinogenic risk due to nitrate through drinking water pathway for (**a**) adult females, (**b**) adult males, (**c**) children, and (**d**) infants in the study area.

The findings in Figure 15 indicate that infants are at a higher health risk compared to adult females, adult males, and children. Furthermore, the results show that males have a greater health risk than females under similar conditions. The study found that areas with a higher HI_{Total} for infants were prevalent throughout the study area, while those for the other three population groups were more sporadic and located in the southwest. This suggests that the health risks associated with NO_3^- are most severe for infants in the study area, and that the risk increases as one moves closer to the southeast of the study area. The proportion of groundwater samples with cumulative non-carcinogenic risk values greater than 1 is highest in infants at 39.02%, followed by children at 14.63%, adult males at 7.32%, and adult females at 2.43%. The study revealed that infants had the highest non-carcinogenic health risk compared to the other populations analyzed. The HI_{Total} values for infants were almost 16.04, 5.33, and 2.67 times higher than adult females, adult males, and children, respectively. This emphasizes the urgency to take immediate action to decrease nitrate concentrations in groundwater sources in the study area.

Based on the study, it can be concluded that the potential health risk associated with excessive NO_3^- concentration is higher in infants and children as compared to adult males and females. The sources of this excessive concentration are mainly urban sewage

and agricultural pollution. To mitigate human health risks caused by NO_3^-, specific measures will be implemented to enhance the quality control of sewage discharge in the industrial new area located in the southwest of the study area. Additionally, the pollution of groundwater from agricultural activities will be addressed by reducing the usage of nitrogen fertilizer and implementing changes in irrigation methods. It should be noted that the adverse effects of nitrate pollution on human health are not limited to the study area and can be a global concern. To mitigate nitrate pollution in groundwater sources, it is imperative for governments and relevant agencies to implement effective monitoring and control measures, particularly in regions where groundwater serves as a primary source of drinking water. Furthermore, it is recommended that health education programs be established to increase awareness of the potential health hazards linked to nitrate pollution in drinking water, particularly among vulnerable populations, such as infants.

5. Conclusions

The main findings of the study are as follows:

1. The groundwater samples have a weakly alkaline nature with low to moderate mineralization and are categorized as HCO_3-Ca type. On average, the cation content is in the order of $Ca^{2+} > Na^+ > Mg^{2+} > K^+$, while the anion content is in the order of $HCO_3^- > SO_4^{2-} > Cl^- > NO_3^- > F^-$. With the exception of NO_3^-, the ion concentrations in almost all samples were within the permissible limits for drinking purposes.
2. The groundwater's major ion sources were found to be primarily from the dissolution of carbonate and silicate rocks, as indicated by principal component analysis, major ion ratios, and mineral saturation index. This process is related to cation exchange. The elevated levels of nitrate in the area are mainly attributed to agricultural activities and urban sewage.
3. Based on the analysis of single irrigation indicators, such as the SAR, Na%, RSC, and PI, it can be concluded that most of the groundwater in the study area is suitable for irrigation purposes. The results of the IWQI study indicate that almost 50% of the groundwater in the area is classified as low to unrestricted when used for irrigation. The EWQI results suggest that except for one groundwater sample, all samples are suitable for drinking water. Additionally, the study found that the groundwater quality for both drinking and irrigation purposes follows a similar trend, decreasing from the northwest to the southeast of the study area. The utilization of groundwater resources should be noticed in the southeastern part.
4. According to the health risk analysis, the risk level for infants is higher than that for children, adult males, and females. To reduce health risks for different groups of people, it is recommended to implement differentiated water supply and targeted water treatment, especially giving more attention to infants.

Author Contributions: Y.W.; writing—original draft preparation, methodology, software, R.L.; data curation, software, X.W.; formal analysis, validation, Y.Y.; data curation, C.W.; funding acquisition, M.L.; investigation, Y.X.; validation, Y.Z.; writing—review and editing, funding acquisition. All authors have read and agreed to the published version of the manuscript.

Funding: This research was funded by Scientific project of Yibin City (SWJTU2021020008).

Data Availability Statement: The data presented in this study are available on request from the corresponding author.

Acknowledgments: We thank two anonymous reviewers for their constructive suggestions which improved our manuscript.

Conflicts of Interest: The authors declare no conflict of interest.

References

1. Abbasnia, A.; Yousefi, N.; Mahvi, A.H.; Nabizadeh, R.; Radfard, M.; Yousefi, M.; Alimohammadi, M. Evaluation of Groundwater Quality Using Water Quality Index and Its Suitability for Assessing Water for Drinking and Irrigation Purposes: Case Study of Sistan and Baluchistan Province (Iran). *Hum. Ecol. Risk Assess. Int. J.* **2018**, *25*, 988–1005. [CrossRef]
2. Nyakundi, R.; Nyadawa, M.; Mwangi, J. Effect of Recharge and Abstraction on Groundwater Levels. *Civ. Eng. J.* **2022**, *8*, 910–925. [CrossRef]
3. Chomba, I.C.; Banda, K.E.; Winsemius, H.C.; Eunice, M.; Sichingabula, H.M.; Nyambe, I.A. Integrated Hydrologic-Hydrodynamic Inundation Modeling in a Groundwater Dependent Tropical Floodplain. *J. Hum. Earth Future* **2022**, *3*, 237–246. [CrossRef]
4. Basack, S.; Goswami, G.; Khabbaz, H.; Karakouzian, M. Flow Characteristics through Granular Soil Influenced by Saline Water Intrusion: A Laboratory Investigation. *Civ. Eng. J.* **2022**, *8*, 863–878. [CrossRef]
5. Mukherjee, I.; Singh, U.K. Groundwater Fluoride Contamination, Probable Release, and Containment Mechanisms: A Review on Indian Context. *Environ. Geochem. Health* **2018**, *40*, 2259–2301. [CrossRef]
6. Al-Mussawi, W. Assessment of Groundwater Quality in UMM ER Radhuma Aquifer (Iraqi Western Desert) by Integration Between Irrigation Water Quality Index and GIS. *J. Babylon Univ. Eng. Sci.* **2014**, *22*, 201–217.
7. Pandey, K.; Kumar, S.; Malik, A.; Kuriqi, A. Artificial Neural Network Optimized with a Genetic Algorithm for Seasonal Groundwater Table Depth Prediction in Uttar Pradesh, India. *Sustainability* **2020**, *12*, 8932. [CrossRef]
8. Ahmed, I.; Tariq, N.; Al Muhery, A. Hydrochemical Characterization of Groundwater to Align with Sustainable Development Goals in the Emirate of Dubai, UAE. *Environ. Earth Sci.* **2019**, *78*, 44. [CrossRef]
9. Jwa, B.; Yza, B.; Hui, Z. Groundwater Chemistry and Groundwater Quality Index Incorporating Health Risk Weighting in Dingbian County, Ordos Basin of Northwest China. *Geochemistry* **2020**, *80*, 125607. [CrossRef]
10. Mohammadi, A.; Ebrahimi, A.A.; Ghanbari, R.; Faraji, M.; Nemati, S.; Abdolahnejad, A. Data on THMs Concentration and Spatial Trend in Water Distribution Network (a Preliminary Study in Center of Iran). *MethodsX* **2019**, *6*, 760–763. [CrossRef]
11. Siddiqi, S.A.; Al-Mamun, A.; Baawain, M.S.; Sana, A. Groundwater Contamination in the Gulf Cooperation Council (GCC) Countries: A Review. *Environ. Sci. Pollut. Res.* **2021**, *28*, 21023–21044. [CrossRef]
12. Alexakis, D.E.; Kiskira, K.; Gamvroula, D.; Emmanouil, C.; Psomopoulos, C.S. Evaluating Toxic Element Contamination Sources in Groundwater Bodies of Two Mediterranean Sites. *Environ. Sci. Pollut. Res.* **2021**, *28*, 34400–34409. [CrossRef]
13. Kafilat Adebola, B.-A.; Joseph Kayode, S.; Adebayo Akeem, O. Integrated Assessment of the Heavy Metal Pollution Status and Potential Ecological Risk in the Lagos Lagoon, South West, Nigeria. *Hum. Ecol. Risk Assess. Int. J.* **2018**, *24*, 377–397. [CrossRef]
14. Mukherjee, I.; Singh, U.K. Assessment of Fluoride Contaminated Groundwater on Food Crops and Vegetables in Birbhum District of West Bengal, India. In *Advance Technologies in Agriculture for Doubling Farmer's Income*; New Delhi Publishers: New Delhi, India, 2018; pp. 225–235. ISBN 978-93-86453-61-7.
15. Adimalla, N.; Qian, H. Groundwater Quality Evaluation Using Water Quality Index (WQI) for Drinking Purposes and Human Health Risk (HHR) Assessment in an Agricultural Region of Nanganur, South India. *Ecotoxicol. Environ. Saf.* **2019**, *176*, 153–161. [CrossRef]
16. Yousefi, M.; Ghoochani, M.; Hossein Mahvi, A. Health Risk Assessment to Fluoride in Drinking Water of Rural Residents Living in the Poldasht City, Northwest of Iran. *Ecotoxicol. Environ. Saf.* **2018**, *148*, 426–430. [CrossRef]
17. Liu, Y.; Hu, G.; Cao, L.; Wang, X.; Chen, M.-H. A Comparison of Monte Carlo Methods for Computing Marginal Likelihoods of Item Response Theory Models. *J. Korean Stat. Soc.* **2019**, *48*, 503–512. [CrossRef]
18. Rahmati, O.; Pourghasemi, H.R.; Melesse, A.M. Application of GIS-Based Data Driven Random Forest and Maximum Entropy Models for Groundwater Potential Mapping: A Case Study at Mehran Region, Iran. *Catena* **2016**, *137*, 360–372. [CrossRef]
19. Arumugam, K.; Elangovan, K. Hydrochemical Characteristics and Groundwater Quality Assessment in Tirupur Region, Coimbatore District, Tamil Nadu, India. *Environ. Geol.* **2009**, *58*, 1509–1520. [CrossRef]
20. Kopittke, P.M.; So, H.B.; Menzies, N.W. Effect of Ionic Strength and Clay Mineralogy on Na–Ca Exchange and the SAR–ESP Relationship. *Eur. J. Soil Sci.* **2006**, *57*, 626–633. [CrossRef]
21. Saleh, A.; Al-Ruwaih, F.; Shehata, M. Hydrogeochemical Processes Operating within the Main Aquifers of Kuwait. *J. Arid Environ.* **1999**, *42*, 195–209. [CrossRef]
22. Wang, L.; Long, F.; Liao, W.; Liu, H. Prediction of Anaerobic Digestion Performance and Identification of Critical Operational Parameters Using Machine Learning Algorithms. *Bioresour. Technol.* **2020**, *298*, 122495. [CrossRef]
23. Paliwal, K.V.; Heine, R.W. Irrigation with Saline Water. *Q. Rev. Biol.* **1972**, *4*, 198. [CrossRef]
24. Spandana, M.P.; Suresh, K.R.; Prathima, B. Developing an irrigation water quality index for vrishabavathi command area. *Int. J. Eng. Res. Technol.* **2013**, *2*, 821–830.
25. Meireles, A.C.M.; de Andrade, E.M.; Chaves, L.C.G.; Frischkorn, H.; Crisostomo, L.A. A New Proposal of the Classification of Irrigation Water. *Rev. Ciênc. Agron.* **2010**, *41*, 349–357. [CrossRef]
26. Xiao, Y.; Xiao, D.; Hao, Q.; Liu, K.; Wang, R.; Huang, X.; Liao, X.; Zhang, Y. Accessible Phreatic Groundwater Resources in the Central Shijiazhuang of North China Plain: Perspective From the Hydrogeochemical Constraints. *Front. Environ. Sci.* **2021**, *9*, 475. [CrossRef]
27. Zhang, Y.; Dai, Y.; Wang, Y.; Huang, X.; Xiao, Y.; Pei, Q. Hydrochemistry, Quality and Potential Health Risk Appraisal of Nitrate Enriched Groundwater in the Nanchong Area, Southwestern China. *Sci. Total Environ.* **2021**, *784*, 147186. [CrossRef] [PubMed]

28. Zhang, Q.; Wang, H.; Wang, L. Tracing Nitrate Pollution Sources and Transformations in the Over-Exploited Groundwater Region of North China Using Stable Isotopes. *J. Contam. Hydrol.* **2018**, *218*, 1–9. [CrossRef] [PubMed]
29. Yao, R.; Yan, Y.; Wei, C.; Luo, M.; Xiao, Y.; Zhang, Y. Hydrochemical Characteristics and Groundwater Quality Assessment Using an Integrated Approach of the PCA, SOM, and Fuzzy c-Means Clustering: A Case Study in the Northern Sichuan Basin. *Front. Environ. Sci.* **2022**, *10*, 907872. [CrossRef]
30. Zhang, Y.; He, Z.; Tian, H.; Huang, X.; Zhang, Z.; Liu, Y.; Xiao, Y.; Li, R. Hydrochemistry Appraisal, Quality Assessment and Health Risk Evaluation of Shallow Groundwater in the Mianyang Area of Sichuan Basin, Southwestern China. *Environ. Earth Sci.* **2021**, *80*, 576. [CrossRef]
31. Zhang, T.; Chen, X.; Jiang, Z.; Lan, G. Characteristics and influencing factors of groundwater in the red layer area of Sichuan basin—A case study of Nanchong city. *Acta Geol. Sichuan* **2005**, *2*, 97–100. (In Chinese)
32. Feng, W.; Fang, H.; Li, Y.; Bai, H. Hydrochemical Characteristics and Water Quality Evaluation of Shallow Groundwater in Red-Layer Area. *Water Power* **2020**, *46*, 12–16+84. (In Chinese)
33. Shi, Z. Environmental Problems of Water Resources and Sustainable Development Management in Sichuan. *Guangdong Sci. Technol.* **2014**, *23*, 90–91. (In Chinese)
34. He, X.; Long, X. Current Situation and Countermeasures of Agricultural Non-point Source Pollution in Suining City. *Sichuan Agric. Sci. Technol.* **2021**, *4*, 81–83. (In Chinese)
35. Luo, S.; Ceng, F.; Yang, H. Analysis and reflection on the current situation of the construction of comprehensive agricultural development projects in Shehong County. *Sichuan Agric. Sci. Technol.* **2014**, *7*, 52–53. (In Chinese)
36. Ceng, S.; Xu, M.; Luo, M.; Yang, Y.; Huang, S. Analysis of hydrochemical characteristics and main ion sources of red-bed groundwater in Suining area, central Sichuan. *Resour. Environ. Yangtze Basin* **2020**, *29*, 220–231. (In Chinese)
37. Ni, J.; Yang, C.; Wu, Y. Evaluation Research on the Forestland Quality Rank of Shehong County Based on GIS. *J. Sichuan For. Sci. Technol.* **2014**, *35*, 57–61. (In Chinese) [CrossRef]
38. Zhou, S.; Tang, F. Practice and Research on Water Pollution Control of Mingyue River in Suining City, Sichuan Province. *China Flood Drought Manag.* **2017**, *27*, 88–89+96. (In Chinese) [CrossRef]
39. Deutsch, W.J. *Groundwater Geochemistry: Fundamentals and Applications to Contamination*; Lewis Publishers: Boca Raton, FL, USA, 1997.
40. Li, P.; Tian, R.; Liu, R. Solute Geochemistry and Multivariate Analysis of Water Quality in the Guohua Phosphorite Mine, Guizhou Province, China. *Expo. Health* **2019**, *11*, 81–94. [CrossRef]
41. Wu, J.; Li, P.; Qian, H.; Duan, Z.; Zhang, X. Using Correlation and Multivariate Statistical Analysis to Identify Hydrogeochemical Processes Affecting the Major Ion Chemistry of Waters: A Case Study in Laoheba Phosphorite Mine in Sichuan, China. *Arab. J. Geosci* **2014**, *7*, 3973–3982. [CrossRef]
42. Wu, J.; Li, P.; Wang, D.; Ren, X.; Wei, M. Statistical and Multivariate Statistical Techniques to Trace the Sources and Affecting Factors of Groundwater Pollution in a Rapidly Growing City on the Chinese Loess Plateau. *Hum. Ecol. Risk Assess. Int. J.* **2020**, *26*, 1603–1621. [CrossRef]
43. Sudheer Kumar, M.; Dhakate, R.; Yadagiri, G.; Srinivasa Reddy, K. Principal Component and Multivariate Statistical Approach for Evaluation of Hydrochemical Characterization of Fluoride-Rich Groundwater of Shaslar Vagu Watershed, Nalgonda District, India. *Arab. J. Geosci.* **2017**, *10*, 83. [CrossRef]
44. Zhang, X.; Guo, Q.; Liu, M.; Luo, J.; Yin, Z.; Zhang, C.; Zhu, M.; Guo, W.; Li, J.; Zhou, C. Hydrogeochemical Processes Occurring in the Hydrothermal Systems of the Gonghe–Guide Basin, Northwestern China: Critical Insights from a Principal Components Analysis (PCA). *Environ. Earth Sci.* **2016**, *75*, 1187. [CrossRef]
45. Kaiser, H.F. The Varimax Criterion for Analytic Rotation in Factor Analysis. *Educ. Psychol. Meas.* **1958**, *23*, 770–773. [CrossRef]
46. Bahrami, M.; Zarei, A.R.; Rostami, F. Temporal and Spatial Assessment of Groundwater Contamination with Nitrate by Nitrate Pollution Index (NPI) and GIS (Case Study: Fasarud Plain, Southern Iran). *Environ. Geochem. Health* **2020**, *42*, 3119–3130. [CrossRef]
47. Spalding, R.F.; Exner, M.E. Occurrence of Nitrate in Groundwater—A Review. *J. Environ. Qual.* **1993**, *22*, 392–402. [CrossRef]
48. El Mountassir, O.; Bahir, M.; Ouazar, D.; Chehbouni, A.; Carreira, P.M. Temporal and Spatial Assessment of Groundwater Contamination with Nitrate Using Nitrate Pollution Index (NPI), Groundwater Pollution Index (GPI), and GIS (Case Study: Essaouira Basin, Morocco). *Environ. Sci. Pollut. Res.* **2022**, *29*, 17132–17149. [CrossRef]
49. Todd, D.K.; Mays, L.W. *Groundwater Hydrology*, 2nd ed.; John Wiley & Sons: Hoboken, NJ, USA, 1980.
50. Eaton; Frank, M. Significance of Carbonates in Irrigation Waters. *Soil Sci.* **1950**, *69*, 123–134. [CrossRef]
51. Osta, M.E.; Masoud, M.; Alqarawy, A.; Elsayed, S.; Gad, M. Groundwater Suitability for Drinking and Irrigation Using Water Quality Indices and Multivariate Modeling in Makkah Al-Mukarramah Province, Saudi Arabia. *Water* **2022**, *14*, 483. [CrossRef]
52. Ayers, R.S.; Westcot, D.W. *The Water Quality in Agriculture*, 2nd ed.; Campina Grande: UFPB. (Studies FAO Irrigation and drainage, 29); Food and Agriculture Organization: Rome, Italy, 1999.
53. Luo, Y.; Xiao, Y.; Hao, Q.; Zhang, Y.; Dong, G. Groundwater Geochemical Signatures and Implication for Sustainable Development in a Typical Endorheic Watershed on Tibetan Plateau. *Environ. Sci. Pollut. Res.* **2021**, *28*, 48312–48329. [CrossRef] [PubMed]
54. Means, B. *Risk-Assessment Guidance for Superfund. Volume 1. Human Health Evaluation Manual. Part A. Interim Report (Final)*; Environmental Protection Agency: Washington, DC, USA, 1989.

55. He, X.; Wu, J.; He, S. Hydrochemical Characteristics and Quality Evaluation of Groundwater in Terms of Health Risks in Luohe Aquifer in Wuqi County of the Chinese Loess Plateau, Northwest China. *Hum. Ecol. Risk Assess. Int. J.* **2019**, *25*, 32–51. [CrossRef]
56. Bawa-Allah, K.A. Assessment of Heavy Metal Pollution in Nigerian Surface Freshwaters and Sediment: A Meta-Analysis Using Ecological and Human Health Risk Indices. *J. Contam. Hydrol.* **2023**, *256*, 104199. [CrossRef] [PubMed]
57. Alexakis, D. Human Health Risk Assessment Associated with Co, Cr, Mn, Ni and V Contents in Agricultural Soils from a Mediterranean Site. *Arch. Agron. Soil Sci.* **2016**, *62*, 359–373. [CrossRef]
58. World Health Organization. *Guidelines for Drinking-Water Quality*, 4th ed.; World Health Organisation: Geneva, Switzerland, 2011.
59. *GB/T 14848–2017*; Gaqs. Standards for Groundwater Quality. General Administration of Quality Supervision: Beijing, China, 2017. (In Chinese)
60. Piper, A. A Graphic Procedure in the Geochemical Interpretation of Water-Analyses. *Eos Trans. Am. Geophys. Union* **1944**, *25*, 914–923. [CrossRef]
61. Mukherjee, I.; Singh, U.K.; Chakma, S. Evaluation of Groundwater Quality for Irrigation Water Supply Using Multi-Criteria Decision-Making Techniques and GIS in an Agroeconomic Tract of Lower Ganga Basin, India. *J. Environ. Manage.* **2022**, *309*, 114691. [CrossRef]
62. Abbasnia, A.; Radfard, M.; Mahvi, A.H.; Nabizadeh, R.; Yousefi, M.; Soleimani, H.; Alimohammadi, M. Groundwater Quality Assessment for Irrigation Purposes Based on Irrigation Water Quality Index and Its Zoning with GIS in the Villages of Chabahar, Sistan and Baluchistan, Iran. *Data Brief* **2018**, *19*, 623–631. [CrossRef]
63. Feth, J.H.; Gibbs, R.J. Mechanisms Controlling World Water Chemistry: Evaporation-Crystallization Process. *Science* **1971**, *172*, 870–872. [CrossRef]
64. Ren, X.; Li, P.; He, X.; Su, F.; Elumalai, V. Hydrogeochemical Processes Affecting Groundwater Chemistry in the Central Part of the Guanzhong Basin, China. *Arch. Environ. Contam. Toxicol.* **2021**, *80*, 74–91. [CrossRef]
65. Nesco, U. Groundwater studies. An international guide for research and practice. In *Geochemistry of Groundwater*; UNESCO: Paris, France, 1977.
66. Adimalla, N. Application of the Entropy Weighted Water Quality Index (EWQI) and the Pollution Index of Groundwater (PIG) to Assess Groundwater Quality for Drinking Purposes: A Case Study in a Rural Area of Telangana State, India. *Arch. Environ. Contam. Toxicol.* **2021**, *80*, 31–40. [CrossRef]
67. Adimalla, N.; Qian, H. Groundwater Chemistry, Distribution and Potential Health Risk Appraisal of Nitrate Enriched Groundwater: A Case Study from the Semi-Urban Region of South India. *Ecotoxicol. Environ. Saf.* **2021**, *207*, 111277. [CrossRef]
68. Zhou, Y.; Li, P.; Xue, L.; Dong, Z.; Li, D. Solute Geochemistry and Groundwater Quality for Drinking and Irrigation Purposes: A Case Study in Xinle City, North China. *Geochemistry* **2020**, *80*, 125609. [CrossRef]
69. Reeve, R.C.; Pillsbury, A.F.; Wilcox, L.V. Reclamation of a Saline and High Boron Soil in the Coachella Valley of California. *Hilgardia* **1955**, *24*, 4. [CrossRef]
70. Richards, L.A. Diagnosis and Improvement of Saline and Alkali Soils. *Soil Sci.* **1954**, *64*, 290. [CrossRef]
71. Bastiaanssen, W.; Loehr, R.A.; Ayers, C.R.; Westcot, D.W.; Barriuso, E.; Calvet, R.; Schiavon, M.; Soulas, G.; Gates, D.; Carvalho, D. *Methods of Chemical Analysis of Water and Wastes*; CRC Press: Boca Raton, FL, USA, 1999.
72. Shu, L.; Zhang, Z.; Lv, J. Ecological environment monitoring and water quality pollution status evaluation of Suining section of Fujiang River Basin. *Sichuan Environ.* **2013**, *32*, 49–53. (In Chinese) [CrossRef]
73. Amiri, V.; Rezaei, M.; Sohrabi, N. Groundwater Quality Assessment Using Entropy Weighted Water Quality Index (EWQI) in Lenjanat, Iran. *Environ. Earth Sci.* **2014**, *72*, 3479–3490. [CrossRef]
74. Xiao, Y.; Liu, K.; Hao, Q.; Xiao, D.; Zhu, Y.; Yin, S.; Zhang, Y. Hydrogeochemical Insights into the Signatures, Genesis and Sustainable Perspective of Nitrate Enriched Groundwater in the Piedmont of Hutuo Watershed, China. *Catena* **2022**, *212*, 106020. [CrossRef]
75. Ravindra, K.; Mor, S. Distribution and Health Risk Assessment of Arsenic and Selected Heavy Metals in Groundwater of Chandigarh, India. *Environ. Pollut.* **2019**, *250*, 820–830. [CrossRef] [PubMed]
76. Naa, B.; Hui, Q.; Pla, B. Entropy Water Quality Index and Probabilistic Health Risk Assessment from Geochemistry of Groundwaters in Hard Rock Terrain of Nanganur County, South India. *Geochemistry* **2019**, *80*, 125544. [CrossRef]

Disclaimer/Publisher's Note: The statements, opinions and data contained in all publications are solely those of the individual author(s) and contributor(s) and not of MDPI and/or the editor(s). MDPI and/or the editor(s) disclaim responsibility for any injury to people or property resulting from any ideas, methods, instructions or products referred to in the content.

water

MDPI

Article

Spatial Optimization of the Groundwater Quality Monitoring Network in the Kingdom of Bahrain

Waleed Al-Zubari *, Ali Al-Shaabani and Nadir Abdulhameid

Department of Natural Resources and Environment, College of Graduate Studies, Arabian Gulf University, Manama P.O. Box 26671, Bahrain; alshabanali@gmail.com (A.A.-S.); nadiragu@gmail.com (N.A.)
* Correspondence: waleed@agu.edu.bh; Tel.: +973-17239880

Abstract: Groundwater resource development, management, and planning essentially rely on their quantitative and qualitative monitoring. The information obtained from the monitoring networks of a given groundwater resource is used as a significant indicator for the status of that resource, and management schemes are subsequently made in order to develop and utilize this resource on a sustainable basis. In this study, the performance of the existing monitoring network of the quality of groundwater in Bahrain was evaluated and was spatially optimized using the geostatistical method of kriging. The estimation variance was used as a criterium in the design process, and variance reduction was used to measure the network performance. The process resulted in an increase in the number of observation points from 15 currently monitored wells to 91 wells, with 74% of these being augmented industrial and commercial wells that were to be self-reported to internalize the cost of groundwater management in their users. It is recommended that temporal optimization procedures for the groundwater level are conducted and that monitored groundwater quality data are stored in a dedicated groundwater management information system (MIS) along with the monitored data of groundwater levels and abstraction to effectively support the process of decision making for groundwater planning and management.

Keywords: geostatistics; GIS; kriging; cost effectiveness; Dammam aquifer; Khobar aquifer zone; self-reporting

1. Introduction

Groundwater monitoring and data acquisition are pre-requisites for the effective management of groundwater resources. Monitoring makes the invisible groundwater visible. The main indicators used in groundwater development, management, and planning are groundwater levels and groundwater quality (e.g., salinity). These two "state variables" are used as indicators for the status of a groundwater resource and reflect the balance between its discharges (e.g., wells, springs, and evapotranspiration) and recharges (e.g., natural or artificial).

Groundwater monitoring is one of the most important tools in groundwater management. In the absence of monitoring, groundwater abstraction and waste disposal would take place without any safeguard for the groundwater resource, and the excessive use and contamination of an aquifer may continue unchecked for years until that groundwater resource is effectively deteriorated and lost. Therefore, the objective of monitoring is to reveal the changes taking place in the groundwater resource over time, and it thereby allows managers to introduce management interventions and restrictions to minimize the negative effect of these impacts. The continued collection of monitoring data allows groundwater managers to measure the effectiveness of these restrictions and their modifications if necessary. Moreover, the continuous monitoring of groundwater is essential to provide historical data that are essential for calibrating groundwater simulation models and that allow reliable simulations of future development and management scenarios [1].

Furthermore, the information obtained from monitoring groundwater resources can play a key role in increasing awareness among water users and stakeholders, and it thus facilitates the introduction of required groundwater demand management measures and aids their participation in groundwater management. In fact, as an awareness tool, the monitoring of groundwater can also lead to participatory self-monitoring, which helps reduce the costs to the water authorities [2].

The design and operation of any groundwater monitoring system needs to be carefully planned and designed so that relevant and useful information for management purposes can be obtained in a sustainable and "cost-effective" manner. In other words, monitoring networks need to be designed to have an optimal configuration, spatially and temporally, that would meet the groundwater management objectives by providing the required information more effectively and efficiently than any other configuration. Otherwise, there will be an inefficient use of the workforce and budget. Therefore, designing a monitoring network becomes an optimization exercise that aims at maximizing the usefulness of the information obtained from the network and the cost incurred in data collection within a set of constraints.

Data collection implies "use" and "worth" for those data, and usually the first data collected contain the most information and have the most worth. Hence, as more data are collected, their marginal worth decreases. However, their marginal cost does not. In this case, an optimal network design would have a configuration that either (1) has the maximum worth of a given budget or (2) has a design such that the marginal worth of the data is equal to their marginal cost. However, while the cost of data collection can be easily obtained for a given observation point in the monitoring network (i.e., the cost of well construction, installing equipment, and lab analysis), the worth of the data for this point is difficult to assess in economic terms. To overcome this difficulty in measuring data worth, surrogates to worth in the form of the measure of accuracy have been developed [3]. Examples of the measure of accuracy that are widely used as surrogates to data worth are the average and maximum errors within a network [4].

Groundwater observation networks, for the groundwater level and quality, are examples of the discontinuous sampling of variables having spatial continuity, i.e., a continuous non-discrete function. The measurement of these state variables at a number of selected points—that constitute the monitoring network—is used to interpolate the variable values in the whole aquifer domain at the unknown points (i.e., non-measurement points). The interpolation of the variable is typically produced in the form of a contour map from which spatial and temporal trends are concluded. One of the most widely applied methods for interpolation is the geostatistical suite of methods of which the most widely used method is kriging interpolation. These methods are used to compute the spatial distribution of the variable based on the existing observation points, and, more importantly, they determine the accuracy of the interpolated distribution. It is this last characteristic of the geostatistical methods that makes them widely applied in optimal network design [5]. The accuracy of the interpolation of the variables in the aquifer domain of interest, measured in the form of the variance in the estimation, is used as an indicator for the optimal sampling locations, and variance reduction is used as a measure of the network performance by computing the change in the estimation variance resulting from adding a fictitious (proposed) sample [6]. The average and the maximum variance within the network are used to dynamically improve the network sampling efficiency. The objective is to obtain a network, which provides a minimum variance estimate of the areal mean from a fixed number of sample stations [7].

The Kingdom of Bahrain is a small island developing state (SIDS) located in the Arabian Gulf (Figure 1). Its groundwater is developed in the Dammam Formation, which forms a small part of the extensive regional aquifer system, termed the Eastern Arabian Aquifer, extending from central Saudi Arabia, where the main recharge area of the aquifer is located in the shores of the Arabian Gulf, including Bahrain. The recharging of the groundwater in Bahrain occurs through the lateral underflow from Eastern Saudi Arabia [8]. Locally, the groundwater system in Bahrain consists of two zones: the Alat aquifer zone

and the Khobar aquifer zone. The Khobar aquifer zone is developed in highly fractured limestones and dolomites and is the principal aquifer in Bahrain. The aquifer provides the majority of groundwater abstraction and is the focus of this research.

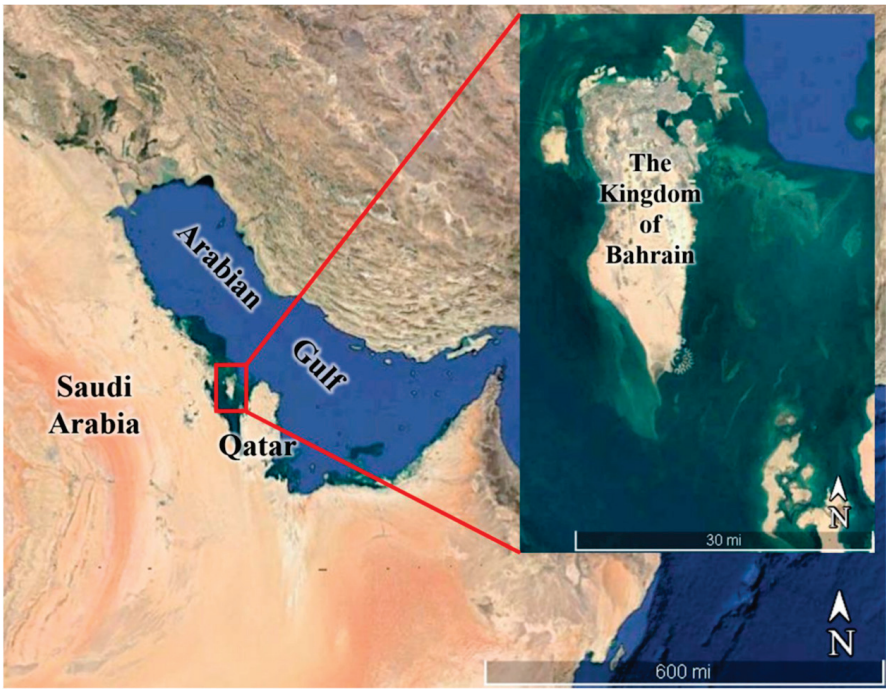

Figure 1. Location of the Kingdom of Bahrain.

Since the 1970s, heavy reliance on groundwater to meet the rapid water demands for the development and expansion of the agricultural and municipal sectors has led to its over-exploitation, which has resulted in a severe decline in groundwater levels, the cessation of natural spring flows, and the deterioration of groundwater quality due to the upward flow from the underlying brackish groundwater and the adjacent saline seawater. In response, the groundwater authorities in Bahrain have been making a number of management interventions on both the supply and demand sides to restore the groundwater, including reducing the reliance on the groundwater in the municipal water supply by increasing the desalination capacity, gradually substituting groundwater with the tertiary treated wastewater from agriculture and landscaping, prohibiting the industrial sector from using the Dammam aquifer's water and directing it to the lower brackish and saline zones [9], and employing a number of irrigation water conservation and efficiency programs that aim at reducing the groundwater use in the agricultural sector. These efforts were successful in reducing the abstraction rates in 2019, causing them to be closer to the recommended safe yield rates. The monitoring of groundwater levels and quality as well as abstraction is becoming crucial to evaluate the effectiveness of groundwater restoration efforts. The availability of information on the groundwater response to these efforts is essential to support decision making in the process of groundwater planning and management in Bahrain.

The groundwater level monitoring program in Bahrain was established in the early 1980s when a dedicated monitoring network was developed for the Dammam aquifer, the principal aquifer in the kingdom. The establishment of the groundwater level network was based on the recommendations of a comprehensive hydrogeological study in Bahrain [8] aiming at the sustainable development and management of the groundwater system in the kingdom. However, regular groundwater quality monitoring was not performed for the Dammam aquifer until 2006. Prior to that, groundwater quality monitoring was carried out in the form of major decadal country-wide surveys in 1970 [10], 1978/1979 [8],

1991/92 [11], 2001/2002 [12], and 2014/2015 [13]. In 2006, the groundwater authority initiated a regular monitoring network of the groundwater quality of the main aquifer zone of the Dammam aquifer, termed the Khobar aquifer zone. The network started with about 44 observation points with samples being collected personally by the staff of the groundwater authority from produced private wells twice a year and being analyzed in government laboratories for salinity and major anions and cations. However, the number of observation points have started to decline gradually, reaching 15 wells in 2019. The decline is attributed to inadequate resources, the shortage of staff, inaccessibility to some wells, and the abandonment of some wells due to a salinity increase. Moreover, during the COVID-19 pandemic (starting in March 2020) monitoring stopped.

The objective of this study was to evaluate the effectiveness of the current groundwater quality monitoring system of the Khobar aquifer zone and to optimize its spatial distribution. The geostatistical optimization approach of kriging and GIS were employed to assess the adequacy of the existing monitoring system, to identify its main gaps, and to upgrade it to enhance its cost effectiveness under the constraints of production well availability, staff limitations, and aquifer limits to provide reliable information for groundwater planning and management. Moreover, it provides a number of recommendations to internalize the cost of groundwater management in groundwater users.

2. Materials and Methods

The methodology of upgrading groundwater quality monitoring network was based primarily on geostatistical methods supported by GIS analysis. Geostatistical methods (synonymous to kriging interpolations) are a group of statistical techniques used to evaluate and predict variations in space and time. Kriging is a local estimation technique of the best linear unbiased estimator (BLUE) for the unknown values of spatial and temporal variables [14]. Its mathematical concept was first introduced by D.K. Krige in 1951 to solve mining-related problem in South Africa, and the method was modified and introduced in the general form of kriging by Matheron in 1971 [15]. Geostatistical analysis, or kriging methods, based on variance, semi-variogram evaluations, and regionalized variable theories is used to compute spatial distributions, to determine the accuracies of those estimated distributions, and to obtain optimal sampling locations for monitoring groundwater. The methods have been applied in various disciplines, such as soil science, surface and sub-surface hydrology, meteorology, atmospheric science, and agriculture [5].

Variance-based approaches were established for the problem of groundwater monitoring network augmentation and upgrading [5] and have been used since the 1980s in upgrading groundwater monitoring networks, e.g., [16–22]. In this approach, the estimation variance and/or a weighted measure of estimation variance are used as criteria in the design process, and variance reduction is used as a measure of network performance. Variance reduction involves a methodical search for the number and locations of sampling sites that minimize the variance in estimation error of the state variable (e.g., water levels, salinity, or pollutant concentrations) of the aquifer. In practice, for groundwater quality monitoring, the search would be for existing operating wells that can be sampled. The search stops when adding new locations does not have a significant impact on reducing the variance, meaning that adding more observation points would not provide significant information (i.e., would not increase certainty of the variable being monitored). The methodology involved in implementing the variance reduction approach in evaluating and enhancing the effectiveness of groundwater quality monitoring network of the Khobar aquifer in Bahrain using Geostatistical Analyst Extension in ArcGIS software (Ver. 10.8) is illustrated in Figure 2. In detail, these procedures are as follows:

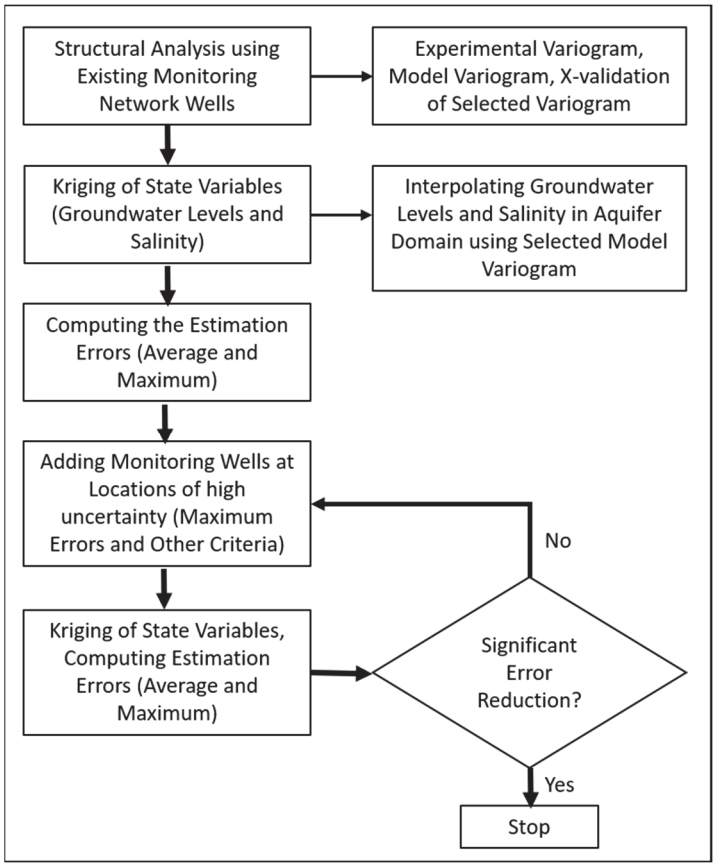

Figure 2. Procedures for monitoring network design.

(1) Data collection and preparation

This involved obtaining the location of the currently monitored wells (i.e., the X and Y coordinates of UTM projection and salinity values in 2019), which were treated as the existing networks of the aquifer that needed to be evaluated for adequacy. Moreover, the existing 15 wells were amended with the operating industrial wells produced from the Khobar aquifer zone. The chemical properties of the industrial wells tapping the Khobar aquifer zone are being analyzed frequently by their owners. However, these analyses are not reported to the groundwater authorities on a regular basis. The data of the currently monitored wells and the industrial wells were obtained from the files of the AEWRD and were verified to obtain their locations by plotting them in a GIS environment on a prepared base map of Bahrain as well as to obtain their operational conditions by interviewing the geotechnicians responsible for collecting the data from the wells.

(2) Conducting a univariate statistical analysis for the data of the existing network

A classical univariate statistical analysis in GIS environment was performed on the existing monitoring network and industrial well data to determine the variables of frequency distribution and spreading patterns (i.e., mean, median, variance, minimum, maximum, skewness, and kurtosis). It should be noted that kriged estimation of the variables provides better estimation if the data used are normally distributed [23]. In the case the data exhibit a log-normal distribution, which is a typical behavior for many hydrogeological variables and parameters, then it is preferable to take the logarithm of the data before performing the geostatistical analysis and estimation [24,25]. This is performed because the structure of the variables is much better (i.e., the variogram shows a better correlation) if the log of the variables is used instead of its raw value [15].

(3) Conducting structural analysis on the data of the regularly monitored wells from the AEWRD using the Geostatistical Analyst Extension of ArcGIS software

The structural analysis involved computing the experimental variogram, fitting the experimental variogram with a model variogram, and cross-validating the model variogram when estimating the value of the existing regularly monitored wells. In practical geostatistics, there are several methods that have been developed for the computation of the experimental variogram. Among these are the "classical" or traditional estimator [26], the Cressi–Hawkins estimator [27], the squared median of the absolute deviation (SMAD) estimator [28], and Omre estimator [29]. In this study, the classical estimator, which is widely used, was adopted to calculate the experimental variogram. The classical estimator equation is as follows:

$$\gamma(h) = \left[\frac{1}{2n(h)}\right]\sum_{i=1}^{n(h)}[Z(x_i+h) - Z(x_i)]^2 \quad (1)$$

where the estimator $\gamma(h)$ is the calculated experimental variogram; $n(h)$ is the number of data pairs separated by the vector, or lag distance, h; and $Z(x_i)$ is measured value of the state variable (i.e., salinity) at coordinate x_i.

An appropriate theoretical model must be fitted to the computed experimental variogram in order to estimate the variable value at different locations in the domain of interest. Several theoretical mathematical models could be fitted to the experimental variogram, which include the spherical, exponential, power, Gaussian, and cubic models [30]. In this study, the spherical model, which is the most commonly used model, was found to be more applicable to the variable of salinity. The model exhibited a linear behavior at small separation distances near the origin, but it flattened out at larger distances and reached a sill limit, i.e., it was transitive, consisting of two separate functions with a discontinuity. The model equations are as follows [31]:

$$\begin{gathered}\gamma(h) = C_0 + C\left[\frac{3h}{2a} - \frac{1}{2}\left(\frac{h}{a}\right)^3\right] \; for\; h < a \\ \gamma(h) = C_0 + C \; for\; h \geq a\end{gathered} \quad (2)$$

where a is the range of influence, C_0 is the nugget variance, and $C_0 + C$ is the sill. C_0 and C represent the random and spatial components of variation, respectively.

After fitting the model, cross-validation (or x-validation) was used to check the reliability and effectiveness of the calculated model variogram in estimating the variable field, i.e., groundwater salinity, in the aquifer. In x-validation, an estimation of each observed data point is made by utilizing the model variogram and the rest of the data set. This process is also called "jack-knifing". At the end of this process, a comparison is made between the estimated values and the observed ones to indicate the goodness of the selected model.

(4) Kriging the salinity using the existing observation points of the monitoring networks and the constructed model variogram using the Geostatistical Analyst Extension of ArcGIS Software

Kriging was used to estimate the values of the salinity at unknown locations in the aquifer. The regularly monitored AEWRD groundwater quality data and the structural variogram model (Equation (2)) were used in the estimation of the state variables' function distribution in the aquifer. The kriging equations are as follows [30]:

$$\begin{gathered}\sum_{i=1}^{n}\lambda_0^j\gamma(x_i - x_j) + \gamma = \gamma(x_i - x_0)\; i = 1, \ldots n \\ \sum_{i=1}^{n}\lambda_0^i = 1\end{gathered} \quad (3)$$

where $\lambda^j{}_0$ is the weighting function of each point j to be used in the estimation of point x_0 and where $\gamma(x_i - x_j)$ is the variogram value for the distance between x_i and x_j.

(5) Calculating the error of kriging estimation using the Geostatistical Analyst Extension of ArcGIS Software

The error maps (maps of distribution of estimated uncertainty %) were useful in that they gave a realistic indication of the variability involved in contrast to kriged maps, which smoothed it out, and that they showed where the interpolated values deviated from the expected statistical structure, thus indicating the best position to place additional wells [32].

The variance in the error of estimation of point x_0 is given as

$$\sigma^2_{x_0} = \sum_{i=1}^{n} \lambda^i_0 \gamma(x_i - x_0) + \mu \quad (4)$$

where μ is the Lagrange multiplier. The associated standard deviation of the estimation was generated for the domain in concern. The average error of the domain was computed, and the location of the maximum error was noted. Furthermore, a contour map for the distribution of the error involved in the estimation of the salinity of the Khobar aquifer zone was produced to indicate the location of high uncertainties. These maps were presented as uncertainty percentage, which is calculated by

$$Uncertainty(\%) = \frac{Error}{Maximum\ Grid\ Error} \times 100 \quad (5)$$

(6) Adding new locations of monitoring well(s) for the aquifer based on the maximum error and other criteria

The uncertainty maps were used to place new monitoring wells based on the maximum error found and were complemented by the existence of a production well. In other words, the existence of groundwater production wells (either government or private) was taken as the criteria for new site selections since augmenting salinity monitoring network is based on collecting samples from existing operating wells. The availability of production wells for augmenting groundwater salinity monitoring network was based on the AEWRD production wells database and was conducted using GIS. This step was performed by adding batches of wells.

(7) Kriging groundwater salinity using both the regularly monitored wells and the newly added well(s) and calculating the associated error of estimation

Using the regularly monitored wells and the newly added ones, kriging was performed to estimate the values of the salinity at unknown locations in the aquifer zones. This was conducted using the same structural variogram model obtained in step (3) in GIS environment. This step was followed by calculating the associated error of the estimation in the form of the standard deviation, the average error of the domain, and the maximum error and by generating uncertainty distribution map for the monitoring network (similar to step 5).

(8) Repeating steps 5 and 6 until no significant reduction in the error is observed

The addition of the wells, kriging them, and calculating the error involved in the estimation was repeated until the rate of improvement became relatively insignificant. While an increase in the sampling density will always decrease the involved errors and increase the sampling reliability, the rate of improvement will be different as more sampling points are added.

The objective was to obtain a "cost-effective" monitoring network that had a minimum variance estimate with a minimum number of sampling points. A plot of the number of wells and the change in the average error and maximum error provided an insight into the "worth of the additional data", i.e., if obtaining more data by adding new wells would provide significant additional information on the state variable being monitored. Here,

a managerial decision had to be made that took into account the available budget and workforce and the information obtained by adding more sampling points.

3. Results and Discussion

As indicated in the methodology section, the first step in analyzing, evaluating, and upgrading the existing monitoring networks of the Khobar aquifer zone was made by taking advantage of the industrial wells (23 wells), which are monitored on a regular basis with respect to their chemical properties by their owners. This increased the number of observation wells from 15 to 38. The following sections include the results of the analysis and evaluation of the quality monitoring network of the Khobar aquifer zone.

3.1. Statistical Analysis

The data statistics of the existing groundwater quality monitoring network (i.e., regularly monitored and the industrial wells) of the Khobar aquifer are summarized in Table 1. The frequency distribution of the quality data (salinity and TDS) of the Khobar aquifer zone is graphically illustrated in Figure 3, and its normal Q-Q plot is shown in Figure 4. The two figures indicate that the distribution of the Khobar data is close to normal, with a slight tendency to tail to the right. However, this does not warrant converting the data into logarithm values (doing so would cause the data to have a strongly skewed distribution to the right).

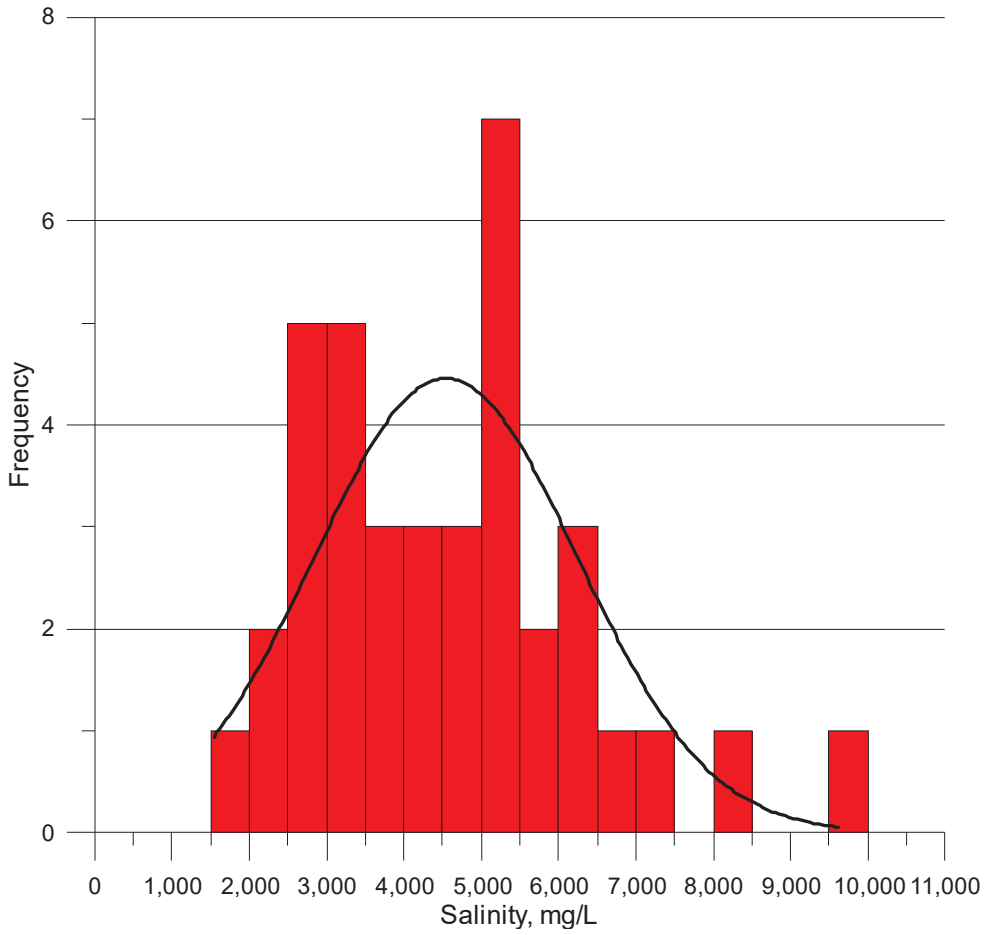

Figure 3. Frequency distribution of the existing groundwater salinity data of the Khobar aquifer zone.

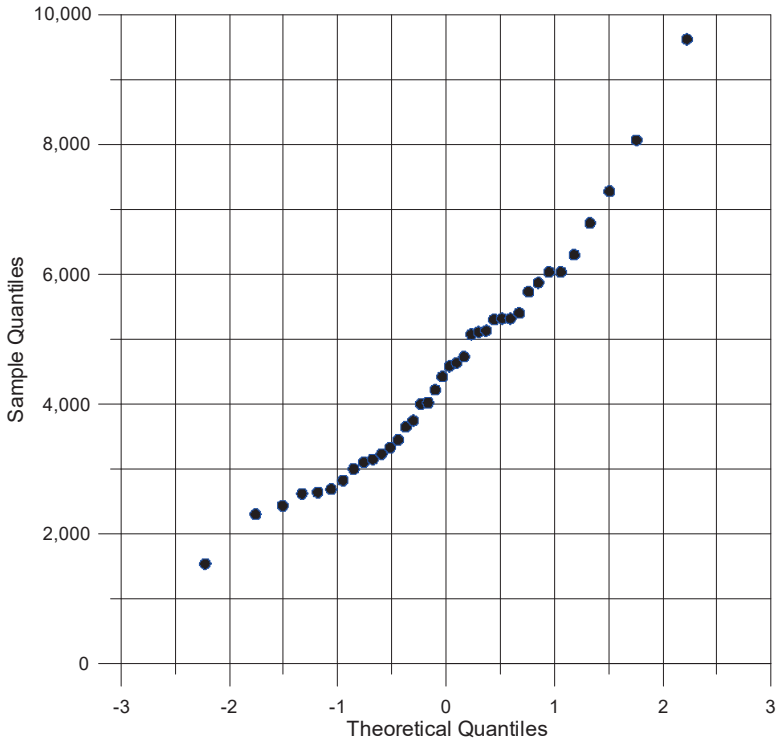

Figure 4. Normal Q-Q plot of the existing groundwater salinity data of the Khobar aquifer zone.

Table 1. Summary statistics of the groundwater salinity data of the Khobar aquifer zone.

Parameter	Value
N	38
Mean	4543
Median	4501
Variance	2,971,181
Standard Deviation	1724
Minimum	1540
Maximum	9616
Skewness	0.8
Kurtosis	0.8

3.2. Structural Analysis

Figures 5 and 6 display the experimental/fitted model variogram and the cross-validation results using the existing observation points of the groundwater quality monitoring network of the aquifer, respectively. The spherical model was found to best fit the variogram of the aquifer quality data, providing more satisfactory cross-validation results than the other models, and it was used in the following analysis.

3.3. Kriging and Kriging Error Analysis of Existing Network

Figure 7a depicts the uncertainty map resulting from kriging the TDS of the Khobar aquifer in Bahrain using the existing monitoring network data (regularly monitored and industrial wells in the Khobar aquifer zone) and the fitted spherical model. The main areas of concern are located in the northwestern and western areas, where the groundwater receives its recharge from the up-gradient parts of the aquifer in Saudi Arabia.

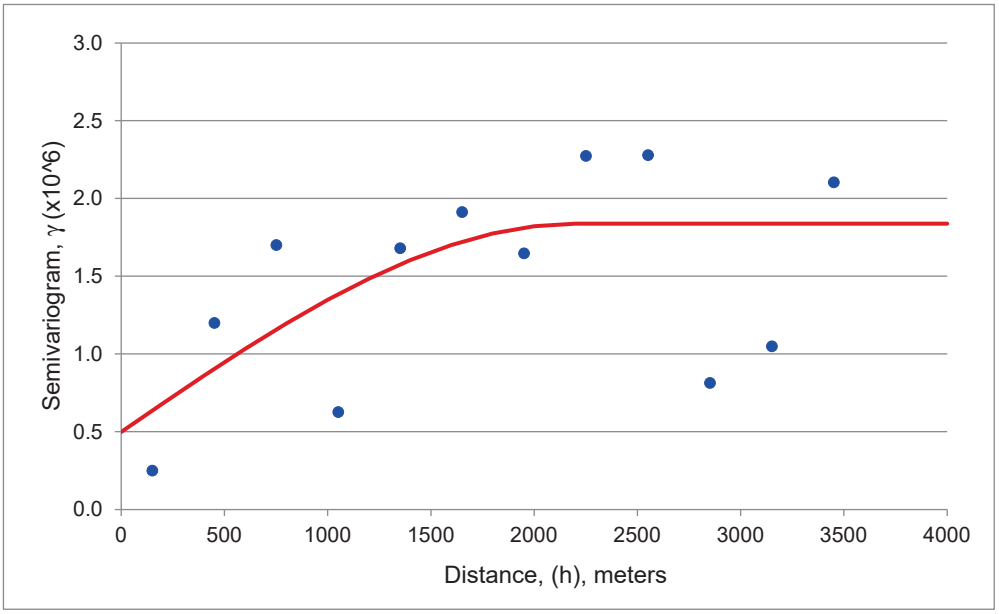

Figure 5. Experimental and fitted spherical model variogram of the existing wells in the Khobar aquifer zone. Parameters of the fitted model variogram (Equation (3)) are nugget (C_0) = 498,540; radius of influence (a) = 2205 m; and sill value (h $\geq$ a) = 1,838,140.

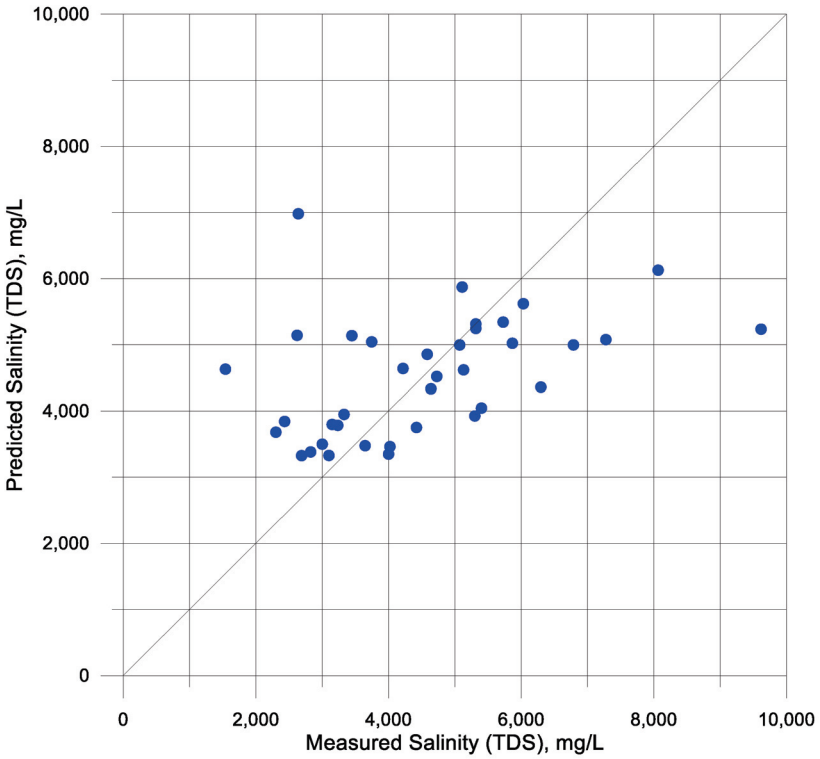

Figure 6. Cross-validation results of the fitted model variogram in estimating the TDS value of the existing monitoring wells in the Khobar aquifer zone.

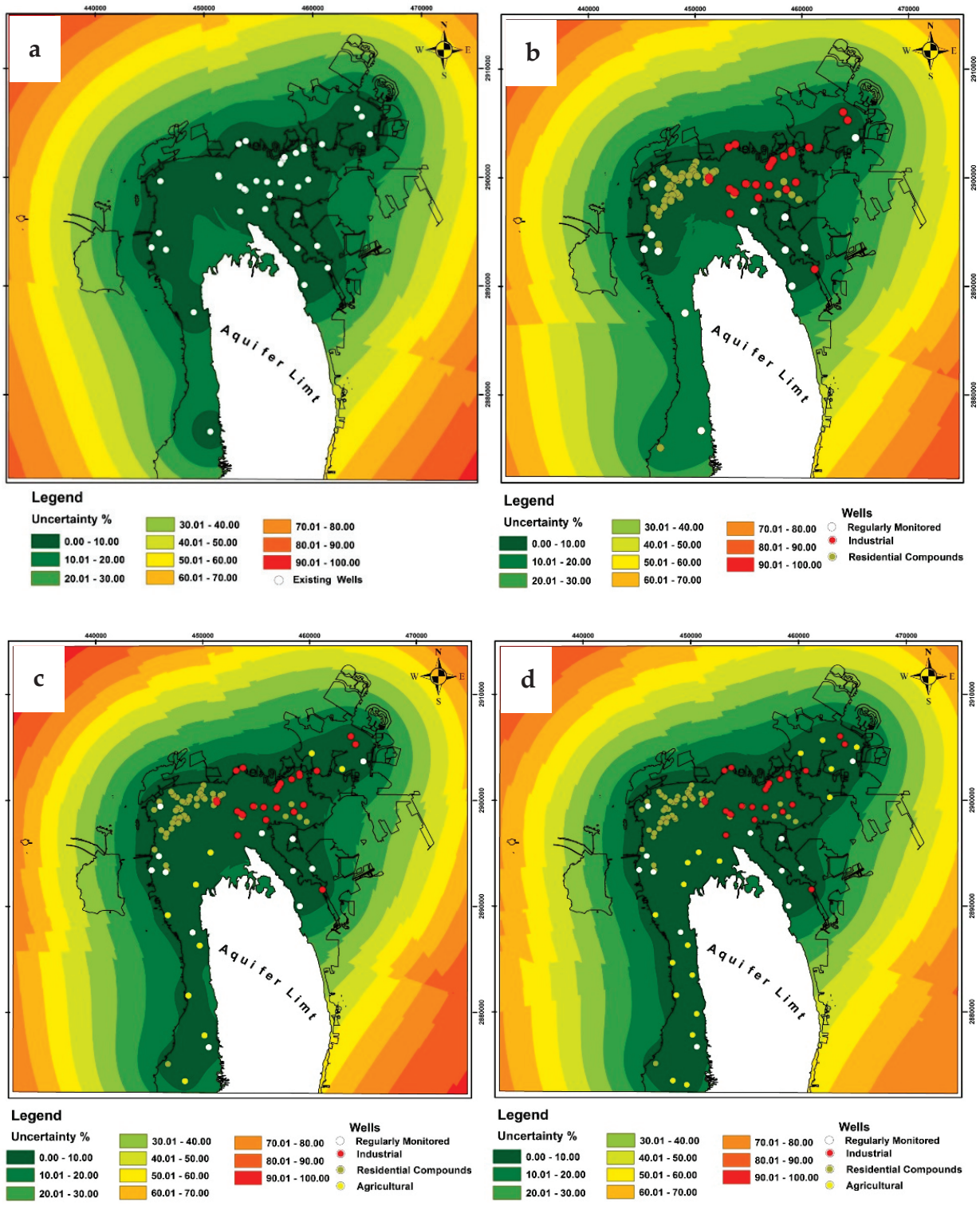

Figure 7. Uncertainty map of (**a**) existing monitoring network of the quality of the Khobar aquifer zone, (**b**) stage 1 of observation well augmentation, (**c**) stage 2 of observation well augmentation, and (**d**) stage 3 of observation well augmentation.

3.4. Upgrading the Existing Monitoring Network

The first step in enhancing the quality monitoring network of the aquifer was to augment the existing monitoring network with the commercial residential compounds. After this stage, it was important to look at the farmers' wells that withdrew their water

from the aquifer. The augmentation of the farmers' wells was performed in two stages, each with nine wells obtained from the well database using GIS. Figure 7b–d illustrate the changes in the spatial uncertainty in these three steps, respectively. Table 2 summarizes the results of the error analysis associated with these stages, while Figure 8 illustrates these results graphically. It can be clearly seen that adding the "commercial" residential compounds will significantly enhance the accuracy of the existing monitoring network (>50% change in accuracy). Similarly, the first stage of adding farmers' wells will cause a relatively considerable enhancement of the accuracy. Therefore, it is highly recommended that these two stages are implemented and that the residential compounds (self-reported) and the first batch of the farmers' wells (sample collection) are included in the monitoring network along with the industrial wells to augment the limited monitoring network of the principal aquifer in Bahrain. The third stage in collecting samples from the farmers' wells will not change the accuracy values significantly, and, hence, adding more wells is not recommended.

Table 2. Maximum and average errors calculated for the estimation of water quality of the Khobar aquifer zone using the existing monitoring network and the various stages of adding new wells.

Stage	Maximum Grid Error	% Change in Maximum Error	Average Grid Error	% Change in Average Error
Existing wells (15 regular and 23 industrial wells)	11.27	-	4.32	-
Stage 1 (44 commercial residential compound wells)	4.83	57.12	1.80	58.35
Stage 2 (9 farmer wells—1)	2.66	44.91	1.46	18.75
Stage 3 (9 framer wells—2)	2.48	6.95	1.38	5.48

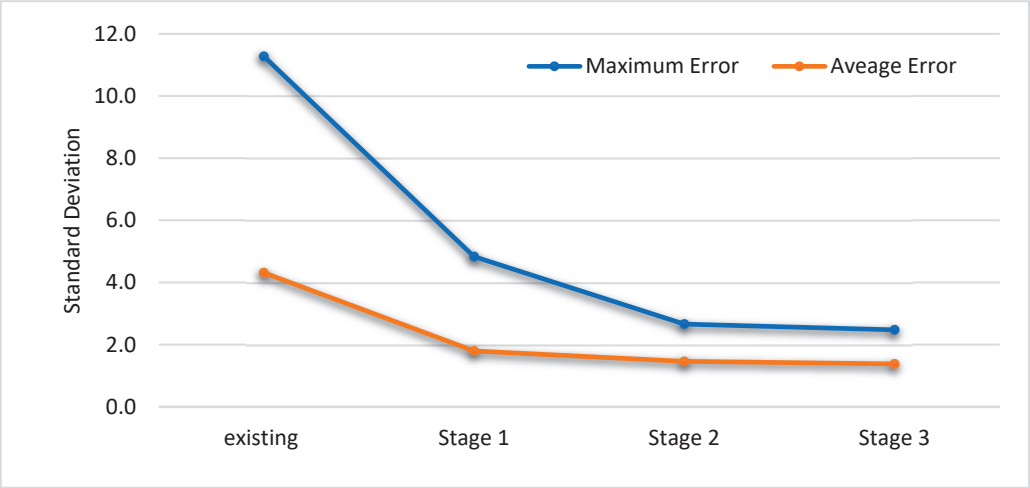

Figure 8. Trends in the maximum and average errors of the Khobar aquifer zone by network upgrading stage.

4. Conclusions

The existing monitoring network of the quality of the Khobar aquifer, the main aquifer zone in the Kingdom of Bahrain, was spatially evaluated for its effectiveness in providing adequate information on the groundwater quality of the kingdom, and recommendations for upgrading and enhancing its cost-effectiveness in the planning and management process were made. The methodological approach involved implementing the variance reduction approach in evaluating and enhancing the effectiveness of the salinity monitoring network of the aquifer, based primarily on the geostatistical method of kriging coupled with GIS, and was constrained by the existence of production wells. In this method, the estimation variance is used as a criterium in the design process, and variance reduction is used to measure the network performance. Variance reduction involves a methodical search

for the number and locations of the sampling sites that minimizes the variance in the estimation error of the groundwater salinity of the aquifer. The search stops when adding new locations does not have a significant impact on reducing the variance, meaning that adding more observation points would not provide significant information (i.e., would not increase the certainty of the monitored variable).

The current quality monitoring network of the Khobar aquifer, consisting of 15 wells, was augmented with an additional 23 industrial wells and was further augmented with 53 commercial residential compound wells to increase the total number of network observation wells to 91 wells. These additional industrial and commercial observation points are to be "self-reported", which will internalize the cost of groundwater monitoring and management in their users and will reduce the cost of the operation of the network. A legislation requiring the certified lab analysis of the quality of the groundwater abstracted by these two sectors on a periodic basis is to be issued by the water authority. It is also recommended to include nine more farmers wells in the network to fill some areal gaps in the aquifer's quality, which will require groundwater authority staff visits to collect the samples and analyses.

It is strongly recommended that monitored data are stored in a dedicated specialized groundwater management information system (MIS) along with the monitored data of groundwater levels and abstraction to effectively support the process of decision making for groundwater planning and management. Moreover, it is recommended that temporal optimization research, i.e., the frequency of sampling, is conducted for the groundwater monitoring system in Bahrain.

Author Contributions: Conceptualization, W.A.-Z.; methodology, W.A.-Z. and A.A.-S.; software, N.A.; validation, W.A.-Z. and A.A.-S.; formal analysis, W.A.-Z. and A.A.-S.; investigation, W.A.-Z., A.A.-S. and N.A.; resources, W.A.-Z., A.A.-S. and N.A.; data curation, A.A.-S.; writing—original draft preparation, W.A.-Z.; writing—review and editing, W.A.-Z.; visualization, N.A.; supervision, W.A.-Z.; project administration, W.A.-Z.; funding acquisition, W.A.-Z. All authors have read and agreed to the published version of the manuscript.

Funding: This research was conducted under the project "Development of an Enabling Environment for Water Demand Management in the Kingdom of Bahrain" funded by the Green Climate Fund (GCF) and was managed by the Water Resources Management Unit (WRMU), the Ministry of Oil and Environment, and the UN Environment on behalf of the Water Resources Council in the Kingdom of Bahrain.

Data Availability Statement: Data sharing not applicable.

Acknowledgments: The authors would like to thank the staff of the WRMU and the Agricultural Engineering and Water Resources Directorate (AEWRD) for their help in providing the data and the information used in this research.

Conflicts of Interest: The authors declare no conflict of interest.

References

1. Anderson, M.P.; Woessner, W.W.; Hunt, J.H. *Applied Groundwater Modeling: Simulation of Flow and Advective Transport*, 2nd ed.; Elsevier: Amsterdam, The Netherlands, 2015.
2. Jollymore, A.; Haines, M.J.; Satterfield, T.; Johnson, M.S. Citizen science for water quality monitoring: Data implications of citizen perspectives. *J. Environ. Manag.* **2017**, *200*, 456–467. [CrossRef] [PubMed]
3. Dawdy, D.R. The worth of hydrologic data. *Water Resour. Res.* **1979**, *15*, 1726–1731. [CrossRef]
4. Candela, L.; Olea, R.A.; Custodio, E. Longnormal kriging for the assessment of reliability in groundwater quality control observation networks. *J. Hydrol.* **1988**, *103*, 67–84. [CrossRef]
5. Singh, C.K.; Katpatal, Y.B. A review of the historical background, needs, design approaches and future challenges in groundwater level monitoring networks. *J. Eng. Sci. Technol. Rev.* **2020**, *13*, 135–153. [CrossRef]
6. Woldt, W.; Bogardi, I. Ground water monitoring network design using multiple criteria decision making and geostatistics. *Water Resour. Bull.* **1992**, *28*, 45–61. [CrossRef]
7. Hughes, J.P.; Lettenmaier, D.P. Data requirements for Kriging: Estimation and network design. *Water Resour. Res.* **1981**, *17*, 1641–1650. [CrossRef]

8. GDC (Groundwater Development Consultants). *Umm Er Radhuma Study, Bahrain Assignment, Vol. III: Groundwater Resources*; Ministry of Water and Agriculture Report; GDC: Riyadh, Saudi Arabia, 1980.
9. Amiri Decree No.12/1980 (1980) Concerning the Use of Groundwater, Government of Bahrain. Government of Bahrain, Official Gazette, 1382 (8 May 1980), pages 3–6 (In Arabic). Available online: https://www.lloc.gov.bh/PDF/L1280.pdf (accessed on 16 December 2022).
10. Italconsult. *Water and Agricultural Studies in Bahrain*; Ministry of Agriculture and Water Report; Italconsult: Riyadh, Saudi Arabia, 1971.
11. Al-Noaimi, M.A. *Evaluation of Bahrain Available Water Resources, Vol. I: Evaluation of Available Water Resources and Utilization Patterns*; Bahrain Center for Studies and Research: Awali, Kingdom of Bahrain, 1993.
12. AEWRD (Agricultural Engineering and Water Resources Directorate). *Groundwater Quality Survey 2001/2002*; Ministry of Works, Municipality Affairs and Urban Planning Report; Government of the Kingdom of Bahrain: Manama, Kingdom of Bahrain, 2003.
13. AEWRD (Agricultural Engineering and Water Resources Directorate). *Groundwater Quality Survey 2014/2015*; Ministry of Works, Municipality Affairs and Urban Planning Report; Manama, Government of the Kingdom of Bahrain: Manama, Kingdom of Bahrain, 2015.
14. Chung, S.Y.; Venkatramanan, S.; Elzain, H.E.; Selvam, S. Supplement of Missing Data in Groundwater-Level Variations of Peak Type Using Geostatistical Methods. In *GIS and Geostatistical Techniques for Groundwater Science*; Venkatramanan, S., Prasanna, M.V., Chung, S.Y., Eds.; Elsevier: Amsterdam, The Netherlands, 2019; pp. 33–42. [CrossRef]
15. Matheron, G. *The Theory of Regionalized Variables and Its Applications*; CGMM, Ecole des Mines, Fontainebleau Report; Ecole des Mines: Paris, France, 1971; Report No. 5. (In French)
16. Sophocleous, M.; Paschetto, J.E.; Olea, R.A. Ground-Water Network Design for Northwest Kansas, Using the Theory of Regionalized Variables. *Ground Water* **1982**, *20*, 48–58. [CrossRef]
17. Rouhani, S. Variance reduction analysis. *Water Resour. Res.* **1985**, *21*, 837–846. [CrossRef]
18. Loaiciga, H.A. An Optimization approach for groundwater quality monitoring network design. *Water Resour. Res.* **1989**, *25*, 1771–1782. [CrossRef]
19. Prakash, M.R.; Singh, V.S. Network design for groundwater monitoring–A case study. *Environ. Geol.* **2000**, *39*, 628–632. [CrossRef]
20. Theodossiou, N.; Latinopoulos, P. Evaluation and optimisation of groundwater observation networks using the kriging methodology. *Environ. Model. Softw.* **2006**, *21*, 991–1000. [CrossRef]
21. Yang, F.; Cao, S.; Liu, X.; Yang, K. Design of groundwater level monitoring network with ordinary kriging. *J. Hydrodyn.* **2008**, *20*, 339–346. [CrossRef]
22. Triki, I.; Moncef, Z.; Hamed, B.D. A geostatistical approach for groundwater head monitoring network optimisation: Case of the Sfax superficial aquifer (Tunisia). *Water Environ. J.* **2013**, *27*, 362–372. [CrossRef]
23. Ahmed, S.; de Marsily, G.; Talbot, A. Combined use of hydraulic and electrical properties of an aquifer in a geostatistical estimation of transmissivity. *Ground Water* **1988**, *26*, 78–86. [CrossRef]
24. Delhomme, J.P. Spatial variability and uncertainty in groundwater flow parameters: A geostatistical approach. *Water Resour. Res.* **1979**, *15*, 269–280. [CrossRef]
25. Neuman, S.P. Statistical characterization of aquifer heterogeneities, An overview. In *Recent Trends in Hydrogeology*; Narsimhan, T.M., Ed.; Geological Society of America Special Paper 189; Geological Society of America: Boulder, CO, USA, 1982; pp. 81–102. [CrossRef]
26. Matheron, G. Principles of Geostatistics. *Econ. Geol.* **1963**, *58*, 1246–1266. [CrossRef]
27. Cressie, N.; Hawkins, D. Robust estimation of the variogram. *Math. Geol.* **1980**, *12*, 115–125. [CrossRef]
28. Dowd, P.A. The Variogram and Kriging: Robust and Resistant Estimators. In *Geostatistics for Natural Resources Characterization, Part 1, NATO ASI Ser., Ser. C. 122*; Verly, G., David, M., Journel, A.G., Marechal, A., Eds.; Springer: Dordrecht, The Netherlands, 1984; pp. 91–107. [CrossRef]
29. Omre, H. The variogram and its estimation. In *Geostatistics for Natural Resources Characterization, Part 1, NATO ASI Ser., Ser. C, 122*; Verly, G., David, M., Journel, A.G., Marechal, A., Eds.; Springer: Dordrecht, The Netherlands, 1984; pp. 107–126. [CrossRef]
30. Marsily, G. *Quantitative Hydrogeology*; Academic Press: San Diego, CA, USA, 1986.
31. Henely, S. *Non-Parametric Geostatistics*; Applied Science Publishers Ltd.: NJ, USA, 1981.
32. Virdee, T.S.; Kottegoda, N.T. A brief review of kriging and its application to optimal interpolation and observation well selection. *Hydrol. Sci. J.* **1984**, *29*, 367–387. [CrossRef]

Disclaimer/Publisher's Note: The statements, opinions and data contained in all publications are solely those of the individual author(s) and contributor(s) and not of MDPI and/or the editor(s). MDPI and/or the editor(s) disclaim responsibility for any injury to people or property resulting from any ideas, methods, instructions or products referred to in the content.

hydrology

MDPI

Article

Purpose-Designed Hydrogeological Maps for Wide Interconnected Surface–Groundwater Systems: The Test Example of Parma Alluvial Aquifer and Taro River Basin (Northern Italy)

Riccardo Pinardi [1], Alessandra Feo [1,*], Andrea Ruffini [2] and Fulvio Celico [1]

[1] Department of Chemistry, Life Sciences and Environmental Sustainability, University of Parma, 43124 Parma, Italy; riccardo.pinardi@studenti.unipr.it (R.P.); fulvio.celico@unipr.it (F.C.)
[2] Territorial Planning Service, Parma Province, 43123 Parma, Italy
* Correspondence: alessandra.feo@unipr.it; Tel.: +39-0521-905-368

Abstract: Hydrogeological maps must synthesize scientific knowledge about the hydraulic features and the hydrogeological behavior of a specific area, and, at the same time, they must meet the expectations of land planners and administrators. Thus, hydrogeological maps can be fully effective when they are purpose-designed, especially in complex interconnected systems. In this case study, purpose-designed graphical solutions emphasize all the hydraulic interconnections that play significant roles in recharging the multilayered alluvial aquifer, where the majority of wells have been drilled for human purposes, artificial channels are used for agricultural purposes, and the shallow groundwater feeds protected groundwater-dependent ecosystems. The hydrogeological map was then designed to be the synthesis of three different and hydraulically interconnected main contexts: (i) the alluvial aquifer, (ii) the hydrographic basin of the Taro losing river, and (iii) those hard-rock aquifers whose springs feed the same river. The main hydrogeological map was integrated with two smaller sketches and one hydrogeological profile. One small map was drawn from a modeling perspective because it facilitates visualization of the alluvial aquifer bottom and the "no-flow boundaries." The other small sketch shows the artificial channel network that emphasizes the hydraulic connection between water courses and groundwater within the alluvial aquifer. The hydrogeological profile was reconstructed to be able to (i) show the main heterogeneities within the aquifer system (both layered and discontinuous), (ii) visualize the coexistence of shallower and deeper groundwater, (iii) emphasize the hydraulic interconnections between subsystems, and (iv) suggest the coexistence of groundwater pathways with different mean residence times.

Keywords: hydrogeological map; interconnected surface–groundwater systems; water resources management

1. Introduction

The natural aquifer recharge is potentially made up of three different components (e.g., [1]): (i) direct recharge, coinciding with the effective infiltration of local precipitation; (ii) indirect recharge, due to losing streams (or occasionally floods from rivers); and (iii) indirect recharge, due to lateral inflow from adjacent upgradient aquifers. The existence of one or more of these components and their proportions where they coexist depend on geological, hydrogeological, hydrological, and geomorphological features. When studying interconnected surface and groundwater systems in vast areas, the groundwater availability in the downgradient aquifer is the net balance between the total input from all the components and the total output from each portion of the interconnected system. As a consequence, in agreement with the general suggestions of Struckmeier and Margat [2], when making hydrogeological maps in these hydraulically interconnected systems, graphic

solutions must be used to enable "scientists" and "non-scientist users" (planners and administrators) to find the information they need to solve problems (applied science) or make decisions (planning and administration), also taking into account the possible cause–effect relationships at the system scale. For example, in terms of planning, a purpose-designed hydrogeological map provides the indispensable scientific knowledge for defining an order of priority when selecting the sub-areas where a vulnerability map must be implemented (more or less urgently) to find the best equilibrium between water resources protection and socio-economic growth. Regarding synthesis, hydrogeological maps must synthesize the scientific knowledge about the hydraulic features and the hydrogeological behavior of a specific area, and, at the same time, they must meet the expectations of the map users, who must find (fast and easily enough) the particular information they need to avoid experiencing negative domino effects when managing water resources in this sort of "basin-in-series" system. Thus, hydrogeological maps can be really and completely effective when they are purpose-designed, especially in complex interconnected systems. This approach to designing hydrogeological maps is of utmost importance in areas where the same water resources have an ecological relevance (e.g., groundwater-dependent ecosystems (GDEs)) and are utilized for human purposes.

The hydrogeological maps can be reconstructed by interpreting and synthesizing data and information from different investigations (e.g., geological surveys, well logging, geophysical investigations, pumping tests, hydraulic heads, discharge measurements, etc.). The type of data used in a specific case depends on several factors, such as (i) the hydrogeological and morphological context, (ii) the scale of the work (e.g., site, basin, regional scales), (iii) the main aims of the studies, and (iv) the available budget.

Based on these considerations, the main aim of the present work is to find and test new graphical solutions for reconstructing purpose-designed hydrogeological maps involving complex surface–groundwater systems where multiple uses and values are associated with water resources. The present map was obtained through a re-interpretation of available data (e.g., geological map, groundwater pathway within the alluvial aquifer, location of springs and "fontanili", stratigraphic profiles, hydraulic properties of rocks) and the reconstruction of original hydrogeological profiles. The map was then used to speculate about the vulnerability of the heterogeneous alluvial aquifer as a function of possible contamination sources located within the Apennine chain, far from the plain, due to surface–groundwater interactions.

The choice of the test area fell on the wide system belonging to the Parma alluvial aquifer and the Taro River basin. From the hydrogeological point of view, it is characterized by several hard-rock mountain aquifers, a flat heterogeneous alluvial aquifer, and a losing river (e.g., [3]). On the other hand, at this site, water resources flowing within the heterogeneous alluvial aquifer feed GDEs and are utilized for drinking, industrial, and agricultural purposes. In agriculture, intensive models prevail in the flat areas, while organic techniques and protected areas and regional and national parks are prevalent within the mountainous Apennines (e.g., [4]). Some mountainous agri-food products (e.g., Parma Ham, Parmigiano Reggiano cheese, mushrooms from Borgotaro) are recognized as Protected Designation of Origin (PDO) or Protected Geographical Indication (PGI) (e.g., [5]), while others are traditional products linked to ancient varieties of animals and plants for which there is an increasing interest in the specific market [6,7]. Industrial activity in Parma is strongly oriented towards the agro-alimentary sector (e.g., large-scale pasta and baked goods and dairy manufacturers, which are world leaders in their sectors). The leading role of the Parma industry is also linked to the production of food machinery, packaging, and preservation machines and equipment. Other industrial sectors, such as pharmaceuticals and perfumery, belong to personal care and well-being [8].

2. Study Area

The research was carried out in the hydrogeological basin of the Taro River and the connected alluvial aquifer developing from the northern Apennine margin to the

Parma plain (Northern Italy; Figure 1). The northern Apennines are a fold-and-thrust belt composed of a pile of NE-verging tectonic units that developed as a result of the Cenozoic collision between the European plate (Corso–Sardinian block) and the Adria plate [9–15]. The tectonic units belong to the Ligurian, Tuscan, and Umbria–Romagna domains. The Ligurian units represent the uppermost tectonic units in the Apennine nappe pile and correspond to allochthonous terrains initially deposited in an oceanic realm (the Ligurian–Piedmontese sector of the Alpine Tethyan ocean) composed of ophiolites and their Jurassic to Eocene sedimentary cover [16–19]. These units tectonically overlie the Tuscan and Umbria–Romagna units, originally deposited on the passive margin of the Adria Plate from the middle Triassic to early Cretaceous and convergent-to-collisional margin since the middle Cretaceous till the present, consisting of a lower succession of carbonate rocks of Mesozoic–Cenozoic age and a thick upper succession of siliciclastic foredeep sediments of the Oligocene–Miocene age [9]. During the orogenetic uplift from the Eocene to the Messinian, episutural and wedge-top basins were set on top of the Ligurian units, giving rise to the Epiligurian Succession [20,21].

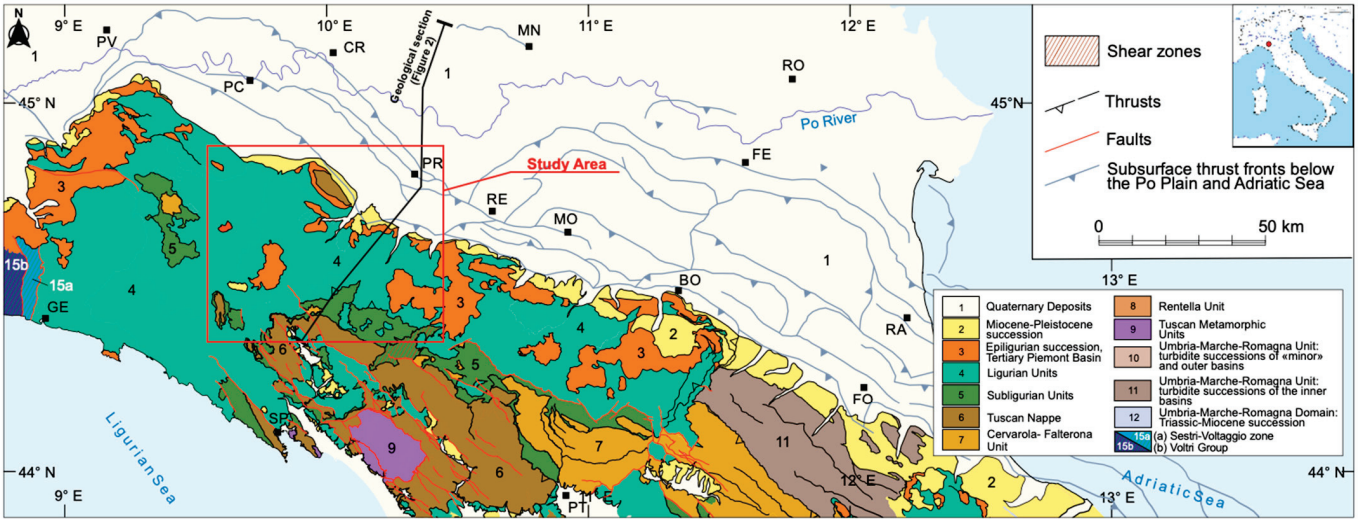

Figure 1. Tectonic map of the northern Apennines (from [9], modified).

From the Messinian to the present, at the front of the chain, the Po Basin represents the northern Apennines foredeep, nowadays filled with Plio-Pleistocene turbidite and deltaic syntectonic marine-regressive sequences, heavily influenced by the uplifts of the several thrust fronts buried under the plain [9,22,23]. Similar to the upper Emilia–Romagna plain and Apennine foothills, the Parma plain is characterized mainly by this marine-to-continental regressive sedimentary succession. The sequence of units (or synthems *sensu* [24]) is characterized at the base by hectometric thicknesses of Pliocene-clay marine sediments, above which progressively more continental deposits from shallow marine and fan deltas to today's plains and foothill alluvial fans discordantly overlapped during the Pleistocene till the present (Figure 2).

Due to their different lithological composition, the geological units of the study area may have different hydrogeological behaviors over the entire Apennines and Po Plain, as studied by several works (e.g., [25–27]) and extensively reported in the specific sections below.

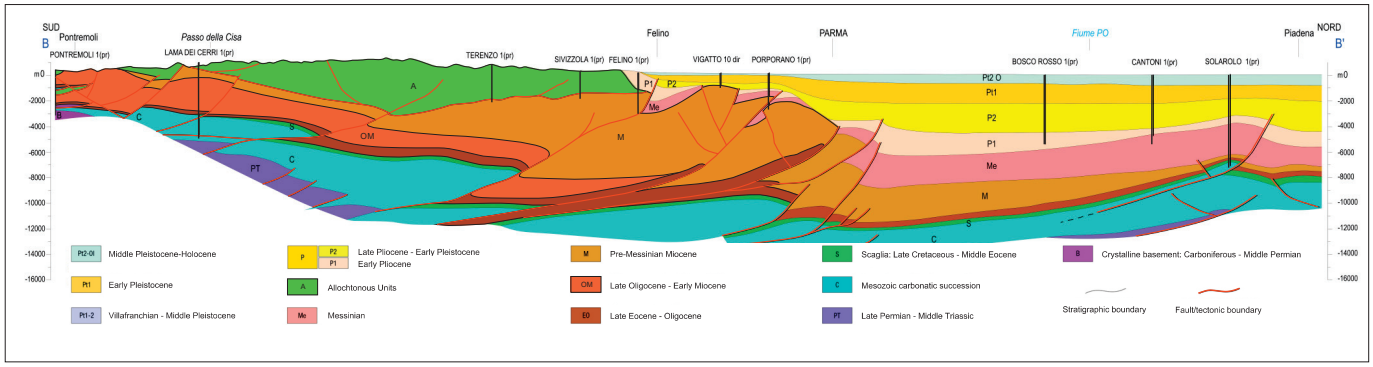

Figure 2. Geological section (from [28], modified).

3. Hydrogeological Subsystems

The main subsystems within the study area are several hard-rock aquifers and one large heterogeneous alluvial aquifer (see details hereafter). Hard-rock aquifers are made mainly of ophiolitic rocks or turbiditic (carbonate and siliciclastic) successions. From the hydrogeological point of view, the alluvial aquifer is downstream of the hard-rock aquifers. Nevertheless, because of the interposition of Pliocene-clay marine sediments, there is no direct groundwater inflow from the ophiolitic or turbiditic aquifers toward the alluvial one (Figure 2). The alluvial aquifer is recharged directly through the effective infiltration of local precipitation and indirectly through the Taro losing river.

Ophiolitic aquifers in the Italian Apennine chain are characterized by hydraulic compartmentalization due to one or more of these factors (e.g., [29–31]; Figure 3): (i) low-permeability fault cores that partially or fully impede groundwater flow (e.g., [32,33]), and/or (ii) displacement of the aquifer bottom due to faulting. Ophiolitic rocks are sometimes characterized by vertical heterogeneity, causing the coexistence of shallow perched temporary groundwater and deeper groundwater [29,34].

Turbiditic aquifers in the Italian Apennine chain are mainly or exclusively made up of sandstones and/or marls. From the hydrogeological point of view, three main conceptual models have been defined, as synthesized below.

In some cases, turbiditic aquifers are characterized by significant vertical heterogeneity due to stress-release fracturing and/or weathering that enhances rock permeability in the near-surface bedrock ([35,36]; Figure 4), according to findings on other hard-rock aquifers (e.g., [37]). In this case, the upper bedrock is characterized by relatively high hydraulic conductivity (around 10^{-6} m/s; [36]) facilitating significant groundwater recharge and flow. Differently, the deeper bedrock is characterized by very low hydraulic conductivity (in the order of 10^{-8} m/s; [36]), and groundwater flow is more significant within possible networks of damage zones associated with faults.

In other contexts, post-depositional processes increase rock permeability in larger volumes as a result of fracture development in the competent layers. Within these successions, there is no contrast in permeability with depth between a shallower and a deeper bedrock and unique groundwater flows in a low-permeability continuum at the basin scale. Despite the significant heterogeneity of the medium, the basin-scale hydraulic continuity is probably due to fracture networks associated with folds and faults that break the lower-permeability layers, therefore minimizing the aquiclude role potentially played by each one of these layers ([38]; Figure 5). In a broader context, this interpretation agrees with the link between fracture zones associated with thrust folds and fluid flow observed by other authors (e.g., [39]).

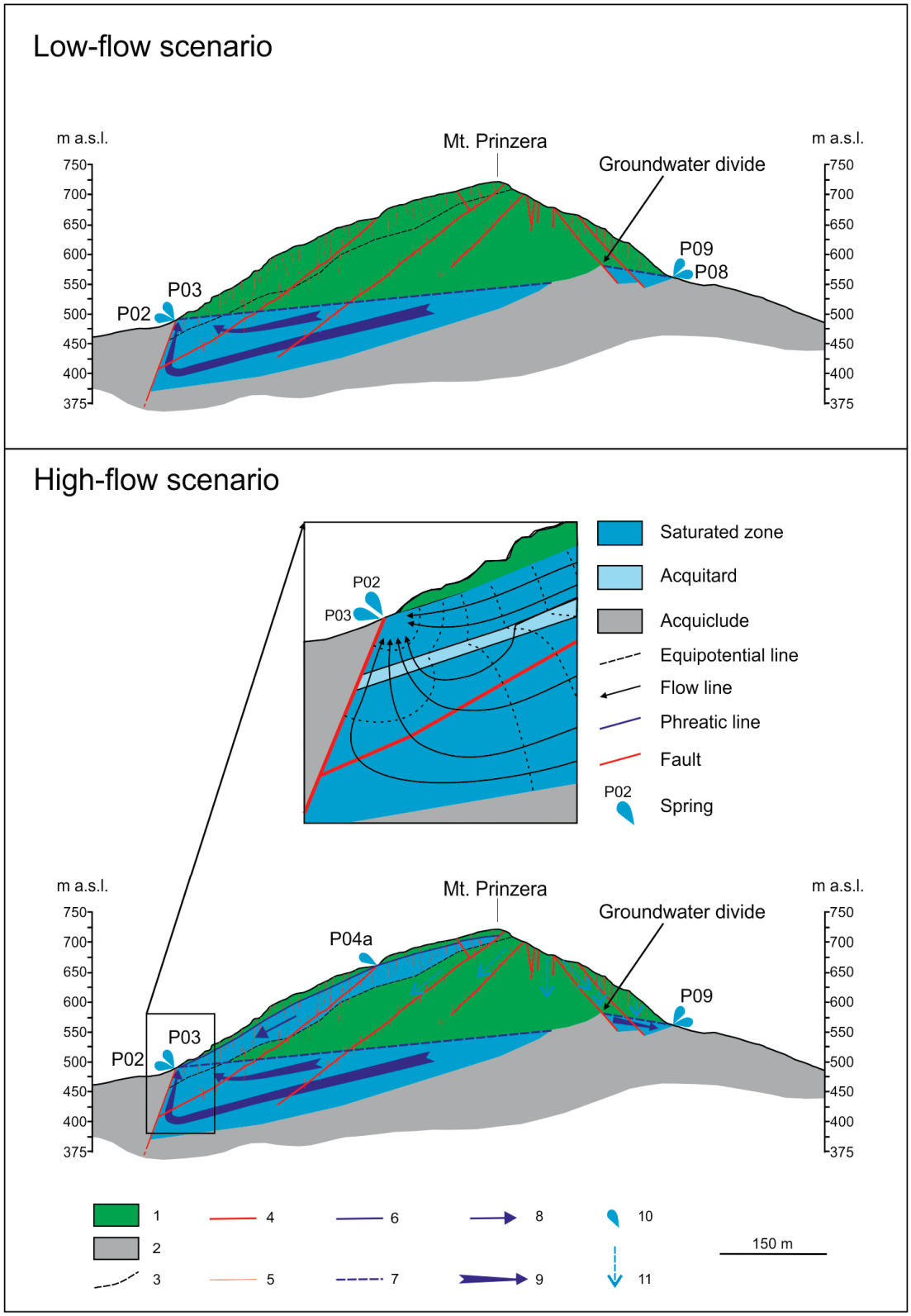

Figure 3. Hydrogeologic conceptual model of the Mt. Prinzera aquifer system. Legend—1: ultramafic aquifer; 2: aquiclude; 3: discontinuous aquitard; 4: fault; 5: fracture; 6: perched groundwater phreatic surface; 7: basal groundwater piezometric surface; 8: flowline of the perched groundwater; 9: flow line of the basal groundwater; 10: springs and their code; 11: infiltration within the unsaturated ultramafic medium (from [29], modified).

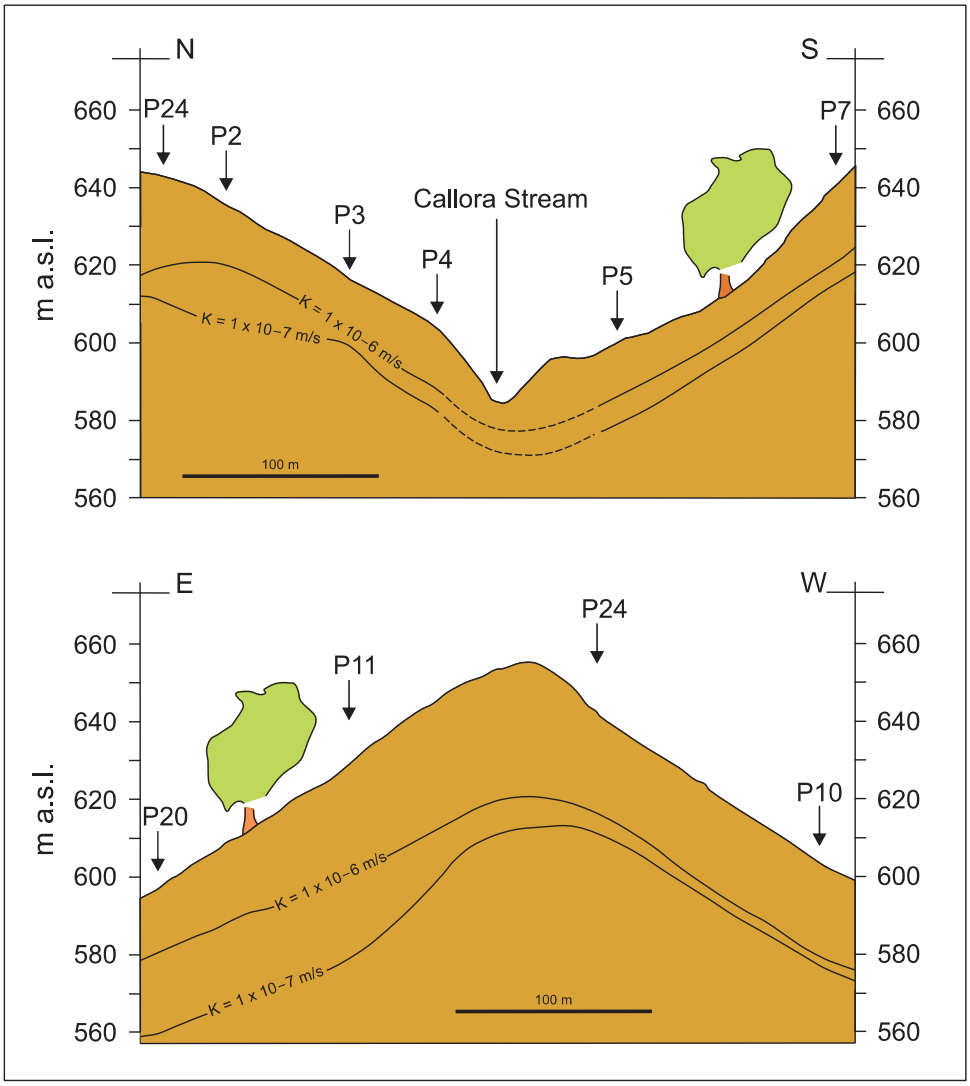

Figure 4. Variation of hydraulic conductivity (K) with depth in a turbiditic aquifer (P2-5, P10, P11, P20, P24 are the codes of the boreholes used to carry out hydraulic tests; from [36], modified).

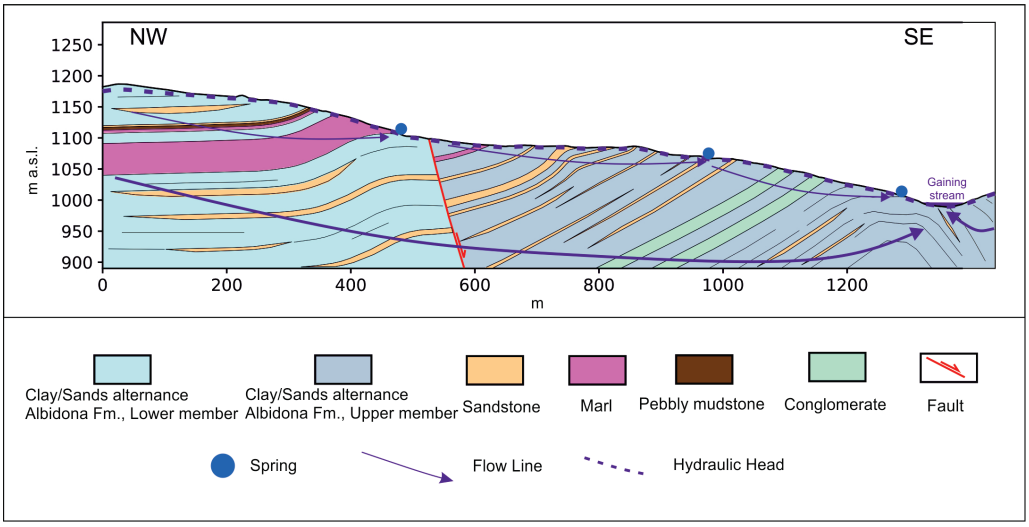

Figure 5. Hydrogeological model of a turbiditic aquifer (from [38], modified).

The main features of the two models described above sometimes coexist and are further complicated by landslide processes, converging in a third conceptual model. In that case, a unique groundwater flows in a low-permeability continuum at the basin scale. Still, significant layered heterogeneity causes the whole system to be characterized by the coexistence of fast and shallow pathways and deeper and more prolonged ones [40]. As demonstrated by merging hydrogeological, microbial, and zoological data in a test site [41,42], rapid percolation is observed in the near-surface unsaturated zone, and fast groundwater flow is observed in the shallow bedrock. Differently, within the deeper bedrock, heterogeneities can cause a significant variation in the hydraulic head with depth [43], and the lower permeability causes the slowdown of groundwater flow. The variation in flow velocities and residence times within the whole heterogeneous system can be further emphasized by very low permeability slip surfaces of landslides that sometimes act as permeability barriers, as demonstrated by Petrella et al. [44] within the study area.

In the wider context of all the hard-rock aquifers, significant groundwater exchange is then possible between adjacent aquifers of the Apennine chain. However, detailed studies have yet to be carried out on this topic at this stage, and purpose-designed investigations must be developed shortly.

The alluvial aquifer corresponds to the Pleistocene alluvial synthem, lithologically defined by alternating gravels, sands, silts, and silty clays and generated in the area by the depositional dynamics of the ancient Taro River. At the bottom of the succession, the high thickness of Pliocene marine clays is considered an extensive regional-scale aquiclude [45]. The contact between the heterogeneous aquifer and bottom aquiclude corresponds to the Pliocene–Pleistocene boundary and is characterized by several undulations due to Apennine tectonic compressive action and subsequent erosion. At the southern end of this aquifer, the Taro River's alluvial terrace (the area's most recent unit) is settled with a stratification parallel to the topographic plane. Moving toward the valley (to the north), a fan of gravel–sand–silt strata open in depth, with gradually smaller angles of inclination as the more recent depositions have originated. The resulting geometric and physical feature of the aquifer arrangement validates its syntectonic nature, contemporaneous with the Apenninic tectonic activations (Figure 6). The groundwater flows from the southwest to the northeast at a basin scale (e.g., [46]) and is recharged by the effective local infiltration and the Taro River waters [3,46–49]. Concerning the hydraulic properties of the system, Zanini et al. [44,46] calculated a hydraulic conductivity varying from 1.2×10^{-5} to 4.9×10^{-5} m/s (mean 2.3×10^{-5} m/s; median 1.7×10^{-5} m/s) in coarse-grained horizons and from 9.3×10^{-9} to 1.3×10^{-7} m/s (mean 1.6×10^{-7} m/s; median 9.7×10^{-8} m/s) in fine-grained layers. The abundance of silt and fine sands, instead of clay, in the fine-grained outcropping layers [50] causes the groundwater to be semi-confined in some sub-areas.

In the northern end of the study area, the shallow groundwater feeds the so-called fontanili (e.g., [46,51,52]; see location in the supplementary Hydrogeological Map), which are small, semi-artificial aquatic ecosystems (*sensu* [53]). These GDEs are typical of the Po River basin, the largest Italian watershed. As demonstrated by Severini et al. [49], they are indirectly recharged also by the losing Taro River.

In the wide context of the whole interconnected system, the losing river causes the heterogeneous alluvial aquifer to be indirectly recharged by the entire hydrographic basin of the Taro, including the surface runoff and groundwater of those hard-rock aquifers whose springs flow out into the Taro River basin. The influence of Taro surface waters on the recharge of the alluvial aquifer is further emphasized by a network of losing artificial open channels used for agricultural purposes (Figure S1).

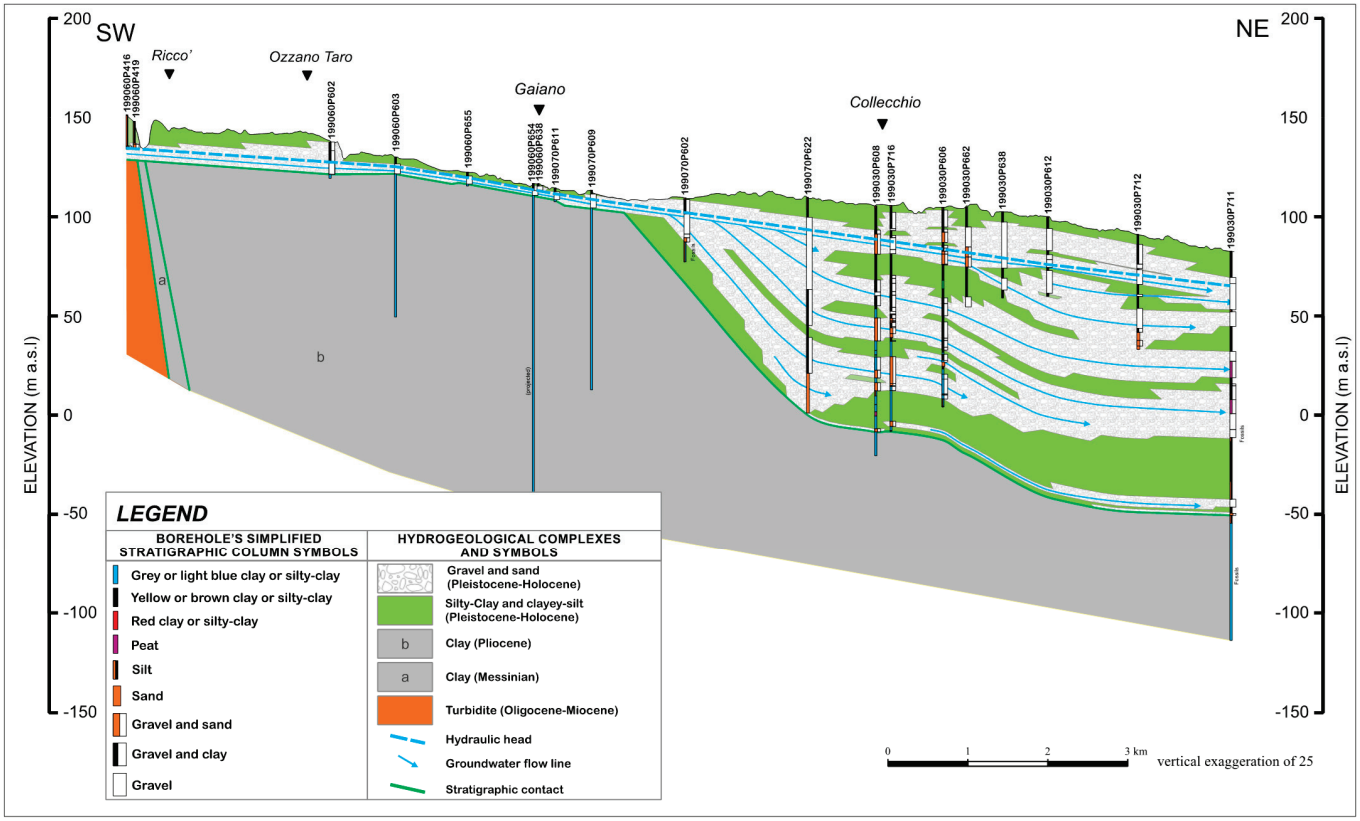

Figure 6. Hydrogeological section showing arrangement of hydrogeological subsystems at the contact between Apennines chain and Parma plain.

4. Materials and Methods

Starting from the lithological composition of the geological units composing this sector of the Apennines and Plains, four hydrogeological subsystems were divided at the basin scale. Official geological mapping (from ISPRA, Regione Emilia–Romagna, and Provincia di Parma), supplemented by outcrop inspections and related scientific literature, has formed the distinction's main basis. To each single geological unit, an expected hydraulic behavior was attributed, and (i) ophiolitic, (ii) turbiditic, (iii) alluvial, and (iv) clay subsystems were defined as the main hydrogeological domains at the study-area scale. The International Hydrogeological Map of Europe 1:1,500,000 (IHME1500) provided by BGR and UNESCO (2019) was used as the standard color reference.

After the initial conceptual subdivision and the analysis of the possible hydraulic interconnection between the Taro River and the multilayered alluvial aquifer (through the reconstruction of original hydrogeological profiles), the main map (available as a supplementary file) was produced to graphically synthesize hydraulic features and interconnections at the basin scale. Mapping was executed with Corel Draw X6 graphic software, and the combination of multiple geological units has necessitated constant comparison with official geological cartography to accurately represent the contacts between the defined hydrogeological subsystems. The topographic chart has been used as the geographical reference base for the map to locate major population centers and anthropogenic structures as potential sources of impact. Geomorphological landforms (landslides, debris, colluvium, etc.) were mostly incorporated into the unit on which they were formed.

The boundary of the Taro River hydrogeological basin has been defined according to topography, surface drainage network, and extension of aquifer hydrogeological subsystems.

Once the representation of subsystems was completed, all the symbols capable of providing hydrogeological insights on a large scale were included in the map.

The main hydrogeological map was integrated with two smaller sketches and one hydrogeological profile. The two smaller maps enable visualizing in detail (i) the alluvial aquifer bottom and (ii) the network of artificial channels within the alluvial aquifer. Because numerical models are increasingly implemented in hydrogeological studies finalized to protect, use, and manage water resources, the small map focused on the aquifer bottom was designed to be easily used for modeling purposes by also emphasizing the "no-flow boundary." Both the bottom and the "no-flow boundary" correspond to the Pliocene-clay marine sediments that act as (i) a hydraulic barrier between the hard-rock aquifers and the alluvial aquifer and (ii) the base of the whole heterogeneous alluvial succession.

The small map focused on the network of artificial channels facilitates an understanding of the wide and pervasive interaction between losing water courses and groundwater within the alluvial aquifer.

The hydrogeological section was added to improve subsurface information. It was reconstructed on the basis of a re-interpretation (from a hydrogeological perspective) of stratigraphic profiles derived from the published database by Regione Emilia–Romagna. At first, after an accurate selection of the above data, the stratigraphic section was constructed having an orthogonal direction to the Apennine front (SW–NE) to obtain a self-constructed perspective of the geological (and hydrogeological) context at the regional scale, considering the nodal zone of the Apennine to Parma Plain transition. In light of the multiple hydraulic interconnections existing within the whole test system and the significant layered heterogeneity of the main alluvial aquifer, the hydrogeological profile was reconstructed so as to be able to (i) show the main heterogeneities within the aquifer system (both layered and discontinuous), (ii) visualize the coexistence of shallower and deeper groundwater, (iii) emphasize the hydraulic interconnections between subsystems, and (iv) suggest the coexistence of groundwater pathways with different mean residence times.

The usual graphical approaches to creating hydrogeological maps could be incomplete and/or ineffective when working on interconnected aquifer systems, where the groundwater pumped for human purposes and feeding GDEs is recharged through direct (local effective infiltration) and indirect processes (losing streams, lateral underground inflow from upgradient aquifers). Therefore, according to other authors (e.g., [30]), in the case of complex systems and/or specific management/protection aims, new and purpose-designed graphical solutions must be applied to enhance the map's effectiveness. In this case study, these solutions show and emphasize all the hydraulic interconnections playing significant roles in recharging the multilayered alluvial aquifer, where the majority of wells have been drilled for drinking/industrial/agricultural purposes, artificial channels are used for agricultural purposes, and the shallow groundwater feeds protected GDEs. The hydrogeological map was then designed to be the synthesis of three different and hydraulically interconnected main contexts: (i) the main heterogeneous alluvial aquifer (the main target of the purpose-designed map), (ii) the hydrographic basin of the Taro River (the losing river that feeds the main alluvial aquifer), and (iii) those hard-rock aquifers (mainly turbiditic and ophiolitic) within the Apennine chain whose springs feed the Taro River. As per the interconnection between the surface and groundwaters within the alluvial plain, a dedicated sketch was added to the main map to clearly show the network of artificial channels utilized for agricultural purposes.

5. Discussion

The purpose-designed hydrogeological map tested at the study area (i) provides effective and partially new graphical solutions to describe the main hydrogeological features and processes characterizing a complex surface–groundwater interconnected system and (ii) points out several important aspects that meet the needs of hydrogeologists and the expectations of the map's users (with emphasis on planners and administrators).

In the latter case, this type of map can be used, for example, as a basis for reconstructing reliable vulnerability maps from the perspective of groundwater and GDE protection against pollution (considering both direct and indirect contamination sources). As a matter

of fact, this test study highlights that the large alluvial aquifer (whose groundwater feeds GDEs and is used to support the economic growth of one of the most important industrial areas in Italy and Europe) is vulnerable to contaminants also coming from the wider upgradient Apennine chain because of the indirect hydraulic connection via the Taro River.

Even if the Parma Apennines are mainly characterized by organic agriculture and protected areas, they could also be of interest for new mining exploitation, taking into consideration the progressive increase in the demand for metals and minerals for lithium-ion batteries. This is the case, for example, in the abandoned Corchia mining district (see location in the supplementary file), which can be defined as mixed sulfide (mostly Cu-bearing) ore deposits set into ophiolitic aquifers. As a matter of fact, mining activities can produce several types of waste, such as wastewater, and have long-lasting and profound adverse effects on the downstream receiving aquatic environments (e.g., [54–61]). Therefore, there is an urgent need to learn from historical mine pollution issues to avoid the negative environmental impacts of new mining activities in the future. This goal can be achieved by understanding how potential mine pollution could be transported from its source through a downstream catchment, and purpose-designed hydrogeological maps give this information to planners and administrators. From a vulnerability perspective, the hydrogeological mapping strategy and solutions proposed here suggest, for example, that Corchia mine reactivation would cause severe environmental damage in the vast interconnected aquatic ecosystem (to groundwater and GDEs) in case of contaminant release.

At the same time, this map will be used to plan and carry out more detailed studies that can help to understand and estimate (i) the magnitude of the expected impact of the possible Corchia mine reactivation, (ii) the transport time between the potential contamination source and each of the subsystems coexisting at the system scale, and (iii) the influence of pumping activities within the heterogeneous alluvial aquifer on the underground contaminant migration pathways.

6. Conclusions

In a broader context, the mapping strategy and solutions presented here are of utmost importance (i) in managing and optimizing water resources abstraction for human purposes (as is evident) as well as (ii) when carrying out effective water–energy–food–land–climate nexus studies (WqEFLC nexus, *sensu* [62]) for sustainable development goals. For example, an effective WqEFLC nexus study must also consider the layered heterogeneity of an alluvial aquifer. In that scenario, groundwater can be pumped through wells drilled and screened at different depths, requiring a lower or higher energy demand. Regarding climate change in particular, graphically showing the hydraulic interconnections between different subsystems that coexist in a wide area facilitates the (rapid and easy) understanding that water availability, as well as the integrity of specific GDEs, in a specific subsystem are both also influenced by climate modifications circumscribed to upstream sub-basins. Therefore, in hydrogeological settings where a changing climate has already been verified at a regional scale (e.g., [63,64] at the study area), more detailed climate studies should be planned to refine this cause–effect relationship.

Even in terms of sustainable development goals, this type of hydrogeological map can be utilized to measure the gross ecosystem product (GEP), which summarizes the value of the contribution of an ecosystem to the economic activity of an area by evaluating the ecosystem services in a single monetary metric [65]. As is known, this approach can consider the contribution of Nature to economic growth and human well-being differently from the conventional gross domestic product (GDP).

The approach proposed here can be applied worldwide, also in hydrogeological settings made up of different lithologies. As a matter of fact, the solutions tested with this map can be used in an easy way in those systems where different factors cause a large aquifer system to be hydraulically interconnected.

Supplementary Materials: The following supporting information can be downloaded at: https://www.mdpi.com/article/10.3390/hydrology10060127/s1, Figure S1: Hydrogeological Map of the Interconnected Surface–Groundwater System of Parma Alluvial Aquifer and Taro River Basin.

Author Contributions: Conceptualization, R.P., A.F., A.R. and F.C.; methodology, R.P., A.F. and F.C.; software, R.P., A.F. and F.C., validation, R.P., A.F., A.R. and F.C.; writing and reviewing the draft, R.P., A.F., A.R. and F.C. All authors have read and agreed to the published version of the manuscript.

Funding: This research received external funding from Provincia di Parma and is funded by the 'Departments of Excellence' program of the Italian Ministry for University and Research (MUR, 2023–2027).

Data Availability Statement: The relevant data can be found as follows: "Regione Emilia Romagna Borehole's Database" at https://servizimoka.regione.emilia-romagna.it/mokaApp/apps/geg/index.html (accessed on 11 May 2023); "Regione Emilia Romagna Water Springs" at https://servizimoka.regione.emilia-romagna.it/mokaApp/apps/rocce_magazzino/index.html (accessed on 11 May 2023); "Regione Emilia Romagna Geological Cartography—Webgis" at https://ambiente.regione.emilia-romagna.it/it/geologia/cartografia/webgis-banchedati/webgis (accessed on 11 May 2023); "ISPRA Geological Cartography at a scale of 1:50.000" at https://www.isprambiente.gov.it/Media/carg/ (accessed on 11 May 2023); "Provincia di Parma PIAE" at http://www.provincia.parma.it/provincia/servizi-e-uffici/servizio-pianificazione-territoriale/ufficio-attivit%C3%A0-estrattive-0 (accessed on 11 May 2023); and "Consorzio Bonifica Parmense irrigation canal network" at https://portale.bonifica.pr.it/map/lizmap/www/index.php/view/map/?repository=pubblica&project=web (accessed on 11 May 2023).

Acknowledgments: This research benefited from the equipment and framework of the COMP-R Initiative.

Conflicts of Interest: The authors declare no conflict of interest.

References

1. Freeze, R.A.; Cherry, J.A. *Groundwater*; Prentice Hall Inc.: Englewood Cliffs, NJ, USA, 1979.
2. Stuckmeier, W.F.; Margat, J. *Hydrogeological Maps. A Guide and a Standard Legend*; International Association of Hydrogeoiogist, Contributions to Hydrogeology, Cerlag Heinz Heisse: Hannover, Germany, 1995; Volume 17, 170p.
3. Iacumin, P.; Venturelli, G.; Selmo, E. Isotopic features of rivers and groundwater of the Parma Province (Northern Italy) and their relationships with precipitation. *J. Geochem. Explor.* **2009**, *102*, 56–62. [CrossRef]
4. Mancini, M.C.; Arfini, F.; Guareschi, M. When Higher Education Meets Sustainable Development of Rural Areas: Lessons Learned from a Community–University Partnership. *Soc. Sci.* **2022**, *11*, 338. [CrossRef]
5. Arfini, F.; Cozzi, E.; Mancini, M.C.; Ferrer-Perez, H.; Gil, J.M. Are Geographical Indication Products Fostering Public Goods? Some Evidence from Europe. *Sustainability* **2019**, *11*, 272. [CrossRef]
6. Mancini, M.C.; Donati, M. *Local Agri-Food Systems in a Global World: Market, Social and Environmental Challenges*; Cambridge Scholars Publishing: Cambridge, UK, 2012.
7. Mancini, M.C.; Consiglieri, C. Innovation and marketing strategies for PDO products: The case of "Parmigiano Reggiano" as an ingredient. *Bio-Based Appl. Econ. J.* **2016**, *5*, 153–174.
8. Parma Manifactures Associations. Parma and Its Enterprises. 2020. Available online: www.upi.pr.it (accessed on 1 January 2023).
9. Conti, P.; Cornamusini, G.; Carmignani, L. An outline of the geology of the Northern Apennines (Italy), with geological map at 1:250,000 scale. *Ital. J. Geosci.* **2020**, *139*, 149–194. [CrossRef]
10. Elter, P.; Grasso, M.; Parotto, M.; Vezzani, L. Structural setting of the Apennine-Maghrebian thrust belt. *Epis. J. Int. Geosci.* **2003**, *26*, 205–211. [CrossRef]
11. Remitti, F.; Vannucchi, P.; Bettelli, G.; Fantoni, L.; Panini, F.; Vescovi, P. Tectonic and sedimentary evolution of the frontal part of an ancient subduction complex at the transition from accretion to erosion: The case of the Ligurian wedge of the northern Apennines, Italy. *GSA Bull.* **2011**, *123*, 51–70. [CrossRef]
12. Carlini, M.; Artoni, A.; Vescovi, P.; Bernini, M.; Remitti, F.; Bettelli, G.; Vannucchi, P.; Aldega, L.; Balestrieri, M.L.; Corrado, S.; et al. Tectonic and erosional exhumation processes in the western Northern Apennines of Italy: Coeval compressional and extensional tectonics affecting an eroding orogenic wedge. In Proceedings of the EGU General Assembly Conference, Vienna, Austria, 7–12 April 2013; p. 12994.
13. Molli, G.; Crispini, L.; Malusà, M.; Mosca, P.; Piana, F.; Federico, L. Geology of the Western Alps-Northern Apennine junction area: A regional review. *Eds Marco Beltrando Angelo Peccerillo Massimo Mattei Sandro Conticelli Carlo Doglioni J. Virtual Explor.* **2010**, *36*, 1–49. [CrossRef]
14. Vescovi, P. *Note Illustrative Della Carta Geologica d'Italia Alla Scala 1:50.000, Foglio 216 "Borgo Val Di Taro"*; Servizio Geologico d'Italia-Regione Emilia Romagna; SELCA: Firenze, Italy, 2002.

15. Boccaletti, M.; Corti, G.; Martelli, L. Recent and active tectonics of the external zone of the Northern Apennines (Italy). *Int. J. Earth Sci.* **2011**, *100*, 1331–1348. [CrossRef]
16. Marroni, M.; Molli, G.; Montanini, A.; Tribuzio, R. The association of continental crust rocks with ophiolites (northern Apen-nines, Italy): Implications for the continent-ocean transition. *Tectonophysics* **1998**, *292*, 43–66. [CrossRef]
17. Marroni, M.; Molli, G.; Montanini, A.; Ottria, G.; Pandolfi, L.; Tribuzio, R. The External Liguride units (Northern Apennine, Italy): From rifting to convergence history of a fossil ocean-continent transition zone. *Ofioliti* **2002**, *27*, 119–132.
18. Vescovi, P.; Fornaciari, E.; Rio, D.; Valloni, R. The basal complex stratigraphy of the Helminthoid Monte Cassio Flysch: A key to the eoalpine tectonics of the Northern Apennines. *Riv. Ital. Di Paleontol. E Stratigr. (Res. Paleontol. Stratigr.)* **1999**, *105*, 101–128.
19. Marroni, M.; Meneghini, F.; Pandolfi, L. A revised subduction inception model to explain the Late Cretaceous, double-vergent orogen in the precollisional western Tethys: Evidence from the Northern Apennines. *Tectonics* **2017**, *36*, 2227–2249. [CrossRef]
20. Amorosi, A.; Ricci Lucchi, F.; Tateo, F. The Lower Miocene siliceous zone: A marker in the palaeogeographic evolution of the northern Apennines. *Palaeogeogr. Palaeoclimatol. Palaeoecol.* **1995**, *118*, 131–149. [CrossRef]
21. Piazza, A.; Artoni, A.; Ogata, K. The Epiligurian wedge-top succession in the Enza Valley (Northern Apennines): Evidence of a syn-depositional transpressive system. *Swiss J. Geosci.* **2016**, *109*, 17–36. [CrossRef]
22. Fantoni, R.; Franciosi, R. Tectono-sedimentary setting of the Po Plain and Adriatic foreland. *Rend. Lincei* **2010**, *21*, 197–209. [CrossRef]
23. Livani, M.; Scrocca, D.; Arecco, P.; Doglioni, C. Structural and stratigraphic control on salient and recess development along a thrust belt front: The Northern Apennines (Po Plain, Italy). *J. Geophys. Res. Solid Earth* **2018**, *123*, 4360–4387. [CrossRef]
24. Salvador, A. *International Stratigraphic Guide: A Guide to Stratigraphic Classification, Terminology, and Procedure*; Geological Society of America: London, UK, 1994.
25. Tazioli, A.; Cervi, F.; Doveri, M.; Mussi, M.; Deiana, M.; Ronchetti, F. Estimating the isotopic altitude gradient for hydrogeo-logical studies in mountainous areas: Are the low-yield springs suitable? Insights from the northern Apennines of Italy. *Water* **2019**, *11*, 1764. [CrossRef]
26. Ronchetti, F.; Piccinini, L.; Deiana, M.; Ciccarese, G.; Vincenzi, V.; Aguzzoli, A.; Malavasi, G.; Fabbri, P.; Corsini, A. Tracer test to asses flow and transport parameters of an earth slide: The Montecagno landslide case study (Italy). *Eng. Geol.* **2020**, *275*, 105749. [CrossRef]
27. Aguzzoli, A.; Arosio, D.; Mulas, M.; Ciccarese, G.; Benedikt, B.; Gerfried, W.; Ronchetti, F. Multidisciplinary non-invasive investigations to develop a hydrogeological conceptual model supporting slope kinematics at Fontana Cornia landslide, Northern Apennines, Italy. *Environ. Earth Sci.* **2022**, *81*, 471. [CrossRef]
28. Martelli, L.; Calabrese, L.; Ercolessi, G.; Molinari, F.C.; Severi, P.; Bonini, M. The New Seismotectonic Map of the Emilia-Romagna Region and Surrounding Areas. Atti del 36° Congresso del Gruppo Nazionale di Geofisicxa della Terra Solida. *Atti. Del.* **2017**, *36*, 14–16.
29. Segadelli, S.; Vescovi, P.; Ogata, K.; Chelli, A.; Zanini, A.; Boschetti, T.; Petrella, E.; Toscani, L.; Gargini, A.; Celico, F. A con-ceptual hydrogeological model of ophiolitic aquifers (serpentinised peridotite): The test example of Mt. Prinzera (Northern Italy). *Hydrol. Process.* **2017**, *31*, 1058–1073. [CrossRef]
30. Segadelli, S.; Vescovi, P.; Chelli, A.; Petrella, E.; De Nardo, M.T.; Gargini, A.; Celico, F. Hydrogeological mapping of hetero-geneous and multi-layered ophiolitic aquifers (Mountain Prinzera, northern Apennines, Italy). *J. Maps* **2017**, *13*, 737–746. [CrossRef]
31. Segadelli, S.; Filippini, M.; Monti, A.; Celico, F.; Gargini, A. Estimation of recharge in mountain hard-rock aquifers based on discrete spring discharge monitoring during base-flow recession. *Hydrogeol. J.* **2021**, *29*, 949–961. [CrossRef]
32. Caine, J.S.; Evans, J.P.; Forster, C.B. Fault zone architecture and permeability structure. *Geology* **1996**, *24*, 1025–1028. [CrossRef]
33. Bense, V.F.; Gleeson, T.; Loveless, S.E.; Bour, O.; Scibek, J. Fault zone hydrogeology. *Earth Sci. Rev.* **2013**, *127*, 171–192. [CrossRef]
34. Segadelli, S.; Adorni, M.; Carbognani, M.; Celico, F.; Tomaselli, M. Combining biological and hydrogeological approaches: The grass Molinia arundinacea as a possible bioindicator of temporary perched aquifers in ophiolitic systems. *Catena* **2022**, *217*, 106448. [CrossRef]
35. Gargini, A.; Vincenzi, V.; Piccinini, L.; Zuppi, G.M.; Canuti, P. Groundwater flow systems in turbidites of the Northern Ap-ennines (Italy): Natural discharge and high speed railway tunnel drainage. *Hydrogeol. J.* **2008**, *16*, 1577. [CrossRef]
36. Petrella, E.; Celico, F. Heterogeneous aquitard properties in sedimentary successions in the Apennine chain: Case studies in southern Italy. *Hydrol. Process. Int. J.* **2009**, *23*, 3365–3371. [CrossRef]
37. Davis, S.N.; De Wiest, R.J.M. *Hydrogeology*; John Wiley & Sons: New York, NY, USA, 1966.
38. Rizzo, P.; Severini, E.; Bucci, A.; Bocchia, F.; Palladino, G.; Riboni, N.; Celico, F. How do turbidite systems behave from the hydrogeological point of view? New insights and open questions coming from an interdisciplinary work in southern Italy. *PLoS ONE* **2022**, *17*, e0268252. [CrossRef]
39. Bonini, M. Interrelations of mud volcanism, fluid venting, and thrust-anticline folding: Examples from the external northern Apennines (Emilia-Romagna, Italy). *J. Geophys. Res. Solid Earth* **2007**, *112*, 1–21. [CrossRef]
40. Deiana, M.; Cervi, F.; Pennisi, M.; Mussi, M.; Bertrand, C.; Tazioli, A.; Ronchetti, F. Chemical and isotopic investigations (δ 18 O, δ 2 H, 3 H, 87 Sr/86 Sr) to define groundwater processes occurring in a deep-seated landslide in flysch. *Hydrogeol. J.* **2018**, *26*, 2669–2691. [CrossRef]
41. Remelli, S.; Petrella, E.; Chelli, A.; Conti, F.D.; Lozano Fondón, C.; Celico, F.; Francese, R.; Menta, C. Hydrodynamic and soil biodiversity characterization in an active landslide. *Water* **2019**, *11*, 1882. [CrossRef]

42. Rizzo, P.; Petrella, E.; Bucci, A.; Salvioli Mariani, E.; Chelli, A.; Sanangelantoni, A.M.; Raimondo, M.; Quagliarini, A.; Celico, F. Studying hydraulic interconnections in low-permeability media by using bacterial communities as natural tracers. *Water* **2020**, *12*, 1795. [CrossRef]
43. Chelli, A.; Francese, R.; Petrella, E.; Carri, A.; Quagliarini, A.; Segalini, A.; Celico, F. A multi-parameter field monitoring system to investigate the dynamics of large earth slides–earth flows in the Northern Apennines, Italy. *Eng. Geol.* **2020**, *275*, 105780. [CrossRef]
44. Petrella, E.; Raimondo, M.; Chelli, A.; Valentino, R.; Severini, E.; Diena, M.; Celico, F. Processes and factors controlling the groundwater flow in a complex landslide: A case study in the Northern Italy. *Hydrol. Process.* **2023**, *37*(5), e14891. [CrossRef]
45. Regione Emilia-Romagna; ENI-AGIP. *Riserve Idriche Sotterranee Della Regione Emilia-Romagna. A Cura di G.M. Di Dio*; Regione Emilia-Romagna, ENI Agip Divisione Esplorazione e Produzione; SELCA: Firenze, Italy, 1998; p. 120.
46. Zanini, A.; Petrella, E.; Sanangelantoni, A.M.; Angelo, L.; Ventosi, B.; Viani, L.; Celico, F. Groundwater characterization from an ecological and human perspective: An interdisciplinary approach in the Functional Urban Area of Parma, Italy. *Rend. Lincei. Sci. Fis. E Nat.* **2019**, *30*, 93–108. [CrossRef]
47. Di Dio, G.; Martini, A.; Lasagna, S.; Zanzucchi, G. *Explanatory notes of the Geologic Map of Italy at the Scale 1:50,000, Sheet No. 199 Parma Sud-Ovest*; Servizio Geologico della Regione Emilia-Romagna, Servizio Geologico Nazionale, ISPRA: Rome, Italy, 2005.
48. Zanini, A.; Ghirardi, M.; Emiliani, R. A multidisciplinary approach to evaluate the effectiveness of natural attenuation at a contaminated site. *Hydrology* **2021**, *8*, 101. [CrossRef]
49. Severini, E.; Ducci, L.; Sutti, A.; Robottom, S.; Sutti, S.; Celico, F. River–Groundwater Interaction and Recharge Effects on Microplastics Contamination of Groundwater in Confined Alluvial Aquifers. *Water* **2022**, *14*, 1913. [CrossRef]
50. Ducci, L.; Rizzo, P.; Pinardi, R.; Solfrini, A.; Maggiali, A.; Pizzati, M.; Balsamo, F.; Celico, F. What Is the Impact of Leaky Sewers on Groundwater Contamination in Urban Semi-Confined Aquifers? A Test Study Related to Fecal Matter and Personal Care Products (PCPs). *Hydrology* **2022**, *10*, 3. [CrossRef]
51. Rossetti, G.; Pieri, V.; Martens, K. Recent ostracods (Crustacea, Ostracoda) found in lowland springs of the provinces of Pia-cenza and Parma (Northern Italy). *Hydrobiologia* **2005**, *542*, 287–296. [CrossRef]
52. Bonaposta, D.; Segadelli, S.; De Nardo, M.T.; Alessandrini, A.; Pezzoli, S. Le potenzialità geologiche dei dati storici am-bientali: Il caso delle sorgenti e dei fontanili in Emilia-Romagna. *Il Geologo dell'Emilia Romagna* **2011**, *1*, 19–34.
53. Kløve, B.; Ala-Aho, P.; Bertrand, G.; Boukalova, Z.; Ertürk, A.; Goldscheider, N.; Widerlund, A. Groundwater dependent ecosystems. Part I: Hydroecological status and trends. *Environ. Sci. Policy* **2011**, *14*, 770–781. [CrossRef]
54. Song, Y.; Ji, J.; Mao, C.; Yang, Z.; Yuan, X.; Godwin, A.A.; Frost, R.L. Heavy metal contamination in suspended solids of Changjiang river—Environmental implications. *Geoderma* **2010**, *159*, 286–295. [CrossRef]
55. Thorslund, J.; Jarsjö, J.; Chalov, S.R.; Belozerova, E.V. Gold mining impact on riverine heavy metal transport in a sparsely monitored region: The upper Lake Baikal Basin case. *J. Environ. Monit.* **2012**, *14*, 2780–2792. [CrossRef]
56. Hu, B.; Li, J.; Bi, N.; Wang, H.; Yang, J.; Wei, H.; Zhao, J.; Li, G.; Yin, X.; Liu, M.; et al. Seasonal variability and flux of patticulate trace elements from the Yellow River: Impacts of the anthropogenic flood event. *Mar. Pollut. Bull.* **2015**, *91*, 35–44. [CrossRef]
57. Oberholster, P.J.; Botha, A.M.; Hill, L.; Strydom, W.F. River catchment responses to anthropogenic acidification in relationship with sewage effluent: An ecotoxicology screening application. *Chemosphere* **2017**, *189*, 407–417. [CrossRef]
58. Zhou, Q.; Yang, N.; Li, Y.; Ren, B.; Ding, X.; Bian, H.; Yao, X. Total concentration and sources of heavy metal pollution in global river and lake water bodies from 1972 to 2017. *Glob. Ecol. Conserv.* **2020**, *22*, e00925. [CrossRef]
59. Atangana, E.; Oberholster, P.J. Using heavy metal pollution indices to assess water quality of surface and groundwater on catchment levels in South Africa. *J. Afr. Earth Sci.* **2021**, *182*, 104254. [CrossRef]
60. Sui, C.; Fatichi, S.; Burlando, P.; Weber, E.; Battista, G. Modeling distributed metal pollution transport in a mine impacted catchment: Short and long-term effects. *Sci. Total Environ.* **2022**, *812*, 151473. [CrossRef]
61. Owens, P.N.; Petticrew, E.L.; Albers, S.J.; French, T.D.; Granger, B.; Laval, B.; Vagle, S. Annual pulses of copper-enriched sediment in a North American river downstream of a large lake following the catastrophic failure of a mine tailings storage facility. *Sci. Total Environ.* **2023**, *856*, 158927. [CrossRef] [PubMed]
62. Rezaei Kalvani, S.; Celico, F. The Water–Energy–Food Nexus in European Countries: A Review and Future Perspectives. *Sustainability* **2023**, *15*, 4960. [CrossRef]
63. D'Oria, M.; Cozzi, C.; Tanda, M.G. Future precipitation and temperature changes over the Taro, Parma and Enza River Basins in Northern Italy. *Ital. J. Eng. Geol. Environ. (Spec. Issue)* **2018**, *1*, 49–63.
64. Todaro, V.; D'Oria, M.; Secci, D.; Zanini, A.; Tanda, M.G. Climate change over the Mediterranean region: Local temperature and precipitation variations at five pilot sites. *Water* **2022**, *14*, 2499. [CrossRef]
65. Ouyang, Z.; Song, C.; Zheng, H.; Polasky, S.; Xiao, Y.; Bateman, I.J.; Daily, G.C. Using gross ecosystem product (GEP) to value nature in decision making. *Proc. Natl. Acad. Sci. USA* **2020**, *117*, 14593–14601. [CrossRef] [PubMed]

Disclaimer/Publisher's Note: The statements, opinions and data contained in all publications are solely those of the individual author(s) and contributor(s) and not of MDPI and/or the editor(s). MDPI and/or the editor(s) disclaim responsibility for any injury to people or property resulting from any ideas, methods, instructions or products referred to in the content.

water

MDPI

Article

Analysis of the Seawater Intrusion Process Based on Multiple Monitoring Methods: Study in the Southern Coastal Plain of Laizhou Bay, China

Hongwei Liu [1,2,3], Lin Gao [4,*], Chuanming Ma [4,*] and Yi Yuan [5]

[1] Chinese Academy of Geological Sciences, No. 26 Baiwanzhuang Street, Beijing 100037, China; liuhenry022@163.com
[2] North China Center for Geoscience Innovation Precambrian Research Centre, China Geological Survey, No. 4, Bahao Road, Tianjin 300170, China
[3] Tianjin Center, China Geological Survey, No. 4, Bahao Road, Tianjin 300170, China
[4] School of Environmental Studies, China University of Geosciences, No. 388, Lumo Road, Wuhan 430074, China
[5] Hubei Provincial Department of Natural Resources Geological Disaster Emergency Response Center, No. 27, Gongzheng Road, Wuhan 430074, China; yuany2019@126.com
* Correspondence: glin@cug.edu.cn (L.G.); machuanming@cug.edu.cn (C.M.); Tel.: +86-027-67883157 (L.G.)

Abstract: Affected by natural factors and human activities, seawater intrusion has become a geo-environmental problem, significantly impacting human production and life. Seawater intrusion weakens coastal areas' geo-environmental carrying capacity, limiting industry and commerce development potential. On the other hand, it may provide convenient deep seawater resources for coastal aquaculture development. Therefore, how to quantitatively analyze seawater intrusion's process, scope, and influencing factors has become a hotspot for hydrogeological researchers. This study uses chemical sampling analysis, environmental isotope, fixed-point, and geophysical methods to monitor long-term seawater intrusion in the southern coastal plain of Laizhou Bay. According to the monitoring data, the chemical type of fresh groundwater changes from Ca·Mg-HCO_3 to Na-HCO_3·Cl, Na·Ca-HCO_3·Cl from south to north, and the changing trend of brackish groundwater is from Mg·Na·Ca-HCO_3, Mg·Ca-HCO_3 to Na-Cl·HCO_3, Na·Mg-Cl. Saline groundwater is mainly of the Na-Cl and Na·Mg-Cl type. Brine is of the Cl-Na type. The relationship between ^{18}O, ^{2}H, and Cl^- shows that groundwater was affected by evaporation, dissolution, and mixing in the runoff process. The relationship between water level and TDS in monitoring wells at different locations and depths confirms the existence of seasonal variations and layered intrusion phenomena in groundwater recharge sources. From July 2018 to December 2019, the south intrusion and north retreat rates were approximately 213.3 m/a and 105.9 m/a, respectively. From August 2016 to December 2019, the seawater intrusion front on the Dawangdong profile generally retreated northward at approximately 27 m/a. The results of this study can provide a scientific basis for the utilization of groundwater in local production and life. Comparative analysis and mutual verification of multiple monitoring methods can provide basic ideas for constructing a multi-source monitoring system for seawater intrusion.

Keywords: groundwater monitoring; seawater intrusion; groundwater aquifer system; Laizhou Bay

1. Introduction

From a global perspective, coastal zones are the most economically developed and densely populated regions [1,2]; approximately 60% of the world's population is widely concentrated within 60 km of a coastal zone [3,4]. Affected by the combined effects of climate change and human activities, coastal areas face ecological and environmental problems, including seawater intrusion [5–8]. The core of the meaning of seawater intrusion is caused by human activity or climate change [9,10]. The most typical intrusion process is the excessive exploitation of groundwater, which causes the hydrodynamic imbalance

of the aquifer and causes the brackish–freshwater transition zone to move inland [11,12]. Seawater intrusion can cause immediate economic losses or problems, such as crop yield loss and industrial water shortages. It will also lead to potential adverse effects on the ecological environment [13,14]. For instance, seawater intrusion will lead to soil salinization in coastal areas, changing soil and vegetation's nitrogen content. Changes in the nitrogen cycle may trigger the decline of some vegetation species and the degradation of ecological functions [15–17]. Concurrently, seawater intrusion can provide convenient deep seawater resources with relatively stable hydration properties for coastal aquaculture [18]. Due to these reasons, based on the dual impact of seawater intrusion on human production and life, the investigation, monitoring, evaluation, prediction, and mechanism of its process have become an essential scientific research topic in the fields of earth science and ecological environment science [7,19,20].

The monitoring target of seawater intrusion is the change in the intrusion transition zone or interface, with indirect reflection factors including changes in vegetation cover, degree of soil salinity, etc., and direct reflection factors including the chemical characteristics of groundwater, groundwater table (or water head), etc. [21,22]. Monitoring methods mainly include the Water Chemical Sampling Analysis Method, Isotope Hydrogeochemical Method, Fixed-point Well Monitoring Method, and Geophysical Monitoring Method (Table 1) [23–27]. The water chemical sampling analysis method is divided into a single index method and a comprehensive index method, which can directly reflect the quality of groundwater [28]. The principle is that chloride ions exist stably, and the mass concentration is significantly different, similar to total dissolved solids (TDS) [29]. This method can quickly identify seawater intrusion based on mastering the hydrogeological conditions of the study area. Maged et al. effectively evaluated the water resources in areas affected by seawater intrusion, such as Mecca, through multiple water quality indices, GIS methods, and partial least squares regression models [30, 31]. With the development of hydrogeochemical isotopic technology, using environmental isotope tracing, such as stable or radioactive isotopes, to monitor seawater intrusion has become an effective method. This method is often combined with the water chemical sampling analysis method. Liu et al. (2016), Maurya et al. (2019), and Qi et al. (2019) [32–34] analyzed the degree of intrusion in different regions by identifying the direction of seawater intrusion and other sources of salinity in the aquifer using data such as groundwater $\delta^{18}O$, $\delta^{2}H$, and water–chemical–ion ratio. The fixed-point well monitoring method refers to drilling wells or relying on existing wells, placing automatic monitor instruments, or regularly taking water samples for testing, which have the advantage of monitoring seawater intrusion at different times and depths in a long sequence. Du et al. (2015) and Lim et al. (2013) [35,36] analyzed the current situation and dynamic change characteristics of seawater intrusion in multiple regions and explored the influence of hydrogeological conditions and groundwater flow system characteristics on seawater intrusion, using data from one-hole multi-layer (different depths) and various groups of one-hole single-layer monitoring wells, respectively. The principle of the geophysical method is that seawater and fresh groundwater have apparent differences in electrical conductivity and magnetic permeability [37–41]. The electromagnetic signal passing through the transition zone between seawater and fresh groundwater will display an abnormal electromagnetic signal, thereby determining the location of the seawater intrusion interface. This method is often combined with the water chemical sampling analysis method to optimize the correction of geophysical parameters [23]. Abdulameer et al. (2018), Wang et al. (2022), and Song et al. (2014) [37,39,40] used a high-density resistivity method or audio magneto telluric, combined with water chemical data or borehole lithology data by setting up multiple monitoring profiles, to accurately delineate the seawater intrusion interface in different regions, and the seawater intrusion status was evaluated. In addition, Alfaifi et al. (2019), El-Kaliouby (2020), Nicolodi et al. (2018), and Yang et al. (2013) [19,42–44] applied various methods, such as the time-domain electromagnetic method (TDEM), aerial remote sensing electromagnetic method, seismic refraction tomography, etc., combined with water chemical data, to analyze the interface, depth, and extent of seawater intrusion in

many regions, and discussed the factors that affect seawater intrusion, such as excessive groundwater extraction, coastal sediment lithology, etc.

Table 1. Comparison of seawater intrusion monitoring methods.

Methodology	Water Chemical Sampling Analysis		Isotope Hydrogeochemical		Monitoring Well	Geophysical Monitoring	
Classification	Single indicator (Cl^-, TDS)	Multiple indicator (Cl^-, Br^-, TDS, etc.)	Stable isotope (^2H, ^{18}O,^{24}S, ^{87}Sr, ^{11}B, ^{37}Cl, ^{87}Br)	Radioactive isotope (^3H, ^{14}C)	Groundwater level	Earth resistance method	Audio-frequency magneto telluric method
Advantages	Most direct and easy-to-use	Comprehensiveness, reducing errors	Identifying the different sources of groundwater salinization		Indirect evidence and reference for the transition zone	Determining the interface between saltwater and freshwater in space and time	
Disadvantages	Hydrogeological conditions and human influence have a large margin of error	Multiple indicators and complex operations	Low sensitivity, multiple isotope identification methods are needed		High requirements for location and depth costly in applications	Equipment parameters need to be set according to the geological conditions to obtain accurate data	

However, most of the above studies used a single method, and more comparative analysis must be carried out using multiple monitoring methods. Based on this, this study uses multiple monitoring methods (including the Water Chemical Sampling Analysis Method, Isotope Hydrogeochemical method, Fixed-point Well Monitoring Method, and Geophysical Monitoring Method) to analyze the situation of seawater intrusion on the southern coastal plain of Laizhou Bay and understand the impact of human activities and seasonal groundwater recharge. We reveal the influencing factors and processes and compare the suitability of monitoring methods to provide an applicability analysis of the above monitoring methods for the construction of a multi-source monitoring system for seawater intrusion.

2. Study Area

The study area is divided into Shouguang County, Changyi County, and Hanting District (Figure 1). It is located on the south bank of Laizhou Bay. The east is adjacent to Qingdao and Yantai City, and the west is adjacent to Zibo City and Dongying City. It is located between 36°41′~37°19′ north latitude and 118°32′~119°10′ longitude. It is classified as a warm temperate continental monsoon climate. The average annual precipitation is 560–660 mm, and the average yearly temperature is 12.3 °C. The total number of rivers is more than 100, each of which is a rain-fed river in the monsoon region, divided into a six-way groundwater aquifer system: Xiaoqing River, Mi River, Bailang River, Wei River, Jiaolai River, and Yu River. The average annual surface runoff volume is 17.0×10^9 m^3. The study area is high in the south and low in the north, with an elevation between 2 and 7 m. The geomorphic types of the study area mainly include coastal plains, beaches, and shallow seas [45]. The coastal area of the study area is a typical silt shale coast in the north of China. It is mainly composed of silt, with an area of about 400 km^2 and a total length of 140 km.

The study area belongs to the fault subsidence settlement area and deposits a set of Minghu town shale. During the Late Pleistocene and Holocene, a group of thick marine sands was deposited due to the influence of three sea transgressions. Most of the area is covered by Quaternary loose deposits with a maximum thickness reaching up to 400 m [46]. Since the Mesozoic, the tectonic movement in the study area has mainly been fault-block motion. The fault tectonic is relatively developed, including the northeast and north-northeast faults. The Yimu fault zone and its derived tectonic control, tectonic engender,

development, magmatic activity, and mineralization of the study area were investigated (Figure 2a). According to the change in the hydrogeological characteristics in the horizontal and vertical directions, Gao et al. (2020), and Hu et al. (2020) [9,18] divided the soil area of Laizhou Bay into six water and geological zones: the bedrock fissures freshwater area, unconsolidated rock pore freshwater area, fresh–salty two-layer structure porewater area, fresh–salty–fresh three-layer structure porewater area, salty–fresh two-layer structure porewater area, and salty–brine pore water of the south coast (Figure 2b).

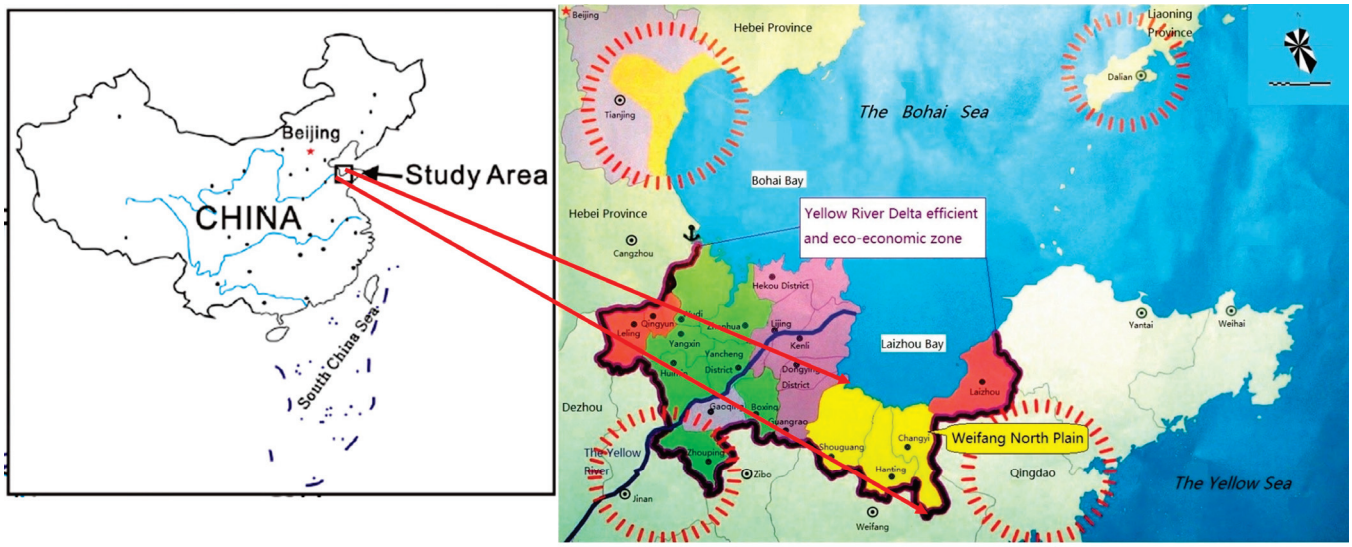

Figure 1. Location and range diagram of the study area.

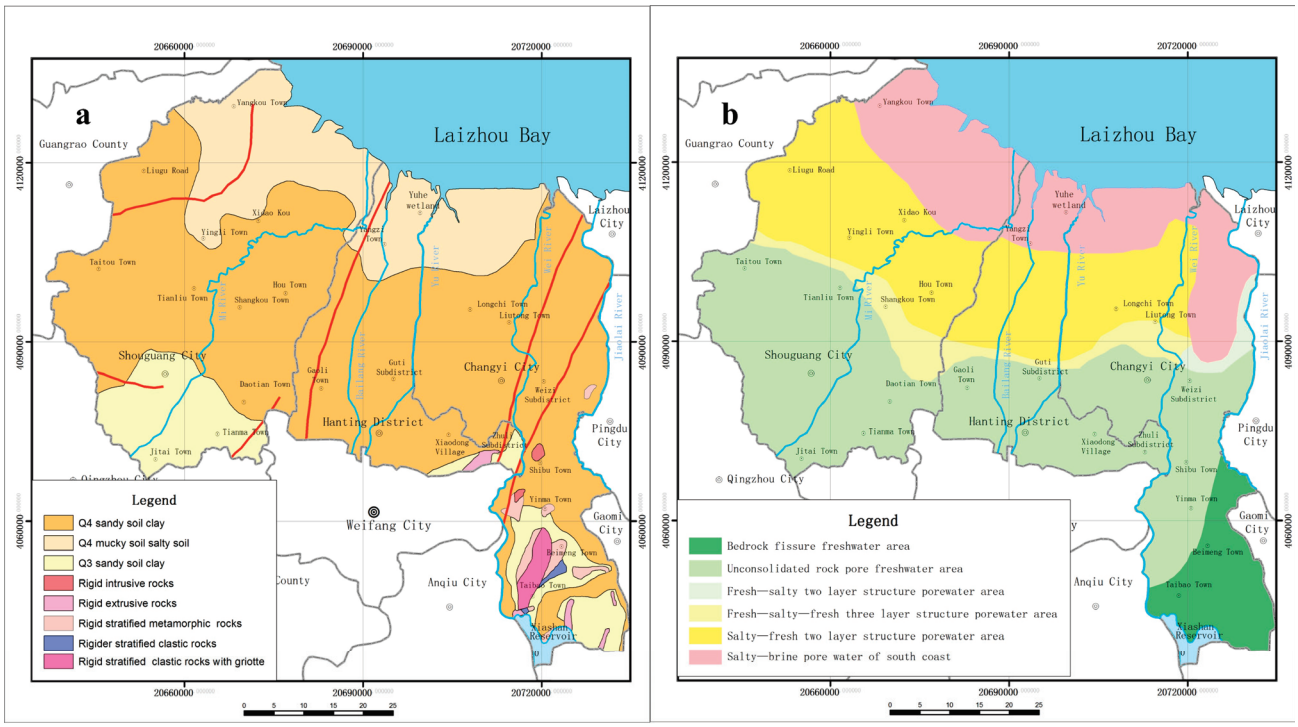

Figure 2. (**a**) Geological map of the study area. (**b**) Hydrogeological map of the study area.

3. Method

In this study, seawater intrusion is a general term for both seawater intrusion and saline groundwater intrusion; the difference between the above two concepts is that the main body of the former is modern seawater, while the latter is ancient seawater (saline water or brine formed by the retention of ancient seawater in the stratum), respectively. Based on the geological and environmental conditions, groundwater flow system, and human activities in the research area, we analyzed the process of seawater intrusion and its influencing factors. The methodology flowchart of this study is shown in Figure 3.

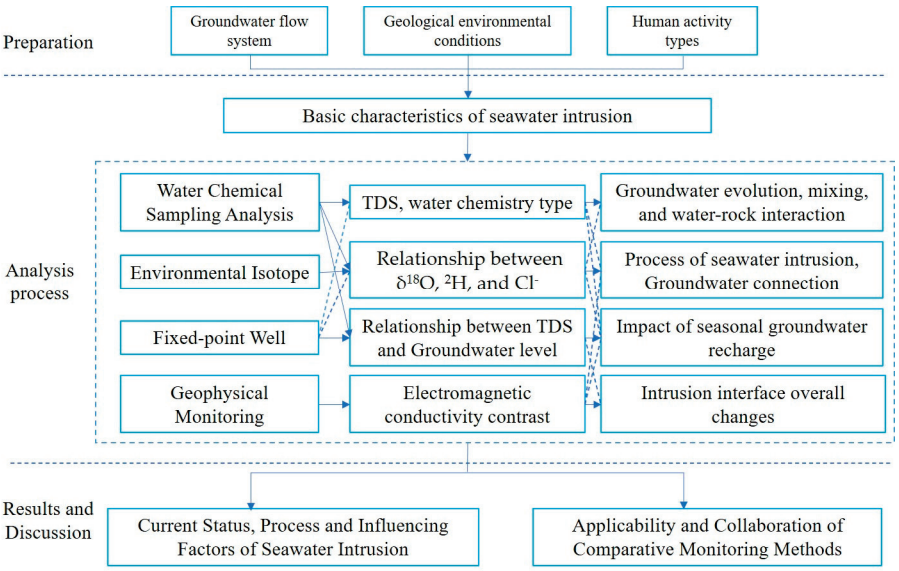

Figure 3. The methodology flowchart of this study.

The water samples for this study were collected in the southern coastal plain of Laizhou Bay from June to July 2018 (Table 2). Sixty-four samples were collected, including one seawater sample, seven surface water samples, and fifty-six groundwater samples. According to the criteria defined by and specification documents, groundwater samples were divided into four types based on the TDS: fresh groundwater (TDS < 1 g/L), brackish groundwater (1 g/L < TDS < 3 g/L), saline groundwater (3 g/L < TDS < 50 g/L), and brine (50 g/L < TDS). Detailed field information, sampling methods, and hydrochemistry analyses are summarized in [47,48]. The automatic monitoring point and electromagnetic profile are shown in Figure 4.

Table 2. Hydrochemistry and isotope compositions of water samples.

Samples	Water Type (m)	TDS (g/L)	Well Depth (m)	Chemical Type	K (mg/L)	Na (mg/L)	Ca (mg/L)	Mg (mg/L)	SO_4 (mg/L)	HCO_3 (mg/L)	Cl (mg/L)	$\delta^{18}O$ VS-MOW (‰)	$\delta^{2}H$ VS-MOW (‰)
0707-09	Brackish groundwater	1.736	5	Na·Ca-HCO_3·Cl	14.5	452	166.8	52.2	174.1	839	457.3	−10	−66.3
225	Brackish groundwater	1.413	12	Ca·Na·Mg-Cl	7.2	157.7	263.9	65.8	135.9	491.2	537.1	−6.3	−46.5
0707-01	Brackish groundwater	2.04	12	Na-HCO_3·Cl·SO_4	7.5	687.7	63.7	43.7	357.1	823.8	467.9	−8.6	−57.4
L45	Brackish groundwater	1.409	18	Ca·Na-SO_4 HCO_3	2	141.8	293	43.6	506.4	497.3	173.7	−9.1	−61.5
16	Brackish groundwater	2.313	18	Na·Mg·Ca-Cl	8.1	446.9	207.6	133.8	293.1	713.9	866.8	−11.8	−58

Table 2. *Cont.*

Samples	Water Type (m)	TDS (g/L)	Well Depth (m)	Chemical Type	K (mg/L)	Na (mg/L)	Ca (mg/L)	Mg (mg/L)	SO_4 (mg/L)	HCO_3 (mg/L)	Cl (mg/L)	$\delta^{18}O$ VS-MOW (‰)	$\delta^{2}H$ VS-MOW (‰)
L35	Brackish groundwater	2.641	18	Na-Cl HCO_3	21.9	895.5	22.3	41	251.9	726.1	1045.8	−10.2	−63.3
L34	Brackish groundwater	2.192	20	Na·Mg·Ca-Cl	1	533.3	156.4	117.8	521.9	500.4	611.5	−9	−51.9
221	Brackish groundwater	2.222	22	Na-Cl·HCO_3·SO_4	27.9	733.6	26.7	23.4	511.5	747.5	524.7	−8.8	−53.9
L31	Brackish groundwater	1.437	23	Na·Ca·Mg-Cl	1	239	174	93.5	139.4	286.8	647	−8.4	−56.7
0724-08	Brackish groundwater	1.457	25	Na-Cl·H CO_3	16.4	440.6	60.9	60.2	165.2	579.7	423.6	−8.5	−58.9
L39	Brackish groundwater	1.033	30	Na-HCO_3·Cl·SO_4	35.9	308.8	22.1	27.5	187.5	552.2	175.5	−9.4	−56.1
L30	Brackish groundwater	1.112	30	Na·Mg·Ca-Cl	14.1	250.4	99.1	63.6	85.3	430.2	384.6	−14.9	−59.6
0705-02	Brackish groundwater	2.555	30	Na-Cl·HCO_3	12.6	741.6	81.9	84.5	180.3	781.1	1063.5	−9.4	−59.6
L33	Brackish groundwater	2.595	70	Na·Mg-Cl	6.3	718.4	69.7	111.6	333	497.3	1107.8	−15.5	−63.9
0707-08	Brackish groundwater	1.238	75	Na·Mg·Ca-HCO_3	2.3	268.4	103.8	72	164.9	579.7	336.8	−13.3	−60.9
0707-07	Brackish groundwater	1.235	80	Mg·Ca·Na-HCO_3	3	152	138.1	129.1	134.8	732.2	312	−9.6	−60.8
L36-2	Brackish groundwater	1.195	200	Na·Ca-Cl·HCO_3	3.1	285.9	87	47.6	167.5	274.6	466.2	−15.5	−71.3
0706-02	Brine	85.767	80	Na-Cl	457.7	26,120	923.8	3018	6836	399.7	48,212	−11.6	−47.5
0705-01	Brine	103.87	90	Na-Cl	694.8	30,690	988.6	4361	7446	799.4	59,290.1	−1.5	−52.4
0724-14	Brine	119.853	100	Na-Cl	830.5	36,770	1122	5048	8162	421	67,709.5	−5.6	−53.9
113	Fresh groundwater	0.496	8	Ca·Na- Cl·HCO_3	5.6	81	73	15.2	121.7	155.6	122.3	−7.7	−49.7
0721-05	Fresh groundwater	0.187	10	Ca·Mg·Na-Cl	1.3	30.9	35.7	19.4	22.3	64.1	46.1	−9.5	−67.4
0724-05	Fresh groundwater	0.547	10	Na·Ca-Cl·HCO_3	0.8	92	77.1	21.7	146.1	192.2	113.4	−8.7	−57.4
0721-11	Fresh groundwater	0.714	15	Na·Mg·Ca-HCO_3	0.5	133.4	58.3	68.9	100.4	353.9	175.5	−5.1	−60.3
0724-02	Fresh groundwater	0.688	18	Ca-HCO_3·Cl	0.3	48.6	205.9	25.1	111.7	341.7	124.1	−7.9	−60.1
0721-06	Fresh groundwater	0.641	20	Ca·Mg-HCl	1	58.8	179	54.4	117.2	277.6	92.2	−11.3	−58.5
0721-10	Fresh groundwater	0.66	20	Na·Mg·Ca-HCO_3	1	164.3	51	45.2	55.4	466.8	109.9	−10.2	−73.6
228	Fresh groundwater	0.386	24	Ca·Mg-HCl	1.2	26	94.1	17.8	45.2	247.1	78	−5.1	−46
0724-06	Fresh groundwater	0.633	24	Ca·Na-HCO_3·Cl	2.6	77.3	169.4	27.9	120.8	250.2	109.9	−7.6	−57.6
132	Fresh groundwater	0.7	26	Ca·Mg·Na-Cl	0.6	66.5	143.5	67.6	123.6	241	177.2	−9.6	−60.2
0721-04	Fresh groundwater	0.627	30	Ca·Mg- HCO_3·Cl	1.1	49.5	178.3	59.9	108.7	277.6	90.4	−4.2	−60.1
0721-07	Fresh groundwater	0.466	35	Mg·Ca·Na-HCO_3	2.6	57.2	84.8	52	27	265.4	109.9	−9.8	−63.5
0708-06	Fresh groundwater	0.652	37	Ca·Mg·Na-HCO_3	1.5	73.1	124.2	41.9	47.9	353.9	186.1	−14.6	−66.2
L29	Fresh groundwater	0.918	40	Na·Mg·Ca-HCO_3	0.8	195.4	72.8	78.4	84.2	515.6	228.7	−4.4	−60
0721-08	Fresh groundwater	0.603	45	Mg·Ca·Na-HCO_3	0.7	61.1	106.1	79.8	67.1	393.6	92.2	−12	−61.5
0708-02	Fresh groundwater	0.863	45	Ca·Mg-Cl·HCO_3	1.5	60.5	193.2	68.2	29.8	451.5	283.6	−9.9	−62.7
L25	Fresh groundwater	0.801	55	Mg·Na·Ca-HCO_3	0.8	134.4	92.6	71.8	59.7	494.3	195	−5.5	−60
0721-02	Fresh groundwater	0.347	60	Ca·Mg- HCO_3	0.7	24.1	107.9	23.4	20.6	259.3	40.8	−12.6	−64.3
0707-05	Fresh groundwater	0.553	60	Ca·Mg-HCO_3·Cl	1.3	48.4	94.8	44.1	19.5	445.4	122.3	−4.3	−58.9
0707-03	Fresh groundwater	0.852	65	Na·Mg·Ca-HCO_3	4.6	161.5	88.1	65.6	79.1	533.9	186.1	−4	−59.4
L27	Fresh groundwater	0.871	65	Mg·Ca·Na-HCO_3	0.9	127.5	113.4	78.7	134.7	424.1	203.8	−10.2	−60.2
0721-01	Fresh groundwater	0.307	70	Ca·Mg-HCO_3	0.9	21.7	88.8	20	12.5	256.3	35.4	−10.5	−62.9
0708-08	Fresh groundwater	0.369	75	Ca·Mg- HCO_3	0.9	31.9	86.7	24.4	7.7	381.4	26.6	−12.7	−66

Table 2. *Cont.*

Samples	Water Type (m)	TDS (g/L)	Well Depth (m)	Chemical Type	K (mg/L)	Na (mg/L)	Ca (mg/L)	Mg (mg/L)	SO_4 (mg/L)	HCO_3 (mg/L)	Cl (mg/L)	$\delta^{18}O$ VS-MOW (‰)	$\delta^{2}H$ VS-MOW (‰)
0708-05	Fresh groundwater	0.392	100	Ca·Mg·Na-HCO_3	1	39.8	86.8	26	13.3	353.9	47.9	−10.2	−64.4
L32	Fresh groundwater	0.637	100	Na·Mg·Ca-HCO_3	1.1	124.9	62.4	47.1	47.4	466.8	120.5	−11.1	−61.1
0707-10	Fresh groundwater	0.543	230	Na- HCO_3·Cl	0.9	173.2	15.8	15.1	79.6	357	79.8	−14.9	−75.4
0707-06	Fresh groundwater	0.394	300	Na·Mg·Ca-HCO_3	0.8	86.5	31.3	26.2	53.9	350.9	19.5	−14.2	−69.1
0725-02	Seawater	30.426	—	Na-Cl	253.4	9089	644.9	1273	2449	109.8	16,661.5	−1	−11
69	Saline groundwater	4.323	13	Na-Cl	8.7	1160	241.4	145.2	153.8	726.1	2251.1	−6.6	−59.2
0724-10	Saline groundwater	3.004	15	Na-Cl·HCO_3	22.1	1022	43.9	55.5	452.4	625.5	1095.4	−8	−59.4
L43	Saline groundwater	3.532	16	Na-Cl	22.1	1182	47.3	65.6	411.7	628.5	1488.9	−10.7	−59
L37	Saline groundwater	4.418	19	Na·Mg-Cl	19.1	995.8	257.7	255.8	545.8	469.9	2109.3	−8.9	−57.5
0706-04	Saline groundwater	47.895	40	Na-Cl	232.6	14,890	574.2	1869	3660	518.7	26,410.2	−13.7	−52.6
L36-3	Saline groundwater	36.101	50	Na·Mg-Cl	121.7	9454	964.8	1903	2733	372.2	20,738.2	−13.7	−56.1
103	Saline groundwater	3.43	60	Na-Cl·SO_4·HCO_3	53.5	1283	2.4	16.7	840.2	893.9	787	−12.3	−57.9
L36-1	Saline groundwater	34.371	90	Na·Mg-Cl	92.9	8606	1108	1875	2405	332.6	20,117.9	−14.4	−61.3
0722-03	Saline groundwater	26.008	145	Na·Mg-Cl	60.1	6256	1606	1511	1573	225.8	14,889	−8.2	−64.6
0725-05	Surface water	0.532	—	Na·Ca-SO_4·HCO_3·Cl	5.8	84.4	84.8	17.1	153.4	143.4	115.2	−5.6	−49.7
0724-04	Surface water	0.542	—	Na-SO_4·HCO_3·Cl	7.4	86.3	70.6	25.6	144.2	125.1	145.3	−5.7	−33.6
0722-08	Surface water	0.559	—	Na·Ca-SO_4·HCO_3·Cl	8.9	85.9	75	26.9	156.2	122	145.3	−3.2	−31.6
0725-03	Surface water	0.956	—	Na-SO_4·Cl	9.6	206.9	91.8	32.1	288.4	100.7	276.5	−2.9	−27.6
0724-12	Surface water	2.78	—	Na-Cl	23.3	744.6	99.9	129.7	278.8	12.2	1497.8	−3.4	−35.2
0724-13	Surface water	4.453	—	Na-Cl	40.2	1242	143.9	192.7	380.1	122	2392.9	−2.4	−32.6
0725-01	Surface water	11.808	—	Na-Cl	79	3075	411.1	483.2	958.9	131.2	6735.5	−1.2	−19.6

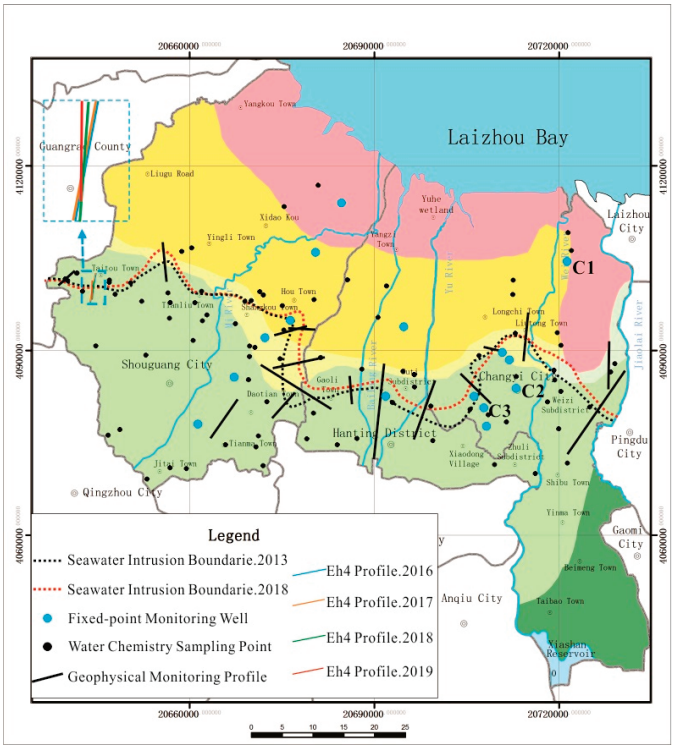

Figure 4. Multiple monitoring method deployment and seawater intrusion boundaries of the study area.

3.1. Water Chemical Sampling Analysis Method

The water samples were tested by Inductively Coupled Plasma Optical Emission Spectrometry (ICP-OES, Optima 8300, PerkinElmer, Waltham, MA, USA, precision ± 0.2‰) for the content of various water chemical ions. A multi-parameter instrument (SX836, Shanghai Sanxin, Shanghai, China) was used to measure water temperature (measurement range: 0~100 °C, resolution: 0.1 °C), conductivity (measurement range: 0~200 mS/cm, resolution: 0.01/0.1 mS/cm), and pH (measurement range: −2.00~19.99 pH, resolution: 0.01 pH). TDS was tested using a Geothermal Blast Drying Oven (DGG-101-1, Tianyu, Tianjin, China, precision ± 1 °C) at 180 °C and a Laboratory Electronic Analytical Balance (XPR504S/AC, Mettler Toledo, Zurich, Switzerland, precision 0.1 mg).

3.2. Environmental Isotope Method

The ^{18}O in the water sample was replaced with standard CO_2 in a glass vacuum equilibrium system (room temperature 25 °C); the generated CO_2 was extracted and collected using a refrigerant (prepared with absolute ethanol and liquid nitrogen, boiling point −78 °C). The ^{2}H in the water sample was converted into hydrogen at high temperature (850 °C) using metallic chromium as a reducing agent, and the hydrogen was absorbed by activated carbon at a low temperature. The collected and generated CO_2 and hydrogen were then sent for Thermal Conversion/Elementary Analyzer-Gas Isotope Ratio Mass Spectrometry Analysis (TC/EA-IRMS, MAT253, Thermo Fisher, Waltham, MA, USA, precision ± 0.2‰, State Key Laboratory of Biogeology and Environmental Geology, China University of Geosciences, Wuhan). Results were normalized to V-SMOW with a precision of ±1.0‰ for $\delta^{2}H$ and 0.1‰ for $\pm\delta^{18}O$, respectively [49].

3.3. Fixed-Point Well Monitoring Method

The monitoring profile is composed of wells C1, C2, and C3. The monitoring instrument is a water level, temperature, and conductivity three-parameter self-recording instrument (CTD-Diver, DI273, SaiNuoXin, Beijing, China, water table precision ±5 cm, electrical conductivity precision ±1% ms/cm). C1 and C2 are fixed-depth single-hole monitoring wells with a depth of 38 m and 30 m, located in the brackish groundwater and the saline groundwater areas; the dynamic type of groundwater is runoff extraction and weak runoff exploitation, respectively. C3 is a single-hole multi-layer monitoring well (including C3-1, C3-2, and C3-3) located in the seawater–fresh groundwater transition area. C3-1 is a shallow groundwater well with a depth of 36 m, and the dynamic type of groundwater at this depth is precipitation–runoff–extraction. C3-2 is a medium–deep groundwater well with a depth of 74 m, and the active type of groundwater at this depth is runoff extraction. C3-3 is a deep groundwater well with a depth of 149 m, and the dynamic type of groundwater at this depth is weak runoff extraction.

3.4. Geophysical Monitoring Method

This study used the audio-frequency magneto telluric method to continuously monitor the changes in seawater intrusion of Dawangdong profiles from 2016 to 2019 (EH4 conductivity imaging system, Geometrics and EMI, San Jose, CA, USA). The horizontal resolution is related to the electrode spacing. In this study, the electrode spacing was 50 m, and the electric field strength at the measuring points of electrodes was greater than 0.01 μV/m, while the magnetic field strength was more significant than 0.01 mGamma. The range and variation characteristics of seawater intrusion were analyzed. The Dawangdong monitoring profile was located east of Dawang Town and south of Taitou Town. The profile point distance was 50 m. The profile angle was 11° from 2016 to 2017. Due to the limitation of field construction conditions, the monitoring profile angle was slightly adjusted from 2018 to 2019, 4° and 0°, respectively. There were three frequency ranges of 10 Hz~1 KHz, 500 Hz~3 KHz, and 750 Hz~96 KHz for monitoring work [23,35]. Data quality assurance methods included the uniform distribution of 5% of the inspection points. The apparent resistivity calculated at the inspection points was consistent with the evident resistivity

curve shape of the original measurement point. The pronounced resistivity curve obtained from a single measurement point was continuous and smooth, without sharp points; the data quality was evaluated by the coherence degree of the entire information vector and the coherence degree of the whole information vector of 90% of the frequency points above 0.5.

4. Results and Discussion

4.1. Water Chemical Sampling Monitoring Results and Discussion

According to the water chemical samples test data (Table 1) and previous research results, the downside of seawater intrusion is insignificant with TDS < 2 g/L, while the impact of TDS over 2 g/L is significant [34,35]. The seawater intrusion boundary on the southern coastal plain of Laizhou Bay was delineated as TDS > 2 g/L, and the TDS contour map (Figure 4) was drawn by interpolation in the geographic information platform (MAPGIS 6.7). The monitoring results show that the boundary distribution in 2013 and 2018 is similar and generally located in the south of Taitou Town–north of Tianliu Town–Hou Town–Gudi Town–north of Liutong Town. In five years, the boundary generally retreated northward. More specifically, the northern part of Tianliu Town, the east of Hou Town, and the eastern part of Liutong Town moved northward, and other areas moved slightly southward or were relatively stable.

Based on the water chemical samples test data (Table 1), Origin 2021 software was used to create a Piper diagram of groundwater and surface water (Figure 5). From Figure 5, there are apparent differences in the water chemical components of different water bodies, arranged in a wide strip from left to right. The left-end member of the strip is groundwater and rainwater. The right end members are brine and seawater, reflecting different water bodies' hadrochemical evolution and action process. The surface water is connected with rainwater (on the left) and seawater (on the right). It is affected by mixing and evaporation-concentration, showing a clear pattern of change from south to north. The mixing line of surface water and seawater should be straight in theory [50,51]. Still, it is a relatively smooth continuous curve with similar chemical composition distribution characteristics to groundwater. This shows that surface water is significantly related to groundwater recharge and discharge. At the estuary, the surface water is subjected to a particular upstream effect of seawater [24,28,52].

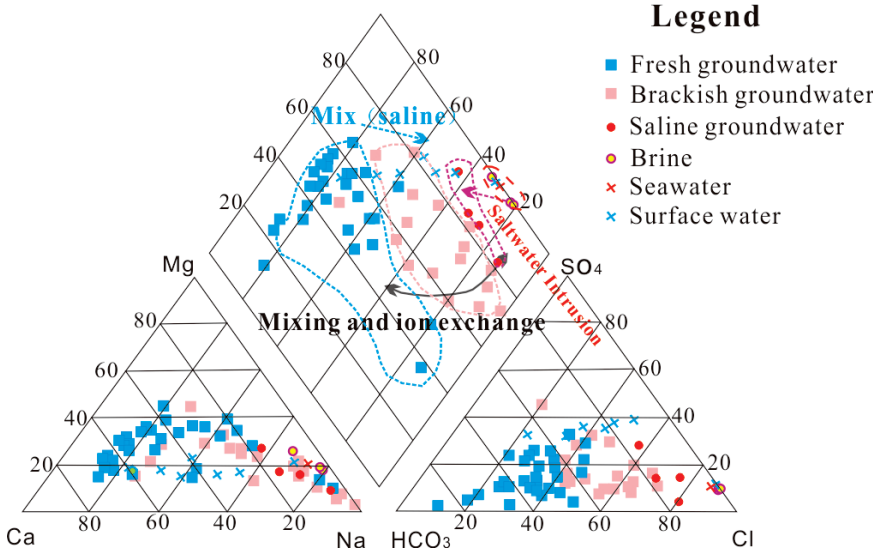

Figure 5. Piper diagram of groundwater and surface water of the study area.

The variation characteristics of groundwater chemical composition along the process show that it is controlled by mixing and water–rock interactions. Affected by leaching and

cationic alternating adsorption [11,21], the chemical type of fresh groundwater changes from Ca·Mg-HCO_3 to Na-HCO_3·Cl, Na·Ca-HCO_3·Cl from south to north, and the changing trend of brackish groundwater is from Mg·Na·Ca-HCO_3, Mg·Ca-HCO_3 to Na-Cl·HCO_3, Na·Mg-Cl. Saline groundwater is mainly of the Na-Cl and Na·Mg-Cl type. Brine is of the Cl-Na type. The distribution characteristics of various ion contents in shallow groundwater show noticeable differences among geomorphic units and exhibit certain regularity. Along the sampling profile of groundwater from south to north, the concentration of various ions in groundwater fluctuates. Among them, the ion HCO_3 concentration shows a trend of slow increase followed by a slight decrease. In mountainous and alluvial plains, the concentrations of various ions in groundwater are relatively low and deliver a slow-increasing trend, while they increase sharply in estuarine plains. The distribution of different groundwater bodies along the route shows a wide band-like distribution. There is no SO_4-type water in many groundwater chemical types, indicating that the mixing effect of groundwater with different salinity is strong. Furthermore, in some relatively low-lying areas in the shallow groundwater at the foot of the mountain, there is a relatively high Cl-content phenomenon, indicating that this area is significantly affected by evaporation and concentration.

4.2. Environmental Isotope Method Results and Discussion

In this study, the correlation between ^{18}O, ^{2}H, and Cl^- was observed to analyze the process of seawater intrusion and the hydraulic connection between different water bodies, using the software Origin 2021 to create a diagram of the correlation between $\delta^{18}O$, ^{2}H, and Cl^- (Figure 6).

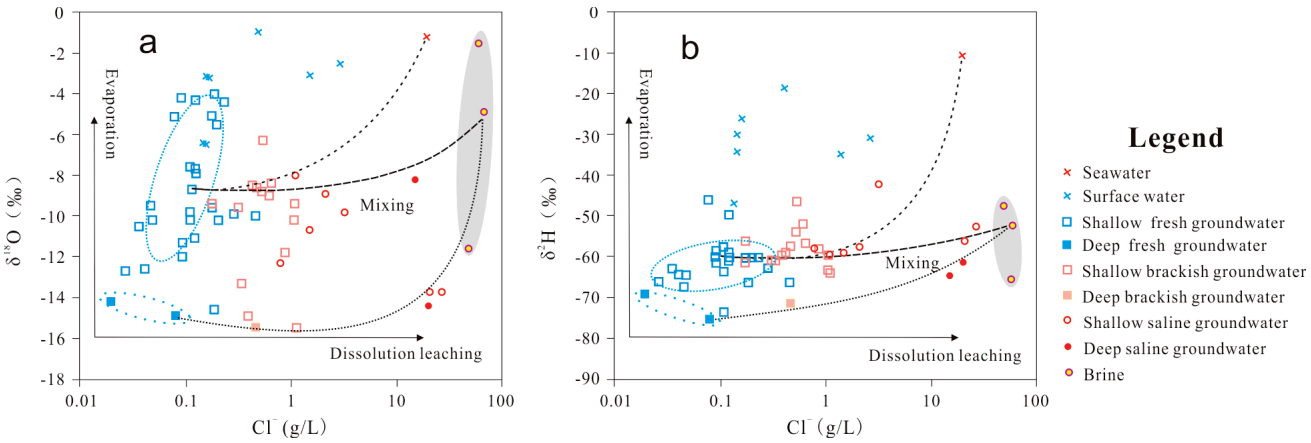

Figure 6. Diagram of correlation between $\delta^{18}O$ (**a**), ^{2}H (**b**), and Cl^- values in groundwater and surface water.

The values of shallow fresh groundwater range from −11.3‰ to −4.2‰ for $\delta^{18}O$ and from −73.6‰ to −46‰ for ^{2}H; the values of deep fresh groundwater range from −11.3‰ to −4.2‰ for $\delta^{18}O$ and from −75.4‰ to −58.9‰ for ^{2}H; the values of shallow brackish groundwater range from −14.9‰ to −6.3‰ for $\delta^{18}O$ and from −66.3‰ to −46.5‰ for ^{2}H; the values of deep brackish groundwater range from −15.5‰ to −9.6‰ for $\delta^{18}O$ and from −71.3‰ to −60.8‰ for ^{2}H; the values of saline groundwater range from −14.4‰ to −6.6‰ for $\delta^{18}O$ and from −64.6‰ to −52.6‰ for ^{2}H; the values of surface water range from −5.6‰ to −1.2‰ for $\delta^{18}O$ and from −49.7‰ to −19.6‰ for ^{2}H. The relationship between $\delta^{18}O$, ^{2}H, and Cl^- shows that the groundwater was affected by various evaporation, dissolution, and mixing in the runoff process. Fresh groundwater was affected by evaporation, resulting in a noticeable change of $\delta^{2}H$ and $\delta^{18}O$; brackish groundwater and saline groundwater were significantly affected by dissolution and mixing; brine was affected by evaporation-concentration and mixing [34]. As described above, deep groundwater to brine water conformed to a gradual mixing pattern from south to

north. In contrast, the mixing pattern of shallow groundwater to brine water was more complex, reflecting that atmospheric precipitation, surface water, and irrigation water influence the recharge sources for shallow groundwater. From the endpoint-element mixing model analysis, fresh groundwater, brackish groundwater, and saline groundwater samples were relatively evenly distributed on the mixing trend line of shallow fresh groundwater–seawater and shallow fresh groundwater-brine, indicating that the shallow freshwater was affected by both brine and seawater intrusion [6,53]. On the trend line of mixing deep fresh groundwater–seawater and deep fresh groundwater–brine, there were sample points of fresh groundwater, brackish groundwater, and saline water. However, the sample points of brackish groundwater were mainly concentrated near the mixing line between fresh water and seawater, indicating that deep groundwater tends to mix more with seawater first and is more affected by seawater intrusion [54]. The deep saline and shallow saline groundwater samples showed a relatively obvious approach, indicating that in some areas, the hydraulic relationship between them is caused by string mining, etc. [55].

4.3. Fixed-Point Wells Monitoring Results and Discussion

The monitoring well's TDS and water level data were analyzed and mapped using the software Grapher 10. The monitoring well C1 was located in the brackish groundwater area. The monitoring data show that the dynamic type of groundwater was runoff extraction (Figure 7).

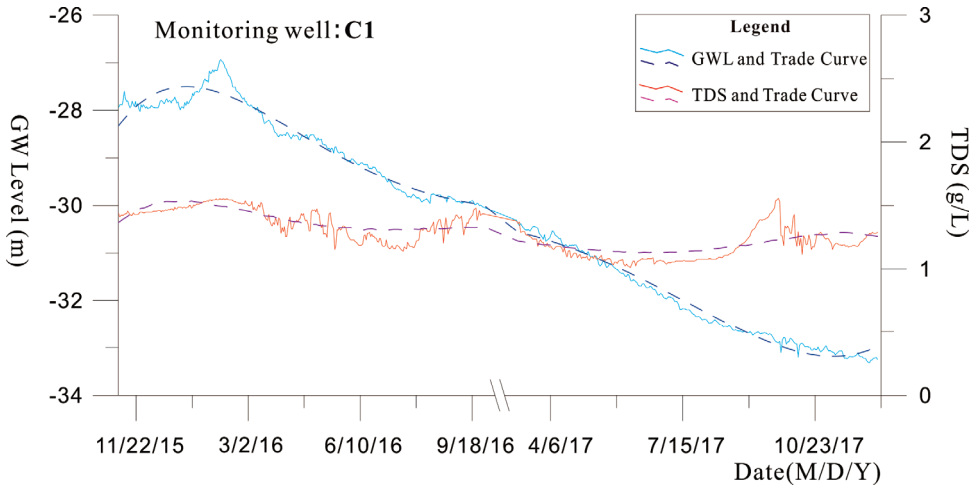

Figure 7. Diagram of correlation between groundwater level and TDS variation in well C1.

During the monitoring period, the groundwater table showed a declining trend, with an average annual decline of more than 3 m, and the TDS was slightly greater than 1 g/L, with a slight change. The more obvious groundwater table rise period appeared in January 2017, and the TDS increased somewhat. According to the TDS and groundwater table correlation, the curve can be divided into two stages; before August 2017, when the groundwater table declined, TDS was positively correlated with the groundwater table, indicating that this area mainly received the lateral recharge of fresh groundwater from the southern region. After August 2017, TDS was negatively correlated with the groundwater table, and the influence of northern seawater intrusion on this area gradually emerged [56].

The monitoring well C2 was severely affected by seawater intrusion in the saline groundwater area. The monitoring data show that the dynamic type of groundwater was weak runoff-exploitation (Figure 8). During the monitoring period, the change in the groundwater table was affected by extraction, and no seasonal variations were observed. The main reason for the lack of obvious seasonal changes was that the salinity here needed to be lowered for agricultural irrigation, mainly for fish farming and the chemical industry [57]. Before March 2017, TDS increased slightly with the groundwater table fluc-

tuation and was relatively stable at approximately 16–17 g/L, indicating a stable saline groundwater or brine recharge source. After March 2017, the TDS and groundwater table showed a significant negative correlation. TDS rose significantly with the fluctuation of the groundwater table; the reason is that the continuous extraction of brackish groundwater caused the lowering of the groundwater level here, breaking the hydraulic balance with the northern saline water, and higher salinity brine from the north began to invade and replenish it [58–60].

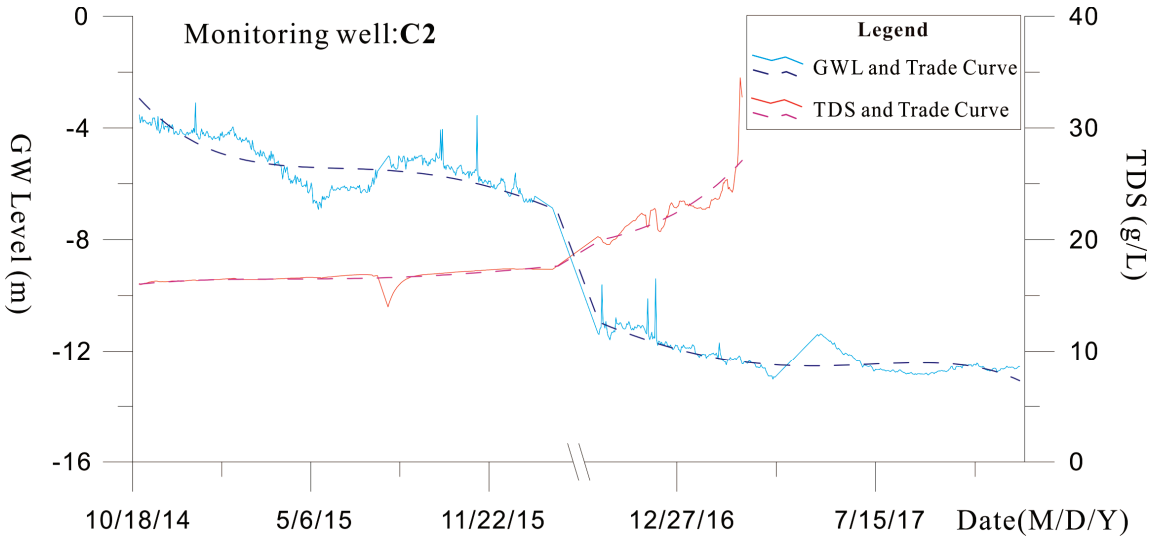

Figure 8. Diagram of correlation between groundwater level and TDS variation in well C2.

The single-hole multi-layer monitoring well C3 was located in the seawater–fresh groundwater transition area. C3-1 is a shallow groundwater well, and the monitoring data show that the dynamic type of groundwater at this depth was precipitation–runoff–extraction (Figure 9a). TDS showed a trend of slightly increasing at the beginning, declining in the middle, and increasing and fluctuating at the end. The groundwater table was in a significant decline stage, and there was a phenomenon of slight decrease followed by a slow recovery in TDS; TDS increased from 1.5 g/L to 0.7 g/L and then expanded to approximately 1 g/L. This indicates that the groundwater was primarily replenished by the runoff of fresh water from the south. Before August 2014, the shallow fresh groundwater was weakly affected by seawater intrusion from the northern region and mainly received fresh groundwater from the southern region. After August 2014, the groundwater table declined, the influence of seawater intrusion was evident, and the increase in saline groundwater recharge in the north led to an increase in TDS. C3-2 is a medium–deep groundwater well. The monitoring data show that the dynamic type of groundwater at this depth was runoff extraction (Figure 9b). The groundwater table change was significantly affected by extraction. During the monitoring period, except for the relatively apparent recovery of the groundwater table in July 2018, the other period maintained a relatively stable decline. The groundwater table generally showed a declining trend. The TDS was significantly positively correlated with the change in the groundwater table, indicating that this area is in the regional groundwater circulation system. The groundwater was mainly recharged by fresh groundwater in the southern region. C3-3 is a deep groundwater well, and the data show that the dynamic type of groundwater at this depth was weak runoff–extraction (Figure 9c). The groundwater table change was affected by extraction, with TDS slightly less than 0.5 g/L, and it was not affected by seawater intrusion. Due to the influence of sedimentary structure and groundwater exploitation, this area has layered seawater intrusion.

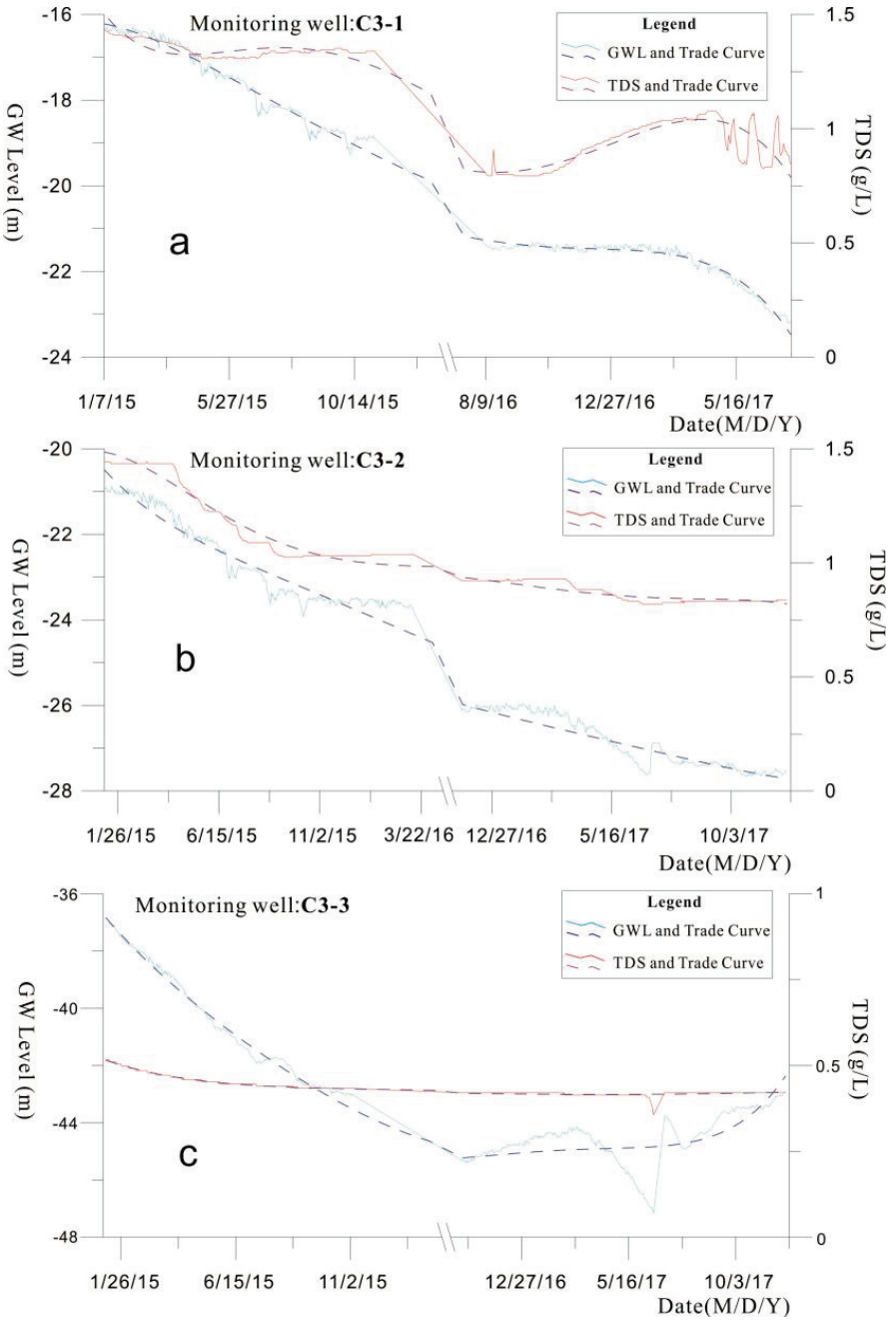

Figure 9. Diagram of correlation between groundwater level and TDS variation in wells C3-1 (**a**), C3-2 (**b**), and C3-3 (**c**).

4.4. Geophysical Monitoring Results and Discussion

We interpolated the resistivity in the software Sufer 12 and obtained a contour profiles map of resistivity values. From the comparison of monitoring profiles (Figure 10), the resistivity contour of the shape is stable and continuous. The resistivity shows a trend of high in the south and low in the north, consistent with the distribution characteristics of saline groundwater and fresh groundwater in the striatum [29,61,62]. According to previous experience and the results of comparative field experiments [21,63–66], it was determined that the seawater intrusion interface was delineated with a resistivity value of 8–10 Ω·m. The monitoring data show that in August 2019, the seawater intrusion front was located near the 2050 m, determined by the resistivity anomaly interpretation. In October 2017, the seawater intrusion front retreated northward by about 100 m to the vicinity of

the 2150 m, with a rate of approximately 85.7 m/a. From July 2018 to December 2019, the seawater intrusion front first showed the characteristics of intrusion to the south and then retreated to the north. Considering the effect of the profile offset angle, the south intrusion and north retreat rates were approximately 213.3 m/a and 105.9 m/a, respectively. From the long-term monitoring data, from August 2016 to December 2019, the seawater intrusion front on the Dawangdong profile retreated northward at approximately 27 m/a.

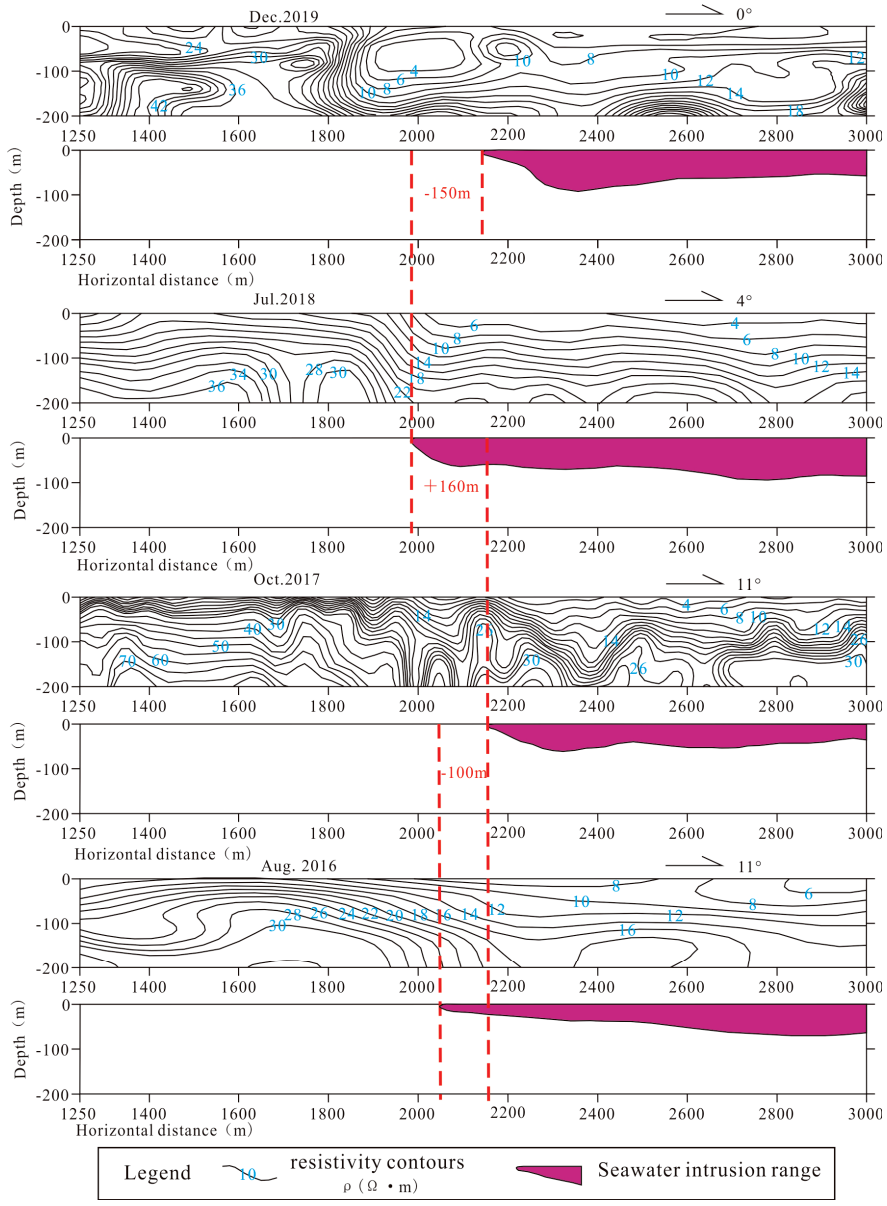

Figure 10. The audio-frequency magneto telluric monitoring date interpretation of seawater intrusion extent comparison.

4.5. Theoretical Implications

Based on the analysis of the results obtained from the above monitoring methods, the water chemical sampling analysis method and the geophysical monitoring method can be used in combination. After obtaining the approximate range and degree of regional seawater intrusion through the water chemical sampling analysis method, further use of geophysical monitoring methods can accurately delineate the boundary between saline and fresh groundwater, determine the burial depth of the top and bottom plates of aquifers containing saline or fresh water, and study the spatial evolution of underground saline

and fresh groundwater bodies [67,68]. The advantage of the cross is that the seawater intrusion interface can be described quickly and accurately, and the degree of seawater intrusion can be determined. After understanding the groundwater flow system, the fixed-point well monitoring method can monitor the long-sequence dynamic characteristics of seawater intrusion at specific points, which can analyze the effect and the response of dynamic groundwater changes on seawater intrusion. This also helps confirm how seawater intrusion is determined by the water chemical sampling analysis method [69]. Combined with the geophysical monitoring method, it can verify the accuracy of the scoping of seawater intrusion. The combination of the environmental isotope method and the water chemical sampling analysis method can analyze and monitor the influencing factors of seawater intrusion. It can clarify the interconnectedness of different water bodies in the intrusion process [70].

4.6. Practical Implications

Based on analyzing the factors and processes affecting seawater intrusion, local authorities must manage groundwater resources in the following aspects: strengthen the management of water resources in the coastal plain area, strictly prohibit deep well drilling in areas where seawater intrusion occurs, precisely control new well drilling, and strictly control groundwater exploitation for irrigation except for human and livestock use [71,72]. Large-scale industrial projects that consume water cannot be built in areas where seawater intrusion occurs. For existing large-scale industrial projects in these areas, a method of centralized water supply from a distance should be adopted instead of exploiting local groundwater.

5. Conclusions

This study conducted a comprehensive analysis of seawater intrusion on the south coast of Laizhou Bay using multiple monitoring methods. From the general study area, the effect of different water bodies on seawater intrusion was analyzed based on the theory of the mixing effect of other water bodies and the water chemistry in groundwater aquifer systems. By combining the water chemical sampling analysis method and the environmental isotope method, the type and extent of seawater intrusion were assessed from a macro perspective. The northern and southern profiles of the study area were selected for fixed-point well monitoring and geophysical monitoring methods, respectively, and the effects of human activities such as groundwater extraction, aquaculture, and hydrogeological conditions on seawater intrusion were investigated. The annual rate of seawater intrusion was quantitatively assessed, and the seawater intrusion front generally showed a trend of retreating backward, with a rate of approximately 27 m/a.

The results show that seawater intrusion vigorously mixes with saline groundwater on the southern coastal plain of Laizhou Bay. Due to the influence of hydrogeological conditions and groundwater extraction, layered seawater intrusion exists. In layered intrusion, shallow fresh groundwater is subject to both saline groundwater mixing and seawater intrusion, while deep freshwater is mainly affected by seawater intrusion. In some areas, shallow saline groundwater is hydraulically connected to deep salty groundwater due to string mining.

Although multiple research methods were used to analyze regional seawater intrusion from various angles in this study, this analysis was based on a detailed geological background. When the geological background conditions of the study area are unclear, the use of the geophysical monitoring method and the fixed-point well monitoring method are limited, and it is necessary to determine the transition zone of seawater intrusion through the water chemical sampling analysis method. However, a high-precision, long-sequence air-ground-well integrated monitoring system has yet to be established in a typical research study. Multi-source monitoring information must be integrated in a true sense to realize the complementary advantages of different monitoring technologies. Therefore, the combined analysis of data from direct and indirect monitoring methods is an idea that deserves further investigation to determine the current status of seawater intrusion.

6. Outlook

With the continuous development of technologies for seawater intrusion monitoring, the three-dimensional integrated monitoring technology of air-ground-wells, which combines multiple methods and integrates multi-source information, was adopted. Taking into account the optimization of monitoring layout and schemes, the continuous improvement of seawater intrusion modeling accuracy using multi-source information has become an important development direction [68,73,74]. For example, high-precision Earth gravity satellite data can be used to decipher the seawater intrusion transition zone and thus more accurately deploy water chemistry sampling holes. The future use of remote sensing, water chemistry, monitoring wells stratified monitoring, and other multi-source techniques means that building a monitoring network [75,76], combined with numerical simulation techniques, is a method of seawater intrusion identification and evaluation of the technical route of direction worth further investigation.

Author Contributions: Conceptualization and design, H.L. and L.G.; methodology, acquisition, and analysis of data, H.L. and L.G.; validation, C.M. and Y.Y.; writing—original draft preparation, H.L.; funding acquisition, H.L. and C.M. All authors have read and agreed to the published version of the manuscript.

Funding: This study was supported by China Geological Survey Projects, grant number 12120113003800, DD20221727.

Data Availability Statement: The data supporting this study's findings are available on request from the corresponding author. The data are not publicly available due to privacy or ethical restrictions. Therefore, they are available from the corresponding author upon reasonable request.

Acknowledgments: The authors thank Zhang Chengyi for her modification of the language structure.

Conflicts of Interest: The authors declare no conflict of interest. The funders had no role in the study's design; in the collection and analyses of data; in the writing of the manuscript; or in the decision to publish the results.

References

1. He, J.; Mai, T.H.T. The Circular Economy: A Study on the Use of Airbnb for Sustainable Coastal Development in the Vietnam Mekong Delta. *Sustainability* **2021**, *13*, 7493. [CrossRef]
2. Werner, A.D.; Bakker, M.; Post, V.E.A.; Vandenbohede, A.; Lu, C.; Ataie-Ashtiani, B.; Simmons, C.T.; Barry, D.A. Seawater Intrusion Processes, Investigation, and Management: Recent Advances and Future Challenges. *Adv. Water Resour.* **2013**, *51*, 3–26. [CrossRef]
3. Barlow, P.M.; Reichard, E.G. L'intrusion d'eau Salée Dans Les Régions Côtières d'Amérique Du Nord. *Hydrogeol. J.* **2010**, *18*, 247–260. [CrossRef]
4. Gogoberidze, G. Tools for Comprehensive Estimate of Coastal Region Marine Economy Potential and Its Use for Coastal Planning. *J. Coast. Conserv.* **2012**, *16*, 251–260. [CrossRef]
5. Garing, C.; Luquot, L.; Pezard, P.A.; Gouze, P. Geochemical Investigations of Saltwater Intrusion into the Coastal Carbonate Aquifer of Mallorca, Spain. *Appl. Geochem.* **2013**, *39*, 1–10. [CrossRef]
6. Maosheng, G.; Yongming, L. Zone, Change of Groundwater Resource and Prevention and Control of Seawater Intrusion in Coastal. *Coast. Sci. Sustain. Dev.* **2016**, *31*, 1197–1203. (In Chinese) [CrossRef]
7. Sun, M.; Wang, T.; Xu, X.; Zhang, L.; Li, J.; Shi, Y. Ecological Risk Assessment of Soil Cadmium in China's Coastal Economic Development Zone: A Meta-Analysis. *Ecosyst. Health Sustain.* **2020**, *6*, 1733921. [CrossRef]
8. Samani, S. Assessment of Groundwater Sustainability and Management Plan Formulations through the Integration of Hydrogeological, Environmental, Social, Economic and Policy Indices. *Groundw. Sustain. Dev.* **2021**, *15*, 100681. [CrossRef]
9. Hu, X.; Gao, L.; Ma, C.; Hu, X. Land Use Zoning of Weifang North Plain Based on Ecological Function and Geo-Environmental Suitability. *Bull. Eng. Geol. Environ.* **2020**, *79*, 2697–2719. [CrossRef]
10. Sekar, S.; Perumal, M.; Roy, P.D.; Ganapathy, M.; Senapathi, V.; Yong Chung, S.; Elzain, H.E.; Duraisamy, M.; Kamaraj, J. A Review on Global Status of Fresh and Saline Groundwater Discharge into the Ocean. *Environ. Monit. Assess.* **2022**, *194*, 915. [CrossRef]
11. Xue, L.; Siyuan, Y. Progress in Seawater Intrusion. *Mar. Geol. Quat. Geol.* **2016**, *36*, 211–217. (In Chinese)
12. Sharan, A.; Lal, A.; Datta, B. A Review of Groundwater Sustainability Crisis in the Pacific Island Countries: Challenges and Solutions. *J. Hydrol.* **2021**, *603*, 127165. [CrossRef]
13. Tully, K.L.; Weissman, D.; Wyner, W.J.; Miller, J.; Jordan, T. Soils in Transition: Saltwater Intrusion Alters Soil Chemistry in Agricultural Fields. *Biogeochemistry* **2019**, *142*, 339–356. [CrossRef]

14. Han, D.; Currell, M.J. Review of Drivers and Threats to Coastal Groundwater Quality in China. *Sci. Total Environ.* **2022**, *806*, 150913. [CrossRef]
15. Noto, A.E.; Shurin, J.B. Early Stages of Sea-Level Rise Lead to Decreased Salt Marsh Plant Diversity through Stronger Competition in Mediterranean-Climate Marshes. *PLoS ONE* **2017**, *12*, e0169056. [CrossRef]
16. Gao, L.; Ma, C.; Wang, Q.; Zhou, A. Sustainable Use Zoning of Land Resources Considering Ecological and Geological Problems in Pearl River Delta Economic Zone, China. *Sci. Rep.* **2019**, *9*, 16052. [CrossRef]
17. Carvalho, A.B.; Inácio de Moraes, G. The Brazilian Coastal and Marine Economies: Quantifying and Measuring Marine Economic Flow by Input-Output Matrix Analysis. *Ocean Coast. Manag.* **2021**, *213*, 105885. [CrossRef]
18. Gao, L.; Hu, X.; Ma, C.; Kuang, H.; Qi, H.; He, Z. Geoenvironmental Risk Evaluation of High-Efficiency Eco-Economic Zone in Weifang City, China. *Nat. Hazards Rev.* **2020**, *21*, 05020005. [CrossRef]
19. El-Kaliouby, H. Mapping Sea Water Intrusion in Coastal Area Using Time-Domain Electromagnetic Method with Different Loop Dimensions. *J. Appl. Geophys.* **2020**, *175*, 103963. [CrossRef]
20. Zhang, Y.; Wang, X.; Xue, Y.; Zou, C.; Luo, M.; Li, G.; Li, L.; Cui, L.; Li, H. Advances in the Study of Submarine Groundwater Discharge (SGD) in China. *Sci. China Earth Sci.* **2022**, *65*, 1948–1960. [CrossRef]
21. Yunzhang, H.; Hong, L.; Ying, L.; Peixin, S.; Jilong, Y.; Ziyuan, H.; Hongwei, L. Hydrogeochemical Recognization of Seawater Intrusion Process at the Typical Profile in Laizhou Bay. *Geol. Surv. Res.* **2015**, *38*, 41–50. (In Chinese)
22. Xiong, G.; Chen, G.; Wu, J.; Fu, T.; Yang, Y.; Xu, X.; Zhu, X.; Yu, H.; Liu, S.; Gao, M.; et al. Seawater Intrusion-Retreat Processes and Groundwater Evolution in Intruded Coastal Aquifers with Land Reclamation: A Case Study of Eastern Jiangsu, China. *Lithosphere* **2021**, *2021*, 1308487. [CrossRef]
23. Gurunadha Rao, V.V.S.; Rao, G.T.; Surinaidu, L.; Rajesh, R.; Mahesh, J. Geophysical and Geochemical Approach for Seawater Intrusion Assessment in the Godavari Delta Basin, A.P., India. *Water. Air. Soil Pollut.* **2011**, *217*, 503–514. [CrossRef] [PubMed]
24. Bo, L.; Shuya, H.; Quansheng, Z. Chemical Characteristics of Groundwater in Coastal Seawater Intrusion Area of Laizhou Bay. *Glob. Geol.* **2020**, *39*, 971–977.
25. Niculescu, B.M.; Andrei, G. Application of Electrical Resistivity Tomography for Imaging Seawater Intrusion in a Coastal Aquifer. *Acta Geophys.* **2021**, *69*, 613–630. [CrossRef]
26. Satish Kumar, V.; Dhakate, R.; Amarender, B.; Sankaran, S. Application of ERT and GPR for Demarcating the Saline Water Intrusion in Coastal Aquifers of Southern India. *Environ. Earth Sci.* **2016**, *75*, 393. [CrossRef]
27. Sherif, M.; El Mahmoudi, A.; Garamoon, H.; Kacimov, A.; Akram, S.; Ebraheem, A.; Shetty, A. Geoelectrical and Hydrogeochemical Studies for Delineating Seawater Intrusion in the Outlet of Wadi Ham, UAE. *Environ. Geol.* **2006**, *49*, 536–551. [CrossRef]
28. Xiaoni, Z.; Zhenxing, W.; Qingzhuang, M.; Bing, Z. Study the Shallow Groundwater Chemical Characteristics in the Typical Area of Zhanghe Catchment Basin. *Geol. Surv. Res.* **2020**, *43*, 265–270. (In Chinese)
29. Giménez-Forcada, E. Use of the Hydrochemical Facies Diagram (HFE-D) for the Evaluation of Salinization by Seawater Intrusion in the Coastal Oropesa Plain: Comparative Analysis with the Coastal Vinaroz Plain, Spain. *HydroResearch* **2019**, *2*, 76–84. [CrossRef]
30. El Osta, M.; Masoud, M.; Alqarawy, A.; Elsayed, S.; Gad, M. Groundwater Suitability for Drinking and Irrigation Using Water Quality Indices and Multivariate Modeling in Makkah Al-Mukarramah Province, Saudi Arabia. *Water* **2022**, *14*, 483. [CrossRef]
31. Masoud, M.; El Osta, M.; Alqarawy, A.; Elsayed, S.; Gad, M. Evaluation of Groundwater Quality for Agricultural under Different Conditions Using Water Quality Indices, Partial Least Squares Regression Models, and GIS Approaches. *Appl. Water Sci.* **2022**, *12*, 244. [CrossRef]
32. Liu, Q.; Li, F.; Li, J.; Luo, B.; Huang, C. Geochemical and Isotopic Evidence of Shallow Groundwater Salinization in a Reclaimed Coastal Zone: The Yellow River Delta, China. *Environ. Earth Sci.* **2016**, *75*, 1107. [CrossRef]
33. Maurya, P.; Kumari, R.; Mukherjee, S. Hydrochemistry in Integration with Stable Isotopes (Δ18O and ΔD) to Assess Seawater Intrusion in Coastal Aquifers of Kachchh District, Gujarat, India. *J. Geochem. Explor.* **2019**, *196*, 42–56. [CrossRef]
34. Qi, H.; Ma, C.; He, Z.; Hu, X.; Gao, L. Lithium and Its Isotopes as Tracers of Groundwater Salinization: A Study in the Southern Coastal Plain of Laizhou Bay, China. *Sci. Total Environ.* **2019**, *650*, 878–890. [CrossRef]
35. Dong, D.; Hongwei, L.; Zhitao, L.; Yunqing, M.; Xueqin, Z. Construction of Sea(Salt)Water Intrusion Monitoring Techniques and Methods System in South Bank of Laizhou Bay. *Environ. Geol.* **2015**, *31*, 49–53.
36. Lim, J.W.; Lee, E.; Moon, H.S.; Lee, K.K. Integrated Investigation of Seawater Intrusion around Oil Storage Caverns in a Coastal Fractured Aquifer Using Hydrogeochemical and Isotopic Data. *J. Hydrol.* **2013**, *486*, 202–210. [CrossRef]
37. Abdulameer, A.; Thabit, J.M.; AL-Menshed, F.H.; Merkel, B. Investigation of Seawater Intrusion in the Dibdibba Aquifer Using 2D Resistivity Imaging in the Area between Al-Zubair and Umm Qasr, Southern Iraq. *Environ. Earth Sci.* **2018**, *77*, 619. [CrossRef]
38. Folch, A.; del Val, L.; Luquot, L.; Martínez-Pérez, L.; Bellmunt, F.; Le Lay, H.; Rodellas, V.; Ferrer, N.; Palacios, A.; Fernández, S.; et al. Combining Fiber Optic DTS, Cross-Hole ERT and Time-Lapse Induction Logging to Characterize and Monitor a Coastal Aquifer. *J. Hydrol.* **2020**, *588*, 125050. [CrossRef]
39. Xili, S.; Peng, S.; Yangfang, S.; Xiangfeng, G. Significance of Seawater Intrusion Interface Divisionin Jijia Area in Yantai City of Shandong Province. *Shandong L. Resour.* **2014**, *30*, 58–60. (In Chinese)
40. Weiping, W.; Chengping, W.; Yongjun, Z.; Shengjun, L.; Xunbiao, M. Application of Airborne Electromagnetic Method in Hydrogeological Survey. *Geol. Surv. China* **2022**, *9*, 113–121. (In Chinese) [CrossRef]

41. Ayolabi, E.A.; Folorunso, A.F.; Odukoya, A.M.; Adeniran, A.E. Mapping Saline Water Intrusion into the Coastal Aquifer with Geophysical and Geochemical Techniques: The University of Lagos Campus Case (Nigeria). *SpringerPlus* **2013**, *2*, 433. [CrossRef]
42. Alfaifi, H.; Kahal, A.; Albassam, A.; Ibrahim, E.; Abdelrahman, K.; Zaidi, F.; Alhumidan, S. Integrated Geophysical and Hydrochemical Investigations for Seawater Intrusion: A Case Study in Southwestern Saudi Arabia. *Arab. J. Geosci.* **2019**, *12*, 372. [CrossRef]
43. Nicolodi, J.L.; Asmus, M.; Turra, A.; Polette, M. Evaluation of Coastal Ecological-Economic Zoning (ZEEC) in Brazil: Methodological Proposal. *Desenvolv. Meio Ambient.* **2018**, *44*, 378–404. [CrossRef]
44. Xueming, Y.; Yongjun, S.; Dong, D.; Jan, F.; Xing, L. The Application of The Audio Ferquency Magnetotelluric Method to The Dynamic Monitoring of Seawater. *Geophys. Geochem. Explor.* **2013**, *37*, 301–305. (In Chinese)
45. Chen, S.m.; Liu, H.W.; Liu, F.T.; Miao, J.J.; Guo, X.; Zhang, Z.; Jiang, W.J. Using Time Series Analysis to Assess Tidal Effect on Coastal Groundwater Level in Southern Laizhou Bay, China. *J. Groundw. Sci. Eng.* **2022**, *10*, 292–301. [CrossRef]
46. Guanquan, C. *Study on The Impact Mechanism and Early Waring Evaluation of Seawater Instrusion in Laizhou Bay Area*; East China Normal University: Shanghai, China, 2013. (In Chinese)
47. He, Z.; Ma, C.; Zhou, A.; Qi, H.; Liu, C.; Cai, H.; Zhu, H. Using Hydrochemical and Stable Isotopic (Δ2H, Δ18O, Δ11B, and Δ37Cl) Data to Understand Groundwater Evolution in an Unconsolidated Aquifer System in the Southern Coastal Area of Laizhou Bay, China. *Appl. Geochem.* **2018**, *90*, 129–141. [CrossRef]
48. China Geological Survey. *Handbook of Hydrogeology*; Geology Press: Bath, UK, 2012. (In Chinese)
49. Yunde, L.; Yiqun, G.; Tingting, Y.; Cunfu, L.; Aiguo, Z. Online Simultaneous Determination of ΔD and Δ18O in Micro-Liter Water Samples by Thermal Conversion/Elemental Analysis-Isotope Ratio Mass Spectrometry. *Rock Miner. Anal.* **2010**, *29*, 643–647. (In Chinese) [CrossRef]
50. Şen, Z. *Practical and Applied Hydrogeology*; Elsevier: Amsterdam, The Netherlands, 2015; ISBN 9780128000755.
51. Siemon, B.; Steuer, A.; Deus, N.; Elbracht, J. Comparison of Manually and Automatically Derived Fresh-Saline Groundwater Boundaries from Helicopter-Borne Em Data at the Jade Bay, Northern Germany. *E3S Web Conf.* **2018**, *54*, 00032. [CrossRef]
52. Dan, L. Comparison of Indicators for the Assessment of Saltwater Intrusion in Coastal Aquifers—Taking Aquifers in Pearl River Estuary as an Example. *Mar. Environ. Sci.* **2020**, *39*, 16–23. (In Chinese) [CrossRef]
53. Sun, Q.; Gao, M.; Wen, Z.; Hou, G.; Dang, X.; Liu, S.; Zhao, G. Hydrochemical Evolution Processes of Multiple-Water Quality Interfaces (Fresh/Saline Water, Saline Water/Brine) on Muddy Coast under Pumping Conditions. *Sci. Total Environ.* **2023**, *857*, 159297. [CrossRef]
54. Han, D.; Cao, G.; McCallum, J.; Song, X. Residence Times of Groundwater and Nitrate Transport in Coastal Aquifer Systems: Daweijia Area, Northeastern China. *Sci. Total Environ.* **2015**, *538*, 539–554. [CrossRef]
55. Thorn, P. Groundwater Salinity in Greve, Denmark: Determining the Source from Historical Data. *Hydrogeol. J.* **2011**, *19*, 445–461. [CrossRef]
56. Jinjie, M. *Dynamic Monitoring and Evolution Study of Saline Intrusion at South Coast of Laizhou Bay*; China University of Geosciences: Beijing, China, 2014.
57. MA, J.; Wei, L.; Xiong, J.; Wu, C.; Zhou, Z.; Zhu, S. Study on the Response of Groundwater Exploitation and Tidal Effects in Coastal Zones to Seawater Intrusion. In Proceedings of the 8th International Conference on Water Resource and Environment, Xi'an, China, 1–4 November 2022. (In Chinese).
58. Sen, L. *The Evolution of Ground-Saline Water and Process Mechanism of Saline Water Intrusion in Southern Laizhou Bay*; China University of Geosciences: Wuhan, China, 2018.
59. Nonner, J.C.; Nonner, J. *Introduction to Hydrogeology*; CRC Press: Boca Raton, FL, USA, 2002; ISBN 9780367805845.
60. Sakai, T.; Omori, K.; Oo, A.N.; Zaw, Y.N. Monitoring Saline Intrusion in the Ayeyarwady Delta, Myanmar, Using Data from the Sentinel-2 Satellite Mission. *Paddy Water Environ.* **2021**, *19*, 283–294. [CrossRef]
61. Subrahmanyam, B.; Trott, C.B.; Murty, V.S.N. Detection of Intraseasonal Oscillations in SMAP Salinity in the Bay of Bengal. *Geophys. Res. Lett.* **2018**, *45*, 7057–7065. [CrossRef]
62. Bouderbala, A.; Remini, B. Geophysical Approach for Assessment of Seawater Intrusion in the Coastal Aquifer of Wadi Nador (Tipaza, Algeria). *Acta Geophys.* **2014**, *62*, 1352–1372. [CrossRef]
63. Hisby, K. Features and Evaluation of Sea/Saltwater Intrusion in Southern Laizhou Bay. *J. Groundw. Sci. Eng.* **2016**, *4*, 141–148. [CrossRef]
64. Yuhai, H. Research and Application of High-Density Resistance Method in Seawater Invasion Investigation of Laizhou Bay. *Mar. Environ. Sci.* **2016**, *35*, 301–305. (In Chinese) [CrossRef]
65. Guanabara, E.; Ltda, K.; Guanabara, E.; Ltda, K. Application of Geophyscial Mehtods to Detecting Sea Water or Saline Water Intrusion:A Case Study of Alluvial-Proluvial Fan of Laizhou Bay. *Mar. Geol. Front.* **2016**, *32*, 58–64. (In Chinese)
66. Abdalla, O.A.E.; Ali, M.; Al-Higgi, K.; Al-Zidi, H.; El-Hussain, I.; Al-Hinai, S. Rate of Seawater Intrusion Estimated by Geophysical Methods in an Arid Area: Al Khabourah, Oman. *Hydrogeol. J.* **2010**, *18*, 1437–1445. [CrossRef]
67. Heydarizad, M.; Pumijumnong, N.; Mansourian, D.; Anbaran, E.D.; Minaei, M. The Deterioration of Groundwater Quality by Seawater Intrusion in the Chao Phraya River Basin, Thailand. *Environ. Monit. Assess.* **2023**, *195*, 424. [CrossRef]
68. Fu, T.; Zhang, Y.; Xu, X.; Su, Q.; Chen, G.; Guo, X. Assessment of Submarine Groundwater Discharge in the Intertidal Zone of Laizhou Bay, China, Using Electrical Resistivity Tomography. *Estuar. Coast. Shelf Sci.* **2020**, *245*, 106972. [CrossRef]
69. Xu, Z.; Tong, J.; Hu, B.X.; Yan, Z. Mapping and Monitoring Seasonal and Tidal Effects on the Salt-Freshwater Interface Using Electrical Resistivity Tomography Techniques. *Estuar. Coast. Shelf Sci.* **2022**, *276*, 108051. [CrossRef]

70. Qi, H.; Ma, C.; He, Z.; Hu, X. Review of Hydrogeochemical and Environmental Isotope Approaches in Groundwater Salinization Study. *Saf. Environ. Eng.* **2018**, *25*, 97–105. (In Chinese)
71. Guo, X.; Ma, C.; Hu, X.; Hu, X.; Yan, W. Application of Groundwater Functional Zoning to Coastal Groundwater Management: A Case Study in the Plain Area of Weifang City, China. *Environ. Earth Sci.* **2019**, *78*, 525. [CrossRef]
72. Zeng, X.; Wu, J.; Wang, D.; Zhu, X. Assessing the Pollution Risk of a Groundwater Source Field at Western Laizhou Bay under Seawater Intrusion. *Environ. Res.* **2016**, *148*, 586–594. [CrossRef]
73. Fan, Y.; Lu, W.; Miao, T.; Li, J.; Lin, J. Optimum Design of a Seawater Intrusion Monitoring Scheme Based on the Image Quality Assessment Method. *Water Resour. Manag.* **2020**, *34*, 2485–2502. [CrossRef]
74. Zghibi, A.; Mirchi, A.; Zouhri, L.; Taupin, J.D.; Chekirbane, A.; Tarhouni, J. Implications of Groundwater Development and Seawater Intrusion for Sustainability of a Mediterranean Coastal Aquifer in Tunisia. *Environ. Monit. Assess.* **2019**, *191*, 696. [CrossRef] [PubMed]
75. Mengya, S.; Bin, S.; Rui, H.; Suping, L.; Chenxi, F.; Zhuo, C. Preliminary Study on Monitoring the Salinity of Seawater with Fiber Bragg Grating. *Geol. J. China Univ.* **2019**, *25*, 125–130. (In Chinese) [CrossRef]
76. Samani, S.; Kardan Moghaddam, H. Optimizing Groundwater Level Monitoring Networks with Hydrogeological Complexity and Grid-Based Mapping Methods. *Environ. Earth Sci.* **2022**, *81*, 453. [CrossRef]

Disclaimer/Publisher's Note: The statements, opinions and data contained in all publications are solely those of the individual author(s) and contributor(s) and not of MDPI and/or the editor(s). MDPI and/or the editor(s) disclaim responsibility for any injury to people or property resulting from any ideas, methods, instructions or products referred to in the content.

hydrology

MDPI

Article

Fuzzy Analytical Solution of Horizontal Diffusion Equation into the Vadose Zone

Christos Tzimopoulos [1], Nikiforos Samarinas [1,*], Basil Papadopoulos [2] and Christos Evangelides [1]

[1] Department of Rural and Surveying Engineering, Aristotle University of Thessaloniki, 54124 Thessaloniki, Greece; tzimo@topo.auth.gr (C.T.)
[2] School of Engineering, Democritus University of Thrace, 67100 Xanthi, Greece
* Correspondence: smnikiforos@topo.auth.gr

Abstract: The process of how soil moisture profiles evolve into the soil and reach the root zone could be estimated by solving the appropriate strong nonlinear Richards' equation. The nonlinearity of the equation occurs because diffusivity D is generally an exponential function of water content. In this work, the boundary conditions of the physical problem are considered fuzzy for various reasons (e.g., machine impression, human errors, etc.), and the overall problem is encountered with a new approximate fuzzy analytical solution, leading to a system of crisp boundary value problems. According to the results, the proposed fuzzy analytical solution is in close agreement with Philip's semi-analytical method, which is used as a reference solution, after testing 12 different types of soils. Additionally, possibility theory is applied, enabling the decision-makers to take meaningful actions and gain knowledge of various soil and hydraulic properties (e.g., sorptivity, infiltration, etc.) for rational and productive engineering studies (e.g., irrigation systems).

Keywords: fuzzy solution; vadose zone; diffusion equation; infiltration; possibility

1. Introduction

Infiltration is a common physical phenomenon of water movement in porous media that is of great interest in many earth and plant sciences. Soil water flow plays an important role in understanding the phenomena of runoff, groundwater recharge, and the transport of contaminants. Especially in the vadose zone, soil moisture strongly influences plants' growing processes, and for irrigation problems, it is important to know how the soil moisture profiles evolve into the soil and reach the root zone. Historically, Buckingham (1907) [1], Gardner and Widsoe (1921) [2], and Richards (1931) [3] are the pioneers in the development of soil water movement, introducing the ideas of capillary potential, capillary conductivity, and diffusion phenomena in the concept of soil water movement, which were completed later by Childs (1936a, 1936b) [4,5]. Klute (1952) [6] presented the equation of flow arising from Darcy's (1856) law [7], while the law of conservation of mass is as follows:

$$\frac{\partial \theta}{\partial t} = \nabla \cdot (K \nabla \Phi)$$

where θ = the moisture content (cm^3/cm^3), K = the unsaturated hydraulic conductivity (cm/s), Φ = the total potential (cm) Φ = Ψ − z, Ψ = the pressure potential or capillary potential (cm), and z = the gravitational component (cm). In the case of one-dimensional horizontal flow or in cases where gravity may be neglected (fine-textured soils), in which the moisture gradient's influence is much more important than gravity, the phenomenon is described by the following equation:

$$\frac{\partial \theta}{\partial t} = \frac{\partial}{\partial x}\left(D \frac{\partial \theta}{\partial x}\right)$$

where D = diffusivity (L^2/T). According to Philip (1957, 1969) [8,9], this equation represents the water movement in a horizontal column and is called the absorption equation because it describes the wetting up of the column under tension.

Many methods exist with their corresponding advantages and disadvantages, such as semi-analytic methods [9], finite difference [10–15], finite element methods [16,17], finite control volume methods [18,19], flux concentration methods [20], and approximate analytical methods [21–25]. Henceforth, our research is focused on approximate analytical methods.

Tolikas et al. (1984) [26] presented a simple analytical solution to the problem of horizontal absorption under the assumption that diffusivity is an exponential function of soil water content. Brutsaert (1982) [27] presented a group of 14 solutions with different diffusivities for the problem of desorption, considering, as pointed out by Crank (1975) [28], that sorption and desorption are related by the correspondence principle. Specifically, if the solution for sorption with a given $D(\theta)$ is $\theta = f(x,t)$ in normalized form, then the function $f1 = 1 - f(x,t)$ is the solution for the desorption problem with the diffusivity $D(1 - \theta)$. Lisle and Parlange (1993) [29] used a large class of transformations in conjunction with symmetry properties to obtain an analytical reduction of the transformed equation for certain diffusivities, emphasizing that the symmetry leaves the equation invariant. Hang and Zhiqiang (1997) [30] presented an approximated analytical solution with the Boltzmann transformation method for the case of an exponential diffusivity form and a profile of soil water content of a finite extent under the assumption that the wetting front is known. Prevedello et al. (2008) [31] derived a new analytical solution of the Boltzmann transformation φ as a function of matrix potential for horizontal water infiltration into a sand soil sample without invoking the concept or use of $D(\theta)$. The derivation assumes that a similarity exists between the soil water retention function and the Boltzmann transformation φ. Tzimopoulos et al. (2015) [32] presented a new approximate analytical solution of the nonlinear diffusion equation, and the solution is given for the transformed equation through the Boltzmann transformation. It is considering the case of an exponential function of the diffusivity under the following assumptions: (a) the profiles of soil water content have a finite extent; (b) the concentration at the boundaries is constant; and (c) the reduced flux of Philip (1973) [20] is of a special form [33]. More recent works have implemented the diffusion equation in applications for volatile organic compound transport [34], mass transfer [35], and Turing pattern formation [36].

The calculation of water flow in the unsaturated zone requires exact knowledge of the initial and boundary conditions and the various soil parameters, and this assumption is based principally on in situ measurements. In general, this assumption is subject to different kinds of uncertainty due to human and machine imprecision. In many cases, the uncertainties were considered in statistical terms as random variables with given mean values, variances, and correlations. However, these methods require exact knowledge of mean values, variances, and correlations and often suffer from an insufficient amount of accurate in situ measurement data. Zadeh (1965) [37] introduced the theory of fuzzy sets and fuzzy logic and covered all these kinds of uncertainty. A significant number of research studies presenting uncertainties were carried out in that field, especially regarding the fuzzy differentiation of functions. Puri and Ralescu (1983) [38] generalized and extended Hukuhara's fundamental study [39] (H-derivative) of a set of values appearing in fuzzy sets. Vorobiev and Seikkala (2002) [40], O'Regan et al. (2003) [41], and Nieto et al. (2006) [42] have worked in the theoretical and applied research fields on fuzzy differential equations with an H-derivative, but their method has presented certain drawbacks since it has led to solutions with increasing support along with increasing time. To overcome this drawback, the generalized derivative gH (gH-derivative) was introduced by [43–46]. The gH-derivative will be used henceforth for a more extensive degree of fuzzy functions than the Hukuhara derivative. In addition, a recent review work by Mazandarani and Xiu (2021) [47] presents a chronological survey on fuzzy differential equations of integer and fractional orders, with the corresponding future perspectives and challenges to be discussed.

In the present article, the problem of fuzzy, unsteady water movement in the vadose zone in the horizontal direction is examined and described by a nonlinear partial diffusion equation with fuzzy conditions. In this context, we developed and propose a new fuzzy analytical solution that has never been presented before in the literature, coupled with the innovative possibility theory (see Section 2.2.1). Specifically, the nonlinear equation was first fuzzified and subsequently translated to a system of second-order crisp boundary value problems called the corresponding system for the fuzzy problem. Subsequently, using the Boltzmann transformation, the crisp problem was transformed to a system of two classical ordinary differential equations [32]. With the help of α-cuts, profiles of moisture content θ versus Boltzmann transformation φ were estimated, as were the storativity (S) and cumulative moisture content (I). In addition, for evaluation purposes, the present analytical solution and the approximated solution of Hang and Zhiqiang (1997) [30] were tested using the semi-analytical solution of Philip as a reference solution.

2. Mathematical Model

2.1. Classical (Crisp) Case

The one-dimensional horizontal nonlinear flow of water in unsaturated soil with initial and boundary conditions for absorption is described by the following equation [6]:

$$\frac{\partial \theta}{\partial t} = \frac{\partial}{\partial x}(D\frac{\partial \theta}{\partial x}) \tag{1}$$

under constant head condition, with initial and boundary conditions as follows:

- Initial condition

$$x \geq 0, t = 0, \theta = \theta_r, \tag{2}$$

- Boundary condition

$$x = 0, t > 0, \theta = \theta_S, x \to \infty, t > 0, \theta = \theta_r. \tag{3}$$

where θ_s = the saturated soil moisture content at x = 0 and θ_r = the residual soil moisture content. The diffusivity D (θ) can be closely expressed by an exponential function [48–50] as follows:

$$D(\theta) = D(\theta_r)e^{\beta(\theta-\theta_r)} \tag{4}$$

The non-dimensional variables are now introduced in Equation (1),

$$\Theta = \frac{\theta - \theta_r}{\theta_S - \theta_r}, X = \frac{x}{L}, \tau = \frac{D_r t}{L^2}, D* = \frac{D}{D_r} = e^{\lambda_1 \Theta}, \tag{5}$$

where L = a characteristic length usually equal to the wetting front, Dr = $D(\theta_r)$ = the diffusivity at the residual soil moisture content, τ = the non-dimensional time, D* = the non-dimensional diffusivity, and $\lambda_1 = \beta\ (\theta_s - \theta_r)$. The advantage of introducing non-dimensional variables is that they allow the generalization of the theory, speeding up the computational processes.

Then, Equation (1) with initial and boundary conditions (2) and (3) becomes the following:

$$\frac{\partial \Theta}{\partial \tau} = \frac{\partial}{\partial X}(D^*(\Theta)\frac{\partial \Theta}{\partial X}) \tag{6}$$

Subjacent to the following:

- Initial condition

$$X \geq 0, \tau = 0, \Theta = 0, \tag{7}$$

- Boundary condition

$$X = 0, \tau > 0, \Theta = 1, X \to \infty, \tau > 0, \Theta = 0. \tag{8}$$

The Boltzmann transformation φ* = Xτ$^{-1/2}$ is now introduced in Equation (6), and due to conditions (7) and (8), Equation (6) is reduced to the following ordinary differential equation:

$$\frac{d}{d\varphi^*}(D^*(\Theta)\frac{d\Theta}{d\varphi^*}) + \frac{\varphi^*}{2}\frac{d\Theta}{d\varphi^*} = 0, \tag{9}$$

The conditions (2) and (3) are transformed into the following:

$$\varphi^* = 0, \ \Theta = 1 \quad \varphi^* \to \varphi_f^*, \ \Theta \to 0, \tag{10}$$

where φ_f^* is the wetting front.

Philip (1957) [8] introduced the term sorptivity in order to define the capacity of the medium to absorb or desorb water by capillarity. He expresses the term as follows:

$$S^* = \int_0^1 \varphi^* d\Theta. \tag{11}$$

The non-dimensional Boltzmann transformation φ* and the non-dimensional sorptivity S* are related to the dimensional Boltzmann transformation φ and the dimensional sorptivity S by the following expressions:

$$\varphi^* = \frac{\varphi}{\sqrt{D_r}}, \ S^* = \frac{S}{(\theta_S - \theta_r)\sqrt{D_r}} \tag{12}$$

Tzimopoulos et al. (2015) [32] proposed the following: (a) an explicit analytical solution, which has the Boltzmann transformation as the dependent variable and the soil water moisture as the independent variable; (b) a simple form for the sorptivity. Both solutions are presented in normalized form. The solutions were tested with 12 soils and showed a close agreement with Philip's semi-analytical method [9], which has been considered a reference method. The solution concerning sorptivity is given as follows:

$$S^* = \sqrt{e^{\lambda_1}(\frac{2}{\lambda_1} - \frac{1}{\lambda_1^2})} \tag{13}$$

or in dimensional form:

$$S = (\theta_S - \theta_r)\sqrt{D_r e^{\lambda_1}(\frac{2}{\lambda_1} - \frac{1}{\lambda_1^2})} \tag{14}$$

The solution concerning Boltzmann transformation is given as follows:

$$\varphi^* = \frac{1}{S^*}\{\frac{1}{\lambda_1}\left(e^{\lambda_1} - e^{\lambda_1\Theta}\right) + E_i(\lambda_1) - E_i(\lambda_1\Theta)\} \tag{15}$$

or in dimensional form:

$$\varphi = \frac{(\theta_S - \theta_r)D_r}{S}\{\frac{1}{\lambda_1}\left(e^{\lambda_1} - e^{\lambda_1\Theta}\right) + E_i(\lambda_1) - E_i(\lambda_1\Theta)\} \tag{16}$$

where $E_i(\lambda_1), E_i(\lambda_1\Theta)$ are the exponential integrals [51,52]. Equation (16) satisfies the boundary conditions (10). Indeed, for the following:

$$\Theta = 1 \to \varphi = \frac{(\theta_S - \theta_r)D_r}{S}\{\frac{1}{\lambda_1}\left(e^{\lambda_1} - e^{\lambda_1}\right) + E_i(\lambda_1) - E_i(\lambda_1)\} = 0. \tag{17}$$

$$\begin{array}{l} \Theta = 1 \\ \rightarrow \lim\limits_{\Theta \to 0}(\Phi) = \lim[\frac{(\theta_S - \theta_r)D_r}{S}\{\frac{1}{\lambda_1}(e^{\lambda_1} - e^{\lambda_1 \Theta}) + E_i(\lambda_1) - E_i(\lambda_1 \Theta)\}] = \\ = \frac{(\theta_S - \theta_r)D_r}{S}\{\frac{1}{\lambda_1}\left(e^{\lambda_1} - 1\right) + E_i(\lambda_1) - \lim\limits_{\Theta \to 0} E_i(\lambda_1 \Theta)\} \end{array} \quad (18)$$

According to Ramanujan et al. (2000) [53], the function $E_i(x) - \gamma - lnx, \gamma \approx 0.5772156649\ldots$ for small values of x is included in the following interval:

$$[1 - \frac{3x}{4}, 1 - \frac{3x}{4} + \frac{11x^2}{36}], x = \lambda_1 \Theta \quad (19)$$

If we choose x = 5×10^{-5} as the minimum value, the above relation gives a value of $E_i(\lambda_1 \Theta)\big|\lambda_1 \Theta = 5 \times 10^{-5} = -8.32631$. With this value of integral, the value of φ is equal to the moisture content front (φ_{front}), which is as follows:

$$\varphi_{front} = \frac{(\theta_S - \theta_r)D_r}{S}\{\frac{1}{\lambda_1}\left(e^{\lambda_1} - 1\right) + E_i(\lambda_1) + 8.32631\} \quad (20)$$

Now the boundary condition $\varphi^* \rightarrow \infty, \Theta \rightarrow 0,$ becomes the following:

$$\text{For} \quad \varphi \geq \varphi_{front}, \ \Theta \approx 0. \quad (21)$$

From the above expressions (14) and (16), it is clear that by knowing the soil moisture contents θ_S, θ_r, and the diffusivity as an exponential function of Θ, it is possible to find the following:

- The sorptivity S;
- The moisture content front φ_{front};
- The water profiles in the form of $\varphi = \varphi(\Theta) = \varphi(\theta)$.

Table 1 shows the parameter values for the 12 different soils under consideration and a comparison of the wetting fronts and sorptivities between the values obtained by the analytical values in this paper and Philip's semi-analytical solution, which is in close agreement with the experimental values and was taken as a reference profile [32].

Table 1. Estimated values of moisture content front and sorptivity for 12 soil types.

a/a	Soil Type	θ_r (cm^3/cm^3)	θ_s (cm^3/cm^3)	D_r cm^2/min	λ_1	$\varphi^{exp}{}_{front}$ ($cm/min^{0.5}$)	$\varphi^{anal}{}_{front}$ ($cm/min^{0.5}$)	S^{exp} ($cm/min^{0.5}$)	S^{anal} ($cm/min^{0.5}$)	Ref.
1	Hagenet sand	0.0540	0.370	9.443×10^{-2}	6.756	5.857	5.870	1.490	1.490	[54]
2	Hayden sandy loam	0.0146	0.510	6.824×10^{-3}	7.256	1.906	1.908	0.780	0.780	[55]
3	Manawatu fine sand. loam	0.0800	0.360	1.168×10^{-3}	11.337	4.490	4.490	1.138	1.138	[56]
4	Adelanto loam	0.0380	0.387	6.678×10^{-8}	18.690	1.010	1.010	0.333	0.333	[57]
5	Edina silt loam	0.0560	0.500	4.214×10^{-3}	7.995	2.013	2.014	0.760	0.760	[54]
6	Nicollet sandy loam	0.0380	0.364	2.151×10^{-5}	13.094	1.346	1.348	0.404	0.404	[58]
7	Fayette silty clay loam	0.0480	0.448	3.418×10^{-4}	9.223	0.960	0.960	0.337	0.337	[58]
8	Panoche clay loam	0.0480	0.443	2.554×10^{-3}	8.731	2.129	2.129	0.730	0.730	[49]
9	Pine silty clay	0.0500	0.463	8.349×10^{-9}	20.262	0.750	0.750	0.294	0.294	[57]
10	Yolo clay	0.0400	0.490	3.265×10^{-4}	6.869	0.360	0.360	0.131	0.131	[59]
11	sample 1	0.0175	0.295	1.13×10^{-3}	9.170	1.710	1.709	0.416	0.416	[60]
12	sample 2	0.0080	0.500	2.992×10^{-1}	6.618	9.930	9.910	3.890	3.890	[60]

The relation

$$S^* = \int_0^1 \varphi^* d\Theta, \tag{22}$$

easily follows the dimensional form of I

$$S = \{\int (\theta - \theta_r) dx\} t^{-1/2} = It^{-1/2} \rightarrow I = St^{1/2} \tag{23}$$

where I = cumulative absorption, L (L^3/L^3). From this one, it follows the flow velocity at x = 0:

$$v|_{x=0} = 0 = \frac{dI}{dt} = St^{-1/2} \tag{24}$$

2.2. Fuzzy Case

In order to facilitate an understanding for readers unfamiliar with the fuzzy and possibility theories, we describe definitions concerning some preliminaries in the fuzzy and possibility theories and definitions about the differentiability of fuzzy numbers.

2.2.1. Fuzzy Theory

Definition 1. *A fuzzy set $\widetilde{U}$ on a universe set X is a mapping $\widetilde{U} : X \rightarrow [0,1]$ or $\mu_{\widetilde{U}} : X \rightarrow [0,1]$, which is called membership function. The value $\mu_{\widetilde{U}}(x), x \in X$ is the membership value of $x \in X$ and expresses the membership degree of $x \in X$, i.e., the truth of fuzzy logical proposition: $T(xis\widetilde{U}|X = x) = \mu_{\widetilde{U}}(x)$.*

The membership function $\mu_{\widetilde{U}}(x)$, defined also as $\widetilde{U}(x)$, has the following properties: (i) $\mu_{\widetilde{U}}$ is upper semicontinuous; (ii) $\mu_{\widetilde{U}}(x)$ = 0 outside of some interval [c, d]; (iii) there are real numbers $c \leq a \leq b \leq d$, such that $\mu_{\widetilde{U}}$ is increasing on [c, a], decreasing on [b, d], and $\mu_{\widetilde{U}}(x)$ = 1 for each $x \in [a,b]$.; (iv) $\widetilde{U}$ is a convex fuzzy set (i.e., $\mu_{\widetilde{U}}(\lambda x + (1-\lambda)x) \geq min\{\mu_{\widetilde{U}}(\lambda x), \mu_{\widetilde{U}}((1-\lambda)x)\}$.

Definition 2. *Let X be a Banach space and $\widetilde{U}$ be a fuzzy set on X. We define the α-cuts of $\widetilde{U}$ as $[\widetilde{U}(x)]_\alpha = \{x \in R | \widetilde{U}(x) \geq \alpha\}, \alpha \in (0,1]$, and for α = 0, we define the following closure:*

$$[\widetilde{U}(x)]_0 = \overline{\left\{x \in R \middle| \widetilde{U}(x) > 0\right\}}.$$

Definition 3. *Let K(X) be the family of all nonempty compact convex subsets of a Banach space. A fuzzy set $\widetilde{U}$ on X is called compact if $[\widetilde{U}]_\alpha \in K(X), \forall \alpha \in [0,1]$. The space of all compact and convex fuzzy sets on X is denoted as $\mathcal{F}$ (X).*

Definition 4. *Let $[\widetilde{U}] \in \mathcal{F}$ (R). The α-cuts of $\widetilde{U}$ are as follows: $[\widetilde{U}]_\alpha = [U_\alpha^-, U_\alpha^+]$. According to the representation theorem of* [61,62]*, the membership function and the α-cut form of a fuzzy number $\widetilde{U}$ are equivalent, and in particular, the α-cuts $[\widetilde{U}]_\alpha = [U_\alpha^-, U_\alpha^+]$ uniquely represent $\widetilde{U}$, provided that the two functions are monotonic (U_α^- increasing, U_α^+ decreasing) and $U_1^- \leq U_1^+$ for $\alpha = 1$. For every $\widetilde{U}, \widetilde{V} \in \mathcal{F}$ (R), the metric structure is given by the Hausdorff distance as follows:*

$$D : \mathcal{F}(R) \times \mathcal{F}(R) \rightarrow R_+ \cup \{0\}, \text{ by } D(U,V) = \sup_{a \in [0,1]} max\{|U_a^- - V_a^-|, |U_a^+ - V_a^+|\}$$

Definition 5. *gH-Differentiability* [63]. *Let $\widetilde{U} : [a,b] \rightarrow R_{\mathcal{F}}$ be such that $[\widetilde{U}]_\alpha = [U_\alpha^-, U_\alpha^+]$. Suppose that the functions U_α^- and U_α^+ are real-valued functions, differentiable w.r.t. (with respect to) x, uniformly w.r.t. $\alpha \in [0,1]$. Then the function $\widetilde{U}(x)$ is gH-differentiable at a fixed $x \in [a,b]$ only if one of the following two cases holds:*

(a) $(U_\alpha^-)'(x)$ *is increasing,* $(U_\alpha^+)'(x)$ *is decreasing as functions of α, and* $(U_1^-)\prime(x) \leq (U_1^+)'(x)]$*, or*

(b) $(U_\alpha^+)'(x)$ *is decreasing,* $(U_\alpha^-)'(x)$ *is increasing as functions of* α*, and* $\left(U_1^+\right)'(x) \leq \left(U_1^-\right)'(x)]$.

Notation: $(U_\alpha^-)'(x) = \frac{\partial U_\alpha^-(x)}{\partial x}, (U_\alpha^+)'(x) = \frac{\partial U_\alpha^+(x)}{\partial x}$. In both of the above cases, the $\widetilde{U}'_\alpha(x)$ derivative is a fuzzy number.

Definition 6. *gH-Differentiable at* x_0*. Let* $\widetilde{U} : [a,b] \to F$ *(R) and* $x_0 \in [a,b]$ *with* $U_\alpha^-(x)$ *and* $U_\alpha^+(x)$ *both being differentiable at* x_0*. We say that* [63]*:*

- $\widetilde{U}$ *is (i)-gH-differentiable at* x_0 *if*

  (i) $\quad [U'_{gH}(x_0)]_\alpha = [(U_\alpha^-)'(x_0), (U_\alpha^+)'(x_0)], \forall \alpha \in [0,1]$

- $\widetilde{U}$ *is (ii)-gH-differentiable at* x_0 *if*

  (ii) $\quad [U'_{gH}(x_0)]_\alpha = [(U_\alpha^+)'(x_0), (U_\alpha^-)'(x_0)], \forall \alpha \in [0,1]$

Definition 7. *g-Differentiability Let* $\widetilde{U} : [a,b] \to F$ *(R) be such that* $[\widetilde{U}]_\alpha = [U_\alpha^-, U_\alpha^+]$*. If* $U_\alpha^-(x)$ *and* $U_\alpha^+(x)$ *are differentiable real-valued functions with respect to x, uniformly for* $\alpha \in [0,1]$*, then f (x) is g-differentiable and we have the following* [63]*:*

$$[U'_g(x)]_\alpha = \left[\inf_{\beta \geq \alpha} min\{(U_\alpha^-)'(x), (U_\alpha^+)'(x)\}, \sup_{\beta \geq \alpha} max\{(U_\alpha^-)'(x), (U_\alpha^+)'(x)\}\right],$$

Definition 8. *The gH-Differentiability implies g-differentiability, but the inverse is not true.*

Definition 9. *[gH-p]-Differentiability. A fuzzy-valued function* $\widetilde{U}$ *of two variables is a rule that assigns to each ordered pair of real numbers (x, t) in a set* $\boldsymbol{D}$ *a unique fuzzy number denoted by* $\widetilde{U}(x,t)$*. Let* $\widetilde{U}(x_0,t_0)$*:* $\boldsymbol{D} \to F$ *(R),* $(x_0, t_0)_\in \boldsymbol{D}$ *and* $U_\alpha^-(x_0,t_0)$*,* $U_\alpha^+(x_0,t_0)$ *are real-valued functions and partially differentiable w.r.t. x. We say that* [46,64]*:*

- $\widetilde{U}(x,t)$ *is [(i)-p]-differentiable w.r.t. x at* (x_0, t_0) *if:*

$$\frac{\partial \widetilde{U}_\alpha(x_0,t_0)}{\partial x_{i.gH}} = [\frac{\partial U_\alpha^-(x_0,t_0)}{\partial x}, \frac{\partial U_\alpha^+(x_0,t_0)}{\partial x}]$$

- $\widetilde{U}(x,t)$ *is [(ii)-p]-differentiable w.r.t. x at* (x_0, t_0) *if:*

$$\frac{\partial \widetilde{U}_\alpha(x_0,t_0)}{\partial x_{ii.gH}} = [\frac{\partial U_\alpha^+(x_0,t_0)}{\partial x}, \frac{\partial U_\alpha^-(x_0,t_0)}{\partial x}]$$

Notation: The same is valid for $\frac{\partial \widetilde{U}_\alpha(x_0,t_0)}{\partial t_{p.gH}}$.

Definition 10. *Let* $\widetilde{U}(x,t)$*:*$\boldsymbol{D} \to F$ *(R), and* $\frac{\partial \widetilde{U}_\alpha(x_0,t_0)}{\partial x_{p.gH}}$ *be [gH-p]-differentiable at* $(x_0, t_0) \in \boldsymbol{D}$ *with respect to x. We say that* [46,64] $\frac{\partial \widetilde{U}_\alpha(x_0,t_0)}{\partial x_{p.gH}}$ *is*

- *[(i)-p]-differentiable w.r.t. x, if the type of [gH-p]-differentiability of both* $\widetilde{U}_\alpha(x_0,t_0)$ *and* $\frac{\partial \widetilde{U}_\alpha(x_0,t_0)}{\partial x_{p.gH}}$ *is the same, then* $\frac{\partial^2 \widetilde{U}_\alpha(x_0,t_0)}{\partial x^2{}_{i.gH}} = [\frac{\partial^2 U_\alpha^-(x_0,t_0)}{\partial x^2}, \frac{\partial^2 U_\alpha^+(x_0,t_0)}{\partial x^2}]$
- *[(ii)-p]-differentiable w.r.t. x, if the type of [gH-p]-differentiability of both* $\widetilde{U}_\alpha(x_0,t_0)$ *and* $\frac{\partial \widetilde{U}_\alpha(x_0,t_0)}{\partial x_{p.gH}}$ *is different, then* $\frac{\partial^2 \widetilde{U}_\alpha(x_0,t_0)}{\partial x^2{}_{i.gH}} = [\frac{\partial^2 U_\alpha^+(x_0,t_0)}{\partial x^2}, \frac{\partial^2 U_\alpha^-(x_0,t_0)}{\partial x^2}]$

2.2.2. Possibility Theory

Definition 11. *A possibility measure* Π *on a set* X *(e.g., a set of reels) is characterized by a possibility distribution* $\pi : X \to [0,1]$ *and is defined by the following:*

$$\forall A \subseteq X, \Pi(A) = sup\{\pi(x), x \in A\}.$$

For finite sets, this definition reduces to the following:

$$\forall \mathrm{A} \subseteq \mathrm{X}, \Pi(\mathrm{A}) = \max\{\pi(\mathrm{x}), \mathrm{x} \in \mathrm{A}\}.$$

Definition 12. *A degree of necessity* $Ness_X$ *on a set* X *(e.g., a set of reals) is characterized by the non-possibility (one minus possibility) of A complement* (A^C).

$$\forall A \subseteq X, Ness_X(A) = 1 - \Pi\left(A^C\right).$$

Definition 13. *A probability distribution p and a possibility distribution* π *are said to be consistent only if* $\pi(u) \geq p(u), \forall u$ [65–68].

Definition 14. *Two possibility distributions* π_X, π'_X *are consistent with the probability distribution* p_X. *The* π_X *distribution is more specific than* π'_X *if it is* $\pi_X < \pi'_X$.

A possibility distribution π^*_x consistent with the probability distribution p_X is called *maximal specificity* if it is more specific that each other possibility distribution π_X:$\pi^*_x(x) < \pi_X(x), \forall x$.

Definition 15. *For a number Y with a known and continuous probability distribution function p, the fuzzy number* $\widetilde{Y}$, *which has a possibility measure* $\Pi(\widetilde{Y}) = \mu_{\widetilde{Y}}$ *is the fuzzy estimator of Y and has an α-cut of* $\Pi_{\widetilde{Y}}(\alpha) = \widetilde{Y}[\alpha]$. *This fuzzy number satisfies the consistency principle and verifies* $P(\widetilde{Y}[\alpha]) = Ness_{\widetilde{Y}}[\alpha] = 1 - \alpha$, *so that the probability of the possibility α-cut is equal to* $1 - \alpha$. *The α-cuts* $\widetilde{Y}[\alpha]$ *are the confidence intervals of P, and the confidence level is α.*

Definition 16. *Conjecture* [68]. *For a function Y = Y (*X_1, X_2, ... X_n*) with unknown probability distribution function, a fuzzy number may be constructed* $\widetilde{Y}^* = \widetilde{Y}(\widetilde{X}^*_1, \widetilde{X}^*_2, \ldots \widetilde{X}^*_n)$, *and the α-cut is equal to the following:*

$$\widetilde{Y}^*[a] = \widetilde{Y}(\widetilde{X}^*_1[a], \widetilde{X}^*_2[a], \ldots \widetilde{X}^*_n[a]).$$

In this case, the fuzzy number$\widetilde{Y}*$ *is the fuzzy estimator of Y and verifies the following:*

$$P(\widetilde{Y}^*[a]) \geq Ness_{\widetilde{Y}^*}[\alpha] = 1 - \alpha,$$

so that the probability of the possibility α-cut is greater than $1 - \alpha$.

2.2.3. Fuzzy Model

We write Equation (1) in its fuzzy form according to [69]:

$$\frac{\partial \widetilde{\Theta}}{\partial \tau} = \frac{\partial}{\partial X}(\widetilde{D}\frac{\partial \widetilde{\Theta}}{\partial X}) \tag{25}$$

with the following:

- Initial condition

$$X \geq 0, \tau = 0, \widetilde{\Theta} = (\widetilde{0}) \tag{26}$$

- Boundary conditions

$$X = 0, \tau > 0, \widetilde{\Theta} = \widetilde{1}, X \to \infty, \tau > 0, \widetilde{\Theta} = \widetilde{0}. \quad (27)$$

The fuzzy parameters were considered to be the following:

(a) The soil moisture contents θ_s (saturated soil moisture content);
(b) θ_r (the residual soil moisture content);
(c) The parameter λ_1 (in the exponent of the diffusivity D).

These parameters are considered symmetrical triangular fuzzy numbers and are illustrated in Figure 1.

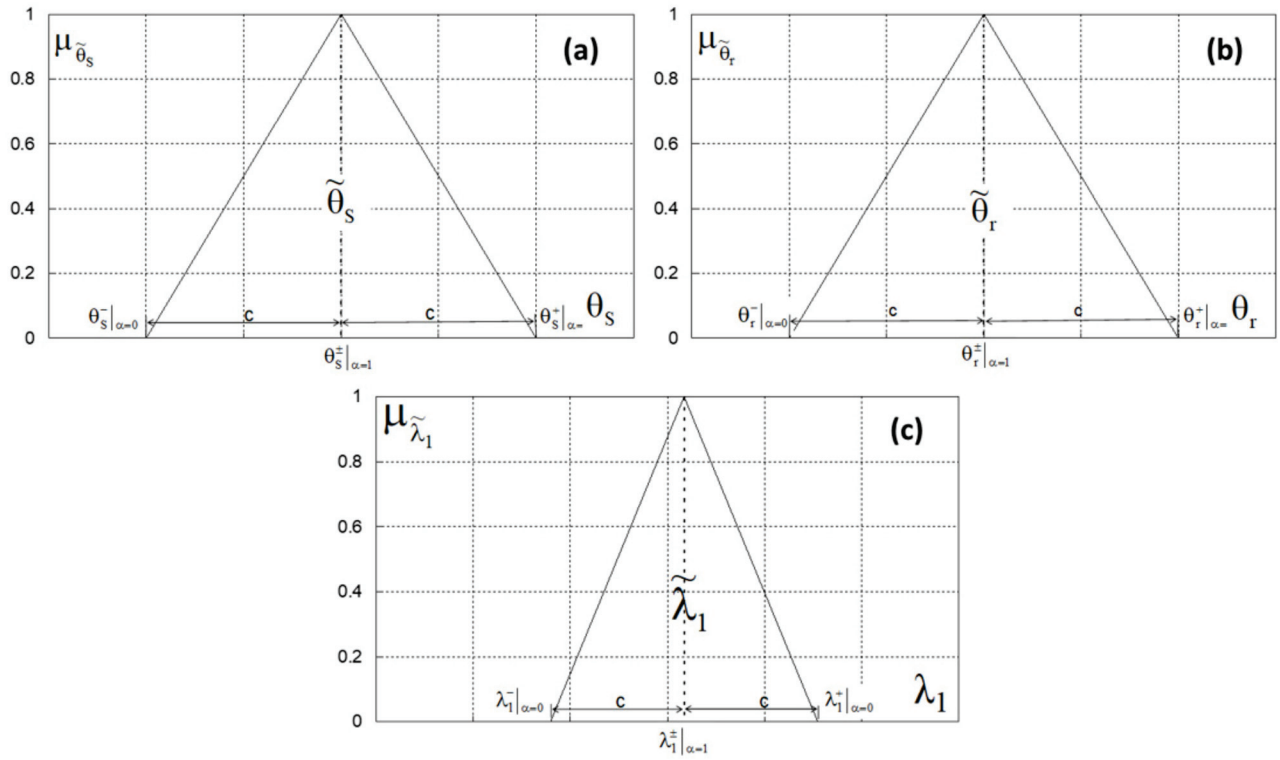

Figure 1. Membership function of (**a**) moisture content θs, (**b**) moisture content θr, and (**c**) parameter λ_1.

We can find solutions to the fuzzy problem of Equation (25) and the initial and boundary conditions (26) and (27) by utilizing the theory of [22,46,63,64,70] and translating the above fuzzy problem to a system of second-order crisp boundary value problems, hereafter called the corresponding system for the fuzzy problem. Therefore, many crisp BVP systems are possible for the fuzzy problem, but in the current work, the solution is restricted to the following systems (Cases A and B), which describe exactly the physical problem.

The following fuzzy expression is valid and is referring to α-cuts:

$$L(\widetilde{\Theta}_\alpha) = [L(\Theta_\alpha^-), L(\Theta_\alpha^+)]$$

In this case, for more convenience, the above expression could be written as follows, related to fuzzy partial differential equations:

$$\frac{\partial \widetilde{\Theta}}{\partial \tau} = \frac{\partial}{\partial X}\left(\widetilde{D}\frac{\partial \widetilde{\Theta}}{\partial X}\right) \Leftrightarrow \underset{\text{Case A}}{\frac{\partial \Theta_\alpha^-}{\partial \tau} = \frac{\partial}{\partial X}\left(D_\alpha^- \frac{\partial \Theta_\alpha^-}{\partial X}\right)}, \underset{\text{Case B}}{\frac{\partial \Theta_\alpha^+}{\partial \tau} = \frac{\partial}{\partial X}\left(D_\alpha^+ \frac{\partial \Theta_\alpha^+}{\partial X}\right)}$$

The main difference between the above two cases is that the operator $(-)$ describes the left side of the α-cut while the (+) describes the right side of the α-cut, constructing in this way a possible range in which the desired value will be.

Case A

For Case A, the following expression arises:

$$\frac{\partial \Theta_{\alpha}^{-}}{\partial \tau} = \frac{\partial}{\partial X}\left(D_{\alpha}^{-} \frac{\partial \Theta_{\alpha}^{-}}{\partial X} \right) \tag{28}$$

Following the same procedure described above for the classical case, the non-dimensional and dimensional forms are presented below:

- Non-dimensional form:

$$\frac{d}{d\varphi^*}(D^*(\Theta^-)\frac{d\Theta^-}{d\varphi^*}) + \frac{\varphi^*}{2}\frac{d\Theta^-}{d\varphi^*} = 0, \tag{29}$$

$$(S^*)_a^- = \left\{ e^{\lambda_1^-}(\frac{2}{\lambda_1^-} - \frac{1}{(\lambda_1^-)^2}) \right\}_{\alpha}^{1/2} \tag{30}$$

$$(\varphi^*)_a^- = \frac{1}{(S^*)_a^-}\left\{ \frac{1}{\lambda_1^-}(e^{\lambda_1^-} - e^{\lambda_1^- \Theta}) + E_i(\lambda_1^-) - E_i(\lambda_1^- \Theta^-) \right\}_{\alpha} \tag{31}$$

- Dimensional form:

$$S_{\alpha}^{-} = [(\theta_s)_{\alpha}^{-} - (\theta_r)_{\alpha}^{-}]\sqrt{D_r^- e^{(\lambda_1)_{\alpha}^-}(\frac{2}{(\lambda_1)_{\alpha}^-} - \frac{1}{((\lambda_1)_{\alpha}^-)^2})} \tag{32}$$

$$\varphi_{\alpha}^{-} = \frac{[(\theta_s)_{\alpha}^{-} - (\theta_r)_{\alpha}^{-}](D_r)_{\alpha}^{-}}{S^-}\{\frac{1}{(\lambda_1)_{\alpha}^-}(e^{(\lambda_1)_{\alpha}^-} - e^{(\lambda_1)_{\alpha}^- \Theta_{\alpha}^-}) + E_i(\lambda_1)_{\alpha}^- - E_i((\lambda_1)_{\alpha}^- \Theta_{\alpha}^-)\} \tag{33}$$

Case B

For Case B, the following expression arises:

$$\frac{\partial \Theta_{\alpha}^{+}}{\partial \tau} = \frac{\partial}{\partial X}\left(D_{\alpha}^{+} \frac{\partial \Theta_{\alpha}^{+}}{\partial X} \right) \tag{34}$$

Following the same procedure described above for the classical case, the non-dimensional and dimensional forms are presented below:

- Non-dimensional form:

$$\frac{d}{d\varphi^*}(D^*(\Theta^+)\frac{d\Theta^+}{d\varphi^*}) + \frac{\varphi^*}{2}\frac{d\Theta^+}{d\varphi^*} = 0, \tag{35}$$

$$(S^*)_a^+ = \left\{ e^{\lambda_1^-}(\frac{2}{\lambda_1^+} - \frac{1}{(\lambda_1^+)^2}) \right\}_{\alpha}^{1/2} \tag{36}$$

$$(\varphi^*)_a^+ = \frac{1}{(S^*)_a^+}\left\{ \frac{1}{\lambda_1^+}(e^{\lambda_1^+} - e^{\lambda_1^+ \Theta}) + E_i(\lambda_1^+) - E_i(\lambda_1^+ - \Theta^+) \right\}_{\alpha} \tag{37}$$

- Dimensional form:

$$S_{\alpha}^{+} = [(\theta_s)_{\alpha}^{+} - (\theta_r)_{\alpha}^{+}]\sqrt{D_r^+ e^{(\lambda_1)_{\alpha}^+}(\frac{2}{(\lambda_1)_{\alpha}^+} - \frac{1}{\left((\lambda_1)_{\alpha}^+\right)^2})} \tag{38}$$

$$\varphi_{\alpha}^{+} = \frac{[(\theta_s)_{\alpha}^{+} - (\theta_r)_{\alpha}^{+}](D_r)_{\alpha}^{+}}{S^{-}} \{ \frac{1}{(\lambda_1)_{\alpha}^{+}} (e^{(\lambda_1)_{\alpha}^{+}} - e^{(\lambda_1)_{\alpha}^{+}\Theta_{\alpha}^{+}}) + E_i(\lambda_1)_{\alpha}^{+} - E_i((\lambda_1)_{\alpha}^{+}\Theta_{\alpha}^{+}) \} \quad (39)$$

3. Results and Discussion

3.1. Construction of the Hang and Zhiqiang Solution

For comparison purposes, the Hang and Zhiqiang (1997) [30] solution was selected mainly due to its simplicity in applications. However, this solution is valid under the following two certain conditions:

1. Diffusivity is an exponential function of Θ;
2. The value of the moisture wetting front is a priori known.

The Hang and Zhiqiang analytical solution initially had the following form:

$$\theta(x,t) = \theta(\varphi) = \frac{1}{\beta} ln[e^{\beta\theta_0} - (\frac{A(e^{\beta\theta_0} - e^{\beta\theta_r}) - 0.5\varphi_{front}^2}{A\varphi_{front}})\varphi - \frac{1}{2A}\varphi^2]$$

In order to make a comparison with Equation (6) and with Philip's reference solution, the above equation is transformed into the following expression:

$$\varphi = \varphi(\theta) = -\alpha + \sqrt{\alpha^2 + 2A(e^{\beta\theta_0} - e^{\beta\theta})},$$

with

$$\alpha = \frac{A(e^{\beta\theta_0} - e^{\beta\theta_r}) - 0.5\varphi_{front}^2}{\varphi_{front}}, \quad A = D_r e^{-\theta_r}$$

The numerical values for φ_{front} were taken from Equation (20).

3.2. Results

Figures 2 and 3 illustrate the profiles of this study versus (vs.) the profiles of the Hang and Zhiqiang solution and Philip's semi-analytical method (the reference method). It is found that the mean relative errors ε_{mean} between the present analytical method and the Hang and Zhiqiang solution are as follows:

(a) Soil sample 1 $\varepsilon_{mean} = 2.669 \times 10^{-2}$;
(b) Soil sample 2 $\varepsilon_{mean} = 8.04 \times 10^{-2}$.

In both cases, these values are the mean of the values φ $\theta_{\alpha=1}, \theta_{\alpha=0}^{-}$, and $\theta_{\alpha=0}^{+}$.

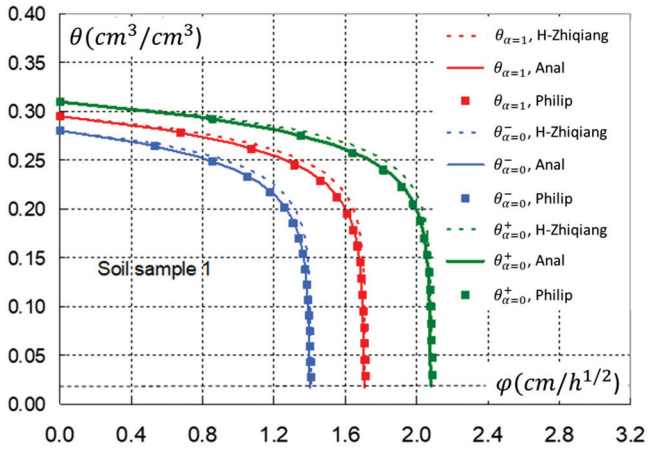

Figure 2. Profiles of moisture content θ versus Boltzmann transformation φ in the case of soil sample 1. The red color corresponds to $\theta_{\alpha=1}$, the blue color to $\theta_{\alpha=0}^{-}$, and the green color to $\theta_{\alpha=0}^{+}$.

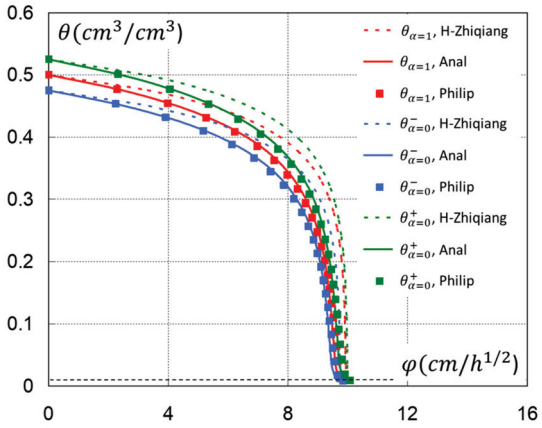

Figure 3. Profiles of moisture content θ versus Boltzmann transformation φ in the case of soil sample 2. The red color corresponds to $\theta_{\alpha=1}$, the blue color to $\theta^{-}_{\alpha=0}$, and the green color to $\theta^{+}_{\alpha=0}$.

Figure 4 is considered very informative for drawing conclusions since it illustrates the membership functions of the profiles (Figure 4a,b) and the sorptivity S (Figure 4c,d) for both samples (1, 2), also giving space for the application of the possibility theory and the meaningful interpretation of the fuzzy results. In that regard and by carefully observing the different cases in Figure 4, we can conclude that, as an example, at α-cut = 0.05, we have valuable information regarding the θ and S intervals of confidence for all cases, which, according to the possibility theory, could provide us with confidence for a probability greater than 95%. For example, in Figure 4b, the interval [0.394, 0.438] denotes that the desired value will be in this range with a probability of >95%.

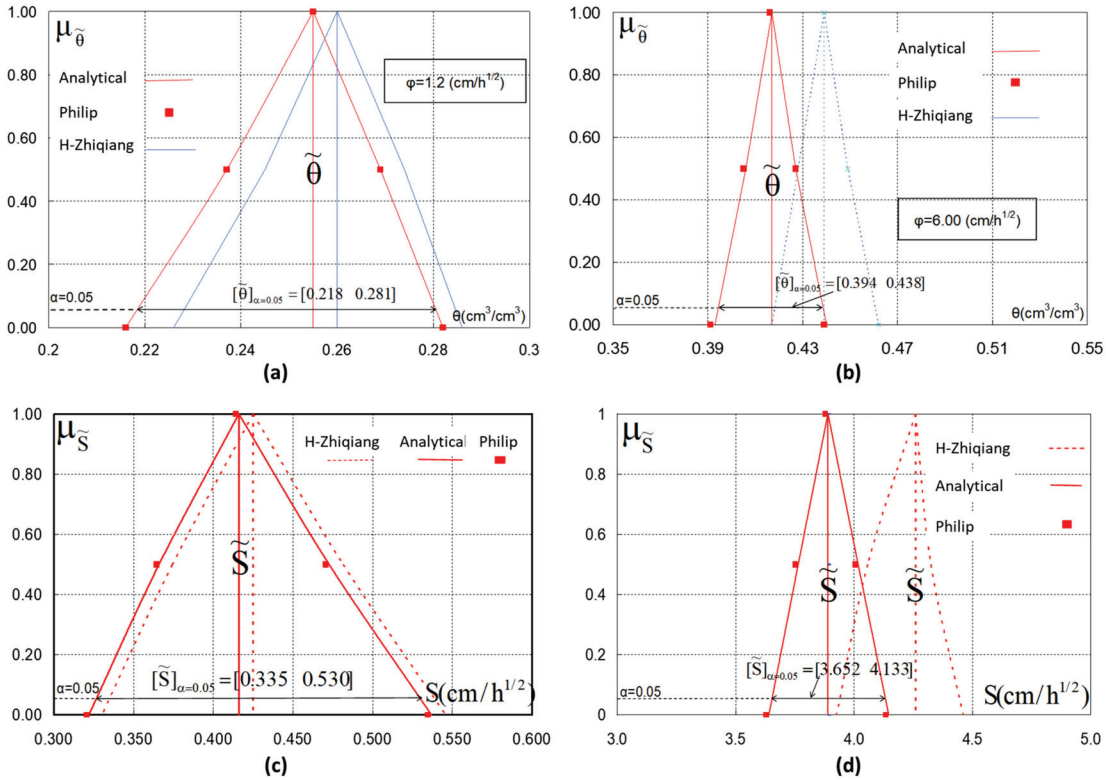

Figure 4. Membership function of (**a**) moisture content θ at φ = 1.2 cm/h$^{1/2}$ in the case of soil sample 1; (**b**) moisture content θ at φ = 6 cm/h$^{1/2}$ in the case of soil sample 2; (**c**) sorptivity in the case of soil sample 1; and (**d**) sorptivity in the case of soil sample 2.

Furthermore, the cumulative infiltration I (cm) vs. time t (h) for the proposed solution, Hang and Zhiqiang solution, and Philip's semi-analytical method is illustrated in Figure 5. Even from the visualization of the results, it is easily observable that the proposed solution is in close agreement with Philip's semi-analytical reference solution. This agreement could allow us to state that the proposed solution is accurate and reliable and can be used for decision-making and planning needs. In contrast, the solution by Hang and Zhiqiang presents some deviations (Table 2).

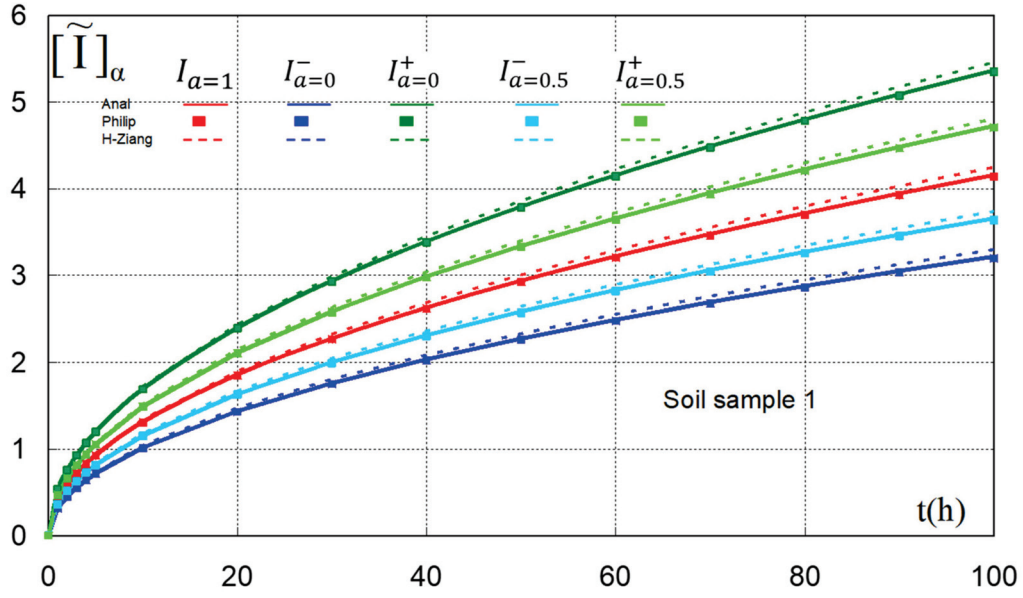

Figure 5. Cumulative absorption I for soil sample 1.

Table 2. Relative error of S between the different solutions related to soil samples 1 and 2.

		Method			Difference	
S	**α-Cut**	**Hang and Zhiqiang (1)**	**Analytical (2)**	**Philip (3)**	**(2) vs. (3)**	**(1) vs. (3)**
Soil sample 1						
S	1	0.425	0.416	0.416	0	0.0254
S−	0.5	0.374	0.366	0.364	0.005	0.0268
S+	0.5	0.481	0.473	0.471	0.0044	0.0225
S−	0	0.33	0.322	0.32	0.0046	0.0293
S+	0	0.546	0.537	0.535	0.0043	0.0206
				mean =	0.0037	0.0249
Soil sample 2						
S	1	4.26	3.89	3.878	0.003	0.09
S−	0.5	4.057	3.764	3.753	0.003	0.075
S+	0.5	4.325	4.017	4.005	0.003	0.074
S−	0	3.926	3.64	3.629	0.003	0.076
S+	0	4.461	4.146	4.134	0.003	0.073
				mean =	0.003	0.078

In addition, Figure 6 illustrates the membership functions for the aforementioned methods, while for the case of the proposed solution, the possibility theory was implemented, leading to the conclusion that for α-cut = 0.05, we have a probability of >95% for our value to be in the interval [1.460, 2.370].

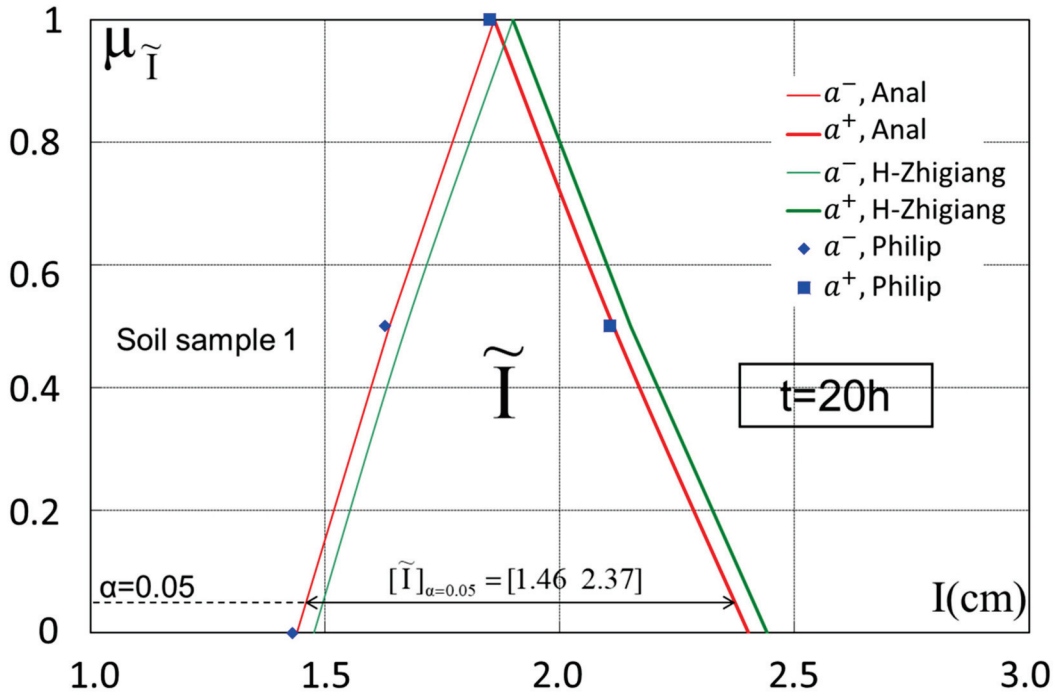

Figure 6. Membership function of cumulative absorption I.

To compare the results produced by the three different methods and for both samples 1 and 2, the mean relative error was chosen as a metric.

Table 2 presents the differences in an analytical way to validate the strong agreement of our proposed solution with Philip's reference solution. Specifically, regarding sample 1, the difference is $\varepsilon_{mean} = 3.7 \times 10^{-3}$, while for sample 2, the difference is $\varepsilon_{mean} = 3.7 \times 10^{-3}$. As it emerged from the visualized results, the deviation between the Hang and Zhiqiang with Philip's reference solution is confirmed here as well, where for samples 1 and 2, we have $\varepsilon_{mean} = 2.5 \times 10^{-2}$ and $\varepsilon_{mean} = 7.8 \times 10^{-2}$, respectively.

4. Conclusions

The proposed fuzzy solution of Richard's equation is based on the Hukuhara theory [39] with the generalized Hukuhara (gH-derivative), as well as its extension to partial differential equations. Today, practical problems useful for engineers can be solved, considering the fuzziness of various sizes.

In the current work, real measurements of 12 different types of soils were used in order to draw reliable conclusions. The application of our proposed solution to real cases of soils has proved that the present analytical solution is in close agreement with Philip's semi-analytical method, which is used as a reference solution that proves the accuracy and reliability of the new fuzzy analytical method. In addition, it was observed to be extremely easy and simple to calculate in comparison to other methods, without affecting the accuracy of the results.

Furthermore, it should be highlighted that according to the possibility theory, for practical cases, such as irrigation, drainage, and water resources projects, the engineers and designers could now have a better understanding of the real physical conditions (including the uncertainties), knowing the confidence intervals of the crisp value of sorptivity and cumulative infiltration with a certain strong probability.

Author Contributions: Conceptualization. C.T.; methodology. C.T. and N.S.; software. C.T.; validation. N.S., B.P. and C.E.; investigation. N.S.; data curation. C.E.; writing—original draft preparation. C.T. and N.S.; writing—review and editing. N.S. and B.P.; visualization. C.T.; All authors have read and agreed to the published version of the manuscript.

Funding: This research received no external funding.

Institutional Review Board Statement: Not applicable.

Informed Consent Statement: Not applicable.

Data Availability Statement: Not applicable.

Conflicts of Interest: The authors declare no conflict of interest.

References

1. Buckingham, E. *Studies on the Movement of Soil Moisture*; Government Publishing Office: Washington, DC, USA, 1907.
2. Gardner, W.; Widtsoe, J.A. The Movement of Soil Moisture. *Soil Sci.* **1921**, *11*, 215–232. [CrossRef]
3. Richards, L.A. Capillary conduction of liquids through porous mediums. *Physics* **1931**, *1*, 318–333. [CrossRef]
4. Childs, E.C. The Transport of Water through Heavy Clay Soils. I. *J. Agric. Sci.* **1936**, *26*, 114–127. [CrossRef]
5. Childs, E.C. The Transport of Water through Heavy Clay Soils. III. *J. Agric. Sci.* **1936**, *26*, 527–545. [CrossRef]
6. Klute, A. A numerical method for solving the flow equation for water in unsaturated materials. *Soil Sci.* **1952**, *73*, 105–116. [CrossRef]
7. Darcy, H. *Les Fontaines Publiques de La Ville de Dijon*; Victor Dalmont: Paris, France, 1956.
8. Philip, J.R. The theory of infiltration. *Soil Sci.* **1957**, *83*, 345–358. [CrossRef]
9. Philip, J.R. Theory of Infiltration. In *Advances in Hydroscience*; Elsevier: Amsterdam, The Netherlands, 1969; pp. 215–296.
10. Shahraiyni, H.T.; Ashtiani, B.A. Comparison of Finite Difference Schemes for Water Flow in Unsaturated Soils. *Int. J. Mech. Ind. Aerosp. Eng.* **2009**, *3*, 10–14.
11. Chávez-Negrete, C.; Domínguez-Mota, F.J.; Santana-Quinteros, D. Numerical Solution of Richards' Equation of Water Flow by Generalized Finite Differences. *Comput. Geotech.* **2018**, *101*, 168–175. [CrossRef]
12. Samarinas, N.; Tzimopoulos, C.; Evangelides, C. Fuzzy Numerical Solution to Horizontal Infiltration. *Int. J. Circuits Syst. Signal Process.* **2018**, *12*, 326–332.
13. Savović, S.; Drljača, B.; Djordjevich, A. A Comparative Study of Two Different Finite Difference Methods for Solving Advection–Diffusion Reaction Equation for Modeling Exponential Traveling Wave in Heat and Mass Transfer Processes. *Ric. Mat.* **2022**, *71*, 245–252. [CrossRef]
14. Samarinas, N.; Tzimopoulos, C.; Evangelides, C. Fuzzy Numerical Solution to the Unconfined Aquifer Problem under the Boussinesq Equation. *Water Supply* **2021**, *21*, 3210–3224. [CrossRef]
15. Samarinas, N.; Tzimopoulos, C.; Evangelides, C. An Efficient Method to Solve the Fuzzy Crank–Nicolson Scheme with Application to the Groundwater Flow Problem. *J. Hydroinformatics* **2022**, *24*, 590–609. [CrossRef]
16. Crevoisier, D.; Chanzy, A.; Voltz, M. Evaluation of the Ross Fast Solution of Richards' Equation in Unfavourable Conditions for Standard Finite Element Methods. *Adv. Water Resour.* **2009**, *32*, 936–947. [CrossRef]
17. Fahs, M.; Younes, A.; Lehmann, F. An Easy and Efficient Combination of the Mixed Finite Element Method and the Method of Lines for the Resolution of Richards' Equation. *Environ. Model. Softw.* **2009**, *24*, 1122–1126. [CrossRef]
18. Arampatzis, G.K.; Tzimopoulos, C.D.; Evangelides, C.H. Numerical Solution of Richards' Equation With Control Volume Method. *J. Mech. Behav. Mater.* **2004**, *15*, 291–308. [CrossRef]
19. Pour, M.; Shoshtari, M.; Adid, A. Numerical Solution of Richards Equation by Using of Finite Volume Method. *World Appl. Sci. J.* **2011**, *14*, 1832–1842.
20. Philip, J.R. On Solving the Unsaturated Flow Equation 1: The Flux Concentration Relation. *Soil Sci.* **1973**, *116*, 328–335. [CrossRef]
21. Tzimopoulos, C.; Papadopoulos, K.; Evangelides, C.; Papadopoulos, B. Fuzzy Solution to the Unconfined Aquifer Problem. *Water* **2018**, *11*, 54. [CrossRef]
22. Tzimopoulos, C.; Papadopoulos, K.; Evangelides, C. Fuzzy Analytical Solution to Horizontal Infiltration. *J. Comput. Methods Sci. Eng.* **2019**, *19*, 913–927. [CrossRef]
23. Tzimopoulos, C.; Papaevangelou, G.; Papadopoulos, K.; Evangelides, C.; Arampatzis, G. Fuzzy Analytical Solution to Vertical Infiltration. *J. Softw. Eng. Appl.* **2020**, *13*, 41–46. [CrossRef]
24. Tzimopoulos, C.; Papadopoulos, K.; Evangelides, C.; Papadopoulos, B. Analytical Solutions of Advection-Dispersion Equation Using Fuzzy Theory. *Desalin. Water Treat.* **2020**, *193*, 302–312. [CrossRef]
25. Tzimopoulos, C.; Samarinas, N.; Papadopoulos, K.; Evangelides, C. Fuzzy Unsteady-State Drainage Solution for Land Reclamation. *Hydrology* **2023**, *10*, 34. [CrossRef]
26. Tolikas, P.K.; Sidiropoulos, E.G.; Tzimopoulos, C.D. A Simple Analytical Solution for the Boussinesq One-Dimensional Groundwater Flow Equation. *Water Resour. Res.* **1984**, *20*, 24–28. [CrossRef]
27. Brutsaert, W. Some Exact Solutions for Nonlinear Desorptive Diffusion. *Z. Angew. Math. Phys.* **1982**, *33*, 540–546. [CrossRef]
28. Crank, J. *The Mathematics of Diffusion*, 1st ed.; Oxford University Press: London, UK, 1975.
29. Lisle, I.G.; Parlange, J.-Y. Analytical Reduction for a Concentration Dependent Diffusion Problem. *ZAMP Z. Angew. Math. Phys.* **1993**, *44*, 85–102. [CrossRef]
30. Hang, L.; Zhiqiang, L. Almost Analytic Solutions and Their Tests of the Horizontal Diffusion Equation for the Movement of Water in Unsaturated Soil. *Appl. Math. Mech.* **1997**, *18*, 647–655. [CrossRef]

31. Prevedello, C.L.; Loyola, J.M.T.; Reichardt, K.; Nielsen, D.R. New Analytic Solution of Boltzmann Transform for Horizontal Water Infiltration into Sand. *Vadose Zone J.* **2008**, *7*, 1170–1177. [CrossRef]
32. Tzimopoulos, C.; Evangelides, C.; Arampatzis, G. Explicit Approximate Analytical Solution of the Horizontal Diffusion Equation. *Soil Sci.* **2015**, *180*, 47–53. [CrossRef]
33. Vauclin, M.; Haverkamp, R. Solutions Quasi Analytiques de l'équation d'absorption de l'eau Par Les Sols Non Saturés. *Agronomie* **1985**, *5*, 597–606. [CrossRef]
34. Huang, J. Analytical Model for Volatile Organic Compound Transport in the Coupled Vadose Zone–Groundwater System. *J. Hydrol. Eng.* **2021**, *26*, 04020058. [CrossRef]
35. Ali, I.; Saleem, M.T. Applications of Orthogonal Polynomials in Simulations of Mass Transfer Diffusion Equation Arising in Food Engineering. *Symmetry* **2023**, *15*, 527. [CrossRef]
36. Ali, I.; Saleem, M.T. Spatiotemporal Dynamics of Reaction–Diffusion System and Its Application to Turing Pattern Formation in a Gray–Scott Model. *Mathematics* **2023**, *11*, 1459. [CrossRef]
37. Zadeh, L.A. Fuzzy logic. *Computer* **1988**, *21*, 83–93. [CrossRef]
38. Puri, M.L.; Ralescu, D.A. Differentials of Fuzzy Functions. *J. Math. Anal. Appl.* **1983**, *91*, 552–558. [CrossRef]
39. Hukuhara, M. Integration Des Applications Measurables Dont La Valeur Est Un Compact Convexe. *Funkc. Ekvacioj* **1967**, *10*, 205–233.
40. Vorobiev, D.; Seikkala, S. Towards the Theory of Fuzzy Differential Equations. *Fuzzy Sets Syst.* **2002**, *125*, 231–237. [CrossRef]
41. O'Regan, D.; Lakshmikantham, V.; Nieto, J. Initial and Boundary Value Problem for Fuzzy Differential Equations. *Nonlinear Anal.* **2003**, *54*, 405–415. [CrossRef]
42. Nieto, J.J.; Rodríguez-López, R. Bounded Solutions for Fuzzy Differential and Integral Equations. *Chaos Solitons Fractals* **2006**, *27*, 1376–1386. [CrossRef]
43. Bede, B.; Gal, S.G. Generalizations of the Differentiability of Fuzzy-Number-Valued Functions with Applications to Fuzzy Differential Equations. *Fuzzy Sets Syst.* **2005**, *151*, 581–599. [CrossRef]
44. Bede, B. A Note on "Two-Point Boundary Value Problems Associated with Non-Linear Fuzzy Differential Equations". *Fuzzy Sets Syst.* **2006**, *157*, 986–989. [CrossRef]
45. Stefanini, L. A Generalization of Hukuhara Difference and Division for Interval and Fuzzy Arithmetic. *Fuzzy Sets Syst.* **2010**, *161*, 1564–1584. [CrossRef]
46. Allahviranloo, T.; Gouyandeh, Z.; Armand, A.; Hasanoglu, A. On Fuzzy Solutions for Heat Equation Based on Generalized Hukuhara Differentiability. *Fuzzy Sets Syst.* **2015**, *265*, 1–23. [CrossRef]
47. Mazandarani, M.; Xiu, L. A Review on Fuzzy Differential Equations. *IEEE Access* **2021**, *9*, 62195–62211. [CrossRef]
48. Gardner, W.R.; Mayhugh, M.S. Solutions and Tests of the Diffusion Equation for the Movement of Water in Soil. *Soil Sci. Soc. Am. J.* **1958**, *22*, 197–201. [CrossRef]
49. Reichardt, K.; Nielsen, D.R.; Biggar, J.W. Scaling of Horizontal Infiltration into Homogeneous Soils. *Soil Sci. Soc. Am. J.* **1972**, *36*, 241–245. [CrossRef]
50. Miller, R.D.; Bresler, E. A Quick Method for Estimating Soil Water Diffusivity Functions. *Soil Sci. Soc. Am. J.* **1977**, *41*, 1020–1022. [CrossRef]
51. Meyer zur Capellen, W. *Integraktafelf—Sammlung Unbestimmter Integrale Elementarer Functionen*; Springer: Berlin/Heidelberg, Germany, 1950.
52. Oldham, K.; Myland, J.; Spanier, J. *An Atlas of Functions*, 2nd ed.; Springer: New York, NY, USA, 2009.
53. Ramanujan, S.; Hardy, G.H.; Seshu Aiyar, P.V.; Wilson, B.M.; Berndt, B.C. *Collected Papers of Srinivasa Ramanujan*; AMS Chelsea Pub.: Providence, RI, USA, 2000.
54. Selim, H.M.; Kirkham, D.; Amemiya, M. A Comparison of Two Methods for Determining Soil Water Diffusivity. *Soil Sci. Soc. Am. J.* **1970**, *34*, 14–18. [CrossRef]
55. Whisler, F.D.; Klute, A.; Peters, D.B. Soil Water Diffusivity from Horizontal Infiltration. *Soil Sci. Soc. Am. J.* **1968**, *32*, 6–11. [CrossRef]
56. Clothier, B.E.; Scotter, D.R.; Green, A.E. Diffusivity and One-Dimensional Absorption Experiments. *Soil Sci. Soc. Am. J.* **1983**, *47*, 641–644. [CrossRef]
57. Jackson, R.D. Porosity and Soil-Water Diffusivity Relations. *Soil Sci. Soc. Am. J.* **1963**, *27*, 123–126. [CrossRef]
58. McBride, J.F.; Horton, R. An Empirical Function to Describe Measured Water Distributions From Horizontal Infiltration Experiments. *Water Resour. Res.* **1985**, *21*, 1539–1544. [CrossRef]
59. Nofziger, D.L. Errors in Gamma-Ray Measurements of Water Content and Bulk Density in Nonuniform Soils. *Soil Sci. Soc. Am. J.* **1978**, *42*, 845–850. [CrossRef]
60. Evangelides, C.; Arampatzis, G.; Tzimopoulos, C. Estimation of Soil Moisture Profile and Diffusivity Using Simple Laboratory Procedures. *Soil Sci.* **2010**, *175*, 118–127. [CrossRef]
61. Negoiţă, C.V.; Ralescu, D.A. Representation Theorems for Fuzzy Concepts. *Kybernetes* **1975**, *4*, 169–174. [CrossRef]
62. Goetshel, R.; Voxman, W. Elementary Fuzzy Calculus. *Fuzzy Sets Syst.* **1986**, *18*, 31–43. [CrossRef]
63. Bede, B.; Stefanini, L. Generalized Differentiability of Fuzzy-Valued Functions. *Fuzzy Sets Syst.* **2013**, *230*, 119–141. [CrossRef]
64. Khastan, A.; Nieto, J.J. A Boundary Value Problem for Second Order Fuzzy Differential Equations. *Nonlinear Anal. Theory Methods Appl.* **2010**, *72*, 3583–3593. [CrossRef]

65. Dubois, D.; Prade, H. When Upper Probabilities Are Possibility Measures. *Fuzzy Sets Syst.* **1992**, *49*, 65–74. [CrossRef]
66. Dubois, D.; Foulloy, L.; Mauris, G.; Prade, H. Probability-Possibility Transformations, Triangular Fuzzy Sets, and Probabilistic Inequalities. *Reliab. Comput.* **2004**, *10*, 273–297. [CrossRef]
67. Dubois, D.; Prade, H. Possibility Theory and Possibilistic Logic: Tools for Reasoning under and about Incomplete Information. In *Intelligence Science III*; Springer: Cham, Switzerland, 2021; pp. 79–89.
68. Mylonas, N. Applications in Fuzzy Statistic and Approximate Reasoning. Ph.D. Thesis, University of Thrace, Komotini, Greece, 2022.
69. Nguyen, H.T. A Note on the Extension Principle for Fuzzy Sets. *J. Math. Anal. Appl.* **1978**, *64*, 369–380. [CrossRef]
70. Tzimopoulos, C.; Papadopoulos, K.; Papadopoulos, B.; Samarinas, N.; Evangelides, C. Fuzzy Solution of Nonlinear Boussinesq Equation. *J. Hydroinformatics* **2022**, *24*, 1127–1147. [CrossRef]

Disclaimer/Publisher's Note: The statements, opinions and data contained in all publications are solely those of the individual author(s) and contributor(s) and not of MDPI and/or the editor(s). MDPI and/or the editor(s) disclaim responsibility for any injury to people or property resulting from any ideas, methods, instructions or products referred to in the content.

water

MDPI

Article

Exploring Multiscale Variability in Groundwater Quality: A Comparative Analysis of Spatial and Temporal Patterns via Clustering

Ismail Mohsine [1,*], Ilias Kacimi [1], Shiny Abraham [2], Vincent Valles [3], Laurent Barbiero [4,5], Fabrice Dassonville [6], Tarik Bahaj [1], Nadia Kassou [1], Abdessamad Touiouine [7], Meryem Jabrane [7], Meryem Touzani [8], Badr El Mahrad [1,9,10] and Tarik Bouramtane [1]

[1] Geosciences, Water and Environment Laboratory, Faculty of Sciences Rabat, Mohammed V University, Rabat 10000, Morocco
[2] Electrical and Computer Engineering Department, Seattle University, Seattle, WA 98122, USA
[3] Mixed Research Unit EMMAH (Environnement Méditerranéen et Modélisation des Agro-Hydrosystèmes), Hydrogeology Laboratory, Avignon University, 84916 Avignon, France
[4] Institut de Recherche pour le Développement, Géoscience Environnement Toulouse, CNRS, University of Toulouse, UMR 5563, 31400 Toulouse, France
[5] Observatoire Midi-Pyrénées, 14 Avenue Edouard Belin, 31400 Toulouse, France
[6] ARS (Provence-Alpes-Côte d'Azur Regional Health Agency), 132, Boulevard de Paris, CEDEX 03, 13331 Marseille, France
[7] Laboratoire de Géosciences, Faculté des Sciences, Université Ibn Tofaïl, BP 133, Kénitra 14000, Morocco
[8] National Institute of Agronomic Research, Rabat 10060, Morocco
[9] Murray Foundation, Brabners LLP, Horton House, Exchange Street, Liverpool L2 3YL, UK
[10] CIMA, FCT-Gambelas Campus, University of Algarve, 8005-139 Faro, Portugal
* Correspondence: ismail.mohsine@um5r.ac.ma

Abstract: Defining homogeneous units to optimize the monitoring and management of groundwater is a key challenge for organizations responsible for the protection of water for human consumption. However, the number of groundwater bodies (GWBs) is too large for targeted monitoring and recommendations. This study, carried out in the Provence-Alpes-Côte d'Azur region of France, is based on the intersection of two databases, one grouping together the physicochemical and bacteriological analyses of water and the other delimiting the boundaries of groundwater bodies. The extracted dataset contains 8627 measurements from 1143 observation points distributed over 63 GWB. Data conditioning through logarithmic transformation, dimensional reduction through principal component analysis, and hierarchical classification allows the grouping of GWBs into 11 homogeneous clusters. The fractions of unexplained variance (FUV) and ANOVA R^2 were calculated to assess the performance of the method at each scale. For example, for the total dissolved load (TDS) parameter, the temporal variance was quantified at 0.36 and the clustering causes a loss of information with an R^2 going from 0.63 to 0.4 from the scale of the sampling point to that of the GWB cluster. The results show that the logarithmic transformation reduces the effect of outliers and improves the quality of the GWB clustering. The groups of GWBs are homogeneous and clearly distinguishable from each other. The results can be used to define specific management and protection strategies for each group. The study also highlights the need to take into account the temporal variability of groundwater quality when implementing monitoring and management programs.

Keywords: groundwater quality; European Union Water Framework Directive; groundwater Bodies; hydrogeological clusters; environmental outliers; PACA region of France

1. Introduction

The supply of drinking water to the population is a major challenge, and among the resources, the issue of groundwater management remains a practical concern in many parts

of the world [1–5] due to the absence or simply the greater vulnerability of surface water to various pollutions [6,7]. Groundwater is a privileged resource, in part because the subsoil effectively filters suspended matter, especially bacteria. The filtering capacity of the aquifer depends on its geological nature, especially its porous characteristics. Once considered an "invisible resource" [8], global economic and population growth now places groundwater in the spotlight [9,10]. Bacteriological quality is a key factor responsible for most drinking water non-compliance and requires a better understanding of the mechanisms responsible for pollution by distinguishing between variations in space and time. Water managers continue to grapple with the question of how to manage this resource, which exhibits great variability in storage over space and time [11]. Following the Water Framework Directive (WFD) adopted by the European Union in 2000 [12–16], an inventory of groundwater bodies (GWB) has been established throughout the EU. In France, the water agencies were in charge of this inventory based on geographical and geological criteria. This inventory has been collected in a French Reference System for Ground Water Bodies [17], regularly updated for about twenty years.

Independently of this inventory, regular water analyses are carried out by the health agencies as part of the monitoring of the quality of water intended for human consumption. These data, the collection of which was initiated more than 30 years ago, have been compiled in another database called SISE-EAUX, which is managed at the national level, but especially at the level of the administrative regions by the regional health agencies [18,19]. This database, continuously updated, includes a wide range of microbiological, physicochemical, and radioactive parameters, making it a valuable source of spatially referenced information on groundwater quality. There are more than 32,000 geo-referenced collection points throughout the country, and each collection point is analyzed several times over time, allowing the measurement of temporal and spatial variability. Despite the large body of information in this database, which allows for a better understanding of key mechanisms shaping water characteristics, the large number of sampling points, even at the scale of the administrative region, does not allow for the development of a monitoring and protection strategy for each catchment point (several thousand) or even for each GWB (typically more than 100). In addition, the highly dimensional nature (sometimes more than 100 parameters) of the data contained in the database makes it difficult to analyze the information using traditional pairwise parameter crossing methods, not to mention that the information may be redundant, with some parameters being more or less related to each other and to environmental conditions.

This work aims to optimize the identification of processes that influence the chemical quality of groundwater bodies, by basing itself on previous research, for a sound management of the resource. Recently, our research team has proposed a classification method to cluster GWBs into homogeneous sets based on multifactorial water quality [20]. This clustering involves a data conditioning step in order to reduce the weight of outliers in the analysis [21] and a dimensional reduction based on principal component analysis [22]. The shift from the collection point scale to the GWB scale and then to the GWB homogeneous grouping scale is accompanied by a loss of part of the information contained in the dataset, which has not been quantified so far. This is one of the objectives of our study, in order to evaluate the relevance and effectiveness of the method leading to the differentiation of a reduced number of spatial units on the final map. The coefficient of determination (R^2) [23] of the analysis of variance (ANOVA) [24] is a relevant tool for this quantification of the rate of information loss during clustering. The higher the R^2, the less information is lost, and the more relevant is the homogeneous clustering of GWB. This study will also focus on the distinction between temporal and spatial variances for a better understanding of the processes taking place in groundwater.

In this framework, the objective of this study is three-fold. It is to (1) analyze the impact of outliers within the dataset without losing the information conveyed by these observations; (2) identify homogeneous subsets of data that allow for better discrimination of processes within each group of GWBs; and (3) quantify the loss of information associated

with the reduction of spatial units from the scale of the collection points to the grouping of GWBs.

2. Materials and Methods

2.1. Study Location

This study was conducted in the Provence-Alpes-Côte d'Azur (PACA) region located in southwestern France (Figure 1). The PACA region, with a surface area of around 31,400 km^2, is characterized by an important altitudinal gradient, ranging from 0 to 4000 m, and by a diversified geology and lithology (Figure 2), as well as a variety of aquifers (Karstic, sedimentary, of fractured basement or accompanying rivers). The water exploitation index (WEI+), the ratio of total annual water withdrawal to the long-term annual average of renewable freshwater resources, is between 30 and 40% [25]. The Rhône River marks the western limit of the region, while its main tributary, the Durance, crosses the region from east to west. Small coastal rivers (Argens, Var, etc.) turned towards the Mediterranean Sea complete the hydrographic network as shown in Figure 2. The population is of around 5 million inhabitants with a considerable increase during the summer periods. For more details regarding the PACA region, the reader may refer to the work of Tiouiouine et al. [20,22].

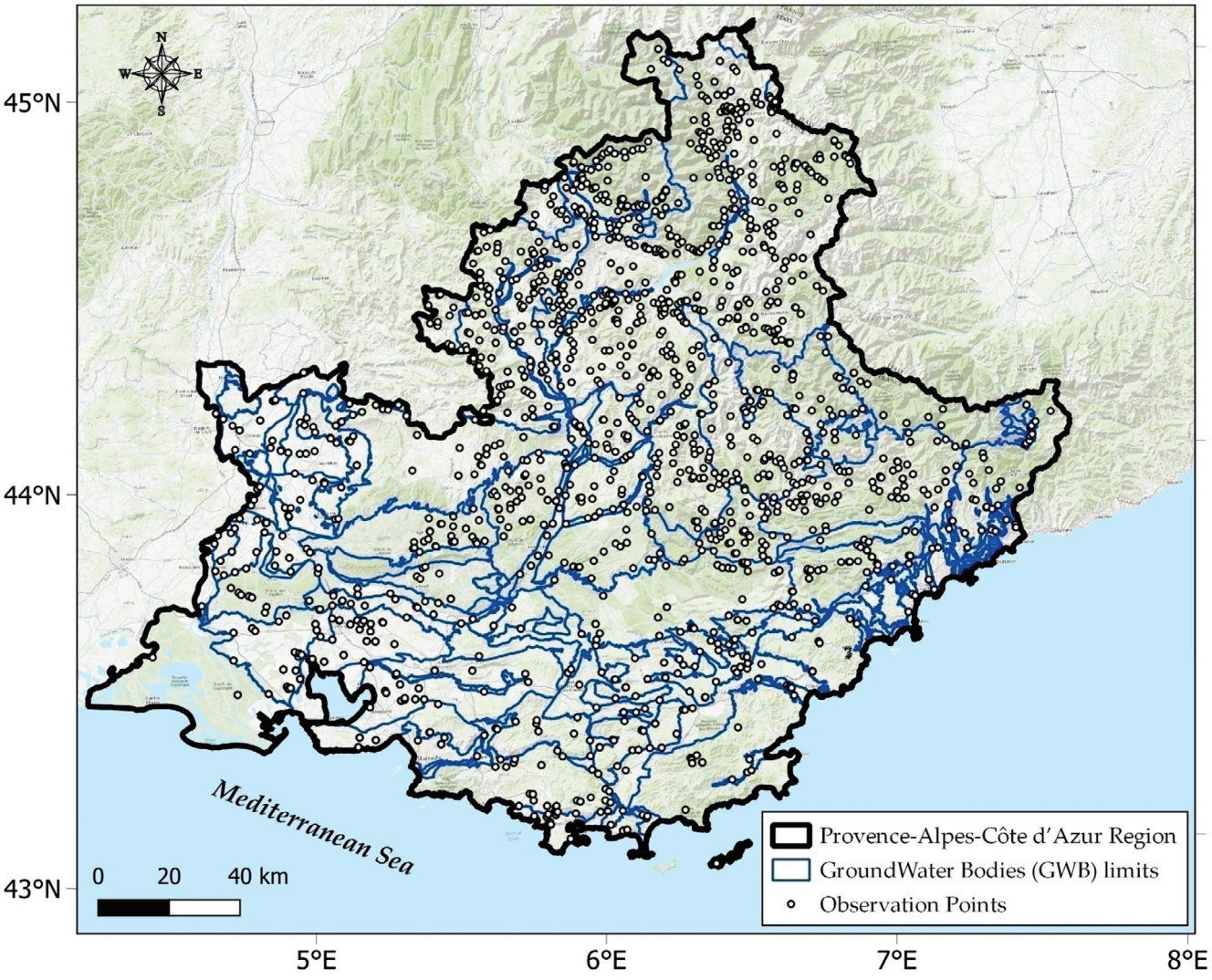

Figure 1. Map distribution of the groundwater bodies (GWB) and observation points within PACA region.

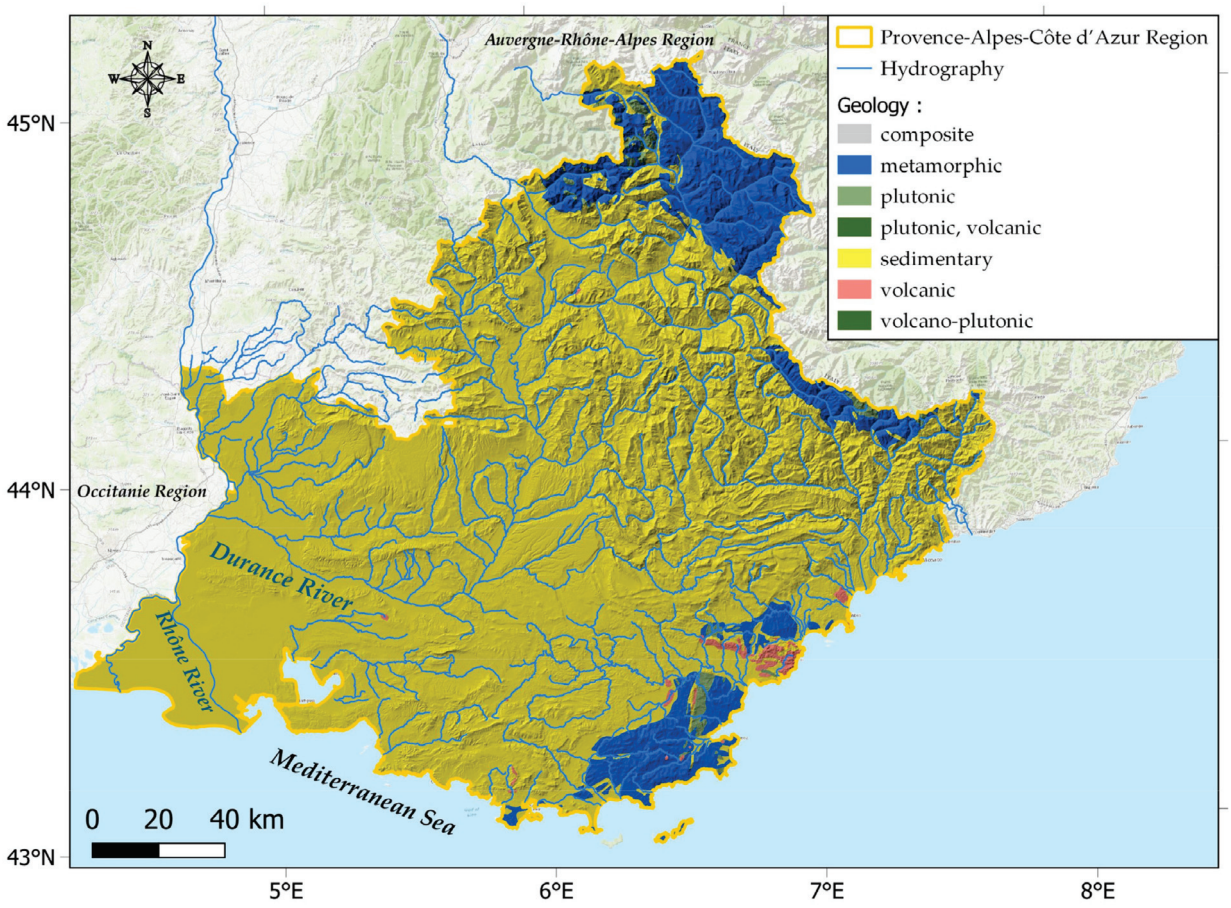

Figure 2. Special distribution of the geological features and hydrographic elements within PACA region.

2.2. Data Sources and Processing

SISE-EAUX is a groundwater quality database maintained by the French Ministry of Health and its regional and departmental services and is intended for the organized storage of health-related information on water [18,19]. It has been progressively computerized since 1994, but its systematic use as a database has been widely adopted since 2000. The database includes 250,000 control points throughout France, covering both raw (untreated) and distributed (potentially treated) water. The analyses were performed by laboratories that have received the necessary approvals and laboratory quality certifications. The data extraction for this study covered the entire PACA region over a period of 14 years, from 2006 to 2020, and focused specifically on raw water before any treatment for potability. The database includes a total of 1143 georeferenced sampling points, the distribution of which is presented in Figure 1. The data extraction provided 9117 water samples, on which between 4 and 24 parameters were analyzed, resulting in a hollow matrix of 9117 samples on 24 parameters. Afterwards, a data cleansing stage took place, which included removing observations with missing values and parameters that had a limited number of samples, such as thermotolerant coliforms and revivable bacteria at 22 and 37 degrees Celsius, along with total coliforms, which exhibited a data deficiency exceeding 95%. In the end, all parameters with more than 2.5% missing values were eliminated, resulting in a data loss of 5.4% compared to the initial extraction. After this cleaning phase, a full matrix of 8627 observations and 18 parameters was retained, which corresponds to an average of 7.55 analyses per sampling point over the 14 years of data collection. The retained parameters are *Enterococcus* (Ent.), *Escherichia coli* (*E. coli*), *electrical conductivity* (EC25), *potassium* (K), *sodium* (Na), *calcium* (Ca), *magnesium* (Mg), *chloride* (Cl), *sulfate* (SO_4), *hydrogenocarbonates* (HCO_3), *nitrates* (NO_3), *fluoride* (F), *total dissolved solids* (TDS), metals

which are *iron* (Fe) and *manganese* (Mn), and metalloids which are arsenic (As) and bore (B). The pH was transformed into H+ concentration to avoid mixing log and non-log units.

The European Water Framework Directive (Directive 2000/60/EC) [16] launched the Water Information System for Europe, in which groundwater bodies correspond to discrete volumes of groundwater residing in one or more aquifers [26]. In France, their inventory is the responsibility of the water agencies with the support of the French Geological Survey (BRGM) and is now listed in the French Reference System for GWB [27]. GWBs can be based on common attributes such as lithological composition, flow characteristics (confined or unconfined), karst properties, and proximity to coastal regions. The 1143 sampling points in the study were associated with 63 groundwater bodies, which were subsequently grouped into 11 GWB groups according to the procedure outlined by Tiouiouine et al. [20].

2.3. Data Treatement and Multivariate Statististical Analysis

Given the complexity of the ecosystem, a series of statistical techniques were employed to analyze the data, including a logarithmic transformation to alleviate the impact of outliers on the data, a principal component analysis (PCA) [28], hierarchical clustering (AHC) [29], kriging, and analysis of variance (ANOVA) [24] with the fraction of variance unexplained (FVU). These methods were used to optimize the identification of the processes that influence the chemical quality of groundwater bodies (GWB) in the PACA region of France.

2.3.1. Log Transformation

The presence of outliers was detected using the Z score defined by:

$$Z = |x - M| / \sigma, \quad (1)$$

where x is the measured value for a given parameter, M is the mean, and σ is the standard deviation. Z values greater than 2.5 and 10 are considered outliers, respectively [21]. The presence of outliers, particularly for microbiological parameters, results in a non-symmetric distribution that deviates from normality. A log transformation of the data was applied according to:

$$y = \log10\ (x + DL), \quad (2)$$

where x denotes the analytical result and DL is the detection limit. The log transformation aims to modify the value scales of the different parameters by dilating the gaps between low values and contracting those between high values [30].

2.3.2. Principal Component Analysis (PCA)

A principal component analysis (PCA) based on the correlation matrix was performed on all parameters [31] in order to reduce the dimensionality of the data space while minimizing the loss of information contained in the dataset. This procedure, based on standardized data centered on the mean and divided by the standard deviation, ensured that each variable had the same weight in the PCA, regardless of the unit used. This method is based on the principle that the resulting factorial axes (principal components) are orthogonal to each other, and therefore carry information related to interdependent processes [32,33].

2.3.3. Hierarchical Clustering

Subsequently, an agglomerative hierarchical clustering (AHC) using the Ward's linkage method [34,35] was performed using the mean values of each groundwater body on the principal components obtained from the PCA. The relative similarities among the GWB were quantified using Euclidean distance, and the levels of similarity at which the GWB were merged were used to construct a dendrogram.

2.3.4. Spatial and Temporal Variability

In order to measure the amount of information lost when downscaling from catchment to GWB and then to grouping of GWBs, an analysis of variance (ANOVA) was conducted with water characteristics as the dependent variable, and individual catchments, GWBs, and groups of GWBs as categorical explanatory variables [36]. The variance explained by the categorical variable was measured by the R^2 [37], according to the formula:

$$R^2 = 1 - (RSS/TSS), \quad (3)$$

where RSS is the residual square sum and TSS is the total square sum. R^2 denotes the percentage of variation in the response variable that is explained by its relationship with the explanatory variables. As the analyses were carried out at several dates on several sampling points, the variance includes on the one hand the temporal variability, which results in different values on the same sampling point, and on the other hand the spatial variability, which results in different averages between the sampling points. The R^2 calculated on the criterion "sampling point" as a non-quantitative explanatory variable corresponds to the spatial variability at this scale. The complement to 1 of the R^2 which is the fraction of variance unexplained (FVU) [38] reflects the temporal variance added to a small part of variance linked to the analytical imprecision, which will be neglected. The same calculation was carried out at the scale of GWBs and groups of GWBs in order to quantify the amount of information contained at these different spatial scales.

2.3.5. Kriging

The spatial structure of each parameter was analyzed by studying the main characteristics of the experimental variograms, such as the range, sill, and nugget effect. The experimental variograms were fitted using spherical models, which were obtained under comparable conditions, (i.e., same number of points and same number of distance classes) [39].

3. Results

3.1. Achieving a Symmetrical Data Distribution

Figure 3 presents the inertia of the factorial axes of the PCAs conducted on the raw and log-transformed data. The first eight principal components accounted for 85.6% of the total variance for all parameters and all samples combined. Despite the high number of parameters and their heterogeneous nature (bacteriological, major ions, metals, metalloids, etc.), the first factorial plane concentrated a significant part of the information, which was significantly higher after log transformation of the data, shifting from 43.2% (10.7 + 32.5) to 51.4% (36.3 + 15.1). The projection of the samples on the factorial plane F1–F2 and F3–F4 (Figure 3) shows that a few samples significantly increase the area of the score plots, with most observations concentrated in a small area (Figure 4a,c). In contrast, after log transformation of the data, the dispersion of observations in the score plots is more uniform (Figure 4b,d). Therefore, in the following, we will consider the log-transformed data.

3.2. PCA Results: General Chemistry and Spatial Distribution of Groundwater

The first factorial axis (F1) in Table 1 contrasted mineralized water without fecal contamination with diluted water contaminated by *E. coli* and *Enterococcus*. This is notably highlighted by high variable contributions (above 0.7) in the majority of major ions, TDS, and electrical conductivity in F1. We assert clearly that this is an axis of water mineral load. The second factorial axis (F2) was mainly scored with waters contaminated by fecal bacteria with *E. coli*. and *Enterococcus* having scored around 0.8. Contaminated waters were rather reductive as shown by the positive coordinates of metals and negative of nitrates. The third factorial axis reflected mainly waters with the highest arsenic, nitrate, fluorine, and boron content, and the fourth factorial axis reflected redox processes, but for waters with low contamination by fecal bacteria.

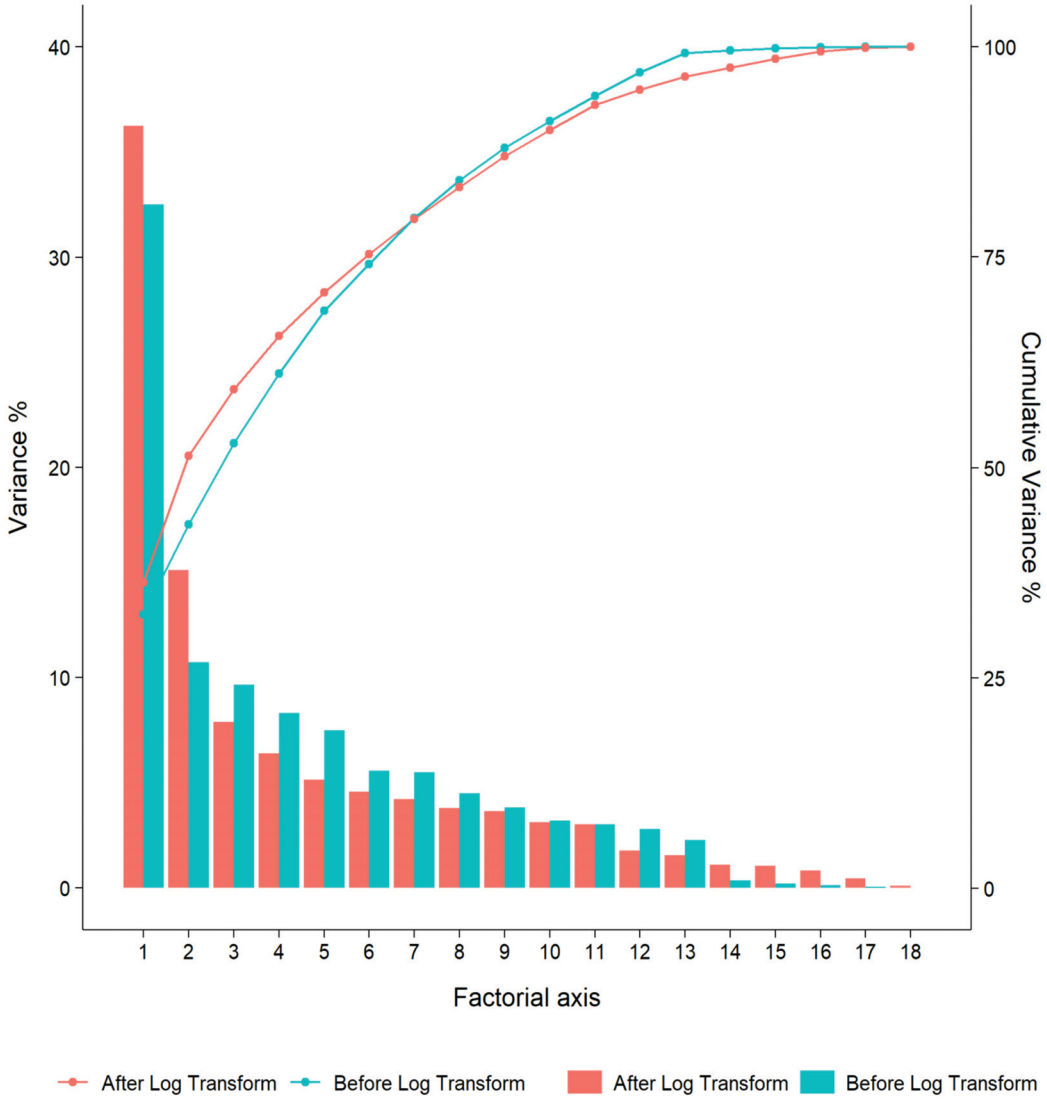

Figure 3. Inertia of the factorial axes of the PCA conducted on the raw and log-transformed data.

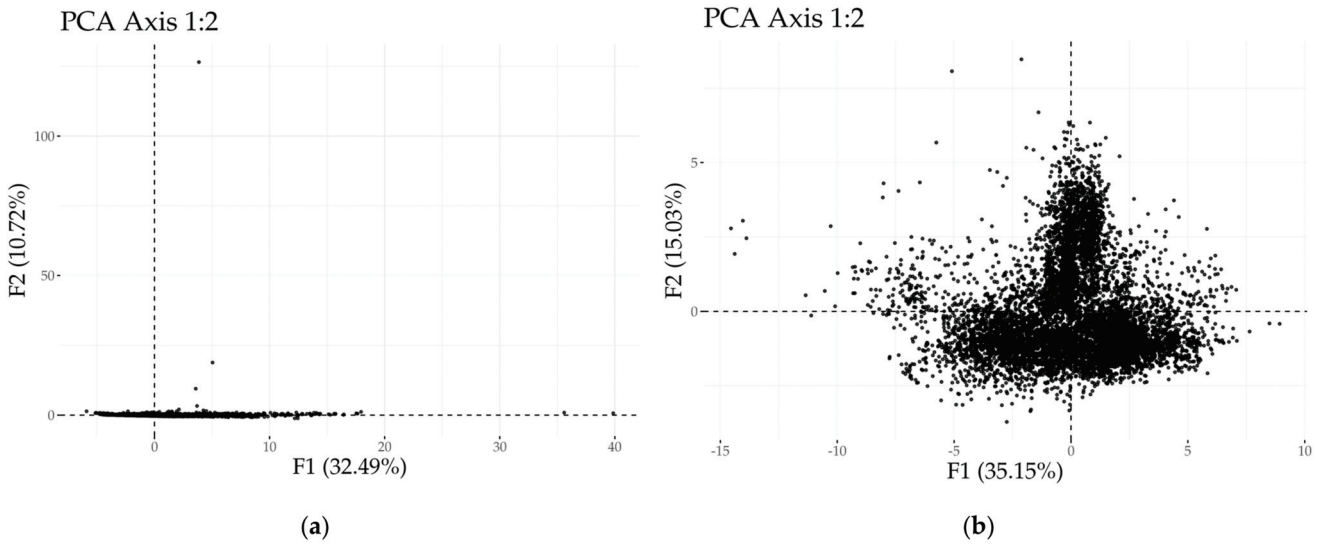

(**a**) (**b**)

Figure 4. *Cont.*

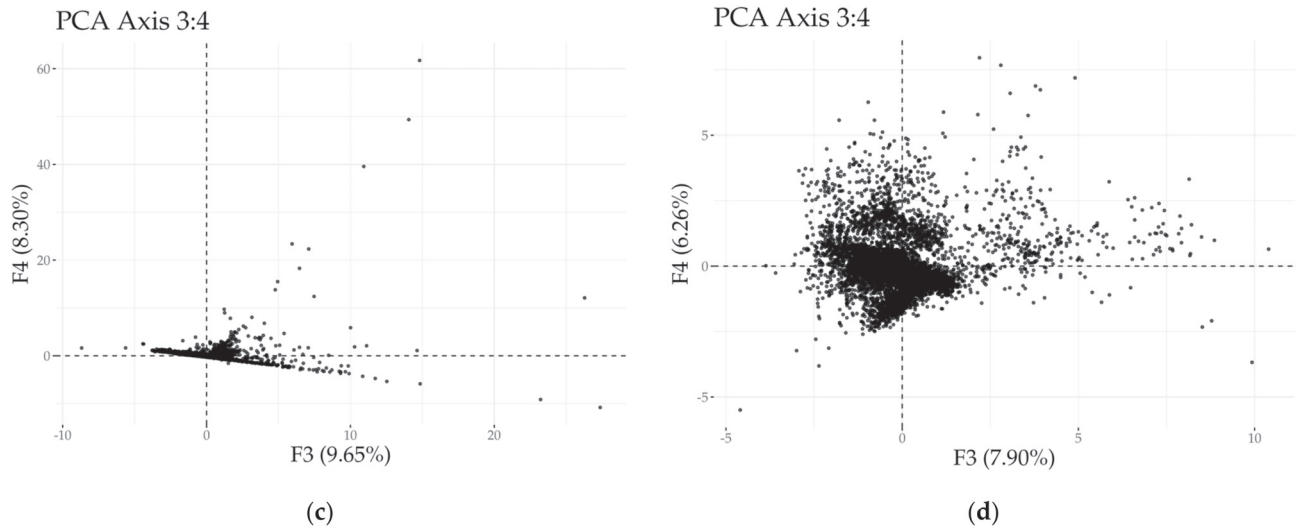

(**c**) (**d**)

Figure 4. Distribution of the observations in factorial plans F1−F2 and F3−F4 for: (**a**,**c**) raw data; (**b**,**d**) log-transformed data.

Table 1. Contribution of the parameters to the first five factorial axes (PCA with log-transformed data).

	F1	F2	F3	F4	F5
Enterococcus	0.035	**0.800**	−0.299	−0.241	0.208
E. coli	0.052	**0.799**	−0.283	−0.244	0.219
K	**0.727**	0.336	0.230	0.002	−0.267
Na	**0.721**	0.392	0.202	0.019	−0.305
Ca	**0.829**	−0.283	−0.299	−0.002	0.094
Mg	**0.723**	−0.015	−0.061	0.116	0.051
Cl	**0.751**	0.344	0.161	−0.006	−0.292
SO_4	**0.729**	0.238	0.144	0.042	−0.067
HCO_3	0.676	−0.420	−0.402	0.011	0.128
EC25	**0.779**	−0.129	−0.215	0.066	−0.012
TDS	**0.912**	−0.226	−0.249	0.045	0.060
pH	−0.378	0.531	−0.189	−0.224	−0.151
Fe	0.070	0.423	−0.109	0.663	−0.167
Mn	0.117	0.380	−0.017	0.541	0.524
As	−0.199	0.074	0.619	0.229	0.219
NO_3	0.531	−0.200	0.245	−0.185	0.079
B	0.554	0.048	0.285	−0.196	0.254
F	0.522	0.055	0.415	−0.277	0.325

Note(s): **Bold** Parameter contribution in the factorial axis of (+/−) 0.7.

3.3. AHC Results: Grouping Groundwater Bodies Using AHC

The clustering of GWBs based on their average coordinates on the first 10 factorial axes is presented in Figure 5, where 11 distinct groups were identified. The mapping of these 11 groups is presented in Figure 6. A strong correlation was observed between the GWB groups and the regional geology and geomorphology. For example, group 9 represents all the accompanying water tables of the hydrographic network, group 11 corresponds to low altitude discontinuous aquifers (karst and fractured aquifers), group 6 groups together sedimentary coastal aquifers, and group 1 identifies high altitude fractured aquifers in crystalline bedrocks.

Figure 6 below shows the main spatial distribution of GWB body group. The main visually observed remark from this clustering is the resemblance between some clusters and the lithological limit. Cluster 1 is located within the coastal crystalline group, cluster 2 corresponds to the alpine crystalline group, clusters 3 and 4 are located within the sedimentary ensembles in altitude, group 5 is exclusive to the sedimentary rocks within

the coastal south to southwest PACA, group 9 is located within the alluvial plains of the Rhone and Durance rivers, group 10 is located also in the sedimentary formations near the alluvial plains, and group 11 is located within two formations, the crystalline coastal formations and near the alluvial plains in the Durance river.

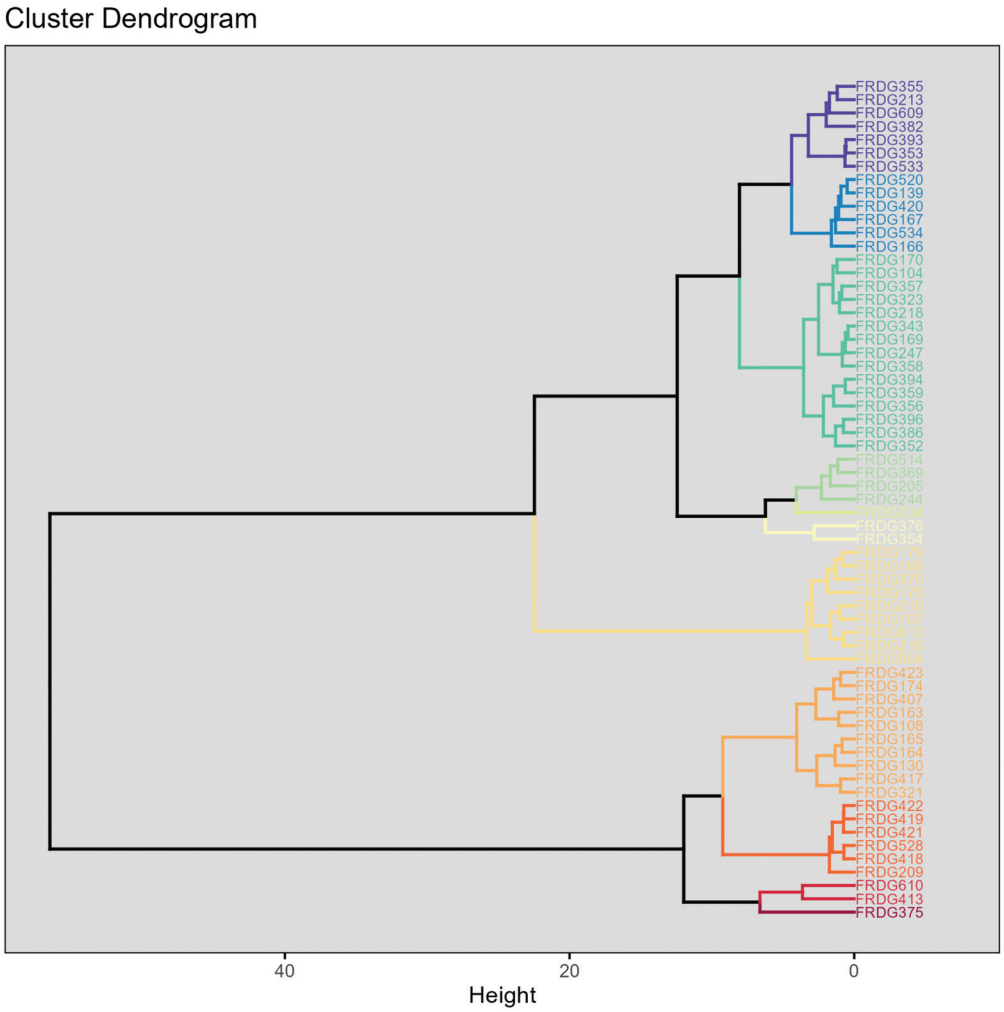

Figure 5. Cluster dendrogram of all groundwater bodies resulting from the agglomerative hierarchical clustering (AHC). FRDGx is an acronym used to represent the French reference of groundwater bodies, where "FR" stands for French reference, "D" refers to the Rhône-Méditerranée Basin, "G" indicates the groundwater body, and "x" signifies the identification code of the particular groundwater body. The colors of each cluster in this dendrogram are reported on Figure 6.

The clustering of GWBs based on their average coordinates on the first 10 factorial axes is presented in Figure 5, where 11 distinct groups were identified. The mapping of these 11 groups is presented in Figure 6. A strong correspondence was observed between GWB groups and regional geology and geomorphology.

Groups 1 and 2 are located in the coastal and alpine crystalline contexts, respectively. Groups 3 and 4 are located in the sedimentary complexes at high altitude and group 5 is exclusive to the sedimentary rocks of the south to southwest coast of the PACA region. Groups 6, 7, and 8 are small and isolated. Group 9 is located in the alluvial plains of the Rhone and Durance rivers and includes all the water tables accompanying the hydrographic network. Group 10 is situated in the sedimentary formations close to the alluvial plains, and group 11 is situated in two formations, the coastal crystalline formations and close to the alluvial plains of the Durance river, which are discontinuous aquifers of low altitude (karst and fractured environments).

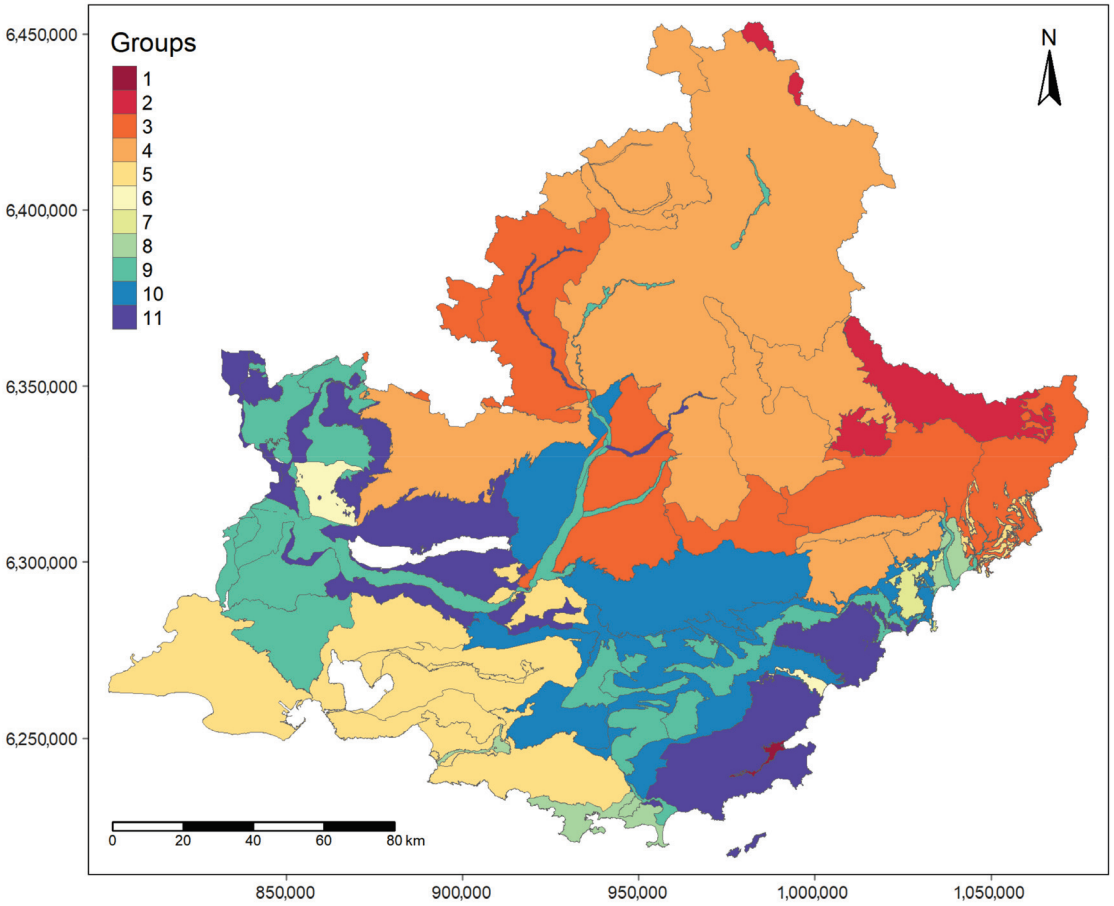

Figure 6. Spatial distribution of groundwater bodies (GWB) clusters resulted from agglomerative hierarchical clustering (AHC).

3.4. Spatial and Temporal Variability

Table 2 summarizes the main characteristics of the variograms obtained for some key parameters (bacteriology and major ions). A significant nugget effect was observed for the bacteriological parameters, combined with a very small range, of the order of a few km. On the other hand, the nugget effect is practically null for electrical conductivity and major ions (represented here by sodium), with a high range of several tens of km.

Table 2. Adjusted special variogram parameters and ANOVA R^2 for *Enterococcus*, *E. coli*, electrical conductivity 25°, and sodium.

Parameter	Nugget	Spherical Semi-Variance	Lag	% Nugget Effect	ANOVA R^2
Enterococcus	0.28	0.12	4000	70.0	0.546
E. coli	0.3	0.22	3000	57.7	0.555
EC25	0.007	0.042	62,000	14.3	0.654
Na	0.08	0.36	150,000	18.2	0.583

The temporal variability evaluated by the R^2 for each parameter is presented in Figure 7. This was high for metals with values reaching 65 to 70%, close to 55 to 60% for trace elements F, B, and As, around 45% for bacteriological parameters, but generally below 40% for major ions.

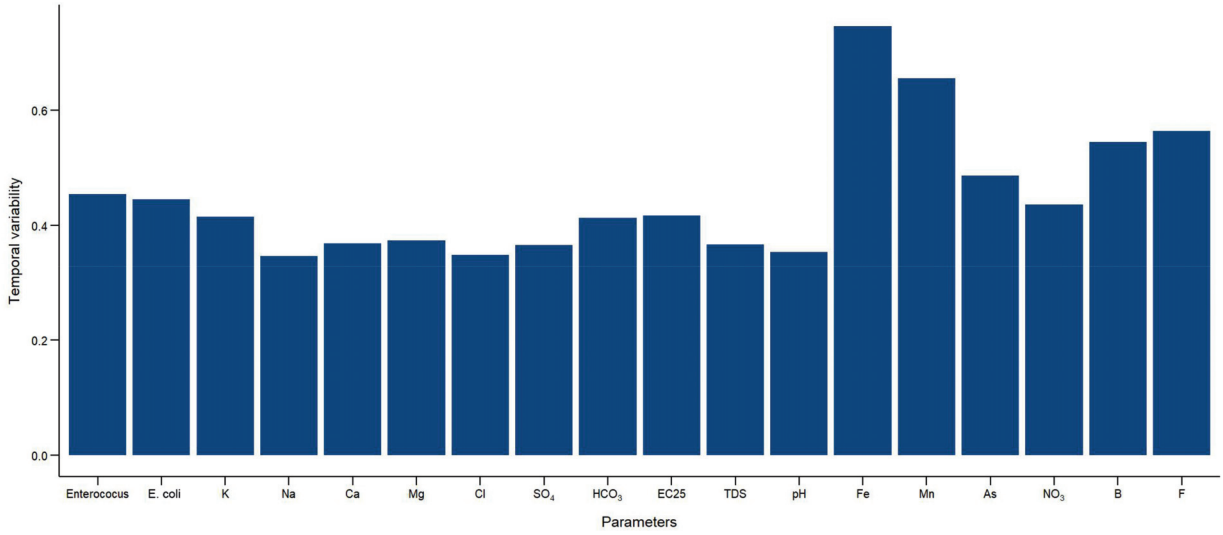

Figure 7. The rate of fraction of variance unexplained FVU within each parameter.

3.5. Determining the Proper Scaling of Groundwater Water Quality

The ratios of variance explained in the two groupings, namely from the scale of collection points to the GWBs and then from GWBs to GWB groups, is presented in Figure 8. In the first aggregation, most of the major ions show a moderate decrease (between 0.7 and 0.99), except for Mg and SO4 ions whose ratio showed a decrease of about 0.6. For nitrates, the ratio was also around 0.6. The ratio for bacteriological parameters showed a moderate decrease (0.55) in spatial variation, while metals and other trace elements showed a decrease in the range of 0.5 to 0.25. At the second aggregation, these ratios decreased slightly on the order of 0.1.

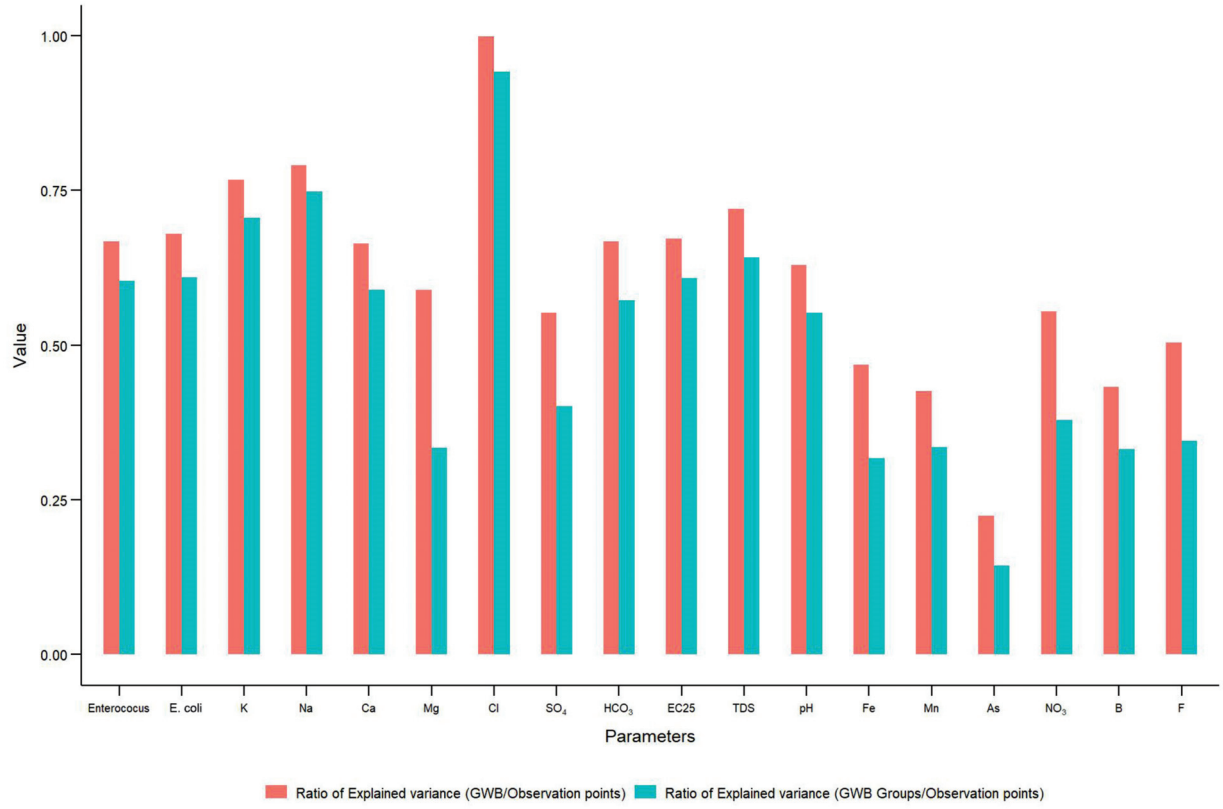

Figure 8. The ratio of explained variance for both the GWB/observation point scale and the GWB groups/observation point scale.

4. Discussion

4.1. Processes of Acquisition of Water Characteristics

The logarithmic transformation of the data clearly allows limiting the weight of outliers, mainly observed for bacteriological parameters. This transformation, already tested on other similar databases [21], allows a stronger concentration of information on the first factorial axes and facilitates the interpretation of the associated processes. The logarithmic transformation of the data also reduces the temporal variability of some parameters, especially bacteriological parameters, a point that will be analyzed in the next paragraph. Minerality is the main factor of variability in the waters of the PACA region. This point has already been emphasized by several studies conducted in the region, whether it is the work of Tiouiouine [20] on which we have relied, or other works conducted in more targeted environments. Thus, minerality is the main factor of water variability within the karst system of Fontaine de Vaucluse and is even identified as a major factor of flow discrimination within the karst [40]. Minerality is also frequently identified as a major variability factor among surface waters on all continents [41]. The second factor of variability in water quality is bacterial contamination, which more specifically affects waters with low mineralization. This is again a classic phenomenon in Mediterranean environments, where late summer storms cause runoff of low mineralized water but with high turbidity and likely to carry a high bacterial load. These waters infiltrate as they flow through the watersheds and contaminate the groundwater. The second factorial axis represents a spatial opposition between mineralized waters with a calcareous carbonate chemical profile and non-carbonate waters that are less mineralized but reductive (attested by the presence of soluble metals) and contaminated by bacteria. The fecal contamination of calcareous, mineralized, and reducing waters appears as the next factor. It can be interpreted as a contrast between more or less old waters in karst environments (i.e., with a higher residence time and which are generally discriminated by higher magnesium contents) [42,43]. Thus, PCA reveals several distinct signatures of fecal contamination, which are represented by distinct factorial axes. There is thus a diversity of situations and mechanisms related to this contamination, as mentioned by Tiouiouine et al. [22]. The mechanisms leading to fecal contamination are not solely limited to surface transport during storm events infiltrating susceptible water catchments, even though this is the most common scenario.

4.2. A Relevant and Efficient Grouping of GWBs

The implementation of a groundwater protection and monitoring policy by health agencies cannot be done on the scale of too many catchment points. A relevant grouping, in homogeneous sets and in coherence with the physicochemical and bacteriological characteristics, is necessary. The knowledge of which catchment points belong to a given GWB is an independent and essential source of information that must obviously be taken into consideration, but the number, 63 in the PACA region and 106 in the neighboring Occitanie region [21], is still too high to implement specific recommendations for each GWB. The reduction in the fineness of description of the information contained in the 8627 water samples collected is drastic when going from 1143 to 63 and then to 11 spatial units (i.e., from sampling points to GWBs and then to groups of GWBs).

The calculation of temporal variability is based on the calculation of R^2 when moving from 8627 collected water samples to 1143 sample points, which resulted in a reduction in the number of data by a factor of 7.5. Temporal variability can also be estimated by the nugget effect observed on the variograms which appears as variance for zero distance, with samples collected from the same point on multiple dates. The comparison between R^2 (Figure 7) and nugget effect for each parameter confirms this. The temporal variability is important, of the order of a third or more of the total variability, less for the chemistry of major ions than for trace elements or bacteriological parameters. In the transition from the observation point scale to the GWB scale, factors that explain changes in variance include differences in borehole characteristics (such as wells or springs), differences in borehole

vulnerability, and heterogeneity of land use in the vicinity of boreholes. The difference in explained variance between groups of GWBs is mainly related to differences in geological characteristics between GWBs. The rates of spatial variability and loss of information during upscaling have different values for different parameters, which can be explained by the diversity of transport mechanisms for these parameters. For bacteriological parameters, the transport of particle fixed bacteria is limited by the pore size, while they enter the boreholes by contamination of runoff water. This leads to a high temporal variability of their concentrations, which can be very sensitive to precipitation events. In general terms, this typology of parameters' behavior is strongly correlated to the spatial structure. Indeed, the parameters that show greater temporal variability are also those that show local spatial variability (Table 2). Thus, there appears to exist a relationship between the local character of spatial variation and the intensity of temporal variability. This constitutes a first basis for a typology of microbiological and physicochemical parameters, which will be the subject of a future publication.

As with temporal variability, the log transformation preserves a greater proportion of the information contained in the dataset. With raw data, almost all spatial information is lost for bacteriological parameters when grouping from catchment points to GWBs and then to GWB groups. The difference is significant and the lack of data conditioning would be detrimental to the methodology. In this sense, this work considerably improves the results previously presented by Tiouiouine [20] in the same PACA region. The loss of spatial information that accompanies the two aggregations varies according to the parameter. For chlorides, the loss is minimal, and the aggregation into GWB groups preserves more than 90% of the initial spatial information. For sodium, electrical conductivity, and E. coli content, more than half of the spatial information is preserved at the GWB group level, with most of the information loss occurring during the first aggregation of the sample points to the corresponding GWBs. For elements with high local variability such as Fe, Mn, and NO3, the loss of information is more important, but about 30–40% of the spatial information is still preserved by the GWB groups. Again, as for the other parameters, the switch from GWBs to GWB groups causes only a minor part of the information loss, the bulk being lost during the first aggregation.

4.3. Methodological Contributions

The present work highlights a series of methodological advances that we feel are relevant to bring together here:

- The log transformation to the data greatly reduces the problem of data non-normality and improves the statistical properties of the dataset, thus enhancing the robustness and reliability of subsequent analyses.
- It also mitigates the effects of outliers without eliminating the information they convey. The integrity of the dataset is thus preserved for analysis.
- The quantification of the loss of information that accompanies the clustering allows the effectiveness of the method to be measured.
- However, the proposed method has certain limitations. In particular, at this stage, the analysis is carried out parameter by parameter, which does not take into account the interrelations between several parameters. A more integrated approach, which could be based on principal components rather than on parameters, could be developed, but it would go beyond the scope of our study. It should be noted, however, that this approach is implicitly supported by the generation of GWB groups, as the classification process takes into account the relationships between different groundwater quality parameters.
- The method applied here is currently being applied in parallel in other French administrative regions and should be the subject of further advances. Whether the groundwater conditions are similar or quite different, there is no reason why the analysis should not be similar to the one conducted here. This method is flexible and applicable to various geological contexts and hydrogeological conditions. The appli-

cability depends on the availability of a statistically significant number of samples per observation point and per GWB. Interpretation will, of course, be guided by the specificities of the region under consideration in terms of geological formations, land use patterns, and possible sources of contamination.

5. Conclusions

The objective of this work was to quantify the spatial variability and temporal variability of the multiparameter quality of groundwater in a region, and to measure the loss of information when implementing the upscaling method proposed by Tiouiouine et al. [20]. This method consists in reducing the dimensionality of the data by PCA, then classifying the groundwater bodies into homogeneous groups according to the average values by GWB.

The analysis of variance shows that the share of temporal variability in the total variance depends strongly on the nature of the quality parameters. The temporal variability is higher for microbiological parameters, and less important for major ions. The analysis of variance made it possible to quantify the loss of information inherent to the grouping and the decrease in the number of units from 1143 sampling points to 63 GWB and then to 11 GWB groups. The amount of information lost also varies according to the quality parameter considered.

The monitoring of water quality for human consumption is the responsibility of the health agencies. The number of 11 homogeneous groups is suitable for the development of a specific roadmap and targeted recommendations for each group of GWB. More specifically, for the PACA region, the detailed analysis of each group will be the next step in our research schedule.

Author Contributions: Conceptualization, I.M., V.V., I.K. and N.K.; methodology, I.M. and V.V.; software, I.M. and V.V.; validation, I.K., L.B. and M.T.; formal analysis, I.M., V.V. and L.B.; investigation, N.K., B.E.M., T.B. (Tarik Bahaj) and T.B. (Tarik Bouramtane); resources, F.D., V.V., A.T. and M.J.; data curation, F.D.; writing—original draft preparation, I.M., L.B., B.E.M. and V.V.; writing—review and editing, I.M., V.V., L.B. and B.E.M.; visualization, I.K., L.B., T.B. (Tarik Bahaj), S.A., M.T. and T.B. (Tarik Bouramtane); supervision, I.K. and V.V.; project administration, I.K.; funding acquisition, S.A. All authors have read and agreed to the published version of the manuscript.

Funding: This research received no external funding.

Data Availability Statement: The data in this study are the property of ARS-PACA and are included in the SISE-Eaux french database.

Acknowledgments: The authors would like to thank the Regional Health Agency (Agence Régional de la Santé, ARS-PACA) for providing the SISE-Eaux database, This study was conducted at the Geosciences, Water and Environment Laboratory of the Faculty of Sciences, Rabat. of Mohammed V University in Rabat In partnership with the UMR EMMAH Hydrogeology Laboratory of the University of Avignon and with the endorsement of the Electrical and Computer Engineering Department of Seattle University.

Conflicts of Interest: The authors declare no conflict of interest.

References

1. Jakeman, A.J.; Barreteau, O.; Hunt, R.J.; Rinaudo, J.-D.; Ross, A.; Arshad, M.; Hamilton, S. Integrated Groundwater Management: An Overview of Concepts and Challenges. In *Integrated Groundwater Management*; Springer: Berlin/Heidelberg, Germany, 2016; pp. 3–20.
2. Priyan, K. Issues and Challenges of Groundwater and Surface Water Management in Semi-Arid Regions. In *Groundwater Resources Development and Planning in the Semi-Arid Region*; Springer: Berlin/Heidelberg, Germany, 2021; pp. 1–17.
3. Syafiuddin, A.; Boopathy, R.; Hadibarata, T. Challenges and Solutions for Sustainable Groundwater Usage: Pollution Control and Integrated Management. *Curr. Pollut. Rep.* **2020**, *6*, 310–327. [CrossRef]
4. Foster, S. Global Policy Overview of Groundwater in Urban Development—A Tale of 10 Cities! *Water* **2020**, *12*, 456. [CrossRef]
5. Closas, A.; Villholth, K.G. Groundwater Governance: Addressing Core Concepts and Challenges. *WIREs Water* **2020**, *7*, e1392. [CrossRef]

6. Walker, D.B.; Baumgartner, D.J.; Gerba, C.P.; Fitzsimmons, K. Surface Water Pollution. In *Environmental and Pollution Science*; Elsevier: Amsterdam, The Netherlands, 2019; pp. 261–292.
7. Li, P.; Karunanidhi, D.; Subramani, T.; Srinivasamoorthy, K. Sources and Consequences of Groundwater Contamination. *Arch. Environ. Contam. Toxicol.* **2021**, *80*, 1–10. [CrossRef] [PubMed]
8. Daly, D. Groundwater—The 'hidden Resource'. In *Proceedings of the Biology and Environment: Proceedings of the Royal Irish Academy*; Royal Irish Academy: Dublin, Ireland, 2009; Volume 109, pp. 221–236.
9. Koundouri, P. Current Issues in the Economics of Groundwater Resource Management. *J. Econ. Surv.* **2004**, *18*, 703–740. [CrossRef]
10. Kemper, K.E. Groundwater—From Development to Management. *Hydrogeol. J.* **2004**, *12*, 3–5. [CrossRef]
11. Ortiz-Letechipia, J.; González-Trinidad, J.; Júnez-Ferreira, H.E.; Bautista-Capetillo, C.; Dávila-Hernández, S. Evaluation of Groundwater Quality for Human Consumption and Irrigation in Relation to Arsenic Concentration in Flow Systems in a Semi-Arid Mexican Region. *Int. J. Environ. Res. Public Health* **2021**, *18*, 8045. [CrossRef] [PubMed]
12. Chave, P. *The EU Water Framework Directive*; IWA Publishing: London, UK, 2001; ISBN 1900222124.
13. Kallis, G.; Butler, D. The EU Water Framework Directive: Measures and Implications. *Water Policy* **2001**, *3*, 125–142. [CrossRef]
14. European Commission. Directive 2014/80/EU Amending Annex II to Directive 2006/ 118/EC of the European Parliament and of the Council on the Protection of Groundwater Against Pollution and Deterioration. *Off. J. Eur. Union* **2014**, *L182*, 52–55.
15. European Commission. Directive 2006/118/EC of the European Parliament and of the Council of 12 December 2006 on the Protection of Groundwater against Pollution and Deterioration. *Off. J. Eur. Union* **2006**, 19–31. Available online: https://eur-lex.europa.eu/legal-content/EN/TXT/?uri=celex%3A32006L0118 (accessed on 21 January 2023).
16. European Commission. Directive 2000/60/EC of the European Parliament and of the Council of 23 October 2000 Establishing a Framework for Community Action in the Field of Water Policy. *Off. J. Eur. Communities* **2000**, *L327*, 1–72.
17. Brugeron, A. *Cartographie et Systèmes d'Information Géographique Pour La Gestion Des Ressources En Eau Souterraine*; HAL: Paris, France, 2012.
18. Pouey, J.; Galey, C.; Chesneau, J.; Jones, G.; Franques, N.; Beaudeau, P. EpiGEH, groupe des référents régionaux; Mouly, D. Implementation of a National Waterborne Disease Outbreak Surveillance System: Overview and Preliminary Results, France, 2010 to 2019. *Eurosurveillance* **2021**, *26*, 2001466. [CrossRef] [PubMed]
19. Beaudeau, P.; Pascal, M.; Mouly, D.; Galey, C.; Thomas, O. Health Risks Associated with Drinking Water in a Context of Climate Change in France: A Review of Surveillance Requirements. *J. Water Clim. Chang.* **2011**, *2*, 230–246. [CrossRef]
20. Tiouiouine, A.; Jabrane, M.; Kacimi, I.; Morarech, M.; Bouramtane, T.; Bahaj, T.; Yameogo, S.; Rezende-Filho, A.T.; Dassonville, F.; Moulin, M.; et al. Determining the Relevant Scale to Analyze the Quality of Regional Groundwater Resources While Combining Groundwater Bodies, Physicochemical and Biological Databases in Southeastern France. *Water* **2020**, *12*, 3476. [CrossRef]
21. Jabrane, M.; Touiouine, A.; Bouabdli, A.; Chakiri, S.; Mohsine, I.; Valles, V.; Barbiero, L. Data Conditioning Modes for the Study of Groundwater Resource Quality Using a Large Physico-Chemical and Bacteriological Database, Occitanie Region, France. *Water* **2023**, *15*, 84. [CrossRef]
22. Tiouiouine, A.; Yameogo, S.; Valles, V.; Barbiero, L.; Dassonville, F.; Moulin, M.; Bouramtane, T.; Bahaj, T.; Morarech, M.; Kacimi, I. Dimension Reduction and Analysis of a 10-Year Physicochemical and Biological Water Database Applied to Water Resources Intended for Human Consumption in the Provence-Alpes-Cote d'azur Region, France. *Water* **2020**, *12*, 525. [CrossRef]
23. Ozer, D.J. Correlation and the Coefficient of Determination. *Psychol. Bull.* **1985**, *97*, 307. [CrossRef]
24. St, L.; Wold, S. Analysis of Variance (ANOVA). *Chemom. Intell. Lab. Syst.* **1989**, *6*, 259–272.
25. Psomas, A.; Bariamis, G.; Roy, S.; Rouillard, J.; Stein, U. *Comparative Study on Quantitative and Chemical Status of Groundwater Bodies: Study of the Impacts of Pressures on Groundwater in Europe, Service Contract, 315/B2020/EEA.58185*; EEA: Copenhagen, Denmark, 2021.
26. Maréchal, J.-C.; Rouillard, J. Groundwater in France: Resources, Use and Management Issues. In *Sustainable Groundwater Management: A Comparative Analysis of French and Australian Policies and Implications to Other Countries*; Springer: Berlin/Heidelberg, Germany, 2020; pp. 17–45.
27. Masses d'eau Souterraines-Métropole-Version État Des Lieux 2019. Available online: https://geo.data.gouv.fr/fr/datasets/1a983edfe5ea441fef359a652e98217c9c3ce3c6 (accessed on 20 March 2021).
28. Ringnér, M. What Is Principal Component Analysis? *Nat. Biotechnol.* **2008**, *26*, 303–304. [CrossRef]
29. Madhulatha, T.S. An Overview on Clustering Methods. *arXiv* **2012**, arXiv:1205.1117. [CrossRef]
30. Cousineau, D.; Chartier, S. Outliers Detection and Treatment: A Review. *Int. J. Psychol. Res.* **2010**, *3*, 58–67. [CrossRef]
31. Pearson, K. On Lines and Planes of Closest Fit to Systems of Points in Space. *Lond. Edinb. Dublin Philos. Mag. J. Sci.* **1901**, *2*, 559–572. [CrossRef]
32. Helena, B.; Pardo, R.; Vega, M.; Barrado, E.; Fernandez, J.M.; Fernandez, L. Temporal Evolution of Groundwater Composition in an Alluvial Aquifer (Pisuerga River, Spain) by Principal Component Analysis. *Water Res.* **2000**, *34*, 807–816. [CrossRef]
33. Rezende-Filho, A.T.; Valles, V.; Furian, S.; Oliveira, C.M.S.C.; Ouardi, J.; Barbiero, L. Impacts of Lithological and Anthropogenic Factors Affecting Water Chemistry in the Upper Paraguay River Basin. *J. Environ. Qual.* **2015**, *44*, 1832–1842. [CrossRef] [PubMed]
34. Day, W.H.E.; Edelsbrunner, H. Efficient Algorithms for Agglomerative Hierarchical Clustering Methods. *J. Classif.* **1984**, *1*, 7–24. [CrossRef]
35. Bouguettaya, A.; Yu, Q.; Liu, X.; Zhou, X.; Song, A. Efficient Agglomerative Hierarchical Clustering. *Expert Syst. Appl.* **2015**, *42*, 2785–2797. [CrossRef]

36. Owamah, H.I. A Comprehensive Assessment of Groundwater Quality for Drinking Purpose in a Nigerian Rural Niger Delta Community. *Groundw. Sustain. Dev.* **2020**, *10*, 100286. [CrossRef]
37. Miles, J. R-Squared, Adjusted R-Squared. In *Encyclopedia of Statistics in Behavioral Science*; R Foundation for Statistical Computing: Vienna, Austria, 2005; ISBN 9780470013199.
38. Achen, C.H. What Does "Explained Variance" Explain?: Reply. *Political Anal.* **1990**, *2*, 173–184. [CrossRef]
39. Cressie, N. The Origins of Kriging. *Math. Geol.* **1990**, *22*, 239–252. [CrossRef]
40. Barbel-Périneau, A.; Barbiero, L.; Danquigny, C.; Emblanch, C.; Mazzilli, N.; Babic, M.; Simler, R.; Valles, V. Karst Flow Processes Explored through Analysis of Long-Term Unsaturated-Zone Discharge Hydrochemistry: A 10-Year Study in Rustrel, France. *Hydrogeol. J.* **2019**, *27*, 1711–1723. [CrossRef]
41. Rezende Filho, A.T.; Furian, S.; Victoria, R.L.; Mascré, C.; Valles, V.; Barbiero, L. Hydrochemical Variability at the Upper Paraguay Basin and Pantanal Wetland. *Hydrol. Earth Syst. Sci.* **2012**, *16*, 2723–2737. [CrossRef]
42. Batiot, C.; Emblanch, C.; Blavoux, B. Total Organic Carbon (TOC) and Magnesium (Mg2+): Two Complementary Tracers of Residence Time in Karstic Systems. *Comptes Rendus Geosci.* **2003**, *335*, 205–214. [CrossRef]
43. Moral, F.; Cruz-Sanjulián, J.J.; Olías, M. Geochemical Evolution of Groundwater in the Carbonate Aquifers of Sierra de Segura (Betic Cordillera, Southern Spain). *J. Hydrol.* **2008**, *360*, 281–296. [CrossRef]

Disclaimer/Publisher's Note: The statements, opinions and data contained in all publications are solely those of the individual author(s) and contributor(s) and not of MDPI and/or the editor(s). MDPI and/or the editor(s) disclaim responsibility for any injury to people or property resulting from any ideas, methods, instructions or products referred to in the content.

water

MDPI

Article

Hydrochemical Characteristics and Water Quality of Shallow Groundwater in Desert Area of Kunyu City, Southern Margin of Tarim Basin, China

Runchi Tang [1,*,†], Shuning Dong [1,2,†], Mengfei Zhang [3], Zhenfang Zhou [1,2], Chenghang Zhang [4], Pei Li [2] and Mengtong Bai [1]

[1] College of Geology and Environment, Xi'an University of Science and Technology, Xi'an 710054, China; dongshuning@cctegxian.com (S.D.); zhouzhenfang@cctegxian.com (Z.Z.); baimt18391505165@163.com (M.B.)
[2] CCTEG Xi'an Research Institute (Group) Co., Ltd., Xi'an 710077, China; lipei@cctegxian.com
[3] Xinjiang Geological Survey Institute of Sinochem Geology and Mine Administration, Urumqi 830017, China; zmf18392362618@163.com
[4] School of Earth Sciences and Engineering, Sun Yat-sen University, Zhuhai 519080, China; zhangchx65@mail2.sysu.edu.cn
* Correspondence: trc1212@stu.xust.edu.cn
† These authors contributed equally to this work.

Abstract: The Tarim Basin in Xinjiang is located in the northwest inland arid region of China, but research shows that the region is rich in groundwater resources. To understand the hydrochemical characteristics and water quality of shallow groundwater in the desert area of the southern margin of the Tarim Basin, the groundwater was systematically sampled and tested. The ion characteristics and evolution mechanism of groundwater were analyzed by mathematical statistics, Schukarev classification, Piper three-line diagram, Gibbs model and ion ratio. Water quality was evaluated by the water quality index method (WQI) and irrigation water suitability-related parameters. The results indicated that the dominant cation in the study area is Na^+, and the main dominant anions are SO_4^{2-} and Cl^-. According to total dissolved solids (TDS), the groundwater mainly belongs to brackish water and semi-saline water. The hydrochemical chemistry types are mainly Cl·SO_4-Na·Mg type, followed by Cl-Na type, and the ion source is mainly the weathering and dissolution of evaporation rock, silicate and sulphate. The hydrochemical process is primarily controlled by evaporation concentration and rock weathering, and the cation exchange is weak. Furthermore, the WQI spatial distribution map shows that the groundwater in the middle of the study area is unsuitable for drinking and there are two areas with high WQI values greater than 500. In contrast, the good-excellent groundwater is scattered in the East. The groundwater generally has high to very high salinity, with significant changes in alkalinity. In addition, 54% of the water samples exceed the magnesium hazard (MH) limit. Therefore, certain measures should be taken before irrigation. This study has important implications for the rational development and reasonable utilization of local groundwater.

Keywords: desert area; groundwater; water quality; hydrochemical characteristics; water quality index

1. Introduction

As an indispensable source of water supply, groundwater is a vital strategic resource to support social and economic development and it plays a significant role in maintaining ecological equilibrium [1,2]. However, in the process of urbanization, industrialization and agricultural activities have a negative impact on groundwater quality. At the same time, excessive exploitation of groundwater leads to enormous pressures put on water supply demand, especially for developing countries such as China [3–5]. China has a shortage of water resources, with a low per capita share. On the other hand, major river basins and lakes are generally polluted, which further exacerbates the current situation

of water shortage [6,7]. The severe water resource problem has become a hot topic of close attention and an unavoidable century challenge in Chinese society [8]. Therefore, there is an urgent need to develop effective water resources management strategies and to strengthen research on the evolution mechanism of groundwater in order to ensure the sustainable development and utilization of water resources.

By analyzing the hydrochemical characteristics and influencing factors of groundwater, its formation and evolution pattern can be better revealed, which provides an essential basis for studying the origin of groundwater. Groundwater quality assessment is very helpful to understand its applicability, and is also necessary for its sustainable planning and management [9]. Among them, the water quality index (*WQI*) is not only an important parameter to evaluate whether the quality of drinking water meets the standard, but also a reference basis for the development, utilization and scientific allocation of water resources [10,11]. Previous researchers have conducted a large number of investigations and research on groundwater quality related issues: Chitsazan [12] investigated the groundwater chemical characteristics in the suburb of Urmia, Iran, and evaluated the quality of drinking water with an index model. It was found that the important processes to control the hydrochemical characteristics are mineral weathering, ion exchange, and human activities; affected by human activities, there are low-hazard pollutants in the suburbs. Tiwari et al. [13] conducted a qualitative evaluation of the mine water in the Sibocaro coalfield through the Piper diagram, saturation index (SI) and relevant parameters of irrigation water suitability. The results showed that the dissolution of minerals and ion exchange are the main processes to control the chemical change of water. The index value of most mine water samples does not exceed the standard, which is suitable for drinking and can be directly used for irrigation. To evaluate the genesis of water quality in Songyuan City, Northeast China, Yan et al. [14] measured the hydrogen and oxygen isotope composition and ion content of groundwater. The results show that the weathering and dissolution of silicate rock is the main factor affecting the ion composition of deep and shallow groundwater. At the same time, long-term artificial exploitation has caused the dispersion of pollutants in the shallow aquifer. In addition, scholars have conducted comprehensive evaluations of groundwater quality based on WQI, combined with multiple statistical analyses, fuzzy logic, geographic information systems, and other methods [15–19].

Due to the scarcity of surface water and atmospheric precipitation, groundwater has become the primary source of water supply in arid and semi-arid areas and is an essential factor affecting the sustainable development of these areas [20,21]. Therefore, scientific evaluation and sustainable development of groundwater are especially important in these areas [22]. The Tarim Basin in Xinjiang is a typical arid and semi-arid area with an arid climate and strong evaporation. Groundwater is an important water resource in this area. In recent years, there have been many studies on the hydrochemical characteristics of groundwater in the Tarim Basin [23–26]. However, these studies are primarily concentrated in the western and southern edge oasis areas of the Tarim Basin, lacking research on ionic characteristics and genetic mechanism of groundwater in desert areas. Furthermore, they mainly focus on the trace elements that affect human health in groundwater, and the comprehensive evaluation of groundwater quality is lacking. For this reason, this paper selects the Kunyu desert area in southern margin of the Tarim Basin as the study area. Combined with a large number of hydrological wells and hydrological borehole data, we analyze the hydrochemical types and causes of groundwater, and reveal the content changes and distribution laws of various chemical components of groundwater in the study area. At the same time, the water quality index method and relevant parameters of irrigation water suitability are used to evaluate water quality. It not only provides theoretical guidance for local groundwater protection and desertification prevention, but also provides a reference for the industrialization process of local reclamation agriculture.

2. Materials and Methods

2.1. Overview of the Research Area

Kunyu City is located in the southwest of Xinjiang Uygur Autonomous Region, at the northern foot of the Kunlun Mountains and the southern margin of the Tarim Basin. Based on the latest Gaofen-2 remote sensing image, the topography of the area was interpreted using remote sensing interpretation markers for each landform. Subsequently, GIS was used to calculate the proportion of each landform, and the interpretation results were verified through field investigations. The interpreted data was authentic and reliable. The mountainous area accounts for 33.3%, the Gobi desert accounts for 63%, and the oasis area only accounts for 3.7%, sporadically scattered among the Gobi desert. The study area is situated at the desert area of the lower Duwa River. The terrain is relatively open and flat, and the topography of small areas is relatively complex with many dunes. The topography is high in the west and low in the east, high in the south and low in the north, mainly developing mobile dunes, fixed-semi-fixed dunes and alluvial plain landforms. According to the information published by the local meteorological office, it belongs to a typical warm temperate inland arid climate. The main climatic characteristics are hot in summer, cold in winter, large diurnal temperature difference, scarce precipitation and strong evaporation. The average annual precipitation is 29 mm, and annual evaporation is 4410 mm. The Duwa River is the major surface water system flowing through the region, flowing from south to northeast, and gradually disappearing in the Gobi desert after passing through the Duwa Reservoir (Figure 1).

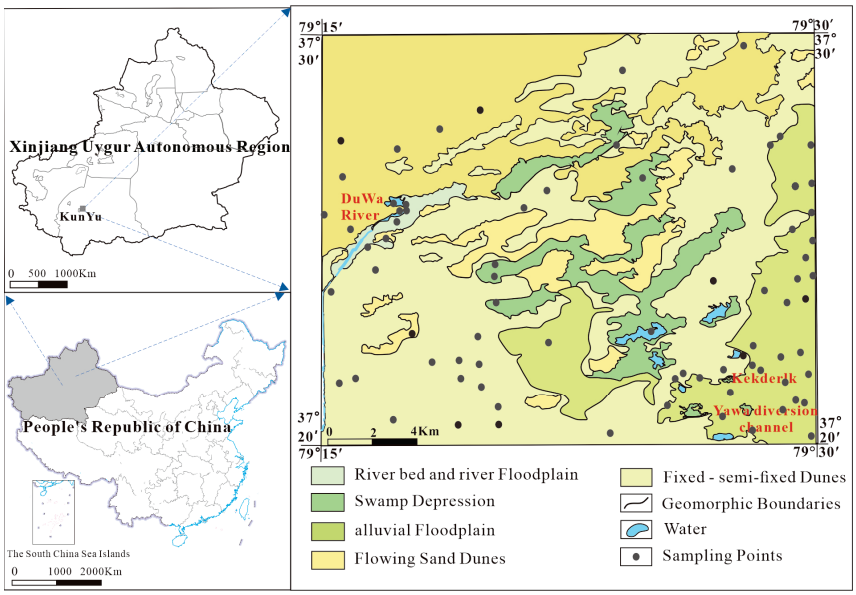

Figure 1. Geomorphology type and location of sampling sites in the study area.

According to field geological surveys and remote sensing image data, the land utilization rate in the research area is relatively low. The southeast and southwest of the study area are mainly residential areas, the southern and central eastern parts are mainly farmland, with jujube trees planted, and the northern parts are vast deserts that have not been utilized.

2.2. Hydrogeological Conditions

According to the lithology and hydrogeological characteristics of Quaternary sediments, combined with pumping tests and previous hydrological borehole data, the Quaternary Holocene (Qh)-Pleistocene (Qp) aquifer group in the study area belongs to pore water in loose rocks. The aquifer is primarily composed of fine sand and silt, with a thickness ranging from 50 to 76 m (the comprehensive histogram in the study area is shown in

Figure S1 of the Supplementary Materials). The depth of the water table varies significantly across different geomorphic types. The flowing dune area in the northwest has a depth of over 5 m, while the fixed and semi-fixed dune area in the southwest and northeast ranges from 3 to 5 m. In the alluvial plain, the water table depth is 1–3 m, whereas, in the central swampy depressions and some parts of the northwest riverbed and floodplain, the depth is less than 1 m. Generally, the water table depth decreases from northwest to southeast, as shown in Figure 2. Combined with the hydrogeological borehole and previous geological data, the area shows a distribution pattern of weak water richness in the northwest and medium in the southeast.

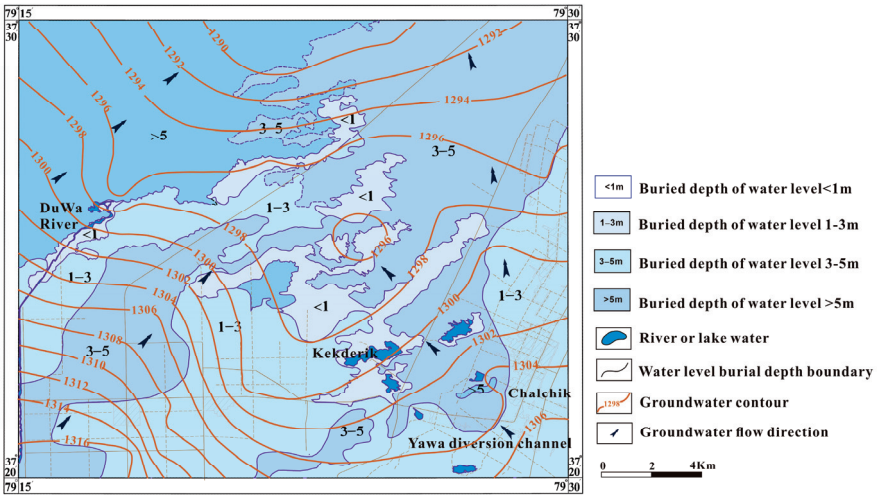

Figure 2. Contour map of phreatic water depth and water level.

In terms of recharge sources, the phreatic water in the area is mainly recharged laterally from the Duwa River, as well as from irrigation infiltration and groundwater lateral recharge. The main discharge methods include artificial mining, evaporation, and transpiration. The overall flow direction is from southwest to northeast, but local areas are affected by rivers, canal systems, field irrigation and groundwater exploitation, which makes the groundwater flow field change to some extent. The ground slope of the floodplain area outside the southern part of the area is small, about 1.67%, and the aquifer particles are mainly sand gravel and gravelly silt. After entering the working area to the north, the slope of the terrain continues to decrease, to only 0.15~0.30‰. Furthermore, the lithology of the aquifer becomes fine sand, and the groundwater flow rate gradually becomes smaller. In Yawa Township in the eastern part of the study area, diving flows from the southeast to the northwest and north under the influence of the Krakash River and the Yawa Dry Drain. The burial depth of groundwater mostly ranges from 1 to 3 m, with a slight topographic slope, and the lithology of the aquifer consisting of fine powder sand, and a hydraulic slope of 0.5‰ to 2‰. The burial depth of groundwater in the middle is mostly less than 1 m, and the groundwater runoff rate is sluggish. In the vertical direction, the shallow vertical runoff is stronger. With the increase in depth, the aquifer compactness increases and the groundwater runoff weakens.

2.3. Sample Collection and Testing

The specific sampling location is shown in Figure 1. Ninety (90) groups of groundwater samples were analyzed altogether in this study, which were obtained from machinery wells, hydrological boreholes, and the Duval River in the study area. The sample collection time was concentrated in late July 2021, with two water samples taken from each borehole and only one sample taken from other locations. The water samples were collected in 500 mL narrow-mouth polyethylene bottles. Before sampling, the sample bottles were washed with the water to be tested 2–3 times. After sampling, the sample bottles were sealed to

prevent leakage and sent to the laboratory for testing as soon as possible. The water sample testing was completed by the Experimental Testing Center of Xi'an Geological Survey Center of China Geological Survey. The main testing indexes included pH, total dissolved solids (TDS), K^+, Na^+, Ca^{2+}, Mg^{2+}, Cl^-, $SO_4{}^{2-}$, $HCO_3{}^-$, $NO_3{}^-$, F^-, total hardness (TH), chemical oxygen demand (COD) and other related components. Electrical conductivity (EC), total dissolved solids (TDS), and pH of the water samples were measured in situ using a pH meter and portable EC instrument. In the laboratory, all water samples were filtered through 0.45 μm membrane filters to separate suspended particles before testing. Major anions (F^-, Cl^-, $SO_4{}^{2-}$, $NO_3{}^-$) were tested using ion chromatography; major cations (Ca^{2+}, Mg^{2+}, Na^+, K^+) were tested by inductively coupled plasma mass spectrometry, and bicarbonate ($HCO_3{}^-$) concentrations were measured using an automatic titrator. TH were measured using EDTA complexometric method. The COD value was determined by potassium permanganate method. The accuracy of test results was examined according to the charge balance error *E* [27], and it was maintained within 5% for all.

2.4. Analysis Method

IBM SPSS 23.0 software was used for the statistical analysis of the data. The groundwater was classified using the Shukarev classification method, and the map of groundwater mineralization distribution and hydrochemical types area was drawn using MapGIS software based on kriging interpolation. The primary ion source of groundwater and the influencing factors of hydrochemical characteristics were determined through the Gibbs diagram and major ion ratio relationship. The quality of drinking water was evaluated by the WQI, and the quality of irrigation water was evaluated by sodium percentage (Na%), sodium adsorption ratio (SAR), permeability index (PI) and magnesium hazard (MH).

2.4.1. Water Quality Index Method (WQI)

WQI can express the comprehensive impact of different water quality parameters on the suitability of drinking water. These parameters were given different weight values (w_i) according to the impact on water quality. Through the analysis of sample test results, nine of these indicators were selected as evaluation factors, and their weights were distributed as follows: TDS and $NO_3{}^-$ were 5, pH, $SO_4{}^{2-}$, COD and F^- were 4, Cl^- was 3, Na^+ was 2, and total hardness (TH) was 1 [28–30].

The water quality index (WQI) can be determined by calculating the relative weight (W_i), quality rating (q_i) and sub-index (SI_i) of each parameter using the equation.

$$W_i = \frac{w_i}{\sum_{i=1}^{n} w_i} \tag{1}$$

$$q_i = \frac{C_i}{S_i} \times 100 \tag{2}$$

$$SI_i = W_i \times q_i \tag{3}$$

where: W_i is the relative weight, w_i is the weight of each parameter, and n is the number of parameters; Q_i is the quality rating, C_i is the value or concentration of each parameter in each water sample; S_i is the drinking water standard of each parameter, and SI_i is the sub-index of each parameter.

WQI is the sum of all sub-indexes SI_i calculated for each parameter of the sample:

$$\text{WQI} = \sum_{i=1}^{n} SI_i \tag{4}$$

2.4.2. Evaluation Method for Suitability of Irrigation Water

When evaluating the suitability of irrigation water, salinity, alkalinity and toxicity are usually considered. High salinity irrigation water will bring about the emergence of saline soil, while high alkalinity irrigation water will cause soil alkalization and hardening, and

high sodium will increase soil alkalinity. The sodium hazard of irrigation water can be expressed by the sodium adsorption ratio (SAR). A higher SAR value indicates that the alkalinity of irrigation water is high [13]. Similarly, the percentage of sodium (Na%) is also a standard index for evaluating the suitability of irrigation water and can be used as the basis for the classification of irrigation water.

If the concentration of Mg^{2+} in irrigation water reaches a high level, magnesium alkalization may occur, thus affecting the organic matter content in the soil and causing crop yield reduction. Therefore, Szaboles and Darab proposed magnesium hazard (MH) to evaluate the applicability of agricultural irrigation water [31]. The permeability index (PI) is another important parameter to measure the suitability of groundwater for irrigation. It represents the ability of water and minerals to migrate through pore space to the plant roots, and is mainly influenced by dissolved ions such as Na^+, Ca^{2+}, $Mg^{2+}$and HCO_3^-, based on which Doneen developed the relevant evaluation criteria according to PI [32]. The calculation formulas of each indicator are listed in Table 1.

Table 1. Evaluation index and calculation formula of irrigation water suitability.

Evaluation Parameters	Calculation Formulas
SAR	$SAR = Na/[(Ca + Mg)/2]^{0.5}$
Na%	$Na\% = (Na + K)/(Ca + Mg + Na + K) \times 100\%$
MH	$MH = Mg/(Ca + Mg) \times 100\%$
PI	$PI = (Na + \sqrt{HCO_3})/(Ca + Mg + Na) \times 100\%$

3. Results and Discussion

3.1. Basic Characteristics of Hydrochemistry

The physicochemical parameters of groundwater in the study area, including statistical indicators such as minimum, maximum, mean and standard deviation, are given in Table 2. From the overall content of each ion, the cation order is $Na^+ > Mg^{2+} > Ca^{2+} > K^+$, of which the content of Na^+ is the largest, with a mean concentration of 696.1 mg/L, which is 5.2, 5.8 and 19.0 times of the content of Mg^{2+}, Ca^{2+} and K^+, respectively. The anion content is ranked as $Cl^- > SO_4^{2-} > HCO_3^- > NO_3^- > F^-$, of which Cl^- and SO_4^{2-} are the primary anions in groundwater, with an average content of 950.4 mg/L and 824.1 mg/L, respectively. The pH of water samples ranges from 6.9 to 9.3, with a mean value of 7.9, which is weakly alkaline overall, and its coefficient of variation (*CV*) is only 4.9%, indicating that the spatial variability of groundwater pH is small. The total hardness (TH) of the water samples varies between 126.4 and 35,350.0 mg/L, with an average value of 1232.8 mg/L. The overall hardness of the groundwater is relatively high, dominated by hard water.

Table 2. Statistical results of main hydrochemical parameters of groundwater.

Project	Na^+	K^+	Ca^{2+}	Mg^{2+}	Cl^-	SO_4^{2-}	HCO_3^-	NO_3^-	COD_{Mn}	F^-	TDS	TH	pH	EC
Min	54.5	1.8	10.9	10.9	49.4	71.3	51.7	0.1	0.8	0.3	714	126.4	6.9	1320.0
Max	4830.0	171.0	592.0	750	7575.0	6416.0	913.0	354.0	7.0	2.9	19,100.0	35,350.0	9.3	8660.0
Mean	696.1	36.8	118.3	135.0	950.4	824.1	341.9	15.2	2.3	1.2	3028.7	1232.8	7.9	3953.4
SD	821.4	30.7	93.6	103.0	1139.6	872.4	212.3	45.3	1.6	0.9	3030.3	3665.5	0.4	1842.9
CV%	118.0	83.5	79.1	76.3	119.9	105.9	62.1	297.3	68.1	74.5	100.0	297.3	4.9	46.6

Note: pH has no unit, the unit of EC is μs/cm, and the unit of other parameters is mg/L.

The distribution map of TDS in the research area is shown in Figure 3. The variation of TDS ranges from 714.0 to 19,100.0 mg/L, and the average value is 3028.7 mg/L. According to its classification standard [33], the groundwater in study area mainly belongs to brackish water and semi-saline, and its distribution area accounts for 63.06% and 20.06% of the total area, respectively. Freshwater is scattered in the southeastern of the study area, making up only 2.59% of the total area. In comparison, saline water is mainly distributed near the Kekderik, with a strip distribution area of about 82.15 km^2, accounting for 20.06%. Mainly

due to the slow groundwater runoff, shallow water level, and strong evaporation, the TDS value in this area is relatively high. COD is an indicator that characterizes organic pollution in water. The COD_{Mn} range in the study area is between 0.8 and 7.0, with an average of 2.3. Most water samples have low CODMn values, which comply with the Class III water regulations in the Sanitary Standard for Drinking Water (GB5749-2006) [34]. Only seven water samples exceed the Class III water limit.

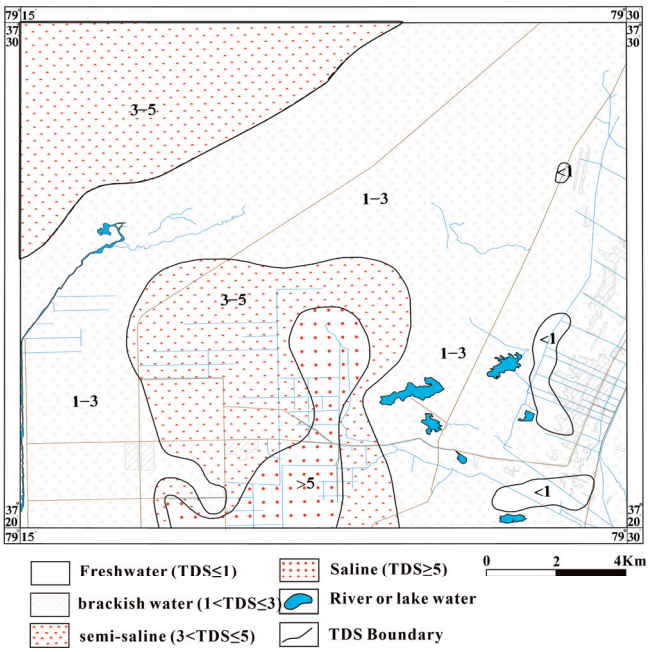

Figure 3. Distribution map of groundwater TDS value.

Correlation analysis can show the close degree between different hydrochemical parameters, which is helpful to better understand the hydrochemical process and ion source. The Pearson correlation analysis results of various indicators are shown in Figure 4. It can be observed from the figure that Na^+ has a strong correlation with K^+, Mg^{2+}, $SO_4{}^{2-}$, Cl^- and TDS, indicating that sodium ions may have many sources. Ca^{2+}, Mg^{2+} strongly correlate with $SO_4{}^{2-}$, but have a poor correlation with $HCO_3{}^-$. TDS has a strong positive correlation with Cl^-, indicating that saline rock may be dissolved along the flow path [35]. However, the correlation between $NO_3{}^-$ and other parameters is weak because its source is mainly artificial, such as the application of nitrogen fertilizer in jujube trees.

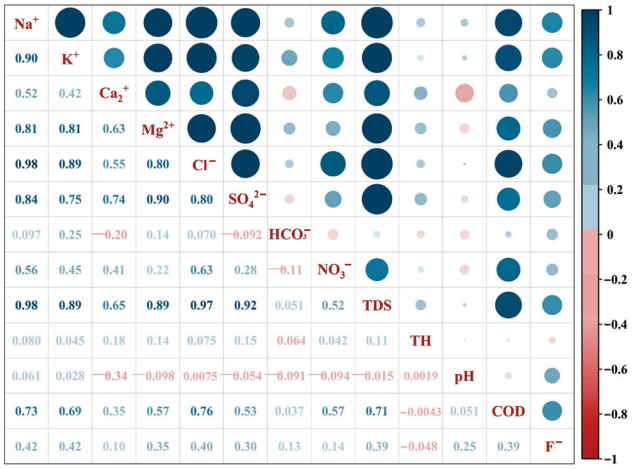

Figure 4. Correlation matrices between parameters.

3.2. Hydrochemical Evolution Characteristics

The Shukarev method is used to classify hydrochemical types based on the concentration and mineralization degree of six common major ions in groundwater. According to the Shukarev method classification [36], the hydrochemical types in the study area can be divided into seven categories (Figure 5). The Cl-SO_4-Na-Mg type and Cl-Na type are predominant, among which the Cl-SO_4-Na-Mg type groundwater is generally distributed in the flowing dunes and fixed-semi-fixed dunes. The groundwater runoff conditions in these areas are poor, and water alternation is medium. The concentration of Cl^-, SO_4^{2-}, Na^+, and Mg^{2+} in groundwater is relatively high, while the content of other ions is relatively low. The Cl-Na type groundwater is found in the northeast desert and the vicinity of Kekderik. Its groundwater depth is shallow, runoff is slow, evaporation is strong, local groundwater is stagnant, salt accumulation is serious, and Na^+ content is high. The groundwater in the southern swamp depression primarily belongs to the Cl-SO_4-Na type. Due to the influence of Karakash River and Yawa diversion channel, the groundwater in the eastern Yawa Township is mainly of Cl-HCO_3-Na-Mg type and Cl-HCO_3-SO_4-Na-Mg type. In addition, Cl-Na-Mg type groundwater is only sporadically distributed in the east near Chalchik.

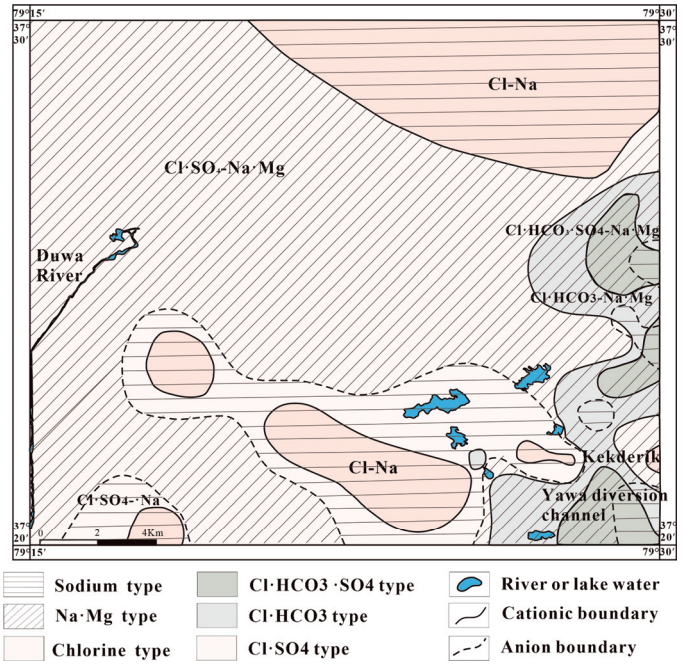

Figure 5. Hydrochemical types of groundwater in the study area.

Figure 6 shows the piper trilinear diagram of groundwater hydrochemistry in the study area. In this diagram, water samples are relatively concentrated, basically falling into Zones IV and II, and more than 90% are distributed in Zone IV. The main anions are close to the Cl^- and SO_4^{2-} ends, and their milligram equivalent percentages are mostly between 40% and 70%, with strong acids (Cl^-, SO_4^{2-}) exceeding weak acids (HCO_3^-). The main cations are close to the Na^+ and Mg^{2+} ends, followed by Ca^{2+}, and the concentration of alkali metal ions (Na^+, K^+) is higher than that of alkaline earth metal ions (Ca^{2+}, Mg^{2+}). The hydrochemical types mainly showed Cl-SO_4-Na type and Cl-Na type. This result is similar to the water chemistry types classified by the Shukarev method.

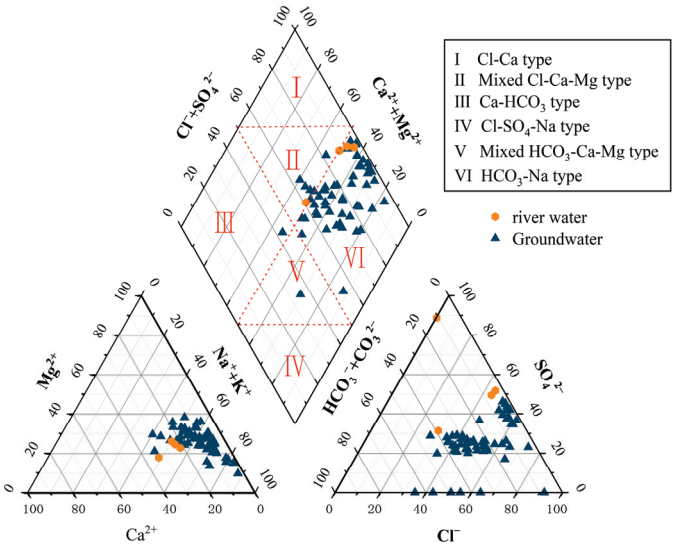

Figure 6. Piper diagram of groundwater chemical composition in the study area.

3.3. Analysis of Hydrochemical Origin of Groundwater

The influence of rock weathering, atmospheric precipitation, evaporation and concentration on groundwater hydrochemistry can be qualitatively analyzed by the Gibbs diagram [37]. In the Gibbs diagram, when the TDS value is low and the ratio of $\gamma Na^+/\gamma(Na^+ + Ca^{2+})$ or $\gamma Cl^-/\gamma(Cl^- + HCO_3^-)$ is greater than 0.5, the groundwater chemical components are mainly influenced by atmospheric precipitation [38]. While higher TDS values and also high $\gamma Na^+/\gamma(Na^+ + Ca^{2+})$ ratio or $\gamma Cl^-/\gamma(Cl^- + HCO_3^-)$ ratio indicate that the groundwater chemical fraction is affected by evaporative concentration, otherwise by rock weathering. It can be seen from Figure 7 that the TDS values of water samples in the study area are high and 98% of them fall within the range of $\gamma Na^+/\gamma(Na^+ + Ca^{2+}) > 0.5$, while the ratio of $\gamma Cl^-/\gamma(Cl^- + HCO_3^-)$ is relatively dispersed, and parts of samples distributed in the region of rock weathering. This shows that the groundwater in this area is affected by both evaporation concentration and rock weathering, and the former is more significant.

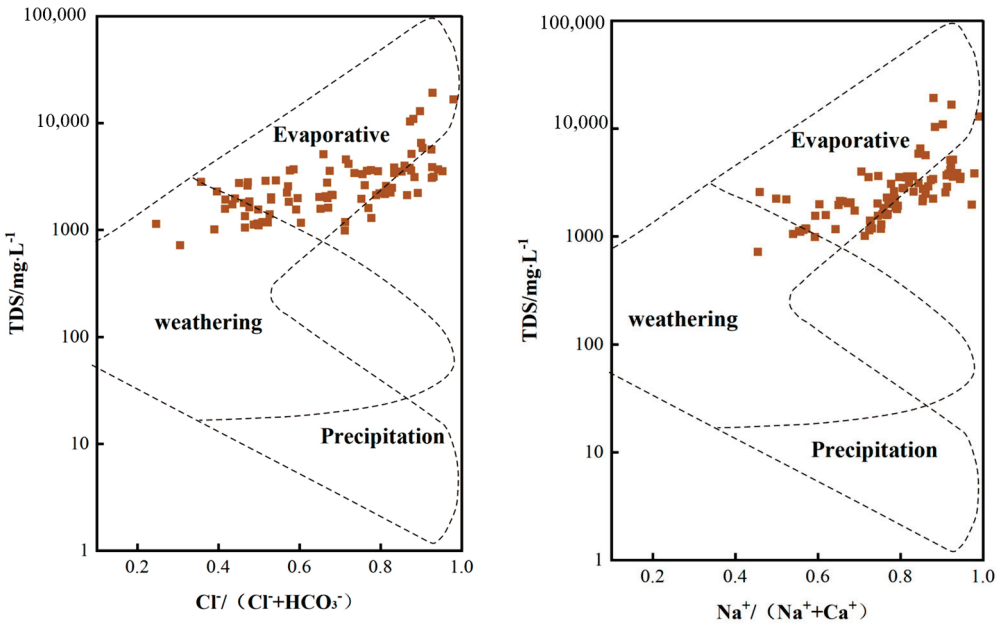

Figure 7. Gibbs diagram of groundwater in the study area.

Groundwater formed under different genesis or conditions often has a large difference in the content ratio between components. Therefore, such ratio coefficients can be used to determine the source of groundwater components. Among them, the relationship of $\gamma(Na^+ + K^+)/\gamma Cl^-$ can be used to determine the sources of K^+ and Na^+ in groundwater. When the $\gamma(Na^+ + K^+)/\gamma Cl^-$ distribution is around the line y = x, the K^+ and Na^+ in groundwater are primarily from rock salt dissolution [39]. Figure 8a shows that K^+ and Na^+ in groundwater in the study area mainly originate from rock salt dissolution, 90% of the water samples fall in the zone where $\gamma(Na^+ + K^+)/\gamma Cl^- > 1$, only a few water sample points fall below. This indicates that the content of Na^+ and K^+ is more than that of Cl^-, which may be caused by the dissolution of silica-aluminate minerals containing sodium and potassium (e.g., feldspar), or there may be alternating cation adsorption.

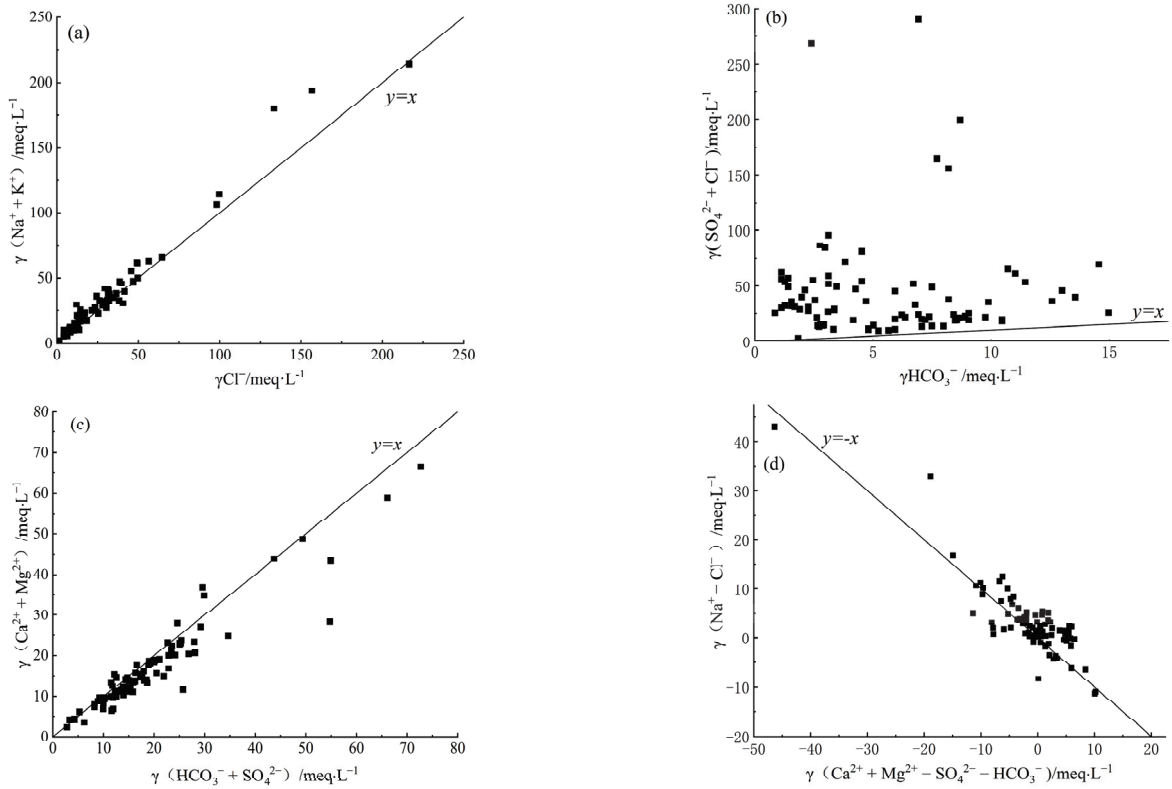

Figure 8. Groundwater ion ratio diagram. (**a**) Scatter plot of $\gamma(Na^+ + K^+)$ versus γCl^-; (**b**) Scatter plot of $\gamma(SO_4^{2-} + Cl^-)$ versus γHCO_3^-; (**c**) Scatter plot of $\gamma(Ca^{2+} + Mg^{2+})$ versus $\gamma(HCO_3^- + SO_4^{2-})$; (**d**) Scatter plot of $\gamma(Na^+ - Cl^-)$ versus $\gamma(Ca^{2+} + Mg^{2+} - HCO_3^- + SO_4^{2-})$.

The dissolution of carbonate rocks in groundwater can be judged by the relationship of $\gamma(SO_4^{2-} + Cl^-)/\gamma(HCO_3^-)$ [39]. As seen from Figure 8b, the groundwater samples all fall above the line y = x, indicating that the chemical composition of groundwater is mainly influenced by the dissolution of evaporite, and the influence of carbonate rocks is weak. The main sources of Mg^{2+} and Ca^{2+} can be determined by analyzing the ratio relationship between $\gamma(Ca^{2+} + Mg^{2+})$ and $\gamma(HCO_3^- + SO_4^{2-})$ [40]. Figure 8c indicates that over 80% of the groundwater samples are located below $\gamma(Ca^{2+} + Mg^{2+})/\gamma(HCO_3^- + SO_4^{2-})$, indicating that Mg^{2+} and Ca^{2+} in groundwater of the study area are primarily from the weathering dissolution of silicate and evaporite, and only a tiny part is related to the weathering dissolution of carbonate rocks. Meanwhile, in Figure 4, both Ca^{2+} and $Mg^{2+}$are strongly correlated with SO_4^{2-}, which further explains that the dissolution of gypsum and magnesium sulfate is an important source of Ca^{2+} and Mg^{2+}.

The ratio relationship between $\gamma(Na^+ - Cl^-)$ and $\gamma(Ca^{2+} + Mg^{2+} - SO_4^{2-} - HCO_3^-)$ is usually used to reveal the cation exchange rate [40]. Groundwater samples fall near the line y = −x, confirming the existence of cation exchange adsorption. The strength

and direction of cation exchange can be inferred from the CAI-1 and CAI-2 indices in the Scholler method [41], which are calculated by Equations (5) and (6), respectively:

$$\text{CAI-1} = \frac{C(Cl^-) - [C(Na^+) + C(K^+)]}{C(Cl^-)} \quad (5)$$

$$\text{CAI-2} = \frac{C(Cl^-) - [C(Na^+) + C(K^+)]}{C(HCO_3^-) + C(SO_4^{2-}) + C(CO_3^-) + C(NO_3^-)} \quad (6)$$

where: C is the ion concentration, in meq/L.

When CAI-1 and CAI-2 are all positive values, it suggests that there is a positive cation exchange, that is, Na^+ and K^+ in water exchange with Ca^{2+} and Mg^{2+} on the surface of mineral particles. Otherwise, if values are negative, the reverse cation exchange occurs, and the greater the absolute value, the stronger the cation alternation [42]. CAI-1 and CAI-2 are negative, with average values of −0.52 and −0.47, respectively. The absolute value is relatively small, indicating that reverse cation alternation has occurred, and this effect is relatively weak.

The analysis results of the ion combination ratio show that Na^+ and K^+ mainly come from salt rock and silica-aluminate minerals dissolution, Mg^{2+} and Ca^{2+} mainly come from weathering dissolution of silicate rocks and evaporite, and SO_4^{2-} mainly comes from sulfate dissolution, which is more consistent with the regional geological background. In the south of the study area, the Late Permian K-feldspar granite strata are exposed near Kunlun Mountain, and the Jurassic, Cretaceous and Paleoproterozoic strata in the area contain evaporites such as gypsum and rock salt of varying thickness. At the same time, a large-scale gypsum mine is developed in the Piaman anticline near the south of Kunyu city. Carbonate rocks have a feeble influence on the chemical composition of groundwater, and it is assumed that desulfurization is one of the important sources of HCO_3^- in water.

3.4. Drinking Water Quality Evaluation

The drinking water quality in the study area was comprehensively evaluated with the Sanitary Standard for Drinking Water (GB5749-2006) [34] as an evaluation index. The limit values and weight values of each factor are shown in Table 3. Meanwhile, the WQI spatial distribution map was drawn according to the calculation results (Figure 9).

Based on the WQI values, groundwater quality can be classified as excellent water (<50), good water (50–100), poor water (100–200), very poor water (200–300) and unsuitable (>300) [43]. The WQI values in the study area range from 43.0 to 1442.9, with a mean value of 224.2, which is relatively large. Only 16 samples belong to the grade of excellent water to good water, and 11 samples belong to the unsuitable category. The rest of the water samples are poor or very poor water. The WQI spatial distribution map shows that most areas in the study area have high WQI values and are not suitable for drinking. Only the groundwater in parts of the eastern regions has low WQI values and is suitable for drinking.

Table 3. List of parameters, weight factors and limits of water quality index.

Indicators	TDS	NO_3^-	SO_4^{2-}	COD	PH	F^-	Cl^-	Na^+	TH
Limit value	1000 mg/L	10 mg/L	250 mg/L	3 mg/L	6.5–8.5	1 mg/L	250 mg/L	200 mg/L	450 mg/L
Weight	5	5	4	4	4	4	3	2	1
Relative weights	0.156	0.156	0.125	0.125	0.125	0.125	0.094	0.063	0.031

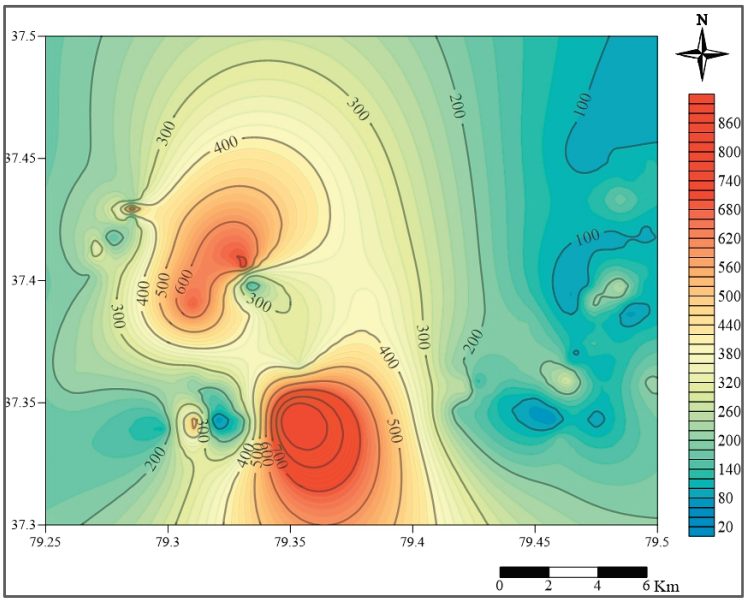

Figure 9. Spatial distribution of water quality index (WQI).

The spatial distribution map of WQI shows that the water quality in the central part of the study area is in the unsuitable category, and two high value areas occur in the lower DuWa River area and near Kekderik. The slow groundwater runoff, shallow depth of burial and strong evaporation in the vicinity of Kekderik result in high TDS values, and the TDS values have a greater weight on the WQI values, which lead to the high WQI values in this area. The sampling survey along the river from the upstream to the downstream of the Duval River found that the water near the starting survey site belonged to brackish. However, the TDS value along the way gradually increased, and the TDS content reached 3960 mg/L at the tail, which was semi-saline water. It reflects that the ion concentration of Duwa River increases with the runoff distance, among which SO_4^{2-}, Na^+ content and TDS value increase more significantly. The river water with high ion concentration recharges the groundwater, causing an increase in the corresponding ion concentration of groundwater in the downstream area; in addition, the dissolution of gypsum mine near this area also has a certain influence on the groundwater quality. The eastern part of the study area is scattered with excellent and good water areas. This is mainly due to the swampy depressions in the area, which mainly receive recharge from irrigation infiltration and river channel infiltration, and the main mining method is artificial mining. The groundwater alternation is stronger, the influence of evaporation is relatively weak, and the ion concentration value is relatively low.

3.5. Irrigation Water Quality Evaluation

Salinity has a significant effect on soil alkalinity and crop growth, and when irrigated with high salinity groundwater, it can lead to soil hardening and inhibit crop growth [44]. The hazard of salinity and alkalinity can be better understood using the United States Salinity Laboratory diagrams (USSL diagrams), where salinity and alkalinity are expressed in terms of electrical conductivity (EC) and sodium adsorption ratio (SAR), respectively [13]. The USSL classification map of the study area was plotted (Figure 10), in which 27% of the groundwater samples distributed in the high salinity region and the remaining 73% fell in the very high salinity region. The SAR values varied between 1.64 and 30.33, with a mean value of 8.47, which were evenly dispersed in the four classification regions S1–S4, and about half of the water samples fell in the high-very high alkalinity region. In summary, the study found that the groundwater in the study area has high-very high salinity overall, but the alkalinity is highly variable and the SAR value is high in some areas, which requires certain measures before it can be used for irrigation.

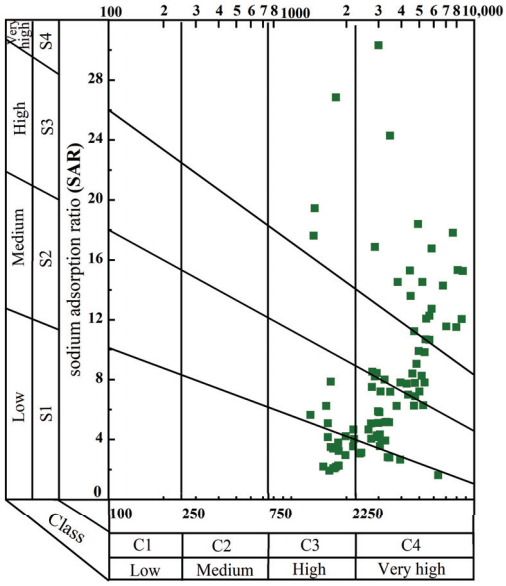

Figure 10. USSL classification chart of groundwater irrigation water quality.

Wilcox plots reflecting salinity and sodium percentage (Na%) allow for the classification of irrigation water [45]. Plotting the samples data into the Wilcox plot (Figure 11), it is found that about 56% of the groundwater samples are in the unsuitable zone, 20% are in the doubtful-unsuitable category, 6% are in the permissible-doubtful category, and only 18% are in the good-permissible category. Most water samples fall within the doubtful or unsuitable range, indicating that the groundwater in this area is not suitable for direct irrigation, mainly due to the high salinity of the groundwater.

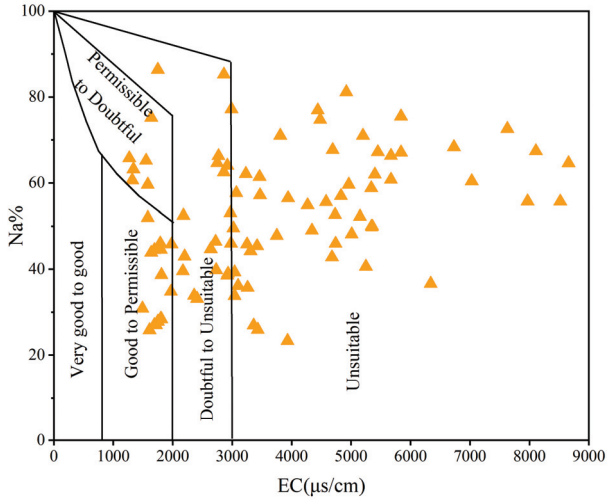

Figure 11. Suitability of groundwater irrigation based on Na%.

Soil permeability is affected by long-term water use and the concentration of calcium, magnesium, sodium, and bicarbonate in the water. The Doneen diagrams based on total salt concentration and permeability index (PI) can be used to characterize the suitability of groundwater for irrigation. In this regard, the PI can be classified into three categories. Class I and II have a maximum permeability of 75% or more and are suitable for irrigation, while class III water indicates a maximum permeability of 25% of the soil and is unsuitable for irrigation [46]. As shown in Figure 12, most of the groundwater samples in the study area belong to category I and only five samples belong to category II, indicating that from the irrigation index (PI), long-term irrigation of groundwater has little impact on soil permeability.

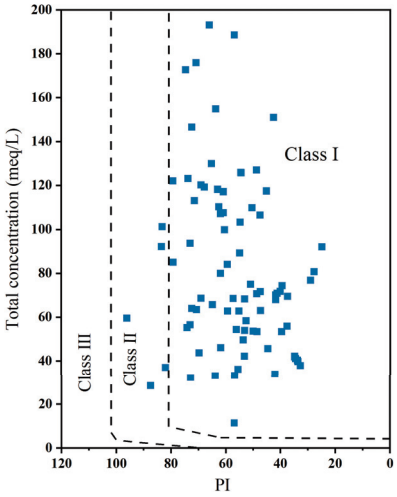

Figure 12. Doneen diagram of groundwater irrigation water quality.

The concentration of magnesium in water is one of the most important parameters to test the suitability of irrigation water. Calcium and magnesium must be present in suitable concentrations to maintain a balance between them. The increase in magnesium concentration in irrigation water will lead to an increase in alkalinity and a decrease in crop yield. Therefore, water with MH value greater than 50% is considered unsuitable for irrigation. The calculated MH values in the study area range from 21.0% to 90.2%, with a mean value of 50.6%, of which 54% of the samples were above the MH limit, indicating that the groundwater magnesium concentration was high and unsuitable for irrigation.

4. Conclusions

In this study, mathematical statistics, Shukalev classification, Gibbs model and ion ratio were applied to analyze the ion characteristics and evolution mechanism of shallow groundwater in Kunyu desert area in the southern edge of Tarim Basin. The research results indicate that the abundance of major cations was in the order of $Na^+ > Mg^{2+} > Ca^{2+} > K^+$, while the major anions trend in the study area was in the following order: $Cl^- > SO_4{}^{2-} > HCO_3{}^- > NO_3{}^- > F^-$. Influenced by the depth of the water table and strong evaporation, the TDS value of groundwater is relatively high and is primarily semi-saline water. The hydrochemical type in the study area is mainly the Cl-SO_4-Na-Mg type. The ions in groundwater are mainly derived from the weathering dissolution of saline rock, silicates and sulfates. The hydrochemical characteristics are mainly controlled by the combination of evaporation concentration and rock weathering. In addition, the desulfation may also have some influence on it.

A comprehensive evaluation of drinking water quality was conducted based on WQI. The overall WQI value in the study area is relatively high, and only parts of the eastern regions have groundwater suitable for drinking. Two high-value WQI areas occur in the lower DuWa River and near Kekdric, which is residential area and farmland. Residents in this area should not use untreated groundwater as drinking water.

Through the USSL classification chart, Wilcox chart, Doneen chart and combining with the SAR and other indicators to evaluate the water quality of irrigation water, it is found that although the PI of groundwater in the study area is suitable, the overall salinity is high-very high, the alkalinity is greatly variable, and the magnesium concentration is high. Therefore, the direct use of groundwater for irrigation will lead to soil hardening and low crop yield, and certain measures need to be taken before it can be used for irrigation.

These water samples are from the same batch, and the sampling time is concentrated in late July 2021. Due to the difficulty of drilling and sampling deep into the desert, there are few samples taken in the northwest region of the study area. Based on data from other parts of the study area, the water level depth values inferred using interpolation methods may slightly differ from the actual values. Furthermore, in a future project research,

batch sampling in different seasons will be considered, so as to compare and study the hydrochemical characteristics and water quality status under different seasons and climatic conditions.

Supplementary Materials: The following supporting information can be downloaded at: https://www.mdpi.com/article/10.3390/w15081563/s1, Figure S1: Comprehensive histogram in the study area.

Author Contributions: All authors contributed to the study's conception and design. S.D. provided the writing ideas and supervised the study; M.Z. collected water samples and sent them for inspection; Z.Z., M.B., C.Z. and P.L. processed and analyzed the data. The first draft of the manuscript was written by R.T., and all authors commented on previous versions of the manuscript. All authors have read and agreed to the published version of the manuscript.

Funding: This research is supported by the National Natural Science Foundation of China (Grant No. 41807221), Tiandi Science and Technology Co. Ltd. Science and Technology Innovation Venture Capital Special Project (2022-2-TD-ZD005), Project of China Geological Survey (DD20179605).

Data Availability Statement: Not applicable.

Acknowledgments: The authors are grateful to the anonymous reviewers for their helpful comments on the manuscript.

Conflicts of Interest: The authors declare no conflict of interest.

References

1. Zhang, P.; Liu, X.; Zhu, W.; Li, C.; Jin, R.; Yan, H.; Gu, C.; Wang, J. Spatio-temporal Changes in Water Conservation Ecosystem Service During 1990–2019 in the Tumen River Basin, Northeast China. *Chin. Geogr. Sci.* **2023**, *33*, 102–115. [CrossRef]
2. Jiang, Y.; Gui, H.; Yu, H.; Wang, M.; Fang, H.; Wang, C.; Chen, C.; Zhang, Y.; Huang, Y. Hydrochemical characteristics and water quality evaluation of rivers in different regions of cities: A case study of Suzhou City in Northern Anhui Province, China. *Water* **2020**, *12*, 950. [CrossRef]
3. Saha, D.; Marwaha, S.; Mukherjee, A. Groundwater resources and sustainable management issues in India. In *Clean and Sustainable Groundwater in India*; Springer: Berlin/Heidelberg, Germany, 2018; pp. 1–11.
4. Jha, M.K.; Shekhar, A.; Jenifer, M.A. Assessing groundwater quality for drinking water supply using hybrid fuzzy-GIS-based water quality index. *Water Res.* **2020**, *179*, 115867. [CrossRef] [PubMed]
5. Çitakoğlu, H.; Demir, A.; Gemici, B. Regionalization and mapping of dissolved oxygen concentration of sakarya basin by L–moments method. *Mühendislik Bilim. Ve Tasarım Derg.* **2021**, *9*, 495–510. [CrossRef]
6. Li, P.; Qian, H. Water resources research to support a sustainable China. *Int. J. Water Resour. Dev.* **2018**, *34*, 327–336. [CrossRef]
7. Wu, J.; Wang, L.; Wang, S.; Tian, R.; Xue, C.; Feng, W.; Li, Y. Spatiotemporal variation of groundwater quality in an arid area experiencing long-term paper wastewater irrigation, northwest China. *Environ. Earth Sci.* **2017**, *76*, 1–14. [CrossRef]
8. Wu, J.; Sun, Z. Evaluation of shallow groundwater contamination and associated human health risk in an alluvial plain impacted by agricultural and industrial activities, mid-west China. *Expo. Health* **2016**, *8*, 311–329. [CrossRef]
9. Li, X.; Wu, H.; Qian, H.; Gao, Y. Groundwater chemistry regulated by hydrochemical processes and geological structures: A case study in Tongchuan, China. *Water* **2018**, *10*, 338. [CrossRef]
10. Singh, C.K.; Shashtri, S.; Mukherjee, S.; Kumari, R.; Avatar, R.; Singh, A.; Singh, R.P. Application of GWQI to assess effect of land use change on groundwater quality in lower Shiwaliks of Punjab: Remote sensing and GIS based approach. *Water Resour. Manag.* **2011**, *25*, 1881–1898. [CrossRef]
11. Abbasnia, A.; Yousefi, N.; Mahvi, A.H.; Nabizadeh, R.; Radfard, M.; Yousefi, M.; Alimohammadi, M. Evaluation of groundwater quality using water quality index and its suitability for assessing water for drinking and irrigation purposes: Case study of Sistan and Baluchistan province (Iran). *Hum. Ecol. Risk Assess. Int. J.* **2019**, *25*, 988–1005. [CrossRef]
12. Chitsazan, M.; Aghazadeh, N.; Mirzaee, Y.; Golestan, Y. Hydrochemical characteristics and the impact of anthropogenic activity on groundwater quality in suburban area of Urmia city, Iran. *Environ. Dev. Sustain.* **2019**, *21*, 331–351. [CrossRef]
13. Tiwari, A.K.; Singh, P.K.; Mahato, M.K. Environmental geochemistry and a quality assessment of mine water of the west Bokaro Coalfield, India. *Mine Water Environ.* **2016**, *35*, 1–11. [CrossRef]
14. Yan, J.; Chen, J.; Zhang, W. Study on the groundwater quality and its influencing factor in Songyuan City, Northeast China, using integrated hydrogeochemical method. *Sci. Total Environ.* **2021**, *773*, 144958. [CrossRef] [PubMed]
15. Chaudhry, A.K.; Sachdeva, P. GIS-based groundwater quality assessment using GQIs and fuzzy-logic approach. *Water Environ. J.* **2022**, *36*, 172–182. [CrossRef]
16. Gharibi, H.; Mahvi, A.H.; Nabizadeh, R.; Arabalibeik, H.; Yunesian, M.; Sowlat, M.H. A novel approach in water quality assessment based on fuzzy logic. *J. Environ. Manag.* **2012**, *112*, 87–95. [CrossRef]

17. Islam, A.T.; Shen, S.; Haque, M.A.; Bodrud-Doza, M.; Maw, K.W.; Habib, M.A. Assessing groundwater quality and its sustainability in Joypurhat district of Bangladesh using GIS and multivariate statistical approaches. *Environ. Dev. Sustain.* **2018**, *20*, 1935–1959. [CrossRef]
18. Maurya, P.K.; Ali, S.A.; Zaidi, S.K.; Wasi, S.; Tabrez, S.; Malav, L.C.; Ditthakit, P.; Son, C.T.; Cabral-Pinto, M.M.S. Assessment of groundwater geochemistry for drinking and irrigation suitability in Jaunpur district of Uttar Pradesh using GIS-based statistical inference. *Environ. Sci. Pollut. Res.* **2023**, *30*, 29407–29431. [CrossRef] [PubMed]
19. ÇITAKOĞLU, H.; Çetin, M.; Çobaner, M.; HAKTANIR, T. Mevsimsel yağışların jeoistatistiksel yöntemle modellenmesi ve gözlemi olmayan noktalarda tahmin edilmesi. *Tek. Dergi* **2017**, *28*, 7725–7745. [CrossRef]
20. Li, P.; Tian, R.; Xue, C.; Wu, J. Progress, opportunities, and key fields for groundwater quality research under the impacts of human activities in China with a special focus on western China. *Environ. Sci. Pollut. Res.* **2017**, *24*, 13224–13234. [CrossRef]
21. Chen, J.; Wu, H.; Qian, H.; Gao, Y. Assessing nitrate and fluoride contaminants in drinking water and their health risk of rural residents living in a semiarid region of Northwest China. *Expo. Health* **2017**, *9*, 183–195. [CrossRef]
22. Chen, J.; Wu, H.; Qian, H.; Li, X. Challenges and prospects of sustainable groundwater management in an agricultural plain along the Silk Road Economic Belt, north-west China. *Int. J. Water Resour. Dev.* **2018**, *34*, 354–368. [CrossRef]
23. Lu, Q.; Liu, F.; Li, Y.; Wang, D. Study on the Relationship between Water Resources Utilization and Economic Growth in Tarim River basin from the Perspective of Water Footprint. *Water* **2022**, *14*, 1655. [CrossRef]
24. Huang, L.; Sun, Z.; Zhou, A.; Bi, J.; Liu, Y. Source and enrichment mechanism of fluoride in groundwater of the Hotan Oasis within the Tarim Basin, Northwestern China. *Environ. Pollut.* **2022**, *300*, 118962. [CrossRef] [PubMed]
25. Wang, W.; Chen, Y.; Wang, W.; Jiang, J.; Cai, M.; Xu, Y. Evolution characteristics of groundwater and its response to climate and land-cover changes in the oasis of dried-up river in Tarim Basin. *J. Hydrol.* **2021**, *594*, 125644. [CrossRef]
26. Wang, W.; Chen, Y.; Wang, W. Groundwater recharge in the oasis-desert areas of northern Tarim Basin, Northwest China. *Hydrol. Res.* **2020**, *51*, 1506–1520. [CrossRef]
27. Kopáček, J.; Hejzlar, J.; Mosello, R. Estimation of organic acid anion concentrations and evaluation of charge balance in atmospherically acidified colored waters. *Water Res.* **2000**, *34*, 3598–3606. [CrossRef]
28. Wu, Z.; Wang, X.; Chen, Y.; Cai, Y.; Deng, J. Assessing river water quality using water quality index in Lake Taihu Basin, China. *Sci. Total Environ.* **2018**, *612*, 914–922. [CrossRef]
29. Ener, E.; Davraz, A. Evaluation of water quality using water quality index (WQI) method and GIS in Aksu River (SW-Turkey). *Sci. Total Environ.* **2017**, *s584–s585*, 131–144.
30. Abbasnia, A.; Alimohammadi, M.; Mahvi, A.H.; Nabizadeh, R.; Yousefi, M.; Mohammadi, A.A.; Pasalari, H.; Mirzabeigi, M. Assessment of groundwater quality and evaluation of scaling and corrosiveness potential of drinking water samples in villages of Chabahr city, Sistan and Baluchistan province in Iran. *Data Brief* **2018**, *16*, 182–192. [CrossRef]
31. Sahoo, S.; Khaoash, S. Impact assessment of coal mining on groundwater chemistry and its quality from Brajrajnagar coal mining area using indexing models. *J. Geochem. Explor.* **2020**, *215*, 106559. [CrossRef]
32. Elsayed, S.; Hussein, H.; Moghanm, F.S.; Khedher, K.M.; Eid, E.M.; Gad, M. Application of irrigation water quality indices and multivariate statistical techniques for surface water quality assessments in the Northern Nile Delta, Egypt. *Water* **2020**, *12*, 3300. [CrossRef]
33. Khosravi, R.; Eslami, H.; Almodaresi, S.A.; Heidari, M.; Fallahzadeh, R.A.; Taghavi, M.; Khodadadie, M.; Peirovi, R. Use of geographic information system and water quality index to assess groundwater quality for drinking purpose in Birjand City, Iran. *Desalin Water Treat* **2017**, *67*, 74–83. [CrossRef]
34. Ministry of Health, PRC. *Sanitary Standard for Drinking Water: GB 5749-2006*; China Standards Press: Beijing, China, 2007.
35. Wu, J.; Li, P.; Qian, H. Hydrochemical characterization of drinking groundwater with special reference to fluoride in an arid area of China and the control of aquifer leakage on its concentrations. *Environ. Earth Sci.* **2015**, *73*, 8575–8588. [CrossRef]
36. Miao, Q.; Li, X.; Xu, Y.; Liu, C.; Xie, R.; Lv, Z. Chemical characteristics of groundwater and source identification in a coastal city. *PLoS ONE* **2021**, *16*, e0256360. [CrossRef]
37. Li, P.; He, X.; Li, Y.; Xiang, G. Occurrence and Health Implication of fluoride in groundwater of loess aquifer in the Chinese Loess Plateau: A Case Study of Tongchuan, Northwest China. *Expo. Health* **2019**, *11*, 95–107. [CrossRef]
38. Akshitha, V.; Balakrishna, K.; Udayashankar, H.N. Assessment of hydrogeochemical characteristics and saltwater intrusion in selected coastal aquifers of southwestern India. *Mar. Pollut. Bull.* **2021**, *173*, 112989. [CrossRef]
39. Ju, Q.; Liu, Y.; Hu, Y.; Wang, Y.; Liu, Q.; Wang, Z. Hydrogeochemical evolution and control mechanism of underground multiaquifer system in coal mine area. *Geofluids* **2020**, *2020*, 8820650. [CrossRef]
40. Li, P.; Wu, J.; Qian, H. Hydrochemical appraisal of groundwater quality for drinking and irrigation purposes and the major influencing factors: A case study in and around Hua County, China. *Arab. J. Geosci.* **2016**, *9*, 15. [CrossRef]
41. Li, P.; Tian, R.; Liu, R. Solute geochemistry and multivariate analysis of water quality in the Guohua phosphorite mine, Guizhou Province, China. *Expo. Health* **2019**, *11*, 81–94. [CrossRef]
42. Zhao, X.; Xu, Z.; Sun, Y. Mechanism of Changes in goaf water hydrogeochemistry: A case study of the menkeqing coal mine. *Int. J. Environ. Res. Public Health* **2022**, *20*, 536. [CrossRef]
43. Gountô, A.; Kouamé, I.K.; Mangoua, J.M.O.; Kouassi, A.K.; Savané, I. Using water quality index for assessing of physicochemical quality of quaternary groundwater in the southern part of Abidjan district (Cte d'Ivoire). *J. Water Resour. Prot.* **2019**, *11*, 14.

44. Esmaeili-Vardanjani, M.; Rasa, I.; Amiri, V.; Yazdi, M.; Pazand, K. Evaluation of groundwater quality and assessment of scaling potential and corrosiveness of water samples in Kadkan aquifer, Khorasan-e-Razavi Province, Iran. *Environ. Monit. Assess.* **2015**, *187*, 53. [CrossRef] [PubMed]
45. Ketata, M.; Gueddari, M.; Bouhlila, R. Suitability assessment of shallow and deep groundwaters for drinking and irrigation use in the £1 Khairat aquifer (Enfidha, Tunisian Sahel). *Environ. Geol.* **2012**, *65*, 313–330. [CrossRef]
46. Doneen, L.D. *Water Quality for Agriculture*; Department of Irrigation: Lalitpur, Nepal, 1964.

Disclaimer/Publisher's Note: The statements, opinions and data contained in all publications are solely those of the individual author(s) and contributor(s) and not of MDPI and/or the editor(s). MDPI and/or the editor(s) disclaim responsibility for any injury to people or property resulting from any ideas, methods, instructions or products referred to in the content.

hydrology

MDPI

Article

Simulation of Surface and Subsurface Water Quality in Hyper-Arid Environments

Ahmed Mohamed [1,*], Ahmed Asmoay [2,*], Saad S. Alarifi [3] and Musaab A. A. Mohammed [4]

[1] Geology Department, Faculty of Science, Assiut University, Assiut 71516, Egypt
[2] Geological Science Department, National Research Centre, Al-Behoos St., Dokki, Cairo 12622, Egypt
[3] Department of Geology and Geophysics, College of Science, King Saud University, P.O. Box 2455, Riyadh 11451, Saudi Arabia
[4] Department of Hydrogeology, Faculty of Earth Sciences and Engineering, University of Miskolc, 3515 Miskolc, Hungary
* Correspondence: ahmedmohamed@aun.edu.eg (A.M.); asmoay@gmail.com (A.A.)

Abstract: Forty-eight water samples (30 groundwater and 18 surface water samples) were collected from the study region. Physical and chemical examinations were performed on the water samples to determine the values of various variables. Several graphs, sheets, and statistical measures, including the sodium solubility percentage (SSP), the sodium absorption ratio (SAR), and Piper's diagram, were used to plot the concentration of the principal ions and the chloride mass balance (CMB). The contents of the variables were compared with the contents in other local areas and the standard allowable safe limits as recommended by the World Health Organization (WHO). Water pH values were neutral for all water samples. Electric conductivity (EC) readings revealed that water samples vacillated from slightly mineralized to excessively mineralized. Water salinities were fresh and very fresh according to the total dissolved solids (TDS) amounts. The hardness of water ranged from medium to hard in the surface water and from medium to very hard in the groundwater samples. Bicarbonate, sodium, and calcium made up the highest amounts in the surface water samples. The highest concentrations of bicarbonate, sulfate, chloride, and sodium were found in the groundwater. Diagrams show the major ion relationships as well as the type and origin of the water. According to Piper's plots, most of the water samples under investigation were Ca-HCO_3 type, Mg water types, followed by SO_4.Ca-Cl water types. This highlighted the elemental preponderance of bicarbonate and alkaline earth (Ca^{2+} + Mg^{2+}). This dominance is caused by evaporite and carbonate minerals dissolving in water because of anthropogenic activities and interaction processes. The groundwater recharge was estimated to be 0.89–1.6 mm/yr based on Chloride Mass Balance. The examined water samples can also be used for cattle, poultry, and irrigation. Additionally, the groundwater is of poorer quality than the surface water, although both types of water are adequate for various industries, with a range of 14 to 94 percent. With the exception of a few groundwater samples, the tested water samples are suitable for a number of applications.

Keywords: surface water; groundwater; sodium absorption ratio; soluble sodium percentage; chloride mass balance; irrigation activities; industrial activities

1. Introduction

Currently, almost one-third of the world's population lives in countries with a water shortage [1]. These include semi-arid regions, which are by nature sparsely populated with water resources. Due to the severe constraints that a lack of water places on both natural and human systems, these regions are potentially highly vulnerable to climate variability and potential future climate change [2].

For many aspects of life and human beings, including drinking, agriculture, industrial operations, hygiene, and reactions, water resources are extremely critical needs. The

growth of villages and urban civilizations is significantly impacted by the availability of water, which can be impacted by precipitation, droughts, and aquifer depletion [3–5]. Since groundwater and surface water are the natural resources that are most frequently contaminated and in short supply globally, monitoring water quality is an important strategy for ensuring water security [6,7]. Anthropogenic activities and natural phenomena have an impact on water quality, degrading groundwater and surface water, and altering how they can be used for agricultural, human, animal, and industrial usage [8]. The measurement of physicochemical characteristics is required for water quality control programs to acquire data that can be used to create an overall picture of water conditions [9–12].

The Nile River is Egypt's primary supply of water, providing 55.5 billion m^3 of water annually, or around 94 percent of all of Egypt's water resources. Egypt's dry climate, with an average annual rainfall of 18 mm, is well-known [13,14]. Furthermore, Egypt's population increased from 66 million in 2002 to approximately 96 million in 2018. As a result, there is considerable water scarcity in Egypt and its water supplies are under stress [15]. About 95% of Egypt's population lives in the Nile Valley and the Delta, where they consume 80% of the country's water supply [16]. In order to fill this gap, the administration opted to use groundwater as a substitute water source, increase agricultural areas, recover desert areas utilizing groundwater, and encourage people to dwell in these areas [14].

The Assiut area is in the middle of the Nile Valley. People from the governorate's desert areas more commonly live on the land along the river's two banks. Approximately 3,119,112 of the governorate's 4,245,215 residents live in rural areas, compared to only 1,126,103 in urban areas [17]. Rural communities that live near water wells use the groundwater without primary treatment, which has a major negative impact on the health of the locals [18,19]. It is possible to categorize water, identify the major ions, and determine how water forms based on the geochemical background [9–12,20]. According to factors like electrical conductivity (EC), sodium absorption ratio (SAR), major ion content, and soluble sodium percentage (SSP), irrigation water quality reflects soil salinity, sodicity risks, water toxicity, and other effects on sensitive salt plants [8,9,21–23]. Numerous scientists worldwide have conducted studies on water quality indices [8,10–12,14,19,24–29].

Although similar studies may be carried out in other sites in Egypt, no previous studies utilizing our proposed methodology have been carried out for the current study area. Therefore, the primary goal of this research is to discuss water geochemistry and evaluate its suitability for a variety of purposes, including irrigation and industrial activities.

2. Material and Methods

2.1. Geology and Hydrogeology

The Assiut Governorate is situated between latitudes 26°50′ and 27°40′ North and longitudes 30°40′ and 31°32′ East; the agricultural area stretches along the two banks of the Nile River. The rate of poverty in Assiut exceeds 60 percent. There are eleven cities (Dairut, El Qusiya, Manfalout, Abnob, Assiut, El Fath, Abou Teg, Sahel Selim, El Badari, Al Ghanayim and Sedfa) in the Assiut Governorate.

The research area is located in the northwestern Assiut district. It represents the low ground that is bordered to the east and west by calcareous plateaus. The two morphological units are represented by the older alluvial plain (agricultural land) and the younger alluvial plain (reclaimed land) [30] (Figures 1 and 2). The Mokkatom group of Eocene rocks, Pliocene deposits, and Quaternary silt makes up the stratigraphic succession in the study region [30,31]. The main sources of water in the study region are groundwater and surface water (the Nile River, secondary canals, and drains). The Quaternary aquifer and the Eocene limestone aquifer are the two main aquifers that represent groundwater reservoirs. Middle Pleistocene (Prenile) coarse and sandy clay cobbles, gravels, and calcareous rocks make up the Quaternary aquifer [32,33]. According to [34,35], this aquifer is recharged from the surface water since the groundwater moves westward. The Quaternary aquifer replenishes the Eocene limestone aquifers [20]. Four land use classes can be identified from the analysis of Landsat 7 images over the study region (Figure 3). These classes are

(1) water that is represented by the Nile River, (2) agricultural lands that include the Nile valley and the reclaimed lands, (3) urban areas, and (4) the desert regions at the eastern and western plateaus.

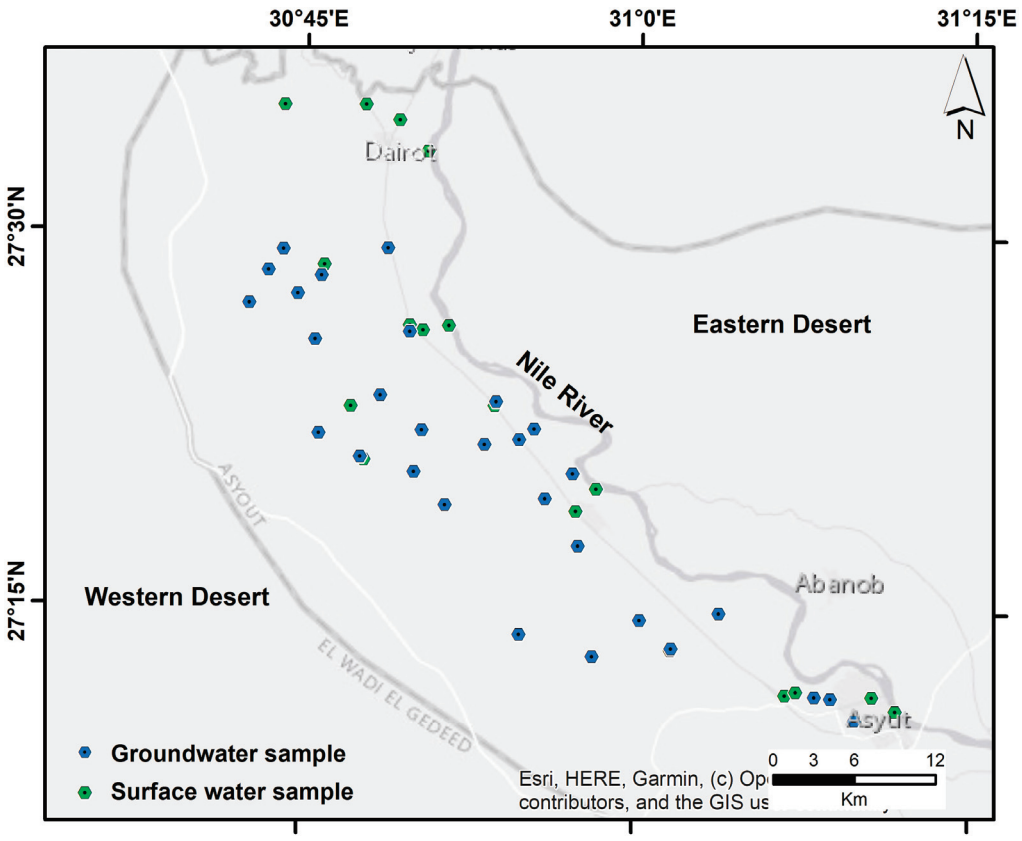

Figure 1. Location map showing the study area.

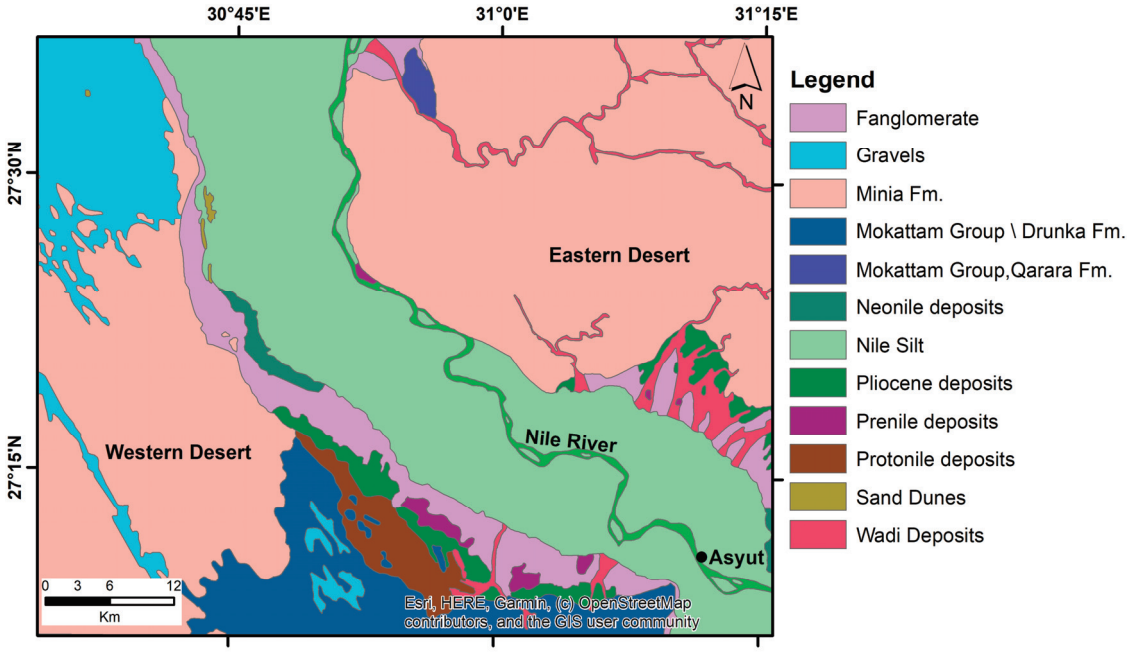

Figure 2. Geological map of the study area (after [31]).

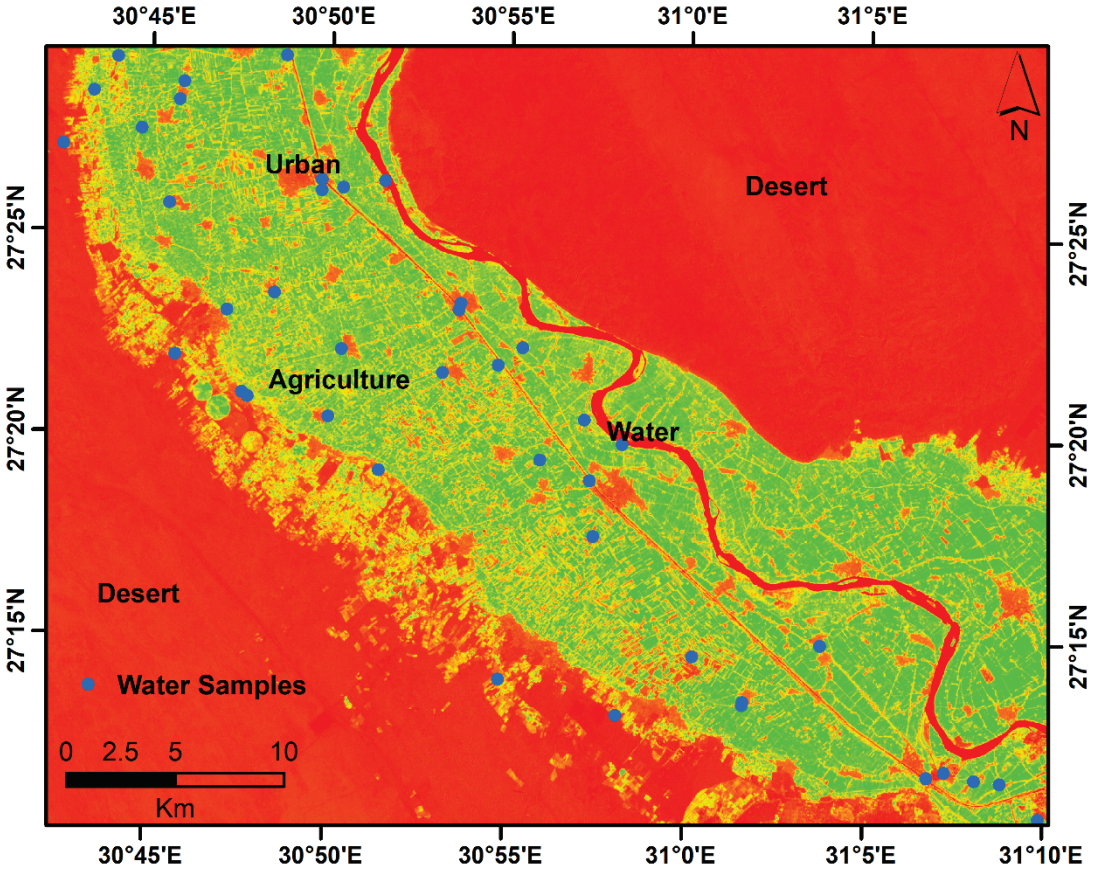

Figure 3. Land-use classification of the study area.

2.2. Climate

The Assiut Governorate is located within Egypt's dry region, which experiences long, hot summers, cold winters, minimal precipitation, and significant evaporation rates. According to the Assiut Meteorological Station, the average daily air temperature in the area is approximately 22.7 °C. Summers are dry and quite hot, with average temperatures reaching 37 °C. December–February are the coldest months, with an average temperature of 18 °C.

2.3. Sampling and Laboratory Methods

In the study region, forty-eight water samples were collected: thirty groundwater samples and eighteen surface water samples. The sterilized polypropylene bottles containing the water samples were sealed tightly for storage. Standard techniques were used to filter the materials and evaluate their physicochemical composition [35]. While Na^+ and K^+ concentrations were checked using a flame photometer, temperature, EC, TDS, and pH were all determined on-site using a pH-meter. Additionally, titration was used in the Assiut University Laboratories to determine the amounts of Ca^{2+}, Mg^{2+}, CO_3^{2-}, HCO_3^-, SO_4^{2-}, and Cl^-. The ionic balances, which were below 5%, indicated the analytical accuracy of the ion readings.

2.4. Sodium Absorption Ratio (SAR)

The relative amounts of calcium, magnesium, and sodium, or SAR, show how these ions affect sodium buildup in soils. This ratio is a more accurate way to calculate the

sodium percentage since it accounts for the root's water deficit caused by high salt and low calcium contents [36]. The following equation for SAR, according to [37], is determined as:

$$SAR = \frac{Na^{+}}{\sqrt{\frac{Ca^{2+}+Mg^{2+}}{2}}}$$

where the concentrations of these cations are expressed in epm (Table 1).

Table 1. Descriptive statistical values for the detected variables in the studied water samples.

Surface Water Samples												
	T (°C)	**pH**	**EC (µS/cm)**	**TDS (ppm)**	**TH (ppm)**	**Ca^{2+} (ppm)**	**Mg^{2+} (ppm)**	**Na^{+} (ppm)**	**K^{+} (ppm)**	**HCO_3^{-} (ppm)**	**Cl^{-} (ppm)**	**SO_4^{2-} (ppm)**
safe limit [38]	-	6.5–8.5	1500	1000	500	75	100	250	12	-	250	250
Valid	18	18	18	18	18	18	18	18	18	18	18	18
Missing	0	0	0	0	0	0	0	0	0	0	0	0
Minimum	22.600	6.390	264.000	204.000	120.000	18.000	21.870	20.700	7.038	175.680	38.998	1.440
Maximum	26.100	7.510	1060.000	854.000	400.000	60.000	89.910	195.500	74.287	488.000	248.171	110.400
Median	24.600	7.115	277.500	213.000	155.000	38.000	29.767	30.450	9.192	249.490	48.417	16.500
Mean	24.483	7.116	375.222	290.778	181.111	34.722	33.264	53.176	16.023	266.875	67.506	30.524
Variance	1.163	0.082	47,696.889	30,576.418	4610.458	146.330	246.275	2305.191	347.419	6942.959	2365.838	1050.773
Std. Deviation	1.078	0.286	218.396	174.861	67.900	12.097	15.693	48.012	18.639	83.324	48.640	32.416
Skewness	−0.090	−0.866	2.419	2.517	2.431	0.304	3.113	1.993	2.762	1.244	3.380	1.634
Groundwater Samples												
	T (°C)	**pH**	**EC (µS/cm)**	**TDS (ppm)**	**TH (ppm)**	**Ca^{2+} (ppm)**	**Mg^{2+} (ppm)**	**Na^{+} (ppm)**	**K^{+} (ppm)**	**HCO_3^{-} (ppm)**	**Cl^{-} (ppm)**	**SO_4^{2-} (ppm)**
Valid	30	30	30	30	30	30	30	30	30	30	30	30
Missing	0	0	0	0	0	0	0	0	0	0	0	0
Minimum	23.000	6.400	207.000	156.000	120.000	30.000	20.655	23.000	5.474	189.100	49.634	7.200
Maximum	32.900	7.000	1452.000	1069.000	1120.000	240.000	170.100	575.000	22.677	915.000	886.325	912.000
Median	25.500	6.720	638.000	496.500	325.000	76.000	52.974	84.550	11.534	375.150	89.365	90.900
Mean	25.973	6.717	713.233	548.500	380.667	85.733	61.394	128.170	11.238	431.087	148.640	151.669
Variance	5.707	0.022	136,597.082	78,828.259	43,896.092	2202.409	1083.732	16,521.013	15.528	28,793.641	29,072.525	37,122.799
Std. Deviation	2.389	0.148	369.590	280.764	209.514	46.930	32.920	128.534	3.941	169.687	170.507	192.673
Skewness	1.544	−0.302	0.548	0.512	1.736	1.612	1.473	2.187	0.663	1.036	3.425	2.719

2.5. Soluble Sodium Percentage (SSP)

SSP is a ratio that assesses the risk from sodium, which causes soil to become less permeable when it reacts with the element Na+ [39]. The following equation is cited by [40] as an estimation of SSP:

$$SSP = \frac{\left(Na^{+} + K^{+}\right) \times 100}{\left(Ca^{2+} + Mg^{2+} + Na^{+} + K^{+}\right)} \quad (1)$$

where the concentrations of these cations are expressed in epm (Table 1).

2.6. Chloride Mass Balance (CMB)

Based on the amount of chloride in precipitation and groundwater, the CMB method is used to estimate the rate of groundwater recharge in dry areas. Chloride is less likely to change in a water system over time. Many researchers, including [41–44], used the CMB method to figure out the recharge rate. The authors used the following equation to figure out how much CMB there was:

$$R = P \cdot Cl_p / Cl_{gw} \quad (2)$$

where R is the recharge rate (mm/yr); P is the average annual precipitation (mm/yr); Cl_p is the average of precipitation-weighted chloride content (ppm); and Cl_{gw} is the mean chloride content in groundwater.

3. Results and Discussion

3.1. Hydrogeochemical Classification Major Ions Correlations

Water temperatures ranged from 22.6 to 26 °C in the surface water and from 23 to 32.9 °C in the groundwater samples (Table 1). The pH readings showed a neutral case which fluctuated between 6.3 and 7.5 (Table 1). EC values varied from 207 to 1452 μS/cm in the water samples to indicate slightly to excessively mineralized water (Table 1: [45]). TDS readings vacillated between 204 and 854 ppm in the surface water samples; in the groundwater samples they ranged from 156 to 1069 ppm (Table 1). TDS readings of the water samples denoted fresh and very fresh water (Table 1: [46]). Total hardness (TH) values ranged from 120 to 400 ppm in the surface water samples to represent hard and very hard water (Table 1; [47]). The groundwater samples included EC values ranging from 207 to 1452 μS/cm to express slightly to excessively mineralized water (Table 1). The values of pH, EC, TDS and TH are agreeable with the standard limits set by [43] except for the TH reading, which increased in the groundwater samples (Table 1). These findings matched with results of examined water in the El Minya Governorate of Egypt [24].

The major ions content can be arranged in descending order according to their mean in the surface water samples into: $HCO_3^- > Cl^- > Na^+ > Ca^{2+} > Mg^{2+} > SO_4^{2-} > K^+$. The means are 266.8, 67.5, 53, 34.7, 33.5., 30, and 16ppm, respectively (Table 1). In the groundwater samples, those means are mapped as: $HCO_3^- > SO_4^{2-} > Cl^- > Na^+ > Ca^{2+} > Mg^{2+} > K^+$, which are 431, 151.6, 148.6, 128, 85.7, 61, and 11ppm, respectively (Table 1). These contents are agreeable with their concentrations in the water in the El Minya Governorate of Egypt [17] and exceed the allowable limits for drinking water in the groundwater samples [43]. The presence of ions in natural water demonstrates the chemical makeup of water. The cation contents of the examined water samples had the highest sodium values (Table 1). In the samples under investigation, bicarbonate concentrations are greater than the chloride and sulphate levels (Table 1). For the classification of water's chemical composition, various approaches were suggested. Some techniques primarily use anions, while others combine anions and cations to produce a clearer image of the type of water. The methods outlined in [36,48] are utilized in the study field as graphical approaches for classifying water. Two triangles and a diamond shape are separated into 4 fields in the [36] diagram. The interactions between the alkalis ($K^+ + Na^+$), alkaline earths ($Ca^{2+} + Mg^{2+}$), the alkalinity ($CO_3^{2-} + HCO_3^-$), and the salinity ($Cl^- + SO_4^{2-}$) are shown in Figure 4. Field No. 1 and Field No. 4 are where most of the water samples were found. The Ca-HCO_3 water type represented by Field No. 4 indicates that calcium and bicarbonate ions predominated due to carbonate mineral dissolution [9,11,12,26,29]. Field No.1 functioned as a SO_4.Ca-Cl water type referring to evaporite mineral dissolution [9,11,12,26,29]. Figure 5 displays the various chemical properties of the water samples as they are projected onto the Piper's diagram's diamond form.

3.2. Major Ions Correlations

Ions that are soluble in water are a result of the interaction between water and rock, evaporation, and precipitation [29,49]. The authors of [29] pointed out the significance of the water–rock interaction process that results in the dissolution of carbonate minerals (Calcite and dolomite) and evaporite minerals (halite and gypsum) in water. This may be stated in the four following equations.

$$CaCO_3 \text{ (calcite)} + H_2CO_3 \rightarrow Ca^{2+} + 2HCO_3^-$$

$$CaMg(CO_3)_2 \text{ (dolomite)} + 2H_2CO_3 \rightarrow Ca^{2+} + Mg^{2+} + 4HCO_3^-$$

$$NaCl \text{ (halite)} \leftarrow\rightarrow Na^+ + Cl^-$$

$$CaSO_4.2H_2O \text{ (gypsum)} \longleftrightarrow Ca^{2+} + SO_4^{2-} + 2H_2O$$

Consequently, the previously mentioned equations revealed that the source of excess Ca^{2+}, Mg^{2+}, HCO_3^- and Cl^- is the dissolution of calcite, dolomite, halite and gypsum minerals (Figure 5). Along with anthropogenic activities like agricultural water drainage, this surplus is the result of the interplay between water and rock [5,29].

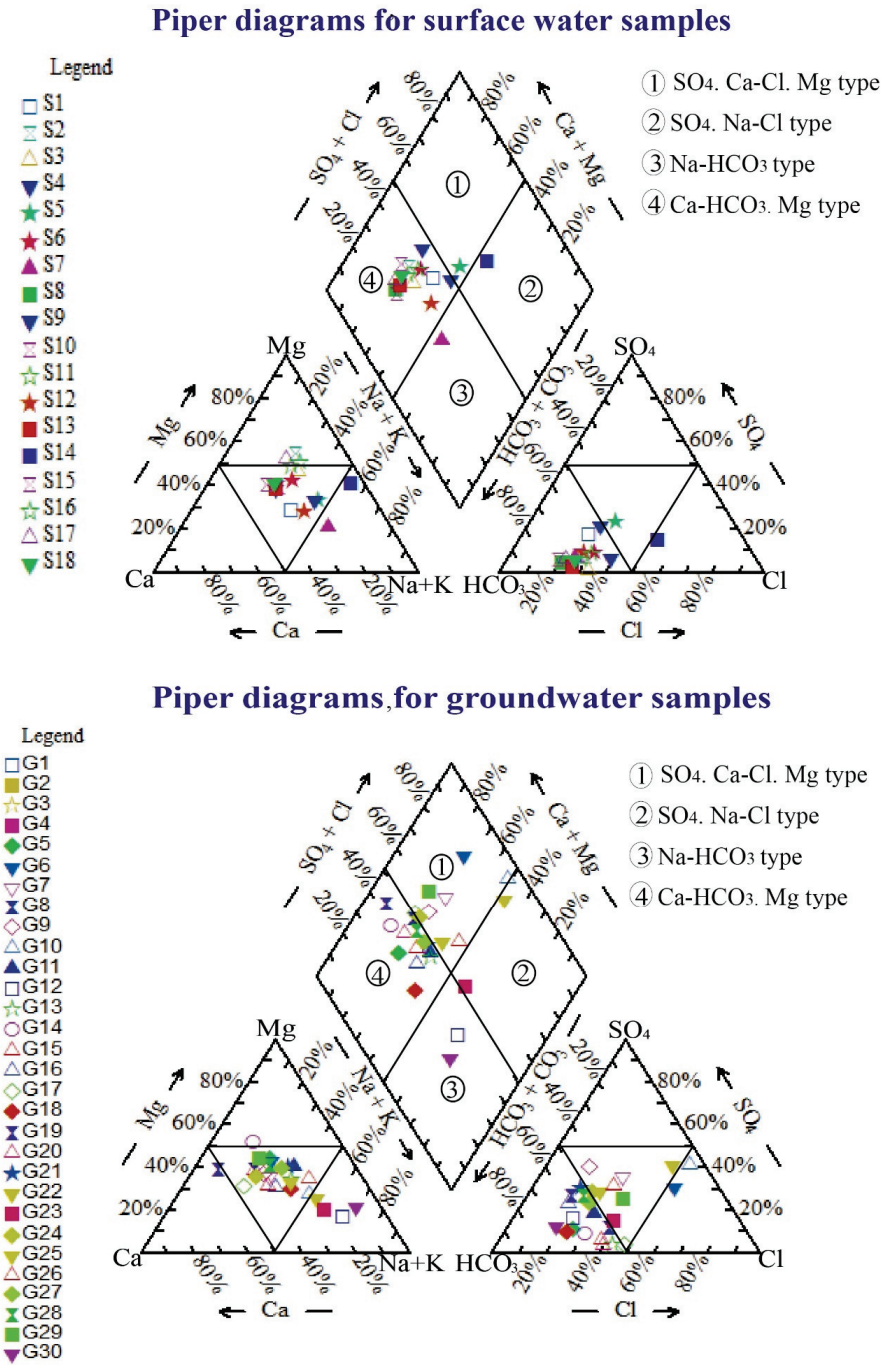

Figure 4. Piper's diagram showing classification of the water samples in the study area.

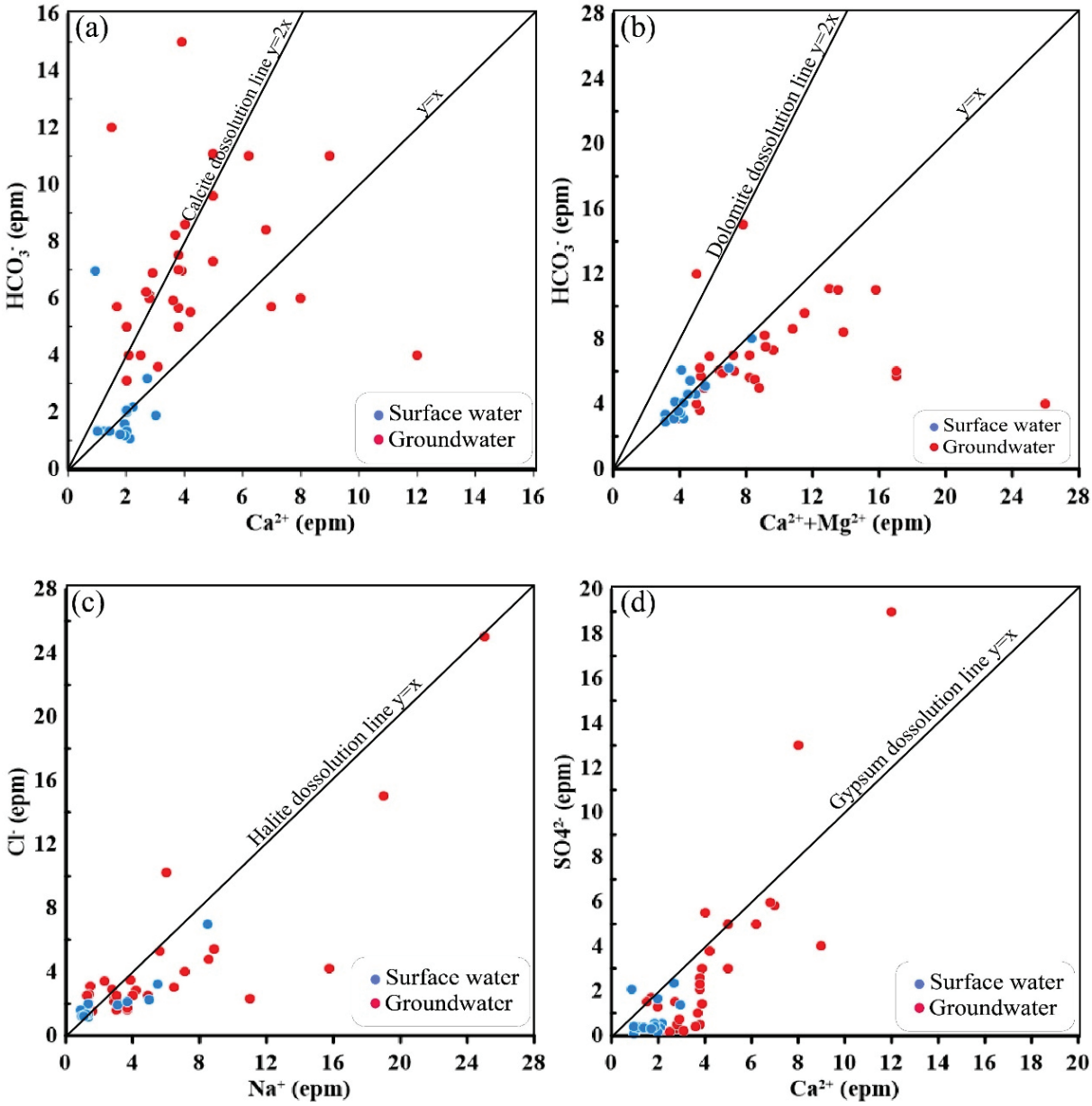

Figure 5. The relationships between the major ions show the dissolution process in the studied water samples (**a**–**d**).

3.3. Chloride Mass Balance (CMB)

The recharge rate (R) of the studied groundwater was shown by CMB to be between 0.89 and 1.6 mm/yr, with a mean of 0.83 mm/yr. The recharge rates (R%) in the study area ranged from 3% to 53%, with an average of 28% of the average annual rainfall. The rest of the rain that fell in the area fell in different ways and did not reach the aquifers as groundwater recharge [50].

3.4. Evaluation of Water for Irrigation

When using irrigation to increase crop output, water quality is a crucial factor. Numerous metrics assess the quality of the water, such as the soluble sodium percentage (SSP) and the sodium absorption ratio (SAR). SAR calculates the salinity risks based on how much sodium the soil has absorbed [37]. The United States Salinity Laboratory staff [51] claims that one may assess the quality of irrigation water by examining the relationship between the SAR on the X-axis and the EC on the Y-axis. Figure 6 shows that, with the exception of

two samples, the surface water samples were low in sodium and had medium salinity [37]. The findings of all surface water samples agree with the conclusions of [24,25] and the samples are suitable for irrigation usage. All groundwater samples range in salinity from low to high and are projected in low sodium water ([37]; Figure 6). Therefore, all of the groundwater samples are suitable for irrigation; these findings are consistent with those of [20,24,26,27].

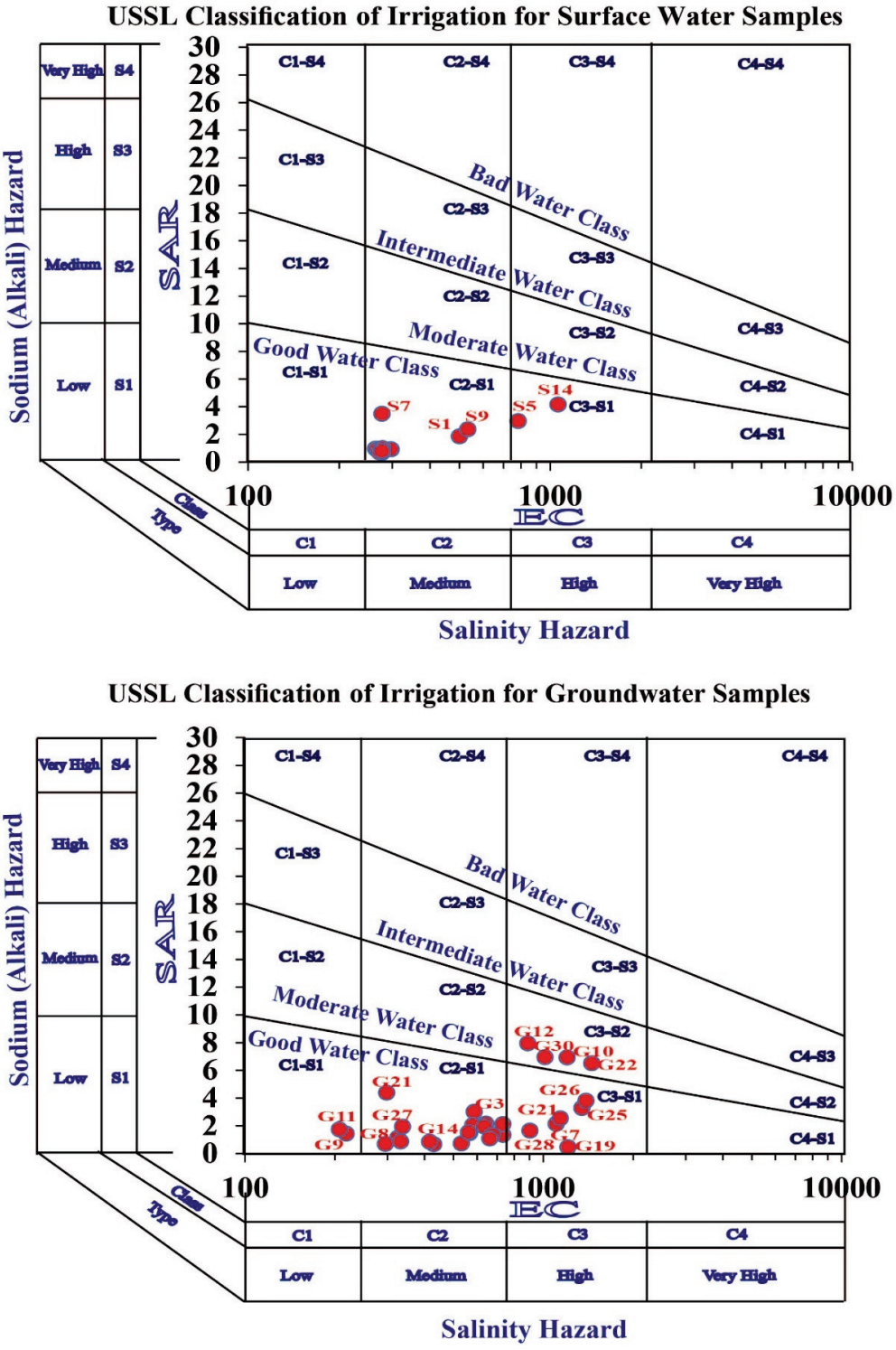

Figure 6. USSL diagram for classification of irrigation waters [36].

The level of sodium concentration in the water was discovered using SSP calculations. It was hypothesized that clay particles absorb Na^+ to concentrate it in soils and displace Mg^{2+} and Ca^{2+} ions, which limits soil permeability when SSP concentrations are above 60 percent [31,52]. With regard to SSP and EC, the Wilcox diagram is a plot sheet that establishes the proportionality of water for irrigation [40]. Figure 7 shows that surface water samples were rated as having good to permissible water quality for irrigation [39]. Meanwhile, the groundwater samples varied in water quality for irrigation from questionable to good, which is consistent with the USSL diagram results (Figures 6 and 7). The authors of [9,20,24–27] all concurred with these findings.

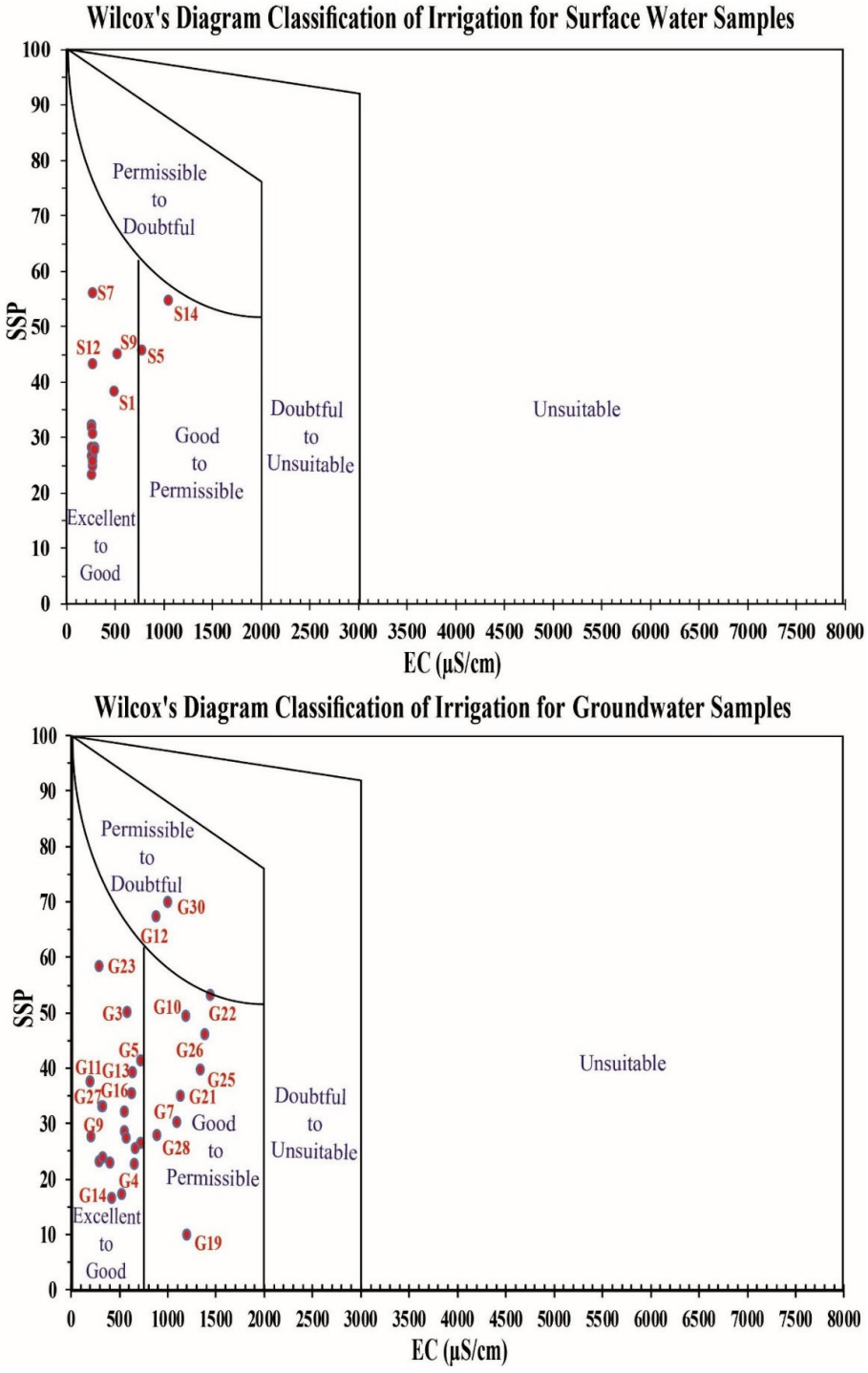

Figure 7. Classification of water irrigation based on the Wilcox diagram.

3.5. Evaluation of Water for Livestock and Poultry

Water quality is greatly impacted by salinity (EC). According to [9,20,24,27] and other researchers, highly salinized water has a negative influence on livestock and poultry as well as plant and soil productivity. For the purposes of using saline water for cattle and poultry, the Food and Agriculture Organization [51] established the standard for water salinity (EC). Table 2 shows that, in accordance with [51], all examined water samples had excellent salinity levels suitable for use with cattle and poultry.

Table 2. Water quality guidelines for livestock and poultry (after [51]).

Salinity (EC μs/cm)	Characters	Water Samples
<1500	Excellent	All the studied water samples
1500–5000	Very satisfactory	-
5000–8000	Satisfactory for livestock, unfit for poultry	-
8000–11,000	Limited for livestock, unfit for poultry	-
11,000–16,000	Very limited use	-
>16,000	Not recommended	-

3.6. Quality Criteria for Industrial Purposes

Water requirements differ by industry [52], and some of these requirements are listed in Table 3. Considering this, the percentages of surface water samples that are suitable for the industries of fruit and vegetable (89%), paper (22%), textile (94%), petroleum (61%), wood chemicals (55%), synthetic rubber (83%), hydraulic cement (94%) and leather tanning (100%) have been calculated (Figure 8).

In addition, the percentages of groundwater samples that were suitable for use were: fruit and vegetable (27%) paper (73%) textile (92%) petroleum (14%) wood chemicals (14%) synthetic rubber (19%) hydraulic cement (54%) and leather tanning industries (73%; Figure 7). Except for the wood sector, the groundwater quality was better than the groundwater quality in El-Obour city [27].

Table 3. Water quality requirements for some industries according to [52].

Parameter	Industries							
	Fruit & Vegetable	Paper	Textile	Petroleum	Wood Chemicals	Synthetic Rubber	Hydraulic Cement	Leather Tanning
pH	6.5–8.5	6–10	6.5–8.5	6–9	6.5–8	6.2–8.3	6.5–8.5	6–8
TDS	500	-	100	1000	1000	-	600	-
TH	250	100	25	350	900	350	-	-
Ca^{2+}	-	20	-	75	100	80	-	-
Mg^{2+}	-	12	-	30	50	36	-	-
HCO_3^-	-	-	-	-	250	-	-	-
Cl^-	250	200	-	300	500	-	250	250
SO_4^{2-}	250	-	-	-	100	-	250	250

Ions expressed in ppm. Note: The absence of values in this table either indicates that the constituent has no limit or that it cannot reach objectionable amounts in water that complies with the other requirements.

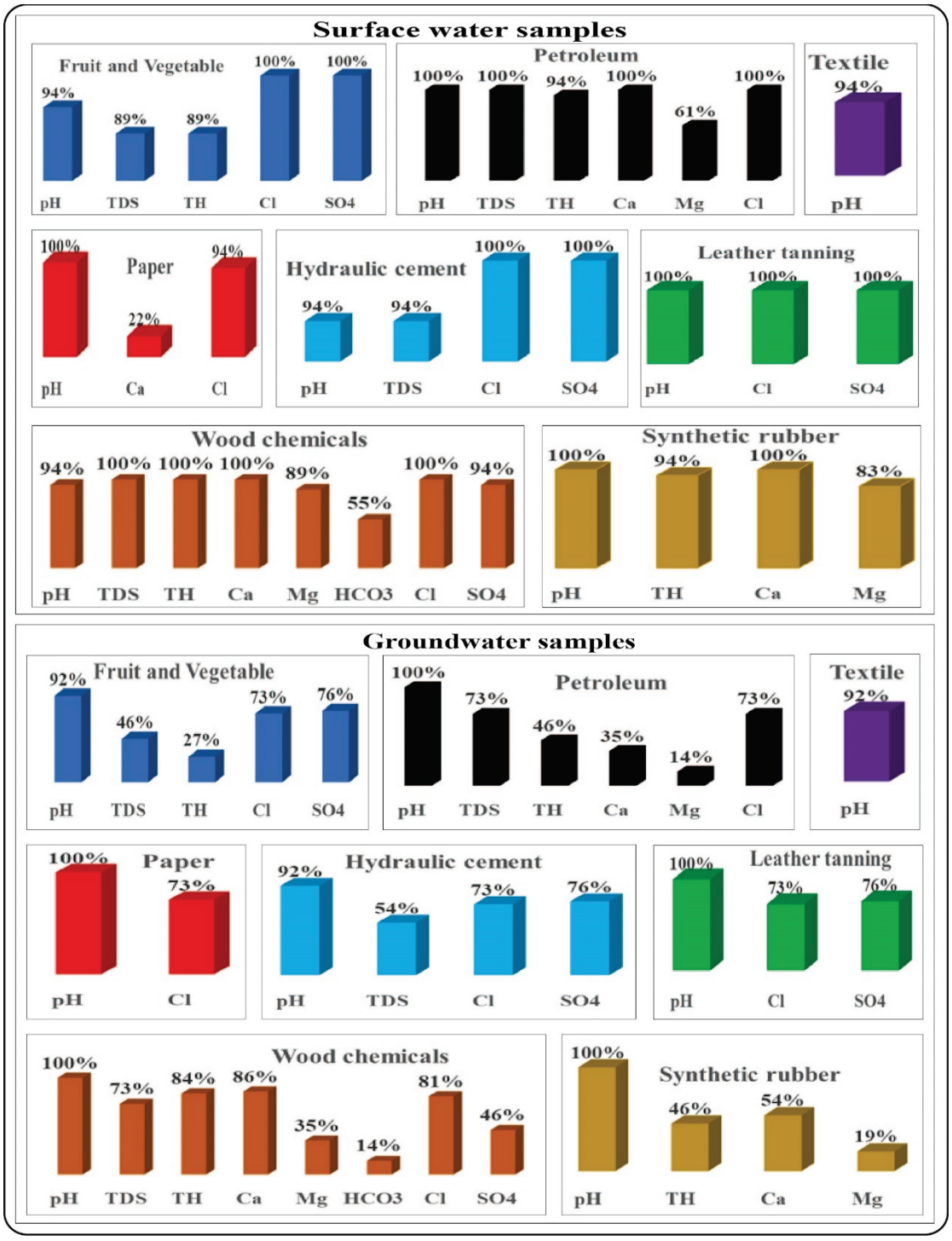

Figure 8. Percentages of the water parameters under investigation that are appropriate for some industries.

4. Conclusions

The pH values of the water samples are neutral. EC results led to the conclusion that the studied water samples are slightly to excessively mineralized. TDS findings expressed that the tested water samples include fresh and very fresh water. The TH readings indicated that the hardness of water samples fluctuate between hard and very hard water. The averages of major ion concentrations revealed that the highest contents in the surface water samples were made up of bicarbonate, chloride, sodium and calcium, respectively. In the groundwater, the highest concentrations were made up of bicarbonate, sulphate, chloride,

sodium and calcium, respectively. The bulk of water samples are characterized by the predominance of bicarbonate ions and the earth's alkaline elements (Ca^{2+} and Mg^{2+}). This was a result of the dissolving of carbonate and evaporite minerals as well as the activities of agricultural water drainage. The examined water samples are suitable for cattle, poultry, and livestock irrigation. The quality of the surface water samples for the use of industrial purposes was often higher than the groundwater samples. The examined water samples had a percentage range of 14 to 94 that made them appropriate for specific sectors. Our recommendation is that the analyzed water samples be used for irrigation, residential purposes, and drinking, except for a few samples from wells whose ion levels exceed the WHO's permissible limits.

Author Contributions: Conceptualization, A.M., A.A. and S.S.A.; methodology, A.A., A.M., S.S.A. and M.A.A.M.; software, A.A.; A.M. and S.S.A.; validation, A.A., S.S.A., A.M. and M.A.A.M.; formal analysis, A.M. and A.A.; investigation, A.A. and S.S.A.; resources, A.M., A.A. and M.A.A.M.; data curation, A.A. and A.M.; writing—original draft preparation, A.A. and A.M.; and writing—review and editing, A.M. and A.A.; visualization, A.A. and A.M.; supervision, A.M., S.S.A. and A.A.; project administration, A.A., A.M. and M.A.A.M.; funding acquisition, S.S.A. All authors have read and agreed to the published version of the manuscript.

Funding: This research was funded by Researchers Supporting Project number (RSP2023R496), King Saud University, Riyadh, Saudi Arabia.

Data Availability Statement: The data is available upon request from the authors.

Acknowledgments: This research was supported by Researchers Supporting Project number (RSP2023R496), King Saud University, Riyadh, Saudi Arabia.

Conflicts of Interest: The authors declare no conflict of interest.

References

1. IPCC. *Climate Change 2001—Impacts, Adaptation and Vulnerability. 3rd Assessment Report of the Intergovernmental Panel on Climate Change*; Cambridge University Press: Cambridge, UK, 2001.
2. Güntner, A. Large-Scale Hydrological Modelling in the Semi-Arid North-East of Brazil. Ph.D. Thesis, Potsdam Institute for Climate Impact Research, Potsdam, Germany, 2002; p. 128.
3. Duran-Encalada, J.A.; Paucar-Caceres, A.; Bandala, E.R.; Wright, G.H. The Impact of Global Climate Change on Water Quantity and Quality: A System Dynamics Approach to the US–Mexican Transborder Region. *Eur. J. Oper. Res.* **2017**, *256*, 567–581. [CrossRef]
4. Chen, S.; Wu, D. Adapting ecological risk valuation for natural resource damage assessment in water pollution. *Environ. Res.* **2018**, *164*, 85–92. [CrossRef] [PubMed]
5. Zhang, Y.; Xu, M.; Li, X.; Qi, J.; Zhang, Q.; Guo, J.; Yu, L.; Zhao, R. Hydrochemical Characteristics and Multivariate Statistical Analysis of Natural Water System: A Case Study in Kangding County, Southwestern China. *Water* **2018**, *10*, 80. [CrossRef]
6. Wu, Z.; Guo, X.; Lv, C.; Wang, H.; Di, D. Study on the quantification method of water pollution ecological compensation standard based on emergy theory. *Ecol. Indic.* **2018**, *92*, 189–194. [CrossRef]
7. Ling, H.; Yan, J.; Xu, H.; Guo, B.; Zhang, Q. Estimates of shifts in ecosystem service values due to changes in key factors in the Manas River basin, northwest China. *Sci. Total Environ.* **2019**, *659*, 177–187. [CrossRef]
8. Ewaid, S.H.; Kadhum, S.A.; Abed, S.A.; Salih, R.M. Development and evaluation of irrigation water quality guide using IWQG V.1 software: A case study of Al-Gharraf Canal, Southern Iraq. *Environ. Technol. Innov.* **2019**, *13*, 224–232. [CrossRef]
9. Jahin, H.S.; Abuzaid, A.S.; Abdellatif, A.D. Using multivariate analysis to develop irrigation water quality index for surface water in Kafr El-Sheikh Governorate, Egypt. *Environ. Technol. Innov.* **2020**, *17*, 100532. [CrossRef]
10. Tanui, F.; Olago, D.; Dulo, S.; Ouma, G.; Kuria, Z. Hydrogeochemistry of a strategic alluvial aquifer system in a semi-arid setting and its implications for potable urban water supply: The Lodwar Alluvial Aquifer System (LAAS). *Groundw. Sustain. Dev.* **2020**, *11*, 100451. [CrossRef]
11. Devi, G.; Goswami, L.; Kushwaha, A.; Sathe, S.S.; Sen, B.; Sarma, H.P. Fluoride distribution and groundwater hydrogeochemistry for drinking, domestic and irrigation in an area interfaced near Brahmaputra floodplain of North-Eastern India. *Environ. Nanotechnol. Monit. Manag.* **2021**, *16*, 100500. [CrossRef]
12. Yuan, Q.-S.; Wang, P.-F.; Chen, J.; Wang, C.; Liu, S.; Wang, X. Influence of cascade reservoirs on spatiotemporal variations of hydrogeochemistry in Jinsha River. *Water Sci. Eng.* **2021**, *14*, 97–108. [CrossRef]
13. Rayan, M.A.; Djebedjian, B. Egypt's water demand, supply and management policies. *Int. Water Demand Manag. Conf. Jordan* **2004**, *30*, 1–24.

14. Moghazy, N.H.; Kaluarachchi, J.J. Assessment of groundwater resources in Siwa Oasis, Western Desert, Egypt. *Alex. Eng. J.* **2019**, *59*, 149–163. [CrossRef]
15. CAPMAS. Annual Bulletin of Statistical Crop Area and Plant Production, Cent. Agency Public Mobilization Stat, 2000–2011. 2019. Available online: https://www.capmas.gov.eg/Pages/Publications.aspx?page_id=5104&Year=23439 (accessed on 10 August 2019).
16. Nour El-Din, M.M. Proposed Climate Change Adaptation Strategy for the Ministry of Water Resources & Irrigation in Egypt. Report of the UNESCO Cairo Office. Joint Programme for Climate Change Risk Management in Egypt, January 2013. 2017. Available online: https://www.eeaa.gov.eg/Uploads/Project/Files/20221123101650781.pdf (accessed on 10 May 2017).
17. CAPMAS. Population Estimates by Sex and Governorate 1/1/2015. Archived (PDF) from the original on 19 October 2015.
18. UNICEF; World Health Organization. *Progress on Sanitation and Drinking Water—2015 Update and MDG Assessment*; WHO: Geneva, Switzerland, 2015.
19. Salman, S.A.; Asmoay, A.A.; El-Gohary, A.; Sabet, H. Evaluation of human risks of surface water and groundwater contaminated with Cd and Pb in the southern El-Minya Governorate, Egypt. *Drink. Water Eng. Sci.* **2019**, *12*, 23–30. [CrossRef]
20. Ibrahim, R.G.M.; Korany, E.A.; Tempelc, R.N.; Gomaa, M.A. Processes of water–rock interactions and their impacts upon the groundwater composition in Assiut area, Egypt: Applications of hydrogeochemical and multivariate analysis. *J. Afr. Earth Sci.* **2019**, *149*, 72–83. [CrossRef]
21. Qureshi, A.S.; Al-Falahi, A. Extent, characterization, and causes of soil salinity in central and southern Iraq and possible reclamation strategies. *Int. J. Eng. Res. Appl.* **2015**, *5*, 84–94.
22. Bortolini, L.; Maucieri, C.; Borin, M. A Tool for the Evaluation of Irrigation Water Quality in the Arid and Semi-Arid Regions. *Agronomy* **2018**, *8*, 23. [CrossRef]
23. Rahi, K.A.; Halihan, T. Salinity evolution of the Tigris River. *Reg. Environ. Chang.* **2018**, *18*, 2117–2127. [CrossRef]
24. Asmoay, A.S.A. Hydrogeochemical Studies on the Water Resources and Soil Characteristics in the Western Bank of the River Nile between Abu Qurqas and Dayr Mawas, El Minya Governorate, Egypt. Ph.D. Thesis, Al-Azhar University, Cairo, Egypt, 2017.
25. Sabet, H.; El-Gohary, A.; Salman, S.; Asmoay, A. Evaluation of Surface Water for Different Uses in the Area Between Abu Qurqas—Dyer Mawas Districts, El Minya Governorate, Egypt. *IJISET Int. J. Innov. Sci. Eng. Technol.* **2017**, *4*, 120–128.
26. El-Gohary, A.M.; Sabet, H.S.; Salman, S.A.; Asmoay, A.S. Hydrogeochemistry of groundwater quality in the area between of Abu Qurqas—Dayer Mawas districts, El Minya Governorate, Upper Egypt. *Int. J. Recent Adv. Multidiscip. Res.* **2017**, *4*, 2493–2497.
27. Zeid, S.A.; Seleem, E.M.; Salman, S.A.; Abdel-Hafiz, M.A. Water quality index of shallow groundwater and assessment for different usages in El-Obour city Egypt. *J. Mater. Environ. Sci.* **2018**, *9*, 1957–1968.
28. Centers for Disease Control and Prevention; U.S. Department of Housing and Urban Development. *Healthy Housing Reference Manual*; U.S. Department of Health and Human Services: Atlanta, GA, USA, 2006.
29. Mohamed, A.; Asmoay, A.; Alshehri, F.; Abdelrady, A.; Othman, A. Hydro-Geochemical Applications and Multivariate Analysis to Assess the Water–Rock Interaction in Arid Environments. *Appl. Sci.* **2022**, *12*, 6340. [CrossRef]
30. Said, R. *The Geological Evolution of the River Nile*; Springer: New York, NY, USA, 1981. [CrossRef]
31. Conoco. Egyptian general authority for petroleum. In *Scale (1:500,000) between El-Minia and Sohag*; Conoco: Ponca City, OK, USA, 1987.
32. Said, R. *The Geology of Egypt*; Balkema Publishing Company: Rotterdam, The Netherlands; Brookfield, WI, USA, 1990; 734p.
33. RIGW. *Hydrogeological Map of Egypt, Assuit and Manfalut, Scale 1:100,000*, 1st ed.; 1994.
34. Sadek, M.A. Isotopic criteria for upward leakage in the alluvial aquifer in north El Minia district, Egypt. *Ann. Geol. Surv. Egypt* **2001**, *XXIV*, 585–596.
35. APHA. *Standard Methods for the Examination of Water and Wastewater*, 19th ed.; American Public Health Association: Washington, DC, USA, 1995.
36. USSL. Diagnosis and improvement of saline and alkaline soils. In *United State Science Laboratory Department, Agriculture Handbook*; USDA: Washington, DC, USA, 1954; Volume 60, 147p.
37. Todd, D.K. *Groundwater Hydrology*, 2nd ed.; John Wiley: New York, NY, USA, 1980; 535p.
38. World Health Organization. *Guidelines for Drinking-Water Quality: Fourth Edition Incorporating the First and Second Addenda*; WHO: Geneva, Switzerland, 2022.
39. Wilcox, L.V. *Classification and Use of Irrigation Waters, USDA, Circular 969*; United States Department of Agriculture: Washington, DC, USA, 1955.
40. Miller, H.J. The amounts of nitrogen as ammonia and as nitric acid and chlorine in the rainwater collected at Rothamsted. *J. Agric. Sci.* **1902**, *1*, 280–303. [CrossRef]
41. Eriksson, E. Composition of Atmospheric Precipitation. *Tellus* **1952**, *4*, 280–303. [CrossRef]
42. Uugulu, S.; Wanke, H. Estimation of groundwater recharge in savannah aquifers along a precipitation gradient using chloride mass balance method and environmental isotopes, Namibia. *Phys. Chem. Earth Parts A/B/C* **2020**, *116*, 102844. [CrossRef]
43. Segobaetso, T.K.; Tafesse, N.T.; Mapeo, R.; Laletsang, K. Groundwater recharge using the chloride mass balance method in the Kanye area, in southeast Botswana. *J. Afr. Earth Sci.* **2022**, *193*, 104534. [CrossRef]
44. Boyd, C.E. *Water Quality: An Introduction*; Kluwer Academic Publisher: New York, NY, USA, 2000; 330p.
45. Piper, A.M. A graphic procedure in the geochemical interpretation of water-analyses. *Eos Trans. Am. Geophys. Union* **1944**, *25*, 914–928. [CrossRef]

46. Bai, X.; Tian, X.; Li, J.; Wang, X.; Li, Y.; Zhou, Y. Assessment of the Hydrochemical Characteristics and Formation Mechanisms of Groundwater in A Typical Alluvial-Proluvial Plain in China: An Example from Western Yongqing County. *Water* **2022**, *14*, 2395. [CrossRef]
47. Gibbs, R.J. Mechanisms Controlling World Water Chemistry. *Science* **1970**, *170*, 1088–1090. [CrossRef]
48. Ayers, R.S.; Westcott, D.W. *Water Quality for Agriculture. Irrigation and Drainage*; Paper No. 29; FAO: Rome, Italy, 1985.
49. Fipps, G. *Irrigation Water Quality Standards and Salinity Management*; Texas A & M University System: College Station, TX, USA, 1998.
50. He, Y.; DeSutter, T.; Casey, F.; Clay, D.; Franzen, D.; Steele, D. Field capacity water as influenced by Na and EC: Implications for subsurface drainage. *Geoderma* **2015**, *245–246*, 83–88. [CrossRef]
51. FAO. *Water for Animal*; Report AGL/MISC/4/85; FAO: Rome, Italy, 1986.
52. Hem, J.D. *Study and Interpretation of the Chemical Characteristics of Natural Water*, 3rd ed.; U.S. Geological Survey: Reston, VA, USA, 1985; 264p.

Disclaimer/Publisher's Note: The statements, opinions and data contained in all publications are solely those of the individual author(s) and contributor(s) and not of MDPI and/or the editor(s). MDPI and/or the editor(s) disclaim responsibility for any injury to people or property resulting from any ideas, methods, instructions or products referred to in the content.

hydrology

MDPI

Article

Modeling a Metamorphic Aquifer through a Hydro-Geophysical Approach: The Gap between Field Data and System Complexity

Francesco Chidichimo [1,*], Michele De Biase [1], Francesco Muto [2] and Salvatore Straface [1]

[1] DIAm, Department of Environmental Engineering, University of Calabria, 87036 Rende, Italy
[2] DIBEST, Department of Biology, Ecology and Earth Sciences, University of Calabria, 87036 Rende, Italy
* Correspondence: francesco.chidichimo@unical.it

Abstract: The productivity of metamorphic aquifers is generally lower than that of the more common alluvial and carbonates ones. However, in some Mediterranean areas, such as the Calabria region (Italy), water scarcity combined with the presence of extensive metamorphic water bodies requires the development of further studies to characterize the hydrodynamic properties of these groundwater systems in order to achieve their sustainable exploitation. The interest in this goal becomes even greater if climate change effects are considered. The purpose of this study was to provide the geological-structural and hydrogeological numerical modeling of a metamorphic aquifer, using direct and indirect data measurement, in a large area of the Sila Piccola in Calabria. The hydrodynamic characterization of the crystalline-metamorphic aquifer, constituted by granite and metamorphic rocks, is extremely complex. The MODFLOW-2005 groundwater model was used to simulate flow phenomena in the aquifer, obtaining hydraulic conductivity values of 2.7×10^{-6} m/s, which turned out to be two orders of magnitude higher than those obtained from the interpretation of the slug-tests performed in the study area. The mathematical model was also able to estimate the presence of a lateral recharge from a neighboring deep aquifer providing a significant water supply to the system under investigation.

Keywords: crystalline-metamorphic aquifer; geological survey; macrostructural and meso-structural analysis; slug tests; electrical resistivity tomography; hydrodynamic properties; aquifer characterization; inverse modeling

1. Introduction

Groundwater in altered and fractured metamorphic aquifers represents the only water resource for many areas, especially in arid and semi-arid regions [1,2]. These aquifers are generally characterized by low water productivity due to their low permeability and porosity. However, the presence of water in these formations depends on various factors such as lithology, tectonics, geodynamics, and climatic conditions. Many studies have shown that their presence is inside the surface mantle and in fissured rocks where the groundwater flow takes place. Moreover, geochemical alteration, tectonic activity, and lithostatic decompression processes are the cause of the generation of cracks inside metamorphic rocks [3–6]. Geodynamic and geomorphic processes affecting the presence of groundwater also have an important influence on the hydraulic conductivity of these geological formations. In crystalline rocks, for example, the hydraulic conductivity can vary up to 12 orders of magnitude [7–10].

The estimate of these parameters, at the aquifer scale, is not the only problem to face for a correct modeling of groundwater flow and transport processes, but also the reconstruction of their spatial pattern is not an easy task. Several methods for the regionalization of hydraulic conductivity or transmissivity, at the aquifer scale, have been proposed, but most of them have been applied to sedimentary or alluvial aquifers. These methods use

extensive hydrodynamic parameter datasets, deduced from pumping or slug tests, to obtain their spatial distribution through geostatistical approaches [11–17]. Geostatistical techniques can be combined with geological facies information to reconstruct the aquifer, as a multiple continuum or a composite medium, providing promising results for the up-scaling of hydrodynamic parameters [18–25]. Further methods based on hydro-geophysical approaches were developed, e.g., [26–30], leading to transmissivity regionalization by combining them with geostatistical techniques, e.g., [31,32]. Such a setup, however, requires thorough field investigations [33].

The characterization of the hydrodynamic properties in hard-rock aquifers, i.e., made up of granite and metamorphic rocks, is a complex problem due to the strong heterogeneity of the system. A network of secondary connections, of different order and degree, takes place among the main fractures, generating a continuous variation in the hydrodynamic properties at different scales and defining the modulus and direction of the groundwater flow, e.g., [34–37]. The field data amount that would be necessary to properly define such systems is difficult to achieve, so the continuum approach is often used in order to deal with large-scale hydrodynamic parameter spatial distributions [38,39]. Although several studies have concluded that the approximation of a fractured medium into a porous one is only valid in densely fractured aquifers [40–42], the scientific debate on this topic is still very open, especially regarding the scale at which this approximation is still suitable [43–47].

In Italy, large areas of the country are covered by metamorphic rocks, and yet the hydrogeological properties of these formations are not well known. Some of the few studies, carried out in the national territory through injection tests, clearly showed the extreme heterogeneity of the rock mass, highlighted by the wide range of values determined for the hydraulic conductivity ($10^{-8} \div 10^{-6}$ m/s) [3,48]. The knowledge of this parameter is of fundamental importance given the extreme variability and heterogeneity of the lithologies with which an aquifer may be constituted. Figure 1 shows representative values of hydraulic conductivity for selected unconsolidated sedimentary materials, and sedimentary and crystalline rocks [49,50].

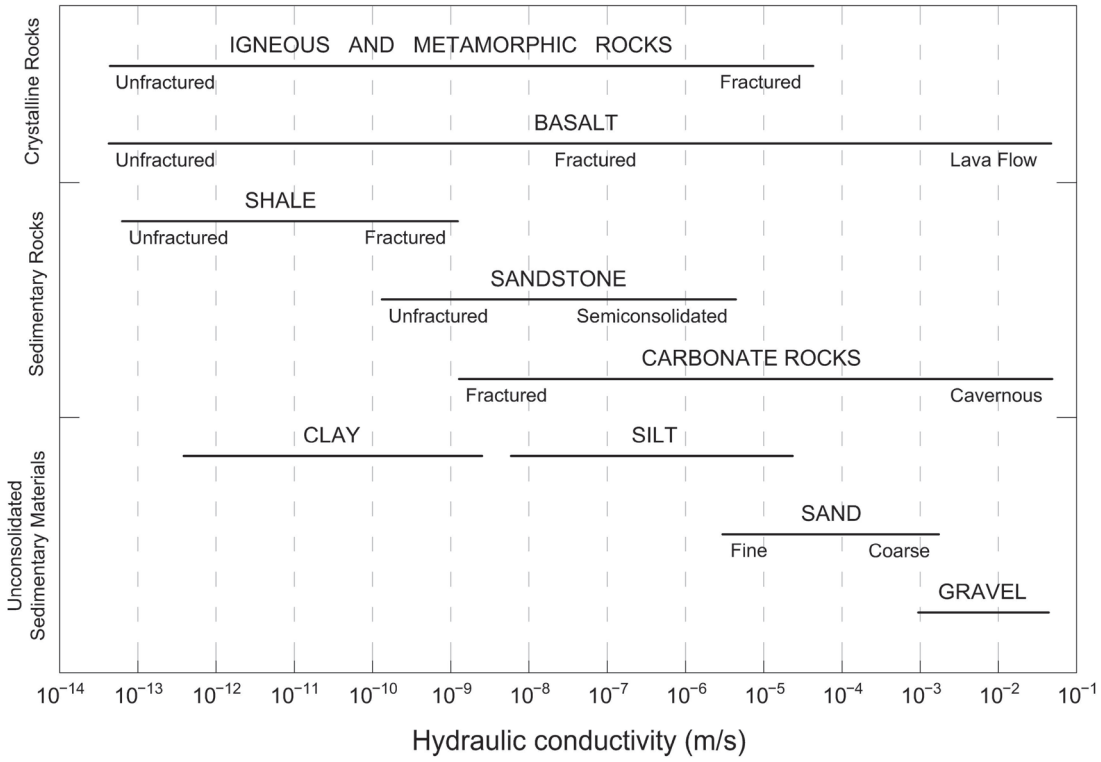

Figure 1. Hydraulic conductivity of selected consolidated and unconsolidated geologic materials (from [49,50]).

In some Mediterranean areas such as in Calabria region, the scarcity of water resources and the considerable extension of metamorphic aquifers (39% of the regional area) would require further studies either on their hydrodynamic properties and their hydraulic behavior in order to achieve their sustainable exploitation.

Interest in these metamorphic aquifers becomes even greater if climate change effects are considered. Many climatic scenarios relating to the Mediterranean area foresee a reduction in rainfall and an increase in storm water events; this will lead to a lower infiltration recharge for aquifers and a higher hydrogeological hazard for the territory [51].

This is the context of our work focusing on the study of a metamorphic aquifer in the Calabrian Arc where a reduction in the average water availability, from one side, and a high risk of landslides in the wettest periods, on the other, represent a major challenge to deal with [52].

The purposes of the study are: (i) to contextualize the geological and structural setting and the gravitational phenomena occurring in a large area of Sila Piccola, Calabria; (ii) to recognize and characterize the geometries of the metamorphic aquifer, located in that zone, using field data derived from springs, wells, and boreholes; (iii) to define the geometric-structural relationships of the geological and lithological units.

2. Materials and Methods

The basin including the slope on the inhabited center of Gimigliano was the object of in-depth study through the realization of continuous-core boreholes. Inclinometers and piezometers were installed at different depths. The obtained data were continuously processed for a significant time interval. Mass movements of variable size and depth were mapped. Particular attention was paid to large landslides, together with other geomorphological processes, which have conditioned the morphology of the entire area.

Geological and regional-scale literature reviews, together with acquired site-specific data, were considered as a starting point. Surface surveys were implemented by geoelectric tomography profiles and by geognostic investigations performed at various depths. A preliminary geological model allowed the planning of these geophysical and geognostic surveys, intended for the support of direct subsurface data and the elaboration of the final geological and hydrogeological models.

The recognition of the geometries and the stratigraphic relationships between the outcropping rocks and the lithological units around the town of Gimigliano, and more generally in the valleys of the Corace and Melito Rivers, were accompanied by macrostructural and meso-structural analysis to better evaluate the level of fracturing of the rock mass.

2.1. Geological Setting

The study area lies within a large sector of the Calabrian chain in the junction zone of the Sila Massif and the Catanzaro Strait (Figure 2). It is located along tectonic lines of a regional extension transversely crossing northern Calabria from the Tyrrhenian to the Ionian margin. The action of these transverse systems of regional faults is more evident in the sector just south of the study area, where the Lamezia-Catanzaro fault zone, e.g., [53–55], represents the master fault of a larger and more extensive system (e.g., Amantea-Gimigliano Fault). In this area, the chain is made up of Paleozoic crystalline rocks, Mesozoic metamorphic ophiolithiferous rocks, and Tertiary-Quaternary deposits (Figure 2). This group of metamorphic units, organized in numerous superimposed lithology associations, belong to the regional geological structure of Northern Calabria [54,56–58] (Figure 2).

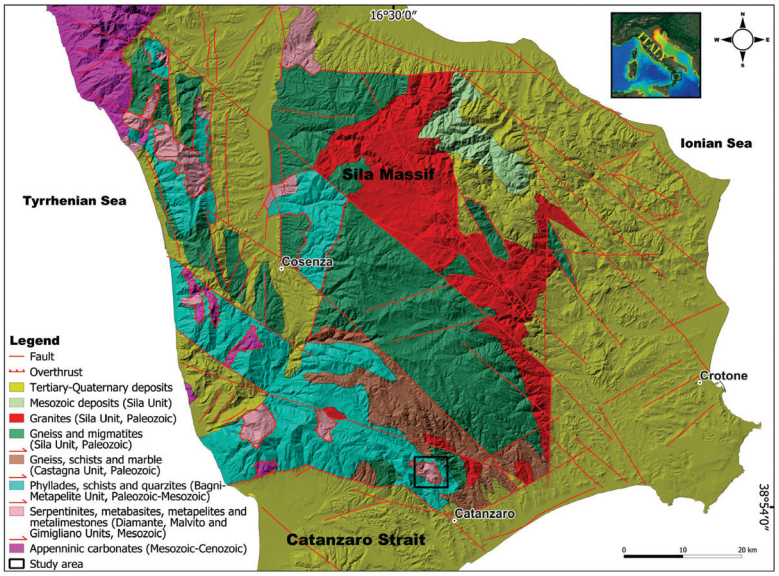

Figure 2. Schematic geological map of the northern Calabria. The black square in the southeastern sector indicates the location of the study area. Modified after Dijk et al. ii 2000 [53] and Tansi et al. ii 2007 [54].

The geometrically lowest units are represented by Apennine Meso-Cenozoic carbonate sequences, overthrusted by alpine and prealpine crystalline and metamorphic rocks of low-mid-high metamorphic grade [59] (Figures 2 and 3). The group of tectonic units in the intermediate position includes mesozoic metaophiolites with metasedimentary cover and sedimentary rocks (Figure 3).

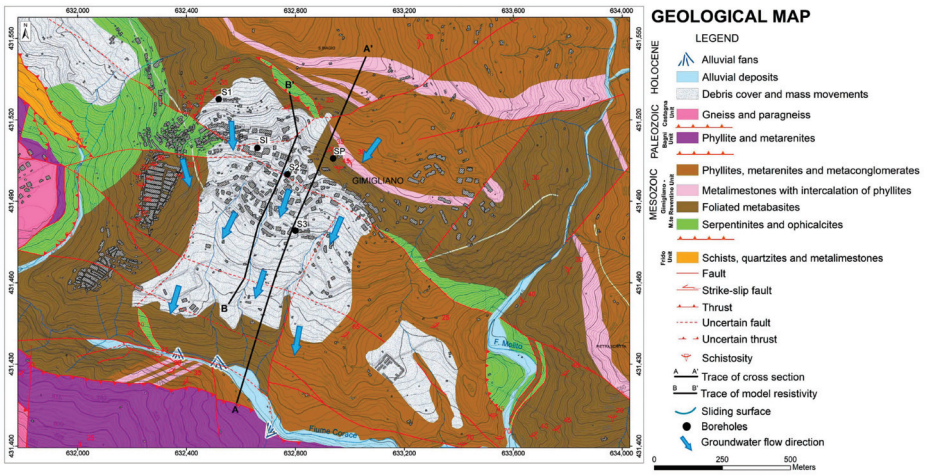

Figure 3. Detailed geological map of the Corace River-Gimigliano village area. A-A' is the geological cross-section trace. In the central sector (white color), the landslide and slope deposits are mapped.

The geolithological and structural analysis is the result of an original geological survey performed at a scale of 1:5000 after the photo-interpretative analysis of a significant portion of the hydrographic basin where the town of Gimigliano is located. In particular, the lithotype out-cropping in the Gimigliano area belongs to a tectonic-metamorphic unit package. From bottom to top, metamorphic rocks consisting of metapelites, metarenites, quartzites, and metalimestones are recognized in a small tectonic window and in boreholes at variable depth (ca., 60 m from surface) (Figure 3). The unit corresponds to the Frido Formation and lies on the carbonate Apennine units.

These rocks are tectonically covered by a complete ophiolitic sequence consisting of serpentinites and metabasites that overlap phyllites, metarenites, and locally thick intervals of crystalline limestones (Gimigliano-Monte Reventino Ophiolitic Unit, Figure 3 and, thanks to the interpretation of the results shown in Figure 4, see also the geological reconstruction of Figure 5). The ophiolite sequences are overthrusted by older metamorphic rocks, schists, and phyllites (Bagni Unit) and by paragneiss (Castagna Unit) (Figures 3 and 5). The reconstruction of the stratigraphic succession is complex because of polydeformed units in a ductile and then brittle environment. However, good superficial exposures of the various lithologies have allowed the identification of the main contacts between the rock associations and their state of deformation (i.e., texture, structure, fracturing, and faulting).

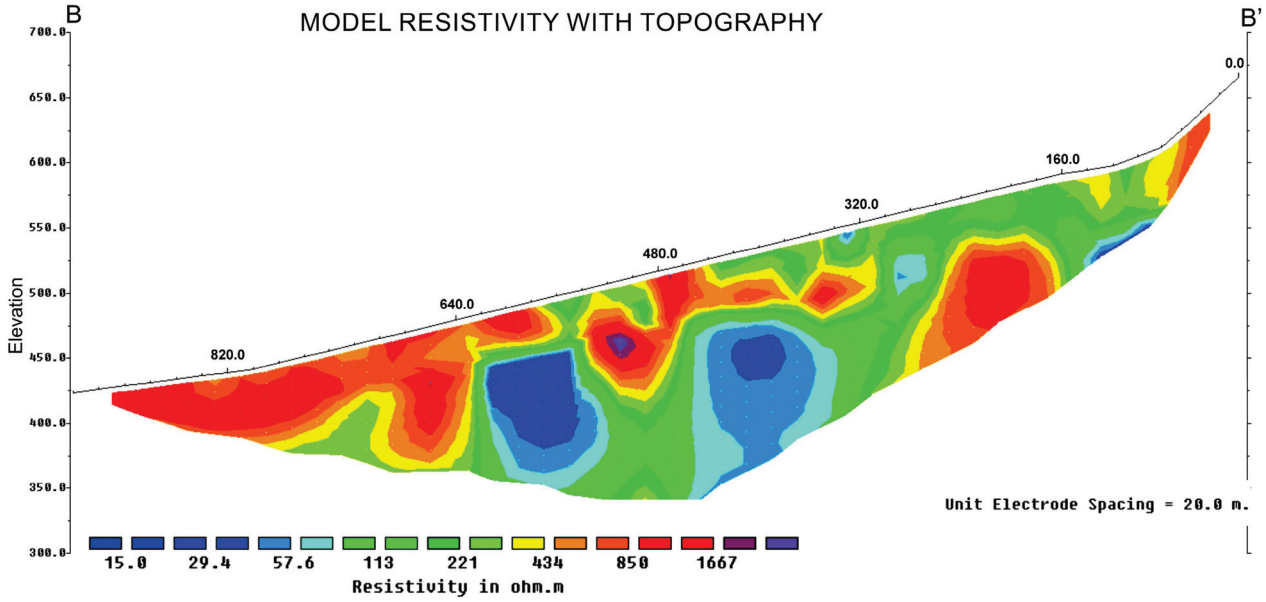

Figure 4. Model of resistivity of the B-B' (ERT) longitudinal section.

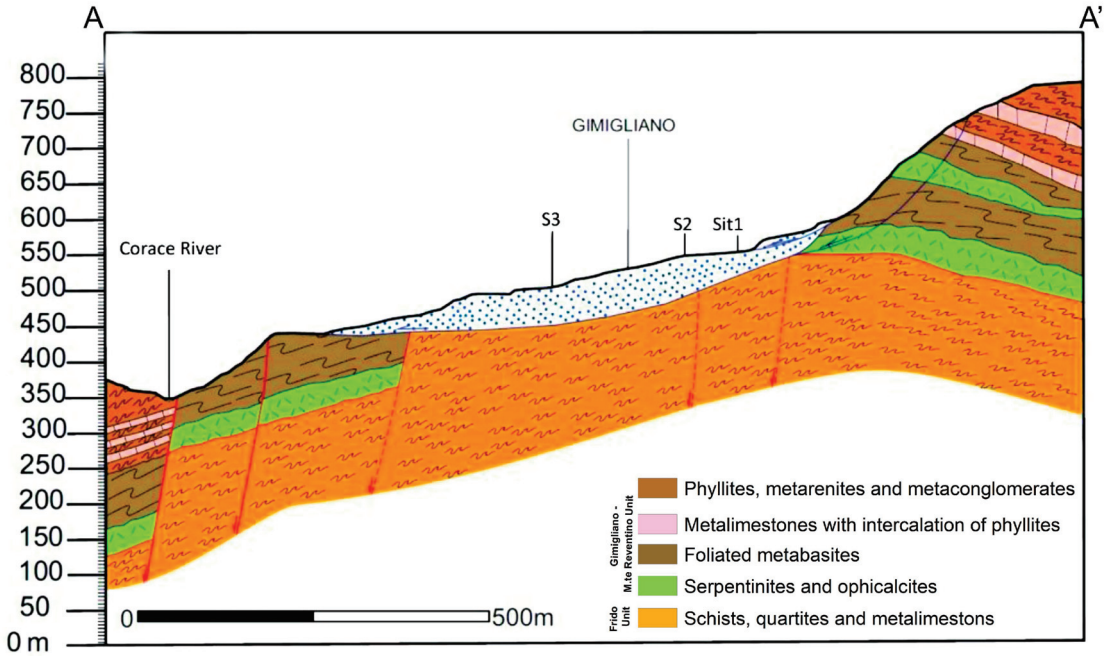

Figure 5. Geological cross-section along the longitudinal A-A' trace (Figure 3). The 2D geological-structural model is the result of the field survey, borehole stratigraphies, and ERT interpretation.

To better investigate the geometries of the lithological units and the most important tectonic structures detected in the field survey, geoelectric tomography profiles were performed. The orientation is shown in Figure 3 and varies between mainly N–S trending and longitudinal to the slope.

The longest longitudinal profile (B-B' in Figures 3 and 4) is about 1 km for a maximum investigation depth of about 200 m. The resistivity model highlights a chaotic and medium-high resistivity distribution of the electro layers (Figure 4). The thickness of this "chaotic" horizon varies between 55 and 60 m, corresponding to the gravitational sliding surface. Below this interval, a resistivity distribution showing sub-vertical geometries with a lateral alternation of low- and high-resistivity rock volumes can be observed.

The interpretation of the geophysical data, together with the field geological analysis and the stratigraphic characterization of boreholes, allowed the implementation of the two-dimensional geological-structural model of Figure 5. The section describes the geometries of vertical succession of the various lithologies, the antiformal fold, the major faults, the depth, and the geometry of the sliding surfaces of gravitational origin.

2.2. Hydrogeological Setting

A series of geognostic investigations were carried out to reconstruct the conceptual hydrogeological model of the study area, according to the indications provided by the geological model. Thirteen boreholes were drilled into the metamorphic aquifer at different depths and locations. During the spring season, the water table depths were measured. They are reported in Table 1 together with the geometrical characteristics of the drilled boreholes.

Table 1. Geometrical characteristics of the boreholes drilled into the aquifer and water table depths measured during the spring season.

Borehole	Diameter (mm)	Borehole Depth (m)	Filter Depth (m)	Water Table Depth (m)
S1a	220	8.00	3.00–8.00	Dry
S1b	160	38.00	33.00–38.00	Dry
S1c	160	51.00	43.00–50.00	Dry
S2a	160	13.00	6.00–13.00	8.75
S2b	160	25.00	16.00–25.00	8.75
S2c	160	42.00	30.00–42.00	8.75
S3a	160	8.00	2.00–8.00	Dry
S3b	160	30.00	14.00–30.00	20.30
S3c	160	48.00	38.00–47.00	33.60
SITa	160	40.00	15.00–25.00	11.95
SITb	160	40.00	0.00–10.00	Dry
SITc	108	40.00	0.00–40.00	10.05
SP	160	60.00	0.00–60.00	32.73

The phreatic aquifer, characterized by low-sodium groundwater rich in calcium and magnesium bicarbonates, flows above the schists' formation, which constitutes the bottom of the groundwater body, whereas the main water circulation occurs within the serpentinites and metabasites formations (Figure 5). Its thickness varies in a range between 10 and 50 m, and the average water table depth stands at around 13 m with respect to the ground level. The aquifer is fed by superficial infiltration provided by rainfall and by a possible underground supply from a neighboring aquifer to the north. This last point is one of the key aspects of the study. The natural aquifer discharge is represented by the Corace river, a permanent water course flowing in the southern boundary of the area under investigation.

Slug tests were performed in no-dry piezometers in order to estimate the value of the hydraulic conductivity of the hard-rock Gimigliano aquifer (Table 2, Figure 3). The acquired data were interpreted using the Bouwer–Rice Method [60] because of the unconfined nature of the aquifer (Figure 6). This method is based on the mathematical model defined as follows:

$$\frac{\partial^2 h}{\partial r^2} + \frac{1}{r}\frac{\partial h}{\partial r} + \frac{K_v}{K_r}\frac{\partial^2 h}{\partial t^2} = 0 \quad (1)$$

where h is the hydraulic head (L), r is the generic radial distance (L), and K_v and K_r are the vertical and horizontal components of the hydraulic conductivity (L/T), respectively. For the initial and boundary conditions, see [60].

Table 2. Summary of the Slug Tests' results carried out in different piezometers. The table shows the lithology and the hydraulic conductivity obtained with the Bouwer–Rice method.

Borehole	Lithology	Hydraulic Conductivity (m/s)
S1a	Highly weathered metabasites	na (dry)
S1b	Highly fractured schists	na (dry)
S1c	Weathered and locally intact metabasites	na (dry)
S2a	Highly weathered phyllites	9.90×10^{-8}
S2b	Highly weathered metabasites	6.77×10^{-8}
S2c	Highly weathered serpentinites	7.51×10^{-8}
S3a	Highly weathered metabasites	na (dry)
S3b	Metabasites with quartz vein	1.80×10^{-7}
S3c	Weathered metabasites reduced to coarse sands	7.44×10^{-8}

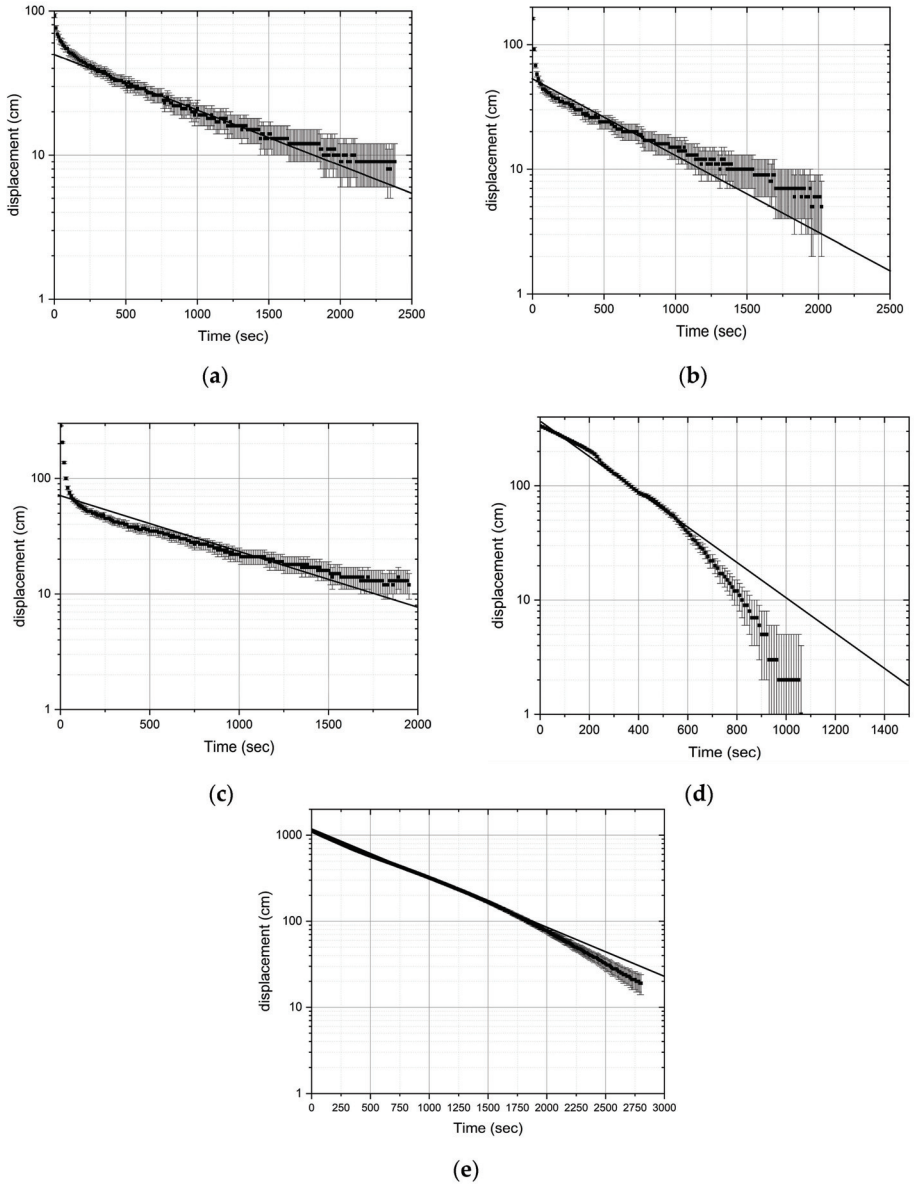

Figure 6. Logarithm of hydraulic head displacement (H) and measurement error bars vs. time plot of slug tests performed in boreholes S2a (**a**), S2b (**b**), S2c (**c**), S3b (**d**), and S3c (**e**) at the Gimigliano study area.

The analytical solution for the mathematical model defined by Equation (1), with the prescribed initial and boundary conditions [60], can be written as [61,62]:

$$ln\left(\frac{H(t)}{H_0}\right) = -\frac{2K_r bt}{r_c^2 ln\left(\frac{R_e}{r_w^*}\right)} \quad (2)$$

where $r_w^* = r_w\sqrt{K_z/K_r}$, H is the variation in the hydraulic head in the well with respect to the static condition (L), t is the total time from the start of the test (T), H_0 is the measurement of the initial displacement due to the slug immediately after the start of the test (L), b is the length of the well screen (L), r_c is the radius of the well casing (L), R_e is the effective radius parameter (L), r_w is the effective radius of the well-filter section (L), and K_z is the vertical component of the hydraulic conductivity (L/T).

If the slug test is performed in boreholes screened across the water table, Bouwer and Rice [61] recommend using an effective casing radius r_c given by the following formula:

$$r_c = \sqrt[2]{r_{nc}^2 + n(r_w^2 - r_{nc}^2)} \quad (3)$$

where r_{nc} is the nominal radius of the well screen (L) and n is the drainable porosity of the filter pack (dimensionless).

The springs falling in the study area were surveyed by cartographic analysis, field campaigns, and published studies. IGM cartography and geological maps of the Calabria region were used [63] along with technical cartography [64]. Among all the emergencies identified at the cartographic level, those with greater importance (more conspicuous water flows provided with continuity throughout the year) were sought in the area as relevant for the research.

Water sources were mostly distributed in the central sector of the slope and landslide area, and according to their conspicuous frequency, the presence of a phreatic aquifer can be confirmed (Figures 7 and 8). The following springs were considered in the study as they are perennials and abundant (Table 3).

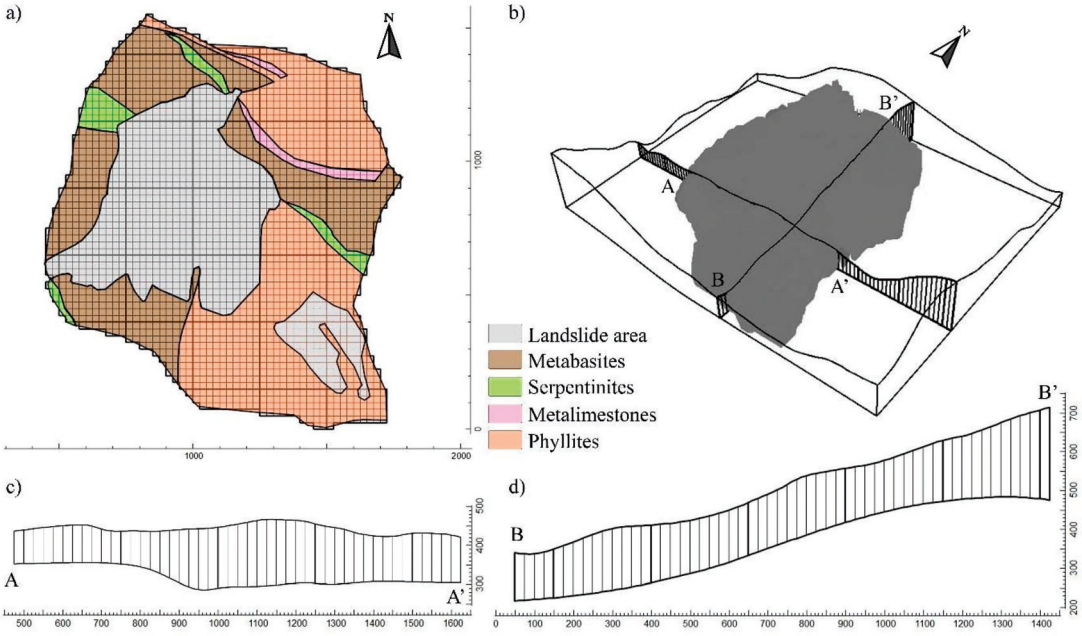

Figure 7. (**a**) Surface geological formations included into the model domain depicting zones with different hydrodynamic parameters; (**b**) 3D view of the model; (**c**) cross-section A-A′ and (**d**) cross-section B-B′ depicting the thickness layout of the model.

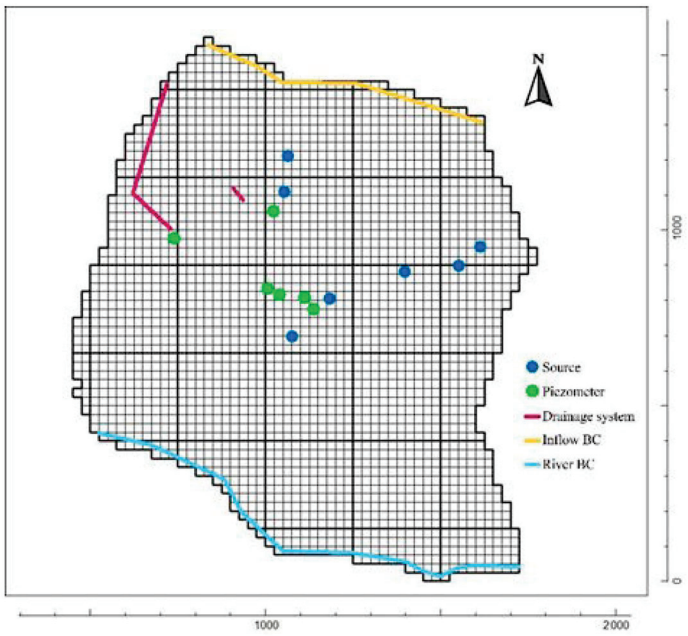

Figure 8. Boundary conditions together with relevant elements included in the model.

Table 3. Springs/Sources (S) detected in the study area. The reported values were observed in February 2011.

Name	Type	Flowrate (L/s)
Calvario	S	1.0
SS Maria di Porto	S	0.1
San Giorgio 1	S	1.0
San Giorgio 2	S	2.0
Agonia	S	1.0
Iannuli	S	2.0
Locco	S	3.5

The aquifer under investigation is mainly located in metabasite, serpentinite, and schist formations. The sources listed in Table 3, some of which have seasonal flowrate variations, are fed by the groundwater flowing in the aforementioned lithologies. Most of them, on the other hand, together with drainage galleries, have a quite constant flowrate during the year.

Two major draining systems were identified during the field campaigns consisting of underground tunnels.

The first one was built around the middle of the last century (in metabasites blocks inside the landslide body). It has a linear envelope with some small branches, likely built to intercept the aquifer. The tunnel is built in reinforced concrete, with the terminal parts (lateral branches and final branch) in stone. The intercepted flow is collected at the beginning of the tunnel toward the Corace river. The tunnel, for safety reasons, is not directly accessible. Finally, an important drainage element, even if made for another purpose, is the tunnel of the railway line (below the downtown), which crosses the landslide slope below the groundwater level, allowing consistent drainage and therefore not negligible for the global water balance. It was verified that the water is conveyed into the Fosso Scavone stream, often dry upstream, with a flowrate in the order of 10 L/s.

2.3. Mathematical Modeling

The mathematical model used to simulate the flow in the Gimigliano aquifer is based on the groundwater flow equation for a three-dimensional case [65]:

$$div\left[\overline{\mathrm{K}}grad(h)\right] = \frac{\partial n}{\partial t} + \mathrm{Q} \quad (4)$$

where $\overline{\mathrm{K}}$ is the hydraulic conductivity tensor (LT^{-1}), h is the hydraulic head (L), n is the porosity (-), and Q represents the incoming/outgoing flow rate per unit volume of the aquifer (T^{-1}). The universal groundwater model MODFLOW-2005 [66] was used to simulate flow phenomena into the aquifer.

The lateral recharge coming from the north domain boundary was estimated by implementing an iterative optimization procedure working in the following way: once all the model parameters were set, a first attempt value of the lateral recharge was defined on the boundary where the recharge is assumed to exist. The iterative optimization procedure was led by the Levenberg–Marquardt algorithm, used to solve non-linear least squares problems, and implemented with the model-independent parameter estimation and uncertainty analysis UCODE-2005 [67]. This algorithm takes full control of the model, running it as many times as necessary to optimize the values of the desired parameter. Thus, the procedure modifies the initial value of the flow rate, assigned to the boundary, until the summation of deviation between calculated and observed hydraulic heads is minimized.

2.3.1. Hydrogeological Model

A three-dimensional heterogeneous model of the phreatic aquifer flowing into the study area, and working in steady state conditions, was developed. The model domain covers an area of about 1.5 km^2 and is based on the morphological and geological reconstruction of the hillside affected by the landslide (Figures 3 and 5). The 3-D geological model was compiled by integrating the surface geological map, with recently acquired and reconstructed vertical cross-sections (Section 2.1). These latter were used to recreate the layout of the aquifer bottom via an ordinary kriging approach. The ground level profile, instead, was realized using DEM data. The whole domain was horizontally discretized by a mesh of 25×25 m^2 square elements. The vertical extent of the model is covered by a single layer, it has a variable thickness (in a range between 10 to 50 m) that follows the trend of the impermeable formation constituting the bottom of the superficial aquifer, and it is designed to replicate the heterogeneity created by the permeable geological formations across the area (Figure 7). The horizontal hydraulic conductivities of the geological formations (Figures 3 and 5) are derived from Table 2. The vertical hydraulic conductivities were set to be a tenth of the horizontal ones, as has been done in many modeling applications, e.g., [68–71]. Faults, and their influence on groundwater flow, were been considered in the model, as their occurrence in the circumscribed model domain is minor, and furthermore, detailed information on their characteristics is not available.

No flow conditions were assigned to the east and west boundaries, while an inlet flow condition was set at the north boundary. The MODFLOW River Package was then used to simulate the surface water/groundwater interaction at the south boundary (Figure 8). The permanent water course, involved as a boundary condition in the modeling process, is the Corace river. Its monthly average flowrate ranges between a maximum of 9.71 m^3/s, in the winter season, and a minimum of 0.446 m^3/s during the summertime [72]. So, the variable flowrate will be proportional to the difference between the river stage and the hydraulic head in the aquifer, i.e., groundwater can leave the aquifer through the river boundary when the hydraulic head in the cell is higher than the river stage; otherwise, surface water can enter the aquifer through the river boundary when the head in the cell is below the river stage.

A natural aquifer recharge from rainfall $N = 41$ mm/y was homogeneously distributed on the model top according to the results of the water balance for the area under investigation.

The water balance can be described using the formula:

$$P_i = E_{t_i} + R_i + N_i + \Delta S_i \quad (5)$$

where P_i is the precipitation (L), E_{t_i} is the evapotranspiration (L), N_i is the infiltration toward the aquifer (L), R_i is the runoff (L), and ΔS_i is the variation in the water storage of the soil (L). All the above-described quantities refer to the i-th month. The evapotranspiration E_{t_i} can be calculated with the method of Thornthwaite [73] based on the relationship existing between potential evapotranspiration and the average monthly temperature. The runoff R_i was obtained using the infiltration curve method based on the Curve Number Method [74]. The water capacity of the ground, or field capacity, can be figuratively represented by a water-soaked sponge retaining its water content as long as the forces at play prevent its runoff. The water amount that does not runoff or evaporate seeps into the ground. If the ground is dry, the first part of this water is used to replenish the water reserve. This water asset will then be used by plants during the periods in which rain is not able to meet their water demand. The water reserve grows, until reaching the field capacity, during the rainy season while yielding the stored water when the net rain ($P_i - R_i$) is less than evapotranspiration. When the water availability exceeds the potential evapotranspiration, and the water reserve reaches the maximum field capacity, the aquifer is recharged. Under these conditions, the variation in the water storage ΔS_i is zero, and the value of the net vertical infiltration comes from the following relation:

$$N_i = P_i - R_i - E_{t_i} \quad (6)$$

Drainage systems and springs, described in Section 2.2 and falling within the domain, were included into the model. Monitored wells and piezometers were also placed within the model and taken into consideration during the calibration procedure initially set-up to estimate the flowrate entering the system from the north inflow boundary condition (Figure 8).

As already said in the previous section, the automatic iterative optimization procedure was driven by UCODE-2005 [68]. The hydraulic head values, calculated at the model observation points and representing the monitoring wells and piezometers, were compared with the measured data. The procedure changed the values of the flowrate until the deviation between calculated and observed values reached a minimum value.

3. Results and Discussion

The first modeling stage, represented by the inversion of the hydraulic head data, was performed to quantify the possible inlet of a flowrate from the northern boundary. The outcomes of the model at the end of the iterative optimization procedure depict a situation in which the calculated hydraulic head distribution always overcomes the observed one by several meters. The sole contribution provided by the rain is sufficient to create conditions for which the entire domain is completely flooded. This unrealistic scenario can only be attributed to the adopted hydraulic conductivity values, which are too low to allow the model to manage even only those forcings of known entity (i.e., rain recharge).

For this reason, the optimization procedure, described in the previous section, was run again to evaluate both the flow rate entering the northern boundary and the value of an equivalent hydraulic conductivity for the aquifer capable of ensuring the compliance with the observed hydraulic heads and even an incoming flow rate at least comparable to that measured at the springs. In this second modeling phase, the aquifer was then turned into a homogeneous medium, without changing the geometrical layout, as the number of available observed data samples was not sufficient to guide and constrain the estimation of the parameters of the previous heterogeneous system. The estimated hydraulic conductivity of the equivalent homogeneous system resulted in a value of 2.7×10^{-6} m/s, which was two orders of magnitude higher than the previous permeabilities. This result, obtained for

the homogeneous configuration, indirectly took also into account the effect of faults in the observed hydraulic head distribution adopted in the inversion process.

The reason of this difference between the slug tests' estimation and the numerical model inversion can be ascribed to different observation scales of the two estimates, local for the first and regional for the second. Metamorphic aquifers, in fact, are characterized by a network of secondary connections of diverse orders and degrees that, among the main fractures, realizes a continuous variation in the hydrodynamic properties at different scales defining the modulus and direction of the groundwater flow. Moreover, the slug tests were all carried out in the landslide body resulting in close permeability values for all of them.

The estimated equivalent hydraulic conductivity value (2.7×10^{-6} m/s) enables a flow rate of 39.7 L/s entering the Northern boundary. This entry flow rate contemporarily fits the hydraulic heads of the monitored wells and piezometers and provides a groundwater flow even after the springs' feed (Figure 9a). In fact, the estimated entering flow rate is of the same order of magnitude as that of the measured springs outlets (Section 2.3.1). The goodness of the fit is shown in the scatterplot having a determination coefficient R^2 equal to 0.95 (Figure 9b).

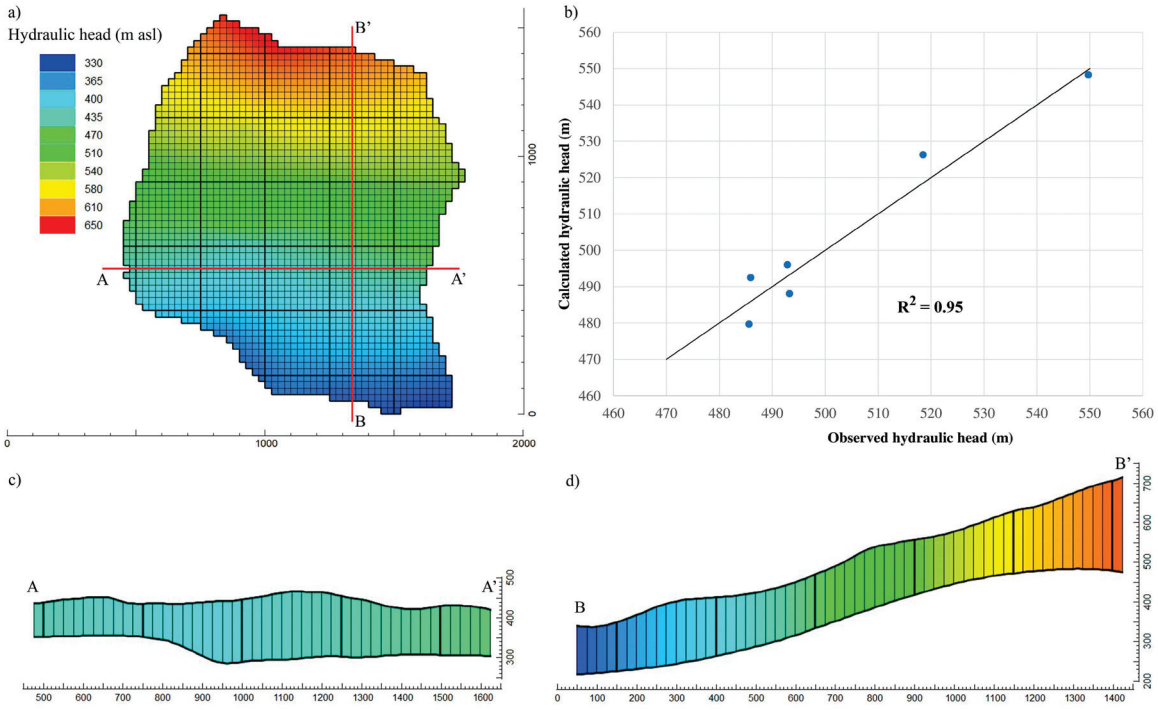

Figure 9. (**a**) Hydraulic head distribution at the end of the optimization procedure; (**b**) scattergraph of the observed and calculated hydraulic head values; (**c**) hydraulic distribution in cross sections A-A' and (**d**) B-B' also displayed in Figure 7.

4. Conclusions

In this work, an extensive campaign of field (hydro-geo-physical) measurements and a first modeling attempt of the Gimigliano aquifer are presented. The mathematical model was able to estimate the equivalent permeability of the Gimigliano aquifer and the presence of a lateral recharge from a deep confining aquifer. The adopted inverse approach provided a hydraulic conductivity of 2.7×10^{-6} m/s and a flow rate entering the northern boundary of 39.7 L/s.

The estimated hydraulic conductivity was almost one order of magnitude higher than the permeabilities estimated by means of slug tests. The reason for this discrepancy between the slug tests' estimation and the numerical model inversion can be found in the different observation scales of the two estimates, very small for the first and regional

for the latter. In fact, aquifers made up of metamorphic rocks include, among the main fractures, a network of secondary connections of different order and degree that determines, at different observation scales, a variation in the aquifer hydraulic properties defining the modulus and direction of the groundwater flow. Moreover, as a validation of our findings, the estimated lateral flow rate feeding the aquifer with a contribution of 39.7 L/s was of the same order of magnitude as the measured springs outlets.

So, as a conclusion, we argue that the hydraulic conductivity of metamorphic aquifers cannot be estimated only by field tests having a local investigation extent, but an inverse modeling approach is required, at a regional scale, which also takes into account the hydrological balance of the aquifer.

Author Contributions: All the authors contributed, in equal measures, to the implementation of the research, to the analysis of the results, and to the drafting the manuscript. All authors have read and agreed to the published version of the manuscript.

Funding: This research was funded by Regione Calabria: Convenzione per lo svolgimento di attività di consulenza tecnico-scientifica e di monitoraggio per i comuni di Gimigliano e Maierato (O.P.C.M. n.3862 del 31/03/2010).

Data Availability Statement: The data presented in this study are available on request from the corresponding author.

Conflicts of Interest: The authors declare no conflict of interest.

References

1. Gustafson, G.; Krásny, J. Crystalline rock aquifers: Their occurrence, use and importance. *Appl. Hydrogeol.* **1994**, *2*, 64–75. [CrossRef]
2. Wright, E.P.; Burgess, W.G. The Hydrogeology of Crystalline Basement Aquifers in Africa. *Geol. Soc. Spec. Publ.* **1992**, *66*, 264. [CrossRef]
3. Baiocchi, A.; Dragoni, W.; Lotti, F.; Piacentini, S.M.; Piscopo, V. A Multi-Scale Approach in Hydraulic Characterization of a Metamorphic Aquifer: What Can Be Inferred about the Groundwater Abstraction Possibilities. *Water* **2015**, *7*, 4638–4656. [CrossRef]
4. Stober, I.; Bucher, K. *Hydrogeology of Crystalline Rocks*; Kluwer Academic Publishers: Dordrecht, The Netherlands, 2003.
5. Dewandel, B.; Lachassagne, P.; Wyns, R.; Maréchal, J.C.; Krishnamurthy, N.S. A generalized 3-D geological and hydrogeological conceptual model of granite aquifers controller by single or multiphase weathering. *J. Hydrol.* **2006**, *320*, 260–284. [CrossRef]
6. Sharp, J.M. *Fractured Rock Hydrogeology*; Taylor & Francis: London, UK, 2014.
7. Tsang, Y.W.; Tsang, C.F.; Hale, F.V.; Dverstorp, B. Tracer transport in a stochastic continuum model of fractured media. *Water Resour. Res.* **1996**, *32*, 3077–3092. [CrossRef]
8. Hsieh, P.A. Scale effects in fluid flow through fractured geological media. In *Scale Dependence and Scale Invariance in Hydrology*; Sposito, G., Ed.; Cambridge Univ. Press: Cambridge, UK, 1998; pp. 35–353.
9. Howard, K.W.K.; Hughes, M.; Charlesworth, D.L.; Ngobi, G. Hydrogeologic evaluation of fracture permeability in crystalline basement aquifers of Uganda. *Hydrogeol. J.* **1992**, *1*, 55–65. [CrossRef]
10. Maréchal, J.C.; Dewandel, B.; Subrahmanyam, K. Use of hydraulic tests at different scales to characterize fracture network properties in the weathered-fractured layer of a hard rock aquifer. *Water Resour. Res.* **2004**, *40*, W11508. [CrossRef]
11. de Marsily, G.; Lavedan, G.; Boucher, M.; Fasanino, G. Interpretation of interference tests in a well field using geostatistical techniques to fit the permeability distribution in a reservoir model. In *Geostatistics for Natural Resources Characterization, Part 2*; NATO Advanced Study Institute: Dordrecht, The Netherlands, 1984; pp. 831–849.
12. Ahmed, S.; de Marsily, G. Comparison of geostatistical methods for estimating transmissivity using data on transmissivity and specific capacity. *Water Resour. Res.* **1987**, *23*, 1717–1737. [CrossRef]
13. Nastev, M.; Savard, M.; Lapcevic, P.; Lefebvre, R.; Martel, R. Hydraulic properties and scale effects investigation in regional rock aquifers, southwestern, Quebec, Canada. *Hydrogeol. J.* **2004**, *12*, 257–269. [CrossRef]
14. Patriarche, D.; Castro, M.C.; Goovaerts, P. Estimating regional hydraulic conductivity fields—A comparative study of geostatistical methods. *Math. Geol.* **2005**, *37*, 587–613. [CrossRef]
15. Razack, M.; Lasm, T. Geostatistical estimation of the transmissivity in a highly fractured metamorphic and crystalline aquifer (Man-Danane Region, Western Ivory Coast). *J. Hydrol.* **2006**, *325*, 164–178. [CrossRef]
16. Li, W.; Englert, A.; Cirpka, O.A.; Vanderborght, J.; Vereecken, H. Twodimensional characterization of hydraulic heterogeneity by multiple pumping tests. *Water Resour. Res.* **2007**, *43*, W04433. [CrossRef]
17. Straface, S.; Yeh, T.C.J.; Zhu, J.; Troisi, S.; Lee, C.H. Sequential aquifer tests at a well field, Montalto Uffugo Scalo, Italy. *Water Resour. Res.* **2007**, *43*, W07432. [CrossRef]

18. Kolterman, C.E.; Gorelick, S.M. Heterogeneity in sedimentary deposits: A review of structure-imitating, process-imitating, and descriptive approaches. *Water Resour. Res.* **1996**, *32*, 2617–2658. [CrossRef]
19. de Marsily, G.; Delay, F.; Gonçalvès, J.; Renard, P.H.; Teles, V.; Violette, S. Dealing with spatial heterogeneity. *Hydrogeol. J.* **2005**, *13*, 161–183. [CrossRef]
20. Straface, S.; Chidichimo, F.; Rizzo, E.; Riva, M.; Barrash, W.; Revil, A.; Cardiff, M.; Guadagnini, A. Joint inversion of steady-state hydrologic and self-potential data for 3D hydraulic conductivity distribution at the Boise Hydrogeophysical Research Site. *J. Hydrol.* **2011**, *407*, 115–128. [CrossRef]
21. Neuman, S.P. Calibration of distributed parameter groundwater flow models viewed as a multiple-objective decision process under uncertainty. *Water Resour. Res.* **1973**, *9*, 1006–1021. [CrossRef]
22. Yeh, W.W.G. Review of parameter estimation procedures in groundwater hydrology: The inverse problem. *Water Resour. Res.* **1986**, *22*, 95–108. [CrossRef]
23. de Marsily, G.; Delhomme, J.P.; Delay, F.; Buoro, A. 40 years of inverse problems in hydrogeology. *C. R. L'academie Sci. Ser. IIA—Earth Planet Sci.* **1999**, *329*, 73–87. [CrossRef]
24. Carrera, J.; Alcolea, A.; Medina, A.; Hidalgo, J.; Slooten, L.J. Inverse problem in hydrogeology. *Hydrogeol. J.* **2005**, *13*, 206–222. [CrossRef]
25. Straface, S. Estimation of transmissivity and storage coefficient by means of a derivative method using the early-time drawdown. *Hydrogeol. J.* **2009**, *17*, 1679–1687. [CrossRef]
26. Kelley, W.E. Geoelectrical sounding for estimating hydraulic conductivity. *Groundwater* **1977**, *15*, 420–425. [CrossRef]
27. Urish, D.W. Electrical resistivity-hydraulic conductivity relationship in glacial outwash aquifers. *Water Resour. Res.* **1981**, *17*, 1401–1408. [CrossRef]
28. Vouillamoz, J.M.; Descloitres, M.; Toe, G.; Legchenko, A. Characterization of crystalline basement aquifers with MRS: Comparison with boreholes and pumping tests data in Burkina Faso. *Near Surf. Geophys.* **2005**, *3*, 205–213. [CrossRef]
29. Straface, S.; Rizzo, E.; Chidichimo, F. Estimation of hydraulic conductivity and water table map in a large scale laboratory model by means of the self-potential method. *J. Geophys. Res.* **2010**, *115*, B06105. [CrossRef]
30. Chidichimo, F.; De Biase, M.; Rizzo, E.; Masi, S.; Straface, S. Hydrodynamic parameters estimation from self-potential data in a controlled full scale site. *J. Hydrol.* **2015**, *522*, 572–581. [CrossRef]
31. Ahmed, S.; de Marsily, G.; Talbot, A. Combined use of hydraulic and electrical properties of an aquifer in a geostatistical estimation of transmissivity. *Groundwater* **1988**, *26*, 78–86. [CrossRef]
32. Fallico, C.; Vita, M.C.; De Bartolo, S.; Straface, S. Scaling Effect of the Hydraulic Conductivity in a Confined Aquifer. *Soil Sci.* **2012**, *177*, 385–391. [CrossRef]
33. Dewandel, B.; Maréchal, J.C.; Bour, O.; Ladouche, B.; Ahmed, S.; Chandra, S.; Pauwels, H. Upscaling and regionalizing hydraulic conductivity and effective porosity at watershed scale in deeply weathered crystalline aquifers. *J. Hydrol.* **2012**, *416–417*, 83–97. [CrossRef]
34. Paillet, F.L. Flow modeling and permeability estimation using borehole flow logs in heterogeneous fractured formations. *Water Resour. Res.* **1998**, *34*, 997–1010. [CrossRef]
35. Maréchal, J.C.; Dewandel, B.; Ahmed, S.; Galeazzi, L.; Zaidi, F.K. Combined estimation of specific yield and natural recharge in a semi-arid groundwater basin with irrigated agriculture. *J. Hydrol.* **2006**, *329*, 281–293. [CrossRef]
36. Le Borgne, T.; Bour, O.; de Dreuzy, J.; Davy, P.; Touchard, F. Equivalent mean flow models for fractured aquifers: Insights from a pumping test scaling interpretation. *Water Resour. Res.* **2004**, *40*, W03512. [CrossRef]
37. Le Borgne, T.; Bour, O.; Paillet, F.L.; Caudal, J.P. Assessment of preferential flow path connectivity, and hydraulic properties at single-borehole and crossborehole scales in a fractured aquifer. *J. Hydrol.* **2006**, *328*, 347–359. [CrossRef]
38. Courtois, N.; Lachassagne, P.; Wyns, R.; Blanchin, R.; Bougaïré, F.D.; Somé, S.; Tapsoba, A. Large-Scale Mapping of Hard-Rock Aquifer Properties Applied to Burkina Faso. *Groundwater* **2010**, *48*, 269–283. [CrossRef]
39. Guihéneuf, N.; Boisson, N.; Bour, O.; Dewandel, B.; Perrin, J.; Dausse, A.; Viossanges, M.; Chandra, S.; Ahmed, S.; Maréchal, J.C. Groundwater flows in weathered crystalline rocks: Impact of piezometric variations and depth-dependent fracture connectivity. *J. Hydrol.* **2014**, *511*, 320–334. [CrossRef]
40. Lee, C.H.; Chang, J.L.; Deng, B.W. A continuum approach for estimating permeability in naturally fractured rocks. *Eng. Geol.* **1995**, *39*, 71–85. [CrossRef]
41. Scanlon, B.R.; Mace, R.E.; Barrett, M.E.; Smith, B. Can we simulate regional groundwater flow in a karst system using equivalent porous media models? Case study, Barton Springs Edwards aquifer, USA. *J. Hydrol.* **2003**, *276*, 135–158. [CrossRef]
42. Lemieux, J.M.; Therrien, R.; Kirkwood, D. Small scale study of groundwater flow in a fractured carbonate-rock aquifer at the St-Eustache quarry, Québec, Canada. *Hydrogeol. J.* **2006**, *14*, 603–612. [CrossRef]
43. Long, J.C.S.; Remer, J.S.; Wilson, C.R.; Witherspoon, P.A. Porous media equivalents for networks of discontinuous fractures. *Water Resour. Res.* **1982**, *18*, 645–658. [CrossRef]
44. Hsieh, P.A.; Neuman, S.P.; Stiles, G.K.; Simpson, E.S. Field determination of the three-dimensional hydraulic conductivity tensor of anisotropic media: 2 Methodology and application to fractured rocks. *Water Resour. Res.* **1985**, *21*, 1667–1676. [CrossRef]
45. Neuman, S.P. Stochastic Continuum Representation of Fractured Rock Permeability as an Alternative to the Rev and Fracture Network Concepts. In Proceedings of the 28th US Symposium on Rock Mechanics, Tucson, AZ, USA, 29 June–1 July 1987.

46. Neuman, S.P. Trends, prospects and challenge in quantifying flow and transport through fractured aquifer. *Hydrogeol. J.* **2005**, *13*, 124–147. [CrossRef]
47. Bradbury, K.R.; Muldoon, M.A.; Zaporec, A.; Levy, J. *Delineation of Wellhead Protection Areas in Fractured Rocks*; US EPA Technical Guidance Document, EPA 570/9-91-009; EPA: Washington, DC, USA, 1991.
48. Baiocchi, A.; Dragoni, W.; Lotti, F.; Piscopo, V. Sustainable yield of fractured rock aquifers: The case of crystalline rocks of Serre Massif (Calabria, Southern Italy). In *Fractured Rock Hydrogeology*; Sharp, J.M., Ed.; Taylor &Francis Group: London, UK, 2014; pp. 79–97.
49. Domenico, P.A.; Schwartz, F.W. *Physical and Chemical Hydrogeology*; John Wiley & Sons: New York, NY, USA, 1990; 824p.
50. Heath, R.C. *Basic Groundwater Hydrology*; U.S. Geological Survey Water-Supply Paper 2220: Washington, DC, USA, 1983; 86p.
51. Dragoni, W. Some considerations on climatic changes, water resources and water needs in the Italian region south of the 43° N. In *Water, Environment and Society in Times of Climatic Change*; Issar, A., Brown, N., Eds.; Kluwer Academic Publishers: Dordrecht, The Netherlands, 1998; pp. 241–271.
52. Bianchini, S.; Cigna, F.; Del Ventisette, C.; Moretti, S.; Casagli, N. Monitoring Landslide-Induced Displacements with TerraSAR-X Persistent Scatterer Interferometry (PSI): Gimigliano Case Study in Calabria Region (Italy). *Int. J. Geosci.* **2013**, *4*, 1467–1482. [CrossRef]
53. Van Dijk, J.P.; Bello, M.; Brancaleoni, G.P.; Cantarella, G.; Costa, V.; Frixa, A.; Golfetto, F.; Merlini, S.; Riva, M.; Torricelli, S.; et al. A regional structural model for the northern sector of the Calabrian Arc (southern Italy). *Tectonophysics* **2000**, *324*, 267–320. [CrossRef]
54. Tansi, C.; Muto, F.; Critelli, S.; Iovine, G. Neogene-Quaternary strike-slip tectonics in the central Calabrian Arc (Southern Italy). *J. Geodyn.* **2007**, *43*, 393–414. [CrossRef]
55. Brutto, F.; Muto, F.; Loreto, M.F.; De Paola, N.; Tripodi, V.; Critelli, S.; Facchin, L. The Neogene-Quaternary geodynamic evolution of the central Calabrian Arc: A case study from the western Catanzaro Trough basin. *J. Geodyn.* **2016**, *102*, 95–114. [CrossRef]
56. Bonardi, G.; Cello, G.; Perrone, V.; Tortorici, L.; Turco, E.; Zupetta, A. Palinspastic restoration of the northern sector of the Calabro-Peloritani arc in a semiquantitative model. *Boll. Soc. Geol. Ital.* **1982**, *101*, 259–274.
57. Tortorici, L. Lineamenti geologico-strutturali dell'Arco Calabro Peloritano (Geologic structural lineaments of the Calabrian-Peloritan Arc). *Soc. Ital. Mineral. Petrogr.* **1982**, *38*, 927940.
58. Critelli, S.; Muto, F.; Perri, F.; Tripodi, V. Interpreting provenance relations from sandstone detrital modes, southern Italy foreland region: Stratigraphic record of the Miocene tectonic evolution. *Mar. Petrol. Geol.* **2017**, *87*, 47–59. [CrossRef]
59. Amodio-Morelli, L.; Bonardi, G.; Colonna, V.; Dietrich, D.; Giunta, G.; Ippolito, F.; Liguori, V.; Lorenzoni, S.; Paglionico, A.; Perrone, V.; et al. L'arco Calabro-Peloritano nell'orogene appenninico Maghrebide. *Mem. Soc. Geol. Ital.* **1976**, *17*, 1–60.
60. Bouwer, H.; Rice, R.C. A slug test for determining hydraulic conductivity of unconfined aquifers with completely or partially penetrating wells. *Water Resour. Res.* **1976**, *12*, 423. [CrossRef]
61. Zlotnik, V. Interpretation of slug and packer tests in anisotropic aquifers. *Groundwater* **1994**, *32*, 761. [CrossRef]
62. Butler, J.J. *The Design, Performance, and Analysis of Slug Tests*; Lewis Publisher CRC Press: Lawrence, KS, USA, 1998; ISBN 1566702305.
63. Pezzotta, G.; Burton, A.N.; Hughes, D.O. *Carta Geologica della Calabria: Nota Illustrativa delle Tavolette Appartenenti al Foglio 242 della Carta Topografica D'italia*; Cassa del Mezzogiorno: Roma, Italy, 1973.
64. Repertorio Nazionale dei Dati Territoriali (RNDT). Available online: https://geodati.gov.it/geoportale/geoviewer/ (accessed on 14 September 2022).
65. Bear, J. *Hydraulics of Groundwater*; McGraw-Hill Publishing: New York, NY, USA, 1979.
66. Harbaugh, A.W. MODFLOW-2005: The U.S. Geological Survey modular ground-water model—The ground-water flow process. In *Book 6: Modeling Techniques, Section A. Ground-Water*; US Geological Survey: Reston, VI, USA, 2005; p. 6-A16.
67. Poeter, E.P.; Hill, M.C.; Banta, E.R.; Steffen, M.; Steen, C. UCODE-2005 and six other computer codes for universal sensitivity analysis, calibration, and uncertainty evaluation constructed using the JUPITER API. In *U.S. Geological Survey Techniques and Methods*; US Geological Survey: Reston, VI, USA, 2008; p. 6-A11.
68. De Biase, M.; Chidichimo, F.; Maiolo, M.; Micallef, A. The Impact of Predicted Climate Change on Groundwater Resources in a Mediterranean Archipelago: A Modelling Study of the Maltese Islands. *Water* **2021**, *13*, 3046. [CrossRef]
69. De Biase, M.; Chidichimo, F.; Micallef, A.; Cohen, D.; Gable, C.; Zwinger, T. Past and future evolution of the onshore-offshore groundwater system of a carbonate archipelago: The case of the Maltese Islands, central Mediterranean Sea. *Front. Water* **2023**, *4*, 1068971. [CrossRef]
70. Haroon, A.; Micallef, A.; Jegen, M.; Schwalenberg, K.; Karstens, J.; Berndt, C.; Garcia, X.; Kühn, M.; Rizzo, E.; Fusi, N.C.; et al. Electrical resistivity anomalies offshore a carbonate coastline: Evidence for freshened groundwater? *Geophys. Res. Lett.* **2021**, *48*, e2020GL091909. [CrossRef]
71. Lemieux, J.M.; Hassaoui, J.; Molson, J.; Therrien, R.; Therrien, P.; Chouteau, M.; Ouellet, M. Simulating the impact of climate change on the groundwater resources of the Magdalen Islands, Québec, Canada. *J. Hydrol. Reg. Stud.* **2015**, *3*, 400–423. [CrossRef]
72. ARPACAL—Centro Funzionale Multirischi. Available online: https://www.cfd.calabria.it/index.php (accessed on 27 February 2023).

73. Thornthwaite, C.W. An Approach toward a Rational Classification of Climate. *Geogr. Rev.* **1948**, *38*, 55–94. [CrossRef]
74. Cronshey, R.; McCuen, R.H.; Miller, N.; Rawls, W.; Robbins, S.; Woodward, D.; Chenoweth, J.; Hamilton, S.; Merkel, W.; Rallison, R.; et al. *Urban Hydrology for Small Watersheds—Technical Release 55*, 2nd ed.; United States Department of Agriculture (USDA): Washington, DC, USA, 1986; p. 164.

Disclaimer/Publisher's Note: The statements, opinions and data contained in all publications are solely those of the individual author(s) and contributor(s) and not of MDPI and/or the editor(s). MDPI and/or the editor(s) disclaim responsibility for any injury to people or property resulting from any ideas, methods, instructions or products referred to in the content.

hydrology

MDPI

Article

Development of Groundwater Flow Models for the Integrated Management of the Alluvial Aquifer Systems of *Dravsko polje* and *Ptujsko polje*, Slovenia

Ada Vengust [1], Anja Koroša [2,*], Janko Urbanc [2] and Nina Mali [2]

[1] Geoinženiring D.O.O., Dimičeva ulica 14, 1000 Ljubljana, Slovenia
[2] Geological Survey of Slovenia, Department of Hydrogeology, Dimičeva ulica 14, 1000 Ljubljana, Slovenia
* Correspondence: anja.korosa@geo-zs.si; Tel.: +386-12-80-9817

Abstract: With increasing exploitation of groundwater resources and implementation of various activities in their recharge areas, it is vital to conduct a comprehensive assessment of aquifers to ensure their conservation and sustainable management. In the present study, we used a comprehensive approach to conceptualise and identify the functioning of two connected aquifer systems in north-eastern Slovenia: the Quaternary porous aquifers *Dravsko polje* and *Ptujsko polje*. The study presents the conceptual models of both aquifers and their interconnectedness using separate mathematical-numerical models with the aim of ensuring an integrated management of these alluvial aquifer systems. It also highlights the importance of understanding connections between such systems for simulating groundwater flow and transport of different contaminants. To describe the entire aquifer system, the study defines its three essential elements: the geometry of the aquifers, their recharge by precipitation, and other boundary conditions. The geometry of the Quaternary aquifers was defined using Sequential Indicator Simulation (SIS) with the ESRI's ArcMap software. Next, LIDAR was used for determining their surface geometry. The hydrogeologic model was designed using the Groundwater Modelling System (GMS) developed by AQUAVEO. We used the MODFLOW 2000 calculation method based on the finite difference method (FDM). The model was calibrated with the PEST module, which was used to calibrate hydraulic conductivity and hydraulic heads between the measured and modelled data. Finally, the model was validated using the Nash–Sutcliffe (NSE) efficiency coefficient. In addition, the model results estimated using the PEST tool were validated with the hydraulic conductivities determined at the pumping sites (pumping tests), each belonging to water protection zones that define the maximum travel time of the particles. This was performed using the MODPATH method. The paper also presents the possibility of modelling heterogeneous but interdependent aquifers in a groundwater body. Modelling the connection between the two aquifers, which are the most important ones in the region, is essential for a comprehensive management of the entire system of water resources. The models allow for a better understanding of groundwater flow in both aquifers. Moreover, their interconnectedness will be used for further studies in this field, as well as for integrated water management.

Keywords: hydrogeological model; Modflow model; aquifer geometry; aquifer recharge; modelling

1. Introduction

Groundwater presents an important source of drinking water, which is why its use and protection has become an important global issue [1]. To achieve comprehensive and integrated management of groundwater resources, various conceptual models were developed worldwide [2–11]. The development of conceptual models relies on frameworks expressing the cause-and-effect structure of groundwater systems. Therefore, different frameworks should be used when dealing with complex natural systems such as aquifers [12]. The main objective of this study is to develop an integrated model of two separate but interconnected aquifers, which will provide a management tool facilitating decision making for the

prevention of groundwater pollution. Regardless of its vital importance to water supply, their recharge area is also a site of diverse and intensive land use, resulting in conflicts of interest. Considering all these aspects, it is imperative to raise the knowledge of the aquifers used in this area. The *Dravska kotlina* groundwater body is located in north-eastern Slovenia and contains two of the largest, interconnected, and most important aquifers used as water resources in Slovenia: the *Dravsko polje* aquifer and the *Ptujsko polje* aquifer. Both are filled with Quaternary sediments of the Drava River and are intergranular aquifers. Their water tables are near the surface and have an average depth of about 8 m. Both aquifers are unconfined and have no overlying low-permeability layers that could protect them from possible pollution. Considering this, they are the most strategic groundwater resources in Slovenia. In recent decades, this area has been affected by high nitrate and pesticide concentrations caused by anthropogenic sources such as animal manure used as fertilizer, synthetic fertilizers, septic systems, and other waste waters. The study area of the two aquifers is intensively used for agriculture. There are many livestock farms in the aquifer recharge area. Contamination of groundwater from diffuse agricultural sources is known to be a major pollution problem [13–17].

The protection of groundwater sources begins with the improvement of groundwater management and the effective implementation of environmental protection measures. The EU Water Framework Directive (2000/60/EC) [18] and its daughter Directive on the Protection of Groundwater Against Pollution (2006/118/EC) [19] established the criteria for defining the qualitative and quantitative status of groundwater. Slovenia recognised this directive in its national regulation: the Water Act [20] and the Regulation on the Protection of Waters Against Pollution Caused by Nitrates from Agricultural Sources [21]. The main objective of this research is to develop a conceptual and hydraulic groundwater flow model on a regional scale, starting from borehole data, grain size distributions and well tests, in order to analyse the overall groundwater flow behaviour. Problems associated with the conceptualisation of groundwater systems have been known for over a decade [22,23]. In recent years, increasing attention has been paid to the development and evaluation of conceptual models [24,25]. The development of an appropriate conceptual model is a critical step in any successful modelling study. A simple model is needed that would be able to capture the behaviour of total groundwater flow in the main aquifers without complex fine-resolution behaviours arising from aquifer heterogeneity. On the other hand, despite their simplicity, such conceptual and numerical models must be accurate and hydrostratigraphically sound. In designing the conceptual models, we defined the study area, created a 3D model of the hydrogeological system, estimated the groundwater recharge from precipitation and surface waters, and defined the boundary conditions (BCs). Previous assessments of groundwater recharge from precipitation and its spatial distribution in the study area were sparse and insufficient. Groundwater recharge in our models was divided into two categories: targeted recharge from surface waters such as rivers, canals, and lakes, and diffuse recharge from infiltration of precipitation through the unsaturated zone into the groundwater. The analysis of groundwater and surface water levels allowed us to define the BCs and the relationship between surface water and groundwater.

This study is the first to evaluate the spatial distribution of long-term average groundwater recharge from precipitation in the *Dravsko polje* and *Ptujsko polje* aquifers as part of the larger *Dravska kotlina* water body. The objective of the research was to develop and present the first hydrogeological model of the interconnected *Dravsko polje* and *Ptujsko polje* aquifers as a basis for integrated management of both aquifers. A detailed overview of the hydrodynamic characteristics of the aquifers was prepared in order to develop a hydrogeological conceptual model that will serve as the foundation for the construction of a numerical groundwater flow and contaminant transport models. The results, along with the geometry of the aquifer and other BCs, can serve as an important input to the development of a numerical model for various contaminants. The model represents a part of the decision support system for groundwater management at national and local levels. Land use in the area under consideration is diverse, and there are considerable conflicts

of interest related to various activities. The model provides the basis for an assessment of the qualitative and quantitative state of the water body, as well as for monitoring its changes due to climate change. The model facilitates the assessment of potential sources of pollution and the development of measures to improve groundwater quality. It provides support for groundwater management intended for water supply, irrigation, and other specific uses. The model also serves to verify the proper delineation of drinking water protection areas.

2. Materials and Methods

2.1. Study Area

2.1.1. Location and Climate of the Study Area

The study area includes two aquifers—*Dravsko polje* and *Ptujsko polje*—which are both part of the *Dravska kotlina* water body (Figure 1). Both aquifers are hydraulically connected.

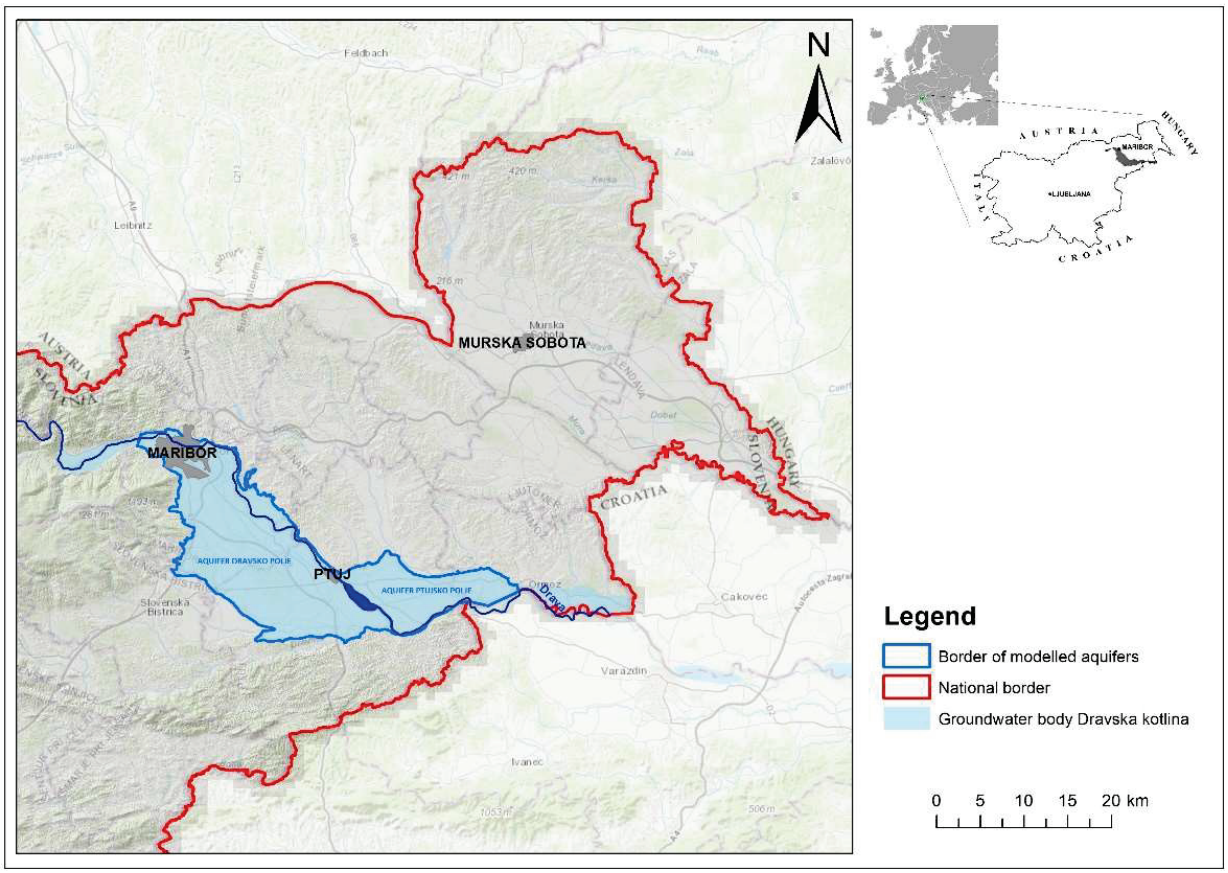

Figure 1. *Dravska kotlina* groundwater body with marked modelled aquifers.

The *Dravsko polje* aquifer is located on the right bank of the Drava River. It covers an area of 293 km^2 and extends from Maribor in the north to Ptuj in the southeast and Slovenska Bistrica in the southwest. In general, it has the shape of a triangle between Maribor, Ptuj, and Pragersko. It is bordered by the Pohorje Massif to the west, Slovenske Gorice Hills to the east and north, and by Haloze and Dravinjske Gorice to the south. A supply canal for the Zlatoličje Hydro Power Plant runs parallel to the Drava River. In the town of Ptuj, the Drava flows into Lake Ptuj, an artificial lake from which the river continues to flow. The *Dravsko polje* aquifer began to form in the Pleistocene when the Drava eroded tertiary sediments and began filling it with sediments. During this process, the Drava also eroded its own sediments, which can be seen in many terraces [26]. There are four terraces; the highest of which is at an altitude of 270 metres. The two upper terraces are inclined towards Ptuj and have a slope of 1.8% [27]. The *Dravsko polje graben* is filled with

Quaternary sediments [26]. The sedimentology of the aquifer is heterogeneous and changes rapidly in the vertical direction. It is mostly composed of gravel and sand and contains layers and lenses of sand. In some areas, there are also clay deposits. Conglomerate is found mainly on the edges of the terraces.

The *Ptujsko polje* aquifer is located on the left bank of the Drava River and extends between Ptuj and the town of Ormož. It borders the *Dravsko polje* aquifer to the west and the *Ormoško polje* aquifer to the east. It is bordered by the hills of Slovenske Gorice to the north and by the Drava River to the south. It has the shape of an elongated triangle with an area of about 91 km^2. The surface is slightly inclined to the east. The *Ptujsko polje* aquifer is filled with Quaternary gravel deposits, the thickness of which varies from 4 m up to 22 m. The aquifer is composed of a very thin layer of gravel. The tertiary base of the Quaternary aquifer consists of conglomerate sand, clay and marl with very low permeability. In the vicinity of Lake Ptuj on the western border, the Ljutomer fault runs in the direction of SW to NE. Between Ptuj and the Ljutomer fault, the base of the Quaternary aquifer consists of Pliocene sediments. The rest of the area east of the fault base consists of Lower Pliocene and Miocene sediments. The tertiary base is strongly undulated [26]. The most important watercourse in the *Ptujsko polje* aquifer is the Drava River. It flows along the southern edge of the aquifer to Ormož. After the construction of the Formin Hydro Power Plant between Markovci and the town of Ptuj, the 5 km long and 1.2 km wide Lake Ptuj was created. A flood control dam was built along this artificial lake. When the Formin Hydro Power Plant was built, the *Ptujsko polje* aquifer was subdivided by an 8.5 km long supply canal between Markovci and Formin and an 8 km long guide canal between Formin and the town of Ormož [26].

The intersection between the two models is the area between the Drava River and Lake Ptuj (Figure 1). Based on the flow budget of the *Drava polje* aquifer, the total discharge below Lake Ptuj and the Drava River is the amount of groundwater that is expected to continue to flow from the *Dravsko polje* into the *Ptujsko polje* aquifer.

2.1.2. Geology and Hydrogeology of the Study Area and Geometry of the Aquifers

To describe the geometry of the bedrock of both aquifers (Figures 2 and 3), we collected lithological data from the archives of the Geological Survey of Slovenia (GeoZS). Data were collected from 2510 boreholes drilled from Pleistocene sediments to the bedrock. The boreholes are spatially distributed throughout the study area, which allows a good definition of the geometry of the aquifer. The study area is crossed by a major fault—the Ljutomer fault. It was included in the bedrock model [28,29]. In the south of the model, the Ljutomer fault shows a slight faulting of the bedrock especially near the Drava River and Lake Ptuj. Both aquifers were treated as a single homogeneous layer consisting mainly of gravel and sand [26]. The homogeneity of the aquifer was verified by a lithological model created using the JewelSuite software [30]. We grouped the lithologic description of the sediments from the boreholes into seven categories (gravel; silt and clay with gravel; silt and clay; conglomerate; gravel, clay, silt; humus and bedrock). The subsurface was drawn using the ESRI ArcMap software with lithologic data obtained from the boreholes and expertise on the study area. Sequential Indicator Simulation (SIS) was used to interpolate the defined lithological units in the 3D model. The model extends from the surface (defined by a digital elevation model) to the bedrock of the Quaternary aquifer. Sequential Indicator Simulation is a stochastic interpolation method based on Juang et al. [31]. For the surface layer, the data from LIDAR were used as Slovenia is completely covered by LIDAR. The models are set to cells with a size of 100 $\times$ 100 m. In both models, we used a porosity value of 0.15, which is typical for porous aquifers.

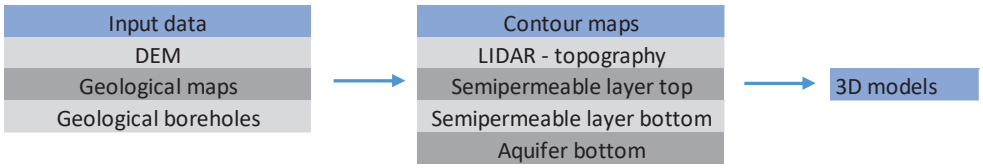

Figure 2. Methodological chart showing the required data and steps for developing 3D models.

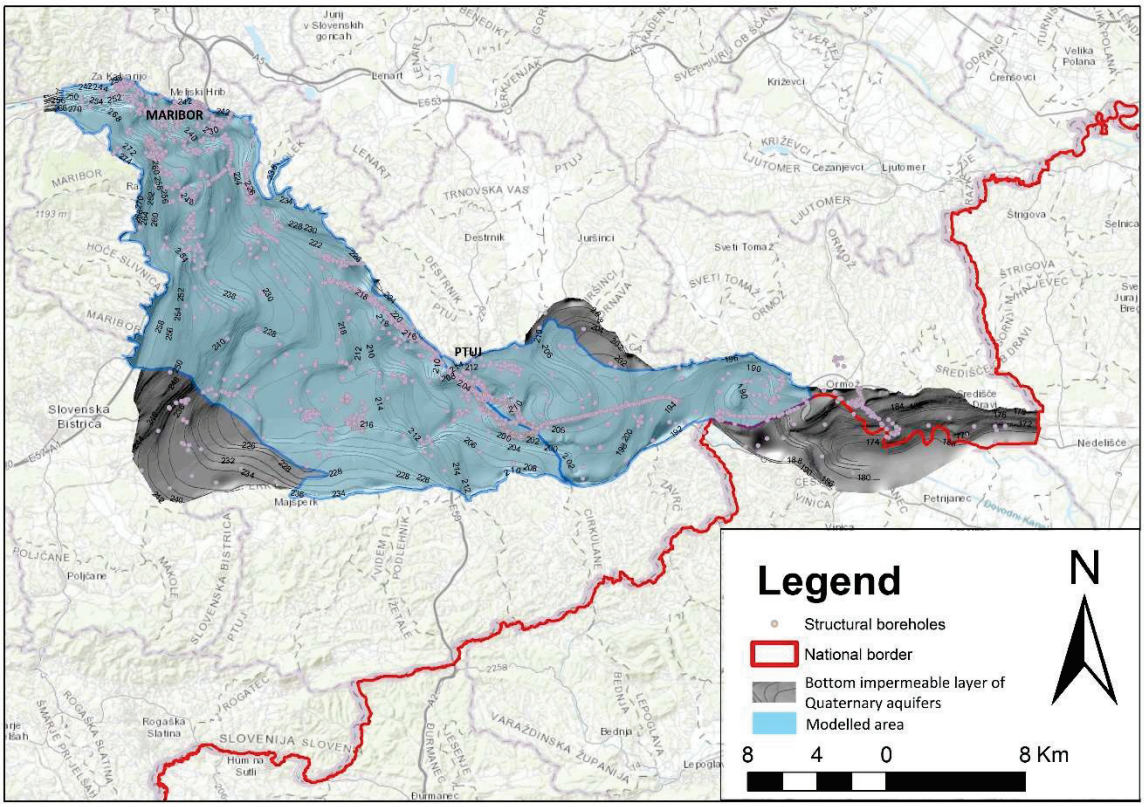

Figure 3. The modelled bottom impermeable layer of Quaternary aquifers.

2.2. Groundwater Flow System and Groundwater Level Monitoring

The groundwater level (GWL) and the upper and lower layers of the model were unified for both models. Based on the measured GWL values of 152 wells in the *Dravsko polje* aquifer and 86 wells in the *Ptujsko polje* aquifer, a GWL map was created using ArcGis software. In addition, the modelled GWLs were compared with the measured (observed) values. For the *Dravsko polje* aquifer, most of the data available were collected between 21 and 25 November 2012, so the GWL map was created for November 2012 (Figure 4). For the *Ptujsko polje* aquifer, most of the data available were collected on 20 March 2015 (Figure 4). For these dates, a medium water level is characteristic.

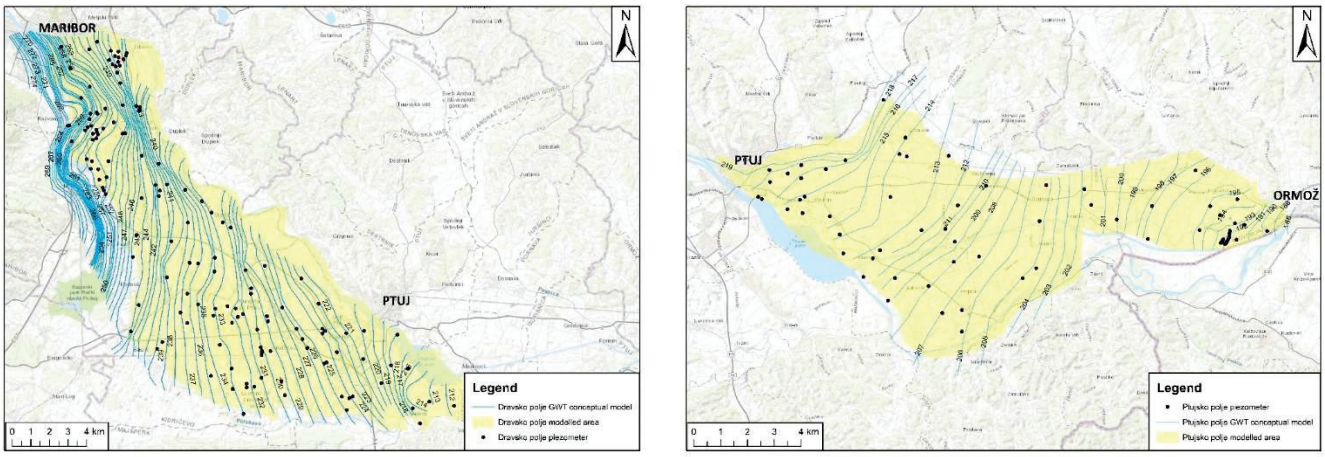

Figure 4. Groundwater level map of the Dravsko polje aquifer (**left**) and groundwater level map of the Ptujsko polje aquifer (**right**).

2.3. Groundwater Recharge Estimation

The groundwater of the *Dravsko polje* aquifer is recharged by infiltration of streams from the Pohorje Massif and by infiltration of precipitation. The *Dravsko polje* aquifer is not homogeneous; moreover, the differences in the way it is recharged are so vast that it was divided into three hydrogeological units, as described by [26]. Each of these units has a separate precipitation margin and a well-defined regime of groundwater recharge and discharge. The first unit covers the north-western part of the territory, which is mainly urbanised. It includes the foothills of the Pohorje Massif of the *Radvanjski potok* and *Razvanjski potok* creeks. In the south, it is bounded by the surface ridge of the *Razvanjski potok* creek ridgeline and the underground ridge extending from Bohova to Dogoše. In this unit, groundwater flow is quite low due to the small precipitation catchment area and the low thickness of the aquifer. The second hydrogeological unit includes part of the *Dravsko polje* aquifer between Bohova and Dogoše in the north and Hotinja vas, Dravski Dvor and Starše in the south of the *Dravsko polje* aquifer. It also includes the hilly outskirts of the *Pivolski potok*, *Hočki potok*, and *Polanski potok* creeks. Groundwater from the second unit of the *Dravsko polje* aquifer is discharged into the Miklavž Spring and the Drava River.

The third and largest hydrogeological unit includes the hilly outskirts of the *Rački potok* creek and the middle part of the *Dravsko polje* aquifer from the border of the Pohorje Massif in the west to the Drava River in the north-east and the Polskava River in the south. Groundwater is discharged from the Pohorje Massif towards the Zlatoličje Canal and the Hajdina and Pobreš springs [32].

The area is largely covered by agricultural land (44%), followed by forested land (20%) and urban (populated) areas, which represent sources of both urban and industrial pollution (19%), while the rest of the area is covered by meadows. Surface activities are also reflected in the quality of the groundwater.

Most of the recharge volume is provided by infiltration of precipitation. The average annual amount of precipitation is between 800 and 1000 mm/year. The long-term mean annual groundwater recharge is estimated at 300–450 mm [33], including evapotranspiration. To determine the long-term mean precipitation, we selected two monitoring stations: one in the north (Maribor—Airport) and one in the south (Ptuj) of the study area (Figure 4). The year with the highest precipitation was 1972 with 1284 mm/year (Ptuj).

Approximately one-third of the average annual precipitation is infiltrated and discharged into the Drava River. The recharge rate of the Quaternary aquifer is estimated at 3 m^3/s [34]. Thus, groundwater discharge equals 2 m^3/s and direct recharge equals 0.8 m^3/s. Surface runoff accounts for the smallest share of the average annual precipitation volume, and about 41% is infiltrated by precipitation (27–47%) [34]. In general, the *Dravsko polje* aquifer has good hydraulic conductivity, ranging from about 68 to 790 m/day [26].

The *Ptujsko polje* aquifer is recharged mainly by precipitation and partly by the Drava River. Groundwater discharges into numerous springs called Zvirenčine at the foot of the high Quaternary gravel terrace. The town of Ormož is supplied with drinking water from the wells in the eastern part of the *Ptujsko polje* aquifer. The supply canal, which belongs to the Formin Hydro Power Plant, affects the groundwater only to a small extent, as all necessary measures were taken to prevent the canal from polluting the groundwater. This canal is sealed only on the eastern side of the *Ptujsko polje* aquifer at a distance of 6 km from Formin in the direction of the town of Ormož to the tertiary base. However, the last 2 km are permeable, allowing water to drain into the Drava River. GWL fluctuations are caused mainly by precipitation and partly by the natural flow of the Drava. Groundwater discharges into the Drava and into springs located along the Drava. The discharge of groundwater into the Drava River is significant for the part after the confluence of the Dravinja River with the Drava River. Before the Dravinja flows into the Drava, an equilibrium is reached between the river and the groundwater, so that it is neither drained nor dammed [35].

In the eastern part between the village of Formin and the town of Ormož, the groundwater no longer flows evenly, as the Formin supply canal is sealed up by the non-permeable tertiary base. Therefore, the groundwater flow is divided into the southern and northern parts of the Formin supply canal. In the northern part, groundwater flows in a W-E direction and discharges into the Drava River, with the last 2 km of the canal being permeable again. Only precipitation has an influence on GWL fluctuation. In this part, water is tapped for the fresh water supply of the town of Ormož. In the southern part of the canal, GWL fluctuation is influenced both by precipitation and the Drava River.

2.4. Conceptual Models of the Study Area

The modelled area of the *Dravsko polje* aquifer is bounded along the western edge by the 'Specified head' BC, which enables a constant flow from the Pohorje Massif to the *Dravsko polje* aquifer. The constant head corresponds to the GWL and is divided into three sections (Figure 5). From the north to the edge of the south-east, the groundwater flow is determined by two BCs: 'Drain', where the groundwater flows further down or into Lake Ptuj, and 'River', where the Drava and Dravinja rivers are located. The 'Drain' stage corresponds to the lower layer of the lake, where the groundwater is higher than the bottom layer of the lake. This is an indication that the groundwater flow exists between the tertiary bottom and the lake bottom. The bottom layer of the lake is shown in Figure 6. It was adapted from [36], which contains an image of the bottom layer, and redrawn using ArcMap.

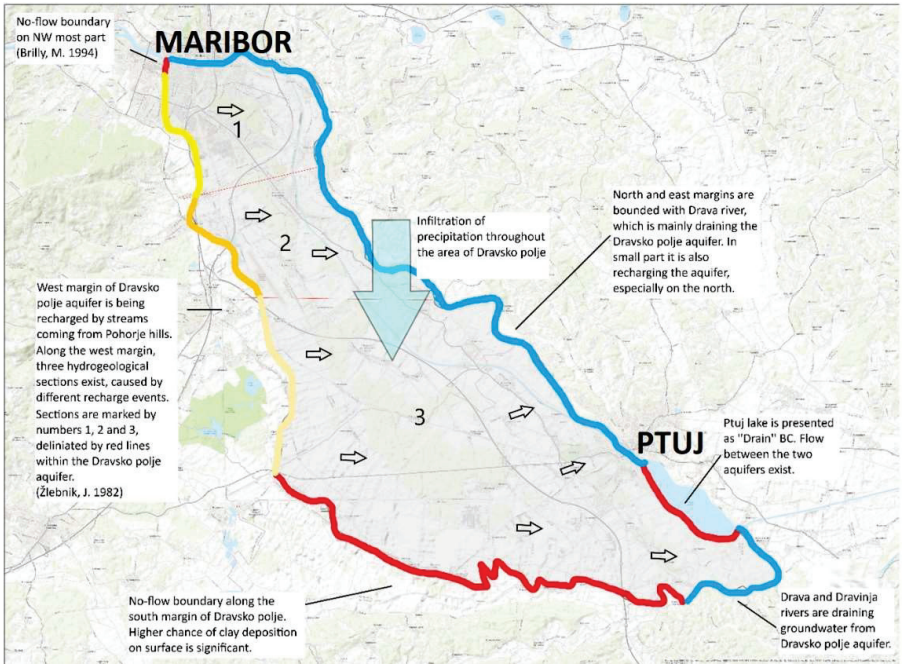

Figure 5. Conceptual model of the *Dravsko polje* aquifer, Žlebnik, L. [26], Brilly, M. [37].

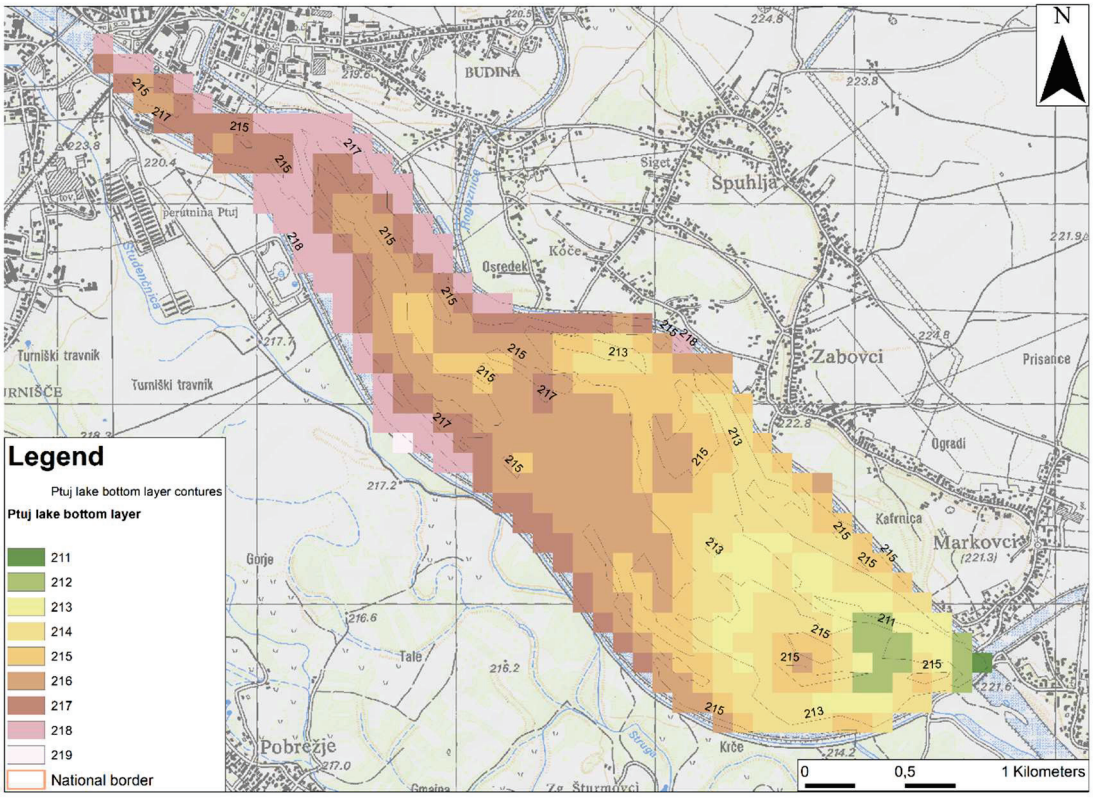

Figure 6. Bottom layer of Lake Ptuj (adapted after Veršič, 2007).

The approximate groundwater flow beneath the lake was calculated based on Darcy's flow for unconfined aquifers. Most of the groundwater is discharged into streams. However, groundwater discharge is substantial in the northern part of the river. The 'River' BC was based on the GWL map; the southern and south-western parts have a 'No-flow' BC. Infiltration of precipitation into the *Dravsko polje* aquifer is 300 mm/yr as 'Recharge' BC [38].

Near the eastern edge of the aquifer and in the south-east, there are two drainages that drain a small amount of groundwater. The model includes 7 pumping fields with a total of 10 wells (Betnava: 40 m^3/day, Dobrovce: 60 m^3/day, Šikole: 44.5 m^3/day, Skorba: 135.5 m^3/day, Kidričevo: 183 m^3/day, Lancova vas: 15.5 m^3/day, Bohova: 50 m^3/day). The total pumping capacity is 528.5 m^3/day. The porosity of the entire model was set to 0.15, as is typical for porous aquifers. The approximate values of water balance were estimated from data in the literature (Table 1).

Table 1. Estimation of the *Dravsko polje* aquifer groundwater flow.

	Wells	**River**	**Recharge from Precipitation**	**Recharge from the Western Boundary (Pohorje)**	**Lake Ptuj**
Flow in [m^3/s]	0	50.000 [34]	106.272 [33]	259.200 [34]	0
Flow out [m^3/s]	528.5	app. 400.000 (groundwater discharges mainly into the river)	0	0	50.000 (calculated based on Darcy's flow)
TOTAL in-out [m^3/s]	415.472				

The conceptual model for the *Ptujsko polje* aquifer is shown in Figure 7. Infiltration by precipitation is described as 'Recharge' BC. A negligible amount of surface water from streams infiltrates from the hills of Slovenske Gorice along the northern edge of the aquifer. Therefore, to simplify the model, the northern edge of the aquifer was defined as a basin with a no-flow BC.

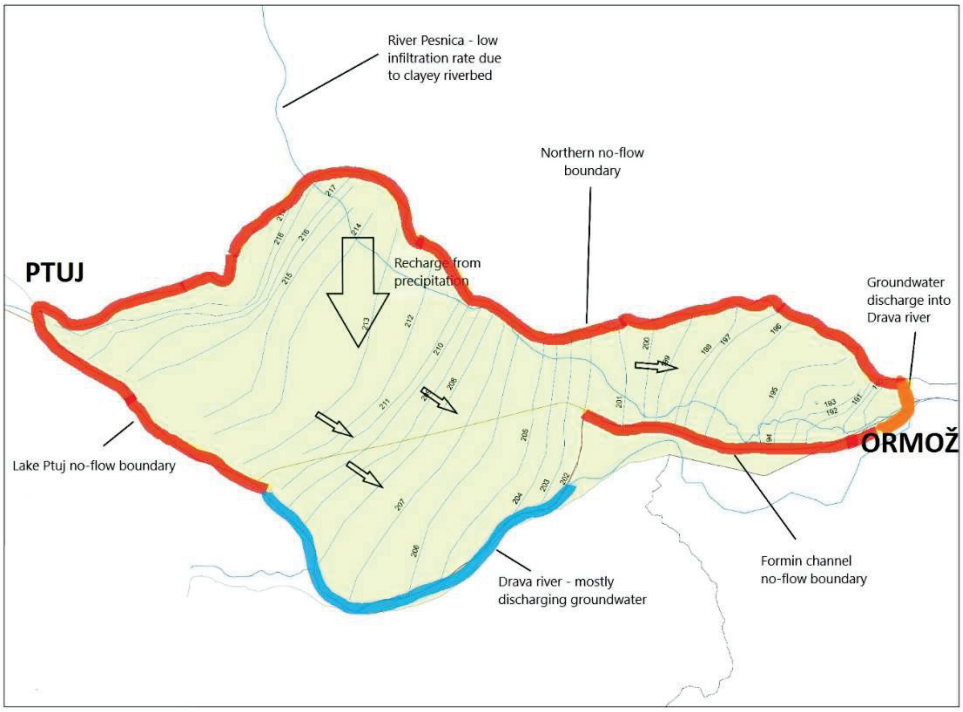

Figure 7. Conceptual model for the *Ptujsko polje* aquifer.

In the eastern part of the aquifer between the village of Formin and the town of Ormož, the supply canal leading to the Formin Hydro Power Plant represents an impermeable boundary, as it is sealed by the impermeable tertiary base of the Quaternary aquifer. However, the last 2 km of this canal are permeable and here, the groundwater is discharged into the Drava River. The eastern part of the *Ptujsko polje* aquifer is also permeable and allows groundwater to discharge into the *Ormož polje* aquifer. Therefore, the canal between the village of Formin and the town of Ormož is without discharge except for the last two kilometres. In the western part of the aquifer, groundwater is discharged mainly into the Drava River. In our model, the Drava was described as 'River' BC. The head stage of the River BC was based on the GWL map. On the west side between Ptuj and Markovci, artificial Lake Ptuj was represented as 'Specified Flow' BC. The recharge rate below the lake was taken from the model of the *Dravsko polje* aquifer, as we assumed that the same amount of groundwater flows from the *Dravsko polje* aquifer into the *Ptujsko polje* aquifer.

The Pesnica River flows through the *Ptujsko polje* aquifer towards *Ormoško polje*. It was neglected, as the amount of water infiltrating into the groundwater is low due to clay deposits at the bottom of the riverbed. In the eastern part of the *Ptujsko polje* aquifer, the *Sejanica pri Mihovcih* pumping station supplies drinking water to the town of Ormož. The water is pumped from 16 pumping wells. However, to avoid depletion of the aquifer, the groundwater is recharged by 5 infiltration fields, where surface water from the canal is infiltrated into the groundwater. The recharge rates are shown in Tables 2 and 3. Table 4 shows the groundwater balance of the *Ptujsko polje* aquifer.

Table 2. Recharge rates from infiltration fields at the *Ptujsko polje* aquifer for the time used in the model.

Infiltration Field	Recharge Rate (m^3/day)
1	347.87
2	581.73
3	0
4	233.37
5	65.03

Table 3. Pumping rates on the east side of the *Ptujsko polje* aquifer for the time used in the model.

Pumping Well	Pumping Rate (m^3/day)
1	255.07
2	0
3	158.97
4	246.73
5	58.83
6	218.37
7	117.50
8	262.57
9	303.77
10	271.37
11	308.87
12	140.67
13	321.10
15	167.33
16	46.57
17	73.43

Table 4. Estimated groundwater flow values for the *Ptujsko polje* aquifer.

	Wells	**Infiltration Fields (m^3/day)**	**Recharge from Precipitation (m^3/day)**	**Recharge from the Western Boundary Lake Ptuj**
Flow in	0	1228	77.433	15.000 (approximated based on the result from the *Dravsko polje* aquifer numerical model)
Flow out	2951.15	0	0	0
TOTAL in-out	93.661			

2.5. Numerical Models and Boundary Conditions (BCs)

Numerical groundwater modelling was performed using the Groundwater Modelling System (GMS 10.1.3) based on MODFLOW 2000, a comprehensive graphical user environment developed by Aquaveo. GMS is compatible with GIS -based graphical pre-processing tools to automate and streamline the modelling process for the conceptualisation and implementation of groundwater flow simulations. The GMS system consists of a graphical user interface (the GMS software) and a number of modelling codes (MODFLOW, MT3DMS, etc.) that provide tools for each phase of groundwater simulation, including site characterisation, model development, calibration, post-processing, and visualisation. GMS supports the appropriate ArcMap version as well as finite difference and finite element models in 2D and 3D, including MOD-FLOW 2000, MODPATH, MT3DMS/RT3D, SEAM3D, FEMWATER, PEST, UTEXAS, MODAEM, and SEEP2D [39].

The *Dravsko polje* and *Ptujsko polje* aquifer models were designed separately. First, conceptual models were created for each area, and then, two numerical models were designed using Modflow 2000. Groundwater flow was modelled with Modflow 2000 using the finite difference method, which uses cell-centred saturated flow. The finite difference method (FDM) is a method used to solve differential equations that are difficult or impossible to solve analytically. In both cases, steady-state models were created. The units describing the flow between the cells are L for unit length and T for unit time. The groundwater flow in the model was calculated using Darcy's law.

The three-dimensional movement of groundwater with constant density through porous earth material may be described by the partial-differential equation:

$$\frac{\partial}{\partial x}\left(K_{xx}\frac{\partial h}{\partial x}\right)+\frac{\partial}{\partial y}\left(K_{yy}\frac{\partial h}{\partial y}\right)+\frac{\partial}{\partial z}\left(K_{zz}\frac{\partial h}{\partial z}\right)+q=S_s\frac{\partial h}{\partial t} \quad (1)$$

where: K_{xx}, K_{yy}, K_{zz}—values of hydraulic conductivity along x, y, and z coordinate axes, which are assumed to be parallel to the main axes of hydraulic conductivity, h—hydraulic head [L], q—volumetric flux per unit volume representing sources and sinks of water, with $q < 0$ for the flow out of the groundwater system, and $q > 0$ for the flow into the system $\left[T^{-1}\right]$, S_s—is the specific storage of the porous media $\left[L^{-1}\right]$, t—time [T].

In general, S_s, K_{xx}, K_{yy} and K_{zz} are functions of space, and q is a function of space and time. Equation (1) describes groundwater flow under non-equilibrium conditions in a heterogeneous and anisotropic medium. The main axes of hydraulic conductivity are aligned with the coordinate directions. Unless the system is very simple, an analytical solution is possible, but usually numerical methods must be used to solve this equation. One approach is the finite difference method, in which the space is described with elements having predetermined head values at the centre of each element. The solution provides the head values at specific points and times [40].

In our model, we used the PEST tool to calibrate hydraulic conductivity and hydraulic heads between the measured and modelled data (hydraulic conductivity with a range from k = 0.01 m/s to $k = 1 \times 10^{-9}$ m/s and recharge from precipitation). The purpose of PEST (parameter estimation) is to assist in data interpretation, model calibration, and predictive analysis.

2.6. Validation of the Modelled Data

The Nash–Sutcliffe [41] efficiency coefficient was used to validate the modelled data. It indicates how well the measured and the simulated data match. The range of the efficiency coefficient is between minus infinity, which corresponds to a very poor model, and 1. The closer the coefficient is to 1, the better the modelled results. The following equation is used:

$$CE = 1 - \frac{\sum_{i=0}^{n}(y_i - y_{SIM,i})^2}{\sum_{i=0}^{n}(y_i - \bar{y})^2} \quad (2)$$

where:

CE—coefficient of efficiency [/];
y_i—measured parameter [m^3/s];
$y_{SIM,i}$—modelled parameter [m^3/s];
$\bar{y}$—mean measured parameter [m^3/s].

The calibration is considered successful if the error between the modelled and the measured data is minimal.

MODPATH was used as a model validation method of hydraulic conductivity with particle tracking simulated using MODPATH [39]. After successfully calibrating the model using PEST, we performed validation of travel times within groundwater protection areas (VVOs). If particles travel from the source to the edge of the protected area within the time frame specified in the regulation, the model has been successfully calibrated. In Slovenia, VVOs are subdivided according to the type of aquifer: a karst aquifer or a porous aquifer. The travel times of pollutants are shorter in the case of a karst aquifer. In our study, we performed validation for porous aquifers. Our aim was to ensure sustainable use of fresh drinking water in the protected areas of the *Dravsko polje* and *Ptujsko polje* groundwater pumping stations, and prevent pollution of this valuable source. In addition to being the most vulnerable direct freshwater source, and; as such; subject to the strictest restrictions, the area around the source is divided into sections that are protected according to their respective distance from the source. These areas are divided into the narrowest inner area (VVO I), the narrowest area (VVO II) and the widest area (VVO III). The strictest measures apply to the inner area, followed by strict measures and finally milder measures for the outer area. The measures for each protected area are based on the travel time (up to 50 days in VVO I and up to 400 days in VVO II) of the pollutant from the intake to the source.

2.7. Uncertainties and Limitations

Numerical groundwater simulations play an important role in the description of dynamic groundwater processes and quantitative assessments of groundwater resources [42]. However, the reliability of numerical groundwater simulations is confounded by uncertainties associated with hydrogeologic structure, spatial local-scale heterogeneity, and parameter values of modelled geological materials. Uncertainties related to hydrogeological structure are often of greatest concern [43]. Hydrogeological structure mainly refers to the spatial distribution of the spatial characteristics of aquifers and aquitards [44]. A proper description or model of their hydrogeological structure is required to accurately resolve uncertainties and effectively evaluate groundwater resources.

While the water balance of the presented porous aquifer system is well understood and previously well researched, a window of data is unpredictable and, therefore, remains unknown. For the purposes of the targeted model, area simplifications had to be applied, which proved sufficient to create a steady-state model of the system. For instance, the amount of precipitation is influenced by numerous factors, such as altitude, outskirts, natural barriers, local climate changes, etc., which have a major impact on groundwater recharge. Another variable is the recharge of groundwater from the outskirts, which is not regularly measured and needed to be inferred from data estimates from more than a decade ago. The same was true for GWLs, which had been measured in different seasons over the

years, and each measurement also required taking into account the weather conditions to achieve the best accuracy. Another factor impossible to measure is whether the riverbed is recharged by groundwater or the aquifer is recharged by a riverbed leakage. Generally, both scenarios are known to be valid, but it is impossible to determine them locally on such a scale. In addition, groundwater flow is generally known, but local changes in flow remain unknown and need to be explored locally for the needs of targeted studies. Therefore, this portion of the data must also be viewed with caution. However, to create a genuine and precise simultaneous model of a large spatial reach, it seems more appropriate to model smaller parts targeting local problems and gradually combine them to form the entire aquifer system.

3. Results

3.1. Groundwater Hydraulic Heads

The steady-state model of the *Dravsko polje* aquifer is presented in Figure 8. A high water level is characteristic for this time of the year. The steady-state model of the *Ptujsko polje* aquifer is presented in Figure 8. Intermediate water level is characteristic for this time of the year. As expected, the calculated flow direction was W-E in the northern part and slightly SE in the southern part. The modelled hydraulic heads were consistent with the expectations of the observed hydraulic heads from the conceptual model. The model of the *Ptujsko polje* aquifer showed the expected development of the calculated hydraulic heads in the flow direction (Figure 9); in the western part, the groundwater flow direction was NW to SE and in the eastern part, parallel to the Drava River, the groundwater flow direction was W-E. Hydraulic head alignment between the computed and the observed values is shown in Figure 8 for *Dravsko polje* and Figure 8 for *Ptujsko polje*.

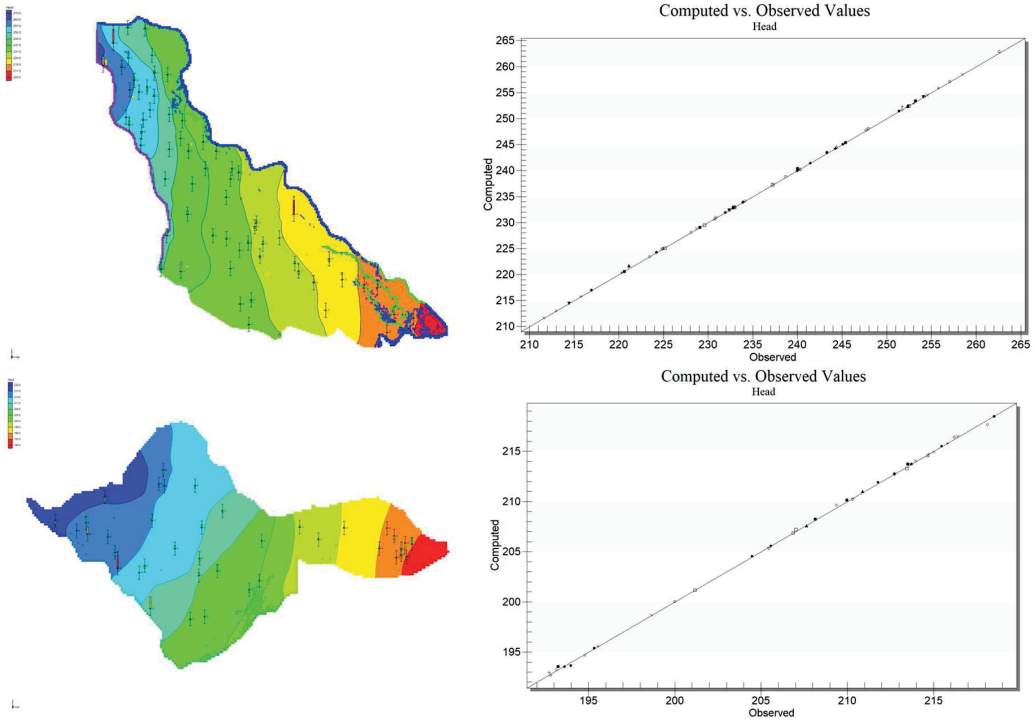

Figure 8. Modelled hydraulic heads in the *Dravsko polje* aquifer; left—model results with observation points in relation to modelled data; right—Comparison between computed and observed hydraulic heads on the *Dravsko polje* aquifer (above). Modelled hydraulic head in the *Ptujsko polje* aquifer; left—model results with observation points in relation to modelled data, where the deviation is less than 0.25 m, marked with a green line, right—deviation between computed vs. observed values in the *Ptujsko polje* aquifer (below).

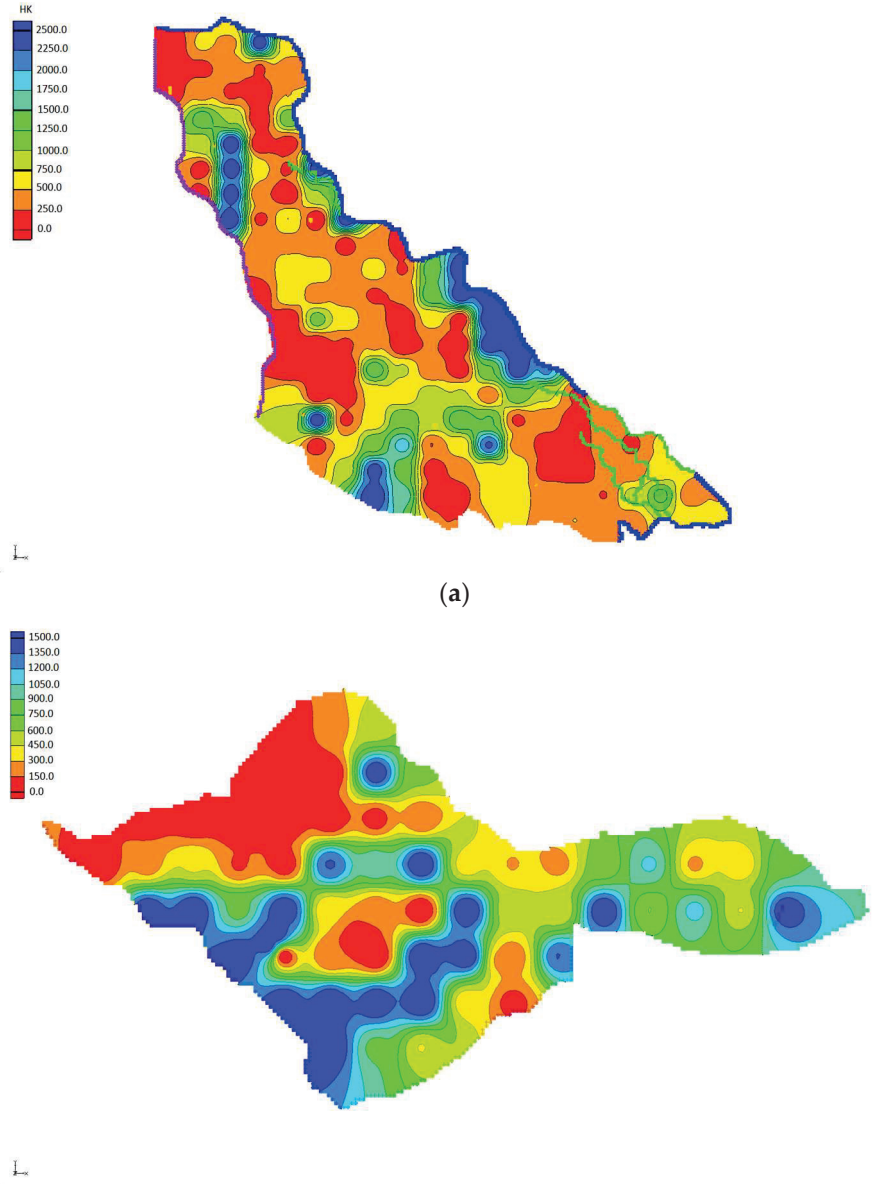

Figure 9. (**a**) Hydraulic conductivity in the *Dravsko polje* aquifer; (**b**) hydraulic conductivity in the *Ptujsko polje* aquifer.

3.2. Hydraulic Conductivity of Aquifers

The modelled hydraulic coefficient of the *Dravsko polje* aquifer ranged from 0.1 m/day to 2500 m/day. Values between 500 and 250 m/day predominate, which is a very good result based on the measured values of hydraulic conductivity [26]. The modelled hydraulic conductivity in the *Ptujsko polje* aquifer ranged from 0.8 to 1500 m/day. Hydraulic conductivity was calculated on the basis of the measured GWL data. The distribution of hydraulic conductivity is shown in Figure 9.

3.3. Flow Budget

As shown in Table 5, the results of the calculated flow budget were well estimated. The total inflow and outflow of the *Dravsko polje* aquifer is higher than predicted, but still sufficient. Most of the groundwater flows into the Drava River and the rest into drains. The calculated discharge into Lake Ptuj was lower than the estimated discharge, which was 50.000 m^3/s; the calculated discharge was 13.632 m^3/s. The results of the modelled flow

budget for the *Ptujsko polje* aquifer were very close to the estimated discharge. The result was considered to be very good. Most of the groundwater flows into the Drava River, and the rest migrates towards the drains.

Table 5. Model flow budget results for the *Dravsko polje* and *Ptujsko polje* aquifers.

	Dravsko Polje		Ptujsko Polje	
	Flow In (m^3/day)	**Flow Out (m^3/day)**	**Flow In (m^3/day)**	**Flow Out (m^3/day)**
Wells		528.5		2.951
Infiltration filed			1228	
Drains		42.984		40.065
Lake Ptuj		13.632	9.765	
River leakage	105.479	482.762	7.457	51.619
Constant head (Pohorje)	299.119	27.617		
Recharge (Precipitation)	162.997		76.205	
Total in-out	567.595	567.539	94.656	94.635

Along the western edge of the *Dravsko polje* aquifer, the model of the general head boundary is divided into three hydrogeological sections: 1, 2, and 3, as described by Žlebnik [26]. Table 6 shows the flow rates for all three sections.

Table 6. Flow rate for the western margin of the *Dravsko polje* aquifer.

Constant Head Section	Flow Rate (m^3/day)
1 section	101.631
2 section	87.947
3 section	81.922

3.4. Interaction between the Aquifers

In the place where the *Dravsko polje* aquifer is connected to the *Ptujsko polje* aquifer, the discharge from Lake Ptuj should be unified. Therefore, it is important to obtain similar values for the two areas. The values for the river should vary, as the conditions on the left and right banks of the river are not necessarily the same. From the *Dravsko polje* aquifer, the lake discharges approximately 14.000 m^3/day. The river discharges 18.000 m^3/day. The inflow from Lake Ptuj into the *Ptujsko polje* aquifer is calculated to be about 10.000 m^3/day, and so, some discrepancy between the inflow and outflow budgets was acknowledged, but it was still acceptable. However, the river leakage was neglected due to the unknown natural interaction with the groundwater and the dimensions of the river bank.

The flow budget with the intersecting part between the *Ptujsko polje* aquifer and the *Dravsko polje* aquifer is presented in Table 7.

Table 7. Flow budget result for the intersecting part *Ptujsko–Dravsko polje* aquifer.

	Ptujsko Polje		Dravsko Polje	
	Flow In	**Flow Out**	**Flow In**	**Flow Out**
Lake (m^3/day)	9.765	0		13.632
River (m^3/day)	4.095	14.525	2.982	17.492
Total in-out	13.860	14.525	2.982	31.124

3.5. Validation of Models

Finally, the data were estimated using the efficiency coefficient by Nash & Sutcliffe (NSE). According to Nash–Sutcliffe's efficiency coefficient, both models were well calibrated, with a result NSE of 1 (Table 8).

Table 8. Nash–Sutcliffe coefficient of efficiency.

	Dravsko Polje	Ptujsko Polje
$(y_i - y_{SIM,i})^2$	1.18	1.32
$(y_i - \bar{y})^2$	9991.77	2806.61
$\bar{y}$	237.53	206.91
NSE	0.99	0.99

3.6. Modelled Data Compared to Travel Times after PEST Calibration

The model results of the *Dravsko polje* and *Ptujsko polje* aquifers were also estimated using the MODPATH model, whereby the validation of hydraulic conductivity was performed. We simulated the particle pathways from the pumping source. The following pumping sites are located along the *Dravsko polje* aquifer sources: Lancova vas, Skorba, Šikole, Dravski dvor, Dobrovce, Bohova, and Betnava. In *Ptujsko polje*, there are pumping sites in Sejanica pri Mihovcih with several pumping wells. For a better visual representation, we used five wells out of seventeen.

We simulated two travel times, which also coincided with our water protection zones (VVO). The first was up to 50 days and the second was up to 400 days. Both results are shown in Figure 10. Based on the results of both travel times, both models were shown to be well calibrated. The travel time frames for 50 (purple line) and 400 (blue line) days both achieve the results within the sections of the VVO. Based on the PEST calibration, the particle travel times were shown to be well correlated. This indicates that the hydraulic conductivity was well calibrated and the effective porosity of the model was realistic.

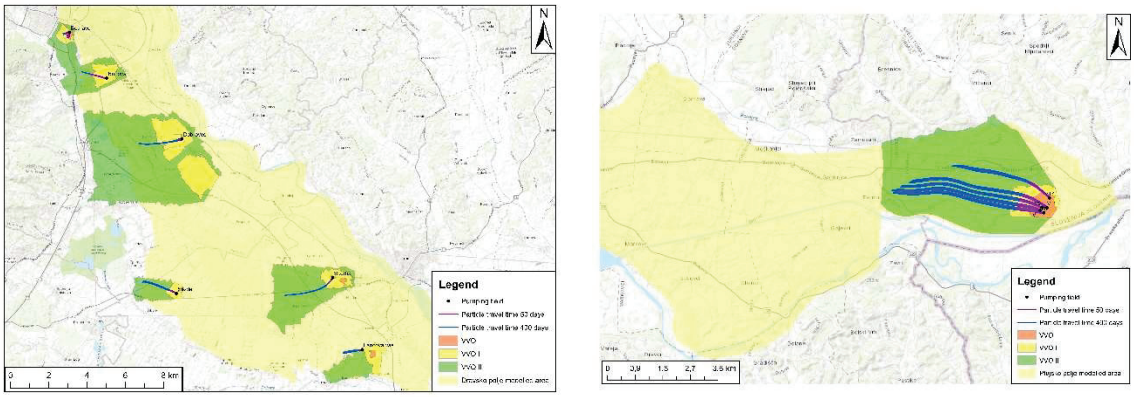

(**a**) (**b**)

Figure 10. (**a**) Modelled travel times for the *Dravsko polje* aquifer; (**b**) Modelled travel times for the *Ptujsko polje* aquifer.

4. Discussion and Conclusions

Sustainable management of hydrological resources is regulated by the European Water Directive (60/2000/EC), which requires each water authority in the EU to prepare a watershed management plan. It is noted that to fulfil these obligations, it is necessary to use integrated management tools and methods, such as computer models, while also taking into account the complexity of water bodies monitoring and uncertain future scenarios brought about by climate change.

Modelling is important to improve our understanding of hydrogeological systems and to assess future conditions in aquifers. Integrated hydrogeological models represent a valuable tool not only in the planning, but also in the implementation and operation of activities related to groundwater management, land use, and water protection action plans. A model provides a description of a specific hydrogeological system. Data availability is extremely important when developing models. For better estimates of the key parameters,

field measurements should be conducted. To assess the degree of validity of the model outputs, uncertainty analysis should also be carried out.

This article presents the first results of two separate hydrogeological numerical models for the *Dravsko polje* and *Ptujsko polje* aquifers, which were combined into an integrated groundwater resource management system. The combination of the two models allowed us to follow and optimise the same approach in groundwater management in this area. It is a tool that helps solve potential problems related to the quantity and quality of groundwater. The models were constructed using different grid-based maps: GWL, lower and upper aquifer layers. Both models were at steady state.

Based on the results, we successfully calibrated both models. From the calibrated model for the *Dravsko polje* and *Ptujsko polje* aquifers, it appeared that the hydraulic heads for both aquifers were well coordinated, and most were within a 25% discrepancy. There are larger discrepancies in hydraulic heads at the western margins of the aquifers, which is to be expected since the aquifers are highly variable. The western margin of the *Dravsko polje* aquifer presented a major modelling challenge. Due to the very high elevation of the tertiary layer and the resulting low thickness of the aquifer (less than 0.5 m), the high GWL, the constant pumping rate, and the unknown recharge rate from the surrounding area, conditions were not ideal. In addition, under such unpredictable conditions, it was very challenging for PEST to calibrate the type of groundwater flow and meet all the given conditions: hydraulic conductivity, GWL within the aquifer thickness, recharge rate, and constant pumping rate.

To achieve the best possible approximation of the model to the natural conditions, it is imperative to continuously measure GWL, infiltration by precipitation, and recharge from the surrounding area, and to update the model regularly. Only then can the model represent a good approximation of the natural conditions. The comparison between the measured and the modelled data shows a very good alignment for both models and indicates that both numerical models provide realistic results of hydraulic pressure distribution and groundwater flow direction.

In addition, the overall water budget of the *Dravsko polje* aquifer and the *Ptujsko polje* aquifer showed only minimal deviation between inflow and outflow, indicating that both models were stable. The modelled water balance data and the estimated water balance data derived from the literature showed that the water balance estimate was consistent with the modelled data. This indicates that the understanding of the groundwater system was correct from the beginning, which facilitated the attainment of correct model results.

Finally, both models were compared to particle travel times from the source of the groundwater protection areas, using the MODPATH procedure for validation. Based on the data presented, the particle travel times were very well aligned. This indicates that the hydraulic conductivity was well calibrated, and the effective porosity was realistic.

However, the models were created separately as this made them easier to present, and the modelled areas were smaller, which gave more control to the BCs. Therefore, we had to unify the intersecting part of the two models. They were connected to the Drava River and Lake Ptuj. Based on the flow budget of the *Drava polje* aquifer, the total discharge below Lake Ptuj and the Drava River was 31.124 m^3/s, and this amount of groundwater was expected to continue to flow into the *Ptujsko polje* aquifer. The modelled flow budget of the *Ptujsko polje* aquifer showed that the inflow at its western edge totalled 13.860 m^3/s, which was less than the amount from the *Dravsko polje* aquifer. Based on these volumes, more than half of the groundwater volume from the *Dravsko polje* aquifer disappeared. However, since the Drava River flows downstream, it is possible that part of the groundwater does not infiltrate into the *Ptujsko polje* aquifer, but enriches the Drava River. It should be kept in mind that Lake Ptuj is artificially regulated, which is another factor for possible discrepancies and a higher probability of errors.

Practice has shown that it is difficult to predict all input values to perfectly match the natural system. However, with such models based on the mathematical background of

cell-to-cell flow rate calculations, we can predict behaviour similar to the natural system, which is exactly the case in our example.

In summary, both models were successfully modelled and validated. Not only did these two models provide a better understanding of groundwater flow in the Drava River water body, but they can also be used to model pollution distribution and infiltration through the saturated zone of the aquifer. The hydraulic model will facilitate the planning of measures for chemical and quantitative improvement of the aquifer. According to the European Water Framework Directive, the groundwater body of the *Dravska* kotlina is classified as a groundwater body with poor chemical and quantitative status. For this reason, measures must be taken to restore its chemical and quantitative status. The hydraulic model of the aquifer is, therefore, essential both for a more detailed definition of the current situation and for predicting the impact of future measures aimed at improving the situation. In addition, these models allow for more accurate simulations of groundwater dynamics and pollutant migration in aquifers, which, in turn, can contribute to more efficient management of groundwater resources. Last but not least, both models together form the basis for a complete decision support system for the management of the entire groundwater body.

Author Contributions: Conceptualization, A.V., A.K., J.U. and N.M. methodology, A.V. and A.K.; software, A.V.; validation, A.V. and A.K.; formal analysis, A.V., A.K., J.U. and N.M.; investigation, A.V., A.K., J.U. and N.M.; resources, J.U.; data curation, A.V. and A.K.; writing—original draft preparation, A.V. and A.K.; writing—review and editing, A.V., A.K., J.U. and N.M.; visualization, A.V. and A.K.; supervision, A.K., J.U. and N.M.; project administration, A.V. and A.K.; funding acquisition, A.V. and A.K. All authors have read and agreed to the published version of the manuscript.

Funding: This study was conducted under the GEOERA HOVER project. This project received funding from the European Union's Horizon 2020 research and innovation programme under grant agreement No 731166. Scientific work was also co-funded by the Slovenian Research Agency (ARRS) in the framework of the Groundwater and Geochemistry (P1-0020) research programme and post-doctoral research project "Urban hydrogeology: Improved methods for determining the occurrence, transport processes and origin of pharmaceuticals in groundwater resources" (Z1-2639).

Data Availability Statement: The data presented in this study are available on request from Geological Survey of Slovenia research databases.

Conflicts of Interest: The authors declare no conflict of interest.

References

1. Moreno, L.J.A.; Zuleta Lemus, D.; Lasso Rosero, J.; Agudelo Morales, D.M.; Sepúlveda Castaño, L.M.; Paredes Cuervo, D. Evaluation of aquifer contamination risk in urban expansion areas as a tool for the integrated management of groundwater resources. Case: Coffee Growing Region, Colombia. *Groundw. Sustain. Dev.* **2020**, *10*, 100298. [CrossRef]
2. Rushton, S.P.; Ormerod, S.J.; Kerby, G. New paradigms for modelling species distributions? *J. Appl. Ecol.* **2004**, *41*, 193–200. [CrossRef]
3. Bagheri, A.; Bondori, A.; Allahyari, M.S.; Damalas, C.A. Modeling farmers' intention to use pesticides: An expanded version of the theory of planned behavior. *J. Environ. Manag.* **2019**, *248*, 109291. [CrossRef] [PubMed]
4. Cui, T.; Sreekanth, J.; Pickett, T.; Rassam, D.; Gilfedder, M.; Barrett, D. Impact of model parameterization on predictive uncertainty of regional groundwater models in the context of environmental impact assessment. *Environ. Impact Assess. Rev.* **2021**, *90*, 106620. [CrossRef]
5. Madani, K.; Mariño, M.A. System dynamics analysis for managing Iran's Zayandeh-rud river basin. *Water Resour. Manag.* **2009**, *23*, 2163–2187. [CrossRef]
6. Prodanovic, P.; Simonovic, S.P. An operational model for support of integrated watershed management. *Water Resour. Manag.* **2010**, *24*, 1161–1194. [CrossRef]
7. Safavi, H.R.; Golmohammadi, M.H.; Sandoval-Solis, S. Expert knowledge based modeling for integrated water resources planning and management in the Zayandehrud River Basin. *J. Hydrol.* **2015**, *528*, 773–789. [CrossRef]
8. Nakić, Z.; Ružičić, S.; Posavec, K.; Mileusnić, M.; Parlov, J.; Bačani, A.; Durn, G. Conceptual model for groundwater status and risk assessment—Case study of the Zagreb aquifer system. *Geol. Croat.* **2013**, *66*, 55–77. [CrossRef]
9. Kaur, M.; Hewage, K.; Sadiq, R. Investigating the impacts of urban densification on buried water infrastructure through DPSIR framework. *J. Clean. Prod.* **2020**, *259*, 120897. [CrossRef]

10. Al-Ghouti, M.A.; Khan, M.; Nasser, M.S.; Al-Saad, K.; Heng, O.E. Recent advances and applications of municipal solid wastes bottom and fly ashes: Insights into sustainable management and conservation of resources. *Environ. Technol. Innov.* **2021**, *21*, 101267. [CrossRef]
11. Liu, B.; Li, Y.; Jiang, W.; Chen, J.; Shu, L.; Liu, J. Understanding groundwater behaviors and exchange dynamics in a linked catchment-floodplain-lake system. *Sci. Total Environ.* **2022**, *853*, 158558. [CrossRef]
12. Skoulikidis, N.T. The environmental state of rivers in the Balkans—A review within the DPSIR framework. *Sci. Total Environ.* **2009**, *407*, 2501–2516. [CrossRef]
13. Lockhart, K.M.; King, A.M.; Harter, T. Identifying sources of groundwater nitrate contamination in a large alluvial groundwater basin with highly diversified intensive agricultural production. *J. Contam. Hydrol.* **2013**, *151*, 140–154. [CrossRef]
14. Li, H.; Wang, Y.; Liu, F.; Tong, L.; Li, K.; Yang, H.; Zhang, L. Volatile organic compounds in stormwater from a community of Beijing, China. *Environ. Pollut.* **2018**, *239*, 554–561. [CrossRef] [PubMed]
15. Lopez, B.; Ollivier, P.; Togola, A.; Baran, N.; Ghestem, J.P. Screening of French groundwater for regulated and emerging contaminants. *Sci. Total Environ.* **2015**, *518–519*, 562–573. [CrossRef]
16. Bunting, S.Y.; Lapworth, D.J.; Crane, E.J.; Grima-Olmedo, J.; Koroša, A.; Kuczyńska, A.; Mali, N.; Rosenqvist, L.; Van Vliet, M.E.; Togola, A.; et al. Emerging organic compounds in European groundwater. *Environ. Pollut.* **2021**, *269*, 115945. [CrossRef] [PubMed]
17. Koroša, A.; Mali, N. Control of organic contaminants in groundwater by passive sampling and multivariate statistical analysis. *J. Environ. Manag.* **2022**, *318*, 115440. [CrossRef]
18. European Commission (EC). Directive 2000/60/EC of the European Parliament and of the Council of 23 October 2000 establishing a framework for Community action in the field of water policy. *Off. J. Eur. Union* **2000**, *327*, 1–73.
19. European Commission (EC). Directive 2006/118/EC of the European Parliament and the Council of 12th of December 2006 on the protection of ground water against pollution and deterioration. *Off. J. Eur. Union* **2006**, *372*, 19–31.
20. Official gazette of the Republic of Slovenia. Water Act (ZV-1). No. 67/02, 2/04–ZZdrI-A, 41/04–ZVO-1, 57/08, 57/12, 100/13, 40/14, 56/15 and 65/20. Available online: http://pisrs.si/Pis.web/pregledPredpisa?id=ZAKO1244 (accessed on 15 February 2023).
21. Official Gazette of the Republic of Slovenia. Regulation on the protection of waters against pollution caused by nitrates from agricultural sources. No. 5/13. Available online: https://eur-lex.europa.eu/legal-content/EN/ALL/?uri=celex%3A31991L0676 (accessed on 15 February 2023).
22. Bredehoeft, J. The conceptualization model problem—Surprise. *Hydrogeol. J.* **2005**, *13*, 37–46. [CrossRef]
23. Hugman, R.; Lotti, F.; Doherty, J. Probabilistic Contaminant Source Assessment—Getting the Most Out of Field Measurements. *Groundwater* **2022**. [CrossRef] [PubMed]
24. Enemark, T.; Peeters, L.J.M.; Mallants, D.; Batelaan, O. Hydrogeological conceptual model building and testing: A review. *J. Hydrol.* **2019**, *569*, 310–329. [CrossRef]
25. Hartmann, A. The Hydrology of Groundwater Systems—From Recharge to Discharge. In *Encyclopedia of Inland Waters*, 2nd ed.; Elsevier: Amsterdam, The Netherlands, 2021; Volume 3, pp. 324–330. [CrossRef]
26. Žlebnik, L. Hydrogeology of the Drava field. *Geologija* **1982**, *1*, 151–164.
27. Žlebnik, L. Hydrogeology of the Ptuj field. *Geologija* **1991**, *34*, 337–352. [CrossRef]
28. Klasinc, M. Pliocenski Vodonosnik Dravskega Polja. Diplomsko delo, Univerza v Ljublajni, Naravoslovno Tehniška Fakulteta, Ljubljana, Slovenia, 2013; pp. 10–25f.
29. Prestor, J.; Drobne, F.; Žlebnik, L. *Hydrogeological Research for the Capture of Underground Water with a Deep Well VG-4/99 in Skorba*; Geological Survey of Slovenia: Ljubljana, Slovenia, 1999.
30. BakerHughes. JewelSuite Geomechanics. 2010. Available online: https://www.bakerhughes.com/oilfield-services-and-equipment-digital/well-planning/jewelsuite-geomechanics (accessed on 12 December 2022).
31. Juang, K.W.; Chen, Y.S.; Lee, D.Y. Using sequential indicator simulation to assess the uncertainty of delineating heavy-metal contaminated soils. *Environ. Pollut.* **2004**, *127*, 229–238. [CrossRef]
32. Žlebnik, L.; Drobne, F. Pliocene Aquifers—The Source of drinking Water for Ptuj and Ormož Region, Slovenia. *Geologija* **1998**, *41*, 339–354. [CrossRef]
33. ARSO. Climatic Conditions in Slovenia. 2018; pp. 1–27. Available online: http://meteo.arso.gov.si/ (accessed on 16 December 2017).
34. Turnšek, A. Groundwater Storage in Quaternary Aquifer of Dravsko Polje. Master's Thesis, University of Ljubljana, Ljubljana, Slovenia, 2016. Available online: https://repozitorij.uni-lj.si/IzpisGradiva.php?lang=eng&id=83631 (accessed on 10 January 2023).
35. Brenčič, M. *Assessment of Changes in the Groundwater Level in the Area of Ptujsko Polje*; Geological Survey of Slovenia: Ljubljana, Slovenia, 2022.
36. Veršič, A. *Environmental Metadata Portal and Online Services*; Mišič water days 2007; Water Management: Hillsboro, TX, USA, 2007.
37. Brilly, M. Groundwater model of the Vrban Plateau. In *Mišičev Vodarski Day: Collection of Papers*; 1994; pp. 44–45.
38. Frantar, P.; Herrmann, F.; Andjelov, M.; Draksler, A.; Wendland, F. Vodnobilančni model MGROWA-SI. In *Bornik Referatov. 29. Mišičev Vodarski dan 2018, Maribor, 06. December. Maribor: Vodnogospodarski biro, 2018. Str. 199-205, Ilustr. Mišičev Vodarski dan. Aquaveo, L.L.C. Groundwater Modeling System*, version 10.1.3; Aquaveo: Provo, UT, USA, 2014.

39. Harbaugh, A.W. *MODFLOW-2005, the U.S. Geological Survey Modular Ground-Water Model–the Ground-Water Flow*; Process: U.S. Geological Survey Techniques and Methods 6-A16. U.S. Geological Survey: Reston, VA, USA, 2005.
40. Nash, J.E.; Sutcliffe, J.V. River flow forecasting through conceptual models part I—A discussion of principles. *J. Hydrol.* **1970**, *10*, 282–290. [CrossRef]
41. Wu, J.C.; Zeng, X.K. Review of the uncertainty analysis of groundwater numerical simulation. *Chin. Sci. Bull.* **2013**, *58*, 3044–3052. [CrossRef]
42. Højberg, A.L.; Refsgaard, J.C. Model uncertainty-parameter uncertainty versus conceptual models. *Water Sci. Technol.* **2005**, *52*, 177–186. [CrossRef]
43. Zhang, Y.; Person, M.; Paola, C.; Gable, C.W.; Wen, X.H.; Davis, J.M. Geostatistical analysis of an experimental stratigraphy. *Water Resour. Res.* **2005**, *41*, 1–20. [CrossRef]
44. Renard, B.; Kavetski, D.; Kuczera, G.; Thyer, M.; Franks, S.W. Understanding predictive uncertainty in hydrologic modeling: The challenge of identifying input and structural errors. *Water Resour. Res.* **2010**, *46*, 1–22. [CrossRef]

Disclaimer/Publisher's Note: The statements, opinions and data contained in all publications are solely those of the individual author(s) and contributor(s) and not of MDPI and/or the editor(s). MDPI and/or the editor(s) disclaim responsibility for any injury to people or property resulting from any ideas, methods, instructions or products referred to in the content.

International Journal of
Environmental Research and Public Health

MDPI

Article

Screening and Optimization of Conditions for the Adsorption of Cd^{2+} in Serpentine by Using Response Surface Methodology

Xufeng Zhang, Liyu Du * and Wenjuan Jin

College of Land and Environment, Shenyang Agricultural University, Shenyang110161, China
* Correspondence: duliyu2006@syau.edu.cn

Abstract: In order to explore the optimal conditions for the adsorption of Cd^{2+} in serpentine, this paper studied the adsorption of simulated cadmium solutions with serpentine as an adsorbent. On the basis of a single factor experiment, four factors including the amount of serpentine, initial pH, the initial concentration of solutions, and adsorption time were selected as the influencing factors, and the adsorption quantity and adsorption rate of serpentine to Cd^{2+} were double response values using the Box–Behnken design. Response surface analyses were used to study the effects of four factors on the adsorption quantity and adsorption rate of serpentine on cadmium, and the interaction between various factors. The results showed that the optimum adsorption conditions were as follows: the amount of serpentine was 1%, the initial pH was 5.5, the initial solution concentration was 40.83 $mg \cdot L^{-1}$, and the adsorption time was 26.78 h. Under these conditions, the theoretical adsorption quantity and adsorption rate of serpentine to Cd^{2+} were 3.99 $mg \cdot g^{-1}$ and 95.24%, respectively. At the same time, after three repeated experiments, the actual adsorption quantity and adsorption rate of serpentine to Cd^{2+} were 3.91 $mg \cdot g^{-1}$ and 94.68%, respectively, and the theoretical value was similar to the actual value. Therefore, it was proved that the experimental design of the regression model is reliable, and it is feasible to use the response surface method to optimize the adsorption conditions of serpentine on Cd^{2+}.

Keywords: serpentine; Cd^{2+}; adsorption; response surface methodology (RSM)

1. Introduction

Industrial wastewater is an important source of pollution relative to the water environment. With the acceleration of industrialization processes, a large amount of industrial heavy metal wastewater containing toxic chemical elements, such as cadmium (Cd), zinc (Zn), and nickel (Ni), enters the environment [1,2]. Among the known heavy metals, Cd is one of the most toxic due to its bioaccumulation in human and animal bodies; moreover, it is almost non-biodegradable, even at low concentrations [3,4]. The majority of Cd contamination in water and wastewater originates from ore processing plants, metal refineries' discharges, mine drainage water, waste batteries' runoff, the manufacture of phosphate fertilizers and pesticides, pigment production, printing, the photographic industry, and rainwater runoff from mining areas [5,6]. In aqueous media, Cd is shown as Cd^{2+}, a highly mobile divalent heavy metal ion that can be easily carried by water and wastewater, leading to the widespread release of this poisonous element [7]. Therefore, methods for effectively treating heavy metal industrial wastewater are urgently needed.

The treatment methods of heavy metal wastewater generally include adsorption, chemical precipitation, redox, ion exchange, membrane separation, electrochemical methods, etc. [8]. Among them, the adsorption method uses porous solid adsorbents to treat wastewater [9], which has the following advantages: low cost, good treatment effects, and no secondary pollution [10,11]. Moreover, it is currently one of the heavy metal wastewater treatment methods that has been popularized and possesses application value. The key to the adsorption method is the choice of adsorbents, and there are various types of

adsorbents. Among these adsorbents, silicate minerals have the advantages of abundant reserves, ample sources, and low cost, and they have a large specific surface area and a special crystal layer structure [12,13]. Silicate minerals can adsorb heavy metals, mainly including surface adsorption and ion exchange. The silicate mineral itself is an excellent adsorbent that has a large specific surface area and surface energy, which can adsorb metal ions on its surface. Ion exchanges refer to the use of interlayer metal examples in silicate minerals, such as Na^+, Al^{3+}, and other metal ions for ion exchange with heavy metal ions; this process belongs to electrostatic adsorption [14,15]. Therefore, it has great potential in the treatment of heavy metal wastewater treatment. Silicate minerals mainly include serpentine, sepiolite, zeolite, bentonite, etc.

Serpentine has a large specific surface area, good pore structure, and strong surface activity [16]. It is a hydrous magnesium-rich silicate mineral, containing 43% MgO, 44.1% SiO_2, 12.9% water, and, usually, some small amounts of other elements [17]. Nevertheless, the stabilization performance of the original serpentine on heavy metals is limited due to finite binding sites, thus hindering its feasibility in application [18]. The modification methods of materials vary, including methods such as doping foreign substances, thermal modification, etc. For example, some studies have reported that the introduction of N doping in carbon materials can alter the electron density of partial C atoms, and the specific surface area of carbon materials can be improved, thereby improving their adsorption and oxidation capacity for pollutants [19]. The characteristics of serpentine adsorbing heavy metals after thermal modification have been studied, and it has been confirmed that thermal activation treatments can increase the specific surface area of serpentine and reorganize its internal structure, greatly improving its ability to adsorb heavy metal ions [20,21]. For this reason, considering the thermal activation modification of serpentine, the purpose is to improve its ability to adsorb heavy metals. Therefore, methods for optimizing and screening the modified serpentine and the adsorption conditions in order to achieve the best repair effect are important for the further development of serpentine as a good repair agent.

Response surface methodology (RSM) is a method oriented toward experimental designs and mathematical modeling optimizations [22]. According to a small number of representative experiments, a mathematical model of various factors and experimental results was established to obtain the best prediction figure of merit and the optimization of process conditions, and the Box–Behnken central combination design was a commonly used response surface method for finding optimal conditions in a multi-factor system [23,24]. Currently, it has been widely used in many fields [25,26], and there have been relatively few studies on the application of response surface methods for optimizing the process of absorbing heavy metals in wastewater by serpentine.

Therefore, from the perspectives of serpentine structure and surface property changes, this article explores the adsorption capacity of Cd^{2+} under different conditions using static adsorption experiments. On the basis of the single factor experiment, the Box–Behnken experimental design is used to optimize the conditions for the adsorption of Cd^{2+} by serpentine in order to provide a theoretical basis for improving the removal effect of Cd^{2+} and to provide an optimized process for the treatment of Cd^{2+} in wastewater.

2. Materials and Methods

2.1. Test Materials

Natural serpentine (S-0): The serpentine was obtained from Xiuyan County, Anshan City, Liaoning Province, China; ground by hand; passed through a 200-mesh sieve; and stored in a plastic sealed bag for later use. The main compositions and contents of serpentine are shown in the Table 1.

Thermally modified serpentine (S-700): The natural serpentine was placed in a muffle furnace and calcined at a constant temperature of 700 °C for 2 h at a heating rate of 5 °C/min. All serpentine used in this article comprised thermally modified serpentine.

Table 1. The main composition and content of serpentine.

Composition	SiO_2	MgO	CaO	Al_2O_3	Fe_2O_3
Content (%)	52.93	46.52	0.85	0.34	0.36

The superficial morphologies of materials were identified by using a scanning electron microscope (SEM). An energy dispersive spectrometer (EDS) was used to determine the element content of the sample, and the crystal textures of the two samples were detected via an X-ray powder diffractometer (XRD) [27].

2.2. Experimental Method

2.2.1. Equilibrium Adsorption Experiment

In this study, 0.5 g of natural serpentine (S-0) and thermally modified serpentine (S-700) was dispensed into a 50 mL centrifuge tube, and then 50 mL of cadmium solution was added at different concentrations. The initial pH of the solution was 6, and the concentrations of the cadmium solution were 40 $mg \cdot L^{-1}$, 80 $mg \cdot L^{-1}$, 120 $mg \cdot L^{-1}$, 160 $mg \cdot L^{-1}$, and 200 $mg \cdot L^{-1}$. These centrifugal tubes were placed in a high-speed constant-temperature oscillator for oscillation, with a rotating speed of 220 $r \cdot min^{-1}$. The temperatures of 25 °C, 35 °C, and 45 °C were used, and an oscillation duration of 24 h was used. Centrifugation and filtration occurred after the oscillations.

2.2.2. Single-Factor Experiment

After the pre-experiment, the amount of serpentine (AS), the initial pH (pH), the initial concentration of the solution (C), and the adsorption time (T) were selected to explore the influence of Cd^{2+} adsorption quantity (AQ) and adsorption rate (AR), and the best range for each influencing factor was preliminarily determined.

The pH was 6, C was 50 $mg \cdot L^{-1}$, and T was 24 h. The influence of different AS (1%, 2%, 3%, 4%, and 5%) on the AQ and AR was investigated.

The AS was 1%, C was 50 $mg \cdot L^{-1}$, and T was 24 h. The influence of different pH (2, 3, 4, 5, and 6) on the AQ and AR was investigated.

The AS was 1%, the pH was 6, and T was 24 h. The influence of different C (10 $mg \cdot L^{-1}$, 20 $mg \cdot L^{-1}$, 50 $mg \cdot L^{-1}$, 100 $mg \cdot L^{-1}$, and 200 $mg \cdot L^{-1}$) on the AQ and AR was investigated.

The AS was 1%, the pH was 6, and C was 50 $mg \cdot L^{-1}$. The influence of different T (0.5 h, 2 h, 6 h, 12 h, and 24 h) on the AQ and AR was investigated.

Each of the above single-factor experiments was carried out three times.

2.2.3. Box–Behnken Center Combination Experiment Design

Based on the single factor experiment, a Box–Behnken design of the central combination experiment was adopted, and four factors of AS, pH, C, and T were selected. The AQ and AR were obtained relative to the Cd^{2+} double response value, and a response surface analysis experiment was designed with four factors and three levels. The three levels of each factor were coded with −1, 0, and 1, as shown in Table 2.

Table 2. Factors and levels in response surface methodology.

Factor	Level		
	−1	**0**	**1**
A AS (%)	1	2	3
B pH	5.5	6	6.5
C C ($mg \cdot L^{-1}$)	40	50	60
D T (h)	20	24	28

2.3. Data Analysis

The concentration of Cd^{2+} in the solution was measured by an atomic absorption spectrophotometer (WYA2200); then, the adsorption quantity and adsorption rate were calculated by using the following formula.

Adsorption quantity:

$$AQ = \frac{v(Co - Ce)}{m} \quad (1)$$

Adsorption rate:

$$AR = \frac{Co - Ce}{Co} \times 100\% \quad (2)$$

Here, in Equations (1) and (2), v denotes the volume of the added Cd^{2+} solution, L; m denotes the amount of the added serpentine, g; Co and Ce denote the Cd^{2+} concentration in the solution before and after adsorption, $mg \cdot L^{-1}$; AQ denotes the adsorption quantity, $mg \cdot g^{-1}$; AR denotes the adsorption rate, %.

The experimental data were analyzed and processed by Origin8.5 and Design Expert12.0.

3. Results and Discussion

3.1. Serpentine Sample Characterization

Natural serpentine (S-0) comprised many irregular flaky structures, while the thermally modified serpentine (S-700) had no layered structure, and the surface of the material comprised a block structure formed by some agglomerated particles (Figure 1).

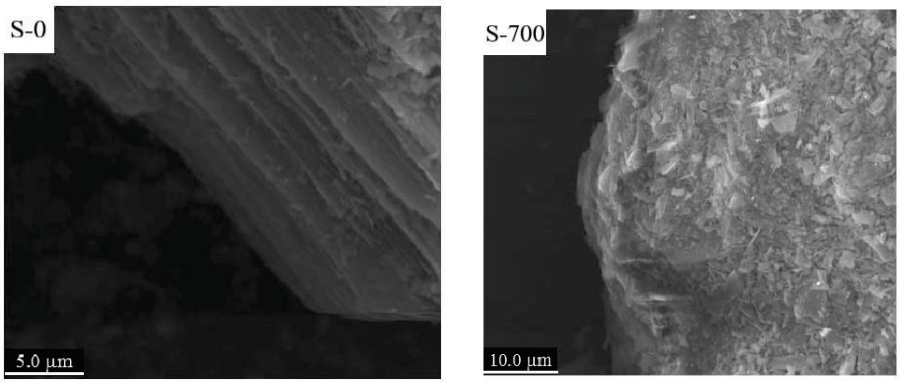

Figure 1. SEM images of two serpentines.

After the thermal modification of serpentine, the content of oxygen (O) decreased, while the content of magnesium (Mg) and silicon (Si) increased, which indicated that the serpentine was dehydrogenated during the thermal activation process (Figure 2).

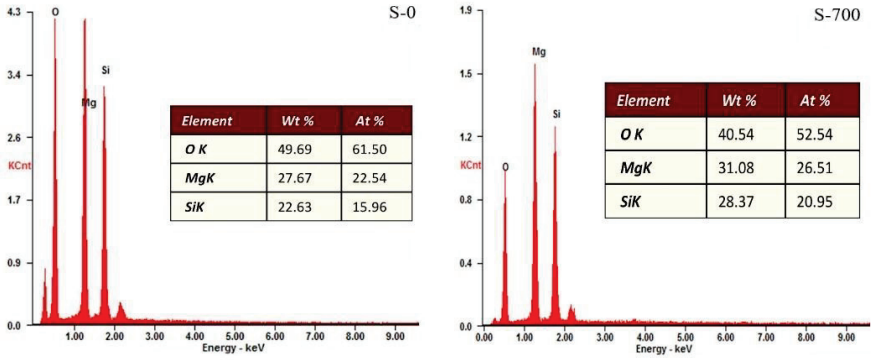

Figure 2. EDS images of two serpentines.

For natural serpentine (S-0), the diffraction peaks (JCPDS 07-0417) attributed to antigorite (a type of serpentine) appeared at 2θ of 12.1°, 24.5°, 35.6°, 37.2°, 41.6°, 42.0°, and 50.2°. When the modification temperature was 700 °C, compared with natural serpentine (S-0), its diffraction peaks obviously changed, and all characteristic diffraction peaks attributed to antigorite disappeared (Figure 3). At the same time, some new diffraction peaks appeared at 2θ of 22.9°, 32.3°, 35.5°, 35.7°, 39.7°, and 52.3°. These diffraction peaks belonged to the characteristic diffraction peaks of forsterite (JCPDS 34-0189), indicating that the crystal structure of serpentine changed when the modification temperature was 700 °C; that is, the serpentine was transformed into forsterite.

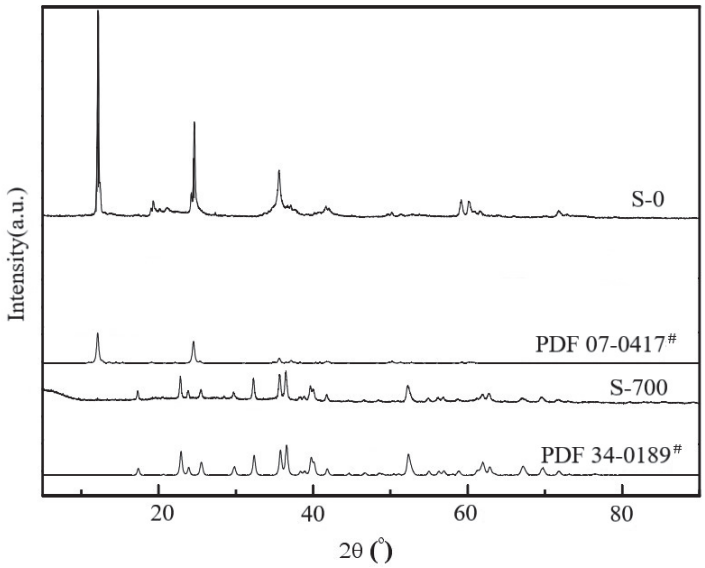

Figure 3. XRD patterns for two serpentines.

Compared with natural serpentine (S-0), the specific surface area and pore volume of thermally modified serpentine (S-700) significantly improved, which was mainly due to the collapse of the layered structure of serpentine at high temperatures and the formation of accumulated slit pores (Table 3).

Table 3. Structural properties of serpentines.

S-T	BET Surface Area ($m^2\ g^{-1}$)	Pore Volume ($cm^3\ g^{-1}$)	Aperture (nm)
S-0	6.1	0.017	11.01
S-700	13.7	0.028	8.10

3.2. Study on the Adsorption Isotherms of Cd^{2+} on Serpentine

A Langmuir isothermal adsorption model was used to fit the adsorption process of natural serpentine (S-0) and heat-modified serpentine (S-700) for Cd^{2+} in order to explore the adsorption characteristics of serpentine for Cd^{2+}.

Langmuir isothermal adsorption model:

$$\frac{C_e}{q_e} = \frac{C_e}{q_m} + \frac{1}{k_L q_m}$$

C_e denotes the balance concentration, $mg \cdot L^{-1}$; q_e denotes the balance adsorption quantity, $mg \cdot g^{-1}$; q_m denotes the maximum adsorption quantity, $mg \cdot g^{-1}$; K_L denotes the adsorption model constant.

The Langmuir isotherm adsorption model can describe the entire adsorption process, indicating that serpentine and Cd^{2+} experienced monolayer adsorption (Figure 4, Table 4).

The maximum adsorption quantity of thermally modified serpentine (S-700) was higher than that of natural serpentine (S-0), indicating that the adsorption effect of thermally modified serpentine (S-700) on Cd^{2+} significantly increased. In addition, when the temperature increased from 25 °C to 45 °C, the adsorption quantity of serpentine to Cd^{2+} increased, indicating that increasing the temperature within a certain temperature range promoted the adsorption.

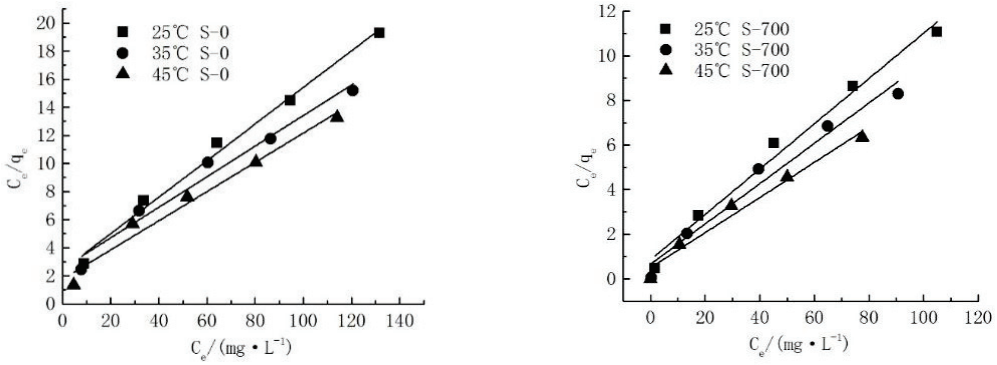

Figure 4. Langmuir isothermal adsorption model of serpentine to Cd^{2+}.

Table 4. Fitting parameters of the Langmuir isotherm adsorption model.

S-T	Temperature	Langmuir		
		R^2	$q_m/(mg \cdot g^{-1})$	K_L
S-0	25 °C	0.9883	7.6982	0.0536
	35 °C	0.9651	9.1971	0.0428
	45 °C	0.9670	9.6246	0.0585
S-700	25 °C	0.9816	9.8774	0.1185
	35 °C	0.9527	11.0693	0.1379
	45 °C	0.9696	12.6904	0.1594

3.3. Single Factor Experiment Results

3.3.1. Effect of the AS on Adsorption Effect

The effect of different ASs on the AQ and AR of Cd^{2+} is shown in Figure 5. It can be observed that the AQ of Cd^{2+} gradually decreased as the AS increased. Specifically, when the AS was 1%, its AQ of Cd^{2+} reached 4.13 $mg \cdot g^{-1}$, but when the AS was 2%, the AQ of Cd^{2+} reduced to 2.48 $mg \cdot g^{-1}$, which was 40% lower than that of 1%. When the AS was 5%, the AQ of Cd^{2+} was only 0.99 $mg \cdot g^{-1}$, which was 76% lower than that of 1%. This change in AQ may be due to the increase in the AS, although the adsorption sites provided by serpentine gradually increased, but the AQ of Cd^{2+} that can be adsorbed per unit area would decrease, resulting in a decrease in AQ. This was similar to the research results of Sun Pengcheng, who used serpentine to adsorb Cd^{2+} in water [28]. Although the AQ of Cd^{2+} in water gradually decreased with the increase in the AS, the AR of Cd^{2+} increased. When the AS was 1%, although the AQ of Cd^{2+} was the largest, the AR of Cd^{2+} was low at this moment, which was only 82.66%. When the AS was 2%, the AR of Cd^{2+} had risen to 99.28%. At this time, the AR reached a very high level. When the AS increased to 3%, 4%, and 5%, it was found that the increase in the AR was not significant and it was maintained at a high level. Under this condition, the AQ of Cd^{2+} also reached a high level, which was 2.48 $mg \cdot g^{-1}$. In summary, the AS was selected as 2%.

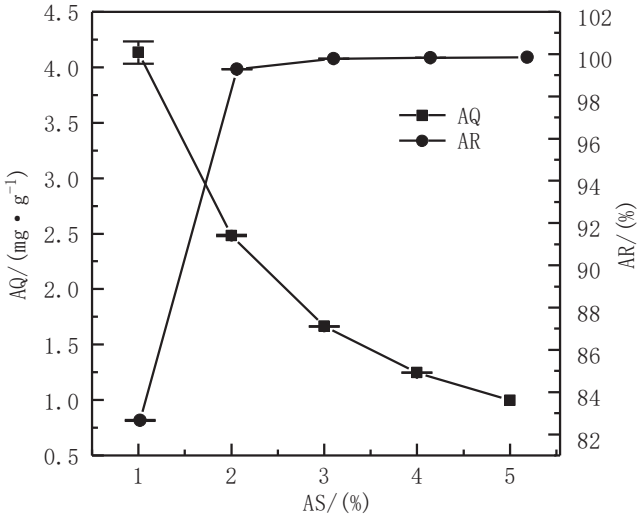

Figure 5. Effect of the AS on adsorption effect.

3.3.2. Effect of the pH on Adsorption Effect

The effect of different pH on the AQ and AR of Cd^{2+} is shown in Figure 6. It can be seen that the AQ and AR of Cd^{2+} gradually increased when the pH increased. Specifically, when the pH was 2, the AQ of Cd^{2+} was 2.96 mg·g^{-1}, and when the pH increased to 6, the AQ also increased to 4.10 mg·g^{-1}, which comprised an increase of 28% compared to when the pH was 2. When the pH was 2, the AR of Cd^{2+} was 59.13%. When the pH increased to 6, the AR of Cd^{2+} also increased to 81.93%. Compared with when the pH was 2, it increased by 38%. It could be seen that when the pH increased from 2 to 6, the AQ and AR of Cd^{2+} greatly improved, and the change in pH had a significant effect on adsorption processes. This change in AQ and AR might be because of the phenomenon where, with an increase in the pH, deprotonation occurred on the surface of the serpentine, and the number of negatively charged sites increased, resulting in an increase in the adsorption of Cd^{2+} on the serpentine [29]. Studies have also shown that adsorbents showed different surface charges in different pH solutions, which led to different removal effects for the heavy metals. For example, studies have shown that the charges on biochemical composite (CFB1-P) surfaces were negative at a pH of over 2.11, while they were positive at a pH beneath 2.11 [30]. Subsequently, measuring the zero potential of serpentine and analyzing the results should be considered. When the pH was 6, the AQ (4.10 mg·g^{-1}) and AR (81.93%) of Cd^{2+} by serpentine reached the highest values, so the pH was selected at 6 for subsequent experiments.

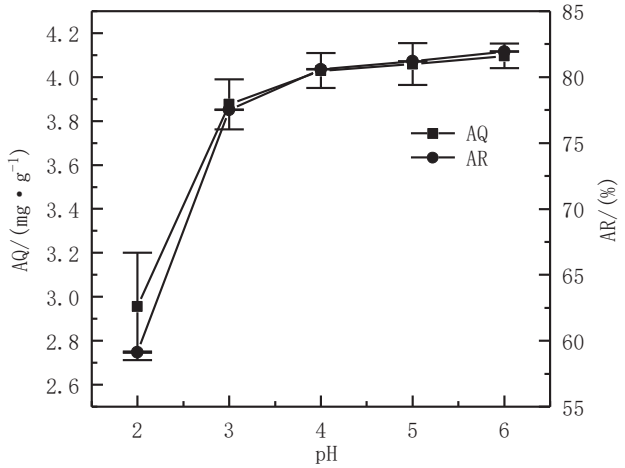

Figure 6. Effect of the pH on adsorption effect.

3.3.3. Effect of the C on Adsorption Effect

The effect of different Cs on the AQ and AR of Cd^{2+} is shown in Figure 7. It can be observed that the AQ of Cd^{2+} continuously increased with the increase in C. Specifically, when C was 10 mg·L^{-1}, the AQ of Cd^{2+} was only 0.99 mg·g^{-1}, but when the C was 50 mg·L^{-1}, the AQ of Cd^{2+} increased to 4.15 mg·g^{-1}. Compared with the C at 10 mg·L^{-1}, it increased by 3.2 times. At this time, it can be observed that there was a significant increase. When the C continued to increase to 200 mg·L^{-1}, it could be seen that the AQ of Cd^{2+} increased to 9.53 mg·g^{-1}, compared with the C at 10 mg·L^{-1} that increased by 8.6 times; the increase was extremely significant. Although the AQ of Cd^{2+} increased with the increase in C, the AR of Cd^{2+} exhibited opposite results. It could be seen that when the C was 10 mg·L^{-1}, the AQ was the smallest, but at this time, the AR reached 99.74%, but, when the C increased to 50 mg·L^{-1}, the AR of Cd^{2+} was 82.91%, which was 17% lower than when the C was 10 mg·L^{-1}. When the C reached 200 mg·L^{-1}, the AQ of Cd^{2+} was the largest, but at this time, the AR was only 47.63%; this may be explained by the continuous increase in C, which would cause the AR of Cd^{2+} to continually decline. This change in the AR of Cd^{2+} in water might be due to the fact that the adsorption sites on the surface of serpentine were certain. When the C was low, the adsorption equilibrium could provide adsorption sites that were relatively sufficient, and the adsorption rate was high; when the C was high, the adsorption sites gradually became saturated, resulting in a gradual decrease in the AR [29]. The coexistence of multiple ions might affect the adsorption effect of serpentine, and, in order to better explore the potential of serpentine in treating cadmium-containing industrial wastewater, the coexisting ion test will be added in subsequent experiments [31]. Considering the change law and value of both AQ and AR, when the C was 50 mg·L^{-1}, the AQ and AR of Cd^{2+} in water were 4.15 mg·g^{-1} and 82.91%, respectively; they were relatively high. Therefore, the C selected for subsequent experiments was 50 mg·L^{-1}.

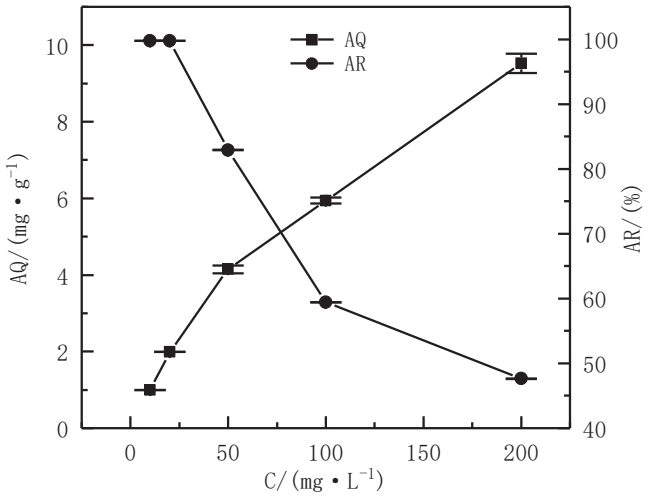

Figure 7. Effect of the C on adsorption effect.

3.3.4. Effect of the T on Adsorption Effect

The effect of different T on the AQ and AR of Cd^{2+} is shown in Figure 8. It can be observed that the AQ and AR of Cd^{2+} both decreased first and then increased with the increase in the T. When the T was 0.5 h, the AQ of Cd^{2+} was 3.17 mg·g^{-1}; when the T reached 2 h, the AQ of Cd^{2+} was 2.91 mg·g^{-1}. Compared with the adsorption time of 0.5 h, it was reduced by 8%. When the T reached 24 h, the AR of Cd^{2+} was 4.10 mg·g^{-1}, which increased by 41% compared with when the T was 2 h. When the T was 0.5 h, the AR of Cd^{2+} was 63.40%. When the T was 2 h, the AR of Cd^{2+} was 58.11%, which was 8% lower than when the T was 0.5 h. When the T was 24 h, the AR of Cd^{2+} was 81.93%, which was increased by 41% when the adsorption time was 2 h. The adsorption was rapid in the first 0.5 h, which might be because of the observation that the adsorption at this stage belonged

to the nonspecific adsorption phase, and the stability efficiency was high and labile [32]. In the next few hours, the combination of the driving force of metal ions and the potential weak retention ability of serpentine resulted in the re-release of metal ions to a certain extent, thereby reducing the AQ and AR [33]. After the adsorption time exceeded 10 h, the AQ and AR of Cd^{2+} gradually increased. When the adsorption time was 24 h, the AQ and AR of Cd^{2+} reached the highest, respectively, at 4.10 $mg \cdot g^{-1}$ and 81.93%. In summary, all subsequent experiments used a T of 24 h.

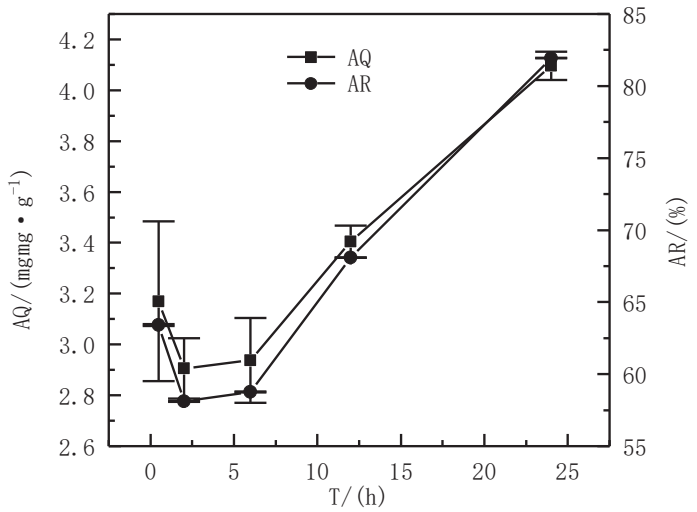

Figure 8. Effect of the T on adsorption effect.

3.4. Experiment Design and Results of RSM

3.4.1. Experiment Design of RSM

Taking the AQ and AR of Cd^{2+} as response values with the AS (A), pH (B), C (C), and T (D) being independent variables, a four-factor three-level central combination design, including 29 experimental programs, was established. Each experiment was repeated three times and averaged. The specific experimental programs are shown in Table 5.

Design-Expert 12.0 was used to perform regression analyses on the experimental data in Table 5, and the quadratic polynomial regression equation was obtained as follows.

$$Y1 = 2.48 - 1.36A - 0.0158B + 0.4167C + 0.0833D + 0.0625AB - 0.09AC - 0.18AD - 0.005BC - 0.02BD - 0.005CD + 0.5765A^2 + 0.009B^2 - 0.0748C^2 - 0.0573D^2$$

$$Y2 = 99.28 + 6.94A - 0.1642B - 2.93C + 0.865D + 1.14AB + 3.39AC + 0.26AD - 0.2025BC - 0.7675BD - 0.2025CD - 5.47A^2 + 0.2983B^2 - 1.05C^2 - 3.57D^2$$

The results of the analysis of variance based on the regression model of the AQ of Cd^{2+} are shown in Table 6. It could be seen that the *p*-value of the regression model was less than 0.0001, reaching an extremely significant level, indicating that the model had practical significance. The regression model resulted in $R^2 = 0.9955$ and $R^2_{Adj} = 0.9910$, indicating that the model could fit the experimental data well and could be used to predict the effect of the AQ of Cd^{2+}. It can also be seen from Table 6 that the *p*-values of the AS(A) and the C (C) were all less than 0.0001, reaching extremely significant levels. The *p*-values of the pH (B) and the T (D) were not significant. It can be inferred that the main and secondary factors affecting the AQ of Cd^{2+} are as follows: A > C > D > B.

Table 5. Experiment design and results of RSM.

Experimental No.	A	B	C	D	Y1 AQ ($mg \cdot g^{-1}$)	Y2 AR (%)
1	−1	−1	0	0	4.65 ± 0.0803	92.99 ± 1.61
2	0	−1	−1	0	1.99 ± 0.0008	99.39 ± 0.04
3	−1	0	0	1	4.33 ± 0.0243	86.56 ± 0.49
4	0	0	0	0	2.49 ± 0.0037	99.75 ± 0.15
5	0	0	0	0	2.48 ± 0.0055	99.21 ± 0.22
6	−1	1	0	0	4.39 ± 0.0254	87.84 ± 0.51
7	0	0	1	−1	2.76 ± 0.0295	92.10 ± 0.98
8	0	0	−1	1	1.99 ± 0.0018	99.29 ± 0.09
9	0	1	0	1	2.46 ± 0.0172	98.58 ± 0.69
10	1	0	1	0	1.97 ± 0.0015	98.59 ± 0.07
11	0	1	1	0	2.87 ± 0.0033	95.78 ± 0.11
12	0	1	−1	0	1.99 ± 0.0004	99.70 ± 0.02
13	1	1	0	0	1.65 ± 0.0031	99.17 ± 0.18
14	0	−1	1	0	2.89 ± 0.0122	96.28 ± 0.41
15	1	0	0	−1	1.66 ± 0.0006	99.41 ± 0.03
16	−1	0	−1	0	3.74 ± 0.0466	93.53 ± 1.17
17	0	1	0	−1	2.38 ± 0.0152	95.23 ± 0.61
18	0	−1	0	1	2.45 ± 0.0085	98.14 ± 0.34
19	0	0	−1	−1	1.96 ± 0.0069	98.10 ± 0.35
20	1	−1	0	0	1.66 ± 0.0003	99.75 ± 0.02
21	0	−1	0	−1	2.29 ± 0.0044	91.72 ± 0.18
22	1	0	−1	0	1.33 ± 0	99.49 ± 0
23	0	0	0	0	2.48 ± 0.0121	99.14 ± 0.48
24	1	0	0	1	1.66 ± 0.0006	99.45 ± 0.04
25	−1	0	0	−1	4.02 ± 0.1325	80.46 ± 2.65
26	0	0	0	0	2.48 ± 0.0005	99.03 ± 0.02
27	0	0	1	1	2.77 ± 0.0301	92.48 ± 1.00
28	−1	0	1	0	4.74 ± 0.1982	79.06 ± 3.30
29	0	0	0	0	2.48 ± 0.0032	99.27 ± 0.13

Table 6. Analysis of variance in regression model based on serpentine AQ of Cd^{2+}.

Source of the Variance	Square-Sum	Degree of Freedom	Average Variance	F Value	*p* Value	Significancy
Model	25.68	14	1.83	222.24	<0.0001	**
A	21.2	1	21.2	2568.79	<0.0001	**
B	0.0026	1	0.0026	0.3153	0.5833	
C	2.10	1	2.10	254.23	<0.0001	**
D	0.0285	1	0.0285	3.46	0.0842	
AB	0.0154	1	0.0154	1.86	0.1940	
AC	0.0319	1	0.0319	3.86	0.0696	
AD	0.0232	1	0.0232	2.81	0.1160	
BC	0.0001	1	0.0001	0.0137	0.9083	
BD	0.0015	1	0.0015	0.1782	0.6793	
CD	0.0000	1	0.0000	0.0047	0.9461	
A^2	1.91	1	1.91	230.86	<0.0001	**
B^2	0.0050	1	0.0050	0.6097	0.4479	
C^2	0.0212	1	0.0212	2.57	0.1309	
D^2	0.0536	1	0.0536	6.50	0.0232	*
Residual	0.1155	14	0.0083			
Lack of fit	0.1153	10	0.0115	239.23	<0.0001	**
Pure Error	0.0002	4	0.0000			
Cor Total	25.79	28				

* $p < 0.05$; ** $p < 0.01$.

The results of analysis of variance based on the regression model of the AR of Cd^{2+} are shown in Table 7. It can be observed that the *p*-value of the regression model is less than 0.0001, reaching an extremely significant level, indicating that the model had practical significance. The regression model resulted in $R^2 = 0.9376$ and $R^2_{Adj} = 0.8752$, indicating that the model could fit the experimental data well and can be used to predict the effect of the AR of Cd^{2+}. It can also be observed in Table 7 that the *p*-values of the AS (A), the C (C), and the T (D) were all less than 0.01, and all reached significant levels, while the pH (B) was not significant. It can be inferred that the main and influential factors of serpentine on the AR of Cd^{2+} are as follows: A > D > C > B.

Table 7. Analysis of variance in regression model based on serpentine AR of Cd^{2+}.

Source of the Variance	Square-Sum	Degree of Freedom	Average Variance	F Value	*p* Value	Significancy
Model	854.14	14	61.01	15.03	<0.0001	**
A	474.01	1	474.01	116.76	<0.0001	**
B	0.3234	1	0.3234	0.0797	0.7819	
C	103.31	1	103.31	25.45	0.0002	**
D	25.46	1	25.46	6.27	0.0253	*
AB	5.22	1	5.22	1.29	0.2758	
AC	46.04	1	46.04	11.34	0.0046	**
AD	9.18	1	9.18	2.26	0.1549	
BC	0.1640	1	0.1640	0.0404	0.8436	
BD	2.36	1	2.36	0.5804	0.4588	
CD	0.1640	1	0.1640	0.0404	0.8436	
A^2	150.36	1	150.36	37.04	<0.0001	**
B^2	0.0062	1	0.0062	0.0015	0.9695	
C^2	12.32	1	12.32	3.04	0.1034	
D^2	55.01	1	55.01	13.55	0.0025	**
Residual	56.84	14	4.06			
Lack of fit	56.53	10	5.65	73.41	0.0004	**
Pure Error	0.3080	4	0.0770			
Cor Total	910.98	28				

* $p < 0.05$; ** $p < 0.01$.

3.4.2. Response Surface Analysis of the Interaction Influence of Various Factors

RSM uses reasonable experimental design to find the optimal process parameters via the analysis of the response surface contour, and it can intuitively evaluate the interaction between various factors using an analysis of the 3D surface graph [34–36]. In the 3D surface graph, the slope of the curved surface indicates the degree of influence of the experimental factor on the response value. The higher the slope, the more significant the influence of the experimental factor on the response value [37,38].

The effect of the interaction between the four factors on the AQ of Cd^{2+} is shown in Figure 9. From these 3D surface graphs, it can be observed that the degree of inclination of the surfaces of graphs (b) and (c) was larger than that of the remaining four graphs, indicating that the interaction between AC and AD had a significant effect on the AQ of Cd^{2+}, while the interaction between other factors had no obvious effects on the AQ of Cd^{2+}.

The effect of the interaction between the four factors on the AR of Cd^{2+} is shown in Figure 10. From these 3D surface graphs, it can be seen that the degree of inclination of the graph (b) was the largest. Then, the slopes of the curved surfaces of the graphs (a) and (c) were the second largest. These were all larger than the curved surfaces of the remaining three graphs, indicating that the interaction between AC had the most obvious impact on the AR of Cd^{2+}, and the interaction between AB and AD also had a significant effect on the AR of Cd^{2+}, while the interaction between the other factors had no obvious effects on the AR of Cd^{2+}.

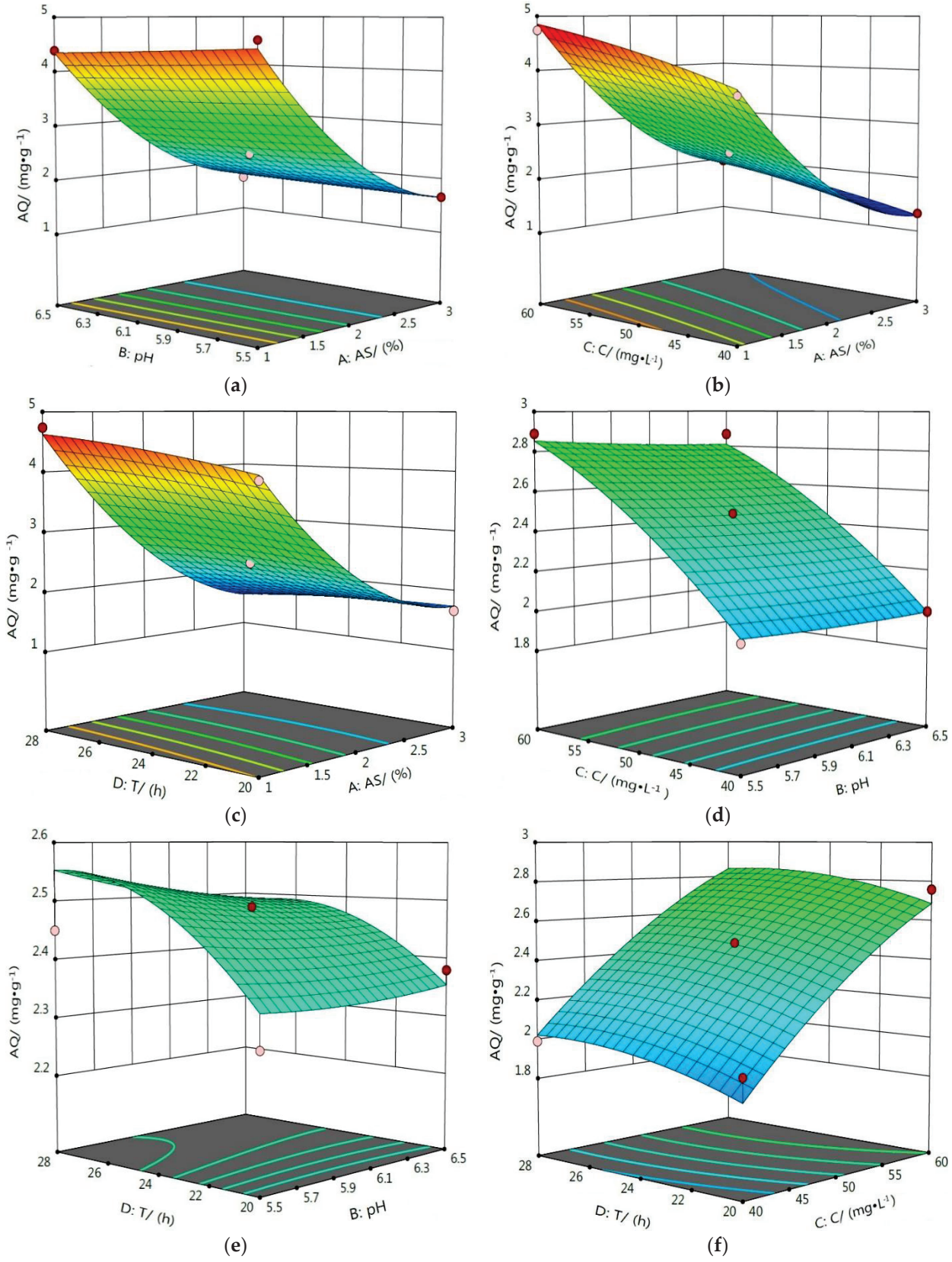

Figure 9. Response surface diagram of the effect of the interaction of various factors on the AQ of Cd^{2+}. Response surface diagram of interaction between AS and pH (**a**), AS and C (**b**), AS and T (**c**), pH and C (**d**), pH and T (**e**), C and T (**f**) on the AQ of Cd^{2+}.

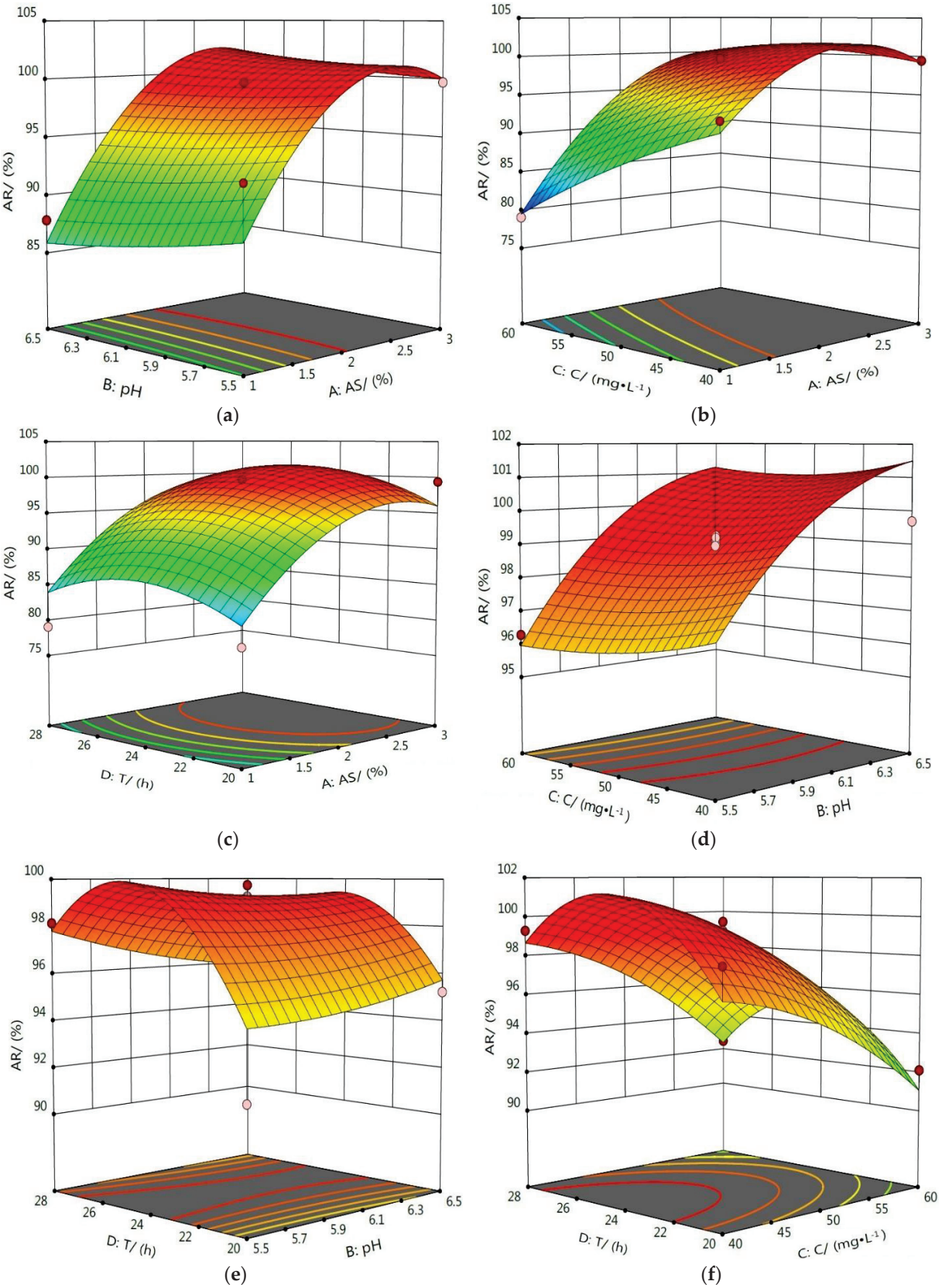

Figure 10. Response surface diagram of the interaction of various factors on the AR of Cd^{2+}. Response surface diagram of interaction between AS and pH (**a**), AS and C (**b**), AS and T (**c**), pH and C (**d**), pH and T (**e**), C and T (**f**) on the AR of Cd^{2+}.

3.5. Determination of Optimal Adsorption Conditions and Verification Experiments

Using the above analysis, a set of prediction data was finally obtained, namely the optimal adsorption conditions for serpentine to adsorb Cd^{2+}. Specifically, the AS was 1%, the pH was 5.5, the C was 40.83 mg·L^{-1}, and the T was 26.78 h. Under these conditions, the AQ of Cd^{2+} was 3.99 mg·g^{-1}, and the AR of Cd^{2+} was 95.24%. Then, in order to verify the accuracy of the prediction data, a set of verification experiments was designed. The values of the four factors were set: The AS was 1%, the pH was 5.5, the C was 41 mg· L^{-1}, and the T was 26.8 h. The results are shown in Table 6. It can be observed in Table 8 that the AQ of Cd^{2+} was 3.91 mg·g^{-1}, and the AR of Cd^{2+} was 94.68%. The data obtained by the verification experiment are similar to the data predicted by the software, which show that optimizing the adsorption conditions of serpentine to Cd^{2+} by RSM is feasible.

Table 8. Verification of experimental results.

Experimental No.	AQ (mg·g^{-1})	AR (%)
1	3.95	95.36
2	3.85	94.11
3	3.93	94.57
Average	3.91	94.68

4. Conclusions

Based on the single factor experiment, the Box–Behnken RSM was adopted and it was analyzed according to Design Expert 12.0. The optimal adsorption conditions obtained by optimizing the factors affecting the adsorption of Cd^{2+} by serpentine were as follows: The AS was 1%, the pH was 5.5, the C was 40.83 mg·L^{-1}, and the T was 26.78 h. Under these conditions, the AQ of Cd^{2+} was 3.99 mg·g^{-1}, the AR of Cd^{2+} was 95.24%, and the experiment had good repeatability. This condition could maximize the adsorption quantity of serpentine on the premise of ensuring a high adsorption rate of Cd^{2+}. The acquisition of this experimental condition could provide further theoretical support for improving the purification efficiency of heavy metal wastewater and for exploring the treatment of cadmium-containing wastewater by serpentine.

Author Contributions: Formal analysis, X.Z.; Data curation, X.Z.; Software, X.Z. and W.J.; Writing—original draft, X.Z.; Writing—review and editing, L.D. All authors have read and agreed to the published version of the manuscript.

Funding: This research received no external funding.

Institutional Review Board Statement: Not applicable.

Informed Consent Statement: Informed consent was obtained from all subjects involved in the study.

Data Availability Statement: Data sharing not applicable.

Conflicts of Interest: The authors declare no conflict of interest.

References

1. Liao, Z.T.; Chen, Z.; Xu, A.; Gao, Q.; Song, K.Y.; Liu, J.H.; Hu, H.Y. Wastewater treatment and reuse situations and influential factors in major Asian countries. *J. Environ. Manag.* **2021**, *282*, 111976. [CrossRef] [PubMed]
2. Liao, Z.T.; Chen, Z.; Wu, Y.H.; Xu, A.; Liu, J.H.; Hu, H.Y. Identification of development potentials and routes of wastewater treatment and reuse for Asian countries by key influential factors and prediction models. *Resour. Conserv. Recycl.* **2021**, *168*, 105259. [CrossRef]
3. Han, G.H.; Wang, J.W.; Sun, H.; Liu, B.B.; Huang, Y.F. A critical review on the removal and recovery of hazardous Cd from Cd-containing secondary resources in Cu-Pb-Zn smelting processes. *Metals* **2022**, *12*, 1846. [CrossRef]
4. Wyszkowska, J.; Borowik, A.; Zaborowska, M.; Kucharski, J. Evaluation of the usefulness of sorbents in the remediation of soil exposed to the pressure of cadmium and cobalt. *Materials* **2022**, *15*, 5738. [CrossRef] [PubMed]
5. Mashhadikhan, S.; Amooghin, A.; Sanaeepur, H.; Shirazi, M. A critical review on cadmium recovery from wastewater towards environmental sustainability. *Desalination* **2022**, *535*, 115815. [CrossRef]

6. Li, X.; Li, Y.P.; Kang, X.R.; Yu, J.P.; Gao, S.; Zhang, J.; Wang, H.; Pan, H.; Yang, Q.G.; Zhuge, Y.P.; et al. Effective utilization of weak alkaline soils with Cd-contamination by wheat and rape intercropping. *Ecotoxicol. Environ. Saf.* **2022**, *248*, 114335. [CrossRef]
7. Zhang, H.; Mindy, R. Cadmium exposure in living organisms: A short review. *Sci. Total Environ.* **2019**, *678*, 761–767. [CrossRef]
8. Chen, B.; Chen, Y.C.; Xu, L.F.; Zhang, Y.M.; Li, H.X. Research and development on industrial heavy metal wastewater treatment technology. 2020 6th International Conference on Energy, Environ. *Mater. Sci.* **2020**, *585*, 012051. [CrossRef]
9. Zou, Z.H.; Hen, S.F.; Han, C.Y.; Zhang, L.Y.; Luo, Y.M. Progress of research on treatment of heavy metal wastewater by adsorption. *Environ. Protect. Sci.* **2010**, *36*, 22–24. (In Chinese)
10. Li, H.B.; Wang, L.; Wei, Y.F.; Yan, W.; Feng, J.T. Preparation of templated materials and their application to typical pollutants in wastewater: A review. *Front. Chem.* **2022**, *10*, 882876. [CrossRef]
11. Zhang, X.G.; Zhang, L. Adsorption of phenol by modified activated carbons. *Environ. Develop.* **2011**, *23*, 182–183. (In Chinese)
12. Hang, X.S.; Wang, H.Y.; Zhou, J.M. Soil heavy-metal distribution and transference to soybeans surrounding an electroplating factory. *Acta Agric. Scand. Sect. B-Soil Plant Sci.* **2010**, *60*, 144–151. [CrossRef]
13. Novikau, R.; Lujaniene, G. Adsorption behavior of pollutants: Heavy metals, radionuclides, organic pollutants, on clays and their minerals (raw, modified and treated): A review. *J. Environ. Manag.* **2022**, *309*, 114685. [CrossRef] [PubMed]
14. Cao, C.Y. *Adsorption Mechanism of Heavy Metals on Serpentine and Its Effects on Heavy Metals Formations in Contaminated Soil*; Shenyang Agricultural University: Shenyang, China, 2017. (In Chinese)
15. Mokhtar, A.; Abdelkarim, S.; Hachemaoui, M.; Adjdir, M.; Zahraoui, M.; Boukoussa, B. Layered silicate magadiite and its composites for pollutants removal and antimicrobial properties: A review. *Appl. Clay Sci.* **2020**, *198*, 105823. [CrossRef]
16. Cheng, D.B.; Cai, C.F. Application of two methods of estimating soil hydraulic properties on purple soil. *J. Soil Water Conserv.* **2007**, *6*, 143–146+158. (In Chinese)
17. Cao, C.Y.; Liang, C.H.; Yin, Y.; Du, L.Y. Thermal activation of serpentine for adsorption of cadmium. *J. Hazard. Mater.* **2017**, *329*, 222–229. [CrossRef]
18. Qu, J.H.; Dong, M.; Bi, F.X.; Tao, Y.; Wang, L.; Jiang, Z.; Zhang, G.S.; Zhang, B.; Zhang, Y. Microwave-assisted one-pot synthesis of β-cyclodextrin modified biochar for stabilization of Cd and Pb in soil. *J. Clean Prod.* **2022**, *346*, 131165. [CrossRef]
19. Qu, J.H.; Xu, Y.; Zhang, X.B.; Sun, M.Z.; Tao, Y.; Zhang, X.M.; Zhang, G.S.; Ge, C.J.; Zhang, Y. Ball milling-assisted preparation of N-doped biochar loaded with ferrous sulfide as persulfate activator for phenol degradation: Multiple active sites-triggered radical/non-radical mechanism. *Appl. Catal. B Environ.* **2022**, *316*, 121639. [CrossRef]
20. Lai, H.Z.; Wang, S.Q.; Yu, N. Mineralogical characteristics of the thermal treatment products of antigorite from Xiuyan, Liaoning. *Acta Mineral. Sin.* **2003**, *2*, 124–128. (In Chinese)
21. Cao, C.Y.; Yu, B.; Wang, M.; Zhao, Y.Y.; Wan, X.; Zhao, S. Immobilization of cadmium in simulated contaminated soils using thermal-activated serpentine. *Soil Sci. Plant Nutr.* **2020**, *66*, 499–505. [CrossRef]
22. Thirugnanasambandham, K.; Sivakumar, V. Optimization of treatment of grey wastewater using electro-fenton technique—Modeling and validation. *Process Saf. Environ. Protect.* **2015**, *95*, 60–68. [CrossRef]
23. Song, L.F.; Yu, X.; Xu, B.; Pang, R.; Zhang, Z.Y. 3D slope reliability analysis based on the intelligent response surface methodology. *Bull. Eng. Geol. Environ.* **2021**, *80*, 735–749. [CrossRef]
24. Xu, J.; Long, Y.Y.; Shen, D.S.; Feng, H.J.; Chen, T. Optimization of fenton treatment process for degradation of refractory organics in pre-coagulated leachate membrane concentrates. *J. Hazard. Mater.* **2016**, *323*, 674–680. [CrossRef] [PubMed]
25. Zheng, H.L.; Jiao, S.J.; Deng, X.L.; Feng, L.; Zhang, H.Q.; Chen, R. Optimization of preparation and application of PPFS by response surface methodology. *Chin. J. Environ. Eng.* **2012**, *6*, 9–14. (In Chinese) [CrossRef]
26. Khataee, A.; Kasiri, M.; Alidokht, L.; Khataee, A.; Kasiri, M.; Alidokht, L. Application of response surface methodology in the optimization of photocatalytic removal of environmental pollutants using nanocatalysts. *Environ. Technol.* **2011**, *32*, 1669–1684. [CrossRef]
27. Liu, J.; Zhou, J.; Wu, Z.H.; Tian, X.; An, X.Y.; Zhang, Y.; Zhang, G.S.; Deng, F.X.; Meng, X.L.; Qu, J.H. Concurrent elimination and stepwise recovery of Pb (II) and bisphenol A from water using β–cyclodextrin modified magnetic cellulose: Adsorption performance and mechanism investigation. *J. Hazard. Mater.* **2022**, *432*, 128758. [CrossRef]
28. Sun, P.C. *Research on the Mechanism of Lead and Cadmium Solidification and Nitrogen Fertilizer Synergy by Three Kinds of Environmental Materials*; China University of Mining & Technology: Beijing, China, 2016. (In Chinese)
29. Liu, W.; Zhao, C.C.; Wang, S.T.; Niu, L.; Wang, Y.L.; Liang, S.X.; Cui, Z. Adsorption of cadmium ions from aqueous solutions using nano-montmorillonite: Kinetics, isotherm and mechanism evaluations. *Res. Chem. Intermed.* **2018**, *44*, 1441–1458. [CrossRef]
30. Qu, J.H.; We, S.Q.; Liu, Y.; Zhang, X.M.; Jiang, Z.; Tao, Y.; Zhang, G.S.; Zhang, B.; Wang, L.; Zhang, Y. Effective lead passivation in soil by bone char/CMC-stabilized FeS composite loading with phosphate-solubilizing bacteria. *J. Hazard. Mater.* **2022**, *423*, 127043. [CrossRef]
31. Qu, J.H.; Tian, X.; Zhang, X.B.; Yao, J.Y.; Xue, J.Q.; Li, K.G.; Zhang, B.; Wang Zhang, Y. Free radicals-triggered reductive and oxidative degradation of highly chlorinated compounds via regulation of heat-activated persulfate by low-molecular-weight organic acids. *Appl. Catal. B Environ.* **2022**, *310*, 121359. [CrossRef]
32. Qu, J.H.; Yuan, Y.H.; Zhang, X.M.; Wang, L.; Tao, Y.; Jiang, Z.; Yu, H.; Dong, M.; Zhang, Y. Stabilization of lead and cadmium in soil by sulfur-iron functionalized biochar: Performance, mechanisms and microbial community evolution. *J. Hazard. Mater.* **2022**, *425*, 127876. [CrossRef]

33. Sdiri, A.; Higashi, T.; Chaabouni, R.; Jamoussi, F. Competitive removal of heavy metals from aqueous solutions by montmorillonitic and calcareous clays. *Water Air Soil Pollut.* **2012**, *223*, 1191–1204. [CrossRef]
34. Wang, F.; Li, X.W.; Liao, L.; Huang, Y.; Hou, J.N.; Yang, J.; Xie, Y.; Tang, R.K.; Li, D. Optimization of enzymatic hydrolysis condition of glucosinolates from rapeseed meal by response surface methododlogy and the preliminary research of its bacteriostasis. *Sci. Technol. Food Ind.* **2017**, *38*, 264–268+273. (In Chinese)
35. Karimifard, S.; Moghaddam, M. Application of response surface methodology in physicochemical removal of dyes from wastewater: A critical review. *Sci. Total Environ.* **2018**, *640*, 772–797. [CrossRef] [PubMed]
36. Nair, A.; Makwana, A.; Ahammed, M. The use of response surface methodology for modelling and analysis of water and wastewater treatment processes: A review. *Water Sci. Technol.* **2014**, *69*, 464–478. [CrossRef]
37. Da, T.X.; Chen, T.; Ma, Y.; Tong, Z.F. Application of response surface method in the separation of radioactive material: A review. *Radiochim. Acta* **2022**, *110*, 51–66. [CrossRef]
38. Manuela, M.; Fátima, B.; Annick, B.; Hannes, W.; Simone, M.; Cristina, D. Valorization of apple tree wood residues by polyphenols extraction: Comparison between conventional and microwave-assisted extraction. *Ind. Crops Prod.* **2017**, *104*, 210–220. [CrossRef]

water

MDPI

Article

Coupling Hydrochemistry and Stable Isotopes (δ^2H, $\delta^{18}O$ and $^{87}Sr/^{86}Sr$) to Identify the Major Factors Affecting the Hydrochemical Process of Groundwater and Surface Water in the Lower Reaches of the Yarlung-Zangbo River, Southern Tibet, Southwestern China

Xiao Yu [1,2], Xingcheng Yuan [3,4], Hongyang Guo [3,*], Yunhui Zhang [3,4], Huawen Cao [5], Tongming Luo [2], Zhaocheng Gong [2] and Haoqing Huang [2]

1 Key Laboratory of Geological Survey and Evaluation of Ministry of Education, China University of Geosciences, Wuhan 430074, China
2 Research Center of Applied Geology of China Geological Survey, Chengdu 610036, China
3 Faculty of Geosciences and Environmental Engineering, Southwest Jiaotong University, Chengdu 611756, China
4 Yibin Research Institute, Southwest Jiaotong University, Yibin 644000, China
5 Chengdu Centre, China Geological Survey, Chengdu 610081, China
* Correspondence: guohongyang855@163.com

Abstract: In Tibet, water resource has been less studied due to remote and harsh conditions. In this study, hydrochemistry and stable isotopes (δ^2H, $\delta^{18}O$ and $^{87}Sr/^{86}Sr$) were employed to investigate the major factors affecting the hydrochemical process of groundwater and surface water in the lower reaches of the Yarlung-Zangbo River, southern Tibet. Groundwater and surface water were weakly alkaline and very soft to moderately hard water. The hydrochemical type of surface water is mainly Ca-HCO_3 (mainstream) and Ca-SO_4-HCO_3 (tributary), while the hydrochemical type of groundwater was mainly Ca-SO_4-HCO_3. Multivariate statistical analysis and Gibbs analysis proposed hydrochemical components were dominated by water-rock interaction. Ion ratio, saturation index, and Sr isotope revealed calcite dissolution and silicate weathering with local sulfide oxidation were involved in water–rock interaction. D-O isotopes indicated the recharge source was mainly derived from atmosphere precipitation. The entropy-weighted water quality index indicated surface water and groundwater reach the standard of drinking purpose in the lower reaches of the Yarlung-Zangbo River. The hydrochemical type varied regularly along the Yarlung-Zangbo River. The dissolution of carbonate rocks and local silicate weather and evaporate dissolution are the primary hydrochemical process along the Yarlung-Zangbo River. This study would provide a preliminary insight for hydrochemical process in the Yarlung-Zangbo River.

Keywords: Yarlung-Zangbo River; water resource; hydrochemistry; isotopes; water quality; southern Tibet

1. Introduction

Water resources are of great significance to human existence. In decades, water resources are becoming scarce, resulting in a shortage of water due to rapid economic development and explosive population growth worldwide. Sustainable water resource exploitation has become an urgent issue that is yet to be resolved [1–3]. Of note, water resources fail to meet the drinking standard due to various natural processes (e.g., water-rock interaction, climate change) and human activities (e.g., municipal sewage and agricultural irrigation). Water quality is determined by the chemical compositions related to water genesis. So far, a large number of research have concentrated on the hydrochemical genesis

and quality of water resource in basin and plain areas [4–8]. In contrast, less studies have concentrated on water resource in the alpine area due to remote location and severe condition. Water resource in the alpine area (e.g., Tibet, Alps, etc.,) are important with regard to the origin of regional rivers such as Yangtze River, Rhine River, and etc. Therefore, the study of water resource in the alpine area will provide unique insights that will be helpful for sustainable water management.

The Qinghai-Tibet Plateau, with an average elevation of over 4000 m, is the highest alpine area on earth. It is rich in water resources and thus is known as the "Asia's Water Tower", feeding more than ten famous Asian rivers such as the Yangtze, Yellow, Yarlung-Zangbo, etc. The water volume of 9×10^8 m^3 has been investigated in the Qinghai-Tibet Plateau, feeding a population of 30×10^8 in the world. Due to the harsh geo-environment, only a few studies on water resource have been conducted in the Qinghai-Tibet Plateau. More knowledge on water resource in the Qinghai-Tibet Plateau is yet to be achieved for sustainable development.

The Yarlung-Zangbo River is located in the southern part of the Tibetan Plateau, with an average elevation of more than 3000 m, making it one of the highest rivers in the world. It originates from the Jemayangtse glacier at the northern foot of the Himalayas, traverses southern Tibet from west to east, and finally flows out of the Chinese into India. Millions of populations are living along the Yarlung-Zangbo River. Previous studies mainly focused on the upper and middle reaches of the Yarlung-Zangbo River. Mao et al., found the spatiotemporal variability of heavy metals and identify the source in the Lhasa River of the Yarlung-Zangbo River [9]. Li et al., investigated the heavy metal distribution along the Yarlung-Zangbo River [10]. Tan et al., analyzed the recharge sources and flow paths of groundwater by O and H isotopes, major ions, and ^{222}Rn concentrations in the middle reaches of the Yarlung-Zangbo River [11]. Shi et al., uncovered the water–rock interaction mechanisms of seasonal river–groundwater circulation using major ions and isotopes (^2H, ^3H, ^{18}O, and Sr) in the middle reaches of the Yarlungzangbo River [12]. So far, less attention has been paid to the lower reaches of the Yarlung-Zangbo River, hampering the comprehensive understanding of water resource in the Yarlung-Zangbo River.

In this study, surface water and groundwater samples were collected for hydrochemical and D-O-Sr isotopic analyses in the lower reaches of the Yarlung-Zangbo River. This study aims to (1) identify the hydrochemical characteristics of groundwater and surface water; (2) recognize the factors controlling the hydrochemical components; (3) assess the quality of groundwater and surface water; (4) provide a comprehensive understanding for hydrochemical process along the whole Yarlung-Zangbo River. The achievements will immensely contribute to the sustainable exploitation of water resource in the Yarlung-Zangbo River.

2. Materials and Methods

2.1. Description of the Study Area

The Yarlung-Zangbo River traverses in the southern Tibet of southwestern China. The study area is located in the lower reaches of the Yarlung-Zangbo River (Figure 1), between the latitude (N) 92.7–93.8° and longitude (E) 28.6–29.2°. The average altitude of the lower reaches of the river is about 3100 m. The lower reaches is about 496.3 km in length, accounting for 24% in total. And the catchment area is about 49,959 km^2, accounting for 21% in total watershed area. The lower reaches of the Yarlung-Zangbo River is located in a humid subtropical climate zone, with an average annual temperature of 8–10 °C. It is dry in winter and spring and rainy in summer and autumn, influenced by the warm and humid Indian Ocean monsoon. The average annual precipitation is higher than 2000 mm and is mainly concentrated in July to September. The annual runoff is mainly recharged by atmospheric precipitation, glacial meltwater, and groundwater.

The lower reaches of the Yangtze River are located at the intersection of the Himalayas, the Nyingchi-Tanggula Range and the Hengduan Mountains, near the Eastern Himalayan Syntaxis where the Eurasian and Indian plates collide [13–15]. The types of strata are vari-

ous in the study area. In the Gacha County, the strata are mainly composed of Triassic slate (carbonaceous), microphyllite, and metamorphic sandstone. In the Lang County, the strata mainly consist of pre-Quakotanian strata, with lithology dominated by granulite, marble, and plagiogneiss. In the Milin County, the strata are comprised of the Cretaceous diorite granite and mica amphibolite. Groundwater is recharged by atmosphere precipitation on the mountain top. Afterwards, it flows along the extensional faults and fractures and finally exposes as springs in the valley. The flow of springs is 0.2 to 1 L/s.

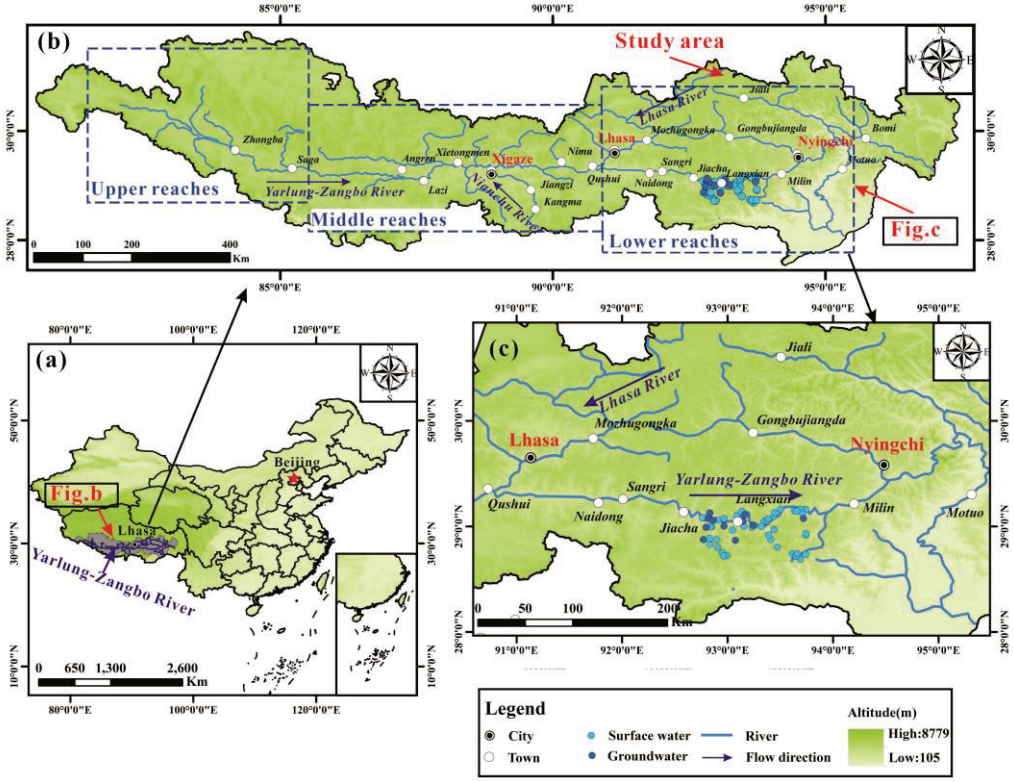

Figure 1. (**a**) Location of the Yarlung Zangbo River in China; (**b**) spatial characteristic of the Yarlung Zangbo River; (**c**) distribution of surface water and groundwater sampling points in the lower reaches of the Yarlung Zangbo River.

2.2. Field Samples and Laboratory Analysis

Field observations and sampling were carried out in July–August of 2019. pH and total dissolved solids (TDS) were measured in situ by a portable multi-meter device (WTW multi 3400i). Before bottling, three-time rinsing was conducted by sampling water. A total of 43 surface water and 11 groundwater samples were collected in this study. All water samples were transported to the laboratory under 3 °C within a week. The experimental analysis was done in the Beijing Createch Testing Technology Co., Ltd., Beijing, China. K^+, Na^+, Ca^{2+}, Mg^{2+}, Cl^-, $SO_4{}^{2-}$, $NO_3{}^-$, and F^- were measured by ion chromatography. $HCO_3{}^-$ was measured by titration with HNO_3. The charge balance error (CBE) was examined by the error within 5% (Equation (1)). Sr and Sr isotope were analyzed using Element XR ICP-MS. D-O isotopes were determined by Finnigan MAT253 mass spectrometer according to the VSMOW standard.

$$\mathrm{CBE}(\%) = \frac{\sum\left(\mathrm{Mg^{2+}}+\mathrm{Ca^{2+}}+\mathrm{Na^{+}}+\mathrm{K^{+}}\right) - \sum(\mathrm{HCO_3^{-}}+\mathrm{SO_4^{2-}}+\mathrm{NO_3^{-}}+\mathrm{Cl^{-}}+\mathrm{F^{-}})}{\sum\left(\mathrm{Mg^{2+}}+\mathrm{Ca^{2+}}+\mathrm{Na^{+}}+\mathrm{K^{+}}\right) + \sum(\mathrm{HCO_3^{-}}+\mathrm{SO_4^{2-}}+\mathrm{NO_3^{-}}+\mathrm{Cl^{-}}+\mathrm{F^{-}})} \times 100 \quad (1)$$

Calculation of saturation index (SI) using Phreeqc 3.0 based on MINTEQ database. As Formula (2):

$$\mathrm{SI} = \log\,(\mathrm{IAP}/\mathrm{K}) \quad (2)$$

where IAP is the product of ion activity and K is the equilibrium constant. A mineral with SI > 0 is supersaturated and precipitates, while a mineral with SI < 0 is unsaturated and dissolves.

3. Results

3.1. Statistical Results of Hydrochemical Parameters

Statistical analysis is usually used to analyze general hydrogeochemical characteristics [16]. In Table 1 and Figure 2, the pH values of surface water and groundwater had a small range from 7.20 to 9.20 and from 7.90 to 8.90, with mean values of 8.35 and 8.47. pH values showed that surface water and groundwater were weakly alkaline. The total hardness (TH) of surface water and groundwater varied from 9.00 to 343.00 mg/L and 54.00 to 259.00 mg/L, with mean values of 92.77 mg/L and 158.18 mg/L. In general, the TH value is subdivided into five degrees, including very soft (0–75 mg/L), soft (75–150 mg/L), medium hard (150–300 mg/L), hard (300–450 mg/L), and very hard (>450 mg/L). In Figure 3a, most of the surface water and groundwater belonged to very soft to moderately hard water. The total dissolved solids (TDS) content of surface water and groundwater varied from 11.00 to 470.00 mg/L and 67.00 to 357.00 mg/L with mean values of 118.42 mg/L and 196.91 mg/L. Both surface water and groundwater were typical of freshwater (Figure 3a). Overall groundwater samples had the higher TH and TDS than those of surface water samples.

Table 1. Statistical analysis of chemical parameters of surface water and groundwater in the lower reaches of Yarlung Zangbo River.

Parameters	pH	TH	TDS	K^+	Na^+	Ca^{2+}	Mg^{2+}	Cl^-	$SO_4{}^{2-}$	$HCO_3{}^-$	$NO_3{}^-$	F^-	Sr^{2+}	$^{87}Sr/^{86}Sr$	$\delta^{18}O$	δD
Max	9.20	343.00	470.00	1.24	6.16	82.70	44.90	2.87	409.00	92.10	0.36	2.02	0.72	0.721	−14.21	−97.12
Min	7.20	9.00	11.00	0.06	0.24	4.00	0.38	0.00	0.01	2.50	0.00	0.00	0.02	0.706	−17.55	−131.82
Mean	8.35	92.77	118.42	0.48	1.62	28.28	7.31	0.39	67.52	43.08	0.12	0.14	0.17	0.710	−15.59	−112.43
SD	0.43	83.86	113.72	0.25	1.52	22.31	9.66	0.49	88.31	23.48	0.08	0.42	0.20	-	-	-
CV	0.05	0.90	0.96	0.52	0.94	0.79	1.32	1.28	1.31	0.54	0.69	2.91	1.18	-	-	-
Skewness	−0.94	1.00	1.22	1.03	1.54	0.92	1.77	2.93	1.77	0.46	0.68	3.89	1.35	-	-	-
Kurtosis	1.09	0.23	0.83	1.16	1.45	−0.24	3.80	13.87	3.77	−0.68	0.02	14.80	0.49	-	-	-
Max	8.90	259.00	357.00	3.07	28.20	82.10	20.80	6.74	213.00	238.00	4.19	0.19	0.71	0.716	−14.73	−108.65
Min	7.90	54.00	67.00	0.19	1.02	21.10	0.38	0.00	6.44	49.70	0.00	0.00	0.04	0.707	−17.33	−132.04
Mean	8.47	158.18	196.91	1.46	6.27	51.91	9.35	1.59	80.07	117.19	0.68	0.09	0.27	0.711	−16.21	−122.53
SD	0.31	75.54	102.43	1.11	7.18	22.60	7.34	1.86	72.76	49.98	1.14	0.07	0.21	-	-	-
CV	0.04	0.48	0.52	0.76	1.14	0.44	0.78	1.16	0.91	0.43	1.67	0.74	0.79	-	-	-
Skewness	−0.61	−0.22	0.30	0.20	2.91	−0.04	0.29	2.25	0.72	1.20	3.00	−0.10	0.98	-	-	-
Kurtosis	−0.69	−1.81	−1.42	−1.93	9.10	−1.95	−1.39	5.14	−1.20	1.82	9.42	−1.64	−0.14	-	-	-

Note: I = surface water; II = groundwater; SD = standard deviation; CV(%) = coefficient of variation; Units of TH, TDS, K^+, Na^+, Ca^{2+}, Mg^{2+}, Cl^-, $SO_4{}^{2-}$, $HCO_3{}^-$, $NO_3{}^-$, F^-, Sr^{2+} are mg/L; units of $\delta^{18}O$, δD are ‰VSMOW, —means no calculation.

Table 2. Statistics of major ions in the whole basin of Yarlung Tsangpo River (mg/L).

River	pH	TDS	K^+	Na^+	Ca^{2+}	Mg^{2+}	Cl^-	$SO_4{}^{2-}$	$HCO_3{}^-$	$NO_3{}^-$	F^-
Global River	8.00	120.00	2.30	6.30	15.00	4.10	7.80	11.20	58.40	1.00	-
Upper reaches	7.77	102.50	1.08	17.67	20.24	4.37	3.25	20.60	70.48	0.17	-
Middle reaches	8.05	304.82	1.29	8.86	41.53	17.97	6.35	98.17	107.98	1.80	-
Lower reaches (this study)	8.35	118.42	0.48	1.62	28.28	7.31	0.39	67.52	43.08	0.12	0.14

Note: Global River is after [17]. Upper reaches is after [18,19]. Middle reaches is after [11,12,20,21].—means data absence.

In terms of ion components, the major cations in surface water ranked as $Ca^{2+} > Mg^{2+} > Na^+ > K^+$, with an average of 28.28, 7.31, 1.62, and 0.48 mg/L. The dominant cations were Ca^{2+} and Mg^{2+}, accounting for 75.03% and 19.40% in total, respectively. The main cations in groundwater had the same order as those in surface water. But groundwater samples possessed slightly higher average concentrations of Ca^{2+} (51.91 mg/L), Mg^{2+} (9.35 mg/L), Na^+ (6.27 mg/L), and K^+ (1.46 mg/L). The dominant cations of groundwater were Ca^{2+} and Mg^{2+}, accounting for 75.24% and 13.55% in total, respectively. Major anion concentrations

in surface water were $SO_4^{2-} > HCO_3^- > Cl^- > F^- > NO_3^-$, with average concentrations of 67.52, 43.08, 0.39, 0.14, and 0.12 mg/L. The anions were mainly SO_4^{2-} and HCO_3^-, accounting for 60.69% and 38.72% in total, respectively. The main anion concentrations in groundwater were $HCO_3^- > SO_4^{2-} > Cl^- > NO_3^- > F^-$, with average concentrations of 117.19, 80.07, 1.59, 0.68, and 0.009 mg/L. The anions were mainly HCO_3^- and SO_4^{2-}, accounting for 58.71% and 40.11% in total, respectively.

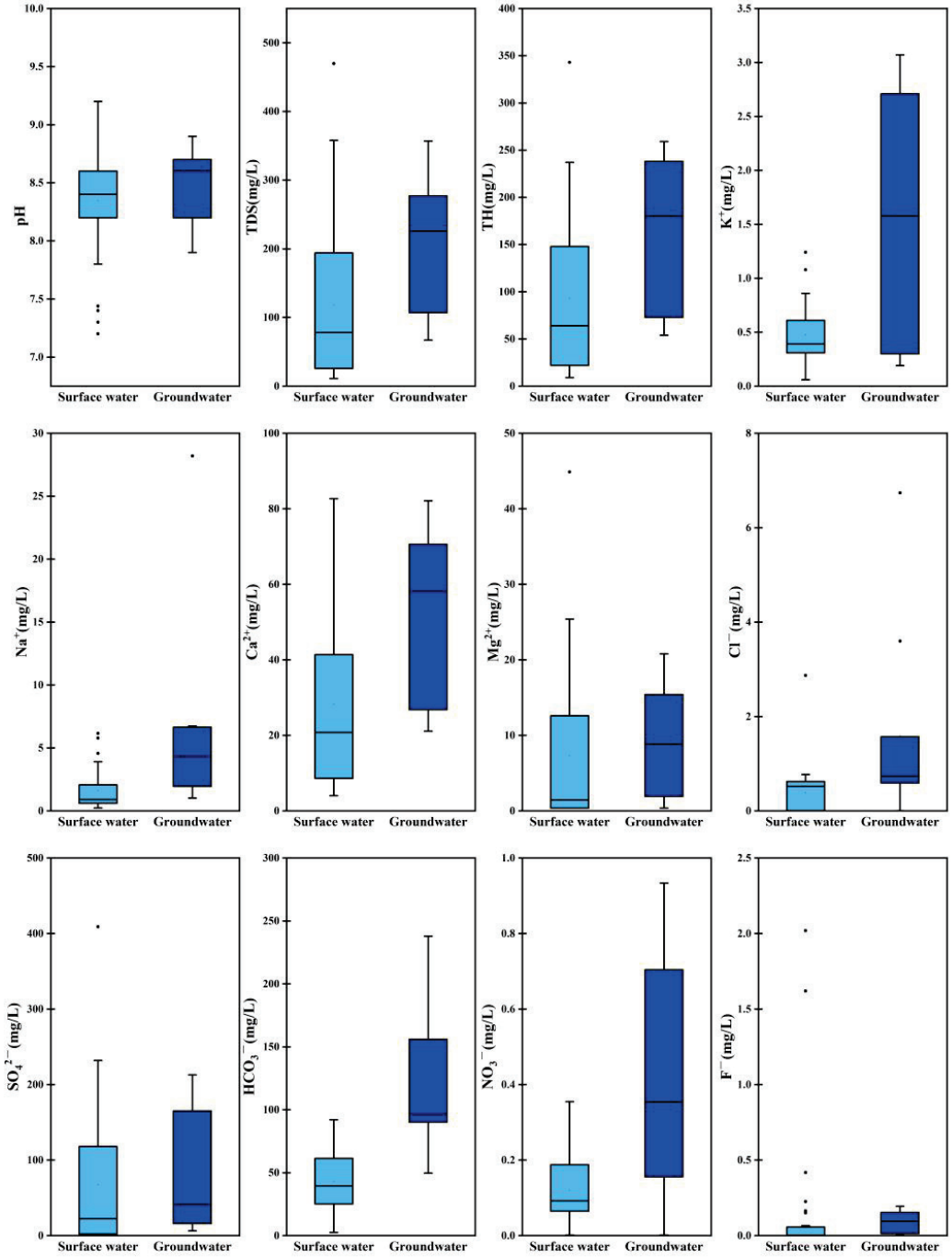

Figure 2. Box diagram of hydrochemical parameters of surface water and groundwater in the lower reaches of Yarlung Zangbo River. Data are from Table 1.

In statistics, variation coefficient is used to evaluate the variability and stability for each variable. In statistics, standard deviation is used to evaluate the dispersion of data. Table 1 shows that the standard deviation of Ca^{2+}, Mg^{2+}, SO_4^{2-}, and HCO_3^- in surface water and groundwater in the study area was relatively large, indicating the large dispersion of

these ions. Hence, the contents of these ions in different downstream areas were obviously different. variation coefficient is used to evaluate the variability and stability for each variable. Variation coefficient has a positive relationship with variability and negative relationship with variable stability, respectively. Lower variation coefficients indicate less factors influencing hydrochemical evolution. As shown in Table 1, the coefficients variation of pH, K^+, and HCO_3^- in surface water and pH and HCO_3^- in groundwater were small, reflecting their relatively constant concentrations in the region. And HCO_3^- concentration in surface water and groundwater was constantly high. In contrast, the coefficients of variation of Mg^{2+}, Cl^-, SO_4^{2-}, and F^- in surface water and Na^+, Cl^-, and NO_3^- in groundwater were large, indicating that their concentrations vary highly and are susceptible to the influence of hydro-meteorological conditions, topography, aquifer media, and human activities. The skewness and kurtosis values of surface and groundwater samples were small, indicating that the statistics of each ionic parameter in surface and groundwater samples were close to normal distribution.

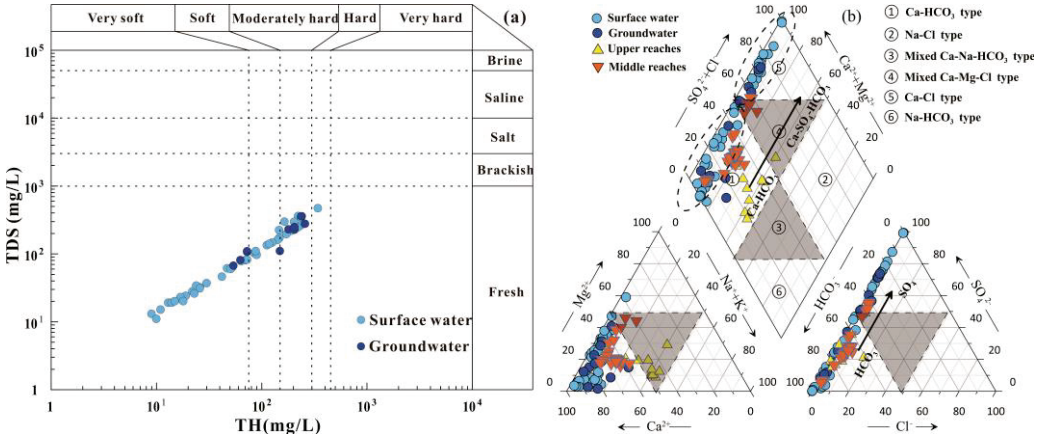

Figure 3. TDS and TH scatter diagram (**a**) and Piper trilinear diagram (**b**) of surface water and groundwater in the Lower reaches of Yarlung Zangbo River. Data are from Tables 1 and 2.

The concentrations of major ions in the lower reaches of the Yarlung-Zangbo River were compared with those in the whole Yarlung-Zangbo River and in the global rivers (Table 2). In Table 2, the concentrations of Ca^{2+}, Mg^{2+}, HCO_3^-, and SO_4^{2-} in the whole Yarlung-Zangbo River during the wet period were about two to three times higher than the global river mean. In the Yarlung-Zangbo River, all ion concentrations in the middle reaches were lower than those in the lower reaches. The phenomenon is probably due to abundant precipitation leading to stronger dilution and lower ion concentrations in the lower reaches. It is noted that Na^+ concentrations in the upper reaches were 10.91 times higher than those in the lower reaches. The higher Na^+ concentrations were induced by silicate weathering existing in igneous rocks of the upper reaches. Ca^{2+}, Mg^{2+}, and SO_4^{2-} concentrations were higher in the lower reaches, especially SO_4^{2-} ion concentration is 3.28 times higher than in the upper reaches of the river. It is presumably due to the effect of oxidative dissolution of Ca and Mg sulfides.

3.2. Hydrochemical Type

Piper trilinear diagram was used to analyze the hydrochemical types of surface water and groundwater in the lower reaches of the Yarlung-Zangbo River. As shown in Figure 3b, the cations of surface water and groundwater basically fell near the Ca^{2+} axis in the trilinear diagram, and the anions were near the HCO_3^- axis in the trilinear diagram. This indicated that the dominant cations of surface water and groundwater were Ca^{2+}, and the dominant anions were HCO_3^- and SO_4^{2-}. The hydrochemical type of surface water was mainly Ca-HCO_3 (mainstream) and Ca-SO_4-HCO_3 (tributary), and the hydrochemical type of groundwater is mainly Ca-SO_4-HCO_3. The hydrochemical type of surface water in the lower reaches of Yarlung-Zangbo River showed a gradual transition from Ca-SO_4-HCO_3

type to Ca-HCO_3 type water from tributary to mainstream area. The hydrochemical type of groundwater was similar to that of surface water in tributary. In Figure 3b, the hydrochemical types of the middle and lower reaches were both Ca-Mg-HCO_3-SO_4 and that of the upper reaches of the river is Ca-Na-HCO_3-SO_4. It indicated that the hydrochemical type of the lower reaches is similar to that of the middle reaches but is different from that of the upper reaches. This is due to the fact that the upstream is more influenced by silicate dissolution, while the cations and anions in the lower reaches are mainly Ca^{2+}, HCO_3^-, and SO_4^{2-}. The hydrochemical type in the lower reaches may be controlled by dissolution of carbonates (calcite, dolomite) and other sulfides oxidation.

3.3. Hydrogen and Oxygen Isotopes

The $\delta^{18}O$ contents of surface water samples in the lower reaches of the Yarlung-Zangbo River varied from −17.55‰ to −17.55‰, with an average value of −15.59‰. δD contents varied from −131.82‰ to −97.12‰, with an average value of −112.43‰. $\delta^{18}O$ contents of groundwater varied from −17.33‰ to −14.73‰, with an average value of −16.21‰ The variation of δD contents ranged from −132.04‰ to −108.65‰, and the average value was −122.53‰ (Table 1).

3.4. Sr Concentration and Sr Isotope

The Sr content of surface water samples in the lower reaches of the Yarlung-Zangbo River varied from 0.02 to 0.72 mg/L, with a mean value of 0.17 mg/L. The $^{87}Sr/^{86}Sr$ ratio varied from 0.70555 to 0.72082, with a mean value of 0.71007. The Sr content of groundwater samples varied from 0.04 to 0.71 mg/L, with a mean value of 0.27 mg/L The variation of $^{87}Sr/^{86}Sr$ ratio ranged from 0.70724 to 0.71620, and the average value was 0.71128 (Table 1).

4. Discussion

4.1. Multivariate Statistical Analysis

4.1.1. Correlation Analysis

Correlation analysis can be used to reveal the source relationship of ions by the correlation between the different factors on the concentration of ions [22–24]. In this study, SPSS 25 software was used to calculate the correlation coefficient matrix of the sample indicators. In Figure 4, there was a good correlation between the TDS, TH, and each ion, indicating a possible common source. The TDS and TH had the highest positive correlation (greater than 0.9) with Ca^{2+}, Mg^{2+}, and SO_4^{2-}, indicating that Ca^{2+}, Mg^{2+}, and SO_4^{2-} were important sources of TDS and TH. In addition, Na^+, Ca^{2+}, Mg^{2+} and Cl^-, SO_4^{2-} and HCO_3^- also showed significant positive correlations, indicating that the TDS and TH were mainly controlled by Na^+, Ca^{2+}, Mg^{2+}, Cl^-, SO_4^{2-}, and HCO_3^-. Sr showed better correlations with Ca^{2+}, Mg^{2+}, and SO_4^{2-}, indicating that the water–rock reaction was stronger in the lower reaches of the Yarlung-Zangbo River. Ca^{2+} had a high correlation with SO_4^{2-} (0.868), indicating that the dissolution of gypsum contributed to Ca^{2+} concentration. The correlation of Ca^{2+}, Mg^{2+}, and HCO_3^- indicated that the dissolutions of calcite and dolomite contribute to hydrochemical compositions of surface water and groundwater. The correlation between Cl^- and NO_3^- is relatively well correlated with correlation coefficient of 0.866, indicating the influence of anthropogenic activities. But the influence of anthropogenic factors was limited due to the low concentration of NO_3^-. Cl^- showed a positive correlation with K^+ and Na^+ with a correlation coefficient of 0.559, indicating the local presence of evaporite dissolution. The comprehensive analysis of various ion correlations can be concluded that the hydrochemical types of surface water and groundwater in the lower reaches of the Yarlung-Zangbo were mainly influenced by water-rock reaction, with less involvements of anthropogenic activities.

4.1.2. Principal Component Analysis

The principal component analysis (PCA) aims to use the dimensionality reduction to transform multiple indicators into a few composite indicators (i.e., principal components).

Each principal component is extracted to explain the information of the raw data variables. The principal component contribution scores can explain the geospatial distribution and temporal variation characteristics of the raw hydrochemical data [25–27].

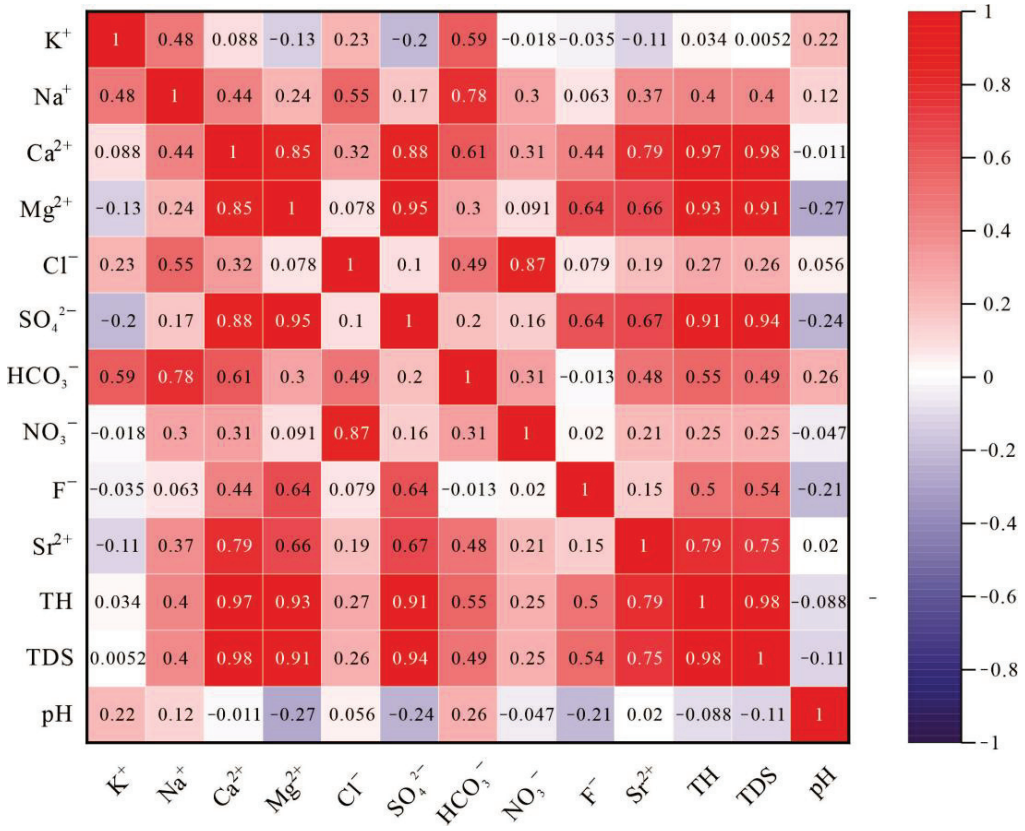

Figure 4. Pearson correlation coefficient matrix for each ion content of surface water and groundwater in the Lower reaches of Yarlung Zangbo River. Data are from Table 1.

To further investigate the relationship between major ions and geological background, principal component analysis was performed in this study. The data were first subjected to the KMO and Bartlett's sphere tests to determine whether factor analysis could be performed. The KOM value was 0.656 (>0.6) and the significant probability of Bartlett's sphere test was 0 (the confidence level of <0.05). The results indicated that the variables had high correlation with each other and were suitable for the PCA. According to the Kaiser–Harris criterion, it is recommended to keep the principal components with eigenvalues greater than 1. In this study, a total of four principal components were extracted to determine the output (Table 3). The three-dimensional spatial plots between the indicators of the first three principal components were derived (Figure 5). In Table 3, the eigenvalues, cumulative contribution of the four principal component factors is 81.662%. The PC1 variance contribution was 48.229%, mainly including seven indicators of the TH, TDS, Ca^{2+}, Mg^{2+}, $SO_4{}^{2-}$, Sr, and $HCO_3{}^{-}$. The PC1 represented the carbonate dissolution, silicate weathering, and the oxidative dissolution of sulfides. The variance contribution of PC2 was 20.600%, which mainly includes four indicators of Na^{+}, K^{+}, Cl^{-}, and $HCO_3{}^{-}$. Evaporite dissolution will increase Na^{+}, K^{+}, and Cl^{-} concentrations. Since the main anion is $HCO_3{}^{-}$, and the concentration of Cl^{-} is very low, and there are various hydrochemical types in the lower reaches of the Yarlung-Zangbo River from the previous paper, $HCO_3{}^{-}$ is classified as the PC2. The variance contribution of PC3 was 11.065%, mainly including two indicators of $NO_3{}^{-}$ and Cl^{-}. There are residential gathering points near the lower reaches of the Yarlung-Zangbo River, which may cause water pollution during human living, and have a greater impact on $NO_3{}^{-}$ and Cl^{-} ions. Therefore, PC3 represents the pollution effect of anthropogenic activities, which has less influence due to the low concentration of $NO_3{}^{-}$.

PC4 variance contribution is 7.75%, which mainly includes one indicator of F^-. Two surface water samples in Ladin Snow Village had F^- ion concentrations of 1.62 mg/L and 2.02 mg/L, indicating that the area may suffer from F^- pollution. Thus, PC4 also represents the pollution by local anthropogenic activities.

Table 3. Results of principal component analysis for each indicator of surface water and groundwater in the lower reaches of Yarlung Zangbo River.

Index	PC1	PC2	PC3	PC4
TH	0.981	−0.099	0.080	−0.054
TDS	0.975	−0.139	0.055	−0.023
Ca^{2+}	0.974	−0.002	0.084	−0.096
Mg^{2+}	0.894	−0.380	0.055	0.082
$SO_4{}^{2-}$	0.889	−0.420	−0.030	0.007
Sr^{2+}	0.790	−0.026	0.095	−0.449
$HCO_3{}^-$	0.596	0.687	0.275	0.001
Na^+	0.512	0.661	0.133	0.165
K^+	0.072	0.657	0.447	0.484
Cl^-	0.394	0.656	−0.592	0.070
$NO_3{}^-$	0.356	0.462	−0.770	−0.097
F^-	0.528	−0.394	−0.054	0.542
pH	−0.097	0.433	0.411	−0.466
Eigenvalue	6.270	2.678	1.438	1.008
Variance/%	48.229	20.600	11.065	7.754
Cumulative % of variance	48.229	68.829	79.894	87.648

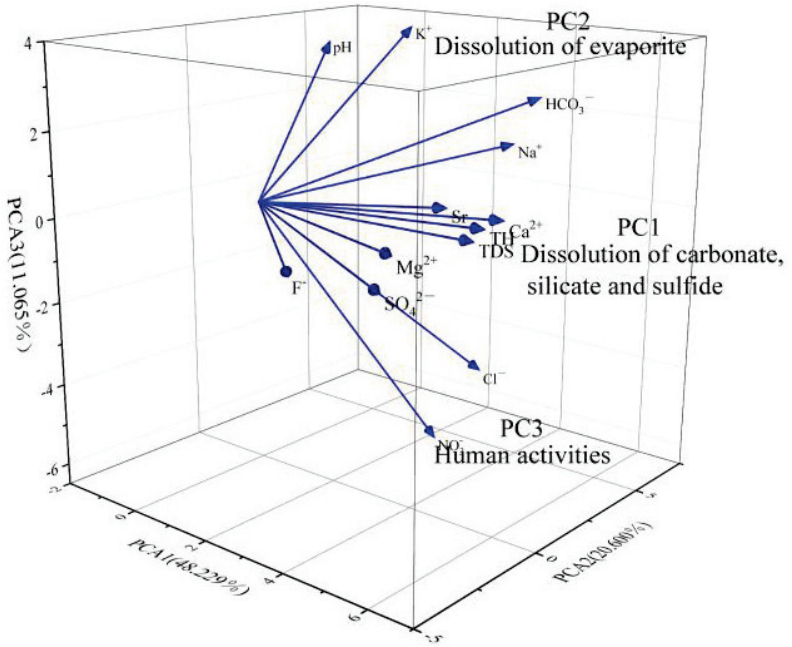

Figure 5. Principal component 3D spatial map of surface water and groundwater in the middle and lower reaches of Yarlung Zangbo River. Data are from Table 1.

4.1.3. Self-Organizing Map

Self-organizing map (SOM) is a network based on competitive learning and consists of an input layer, an output layer, and weight vectors, where the neurons in the output layer are arranged in a matrix in a one- or two-dimensional space. They compete with each other for opportunity to adjust the weight vectors based on the input vectors. Finally, the neurons in the output layer are presented in the output space in a meaningful topology based on the features of the input vectors [28–30].

All the parameters of surface and groundwater sample were mapped onto neurons by the SOM, and the correlations between indicators were compared based on the feature images formed by the neurons (Figure 6). First, all samples were divided into two categories: surface water (group 1) and groundwater (group 2). The feature images were analyzed by establishing a right-angle coordinate system with the image orthocenter as the origin, and the activation positions of neurons are the same, which indicates positive correlation [31]. In Figure 6, the high correlation between Na^+, K^+, Cl^-, HCO_3^-, and NO_3^- and the characteristic images of surface water and groundwater groupings indicated that these ions aggregated to a similar extent in surface water and groundwater. And it is speculated that there may be direct mixing between surface water and groundwater. As shown in Figure 6, the group of the TDS, TH, Ca^{2+}, Mg^{2+}, SO_4^{2-}, and Sr^{2+} were highly correlated with group of K^+, Na^+, Cl^-, and HCO_3^-. The SOM result proposed that these may have a common origin of water–rock interaction between surface water and groundwater. It was consistent with the Pearson correlation coefficient matrix analysis and principal component PCA classification. NO_3^- and Cl^- are closely related, indicating the source of local anthropogenic activities.

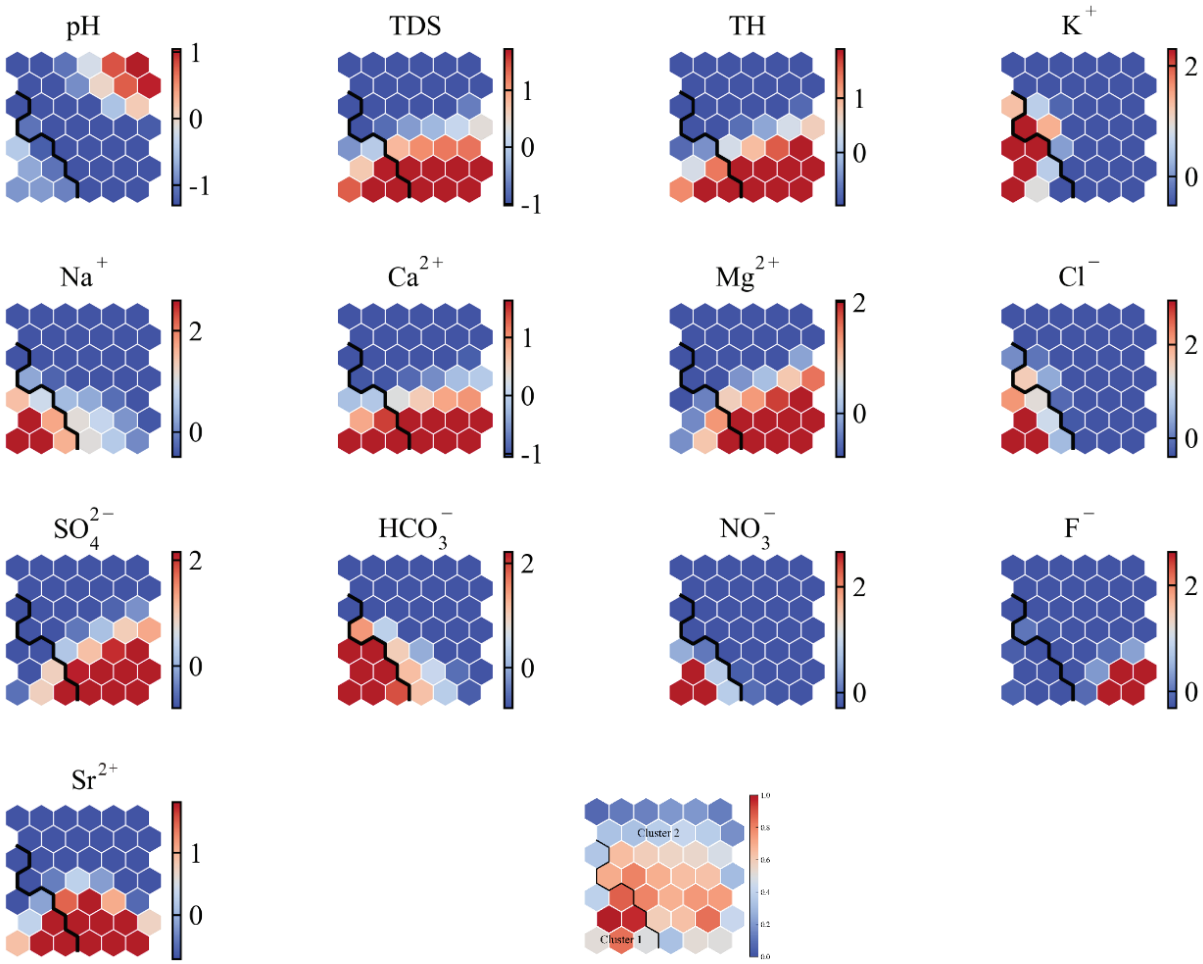

Figure 6. Characteristic map of main indicators of surface water and groundwater in the lower reaches of Yarlung Zangbo River mapped to SOM. Data are from Table 1.

4.2. Governing Factors of Hydrochemical Compositions

4.2.1. Gibbs Analysis

The Gibbs diagram was used to classify the mechanisms controlling the chemical fraction of groundwater into three types: precipitation, water–rock interaction, and evaporanspiration [32]. The Gibbs ratio was obtained by the ratio of $Na^+/(Na^+ + K^+)$ and $Cl^-/(Cl^- + HCO_3^-)$ to the total dissolved solid (TDS) to visualize the different control-

ling factors on hydrogeochemical compositions. In Figure 7, surface water samples and groundwater samples in the lower reaches of the Yarlung-Zangbo River, as well as sample sites in the middle and upper reaches of the Yarlung-Zangbo River, were distributed in the area of rock dominance, indicating water–rock interaction is the main factor affecting hydrochemical compositions.

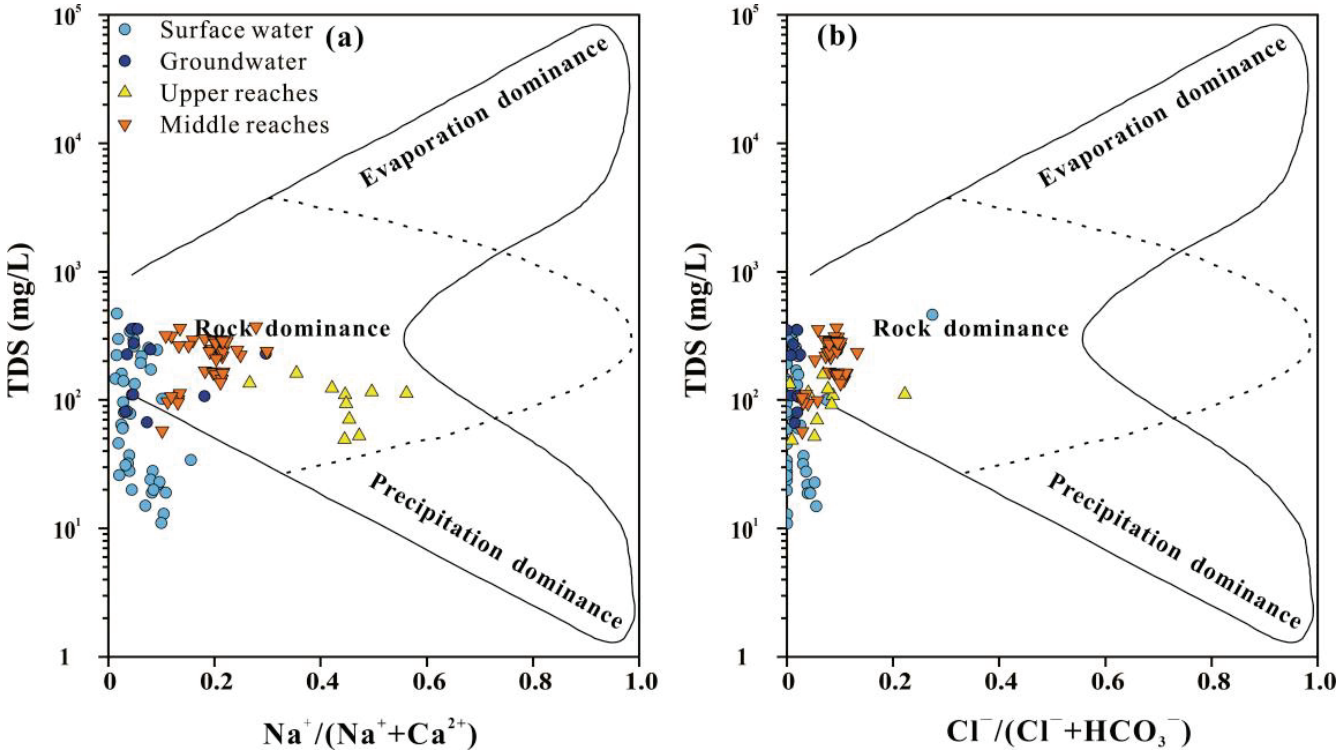

Figure 7. (**a**,**b**) Gibbs diagram of the water resource in the Yarlung-Zangbo River. Data are from Tables 1 and 2.

4.2.2. Ion Ratio Analysis

The ratio coefficients between various hydrochemical components have been used to determine the hydrochemical process [33,34]. The ion ratios of each component in the lower, middle, and upper reaches of the Yarlung-Zangbo River were also compared and analyzed as a way to further understand the characteristics of hydrochemical changes along the whole Yarlung-Zangbo River.

Silicate weathering, carbonate, and evaporative mineral dissolution can be determined by the correlation ratios of Ca^{2+}, Mg^{2+}, Na^{+}, and HCO_3^{-} [17]. All samples in the upper, middle, and lower reaches of the Yarlung-Zangbo River were located in the silicate and carbonate dominating zones (Figure 8), indicating that silicate weathering and carbonate dissolution were the main types of water–rock interaction. Figure 8 also showed that from the upper to lower reaches of the Yarlung-Zangbo River, the dominated type of water-rock interaction displayed a gradual transition from silicate dissolution to carbonate dissolution.

The molar ratio relationship between (K^{+} + Na^{+}) and Cl^{-} can reflect the sources of Na^{+} and K^{+} [33]. As shown in Figure 9a, both surface water and groundwater in the lower reaches of the Yarlung-Zangbo River fell below the y = x line and close to the K^{+} + Na^{+} axis, indicating the occurrence of silicate weathering. Since the Cl^{-} concentration is not sufficient to balance Na^{+} + K^{+}, it indicated that there are other minerals dissolved to provide Na^{+} and K^{+} concentrations, such as dissolution of silicate minerals (sodium, potassium feldspar, etc.,). In addition, excess Na^{+} and K^{+} concentrations existed in the upper and middle reaches, indicating the silicate weathering.

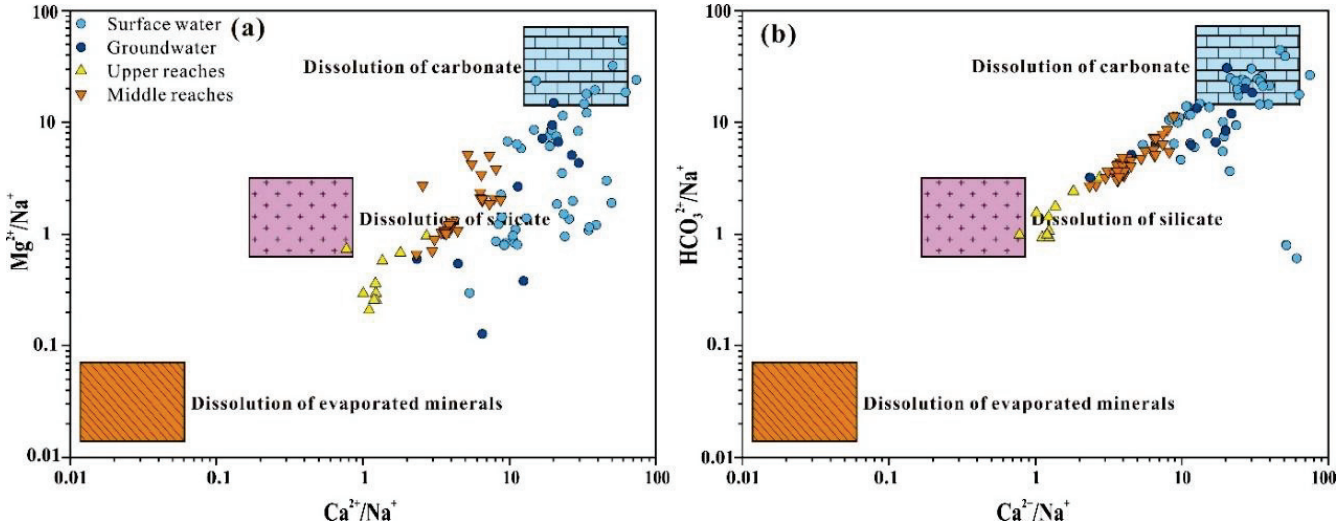

Figure 8. Ratio diagram of $Ca^{2+}/Na^{+} - Mg^{2+}/Na^{+}$ (**a**) and $Ca^{2+}/Na^{+} - HCO_3{}^{-}/Na^{+}$ (**b**). Data are from Tables 1 and 2.

Ca^{2+} and Mg^{2+} concentrations in groundwater mainly come from dissolution of carbonates or silicates and evaporites, so the molar ratio between $(Ca^{2+} + Mg^{2+})/(HCO_3{}^{-} + SO_4{}^{2-})$ can be used to determine the main source of Ca^{2+} and Mg^{2+} [35]. When the ratio is close to 1, it indicates that carbonates (calcite, dolomite) dissolution and silicates weathering are the main source of Ca^{2+} and Mg^{2+}. When this ratio is much greater than 1, it indicates that dissolution of carbonate minerals is the main source of Ca^{2+} and Mg^{2+}. When this ratio is much less than 1, it indicates that evaporite dissolution and silicate weathering are the main source of Ca^{2+} and Mg^{2+}. As shown in Figure 9b, most of the surface water and groundwater are located near the y = x line. Hence, Ca^{2+} and Mg^{2+} in surface water and groundwater in the lower reaches of the Yarlung-Zangbo River mainly originated from the dissolution and weathering of carbonate and silicate minerals, as well as those in the middle and upper reaches of the Yarlung-Zangbo River.

The molar ratios of Ca^{2+} and $(Ca^{2+} + Mg^{2+})$ against $HCO_3{}^{-}$ can determine the dissolution of carbonate rocks [33]. As shown in Figure 9c,d, some points fell on the y = x line and the remaining more points fall on the Ca^{2+} and $Ca^{2+} + Mg^{2+}$ side, indicating calcite dissolution dominated the water–rock interaction in the lower reaches of the Yarlung-Zangbo River. The excess Ca^{2+} and Mg^{2+} were presumed to be derived from the dissolution of Ca- and Mg- bearing silicate minerals. The $Ca^{2+}/HCO_3{}^{-}$ and $(Ca^{2+} + Mg^{2+})/HCO_3{}^{-}$ ratios of water samples in the middle and upper reaches of the Yarlung-Zangbo River showed the dissolution and weathering of carbonate and silicate minerals.

Molar ratio of Ca^{2+} and $SO_4{}^{2-}$ equal to 1:1 would indicate that Ca^{2+} and $SO_4{}^{2-}$ concentrations originated from the dissolution of gypsum [27]. As shown in Figure 9e, some surface water samples were located on the y = x line, from which it can be judged that a small portion of Ca^{2+} and $SO_4{}^{2-}$ in surface water also originates from the dissolution of gypsum. While most of surface water and groundwater samples fell above or below the y = x line. And the cause of this phenomenon may be cation exchange process. The sample points in the middle reaches of the Yarlung-Zangbo River mainly fell on the y = x line, indicating that gypsum dissolution also exists in the middle reaches. The sample points in the upper reaches fell below the 1:1 line, which may also be influenced by the cation exchange process.

The molar ratio between Ca^{2+} and Mg^{2+} is called the calcium–magnesium coefficient. Calcium-containing minerals are more insoluble than magnesium-containing minerals. When the water–rock interaction is very strong, the insoluble ions mainly exist in water. The ratio coefficient of Ca^{2+}/Mg^{2+} is positively correlated with the degree of water–rock interaction. As shown in Figure 9f, both surface water and groundwater samples were

biased toward the Ca^{2+} axis, indicating that obvious water–rock interaction occurs in surface water and groundwater.

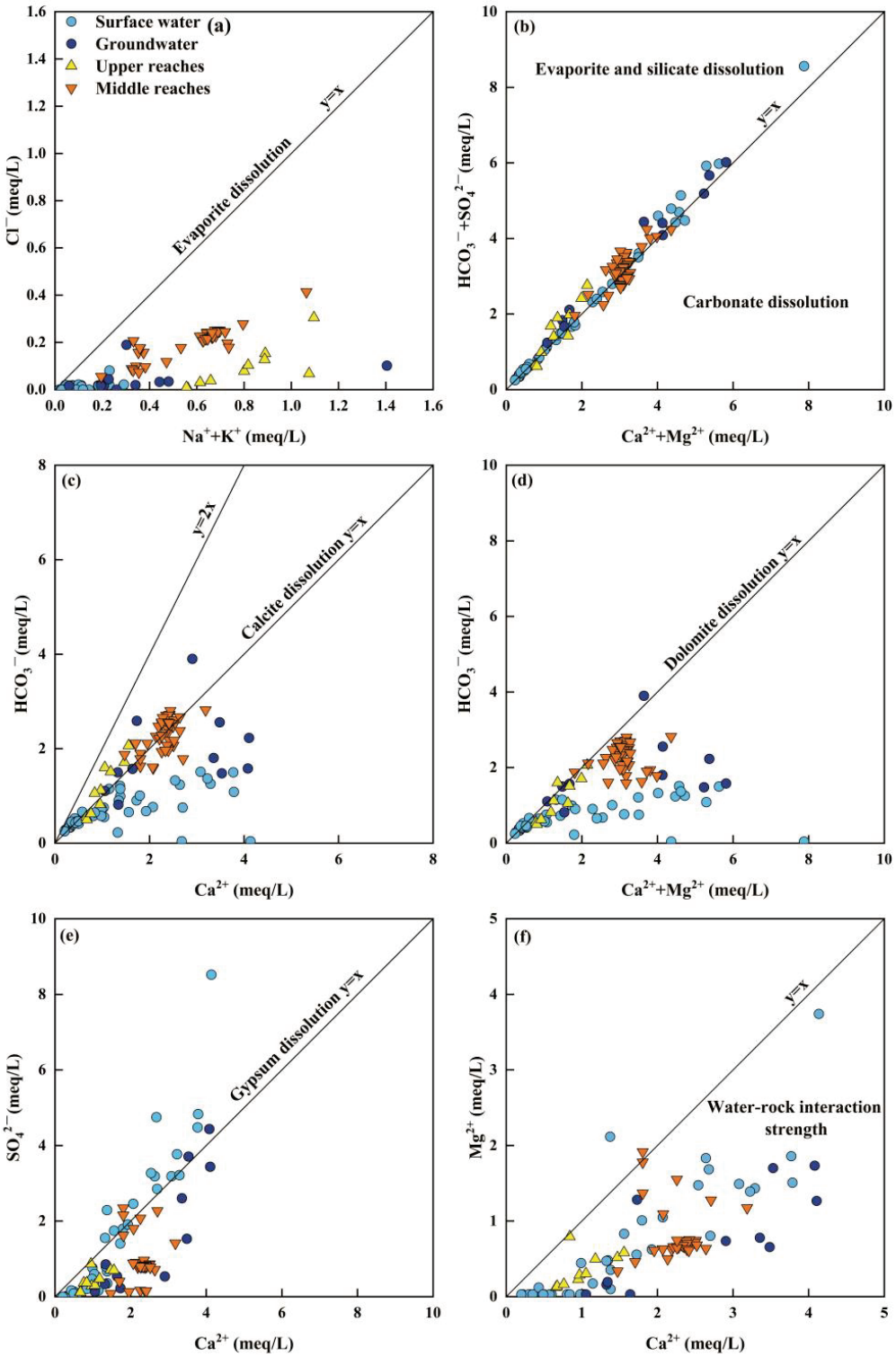

Figure 9. Molar ratio diagram of ion combination. Data were from Tables 1 and 2. (**a**) $(K^+ + Na^+)/Cl^-$; (**b**) $(Ca^{2+} + Mg^{2+})/(HCO_3^- + SO_4^{2-})$; (**c**) Ca^{2+}/HCO_3^-; (**d**) $(Ca^{2+} + Mg^{2+})/HCO_3^-$; (**e**) Ca^{2+}/SO_4^{2-}; (**f**) Ca^{2+}/SO_4^{2-}.

4.2.3. Ion Exchange

Ion exchange process can be verified by the relationship between the $(Ca^{2+} + Mg^{2+}) - (SO_4^{2-} + HCO_3^-)$ and $(Na^+ + K^+ - Cl^-)$ [30]. As shown in Figure 10a, the surface water

and groundwater samples, and mid- and upstream water samples in the lower reaches of the Yarlung-Zangbo River all fell near the straight line with a slope of −1. The slope of the linear distribution of the surface water samples is −0.9953 and R2 is 0.1011; the slope of the linear distribution of the groundwater samples is −0.6615 and R2 is 0.6063; the slope of the linear distribution of the upstream water samples is −0.9582 and R2 is 0.0. The results showed that the cation exchange is an important factor affecting water chemistry in the Yarlung-Zangbo River.

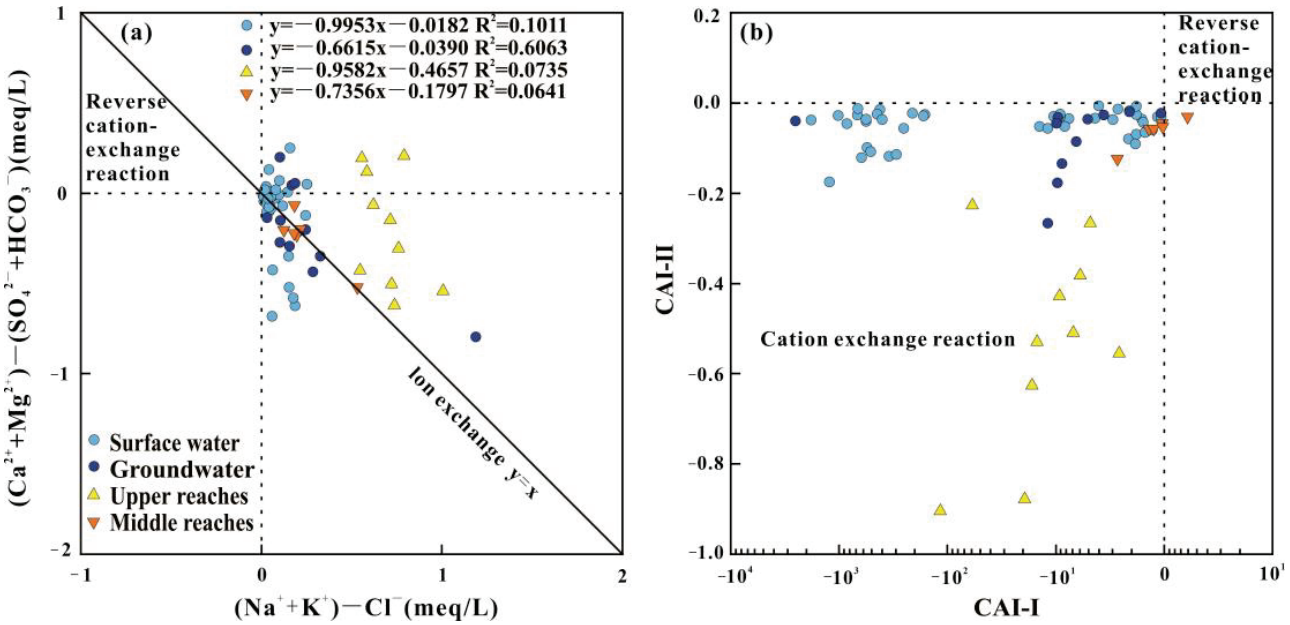

Figure 10. Ion combination ratio diagram of ion exchange. Data are from Tables 1 and 2.

Cation exchange interaction can also be analyzed using the choroalkaline index [36]. Where the indices CAI-I (=(Cl^- − (Na^+ + K^+))/Cl^-) and CAI-II (=(Cl^- − (Na^+ + K^+))/(HCO_3^- + SO_4^{2-} + CO_3^{2-} + NO_3^-)) are positive, it indicates that Na^+ and K^+ in water have been exchanged by Ca^{2+} and Mg^{2+} in the surrounding rocks, while negative values indicate the presence of reverse exchange, and the absolute value The larger the value, the stronger the ion-exchange interaction, and if the value is equal to 0, it means that there is no ion-exchange interaction in the water chemistry process. Figure 10b shows the CAI-I and CAI-II relationships of surface water, groundwater, and water samples from the lower reaches of the Yarlung-Zangbo River and the middle and upper reaches of the Yarlung-Zangbo River, and it can be seen that the vast majority of water samples are less than 0, indicating that Ca^{2+} and Mg^{2+} in surface water, groundwater, and water samples from the middle and upper reaches of the Yarlung-Zangbo River have been exchanged by Na^+ and K^+ in the surrounding rocks.

4.2.4. Saturation Index Analysis

The saturation index (SI) calculated by Phreeqc 3.0 is used to assess the equilibrium state of various minerals in water [37]. In this study, SI values of calcite, dolomite, gypsum, and halite were calculated for surface water and groundwater samples (Figure 11). The results showed that the SI of calcite, dolomite, gypsum, and halite were all less than 0 and thus were undersaturated. The SI values of calcite, dolomite, gypsum, and halite had the order as $SI_{halite} < SI_{gypsum} < SI_{dolomite} < SI_{calcite}$. Therefore, calcite dissolution is the predominant process in surface water and groundwater. It was consistent with the results of ion ratio analysis.

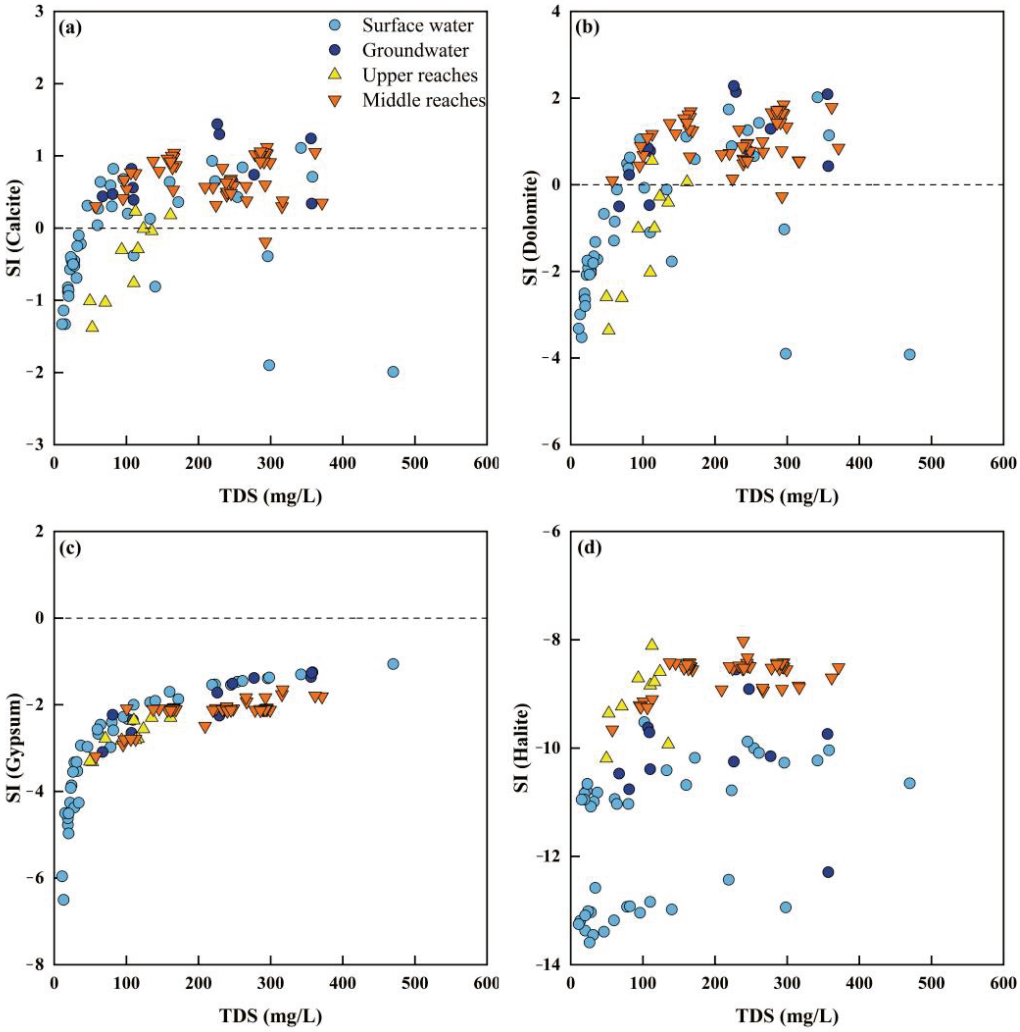

Figure 11. Relationship between saturation index (SI) of different minerals in surface water and groundwater and total dissolved solids (TDS). (**a**) SI (calcite); (**b**) SI (dolomite); (**c**) SI (gypsum), and (**d**) SI (halite). Data are from Tables 1 and 2.

4.2.5. Water–Rock Interaction Implied by Sr Isotope

The variation of strontium concentration and strontium isotope of surface and groundwater can be used to identify the main water-rock interaction [38–40]. The mean values of Sr content and $^{87}Sr/^{86}Sr$ ratio of groundwater were higher than those of surface water in the lower reaches of the Yarlung-Zangbo River. Most of the $^{87}Sr/^{86}Sr$ ratios of surface water and groundwater samples in the lower reaches of the Yarlung-Zangbo River were greater than the mean value of modern seawater (0.70907) and the mean value of the middle reaches of the Yarlung-Zangbo River (0.71136) [12], respectively (Figure 12a). It indicated that a large amount of Sr^{2+} was dissolved from the rocks during the runoff. Meanwhile, the surface water and groundwater in the lower reaches experienced water–rock interaction, and then increased $^{87}Sr/^{86}Sr$ ratio in surface water and groundwater (Figure 12b). This indicates that the $^{87}Sr/^{86}Sr$ ratios in surface and groundwater in the lower reaches of the Yarlung-Zangbo River are influenced by water–rock interaction. The $^{87}Sr/^{86}Sr$ ratios of most surface water and groundwater samples in the lower reaches of the Yarlung-Zangbo River lied in the source field between carbonate rock (0.708–0.709) and silicate rock (0.716–0.720), indicating that Sr content in surface water and groundwater in the lower reaches of the Yarlung-Zangbo River is dominated by carbonate rock and silicate rock weathering. In terms of regional distribution (Figure 12b), the $^{87}Sr/^{86}Sr$ ratios in surface water and groundwater are higher in the eastern mainstem of the lower reaches of the

Yarlung-Zangbo River and lower in the western mainstem, with an overall trend of increasing along the river runoff path. The southwestern and southeastern tributaries show higher $^{87}Sr/^{86}Sr$ ratios, which may be due to the tributary areas being more influenced by silicate rock weathering.

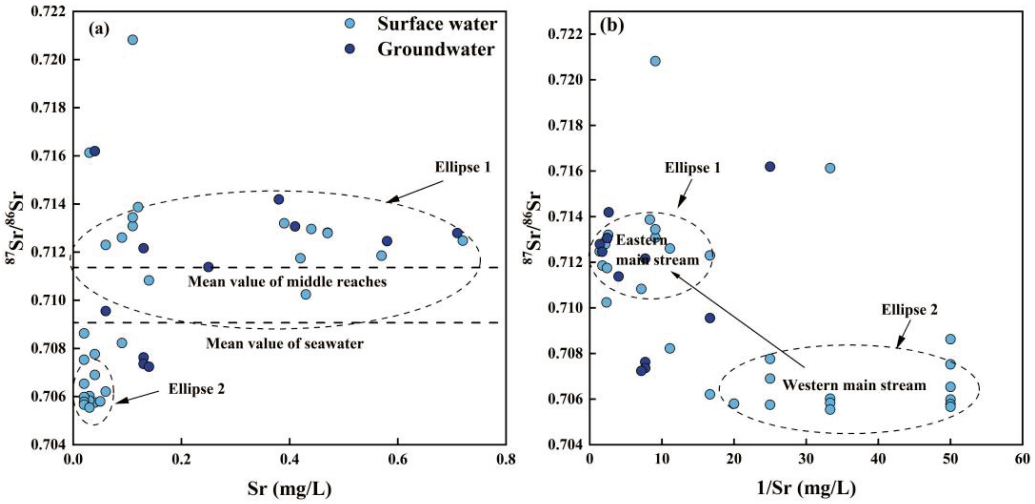

Figure 12. $^{87}Sr/^{86}Sr$ vs. Sr (**a**) and$^{87}Sr/^{86}Sr$ vs. 1/Sr (**b**) of surface water and groundwater samples in the lower reaches of the Yarlung Zangbo River. Data were from Tables 1 and 2.

It was shown that the strontium isotopic compositions in different minerals are significantly different, and the $^{87}Sr/^{86}Sr$ average ratio of 0.7075 and lower Mg^{2+}/Ca^{2+} ratio (~0.1) can be considered as the end member of dissolved limestone; $^{87}Sr/^{86}Sr$ average ratio of 0.7093 and higher Mg^{2+}/Ca^{2+} values (~1.05) as the end member of dissolved dolomite. $^{87}Sr/^{86}Sr$ mean ratio of 0.7200 and moderate Mg^{2+}/Ca^{2+} values (~0.7) are used as end members of dissolved silicate rocks [41]. As can be seen in Figure 13a, most of the surface water and a small portion of the groundwater sample points were concentrated around the limestone end member, indicating that they are mainly affected by calcite dissolution. The remaining portion of the surface water and most of the groundwater sample points were distributed near the limestone and silicate rock mixing line. This indicated that the surface water and groundwater samples in this part are mainly controlled by calcite dissolution and silicate weathering.

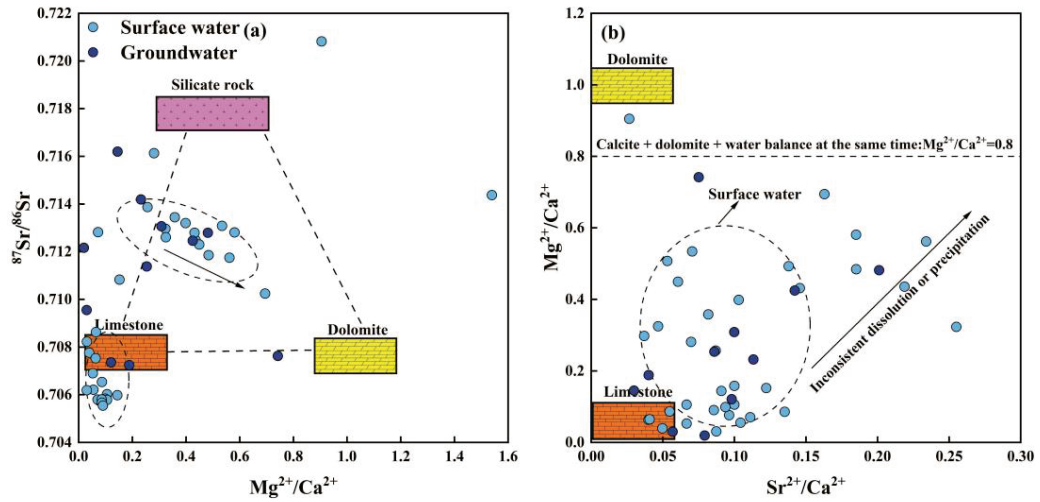

Figure 13. $^{87}Sr/^{86}Sr$ vs. Mg^{2+}/Ca^{2+} (**a**) and Mg^{2+}/Ca^{2+} vs. Sr^{2+}/Ca^{2+} (**b**) of surface water and groundwater samples in the lower reaches of the Yarlung Zangbo River. Data are from Table 1.

During the dissolution of carbonate minerals, Sr behaves similarly to Mg. Ca^{2+} and Mg^{2+} in groundwater correlate well with the variation of Sr, indicating that alkaline earth metals have similar origin. Therefore, the ratios of Mg^{2+}/Ca^{2+} and Sr^{2+}/Ca^{2+} can be used to trace the water–rock reaction [42]. As shown in Figure 13b, most samples of surface water and groundwater were more concentrated and can also be analyzed with an approximate three-terminal member mixture, i.e., a mixture of limestone aquifer water, dolomite aquifer water, and surface water. It indicated the direct mixing of surface water with groundwater, which affects the chemical composition of surface water. Only a few water samples in Figure 8b had high Mg^{2+}/Ca^{2+} and Sr^{2+}/Ca^{2+} ratios, indicating a small effect of non-conformable dissolution/precipitation of carbonate rocks. Non-conformable dissolution/precipitation will elevate the Mg^{2+} content in water, does not result in significantly larger Mg^{2+}/Ca^{2+} ratios in surface and groundwater than the water in which calcite and dolomite are in simultaneous equilibrium Mg^{2+}/Ca^{2+} ratio (0.8).

4.2.6. Recharge Sources Determined by D-O Isotopes

Using δD and $\delta^{18}O$ data of rainfall precipitation, surface water, and groundwater, δD-$\delta^{18}O$ scatter diagrams can be plotted, and by comparison with global meteoric water line (GMWL) or regional atmospheric precipitation lines, the fractionation effect of δD and $\delta^{18}O$ in water bodies can be analyzed in depth to reveal the occurrence process and driving mechanism and provide a tracer for hydrogeological studies.

In the δD-$\delta^{18}O$ scatter plotting diagram (Figure 14a), it can be seen that both surface water and groundwater samples were close to the local atmospheric precipitation line (LMWL) [43] and the global atmospheric precipitation line (GMWL) [44]. The results indicated that surface water and groundwater were derived from local atmospheric precipitation. A small portion of surface water samples in the lower reaches of the Yarlung-Zangbo River were located to the right of the atmospheric precipitation line and the GMWL, indicating that surface water was less influenced by evapotranspiration. The slope of the surface water line in the lower reaches of the Yarlung-Zangbo River was 9.21, close to the local atmospheric precipitation line of 8.08, while the intercept (31.146) is higher than the local atmospheric precipitation line (12.37). The results were due to the water hydration with silicate minerals during runoff, resulting in the $\delta^{18}O$ depletion and slight δD enrichment in surface water. And the strong oxygen isotope exchange caused $\delta^{18}O$ loss and kinetic fractionation during ice melt, which can have an impact on δD and $\delta^{18}O$ balance. Therefore, most of the surface water samples were located to the left of the atmospheric precipitation line and global meteoric water line (GMWL) in the lower reaches of the Yarlung-Zangbo River. Moreover, surface water mainly originates from the middle and upper reaches of mainstream and tributary water atmospheric precipitation and ice melt. The δD and $\delta^{18}O$ values of most groundwater samples were located below the atmospheric precipitation line in the lower reaches of the Yarlung-Zangbo River and the global atmospheric precipitation line. It may be influenced by the isotope elevation effect and kinetic fractionation, resulting in lower δD and $\delta^{18}O$ values in groundwater. Groundwater was mainly recharged from atmospheric precipitation, ice and snow melt water, whose recharge elevation was higher than that of surface water. A comparative analysis of the surface water lines of the Yarlung-Zangbo River (Figure 14b) showed that the deviation was greatest in the middle and lower reaches (slope of 5.79) and less in the upper reaches (slope of 7.088 and 9.21). It indicated that the middle reaches of the Yarlung-Zangbo River was subject to stronger evaporation and the upper reaches and lower reaches of the Yarlung-Zangbo River were subject to weaker evaporation.

4.3. Assessment of Groundwater Quality Based on EWQI

The entropy-weighted water quality index (EWQI) method has been widely used to assess the combined impact of water chemistry parameters on overall water quality [45–47]. When the EWQI value is below 100, it means that the water quality reaches the permit limit for drinking water. Twelve surface and groundwater parameters were selected for EWQI

calculations, including pH, TH, TDS, K^+, Na^+, Ca^{2+}, Mg^{2+}, Cl^-, $SO_4{}^{2-}$, $HCO_3{}^-$, $NO_3{}^-$, and F^-. The procedure was described as Zhang et al. [48]. The results showed that the EWQI values of surface water varied from 1.84 to 81.34 with a mean value of 11.93, and the EWQI values of groundwater varied from 7.14 to 21.77 with a mean value of 16.13. The EWQI values of groundwater were slightly higher than those of surface water. The surface water and groundwater quality can be classified into five classes according to EWQI. In Figure 15, it showed that most of the surface water and all groundwater samples belonged to excellent water of class 1. Only 2 surface water samples were good water of class 2 and also meet the WHO drinking standards. The two surface water samples exceeded the fluoride standard of 1.62 mg/L and 2.02 mg/L, respectively, and may have been affected by contamination from human activities. Figure 15 also shows a better linear trend of EWQI and TDS for surface water and groundwater samples.

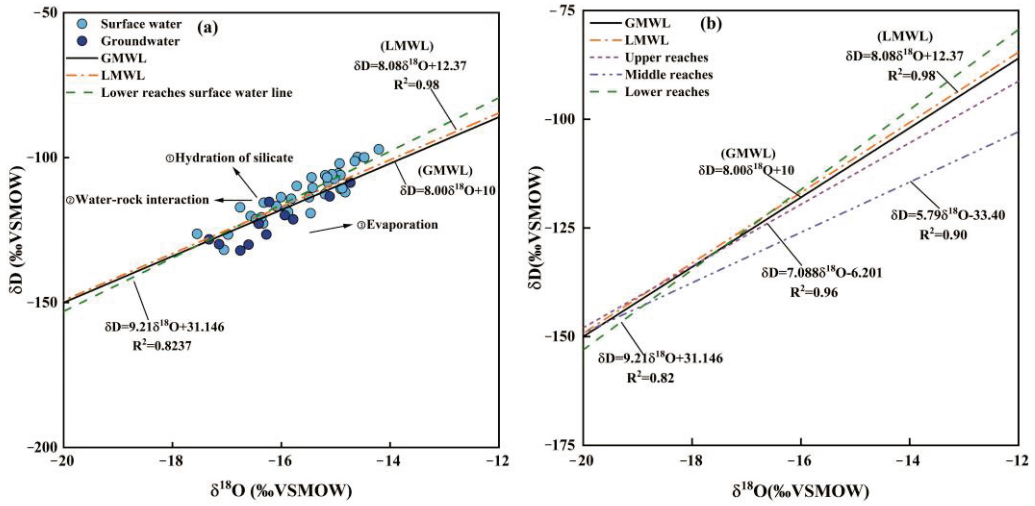

Figure 14. Relationship between surface water and groundwater δD and $\delta^{18}O$ in the middle and lower reaches of the Yarlung Zangbo River (**a**) and comparison of surface water lines in the middle and lower reaches, middle and upper reaches of the Yarlung Zangbo River (**b**). Data are from Tables 1 and 2.

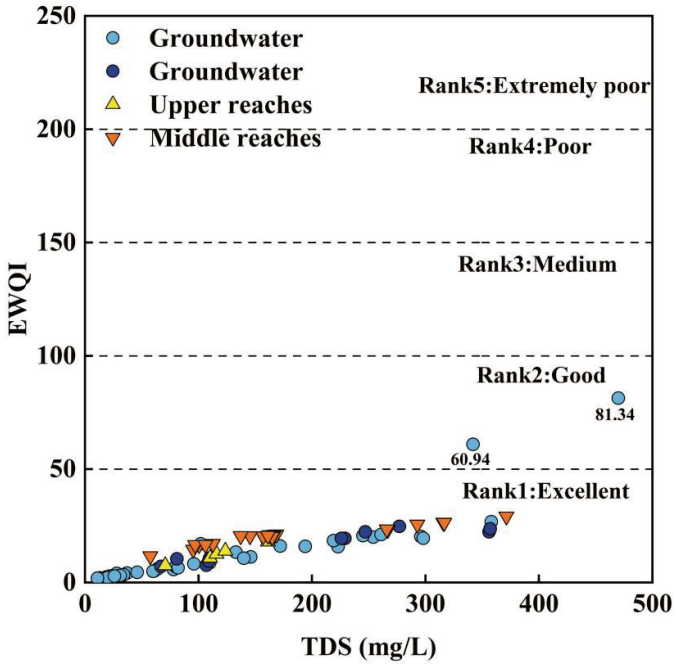

Figure 15. Relationship between surface water and groundwater EWQI and TDS.

4.4. Hydrochemical Conceptual Model of the Yarlung-Zangbo River

As shown in Table 2, the pH values increased from the upper to the lower reaches of the Yarlung-Zangbo River and was weakly alkaline. The TDS and most of the ion concentrations in the upper and lower reaches of the river were lower than those in the middle reaches of the river, which is mainly due to the relatively strong evaporation in the middle reaches of the river and the dilution effect of snow melting in the upper reaches and increasing rainfall recharge in the lower reaches. Hydrochemical type was Ca-Na-HCO_3-SO_4 in the upper reaches of the Yarlung-Zangbo River, whose hydrochemical compositions were determined by silicate weathering and carbonate dissolution. Hydrochemical type was Ca-HCO_3 and Ca-HCO_3-SO_4 in the middle reaches of the Yarlung-Zangbo River, and the main ions were derived from carbonate and evaporite dissolution. Hydrochemical type was Ca-HCO_3 and Ca-SO_4-HCO_3 in the lower reaches of the Yarlung-Zangbo River, and the main ions were derived from carbonate and evaporite dissolution. Therefore, it can be concluded that the whole basin of the Yarlung-Zangbo River is controlled by the dissolution of carbonate rocks (Figure 16). Combined with Figure 10a,b, it shows that from the upstream to the lower reaches of the river, the controlling factor of water chemistry changes from water–rock action to water–rock action and atmospheric precipitation, and the main form of water–rock action shows a trend of transition from silicate weathering and dissolution to carbonate weathering and dissolution. Considering the low concentration of Cl and NO_3, anthropogenic activities were weak in the whole basin of the Yarlung-Zangbo River (Table 4).

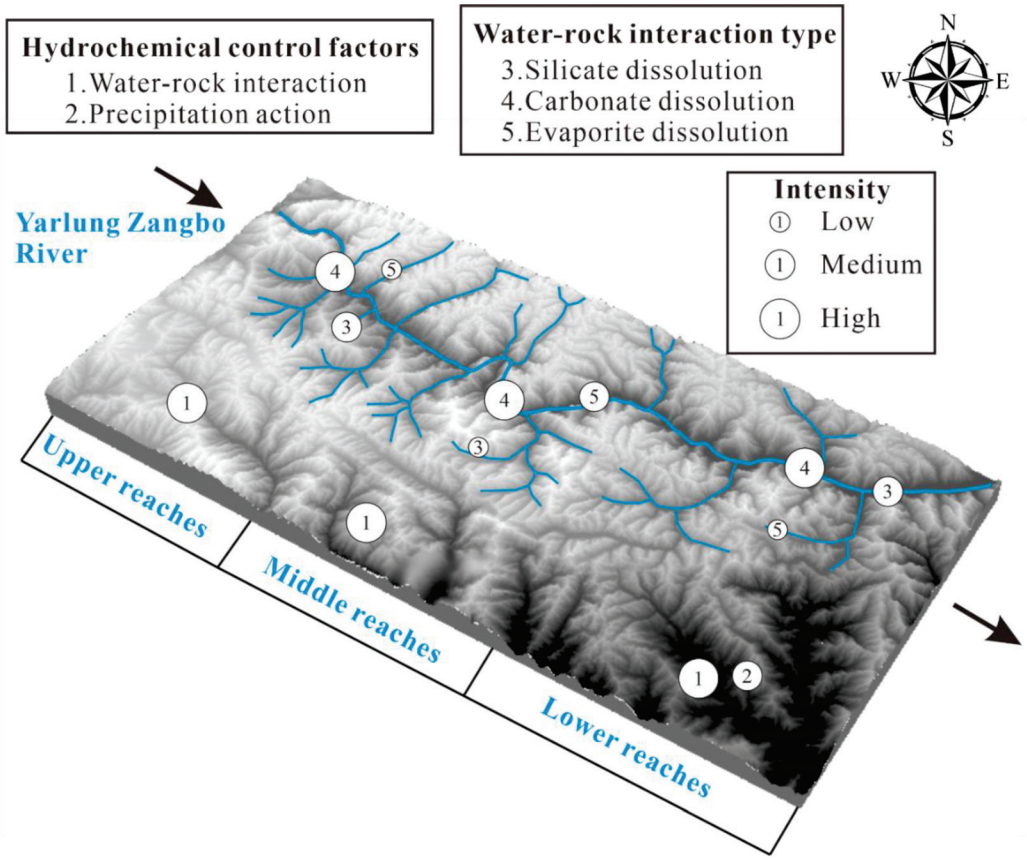

Figure 16. Schematic diagram of hydrochemical control factors in the middle and lower reaches, middle reaches and upper reaches of Yarlung Zangbo River.

Table 4. Comparison of hydrochemical characteristics between the lower reaches and the middle and upper reaches of the Yarlung Zangbo River.

Reach	Upper Reaches	Middle Reaches	Lower Reaches
Geographical position	Jiema yangzongqu—Lizi section	Shigatse—Gyaca section	Gyaca—Millin section
Hydrochemical type	Ca-Na-HCO_3-SO_4	Ca-HCO_3 and Ca-HCO_3-SO_4	Ca-HCO_3 and Ca-SO_4-HCO_3
Controlling factors	Water–rock interaction	Water–rock interaction	Water–rock interaction, Atmospheric precipitation
Ion source	Silicate rock, Carbonate rock, Evaporite rock	Carbonate rock, Evaporite rock, Silicate rock	Carbonate rock, Silicate rock, Evaporite rock
Influence of human factors	Very low	Very low	Low

5. Conclusions

Hydrochemistry and stable isotopes (δ^2H, $\delta^{18}O$ and $^{87}Sr/^{86}Sr$) were integrated to identify the major factors affecting the hydrochemical process of groundwater and surface water in the lower reaches of the Yarlung-Zangbo River, southern Tibet. The hydrochemical compositions were further analyzed to reveal the spatial characteristics of water–rock interaction along the Yarlung-Zangbo River. Four main conclusions were achieved as follows:

(1) Surface water and groundwater were weakly alkaline and belonged to very soft to moderately hard fresh water. Major cations in surface water and groundwater ranked as $Ca^{2+} > Mg^{2+} > Na^+ > K^+$. Major anion concentrations in surface water were $SO_4^{2-} > HCO_3^- > Cl^- > F^- > NO_3^-$, and major anion concentrations in groundwater were $HCO_3^- > SO_4^{2-} > Cl^- > NO_3^- > F^-$, respectively. The hydrochemical type of surface water is mainly Ca-HCO_3 (mainstream) and Ca-SO_4-HCO_3 (tributary), while the hydrochemical type of groundwater was mainly Ca-SO_4-HCO_3.

(2) Hydrochemical compositions of surface water and groundwater were mainly affected by water–rock interaction. Silicate weathering, calcite dissolution, and cation exchange were involved in water–rock interaction of surface water and groundwater. Evaporite dissolution locally occurred in the tributary area. Surface water and groundwater were recharged by atmosphere precipitation and local snow melting. Stronger evaporation occurred in the middle reaches than that in the upper reaches and lower reaches of the Yarlung-Zangbo River.

(3) The EWQI values indicated most of the surface water and all groundwater samples belonged to excellent water of class 1. Only 2 surface water samples, having higher fluoride concentrations of 1.62 mg/L and 2.02 mg/L, were good water of class 2. Therefore, surface water and groundwater reach the standard of drinking purpose in the lower reaches of the Yarlung-Zangbo River.

(4) Hydrochemical process displayed a changing trend along the Yarlung-Zangbo River. Hydrochemical type was Ca-Na-HCO_3-SO_4 in the upper reaches of the Yarlung-Zangbo River, whose hydrochemical compositions were determined by silicate weathering and carbonate dissolution. Hydrochemical type was Ca-HCO_3 and Ca-HCO_3-SO_4 in the middle reaches of the Yarlung-Zangbo River, and the main ions were derived from carbonate and evaporite dissolution. Hydrochemical type was Ca-HCO_3 and Ca-SO_4-HCO_3 in the lower reaches of the Yarlung-Zangbo River, and the main ions were derived from carbonate and evaporite dissolution. Therefore, the Yarlung-Zangbo River is controlled by the dissolution of carbonate rocks and local silicate weather and evaporate dissolution. In this study, a hydrochemical-type transition of Ca-Na-HCO_3-SO_4 $\rightarrow$ Ca-HCO_3 and Ca-HCO_3-SO_4 $\rightarrow$ Ca-HCO_3 and Ca-SO_4-HCO_3 has been identified along the Yarlung-Zangbo River. The different hydrochemical types would be produced by relevant water-rock interactions. The achievements would be helpful for understanding the hydrochemical processes in the catchment of the Yarlung-Zangbo River, providing a vital reference for water resource management.

Author Contributions: Data curation, X.Y. (Xingcheng Yuan) and H.H.; formal analysis, Z.G. and T.L.; funding acquisition, X.Y. (Xiao Yu); investigation, X.Y. (Xiao Yu), Y.Z., H.C. and T.L.; methodology, H.G.; software, X.Y. (Xingcheng Yuan) and H.G.; supervision, Y.Z.; writing—original draft, X.Y. (Xiao Yu) and X.Y. (Xingcheng Yuan); writing—review and editing, H.G. and Y.Z. All authors have read and agreed to the published version of the manuscript.

Funding: This research was funded by National Natural Science Foundation of China grant number 42072313. And The APC was funded by Research Center of Applied Geology of China Geological Survey.

Data Availability Statement: The data presented in this study are available on request from the corresponding author.

Acknowledgments: We thank two anonymous reviewers for their constructive suggestions which improved our manuscript.

Conflicts of Interest: The authors declare that they have no known competing financial interests or personal relationships that could have appeared to influence the work reported in this paper.

References

1. Li, C.; Gao, X.; Li, S.; Bundschuh, J. A review of the distribution, sources, genesis, and environmental concerns of salinity in groundwater. *Environ. Sci. Pollut. Res.* **2020**, *27*, 41157–41174. [CrossRef] [PubMed]
2. Li, P. To Make the Water Safer. *Expo. Health* **2020**, *12*, 337–342. [CrossRef] [PubMed]
3. Uddin, M.G.; Nash, S.; Olbert, A.I. A review of water quality index models and their use for assessing surface water quality. *Ecol. Indic.* **2021**, *122*, 107218. [CrossRef]
4. Elshall, A.S.; Arik, A.D.; El-Kadi, A.I.; Pierce, S.; Ye, M.; Burnett, K.M.; Wada, C.A.; Bremer, L.L.; Chun, G. Groundwater sustainability: A review of the interactions between science and policy. *Environ. Res. Lett.* **2020**, *15*, 093004. [CrossRef]
5. Medici, G.; Langman, J.B. Pathways and Estimate of Aquifer Recharge in a Flood Basalt Terrain; A Review from the South Fork Palouse River Basin (Columbia River Plateau, USA). *Sustainability* **2022**, *14*, 11349. [CrossRef]
6. Qu, S.; Duan, L.; Shi, Z.; Liang, X.; Lv, S.; Wang, G.; Liu, T.; Yu, R. Hydrochemical assessments and driving forces of groundwater quality and potential health risks of sulfate in a coalfield, northern Ordos Basin, China. *Sci. Total Environ.* **2022**, *835*, 155519. [CrossRef]
7. Subba Rao, N.; Dinakar, A.; Sun, L. Estimation of groundwater pollution levels and specific ionic sources in the groundwater, using a comprehensive approach of geochemical ratios, pollution index of groundwater, unmix model and land use/land cover—A case study. *J. Contam. Hydrol.* **2022**, *248*, 103990. [CrossRef]
8. Zhang, Y.; Hou, K.; Qian, H.; Gao, Y.; Fang, Y.; Xiao, S.; Tang, S.; Zhang, Q.; Qu, W.; Ren, W. Characterization of soil salinization and its driving factors in a typical irrigation area of Northwest China. *Sci. Total Environ.* **2022**, *837*, 155808. [CrossRef]
9. Mao, G.; Zhao, Y.; Zhang, F.; Liu, J.; Huang, X. Spatiotemporal variability of heavy metals and identification of potential source tracers in the surface water of the Lhasa River basin. *Environ. Sci. Pollut. Res.* **2019**, *26*, 7442–7452. [CrossRef]
10. Li, Z.; Liu, J.; Chen, H.; Li, Q.; Yu, C.; Huang, X.; Guo, H. Water environment in the Tibetan Plateau: Heavy metal distribution analysis of surface sediments in the Yarlung Tsangpo River Basin. *Environ. Geochem. Health* **2020**, *42*, 2451–2469. [CrossRef]
11. Tan, H.; Chen, X.; Shi, D.; Rao, W.; Liu, J.; Liu, J.; Eastoe, C.J.; Wang, J. Base flow in the Yarlungzangbo River, Tibet, maintained by the isotopically—depleted precipitation and groundwater discharge. *Sci. Total Environ.* **2021**, *759*, 143510. [CrossRef]
12. Shi, D.; Tan, H.; Chen, X.; Rao, W.; Basang, R. Uncovering the mechanisms of seasonal river–groundwater circulation using isotopes and water chemistry in the middle reaches of the Yarlungzangbo River, Tibet. *J. Hydrol.* **2021**, *603*, 127010. [CrossRef]
13. Cao, H.-W.; Pei, Q.-M.; Santosh, M.; Li, G.-M.; Zhang, L.-K.; Zhang, X.-F.; Zhang, Y.-H.; Zou, H.; Dai, Z.-W.; Lin, B.; et al. Himalayan leucogranites: A review of geochemical and isotopic characteristics, timing of formation, genesis, and rare metal mineralization. *Earth. Sci. Rev.* **2022**, *234*, 104229. [CrossRef]
14. Zhang, Y.-h.; Cao, H.-w.; Hollis, S.P.; Tang, L.; Xu, M.; Jiang, J.-s.; Gao, S.-b.; Wang, Y.-s. Geochronology, geochemistry and Sr-Nd-Pb-Hf isotopes of the Early Paleogene gabbro and granite from Central Lhasa, southern Tibet: Petrogenesis and tectonic implications. *Int. Geol. Rev.* **2019**, *61*, 868–894. [CrossRef]
15. Zhang, Y.-H.; Yao, R.-W.; Wang, Y.; Duo, J.; Cao, H.-W. Zircon U–Pb and sericite Ar–Ar geochronology, geochemistry and S–Pb–Hf isotopes of the Zebuxia Pb–Zn deposit, Tibet, southwestern China. *Ore. Geol. Rev.* **2022**, *148*, 104999. [CrossRef]
16. Yan, J.; Chen, J.; Zhang, W. Impact of land use and cover on shallow groundwater quality in Songyuan city, China: A multivariate statistical analysis. *Environ. Pollut.* **2022**, *307*, 119532. [CrossRef]
17. Gaillardet, J.; Dupré, B.; Louvat, P.; Allègre, C.J. Global silicate weathering and CO_2 consumption rates deduced from the chemistry of large rivers. *Chem. Geol.* **1999**, *159*, 3–30. [CrossRef]
18. Yan, Y.P.; Niu, F.X.; Liu, J.; Liu, X.T.; Li, Y.; Peng, H.; Yan, D.H.; Xiao, S.B. Hydrochemical characteristics and sources of the upper Yarlung Zangbo River in summer. *China Environ. Sci.* **2022**, *42*, 815–825. (In Chinese and English Abstract)
19. Chen, W. Hydrochemical Characteristics in the Upper Reaches of the Yarlung Zangbo River in Summer. Master's Thesis, China Three Gorges University, Yichang, China, 2021. (In Chinese and English Abstract)

20. Liu, J.; Li, Y.; Gao, Z.; Wang, M.; Ma, Y.; Shi, M.; Zhang, H. Ionic composition characteristics and their controlling factors in the main stream of the Yarlung Zangbo River. *J. Glaciol. Geocryol.* **2019**, *41*, 697–708. (In Chinese and English Abstract)
21. Li, Y.Z.; Gao, Z.J.; Liu, J.T.; Wang, M.; Han, C. Hydrogeochemical and isotopic characteristics of spring water in the Yarlung Zangbo River Basin, Qinghai-Tibet Plateau, Southwest China. *J. Mt. Sci.* **2021**, *18*, 2061–2078. [CrossRef]
22. Duan, R.; Li, P.; Wang, L.; He, X.; Zhang, L. Hydrochemical characteristics, hydrochemical processes and recharge sources of the geothermal systems in Lanzhou City, northwestern China. *Urban Clim.* **2022**, *43*, 101152. [CrossRef]
23. Li, P.; He, X.; Guo, W. Spatial groundwater quality and potential health risks due to nitrate ingestion through drinking water: A case study in Yan'an City on the Loess Plateau of northwest China. *Hum. Ecol. Risk Assess. Int. J.* **2019**, *25*, 11–31. [CrossRef]
24. Zhang, L.; Li, P.; He, X. Interactions between surface water and groundwater in selected tributaries of the Wei River (China) revealed by hydrochemistry and stable isotopes. *Hum. Ecol. Risk Assess. Int. J.* **2021**, *28*, 79–99. [CrossRef]
25. Seyedrahimi-Niaraq, M.; Mahdiyanfar, H.; Mokhtari, A.R. Integrating principal component analysis and U-statistics for mapping polluted areas in mining districts. *J. Geochem. Explor.* **2022**, *234*, 106924. [CrossRef]
26. Zeinalzadeh, K.; Rezaei, E. Determining spatial and temporal changes of surface water quality using principal component analysis. *J. Hydrol. Reg. Stud.* **2017**, *13*, 1–10. [CrossRef]
27. Zhang, Y.; Xu, M.; Li, X.; Qi, J.; Zhang, Q.; Guo, J.; Yu, L.; Zhao, R. Hydrochemical Characteristics and Multivariate Statistical Analysis of Natural Water System: A Case Study in Kangding County, Southwestern China. *Water* **2018**, *10*, 80. [CrossRef]
28. Bigdeli, A.; Maghsoudi, A.; Ghezelbash, R. Application of self-organizing map (SOM) and K-means clustering algorithms for portraying geochemical anomaly patterns in Moalleman district, NE Iran. *J. Geochem. Explor.* **2022**, *233*, 106923. [CrossRef]
29. Qu, S.; Shi, Z.; Liang, X.; Wang, G.; Han, J. Multiple factors control groundwater chemistry and quality of multi-layer groundwater system in Northwest China coalfield— Using self-organizing maps (SOM). *J. Geochem. Explor.* **2021**, *227*, 106795. [CrossRef]
30. Yao, R.; Yan, Y.; Wei, C.; Luo, M.; Xiao, Y.; Zhang, Y. Hydrochemical Characteristics and Groundwater Quality Assessment Using an Integrated Approach of the PCA, SOM, and Fuzzy c-Means Clustering: A Case Study in the Northern Sichuan Basin. *Front. Environ. Sci.* **2022**, *10*, 648. [CrossRef]
31. Yu, J.; Tian, Y.; Wang, X.; Zheng, C. Using machine learning to reveal spatiotemporal complexity and driving forces of water quality changes in Hong Kong marine water. *J. Hydrol.* **2021**, *603*, 126841. [CrossRef]
32. Gibbs, R.J. Mechanisms controlling world water chemistry. *Science* **1970**, *170*, 1088–1090. [CrossRef]
33. Li, C.; Gao, X.; Liu, Y.; Wang, Y. Impact of anthropogenic activities on the enrichment of fluoride and salinity in groundwater in the Yuncheng Basin constrained by Cl/Br ratio, δ18O, δ2H, δ13C and δ7Li isotopes. *J. Hydrol.* **2019**, *579*, 124211. [CrossRef]
34. Subba Rao, N.; Sunitha, B.; Sun, L.; Deepthi Spandana, B.; Chaudhary, M. Mechanisms controlling groundwater chemistry and assessment of potential health risk: A case study from South India. *Geochemistry* **2020**, *80*, 125568. [CrossRef]
35. Gao, X.; Li, X.; Wang, W.; Li, C. Human Activity and Hydrogeochemical Processes Relating to Groundwater Quality Degradation in the Yuncheng Basin, Northern China. *Int. J. Environ. Res. Public Health* **2020**, *17*, 867. [CrossRef] [PubMed]
36. Xiao, Y.; Hao, Q.; Zhang, Y.; Zhu, Y.; Yin, S.; Qin, L.; Li, X. Investigating sources, driving forces and potential health risks of nitrate and fluoride in groundwater of a typical alluvial fan plain. *Sci. Total Environ.* **2022**, *802*, 149909. [CrossRef]
37. Xiao, Y.; Liu, K.; Hao, Q.; Xiao, D.; Zhu, Y.; Yin, S.; Zhang, Y. Hydrogeochemical insights into the signatures, genesis and sustainable perspective of nitrate enriched groundwater in the piedmont of Hutuo watershed, China. *Catena* **2022**, *212*, 106020. [CrossRef]
38. Shoedarto, R.M.; Tada, Y.; Kashiwaya, K.; Koike, K.; Iskandar, I.; Malik, D.; Bratakusuma, B. Investigation of meteoric water and parent fluid mixing in a two-phase geothermal reservoir system using strontium isotope analysis: A case study from Southern Bandung, West Java, Indonesia. *Geothermics* **2021**, *94*, 102096. [CrossRef]
39. Temizel, E.H.; Gültekin, F.; Ersoy, A.F.; Gülbay, R.K. Multi-isotopic (O, H, C, S, Sr, B, Li) characterization of waters in a low-enthalpy geothermal system in Havza (Samsun), Turkey. *Geothermics* **2021**, *97*, 102240. [CrossRef]
40. Yan, Y.; Zhou, X.; Liao, L.; Tian, J.; Li, Y.; Shi, Z.; Liu, F.; Ouyang, S. Hydrogeochemical Characteristic of Geothermal Water and Precursory Anomalies along the Xianshuihe Fault Zone, Southwestern China. *Water* **2022**, *14*, 550. [CrossRef]
41. Cherchali, M.E.H.; Liégeois, J.P.; Mesbah, M.; Daas, N.; Amrous, K.; Ouarezki, S.A. Central Hoggar groundwaters and the role of shear zones: $^{87}Sr/^{86}Sr$, $\delta^{18}O$, $\delta^{2}H$ and 14C isotopes, geochemistry and water-rock interactions. *Appl. Geochem.* **2021**, *137*, 105179. [CrossRef]
42. Fantong, W.Y.; Kamtchueng, B.T.; Ishizaki, Y.; Fru, E.C.; Fantong, E.B.; Wirmvem, M.J.; Aka, F.T.; Nlend, B.; Harman, D.; Ueda, A.; et al. Major ions, $\delta^{18}O$, $\delta^{13}C$ and $^{87}Sr/^{86}Sr$ compositions of water and precipitates from springs along the Cameroon volcanic line (Cameroon, west Africa): Implications for provenance and volcanic hazards. *J. Afr. Earth Sci.* **2019**, *150*, 12–22. [CrossRef]
43. Song, H.W.; Meng, Y.C.; Jiang, F.T.; Li, L.X.; Li, Y.Q.; Du, C.H. Isotope characteristics of surface water and groundwater in the middle reaches of Yarlung Zangbo river and their indicators. *J. Arid Land Resour. Environ.* **2021**, *35*, 122–128. (In Chinese and English Abstract)
44. Craig, H. Isotopic variations in meteoric waters. *Science* **1961**, *133*, 1702–1703. [CrossRef]
45. Adimalla, N. Application of the Entropy Weighted Water Quality Index (EWQI) and the Pollution Index of Groundwater (PIG) to Assess Groundwater Quality for Drinking Purposes: A Case Study in a Rural Area of Telangana State, India. *Arch. Environ. Contam. Toxicol.* **2021**, *80*, 31–40. [CrossRef]

46. Amiri, V.; Rezaei, M.; Sohrabi, N. Groundwater quality assessment using entropy weighted water quality index (EWQI) in Lenjanat, Iran. *Environ. Earth Sci.* **2014**, *72*, 3479–3490. [CrossRef]
47. Unigwe, C.O.; Egbueri, J.C. Drinking water quality assessment based on statistical analysis and three water quality indices (MWQI, IWQI and EWQI): A case study. *Environ. Dev. Sustain.* **2022**, 1–22. [CrossRef]
48. Zhang, Y.; Dai, Y.; Wang, Y.; Huang, X.; Xiao, Y.; Pei, Q. Hydrochemistry, quality and potential health risk appraisal of nitrate enriched groundwater in the Nanchong area, southwestern China. *Sci. Total Environ.* **2021**, *784*, 147186. [CrossRef]

International Journal of
Environmental Research and Public Health

MDPI

Article

Performance and Enhancement of Various Fillers Guiding Vanadium (V) Bioremediation

Liting Hao *, Lin Li, Bangyan Wang, Xinli Wang, Jinkai Shi, Chen Shi and Xiaodi Hao *

Sino-Dutch R&D Centre for Future Wastewater Treatment Technologies/Key Laboratory of Urban Stormwater System and Water Environment, Beijing University of Civil Engineering and Architecture, Beijing 100044, China
* Correspondence: haoliting@bucea.edu.cn (L.H.); xdhao@hotmail.com (X.H.)

Abstract: Bioremediation of vanadium (V) pollution in groundwater is an emerging topic. However, knowledge of V in a biogeochemical process is limited and long-term effective removal methods are lacking. V(V) remediation processes by various kinds of auxiliary fillers (maifanite-1, maifanite-2, volcanic rock, green zeolite and ceramsite), agricultural biomass and microbial enhancing were explored in this study. In tests without inocula, the V(V) removal efficiencies of ceramsite (inert filler) and maifanite-2 (active filler) were 84.9% and 60.5%, respectively. When inoculated with anaerobic sludge, 99.9% of V(V) could be removed with the synergistic performance of straw and maifanite-2. TOC (Total Organic Carbon), trace elements and three-dimensional fluorescence analyses confirmed that maifanite-2 was the most suitable among various fillers in biological V(V) removal systems with straw. This study provides a collaborative method (adsorption–biology) by using straw with maifanite-2 in V(V)-contaminated groundwater. The knowledge gained in this study will help develop permeable reactive barrier technology to repair polluted groundwater to put forward a reasonable, effective and sustainable environmental treatment strategy.

Keywords: vanadium (V); fillers; straw; adsorption; bioremediation

1. Introduction

In modern industry, vanadium (V) is widely used in various fields, particularly in aerospace, steelmaking, chemical production and batteries [1]. It is estimated that the annual consumption of V will reach 130.1 kilotons by 2024 [2]. V mining, fossil fuel smelting and product manufacturing have caused heavy V pollution [3]. V concentration of the fly ash pits was reported to be as high as 58.6 mg/L [4]. People who took 4.5–18 mg V/d for 6–10 weeks suffered from green tongue, spasms and diarrhea, and even harmed to nerve tissues [5,6]. Therefore, V contamination is in urgent need of treatment.

In recent years, one reliable approach to V pollution has been the adsorption, and researchers have primarily focused on low-cost adsorbents, such as agricultural by-products and industrial wastes [7–9]. Corn straw, wheat straw and so on have been widely used as low-cost adsorbents [10,11]. Volcanic rocks have good physical properties such as great porosity and specific surface areas, which make them excellent adsorbents [12]. Zeolite and ceramsite have good adsorption and ion exchange capacities [13].

Furthermore, numerous microbes could reduce V(V) to V(IV) to reduce its toxicity. The toxicity of V increases with its valence and solubility, and V(V) is the most toxic [14]. Heterotrophic microorganisms with organic and inorganic substances as electron donors have attracted the interest of scholars. Organic electron donors such as straw and sawdust and inorganic electron donors such as H_2, S (0), Fe (0) and FeS were proved to be effective in microbial V(V) reduction [15–19]. The aggregation of heterotrophic bacteria in volcanic pores can adequately degrade and utilize COD, which is conducive to the growth of microorganisms [20]. It has been reported that maifanite can provide trace elements that are a part of the microbial enzyme system. Studies have shown that coenzymes and

cofactors of anaerobes are highly dependent on the existence of trace elements (Fe, Mo and Ni) [21]. Adding trace element Fe can improve the enzyme activity of anaerobic digestion, promoting the growth of anaerobic-activated sludge [22]. Moreover, trace elements elevate the enzyme reaction related to the degradation of COD and accelerate the biochemical reaction of microorganisms so as to promote metabolism and enhance the microbial reduction of V(V) [12,23].

There are several methods used for the treatment of V, and each method has several advantages and disadvantages. To find a more efficient, pollution-free and economic way, the adsorptive and biological combined removal using several auxiliary filters (maifanite-1, maifanite-2, volcanic rock, green zeolite and ceramsite) was investigated. Microbial-enhanced adsorptive removal of V(V) was carried out in this work. The best V(V) removal performance was revealed by the analysis of the whole combined process. The effect of various kinds of auxiliary fillers on the V(V) bio-reduction process was explored. The results obtained in this study can contribute to the effective bioremediation of a V(V)-contaminated environment.

2. Methods and Materials

2.1. Preparation of Materials

Maifanite-1, maifanite-2, black volcanics, green zeolite and ceramsite came from Linyi of Shandong Province, Dengfeng of Henan Province, Zhangjiakou of Hebei Province, Weixian of Shandong Province and Zhengzhou of Henan Province (China), respectively. In total, 1–3 mm straw and 3–5 mm fillers were screened, rinsed with tap water and deionized water (3 times), then put into the 40 °C oven. Serum bottles, rubber stoppers, aluminum caps, beakers, tweezers and volumetric bottles were washed with deionized water. The materials above along with centrifugal tubes and 0.45 μm filter membranes were disinfected by UV (4 h) prior to use.

2.2. Experimental Procedure

In order to determine the synergetic effect with fillers, straw addition and microbial addition were considered in the two tests. Batch experimental reactors and the specific experimental settings are shown in Figure S1 and Table 1, respectively. There were 6 groups with a total of 12 serum bottles in Test 1. In total, 250 mL actual groundwater in Beijing with $NaVO_3$ (75 mg/L V(V)) and 2.5 g straw were added to each reactor. Then, 10 g prepared fillers (maifanite-1, maifanite-2, black volcanics, green zeolite and ceramsite) were added to reactors, labeled MF-1, MF-2, BV, GZ, CM. The blank group was set up without fillers. All reactors were put in the dark (35 ± 2 °C).

Table 1. Experimental settings.

	Group	Straw (g)	Filler (10 g)	Sludge (mL)	Initial V(V) Concentration (mg/L)
Test 1	MF-1	2.5	Maifanite-1	0	75
	MF-2	2.5	Maifanite-2	0	75
	BV	2.5	Black volcanics	0	75
	GZ	2.5	Green zeolite	0	75
	CM	2.5	Ceramsite	0	75
	blank	2.5	blank	0	75
Test 2	MF-1-S	2.5	Maifanite-1	12.5	75
	MF-2-S	2.5	Maifanite-2	12.5	75
	BV-S	2.5	Black volcanics	12.5	75

To enhance the V(V) bio-reduction process, sludge was added in Test 2 (3 groups, 6 serum bottles) as inocula. Sludge was taken from the secondary sedimentation tank of Beijing Gaobeidian sewage treatment plant and domesticated (3 months) by refreshing the fresh nutrient solution once every 3 d. Nutrient solution contained the following components (per liter): NH_4Cl (0.1557 g), $CaCl_2$ (0.2464 g), $MgCl_2 \cdot 6H_2O$ (1.0572 g), NaCl (0.4459 g),

KCl (0.0283 g), $NaHCO_3$ (0.8082 g), KH_2PO_4 (0.0299 g), $C_6H_{12}O_6$ (0.7500 g) and $NaVO_3$ (0.1795 g). Sludge was centrifuged 30 min (3000× *g*) with supernatant skimmed, and the precipitated part was transferred to reactors (maifanite-1, maifanite-2 or black volcanics). Next, 250 mL actual groundwater in Beijing with $NaVO_3$ (75 mg/L V(V)), 2.5 g straw and 10 g prepared fillers were also added, the same as Test 1, labeled MF-1-S, MF-2-S, BV-S. The whole experimental period was 168 h with the sampling time every 24 h. After passing through the 0.45 μm membrane, liquid samples were refrigerated at 4 °C for further analysis. The information of chemical reagents and instruments used in this study are shown in the Table S1.

2.3. Analysis Methods

Aqueous samples were filtered using 0.45 μm membrane before analysis. V(V) existence was analyzed by spectrophotometry. 2-(5-bromo-2-pyridylazo)-5-diethylaminophenol (5-Br-PADAP) was used as a chelating agent for determining V(V) at 601 nm [18]. The total V and microelement in the solution were determined by ICP-OES (ICAP7200, Thermo Fisher Scientific, Waltham, MA, USA). TOC was analyzed by TOC analyzer (vario TOC cube, DKSH, Zürich, Switzerland). The pH level was monitored by using a pH meter. The three-dimensional fluorescence excitation emission matrix (EEM) quantified the changes in different areas of DOM (dissolved organic matter). The total microorganisms' count was determined using 3 M Petrifilm™ (6406, Saint Paul, MN, USA).

The V(V) removal efficiency (*RE*) was calculated by Equation (1).

$$RE = \frac{C_0 - C_e}{C_0} \times 100\% \quad (1)$$

C_0: the initial concentration (mg/L); C_e: the final concentration (mg/L).

3. Results and Discussion

3.1. Effect of Different Fillers on V(V) Removal Process

In the tests without inocula, V(V) decreased continuously in all groups. It was the most obvious in Group CM (ceramsite), and V(V) removal was the fastest from beginning to end, with its efficiency as high as 84.9% in 168 h. V(V) removal efficiency was 66.0% in Group GZ (green zeolite). The removal efficiency of V(V) in Group MF-2 (maifanite-2) was about 60.5% (168 h), and that in Group MF-1 (maifanite-1) and Group BV (black volcanics) were about 52.1% and 53.4% (Figure 1a). TOC in each group was stable for a short time after the rapid accumulation on the first day and then decreased slightly, then gradually increased after 72 h (Figure 2). This might be owing to the straw continuing to dissolve out of carbon and into the liquid. TOC increased at the beginning. Subsequently, microbial growth and V(V) reduction by using carbon might be faster than that of straw dissolution. TOC concentration in the liquid samples decreased slightly. Then, microbes were resistant to the toxicity of the external environment, and probably did not urgently reduce the toxicity. Thus, the amount of carbon dissolved was greater than that utilized by microorganisms at this stage. TOC in almost all groups was higher than that in the blank group at 144 h. This might be owing to auxiliary fillers enhancing carbon dissolution. In the Group CM, TOC at the endpoint was 434.1 mg/L. The status of the higher TOC concentration in liquid samples (Group CM) might be reflected by the large number of organic substrates dissolving from straw with fewer being consumed microbiologically.

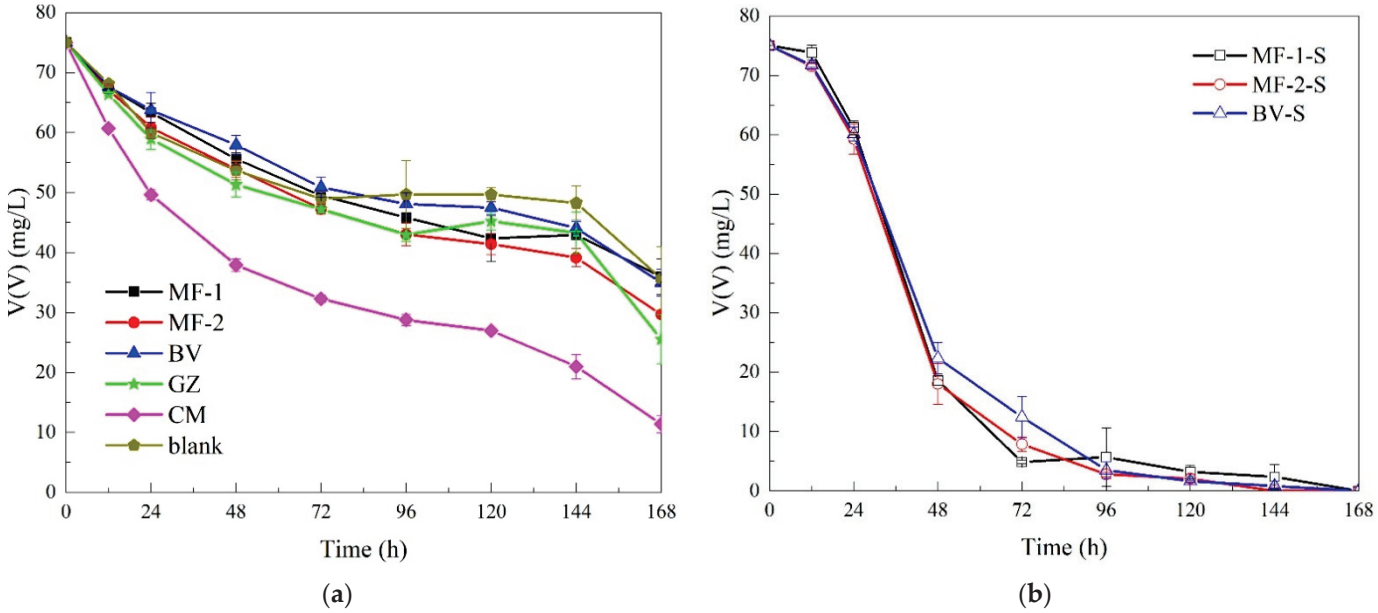

Figure 1. (**a**) V(V) removal by straw and various fillers (Group MF-1, MF-2, BV, GZ, CM and blank); (**b**) enhanced by additional inocula (Group MF-1-S, MF-2-S and BV-S).

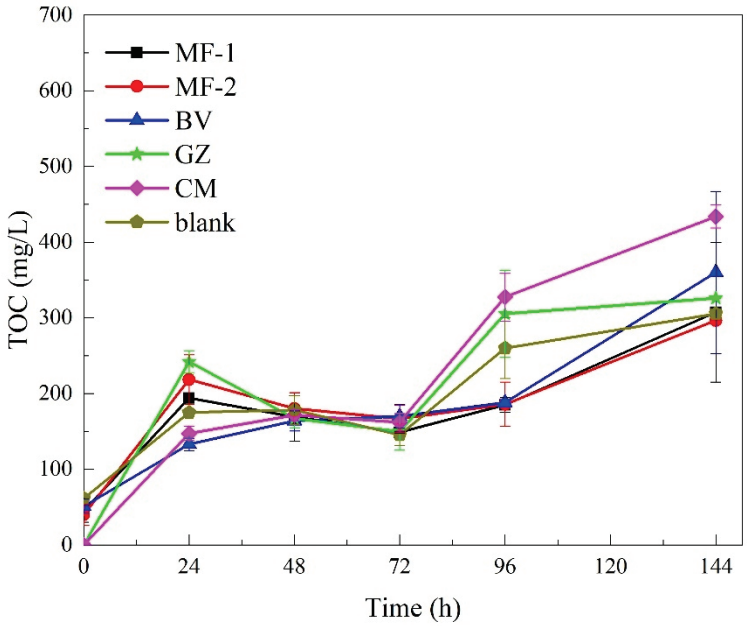

Figure 2. TOC during V(V) removal processes by straw and various fillers (Group MF-1, MF-2, BV, GZ, CM and blank).

From EEM results, it could be seen that the soluble microbial products (IV zone) of all kinds of fillers showed an upward trend (Table 2). It showed that there were indigenous microorganisms in the straw. However, the humus-like substance (V zone) showed a certain difference. It increased slowly in the reactors with maifanite and black volcanics (Group MF-1, MF-2, BV), while it clearly decreased with green zeolite and ceramsite (Group GZ, CM). Maifanite and black volcanics as active fillers cooperated with in situ microorganisms to hydrolyze straw, and the strength of humus-like substances (V zone) increased. Similar reports were reported in previous studies, such as the strong affinity and adhesion of black volcanics to biofilms [20]. Heterotrophic bacteria were proven to make fuller use of substrates to complete the enrichment process in volcanic pores [12]. In comparison, green

zeolite and ceramsite had good adsorption properties as inert fillers. V(V) pollutants in the solution and humus-like substances could be adsorbed, so the strength of the V zone decreased slowly.

Table 2. Three-dimensional fluorescence graph at 0, 72 and 168 h.

Group \ Time	0 h	72 h	168 h
MF-1-S	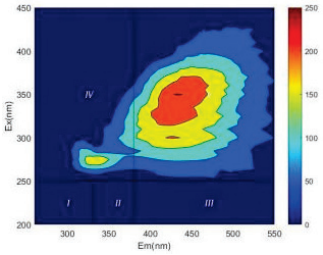	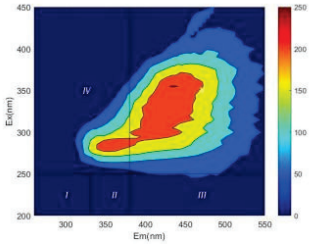	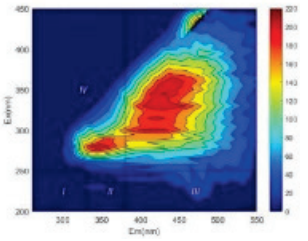
MF-1	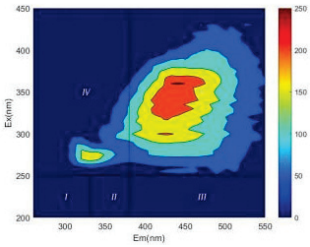	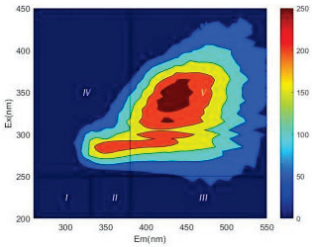	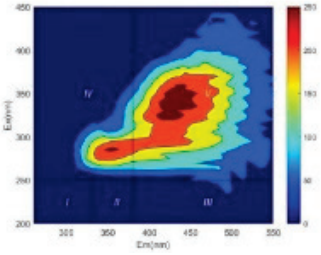
MF-2-S	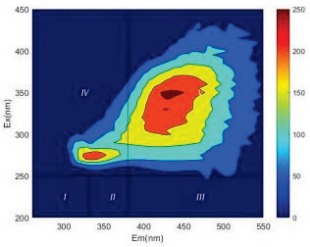	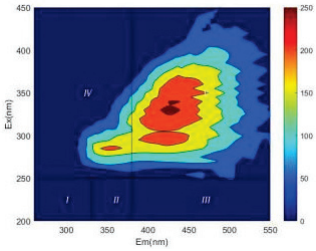	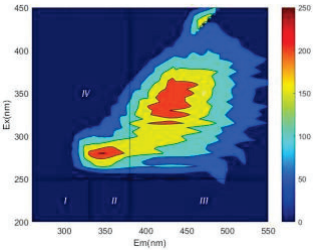
MF-2	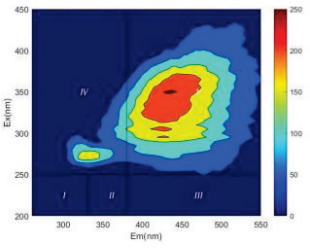	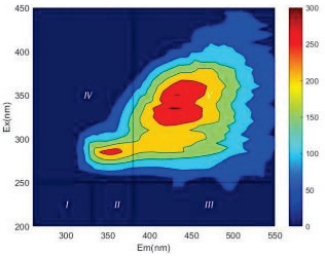	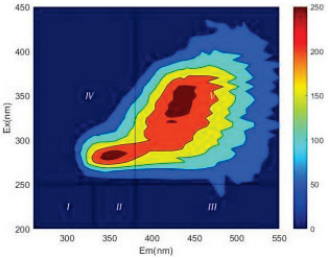
BV-S	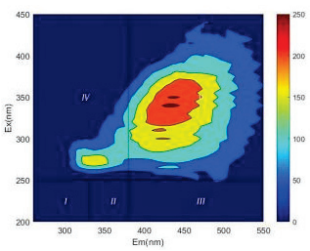	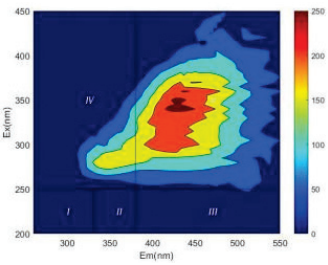	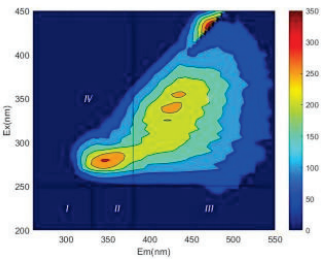

Table 2. *Cont.*

Group \ Time	0 h	72 h	168 h
BV	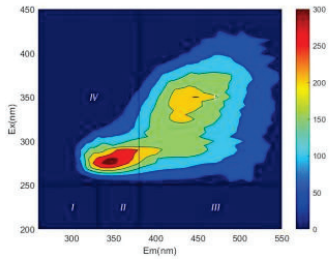	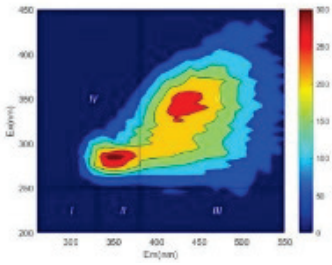	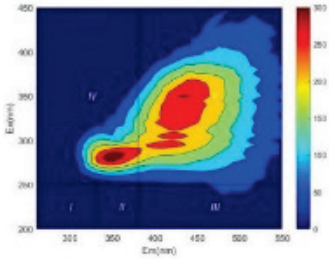
GZ	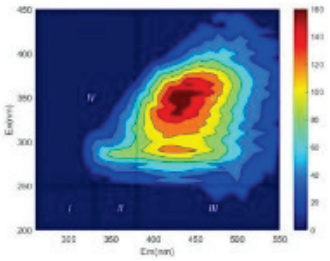	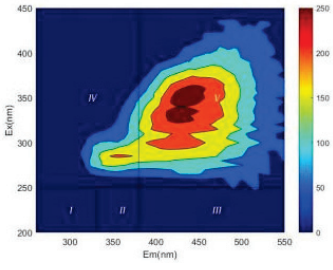	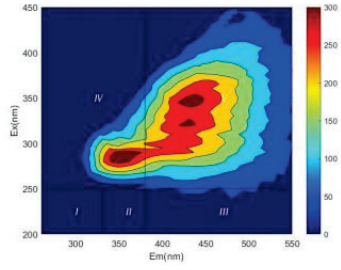
CM	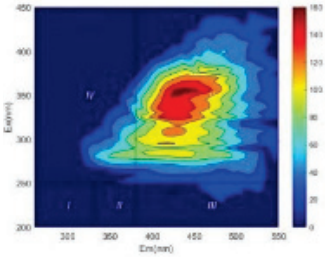	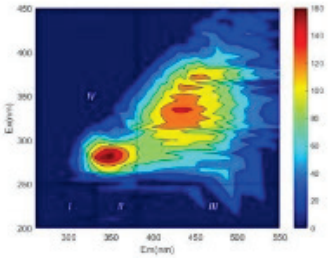	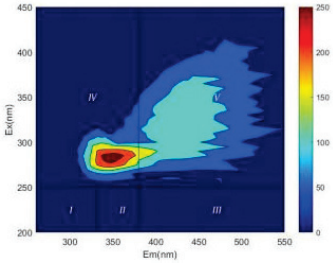
Blank	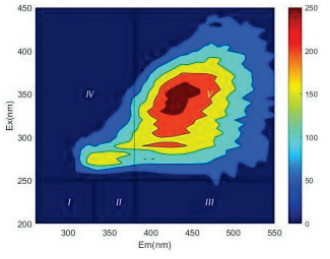	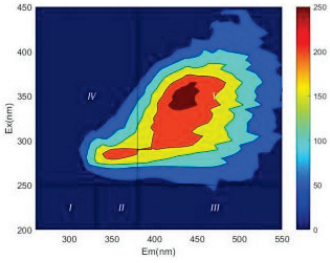	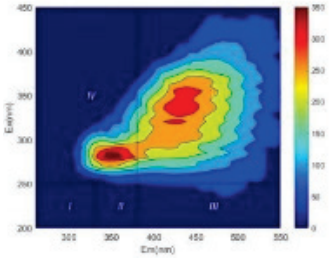

3.2. Synergism between Various Fillers and Microbes

Among the three kinds of fillers inoculated with domesticated sludge, V(V) removal in Group MF-2-S was the most significant (>99.9%, 144 h), while those in Group MF-1-S and Group BV-S reached more than 99.9% by 168 h (Figure 1b). Tests with operation conditions and performance results in this study and previous studies are shown in Table S2. The 3 M test results showed that different fillers combined with a solid carbon source had a significant enrichment effect on microbes (from 10^5 to 10^6). At the same time, the filler had a more pronounced enrichment effect on the primordial microbes. Compared with the original microbes, domesticated microbes need adapt to the conditions of using macromolecular carbon sources (lignin, cellulose and so on). The number of colonies in Groups MF-1-S and MF-2-S with maifanite were consistent with better removal of V(V) performance, especially with maifanite-2 (Table 3). The micropore sponge structure of maifanite could increase the activity of microorganisms [24,25]; moreover, its amendment was adequate to buffer the pH to improve the microbial living environment [26]. These two reasons might further enhance the V(V) bio-reduction. In addition, maifanite could

promote the degradation of organic matter and enhance the immobilization of heavy metals [26]. Furthermore, the dissolution of elements such as calcium and zinc from maifanite could be helpful for mineralization [27]. Oxides and calcium carbonates might cause precipitation reactions to fix heavy metals [28].

Table 3. Total number of bacteria analyzed by 3M.

Group	0 h ($\times 10^5$)	168 h ($\times 10^6$)
MF-1-S	1.5	6.7
MF-1	0	8.7
MF-2-S	1.5	8.6
MF-1	0	8.9
BV-S	1.5	6.1
BV	0	5.7

Three-dimensional fluorescence detection showed that maifanite and black volcanics significantly enhanced the microbial activity in reactors with sludge. It was shown that the addition of maifanite could increase the humic-like substances [29], the main substance produced by hydrolysis and the dissolution of straw. Humus could promote electron transfer in the system [30]. For example, dissolved humus used as an electron shuttle promoted the reduction of Fe (III) in the sediment [31,32]. Humus transferred electrons from the bacteria to the oxide surface and enhanced extracellular electron conduction, significantly accelerating the microbial reduction of iron oxide and metal ions [33,34]. Meanwhile, it was used as a recyclable electron shuttle to accelerate the redox process in the redox treatment of pollutants [30]. Hydroxyl in humus could provide electrons with the ability to reduce heavy metals, and the reaction rate is closely related to the pH of the reaction system [35]. In acidic conditions, the reduced V(IV) bound to oxygen-supplying atoms on the carboxylic acid site of humic acid [36]. V(IV) formed a stable complex with humic acid [37]. It was speculated that humus-like substances accelerated the electron transfer in the process of V(V) reduction and helped to maintain the stable state after V(V) reduction.

The intensities (I and II regions) of all groups constantly changed during the test, which may come from the hydrolysis of straw and the degradation of substances in the V region [38,39]. The intensity of soluble microbial products (IV region) in the early stage (0 h) of Groups MF-1-S, MF-2-S and BV-S was more obvious (Table 2). The soluble microbial by-product in the IV region was related to cellular substances and their secretions and showed the microbial activity [40]. Tryptophan-like substances in dissolved organic matter can bind to heavy metals [41]. Therefore, it was speculated that tryptophan produced in the biological system complexed with V(V), which may be the potential mechanism of V(V) removal in this study. In the meantime, soluble microbial products contained hydroxyl, carboxyl and other functional groups helpful for microbial V(V) bio-reduction [42].

In addition to carbon, trace elements played a crucial role in the growth and metabolism of anaerobic microorganisms [43]. Trace elements were commonly parts of the cofactors in the enzyme system, and were vital to the enzyme system [21]. The coenzymes and cofactors of anaerobes were highly dependent on the existence of these metals (Ni, Fe and Mo) [21]. Trace elements often existed in some reductase, such as F420-reductase containing Fe and Ni in the reductive pathway from CO_2 to CH_4 [44]. In this study, the trace elements in the initial V contamination solution were detected. Fe and Mo were below the detection limit in the initial solution. Mo and Fe in the liquid samples were also determined at the end of the experiment. A higher Fe concentration (42–73 mg/L) was detected in all the experimental groups inoculated with sludge and the Mo concentration was 0.4–7.1 mg/L (Figure 3). The addition of inocula accelerated the dissolution of trace element Fe from maifanite. Fe was reported to improve the microbial enzyme activity of the anaerobic digestion of agricultural and forestry wastes [45]. It was speculated that the presence of microorganisms promoted the dissolution process of trace elements. It was also reported that maifanite could extract

cations such as Fe and Mg [46]. Biofilm could use trace elements (such as Fe) as growth sources [46]. In the dissolution tests, all the experimental groups (MF-1-S, MF-2-S and BV-S) had a certain amount of Mo. Mo was an element in the cofactor of nitrate reductase [47].

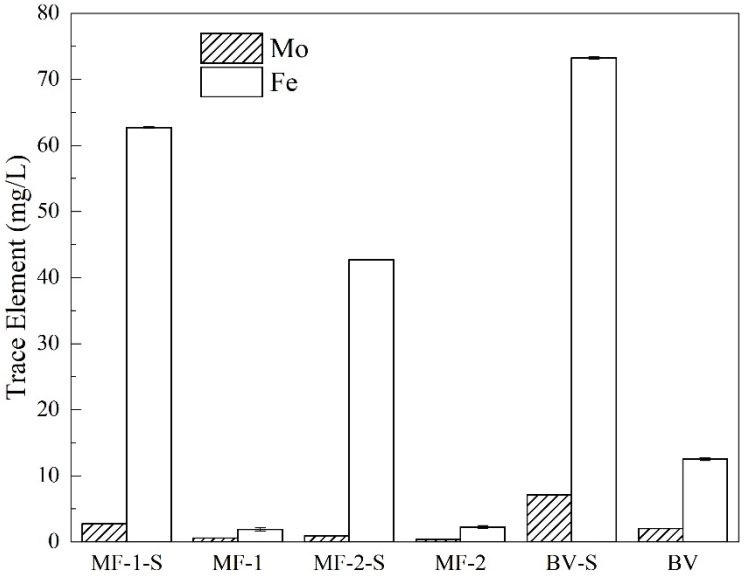

Figure 3. Trace elements' concentration (Mo and Fe) in Groups MF-1, MF-1-S, MF-2, MF-2-S, BV and BV-S.

Trace elements played an essential role in improving the stable operation of the anaerobic reactor [22]. The addition of trace elements such as Fe, Mo and Ni can accelerate the transformation rate of the substrate [23], thus enhancing the reduction efficiency of V(V). The detection of trace elements in this experiment showed that maifanite and black volcanics can continuously dissolve a certain amount of trace elements with microbes in reactors. The dissolution of Fe and Mo from black volcanics was more than that from maifanite. However, in the macro reaction system, trace elements were accompanied by the dynamic process of dissolution–consumption. To some extent, it might be reflected in the low utilization efficiency in the black volcanics group. It may be one of the reasons that its V(V) removal performance was worse than that with maifanite.

3.3. Geochemical and Environmental Implications

Maifanite and black volcanics used in this study are widely distributed and are low-cost materials. The physical and chemical properties of the above materials produced by various producing areas and mining methods are different. Active auxiliary fillers combined with straw have been shown to enable VRB (Vanadium Reducing Bacteria) in the reactors to make good use of the dissolved substrate and trace elements as nutrients. In the early stages, there was a certain intensity about the soluble microbial products (IV zone). VRB quickly adapted to the high V(V) concentration environment in inocula and removed V(V) pollutants rapidly and stably. In addition, the adsorption of straw and fillers, and the participation by in situ microbes cannot be ignored. Even with the lack of enhanced VRB, V(V) removal efficiency still reached more than 50%. This was also shown by the 3 M results. Although the high concentration of V(V) was obviously toxic to organisms, it had an obvious enrichment effect for microbes with the supplement of straw and fillers. To some extent, Group MF-2-S, with the best enrichment effect, showed the best V(V) remediation performance. Thus, V(V) bio-reduction was enhanced by auxiliary fillers, and maifanite-2 was the most suitable filler for the straw biological V(V) removal system in the study. It has significant implications for the remediation of V(V) contaminated groundwater.

4. Conclusions

Based on the current concept of treating pollution by using waste material, this study further studied the effect of auxiliary fillers (active fillers and inert fillers) along with agricultural wastes on V pollution. The effect of additional fillers was explored on the microbial V(V) removal system using straw as a carbon source. Inert fillers such as ceramsite had better V(V) adsorption performance (>84.9%). Fillers also showed significant adsorption to various complex carbon sources dissolved from straw. Group MF-2-S (maifanite-2 + straw + sludge) achieved the best V(V) removal performance (>99.9%, 144 h) in the study by the collaborative method (adsorption–biology). The results confirmed that maifanite and other active fillers could enrich a large number of microbes coordinating with straw, and could continuously dissolve a certain amount of trace elements (Mo and Fe) during inocula-enhanced processes. This study improves the efficient, low-cost and long-term technical support for the treatment of V contamination in groundwater.

Supplementary Materials: The following supporting information can be downloaded at: https://www.mdpi.com/article/10.3390/ijerph192214926/s1. Table S1: (a): Information of main chemical reagents used in the study; (b): The main instruments used in the study; Table S2: Tests with operation conditions and performance results in this study and previous studies; Figure S1: The experimental reactors. References [48–52] are cited in supplementary materials.

Author Contributions: Conceptualization, L.H. and B.W.; methodology, B.W.; software, B.W. and L.L.; validation, X.W. and J.S.; formal analysis, B.W. and L.L.; investigation, B.W. and L.L.; resources, L.H. and X.H.; data curation, L.L.; writing—original draft preparation, L.L.; writing—review and editing, L.H., C.S. and X.H.; visualization, L.L.; supervision, L.H. and X.H.; project administration, L.H.; funding acquisition, L.H. and C.S. All authors have read and agreed to the published version of the manuscript.

Funding: This research work was supported by the National Natural Science Foundation of China (NSFC) (No. 51908021), R&D Program of Beijing Municipal Education Commission (No. KM202210016006), BUCEA Pyramid Talent Training Project (No. JDYC20220816), BUCEA Scientific Research Ability Improvement Program for Young Teachers (No. X21015) and BUCEA Post Graduate Innovation Project (No. PG2022068).

Institutional Review Board Statement: Not applicable.

Informed Consent Statement: Not applicable.

Data Availability Statement: The data presented in this study are available on request from the corresponding author. The data are not publicly available due to privacy.

Conflicts of Interest: The authors declare no conflict of interest.

References

1. Imtiaz, M.; Rizwan, M.S.; Xiong, S.; Li, H.; Ashraf, M.; Shahzad, S.M.; Shahzad, M.; Rizwan, M.; Tu, S. Vanadium, recent advancements and research prospects: A review. *Environ. Int.* **2015**, *80*, 79–88. [CrossRef] [PubMed]
2. Lee, J.; Kim, E.; Chung, K.W.; Kim, R.; Jeon, H.S. A review on the metallurgical recycling of vanadium from slags: Towards a sustainable vanadium production. *J. Mater. Res. Technol.* **2021**, *12*, 343–364. [CrossRef]
3. Burke, I.T.; Peacock, C.L.; Lockwood, C.L.; Stewart, D.I.; Mortimer, R.J.; Ward, M.B.; Renforth, P.; Gruiz, K.; Mayes, W.M. Behavior of aluminum, arsenic, and vanadium during the neutralization of red mud leachate by HCl, gypsum, or seawater. *Environ. Sci. Technol.* **2013**, *47*, 6527–6535. [CrossRef] [PubMed]
4. Jia, L.; Anthony, E.J.; Charland, J.P. Investigation of vanadium compounds in ashes from a CFBC firing 100 petroleum coke. *Energy Fuels* **2002**, *16*, 397–403. [CrossRef]
5. Anke, M. Vanadium-an element both essential and toxic to plants, animals and humans. *Anal. Real Acad. Nac. Farm.* **2004**, *70*, 961–999.
6. Cooper, R.G. Vanadium pentoxide inhalation. *Indian J. Occup. Environ. Med.* **2007**, *11*, 97. [CrossRef]
7. Gogoi, H.; Zhang, R.; Matusik, J.; Leiviskä, T.; Rämö, J.; Tanskanen, J. Vanadium removal by cationized sawdust produced through iodomethane quaternization of triethanolamine grafted raw material. *Chemosphere* **2021**, *278*, 130445. [CrossRef]
8. He, W.; Liao, W.; Yang, J.; Jeyakumar, P.; Anderson, C. Removal of vanadium from aquatic environment using phosphoric acid modified rice straw. *Bioremediat. J.* **2020**, *24*, 80–89. [CrossRef]

9. Zhang, R.; Leiviskä, T.; Tanskanen, J.; Gao, B.; Yue, Q. Utilization of ferric groundwater treatment residuals for inorganic-organic hybrid biosorbent preparation and its use for vanadium removal. *Chem. Eng. J.* **2019**, *361*, 680–689. [CrossRef]
10. Hu, Y.; Liu, T.; Chen, N.; Feng, C.; Lu, W.; Guo, H. Simultaneous bio-reduction of nitrate and Cr(VI) by mechanical milling activated corn straw. *J. Hazard. Mater.* **2022**, *429*, 128258. [CrossRef]
11. Hao, L.; He, Y.; Shi, C.; Hao, X. Performance and mechanisms for V(V) bio-reduction by straw: Key influencing factors. *RSC Adv.* **2021**, *11*, 27246–27256. [CrossRef] [PubMed]
12. Deng, J.; Zhou, R.; Shan, X.; Ruan, W. Biomass Substrate Carrying Bacteria for Treatment of Micro-polluted River Water. *China Water Wastewater* **2021**, *37*, 8.
13. Wu, H.; Fan, J.; Zhang, J.; Ngo, H.H.; Guo, W.; Liang, S.; Lv, J.; Lu, S.; Wu, W.; Wu, S. Intensified organics and nitrogen removal in the intermittent-aerated constructed wetland using a novel sludge-ceramsite as substrate. *Bioresour. Technol.* **2016**, *210*, 101–107. [CrossRef] [PubMed]
14. Yang, J.; Wang, M.; Jia, Y.; Gou, M.; Zeyer, J. Toxicity of vanadium in soil on soybean at different growth stages. *Environ. Pollut.* **2017**, *231*, 48–58. [CrossRef]
15. Hao, L.; He, Y.; Shi, C.; Hao, X. Biologically removing vanadium(V) from groundwater by agricultural biomass. *J. Environ. Manag.* **2021**, *296*, 113244. [CrossRef]
16. Hao, L.; Liu, Y.; Chen, N.; Hao, X.; Zhang, B.; Feng, C. Microbial removal of vanadium(V) from groundwater by sawdust used as a sole carbon source. *Sci. Total Environ.* **2021**, *751*, 142161. [CrossRef]
17. Xu, X.; Xia, S.; Zhou, L.; Zhang, Z.; Rittmann, B.E. Bioreduction of vanadium(V) in groundwater by autohydrogentrophic bacteria: Mechanisms and microorganisms. *J. Environ. Sci.* **2015**, *30*, 122–128. [CrossRef]
18. Zhang, B.; Qiu, R.; Lu, L.; Chen, X.; He, C.; Lu, J.; Ren, Z. Autotrophic vanadium(V) bioreduction in groundwater by elemental sulfur and zerovalent iron. *Environ. Sci. Technol.* **2018**, *52*, 7434–7442. [CrossRef]
19. He, C.; Zhang, B.; Lu, J.; Qiu, R. A newly discovered function of nitrate reductase in chemoautotrophic vanadate transformation by natural mackinawite in aquifer. *Water Res.* **2021**, *189*, 116664. [CrossRef]
20. Hao, X.; Wei, L.; Qiu, F. Experimental study on enhancing nitrogen removal by effluent recirculation in a BAF reactor with crushed lava packed as carriers. *Chin. J. Environ. Eng.* **2009**, *3*, 239–245.
21. Zandvoort, M.H.; Hullebusch, E.D.; Fermoso, F.G.; Lens, P.N.L. Trace metals in anaerobic granular sludge reactors: Bioavailability and dosing strategies. *Eng. Life Sci.* **2006**, *6*, 293–301. [CrossRef]
22. Zhang, W.; Wu, S.; Guo, J.; Zhou, J.; Dong, R. Performance and kinetic evaluation of semi-continuously fed anaerobic digesters treating food waste: Role of trace elements. *Bioresour. Technol.* **2015**, *178*, 297–305. [CrossRef] [PubMed]
23. Cai, Y.; Hua, B.; Gao, L.; Hu, Y.; Yuan, X.; Cui, Z.; Zhu, W.; Wang, X. Effects of adding trace elements on rice straw anaerobic mono-digestion: Focus on changes in microbial communities using high-throughput sequencing. *Bioresour. Technol.* **2017**, *239*, 454–463. [CrossRef] [PubMed]
24. Awasthi, M.K.; Wang, Q.; Awasthi, S.K.; Wang, M.; Chen, H.; Ren, X.; Zhao, J.; Zhang, Z. Influence of medical stone amendment on gaseous emissions, microbial biomass and abundance of ammonia oxidizing bacteria genes during biosolids composting. *Bioresour. Technol.* **2018**, *247*, 970–979. [CrossRef] [PubMed]
25. Yan, X.; Wang, B.; Zhang, J. Liquefaction of cotton seed in sub-critical water/ethanol with modified medical stone for bio-oil. *Bioresour. Technol.* **2015**, *197*, 120–127. [CrossRef] [PubMed]
26. Wang, Q.; Wang, Z.; Awasthi, M.K.; Jiang, Y.; Li, R.; Ren, X.; Zhao, J.; Shen, F.; Wang, M.; Zhang, Z. Evaluation of medical stone amendment for the reduction of nitrogen loss and bioavailability of heavy metals during pig manure composting. *Bioresour. Technol.* **2016**, *220*, 297–304. [CrossRef]
27. Li, R.; Liu, J.; Li, Y.; Cao, S.; Chen, G. Review on the Application Effects of 'Medica' Healthy-stone in Hunan Province. *Hunan Agric. Sci.* **2007**, 120–122.
28. Giagnoni, L.; Borges, L.G.; Giongo, A.; Silveira, A.; Ardissone, A.N.; Triplett, E.W.; Mench, M.; Renella, G. Dolomite and compost amendments enhance cu phytostabilization and increase microbiota of the leachates from a cu-contaminated soil. *Agronomy* **2020**, *10*, 719. [CrossRef]
29. Wang, Q.; Awasthi, M.K.; Zhao, J.; Ren, X.; Wang, M.; Li, R.; Wang, Z.; Zhang, Z. Utilization of medical stone to improve the composition and quality of dissolved organic matter in composted pig manure. *J. Clean. Prod.* **2018**, *197*, 472–478. [CrossRef]
30. Yang, Z.; Du, M.; Jiang, J. Reducing capacities and redox potentials of humic substances extracted from sewage sludge. *Chemosphere* **2016**, *144*, 902–908. [CrossRef]
31. Lovley, D.R.; Coates, J.D.; Blunt-Harris, E.L.; Phillips, E.J.; Woodward, J.C. Humic substances as electron acceptors for microbial respiration. *Nature* **1996**, *382*, 445–448. [CrossRef]
32. Nevin, K.P.; Lovley, D.R. Potential for nonenzymatic reduction of Fe(III) via electron shuttling in subsurface sediments. *Environ. Sci. Technol.* **2000**, *34*, 2472–2478. [CrossRef]
33. Roden, E.E.; Kappler, A.; Bauer, I.; Jiang, J.; Paul, A.; Stoesser, R. Extracellular electron transfer through microbial reduction of solid-phase humic substances. *Nat. Geosci.* **2010**, *3*, 417–421. [CrossRef]
34. Zhou, S.; Chen, S.; Yuan, Y.; Lu, Q. Influence of humic acid complexation with metal ions on extracellular electron transfer activity. *Sci. Rep.* **2015**, *5*, 17067. [CrossRef]
35. Wittbrodt, P.R.; Palmer, C.D. Effect of temperature, ionic strength, background electrolytes, and Fe(III) on the reduction of hexavalent chromium by soil humic substances. *Environ. Sci. Technol.* **1996**, *30*, 2470–2477. [CrossRef]

36. Lu, X.; Johnson, W.D.; Hook, J. Reaction of vanadate with aquatic humic substances: An ESR and 51V NMR study. *Environ. Sci. Technol.* **1998**, *32*, 2257–2263. [CrossRef]
37. Ortiz-Bernad, I.; Anderson, R.T.; Vrionis, H.A.; Lovley, D.R. Vanadium respiration by Geobacter metallireducens: Novel strategy for in situ removal of vanadium from groundwater. *Appl. Environ. Microbiol.* **2004**, *70*, 3091–3095. [CrossRef] [PubMed]
38. Luo, K.; Yang, Q.; Li, X.; Chen, H.; Liu, X.; Yang, G.; Zeng, G. Novel insights into enzymatic-enhanced anaerobic digestion of waste activated sludge by three-dimensional excitation and emission matrix fluorescence spectroscopy. *Chemosphere* **2013**, *91*, 579–585. [CrossRef]
39. Wang, Y.; Zhang, J.; Sun, Y.; Yu, J.; Zheng, Z.; Li, S.; Cui, Z.; Hao, J.; Li, G. Effects of intermittent mixing mode on solid state anaerobic digestion of agricultural wastes. *Chemosphere* **2020**, *248*, 126055. [CrossRef]
40. Bridgeman, J.; Baker, A.; Marquet, C.C.; Carstea, E. Determination of changes in wastewater quality through a treatment works using fluorescence spectroscopy. *Environ. Technol.* **2013**, *34*, 3069–3077. [CrossRef]
41. Wu, J.; Zhang, H.; He, P.; Shao, L. Insight into the heavy metal binding potential of dissolved organic matter in MSW leachate using EEM quenching combined with PARAFAC analysis. *Water Res.* **2011**, *45*, 1711–1719. [CrossRef] [PubMed]
42. Liu, W.; Cheng, S.; Yin, L.; Sun, Y.; Yu, L. Influence of soluble microbial products on the long-term stability of air cathodes in microbial fuel cells. *Electrochim. Acta* **2018**, *261*, 557–564. [CrossRef]
43. Takashima, M.; Speece, R.E. Mineral nutrient requirements for high-rate methane fermentation of acetate at low SRT. *Res. J. Water Pollut. Control Fed.* **1989**, *61*, 1645–1650.
44. Michel, R.; Massanz, C.; Kostka, S.; Richter, M.; Fiebig, K. Biochemical Characterization of the 8-hydroxy-5-deazaflavin-reactive Hydrogenase from Methanosarcina barkeri Fusaro. *Eur. J. Biochem.* **1995**, *233*, 727–735. [CrossRef]
45. Khatri, S.; Wu, S.; Kizito, S.; Zhang, W.; Li, J.; Dong, R. Synergistic effect of alkaline pretreatment and Fe dosing on batch anaerobic digestion of maize straw. *Appl. Energy* **2015**, *158*, 55–64. [CrossRef]
46. Tsai, W.; Su, T.; Hsu, H.; Lin, K.; Lin, C.; Tai, T. Preparation of mesoporous solids by acid treatment of a porphyritic andesite (wheat–rice–stone). *Microporous Mesoporous Mater.* **2007**, *102*, 196–203. [CrossRef]
47. Jacques, J.G.; Burlat, B.; Arnoux, P.; Sabaty, M.; Guigliarelli, B.; Léger, C.; Pignol, D.; Fourmond, V. Kinetics of substrate inhibition of periplasmic nitrate reductase. *Biochim. Biophys. Acta-Bioenerg.* **2014**, *1837*, 1801–1809. [CrossRef]
48. Zhang, B.; Li, Y.; Fei, Y.; Cheng, Y. Novel pathway for vanadium (V) bio-detoxification by gram-positive *Lactococcus raffinolactis*. *Environ. Sci. Technol.* **2021**, *55*, 2121–2131. [CrossRef]
49. Wang, G.; Zhang, B.; Li, S.; Yang, M.; Yin, C. Simultaneous microbial reduction of vanadium (V) and chromium (VI) by Shewanella loihica PV-4. *Bioresour. Technol.* **2017**, *227*, 353–358. [CrossRef]
50. Shi, C.; Cui, Y.; Lu, J.; Zhang, B. Sulfur-based autotrophic biosystem for efficient vanadium (V) and chromium (VI) reductions in groundwater. *Chem. Eng. J.* **2020**, *395*, 124972. [CrossRef]
51. Ali, M.M.S.; Imam, D.M.; El-Nadi, Y.A. Vanadium (V) removal and recovery by adsorption onto modified activated carbon derived from natural hydroxyapatite. *J. Iran. Chem. Soc.* **2021**, *18*, 2771–2784. [CrossRef]
52. He, Q.; Si, S.; Zhao, J.; Yan, H.; Sun, B.; Cai, Q.; Yu, Y. Removal of vanadium from vanadium-containing wastewater by amino modified municipal sludge derived ceramic. *Saudi J. Biol. Sci.* **2018**, *25*, 1664–1669. [CrossRef] [PubMed]

remote sensing

MDPI

Article

Dynamics of Spatiotemporal Variation of Groundwater Arsenic Due to Salt-Leaching Irrigation and Saline-Alkali Land

Shuhui Yin [1,2,†], Yuan Tian [1,2,†], Linsheng Yang [1,2], Qiqian Wen [1,2] and Binggan Wei [1,2,*]

[1] Key Laboratory of Land Surface Pattern and Simulation, Institute of Geographic Sciences and Natural Resources Research, Chinese Academy of Sciences, Beijing 100101, China
[2] College of Resources and Environment, University of Chinese Academy of Sciences, Beijing 100049, China
* Correspondence: weibg@igsnrr.ac.cn; Tel.: +86-(0)-10-64856504
† These authors contributed equally to this work.

Abstract: Determining the link between the evolution of salt-leaching irrigation, saline-alkali land, and groundwater arsenic (As) is essential to prevent groundwater arsenic pollution and implement appropriate soil salinization control projects. The objectives of our study were to explore the spatiotemporal correlation of saline-alkali land and salt-leaching irrigation with groundwater As in the Hetao Plain. Therefore, groundwater As concentrations during Period I (2006–2010) and Period II (2016–2020) were collected by historical data and chemical measurements. Salt-leaching irrigation area and saline-alkali land area in Period I and Period II were extracted through remote sensing data. With the increase of the salt-leaching irrigation area level (SLIAL) and saline-alkali land area level (SALAL), the variation trend in groundwater As concentration slightly fluctuated, with an increase in the SLIAL at the low SALAL, which may be because short-term flooding may not considerably enhance As mobilization. Lower groundwater As concentrations appeared in regions with higher SLIAL and lower SALAL. A larger saline-alkali land area (higher SALAL) increased the groundwater As concentration. The path analysis model confirmed that salt-leaching irrigation may increase groundwater salinity to affect groundwater As levels and to decrease the saline-alkali land area. From Periods I to II, the difference in path analysis results may imply that the decrease in the saline-alkali land area may have influenced As mobilization due to competitive adsorption caused by the increase in total dissolved solids (TDS) in groundwater. Our results provide new insights for the impacts of saline-alkali land and salt-leaching irrigation both on groundwater As concentration and the geochemical processes of As enrichment in arid and semi-arid areas with more serious salinization.

Keywords: saline-alkali land; salt-leaching irrigation; groundwater; arsenic; spatiotemporal variation

1. Introduction

Soil salinization has become an urgent global environmental and socioeconomic issue, especially in arid and semi-arid areas [1]. Poor drainage may generate soil salinity problems because capillary action causes the rise of the water table to accumulate salts in the soil near the root zone of the plants in the agricultural irrigation system [2]. The Hetao Plain is a representative salinization-irrigated district that is affected by serious soil secondary salinization caused by inappropriate irrigation, poor drainage, and high groundwater levels [3–5]. Land use patterns, the texture, the structure, and the capacity of the soil can affect groundwater quality [6,7]. Urbanization affects the hardness of groundwater, where soft groundwater is characterized by agricultural areas and hard groundwater is characterized by a mineralized subsoil in the state of Morelos, Mexico [6]. Aquifers were susceptible to nitrate contamination in the area localized to most agricultural activity in Flamouria Basin in Northern Greece [7]. Saline-alkali land has markedly higher concentrations of total dissolved solids (TDS), Na^+, and HCO_3^- in groundwater than other land types in Shuangliao City, Northeast China [8]. In autumn, intensive flooding

irrigation is used to leach salt from the soil to maintain the soil salinity within a reasonable range in the Hetao Plain [3,5]. Intense short-term flood salt-leaching irrigation in autumn typically results in significant groundwater recharge, raising the water table [9]. Soil salts can be leached into groundwater or transferred to neighboring areas without irrigation due to significant lateral groundwater gradients [3]. Soil salt-leaching into groundwater led to an increase in the groundwater TDS content and enhanced groundwater salinization [5,10,11]. Moreover, salt-leaching irrigation in saline-alkali land elevates the concentrations of HCO_3^-, SO_4^{2-},Ca^{2+}, Na^+, and Cl^- in the groundwater [12]. In addition, the rise in the water table and TDS concentration in the groundwater also affects the distribution and evolution of saline-alkali land [3,5,13,14]. Thus, the salinization of groundwater and soil is interrelated. The distribution of saline-alkali land and salt-leaching irrigation may change the hydrogeochemical properties of groundwater. It is important that the relationship between irrigated soil quality and trace elements' concentration in the groundwater should be investigated in the agricultural irrigation area [15].

Chronic arsenic (As) exposure induces several types of cancer (e.g., lung and bladder cancer) [16], endothelial dysfunction [17], impairment of intestinal stromal cells [18], chronic kidney disease [19], hypertension, and skin lesions [20]. The World Health Organization (WHO) recommends 10 μg/L as the maximum permissible concentration of As in drinking water [21]. The Hetao Basin is a typical region with geologically high As (>10 μg/L) in groundwater, which has affected the public health of 300,000 people for decades [22–24]. In the Hetao Basin, the release of As into groundwater is usually influenced by the reductive dissolution of Fe(III) oxides through the degradation of organic matter and the oxidation of sulfide (H_2S), as well as As desorption caused by an increase in pH and the coexistence of anions, such as HCO_3^- and PO_4^{3-} [25]. Groundwater with high As concentrations is accompanied by low concentrations of NO_3^- and SO_4^{2-} and high concentrations of dissolved Fe, Mn, HCO_3^-, P, and S^{2-} in the shallow alluvial-lacustrine aquifers in the Hetao Basin [22]. The coexistence of high As and saline groundwater was observed in the Hetao Basin [24,26]. Salinization processes may influence the mobilization of As in groundwater [10,11,24]. This can be attributed to the simultaneous As enrichment and SO_4^{2-} reduction in the reductive aquifer when the TDS concentration is below 3000 mg/L [24]. The increase in salinity may promote flocculation of iron oxides, which can limit As enrichment in groundwater [10,27]. However, increasing the salinity and bicarbonate in groundwater can promote the release of As via competing adsorption in aquifers [28,29]. In general, salt-leaching irrigation can transfer soil salt into groundwater, which affects the distribution of saline-alkali land, the water table, the salinity, and related salt ion concentrations of groundwater [3,5,8]. Subsequently, the release of As into groundwater may be limited or promoted owing to the changes in the water table, the salinity, and related salt ion concentrations of groundwater [10,11,24]. Therefore, we assume that spatial and temporal distribution of As in groundwater may be associated with the distribution of saline-alkali land and salt-leaching irrigation. Exploring the effects of saline-alkali land and salt-leaching irrigation on groundwater As may be helpful to prevent groundwater arsenic pollution and to better implement appropriate soil salinization control projects.

Remote sensing satellite image data can easily characterize the macroscopic changes of the surface environment in a large geographical area, including land use (also includes evolution of wetlands and saline-alkali land), active faults, rivers, and vegetation types [8,30–34]. Correlatively, the impacts of wetland evolution, active faults, and the distance from the river on groundwater As concentration have been clearly explained [30–32]. Studies on soil salinization, salt-leaching irrigation, and groundwater chemistry have mostly focused on the microscopic scale, including the transport of soil salt ions between soil and groundwater due to salt-leaching irrigation and the distribution relationships of groundwater depth, salinity, and soil salt content [3,12,14,35]. However, these studies were mainly based on chemical experiments, and the effects of soil salinization and salt-leaching irrigation on groundwater chemistry at a larger scale cannot be economically and rapidly characterized. Our study explores fresh insight into the quantitative relationship between

the evolution of salt-leaching irrigation and saline-alkali land at the macroscopic scale based on remote sensing data with spatiotemporal variation of groundwater As in the Hetao Plain, which can be used at a larger geographical scale and even a global scale.

The objectives of this study were to: (1) characterize the spatiotemporal variation of groundwater As in shallow aquifers, (2) determine the spatiotemporal distribution of salt-leaching irrigation areas and saline-alkali land using remote sensing imagery, and (3) assess the quantitative relationship between salt-leaching irrigation, saline-alkali land, and groundwater As.

2. Materials and Methods

2.1. Geological and Hydrological Setting

The study area is the flat plain of the Hetao Basin, the Hetao Plain, which is located in the arid and semi-arid areas from the south of the Langshan Mountains, adjacent to the north of the Yellow River. The study area has a total area of 8949 km^2 from the east of the Ulanbuh Desert to the west of Wuliangsuhai Lake (excluding Ulanbuh Desert) (Figure 1). The average annual precipitation ranges from 130 to 220 mm, while the annual evaporation ranges from 2000 to 2500 mm [24]. The elevation is in the range of 1021–1100 m.

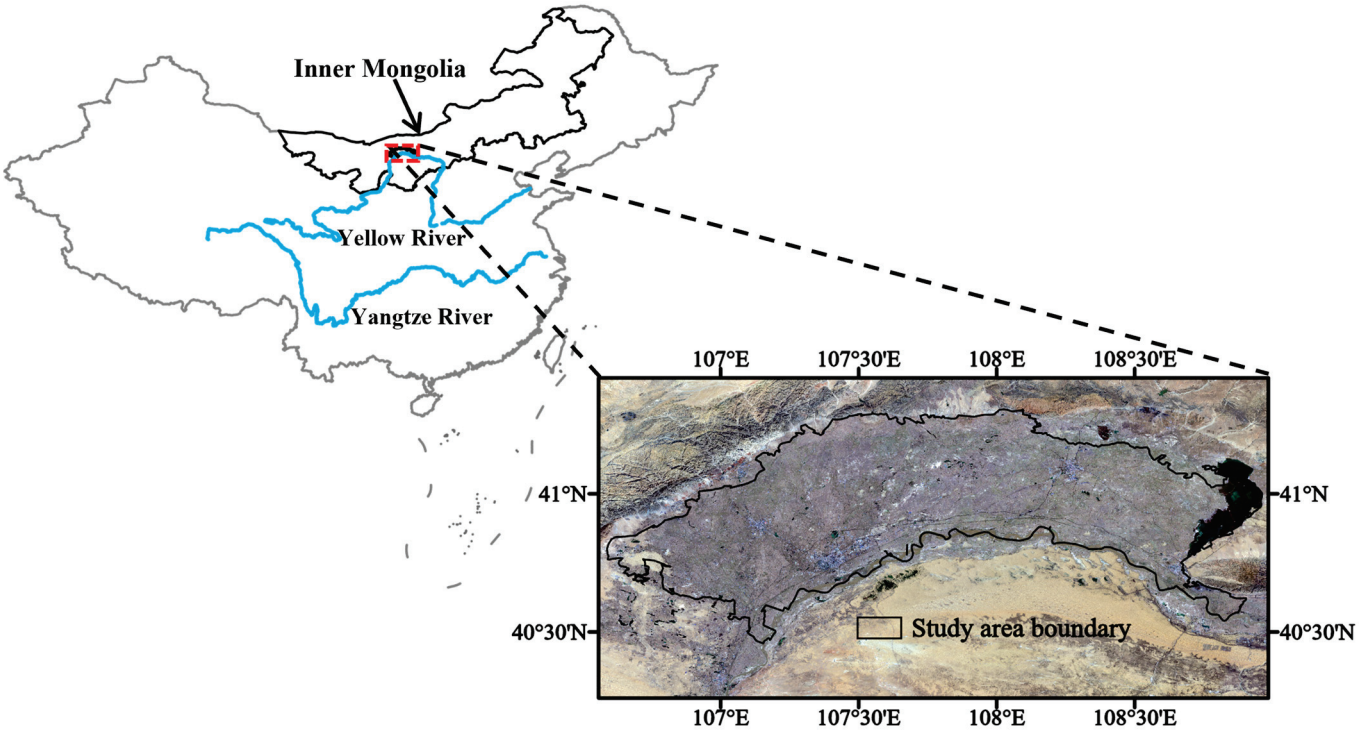

Figure 1. Geographical site and Landsat true-color composite images of Hetao Plain.

Hetao Basin, located in the northern margin of the Ordos Syncline of the North China Platform, is regarded as one of the Cenozoic rift basins. Tectonic movement and the paleo-climate affect the sedimentary environment, paleo-geography, and lithology. Great amounts of salinity (such as calcite and gypsum) were accumulated due to the occurrence of red or deep-brown sediments in an oxidative environment during the Tertiary period. Inland lacustrine sediments had locally been deposited and thick Mid-Cenozoic sedimentary formation had developed in relation to the closed geologic structure and continuous tectonic subsidence during the Quaternary period [22,36]. Fluvial and lacustrine sediments with silt and fine sand were deposited during the Quaternary period in the Hetao Plain [37].

The aquifers overlying clay layers at a depth of 40 m (<40 m BLS) are regarded as shallow groundwater [25]. The shallow aquifers are generally multi-layered, varying from unconfined to leaky-confined in the shallow deposits, which is characterized as an

interbedding of silt and fine sands rich in organic matter with a relatively low hydraulic gradient and groundwater flow rates [22,36,37]. The north area is the weak runoff area with lower permeability due to higher clay particle content, and the south area near the Yellow River is the strong runoff area with higher permeability [38]. The depth of the water table generally changes from 2 to 20 m multi-yearly, affected by Yellow River irrigation in Hetao Basin, and the depth of the water table is approximately 1 m BLS in the flat plain [35,36]. The recharge to shallow groundwater includes irrigation channels, rainfall infiltration, and surface water, while the discharge paths include evapotranspiration, drainage, and pumping in the study area [29,37]. The flow direction of shallow groundwater is generally from northwest to southeast and north, and from southwest to north and south [29,30,38].

2.2. Groundwater as Dataset

Shallow groundwater is more vulnerable to saline soil leaching contamination [10]. Aquifers above the clay layer host shallow groundwater (<40 m BLS), including alluvial-lacustrine aquifers and alluvial-pluvial aquifers [23,25,37]. Therefore, we mainly selected groundwater samples below 40 m for analysis. Groundwater data, including As concentration, coordinates, well depths, and sampling times for each sample, were collected from historical documents [22,23,30,35,37,38]. These shallow groundwater samples were collected in the Holocene and late Pleistocene aquifers. The lithology of the aquifers was mainly composed of silt and fine sand and the aquifers were above the clay layer. Therefore, all sampled sites can be affected by the surface recharge. Samples were collected between July and September in 2006, 2007, 2008, 2009, 2010, 2016, and 2017. Moreover, the contents of trivalent As as (As (III)), total dissolved solids (TDS), pH, Na^+, Cl^-, $HCO_3{}^-$, and $SO_4{}^{2-}$ in shallow groundwater samples were collected. In addition, 73 shallow groundwater samples (<40 m BLS) collected in August 2020 were analyzed. TDS content and pH were measured with a portable water quality instrument. Arsenic concentration was tested by inductively coupled plasma mass optical emission spectroscopy (ICP–OES). The $SO_4{}^{2-}$ concentration was determined by ion chromatograph. Interannual variations in groundwater As from 2006 to 2010 were not significant [23]. From 2011 to 2016, water-saving reconstruction was widely applied in the irrigation area of the Hetao Plain. This water-saving reconstruction markedly decreased the groundwater table [39], possibly impacting the distribution of saline-alkali land and the concentration of As in groundwater. Therefore, the groundwater As data were divided into two periods for analysis: 2006–2010 (Period I) and 2016–2020 (Period II) (Figure 2).

2.3. Remote Sensing Image Acquisition and Preprocessing

Remote sensing images used in this study were obtained from the Google Earth Engine (GEE) platform. Remote sensing images in 2006 and 2010 were from Landsat 5 ETM. Remote sensing images in 2016 and 2020 were from Landsat 8 OLI/TIRS. The spatial resolution of all the images was 30 m. Remote sensing images with the minimum cloud amount were selected in the GEE platform and then radiometric correction, image fusion, and other image preprocessing operations of Landsat images were completed.

2.4. Salt-Leaching Irrigation Information Extraction

In the Hetao Plain, water is irrigated to leaching saline soil in the autumn from the end of October to the beginning of November each year. The temporary water bodies are formed in the surface that did not exist at other times of the year. After extracting water bodies during the period and subtracting those long-term stable water bodies, such as rivers and lakes, the distribution of salt-leaching irrigation water information can be obtained. Salt-leaching irrigation can transport partial soil salts and some ions into groundwater with irrigation water or transport to adjacent areas [3,11,17]. To analyze the relationships among the distribution of salt-leaching irrigation, saline-alkali land, and groundwater arsenic concentration, we extracted the information of salt-leaching irrigation water in autumn of the previous year (Period I corresponding to 2005–2009 and Period II corresponding to

2015–2019) (Figure 3a). We observed that the salt-leaching irrigation position moderately change in each autumn, respectively, within the two periods. Therefore, we extracted the information about salt-leaching irrigation water in 2005, 2009, 2015, and 2019. To extract the distribution of the salt-leaching irrigation water with high accuracy from the remote sensing images, the Automated Water Extraction Index (*AWEI*) [40] was utilized for extracting water information based on Equations (1) and (2):

$$AWEI_{nsh} = 4 \times \left(\rho_{(\text{green})} - \rho_{(\text{SWIR1})}\right) - \left(0.25 \times \rho_{(\text{NIR})} + 2.75 \times \rho_{(\text{SWIR2})}\right) \quad (1)$$

$$AWEI_{sh} = \rho_{(\text{blue})} + 2.5 \times \rho_{\ (\text{green})} - 1.5 \times \left(\rho_{(\text{NIR})} + \rho_{(\text{SWIR1})}\right) - 0.25 \times \rho_{(\text{SWIR2})} \quad (2)$$

where $AWEI_{\text{nsh}}$ can effectively remove pixels without a water body, including dark-built surfaces in areas with urban background, and $AWEI_{\text{sh}}$ primarily further eliminates shadow pixels that $AWEI_{\text{nsh}}$ may not effectively remove. $\rho_{(\text{blue})}$ refers to the gray value in the blue band of the images, $\rho_{(\text{green})}$ is the gray value in the green band of the images, $\rho_{(\text{NIR})}$ is the gray value in the near-infrared band of the images, $\rho_{(\text{SWIR1})}$ refers to the gray value in the shortwave infrared 1 band of the images, and $\rho_{(\text{SWIR2})}$ is the gray value in the shortwave infrared 2 band of the images. The surface water was extracted by the application of a threshold close to that in [40].

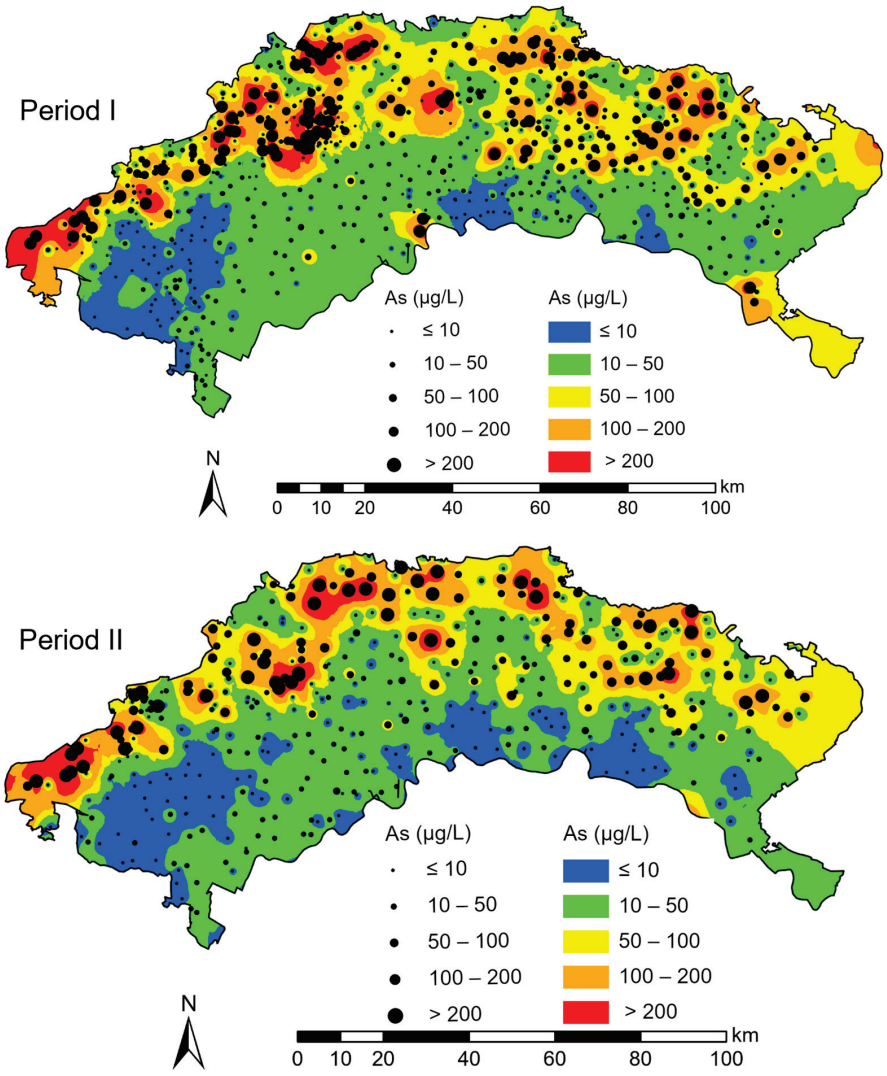

Figure 2. Spatial distribution of arsenic concentrations in sampling sites and in the IDW interpolation method.

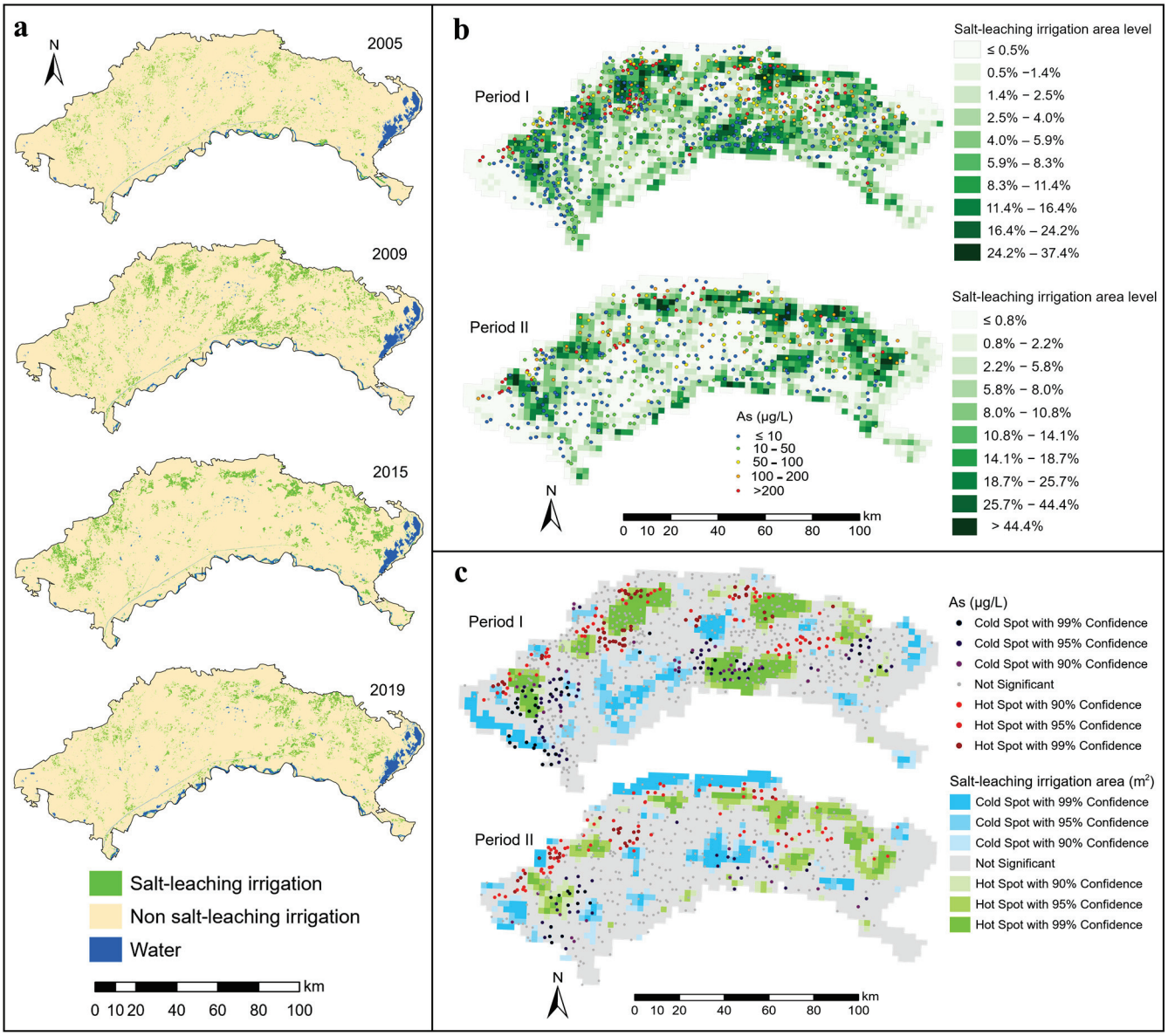

Figure 3. Spatial distribution and hotspots of salt-leaching irrigation and groundwater arsenic concentrations ((**a**) Salt-leaching irrigation information, (**b**) Covering area percentages of salt-leaching irrigation and groundwater arsenic concentrations, (**c**) Hotspots of salt-leaching irrigation area and groundwater arsenic concentrations).

2.5. Saline-Alkali Land Information Extraction

Supervised classification (random forest algorithm) was applied to obtain saline-alkali land information. The training samples used in the supervised classification were obtained according to a field survey and high-resolution images on Google Earth. The variation in land cover caused by seasonal changes affects the precision of the saline-alkali land interpretation. Therefore, the spring image was selected for saline-alkali land research when the amounts of vegetation and soil water content at the surface were lower [33]. Saline-alkali land varied slightly between 2006–2008, 2008–2010, 2016–2017, and 2018–2020. Therefore, we extracted information on saline-alkali land in 2006, 2010, 2016, and 2020 (Figure 4a). The land use of the study area was divided into three types: saline-alkali land (200–250 sample points), non-saline-alkali land (200–250 sample points), and water (100–150 sample points). In the Google Earth Engine (GEE) platform, the sample points were randomly separated into 7:3, which were used for training and verification sample

points of the land use classification algorithm. The classified products and sample points were then analyzed using the confusion matrix analysis. The overall accuracy and Kappa accuracy were calculated to assess the classification effect or misclassification error of the various classification algorithms. The overall accuracy remained in the range of 92–97%, and the Kappa accuracy remained in the range of 91–96%.

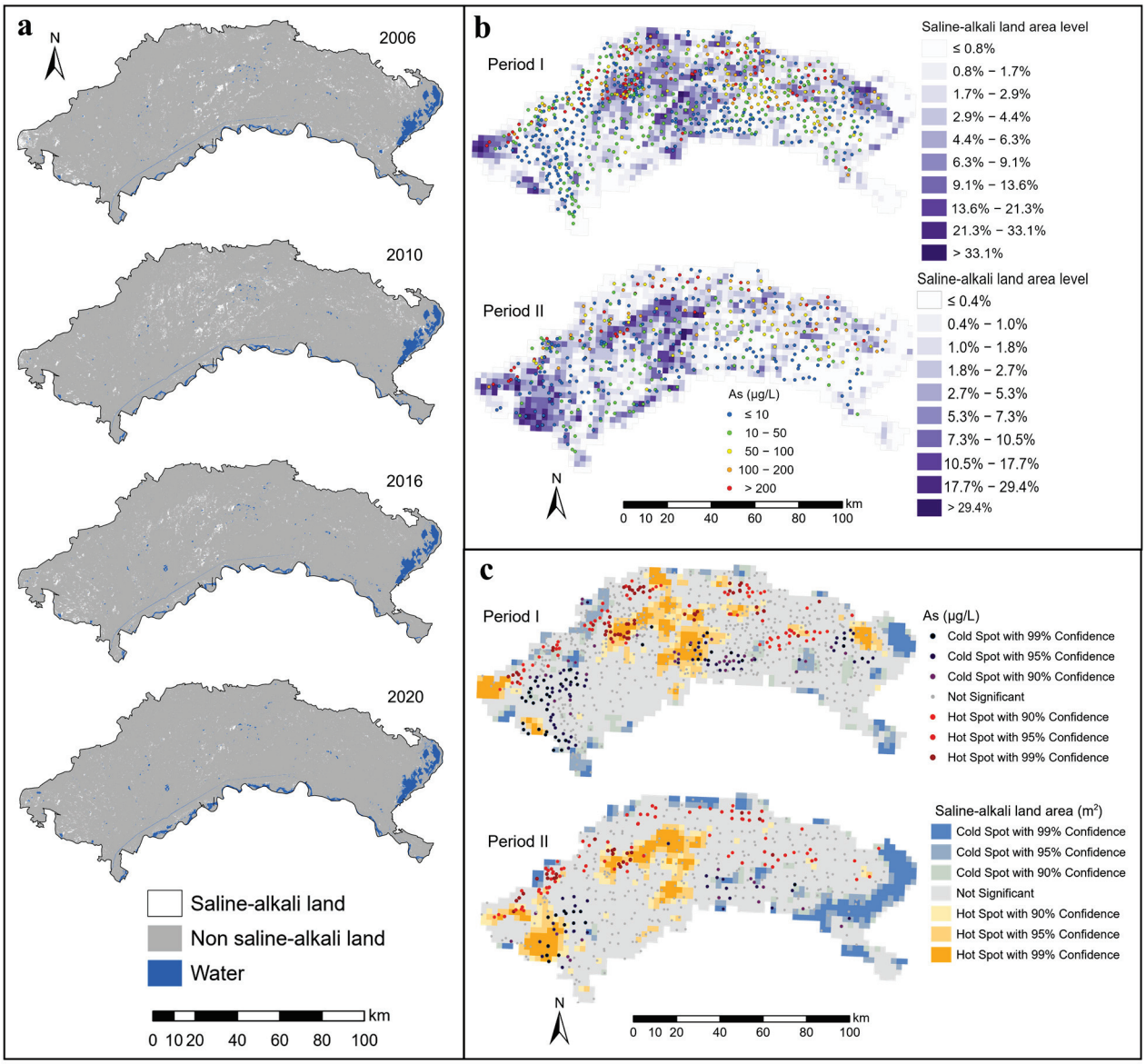

Figure 4. Spatial distribution and hotspots of saline-alkali land and groundwater arsenic concentrations ((**a**) Saline-alkali land information, (**b**) Covering area percentages of saline-alkali land and groundwater arsenic concentrations, (**c**) Hotspots of saline-alkali land area and groundwater arsenic concentrations).

2.6. Data Analysis Methods

Statistics and classification: The study area was divided into 1505 evaluation units of 2.5 × 2.5 km fishnets, and the covering area percentages of salt-leaching irrigation and saline-alkali land in each fishnet were calculated. Subsequently, the covering area percentages of salt-leaching irrigation and saline-alkali land in fishnets were classified into ten levels using the Natural Breaks Jenks method. The classification results were recorded as 'salt-leaching irrigation area level' and 'saline-alkali land area level' in Figures 3b and 4b. The Natural

Breaks Jenks Method can minimize the variance within classes and can maximize the variance between classes to make the classification most appropriate [41].

Hotspot analysis: Getis-Ord Gi* was used to calculate the hotspots and cold spots of the salt-leaching irrigation area, saline-alkali land area, and groundwater arsenic concentration in this study (Figures 3c and 4c). A high z-score refers to the hotspot, while a low z-score represents the cold spot. Before hotspot analysis, the K-S (Kolmogorov–Smirnov) test was applied to judge whether the data conform to the normal distribution. For the data that do not conform to normal distribution, Box-Cox transformation was performed. Hotspot analysis was conducted in the spatial statistics toolbox of ArcGIS Pro 2.8. The Gi* was calculated as [42]:

$$G_i^* = \frac{\sum_{j=1}^{n} \omega_{i,j} x_j - \overline{X} \sum_{j=1}^{n} \omega_{i,j}}{S \sqrt{\frac{n \sum_{j=1}^{n} \omega_{i,j}^2 - \left(\sum_{j=1}^{n} \omega_{i,j}\right)^2}{n-1}}}$$

where x_j is the attribute value of j, $\omega_{i,j}$ refers to the spatial weight among feature i, n is the total number of features, $\overline{x}$ is the mean value of all element values, and S is the standard deviation of all element values.

Path analysis: A path model was used to evaluate the relationships among salt-leaching irrigation area, saline-alkali land area, As, and other ions' concentrations in groundwater. The model shows the direct and indirect effects of single factors and interactive factors on the receptor through multiple regression [43]. Before establishing a path model, the K-S (Kolmogorov–Smirnov) test was applied to determine whether the data conformed to the normal distribution. Box-Cox transformation was performed if the data did not conform to normal distribution. Path analysis was established in SPSSAU and was added or deleted by the significance of test parameters of each path (p-value < 0.05) to debug the model.

3. Results

3.1. Spatiotemporal Variations in Groundwater as Concentrations

In Period I, the As concentrations in the groundwater samples ranged from 0 to 999 μg/L. The mean and median concentrations were 76.90 and 21.60 μg/L, respectively. Approximately 64% of the total groundwater samples had As concentrations higher than 10 μg/L, and approximately 30.7% of the total samples had As concentrations higher than 50 μg/L. Figure 2 shows the extrapolation map of groundwater As using the inverse distance weighting (IDW) interpolation method. The groundwater samples with As concentrations higher than 50 μg/L mostly occurred along the northern edge of the study area adjacent to northern mountainous areas.

In Period II, the mean and median As concentrations were 67.85 and 14.80 μg/L, respectively, and the As concentrations ranged from 0.05 to 946.20 μg/L. Groundwater samples with As concentrations higher than 10 and 50 μg/L accounted for approximately 58% and 29.7% of the total groundwater samples, respectively. Figure 2 shows that the spatial distribution of groundwater As varied slightly between Periods I and II. Higher As concentrations in the groundwater were mainly found along the northern edge of the study area. The mean groundwater As concentration in Period II from the study area was slightly lower than that in Period I, whereas there was no obvious change in the spatial distribution trend of groundwater As between Periods I and II. In addition, areas with As concentrations higher than 10 μg/L decreased. The area with an As concentration in the range of 10–50 μg/L increased in the mid-west and southeast regions. The figure shows that the area with As concentrations higher than 50 μg/L expanded between Periods I and II.

3.2. Relationship between Salt-Leaching Irrigation Area Distribution and Groundwater as Concentrations

The results of the Automated Water Extraction Index procedure suggested that salt-leaching irrigation was mainly distributed along the front of the northern mountainous region and the areas along the Yellow River (Figure 3a). Salt-leaching irrigation distribution

was widespread in other areas but sparse in the central areas, as indicated by hot and cold spots in the salt-leaching irrigation area. Salt-leaching irrigation hotspots occurred in the northern edge of the study area and some areas in the south (Figure 3c). Many farmlands are located in these areas. Autumn irrigation is an efficient way to control soil salinity in farmlands by leaching salts from the root zone to non-irrigated adjacent areas under significant lateral groundwater gradients [3].

From the perspective of spatial location relationships, cold spots of groundwater As were more likely to be found in the hotspots of the salt-leaching irrigation area located near the Yellow River, while hotspots of groundwater As were more likely to be found in the hotspots of the salt-leaching irrigation area near the northern mountainous region (Figure 3c). The quantitative relationship between the salt-leaching irrigation area level (SLIAL) and the proportion of As concentrations exceeding 10 μg/L was estimated by spatial overlay analysis. The results are shown in Figure 5. With the increase in SLIAL, the proportion of As concentrations exceeding 10 μg/L increased marginally and then fluctuated. Figure 6a shows the annual variation in As concentration in groundwater corresponding to the salt-leaching irrigation distribution. Disappeared salt-leaching irrigation refers to the regions where salt-leaching irrigation land was observed in Period I and did not appear in Period II. Newly increased salt-leaching irrigation refers to the regions where salt-leaching irrigation land did not appear in Period I and has newly appeared in Period II. The results of the Mann–Whitney test indicated that there was no significant difference in total As concentrations in groundwater between the disappeared salt leaching irrigation and the newly increased salt-leaching irrigation from Period I to Period II.

3.3. Relationship between Saline-Alkali Land Distribution and Groundwater as Concentrations

The results of the supervised classification revealed that the saline-alkali land was concentrated in the western, central, and northeastern regions during Period I (Figure 3). Saline-alkali land had the highest spatial aggregation with a contiguous chunk distribution. From Period I to Period II, the saline-alkali land area increased in the west and the degree of spatial aggregation also increased, while saline-alkali land changed from widespread distribution to fragmented distribution in the central area. The distribution of saline-alkali land gradually fragmented from Period I to Period II across the Hetao Plain. In the region with more salt-leaching irrigation areas, the areas of saline-alkali land were smaller (Figures 3 and 4). The hotspots of the saline-alkali land area are more likely to appear in the areas near the northern mountainous region (Figures 3c and 4c).

From the perspective of spatial location relationships, hotspots of groundwater As were more likely to occur in the areas near the northern mountainous region (Figure 4c), where groundwater flows converge [38]. The quantitative relationship between the saline-alkali land area level (SALAL) and the proportion of As concentrations exceeding 10 μg/L was estimated by spatial overlay analysis. The results are shown in Figure 5. The proportion of As concentrations exceeding 10 μg/L generally increased and then decreased with the increase in SALAL both in Period I and Period II (Figure 5). During Period I, the proportion of As concentrations exceeding 10 μg/L increased when SALAL was less than 7, and the proportion of arsenic concentrations exceeding 10 μg/L decreased when SALAL exceeded 7. However, in Period II, the proportion of arsenic concentrations exceeding 10 μg/L increased when SALAL was lower than 2, and the proportion of arsenic concentrations exceeding 10 μg/L decreased when SALAL exceeded 2. Figure 6b shows the annual variation in groundwater arsenic concentrations in correlation with the saline-alkali land distribution. The results showed that there was no significant difference in total arsenic concentration between the disappeared saline-alkali land and the newly increased saline-alkali land from Period I to Period II.

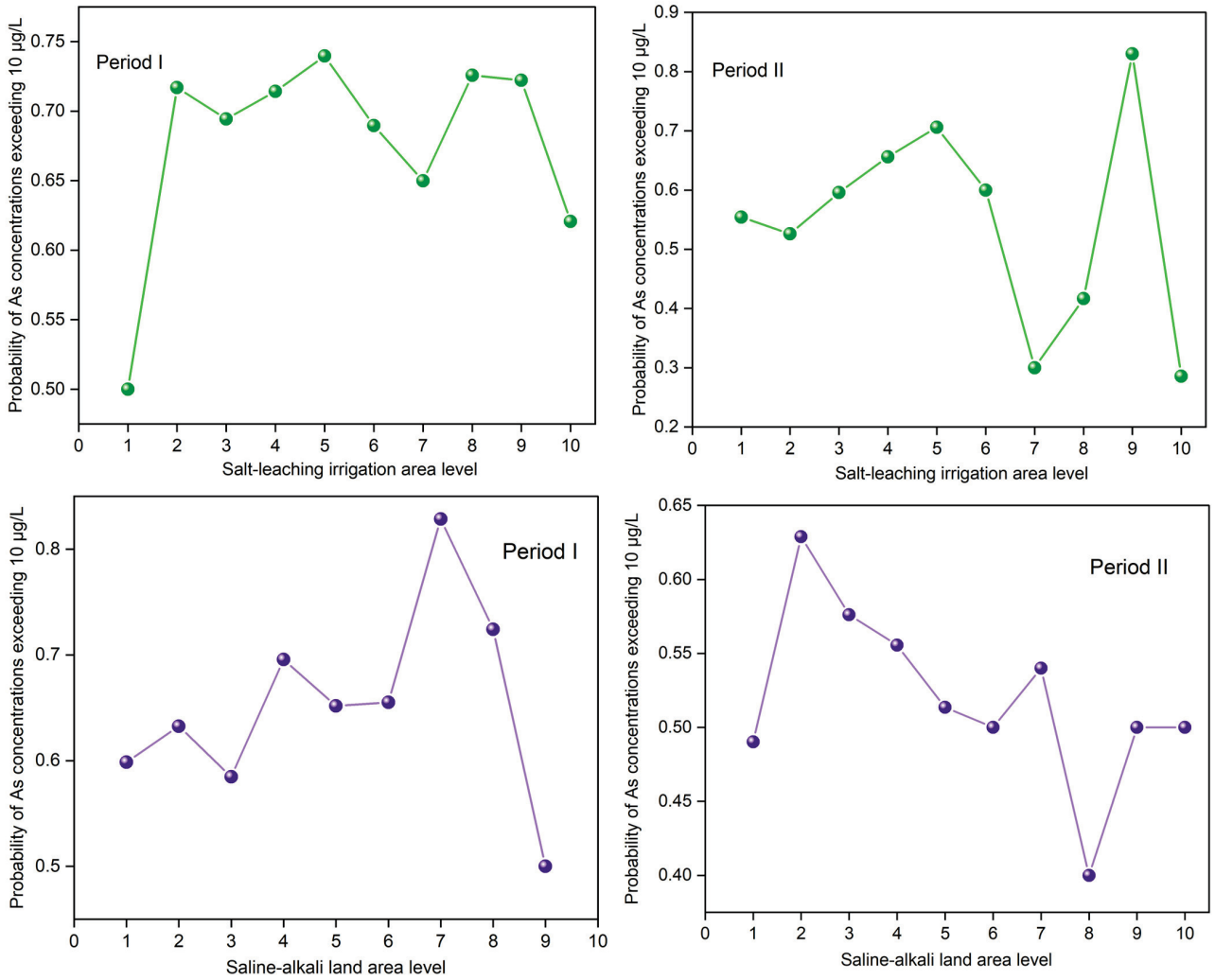

Figure 5. Relationships between the proportion of As concentrations in the groundwater exceeding 10 μg/L with the salt-leaching irrigation area level (SLIAL) and the saline-alkali land area level (SALAL).

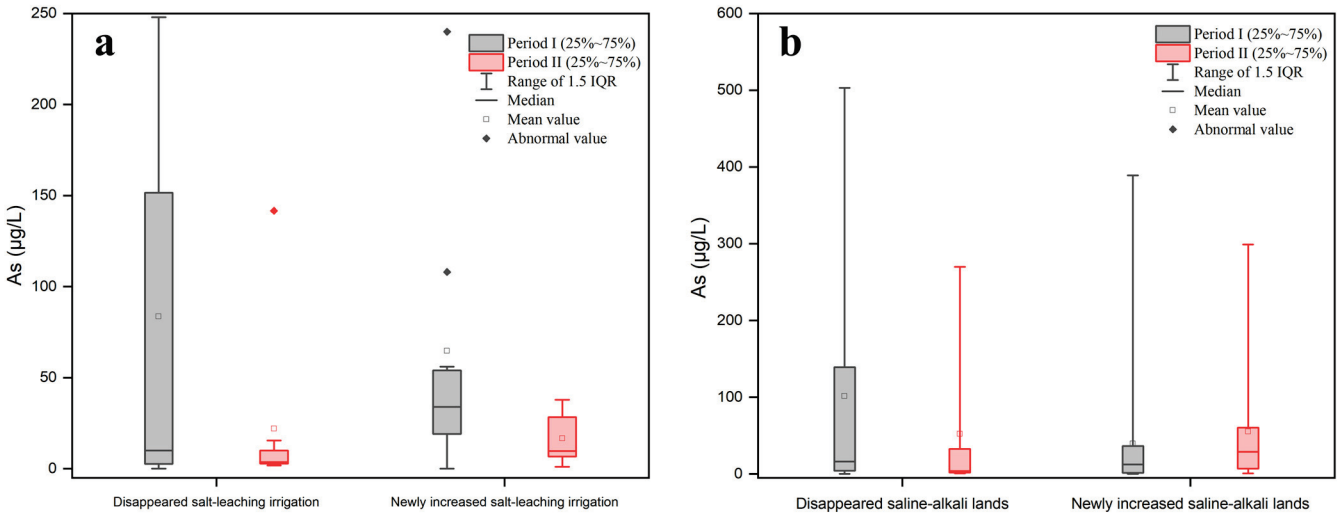

Figure 6. Annual variation in As concentrations in groundwater with salt-leaching irrigation and saline-alkali land distribution ((**a**) Annual variation in As concentrations in groundwater with salt-leaching irrigation, (**b**) Annual variation in As concentrations in groundwater with saline-alkali land distribution).

4. Discussion

4.1. The Impact of Salt-Leaching Irrigation and Saline-Alkali Land on as Transport

Flooding usually induces anoxic conditions that promote the release of As from soil and sediment [44]. However, seasonal short-term flooding may not considerably enhance As mobilization [45]. The proportion of As concentrations exceeding 10 μg/L may be enhanced with increasing SLIAL. In addition, salt-leaching irrigation usually increases the contents of Na^+, Mg^{2+}, Ca^{2+}, HCO_3^-, and SO_4^{2-} in groundwater and decreases the contents of Ca^{2+}, SO_4^{2-}, Na^+, and Cl^- in the soil of saline-alkali land [12]. Therefore, the distribution of saline-alkali land should be considered when exploring the impact of salt-leaching irrigation on As in groundwater.

During Period I, lower As concentrations generally occurred in areas with higher SLIAL and lower SALAL, accompanied by a higher proportion of As (III) (Figure 7). The large ratio of $n(Na^+)/n(Cl^-)$ (>0.86) indicates that the salinity in groundwater originated from leaching rather than sedimentation [46,47]. Figure 8 shows a larger ratio of $n(Na^+)/n(Cl^-)$, higher TDS concentration, and higher SO_4^{2-} concentration in areas with higher SLIAL and lower SALAL, implying that salinity in groundwater in these areas is mainly derived from leaching saline soils. Areas with higher SLIAL and lower SALAL values suggested that salt-leaching irrigation in the previous year transferred salt from the soil into the groundwater. This decreased the redox condition of the groundwater. Less reductive conditions of high-saline groundwater (TDS > 3000 mg/L) prevented As enrichment with the reduction of SO_4^{2-} [24]. A simultaneously higher proportion of As (III), higher TDS, and higher SO_4^{2-} in the areas with higher SLIAL and lower SALAL implied that salt-leaching irrigation carried the soil salt ions into groundwater, limiting As enrichment in groundwater by decreasing reductive conditions and preventing the participation of SO_4^{2-} in the redox process. Therefore, less saline-alkali land associated with more salt-leaching irrigation may decrease the arsenic concentration in groundwater.

Higher As concentrations tended to occur in areas with higher SLIAL and SALAL, accompanied by a relatively higher proportion of As (III) (Figure 7). Moreover, a lower ratio of $n(Na^+)/n(Cl^-)$ (<0.86), lower TDS concentration (TDS < 3000), and lower SO_4^{2-} concentrations in the groundwater were observed in these areas. This suggests that more salt-leaching irrigation in the previous year did not transfer more salt from the soil to the groundwater in these areas. These areas also showed higher salt-leaching irrigation in the previous year, while saline-alkali land areas were not reduced. There could be serious soil secondary salinization phenomena in which groundwater salt is brought to the surface soil in the spring after salt-leaching irrigation in these areas. Irrigation can result in an increase in the groundwater table, and soluble salts from groundwater easily pass through the vadose zone and accumulate in shallow soil when the water table is relatively high [5]. A relatively high groundwater table can enhance groundwater reduction conditions [23]. A higher proportion of As (III) and lower SO_4^{2-} concentrations also indicate higher reduction conditions for groundwater from these areas. As enrichment occurred simultaneously with the reduction of SO_4^{2-} in the reductive groundwater with TDS below 3000 [24]. Therefore, a synergistic increase in salt-leaching irrigation and saline-alkali land may increase the As concentration in the groundwater.

Slightly higher groundwater As was found in areas with lower SLIAL and higher SALAL, while the proportion of As (III) decreased (<40%) (Figure 7). The pH and HCO_3^- contents in groundwater from these areas were relatively higher (Figure 8). In relatively oxidized groundwater, higher pH and HCO_3^- concentrations usually promote As desorption in groundwater [27,48]. In addition, areas with lower and higher SALAL were more likely to have low-lying downstream discharge areas [10]. Significant lateral movement of groundwater and transportation of salt were observed during the salt-leaching irrigation period, inducing the movement of water and salts from the root zone to adjacent areas [3]. With a decrease in elevation and groundwater flow, salt ions moved downstream to the discharge zone, causing the discharge zone to be more likely to be saline-alkaline land [10]. In the discharge areas, strong evaporation enhanced the weathering of carbonate

and increased the HCO_3^- concentration and pH in groundwater, which promoted the desorption of As in groundwater [25,48], indicating that saline-alkali land may increase the As concentration in groundwater.

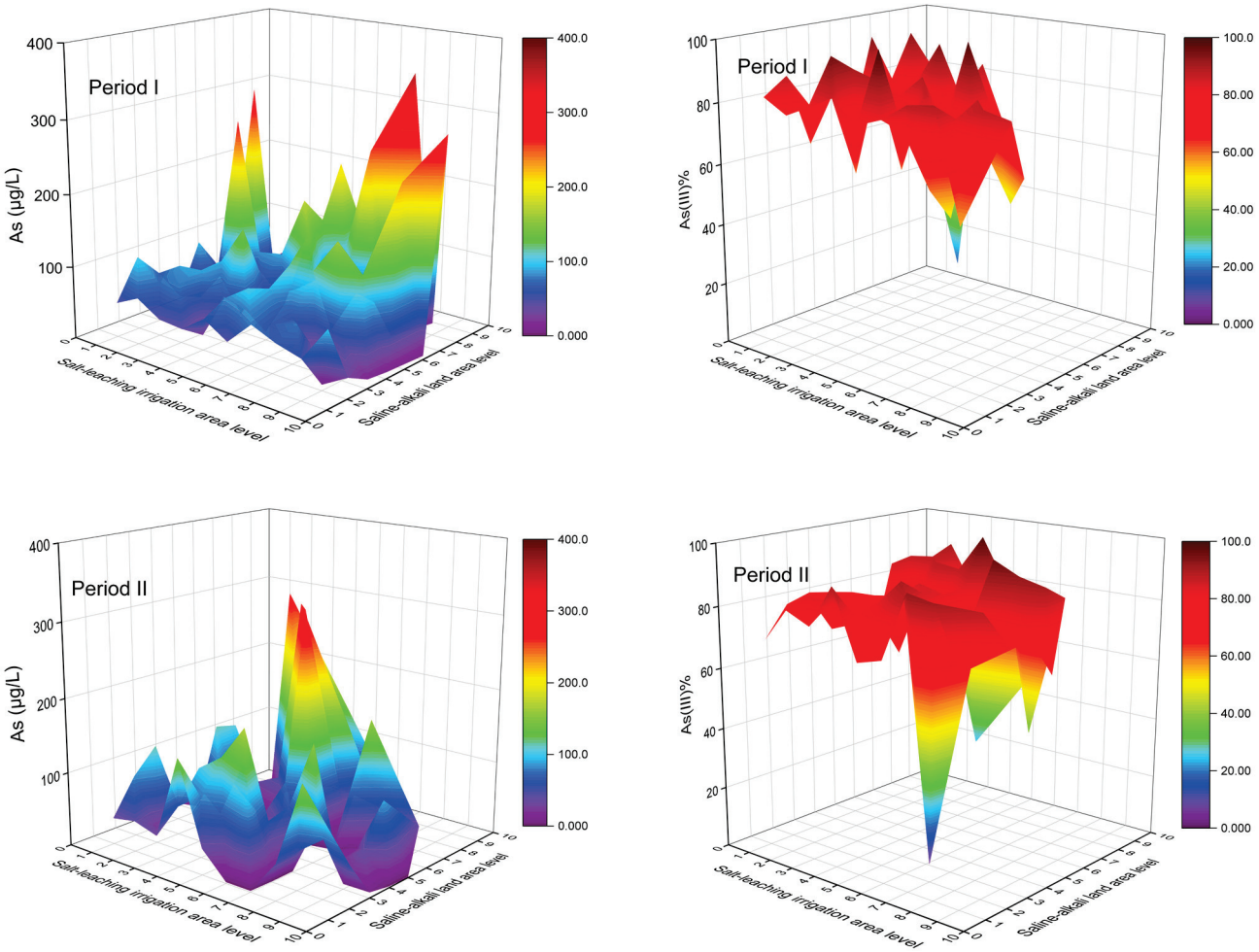

Figure 7. The variations of total arsenic concentrations and proportion of As (III) concentrations to total arsenic concentrations under the combined influence of SLIAL and SALAL.

In Period II, lower groundwater As levels were also observed in areas with higher SLIAL and lower SALAL. However, higher groundwater As levels were more likely to occur in areas with lower SLIAL and higher SALAL (Figure 7). Higher pH, TDS concentration, SO_4^{2-} concentration, and a lower proportion of As (III) (<40%) in groundwater were also observed in these areas. Higher TDS concentrations (>3000 mg/L) occurred in areas with higher SLIAL and SALAL (Figure 8). This phenomenon might be associated with the decrease in the saline-alkali land area from Period I to Period II. From 2011 to 2016, the large-scale implementation of water-saving reconstruction in irrigation areas of the Hetao Plain considerably reduced the groundwater table [40]. With a decrease in the groundwater table, fewer groundwater salts returned to the surface soil, and the saline-alkali land area gradually decreased [13], possibly elevating salinity in groundwater. The increase in groundwater salinity usually weakens the reductive dissolution of As but promotes the desorption of As via competing adsorption with HCO_3^- [11,24,28,49]. Consequently, the decrease in saline-alkali land area from Period I to Period II may have increased the desorption of As in groundwater.

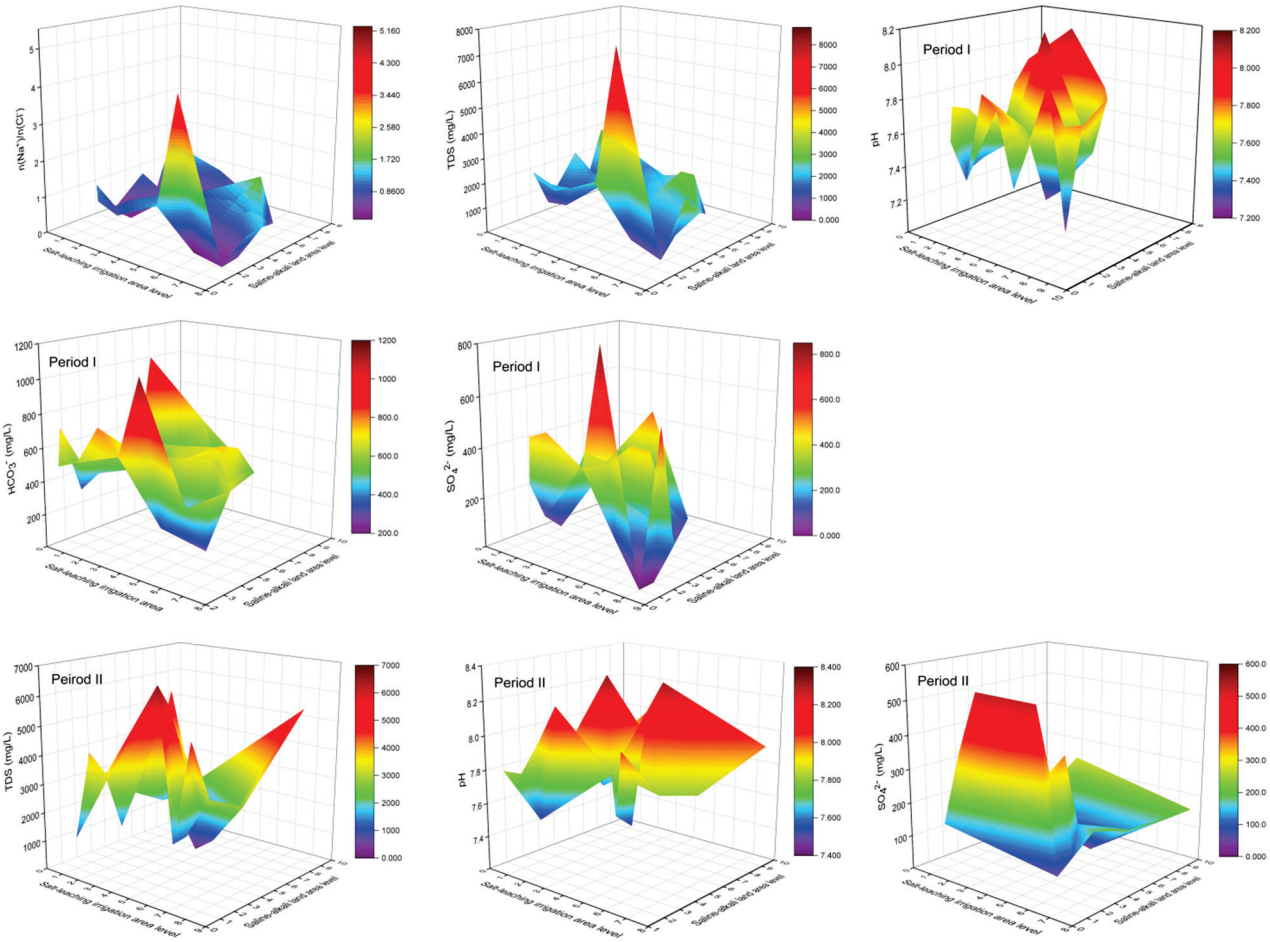

Figure 8. The variations of n(Na+)/n(Cl$^-$) ratio, TDS, pH, SO_4^{2-}, and HCO_3^- under the combined influence of SLIAL and SALAL.

The reductive dissolution of As-rich Fe (oxyhydr)oxide is the dominant reaction for As transport in groundwater, and As desorption generated by alkaline pH and increased HCO_3^- is another significant process of As transport in the Hetao Basin [25]. Relative contributions of the two geochemical processes largely depend on redox conditions, pH, and competing anion concentrations in groundwater. Therefore, the covered area of salt-leaching irrigation and saline-alkali land may influence groundwater As mobilization through different geochemical processes. A path analysis model was used to estimate the influence path of salt-leaching irrigation and saline-alkali land on groundwater As mobilization across the Hetao Plain (Figure 9).

The results showed that the salt-leaching irrigation area was negatively correlated with the saline-alkali land area in both Periods I and II. In Period I, the salt leaching irrigation area negatively affected the HCO_3^- concentration, while the HCO_3^- concentration positively affected the As concentration in the groundwater. Previous research has revealed that increasing the HCO_3^- concentration and pH promotes the release of As in groundwater due to competing adsorption [25]. Therefore, salt-leaching irrigation may restrain the release of As. The saline-alkali land area showed a negative correlation with the SO_4^{2-} concentration, while the SO_4^{2-} concentration showed a negative relationship with the As concentration in the groundwater. Decreased levels of SO_4^{2-} promote As enrichment in groundwater [10,22]. This suggests that saline-alkali land can increase the As content in groundwater. In Period II, the saline-alkali land area showed a direct negative effect on the TDS concentration and an indirect negative effect on the SO_4^{2-} concentration. TDS content was directly negatively associated with the As concentration. Generally,

a higher TDS content limits the enrichment of As in groundwater from Rachna Doab, Punjab Pakistan, and the Datong Basin, China [10,11]. However, the SO_4^{2-} concentration showed no significant effects on the As concentration. This variation may be related to the decrease in saline-alkali land area from Period I to Period II due to water-saving irrigation in the study area, which increased the TDS concentration and enhanced the oxidization of groundwater. The results implied that salt-leaching irrigation can partially flush soil salinity into groundwater to reduce the saline-alkali land area and elevate the ion concentration in groundwater. Salt-leaching irrigation considerably elevated the contents of Na^+, Mg^{2+}, Ca^{2+}, HCO_3^-, and SO_4^{2-} in groundwater [12]. These ions may affect As concentrations in the groundwater. We represent the above geochemical process of the impacts of salt-leaching irrigation and saline-alkali land on As transport in the adjacent shallow aquifers in Figure 10.

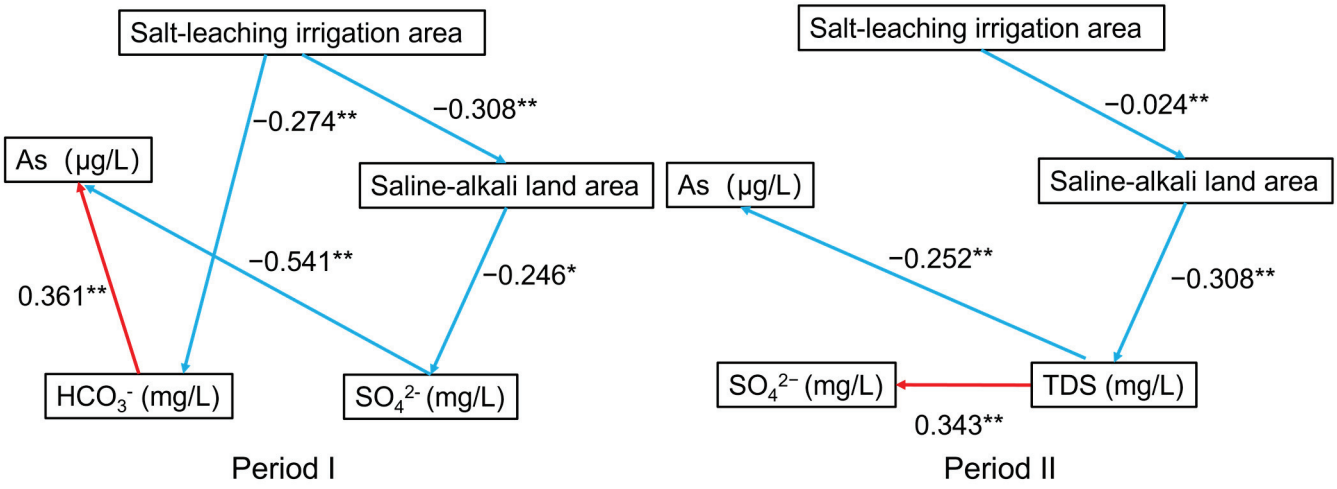

Figure 9. The results of path analysis (* $p < 0.05$, ** $p < 0.01$, red represents positive correlation and blue represents negative).

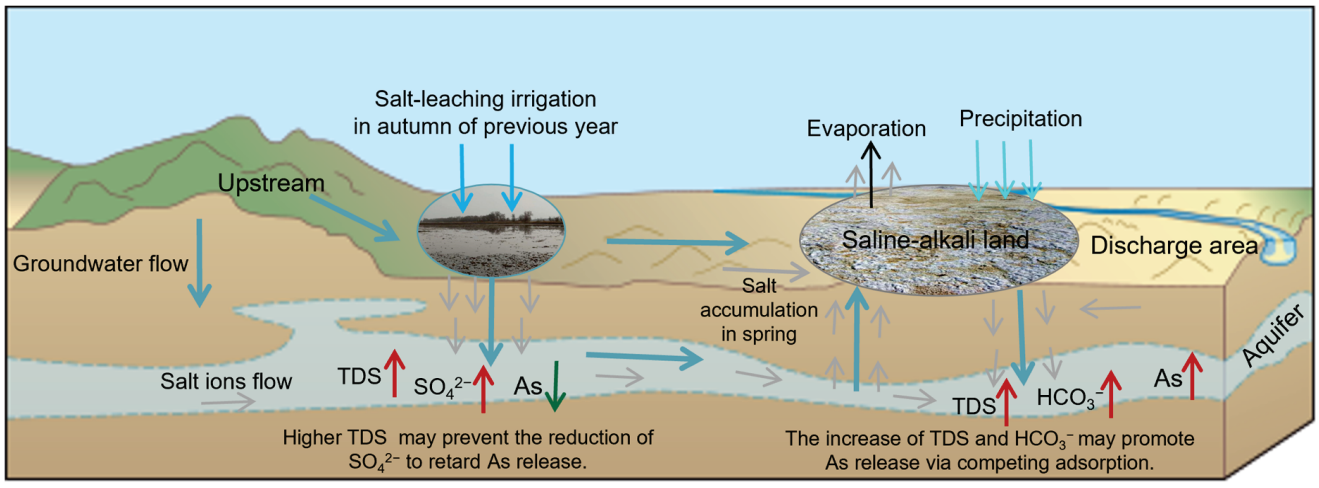

Figure 10. Schematic illustration of the impacts of salt-leaching irrigation and saline-alkali land on As transport in the adjacent shallow aquifers.

Previous studies had confirmed the effects of salt-leaching irrigation on the salinity and related salt ions' concentrations of saline-alkali land soil and groundwater, the impacts of saline-alkali land on salt ions' concentrations in groundwater, and the influence of groundwater salinity on As transport [3,8,12,14,34]. This paper has addressed this gap in the influence of the distribution of saline-alkali land and salt-leaching irrigation on

As transport in groundwater, which is not directly discussed in previous studies. Our results indicated that although salt-leaching irrigation is helpful to reduce the saline-alkali land area, the treatment of saline-alkali land may affect the control of arsenic pollution in groundwater. We suggest that the treatment of saline-alkali land should not only consider its influence on the water table and salt ions' concentrations, but also pay more attention to the mobilization of other pollutants caused by the changes in salt ions' concentrations in groundwater.

4.2. Limitations of the Study and Future Works

Arsenicosis was firstly recognized in 1990 in the center of Inner Mongolia [50]. Guo et al. found that Wuyuan and Alashan were highly contaminated areas [51]. Arsenic concentrations of 96.2% in water samples were above 50 μg/L in the Wuyuan area and 69.3% in the Alashan area [51]. The risk of arsenic pollution also existed in the arid and semi-arid reducing aquifers around the Hetao Plain. Arsenic concentration ranges changed from <1 to 1860 μg/L in the Huhhot Basin, <1.0 to 1300 μg/L in the Datong Basin, and <0.01 to 177 μg/L with an average concentration of 27.3 μg/L in the Yinchuan Basin [30,50]. A more careful comparison study at a larger spatial scale and in past times about the harmful parameters around the Hetao Plain should be further undertaken. This study quantified the impact of the distribution of saline-alkali land and salt-leaching irrigation on groundwater As migration. For the convenience of analysis, the salinization degree of saline-alkali land is not classified in this paper because salt-leaching irrigation is difficult to be classified according to the amount of irrigation water. It is ignored that the influence of saline-alkali land has different salinization degrees on groundwater As in this paper. Except for groundwater total arsenic concentrations, partial data of other ions were missing. For the influence of the evolution of saline-alkali land and salt-leaching irrigation on geochemical processes of groundwater As, preliminary guesses only have been made based on the trends and correlations between ion concentrations in groundwater. For future studies, the impact of the evolution of saline-alkali land and salt-leaching irrigation on groundwater arsenic geochemical processes needs to be further quantified through long-term observations and experiments. Moreover, our study also suggested that the effects of salt-leaching irrigation and saline-alkali land distribution on groundwater As concentrations are not linear due to the diverse effects of groundwater salinity on groundwater arsenic. Advanced models and methods are needed to simulate a reasonable range in the water amount and area of salt-leaching irrigation, which is expected to contribute to groundwater arsenic elimination in the future.

5. Conclusions

The results of this study indicate that salt-leaching irrigation and saline-alkali land influence the As concentration in groundwater. In general, the groundwater As concentration fluctuated slightly, with an increase in the SLIAL and with low SALAL. Likely, seasonal short-term flooding may not markedly enhance As mobilization. Lower groundwater As concentrations appeared in the regions with high SLIAL and low SALAL due to the increase in TDS generated by leaching soil salt into the groundwater, which may retard the accumulation of As in groundwater. A larger saline-alkali land area (high SALAL) increased the groundwater As concentration due to the introduction of salt ions. This may be related to the increase in the HCO_3^- concentration promoting As release via competing adsorption or the increase in the SO_4^{2-} concentration enhancing As release in reductive groundwater with lower TDS. The path analysis model confirmed that salt-leaching irrigation may increase groundwater salinity by leaching soil salt into the groundwater to affect groundwater As. From Periods I and II, the decrease in the saline-alkali land area may impact As mobilization due to competitive adsorption caused by the increase in the TDS concentration in groundwater. Salt-leaching irrigation in the autumn is one of the effective ways to control soil salinity in the Hetao Plain, but our study showed that this measure had adverse effects on groundwater quality. We suggest that the current measures,

including policy and engineering to control soil salinity, should be changed to protect groundwater resources.

Author Contributions: Conceptualization, B.W.; methodology, software, data collection and analysis, S.Y., Y.T. and B.W.; chemical experiment, S.Y. and Q.W.; writing—review and editing, all authors; funding acquisition, B.W. and L.Y. All authors have read and agreed to the published version of the manuscript.

Funding: Funding for this study was provided by the National Natural Science Foundation of China (Grant No. 41977400), the Second Tibetan Plateau Scientific Expedition and Research Program (STEP) (Grant No. 2019QZKK0607), and the Central Government Guides Local Science and Technology Development Program (Grant Nos. 2021ZY0047, XZ202201YD0014C).

Conflicts of Interest: The authors declare that they have no known competing financial interest or personal relationships that could have appeared to influence the work reported in this paper.

References

1. Hassani, A.; Azapagic, A.; Shokri, N. Global predictions of primary soil salinization under changing climate in the 21st century. *Nat. Commun.* **2021**, *12*, 6663. [CrossRef] [PubMed]
2. Kumar, S.; Kumar, M.; Chandola, V.K.; Kumar, V.; Saini, R.K.; Pant, N.; Kumari, N.; Srivastava, A.; Singh, S.; Singh, R.; et al. Groundwater Quality Issues and Challenges for Drinking and Irrigation Uses in Central Ganga Basin Dominated with Rice-Wheat Cropping System. *Water* **2021**, *13*, 2344. [CrossRef]
3. Mao, W.; Zhu, Y.; Wu, J.; Ye, M.; Yang, J. Evaluation of effects of limited irrigation on regional-scale water movement and salt accumulation in arid agricultural areas. *Agric. Water Manag.* **2022**, *262*, 107398. [CrossRef]
4. Sun, Y.; Li, X.; Shi, H.; Cui, J.; Wang, W.; Ma, H.; Chen, N. Modeling salinized wasteland using remote sensing with the integration of decision tree and multiple validation approaches in Hetao irrigation district of China. *Catena* **2022**, *209*, 105854. [CrossRef]
5. Zheng, N.; Guo, M.; Yue, W.; Teng, Y.; Zhai, Y.; Yang, J.; Zuo, R. Evaluating the impact of flood irrigation on spatial variabilities of soil salinity and groundwater quality in an arid irrigated region. *Hydrol. Res.* **2020**, *52*, 229–240. [CrossRef]
6. Loaiza, J.G.; Bustos-Terrones, Y.; Bustos-Terrones, V.; Monjardín-Armenta, S.A.; Quevedo-Castro, A.; Estrada-Vazquez, R.; Rangel-Peraza, J.G. Evaluation of the Hydrochemical and Water Quality Characteristics of an Aquifer Located in an Urbanized Area. *Appl. Sci.* **2022**, *12*, 6879. [CrossRef]
7. Bannenberg, M.; Ntona, M.M.; Busico, G.; Kalaitzidou, K.; Mitrakas, M.; Vargemezis, G.; Fikos, I.; Kazakis, N.; Voudouris, K. Hydrogeological and Hydrochemical Regime Evaluation in Flamouria Basin in Edessa (Northern Greece). *Environments* **2020**, *7*, 105. [CrossRef]
8. Liu, M.; Xiao, C.; Liang, X.; Wei, H. Response of groundwater chemical characteristics to land use types and health risk assessment of nitrate in semi-arid areas: A case study of Shuangliao City, Northeast China. *Ecotoxicol. Environ. Saf.* **2022**, *236*, 113473. [CrossRef]
9. Xu, X.; Huang, G.; Qu, Z.; Pereira, L.S. Assessing the groundwater dynamics and impacts of water saving in the Hetao Irrigation District, Yellow River basin. *Agric. Water Manag.* **2010**, *98*, 301–313. [CrossRef]
10. Parvaiz, A.; Khattak, J.A.; Hussain, I.; Masood, N.; Javed, T.; Farooqi, A. Salinity enrichment, sources and its contribution to elevated groundwater arsenic and fluoride levels in Rachna Doab, Punjab Pakistan: Stable isotope (δ^2H and δ^{18}O) approach as an evidence. *Environ. Pollut.* **2021**, *268*, 115710. [CrossRef]
11. Li, J.; Wang, Y.; Xie, X. Cl/Br ratios and chlorine isotope evidences for groundwater salinization and its impact on groundwater arsenic, fluoride and iodine enrichment in the Datong basin, China. *Sci. Total Environ.* **2016**, *544*, 158–167. [CrossRef]
12. Liu, X.; Xu, Z.; Qu, Z. *Study on the Law of Ion Migration of Soil and Groundwater in Different Types of Saline-Alkali Land in Arid Salinization Irrigation District*; American Geophysical Union: Washington, DC, USA, 2019.
13. Dou, X.; Shi, H.; Miao, Q.; Tian, F.; Yu, D.; Zhou, L.; Liang, Z. Temporal and Spatial Variability Analysis of Soil Water and Salt and the Influence of Groundwater Depth on Salt in Saline Irrigation Area. *J. Soil Water Conserv.* **2019**, *33*, 246–253. [CrossRef]
14. Khasanov, S.; Li, F.; Kulmatov, R.; Zhang, Q.; Qiao, Y.; Odilov, S.; Yu, P.; Leng, P.; Hirwa, H.; Tian, C.; et al. Evaluation of the perennial spatio-temporal changes in the groundwater level and mineralization, and soil salinity in irrigated lands of arid zone: As an example of Syrdarya Province, Uzbekistan. *Agric. Water Manag.* **2022**, *263*, 107444. [CrossRef]
15. Zafar, M.M.; Sulaiman, M.A.; Prabhakar, R.; Kumari, A. Evaluation of the suitability of groundwater for irrigational purposes using irrigation water quality indices and geographical information systems (GIS) at Patna (Bihar), India. *Int. J. Energy Water Resour.* **2022**, 2522-0101. [CrossRef]
16. Shao, K.; Zhou, Z.; Xun, P.; Cohen, S.M. Bayesian benchmark dose analysis for inorganic arsenic in drinking water associated with bladder and lung cancer using epidemiological data. *Toxicology* **2021**, *455*, 152752. [CrossRef]
17. Farzan, S.F.; Eunus, H.E.M.M.; Haque, S.E.; Sarwar, G.; Hasan, A.K.M.R.; Wu, F.; Islam, T.; Ahmed, A.; Shahriar, M.; Jasmine, F.; et al. Arsenic exposure from drinking water and endothelial dysfunction in Bangladeshi adolescents. *Environ. Res.* **2022**, *208*, 112697. [CrossRef]

18. Kellett, M.P.; Jatko, J.T.; Darling, C.L.; Ventrello, S.W.; Bain, L.J. Arsenic exposure impairs intestinal stromal cells. *Toxicol. Lett.* **2022**, *361*, 54–63. [CrossRef] [PubMed]
19. Cheng, Y.-Y.; Huang, N.-C.; Chang, Y.-T.; Sung, J.-M.; Shen, K.-H.; Tsai, C.-C.; Guo, H.-R. Associations between arsenic in drinking water and the progression of chronic kidney disease: A nationwide study in Taiwan. *J. Hazard. Mater.* **2017**, *321*, 432–439. [CrossRef]
20. Wei, B.; Yu, J.; Wang, J.; Yang, L.; Li, H.; Kong, C.; Xia, Y.; Wu, K. The relationships between arsenic methylation and both skin lesions and hypertension caused by chronic exposure to arsenic in drinking water. *Environ. Toxicol. Pharmacol.* **2017**, *53*, 89–94. [CrossRef]
21. WHO; UNICEF. *Arsenic Primer—Guidance on the Investigation & Mitigation of Arsenic Contamination*, 3rd ed.; WHO: Geneva, Switzerland; UNICEF: New York, NY, USA, 2018. Available online: https://www.unicef.org/wash/files/UNICEF_WHO_Arsenic_Primer.pdf (accessed on 1 May 2022).
22. Guo, H.; Yang, S.; Tang, X.; Li, Y.; Shen, Z. Groundwater geochemistry and its implications for arsenic mobilization in shallow aquifers of the Hetao Basin, Inner Mongolia. *Sci. Total Environ.* **2008**, *393*, 131–144. [CrossRef]
23. Guo, H.; Zhang, Y.; Jia, Y.; Zhao, K.; Li, Y.; Tang, X. Dynamic behaviors of water levels and arsenic concentration in shallow groundwater from the Hetao Basin, Inner Mongolia. *J. Geochem. Explor.* **2013**, *135*, 130–140. [CrossRef]
24. Jia, Y.; Guo, H.; Xi, B.; Jiang, Y.; Zhang, Z.; Yuan, R.; Yi, W.; Xue, X. Sources of groundwater salinity and potential impact on arsenic mobility in the western Hetao Basin, Inner Mongolia. *Sci. Total Environ.* **2017**, *601–602*, 691–702. [CrossRef] [PubMed]
25. Gao, Z.P.; Jia, Y.F.; Guo, H.M.; Zhang, D.; Zhao, B. Quantifying Geochemical Processes of Arsenic Mobility in Groundwater from an Inland Basin Using a Reactive Transport Model. *Water Resour. Res.* **2020**, *56*, e2019WR025492. [CrossRef]
26. Gao, C.; Liu, W.; Feng, C.; Liu, B.; Jianxin, S. Distribution Characteristics of Saline Groundwater and High-arsenic Groundwater in the Hetao Plain, Inner Mongolia. *Acta Geosci. Sin.* **2014**, *35*, 139–148.
27. Smedley, P.L.; Kinniburgh, D.G. A review of the source, behaviour and distribution of arsenic in natural waters. *Appl. Geochem.* **2002**, *17*, 517–568. [CrossRef]
28. Bundschuh, J.; Litter, M.I.; Parvez, F.; Román-Ross, G.; Nicolli, H.B.; Jean, J.-S.; Liu, C.-W.; López, D.; Armienta, M.A.; Guilherme, L.R.G.; et al. One century of arsenic exposure in Latin America: A review of history and occurrence from 14 countries. *Sci. Total Environ.* **2012**, *429*, 2–35. [CrossRef]
29. Gao, Z.; Guo, H.; Li, S.; Wang, J.; Ye, H.; Han, S.; Cao, W. Remote sensing of wetland evolution in predicting shallow groundwater arsenic distribution in two typical inland basins. *Sci. Total Environ.* **2022**, *806*, 150496. [CrossRef]
30. Zhang, H.; Zhang, X.; Liu, W.; Yeh, P.J.F.; Ye, P.; He, X. Impacts of active tectonics on geogenic arsenic enrichment in groundwater in the Hetao Plain, Inner Mongolia. *Quat. Sci. Rev.* **2022**, *278*, 107343. [CrossRef]
31. Choudhury, R.; Nath, B.; Khan, M.R.; Mahanta, C.; Ellis, T.; van Geen, A. The Impact of Aquifer Flushing on Groundwater Arsenic Across a 35-km Transect Perpendicular to the Upper Brahmaputra River in Assam, India. *Water Resour. Res.* **2018**, *54*, 8160–8173. [CrossRef]
32. Kellner, E.; Hubbart, J.A.; Ikem, A. A comparison of forest and agricultural shallow groundwater chemical status a century after land use change. *Sci. Total Environ.* **2015**, *529*, 82–90. [CrossRef]
33. Guo, Z.; Ruan, B.; Guan, X.; Wang, S.; Li, Y. Analysis on Spatial-temporal Evolution of Soil Salinity and Its Driving Factors in Hetao Irrigation District during Recent 30 years. *China Rural Water Conserv. Hydropower* **2016**, *9*, 159–162+167.
34. Cui, G.; Lu, Y.; Zheng, C.; Liu, Z.; Sai, J. Relationship between Soil Salinization and Groundwater Hydration in Yaoba Oasis, Northwest China. *Water* **2019**, *11*, 175. [CrossRef]
35. Fu, Y.; Cao, W.; Pan, D.; Ren, Y. Changes of groundwater arsenic risk in different seasons in Hetao Basin based on machine learning model. *Sci. Total Environ.* **2022**, *817*, 153058. [CrossRef]
36. Guo, H.; Zhou, Y.; Jia, Y.; Tang, X.; Li, X.; Shen, M.; Lu, H.; Han, S.; Wei, C.; Norra, S.; et al. Sulfur Cycling-Related Biogeochemical Processes of Arsenic Mobilization in the Western Hetao Basin, China: Evidence from Multiple Isotope Approaches. *Environ. Sci. Technol.* **2016**, *50*, 12650–12659. [CrossRef] [PubMed]
37. Gao, Z.; Weng, H.; Guo, H. Unraveling influences of nitrogen cycling on arsenic enrichment in groundwater from the Hetao Basin using geochemical and multi-isotopic approaches. *J. Hydrol.* **2021**, *595*, 125981. [CrossRef]
38. Zhang, Y.; Cao, W.; Wang, W.; Dong, Q. Distribution of groundwater arsenic and hydraulic gradient along the shallow groundwater flow-path in Hetao Plain, Northern China. *J. Geochem. Explor.* **2013**, *135*, 31–39. [CrossRef]
39. Zhang, Q.; Qiang, Q.; Li, J.; Chen, J.; Li, Q. Groundwater Dynamic Changing under Water-saving Irrigation Conditions of Hetao Irrigation District. *J. Irrig. Drain.* **2018**, *37*, 97–101. [CrossRef]
40. Feyisa, G.L.; Meilby, H.; Fensholt, R.; Proud, S.R. Automated Water Extraction Index: A new technique for surface water mapping using Landsat imagery. *Remote Sens. Environ.* **2014**, *140*, 23–35. [CrossRef]
41. Amirruddin, A.D.; Muharam, F.M.; Ismail, M.H.; Ismail, M.F.; Tan, N.P.; Karam, D.S. Hyperspectral remote sensing for assessment of chlorophyll sufficiency levels in mature oil palm (*Elaeis guineensis*) based on frond numbers: Analysis of decision tree and random forest. *Comput. Electron. Agric.* **2020**, *169*, 105221. [CrossRef]
42. Zhang, L.; Tao, Z.; Wang, G. Assessment and determination of earthquake casualty gathering area based on building damage state and spatial characteristics analysis. *Int. J. Disaster Risk Reduct.* **2022**, *67*, 102688. [CrossRef]
43. Feng, K.; Wang, T.; Liu, S.; Yan, C.; Kang, W.; Chen, X.; Guo, Z. Path analysis model to identify and analyse the causes of aeolian desertification in Mu Us Sandy Land, China. *Ecol. Indic.* **2021**, *124*, 107386. [CrossRef]

44. Weber, F.-A.; Hofacker, A.F.; Voegelin, A.; Kretzschmar, R. Temperature Dependence and Coupling of Iron and Arsenic Reduction and Release during Flooding of a Contaminated Soil. *Environ. Sci. Technol.* **2010**, *44*, 116–122. [CrossRef] [PubMed]
45. Stuckey, J.W.; Schaefer, M.V.; Kocar, B.D.; Benner, S.G.; Fendorf, S. Arsenic release metabolically limited to permanently water-saturated soil in Mekong Delta. *Nat. Geosci.* **2016**, *9*, 70–76. [CrossRef]
46. Asaf, L.; Nativ, R.; Hassan, M.A.; Shain, D.; Geyer, S.; Ziv, B. Influence of small- and large-scale variables on the chemical and isotopic compositions of urban rainwater, as illustrated by a case study in Ashdod, Israel. *J. Geophys. Res. Atmos.* **2005**, *110*, D11307. [CrossRef]
47. Vengosh, A.; Helvacı, C.; Karamanderesi, İ.H. Geochemical constraints for the origin of thermal waters from western Turkey. *Appl. Geochem.* **2002**, *17*, 163–183. [CrossRef]
48. Wang, Y.; Li, J.; Ma, T.; Xie, X.; Deng, Y.; Gan, Y. Genesis of geogenic contaminated groundwater: As, F and I. *Crit. Rev. Environ. Sci. Technol.* **2021**, *51*, 2895–2933. [CrossRef]
49. Bhattacharya, P.; Claesson, M.; Bundschuh, J.; Sracek, O.; Fagerberg, J.; Jacks, G.; Martin, R.A.; del Storniolo, A.R.; Thir, J.M. Distribution and mobility of arsenic in the Río Dulce alluvial aquifers in Santiago del Estero Province, Argentina. *Sci. Total Environ.* **2006**, *358*, 97–120. [CrossRef]
50. Guo, H.; Wen, D.; Liu, Z.; Jia, Y.; Guo, Q. A review of high arsenic groundwater in Mainland and Taiwan, China: Distribution, characteristics and geochemical processes. *Appl. Geochem.* **2014**, *41*, 196–217. [CrossRef]
51. Guo, X.; Fujino, Y.; Kaneko, S.; Wu, K.; Xia, Y.; Yoshimura, T. Arsenic contamination of groundwater and prevalence of arsenical dermatosis in the Hetao plain area, Inner Mongolia, China. *Mol. Cell. Biochem.* **2001**, *222*, 137–140. [CrossRef]

water

MDPI

Article

In Situ Pumping–Injection Remediation of Strong Acid–High Salt Groundwater: Displacement–Neutralization Mechanism and Influence of Pore Blocking

Fang Yuan [1], Jia Zhang [1], Jian Chen [2,*], Honghan Chen [1] and Samuel Barnie [3]

[1] Beijing Key Laboratory of Water Resources and Environmental Engineer, School of Water Resources and Environment, China University of Geosciences, Beijing 100083, China
[2] Chinese Academy of Environmental Planning, Beijing 100012, China
[3] Department of Water and Sanitation, University of Cape Coast, Cape Coast, Ghana
* Correspondence: chenjian@caep.org.cn

Abstract: Acid-polluted groundwater may cause many environmental problems due to its corrosivity. Pumping and injection technology is a commonly used remediation technology, and its main principles are displacement and neutralization. However, due to the high salinity in groundwater, blockage easily occurs and reduces the efficiency. The mechanism of pumping and remediation of strong acid–high salinity groundwater is unclear, and the mechanism and effect of pore blocking are unknown. In this paper, based on an actual polluted site, a field pumping test was carried out. Through groundwater monitoring and drilling core sampling, the process and mechanism of acid groundwater pumping–injection remediation were clarified, and the principle and impact of pore blockage are revealed. The results showed that increasing the injection pressure can effectively improve the repairing efficiency. When the pressure increased from 0.2 MPa to 0.3 MPa, the water injection efficiency per unit time was increased by more than 20%. The principle of pumping–injection remediation of acidic groundwater was mainly displacement, accounting for more than 93%, while neutralization only contributed less than 0.1%. Although the neutralization contribution was small, the neutralization interface of injected alkaline water and acidic groundwater was the main place for precipitation. The precipitation was mainly formed around the injection well, the amount of which decreases greatly with the increase in displacement distance. This was because the formation of precipitation required both an appropriate concentration of Fe and high pH (5.63). Affected by neutralization and dispersion, the pH of the acid–base water interface decreased and the necessary conditions for the formation of precipitation were not met. Therefore, in the actual pumping–injection restoration project, optimization can be carried out from two perspectives of appropriately increasing the injected water pressure and reducing the injected water pH. This study has important reference value for the control and remediation of such acid-polluted groundwater.

Keywords: pumping–injection; blocking; Fe precipitation; groundwater pollution

1. Introduction

Pump-and-treat (PAT) is one of the most widely used remediation technologies for contaminated aquifers [1–3], mostly implemented for the remediation of groundwater polluted with high concentrations of soluble pollutants, which can be very effective for source removal and plume control [4–7]. In a typical PAT system, contaminated groundwater is pumped from the aquifer and treated above ground, then injected back into the aquifer or discharged [8–10]. By contrast, the traditional technology with only extraction, the pumping–injection technology with the addition of injection wells, has a higher displacement efficiency for pollutants [11].

Strong acid–high salt polluted groundwater is mostly caused by chemical weathering [12,13], acid leakage, discharge of acidic mine wastewater and chemical wastew-

ater [14,15]. Acid groundwater pollution has been reported in the United States, South Korea, Australia, The Netherlands, etc. [16–18]. The Chemical Safety Clearing-house (CSC) system (https://CSC.me.go.kr, accessed on 7 August 2021), established by the Korean Ministry of Environment, reported that twenty-nine sulfuric acid leaks and eight hydrofluoric acid spills occurred between 2000 and 2018 [15]. In Australia, acid groundwater pollution caused by acidic soils is one of the major environmental and socio-economic problems [19]. Acid water enters the aquifer, increasing the dissolution of the aquifer medium that may significantly change the hydrogeological conditions [13], corrode aquiclude and cause cross-strata pollution, etc. The quality of the lower confined water is usually good and often used as a source of water supply; its pollution, therefore, may lead to greater environmental risks because its control and restoration is more difficult and costly. Therefore, increasing pH is the key to reducing the corrosiveness. Using the pumping–injection technology, injecting neutral or alkaline water combined with pumping for hydraulic control can achieve the purpose of rapidly increasing the pH of groundwater. However, acidic groundwater can dissolve minerals of the aqueous medium [20–23], resulting in a large amount of iron, aluminum, calcium, magnesium, etc. [15,24,25]. When the injected alkaline water contacts with the acid-polluted groundwater, the pH at the acid–base water interface rises rapidly, and the concentration of iron is also high, reaching the conditions for the formation of precipitation, which is easy-to-form iron oxide/hydroxide precipitation. The precipitation blocks the pores of the medium and reduces the permeability on account of the increased pH and high iron concentration [19,26]. It follows that when the pumping–injection technology is used to remediate acidic–high salt groundwater, it is easy to generate precipitation during the process of injecting alkaline water, reduce the permeability, decrease the effective influence radius and extend the repair time. From a summary of various studies, the causes of blockage can be summarized into three aspects. Firstly, hydrodynamic conditions, which is mainly the given water pressure during the water injection process [27,28]. Secondly, hydrochemical conditions, that is, differences in pH, iron concentration, etc., between injected water and polluted groundwater [29–32]. The last is the inherent permeability, particle size and porosity of the aqueous medium [33–35]. The increased injection pressure causes the higher hydraulic gradient, and the groundwater flow rate increases, resulting in a shorter residence time and less precipitation. At the same time, it can open up the water injection channel and increase the permeability, which will slow down the reduction in the water injection capacity caused by blockage. Differences in water quality between groundwater and injected water are also critical to the impact of injection. Previous studies have proposed the affinity theory between artificial recharge water and groundwater in aquifers, considered that injected water and original groundwater had good chemical affinity when chemical phases and soluble salt concentrations were similar and that the risk of problems, such as blockage and changes in water quality, was relatively small [29]. So, the chemical blockage usually formed by mineral precipitation mainly occurs in the front of the recharge water flow in the aquifer, that is, the mixed zone of groundwater and recharge water. For example, the blockage formed by iron precipitation often occurs near the infiltration zone [30]. The difference of the particle size and porosity of the aqueous medium has obvious influence on the blocking process and blocking degree [36,37]. For instance, in the injection of fine sand aquifers, the upper limit of the particulate matter content of the injection water quality was very low [37], while for sandy limestone aquifers with significant secondary pores, water with extremely high particulate matter content was continuously injected for 4 years [32]. Yan's research showed that in the same area, different wells have different rock and soil particle sizes in aquifers; the recharge was also different, and the coarser the particles, the better the recharge effect [38]. Huang conducted a laboratory injection experiment on two kinds of sand samples with particle sizes of 0.59 mm and 0.34 mm, respectively. The sand column with a smaller particle size was more likely to be blocked, while the sand column with a particle size of 0.59 nm had a longer duration of decrease in the permeability coefficient [39].

This study is based on a chemical-polluted site. The groundwater is strongly acidic, which may corrode the aquiclude and contaminate the lower confined water. Therefore, a combination of pump and injection technology is used to inject alkaline water to displace and neutralize the acidic groundwater, so as to achieve the purpose of rapidly increasing pH and eliminating environmental risks. The hydrochemical conditions of the study area are relatively stable with a good uniform aquifer medium, which is mainly aeolian sand. The pH of the groundwater in the heavily polluted area is 1~3 and the iron concentration is extremely high. The injected water quality remains stable, with a pH of 8~8.5. It is easy to produce iron precipitation during the water injection to block the pores and affect the pumping effect. The objective of this study is to explore the principle of the pumping–injection process and the reasons for pore blockage based on the partition and staged water injection pressure test. The research includes: 1. Variation in injection volume and dynamic displacement process of groundwater under different injection pressures; 2. the change in groundwater pH in different zones at different water injection stages; 3. the influence and mechanism of water injection pressure on the blocking degree of aqueous medium during displacement–neutralization restoration.

2. Materials and Methods

2.1. Study Site

The study site is located in the desert area of China. A factory there produced dye intermediates from 1998 to 2014. Groundwater pollution was caused by the discharge of wastewater to the outside of the factory. Sulfuric acid was one of the main raw materials. Therefore, the groundwater is strongly acidic, with a pH of 1~3.

2.1.1. Hydrogeology Conditions

The unconfined aquifer was mainly Quaternary silty-fine sand, and the water level was 13.9~19.7 m below the surface. The thickness was about 25 m with a permeability coefficient of about 3 m/d, while the porosity was about 0.2. The aquiclude was silty clay with a thickness of about 3 m. The minerals were dominated by clay minerals as well as calcite, dolomite, pyrite, etc., which easily react with acid and dissolve. The confined aquifer under the aquiclude was about 100 m thick with the interbedded pebble gravel and silty clay. The confined aquifer was a groundwater resource rich in amount and quality.

2.1.2. Characteristics of Groundwater Pollution

The polluted area of pH less than 3 was about 51,600 m^2 in the site. The study area is located in the heavily polluted groundwater area (Figure 1d) with strong acidity. Since the aqueous medium contained a large amount of iron-bearing minerals that can be easily dissolved by the acidic groundwater, this resulted in a high Fe concentration in the groundwater, up to 8900 mg/L.

According to the characteristics of groundwater acid pollution, the study area was set up in the area with the strongest acidity (pH < 3) (Figure 1b). The study area was about 1596 m^2, 42 m long and 38 m wide. It was divided into east and west, two areas by the injection well I1. The specific locations of injection wells, pumping wells and monitoring wells are shown in Figure 2. The pH of the observation wells W1~W6 on the western zone was 1.81~2.66, and the pH of the observation well E1 on the eastern zone was 1.2. The iron concentration in the western zone was 64.3~264.2 mg/L, and the concentration in the eastern zone was as high as 8880 mg/L. In order to control and remediate polluted groundwater, several pumping wells had been set up and extracted for 5 years on the site, but the increase in pH was extremely slow. According to the long-term monitoring well data of X3, the pH was still fluctuating between 0.4 and 1.4 (Figure S1). So, to solve the problem of acid groundwater corroding the aquiclude as soon as possible, a combination of pumping and injection to inject alkaline water was proposed in order to rapidly increase the pH and reducing environmental risks.

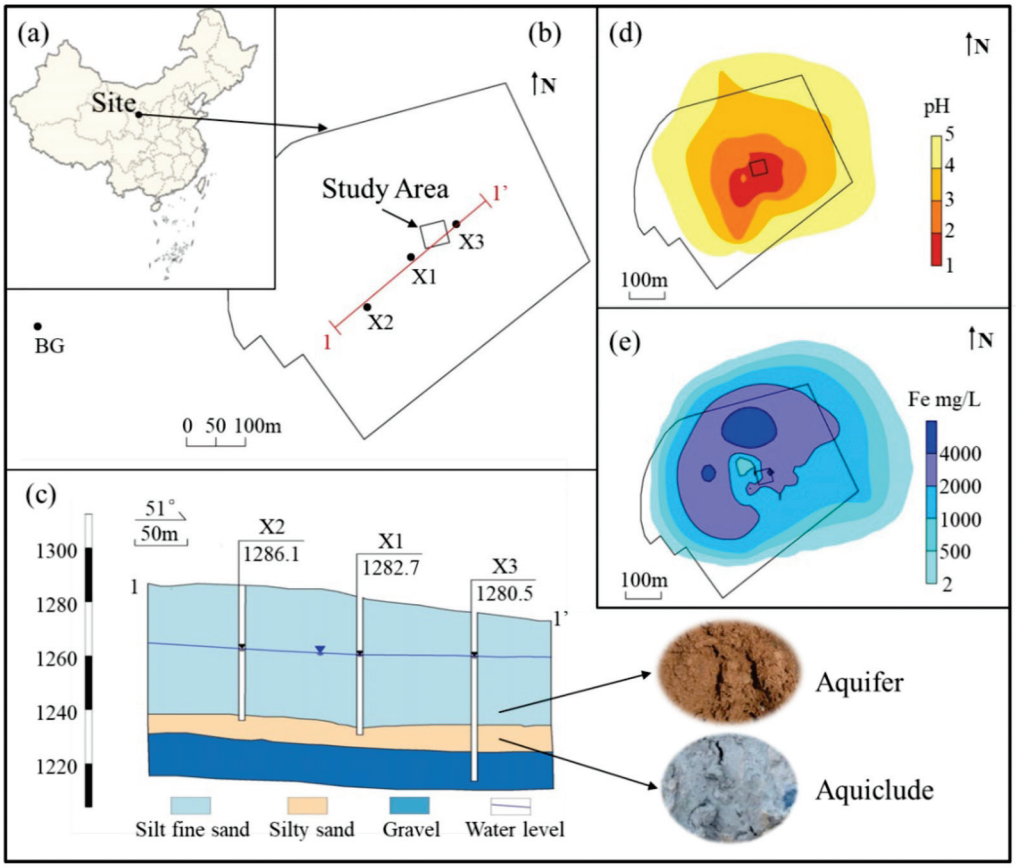

Figure 1. (**a**) The study site was located in the desert area of China. Rectangular in (**b**) is the study area, red line is the cross section and the background point (BG) is about 325 m upstream, west of the site; (**c**) is details of the hydrogeological section with phones of aquifer (silty-fine sand) and aquiclude (silty clay); (**d**,**e**) are the polluted range of H^+ and Fe, respectively.

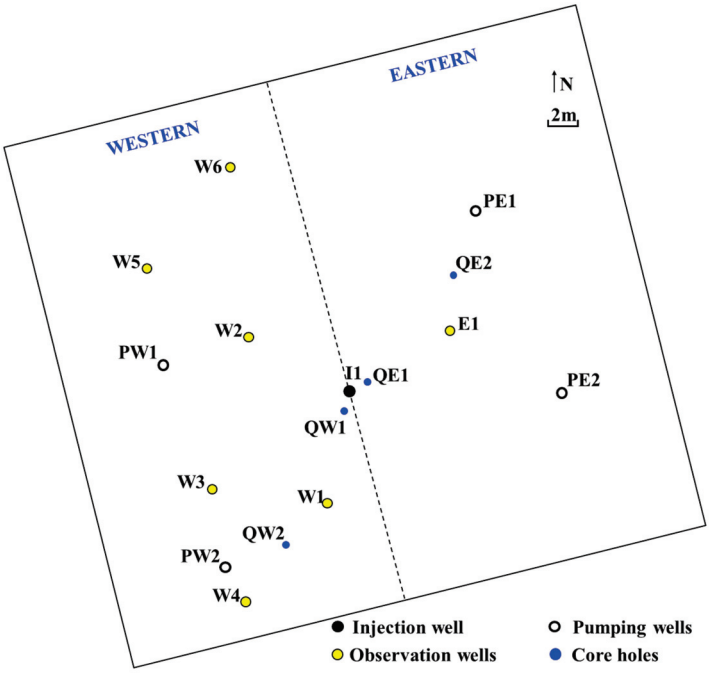

Figure 2. Layout of study area: the injection well I1 divided study area into eastern zone and western zone, with two pumping wells and several monitor wells in each zone.

2.2. Operational Details

2.2.1. Pump–Treat–Inject Process

The pump–treat–inject process is shown in Figure 3. Firstly, the acid-polluted groundwater with pH < 2 was extracted from the pumping well, and the Fe concentration was 912~2180 mg/L, then transported to the surface treatment system (Table 1).

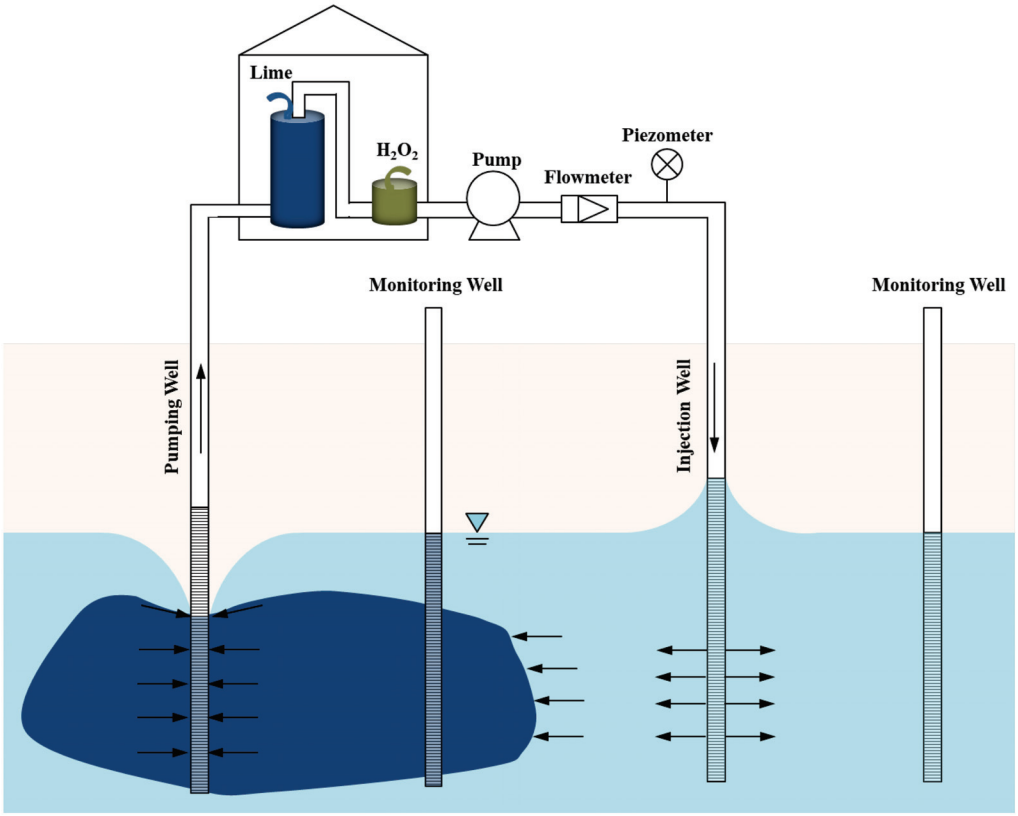

Figure 3. The acid-polluted groundwater was extracted from the pumping well, then transported to the surface treatment system and finally, injected back to the aquifer from the injection well. Changes in groundwater quality throughout the process were obtained from monitoring wells.

Table 1. Water quality of monitor wells, pumping and injecting water in the study area.

Index	Pumped Groundwater	Injection Water (Average Value)	Monitor Well						
			Western Zone						Eastern Zone
			W1	W2	W3	W4	W5	W6	E1
pH	1.29~1.8	8.5	2.15	2.24	2.03	1.81	2.57	2.66	1.2
Fe (mg/L)	912~2180	—	213.6	229.1	264.2	243.1	66.02	64.3	8880
COD (mg/L)	1249~4650	1610	820	94.5	1226.5	2287	320.5	311	9240
HAc (mg/L)	1050~3900	1560	728	520	1086	2130	290	280	8224
Distance to the injection well (m)			8	8.2	12.3	16.6	17.15	18.2	8.45

After adjusting the pH with lime milk, the pH of the effluent was stabilized at about 8.5, and the Fe formed precipitation as the pH was raised to alkaline, so the Fe concentration was lower than the detection limit. The precipitation in the treated groundwater was removed by pressure filtration. Finally, the treated groundwater was injected back into the aquifer from the injection well.

In addition, there was also chemical oxygen demand (COD) pollution in the groundwater. The COD concentration in the extracted groundwater was 1249~4650 mg/L. During

the treatment at the ground station, part of the organic matter was oxidized and removed by hydrogen peroxide, and the COD was reduced to about 1610 mg/L. The main component was acetic acid, which was difficult to oxidize by hydrogen peroxide. So, the main goal of this study was to increase the pH of groundwater so as to reduce the risk of acid groundwater corroding the aquiclude and avoid contaminating the underlying confined aquifer. Since acetic acid is less biologically toxic and can be used as a good carbon source by microorganisms and be gradually removed from the aquifer by natural attenuation, it will, therefore, not be discussed in depth in this study.

2.2.2. Experimental Process

The study area was divided into the eastern zone and the western zone by the center injection well (I1) (Figure 2), and there were two pumping wells, PW1 and PW2 and PE1 and PE2 at the two zones, respectively. (The distance to the water injection wells was 15 m, 13.3 m, 15.7 m and 15.1 m, respectively.) The open and close of the pumping wells on both sides can control the flow direction of the injected water. The pumping wells in the western zone (PW1 and PW2) were opened during the whole process, and the pumping wells in the eastern zone (PE1 and PE2) were opened on the 26th day. Therefore, most of the injected water flowed to the west in the previous stage. Combined with the injection pressure, the experiment was divided into 2 major stages (Table 2). The injection test lasted for 57 days and the total amount of water injected was 15,662 m^3. The pumping rate of PW1 and PW2 was about 3 m^3/h, of PE1 and PE2 was about 6 m^3/h and the total pumping volume was about 17,424 m^3.

Table 2. Water injection pressure, volume and pumping wells at each stage.

Stage	Stage 1			Stage 2	Total
	Stage 1.1	Stage 1.2	Stage 1.3		
Time	0~8th	9~19th	20th~30th	31st~57th	57 d
Injection pressure (MPa)	0~0.2	0.24~0.25	0.28~0.29	0.3~0.32	—
Injection volume (m^3)	2022	2783	2671	8186	15,662
Pumping wells		PW1, PW2		PW1, PW2, PE1, PE2	—

At the first stage (the first 30 days), in order to determine the relationship between the water injection pressure and the displacement efficiency, the step-by-step pressurization method was adopted for water injection, and the pressure was increased from 0 to 0.29 MPa in three steps. In order to study the change in injection rate and the effect on pH, as well as the change in the permeability of the 6 observation wells W1~6, which were set up at different distances (8 m, 8.2 m, 12.3 m, 16.6 m, 17.15 m, 18.2 m to the water injection wells, respectively) under different pressures.

The second stage was from the 31st to the 57th day, with a given pressure of 0.3 to 0.32 MPa. The aim of this stage was mainly to observe the operation of the eastern zone at a higher constant pressure. There was an observation well, E1 (8.45 m away from the water injection well), in the eastern zone. The displacement efficiency of the 1.1 stage of the western area was compared, that is, the attenuation of the injected water volume and the amount of precipitation.

2.3. Sample Collection and Analysis

2.3.1. Water Sample Analysis

During the test period, water samples from each monitoring well were taken regularly with Baylor tubes and then passed through a 0.25-micrometer filter membrane before testing. PH was measured on-site with a multiparameter water quality monitor (Manta, Eureka). COD was determined by a COD rapid analyzer (5B-3C, Beijing Lianhua Yongxing Technology Development Co., Ltd, Beijing, China). Fe was measured by inductively

coupled plasma emission spectroscopy (iCAP 7000, Thermo, Waltham, MA, USA) at a wavelength of 259.94 nm.

2.3.2. Core Analysis

In order to verify the occurrence of precipitation and compare the amount of precipitation of the different distance to the injection well at different zones, two coring holes were set up in the two zones, respectively (Figure 2), after the experiment. QW1 and QE1 were 1 m away from the injection well and QW2 and QE2 were 11.5 m away. A control point (OS) at the pH≈2 area outside the experimental area and a background point (BG) were set. About 1 m of core was taken at the upper, middle and lower depths of the aquifer at each point, respectively, and mixed evenly. Then, 1 mol/L HCl was used to extract the iron precipitate on the core surface referring to the BCR leaching method for heavy metal acid soluble state [40]. Since 1 mol/L HCl cannot completely dissolve all iron minerals on the aqueous medium in a short period of time, this part of the dissolution can be considered as the less stable secondary iron-bearing minerals that were used to characterize the precipitation amount on the aqueous medium surface during the experiment. A total of 20 mL of 1 mol/L HCl and 10 g of core in 40 mL were put in a brown reagent bottle, and then, we placed the bottle on a 25 °C shaker and shook it for 16 h at 200 rmp. After sampling, it was passed through a 0.25-micrometer filter membrane to measure Fe. The test method is the same as that described in 2.3.1. The core surface topography was analyzed by cold field emission scanning electron microscopy (S-4800, Hitachi, Japan).

2.4. Analysis of the Data

2.4.1. Breakthrough Time

The migration process from injection wells to pumping wells and monitoring wells is a typical convective diffusion process. The solute concentration in observation wells and pumping wells showed an s-shaped upward trend [41]. The time from the start of injection to the solute concentration increase (or decrease) to 50% of the stable value is defined as the injected water migration to the monitoring well, which is recorded as t_a. The midpoint of the concentration of the breakthrough curve is only determined by the convection process and is not affected by the dispersion effect, so the particle convection process is identified by obtaining the time corresponding to this midpoint [42]. A representative S-type curve Boltzmann function is chosen for C–t series fitting to calculate the time t_a [42,43].

$$C = \frac{C_1 - C_2}{1 + exp\left(\frac{t - t_a}{d_t}\right)} + C_2 \quad (1)$$

C_1 is the initial concentration before injection (mg/L), C_2 is the concentration in the observation well after injection increase/decrease to a stable value (mg/L), t_a is the center of the curve (d) and d_t is the time constant.

2.4.2. Neutralized H^+ Content

During the injection, H^+ in the groundwater was consumed by neutralization with injected water. This amount of H^+ can be calculated according to the OH^- concentration of injected water and the difference in OH^- concentration when it reached the observation well. The time difference between the breakthrough time of COD and pH in the observation well was the time used for neutralization that can be calculated by the following formula:

$$t_{ne} = t_{pH} - t_{COD} \quad (2)$$

$$\mu = \frac{S}{t_{COD}} \quad (3)$$

$$q_n = \mu t_{ne} LMn(C_I - C_a) \quad (4)$$

T_{ne}, t_{COD}, and t_{pH} are neutralized time, breakthrough time of COD and pH in the observation well (d), μ is actual velocity of groundwater (m/d), q_n is the amount of neutralized H^+ (mol), S is the distance between observation well and injection well (m), L is the length of the water-passing section at the observation well in the equilibrium area (m) (using the numerical simulation method to construct a numerical model and based on the particle tracking module, acquire the streamline of each equilibrium zone, thereby the length of the water-passing section is obtained), M is the thickness of aquifer thickness (the site aquifer thickness is 25 m), n is porosity (0.2) and C_I and C_a are the OH^- concentration of the injected water and the OH^- concentration of the observation well breakthrough, respectively (mol/L).

2.4.3. Extracted H^+ Content

The amount of extracted H^+ is calculated by the equilibrium method. The area surrounded by the streamline from each pumping well to the injection well obtained by the numerical model is an equilibrium area. The time for the injected water breakthrough to the pumping well is an equilibrium period. The amount of H^+ extracted in each equilibrium zone can be calculated according to the volume of water pumped and the H^+ concentration of the extracted water using the following formula:

$$Q_P = Q_{OS} + Q_{IN} \tag{5}$$

$$Q_p C_P = Q_{OS} C_{OS} + Q_{IN} C_{IN} \tag{6}$$

The proportion of the injected water in the equilibrium area of the pumped water:

$$x = \frac{Q_{IN}}{Q_P} = \frac{C_{OS} - C_p}{C_{OS} - C_{IN}} \tag{7}$$

The amount of extracted H^+ is:

$$x = \frac{Q_{NN}}{Q_P} \frac{C_{OS} - C_p}{C_{OS} - C_{IN}} \tag{8}$$

Q_P is the pumping volume of the pumping wells in the equilibrium zone (L); Q_{OS} and Q_{IN} are the volume of water entering the pumping well from outside and inside the equilibrium zone, respectively, (L), C_P, C_{OS} and C_{IN} are the H^+ concentration of the pumping well, outside the equilibrium zone and inside the equilibrium zone, respectively, (mol/L), and q_P is the amount of extracted H^+ (mol).

3. Results and Discussion

3.1. Displacement of Acidic Groundwater by Injected Water

3.1.1. Water Injection Process

In stage 1 (the first 30 days), in order to study the relationship between the water injection pressure and displacement efficiency, the injection was carried out in a step-by-step pressurization method (Figure 4), and the pressure was increased from 0 to 0.29 MPa in three steps. The pumping wells PW1 and PW2 on the western zone were opened, and PE1 and PE2 on the eastern zone were closed, so most of the injected water flowed to the west side. The pressure in stages 1.1 to 1.3 gradually increased and the initial injection rates were 11.82 m^3/h, 11 m^3/h and 10.3 m^3/h, respectively. The injection rate in the first two stages gradually decreased with time and was basically stable in the 1.3 stage. The injection rate (q) and time (t) were fitted with linear equation and the slope was the decay rate of each stage (Text S1). The decay rates of the three stages were 0.33, 0.1 and 0.008, respectively, indicating that with the increase in pressure and the injected water flow to the periphery, the decay rate decreased. In stage 2 (31~57 days), the injection pressure was high and stable. Due to the opening of the eastern zone's pumping wells and the high injection pressure, the injected water mainly flowed to the east side and the initial injection rate

increased to 15.53 m^3/h, which was significantly higher than that in the 1.1 stage. However, as the injection progressed, the injection rate also decreased linearly with a decay rate of 0.30, slightly less than the 1.1 stage. Stage 1 injected 7476 m^3 of water in 30 days and stage 2 injected 8186 m^3 of water in 27 days. Although the decay rate gradually decreased with the gradual pressurization, the decay rate of stage 2 was similar to that of stage 1.1, but due to the large initial flow rate, the total injection volume was still higher than that of stage 1, and the per unit time water injection efficiency was improved by more than 20%.

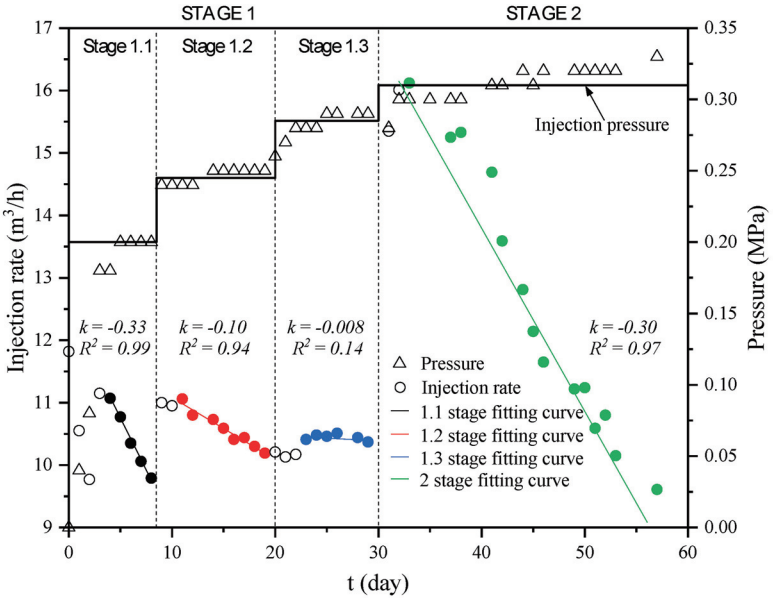

Figure 4. Injection rate and its *q*–*t* fitting curve under different pressure at each stage.

The decrease in the initial injection rate and the injection volume at each stage may be caused by the decrease in permeability of the aquifer. The groundwater was acidic with a pH of less than 3, while the injected water was alkaline with a pH of about 8.5, which led to the increase in pH in the groundwater. Due to the high iron concentration in groundwater, precipitation was easy to generate when pH rose and the precipitation deposited in the pores of the aquifer, causing blockage and poor permeability. However, as the injected water flowed to the periphery and the injection pressure increased, the water-passing section became wider and the groundwater flow rate was faster. The faster flow rate shortened the residence time and reduced the amount of precipitation. At the same time, the cross-section of water increased, less precipitation was distributed to each pore and the injection rate decay was gradually reduced. The initial injection rate of stage 2 was high mainly because most of the water flowed to the east side where the degree of blockage was low and the groundwater flow rate was faster when the pressure was high, so the neutralization time was shortened, resulting in the precipitation being slightly less than in the 1.1 stage. As the injected water's pH increased, the precipitation gradually formed and the injection rate decreased.

3.1.2. Flow and Dispersion Process of Acidic Groundwater

The displacement process of injected water to groundwater can be characterized by the change in the COD concentration of observation wells at different distances. This was mainly due to the large difference in COD concentrations between injected water and groundwater. Additionally, the pollutants, such as acetic acid represented by COD, mainly flow and disperse. In the process of groundwater displacement, pollutants, such as acetic acid represented by COD, were mainly migrating by convection and dispersion. Therefore, the migration of injected water and polluted acidic groundwater can be reflected by observing the change in COD concentration with time at the monitoring well.

With the progress of water injection, the COD concentration of the observation well on the western zone gradually increased (Figure 5), and the COD concentration of the observation well on the eastern zone quickly decreased to the injected water concentration after the pumping well on the eastern zone was opened (26 d). The COD concentration–time series was fitted with the Boltzmann function, and the midpoint of the concentration was the breakthrough time (t_{COD}) of the injected water (Table S1, Figure S1), which can reflect the flow process. The injected water migrated to W1 and W2 on the 5~6th day, to W3, W4 and W5 on the 11~20th day, and to W6 and E1 on the 21.82nd to the 26.5th day, respectively. Fitting of the actual breakthrough time (t_{COD}) and migration distance of injected water was conducted and then compared with the theoretical migration curve. (See Table S2 for details.) The numerical simulation method was used to build a numerical model (Text S2). The water level data were extracted from the model and divided to acquire the hydraulic gradient of each subdivided unit. The migration velocity and migration time of each unit were calculated according to the permeability coefficient and the pumping test before the experiment. The theoretical migration curve was obtained by fitting the time and migration distance according to the unchanged permeability coefficient and did not take precipitation into account. The fitting curve of actual breakthrough time is on the right side of the theoretical migration curve, indicating that the actual breakthrough time lags behind the theoretical value and the farther the distance is, the longer the lag time is (Figure 5b). The actual migration time was used to calculate the migration velocity (Table S3), and the velocities of the two observation wells at different distances in the same radial direction were compared. The speed of migration from injection well I1 to W1 was 1.62 m/d, from W1 to W4 was 0.71 m/d, from I1 to W2 was 1.44 m/d and from W2 to W5 was 0.63 m/d. This demonstrated that the farther the injected water diffused, the lower the hydraulic gradient, and the longer the distance, the slower the migration speed. With the progress of injection, the rate of COD concentration increased/decreased, and injected water concentration in each observation well was also different. It rose faster to the stable concentration at closer observation wells due to the dispersion effect, and the farther the distance, the longer the dispersion. When injected water migrated to W1 and W2, the dispersion was only 6~7 cm, while it migrated to 16~17 m when the dispersion was about 1.5 m. In addition, the increase in pressure can also slow down the dispersion effect, so the COD concentration of E1 decreased from breakthrough to stable faster than W1 and W2.

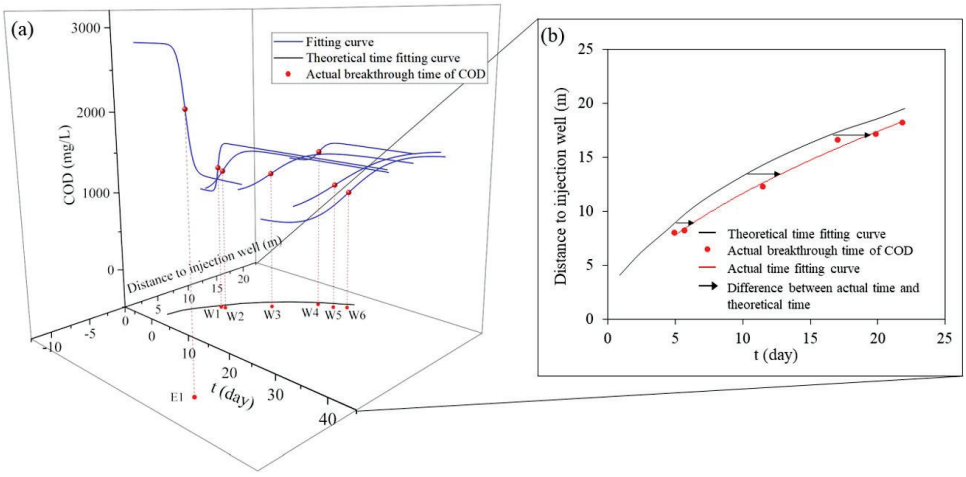

Figure 5. (**a**) COD concentration and time fitting curve of observation wells at different distances from injection wells and projection of actual breakthrough time on the two-dimensional plane. (**b**) Actual breakthrough time and its fitting curve compared to theoretical time fitting curve.

3.1.3. Attenuation of Permeability of Aqueous Medium

According to the numerical simulation results, water level data were extracted. W1~W4 and W2~W5 were two sets of observation wells in the same radial direction, respectively.

According to the actual velocity and water level data, the permeability coefficients of I1~W1 and W1~W4 were 1.4 m/d and 2.59 m/d, respectively, and the permeability coefficients of I1~W2 and W2~W5 were 1.33 m/d and 2.48 m/d, respectively (Table S3). It follows that the permeability coefficient near the water injection well reduced significantly, while the permeability of the farther area decreased less, indicating that the blockage was mainly generated in the area close to the injection well.

3.2. Displacement–Neutralization Process of Acidic Groundwater

3.2.1. Dynamic Variation of Groundwater pH

In order to observe the displacement–neutralization process of acidic groundwater, the observation of pH in the observation wells was carried out, and the results are shown in Figure 6. The change characteristics of pH were similar to COD in general. The closer the distance was, the earlier the breakthrough time was and the faster it was to stabilize. The pH of monitoring wells all gradually increased to more than 4.5 (Figure 9). The H^+ of the W1 that was close to the injection well was 4.57 mol/L on the 6th day and rapidly decreased to about 0.1 mol/L on the 10th day, and the final pH was about 6.5 (Figure S2). On the other hand, the H^+ of the farther observation well W5 was 2.29 mol/L on the 29th day and decreased to 0.15 M in 37 days with a final pH of around 4.5.

The pH did not rise to the same level as the injected water because of the neutralization of the medium that consumed OH^- during the migration of the injected water. The farther the migration, the more OH^- was consumed, so the pH of the farther observation wells increased less. As the injected water migrated, an acid–base water neutralization interface formed as a result of the dispersion with groundwater. The pH of the injection well side was high, while the pH of the groundwater side was low, and the pH gradually decreased from the injection water side to the groundwater side. The interface gradually migrated to the periphery with the injection process. The farther the migration, the longer the dispersion distance, and the larger the interface width, the slower the pH rise will be.

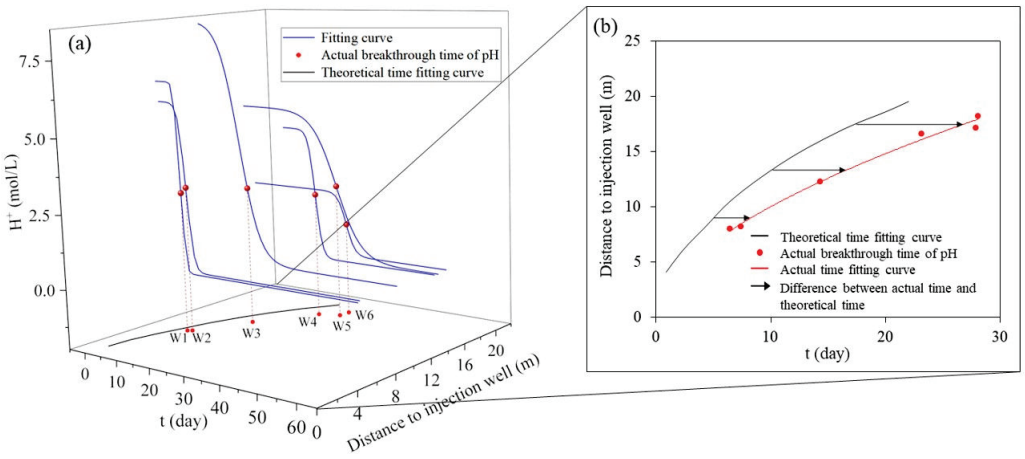

Figure 6. (**a**) The pH and time fitting curve of observation wells at different distances from injection wells and projection of actual breakthrough time on the two-dimensional plane. (**b**) The pH actual breakthrough time and its fitting curve compared to theoretical time fitting curve.

3.2.2. Neutralization Amount of H^+ in Groundwater

Although the overall trend of pH was basically the same as that of COD in each monitoring well, the time pH rose obviously lagged behind that of COD (Figure 7). This may be because of the neutralization between the acidic groundwater and injected water consuming the H^+ and OH^- at the acid–base water interface. The time difference was the neutralization time. A numerical simulation method was used to build a numerical model to calculate the amount of neutralized H^+. Based on the particle tracking module, four equilibrium zones were determined, named PW1, PW2, PE1 and PE2, respectively (Text S2). According to the envelope of each equilibrium area, the length of the water-passing section

of each observation well can be obtained. Combined with the groundwater flow rate, the H^+ neutralization amount can be calculated (Table S4).

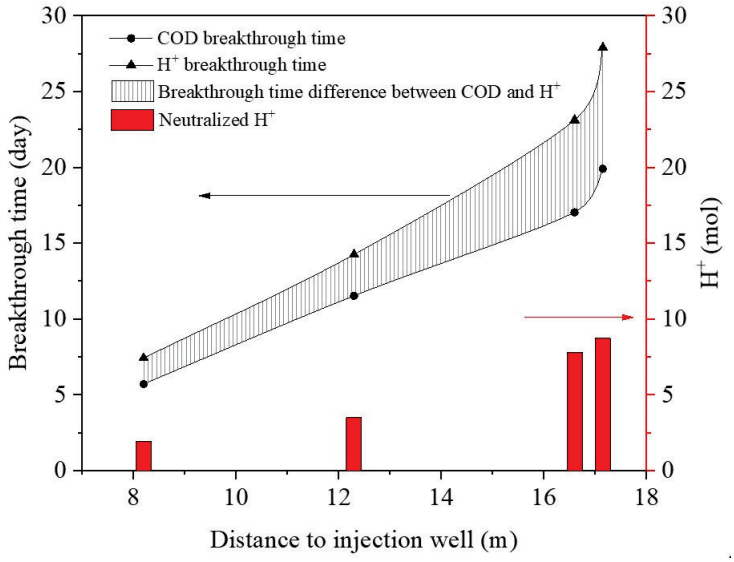

Figure 7. The breakthrough time difference between COD and pH, and the amount of H^+ neutralization in the western zone of different distances to injection well.

As the injected water moved outward, the farther the observation wells in the west area were, the longer the neutralization time was, and the amount of neutralized H^+ gradually increased (Figure 7). From W1 to W5, the amount of H^+ neutralization increased from 1.95 mol to 8.72 mol. The neutralization time of E1 in the eastern zone was slightly shorter than the observation wells W1 and W2 of the approximate distance in the western zone, indicating that the increase in pressure was beneficial to shorten the neutralization time and reduce the amount of H^+ neutralized. The neutralized H^+ amounts of PE1 and PE2 in the eastern zone were 1.67 mol and 5.23 mol, respectively, and PW1 and PW2 in the western zone were 8.72 mol and 7.81 mol, respectively. From this, it can be speculated that the neutralization amount and precipitation amount in the eastern zone were less than the western zone.

3.2.3. Equilibrium Analysis of H^+ in Groundwater

On the basis of the H^+ neutralization amount analysis, the displacement amount of H^+ in groundwater will be further counted and the equilibrium analysis of H^+ in groundwater will be carried out. The four equilibrium zones are shown in Figure 8. The equilibrium period was calculated as the injected water migrated to the pumping well; that is, the groundwater in the equilibrium zone was completely displaced once. The balance item of each zone mainly includes the groundwater volume extracted from the equilibrium zone, outside the zone and the total pumped water. The calculation method and process of each equilibrium item are shown in the Supplementary Materials.

After the start of the injection experiment, the pH of the pumping wells also gradually increased. Before that, according to the long-term monitoring data of the pumping well in the heavily polluted area, the pH remained basically stable for a long time (Figure S3), and the pH was as low as about 1. Since the pH of the study area was slightly higher than that of the outside after the start of water injection, the proportion of the water extracted in the study area increased, so the pH of the pumping wells increased. When the injected water had completely displaced the groundwater of the equilibrium zone, the pumping wells extracted the low-pH groundwater outside the study area and the injected water at a stable ratio, and then the pH rose to a stable level. Taking the initial pH of the pumping well as the pH of the outside and the pH in the stable state as the pH in the equilibrium

zone, the H^+ amounts extracted from the equilibrium areas of PW1, PW2, PE1 and PE2 were 8085.62 mol, 25,049.46 mol, 27,048.87 mol and 29,433.67 mol, respectively (Table 3).

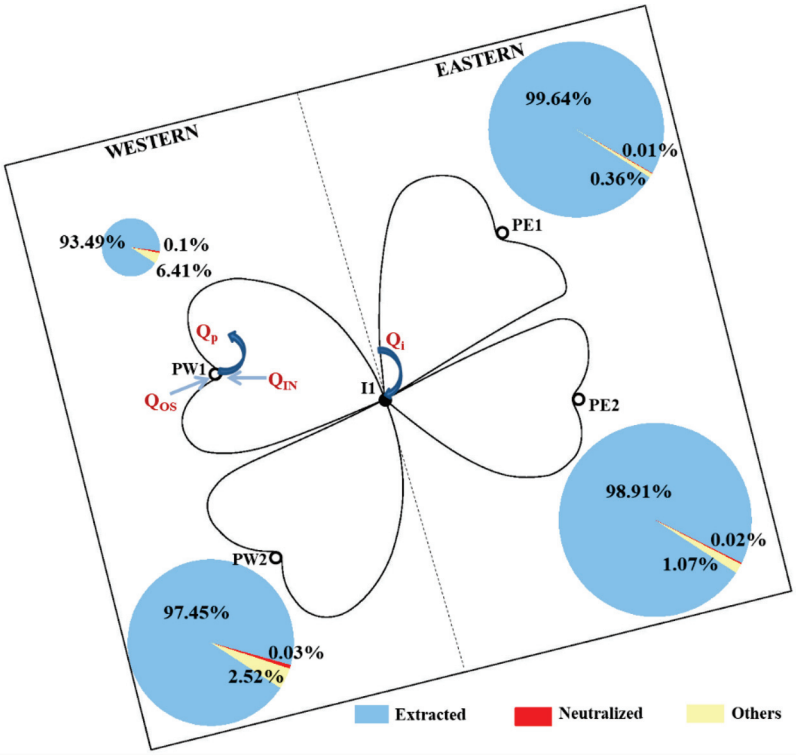

Figure 8. The displacement, neutralization and other proportions of H^+ in each equilibrium area (the size of the circle represents the total amount of H^+).

Table 3. Neutralized, extracted and other part amounts and proportion of H^+ in each equilibrium area.

Equilibrium Area	Total (mol)	Neutralized		Extracted		Others	
		Amount	Proportion (%)	Amount	Proportion (%)	Amount	Proportion (%)
PW1	8648.69	8.72	0.10	8085.62	93.49	554.34	6.41
PW2	25,705.49	7.81	0.03	25,049.46	97.45	648.22	2.52
PE1	27,146.96	1.67	0.01	27,048.87	99.64	96.42	0.36
PE2	29,756.84	5.23	0.02	29,433.67	98.91	317.95	1.07

According to the envelope area and interpolation calculation results of each equilibrium zone, the total amount of H^+ in each zone was 8648.69 mol, 25,705.49 mol, 27,146.96 mol and 29,756.84 mol, respectively. The extracted amount from each equilibrium zone accounts for more than 93% of the total. Neutralization accounted for less than 0.2%. The rest is due to calculation errors and other parts, such as residuals on the medium, accounting for 0.3~7%. It can be seen that the pH increase in each zone was mainly due to the displacement of injected water.

Although the proportion of neutralization was small, it was the neutralization that obviously led to the reduction in permeability, thereby reducing the efficiency of injection–extraction, which had become an important restrictive factor for the restoration project and cannot be ignored. It is necessary to develop the mechanism analysis and optimized design of adsorption engineering process parameters for the blocking problem.

Above all, the main principle of the pumping–injection process is the displacement process, which plays a major role in the remediation process. In addition, the neutralization of the acid–base water contact will also increase the pH, which is the secondary contribu-

tion. Therefore, the remediation mechanism of this site is the displacement–neutralization mechanism.

3.3. Blocking Mechanism

3.3.1. Iron Concentration

The iron concentration of each monitoring well gradually decreased due to the displacement of the injected water. The iron of observation wells W1~3, which were closer to the water injection well, were lower than the detection limit when the pH rose to about 5.63 (Figure 9), indicating that under the hydrochemical conditions of this site, iron began to precipitate at this pH. Then, the slow pH rise may be caused by the precipitation of iron hydrolysis and the supply of H^+ [11]. When the pH of W4 was 3.22, the iron decreased to 0.286 mg/L and the pH was always lower than 5.63, which did not meet the conditions for precipitation, and the iron concentration finally dropped to undetectable levels because the injected water completely displaced the groundwater. However, the pH of W5~6 did not reach 5.63, iron was still detected in a certain amount after the injected water was displaced completely and the concentration was relatively stable, which may be due to the continuous desorption of iron adsorbed on the medium.

$$Fe^{3+} + H_2O \rightarrow FeOH^{2+} + H^+ \quad (9)$$

$$Fe^{3+} + 2H_2O \rightarrow FeOH_2^+ + 2H^+ \quad (10)$$

$$Fe^{3+} + 3H_2O \rightarrow Fe(OH)_{3(s)} + 3H^+ \quad (11)$$

$$Fe^{3+} + 2H_2O \rightarrow Fe(OOH) + 3H^+ \quad (12)$$

According to the change in iron concentration combined with the law of pH increase, it can be seen that 5.63 is the critical pH at which precipitation occurs. The closer to the injection well the narrower neutralization interface (Table S5) was, the faster the pH increased (Figure 10) and soon rose to above 5.63, while the iron concentration was still high enough to produce precipitation. Therefore, the closer to the injection well, the greater the amount of precipitation was. Whereas, in the area far from the injection well, pH could not rise to the critical pH of 5.63 due to the neutralization of the medium along the process, and as the neutralization interface is wide, the pH rose slowly. When the pH was still low, the iron concentration dropped to a very low concentration owing to the displacement of injected water and the conditions for precipitation were not met. With the increased injection pressure, the precipitation interface gradually expanded. In stage 1.1, the injection rate reduced linearly, indicating that the precipitation had been formed. After pressurization in stage 1.2, the velocity of groundwater increased and promoted the outward migration of injected water simultaneously, the precipitation interface around the injection well expanded outward and continued to generate precipitation and the injection rate decreased again. However, in stage 1.3, it continued to increase the pressure and the injection rate was basically stable. This was because the injected water diffused farther and the pH could not rise to 5.63, while the iron had dropped to a very low concentration that could not produce precipitation. So, the permeability of the aquifer did not change, and the flow rate was basically stable. In stage 2, the pressure increased and most of the water migrated to the east. Due to the formation of precipitation, the injection rate also dropped linearly, and the decay rate was slightly lower than that in stage 1.1, indicating that the pressure increase can slightly reduce the production of precipitation.

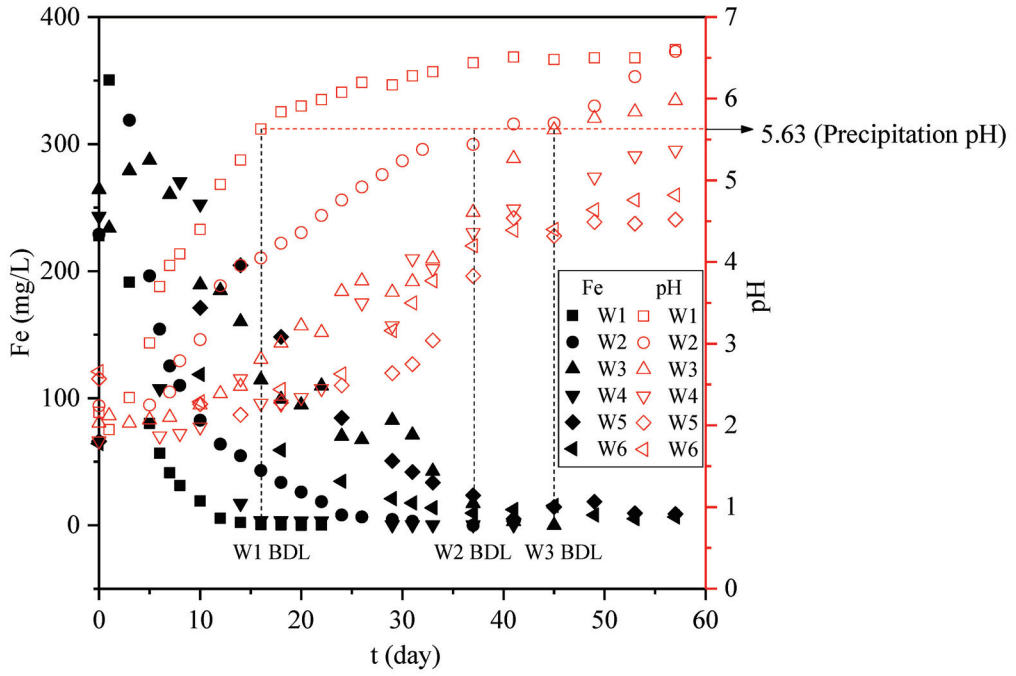

Figure 9. Concentration of Fe and pH in each observation well (BDL is Below Detection Limit).

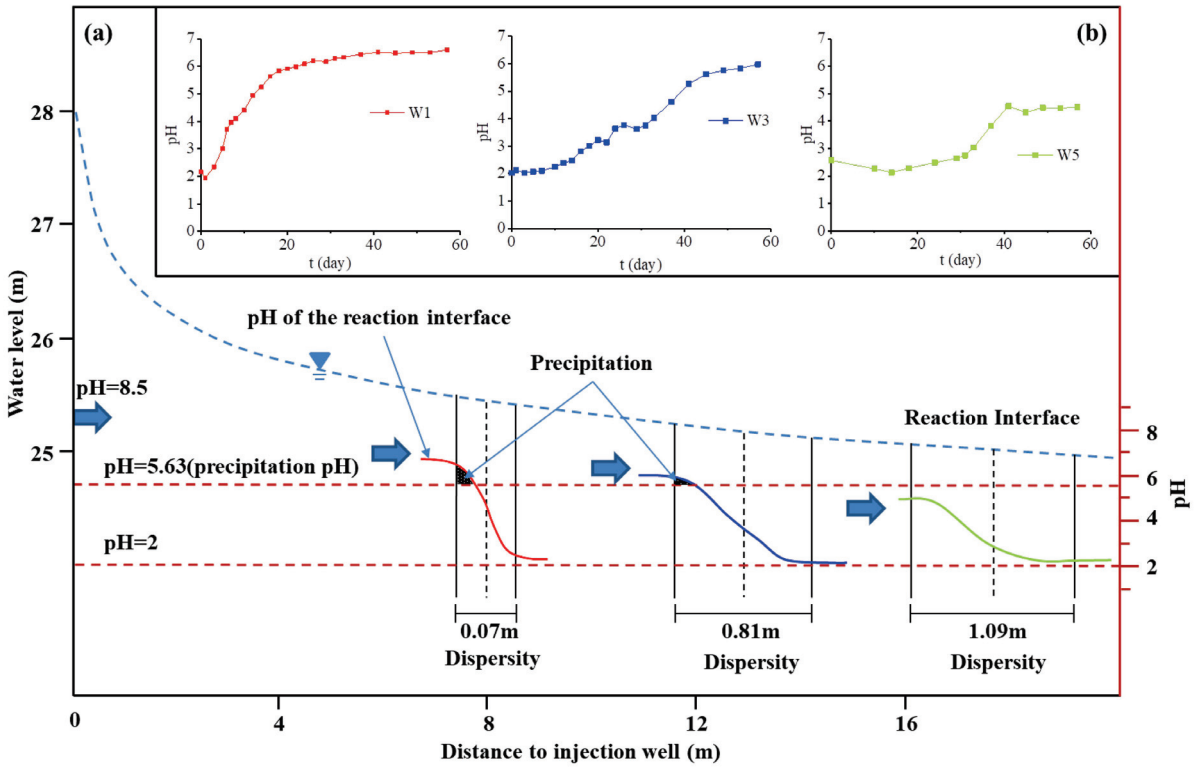

Figure 10. The migration process of the neutralization interface gradually moved away from the injection well (**a**) and its pH changes and precipitation at different distances (**b**). (Water level is the relative water level elevation that the elevation of the aquiclude is set to 0).

3.3.2. Mineralogical Analysis

After the test, cores were taken from the eastern zone, western zone, the control point OS (areas with pH ≈ 2 outside the study area) and the background point BG. HCl was used to dissolve the iron precipitation on the core surface, and we compared the amount of

iron precipitation in the area close to the injection well (1 m) and the area far away (11.5 m) of the two zones.

Fe dissolved in the two points CW1 and CE1 near the injection well in the study area was about 3000 mg/kg, which was significantly higher than the 162.8 mg/kg of OS (Figure 11). The Fe content of CW1 in the western zone was slightly higher than that of CE1 in the eastern zone. The Fe content of CW2 and CE2 at the two points far from the injection well were similar to that of OS and less than BG. Due to the difference in the content of iron-bearing minerals and dissolution on the surface of the medium, it can be seen that the iron precipitation at these two points was either very small or no precipitation was generated. Combined with the previous judgment, a small amount of precipitation occurred in the western zone far from the injection well. In summary, aquifer medium near the water injection well was covered by a large amount of iron precipitation, so a large amount of Fe was dissolved by HCl, while the amount of precipitation far away was very small. The precipitation in the east area was slightly less than that in the west, indicating that high injection pressure can reduce the formation of precipitation.

Comparing the surface topography of the two points CW1 and CW2 in the western zone, the outside point OS and the background point BG indicated that compared with BG under natural conditions, the surface of the medium became significantly uneven in the acidic environment. Additionally, some floccule obviously attached to the surface of the medium in the study area, while there were more on the surface of the point close to the injection well, which also showed that there is more precipitation closer to the well.

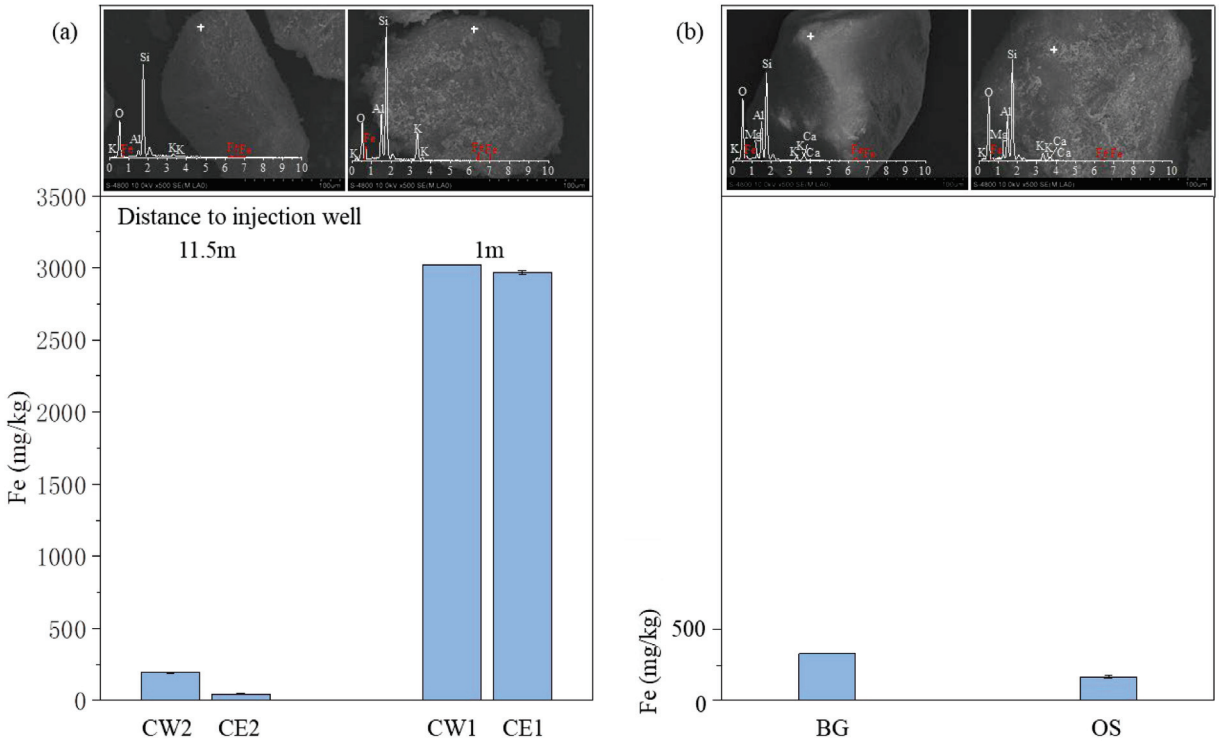

Figure 11. (**a**) Surface topography and Fe content of the core of two coring holes at 1 m and 11.5 m to injection well, respectively, compared with (**b**) the background point BG and the control point OS.

4. Conclusions

This paper was based on an acidic–high-iron-polluted site. Through a partition and staged water injection pressure experiment, we injected water with a pH of about 8.5 in a heavily polluted area with a groundwater pH of 1~3, and groundwater was pumped around to explore the remediation effect and influencing factors. The results showed that in the case of step-by-step pressurized water injection, the permeability was reduced due to the formation of precipitation, and the initial injection rate, injection volume and decay rate

at each stage were decreased. The increase in pressure can slightly reduce the generation of precipitates. When the pressure increased from 0.2 MPa to 0.3 MPa, the water injection efficiency per unit time was increased by more than 20%. The principle of pump–injection remediation of acidic groundwater was mainly displacement, accounting for more than 93%, while neutralization only contributed less than 0.1%. Although the neutralization contribution was small, the neutralization interface was the main place for precipitation, which was the important constraint factor for the restoration project and cannot be ignored. The acid–base water neutralization interface was formed owing to the dispersion. The closer to the water injection well, the narrower the neutralization interface, the pH rising rapidly and the iron concentration being high result in more iron precipitation. In the area far from the injection well, pH did not rise to the condition to generate precipitation due to the neutralization of the medium along the process, and the iron concentration dropped to a very low concentration, so the conditions for precipitation were not met.

Supplementary Materials: The following supporting information can be downloaded at: https://www.mdpi.com/article/10.3390/w14172720/s1, Text S1: Linear fitting formula for injection rate and time of each stage, Text S2: The groundwater numerical simulation software groundwater model system (GMS) was used to simulate the seepage field of the experimental area, Text S3: Calculation of Dispersion, Table S1: The breakthrough times of COD, H+ and neutralization times obtained by fitting the C-t sequence with the Boltzmann function, Table S2: Theoretical time of each section according to the numerical model, Table S3: Actual migration velocity (μ) and permeability coefficient (K) after water injection of two sections in the same radial direction with different distances from the injection well, Table S4: Calculation of neutralized H+ in each equilibrium area, Table S5: Dispersion at each observation well, Figure S1: COD~t fitting curves of monitor wells, Figure S2: pH~t fitting curves of monitor wells, Figure S3: pH data of monitor well X1 and long-term pumping wells P1 and P2 in the site. Reference [44] is cited in the Supplementary Materials.

Author Contributions: Conceptualization, F.Y. and J.Z.; Methodology, F.Y., J.Z., H.C. and J.C.; Investigation, S.B. All authors have read and agreed to the published version of the manuscript.

Funding: This work was supported by National Key R&D Program of China [grant number 2018YFC1800400]; and National Science and Technology Major Project in the 13th Five-Year Plan Period [grant number 2016ZX05040-002-003-001].

Institutional Review Board Statement: Not applicable.

Informed Consent Statement: Not applicable.

Data Availability Statement: Not applicable.

Acknowledgments: The authors would like to thank the editor and reviewers for their constructive and valuable comments and suggestions, which significantly improved the quality of this work.

Conflicts of Interest: The authors declare no conflict of interest.

References

1. Güngör-Demirci, G.; Aksoy, A. Variation in time-to-compliance for pump-and-treat remediation of mass transfer-limited aquifers with hydraulic conductivity heterogeneity. *Environ. Earth Sci.* **2010**, *63*, 1277–1288. [CrossRef]
2. Ciampi, P.; Esposito, C.; Cassiani, G.; Deidda, G.P.; Rizzetto, P.; Papini, M.P. A field-scale remediation of residual light non-aqueous phase liquid (LNAPL): Chemical enhancers for pump and treat. *Environ. Sci. Pollut. Res.* **2021**, *28*, 35286–35296. [CrossRef] [PubMed]
3. Antelmi, M.; Renoldi, F.; Alberti, L. Analytical and Numerical Methods for a Preliminary Assessment of the Remediation Time of Pump and Treat Systems. *Water* **2020**, *12*, 2850. [CrossRef]
4. Truex, M.; Johnson, C.; Macbeth, T.; Becker, D.; Lynch, K.; Giaudrone, D.; Frantz, A.; Lee, H. Performance Assessment of Pump-and-Treat Systems. *Groundw. Monit. Rem.* **2017**, *37*, 28–44. [CrossRef]
5. Park, Y.-C. Cost-effective optimal design of a pump-and-treat system for remediating groundwater contaminant at an industrial complex. *Geosci. J.* **2016**, *20*, 891–901. [CrossRef]
6. Matott, L.S.; Rabideau, A.J.; Craig, J.R. Pump-and-treat optimization using analytic element method flow models. *Adv. Water Resour.* **2006**, *29*, 760–775. [CrossRef]

7. Thornton, S.F.; Baker, K.M.; Bottrell, S.H.; Rolfe, S.A.; McNamee, P.; Forrest, F.; Duffield, P.; Wilson, R.D.; Fairburn, A.W.; Cieslak, L.A. Enhancement of in situ biodegradation of organic compounds in groundwater by targeted pump and treat intervention. *Appl. Geochem.* **2014**, *48*, 28–40. [CrossRef]
8. Bortonea, I.; Ertob, A.; Nardoc, A.D.; Santonastasoc, G.F.; Chianesec, S.; Musmarrac, D. Pump-and-treat configurations with vertical and horizontal wells to remediate an aquifer contaminated by hexavalent chromium. *J. Contam. Hydrol.* **2020**, *235*, 103725. [CrossRef]
9. Kahler, D.M.; Kabala, Z.J. Acceleration of groundwater remediation by deep sweeps and vortex ejections induced by rapidly pulsed pumping. *Water Resour. Res.* **2016**, *52*, 3930–3940. [CrossRef]
10. Teramoto, E.H.; Pede, M.A.Z.; Chang, H.K. Impact of water table fluctuations on the seasonal effectiveness of the pump-and-treat remediation in wet–dry tropical regions. *Environ. Earth Sci.* **2020**, *79*, 435. [CrossRef]
11. Sadeghfam, S.; Hassanzadeh, Y.; Khatibi, R.; Nadiri, A.A.; Moazamnia, M. Groundwater Remediation through Pump-Treat-Inject Technology Using Optimum Control by Artificial Intelligence (OCAI). *Water Resour. Manag.* **2019**, *33*, 1123–1145. [CrossRef]
12. Takem, G.E.; Kuitcha, D.; Ako, A.A.; Mafany, G.T.; Takounjou-Fouepe, A.; Ndjama, J.; Ntchancho, R.; Ateba, B.H.; Chandrasekharam, D.; Ayonghe, S.N. Acidification of shallow groundwater in the unconfined sandy aquifer of the city of Douala, Cameroon, Western Africa: Implications for groundwater quality and use. *Environ. Earth Sci.* **2015**, *74*, 6831–6846. [CrossRef]
13. Vahedian, A.; Aghdaei, S.A.; Mahini, S. Acid Sulphate Soil Interaction with Groundwater: A Remediation Case Study in East Trinity. *APCBEE Proc.* **2014**, *9*, 274–279. [CrossRef]
14. Caraballo, M.A.; Macias, F.; Nieto, J.M.; Ayora, C. Long term fluctuations of groundwater mine pollution in a sulfide mining district with dry Mediterranean climate: Implications for water resources management and remediation. *Sci. Total Environ.* **2016**, *539*, 427–435. [CrossRef]
15. Shin, D.; Kim, Y.; Moon, H.S. Fate and toxicity of spilled chemicals in groundwater and soil environment I: Strong acids. *Environ. Health Toxicol.* **2018**, *33*, e2018019. [CrossRef]
16. Ha, Q.K.; Choi, S.; Phan, N.L.; Kim, K.; Phan, C.N.; Nguyen, V.K.; Ko, K.S. Occurrence of metal-rich acidic groundwaters around the Mekong Delta (Vietnam): A phenomenon linked to well installation. *Sci. Total Environ.* **2019**, *654*, 1100–1109. [CrossRef]
17. Appleyard, S.; Wong, S.; Willis-Jones, B.; Angeloni, J.; Watkins, R. Groundwater acidification caused by urban development in Perth, Western Australia: Source, distribution, and implications for management. *Aust. J. Soil Res.* **2005**, *42*, 579–585. [CrossRef]
18. Paulson, A.J.; Balistrieri, L. Modeling Removal of Cd, Cu, Pb, and Zn in Acidic Groundwater during Neutralization by Ambient Surface Waters and Groundwaters. *Environ. Sci. Technol.* **1999**, *33*, 3850–3856. [CrossRef]
19. Indraratna, B.; Pathirage, P.U.; Banasiak, L.J. Remediation of acidic groundwater by way of permeable reactive barrier. *Environ. Geotech.* **2017**, *4*, 284–298. [CrossRef]
20. Shin, D.; Lee, Y.; Park, J.; Moon, H.S.; Hyun, S.P. Soil microbial community responses to acid exposure and neutralization treatment. *J. Environ. Manag.* **2017**, *204*, 383–393. [CrossRef]
21. Sung, P.H.; Doyun, S.; Hee, S.M.; Young-Soo, H.; Seonjin, H.; Yoonho, L.; Eunhee, L.; Hyun, J.; Yu, S.H. A Multidisciplinary Assessment of the Impact of Spilled Acids on Geoecosystems: An Overview. *Environ. Sci. Pollut. Res.* **2020**, *27*, 9803–9817.
22. Jeon, I.; Nam, K. Change in the site density and surface acidity of clay minerals by acid or alkali spills and its effect on pH buffering capacity. *Sci. Rep.* **2019**, *9*, 9878. [CrossRef] [PubMed]
23. Zhang, Y.; Dai, Y.; Wang, Y.; Huang, X.; Pei, Q. Groundwater chemistry, quality and potential health risk appraisal of nitrate enriched groundwater in the Nanchong area, southwestern China. *Sci. Total Environ.* **2021**, *784*, 147186. [CrossRef]
24. Olías, M.; Cánovas, C.R.; Basallote, M.D.; Macías, F.; Pérez-López, R.; González, R.M.; Millán-Becerro, R.; Nieto, J.M. Causes and impacts of a mine water spill from an acidic pit lake (Iberian Pyrite Belt). *Environ. Pollut.* **2019**, *250*, 127–136. [CrossRef]
25. Zhang, Y.; He, Z.; Tian, H.; Huang, X.; Zhang, Z.; Liu, Y.; Xiao, Y.; Li, R. Hydrochemistry appraisal, quality assessment and health risk evaluation of shallow groundwater in the Mianyang area of Sichuan Basin, southwestern China. *Environ. Earth Sci.* **2021**, *80*, 576. [CrossRef]
26. Gazea, B.; Adam, K.; Kontopoulos, A. A review of passive systems for the treatment of acid mine drainage. *Miner. Eng.* **1996**, *9*, 23–42. [CrossRef]
27. Jiankang, Z.; Yong, Z.; Jin, C. Application Research on Pressure Recharge in Underground-water Source Heat Pump System. *Explor. Eng. (Rock Soil Drill. Tunn.)* **2010**, *37*, 55–58.
28. Wu, J.Q.; Zhang, J.Z.; Li, X.H.; Shi, F.F.; Zhang, P.; Bai, M. Experiment on artificial pressure re-injection of geothermal water in Xi'an suburb. *J. Water Resour. Water Eng.* **2014**, *25*, 215–218.
29. Zhao, B.l.; Mu, Z.Y.; Wu, J.X. *Articifial Recharge of Groundwater (Translated Version)*; Water Conservancy Press: Beijing, China, 1980; pp. 32–33.
30. Du, X.Q.; Lu, Y.; Li, S.T.; Ye, X.Y.; Wang, Z.J. Mechanism, Prediction and Control of Suspended Matter Blocking in Artificial Recharge of Groundwater. In Proceedings of the 8th China Water Forum, Harbin City, China, 2–3 August 2010; p. 146.
31. Akhtar, M.S.; Nakashima, Y.; Nishigaki, M. Clogging mechanisms and preventive measures in artificial recharge systems. *J. Groundw. Sci. Eng.* **2021**, *9*, 21.
32. Pavelic, P.; Vanderzalm, J.; Dillon, P.; Herczeg, A.; Magareyd, P. *Assessment of the Potential for Well Clogging Associated with Salt Water Interception and Deep Injection at Chowilla, SA*; CSIRO: Canberra, Australia, 2007.
33. Dou, Z.; Zhang, X.; Zhuang, C.; Yang, Y.; Wang, J.; Zhou, Z. Saturation dependence of mass transfer for solute transport through residual unsaturated porous media. *Int. J. Heat Mass Transfer* **2022**, *188*, 122595. [CrossRef]

34. Dou, Z.; Tang, S.; Zhang, X.; Liu, R.; Zhuang, C.; Wang, J.; Zhou, Z. Influence of Shear Displacement on Fluid Flow and Solute Transport in a 3D Rough Fracture. *Lithoshere* **2021**, *2021*, 1569736. [CrossRef]
35. Guo, Q.; Zhou, Z.; Huang, G.; Zhi, D. Variations of Groundwater Quality in the Multi-Layered Aquifer System near the Luanhe River, China. *Sustainability* **2019**, *11*, 994. [CrossRef]
36. Mengying, L. *Investigation on Environmental Impact of Subway Construction in Jinan*; Shanghai Jiao Tong University: Shanghai, China, 2018.
37. Olsthoorn, T.N. The clogging of recharge wells, main subjects. In *KIWA-Communications*; KIWA: Rijswijk, The Netherlands, 1982.
38. Yan, Y.; Yang, R.; Wang, X.; Yan, F.G.; Zhang, D. Analysis on Influencing Factors of Groundwater Recharge in Hohhot Area. *West. Resour.* **2014**, *6*, 193–195.
39. Huang, X.D.; Shu, L.C.; Liu, P.G.; Wang, E. An experimental study on the problem of blockage during recharging of water injection wells. *J. Hydraul. Eng.* **2009**, *40*, 430–434.
40. Dandan, L.; Fei, L.; Deren, M. Optimization of Soil Heavy Metal Sequential Extraction Procedures. *Geoscience* **2015**, *29*, 7.
41. Fetter, C.W. *Contaminant Hydrogeology*; Waveland Press, Inc.: Long Grove, IL, USA, 2008; p. 500.
42. Zhao, H.; Zhang, J.; Chen, H.; Wang, L.; Yang, Z. Localization of Groundwater Contaminant Sources Using Artificially Enhanced Catchment. *Water* **2020**, *12*, 1949. [CrossRef]
43. Siyu, Y.; Zhiping, L.; Shuli, W.; Qiaoling, Y.; Lili, L. Multi-model comparative analysis of nitrobenzene penetration curve in the sandy strata. *Geotech. Investig. Surv.* **2020**, *48*, 40–46.
44. Bu, X.F.; Wan, W.F. Experimental Research on the Hydrodynamic Dispersion Characteristics of Loess Medium in Hilly Area of Western Henan Province. *China Rural Water Hydropower* **2021**, *12*, 27–31.

MDPI AG
Grosspeteranlage 5
4052 Basel
Switzerland
Tel.: +41 61 683 77 34

MDPI Books Editorial Office
E-mail: books@mdpi.com
www.mdpi.com/books

Disclaimer/Publisher's Note: The title and front matter of this reprint are at the discretion of the Topic Editors. The publisher is not responsible for their content or any associated concerns. The statements, opinions and data contained in all individual articles are solely those of the individual Editors and contributors and not of MDPI. MDPI disclaims responsibility for any injury to people or property resulting from any ideas, methods, instructions or products referred to in the content.

Academic Open
Access Publishing

mdpi.com

ISBN 978-3-7258-4636-8